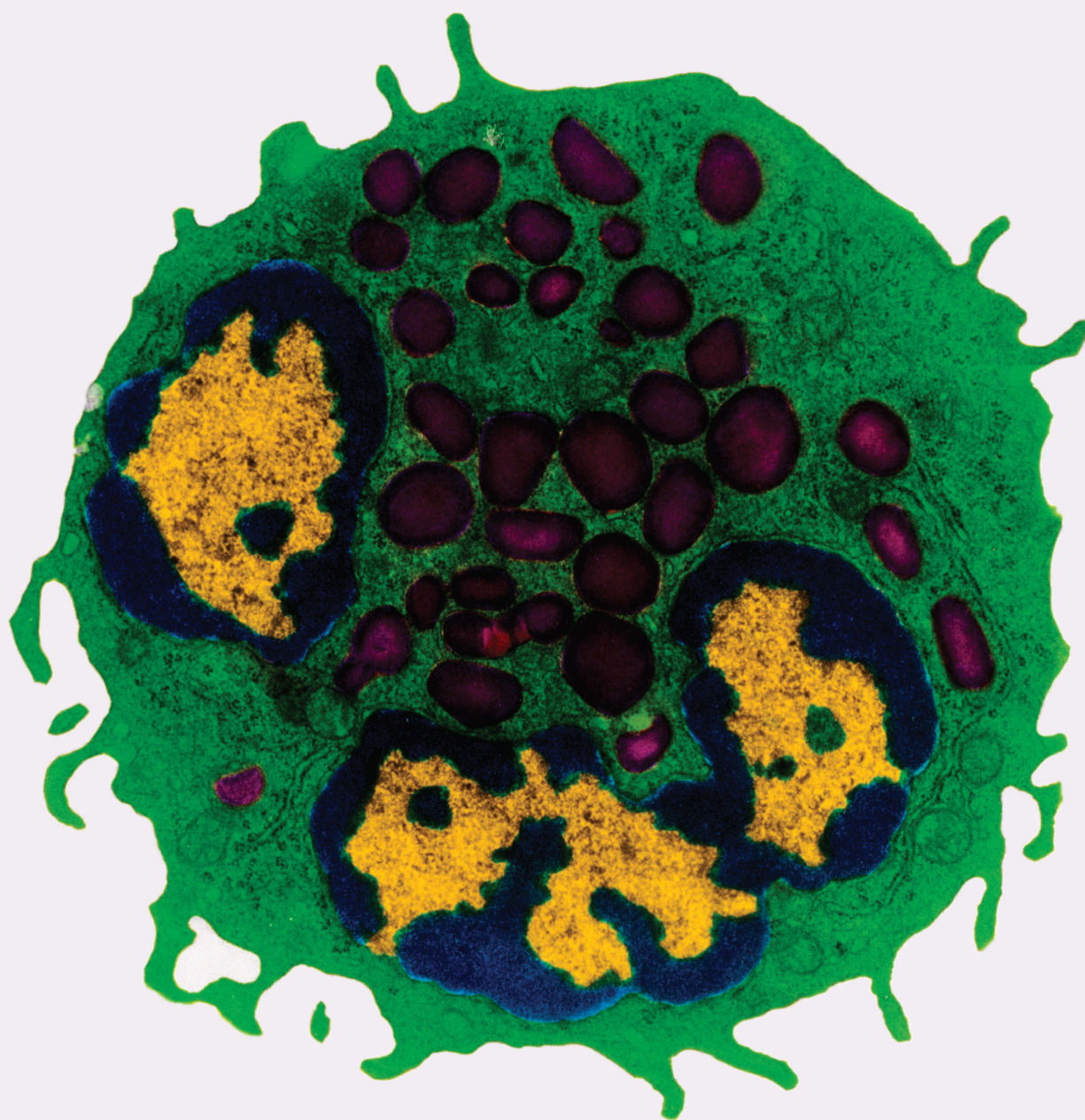# Dual Role of Inflammatory Mediators in Cancer

Lead Guest Editor: Jinhua Pan
Guest Editors: Jiang Pi and Bin Liu
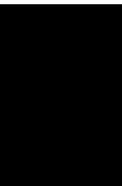
Dual Role of Inflammatory Mediators in Cancer

Dual Role of Inflammatory Mediators in Cancer

Lead Guest Editor: Jinhua Pan
Guest Editors: Jiang Pi and Bin Liu

Contents

Contents

Contents

Research Article

High-Fat Mouse Model to Explore the Relationship between Abnormal Lipid Metabolism and Enolase in Pancreatic Cancer

Lin Qin,[1,2,3,4,5] **Kai Sun,**[6] **Li Shi,**[1,4,5] **Yushan Xu** ![ORCID],[1,4,5] **and Rongping Zhang** ![ORCID][3]

[1]*Department of Endocrinology, The First Affiliated Hospital of Kunming Medical University, Kunming, Yunnan 650000, China*
[2]*School of Pharmaceutical Science, Kunming Medical University, Kunming, Yunnan 650500, China*
[3]*School of Chinese Materia Medica and Yunnan Key Laboratory of Southern Medicine Utilization, Yunnan University of Chinese Medicine, Kunming, Yunnan 650500, China*
[4]*Yunnan Province Clinical Research Center for Metabolic diseases, Kunming, Yunnan 650000, China*
[5]*Yunnan Clinical Medical Center for Endocrine and Metabolic Diseases, Kunming, Yunnan 650000, China*
[6]*Affiliated Hospital of Yunnan University, Qingnian Road, Kunming, Yunnan 650000, China*

Correspondence should be addressed to Yushan Xu; xuysh@ydyy.cn and Rongping Zhang; zhrpkm@ynutcm.edu.cn

Malignant tumors have become a major social health problem that seriously threatens human health, among which pancreatic cancer has a high degree of malignancy, difficult diagnosis and treatment, short survival time, and high mortality. More and more attention has been paid to abnormal lipid metabolism as a momentous carcinogenesis mechanism. Here, we explored the relationship between abnormal lipid metabolism, enolase, and pancreatic cancer by clinical data analysis. A high-fat mouse model was constructed, and then, a subcutaneous tumorigenesis mouse model of carcinoma of pancreatic cells and a metastatic neoplasm mouse pattern of pancreatic carcinoma cells injected through the tail vein were constructed to explore whether abnormal lipid metabolism affects the progression of pancreatic cancer in mice. We constructed a high-lipid model of pancreatic carcinoma cell lines and knockdown and overexpressed enolase in pancreatic carcinoma cell lines and investigated whether high lipid regulates epithelial-mesenchymal transition (EMT) by upregulating enolase (ENO), thereby promoting the cells of pancreatic carcinoma to invade and migrate. Triglycerides, total cholesterol, free cholesterin, high-density lipoprotein cholesterol (HDL-C), low-density lipoprotein cholesterol (LDL-C), and neuron-specific enolase (NSE) from pancreatic cancer patients and nonpancreatic cancer patients were tested. The differences in blood lipids between patients with and without pancreatic carcinoma were compared, and the correlation between blood lipids and neuron-specific enolase was analyzed. We confirmed that the serum triglyceride level of pancreatic cancer patients at initial diagnosis is overtopping nonpancreatic cancer patients, and the neuron-specific enolase level of patients with pancreatic carcinoma is better than nonpancreatic carcinoma sufferers. Triglyceride level is positively correlated with neuron-specific enolase level, and serum triglyceride level has predictive value for pancreatic cancer. Hyperlipidemia can promote tumor growth and increase the expression levels of ENO1, ENO2, and ENO3 in subcutaneous tumor formation of pancreatic cancer in mice. Additional hyperlipidemia promoted pancreatic carcinoma metastasis in the lung in mice injected through the tail vein, which confirmed that hyperlipidemia accelerated the process of EMT by increasing the expression of ENO1, ENO2, and ENO3, therefore promoting the pancreatic cancer cell metastasis.

1. Introduction

Malignancy has become a major public health issue that seriously threatens human health, among which pancreatic cancer has a high degree of malignancy, difficult diagnosis and treatment, short survival time, and high mortality [1]. Dys-lipidemia more and more is considered a significant mechanism of tumorigenesis. The basic test indexes of blood lipid included total cholesterol (TC), low-density lipoprotein cholesterol (LDL-C), high-density lipoprotein cholesterol (HDL-C), and triglyceride (TG) [2]. The metastatic ability of carcinoma cells is strongly linked to lipid metabolic

enzymes, In melanoma metastasis, mammary carcinoma, and prostate cancer, the metastatic ability of carcinoma cells is strongly linked to lipid metabolic enzymes [3]. HDL and LDL major cholesterol carriers function through receptor-mediated mechanisms in tumor cells. The effect of HDL cholesterol on cancer is related to its antioxidant and anti-inflammatory properties, and some prospective studies have shown that prediagnosis HDL cholesterol levels are significantly associated with the incidence of breast, prostate, colon, lung, and liver cancers. Serum triglyceride level is significantly increased in patients with colorectal cancer (CRC), and hypertriglyceridemia is positively correlated with the occurrence of colorectal adenoma [4]. Elevated triglyceride can be a colorectal adenoma risk factor for the potential occurrence and development. Enolase (ENO) is an ancient enzyme with a highly conserved structure, including ENO1, ENO2, and ENO3. The active ENO exists as a dimer and consists of two relatively parallel subunits [5]. ENO1 is widely distributed in various tissues, ENO2 is mainly found in neurons, and ENO3 is mainly found in muscle tissues [6]. As a key enzyme in the glycolytic pathway, ENO is related to the prognosis of many such as tumors and other diseases. ENO1 expression is significantly upregulated in all kinds of malignancies, ranging from glioma, nasal laryngeal carcinoma, mammary cancer, and pancreatic cancer to uterine cancer, etc. Studies have found that in pancreatic cancer, the expression of ENO1 is positively correlated with clinical stage and lymphatic metastasis and negatively correlated with survival time [7]. The median survival of patients with high ENO1 expression in pancreatic carcinoma is as short as 8 months, while the median survival time is more than 30 months with low ENO1 expression [8]. ENO1 and related antibodies can reference as underlying biomarkers in the diagnosis and prognosis of tumor. ENO2 is an important tumor marker for the diagnosis, prognosis, and follow-up of lung cancer [9]. The objective was to investigate what is the effect of ENO in abnormal lipid metabolism and how it impacts the progression of carcinoma of pancreas and its mechanism. A basis for individualized diagnosis and therapeutic of pancreatic cancer patients in the future.

The incidence of pancreatic cancer increased in recent years; obesity might be involved, The incidence of pancreatic cancer increased in recent years [10]. Pancreatitis and pancreatic cancer are both pancreatic diseases with common risk factors and pathological features, suggesting a strong correlation between them, which may also be the key to cancer transformation [11]. Acinar-to-ductal metaplasia is observed in chronic pancreatitis. ADM is considered to be a precursor of pancreatic cancer [12]. Oxidative stress and inflammatory response can promote the development of pancreatitis and act together with genetic factors, such as oncogenic KRAS mutation and tumor suppressor gene inactivation, thus initiating and accelerating pancreatic intraepithelial neoplasia [13]. PANIN ultimately leads to pancreatic cancer [14]. Studies have also found that hyperglycemia can increase the incidence rate and sprout of pancreatic cancer in varied ways, and elevated fasting blood glucose can significantly affect the incidence of pancreatic cancer, suggesting that hyperglycemia is closely related to pancreatic cancer

[15]. Hyperglycemia is associated with genomic instability by increasing the level of O-GlcNacylation after translation, leading to an imbalance in the nucleotide pool and ultimately to the induction of KRAS mutations, thus becoming an initiating event in pancreatic cancer [16].

Enolase (EC4.2.1.11) is a highly conservative glycosome that catalyzes 2-phospho-D-glyceric acid (2-PGA) to convert to phosphoenolpyruvate (PEP) during glycolysis [17]. Enolase isoenzymes function as homodimers ($\alpha\alpha$, $\beta\beta$, and $\gamma\gamma$) or heterodimers ($\alpha\beta$ or $\alpha\gamma$), catalyzing 2-phosphoglycerate in glycolysis to convert to phosphoenolpyruvate (PEP) [18]. The expression of enolase in mammals is tissue-specific, α-enolase (ENO1) is widely found in a variety of tissues, β-enolase (ENO3) is mainly expressed in muscle tissues, and γ-enO2 is very active in neuronal tissues, so it is also called neuron-specific enolase (NSE) [19]. γ-Enolase (ENO2) is the encoding gene located on human chromosome 12. It is composed of two enolase isoenzymes, $\gamma\gamma$ and $\alpha\gamma$ [20]. It is an acid dimer protein with 433 amino acids. By the way, γ-enolase also is major in lung cancer diagnosis and prognosis and likely plays a part in predicting chemotherapy response and recurrence in acute leukemia [21]. γ-Enolase phosphorylates GSK-3β to enhance the activity of Akt and induce cell proliferation, resulting in the increased expression of multiple glycolytic-related genes in acute leukemia cells. Elevated γ-enolase expression is also associated with neuroblastoma, cervical cancer, melanoma, renal cell carcinoma, and other diseases [22]. ENO2 serves as a potential target for these tumors [23]. A positive correlation was found by Chang et al. between serum triglyceride extent and the NSE level of ischemic stroke patients [24]. However, there are few studies on the effect of abnormal lipid metabolism on ENO and its further effect on pancreatic carcinoma, which is worthy of further investigation.

2. Materials and Methods

2.1. Preparation of Animals. This research was supported by the Kunming University of Medical Sciences (Approval number: kmmu2021426).

As laboratory animals, 6-8-week-old male C57 and Panc-02 mice weight 20 g-30 g ($n = 12$, each group), and Panc-02 mouse pancreatic cancer cells were provided by Olubiol (Kunming, Yunnan, China). The mice were housed in an animal facility and handled in accordance with the Guide for the Care and Use of Laboratory Animals of Kunming Medical University Hospital. All mice were housed under ambient conditions (standard humidity and temperature) with a 12 h light/dark cycle. The 7-week-old mice were used for experimentation after an adaptation period of 1 week. All mice were specifically pathogen-free and were maintained under the same environmental conditions without differences in food intake.

2.2. The Research Object. All 208 pancreatic carcinoma patients admitted to the First Affiliated Hospital of Kunming Medical University from January 2016 to June 2022 were enrolled as the study group, including 117 males and 91 females. The inclusion criteria of the pancreatic cancer group were as follows: malignant cells of pancreatic cancer

were detected by pancreatic cancer surgery or biopsy, which met the diagnostic criteria of pancreatic cancer. Exclusion criteria for the pancreatic cancer group were as follows: age < 18 years and without a pathological diagnosis of pancreatic cancer. The control group included 1350 randomly selected people who underwent physical examination in our hospital during the same period. The exclusion criteria of the control group included those who were younger than 18 years old, had pancreatic occupation on ultrasound, or had a history of pancreatic cancer. There were 662 males and 688 females in the control group. There was no statistical significance in the sex ratio between the two groups ($P > 0.05$).

2.3. The Indicators. The indicators used in this study include gender, age, aspartate aminotransferase (AST) levels (IU/L), alanine aminotransferase (ALT) levels (IU/L), serum creatinine (Cre) levels (μmol/L), serum uric acid (UA) levels (μmol /L), fasting venous glucose levels (mmol/L), total cholesterol (TC) levels (mmol/L), free cholesterol (F-CHOL) levels (mmol/L), triglyceride (TG) levels (mmol/L), high-density lipoprotein cholesterol (HDL-C)(mmol/L), low-density lipoprotein cholesterol (LDL-C) (mmol/L), and neuron-specific enolase (NSE) (ng/mL). All indicators were collected from the Clinical Data Management Center of the First Affiliated Hospital of Kunming Medical University.

2.4. Detection Method. Roche Cobas 8000 automatic biochemical analyzer was used to measure blood biochemical-related indexes (fasting blood in the morning): total protein (biuret method), blood glucose (hexokinase method), total cholesterol (cholesterol oxidase method), triglyceride (GPO-PAP method), and low-density lipoprotein cholesterol (surfactant clearance method). Tumor markers were detected by the Cobas 6000 instrument. Within two hours, the professional inspectors of the Central Laboratory of the First Affiliated Hospital of Kunming Medical University shall complete the inspection with original reagents according to the standard procedures of the instrument usage instructions and strictly control the quality. An abdominal ultrasound examination was completed in the Imaging Department of the First Affiliated Hospital of Kunming Medical University.

2.5. Immunohistochemistry Was Used to Detect Clinical Specimens. The surgical sections of patients with clinical pancreatic cancer were collected for immunohistochemical staining. The specific steps were as follows: (a) baking sheet: put the tissue sheet into a 64°C incubator and bake for 1 h; (b) dewaxing: put the glass slide into xylene I (10 min) and xylene II (10 min); (c) hydration: 100% alcohol I and II (5 min), 100% alcohol (5 min), 95% alcohol (5 min), 80% alcohol (3 min), and 70% alcohol (2 min); rinse with PBS 3 times, 5 min each time; (d) antigen repair: pour citrate buffer into the pressure cooker and boil it, then put the slide in, cover the pot tightly, start the timer when a large number of bubbles emerge from the exhaust valve, boil for 3 minutes, turn off the heat, open the cover after exhaust, and cool to room temperature; rinse with PBS 3 times, 5 min each time;

(e) blocking: incubation with 3% H_2O_2 water for 20 min at room temperature to inactivate endogenous peroxidase activity; rinse with PBS 3 times, 5 min each time; (f) block: 5% bovine serum albumin V was incubated at 37°C for 30 min; (g) incubation of primary antibody: according to the antibody instructions, the appropriate dilution ratio was selected to dilute the primary antibody with 2% bovine serum albumin V, and the diluted primary antibody was added to the glass slide by drop and placed in the refrigerator at 4°C overnight. In the next day, the primary antibody was placed in the temperature box at 37°C for rewarming for 30 min and then washed with PBS three times, 5 min each time; (h) incubation of secondary antibody: goat anti-rabbit secondary antibody (diluted in PBS, 1 : 500) was added to the tissue block and incubated at 37°C for 30 min and then washed with PBS 3 times, 5 min each time; (i) DAB color development: DAB staining droplets were added to the tissue blocks for staining, and the slides were placed under a microscope to observe the staining. After obvious staining, the staining solution was washed with PBS, and the staining solution was washed with PBS 3 times, 5 min each time; (j) hematoxylin counterstaining: the slide was stained in hematoxylin for 5 min, washed with distilled water, put into alcohol hydrochloric acid solution for differentiation, differentiation for 10-15 s, and put into tap water to return blue for at least 15 min; (k) dehydration: 70% alcohol (2 min), 80% alcohol (3 min), 95% alcohol (5 min), 100% alcohol I (5 min), and 100% alcohol II (5 min); (l) transparent: xylene I (10 min) and xylene II (10 min); (m) seal: seal the film with neutral gum; (n) analysis: for microscopic observation, 5 visual fields were selected to take films and the positive rate was calculated.

2.6. Mouse Pancreatic Cancer Cell Panc-02 Cell Culture

2.6.1. Cell Recovery. According to the records, the frozen cells were removed from liquid nitrogen and quickly shaken in a 37°C water bath. After they were dissolved, the cells were quickly brought to the ultraclean workbench. The cells were transferred to a 15 mL centrifuge tube containing 10 mL complete medium, mixed, and centrifuged at 1000 rpm for 5 min at room temperature. The supernatant was poured out and DMEM complete medium was added. After blowing and mixing, the cell suspension was transferred into T-25 culture flask and cultured in an incubator with 5% CO_2 at 37°C.

2.6.2. Cell Passage. When the cell density reached 80%, carefully absorb and discard the culture medium in the cell culture dish with a pipette gun on the ultraclean workbench, slowly add 3 mL sterile PBS from the edge of the dish with a pipette gun, absorb and discard PBS with a pipette gun, and wash twice. When most of the cells became round and separated from each other, an appropriate amount of complete medium containing fetal bovine serum was added to terminate the digestion. The single cell suspension was made by gently blowing and was centrifuged at 1000 rpm for 5 min, the medium was discarded, and the cells were resuspended by adding a complete medium containing fetal

bovine serum. Then, it was divided into culture bottles for further culture and subcultured according to 1 : 3.

2.6.3. Cell Cryopreservation.

When the cell density reached 80%, the culture medium in the cell culture dish was carefully sucked and discarded with the pipette gun on the ultraclean workbench, 3 mL sterile PBS was slowly added from the edge of the dish with the pipette gun, the PBS was sucked and discarded with the pipette gun, and the washing was repeated twice. When most of the cells became round and separated from each other, an appropriate amount of DMEM complete medium containing fetal bovine serum was added to terminate the digestion, and the single cell suspension was made by gently blowing and centrifuged at 1000 rpm for 5 min, and the medium was discarded. The cells were resuspended by adding 1 mL of frozen storage solution and transferred to the frozen storage tube and placed in the frozen storage box at -80°C overnight and then transferred to liquid nitrogen for storage.

2.7. Blood Samples Were Taken from Mice to Detect Blood Lipids.

There are 24 C57 mice (male) aged 6-8 weeks, of which 12 mice were fed with high fat and 12 mice were fed with normal. After 6 weeks, blood samples were collected from the eye socket of mice and placed in heparin anticoagulant tubes for 2 hours. After that, the samples were separated at 3000 rpm/heart for 15 min at 2-8°C. The thawed samples were centrifuged again and then tested for triglyceride, total cholesterol, HDL cholesterol, and LDL cholesterol levels.

2.8. Tumor Formation by Subcutaneous Injection.

Six mice were randomly selected from 12 mice with hyperlipidemia after 6 weeks of high-fat feeding, 6 mice were randomly selected from 12 mice with normal blood lipids, 6 mice were also randomly selected from 12 mice with normal blood lipids, and 6 mice were also randomly selected from 12 mice with normal blood lipids at 8 weeks. 100μ of PANC-02 mouse pancreatic cancer cells (7×10^6 cells) was subcutaneously injected into C57 mice. We checked whether the cell name corresponds to the group of animals one by one; check whether the cell name corresponds to the group of animals one by one. The air in the syringe should be discharged after the syringe inhales the cells. Pinch the skin at the injection site with your hand, stab the needle into the subcutaneous area and groin observedly, draw back if no blood, and then, advance the cells; hold for 7-10 s, pull out the needle, and locally compress it with a cotton ball or swab for a while. The long and short diameters of the implanted subcutaneous tumors were measured with vernier calipers every 2 days from 3 days after subcutaneous tumor modeling, and the tumor volume was calculated according to the formula $V = A \times B^2 \times 0.5$ (V represents the tumor volume, A is the long diameter, and B is the short diameter). On the 12th day after subcutaneous tumorization, the animals were sacrificed by cervical dislocation, and the tumor pieces were slowly removed with ophthalmic scissors and ophthalmic tweezers and then weighed on an electronic balance. The tumor mass was measured by analytical balance and recorded.

2.9. Tumor Formation by Tail Vein Injection.

Twelve mice were given a high-fat diet (high-fat group), while the other twelve mice were given a normal diet (control group). Blood lipids were measured after six weeks, and at the 8th week, six mice from each group were randomly selected for tail vein injection with pancreatic cancer cells. $100 \mu L$ of PANC-02 mouse pancreatic cancer cells (5×10^6 PANC -02 cells) was injected into C57 mice through tail vein. Pancreatic cancer cells (PANC-02 cells) may metastasize to the spleen, lung, pancreas, and brain, causing tissue lesions. Body weight was monitored every 3-4 d after 3 days of surgery. An electronic scale was used to record the weight changes of mice. The steps are as follows: step 1: place the electronic scale on a hard and flat surface; step 2: press the "on/off" button, and the scale will be cleared within 3 seconds; and step 3: please place the item to be weighed in the container, and the weight will be displayed on the electronic screen. After the body weight of C57 mice decreased abruptly, metastatic foci may be formed. On the 42nd day after the tail vein injection of pancreatic cancer cells into the model, C57 mice were anesthetized by intraperitoneal injection of 1.5 vol% isoflurane (1 L/min) through a 1 mL syringe according to their body weight. After that, the abdomen was disinfected and the skin was prepared. Lung tissue was removed from mice.

2.10. QPCR Detection.

Total RNA extraction: cells were mixed with $700 \mu L$ of RNA extract, thoroughly blown and mixed, and then stood for 10 min; $140 \mu L$ of chloroform was added and thoroughly mixed. Centrifugation at 12000 g for 15 min at 4°C showed that the liquid was divided into three layers, and RNA was retained in the colorless upper aqueous phase. Gently draw the upper aqueous phase into a new EP tube and record the volume of the supernatant. Then, the same volume of 100% isopropanol was added and centrifuged at room temperature for 10 min at 12000 g for 10 min at 4°C. It was observed that more white RNA precipitates were generated at the bottom of the tube. Carefully tilt the tube mouth to discard the supernatant, blot the tube mouth with absorbent paper, add $500 \mu L$ 75% ethanol to the precipitation (the amount of ethanol added is half of the supernatant), centrifuge at 7500 g for 5 minutes at 4°C, and make the precipitation adhere to the bottom of the tube. Discard the supernatant, invert the centrifuge tube onto absorbent paper, and blot the remaining liquid with a pipette gun. Blow in a ventilated kitchen for 5 minutes to remove as much residual liquid as possible. Add $60 \mu L$ of RNase water to the dried RNA precipitate and leave for 15 minutes to dissolve the RNA completely. Freeze in the refrigerator at -80°C. Reverse transcription: SureScript First-Strand cDNA Synthesis Kit (Xavir, Guangzhou, China) was used. After brief centrifugation, the reaction was carried out in CFX96 real-time quantitative PCR instrument according to the following conditions: predenaturation at 95°C for 1 min, denaturation at 95°C for 20 s, annealing at 55°C for 20 s, and extension at 72°C for 30 s, 40 cycles; and the final extension was made at 72°C for 5 min 4°C. Fluorescence was collected and recorded, amplification curve and dissolution curve were made, and Ct values were read. The primer sequence

is as follows: GAPDH F: CCTTCCGTGTTCCTACCCC; GAPDH R: GCCCAAGATGCCCTTCAGT; E-cadherin F: GGGACAAAGAAACAAAGGT; E-cadherin R: GACACG GCATGAGAATAGA; N-cadherin F: CCCCCAAGTCC AACATTTC; N-cadherin R: CCGCCGTTTCATCCAT ACC; vimentin F: GCAGCCTCTATTCCTCATC; vimentin R: TGCAGTTCTACCTTCTCGT; a-SMA F: TGCCGA GCGTGAGATTGT; a-SMA R: CTTCATGGTGCTGGGT GC; ENO1 F: GGCAACCCTGAAGTCATCCT; ENO1 R: AATCCACCCTCATCACCCAC; ENO2 F: GGATGGGAC TGAGAATAAA; ENO2 R: AGCAATGTGGCGATAG AGG; ENO3 F: GGGGGATGAGGGTGGCTTT; and ENO3 R: GGGGTTGGTTACCGTGAGG. Analysis of experimental results: the dissolution curve was smooth with only one large single peak, and the primer specificity was good. The data were available. The Ct values were read, and the relative gene expression was calculated using the $2^{-\triangle\triangle Ct}$ method. Specifically, the first step was calculated as $\triangle Ct = Ct$ (target gene) − Ct (reference gene). $\triangle\triangle CT = \triangle CT$ (experimental group) − $\triangle CT$ (control group); finally, the $2^{-\triangle\triangle CT}$ value was calculated as the relative expression level of mRNA.

2.11. Western Blotting Detection

2.11.1. Tissue/Cell Protein Extraction. Preparation of RIPA lysate: 1 mL RIPA lysate with 10 μL of 100x protease inhibitors (if phosphorylated antibodies need to be checked to add the corresponding phosphatase inhibitors) on ice for use. Discard the medium, wash the cells with precooled PBS for 3 times, add the corresponding amount of cell lysate, lysate on ice for 10 min, scrape the cells with cells, and transfer to EP tube. Weigh 50-100 mg of tissue and add 500-1000 μL RIPA lysate to the tissue homogenizer and homogenize on ice. Centrifuge the above lysed sample at 16000 g for 15 min at 4°C, take the supernatant, and divide it into 80 μL each.

2.11.2. Determination of Protein Concentration and Denaturation. Determination of protein concentration with BCA protein quantification kit: add 0, 0.25, 0.05, 0.1, 0.2, 0.3, 0.4, and 0.5 mg/mL of the standard volume of 20 μL, after 50 times of sample dilution, add 20 μL of the diluted sample to make 3 rewells, and add 200 μL of BCA working solution (BCA reagent A and B 50 : 1 preparation). The absorbance value was measured at 562 nm after 30 minutes at 37°C. Protein denaturation reserve: take 80 μL protein sample for quantification 3.8-6 μg/μL (concentration < 3.8 μg/μL ≥ 0.5 μg/μL quantitative denaturation according to the lowest), mix with appropriate 5× protein loading buffer and boil in boiling water bath for 10 min, cool to room temperature, and store at -80°C.

2.11.3. SDS-PAGE Electrophoresis. Separation glue: distilled water, 30% acrylamide, 1 M Tris-HCl (pH 8.8), 10% SDS, 10% ammonium persulfate, and TEMED preparation according to the different target protein preparation of different concentrations of glue. Concentrated glue: concentrated glue (5 mL) 3.4 mL of distilled water, 30% acrylamide 0.83 mL, 1 Tris-HCl (pH 6.8) 0.63 mL, 10% SDS 0.05 mL, 10% ammonium persulfate 0.05 mL, and TEMED preparation 0.01 mL. After the glue is prepared, add distilled water liquid seal, discard the distilled water after 30 min, and blot the water with paper. The concentrated glue can be used 10 min after it is prepared. SDS-PAGE electrophoresis: 10 μL sample loading and 80 V stable pressure electrophoresis for about 30 min; when the protein sample is to the separation glue concentrated glue interface, change to 120 V stable pressure electrophoresis; when bromophenol blue run to the bottom, about 90 minutes, take out the gel.

2.11.4. Membrane Transfer. The PVDF membrane should be soaked in methanol for 5 minutes and then balanced in the membrane transfer buffer for 15 minutes. The membrane was transferred to the electroconverter at 4°C and 300 mA for 1 h. Block: remove PVDF membrane and rinse with TBST once, cut the excess membrane on the edge, and block in 5% BSA at 37°C for 30 min (or overnight at 4°C).

2.12. Statistical Analysis.
SPSS20.0 software was used for data processing. The normal distribution of measurement data was expressed as mean ± standard deviation (X ± S), and t-test was used for comparison between the two groups. The receiver operating characteristic curve (ROC curve) was used to evaluate the prognostic value. $P < 0.05$ was considered statistically significant.

3. Results

3.1. Expression and Correlation Analysis of Triglyceride and NSE in Pancreatic Cancer Patients. The comparison of clinical data between pancreatic cancer patients and the control group showed that TG and NSE of pancreatic cancer patients were higher than the control group, and there was a significant positive correlation between triglyceride and neuron-specific enolase (NSE) ($P = 0.0004$) (Figures 1(a)–1(c)). ROC curve evaluation showed that triglyceride had a certain predictive value in pancreatic cancer (AUC = 0.7678 > 0.7). AUC > 0.7 is considered to have predictive value; AUC < 0.7 has no predictive value (Figure 1(d)). By analyzing the clinical indicators of pancreatic cancer patients and the control group and exploring the relationship between abnormal lipid metabolism, enolase, and pancreatic cancer, we drew the following conclusions: the triglyceride level of pancreatic cancer patients at initial diagnosis was higher than that of the control group. The level of NSE in pancreatic cancer patients was higher than the control group (Figure 1(e)). Triglyceride level was positively correlated with NSE. Human growth hormone (HGH), ferritin (FER), and pepsinogen 1 were correlated with triglyceride (pepsinogen 1), total bile acid (TBA), gamma-glutamyl transpeptidase (GGT), cholinesterase (PChE), urea nitrogen (BUN), blood uric acid UA, high-density lipoprotein cholesterol (HDL-C), low-density lipoprotein cholesterol (LDL-C); CEA, CA125, CA153, CA199, CK-19, ferritin (FER), prostate specific antigen (PSA), aspartate aminotransferase (AST), total bilirubin (TB), indirect bilirubin (IDBIL), and alkaline phosphatase (ALP) were correlated with NSE (Figure 1(f)).

(a)   (b)   (c)   (d)

(e)

(f)
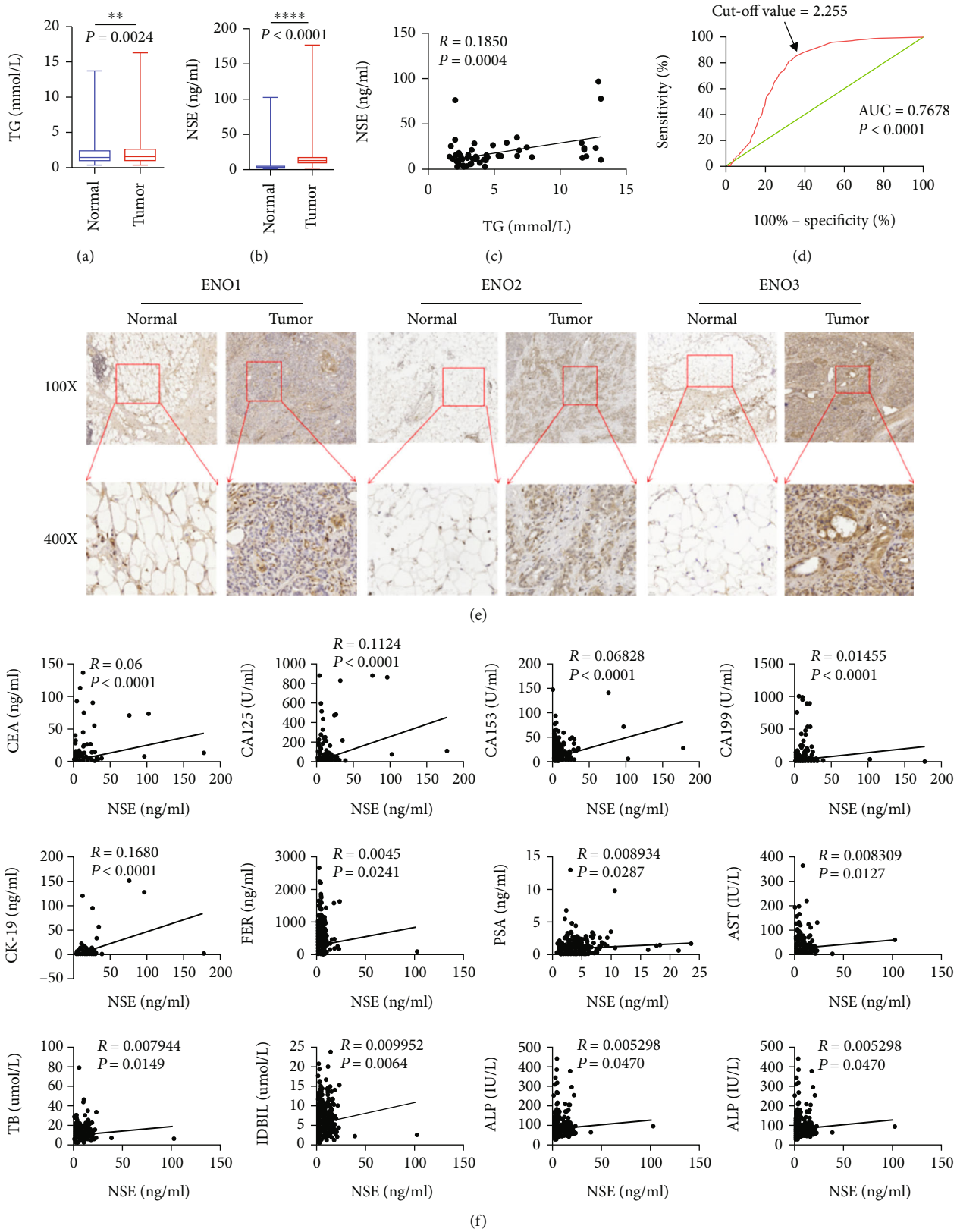
FIGURE 1: Clinical data analysis of pancreatic cancer patients and control group. (a–c) Expression and correlation analysis of triglyceride and NSE in pancreatic cancer patients. (d) ROC curve was used to evaluate the predictive value of triglyceride in pancreatic cancer. (e) Immunohistochemistry was used to detect the expression of ENO1, ENO2, and ENO3 in clinical tissues. (f) Analysis of neuron-specific enolase (NSE) and tumor-related indicators.
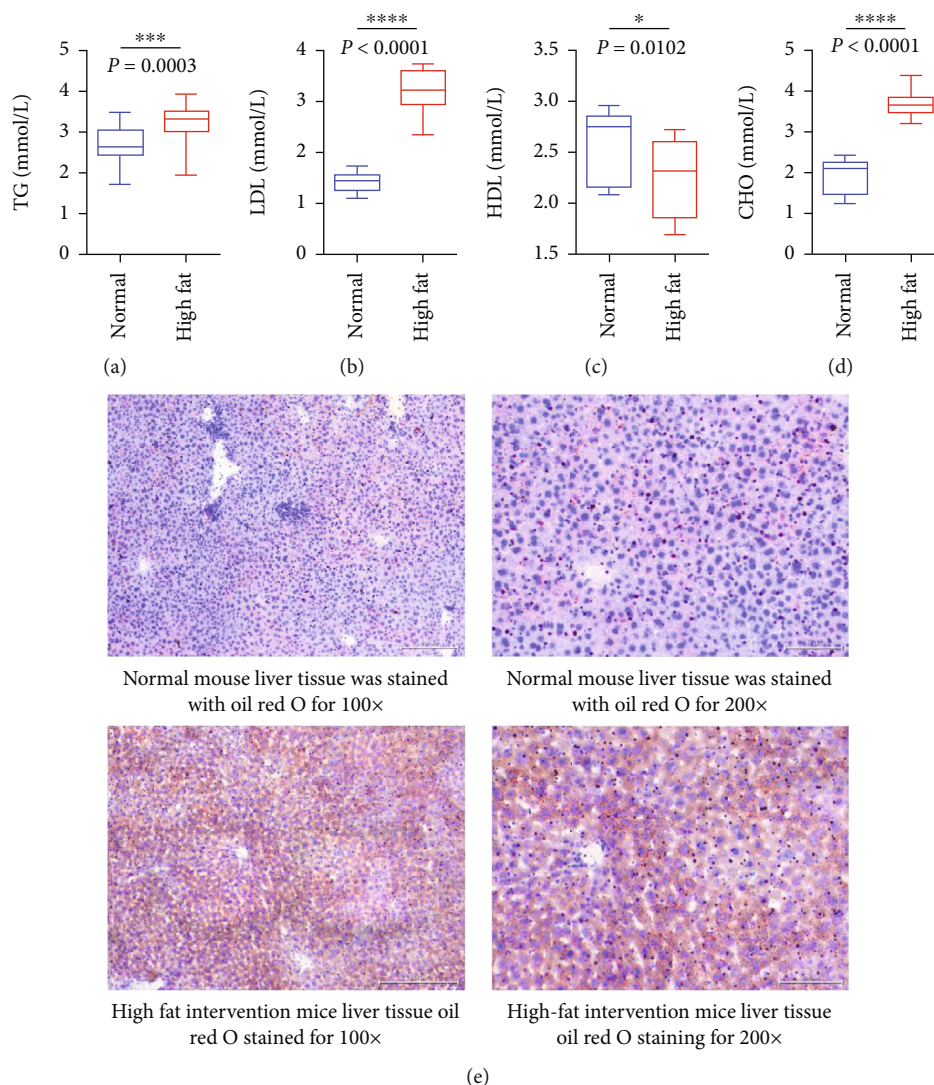
FIGURE 2: Establishment and identification of mouse hyperlipidemia model. (a) The expression of triglyceride TG in the four blood lipids of mice. (b) The expression of low-density lipoprotein cholesterol and LDL in the four blood lipids of mice. (c) The expression of high-density lipoprotein cholesterol HDL in the four blood lipids of mice. (d) The expression of total cholesterol CHO in the four items of blood lipid detected by total cholesterol CHO in mice. (e) The results of oil Red O staining in liver tissue of mice. The results showed that the fat content in the liver tissue of mice in the high-fat feeding group was significantly higher than that in the ordinary feeding group.

3.2. Identification of Mouse Hyperlipidemia Model. C57 mice in the high-fat group were fed with a high-fat diet, while C57 mice in the normal group were fed with an ordinary diet. After 6 weeks, four blood lipids were detected by a biochemical analyzer. The results of oil Red O staining in liver tissue showed that the hyperlipidemia mouse model was successfully established. Four blood lipids (triglyceride (TG), low-density lipoprotein cholesterol (LDL), high-density lipoprotein cholesterol (HDL), and total cholesterol (CHO)) in mice were detected (Figures 2(a)–2(d)). Compared with the mice in the high-fat feeding group, triglyceride (TG) increased, low-density lipoprotein cholesterol (LDL) increased, high-density lipoprotein cholesterol (HDL) decreased, and total cholesterol (CHO) increased, all with statistical significance. The results of oil Red O staining of mouse liver tissue showed that the fat content of liver tissue in the high-fat

feeding group was significantly higher than that in the ordinary feeding group (Figure 2(e)).

3.3. The Construction of Pancreatic Cancer Subcutaneous Tumor Animal Model. Mice in the high-fat group and control group were injected with PANC-02 cells subcutaneously to establish the animal model of pancreatic cancer tumorigenesis (Figure 3(a)). The curve of tumor volume change in mice showed a gradual upward trend; the volume of the control group increased after decreasing (Figure 3(b)). The curve of weight change of mice after subcutaneous tumor formation showed that the weight of the high-fat group showed a trend of first increasing and then decreasing (Figure 3(c)), while the weight of the control group gradually decreased. The tumor growth curve (Figure 3(d)) showed that compared with the control group, the tumors in the
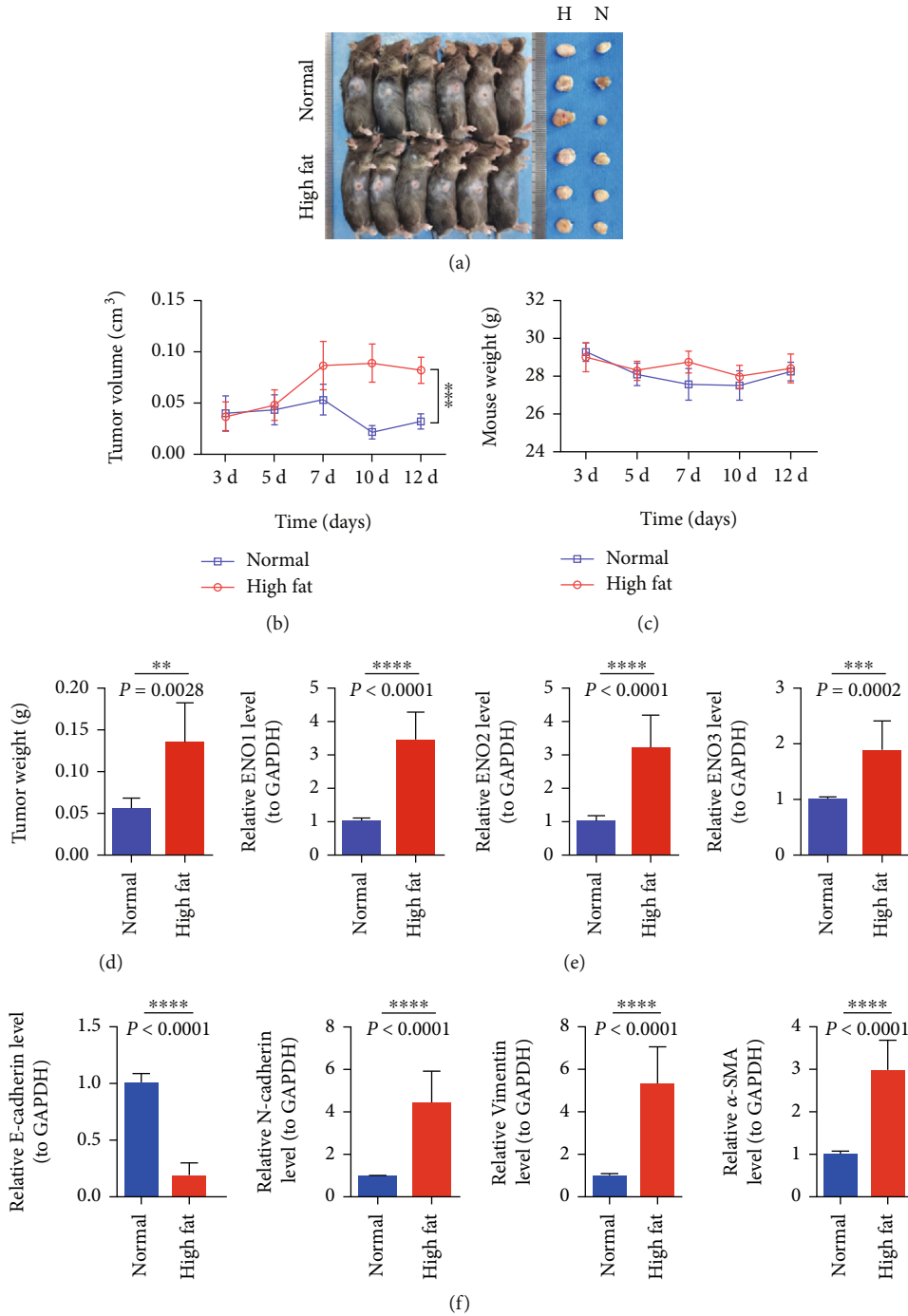
FIGURE 3: To construct a subcutaneous tumor animal model of pancreatic cancer. (a) Individual and tumor differences in mice; the tumors in the high-fat group were relatively larger. (b) Differences in tumor volume in mice. (c) Body weight growth curves of mice inoculated with tumor. (d) Tumor weight statistics after in vitro. (e) ENO1/ENO2/ENO3 indexes related to tumor enolase in mouse subcutaneous tumorigenesis test. (f) Expression of EMT-related genes E-cadherin/N-cadherin/vimentin/α-SMA. *** represents $P < 0.001$, and **** represents $P < 0.0001$.

high-fat group grew relatively faster, and the difference between the two groups was statistically significant.

3.4. Expression of Enolase-Related Indexes and EMT-Related Genes in Mouse Subcutaneous Tumorigenesis. QPCR test declares that enolase-related indicators ENO1/ENO2/ENO3 in the high-fat group were significantly higher than

those in the control group (Figure 3(e)). The expression of EMT-related genes N-cadherin, vimentin, and α-SMA in the high-fat group was significantly higher than that in the control group, and the expression of E-cadherin in the high-fat group was significantly lower than that in the control group (Figure 3(f)). These results suggested that the enolase ENO1/ENO2/ENO3 of subcutaneous tumor
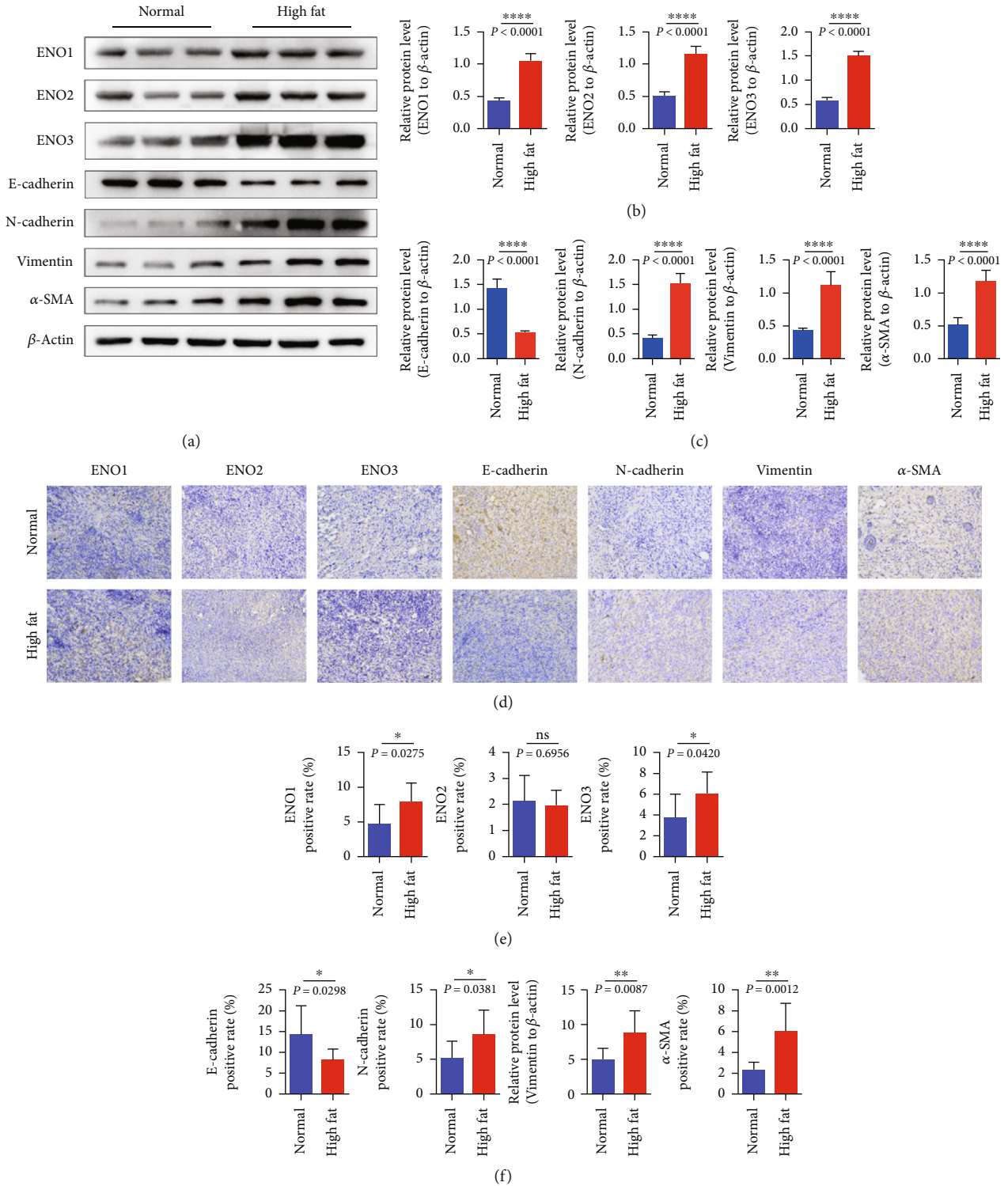
FIGURE 4: Indexes related to tumor enolase in subcutaneous tumorigenesis of mice. (a–c) The expression of ENO1/ENO2/ENO3 and EMT-related genes E-cadherin/N-cadherin/vimentin/α-SMA detected by western blotting in each group of mouse subcutaneous tumor-forming experiment. (d) The expressions of ENO1/ENO2/ENO3 and EMT-related genes E-cadherin/N-cadherin/vimentin/α-SMA were detected by immunohistochemistry. Ns represents no statistical significance, * represents $P < 0.05$, and ** represents $P < 0.01$.

(a)

(b)

(c)

(d)

(e)

(f)

(g)

Figure 5: Continued.

(h)
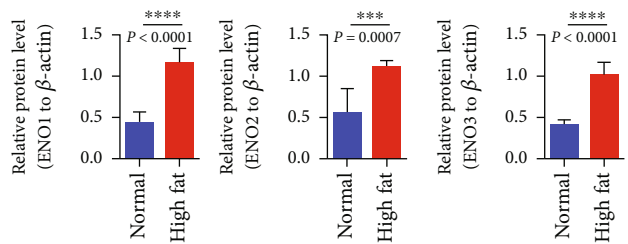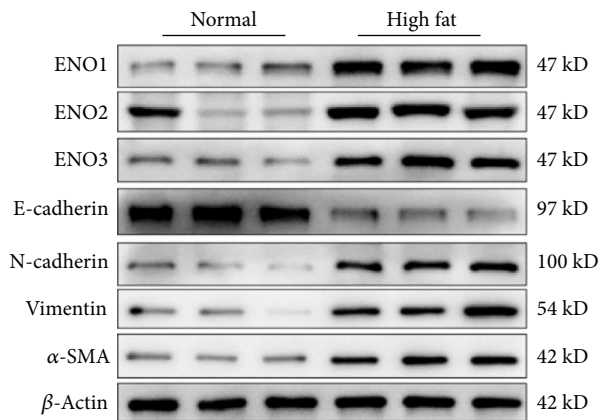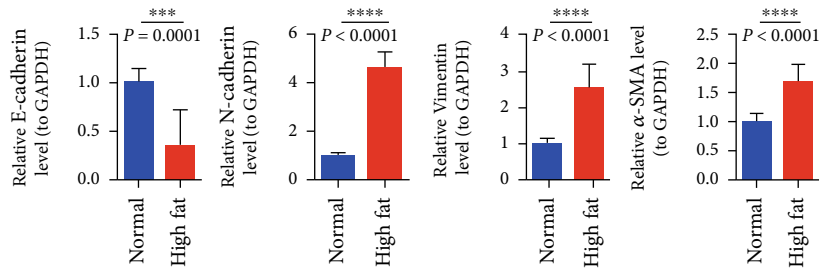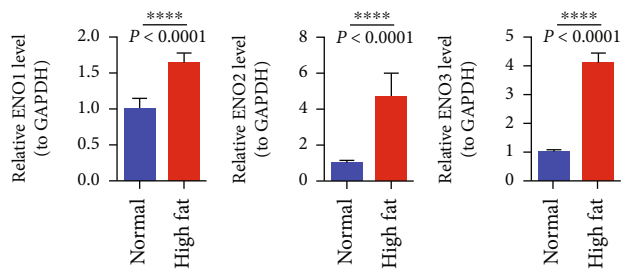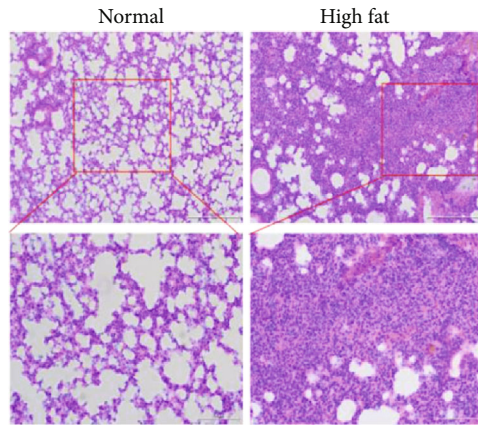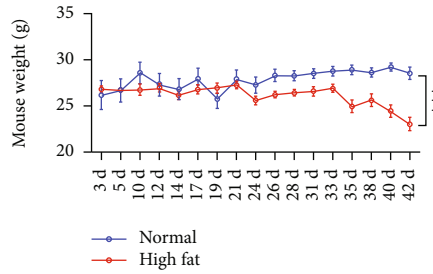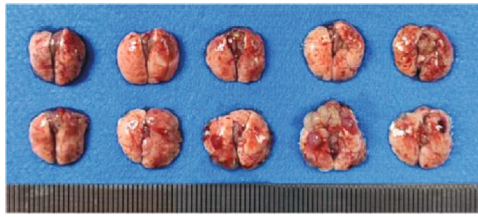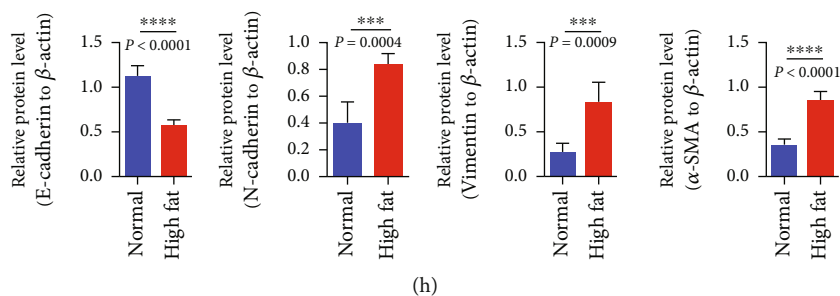
FIGURE 5: (a) The pulmonary metastatic nodule picture of the lungs. (b) The body weight monitoring map. (c) The HE staining in each group of the tail vein injection. (d, e) QPCR was used to detect the expression of enolase-related indicators ENO1/ENO2/ENO3 and EMT-related genes E-cadherin/N-cadherin/vimentin/α-SMA in the lungs of each group after tail vein injection. (f–h) Western blotting was used to detect the expression of enolase-related indicators ENO1/ENO2/ENO3 and EMT-related genes E-cadherin/N-cadherin/ vimentin/α-SMA in the lungs of mice injected through tail vein. *** represents $P < 0.001$ and **** represents $P < 0.0001$.

in the high-fat group increased and promoted the process of EMT (Figure 4).

3.5. The Animal Model of Pancreatic Cancer Tail Vein Tumor. Pancreatic cancer cells were injected into the tail vein of high-fat mice and control mice. It was confirmed that hyperlipidemias accelerated the process of EMT and promoted the metastasis of pancreatic cancer cells by stimulating enolase-related indicators ENO1/ENO2/ENO3. The hyperlipidemia model was established in C57 mice. PANC-02 pancreatic cancer cells were injected into the tail vein of both the high-fat group and control group, and the experiment was terminated 42 days later. Lung metastatic nodules of pancreatic cancer cells were observed in mice. The lung was removed and the metastatic nodules of lung tissue were detected. The lung physiology figure showed that the number and volume of metastatic nodules in the high-fat group were larger than those in the control group (Figure 5(a)).

The curve of weight change (Figure 5(b)) showed that the weight of the high-fat group increased first and then decreased, while the weight of the control group gradually increased, and the weight of the high-fat group was significantly lower than that of the control group after 21 days, and the difference was obvious. HE staining showed that the control group had normal lung tissue structure, intact alveoli, no edema, inflammatory cell infiltration, and no tumor cell metastasis. In the high-fat group, the alveolar structure of lung tissue was incomplete, and a large number of tumor cells could be seen metastasis. These results suggest that hyperlipidemia may enhance the ability of pancreatic cancer cells to metastasize to the lung (Figure 5(c)). We detect the expression of enolase-related indicators ENO1/ENO2/ENO3 and EMT markers in lung tumor tissues, and further explore the effect of hyperlipidemia on enolase activation and metastasis in pancreatic cancer cells at the molecular level. QRT-PCR results showed (Figure 5(d)) that enolase-related indicators ENO1/ENO2/ENO3 in the high-fat group were significantly higher than those in the control group. The expression of EMT-related genes N-cadherin, vimentin, and α-SMA in the high-fat group was significantly higher than that in the control group, and the expression of E-cadherin in the high-fat group was significantly lower than that in the control group. These results suggested that hyper-

lipidemia increased enolase expression and accelerated the process of EMT. Western blotting results showed (Figure 5(f)) that enolase-related indicators ENO1/ENO2/ ENO3 in the high-fat group were significantly higher than those in the control group. The expression of EMT-related genes N-cadherin, vimentin, and α-SMA in the high-fat group was significantly higher than that in the control group, and the expression of E-cadherin in the high-fat group was significantly lower than that in the control group (Figures 5(g) and 5(h)). The results were consistent with those of qPCR. These results suggest that hyperlipidemia increases enolase and promotes EMT.

3.6. Upregulation of Enolase Can Accelerate the Process of EMT and Aggravate the Malignant Behavior of Pancreatic Cancer Cells. Human pancreatic cancer cell PANC-1 high-fat cell model was established by oleic acid. It was confirmed that high-fat upregulated enolase accelerated the process of EMT and aggravated the malignant behavior of pancreatic cancer cells at the cellular level. To establish a high-fat cell model, PANC-1 cells were stimulated with oleic acid at concentrations of 10 nM, 50 nM, 80 nM, 100 nM, and 150 nM, respectively. After oil Red O staining, the number of oil Red O stained cells in the microscopic field increased with the increase of oleic acid concentration (Figure 6(a)). The results showed that the number of adipogenic cells increased with the increase of oleic acid concentration, and the percentage of adipogenic cells was higher when the concentration was 100 nM.

In order to explore the effect of high fat and hyperlipidemiaon on the migration and invasion of pancreatic cancer cells, a high-fat cell model was established, and the migration and invasion levels of cells were detected by transwell chamber assay. The results showed that the migration and invasion levels of cells in the high-fat group were enhanced compared with those in the control group (Figures 6(b) and 6(c)). These results indicated that high fat could promote the migration and invasion of pancreatic cancer cells. We detect the expression of enolase-related indicators ENO1/ENO2/ENO3 and EMT markers in high-fat cells and control cells, and further explore the effect of high fat on enolase level and migration ability of pancreatic cancer cells at the molecular level. Western blotting results showed

(a)

(b)

(c)

(d)

(e)
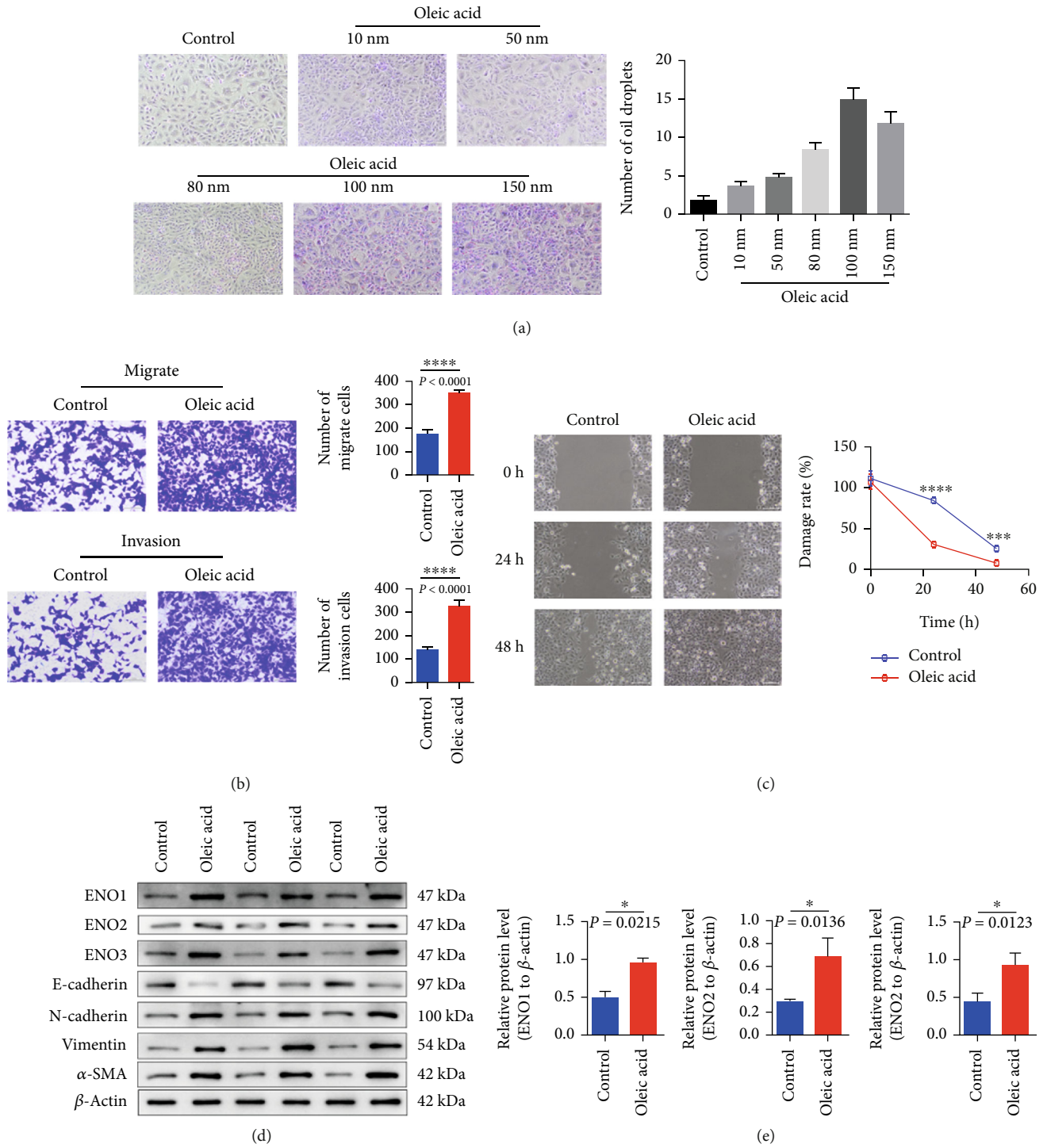
Figure 6: Continued.

(f)

(g)

(h)
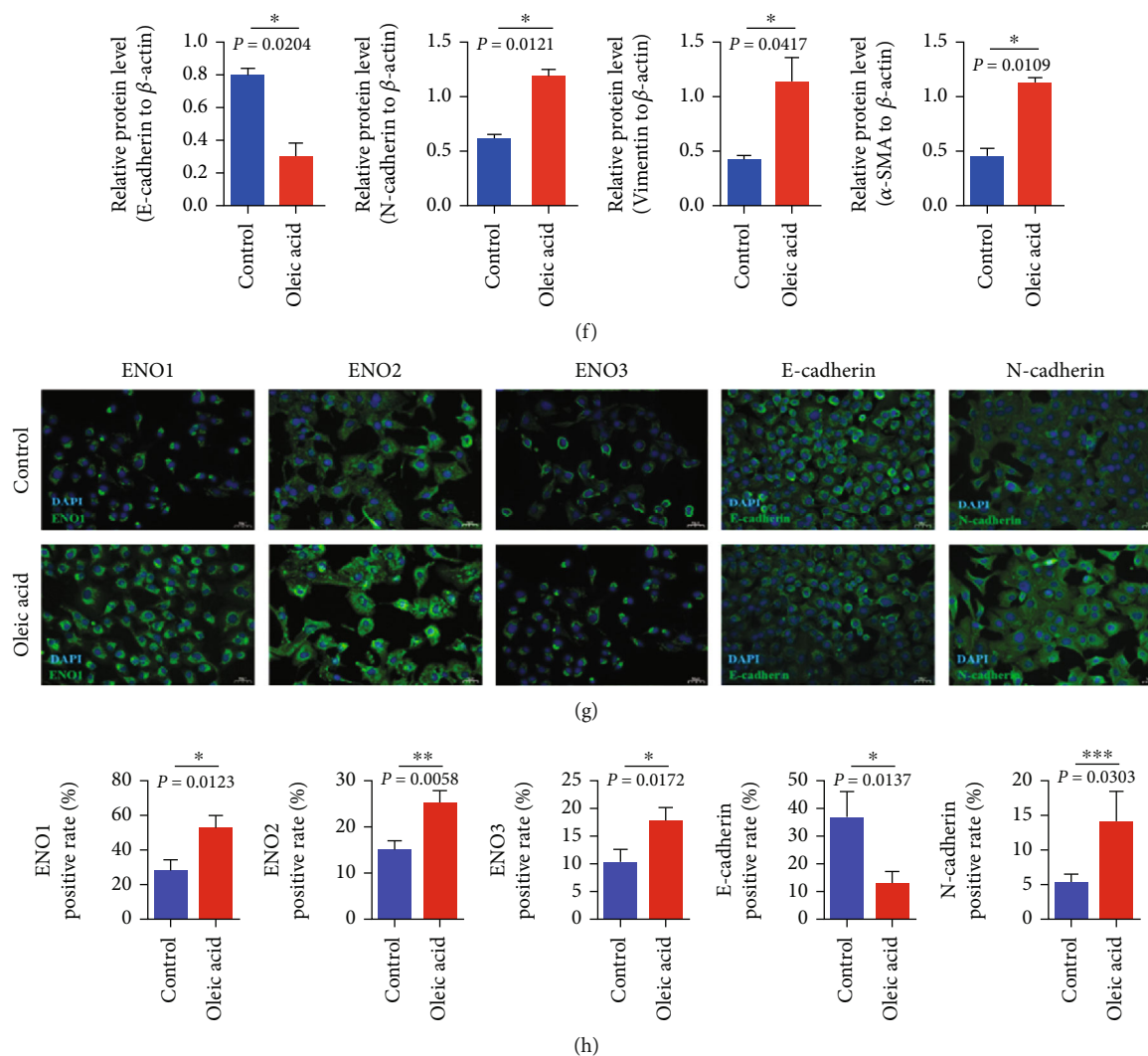
Figure 6: The cellular level confirmed that high-lipid upregulated enolase, accelerated the process of EMT, and aggravated the malignant behavior of pancreatic cancer cells. (a) PANC-1 cells were treated with different concentrations of oleic acid, and lipid formation was examined by oil Red O staining. (b, c) PANC-1 cells were stimulated with 100 nM oleic acid to detect cell migration and invasion. (d–f) WB was used to detect the expression of enolase-related indicators ENO1/ENO2/ENO3 and EMT-related indicators E-cadherin/N-cadherin/vimentin/α-SMA. (g, h) The expression of enolase-related indicators ENO1/ENO2/ENO3 was detected by immunofluorescence. Expression of EMT-related genes E-cadherin/N-cadherin.

that the enolase-related indicators ENO1/ENO2/ENO3 and the expression of EMT-related indexes N-cadherin, vimentin, and α-SMA of PANC-1 cells in the oleic acid intervention group were significantly higher than those in the control group (Figures 6(d)–6(f)). These results suggest that high fat promotes the expression of enolase and accelerates the process of EMT in pancreatic cancer cells.

In order to further clarify the effect of high fat on enolase-related indicators ENO1/ENO2/ENO3 and EMT markers of pancreatic cancer cells, immunofluorescence detection was performed. The results showed (Figures 6(g) and 6(h)) that the enolase-related indicators ENO1/ENO2/ENO3 of PANC-1 cells treated with oleic acid were significantly increased compared with the control group. The expression of EMT-related index N-cadherin in PANC-1 cells treated with oleic acid was higher than that in the control

group, and the expression of E-cadherin in PANC-1 cells treated with oleic acid was lower than that in the control group. These results further suggested that, at the protein level, high fat increased enolase expression in pancreatic cancer cells accelerated EMT progression.

4. Discussion

The incidence of adenocarcinoma varies widely across regions, with lifestyle and environmental factors playing a significant role. Smoking is the most commonly known risk factor, and diabetes, high fat, chronic pancreatitis, and genetic mutations all contribute to an increased risk of pancreatic cancer [25]. ENO2 (also known as γ-enolase, neuron-specific enolase, and NSE) can catalyze the conversion of 2-phosphoglycerate to phosphoenolpyruvate in glycolysis [26].

It has two isoenzymes and is a very important enzyme in glycolysis. ENO2 is mainly found in neuronal cells and neuroendocrine cells [27]. Abnormal expression of ENO2 is associated with a variety of neurological injuries, which can be used as a marker to evaluate neuronal death in different CNS injuries [28]. ENO2 is highly expressed in tumor patients, especially in neurogenic and neuroendocrine tumors, and is considered to be the most important tumor marker of poorly differentiated neuroendocrine tumors. In addition, exposure to ENO2 in carcinogenic pollutants cadmium and arsenic can also be used as a marker [29]. Remodeling of actin cytoskeleton leads to cell migration. It has been found that ENO2 can bind actin and tubulin, thereby affecting microtubule motility and cell migration [30]. ENO2 depends on gamma-1-syntrophin to colocalize actin. γ-Enolase controls neuronal survival, differentiation, and neurite regeneration through the activation of PI3K/Akt and MAPK/ERK signaling pathways, thereby regulating cytoskeletal reorganization and cell remodeling [31]. RhoA inhibits axon elongation, while ENO2 inactivates RhoA through PI3K [32]. By analyzing the clinical-related indexes of pancreatic cancer patients and the control group, this study found that the triglyceride level of pancreatic cancer patients was higher than that of the control group at the initial diagnosis [33]. The level of neuron-specific enolase (NSE) in pancreatic cancer patients was higher than that in the control group [3]. Triglyceride level was positively correlated with NSE. It is suggested that triglyceride is a warning indicator of pancreatic cancer [34]. Blood lipid analysis combined with ENO2 analysis is helpful to evaluate the condition of pancreatic cancer patients.

Triglycerides, an important component of blood lipids, were found to be more likely to develop lung cancer in people with hypertriglyceridemia in an Austrian study [35]. Other studies have confirmed that the lipid content of some dendritic cells (DC) is increased, especially the triglyceride content [36]. There should be a high level of lipids, especially triglycerides, in tumor cells, which further stimulates and promotes the expression of ENO1 [37]. A long-term high-fat diet is an important contributor to obesity, which increases the risk of pancreatic cancer. In this study, it was found that the tumor volume of mice in the high-fat group increased faster in the subcutaneous tumorigenesis test, and the lung metastasis of mice in the high-fat group was more frequent in the tail vein injection [38]. Triglyceride storage in vitro, lipid droplet formation, and lipid accumulation in vivo of mouse pancreatic cancer cells can positively regulate tumor growth [39]. HE staining was used to observe the lesion morphology. PCR, WB, and immunohistochemistry were used to detect ENO1, ENO2, ENO3, and EMT indicators (E-cadherin, N-cadherin, and vimentin). It was found that enolase increased significantly in the high-fat group, and EMT indicators also showed a positive effect. These results indicated that high fat could increase enolase, promote EMT, and accelerate the development of pancreatic cancer in mice. Triglycerides exist in peripheral blood in pancreatic cancer cells in large quantities, which leads to the increase of triglyceride level in the circulating blood of patients [40]. The high concentration of triglyceride in the

pancreas and peripancreas can hydrolyze pancreatic enzymes and produce a large amount of free fatty acids locally to induce acidosis, which can activate trypsinogen, thus triggering a series of activation of trypsinogen and then leading to severe self-digestion of the pancreas. High levels of triglyceride can damage vascular endothelium and increase blood viscosity. In severe pancreatitis, a large number of plasma components seep out and blood is concentrated under the action of various inflammatory factors. In this study, oleic acid was used to construct a high-fat pancreatic cancer cell model (PANC-1 cell line) to detect the biological behavior of pancreatic cancer cells after an intervention. It was found that the expressions of ENO1, ENO2, and ENO3 of PANC-1 cells were increased under high-fat conditions, and the migration and invasion ability of cancer cells was enhanced. Immunofluorescence detection of pancreatic cancer cells in the high-fat group and the control group showed that the trend of EMT-related indicators was consistent with that of the animal model, suggesting that high fat promoted the process of EMT. The trend is consistent; in in vivo and in vitro experimental results, it is concluded that high cholesterol and obesity caused by high-fat diet, which degrades the pancreas, induces inflammation, promotes the enolization enzyme expression, increases the risk of pancreatic cancer, and accelerates the progress of pancreatic cancer; low-fat diet helps pancreatic cancer prevention but also for the future further research provides the basis for pancreatic cancer.

5. Conclusion

In in vivo experiments, mouse models of subcutaneous tumorigenesis and metastasis of pancreatic cancer cells injected into the tail vein were constructed. In in vitro cell experiments, PANC-1 cells were intervened with oleic acid to construct a high-fat cell model. Enolase-related indicators ENO1/ENO2/ENO3 and EMT-related indicators were detected. The hyperlipidemia mouse model was established, and the hyperlipidemia animal model was successfully established by lipid four items and oil Red O staining. Subcutaneous tumorigenesis of pancreatic cancer cells in the hyperlipidemia group and control group showed that hyperlipidemia promoted tumor growth. Enolase-related indicators ENO1/ENO2/ENO3 and EMT-related indicators E-cadherin/N-cadherin/vimentin/α-SMA were detected by qPCR, western blotting, and immunohistochemistry. It was found that hyperlipidemia could increase the expression of enolase-related indicators ENO1/ENO2/ENO3 in subcutaneous tumorigenesis tissues and accelerate the process of EMT. The results of tail vein injection of pancreatic cancer cells in the hyperlipidemia group and control group showed that hyperlipidemia increased the expression of enolase-related indicators ENO1/ENO2/ENO3 in metastatic tumor tissues, accelerated the process of EMT, and promoted the metastasis of pancreatic cancer cells. PANC-1 cells were treated with oleic acid to establish a high-lipid cell model. With the increase of oleic acid concentration, cell adipogenesis was enhanced. After oleic acid intervention in PANC-1 cells to establish a high-lipid cell model, it was confirmed

at the cell level that high lipid enhanced the migration and invasion ability of pancreatic cancer cells by increasing the expression of enolase-related indicators ENO1/ENO2/ENO3.

Abbreviations

ADM: Acinar-to-ductal metaplasia
CCK8: Cell Counting Kit-8
DAB: Diaminobenzidine
ECL: Electrochemiluminescence
EMT: Epithelial-mesenchymal transition
ENO: Alpha-enolase
FAK: Focal adhesion kinase
GAL-3: Galactase-3
HDL-C: High-density lipoprotein
HE: Hematoxylin-eosin
HTG: Hypertriglyceridemia
HTGP: HTG-induced pancreatitis
IS: Ischemic stroke
LDL-C: Low-density lipoprotein
NSE: Neuron-specific enolase
OD: Optical density
PANIN: Pancreatic intraepithelial neoplasia
PDAC: Pancreatic adenocarcinoma
PI: Propidium iodide
PTL: Pancreatic triglyceride lipase
ROC: Receiver operating characteristic
ROCK: Rho-associated kinase
SCR: Serum creatinine.

Data Availability

All data generated or analyzed during this study are included in this article.

Conflicts of Interest

The authors have no conflicts of interest regarding the material in this article.

Authors' Contributions

Lin Qin, Kai Sun, and Li Shi have contributed equally to this work.

Acknowledgments

References

[1] S. Hashmi, Y. Wang, D. S. Suman et al., "Human cancer: is it linked to dysfunctional lipid metabolism?," *Biochimica et Biophysica Acta (BBA)-General Subjects*, vol. 1850, no. 2, pp. 352–364, 2015.

[2] R. Sánchez-Martínez, S. Cruz-Gil, M. G. de Cedrón et al., "A link between lipid metabolism and epithelial-mesenchymal transition provides a target for colon cancer therapy," *Oncotarget*, vol. 6, no. 36, pp. 38719–38736, 2015.

[3] P. M. Cruz, H. Mo, W. J. McConathy, N. Sabnis, and A. G. Lacko, "The role of cholesterol metabolism and cholesterol transport in carcinogenesis: a review of scientific findings, relevant to future cancer therapeutics," *Frontiers in Pharmacology*, vol. 4, p. 119, 2013.

[4] S. J. Chang, M. F. Hou, S. M. Tsai et al., "The association between lipid profiles and breast cancer among Taiwanese women," *Clinical Chemical Laboratory Medicine*, vol. 45, no. 9, pp. 1219–1223, 2007.

[5] T. J. Kim, J. E. Kim, Y. H. Choi et al., "Obesity-related parameters and colorectal adenoma development," *Journal of Gastroenterology*, vol. 52, no. 12, pp. 1221–1229, 2017.

[6] L. Avilán, M. Gualdrón-López, W. Quiñones et al., "Enolase: A Key Player in the Metabolism and a Probable Virulence Factor of Trypanosomatid Parasites—Perspectives for Its Use as a Therapeutic Target," *Enzyme Research*, vol. 2011, Article ID 932549, 14 pages, 2011.

[7] J. C. López López, N. Fernández Alonso, J. Cuevas Álvarez, T. García-Caballero, and J. C. Pastor Jimeno, "Immunohistochemical assay for neuron-specific enolase, synaptophysin, and RB-associated protein as a diagnostic aid in advanced retinoblastomas," *Clinical Ophthalmology*, vol. 12, pp. 1171–1179, 2018.

[8] L. Wang, R. Bi, H. Yin, H. Liu, and L. Li, "ENO1 silencing impaires hypoxia-induced gemcitabine chemoresistance associated with redox modulation in pancreatic cancer cells," *American Journal of Translational Research*, vol. 11, no. 7, pp. 4470–4480, 2019.

[9] P. Cancemi, M. Buttacavoli, E. Roz, and S. Feo, "Expression of alpha-enolase (ENO1), Myc promoter-binding protein-1 (MBP-1) and matrix metalloproteinases (MMP-2 and MMP-9) reflect the nature and aggressiveness of breast tumors," *International Journal of Molecular Sciences*, vol. 20, no. 16, p. 3952, 2019.

[10] O. J. P. De La, L. L. Emerson, J. L. Goodman et al., "Notch and Kras reprogram pancreatic acinar cells to ductal intraepithelial neoplasia," *Proceedings of the National Academy of Sciences of the United States of America*, vol. 105, no. 48, pp. 18907–18912, 2008.

[11] W. Liu, B. Chakraborty, R. Safi, D. Kazmin, C. Y. Chang, and D. P. McDonnell, "Dysregulated cholesterol homeostasis results in resistance to ferroptosis increasing tumorigenicity

and metastasis in cancer," *Nature Communications*, vol. 12, no. 1, p. 5103, 2021.

[12] C. Hu, S. Tien, P. Hsieh et al., "High glucose triggers nucleotide imbalance through O-GlcNAcylation of key enzymes and induces KRAS mutation in pancreatic cells," *Cell Metabolism*, vol. 29, no. 6, pp. 1334–1349.e10, 2019.

[13] M. A. Isgro, P. Bottoni, and R. Scatena, "Neuron-specific enolase as a biomarker: biochemical and clinical aspects," *Advances in Experimental Medicine and Biology*, vol. 867, pp. 125–143, 2015.

[14] M. Piast, I. Kustrzeba-Wójcicka, M. Matusiewicz, and T. Banaś, "Molecular evolution of enolase," *Acta Biochimica Polonica*, vol. 52, no. 2, pp. 507–513, 2005.

[15] S. Raimondi, P. Maisonneuve, and A. B. Lowenfels, "Epidemiology of pancreatic cancer: an overview," *Nature reviews Gastroenterology & Hepatology*, vol. 6, no. 12, pp. 699–708, 2009.

[16] M. A. Soh, S. H. Garrett, S. Somji et al., "Arsenic, cadmium and neuron specific enolase (ENO2, *γ*-enolase) expression in breast cancer," *Cancer Cell International*, vol. 11, no. 1, p. 41, 2011.

[17] A. Hafner, N. Obermajer, and J. Kos, "*γ*-Enolase C-terminal peptide promotes cell survival and neurite outgrowth by activation of the PI3K/Akt and MAPK/ERK signalling pathways," *The Biochemical Journal*, vol. 443, no. 2, pp. 439–450, 2012.

[18] H. Ulmer, W. Borena, K. Rapp et al., "Serum triglyceride concentrations and cancer risk in a large cohort study in Austria," *British Journal of Cancer*, vol. 101, no. 7, pp. 1202–1206, 2009.

[19] R. Arai, S. Soda, T. Okutomi et al., "Lipid accumulation in peripheral blood dendritic cells and anticancer immunity in patients with lung cancer," *Journal of Immunology Research*, vol. 2018, Article ID 5708239, 8 pages, 2018.

[20] J. Incio, H. Liu, P. Suboj et al., "Obesity-induced inflammation and desmoplasia promote pancreatic cancer progression and resistance to chemotherapy," *Cancer Discovery*, vol. 6, no. 8, pp. 852–869, 2016.

[21] S. T. Tsai, I. H. Chien, W. H. Shen et al., "*ENO1*, a potential prognostic head and neck cancer marker, promotes transformation partly via chemokine *CCL20* induction," *European Journal of Cancer*, vol. 46, no. 9, pp. 1712–1723, 2010.

[22] H. Yin, L. Wang, and H. Liu, "ENO1 overexpression in pancreatic cancer patients and its clinical and diagnostic significance," *Gastroenterology Research and Practice*, vol. 2018, Article ID 3842198, 7 pages, 2018.

[23] P. Zhan, S. Zhao, H. Yan et al., "*α*-Enolase promotes tumorigenesis and metastasis via regulating AMPK/mTOR pathway in colorectal cancer," *Molecular Carcinogenesis*, vol. 56, no. 5, pp. 1427–1437, 2017.

[24] G. Chang, K. Liu, C. Hsieh et al., "Identification of alpha-enolase as an autoantigen in lung cancer: its overexpression is associated with clinical outcomes," *Clinical cancer research : an official journal of the American Association for Cancer Research*, vol. 12, no. 19, pp. 5746–5754, 2006.

[25] S. H. Jiang, F. Y. Dong, L. T. Da et al., "Ikarugamycin inhibits pancreatic cancer cell glycolysis by targeting hexokinase 2," *The FASEB Journal*, vol. 34, no. 3, pp. 3943–3955, 2020.

[26] M. S. Yeo, V. V. Subhash, K. Suda et al., "FBXW5 promotes tumorigenesis and metastasis in gastric cancer via activation of the FAK-Src signaling pathway," *Cancers*, vol. 11, no. 6, p. 836, 2019.

[27] C. Huang, Y. Sun, L. Lv, and Y. Ping, "ENO1 and cancer," *Molecular Therapy Oncolytics*, vol. 24, pp. 288–298, 2022.

[28] J. Chen, S. Chiu, K. Chen, Y. Huang, Y. Liao, and C. Yu, "Enolase 1 differentially contributes to cell transformation in lung cancer but not in esophageal cancer," *Oncology Letters*, vol. 19, no. 4, pp. 3189–3196, 2020.

[29] B. Liu, S. Lu, Y. Hu, X. Liao, M. Ouyang, and Y. Wang, "RhoA and membrane fluidity mediates the spatially polarized Src/FAK activation in response to shear stress," *Scientific Reports*, vol. 4, no. 1, p. 7008, 2014.

[30] B. Deng, R. Liu, X. Tian, Z. Han, and J. Chen, "Simulated microgravity inhibits the viability and migration of glioma via FAK/RhoA/Rock and FAK/Nek2 signaling," *In Vitro Cellular & Developmental Biology Animal*, vol. 55, no. 4, pp. 260–271, 2019.

[31] Y. Zhang, J. Yan, H. Xu et al., "Extremely low frequency electromagnetic fields promote mesenchymal stem cell migration by increasing intracellular Ca2+ and activating the FAK/Rho GTPases signaling pathways in vitro," *Stem Cell Research & Therapy*, vol. 9, no. 1, p. 143, 2018.

[32] A. M. M. González and J. Bosch, "*γ*-Enolase C-terminal peptide promotes cell survival and neurite outgrowth by activation of the PI3K/Akt and MAPK/ERK signalling pathways," *Biochemical Journal*, vol. 443, no. 2, pp. 439–450, 2012.

[33] T. Zeng, Y. Cao, T. Gu et al., "Alpha-enolase protects hepatocyte against heat stress through focal adhesion kinase-mediated phosphatidylinositol 3-kinase/Akt pathway," *Frontiers in Genetics*, vol. 12, p. 693780, 2021.

[34] K. Jiang, C. Dong, Z. Yin et al., "Exosome-derived ENO1 regulates integrin *α*6*β*4 expression and promotes hepatocellular carcinoma growth and metastasis," *Cell Death & Disease*, vol. 11, no. 11, p. 972, 2020.

[35] L. Sun, T. Lu, K. Tian et al., "Alpha-enolase promotes gastric cancer cell proliferation and metastasis via regulating AKT signaling pathway," *European Journal of Pharmacology*, vol. 845, pp. 8–15, 2019.

[36] R. Gumus, O. Capik, B. Gundogdu et al., "Low vitamin D and high cholesterol facilitate oral carcinogenesis in 4NQO-induced rat models via regulating glycolysis," *Oral Diseases*, vol. 29, no. 3, pp. 978–989, 2023.

[37] T. Lofterød, E. S. Mortensen, H. Nalwoga et al., "Impact of prediagnostic triglycerides and HDL-cholesterol on breast cancer recurrence and survival by breast cancer subtypes," *BMC Cancer*, vol. 18, no. 1, p. 654, 2018.

[38] S. Honeder, T. Tomin, L. Nebel et al., "Adipose triglyceride lipase loss promotes a metabolic switch in A549 non-small cell lung cancer cell spheroids," *Molecular & Cellular Proteomics : MCP*, vol. 20, p. 100095, 2021.

[39] X. X. Wang, G. Q. Yin, Z. H. Zhang et al., "TWIST1 transcriptionally regulates glycolytic genes to promote the Warburg metabolism in pancreatic cancer," *Experimental Cell Research*, vol. 386, no. 1, p. 111713, 2020.

[40] G. Generoso, C. C. P. S. Janovsky, and M. S. Bittencourt, "Triglycerides and triglyceride-rich lipoproteins in the development and progression of atherosclerosis," *Current Opinion in Endocrinology, Diabetes, and Obesity*, vol. 26, no. 2, pp. 109–116, 2019.

Research Article

LINC01088/miR-22/CDC6 Axis Regulates Prostate Cancer Progression by Activating the PI3K/AKT Pathway

Jianwei Li,[1] Xinghua Huang,[1] Haodong Chen,[1] Caifu Gu,[2] Binyu Ni,[3] and Jianhua Zhou [1]

[1]*Department of Urology, Longgang District People's Hospital of Shenzhen, Guangdong 518000, China*
[2]*Department of Thyroid and Breast Surgery, Longgang Central Hospital, Shenzhen, Guangdong 518000, China*
[3]*Department of Pediatrics, Longgang District People's Hospital of Shenzhen, Shenzhen, Guangdong 518000, China*

Correspondence should be addressed to Jianhua Zhou; jianhua_zhoulg@163.com

Jianwei Li and Xinghua Huang contributed equally to this work.

Background. Prostate cancer (PCa) harms the male reproductive system, and lncRNA may play an important role in it. Here, we report that the LINC01088/microRNA- (miRNA/miR-) 22/cell division cycle 6 (CDC6) axis regulated through the phosphatidylinositide 3-kinases- (PI3K-) protein kinase B (AKT) signaling pathway controls the development of PCa. *Methods.* lncRNA/miRNA/mRNA associated with PCa was downloaded and analyzed by Gene Expression Omnibus. The expression and correlation of LINC01088/miR-22/CDC6 in PCa were analyzed and verified by RT-qPCR. Dual-luciferase was used to analyze the binding between miR-22 and LINC01088 or CDC6. Cell Counting Kit-8 and Transwell were used to analyze the effects of LINC01088/miR-22/CDC6 interactions on PCa cell viability or migration/invasion ability. Localization of LINC01088 in cells was analyzed by nuclear cytoplasmic separation. The effect of LINC01088/miR-22/CDC6 interaction on downstream PI3K/AKT signaling was analyzed by Western blot. *Results.* LINC01088 or CDC6 was upregulated in prostate tumor tissues or cells, whereas miR-22 was downregulated, miR-22 directly targets both LINC01088 and CDC6. si-LINC01088 inhibits the PCa process by suppressing the PI3K/AKT pathway. CDC6 reverses si-linc01088-mediated cell growth inhibition and reduction of PI3K and AKT protein levels. *Conclusion.* Our results demonstrate that the LINC01088/miR-22/CDC6 axis functions in PCa progression and provide a promising diagnostic and therapeutic target.

1. Introduction

Prostate cancer (PCa) is a cancer that affects men and is very common worldwide. It accounts for 21% of all new cases of cancer in men. Unfortunately, it causes significant illness and death in those affected [1, 2]. Early systematic screening has a very positive effect on the prevention and treatment of prostate cancer, and the available set of PC biomarkers is growing [3]; there is still a significant unmet need for new and more effective treatments.

Long noncoding RNAs (lncRNAs), which are greater than 200 nucleotides and do not code for proteins, significantly impact cancer tumorigenesis and metastasis when their expression is altered [4]. lncRNAs primarily function through the regulation of competing endogenous RNAs (ceRNAs), which act as sponges for miRNAs that would otherwise target specific genes. Several lncRNAs, including MEG3, FOXP4-AS1, and H19, have been implicated in prostate cancer [5–7]. However, the molecular mechanism by which LINC01088, which is considered an oncogene in most cancers [8, 9], operates in prostate cancer has not yet been elucidated.

miR-22 impedes the progression of different cancer types, including bladder, colorectal, and gastric cancers [10–12]. Similarly, miR-22, which is an androgen receptor (AR) cistrome member, suppresses process of cancer cells such as LNCaP or PC3 in PCa [13]. The ceRNA role of

miRNA targeting lncRNAs or mRNA 3$'$untranslated region (UTR) in PCa has been reported. For instance, miR-22 targets the HOTAIR and 3$'$UTR of *HMGB1*, affecting PCa prognosis [14]. Additionally, miR-22 has been shown to regulate multiple signaling pathways in PCa cells. Specifically, miR-22 activates Wnt/β-catenin signaling in carcinoma [15]. Dhar et al. found that MTA1-activated miR-22 regulates PCa invasiveness [16]. Moreover, miR-22 regulates the PI3K/AKT pathway in various cancers, such as ovarian cancer and osteosarcoma [17, 18]. Nevertheless, whether miR-22 activates the PI3K/AKT pathway in PCa remains unclear.

Cell division cycle 6 (CDC6) is a novel cancer target that regulates the DNA replication process and is considered an early indicator of malignancy [19]. CDC6 has been recognized as a cancer diagnosis biomarker in various cancers [20, 21]. For instance, Mahadevappa et al. found the prognostic significance of CDC6 in breast cancer [22]. However, only few studies have investigated the CDC6 expression in PCa [23]; therefore, CDC6 requires further investigation.

The AR and frequent activation of PI3K signaling are key factors in the progression of PCa [24]. The PI3K/AKT signaling pathway, which is cross-regulated through several reciprocal inhibitory loops with AR pathways, is the driver of prostate tumor development [25, 26]. Recent research by Tan et al. showed that PI3K/AKT axis inactivation suppresses prostate tumorigenesis [27]. Dai et al. confirm that inhibition of the PI3K/AKT signaling pathway facilitates PCa cell autophagy [28]. PI3K and AKT inhibitors will soon be introduced as antitumor drugs and are currently in preclinical and clinical development [29–31].

This study is aimed at understanding the interaction and mechanism of the LINC01088/miR-22/CDC6 axis and exploring its possibility as a biomarker for systematic screening of PCa.

2. Materials and Methods

2.1. Samples. Ten pairs of fresh frozen PCa and adjacent tissues were obtained from the Longgang District People's Hospital of Shenzhen (Shenzhen, China), along with pathological information. All patients were histologically confirmed to have a prostate tumor. The experiments was approved by the institutional ethics committees of Longgang District People's Hospital of Shenzhen (Shenzhen, China; approval no. 2022071) and conducted in accordance with the Declaration of Helsinki.

2.2. Microarray Raw Data Analyses. Datasets were from Gene Expression Omnibus. The series (GSE104749) dataset were utilized to analyze lncRNA/mRNA expression profiles in PCa and categorized as follows: control (4 benign prostatic hyperplasia (BPH) fine-needle aspiration biopsy tissues), and PCa (4 PCa fine-needle aspiration biopsy tissues). The GEO series (GSE45604) dataset was utilized to analyze miRNA expression profiles in PCa and categorized as follows: normal (10 normal prostate tissues) and PCa (10 PCa tissues). Expression of dysregulated RNA was identified to meet the |fold change| ≥ 1.5 criteria. GEPIA2 was used for The Cancer Genome Atlas (TCGA) survival

analysis. Candidate genes and cancer subtypes were chosen as the inputs to generate survival curves for disease-free survival. Statistical significance was defined as $P < 0.05$.

2.3. Predicted Targets of LINC01088 and miR-22. The interactions between LINC01088 and miR-22 were predicted using LncBase v.3 (https://diana.e-ce.uth.gr/lncbasev3/interactions). Putative targets of miR-22 were predicted using TargetScan (http://www.targetscan.org/vert_72/) and TarBase v.8 (https://dianalab.e-ce.uth.gr/html/diana/web/index.php?r=tarbasev8%2Findex).

2.4. Cell Culture and Transfection. Human PCa cell lines (LNCAP, PC3, C4-2, and 22RV1) and prostate epithelial cells (RWPE-2) were purchased from American Type Culture Collection (ATCC; VA, USA). LNCAP, PC3, C4-2, 22RV1, and RWPE-2 cells were maintained in RPMI-1640 (HyClone, UT, USA) with 10% fetal bovine serum (FBS; HyClone). Lipofectamine 3000 (Invitrogen; Thermo Fisher Scientific, Inc.) were transfected into cells and used in subsequent experiments 48 h later.

2.5. Nucleocytoplasmic Separation and RT-qPCR Assay. Cytoplasmic and Nuclear RNA Purification Kit (bioWORLD; OH, USA) was isolated from cells according to the manufacturer's instructions. Total RNA was extracted from tissues or cells using a TRIzol reagent. After centrifugation at $12000 \times g$ (4°C, 10 min), RNA was reverse-transcribed to cDNA and analysis using One-Step SYBR Green RT-qPCR Kit (Biomarker, Beijing, China) and performed at conditions: 95°C for 1 min followed by 40 cycles of 95°C for 6 s and 60°C for 32 s. Sequences of the primers were as follows: *LINC01088* forward, 5$'$-TAGGGT GCCTTCACCTGCTA-3$'$ and *LINC01088* reverse, 5$'$-TACA CCCGGTGGAAAACTCC-3$'$; *CDC6* forward, 5$'$-GATCAA CTGGACAGCAAAGG-3$'$ and *CDC6* reverse, 5$'$-CTAGGT AGAATTCTATCTGT-3$'$; miR-22 forward, 5$'$-ACACTCCAG CTGGGAGTTCTTCAGTGGCAA-3$'$ and miR-22 reverse, 5$'$-CTCAACTGGTGTCGTGGA-3$'$; 18sRNA forward, 5$'$-CCTG GATACCGCAGCTAGGA-3$'$ and 18sRNA reverse, 5$'$-GCGG CGCAATACGAATGCCCC-3$'$; and U6 forward, 5$'$-CTCG CTTCGGCAGCACA-3$'$ and U6 reverse, 5$'$-AACGCTTCA CGAATTTGCGT-3$'$. RNA levels were calculated using the $2^{-\Delta\Delta Ct}$ method [32].

2.6. RNA Pull-Down Assay. Biotin-labeled *LINC01088* and miR-22 were transfected into PCa cells. After 24 h, cells were lysed with RIPA lysis buffer and then incubated (12 min) with Dynabeads M-280 Streptavidin (Invitrogen), followed by RT-qPCR analysis. Biotinylated RNA was obtained from Sangon Biotech.

2.7. Transient LINC01088 Silencing. The siRNA sequences were as follows: si-LINC01088-1, 5$'$-CCTTAAAGTAG CAATCTTAdTdT-3$'$; si-LINC01088-2, 5$'$-GAGAAATTG GACCAGACAAdTdT-3$'$; si-LINC01088-3, 5$'$-AGTCTG CATTGAAGATGTAdTdT; and si-NC, 5$'$-TTCTCCGAA CGTGTCACGdTdT-3$'$.

(a)

(b)

(c)

(d)

(e)

(f)
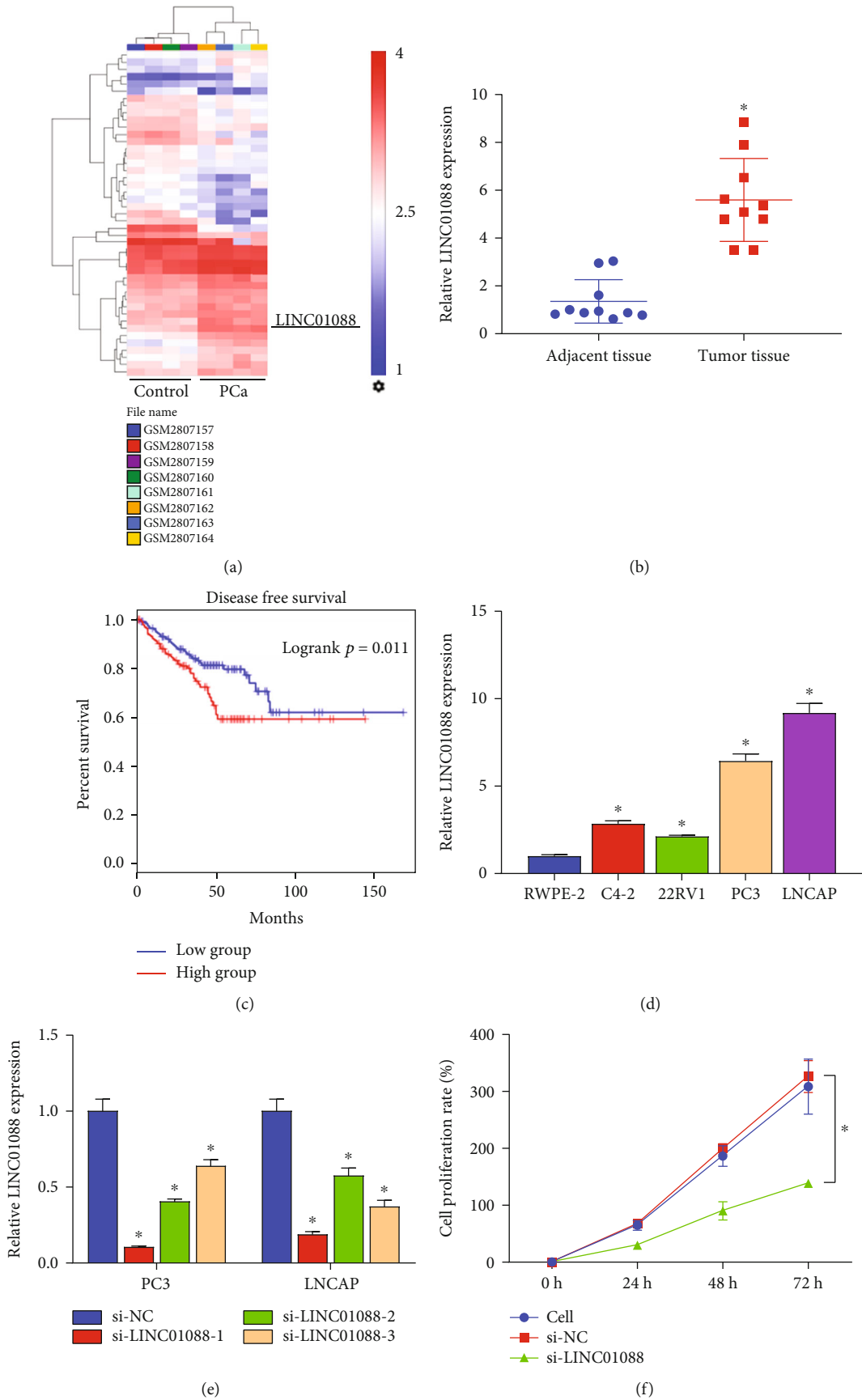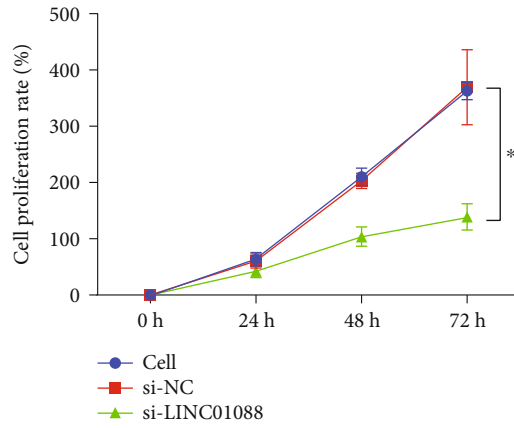
Figure 1: Continued.

(g)
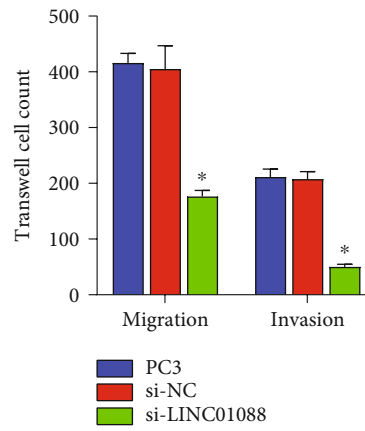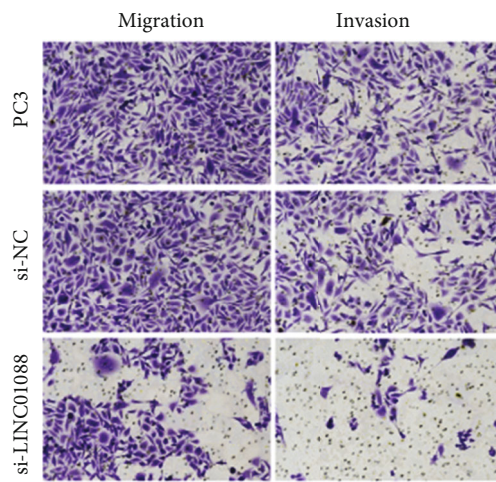
(h)
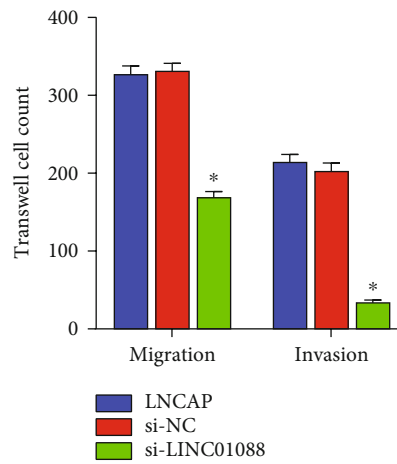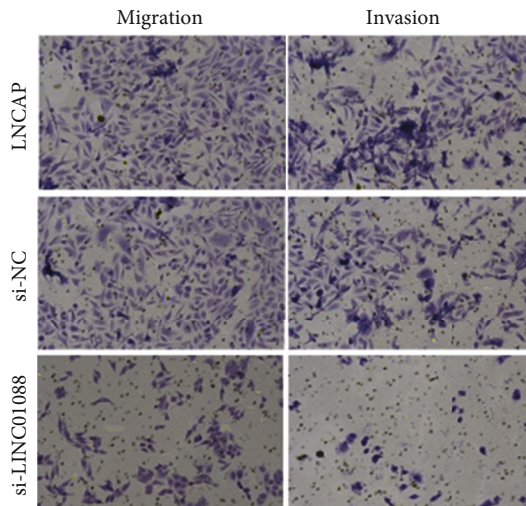
(i)

Figure 1: Continued.

(j)
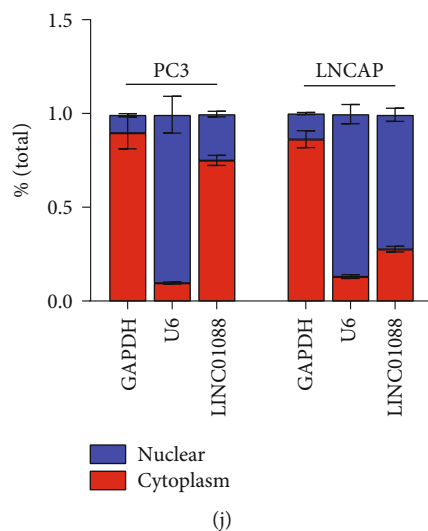
FIGURE 1: LINC01088 is a new potential target that promotes PCa development. (a) Hierarchical clustering heat map shows differentially expressed lncRNA including LINC01088 between the PCa and control groups. (b) Relative expression levels of LINC01088 between the PCa tumor tissues and adjacent tissues. (c) The disease-free survival rate was calculated in the LINC01088-high or LINC01088-low groups by TCGA survival analysis on the GEPIA2 database. (d) Relative expression of LINC01088 in RWPE-2 and four PCa cell lines (C4-2, 22RV1, PC3, and LNCaP). (e) RT-qPCR analysis of the inhibition efficiency of 3 si-LINC01088 in PC3 and LNCAP cells. CCK8 analysis of the effect of si-LINC01088 on the viability rate of (f) PC3 and (g) LNCAP cells. Transwell analysis of the effects of si-LINC01088 on migration and invasion of (h) PC3 and (i) LNCAP cells. (j) RT-qPCR analysis of LINC01088 localization in PC3 and LNCAP cells. $^*P < 0.05$.

2.8. Cell Viability Assay. To assess cell viability, PC3 and LNCAP cells (4×10^3) were treated with $10\,\mu L$ of CCK-8 reagent (Solarbio) at 0, 24, 48, and 72 hours. After 60 min of incubation (in the dark) at 37°C, the absorbance of the samples was determined at 450 nm using an enzyme-labeled instrument (Thermo Fisher Scientific).

2.9. Migration and Invasion Assays. Migration of PC3 and LNCAP cells was verified using Transwell inserts (BD Biosciences) with a porous polycarbonate membrane. Cells were maintained in serum-free medium (upper chamber), and a medium (10% FBS) was added to the lower chamber, for 24 h. The difference with migration is that the invasion assay preincubates Matrigel (BD Biosciences) on Transwell inserts. Then, it was fixed with absolute alcohol, stained with crystal violet, and counted.

2.10. Dual-Luciferase Reporter Assay. Inserted LINC01088 or CDC6 3′UTR into psi-CHECK2 and transfected into 293 T cells (ATCC) with miR-22 mimic using lipofectamine 3000 at 37°C for 4 h. Luciferase activity was measured using the dual-luciferase reporter assay system (Promega) at 490 nm after 48 h of culture. Firefly luciferase values were normalized using the ratio of firefly to Renilla luciferase activity.

2.11. Western Blotting. Denatured proteins from PCa cells were resolved by 10% SDS-PAGE (Beyotime). The separated bands were subsequently transferred to PVDF membranes and incubated (12 h; 4°C) with PI3K (1 : 1200, ab191606), AKT (1 : 500, ab8805), p-PI3K (1 : 500, ab182651), p-AKT (1 : 500, ab38449), CDC6 (1 : 1,000, ab109315), and

GAPDH (1 : 3000, ab8245) primary antibodies. They were then incubated (2 h, 25°C) with goat anti-rabbit antibody (1 : 12,000, ab205718). Antibodies were obtained from Abcam (Cambridge, UK).

2.12. Statistical Analysis. Mean ± SD values were used to present the data, and GraphPad Prism 9 was utilized for statistical analysis. Initially, one-way ANOVA was performed, followed by a Bonferroni post hoc test to establish the presence of a statistically significant change overall. Subsequently, a Student's t-test was employed to examine the difference between any two groups. Statistical significance was defined as $P < 0.05$.

3. Results

3.1. LINC01088 Is Upregulated in PCa. We conducted a comprehensive inquiry into the potential role of a recently discovered long noncoding RNA (lncRNA) in the advancement of prostate cancer (PCa). Our investigation primarily involved lncRNA chip data, which revealed that 45 differentially expressed transcripts lncRNAs, were identified in PCa specimens compared to the control group. Of these transcripts, LINC01088 exhibited the most significant log-fold change (logFC) value, thereby implying its potential as a target for further research (Figure 1(a)). Additionally, we validated the overexpression of LINC01088 in PCa tissues (Figure 1(b)), which was linked with decreased disease-free survival in PCa patients, and associated with diverse clinicopathological features of PCa (Figure 1(c)). The expression of LINC01088 was notably heightened in PCa cells in

(a)

(b)

(c)

(d)

Figure 2: Continued.

(e)

(f)
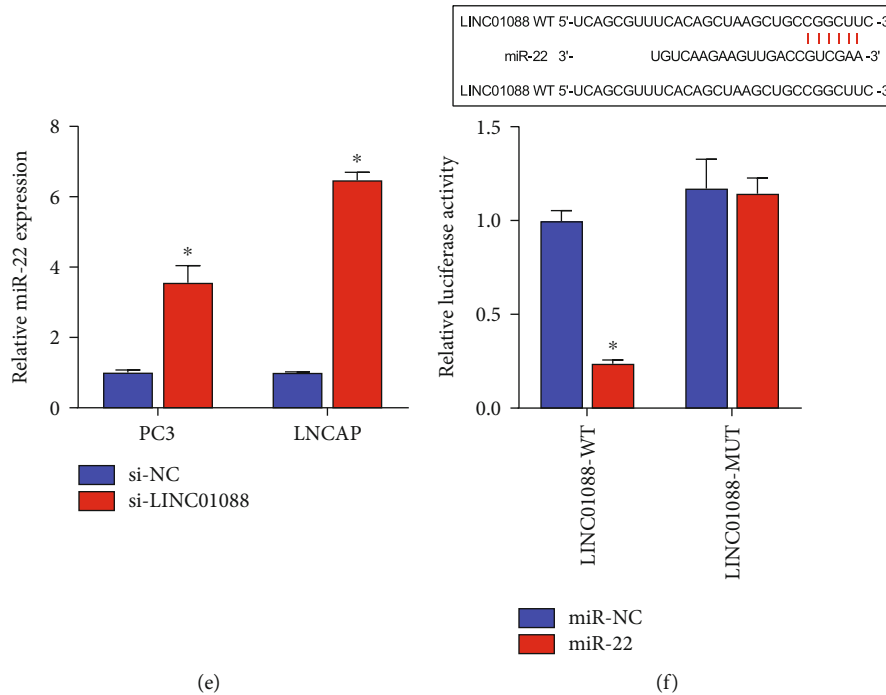
FIGURE 2: LINC01088 sponge adsorbs miR-22. (a) Hierarchical clustering heat map shows differentially expressed miRNA between the PCa and control groups. (b) The miRNA chip and the lncRNA database were combined to analyze the potential miRNAs that bind to LINC01088. (c) Relative expression of miR-22 between the PCa tumor tissues and adjacent tissues. (d) Relative expression of miR-22 in RWPE-2 and four PCa cell lines (C4-2, 22RV1, PC3, and LNCaP). (e) RT-qPCR analysis of the effect of si-LINC01088 on the expression of miR-22 in PC3 and LNCAP cells. (f) Dual-luciferase assay analysis of the binding of LINC0108 to miR-22. $*P < 0.05$.

comparison to RWPE-2 cells (Figure 1(d)), particularly in PC3 and LNCAP cells, highlighting the significant role of LINC01088 in PCa progression. Subsequent findings illustrated that siRNA-LINC01088-1 was the most potent inhibitor of LINC01088 among the three siRNAs in PC3 and LNCAP cells, and we used it as an antagonist for further molecular mechanistic studies (Figure 1(e)). Our findings indicate that the reduction of LINC01088 expression results in a diminished cellular viability, as well as decreased migratory and invasive capacity of both PC3 and LNCAP cell lines (as depicted in Figures 1(f)–1(i)). Moreover, based on our observations, LINC01088 is preferentially localized in the cytoplasmic region of these cells (Figure 1(j)), implying that its effect on prostate cancer pathophysiology may be mediated by a competing endogenous RNA (ceRNA) mechanism.

3.2. LINC01088 Directly Targeted miR-22. Based on miRNA chip data analysis results, 64 differentially expressed hsa-miRNAs were identified with 5 upregulated and 59 downregulated hsa-miRNAs using 10 PCa and 10 normal prostate samples (Figure 2(a)), the joint analysis of LncBase v3 database and miRNA chip data showed that miR-22 was the only intersection among the down-regulated miRNAs (Figure 2(b)) and miR-22 was downregulated in both tissues and cells of PCa (Figures 2(c) and 2(d)). Moreover, suppressing the expression of LINC01088 increased the expression of miR-22 (Figure 2(e)). Subsequent experiments confirmed that LINC01088 directly targets miR-22 (Figure 2(f)). Here, we confirmed that LINC01088 can adsorb miR-22 to regulate PCa development.

3.3. CDC6 Directly Targeted miR-22. Given that miRNAs possess the capacity to regulate transcription and translation via the binding to the 3'UTR of mRNAs [33], we analyzed PCa-related differentially expressed mRNAs in the GEO dataset. The mRNA chip data analysis showed that 1,067 oncogenes were upregulated (Figure 3(a)). The combined analysis of the TargetScan database and TarBase V.8 database showed that 20 genes had overlapped, among which 2 genes had potential binding sites, namely, VASH1 and CDC6 (Figure 3(b)). A previous investigation revealed that VASH1 was downregulated in PCa [34], while the augmented expression of CDC6 conspicuously truncated the disease-free survival of PCa patients (Figure 3(c)). Therefore, we designated the CDC6 gene as a plausible target for subsequent verification. Our finding substantiated that CDC6 was highly expressed within PCa tissues and cells (Figures 3(d) and 3(e)). In addition, our dual-luciferase assay validated that CDC6 directly targeted miR-22 (Figure 3(f)). Following the suppression of LINC01088, the expression of CDC6 was downregulated within PC3 and LNCAP cells (Figure 3(g)).

3.4. LINC01088 Is Positively Correlated with CDC6. The association between LINC01088 and CDC6 was verified by constructing an overexpression plasmid for CDC6 (ov-CDC6). Results indicated that CDC6 were upregulated in ov-CDC6-transfected PC3 and LNCAP cells, confirming the effectiveness of CDC6 overexpressed plasmid (Figure 3(h)). In addition, after cotransfection of PC3 and LNCAP cells with ov-CDC6 and si-LINC01088, excessive CDC6 reversed the inhibition of LINC01088 expression by

(a)

(b)

(c)

(d)
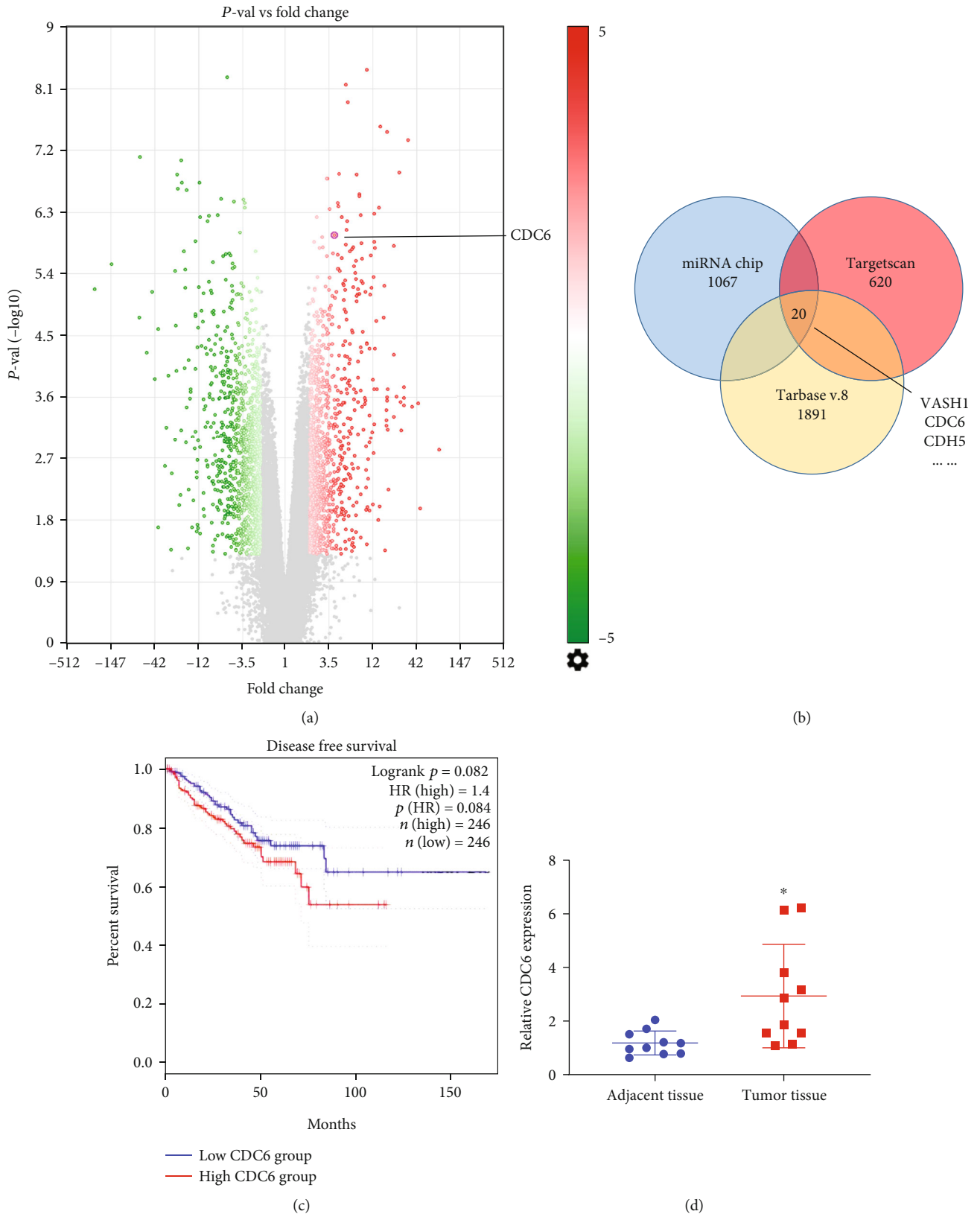
FIGURE 3: Continued.
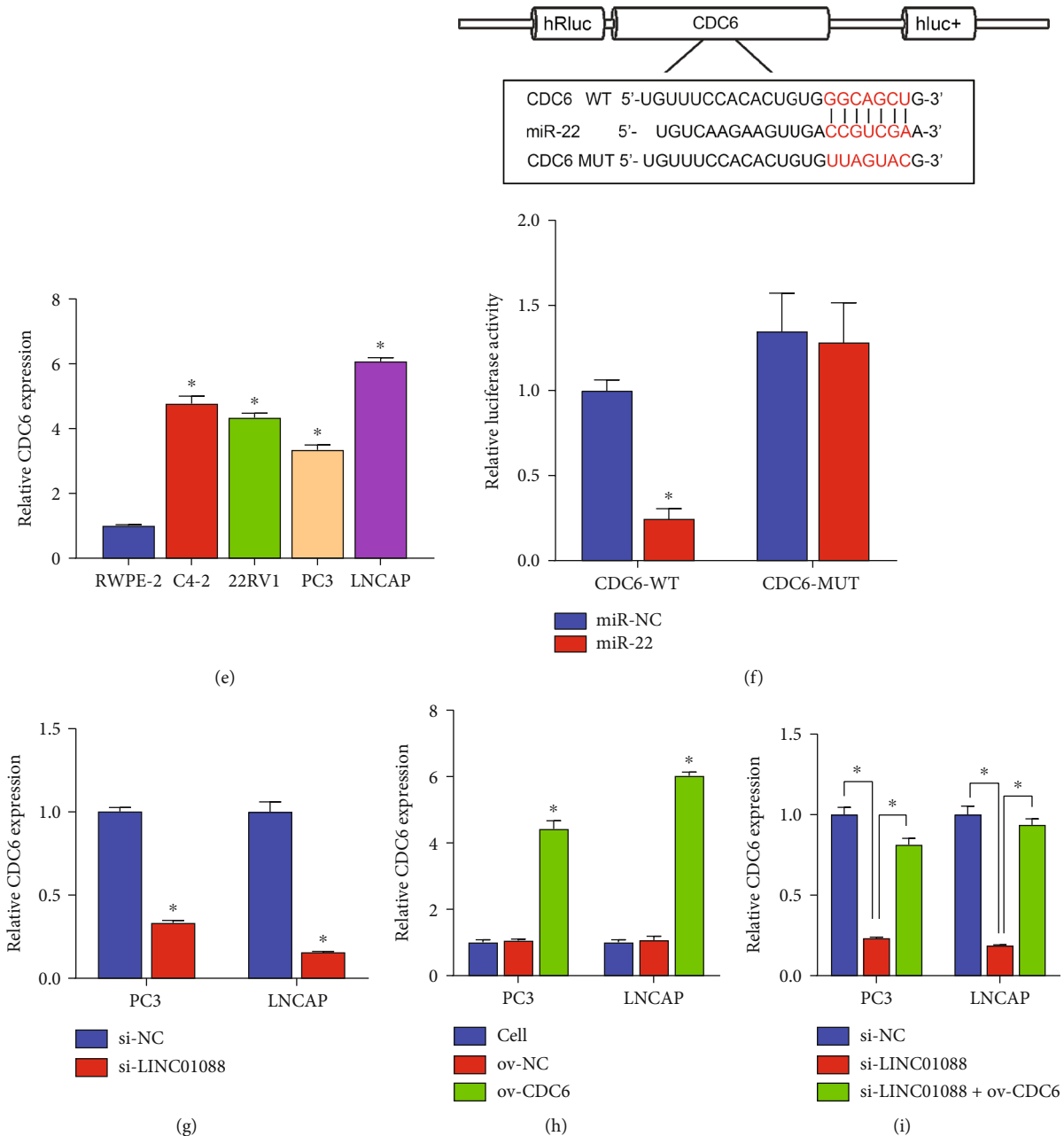
FIGURE 3: CDC6 targets miR-22 and reverses the effects of si-LINC01088 in PC3 and LNCAP cells. (a) Scatter plot shows differentially expressed mRNAs between the PCa and control groups. (b) The dual-luciferase reporter assay shows the relative luciferase activity of the CDC6-WT or CDC6-MUT plasmid between the miR-NC and miR-22 groups. (c) The disease-free survival rate was calculated in the CDC6-high or CDC6-low groups by TCGA survival analysis on the GEPIA2 database. (d) Relative expression levels of LINC01088 between the PCa tumor tissues and adjacent tissues. (e) Relative expression of LINC01088 in RWPE-2 and four PCa cell lines (C4-2, 22RV1, PC3, and LNCaP). (f) Dual-luciferase assay analysis of the binding of CDC6 to miR-22. (g) RT-qPCR analysis of the effect of si-LINC01088 on the expression of CDC6 in PC3 and LNCAP cells. (h) RT-qPCR verified the validity of overexpressing CDC6 plasmid. (i) RT-qPCR analysis of the reversal of LINC01088 expression by overexpressing CDC6 on si-LINC01088. $^{*}P < 0.05$.

si-LINC01088. (Figure 3(i)). Thus, miR-22 directly targets both LINC01088 and CDC6, and LINC01088 is positively correlated with CDC6.

3.5. The LINC01088/miR-22/CDC6 Axis Affects PCa Development through PI3K/AKT Signaling. Next, to identify the key regulatory signaling pathway, we analyzed enriched signaling pathways associated with the differentially expressed

genes using the DAVID database. Among the top 10 enriched pathways, the PI3K/AKT pathway associated with 45 participating differential genes, which is the highest number of genes, was selected (Figure 4(a)). Based on Western blotting, knockdown of LINC01088 in PC3 and LNCAP cells resulted in decreased CDC6, p-PI3K, and p-AKT protein levels (Figure 4(b)). ov-CDC6 reversed the effects of LINC01088 (Figure 4(c)). Moreover, si-LINC01088 can inhibit the

(a)

(b)

Figure 4: Continued.

(c)

(d)

(e)

Figure 4: Continued.

(f)
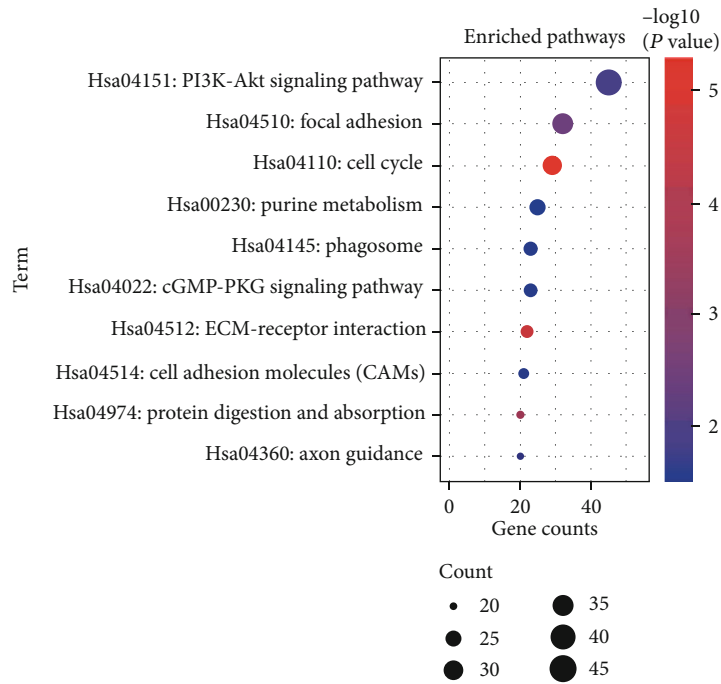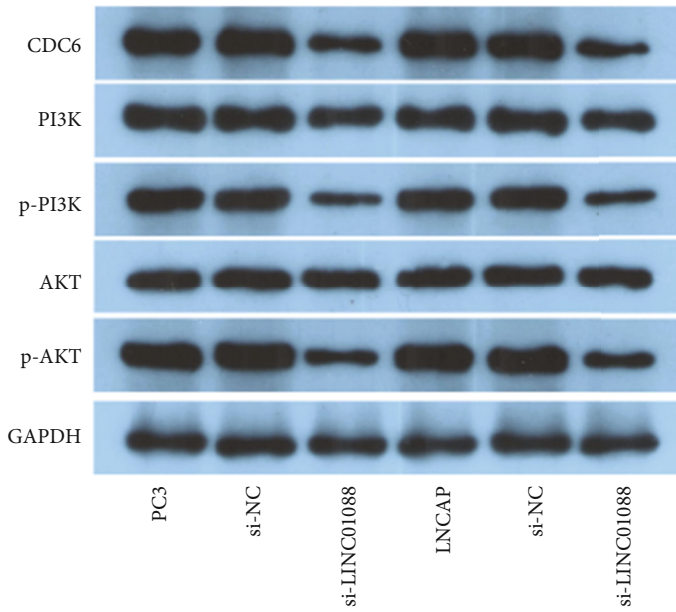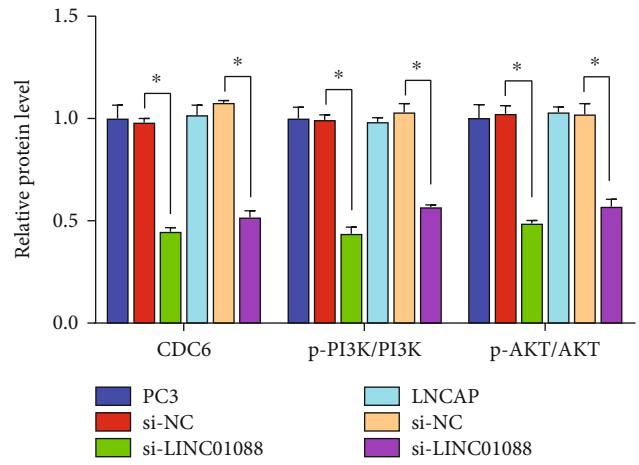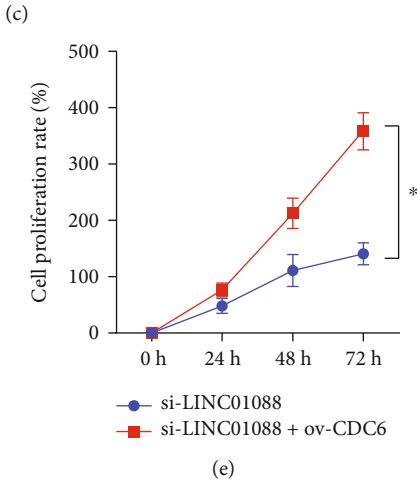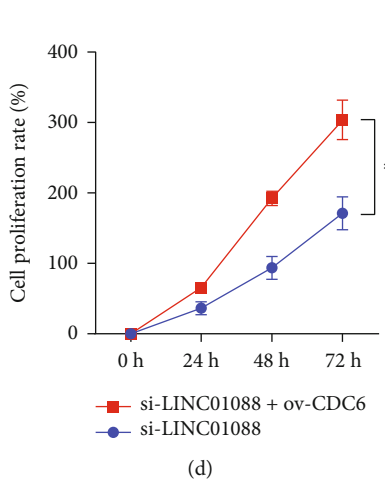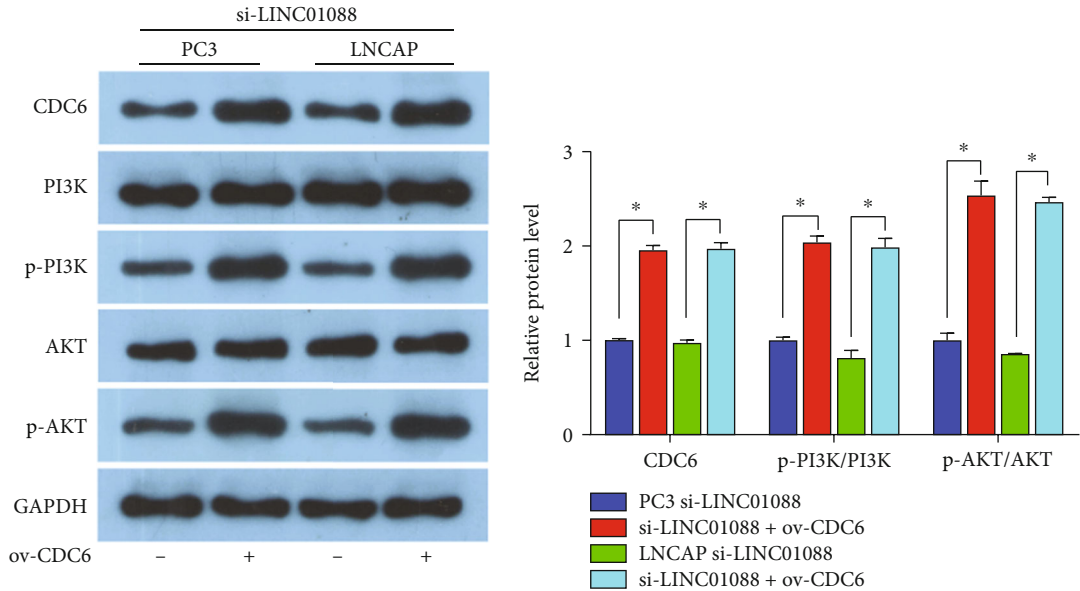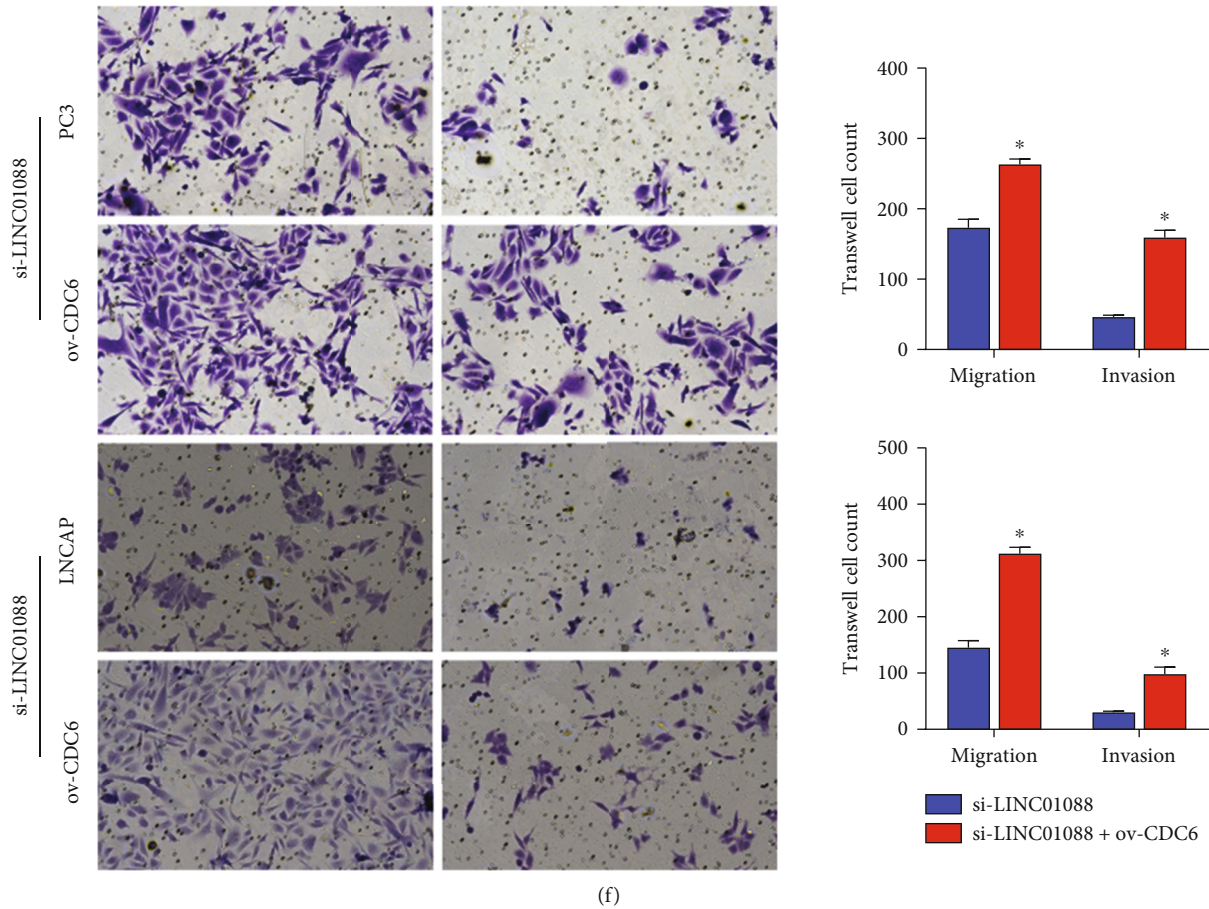
Figure 4: si-LINC01088 suppresses PCa cell growth via the PI3K/AKT pathway. (a) Top 10 KEGG pathway enrichment analysis. (b) Western blot analysis of si-LINC01088-mediated protein levels of CDC6, PI3K, p-PI3K, AKT, and p-AKT. (c) Western blot analysis of si-LINC01088/ov-CDC6-mediated protein levels of CDC6, PI3K, p-PI3K, AKT, and p-AKT. CCK8 analysis of the effect of si-LINC01088/ov-CDC6 co-action on the viability rate of (d) PC3 and (e) LNCAP cells. Transwell analysis of the effect of si-LINC01088/ov-CDC6 coaction on migration and invasion of (f) PC3. $^*P < 0.05$.

4. Discussion

viability rate (Figures 4(d) and 4(e)) and migration/invasion of PC3 and LNCAP cells (Figure 4(f)). Taken together, LINC01088 affects PI3K-AKT signaling through sponge adsorption of miR-22 and regulates CDC6, thereby regulating PCa development.

4. Discussion

Our aim was to identify a novel lncRNA with potential therapeutic value in the treatment of PCa. Initially, we investigated the oncogenic function of LINC01088 and CDC6 and the tumor-suppressing role of miR-22 in PCa. LINC01088 and CDC6 expression were both upregulated in PCa tissues and cells, unlike miR-22, promoting PCa cell growth in vitro. We discovered that LINC01088 sponges miR-22, CDC6 is the target of miR-22, and LINC01088 is coordinately upregulated with CDC6 in PCa progression. Furthermore, LINC01088 activates the PI3K/AKT pathway.

LINC01088 is an influential regulatory factor in various cancers [8, 9]. For instance, Peng et al. discovered that LINC01088 promotes glioma progression [35], and Liu et al. observed that LINC01088 promotes proliferation and

migration of non-small-cell lung cancer [8]. In a similar vein, our research showed that LINC01088 is upregulated in PCa, and its overexpression significantly reduces the disease-free survival of PCa patients. LINC01088 promotes PCa cell viability rate and migration/invasion via the PI3K/AKT signaling, indicating that LINC01088 has an oncogenic role in promoting PCa development. When LINC01088 was suppressed, the growth of PCa cells is restricted. Furthermore, LINC01088 plays a role as a ceRNA, a miRNA sponging factor, in cancers. For instance, Zang et al. found that LINC01088 inhibits the tumorigenesis of ovarian epithelial cells by sponging miR-24-1-5p [36], and Li et al. found that LINC01088 plays a ceRNA role by sponging miR-22 in the progression of colorectal cancer [9]. In our study, we demonstrated that LINC01088 sponges miR-22 and negatively regulative miR-22 in PCa. Moreover, suppressing the expression of LINC01088 promoted the expression of miR-22 in PCa cells.

miR-22 regulates the target gene to affect posttranscription or translation in PCa progression [13, 14]. Bioinformatics predicted that miR-22 targets CDC6, and the target mechanisms were proved by dual-luciferase reporter

assay. Furthermore, CDC6 expression was negatively correlated with miR-22 expression in PCa tissues and cells. Notably, CDC6 promotes PCa progression [37, 38]. Moreover, LINC01088 is coordinately upregulated with miRNA target genes in the ceRNA axis. In our study, LINC01088 was coordinately upregulated with CDC6, si-LINC01088 reduced CDC6 expression in PCa cells, and CDC6 reversed si-LINC01088-mediated PI3K and AKT protein expression reduction in PCa cells. In addition, the slow growth of PCa cells caused by the inhibition of LINC01088 expression was significantly alleviated by the overexpression of CDC6. These results suggest that LINC01088 exerts oncogenic effects through the miR-22/CDC6 axis.

The PI3K/AKT pathway directly controls PCa [39, 40]. Shorning et al. found the PI3K-AKT signaling and PCa at the intersection of AR-MAPK-Wnt [41]. In the present study, at the time of suppression of cell viability rate, promotion of cell apoptosis, and suppression of migration/invasion, PI3K/AKT phosphorylation levels were reduced. LINC01088, miR-22, and CDC6 control the PI3K/AKT pathways to regulate PCa progression. si-LINC01088 or miR-22 suppressed PCa cell growth and decreased PI3K/AKT phosphorylation levels. CDC6 promoted cancer cell growth and enhanced PI3K/AKT signaling and reversed the effect of si-LINC01088 on PCa cells.

Interlaboratory variability may also affect the development of therapeutic strategies targeting the LINC01088/miR-22/CDC6 axis. Despite the potential limitations, this study provides a foundation for further research on the LINC01088/miR-22/CDC6 axis as a potential therapeutic target for PCa treatment. Future studies can build upon these findings and investigate the molecular mechanisms underlying the regulatory interactions among LINC01088, miR-22, and CDC6 in PCa. Therefore, it is important to conduct validation studies to confirm the therapeutic potential of this axis across multiple laboratories and patient populations before initiating clinical trials.

In conclusion, this study confirms the LINC01088/miR-22/CDC6 axis as a potential therapeutic target, providing more directions and theoretical basis for the treatment of PCa.

Data Availability

The authors declare that all other data supporting our findings are available within the article and from the corresponding authors upon reasonable request.

Conflicts of Interest

The authors declare no conflicts of interest.

Authors' Contributions

Jianwei Li and Xinghua Huang contributed equally to this work and are co-first authors.

References

[1] R. L. Siegel, K. D. Miller, and A. Jemal, "Cancer statistics, 2020," *CA: a Cancer Journal for Clinicians*, vol. 70, no. 1, pp. 7–30, 2020.

[2] M. P. Huynh-Le, C. C. Fan, R. Karunamuni et al., "Polygenic hazard score is associated with prostate cancer in multi-ethnic populations," *Nature Communications*, vol. 12, no. 1, p. 1236, 2021.

[3] S. Salciccia, A. L. Capriotti, A. Lagana et al., "Biomarkers in prostate cancer diagnosis: from current knowledge to the role of metabolomics and exosomes," *International Journal of Molecular Sciences*, vol. 22, no. 9, p. 4367, 2021.

[4] A. Bhan, M. Soleimani, and S. S. Mandal, "Long noncoding RNA and cancer: a new paradigm," *Cancer Research*, vol. 77, no. 15, pp. 3965–3981, 2017.

[5] X. Wu, Y. Xiao, Y. Zhou, Z. Zhou, and W. Yan, "LncRNA FOXP4-AS1 is activated by PAX5 and promotes the growth of prostate cancer by sequestering miR-3184-5p to upregulate FOXP4," *Cell Death & Disease*, vol. 10, no. 7, p. 472, 2019.

[6] M. Zhu, Q. Chen, X. Liu et al., "lncRNA H19/miR-675 axis represses prostate cancer metastasis by targeting TGFBI," *The FEBS Journal*, vol. 281, no. 16, pp. 3766–3775, 2014.

[7] M. Wu, Y. Huang, T. Chen et al., "LncRNA MEG3 inhibits the progression of prostate cancer by modulating miR-9-5p/QKI-5 axis," *Journal of Cellular and Molecular Medicine*, vol. 23, no. 1, pp. 29–38, 2019.

[8] J. Q. Liu, Y. H. Feng, S. Zeng, and M. Z. Zhong, "linc01088 promotes cell proliferation by scaffolding EZH2 and repressing p21 in human non-small cell lung cancer," *Life Sciences*, vol. 241, article 117134, 2020.

[9] C. Li, B. Pan, X. Wang et al., "Upregulated LINC01088 facilitates malignant phenotypes and immune escape of colorectal cancer by regulating microRNAs/G3BP1/PD-L1 axis," *Journal of Cancer Research and Clinical Oncology*, vol. 148, no. 8, pp. 1965–1982, 2022.

[10] M. Xu, J. Li, X. Wang et al., "MiR-22 suppresses epithelial-mesenchymal transition in bladder cancer by inhibiting Snail and MAPK1/Slug/vimentin feedback loop," *Cell Death & Disease*, vol. 9, no. 2, p. 209, 2018.

[11] Y. Liu, X. Chen, R. Cheng et al., "The Jun/miR-22/HuR regulatory axis contributes to tumourigenesis in colorectal cancer," *Molecular Cancer*, vol. 17, no. 1, p. 11, 2018.

[12] D. Tong, J. Zhang, X. Wang et al., "_MiR-22_ , regulated by MeCP2, suppresses gastric cancer cell proliferation by inducing a deficiency in endogenous S-adenosylmethionine," *Oncogene*, vol. 9, no. 11, p. 99, 2020.

[13] L. Pasqualini, H. Bu, M. Puhr et al., "miR-22 and miR-29a are members of the androgen receptor cistrome modulating LAMC1 and Mcl-1 in prostate cancer," *Molecular Endocrinology*, vol. 29, no. 7, pp. 1037–1054, 2015.

[14] Z. H. Deng, G. S. Yu, B. Pan et al., "Rs145204276 and rs4759314 affect the prognosis of prostate cancer by modulating the GAS5/miR-1284/HMGB1 and HOTAIR/miR-22/HMGB1 signalling pathways," *Artificial Cells, Nanomedicine, and Biotechnology*, vol. 48, no. 1, pp. 435–442, 2020.

[15] S. Yuan, P. Zhang, L. Wen et al., "*miR-22* promotes stem cell traits via activating Wnt/ *β*-catenin signaling in cutaneous squamous cell carcinoma," *Oncogene*, vol. 40, no. 39, pp. 5799–5813, 2021.

[16] S. Dhar, A. Kumar, C. R. Gomez et al., "MTA1-activated Epi-microRNA-22 regulates E-cadherin and prostate cancer invasiveness," *FEBS Letters*, vol. 591, no. 6, pp. 924–933, 2017.

[17] H. Wu, J. Liu, Y. Zhang, Q. Li, Q. Wang, and Z. Gu, "miR-22 suppresses cell viability and EMT of ovarian cancer cells via NLRP3 and inhibits PI3K/AKT signaling pathway," *Clinical & Translational Oncology*, vol. 23, no. 2, pp. 257–264, 2021.

[18] C. Y. Meng, Z. Q. Zhao, R. Bai et al., "MicroRNA-22 mediates the cisplatin resistance of osteosarcoma cells by inhibiting autophagy via the PI3K/Akt/mTOR pathway," *Oncology Reports*, vol. 43, no. 4, pp. 1169–1186, 2020.

[19] N. Lim and P. A. Townsend, "Cdc6 as a novel target in cancer: oncogenic potential, senescence and subcellular localisation," *International Journal of Cancer*, vol. 147, no. 6, pp. 1528–1534, 2020.

[20] C. An, G. Liu, S. Cheng et al., "A pilot study of cdc6 as a biomarker for circulating tumor cells in patients with lung cancer," *Journal of Clinical Laboratory Analysis*, vol. 34, no. 6, article e23245, 2020.

[21] Y. Hu, L. Wang, Z. Li et al., "Potential prognostic and diagnostic values of CDC6, CDC45, ORC6 and SNHG7 in colorectal cancer," *Oncotargets and Therapy*, vol. 12, pp. 11609–11621, 2019.

[22] R. Mahadevappa, H. Neves, S. M. Yuen et al., "The prognostic significance of Cdc6 and Cdt1 in breast cancer," *Scientific Reports*, vol. 7, no. 1, p. 985, 2017.

[23] Y. Gao, Y. Liu, Y. Liu et al., "UHRF1 promotes androgen receptor-regulated _CDC6_ transcription and anti- androgen receptor drug resistance in prostate cancer through KDM4C-Mediated chromatin modifications," *Cancer Letters*, vol. 520, pp. 172–183, 2021.

[24] M. Crumbaker, L. Khoja, and A. M. Joshua, "AR signaling and the PI3K pathway in prostate cancer," *Cancers*, vol. 9, no. 12, p. 34, 2017.

[25] B. S. Carver, C. Chapinski, J. Wongvipat et al., "Reciprocal feedback regulation of PI3K and androgen receptor signaling in PTEN-deficient prostate cancer," *Cancer Cell*, vol. 19, no. 5, pp. 575–586, 2011.

[26] M. A. De Velasco, Y. Kura, K. Sakai et al., "Targeting castration-resistant prostate cancer with androgen receptor antisense oligonucleotide therapy," *JCI Insight*, vol. 4, no. 17, article e122688, 2019.

[27] M. Tan, J. Xu, J. Siddiqui, F. Feng, and Y. Sun, "Depletion of SAG/RBX2 E3 ubiquitin ligase suppresses prostate tumorigenesis via inactivation of the PI3K/AKT/mTOR axis," *Molecular Cancer*, vol. 15, no. 1, p. 81, 2016.

[28] H. Dai, W. Hu, L. Zhang et al., "FGF21 facilitates autophagy in prostate cancer cells by inhibiting the PI3K-Akt-mTOR signaling pathway," *Cell Death & Disease*, vol. 12, no. 4, p. 303, 2021.

[29] A. J. Armstrong, S. Halabi, P. Healy et al., "Phase II trial of the PI3 kinase inhibitor buparlisib (BKM-120) with or without enzalutamide in men with metastatic castration resistant prostate cancer," *European Journal of Cancer*, vol. 81, pp. 228–236, 2017.

[30] L. Graham, K. Banda, A. Torres et al., "A phase II study of the dual mTOR inhibitor MLN0128 in patients with metastatic castration resistant prostate cancer," *Investigational New Drugs*, vol. 36, no. 3, pp. 458–467, 2018.

[31] M. P. Kolinsky, P. Rescigno, D. Bianchini et al., "A phase I dose-escalation study of enzalutamide in combination with the AKT inhibitor AZD5363 (capivasertib) in patients with metastatic castration- resistant prostate cancer," *Annals of Oncology*, vol. 31, no. 5, pp. 619–625, 2020.

[32] K. J. Livak and T. D. Schmittgen, "Analysis of relative gene expression data using real-time quantitative PCR and the $2^{-\Delta\Delta}$ $-C_{-T}$ method," *Methods*, vol. 25, no. 4, pp. 402–408, 2001.

[33] M. R. Fabian, N. Sonenberg, and W. Filipowicz, "Regulation of mRNA translation and stability by microRNAs," *Annual Review of Biochemistry*, vol. 79, no. 1, pp. 351–379, 2010.

[34] Z. Jiang, Y. Zhang, X. Chen, P. Wu, and D. Chen, "Long non-coding RNA RBMS3-AS3 acts as a microRNA-4534 sponge to inhibit the progression of prostate cancer by upregulating VASH1," *Gene Therapy*, vol. 27, no. 3-4, pp. 143–156, 2020.

[35] T. Peng, D. L. Chen, and S. L. Chen, "LINC01088 promotes the growth and invasion of glioma cells through regulating small nuclear ribonucleoprotein polypeptide A transcription," *Bioengineered*, vol. 13, no. 4, pp. 9172–9183, 2022.

[36] W. Zhang, J. Fei, S. Yu et al., "*LINC01088* inhibits tumorigenesis of ovarian epithelial cells by targeting *miR-24-1-5 p*," *Scientific Reports*, vol. 8, no. 1, p. 2876, 2018.

[37] Y. H. Kim, Y. J. Byun, W. T. Kim et al., "CDC6 mRNA expression is associated with the aggressiveness of prostate cancer," *Journal of Korean Medical Science*, vol. 33, no. 47, article e303, 2018.

[38] H. Li, W. Xu, T. Wang et al., "miR-26a inhibits the proliferation and migration of prostate cancer by targeting CDC6," *Minerva Medica*, vol. 112, no. 5, pp. 661–663, 2021.

[39] T. M. Morgan, T. D. Koreckij, and E. Corey, "Targeted therapy for advanced prostate cancer: inhibition of the PI3K/Akt/ mTOR pathway," *Current Cancer Drug Targets*, vol. 9, no. 2, pp. 237–249, 2009.

[40] N. M. Roudsari, N. A. Lashgari, S. Momtaz et al., "Inhibitors of the PI3K/Akt/mTOR pathway in prostate cancer chemoprevention and intervention," *Pharmaceutics*, vol. 13, no. 8, p. 1195, 2021.

[41] B. Y. Shorning, M. S. Dass, M. J. Smalley, and H. B. Pearson, "The PI3K-AKT-mTOR pathway and prostate cancer: at the crossroads of AR, MAPK, and WNT signaling," *International Journal of Molecular Sciences*, vol. 21, no. 12, p. 4507, 2020.

Research Article

Building an Immune-Related Genes Model to Predict Treatment, Extracellular Matrix, and Prognosis of Head and Neck Squamous Cell Carcinoma

Yushi Yang [iD],[1] **Yang Feng,**[2] **Qin Liu,**[3] **Ji Yin** [iD],[4] **Chenglong Cheng,**[1] **Cheng Fan** [iD],[3] **Chenhui Xuan,**[5,6] **and Jun Yang**[7]

[1]*Department of Otolaryngology and Ophthalmology, Anji County People's Hospital, Zhejiang, China*
[2]*Department of Radiation Oncology, Shanghai Ninth People's Hospital, Shanghai Jiaotong University School of Medicine, Shanghai, China*
[3]*Department of Neurosurgery, Anyue County People's Hospital, Sichuan, China*
[4]*The Affiliated Traditional Chinese Medicine Hospital of Southwest Medical University, Sichuan, China*
[5]*Department of Endocrinology, The Affiliated Third Hospital of Chengdu Traditional Chinese Medicine University, Sichuan, China*
[6]*Department of Endocrinology, Chengdu Pidu District Hospital of Traditional Chinese Medicine, Sichuan, China*
[7]*Department of Cardiology, Anyue County People's Hospital, Sichuan, China*

Correspondence should be addressed to Yushi Yang; 2467394035@qq.com

Due to the considerable heterogeneity of head and neck squamous cell carcinoma (HNSCC), individuals with comparable TNM stages who receive the same treatment strategy have varying prognostic outcomes. In HNSCC, immunotherapy is developing quickly and has shown effective. We want to develop an immune-related gene (IRG) prognostic model to forecast the prognosis and response to immunotherapy of patients. In order to analyze differential expression in normal and malignant tissues, we first identified IRGs that were differently expressed. Weighted gene coexpression network analysis (WGCNA) was used to identify modules that were highly related, and univariate and multivariate Cox regression analyses were also used to create a predictive model for IRGs that included nine IRGs. WGCNA identified the four most noteworthy related modules. Patients in the model's low-risk category had a better chance of survival. The IRGs prognostic model was also proved to be an independent prognostic predictor, and the model was also substantially linked with a number of clinical characteristics. The low-risk group was associated with immune-related pathways, a low incidence of gene mutation, a high level of M1 macrophage infiltration, regulatory T cells, CD8 T cells, and B cells, active immunity, and larger benefits from immune checkpoint inhibitors (ICIs) therapy. The high-risk group, on the other hand, had suppressive immunity, high levels of NK and CD4 T-cell infiltration, high gene mutation rates, and decreased benefits from ICI therapy. As a result of our research, a predictive model for IRGs that can reliably predict a patient's prognosis and their response to both conventional and immunotherapy has been created.

1. Introduction

Head and neck cancer ranks as the 6th most prevalent malignancy worldwide, with an annual incidence of 930,000 cases and 470,000 deaths [1]. Head and neck squamous cell carcinoma (HNSCC) is the majority of head and neck cancer, and the major risk factors for the development of HNSCC include tobacco, alcohol consumption, and human papillomavirus infection [1]. The main reasons for death in advanced HNSCC patients are local recurrence, remote metastasis, and therapeutic failure owing to resistance to routine chemotherapy [2]. In the last years, immune checkpoint inhibitors (ICIs) are regarded as revolutionary agents in medicinal therapy for malignant tumors, especially for HNSCC [3].

Cancer immunotherapy operates on the basis that the host's immune system may get activated by the cancer cells, which identifies and eliminates them [4]. While immune checkpoints can prevent overwhelming inflammatory

responses and the progression of autoimmunity, they can as well be operated as a mechanism of tumor immune evasion [5]. ICIs reactivate immune responses against cancer by blocking immune checkpoint pathways, including antiprogrammed death-1, antiprogrammed death-1 ligand, and anticytotoxic T-lymphocyte-associated protein 4 antibodies [5]. Nevertheless, the main restriction of this treatment is the poor patient response rate. Only a small percentage of HNSCC patients respond to immunotherapy, and the responses seen are usually durable and profound, but many others show widespread resistance to immunotherapy [6]. Therefore, novel therapeutic markers demand to urgent study to identify the ideal subgroup of HNSCC for immunotherapy.

In the research, we attempted to construct a prognostic signature for HNSCC that can predict the efficacy of routine therapy and immunotherapy. First, we assessed immune-related genes (IRGs) of HNSCC and identified survival-associated differentially expressed IRGs in significantly relevant modules by weighted gene coexpression network analysis (WGCNA) to develop an IRGs prognostic model. We then estimated its predictive value among HNSCC patients, examined the immune profile of the prognostic model, and characterized it with gene mutation, N6-methyladenosine (m^6A) mRNA stats, tumor immune dysfunction and exclusion (TIDE) score, tumor inflammation signature (TIS) score, and chemotherapeutic efficacy. Conclusively, the IRGs prognostic model was a prospective prognostic signature for precise prediction of patient prognosis and reaction to traditional treatment and immunotherapy.

2. Materials and Methods

2.1. Preparation of Data. The RNA-seq data and clinicopathological features of HNSCC samples (The Cancer Genome Atlas (TCGA)-HNSCC and GSE65858) were procured from the TCGA (http://portal.gdc.cancer.gov) and gene expression omnibus (GEO) (http://www.ncbi.nlm.nih.gov/geo/) [7]. The gene transfer format files with gene names and the transcript annotation of the genome available were obtained in the Ensemble database (http://asia.ensembl.org) [8]. A dataset of recognized IRGs was acquired in the InnateDB (http://www.innatedb.com) databases and the ImmPort database (http://www.immport.org) [9]. The somatic mutation data of HNSCC patients were retrieved from the TCGA.

2.2. Identification of Significantly Relevant Modules with WGCNA. Differential expression analysis ($|\log2FC| > 0.585$, false discovery rate (FDR) <0.05) was utilized to recognize differentially expressed IRGs. The gene ontology (GO) and Kyoto Encyclopedia of Genes and Genomes (KEGG) analyses were employed to analyze these differentially expressed IRGs (P value <0.05) [10].

After that, significantly relevant modules were obtained using WGCNA. First, a similarity matrix that calculates Pearson's correlation coefficient between two genes was constructed in light of expression data. Second, an adjacency matrix with a network type of sign was acquired based on the similarity matrix by selecting five as the soft threshold and further converted to a topological matrix with the topological overlap

measure, which was used to depict the degree of association between genes. Then, genes were grouped at a distance of 1-TOM, and gene modules were recognized using the dynamic hybrid tree-cut algorithm. Lastly, nine modules were determined based on a minimal cluster size of 25, a correlation coefficient greater than 0.9, and a merging threshold function of 0.25. These modules (the green, pink, brown, and red modules) were recognized as significantly relevant modules.

Finally, to show as many protein interactions as possible in the different modules, the protein–protein interaction networks (PPI) of these IRGs in significantly relevant modules were retrieved, respectively, from STRING (http://string-db.org) and were visualized separately by Cytoscape 3.8.2 software (minimum required interaction score >0.2) [11]. And these IRGs in significantly relevant modules were analyzed individually by GO and KEGG (P-value <0.05).

2.3. Development and Evaluation of Prognostic Model. Univariate Cox regression and Kaplan–Meier (KM) analysis were carried out to identify the association of these IRGs in significantly relevant modules with survival, and twenty IRGs with $P < 0.05$ were determined to be survival-associated IRGs. These survival-related IRGs were utilized by multivariate Cox regression analysis to construct an IRGs prognostic model with nine IRGs. The specific risk score for each patient was calculated, and the risk score formula was as follows:

$$\sum_{i=1}^{k} 1 \sqrt{i} Si. \tag{1}$$

We used KM survival analysis to evaluate the prognostic ability of the model in the TCGA and GEO cohorts. Chi-squared test was applied to investigate the association between the prognostic model and clinical characteristics. Wilcoxon signed-rank test was carried out to compute the risk score differences among distinct groups of clinical features. Univariate and multivariate Cox analyses were utilized to verify that the signature was an independent predictor of clinical prognosis. Finally, decision curve analysis (DCA) was employed to assess the net benefit of five markers for clinical decision-making, and a nomogram integrating prognostic signatures was built to predict the survival rates of patients.

2.4. Exploration of Molecular and Immunological Characteristics and ICIs Therapeutics. Gene set enrichment analysis (GSEA) based on the KEGG and HALLMARK genes was applied to identify the signaling pathways in different groups ($P < 0.05$ and FDR <0.25). The gene mutation analysis was used to identify the quantity and quality of gene mutations among the signature subgroups. Wilcoxon signed-rank test was employed to investigate differences in expression levels of m^6A-related genes in different groups.

To analyze the immune characteristics of this model, the relative proportion of immune cells was computed using CIBERSORT (http://cibersort.stanford.edu/) [12]. Single-sample GSEA (ssGSEA) was applied to identify differences of immune function between different groups. Survival status was compared with the immune cell proportions and immune function

between different groups. And we carried out Wilcoxon signed-rank test to explore the expression level of ICIs-related molecules among different groups.

TIDE score was obtained from TIDE (http://tide.dfci.harvard.edu/), and TIS score was computed based on the expression of the 18 genes [13, 14]. Then, the time-dependent receiver-operating characteristic (ROC) curve analyses were performed to acquire the area under the curve (AUC) and compare the prognostic value among the model, TIDE, and TIS. To evaluate the sensitivity of chemotherapy in the IRGs prognostic model, Wilcoxon signed-rank test was used to compare the difference in the half inhibitory concentration (IC_{50}) among the prognostic model subgroups.

3. Results

3.1. Identification of Significantly Related Modules. By performing differential expression analysis and intersecting these genes with identified IRGs, 920 differentially expressed IRGs were extracted, of which 726 were upregulated and 194 were downregulated (*Supplementary 1*). In total, 920 IRGs were enriched in various GO and KEGG terms (details in *Supplementary 2*), and the first 30 GO and KEGG terms are presented in *Supplementary 1* (Figures S1B and S1C). Nine significantly related modules were recognized by WGCNA on the basis of the scale-free network (*Supplementary 3*). PPI was constructed separately, and GO and KEGG were conducted respectively on the genes of the green, pink, brown, and red modules (*Supplementary 4*).

3.2. Development of IRGs Prognostic Index. To construct an IRGs prognostic model, 20 survival-associated IRGs were extracted in accordance with these genes of significantly relevant modules (the green, pink, brown, and red modules), shown in Figure 1(a) and *Supplementary 5*. Among 20 survival-associated IRGs, nine IRGs were identified via multivariate Cox regression analysis, thereby establishing the prognostic model (Figure 1(b)). Although some genes had *P*-values greater than 0.05 in the multivariate Cox regression analysis, these genes still had some prognostic value. On the basis of the respective median risk score, 249 patients were assigned to the high-risk group and 250 patients to the low-risk group in TCGA, 143 patients to the high-risk group, and 127 patients to the low-risk group in GEO.

3.3. Estimation of the Risk Assessment Signature. KM analysis demonstrated that survival rates were remarkably lower in high-risk HNSCC patients (Figures 1(c) and 1(d)). Besides, the risk score distribution for HNSCC patients is presented in Figures 1(e) and 1(f), indicating that the clinical prognosis of patients in the high-risk group was generally worse. Based on a set of χ^2 tests, the strip chart (Figure 2(a)) and consequent scatter diagrams show that risk scores are strongly related to clinico-pathological characteristics of HNSCC patients, including pathological stage (Figure 2(b)), clinical stage (Figure 2(c)), T stage (Figure 2(d)) and N stage (Figure 2(e)). Univariate and multivariate Cox regression analysis validated that the model was an independent prognostic risk factor (Figures 2(f) and 2(g), details in *Supplementary 6*). The result

of DCA indicated that the prognostic model was more precise than other conventional clinico-pathological characteristics (Figure 3(a)). The nomogram combining the IRGs prognostic model and clinico-pathological characteristics was dependable and sensitive for survival prediction of HNSCC patients (Figure 3(b)).

3.4. Investigation of Molecular Characteristics. Genes in the low-risk group were largely enriched in cell adhesion molecules, chemokines, and immune-related pathways, whereas genes in the high-risk group were majorly enriched in focal adhesion (Figures 4(a) and 4(b), details in *Supplementary 7*). The results of gene mutation analysis displayed that more genes were mutated in the high-risk group (Figures 4(c) and 4(d)). The commonest type of mutation was the missense variant mutations, followed by nonsense mutation and multiple mutations of a gene. The top 10 genes having the greatest mutation rate were TP53, TTN, FAT1, CDKN2A, MUC16, CSMD3, PIK3CA, NOTCH1, SYNE1, and LRP1B. Mutations in the TP53, TTN, CDKN2A, and NOTCH1 genes were more frequent among the high-risk group, whereas mutations in the NSD1 and FLG genes were more prevalent among the other group. Comparing m^6A-related mRNAs in different groups revealed that the expression levels of YTHDC2, YTHDF1, ALKBH5, IGFBP2, and FTO ($P < 0.001$), RBM15B, VIRMA, YTHDC1, and HNRNPC ($P < 0.01$), and HNRNPA2B1 ($P < 0.05$) were statistically different (Figure 4(e)).

3.5. Evaluation of Immunological Characteristics. Based on CIBERSORT, we found that NK-cell resting, eosinophil, T-cell $CD4^+$ naive, mast cell resting, M0 macrophage were more plentiful in the high-risk group, and T-cell follicular helper, T-cell $CD8^+$, mast cell activated, regulatory T-cell, B-cell naive, B-cell plasma, B-cell memory, myeloid dendritic cell resting, monocyte, M1 macrophage were more plentiful in the low-risk group (Figures 5(a) and 5(b), details in *Supplementary 8*). The vast majority of immune functions were statistically different among distinct groups, except for antigen-presenting cell coinhibition, macrophages, major histocompatibility complex class I, response to type I Interferon, and parainflammation (Figure 6(a)). The relationship between immune cell proportions and immune function and survival status was analyzed (*Supplementary 9* and *Supplementary 10*). We also explored whether the model was associated with ICIs and found statistically significant differences in the expression of CTLA-4, PDCD1, LAG3, TIGIT, BTLA, and others in different groups (Figure 6(b)).

3.6. Exploration of ICIs Therapeutics. To estimate the underlying clinical efficacy of immunotherapy of the prognostic model, TIDE was used to evaluate this, and lower TIDE prediction scores indicated a higher likelihood of patients benefiting from treatment with ICIs, as represented by a lower potential for immune evasion. In our results, no statistical differences in TIDE scores were found between distinct groups, but TIDE scores were low in both groups, indicating that both groups were able to benefit better from treatment with ICIs (Figure 7(a)). In addition, we found that the low-risk group had a higher microsatellite instability (MSI) score
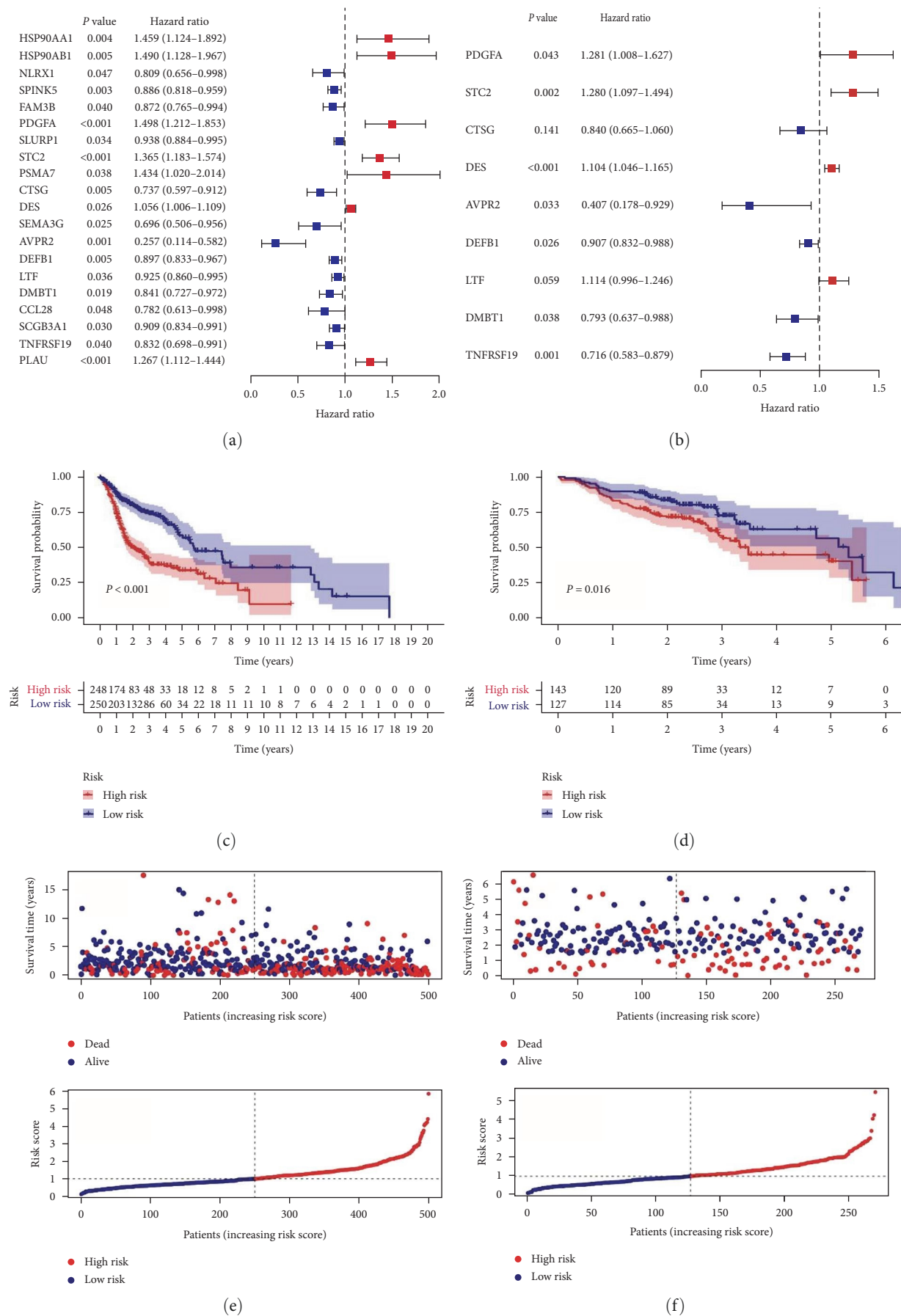
FIGURE 1: Prognostic analysis of distinct prognostic signature groups: (a) univariate Cox analysis of 20 IRGs; (b) multivariate Cox regression analysis of nine IRGs; (c and d) Kaplan–Meier survival analysis; (e and f) risk scores and survival outcome.

(a)

(b)

(c)

(d)

(e)

FIGURE 2: Continued.

	P value	Hazard ratio	
Age	0.035	1.380 (1.023–1.861)	
Gender	0.120	0.779 (0.568–1.067)	
Grade	0.203	1.161 (0.923–1.459)	
Stage	<0.001	1.452 (1.206–1.748)	
Risk score	<0.001	1.851 (1.582–2.166)	

Hazard ratio

(f)

	P value	Hazard ratio	
Age	0.009	1.509 (1.108–2.056)	
Gender	0.038	0.708 (0.511–0.980)	
Grade	0.905	0.985 (0.769–1.262)	
Stage	<0.001	1.537 (1.275–1.854)	
Risk score	<0.001	2.060 (1.715–2.474)	

Hazard ratio

(g)
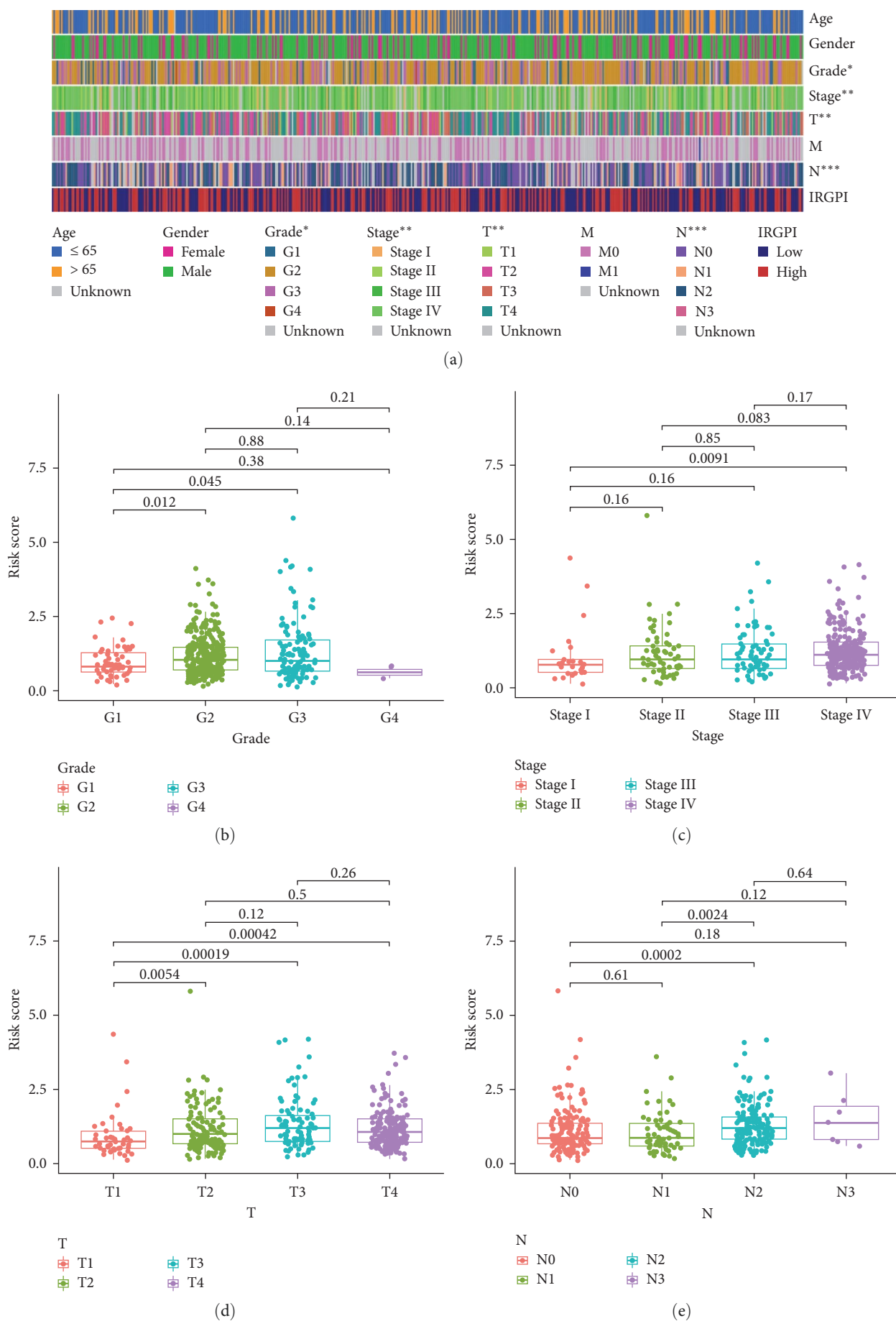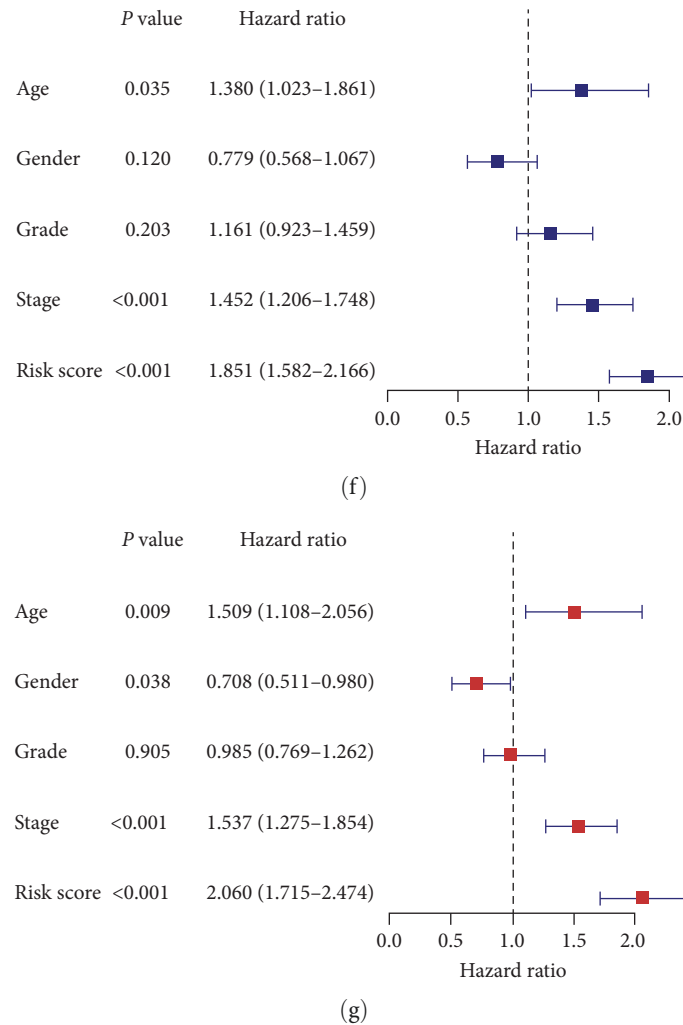
FIGURE 2: Assessment of clinical characteristics for the model: (a–e) the relationship between the model and traditional clinical characteristics; (f and g) univariate and multivariate Cox analysis of the model and traditional clinical characteristics. $*P < 0.05$, $**P < 0.01$, $***P < 0.001$.

and T-cell dysfunction score, whereas the high-risk group had a higher T-cell exclusion score. The AUC of the ROC analysis for 3-year survival prediction showed that the model was more accurate than TIDE and MSI. The AUC values for the 1-, 2-, and 3-year ROC curves in the IRGs prognostic model were all high, indicating that the model had superior sensitivity and specificity for survival prediction (Figure 7(b)). Beyond ICIs blocking therapy, we found that the IC_{50} of docetaxel, gemcitabine, and methotrexate were statistically different among different groups; while the difference in IC_{50} for cisplatin and paclitaxel was minimal (Figure 7(c)).

3.7. Role of PDGFA in HNSC Progression. To clarify the role of PDGFA in HNSC progression, we found by analyzing the TCGA database that: PDGFA expression levels showed a significant positive correlation with TGF-β by Figure 8(a). Correspondingly, we found that PDGFA expression levels were significantly higher in the tissues of HNSC patients with higher epithelial-mesenchymal transition (EMT) viability compared to those with lower EMT viability (Figure 8(b)).

The above data suggest that the aberrant expression of PDGFA expression levels in HNSC may promote distal metastasis of HNSC by promoting EMT and thereby. Further, we performed a knockdown of PDGFA in HNSC and verified the knockdown efficiency by the western blot (WB) (Figure 8(c)). Based on this, we found by transwell assay that: PDGFA knockdown could significantly inhibit the metastatic potential of HNSC cells in vitro (Figure 8(d)). The current first-line treatment regimen of HNSC is still dominated by radiotherapy, and the activation of EMT is closely associated with chemoresistance, according to which we speculate that the abnormal expression of PDGFA may confer chemoresistant properties to HNSC cells. To test our conjecture, we performed 5-Fu treatment in control and PDGFA cells and detected the apoptosis rate by flow assay, and found that: PDGFA knockdown could significantly promote apoptosis induced by 5-Fu treatment, i.e., PDGFA could enhance HNSC for chemotherapy accordingly (Figure 8(e)). In addition, we found that PDGFA expression levels were significantly elevated in HNSC compared to normal tissues
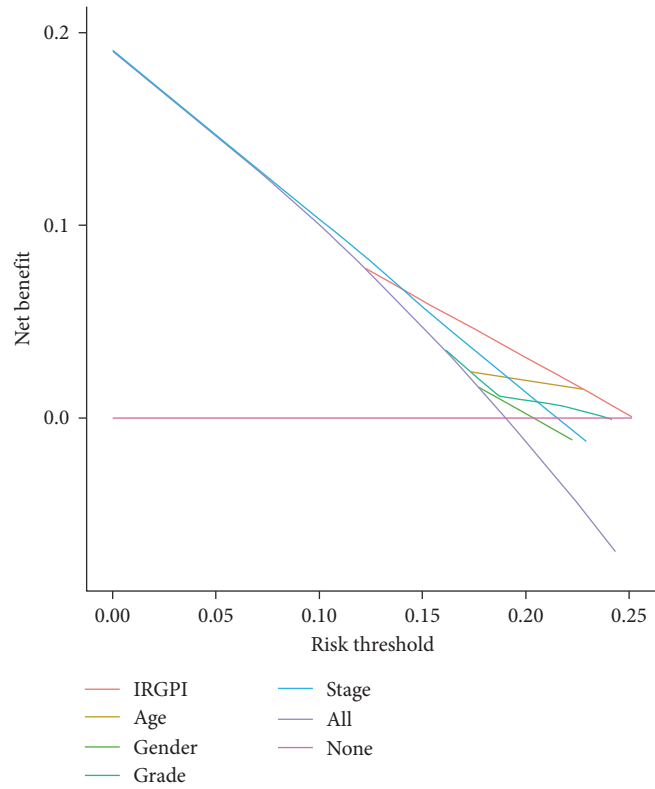
(a)
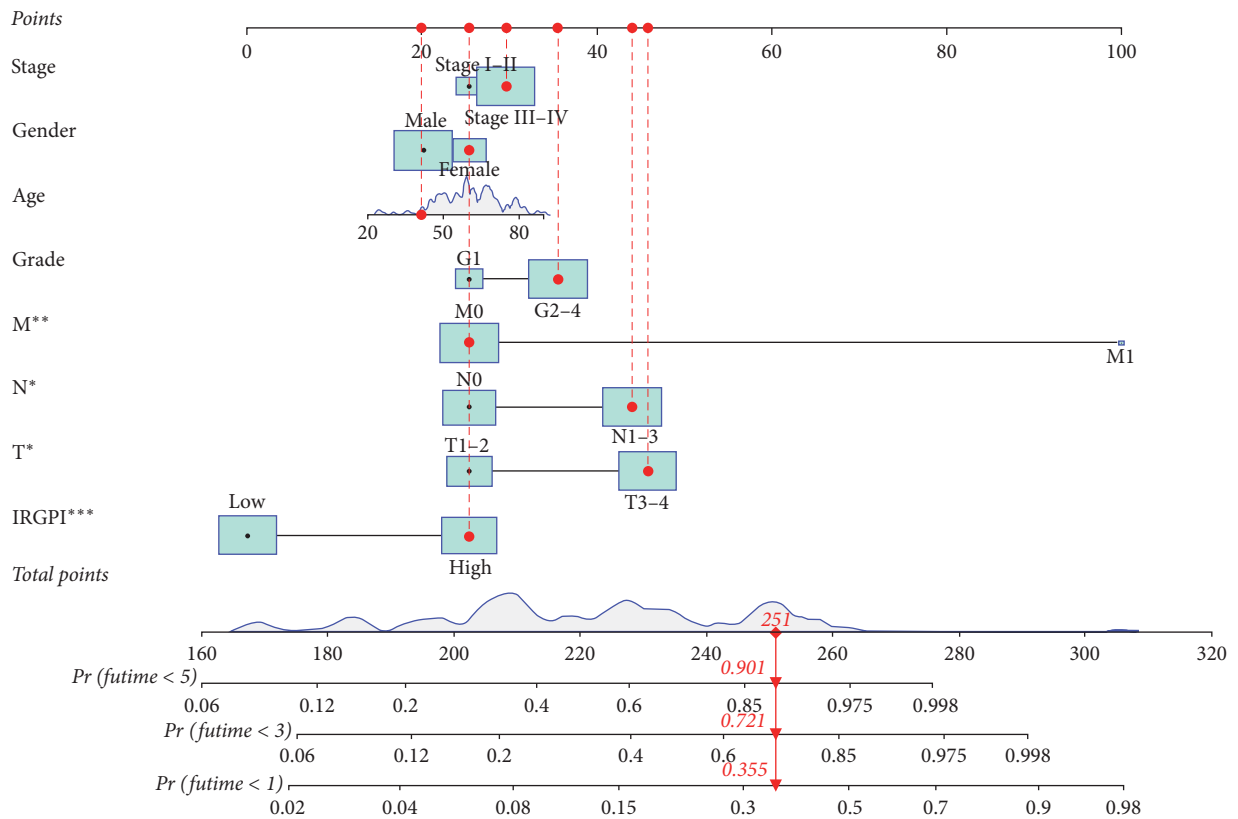
(b)

Figure 3: Exploration of the model: (a) the DCA of the risk model; (b) a nomogram based on clinical characteristics and risk groups. $^*P < 0.05$, $^{**}P < 0.01$, $^{***}P < 0.001$.

(a)

(b)

(c)

(d)
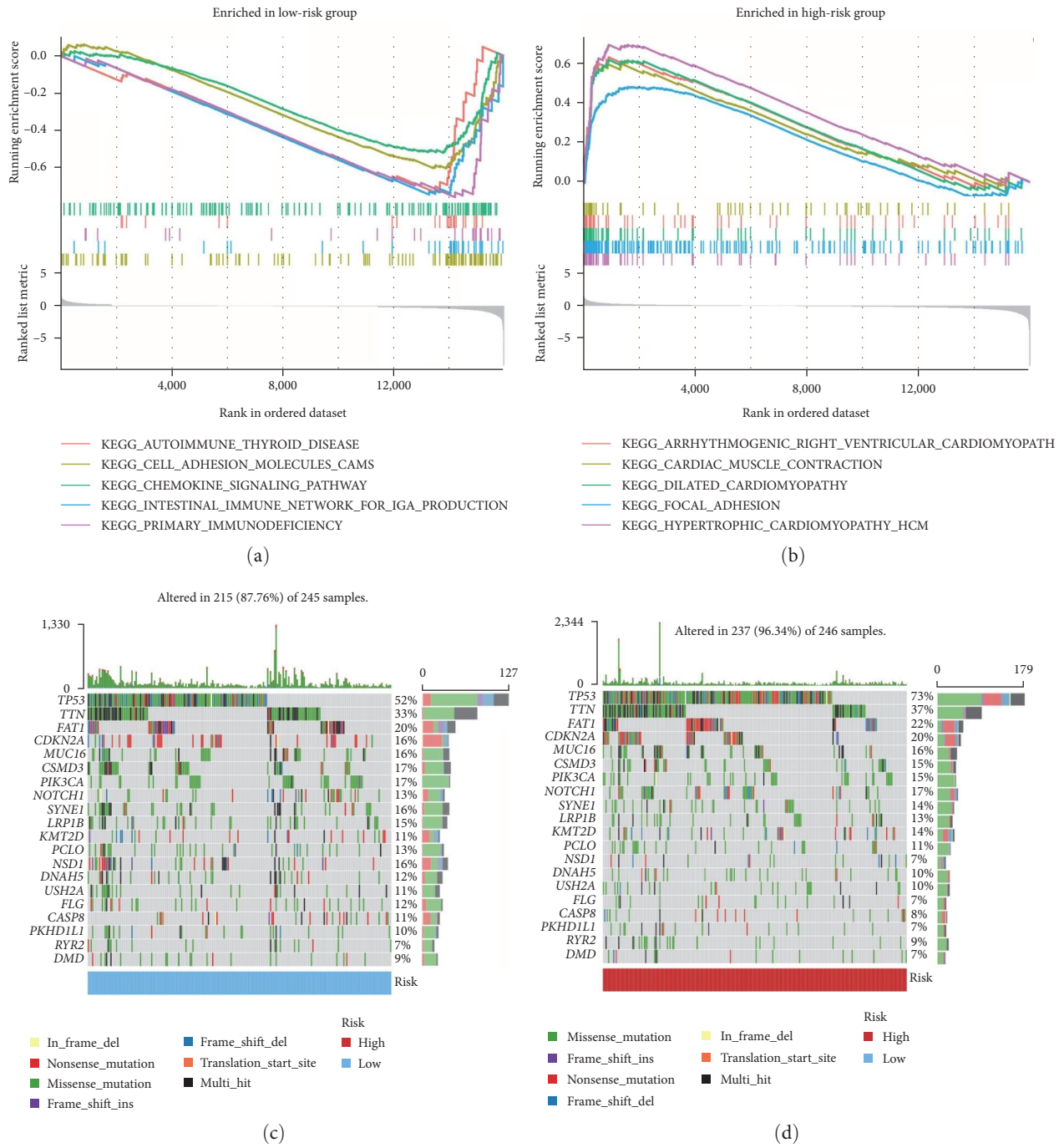
FIGURE 4: Continued.
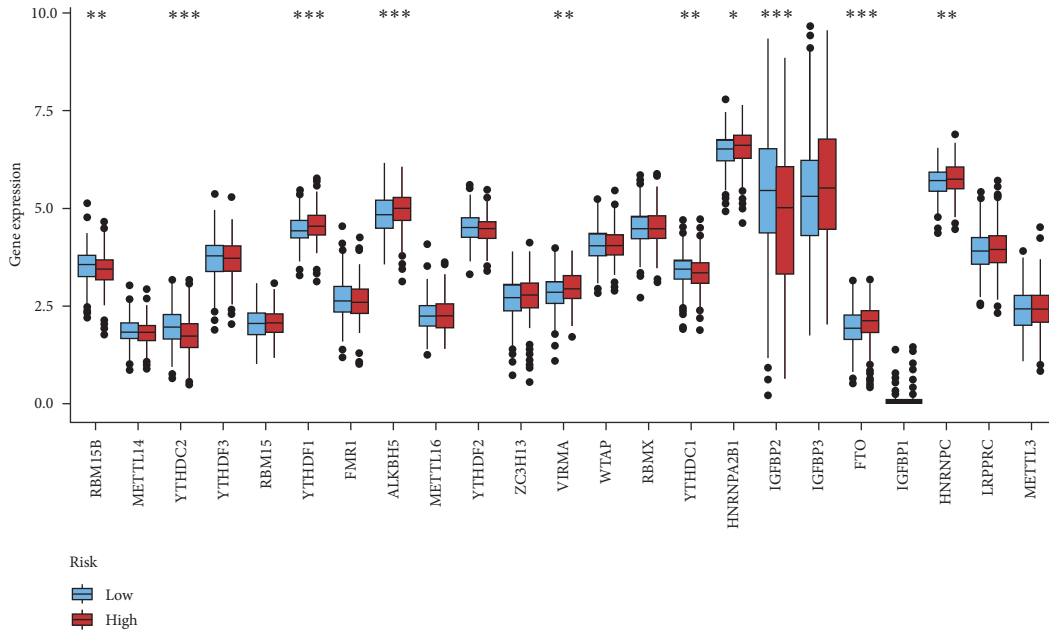
(e)

FIGURE 4: Molecular features of distinct groups: (a and b) genes enriched in distinct groups; (c and d) gene mutation analysis of distinct groups; (e) differences of m^6A-related genes expression among distinct groups. $*P < 0.05$, $**P < 0.01$, $***P < 0.001$.

(a)
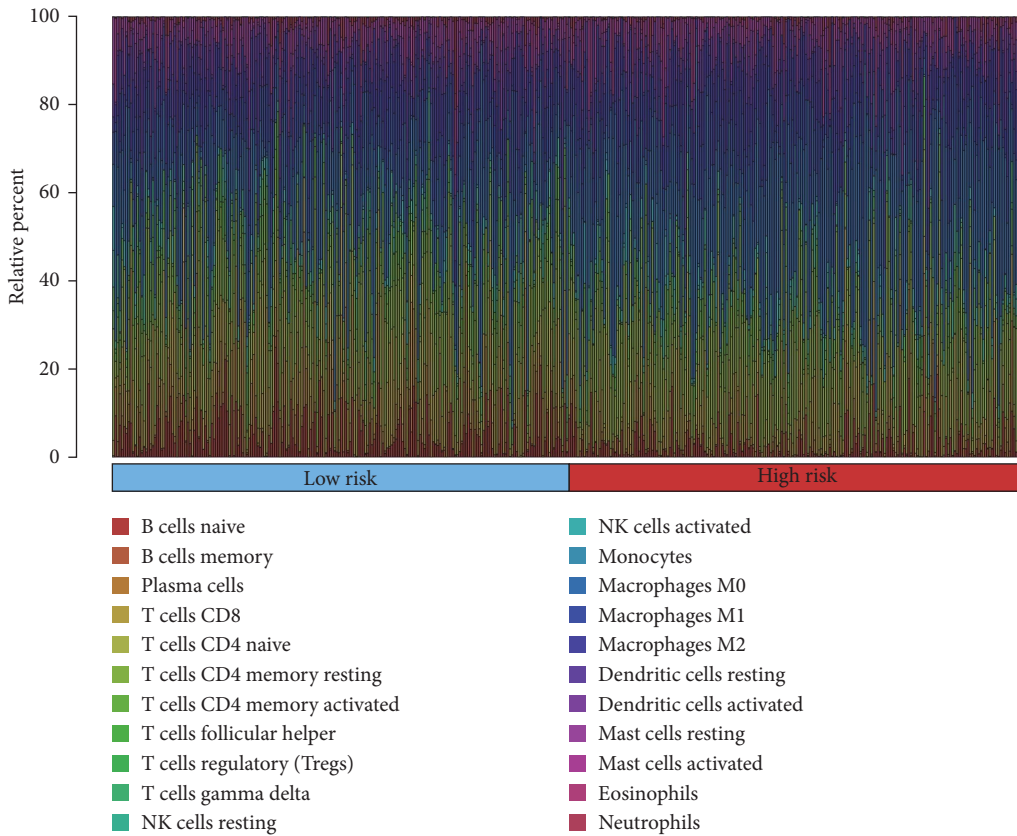
FIGURE 5: Continued.
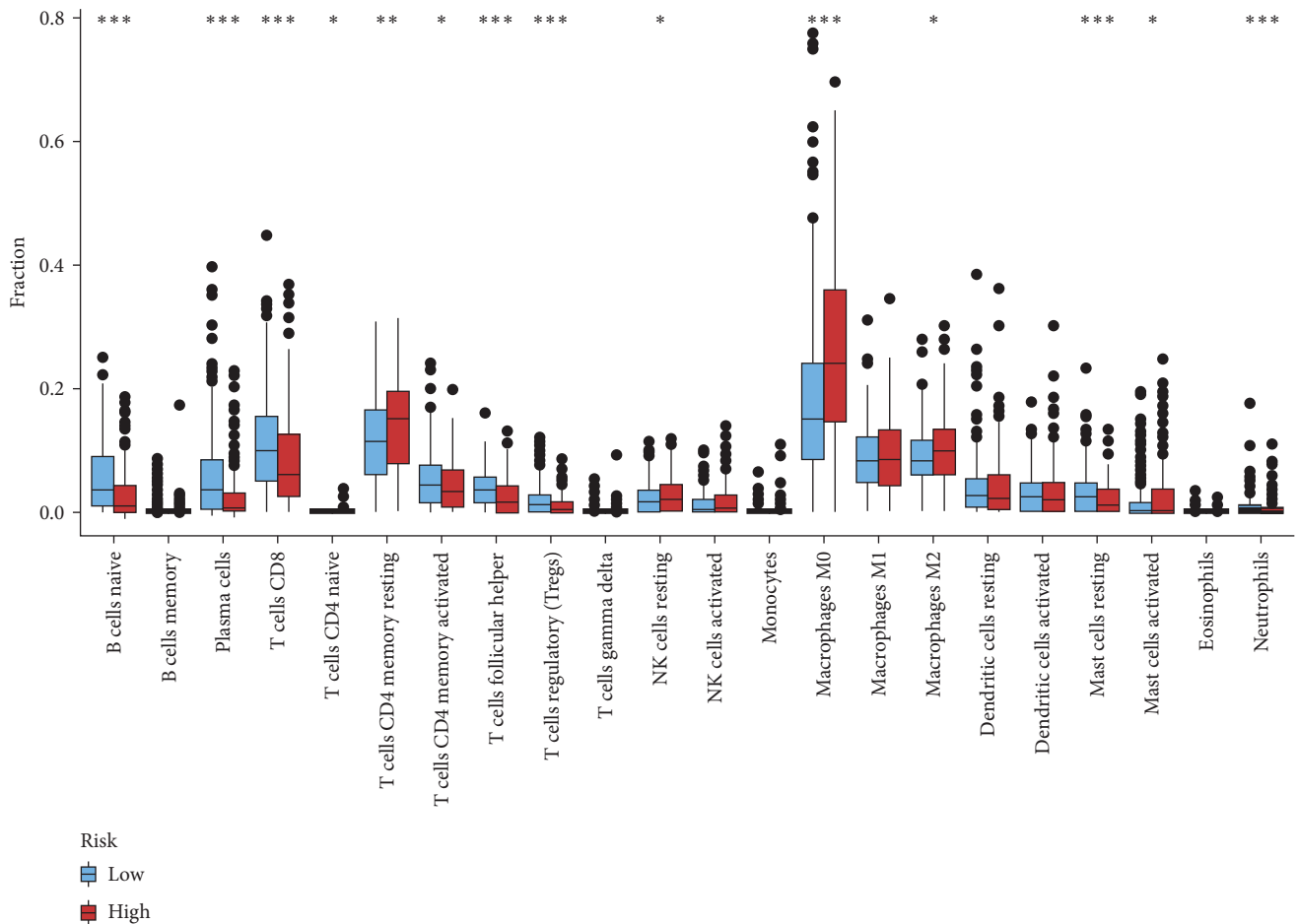
(b)

FIGURE 5: The landscape of the TME in the TCGA-HNSCC set: (a) the proportion of TME cells in the TCGA set; (b) the proportion of each TME cell type in distinct groups. $^{*}P < 0.05$, $^{**}P < 0.01$, $^{***}P < 0.001$.

(Figure 8(f)). And the abnormally elevated level of its expression predicted poor prognosis of patients (Figures 8(g)–8(i)).

4. Discussion

ICIs therapeutics have been demonstrated to be an accurate and safe therapy for relapsed or refractory HNSCC patients [15, 16]. As the general response rate to treatment with ICIs remains low, it is crucial to ascertain those patients who could profit most from those treatments [17, 18]. Over the past few years, although there have been many evaluations of various prognostic signatures for HNSCC, we remain without identifying a validated biomarker for predicting immunotherapy and immune system response. We emphasize the necessity of identifying the optimal treatment population and prognostic genes for response to immunotherapy.

WGCNA is a virtual approach to finding modules of strongly correlated genes, modules, and external sample characteristics and can help recognize potential IRGs or therapeutic targets [19, 20]. WGCNA was used to identify nine IRGs, and the IRGs prognostic model was developed based on TCGA. The model has been shown to be an effective IRGs for HNSCC, with better survival in patients with the low-risk group.

Various studies have indicated that a variety of immune-related biomarkers are related to the outcome of patients with various malignancies, particularly HNSCC [21–23]. Wang et al. [24] set up a nine IRGs signature to analyze the tumor microenvironment and indicate the prognosis for HNSCC. She et al. [25] identified 27 IRGs and established a signature that offers a thorough overview of the immune microenvironment and prognosis of HNSCC. In this study, some of the IRGs that have been recognized during modeling play an important role in the malignant phenotype of different cancer types, especially HNSCC. Humphries et al. reported that CTSG was highly expressed in HNSCC tissues in contrast to paraneoplastic tissues and affected cancer progression and metastasis by activating and inhibiting a large network of protein hydrolytic interactions [25]. Yang et al. found that STC2 facilitates HNSCC proliferation and metastasis by modulating the G1/S cell cycle transition [25]. Zhang et al. [26] demonstrated that the re-expression of LTF could impair the malignancy of HNSCC cells. In summary, the IRGs prognostic model we developed in the study was a novel model that could recognize new biomarkers to be further studied.

The results of GSEA showed that the low-risk group was enriched in cell adhesion molecules, chemokines, and immune-

(a)

(b)
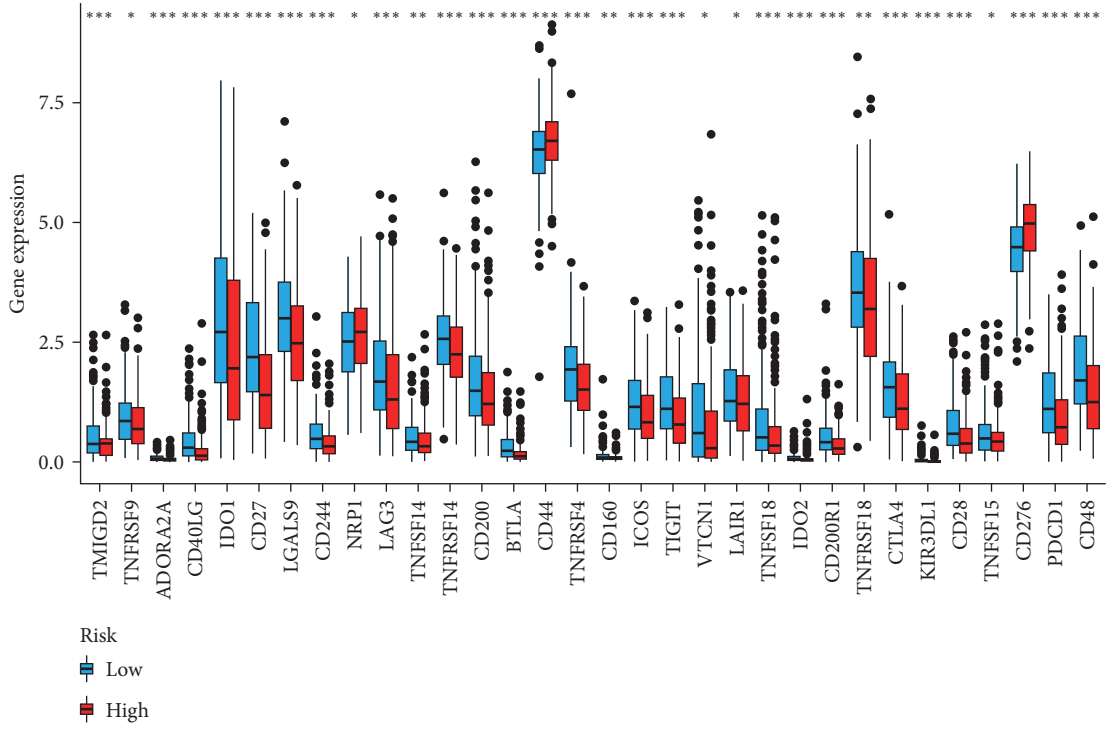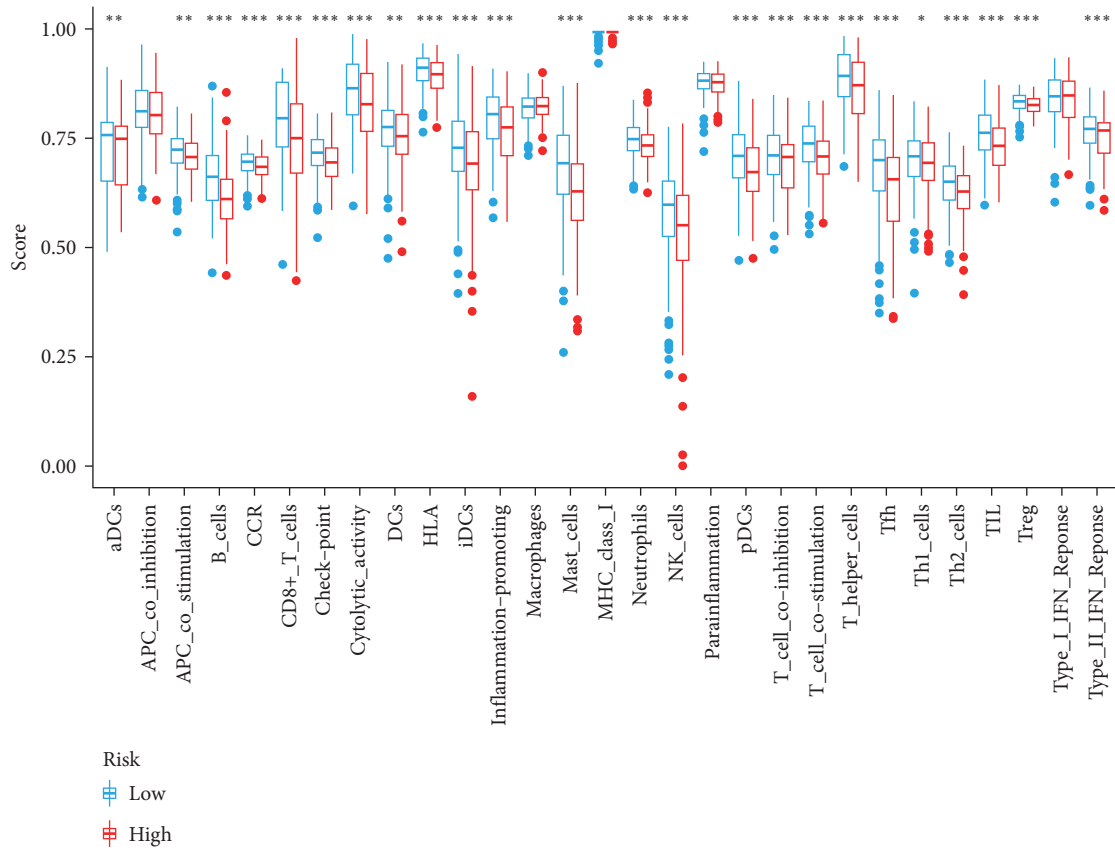
FIGURE 6: Evaluation of immune-related functions and ICIs-related molecules: (a) immune-related function analyzed by the ssGSEA in distinct groups; (b) differences of checkpoint-related genes expression among diverse groups. $^*P < 0.05$, $^{**}P < 0.01$, $^{***}P < 0.001$.
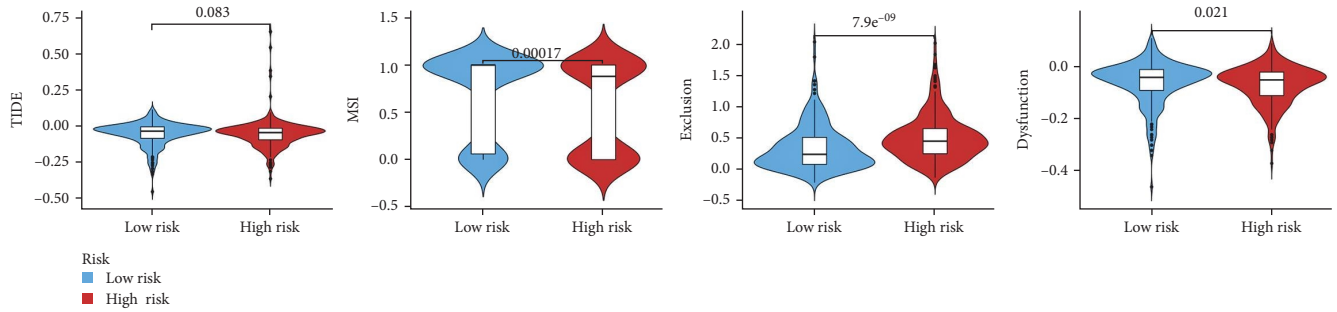
(a)
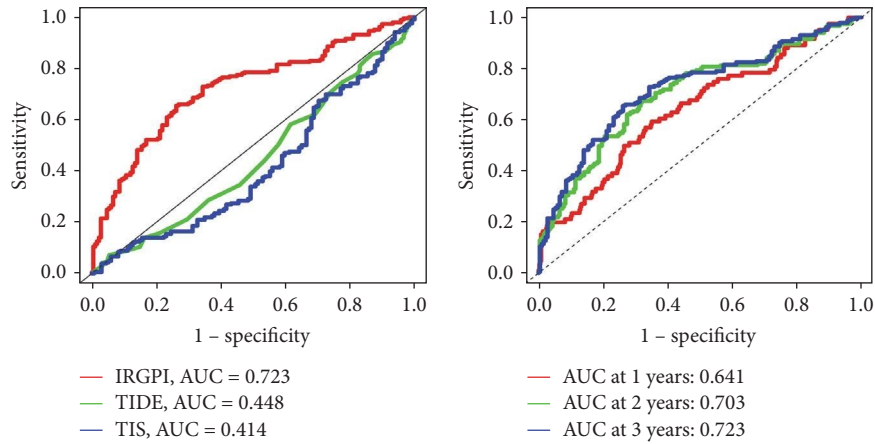
(b)
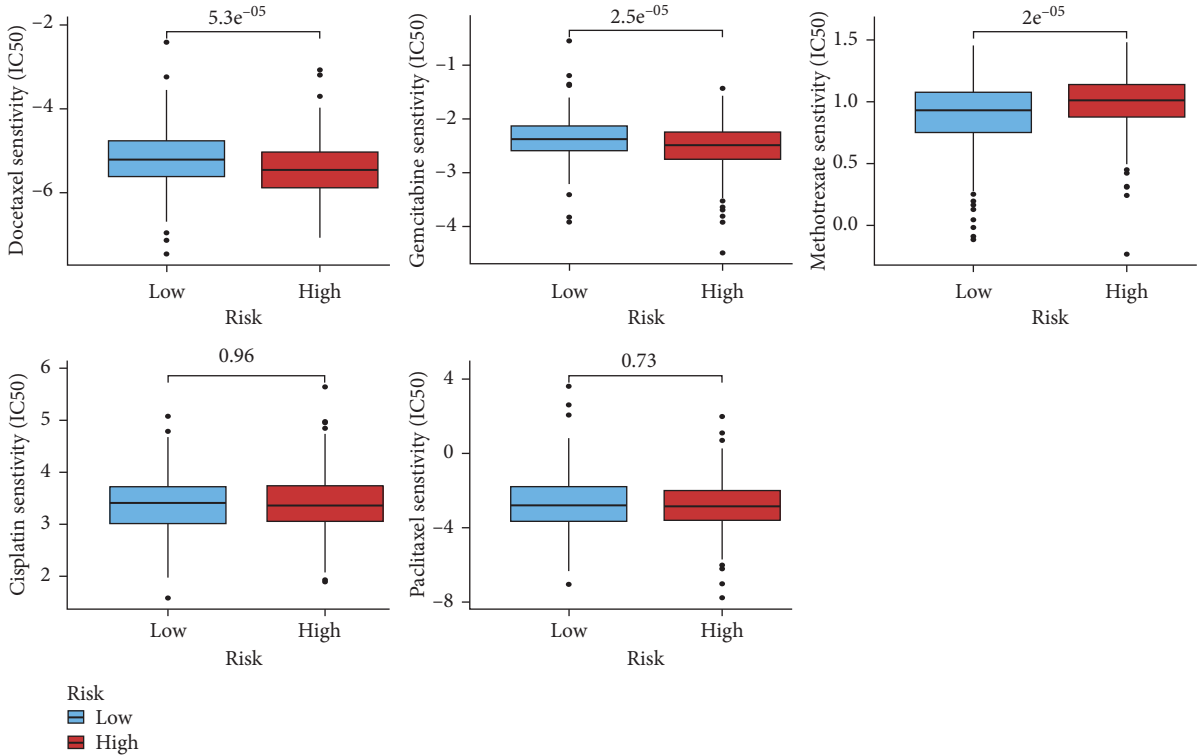
(c)

FIGURE 7: Exploration of ICIs therapeutics in different risk groups: (a) TIDE, MSI, T-cell exclusion, and dysfunction score in distinct groups; (b) ROC analysis of the IRGs prognostic model, TIDE, and TIS on 3-year and ROC analysis of the model in 1-, 2-, and 3-year; (c) differences of IC_{50} of chemotherapeutics among different groups.

(a)

(b)

(c)

(d)

(e)

FIGURE 8: Continued.

(f)

(g)

(h)

(i)
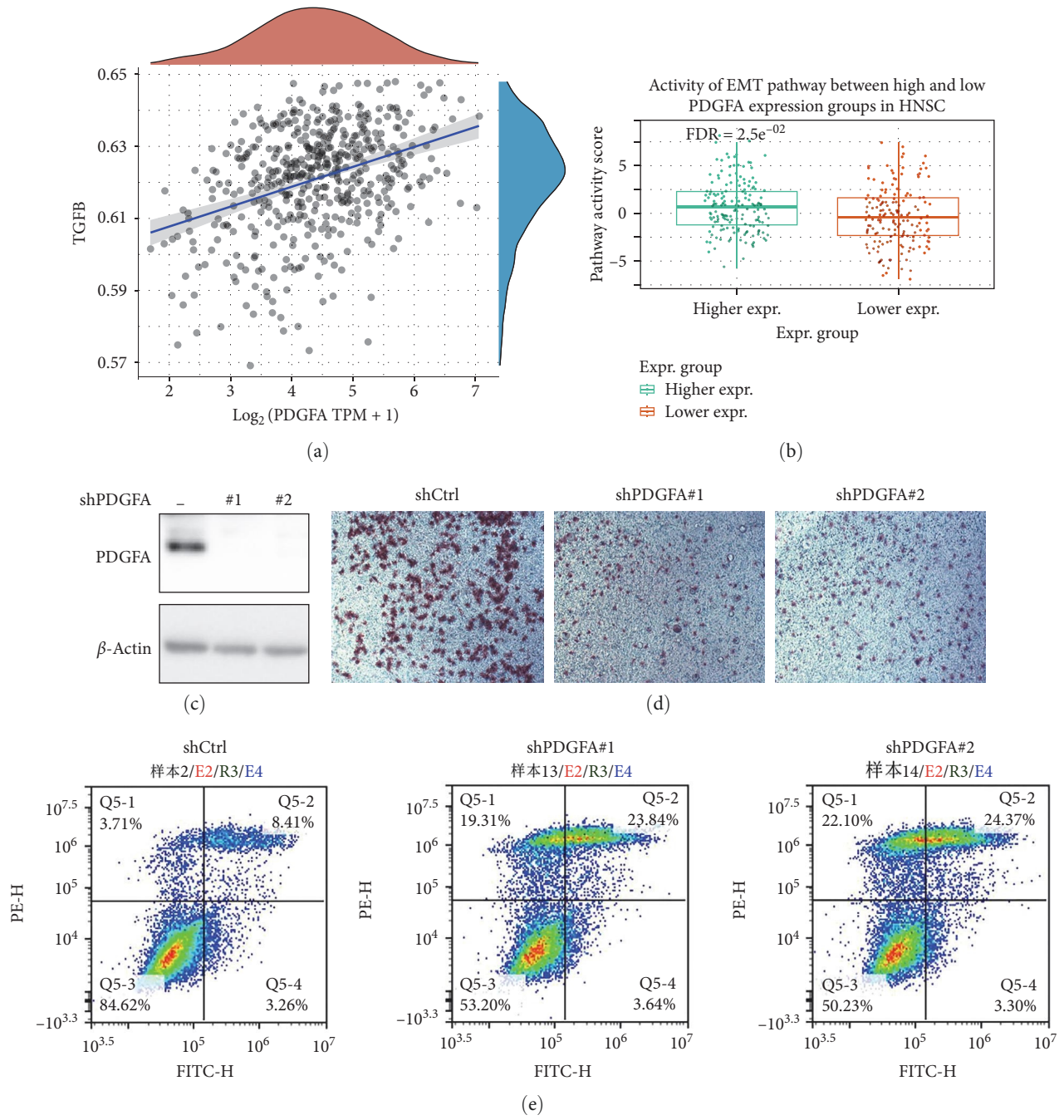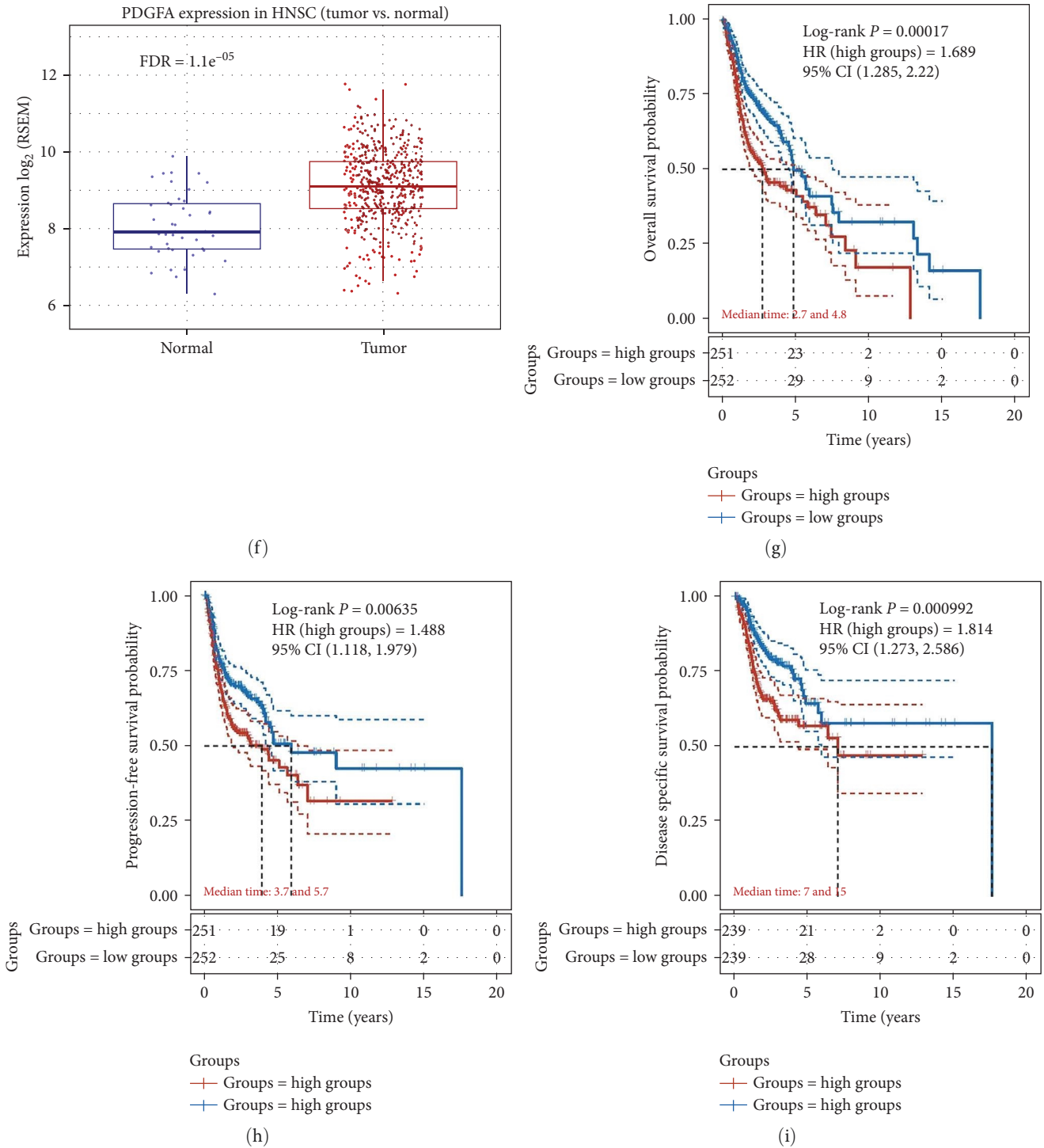
FIGURE 8: Role of PDGFA in HNSC progression: (a) correlation of PDGFA with TGF-β based on TCGA database; (b) PDGFA expression levels in the tissues of HNSC patients; (c) WB analysis validation for PDGFA knockdown in HNSC; (d) PDGFA knockdown inhibit the metastatic potential of HNSC cells in vitro; (e) immunofluorescence detection of the apoptosis rate in control and PDGFA knocked down cells; (f) PDGFA expression levels in HNSC and normal tissues; (g–i) PDGFA expression levels predict the prognosis in HNSC patient.

related pathways, whereas the high-risk group was enriched in focal adhesion, which implied that the low-risk group was characterized by immune activation and suppression of tumor progression. The gene mutations of the high- and low-risk groups showed that the most prevalent type of mutation was the missense variant mutation, next to nonsense mutations and

multiple mutations of a gene, as mentioned previously [26]. TP53 mutation was the most frequent mutation between different groups (73% vs. 52%). The majority of HNSCC patients (about 70%) have the TP53 mutation, while the incidence of this genetic change varies according to the head and neck area [27]. Furthermore, TP53 mutation is related to more invasive

disease and poorer patient prognosis in HNSCC [27]. Thus, the low-risk group with low TP53 mutations had a better prognosis, in agreement with our results. DNA methylation is a form of chemical modification of DNA that can alter genetic expression without altering the DNA sequence [28, 29]. Methylation-related genes in HNSCC have been extensively studied in recent years [30, 31]. In this study, some m^6A-related genes not only differed significantly different among different groups but also correlated with the prognosis of various malignancies, such as FTO, ALKBH5, YTHDF1, and YTHDC2, in agreement with our results [32–35]. In addition, we found that abnormal expression of PDGFA expression levels in HNSC may promote distal metastasis of HNSC by promoting EMT and thus HNSC.

A comprehensive understanding of the immunological landscape can help find new ways to treat HNSCC. CD4$^+$ T cells and NK cells were more prevalent in the high-risk group, whereas CD8$^+$ T cells, M1 macrophages, regulatory T cells, and B cells were more common in the low-risk group. A large number of researches have indicated that CD4$^+$ T cells are related to poor prognosis [32–35]. Conversely, the high density of CD8$^+$ T cells and M1 macrophages are indicative of a good prognosis [36–39]. These research findings are in accordance with ours. However, regulatory T cells and B cells were negatively related to the prognosis of patients in some researches, while others indicated the opposite [40–42]. Similarly, the results of the immune function analysis showed that the low-risk group had more immune activities, which predicted a better prognosis for the low-risk group. Furthermore, our results indicated that the low-risk group was positively associated with the expression of most ICIs, including CTLA-4, PDCD1, LAG3, TIGIT, and BTLA, suggesting that patients in the low-risk group might be able to benefit more from ICI therapy.

TIDE has been developed based on two different mechanisms of tumor immune escape: T-cell dysfunction in cytotoxic T lymphocytes (CTL)-high tumors and T-cell exclusion in CTL-low tumors [43]. In our study, there was no significant difference in TIDE scores between different risk groups, but both their TIDE scores were low. The high-risk group had a higher T-cell exclusion score and lower T-cell dysfunction score, and higher MSI score, which indicated that these patients had higher levels of T-cell exclusion. On the contrary, the low-risk group had a higher T-cell dysfunction score, MSI score, and lower T-cell exclusion score than the high-risk group, which demonstrated that these patients had higher levels of T-cell dysfunction and more MSI. Some researches have demonstrated the prevalence of MSI in HNSCC, and the high mutational burden caused by MSI makes the tumor immunogenic and sensitive to anti-PD1 therapy [44, 45]. TIS, an 18 gene signature developed by NanoString Technologies, has been verified in HNSCC clinical trials (KEYNOTE-012 and KEYNOTE-055) using single-agent pembrolizumab treatment, demonstrating a positive association with response and survival [16, 46]. In the research, the predictive value of the prognostic model was higher than that of TIDE and TIS, and the model consisted of only nine genes and was, therefore, easier to detect than TIDE and TIS. Our findings indicated that the IC$_{50}$ of docetaxel, gemcitabine, and methotrexate were statistically different between different groups, whereas the difference in IC$_{50}$ for cisplatin and paclitaxel was little.

However, the current study has several shortcomings and limitations. First, though external validation has been carried out to verify the predictive power of the model, the exact molecular mechanisms of the nine IRGs have not been explored in the present study. Second, our total sample size is relatively small, and the normal to tumor sample counts are nonproportional. Third, the results may be biased as the majority of samples from TCGA are nonmetastatic. Therefore, in order to further examine and validate our model, we want to recollect more clinical samples, increase the size of our sample, and carefully follow-up on our results.

5. Conclusion

In summary, this study demonstrated that a promising IRGs prognostic model might facilitate the differentiation of immune and molecular features, forecast patient prognosis, and aid in distinguishing those who could benefit from antitumor immunotherapy for HNSCC.

Data Availability

Publicly available datasets were analyzed in this study; these can be found in TCGA (https://portal.gdc.cancer.gov/) and GEO (http://www.ncbi.nlm.nih.gov/geo/).

Conflicts of Interest

The authors declare that they have no conflicts of interest.

Authors' Contributions

YY, YF, and QL drafted the manuscript. CC, CX, and CF designed the figures and tables. JY performed data analysis. YY and JY revised the manuscript. All authors contributed to the article and approved the submitted version. YY, YF, and QL contributed equally to this work.

Acknowledgments

We are very appreciative of the raw data provided by TCGA and the GEO database.

Supplementary Materials

Supplementary 1. Determination of differentially expressed IRGs in HNSCC.

Supplementary 2. The details of GO and KEGG enrichment analysis.

Supplementary 3. Identification of modules by the WGCNA analysis.

Supplementary 4. Analysis of genes in significantly relevant modules.

Supplementary 5. Kaplan–Meier survival curves of twenty survival-associated IRGs ($P < 0.05$).

Supplementary 6. The detailed values of univariate and multivariate Cox regression analysis.

Supplementary 7. The GSEA in different groups.

Supplementary 8. The relative proportion of various immune cells by CIBERSORT.

Supplementary 9. Kaplan–Meier survival curves of immune cell proportion ($P < 0.05$).

Supplementary 10. Kaplan–Meier survival curves of immune function ($P < 0.05$).

References

[1] H. Sung, J. Ferlay, R. L. Siegel et al., "Global cancer statistics 2020: GLOBOCAN estimates of incidence and mortality worldwide for 36 cancers in 185 countries," *CA: A Cancer Journal for Clinicians*, vol. 71, no. 3, pp. 209–249, 2021.

[2] S. Marur and A. A. Forastiere, "Head and neck squamous cell carcinoma: update on epidemiology, diagnosis, and treatment," *Mayo Clinic Proceedings*, vol. 91, no. 3, pp. 386–396, 2016.

[3] J. D. Cramer, B. Burtness, Q. T. Le, and R. L. Ferris, "The changing therapeutic landscape of head and neck cancer," *Nature Reviews Clinical Oncology*, vol. 16, pp. 669–683, 2019.

[4] R. L. Ferris, "Immunology and immunotherapy of head and neck cancer," *Journal of Clinical Oncology*, vol. 33, no. 29, pp. 3293–3304, 2015.

[5] A. G. Ramsay, "Immune checkpoint blockade immunotherapy to activate anti-tumour T-cell immunity," *British Journal of Haematology*, vol. 162, no. 3, pp. 313–325, 2013.

[6] J. Moskovitz, J. Moy, and R. L. Ferris, "Immunotherapy for head and neck squamous cell carcinoma," *Current Oncology Reports*, vol. 20, Article ID 22, 2018.

[7] G. Wichmann, M. Rosolowski, K. Krohn et al., "The role of HPV RNA transcription, immune response-related gene expression and disruptive *TP53* mutations in diagnostic and prognostic profiling of head and neck cancer," *International Journal of Cancer*, vol. 137, no. 12, pp. 2846–2857, 2015.

[8] F. Cunningham, J. E. Allen, J. Allen et al., "Ensembl 2022," *Nucleic Acids Research*, vol. 50, no. D1, pp. D988–D995, 2022.

[9] K. Breuer, A. K. Foroushani, M. R. Laird et al., "InnateDB: systems biology of innate immunity and beyond—recent updates and continuing curation," *Nucleic Acids Research*, vol. 41, no. D1, pp. D1228–D1233, 2013.

[10] G. Yu, L.-G. Wang, Y. Han, and Q.-Y. He, "clusterProfiler: an R package for comparing biological themes among gene clusters," *OMICS: A Journal of Integrative Biology*, vol. 16, no. 5, pp. 284–287, 2012.

[11] D. Szklarczyk, A. L. Gable, K. C. Nastou et al., "The STRING database in 2021: customizable protein–protein networks, and functional characterization of user-uploaded gene/measurement sets," *Nucleic Acids Research*, vol. 49, no. D1, pp. D605–D612, 2021.

[12] C. B. Steen, C. L. Liu, A. A. Alizadeh, and A. M. Newman, "Profiling cell type abundance and expression in bulk tissues with CIBERSORTx," in *Stem Cell Transcriptional Networks*, B. Kidder, Ed., vol. 2117 of *Methods in Molecular Biology*, pp. 135–157, Humana, New York, NY, 2020.

[13] D. Damotte, S. Warren, J. Arrondeau et al., "The tumor inflammation signature (TIS) is associated with anti-PD-1 treatment benefit in the CERTIM pan-cancer cohort," *Journal of Translational Medicine*, vol. 17, Article ID 357, 2019.

[14] J. Fu, K. Li, W. Zhang et al., "Large-scale public data reuse to model immunotherapy response and resistance," *Genome Medicine*, vol. 12, Article ID 21, 2020.

[15] E. E. W. Cohen, D. Soulières, C. Le Tourneau et al., "Pembrolizumab versus methotrexate, docetaxel, or cetuximab for recurrent or metastatic head-and-neck squamous cell carcinoma (KEYNOTE-040): a randomised, open-label, phase 3 study," *The Lancet*, vol. 393, no. 10167, pp. 156–167, 2019.

[16] T. Y. Seiwert, B. Burtness, R. Mehra et al., "Safety and clinical activity of pembrolizumab for treatment of recurrent or metastatic squamous cell carcinoma of the head and neck (KEYNOTE-012): an open-label, multicentre, phase 1b trial," *The Lancet Oncology*, vol. 17, no. 7, pp. 956–965, 2016.

[17] Y. Chen, Z.-Y. Li, G.-Q. Zhou, and Y. Sun, "An immune-related gene prognostic index for head and neck squamous cell carcinoma," *Clinical Cancer Research*, vol. 27, no. 1, pp. 330–341, 2021.

[18] K. Du, J. Zou, B. Wang et al., "A metabolism-related gene prognostic index bridging metabolic signatures and antitumor immune cycling in head and neck squamous cell carcinoma," *Frontiers in Immunology*, vol. 13, Article ID 857934, 2022.

[19] T. Krüger, "Editorial change at statistical applications in genetics and molecular biology," *Statistical Applications in Genetics and Molecular Biology*, vol. 17, no. 4, Article ID 20180046, 2018.

[20] H. Wang, X. Wu, and Y. Chen, "Stromal-immune score-based gene signature: a prognosis stratification tool in gastric cancer," *Frontiers in Oncology*, vol. 9, Article ID 1212, 2019.

[21] W. Hong, L. Liang, Y. Gu et al., "Immune-related lncRNA to construct novel signature and predict the immune landscape of human hepatocellular carcinoma," *Molecular Therapy Nucleic Acids*, vol. 22, pp. 937–947, 2020.

[22] J. Yin, X. Li, C. Lv et al., "Immune-related lncRNA signature for predicting the immune landscape of head and neck squamous cell carcinoma," *Frontiers in Molecular Biosciences*, vol. 8, Article ID 689224, 2021.

[23] Y. Lv, S.-Y. Lin, F.-F. Hu et al., "Landscape of cancer diagnostic biomarkers from specifically expressed genes," *Briefings in Bioinformatics*, vol. 21, no. 6, pp. 2175–2184, 2020.

[24] Z. Wang, H. Yuan, J. Huang et al., "Prognostic value of immune-related genes and immune cell infiltration analysis in the tumor microenvironment of head and neck squamous cell carcinoma," *Head & Neck*, vol. 43, no. 1, pp. 182–197, 2021.

[25] Y. She, X. Kong, Y. Ge et al., "Immune-related gene signature for predicting the prognosis of head and neck squamous cell carcinoma," *Cancer Cell International*, vol. 20, Article ID 22, 2020.

[26] J. Zhang, T. Ling, H. Wu, and K. Wang, "Re-expression of *Lactotransferrin*, a candidate tumor suppressor inactivated by promoter hypermethylation, impairs the malignance of oral squamous cell carcinoma cells," *Journal of Oral Pathology & Medicine*, vol. 44, no. 8, pp. 578–584, 2015.

[27] G. Zhou, Z. Liu, and J. N. Myers, "*TP53* mutations in head and neck squamous cell carcinoma and their impact on disease progression and treatment response," *Journal of Cellular Biochemistry*, vol. 117, no. 12, pp. 2682–2692, 2016.

[28] A. L. Mattei, N. Bailly, and A. Meissner, "DNA methylation: a historical perspective," *Trends in Genetics*, vol. 38, no. 7, pp. 676–707, 2022.

[29] M. Kulis and M. Esteller, "DNA methylation and cancer," *Advances in Genetics*, vol. 70, pp. 27–56, 2010.

[30] S. Virani, E. Light, L. A. Peterson et al., "Stability of methylation markers in head and neck squamous cell carcinoma," *Head & Neck*, vol. 38, no. S1, pp. E1325–E1331, 2016.

[31] C. Zhou, M. Ye, S. Ni et al., "DNA methylation biomarkers for head and neck squamous cell carcinoma," *Epigenetics*, vol. 13, no. 4, pp. 398–409, 2018.

[32] X. Zhao, Y. Chen, Q. Mao et al., "Overexpression of YTHDF1 is associated with poor prognosis in patients with hepatocellular carcinoma," *Cancer Biomarkers*, vol. 21, no. 4, pp. 859–868, 2018.

[33] S. Sun, Q. Han, M. Liang, Q. Zhang, J. Zhang, and J. Cao, "Downregulation of m^6 A reader YTHDC2 promotes tumor progression and predicts poor prognosis in non-small cell lung cancer," *Thoracic Cancer*, vol. 11, no. 11, pp. 3269–3279, 2020.

[34] A. Strick, F. von Hagen, L. Gundert et al., "The N^6 -methyladenosine (m^6 A) erasers alkylation repair homologue 5 (ALKBH5) and fat mass and obesity-associated protein (FTO) are prognostic biomarkers in patients with clear cell renal carcinoma," *BJU International*, vol. 125, no. 4, pp. 617–624, 2020.

[35] Y. Nagaki, S. Motoyama, T. Yamaguchi et al., "m^6 A demethylase ALKBH5 promotes proliferation of esophageal squamous cell carcinoma associated with poor prognosis," *Genes to Cells*, vol. 25, no. 8, pp. 547–561, 2020.

[36] G. Bindea, B. Mlecnik, M. Tosolini et al., "Spatiotemporal dynamics of intratumoral immune cells reveal the immune landscape in human cancer," *Immunity*, vol. 39, no. 4, pp. 782–795, 2013.

[37] W. H. Fridman, L. Zitvogel, C. Sautès–Fridman, and G. Kroemer, "The immune contexture in cancer prognosis and treatment," *Nature Reviews Clinical Oncology*, vol. 14, pp. 717–734, 2017.

[38] A. J. Gentles, A. M. Newman, C. L. Liu et al., "The prognostic landscape of genes and infiltrating immune cells across human cancers," *Nature Medicine*, vol. 21, pp. 938–945, 2015.

[39] D. H. Josephs, H. J. Bax, and S. N. Karagiannis, "Tumour-associated macrophage polarisation and re-education with immunotherapy," *Frontiers in Bioscience (Elite Ed)*, vol. 7, no. 2, pp. 334–351, 2015.

[40] A. Sarvaria, J. A. Madrigal, and A. Saudemont, "B cell regulation in cancer and anti-tumor immunity," *Cellular & Molecular Immunology*, vol. 14, pp. 662–674, 2017.

[41] P. Tsou, H. Katayama, E. J. Ostrin, and S. M. Hanash, "The emerging role of B cells in tumor immunity," *Cancer Research*, vol. 76, no. 19, pp. 5597–5601, 2016.

[42] D. Wolf, S. Sopper, A. Pircher, G. Gastl, and A. M. Wolf, "Treg (s) in cancer: friends or foe?" *Journal of Cellular Physiology*, vol. 230, no. 11, pp. 2598–2605, 2015.

[43] P. Jiang, S. Gu, D. Pan et al., "Signatures of T cell dysfunction and exclusion predict cancer immunotherapy response," *Nature Medicine*, vol. 24, pp. 1550–1558, 2018.

[44] J. C. Dudley, M.-T. Lin, D. T. Le, and J. R. Eshleman, "Microsatellite instability as a biomarker for PD-1 blockade," *Clinical Cancer Research*, vol. 22, no. 4, pp. 813–820, 2016.

[45] R. Mandal, R. M. Samstein, K.-W. Lee et al., "Genetic diversity of tumors with mismatch repair deficiency influences anti-PD-1 immunotherapy response," *Science*, vol. 364, no. 6439, pp. 485–491, 2019.

[46] W. J. Ho and R. Mehra, "Pembrolizumab for the treatment of head and neck squamous cell cancer," *Expert Opinion on Biological Therapy*, vol. 19, no. 9, pp. 879–885, 2019.

Hindawi

Research Article

LINC00174 Promotes Colon Cancer Progression by Regulating Inflammation and Glycolysis by Targeting the MicroRNA-2467-3p/Enolase 3 Axis

Sheng Xu [iD],[1] **Jiawei Lin,**[1] **Rong Chen,**[1] **Junjie Xie** [iD],[2] **Enquan Yuan,**[1] **Fajie Cen,**[1] **and Fanbiao Kong**[1]

[1]*Department of General Surgery, People's Hospital of Guangxi Zhuang Autonomous Region, 530021 Nanning, China*
[2]*Oncology Department, General Hospital of Central Theater Command, Wuluo 627, Wuhan, 430070 Hubei Province, China*

Correspondence should be addressed to Sheng Xu; feisheng00@163.com and Junjie Xie; junjie0219@sina.com

Objective. To elucidate the mechanism by which LINC00174 promotes colon cancer progression by targeting the microRNA-2467-3p (miR-2467-3p)/enolase 3 (ENO3) axis to regulate inflammation and glycolysis. *Methods*. The expression of LINC00174 and ENO3 in colon cancer tissues, its relationship with survival rate, and correlation were analyzed using bioinformatic analysis. The effects of LINC00174 overexpression and silencing on the biological behavior of and inflammation in colon cancer cells were analyzed via transfection experiments. The target relationships between miR-2467-3p or LINC00174 and ENO3 were verified using sequence prediction and the dual-luciferase reporter assay, respectively. Furthermore, LINC00174- and/or miR-2467-3p-overexpressing cells were prepared to determine the effects on ENO3 protein levels and glycolysis. Finally, the effects of LINC00174 and/or miR-2467-3p overexpression on colon cancer, ENO3 protein levels, and inflammation were analyzed using a tumor-bearing mice model. *Results*. LINC00174 and ENO3 were overexpressed and associated with a lower survival rate. LINC00174 was positively correlated with ENO3 in colon cancer tissues. Furthermore, the overexpression of LINC00174 in colon cancer cell lines promoted the proliferation, migration, and invasion of colon cancer cells and inflammation but inhibited apoptosis. The overexpression of miR-2467-3p inhibited ENO3 protein levels, which was attenuated via LINC00174 overexpression. Furthermore, it inhibited the biological behavior of and inflammation and glycolysis in colon cancer cells and blocked their LINC00174-induced promotion. Moreover, using animal experiments, the regulatory effects of LINC00174 on tumor growth, ENO3 protein levels, and inflammation via miR-2467-3p were confirmed. *Conclusion*. LINC00174 promotes the glycolysis, inflammation, proliferation, migration, and invasion of colon cancer cells and inhibits apoptosis. The cancer-promoting mechanism of LINC00174 is related to targeting miR-2467-3p to promote ENO3 protein levels.

1. Introduction

A global statistical report revealed 1,148,515 new cases of colon cancer and 576,858 colon cancer-related deaths in 2020, accounting for 6.0% and 5.8% of all tumors, respectively; this makes colon cancer the fifth most common cancer type [1]. Surgery or combination chemotherapy is the main treatment strategy to decrease tumor burden and prolong patient survival [2, 3]. Nevertheless, patients with

colon cancer have a poor prognosis, with an overall 5-year survival rate of approximately 60% [4, 5]. However, the detection of this cancer type is difficult at an early stage, and the survival rate of advanced colon cancer is only 8%–30% [6, 7]. Colon cancer is also associated with chronic inflammation, and diseases such as ulcerative colitis may further progress to colon cancer [8, 9]. Furthermore, chronic inflammation is conducive to tumor cell metastasis [10, 11]. Moreover, increased interleukin- (IL-)

1β and IL-8 levels promote the migration and invasion of colon cancer cells [12, 13]. Therefore, it is extremely crucial to determine colon cancer pathogenesis.

Long noncoding RNAs (lncRNAs) can competitively adsorb microRNAs (miRNAs) and inhibit their posttranscriptional gene expression [14]. Furthermore, they can promote colon cancer progression by inducing inflammation, such as taurine upregulated 1 [15, 16]. LINC00174 has been recently discovered as a cancer-promoting lncRNA; it plays a role in promoting the progression of liver cancer [17], breast cancer [18], and osteosarcoma [19]. A sequencing-based study reported that LINC00174 is associated with colon cancer prognosis and is involved in regulating glucose metabolism [20]. However, the effect and mechanism of LINC00174 on the biological behavior of colon cancer cells remain unclear.

Tumor cells produce ATP mainly via glycolysis, even if the oxygen supply is sufficient; this is known as the Warburg effect [21, 22]. Tumor cells can rapidly obtain energy via glycolysis, which is conducive to tumor cell growth [23]. The Warburg effect can increase the aggressiveness of colon cancer cells; therefore, reversing glycolysis can be a potential approach to treat colon cancer [24, 25]. Enolase 3 (ENO3) is a β-enolase that regulates striated muscle development [26]. Genomic analysis revealed that ENO3 is associated with the risk of colon cancer and that it is involved in the regulation of glycolysis [27]. Elevated levels of glycolysis result in the activation of inflammatory pathways [28], which are also involved in tumor progression [29]. However, this mechanism remains unvalidated at the cellular and animal levels, and the mechanism by which ENO3 expression is regulated remains unclear.

The present study is aimed at determining the mechanism by which LINC00174 regulates ENO3, glycolysis, and inflammation and elucidates its effects on colon cancer. Our goal is to provide a novel theoretical foundation for colon cancer diagnosis and treatment.

2. Materials and Methods

2.1. Bioinformatic Analysis.
Colon cancer cases in The Cancer Genome Atlas (TCGA) database were analyzed using the starBase tool. For differential analysis, 471 tumor tissue samples and 41 normal tissue samples were included. For survival analysis, 447 samples were included. The survival rate of the LINC00174 or ENO3 high- and low-expression groups was analyzed and compared using the logrank test. Further, the correlation between LINC00174 and ENO3 in colon tissues was analyzed using the Pearson test.

2.2. Cell Culture.
FHC, a human colon epithelial cell line (CRL-1831); Caco-2, a colon cancer cell line (HTB-37); SW480 (CCL-228); COLO201 (CCL-224); and HCT116 (CCL-247EMT) were acquired from American Type Culture Collection (Manassas, VA, USA). All cell lines were maintained in Dulbecco's modified Eagle medium (DMEM) (Gibco, USA) supplemented with 10% fetal bovine serum (FBS), 100 mg/mL streptomycin, and 100 units/mL penicillin (Sigma-Aldrich, USA). The cells were cultured in a 5% CO_2 incubator at 37°C and 95% humidity. In some experiments, the cells were treated with 5 mM 2-deoxy-d-glucose (2-DG) for 48 h to inhibit cellular glycolysis.

2.3. Cell Transfection.
Transfection experiments to silence LINC00174 were performed using Caco-2 cells with relatively high LINC00174 expression. Transfection experiments to overexpress LINC00174 were performed using COLO201 cells. Moreover, Caco-2 cells were used to cotransfect LINC00174 and the miR-2467-3p mimic. siLINC00174, siENO3, LINC00174, miR-2467-3p mimic, and corresponding siNC/NC/mimic NC were obtained from GenePharma Co., Ltd. (China). Briefly, 50 pmol (0.67 μg) plasmid was diluted with 25 μL of serum-free DMEM (reagent A). Then, 1 μL of Entranster™-R4000 (Engreen) and 24 μL of serum-free DMEM were mixed for 25 min (reagent B). The transfection complex was prepared by thoroughly mixing 25 μL of reagent A and 25 μL of reagent B (aspirate 10 times using a pipette) and standing for 15 min. Cells in 0.45 mL of complete medium were transfected with 50 μL of the transfection complex. siNC/NC/mimic NC plasmids were used as controls.

2.4. RT-qPCR.
For analysis, 400 μL of TRIzol (Thermo Fisher, USA) was added to the cells or tissues in a 1.5 mL sterile RNase-free EP tube. The cells or tissues were ground to a homogenate, followed by the addition of 600 μL of TRIzol and mixing for 5 min. Then, the cells were centrifuged for 5 min (4°C, 12,000 × g), and the pellet was discarded. TRIzol and chloroform were mixed at a ratio of 1 : 2 and added to the supernatant of the previous step, followed by shaking for 15 s. Thereafter, isopropanol was added to precipitate the RNA in the aqueous phase. The collected RNA pellet was carefully washed with 75% ethanol to remove impurities. RNA was redissolved in diethylpyrocarbonate-treated water and stored at −80°C. RNA was reverse transcribed into cDNA using the PrimeScript RT reagent kit (RR047A, Takara) under the following conditions: 37°C/15 min and 98°C/5 min. qPCR amplification was performed using the SYBR Green reagent (Takara, Japan) under the following conditions: 94°C for 3 min, followed by 40 cycles at 94°C for 15 s, 58°C for 20 s, and 72°C for 30 s. The expression of LINC00174 and mRNAs was normalized to that of GAPDH using the $2^{-\Delta\Delta Ct}$ method. The expression of miR-2467-3p, miR-3918, and miR-542-3p was normalized to that of U6. The primers used were as follows: LINC00174 F: 5′-AAGCCCCTGGGGAATGTTTC-3′, R: 5′-AAGCCCCTG GGGAATGTTTC-3′; IL-1β F: 5′-TCCTTGCCCCTTCCATG AACC-3′, R: 5′-TTACTTGGCACCCTGTTTGC-3′; IL-8 F: 5′-GGCAGCCTTCCTGATTTCTG-3′, R: 5′-AATTTCTGT GTTGGCGCAGTG-3′; IL-10 F: 5′-GAGATGCCTTCAGC AGAGTGA-3′, R: 5′-ACTCATGGCTTTGTAGATGCCT-3′; GAPDH F: 5′-TTTCTGACTCCGTGAACCGC-3′, R: 5′-AGTCCTTCCACGATACCAAAGTT-3′; miR-2467-3p F: 5′-CCTGAGGCTCTGTTAGCCTT-3′, R: 5′-ACAGACCCTGA GCCTCTC-3′; miR-3918 F: 5′-GGTTAAGCCATGGGAC AGGG-3′, R: 5′-CTACGAACCAGGTGCAGGG-3′; miR-542-3p F: 5′-TCGGGGATCATCATGTCACG-3′, R: 5′-

GAGTGGCTCCCAGACCTTTC-3′; and U6 F: 5′-CTCGCT
TCGGCAGCACA-3′, R: 5′-AACGCTTCACGAATTTGCG
T-3′.

2.5. Measurement of IL-1β, IL-8, and IL-10 Levels via Enzyme-Linked Immunosorbent Assay (ELISA).

In transfection experiments, Caco-2 cells with relatively high LINC00174 expression were used to silence LINC00174, whereas COLO201 cells were used to overexpress LINC00174. The cells were collocated and centrifuged at $1000 \times g$ for 15 min at 4°C. The supernatant was collected and transferred into 96-well plates. The levels of IL-1β, IL-8, and IL-10 were measured using ELISA kits (Invitrogen, USA) following the manufacturer's instructions. Optical density (OD) was measured using a microplate reader (Biotek, Winooski, VT, USA). The levels of IL-1β, IL-8, and IL-10 were expressed as microgram per milliliter.

2.6. Cell Counting Kit-8 (CCK-8) Assay.

The cell suspension (100 μL) at a density of 5×10^4/mL was added into the wells of a 96-well plate. After 24, 48, and 72 h, 10 μL of the CCK-8 solution was added. The plates were gently mixed on an orbital shaker for 1 min at 37°C to ensure uniform mixing. The plates were then incubated for 2 h for the dehydrogenation reaction. The OD was measured at a wavelength of 450 nm using a microplate reader (Biotek).

2.7. Flow Cytometry.

Cells were collected and trypsinized without EDTA. After washing with PBS and centrifuging the samples two times at 2000 rpm for 5 min, 5×10^5 cells were collected and resuspended in 500 μL of binding buffer. Then, 5 μL of annexin V-fluorescein isothiocyanate and propidium iodide (Sanjiang Biological Technology Co., Ltd., China) was used to mark apoptotic cells (15 min in the dark). After 30 min, flow cytometry (BD FACSCalibur, USA) was performed for detection. Normal cells were used for fluorescence compensation modulation to set the position of the cross gates.

2.8. Scratch Healing Assay.

Cells were grown to 90%–95% confluency in 6-well plates to form a monolayer under the abovementioned conditions. Then, a 200 μL pipette tip was used to make vertical scratches from top to bottom. This was considered 0 h, and the scratch width was recorded. After the streaked cells were washed away, the cells were cultured in serum-free medium. Photographs were captured after 24 h to assess scratch healing.

2.9. Transwell Assay.

Matrigel (1:8 dilution; Corning, USA) was added to the upper chamber, and the sample was incubated at 37°C for 30 min. Then, 600 μL of complete medium (20% FBS) was added to the lower chamber of the 24-well Transwell device. The cells (5×10^4/mL) were cultured in serum-free medium at 37°C for 24 h for starvation treatment. After digestion, 100 μL of cell solution (5×10^4/mL) was added to the hydrated Transwell chamber. After 24 h, the uninvaded cells were washed away, and the infiltrated cells in the lower chamber were fixed with 95% ethanol and stained with 0.1% crystal violet for 20 min at room temperature (25°C). The number of cells was counted in five random fields in a ×400-fold field of view.

2.10. Analysis of Glycolysis Levels.

Glycolysis level was determined by detecting glucose intake and lactic acid secretion. Briefly, 1×10^5 cells were seeded in a Petri dish and incubated for 24 h under the abovementioned conditions. Then, the medium was removed, and 5 mL of medium without FBS and L-glutamine was added. After incubation for 8 h, the supernatant was collected via centrifugation. Glucose intake was detected using the Amplex Red Glucose/Glucose Oxidase Assay Kit (Molecular Probes, CA, USA). Lactic acid production was detected using a lactic acid detection kit (BioVision, CA, USA).

2.11. Dual-Luciferase Reporter Assay.

For the dual-luciferase reporter assay, 1 μg of wild-type (wt) LINC00174/ENO3-pGL4 (Promega Corporation, USA) or mutant LINC00174/ENO3-pGL4 (induced using the QuickMutation™ Kit, Beyotime, China), 50 nmol miR-2467-3p mimic/mimic NC, and 150 ng Renilla luciferase plasmid (Beyotime) were transfected into 3×10^4 cells using Lipofectamine® 2000 at 37°C for 36 h. Luciferase activity was measured using the dual-luciferase reporter gene detection kit (Promega Corporation). All data were normalized to Renilla luciferase activity.

2.12. Western Blotting.

The cells or tissues were collected and incubated with RIPA lysis solution on ice for 30 min. Then, total protein was obtained via centrifugation at $12000 \times g$ for 20 min at 4°C. Sodium dodecyl sulfate-polyacrylamide gel electrophoresis was performed to separate the proteins. The rabbit monoclonal primary antibody of ENO3 (1:1000) (ab157474, Abcam, USA) was added to the membrane (4°C, overnight). Then, the membrane was washed two times with Tris-buffered saline/0.1% Tween (TBST) solution. The membrane was then incubated with secondary antibodies (1:2000, ab6721) for 2 h at 37°C. The membrane was washed three times with TBST. The protein blots were visualized using an ECL kit (Solarbio) and detected using IPP6.0 (Media Cybernetics, USA).

2.13. Construction of the Syngeneic Model.

Four-week-old male normal BALB/C mice (Charles River Co., Ltd., China) were used to detect cell tumorigenesis. The animals were housed in an environment of 24°C±1°C and 60% ± 5% relative humidity. In total, 24 mice were grouped using the random number table method, with 6 mice in each group. Briefly, 5×10^6 CT26-wt cells were resuspended in 200 μL of PBS and injected into the armpit area of the mice. Twenty-eight days after transplantation, the mice were sacrificed and tumors were collected for weighing. The animals were euthanized when the diameter of the tumor was >2 cm (not involved in this experiment). Protocols involving animals were approved by the ethics committee of the People's Hospital of Guangxi Zhuang Autonomous Region.

2.14. Statistical Analysis.

All experiments were independently performed in triplicate. Data were expressed as mean ± SD. Statistical analysis was performed using one-way analysis of variance and Tukey's multiple comparison tests (GraphPad

Prism version 7.0). The *t*-test was used to analyze the differences between the two groups. Survival analysis was performed using the logrank test. A *P* value of < 0.05 was considered statistically significant.

3. Results

3.1. LINC00174 Is Overexpressed in Colon Cancer and Associated with a Poor Prognosis. To preliminarily analyze LINC00174 expression in colon cancer, LINC00174 expression in colon cancer tissues in TCGA database was obtained for analysis. LINC00174 expression was significantly increased in colon cancer tissues (Figure 1(a)). Patients with high LINC00174 expression had a significantly decreased survival rate ($P = 0.025$) (Figure 1(b)). Compared with normal colon epithelial cells, LINC00174 expression was significantly upregulated in colon cancer cell lines (Figure 1(c)). This suggests that LINC00174 plays a positive role in colon cancer. Caco-2 cells with relatively high LINC00174 expression and COLO201 cells with relatively low LINC00174 expression were used in the subsequent experiments.

3.2. Silencing or Overexpression of LINC00174 Affects the Growth, Migration, and Invasion of Caco-2 Cells. To determine the effects of LINC00174 on colon cancer cells, Caco-2 was used as a model cell line for LINC00174 silencing. Figure 2(a) illustrates the transfection results. Cell viability was significantly decreased after LINC00174 silencing (Figure 2(b)). After LINC00174 inhibition, the apoptosis rate increased from approximately 5% to approximately 20% (Figure 2(c)). The level of scratch healing was significantly decreased in the siLINC00174 group after 24 h (Figure 2(d)). Furthermore, the number of cells that invaded the lower chamber of the Transwell device was lower in the siLINC00174 group than in the siNC group (Figure 2(e)).

COLO201 cells with relatively low LINC00174 expression were used to overexpress LINC00174 (Figure 2(f)). When LINC00174 expression increased in the cells, the proliferation ability significantly increased, whereas the apoptosis rate decreased (Figures 2(g) and 2(h)). Increasing LINC00174 expression increased the scratch healing rate from 60% to approximately 90% after 24 h (Figure 2(i)). The number of cells that invaded the lower chamber of the Transwell device was higher in the LINC00174 group than in the NC group (Figure 2(j)).

3.3. Silencing or Overexpression of LINC00174 Affects Inflammation in Caco-2 Cells. A decrease in LINC00174 expression decreased the expression of the proinflammatory factors IL-1β and IL-8 (Figures 3(a) and 3(b)) but increased the mRNA expression of the anti-inflammatory factor IL-10 (Figure 3(c)). These results suggest that LINC00174 silencing inhibits the malignant biological behavior of and inflammation in colon cancer cells. ELISA revealed that IL-1β and IL-8 levels were significantly decreased in the siLINC00174 group, whereas IL-10 levels were significantly increased in the siLINC00174 group compared with the siNC group (Figures 3(d)–3(f)). Moreover, LINC0017 overexpression promoted the mRNA expression of the proinflammatory

factors IL-1β and IL-8 (Figures 3(g) and 3(h)) but decreased that of the anti-inflammatory factor IL-10 (Figure 3(i)). This further confirms the promoting effects of LINC00174 on colon cancer. In contrast, when LINC00174-overexpressing cells were treated with 2-DG, a glycolytic inhibitor, or ablated with ENO3 (siENO3), the effects of LINC00174 overexpression on the inflammatory factors were significantly abolished (Figures 3(g)–3(l)). Compared with the LINC00174 group, IL-1β and IL-8 levels were significantly decreased in the LINC00174+2-DG and LINC00174 +siENO3 groups (Figures 3(g), 3(h), 3(j), and 3(k)), whereas IL-10 levels were significantly increased in these two groups (Figures 3(i) and 3(l)).

3.4. Construction of the LINC00174/miR-2467-3p/ENO3 Axis. TCGA analysis revealed that ENO3 expression was increased in colon cancer tissues (Figure 4(a)). Patients with high ENO3 expression had a significantly decreased survival rate ($P = 0.025$) (Figure 4(b)). Using the colon cancer samples in TCGA database, LINC00174 was found to be positively correlated with ENO3 ($r = 0.458$, $P < 0.001$) (Figure 4(c)). The respective target miRNAs of LINC00174 and ENO3 were predicted, and three common miRNAs were identified: miR-2467-3p, miR-3918, and miR-542-3p (Figure 4(d)). To determine the differences in these three miRNAs, the effects of LINC00174 alterations on them were examined. LINC00174 silencing increased miR-2467-3p levels in Caco-2 cells; however, it had no significant effects on miR-3918 and miR-542-3p levels (Figure 4(e)). Similarly, LINC00174 overexpression suppressed miR-2467-3p levels in COLO201 cells; however, the effects on the other two miRNAs were not statistically significant (Figure 4(f)). Taken together, these results suggest that miR-2467-3p is a key miRNA in colon cancer regulation via LINC00174.

3.5. LINC00174 Targets miR-2467-3p to Regulate ENO3. To preliminarily verify the LINC00174/miR-2467-3p/ENO3 axis, cell experiments were performed; the results demonstrated that LINC00174 bound to miR-2467-3p and that miR-2467-3p bound to the 3′-UTR of ENO3 (Figures 5(a)–5(d)). Furthermore, miR-2467-3p-overexpressing COLO201 cells were constructed (Figure 5(e)). Elevated miR-2467-3p levels inhibited ENO3 protein levels (Figure 5(f)). This suggests that LINC00174 targets miR-2467-3p to regulate ENO3.

3.6. LINC00174/miR-2467-3p Regulates ENO3 Expression and Colon Cell Biological Behavior and Glycolysis. To determine the LINC00174/miR-2467-3p/ENO3 axis and its effect on colon cells, COLO201 cells overexpressing LINC00174 and/or miR-2467-3p were constructed via transfection. Elevated LINC00174 levels increased ENO3 protein levels, whereas miR-2467-3p inhibited ENO3 protein levels (Figures 6(a) and 6(b)). Furthermore, LINC00174 overexpression reversed ENO3 repression via miR-2467-3p. This suggests that LINC00174 promotes ENO3 protein levels by targeting miR-2467-3p.

Elevated miR-2467-3p levels decreased cell proliferation ability, whereas LINC00174 overexpression not only

(a)

(b)

(c)
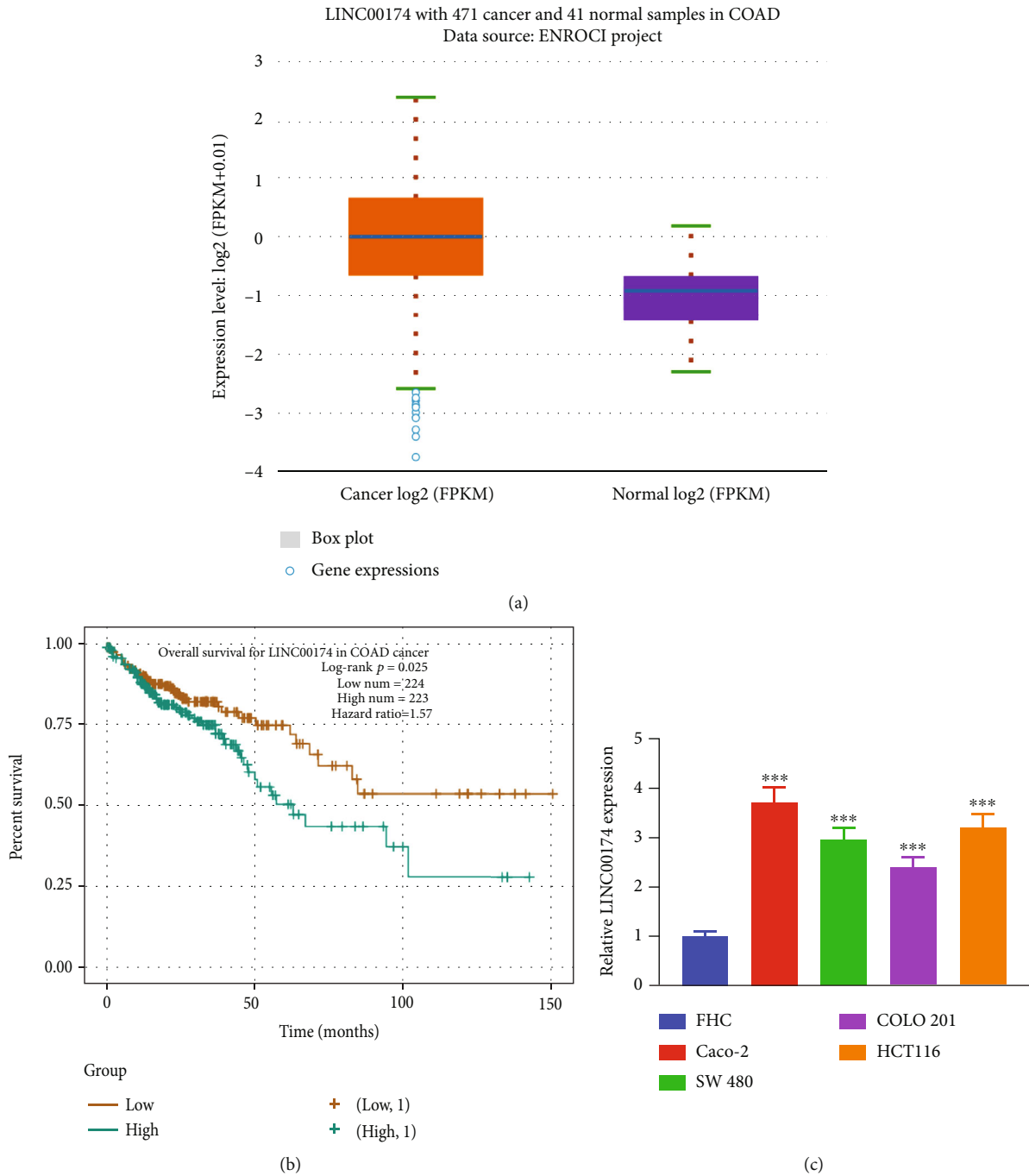
Figure 1: LINC00174 is overexpressed in colon cancer and associated with poor prognosis. (a) LINC00174 expression in colon cancer tissues in The Cancer Genome Atlas database. (b) The relationship between different LINC00174 levels and the survival rate of patients with colon cancer. (c) LINC0017 expression in human colonic epithelial cells and colon cancer cell lines. ***$P < 0.001$ vs. FHC.

promoted cell proliferation ability but also reversed the inhibitory effects of miR-2467-3p on the cells (Figure 6(c)). Furthermore, miR-2467-3p overexpression blocked the antiapoptotic effect of LINC00174 (Figures 6(d) and 6(e)). Compared with the NC+mimic NC group, the migration and invasive abilities of the LINC00174+mimic NC group were increased. Furthermore, the migration and invasive abilities of the LINC00174+mimic group were significantly lower than those of the LINC00174+mimic NC group and significantly higher than those of the NC+mimic group

(Figures 7(a)–7(d)). LINC00174 overexpression reversed the inhibitory effects of miR-2467-3p on cell motility. Taken together, the results suggest that the function of LINC00174 in regulating colon cancer is inseparable from that of miR-2467-3p.

Tumor cells absorb large amounts of glucose via glycolysis and produce lactate. Because ENO3 is involved in sugar metabolism and glycolysis, we elucidated the effects of LINC00174 and/or miR-2467-3p overexpression on glycolysis levels. Elevation of miR-2467-3p decreased glucose

(a)

(b)

(c)

(d)

(e)

FIGURE 2: Continued.

(f)

(g)

(h)

(i)

(j)
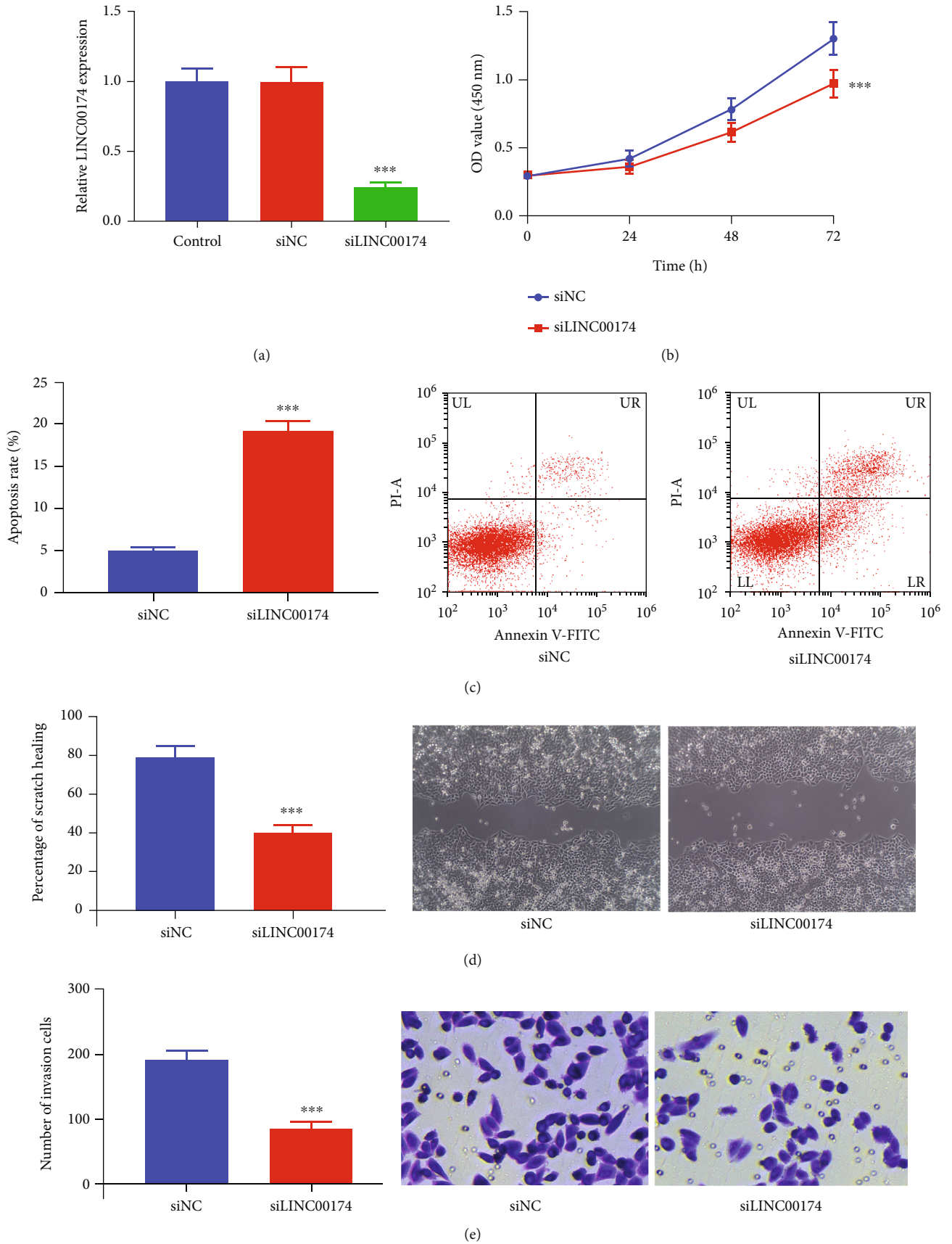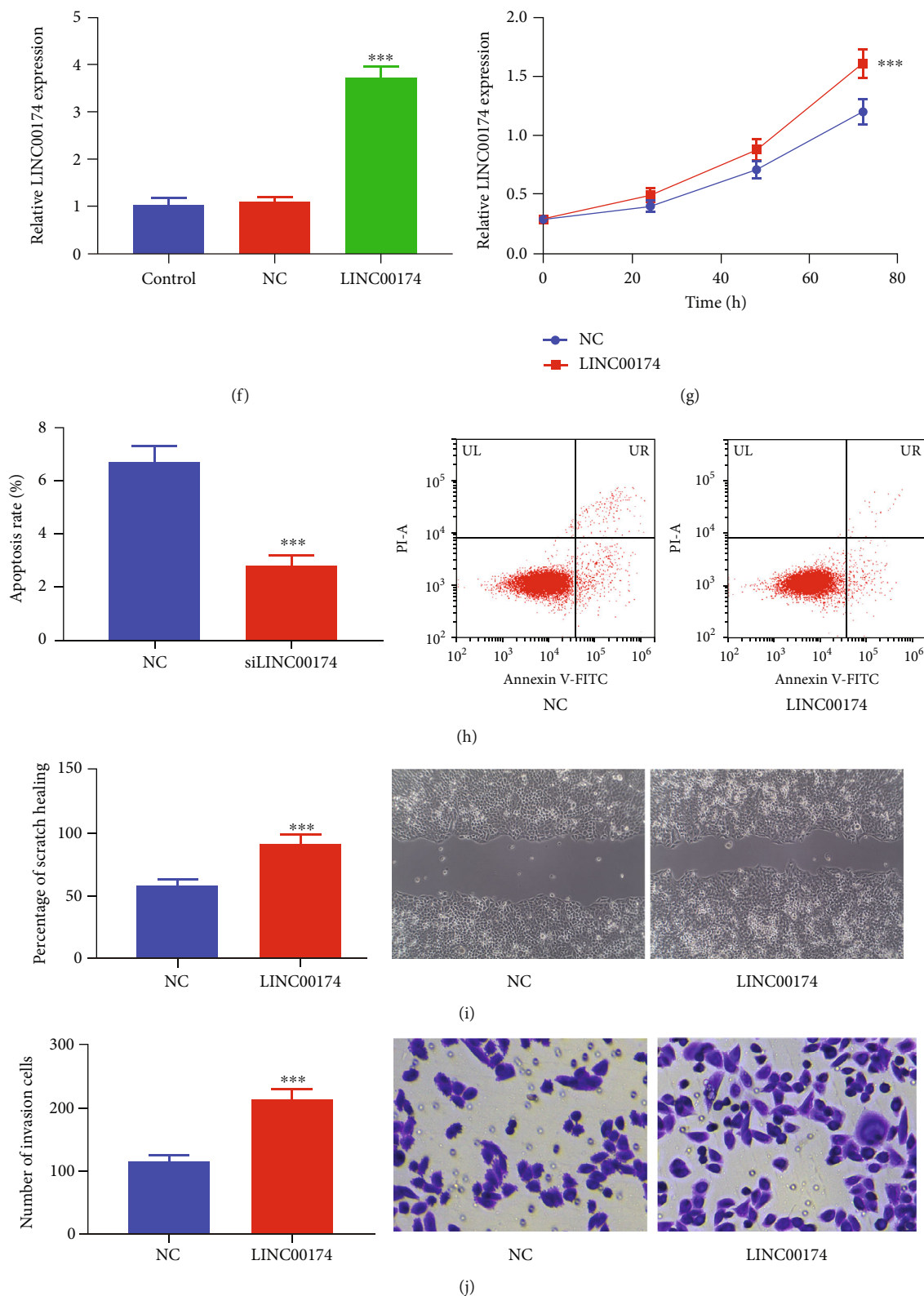
FIGURE 2: Silencing or overexpression of LINC00174 affects the growth, migration, and invasion of Caco-2 cells. (a) Construction of LINC00174-silenced Caco-2 cells. (b) Effects of LINC00174 silencing on proliferation ability. (c) Effects of LINC00174 silencing on the apoptosis of Caco-2 cells. (d) Effects LINC00174 silencing on cell migration. (e) Effects of LINC00174 silencing on the invasion of Caco-2 cells. ***$P < 0.001$ vs. siNC. (f) Construction of LINC00174-overexpressing Caco-2 cells. (g) Effects of LINC00174 overexpression on proliferation ability. (h) Effects of LINC00174 overexpression on the apoptosis of COLO201 cells. (i) Effects of LINC00174 overexpression on cell migration. (j) Effects of LINC00174 expression on the invasion of COLO201 cells. ***$P < 0.001$ vs. NC.

(a)

(b)

(c)

(d)

(e)

(f)

(g)

(h)

Figure 3: Continued.

(i)

(j)

(k)

(l)
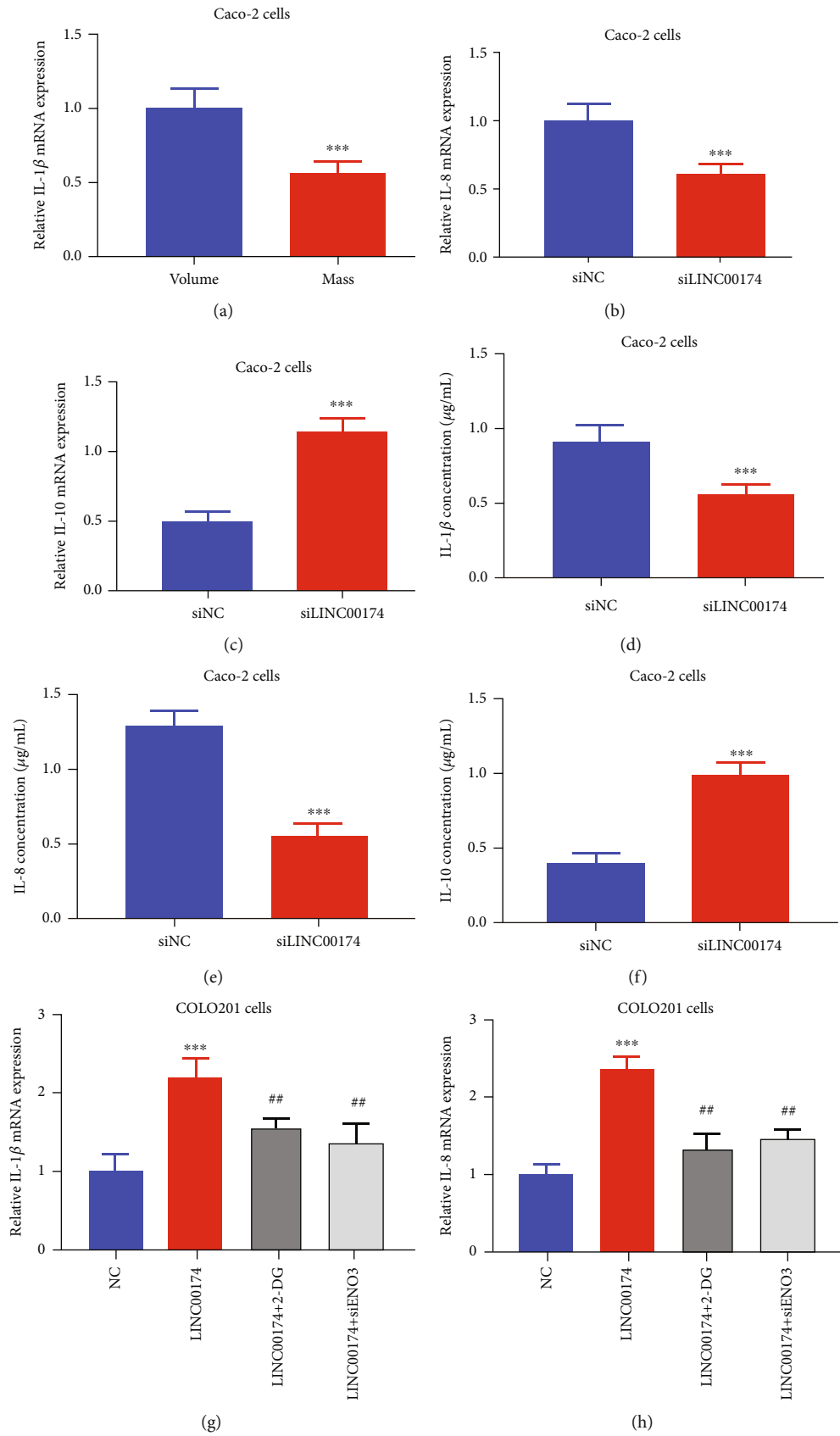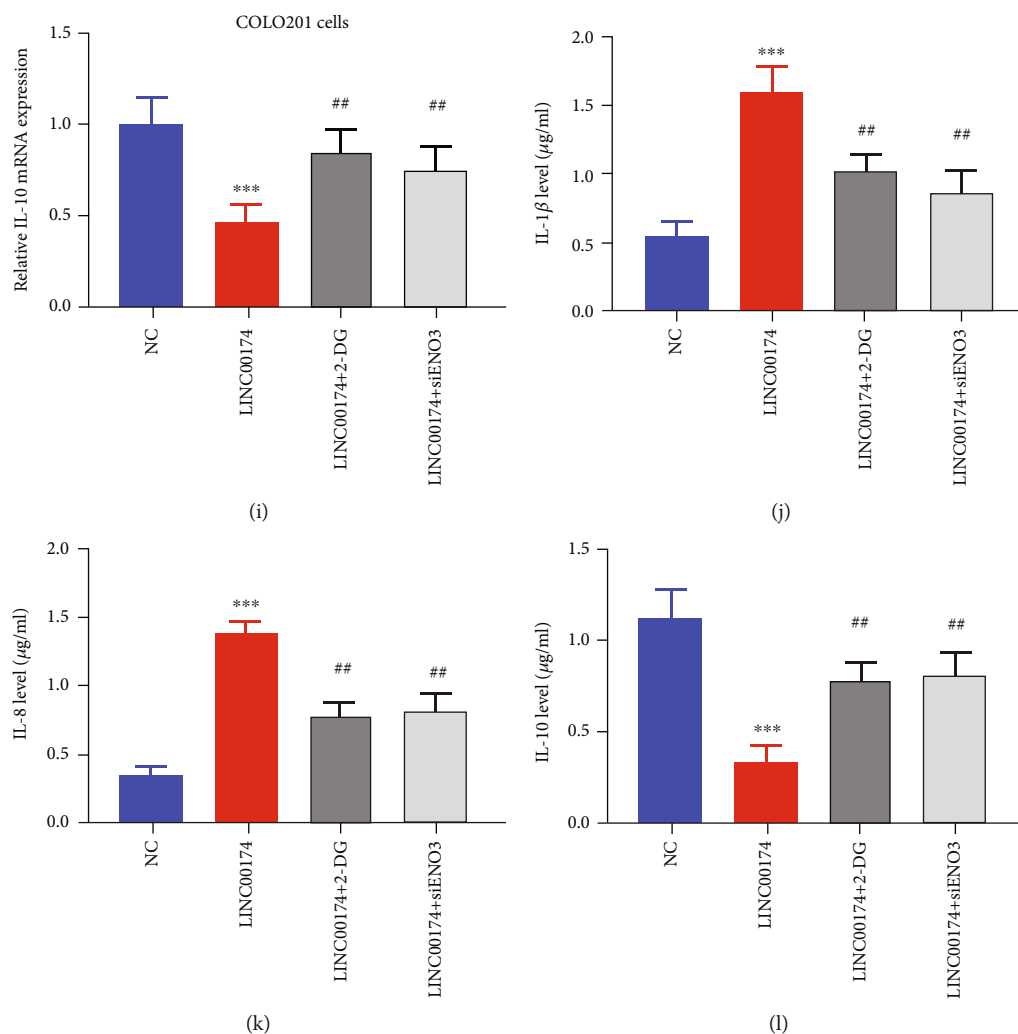
FIGURE 3: Silencing or overexpression of LINC00174 affects inflammation in colon cancer cells. (a–c) Effects of LINC00174 silencing on the transcription of the proinflammatory genes IL-1β and IL-8 and the anti-inflammatory gene IL-10 in Caco-2 cells. ***$P < 0.001$ vs. siNC. (d–f) Effects of LINC00174 silencing on the expression of the proinflammatory genes IL-1β and IL-8 and the anti-inflammatory gene IL-10 in Caco-2 cells. ***$P < 0.001$ vs. siNC. (g–i) Effects of LINC00174 overexpression or 2-deoxy-d-glucose (2-DG) (a glycolytic inhibitor) or ENO3 ablation on the mRNA expression of the proinflammatory genes IL-1β and IL-8 and anti-inflammatory gene IL-10 in COLO201 cells. ***$P < 0.001$ vs. NC and ##$P < 0.05$ vs. LINC00174. (j–l) Effects of LINC00174 overexpression or 2-DG or ENO3 ablation on the levels of the proinflammatory genes IL-1β and IL-8 and anti-inflammatory gene IL-10 in Caco-2 cells. ***$P < 0.001$ vs. NC and ##$P < 0.05$ vs. LINC00174.

uptake and inhibited lactate production in COLO201 cells. However, LINC00174 overexpression not only promoted glucose uptake and increased lactate accumulation in colon cancer cells but also blocked the inhibitory effects of miR-2467-3p on glycolysis (Figures 7(e) and 7(f)). This suggests that LINC00174/miR-2467-3p not only regulates ENO3 but also regulates glycolysis.

3.7. LINC00174 Regulates ENO3 Protein Levels, Tumor Growth, and Inflammation by Targeting miR-2467-3p. To further verify the effects and mechanism of LINC00174 on colon cancer cells *in vivo*, COLO201 cells with LINC00174 and/or miR-2467-3p overexpression were used to construct a tumor-bearing mice model. LINC00174 overexpression increased tumor volume and mass by approximately 1.8-fold, whereas miR-2467-3p overexpression inhibited tumor growth to half of that observed in the NC+mimic NC group

(Figures 8(a) and 8(b)). The tumor volume and mass of the mice in the LINC00174+mimic group were significantly lower than those of the mice in the LINC00174+mimic NC group and significantly higher than those of the mice in the NC+mimic group (Figures 8(a) and 8(b)). This indicates that miR-2467-3p overexpression blocks the *in vivo* promoting effects of LINC00174 on colon cancer and confirms that these effects are inseparable from those of miR-2467-3p. In addition, LINC00174 and miR-2467-3p promoted and inhibited ENO3 protein levels in vivo, respectively (Figure 8(c)). Moreover, LINC00174 overexpression reversed the inhibitory effects of ENO3 protein levels on tumor tissues via miR-2467-3p (Figure 8(c)). These findings further confirm that LINC00174 increases ENO3 protein levels by targeting miR-2467-3p *in vivo*.

We also elucidated the inflammation levels in the tumor tissues of each group and observed that the mRNA

(a)

(b)

Figure 4: Continued.

(c)

(d)

(e)

(f)
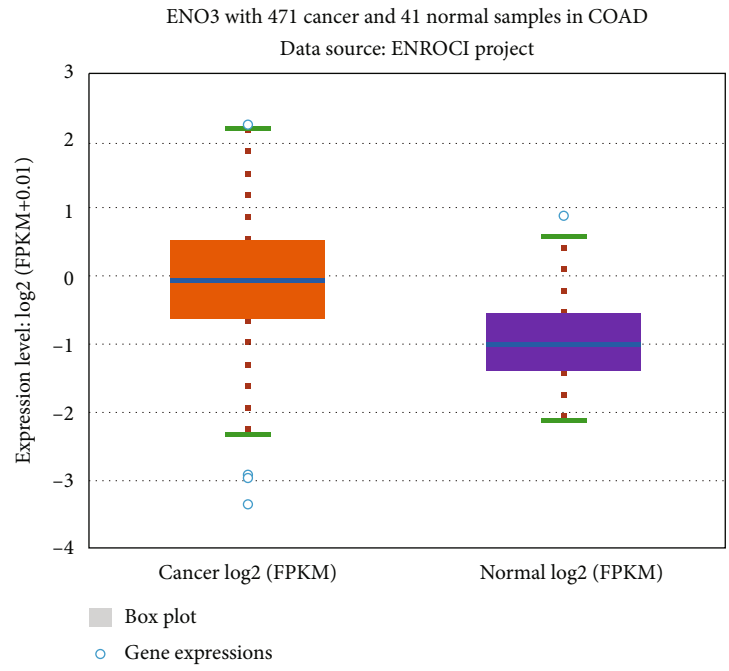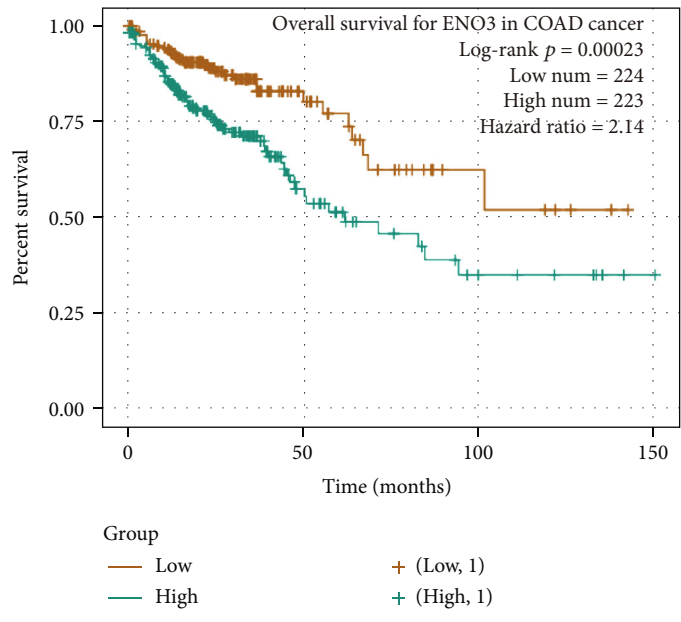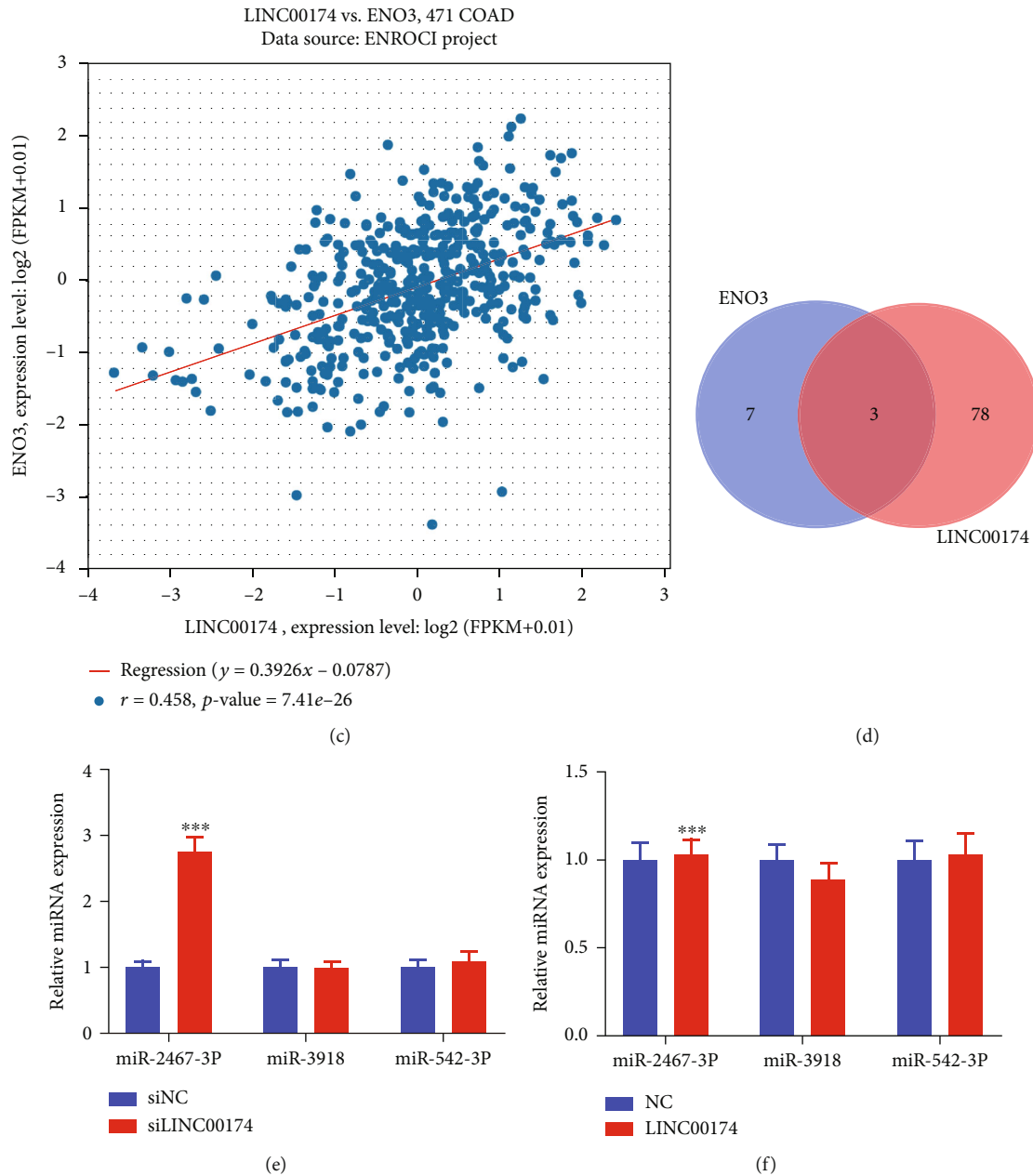
FIGURE 4: Construction of the LINC00174/miR-2467-3p/ENO3 axis. (a) ENO3 expression in colon cancer tissues in The Cancer Genome Atlas database. (b) The relationship between different ENO3 levels and the survival rate of patients with colon cancer. (c) Correlation between LINC00174 and ENO3 in colon tissues. (d) The target miRNAs of LINC00174 and ENO3; three common miRNAs were identified: miR-2467-3p, miR-3918, and miR-542-3p. (e) Effects of LINC00174 silencing on the expression of miR-2467-3p, miR-3918, and miR-542-3p in Caco-2 cells. (f) Effects of LINC00174 overexpression on the expression of miR-2467-3p, miR-3918, and miR-542-3p in COLO201 cells. ***$P < 0.001$ vs. siNC or NC.

expression of IL-1β and IL-8 was increased but that of IL-10 decreased after LINC00174 overexpression. miR-2467-3p overexpression had opposite effects (Figures 8(d)–8(f)). In addition, the mRNA expression of IL-1β and IL-8 was higher in the LINC00174+mimic group than in the LINC00174+ mimic NC group and lower in the NC+mimic group; however, the mRNA expression of IL-10 was lower in the LINC00174+ mimic NC group and higher in the NC+mimic group compared to NC+mimic NC group (Figures 8(a)–8(f)). miR-

2467-3p overexpression blocked the promoting effects of LINC00174 on inflammation, suggesting that the mechanism by which LINC00174 promotes inflammation in colon cancer is inseparable from miR-2467-3p at the *in vivo* level.

4. Discussion

The interaction between innate genetic risk factors and environmental carcinogenic factors is an important aspect that

(a)

(b)

(c)

(d)

(e)

(f)
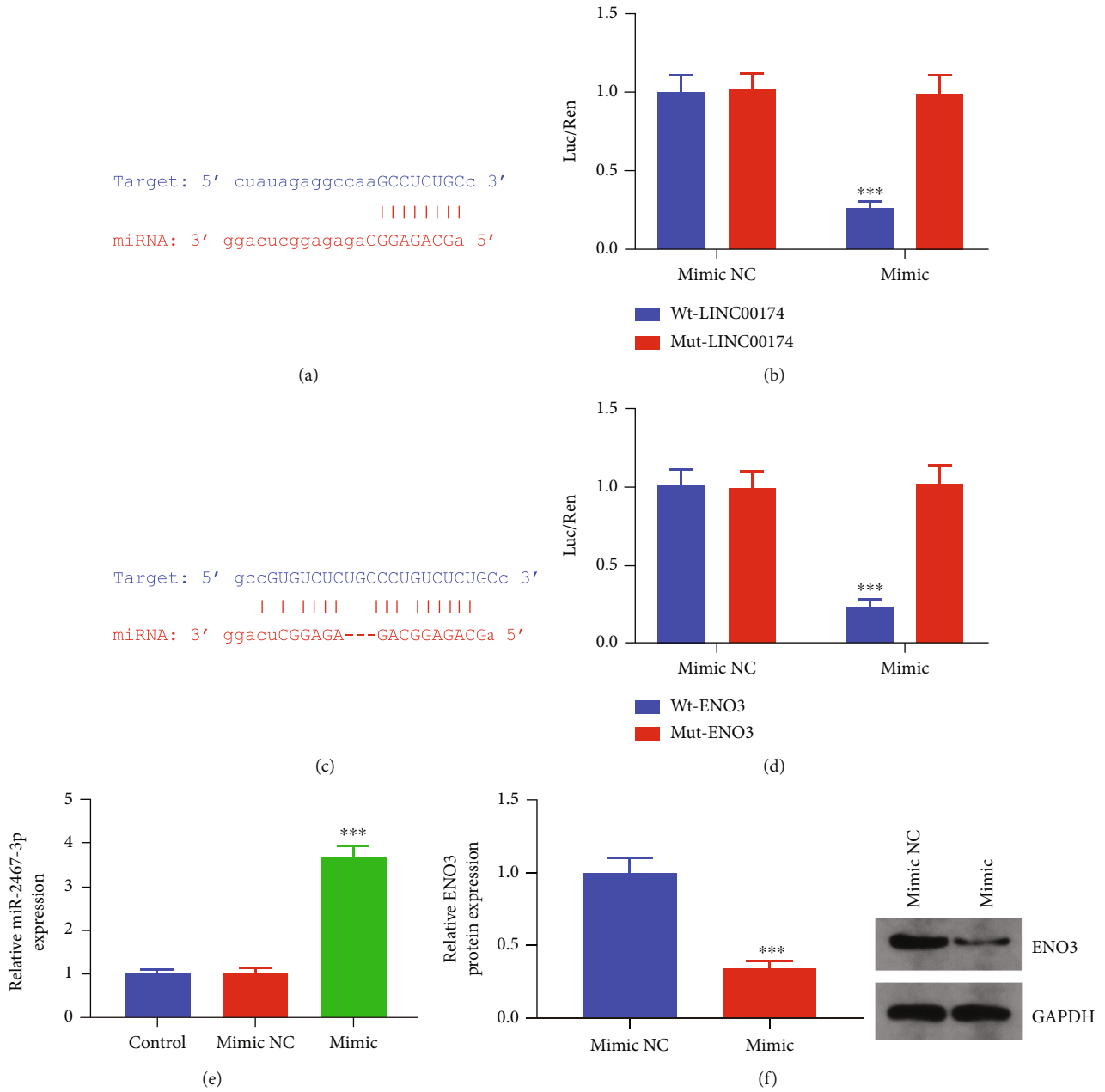
Figure 5: LINC00174 targets miR-2467-3p to regulate ENO3. (a) Binding sites of LINC00174 and miR-2467-3p. (b) Dual-luciferase reporter assay to verify the targeted binding between LINC00174 and miR-2467-3p. (c) Binding sites of ENO3 and miR-2467-3p. (d) Dual-luciferase reporter assay to verify the targeted binding between ENO3 and miR-2467-3p. (e) Construction of miR-2467-3p-overexpressing COLO201 cells. (f) Effects of miR-2467-3p overexpression on ENO3 protein levels in cells.

leads to colon cancer [30, 31]. Inflammatory bowel disease and other conditions may also lead to colon cancer, and inflammation is a crucial factor involved in colon cancer progression [32, 33]. In addition to surgery and chemotherapy, new immunotherapies are constantly being used in clinical settings; however, the prognosis of patients with colon cancer remains poor [34, 35]. Furthermore, most patients lose the best opportunity for surgery at the time of diagnosis and exhibit infiltration and metastasis [36, 37]. Therefore, it is important to analyze the mechanism underlying colon cancer progression. Glycolysis and inflammation have a

close interrelationship in cancer cells. In these cells, glycolysis is often upregulated so as to facilitate their rapid growth and proliferation [38]. This phenomenon is commonly called the Warburg effect. In addition, glycolysis can lead to the production of reactive oxygen species, which can cause cellular damage and trigger inflammatory responses [39]. The chronic activation of the inflammatory pathways in cancer cells can lead to the recruitment of immune cells and release of cytokines and chemokines, thereby promoting tumor growth and metastasis. Furthermore, inflammation in the tumor microenvironment can induce glycolysis in

(a)

(b)

(c)

(d)

(e)
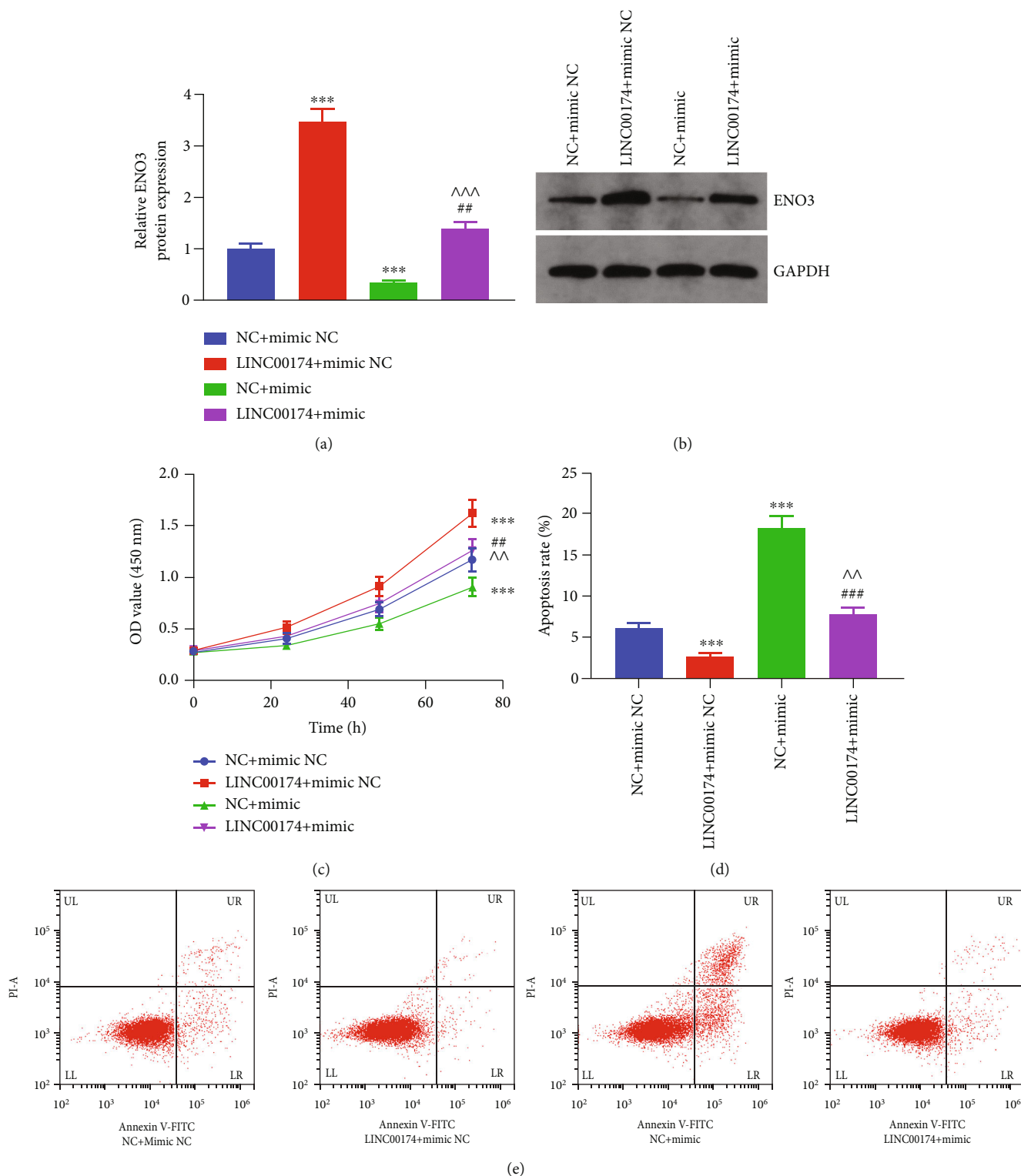
Figure 6: LINC00174/miR-2467-3p regulates ENO3 expression and inhibits cell proliferation. (a, b) Effects of LINC00174 and/or miR-2467-3p expression on ENO3 protein levels. (c) Effects of LINC00174 and/or miR-2467-3p overexpression on cell proliferation ability. (d) Effects of LINC00174 and/or miR-2467-3p overexpression on the apoptosis of COLO201 cells. $^{***}P < 0.001$ vs. NC+mimic NC, $^{\#\#}P < 0.01$ and $^{\#\#\#}P < 0.001$ vs. LINC00174+mimic NC, and $^{\wedge\wedge}P < 0.01$ vs. NC+mimic. (e) Representative images of flow cytometry results.

neighboring cells, resulting in a positive feedback loop that fuels cancer progression [40]. Therefore, glycolysis and inflammation are mutually reinforcing processes driving cancer development and progression [41]. Nevertheless, the relationship between glycolysis and inflammation in cancer cells is complex and multifaceted. While glycolysis

(a)

(b)

(c)

(d)

(e)

(f)
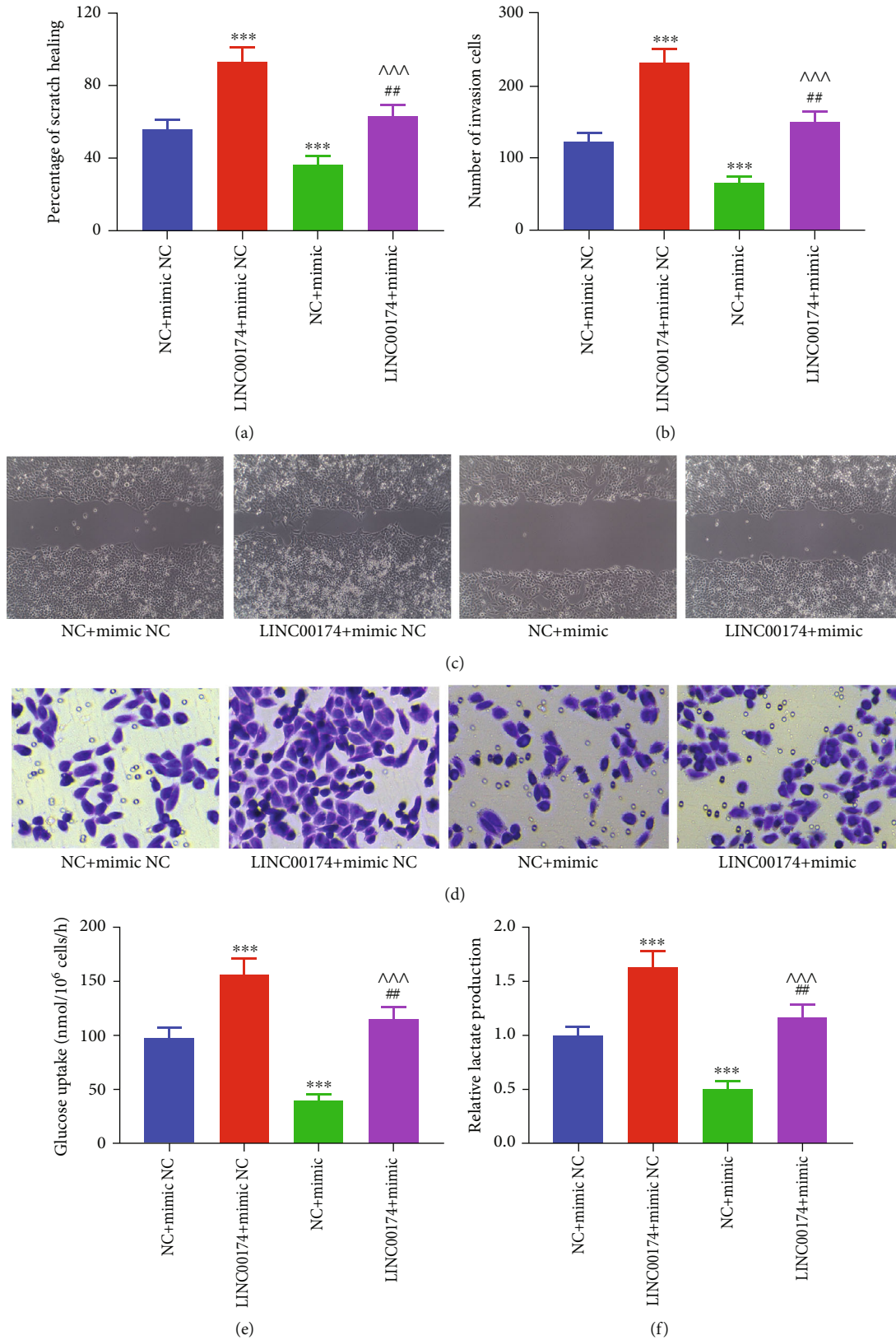
FIGURE 7: LINC00174/miR-2467-3p regulates colon cancer cell migration, invasion, and glycolysis. (a, c) Effects of LINC00174 and/or miR-2467-3p overexpression on cell migration. (b, d) Effects of LINC00174 and/or miR-2467-3p expression on the invasion of COLO201 cells. (e) Effects of LINC00174 and/or miR-2467-3p overexpression on glucose uptake. (f) Effects of LINC00174 and/or miR-2467-3p overexpression on lactate production in COLO201 cells. $***P < 0.001$ vs. NC+mimic NC, $^{\#\#}P < 0.01$ vs. LINC00174+mimic NC, and $^{\wedge\wedge\wedge}P < 0.001$ vs. NC+mimic.

(a)

(b)

(c)

(d)

(e)

Figure 8: Continued.

(f)
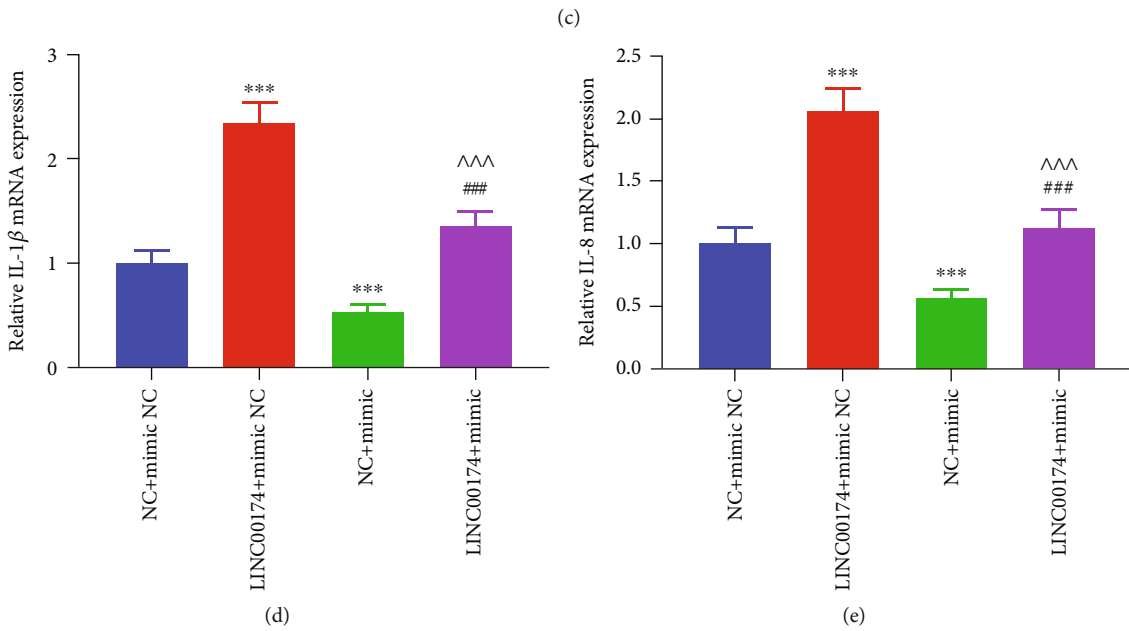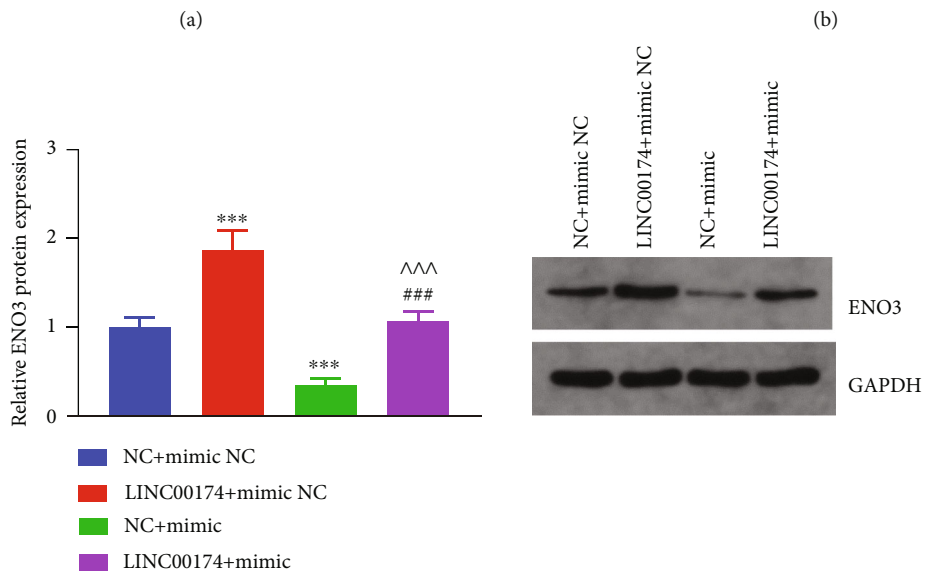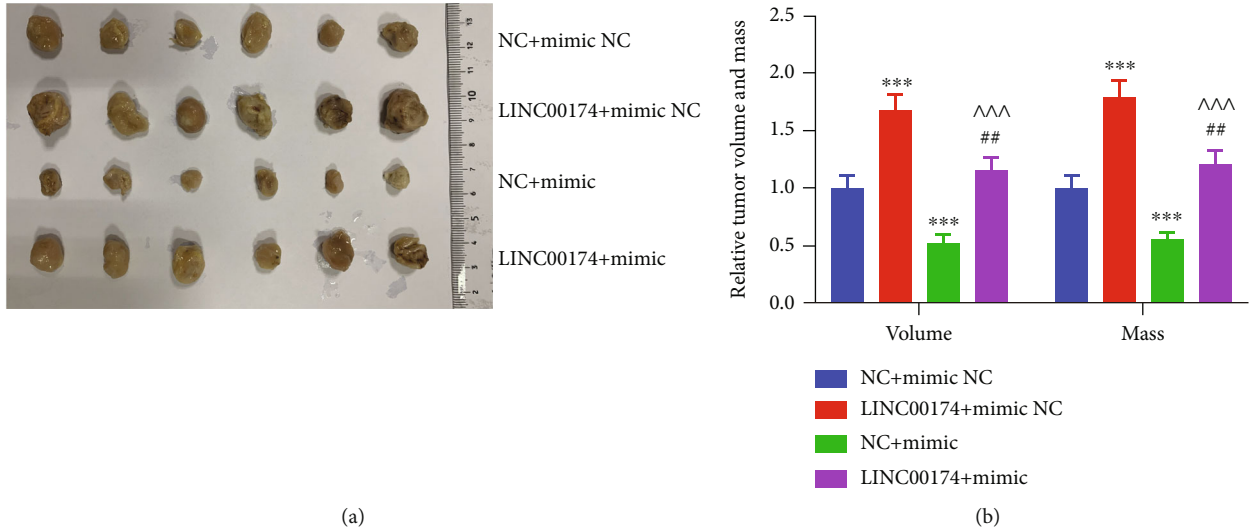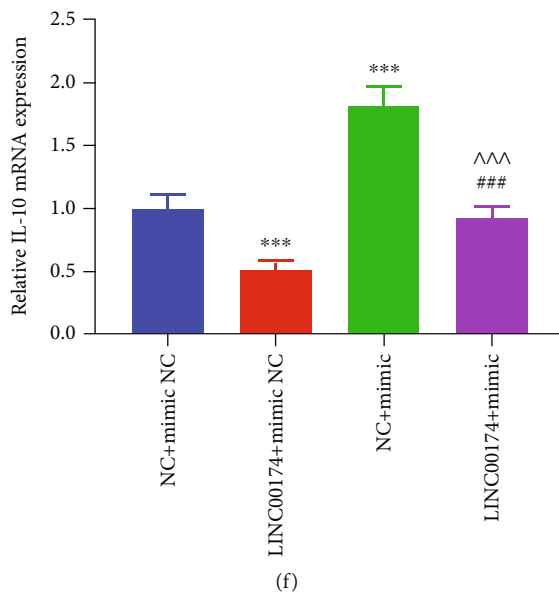
FIGURE 8: LINC00174 regulates ENO3 protein levels, tumor growth, and inflammation in tumor tissues by targeting miR-2467-3p. (a, b) Effects of LINC00174 and/or miR-2467-3p overexpression on tumor volume and mass in a tumor-bearing mice model. (c) Effects of LINC00174 and/or miR-2467-3p overexpression on ENO3 protein levels in tumor tissues. (d, e) Effects of LINC00174 and/or miR-2467-3p overexpression on the transcription of the proinflammatory genes IL-1β and IL-8 in tumor tissues. (f) Effects of LINC00174 and/or miR-2467-3p overexpression on the transcription of the anti-inflammatory gene IL-10. $^{***}P < 0.001$ vs. NC+mimic NC, $^{\#\#}P < 0.01$ and $^{\#\#\#}P < 0.001$ vs. LINC00174+mimic NC, and $^{\wedge\wedge\wedge}P < 0.001$ vs. NC+mimic.

is important for cancer cell survival, it also induces inflammatory responses that contribute to tumor progression [42]. Therefore, identifying strategies that target both glycolysis and inflammation may be effective in improving cancer therapy.

lncRNAs are recently discovered novel tumor diagnostic and therapeutic targets. For example, DNAJC3-AS1 [43], EGOT [44], and LINC00261 [45] are considered clinical markers of colon cancer and are involved in regulating cell proliferation and invasion. LINC00174 (ENSG00000179406) is overexpressed in liver cancer [17], glioblastoma [46], and thymic epithelial tumors [47] and exerts a cancer-promoting function. Recent studies have reported that LINC00174 is associated with the malignant pathological features of patients with colorectal cancer and that it promotes tumor progression and metastasis [48, 49]. However, the effect and mechanism of LINC00174 on the biological behavior of and inflammation in colon cancer cells remain unclear. To this end, preliminary analysis of the colon cancer samples in TCGA database revealed that LINC00174 is overexpressed and associated with a lower survival rate. Furthermore, *in vitro* experiments using colon cancer cell lines revealed that LINC00174 overexpression promotes colon cancer cell proliferation, migration, invasion, and inflammation and inhibits apoptosis. These findings suggest that LINC00174 plays tumor- and inflammation-promoting roles in colon cancer and is a biomarker for colon cancer.

Next, to analyze the mechanism by which LINC00174 promotes colon cancer, TCGA database was used to identify ENO3, which is positively correlated with LINC00174 in colon cancer tissues. Similar to LINC00174, ENO3 was also overexpressed in colon cancer and related to a poor prognosis. Thereafter, the respective target miRNAs of LINC00174 and ENO3 were predicted, and three common miRNAs were identified: miR-2467-3p, miR-3918, and miR-542-3p. To distinguish these three miRNAs, we determined the effects of LINC00174 alterations on them. LINC00174 silencing increased miR-2467-3p levels in Caco-2 cells, whereas LINC00174 overexpression decreased miR-2467-3p levels in COLO201 cells. However, the effects on the other two miRNAs were not statistically significant. Using molecular cell experiments, we confirmed that miR-2467-3p binds to LINC00174 and ENO3 and that miR-2467-3p inhibits ENO3 protein levels, which are, in turn, regulated by LINC00174. A study reported that miR-2467-3p can inhibit the metastasis of colorectal cancer cells [50]. This suggests that miR-2467-3p is a key miRNA for LINC00174 in regulating colon cancer and ENO3 protein levels.

In the present study, we observed that LINC00174 can bind to miR-2467-3p, thereby inhibiting its expression. In turn, miR-2467-3p can target and downregulate ENO3 expression. Therefore, LINC00174 indirectly regulates ENO3 expression by modulating miR-2467-3p levels. We observed that LINC00174 expression was increased, leading to a decrease in miR-2467-3p levels and an increase in ENO3 expression. This was associated with altered glucose metabolism and increased proliferation in cancer cells. Therefore, LINC00174 may play a critical role in regulating glucose metabolism and cancer cell proliferation by modulating miR-2467-3p expression and ENO3 protein levels. Nevertheless, additional studies are warranted to fully understand the molecular mechanisms involved in this

regulatory network and its potential as a therapeutic target for cancer. ENO3 encodes β-enolase and is mainly expressed in the skeletal muscle and liver. It plays an important role in both glycogen and cholesterol metabolism [51, 52]. ENO3 deficiency can lead to metabolic myopathy [53]. Furthermore, ENO3 may have a unique function in promoting glycolysis in tumor cells. To date, several sequencing-based studies have reported that ENO3 is involved in glycolysis and colorectal or colon cancer and that elevated ENO3 promotes ATP production or glycolysis under hypoxic conditions [27, 54]. Furthermore, genome analysis using the Gene Expression Omnibus database revealed that ENO3 is involved in glycolysis regulation; LASSO Cox analysis revealed that ENO is associated with prognosis [55]. Glycolysis also regulates the biological behavior of colon cancer cells [56, 57]. In the present study, we observed that miR-2467-3p targets ENO3 expression, inhibits the malignant biological behavior of and glycolysis in colon cancer cells, and alleviates the cancer-promoting effects of LINC00174. Moreover, LINC00174 promotes glycolysis and blocks the inhibitory effects of miR-2467-3p on colon cancer cells and glycolysis. In addition, the regulatory effects of LINC00174 on tumor growth and ENO3 protein levels via miR-2467-3p were confirmed via animal experiments. In animal models, elevated LINC00174 expression promoted the mRNA expression of IL-1β and IL-8 but inhibited IL-10 expression. Furthermore, miR-2467-3p overexpression blocked the promoting effects of LINC00174 on inflammation. This further suggests that in colon cancer, the increase in LINC00174 expression promotes ENO3 protein levels at the posttranscriptional level by targeting miR-2467-3p, which, in turn, promotes glycolysis and inflammation, thereby promoting colon cancer progression. Because colon cancer cells require high glucose levels to sustain their rapid growth, they adapt themselves by promoting glycolysis via the Warburg effect. The complex regulation among LINC00174, miR-2467-3p, and ENO3 can be critical for cancer cell survival and proliferation, and interfering with this regulatory network can be a promising approach to developing effective cancer therapies.

5. Conclusion

LINC00174 can promote colon cancer cell glycolysis, inflammation, proliferation, migration, and invasion and inhibit apoptosis. The cancer-promoting mechanism of LINC00174 is related to targeting miR-2467-3p to promote ENO3 protein levels. Nevertheless, the function and mechanism of LINC00174 in colon cancer should be further confirmed at the clinical level. Furthermore, the mechanism by which LINC00174 promotes glycolysis should be confirmed *in vivo*.

Data Availability

The datasets generated during and/or analyzed during the current study are available from the corresponding authors on reasonable request.

Ethical Approval

This study was performed according to the principles of the Declaration of Helsinki. The Ethics Committee of the People's Hospital of Guangxi Zhuang Autonomous Region approved this study (no. 20204532AA).

Disclosure

Sheng Xu, Jiawei Lin, and Rong Chen are the co-first authors.

Conflicts of Interest

The authors have no relevant financial or nonfinancial interests to disclose.

Authors' Contributions

All authors contributed to study conception and design. Cell experiments were performed by Sheng Xu, Jiawei Lin, and Rong Chen. Animal experiments were performed by Junjie Xie and Enquan Yuan. Data collection and analysis were performed by Fajie Cen and Fanbiao Kong. The initial draft of the manuscript was written by Junjie Xie. All authors commented on the previous versions of the manuscript. All authors have read and approved the final manuscript.

References

[1] H. Sung, J. Ferlay, R. L. Siegel et al., "Global cancer statistics 2020: GLOBOCAN estimates of incidence and mortality worldwide for 36 cancers in 185 countries," *CA: a Cancer Journal for Clinicians*, vol. 71, no. 3, pp. 209–249, 2021.

[2] J. Tie, J. D. Cohen, Y. Wang et al., "Circulating tumor DNA analyses as markers of recurrence risk and benefit of adjuvant therapy for stage III colon cancer," *JAMA Oncology*, vol. 5, no. 12, pp. 1710–1717, 2019.

[3] J. A. Meyerhardt, Q. Shi, C. S. Fuchs et al., "Effect of celecoxib vs placebo added to standard adjuvant therapy on disease-free survival among patients with stage III colon cancer: the CALGB/SWOG 80702 (Alliance) randomized clinical trial," *JAMA*, vol. 325, no. 13, pp. 1277–1286, 2021.

[4] H. J. Schmoll, C. Twelves, W. Sun et al., "Effect of adjuvant capecitabine or fluorouracil, with or without oxaliplatin, on survival outcomes in stage III colon cancer and the effect of oxaliplatin on post-relapse survival: a pooled analysis of individual patient data from four randomised controlled trials," *The Lancet Oncology*, vol. 15, no. 13, pp. 1481–1492, 2014.

[5] C. Kaltenmeier, C. Shen, D. S. Medich et al., "Time to surgery and colon cancer survival in the United States," *Annals of Surgery*, vol. 274, no. 6, pp. 1025–1031, 2021.

[6] E. Rosander, T. Holm, A. Sjövall, F. Hjern, C. E. Weibull, and C. Nordenvall, "Preoperative multidisciplinary team assessment is associated with improved survival in patients with locally advanced colon cancer; a nationwide cohort study in 3157 patients," *European Journal of Surgical Oncology*, vol. 47, no. 9, pp. 2398–2404, 2021.

[7] Y. Yuan, W. W. Xiao, W. H. Xie et al., "Neoadjuvant chemoradiotherapy for patients with unresectable radically locally advanced colon cancer: a potential improvement to overall

survival and decrease to multivisceral resection," *BMC Cancer*, vol. 21, no. 1, p. 179, 2021.

[8] D. Yao, M. Dong, C. Dai, and S. Wu, "Inflammation and inflammatory cytokine contribute to the initiation and development of ulcerative colitis and its associated cancer," *Inflammatory Bowel Diseases*, vol. 25, no. 10, pp. 1595–1602, 2019.

[9] E. Pagano, J. E. Elias, G. Schneditz et al., "Activation of the GPR35 pathway drives angiogenesis in the tumour microenvironment," *Gut*, vol. 71, no. 3, pp. 509–520, 2022.

[10] M. D. Wellenstein, S. B. Coffelt, D. E. M. Duits et al., "Loss of p53 triggers WNT-dependent systemic inflammation to drive breast cancer metastasis," *Nature*, vol. 572, no. 7770, pp. 538–542, 2019.

[11] S. Hibino, T. Kawazoe, H. Kasahara et al., "Inflammation-induced tumorigenesis and metastasis," *International Journal of Molecular Sciences*, vol. 22, no. 11, p. 5421, 2021.

[12] G. Cui, G. Li, Z. Pang, J. Florholmen, and R. Goll, "The presentation and regulation of the IL-8 network in the epithelial cancer stem-like cell niche in patients with colorectal cancer," *Biomedicine & Pharmacotherapy*, vol. 152, article 113252, 2022.

[13] A. Meirovitz, L. Baider, T. Peretz, S. Stephanos, and V. Barak, "PTX treatment of colon cancer: mode of action based on tumor marker and cytokine kinetics," *Anticancer Research*, vol. 42, no. 11, pp. 5487–5496, 2022.

[14] M. D. Paraskevopoulou and A. G. Hatzigeorgiou, "Analyzing miRNA-lncRNA interactions," *Methods in Molecular Biology*, vol. 1402, pp. 271–286, 2016.

[15] L. Wang, K. B. Cho, Y. Li, G. Tao, Z. Xie, and B. Guo, "Long noncoding RNA (lncRNA)-mediated competing endogenous RNA networks provide novel potential biomarkers and therapeutic targets for colorectal cancer," *International Journal of Molecular Sciences*, vol. 20, no. 22, p. 5758, 2019.

[16] S. Baliou, A. Kyriakopoulos, D. Spandidos, and V. Zoumpourlis, "Role of taurine, its haloamines and its lncRNA TUG1 in both inflammation and cancer progression. On the road to therapeutics? (review)," *International Journal of Oncology*, vol. 57, no. 3, pp. 631–664, 2020.

[17] J. T. Zhao, B. J. Chi, Y. Sun et al., "LINC00174 is an oncogenic lncRNA of hepatocellular carcinoma and regulates miR-320/ S100A10 axis," *Cell Biochemistry and Function*, vol. 38, no. 7, pp. 859–869, 2020.

[18] H. Xu, D. Han, K. Wang, T. Zhang, and G. C. Gao, "LINC00174 triggers the malignant development of breast cancer by negatively regulating miR-1827 level," *European Review for Medical and Pharmacological Sciences*, vol. 25, no. 21, pp. 6447–6453, 2021.

[19] C. Zheng, R. Li, S. Zheng, H. Fang, M. Xu, and L. Zhong, "LINC00174 facilitates cell proliferation, cell migration and tumor growth of osteosarcoma via regulating the TGF-β/ SMAD signaling pathway and upregulating SSH2 expression," *Frontiers in Molecular Biosciences*, vol. 8, article 697773, 2021.

[20] L. Jin, C. Li, T. Liu, and L. Wang, "A potential prognostic prediction model of colon adenocarcinoma with recurrence based on prognostic lncRNA signatures," *Human Genomics*, vol. 14, no. 1, p. 24, 2020.

[21] W. H. Koppenol, P. L. Bounds, and C. V. Dang, "Otto Warburg's contributions to current concepts of cancer metabolism," *Nature Reviews. Cancer*, vol. 11, no. 5, pp. 325–337, 2011.

[22] J. Yang, B. Ren, G. Yang et al., "The enhancement of glycolysis regulates pancreatic cancer metastasis," *Cellular and Molecular Life Sciences*, vol. 77, no. 2, pp. 305–321, 2020.

[23] M. G. Vander Heiden, L. C. Cantley, and C. B. Thompson, "Understanding the Warburg effect: the metabolic requirements of cell proliferation," *Science*, vol. 324, no. 5930, pp. 1029–1033, 2009.

[24] L. Ji, W. Shen, F. Zhang et al., "Worenine reverses the Warburg effect and inhibits colon cancer cell growth by negatively regulating HIF-1α," *Cellular & Molecular Biology Letters*, vol. 26, no. 1, p. 19, 2021.

[25] W. Zhu, Y. Huang, Q. Pan, P. Xiang, N. Xie, and H. Yu, "MicroRNA-98 suppress Warburg effect by targeting HK2 in colon cancer cells," *Digestive Diseases and Sciences*, vol. 62, no. 3, pp. 660–668, 2017.

[26] R. Wigley, R. S. Scalco, A. R. Gardiner et al., "The need for biochemical testing in beta-enolase deficiency in the genomic era," *JIMD Reports*, vol. 50, no. 1, pp. 40–43, 2019.

[27] G. Mao, J. Wu, H. Cui et al., "A novel glycolysis and hypoxia combined gene signature predicts the prognosis and affects immune infiltration of patients with colon cancer," *International Journal of General Medicine*, vol. 15, pp. 1413–1427, 2022.

[28] S. Wang, H. Yu, J. Gao et al., "PALMD regulates aortic valve calcification *via* altered glycolysis and NF- κB-mediated inflammation," *The Journal of Biological Chemistry*, vol. 298, no. 5, article 101887, 2022.

[29] W. Li, M. Xu, Y. Li et al., "Comprehensive analysis of the association between tumor glycolysis and immune/inflammation function in breast cancer," *Journal of Translational Medicine*, vol. 18, no. 1, p. 92, 2020.

[30] D. N. Jackson and A. L. Theiss, "Gut bacteria signaling to mitochondria in intestinal inflammation and cancer," *Gut Microbes*, vol. 11, no. 3, pp. 285–304, 2020.

[31] E. E. Low, J. Demb, L. Liu et al., "Risk factors for early-onset colorectal cancer," *Gastroenterology*, vol. 159, no. 2, pp. 492–501.e7, 2020.

[32] J. E. Axelrad, S. Lichtiger, and V. Yajnik, "Inflammatory bowel disease and cancer: the role of inflammation, immunosuppression, and cancer treatment," *World Journal of Gastroenterology*, vol. 22, no. 20, pp. 4794–4801, 2016.

[33] A. S. Faye, A. K. Holmer, and J. E. Axelrad, "Cancer in inflammatory bowel disease," *Gastroenterology Clinics of North America*, vol. 51, no. 3, pp. 649–666, 2022.

[34] M. Chalabi, L. F. Fanchi, K. K. Dijkstra et al., "Neoadjuvant immunotherapy leads to pathological responses in MMR-proficient and MMR-deficient early-stage colon cancers," *Nature Medicine*, vol. 26, no. 4, pp. 566–576, 2020.

[35] A. E. Snook, T. R. Baybutt, B. Xiang et al., "Split tolerance permits safe Ad5-GUCY2C-PADRE vaccine-induced T-cell responses in colon cancer patients," *Journal for Immunotherapy of Cancer*, vol. 7, no. 1, p. 104, 2019.

[36] E. L. Van Blarigan, C. S. Fuchs, D. Niedzwiecki et al., "Association of survival with adherence to the American Cancer Society nutrition and physical activity guidelines for cancer survivors after colon cancer diagnosis," *JAMA Oncology*, vol. 4, no. 6, pp. 783–790, 2018.

[37] T. Yoshino, G. Argilés, E. Oki et al., "Pan-Asian adapted ESMO clinical practice guidelines for the diagnosis treatment and follow-up of patients with localised colon cancer," *Annals of Oncology*, vol. 32, no. 12, pp. 1496–1510, 2021.

[38] H. Lincet and P. Icard, "How do glycolytic enzymes favour cancer cell proliferation by nonmetabolic functions?," *Oncogene*, vol. 34, no. 29, pp. 3751–3759, 2015.

[39] D. G. Franchina, C. Dostert, and D. Brenner, "Reactive oxygen species: involvement in T cell signaling and metabolism," *Trends in Immunology*, vol. 39, no. 6, pp. 489–502, 2018.

[40] L. Li, R. Yu, T. Cai et al., "Effects of immune cells and cytokines on inflammation and immunosuppression in the tumor microenvironment," *International Immunopharmacology*, vol. 88, no. 106939, p. 106939, 2020.

[41] G. M. Pitari, P. Li, J. E. Lin et al., "The paracrine hormone hypothesis of colorectal cancer," *Clinical Pharmacology and Therapeutics*, vol. 82, no. 4, pp. 441–447, 2007.

[42] N. Dehne, J. Mora, D. Namgaladze, A. Weigert, and B. Brüne, "Cancer cell and macrophage cross-talk in the tumor microenvironment," *Current Opinion in Pharmacology*, vol. 35, pp. 12–19, 2017.

[43] B. Han, Y. Ge, J. Cui, and B. Liu, "Down-regulation of lncRNA DNAJC3-AS1 inhibits colon cancer via regulating miR-214-3p/LIVIN axis," *Bioengineered*, vol. 11, no. 1, pp. 524–535, 2020.

[44] Y. Liu, B. Zhang, W. B. Cao, H. Y. Wang, L. Niu, and G. Z. Zhang, "Study on clinical significance of lncRNA EGOT expression in colon cancer and its effect on autophagy of colon cancer cells," *Cancer Management and Research*, vol. Volume 12, pp. 13501–13512, 2020.

[45] Z. Zhou and J. Ma, "Expression and clinical significance of long-chain noncoding RNA LINC00261 in colon cancer," *Clinical Laboratory*, vol. 65, no. 12/2019, 2019.

[46] Z. Wang, Q. Wang, Z. Bao et al., "LINC00174 is a favorable prognostic biomarker in glioblastoma via promoting proliferative phenotype," *Cancer Biomarkers*, vol. 28, no. 4, pp. 421–427, 2020.

[47] C. Tito, F. Ganci, A. Sacconi et al., "LINC00174 is a novel prognostic factor in thymic epithelial tumors involved in cell migration and lipid metabolism," *Cell Death & Disease*, vol. 11, no. 11, p. 959, 2020.

[48] Y. Ma, Y. Li, Y. Tang, N. Tang, D. Wang, and X. Li, "LINC00174 facilitates proliferation and migration of colorectal cancer cells via miR-3127-5p/ E2F7 axis," *Journal of Microbiology and Biotechnology*, vol. 31, no. 8, pp. 1098–1108, 2021.

[49] Y. Shen, X. Gao, W. Tan, and T. Xu, "STAT1-mediated upregulation of lncRNA LINC00174 functions a ceRNA for miR-1910-3p to facilitate colorectal carcinoma progression through regulation of TAZ," *Gene*, vol. 666, pp. 64–71, 2018.

[50] H. Xiao and M. Liu, "Circular RNA hsa_circ_0053277 promotes the development of colorectal cancer by upregulating matrix metallopeptidase 14 via miR-2467-3p sequestration," *Journal of Cellular Physiology*, vol. 235, no. 3, pp. 2881–2890, 2020.

[51] G. P. Comi, F. Fortunato, S. Lucchiari et al., "β-Enolase deficiency, a new metabolic myopathy of distal glycolysis," *Annals of Neurology*, vol. 50, no. 2, pp. 202–207, 2001.

[52] X. Jia and T. Zhai, "Integrated analysis of multiple microarray studies to identify novel gene signatures in non-alcoholic fatty liver disease," *Frontiers in Endocrinology*, vol. 10, p. 599, 2019.

[53] M. A. Tarnopolsky, "Myopathies related to glycogen metabolism disorders," *Neurotherapeutics*, vol. 15, no. 4, pp. 915–927, 2018.

[54] J. Chen, Z. Zhang, J. Ni et al., "ENO3 promotes colorectal cancer progression by enhancing cell glycolysis," *Medical Oncology*, vol. 39, no. 6, p. 80, 2022.

[55] J. Zhu, S. Wang, H. Bai et al., "Identification of five glycolysis-related gene signature and risk score model for colorectal cancer," *Frontiers in Oncology*, vol. 11, article 588811, 2021.

[56] J. Huang, M. Yang, Z. Liu et al., "PPFIA4 promotes colon cancer cell proliferation and migration by enhancing tumor glycolysis," *Frontiers in Oncology*, vol. 11, article 653200, 2021.

[57] M. Liu, Y. Hu, S. Lu et al., "IC261, a specific inhibitor of CK1δ/ε, promotes aerobic glycolysis through p53-dependent mechanisms in colon cancer," *International Journal of Biological Sciences*, vol. 16, no. 5, pp. 882–892, 2020.

Hindawi

Research Article

Effects of CAR-T Cell Therapy on Immune Cells and Related Toxic Side Effect Analysis in Patients with Refractory Acute Lymphoblastic Leukemia

Lianlian Li (ID)**, Jie Gao, Zhaojun Sun, Xiaolei Li, Ning Wang, and Rui Zhang**

Department of Hematology, Cangzhou People's Hospital, Cangzhou City, Hebei Province, China

Correspondence should be addressed to Lianlian Li; lianlianlidr@126.com

Objective. To observe the effects of chimeric antigen receptor T (CAR-T) cell immunotherapy on immune cells and related toxic side effects in patients with refractory acute lymphoblastic leukemia (ALL). *Methods.* A retrospective study was conducted in 35 patients with refractory ALL. The patients were treated with CAR-T cell therapy in our hospital from January 2020 to January 2021. The efficacy was evaluated at one and three months post treatments. The venous blood of the patients was collected before treatment, 1 month after treatment, and 3 months after treatment. The percentage of regulatory T cells (Treg cells), natural killer (NK) cells, and T lymphocyte subsets (CD3+, CD4+, and CD8+ T cells) was detected by flow cytometry. The ratio of CD4+/CD8+ was calculated. Patient's toxic side effects such as fever, chills, gastrointestinal bleeding, nervous system symptoms, digestive system symptoms, abnormal liver function, and blood coagulation dysfunction were monitored and recorded. The incidence of toxic and side effects was calculated, and the incidence of infection was recorded. *Results.* After one month of CAR-T cell therapy in 35 patients with ALL, the efficacy evaluation showed that complete response (CR) patients accounted for 68.57%, CR with incomplete hematological recovery (CRi) patients accounted for 22.86%, and partial disease (PD) patients accounted for 8.57%, and the total effective rate was 91.43%. In addition, compared with that before treatment, the Treg cell level in CR+CRi patients treated for 1 month and 3 months decreased prominently, and the NK cell level increased dramatically ($P < 0.05$). Compared with that before treatment, the levels of CD3+, CD4+, and CD4+/CD8+ in patients with CR+CRi in the 1-month and 3-month groups were markedly higher, and the levels of CD4+/CD8+ in the 3-month group were memorably higher than those in the 1-month group ($P < 0.05$). During CAR-T cell therapy in 35 patients with ALL, fever accounted for 62.86%, chills for 20.00%, gastrointestinal bleeding for 8.57%, nervous system symptoms for 14.29%, digestive system symptoms for 28.57%, abnormal liver function for 11.43%, and coagulation dysfunction for 8.57%. These side effects were all relieved after symptomatic treatment. During the course of CAR-T therapy in 35 patients with ALL, 2 patients had biliary tract infection and 13 patients had lung infection. No correlations were found between the infection and age, gender, CRS grade, usage of glucocorticoids or tocilizumab, and laboratory indicators such as WBC, ANC, PLT, and Hb ($P > 0.05$). *Conclusion.* CAR-T cell therapy had a good effect on patients with refractory ALL by regulating the immune function of the body via mediating the content of immune cells. CAR-T cell therapy may have therapeutic effect on refractory ALL patients with mild side effects and high safety.

1. Introduction

Acute lymphoblastic leukemia (ALL) is a clinically common hematological tumor, accounting for about 20% to 30% of acute leukemia in adults. Clinical manifestations of ALL include the inhibition of bone marrow hematopoietic function and the proliferation and infiltration of leukemia cells,

etc. ALL has a high recurrence rate and poor prognosis, which seriously affects the life of patients [1, 2]. The incidence rate of ALL is high, accounting for 15% of leukemia and about 35% of acute leukemia. At present, the main clinical treatment of ALL is chemotherapy and/or hematopoietic stem cell inhibition therapy. However, the recurrence rate and mortality rate of patients are still at a high level.

Previous studies have concluded that chemotherapy has a two-year disease-free survival rate of 39.0% and a two-year overall survival rate of 58.4% for patients with ALL [3, 4]. How to improve the prognosis of refractory ALL patients has become the focus of current medical research.

Chimeric antigen receptor T (CAR-T) cell is a T cell with the ability to recognize and kill tumors, and key cytokines such as IL-12 could be expressed on the basis of whose organizational structure. Intensifying the activation reaction of T cells has a good effect in the treatment of ALL and can improve the long-term survival rate of patients by enhancing the immune response [5, 6]. In recent years, foreign scholars believe that CAR-T cell therapy has shown good efficacy in children with refractory ALL, with tolerable safety, high response rate, and excellent persistence [7]. However, the effects of CAR-T cells on immune cells in patients with refractory ALL have been reported less.

In this study, 35 patients with refractory ALL admitted in our hospital during January 2020 to January 2021 were chosen as subjects, aiming to analyze the effects of CAR-T immunotherapy on immune cells and related toxic side effects in patients with refractory ALL.

2. Materials and Methods

2.1. General Materials. Thirty-five patients with refractory ALL during January 2020 to January 2021 were chosen as subjects. The clinical data of the patients were collected and retrospectively analyzed. Inclusion criteria were as follows: (1) all patients were initially diagnosed patients who failed to respond to two standard protocols or ALL patients who recurred within 12 months after consolidation and intensive treatment after CR or who recurred twice or more [8]. (2) The patient's age was between 18 and 65 years old. (3) The patients and their family members were informed and had good compliance and could cooperate with the examination and treatment. All of them signed an informed consent form. Exclusion criteria were as follows: (1) patients with severe cardiovascular and cerebrovascular diseases, (2) patients with nervous system diseases, (3) patients with other malignant tumors, and (4) patient complicated with infection. The subjects included 18 males and 17 females, with an average age of 38.16 ± 6.85 years. The operation of this experiment was approved by the hospital Ethics Association. The experimental process is shown in Figure 1.

2.2. Methods. To prepare CAR-T cells, 40-60 mL of peripheral blood was collected from experimental subjects, anticoagulation with heparin: T lymphocytes were activated and expanded after isolation and purification, and CAR-T cells were amplified again after specific CAR transfection. CAR-T cells were frozen after quality inspection. CAR-T cells were infused intravenously for the treatment. All patients received chemotherapy about 30 days before CAR-T cell infusion. Appropriate chemotherapy programs were chosen by physicians according to the patient's condition and previous treatment to reduce the tumor load of patients, aiming to prevent the occurrence of cytokine release syndrome (CRS) or reduce the severity of CRS. Detect the recovery of
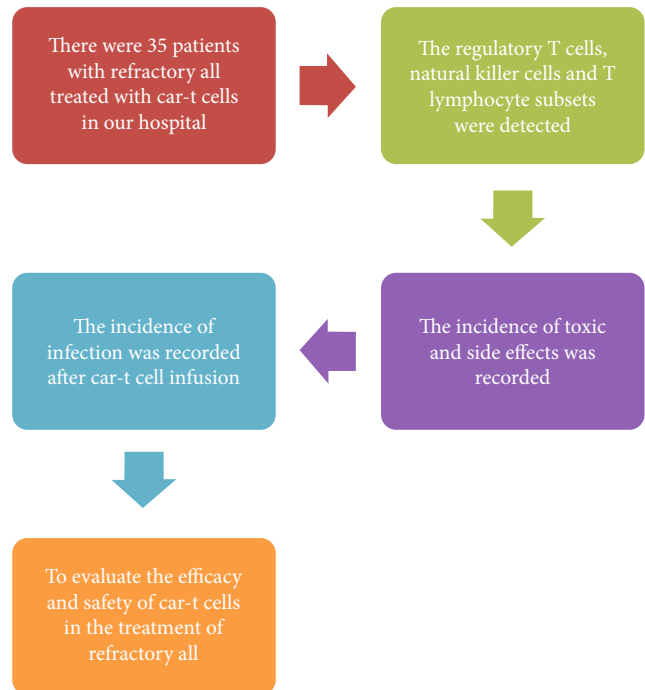
FIGURE 1: The experimental process.

patient's blood routine. About 3 days before cell infusion, fludarabine (Flu)+cyclophosphamide (CY) pretreatment scheme (FC) was given as follows: Flu 25 mg/m² and CY 300 mg/m²/d, continuously injected intravenously for 3 days. According to the existing literature report in the United States [7], in the CAR-T cell reinfusion therapy, the amount of CAR-T cell reinfusion should be 10^6-10^7 cells/ kg body weight. According to the number of T cells collected from the patient, the reinfusion plan was formulated as appropriate, and the infusion volume was 10^6-10^7 cells/kg body weight.

2.3. Outcome Measures

2.3.1. Efficacy Analysis. The efficacy evaluation included complete response (CR), CR with incomplete clinical recovery (CRi), and partial disease (PD). Among them, CR represented the recovery of bone marrow hematopoiesis, with primitive cells < 5%, no primitive cells in peripheral blood, absolute value of platelets $> 100 \times 10^9$/L, absolute value of neutrophil $> 1 \times 10^9$/L, and no recurrence occurs in 4 weeks. CRi referred to the recovery of bone marrow hematopoiesis, with primitive cells < 5% and no primitive cells in peripheral blood, but the absolute value of patient's platelet $\leq 100 \times 10^9$/L, absolute value of neutrophil $\leq 1 \times 10^9$/L, and no recurrence in 4 weeks. PD represented 25% increase of primitive cells found in bone marrow or peripheral blood, or extramedullary infiltration occurs.

2.3.2. Detection of Serum Indicators. The venous blood of patients was collected before treatment, 1 month after treatment, and 3 months after treatment and stored in heparin anticoagulant tubes. After centrifuged at 1500 r/min for

TABLE 1: CRS grade.

Indicators	Grade 1	Grade 2	Grade 3	Grade 4
Fever	Body temperature ≥ 38°C	Body temperature ≥ 38°C	Body temperature ≥ 38°C	Body temperature ≥ 38°C
Hypotension	No	No need to use antihypertensive drugs	1 antihypertensive drug is required, with or without vasopressin	Multiple antihypertensive drugs are required (excluding vasopressin)
		And/or		
Hypoxemia	No	Need low flow nasal catheter oxygen inhalation	Need high flow nasal catheter oxygen inhalation and circulatory respirator	Need positive pressure ventilation

5 min, the supernatant was carefully separated and stored into the refrigerator at -80°C to avoid repeated freezing and thawing. The percentage of regulatory T (Treg) cells, natural killer (NK) cells, and T lymphocyte subsets CD3+, CD4+, and CD8+ T cells was detected by TUNEL Flow Cytometry Analysis Kit (purchased from Wuhan Purity Biotechnology Co., Ltd., Hongshan District, Wuhan, Hubei Province, China) and HLA-B27 Assay Kit (purchased from Guangzhou Jincheng Biotechnology Co., Ltd., Tianhe District, Guangzhou, Guangdong Province, China). The ratio of CD4+/CD8+ T cells was calculated.

2.3.3. Toxic and Side Effects. Closely observe the patient's condition changes and monitor and record the patient's toxic and side effects such as fever, chills, gastrointestinal bleeding, nervous system symptoms (dizziness, headache, irritability, aphasia, photophobia, etc.), digestive system symptoms (vomiting, nausea, etc.), abnormal liver function, and blood coagulation dysfunction. The incidence of side effects was calculated.

2.3.4. Infection. After CAR-T cell infusion treatment, the presence of infection was comprehensively judged according to laboratory indicators, imaging, histopathology, and/or microbiological examination. Infection within 30 days after infusion requires intravenous antibiotics or hospitalization when severe infection occurs. The age, gender, cytokine release syndrome (CRS) grade (Table 1), whether there was a usage of glucocorticoid and tocilizumab, and laboratory indicators including white blood cell (WBC), neutrophil (ANC), platelet count (PLT), and hemoglobin (Hb) were collected.

2.4. Statistical Analysis. SPSS 20.0 software was used to analyze the experimental data. Measurement data such as Treg cells, NK cells, CD3+, CD4+, and CD4+/CD8+ were represented as $(\bar{x} \pm s)$. Repeated measurement ANOVA was used for comparison among groups, and these with statistical differences were further compared with the Tukey test. The SNK-q test was used for comparison of multiple sample averages between groups. Enumeration data such as curative effect and adverse reaction were expressed as %, and χ^2 test was used for comparison between groups. $P < 0.05$ indicated that the statistical results were statistically significant.
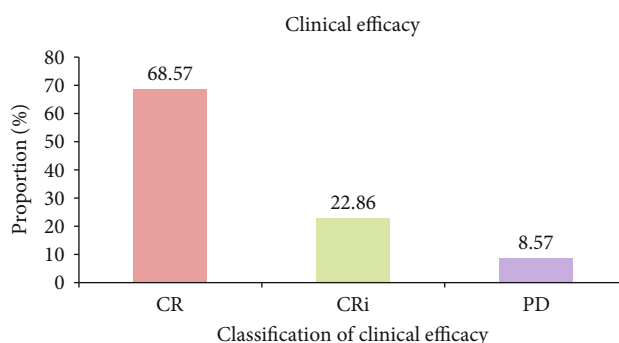
FIGURE 2: Analysis of curative effect after treatment.

3. Results

3.1. Analysis of Curative Effect after Treatment. After one month of CAR-T cell therapy in 35 patients with ALL, the efficacy evaluation showed that CR patients accounted for 68.57% (24 cases), CRi patients accounted for 22.86% (8 cases), and PD patients accounted for 8.57% (3 cases), and the total effective rate was 91.43% (Figure 2).

3.2. Comparison of Treg Cell Level before and after Treatment. The patients were grouped according to the time after treatment, and the Treg cell level was detected. Compared with that before treatment, the Treg cell level in CR +CRi patients treated for 1 month and 3 months decreased prominently, and the NK cell level increased dramatically ($P < 0.05$, Table 2).

3.3. Comparison of T Lymphocyte Subsets before and after Treatment. Compared with that before treatment, the levels of CD3+, CD4+, and CD4+/CD8+ in patients with CR +CRi in the 1-month and 3-month groups were markedly higher, and the levels of CD4+/CD8+ in the 3-month group were memorably higher than those in the 1-month group ($P < 0.05$, Table 3).

3.4. Analysis of Side Effects after Treatment. During CAR-T cell therapy in 35 patients with ALL, fever accounted for 62.86%, chills for 20.00%, gastrointestinal bleeding for 8.57%, nervous system symptoms for 14.29%, digestive system symptoms for 28.57%, abnormal liver function for 11.43%, and coagulation dysfunction for 8.57%. These

TABLE 2: Comparison of Treg cell level before and after treatment ($\bar{x} \pm s$).

Groups	Treg cells (%)	NK cells (%)
Before treatment ($n = 35$)	8.16 ± 2.86	11.78 ± 0.62
CR+CRi patients treated for 1 month ($n = 32$)	7.05 ± 1.25[a]	13.25 ± 0.56[a]
CR+CRi patients treated for 3 months ($n = 32$)	6.15 ± 2.13[ab]	15.02 ± 0.32[ab]
PD patients treated for 1 month ($n = 3$)	10.85 ± 1.16[bc]	11.64 ± 0.89
F	7.500	17.770
P	<0.001	<0.001

[a]$P < 0.05$ compared with before treatment; [b]$P < 0.05$ compared with CR+CRi patients treated for 1 month; [c]$P < 0.05$ compared with CR+CRi patients treated for 3 months.

TABLE 3: Comparison of T lymphocyte subsets before and after treatment ($\bar{x} \pm s$).

Groups	CD3+ (%)	CD4+ (%)	CD8+ (%)	CD4+/CD8+ (%)
Before treatment ($n = 35$)	66.52 ± 9.12	31.95 ± 9.82	31.56 ± 7.45	1.01 ± 0.45
CR+CRi patients treated for 1 month ($n = 32$)	72.45 ± 8.56[a]	38.45 ± 8.45[a]	30.79 ± 5.26	1.25 ± 0.26[a]
CR+CRi patients treated for 3 months ($n = 32$)	73.26 ± 8.66[a]	42.59 ± 8.75[a]	29.62 ± 5.12	1.44 ± 0.31[ab]
PD patients treated for 1 month ($n = 3$)	67.45 ± 12.05	32.15 ± 4.56	31.05 ± 12.45	1.04 ± 0.25
F	4.010	8.340	0.540	8.700
P	0.010	<0.001	0.657	<0.001

[a]$P < 0.05$ compared with before treatment; [b]$P < 0.05$ compared with CR+CRi patients treated for 1 month.
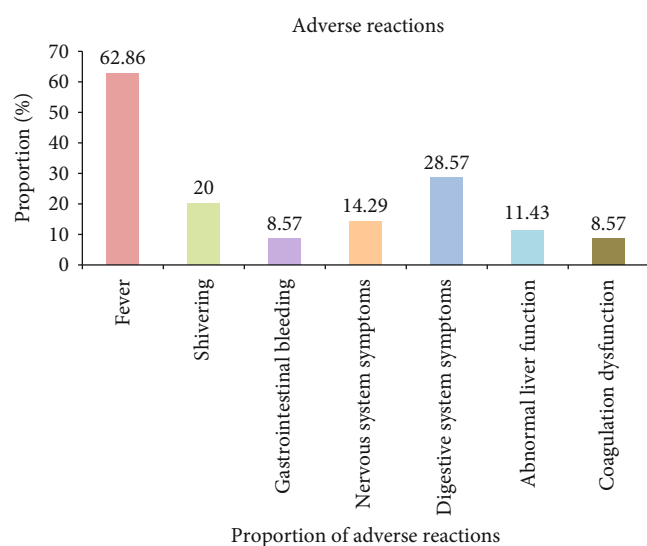
FIGURE 3: Analysis of side effects after treatment.

side effects were all relieved after symptomatic treatment (Figure 3).

3.5. Infection Analysis. During the course of CAR-T therapy in 35 patients with ALL, 2 patients had biliary tract infection and 13 patients had lung infection. No correlations were found between the infection and age, gender, CRS grade, usage of glucocorticoids or tocilizumab, and laboratory indicators such as WBC, ANC, PLT, and Hb ($P > 0.05$, Table 4).

4. Discussion

ALL is a common malignant hematological disease, accounting for 80% of acute leukemia in children. At present, the clinical treatment effect of ALL is good with the CR rate of as high as 70%-90%, but some patients show refractory ALL or easy to relapse. About 30% of ALL patients have relapses after conventional induction remission, and the cure rate of refractory or relapses is low, only about 5% [9, 10]. Therefore, how to improve the cure rate and quality of life of patients with refractory ALL has become the focus of current research.

CAR-T cell therapy is to transform T cells into T cells carrying a single-chain variable fragment (scFV) with specific extracellular recognition antigen by genetic engineering, which has the function of targeting to kill tumor cells. After *in vitro* expansion, CAR-T cells are transfused back to patients to improve their immune function and kill abnormal leukemia cells in the body, which can help improve the life quality and prolong the lives of patients with ALL [11, 12]. As a new immunotherapy, CAR-T cell therapy provides a treatment option for hematologic malignancies. At the same time, some scholars are studying the application value of CAR-T cell therapy in solid tumors. Berdeja et al. [13] have concluded that the CAR-T cell assay shows a high-quality response, and a single cilta-cell infusion at a target dose of 0.75×10^6 CAR-positive live T cells per kilogram can produce an early, deep, and durable response in patients with multiple myeloma who have undergone extensive pretreatment, with a controllable safety profile. In this study, after one month of CAR-T cell therapy, the efficacy

TABLE 4: Analysis of infection after CAR-T treatment.

Groups	No infection occurs ($n = 20$)	Infection occurs ($n = 15$)	t / χ^2	P
Age (year)	35.25 ± 15.48	31.26 ± 12.33	0.821	0.418
Gender				
Male	8 (40.00)	10 (66.67)	2.440	0.118
Female	12 (60.00)	5 (33.33)		
CRS grade				
Grade 1	7 (35.00)	3 (20.00)	2.426	0.489
Grade 2	6 (30.00)	5 (33.33)		
Grade 3	6 (30.00)	4 (26.67)		
Grade 4	1 (5.00)	3 (20.00)		
Usage of glucocorticoids				
Yes	11 (55.00)	9 (60.00)	0.088	0.767
No	9 (45.00)	6 (40.00)		
Usage of tocilizumab				
Yes	15 (75.00)	11 (73.33)	0.013	0.911
No	5 (25.00)	4 (26.67)		
Initial WBC ($\times 10^9$/L)	4.52 ± 1.85	4.43 ± 1.97	0.139	0.891
Initial ANC ($\times 10^9$/L)	2.53 ± 0.28	3.05 ± 1.26	1.796	0.082
Initial PLT ($\times 10^9$/L)	127.49 ± 10.23	131.25 ± 15.48	0.865	0.393
Initial Hb ($\times 10^9$/L)	102.25 ± 20.42	97.26 ± 18.48	0.745	0.462

evaluation showed that CR patients accounted for 68.57%, CRi patients accounted for 22.86%, and PD patients accounted for 8.57%, with the total effective rate of 91.43%. During the CAR-T cell therapy, fever accounted for 62.86%, chills for 20.00%, gastrointestinal bleeding for 8.57%, nervous system symptoms for 14.29%, digestive system symptoms for 28.57%, abnormal liver function for 11.43%, and coagulation dysfunction for 8.57%. These side effects were all relieved after symptomatic treatment. These results suggested that CAR-T cells were effective in the treatment of refractory ALL without serious side effects. After symptomatic treatment, the side effects were relieved with high safety, which was similar to the research results of Li and Chen [14].

Studies have proved that the occurrence and development of ALL are closely related to the changes of immune function [15, 16]. The change of cellular immunity is more closely related to ALL. Among them, Treg cells, NK cells, and T lymphocyte subsets can mediate the change of cellular immune function. Treg cells can regulate the body's peripheral tolerance monitoring and autoimmune response, so leukemia cells will be regarded as normal cells, and the effect of immunotherapy will be weakened by inhibiting specific antitumor T cells [17, 18]. Niu et al. [19] believed that the increase of Treg cell level indicated the failure of ALL treatment or recurrence. NK cells have cytotoxic function and immune regulation function and are the first line of defense against infection and tumor. After a period of effective treatment for ALL, the NK cell level gradually recovers and the immune function of the body is enhanced [20]. T lymphocyte subsets mainly include CD3+, CD4+, and CD8+. Among them, the level of CD3+ reflects the number of T

lymphocytes in the body, CD4+ determines the change of immune cell function in the body, and CD8+ is an immunosuppressive factor. Therefore, the ratio of CD4+/CD8+ reflects the changes of cellular immune function [21]. In this study, compared with that before treatment, the Treg cell level in CR+CRi patients treated for 1 month and 3 months decreased prominently, and the NK cell level increased dramatically. Compared with that before treatment, the levels of CD3+, CD4+, and CD4+/CD8+ in patients with CR+CRi in the 1-month and 3-month groups were markedly higher, and the levels of CD4+/CD8+ in the 3-month group were memorably higher than those in the 1-month group. It was suggested that CAR-T cell therapy improved the cellular immune function of the body by mediating the changes of Treg cells, NK cells, and T lymphocyte subsets, which was helpful to control the patient's condition. During the course of CAR-T therapy in 35 patients with ALL, 2 patients had biliary tract infection and 13 patients had lung infection. In addition, no correlations were found between the infection and the age, gender, CRS grade, usage of glucocorticoids or tocilizumab, and laboratory indicators such as WBC, ANC, PLT, and Hb. No related factors of infection were found in the present study. However, some reports indicated that [22, 23] the more severe CRS after CAR-T cell treatment was, the greater the possibility of infection was. After infusion of CAR-T cells, it is sometimes difficult to distinguish infection and CRS reaction. Thus, the prevention, diagnosis, and treatment of infection after CAR-T treatment need further research. Studies have also found that early stage after CAR-T infusion is affected by pretreatment by depigmentation, and later stage is related to cytokine-mediated cytopenias. Some patients may experience prolonged cytopenia

and require blood transfusion or growth factor support, during which the patient's immune function is significantly reduced and the infection rate increases [24, 25]. The absence of infectious factors that was identified in this study may be due to the small number of cases included in this study and the single-centre retrospective study, which might have data bias.

In general, CAR-T cell therapy had a good effect on patients with refractory ALL by regulating the immune function of the body via mediating the content of immune cells. This therapy may have a therapeutic effect on refractory ALL patients with mild side effects and high safety. However, due to the limitation of research time and sample size in this experiment, the long-term prognosis of patients was not followed up and there was no control group. In the future, the mechanism of Treg cells influencing the curative effect of CAR-T cells will be further clarified through *in vivo* and *in vitro* experiments. We need to verify whether the therapeutic effect of CAR-T cells can be improved and the recurrence can be reduced by intervening Treg cells. Therefore, the sample size and research time will be expanded for in-depth exploration in our following study.

Data Availability

The datasets used and/or analyzed during the current study are available from the corresponding author on reasonable request.

Conflicts of Interest

The authors declare that they have no competing interests.

Acknowledgments

References

[1] H. Inaba and C. G. Mullighan, "Pediatric acute lymphoblastic leukemia," *Haematologica*, vol. 105, no. 11, pp. 2524–2539, 2020.

[2] H. Inaba and C. H. Pui, "Immunotherapy in pediatric acute lymphoblastic leukemia," *Cancer Metastasis Reviews*, vol. 38, no. 4, pp. 595–610, 2019.

[3] P. A. Brown, L. Ji, X. Xu et al., "Effect of postreinduction therapy consolidation with blinatumomab *vs* chemotherapy on disease-free survival in children, adolescents, and young adults with first relapse of B-cell acute lymphoblastic leukemia: a randomized clinical trial," *Journal of the American Medical Association*, vol. 325, no. 9, pp. 833–842, 2021.

[4] F. El Chaer, M. Keng, and K. K. Ballen, "MLL-rearranged acute lymphoblastic leukemia," *Current Hematologic Malignancy Reports*, vol. 15, no. 2, pp. 83–89, 2020.

[5] J. Qu, Q. Mei, L. Chen, and J. Zhou, "Chimeric antigen receptor (CAR)-T-cell therapy in non-small-cell lung cancer (NSCLC): current status and future perspectives," *Cancer Immunology, Immunotherapy*, vol. 70, no. 3, pp. 619–631, 2021.

[6] N. Dasyam, P. George, and R. Weinkove, "Chimeric antigen receptor T-cell therapies: optimising the dose," *British Journal of Clinical Pharmacology*, vol. 86, no. 9, pp. 1678–1689, 2020.

[7] C. Roddie, J. Dias, M. A. O'Reilly et al., "Durable responses and low toxicity after fast off-rate CD19 chimeric antigen receptor-T therapy in adults with relapsed or refractory B-cell acute lymphoblastic leukemia," *Journal of Clinical Oncology*, vol. 39, no. 30, pp. 3352–3363, 2021.

[8] S. Aamir, M. Y. Anwar, F. Khalid, S. I. Khan, M. A. Ali, and Z. E. Khattak, "Systematic review and meta-analysis of CD19-specific CAR-T cell therapy in relapsed/refractory acute lymphoblastic leukemia in the pediatric and young adult population: safety and efficacy outcomes," *Clinical Lymphoma, Myeloma & Leukemia*, vol. 21, no. 4, pp. e334–e347, 2021.

[9] K. Wudhikarn, J. R. Flynn, I. Rivière et al., "Interventions and outcomes of adult patients with B-ALL progressing after CD19 chimeric antigen receptor T-cell therapy," *Blood*, vol. 138, no. 7, pp. 531–543, 2021.

[10] M. Medinger, D. Heim, C. Lengerke, J. P. Halter, and J. R. Passweg, "Akute lymphoblastische leukämie – Diagnostik und Therapie," *Therapeutische Umschau*, vol. 76, no. 9, pp. 510–515, 2019.

[11] I. Aldoss, S. J. Forman, and V. Pullarkat, "Acute lymphoblastic leukemia in the older adult," *Journal of Oncology Practice/American Society of Clinical Oncology*, vol. 15, no. 2, pp. 67–75, 2019.

[12] A. D. McLellan and S. M. Ali Hosseini Rad, "Chimeric antigen receptor T cell persistence and memory cell formation," *Immunology and Cell Biology*, vol. 97, no. 7, pp. 664–674, 2019.

[13] J. G. Berdeja, D. Madduri, S. Z. Usmani et al., "Ciltacabtagene autoleucel, a B-cell maturation antigen-directed chimeric antigen receptor T-cell therapy in patients with relapsed or refractory multiple myeloma (CARTITUDE-1): a phase 1b/2 open-label study," *The Lancet*, vol. 398, no. 10297, pp. 314–324, 2021.

[14] X. Li and W. Chen, "Mechanisms of failure of chimeric antigen receptor T-cell therapy," *Current Opinion in Hematology*, vol. 26, no. 6, pp. 427–433, 2019.

[15] S. P. Hunger and E. A. Raetz, "How I treat relapsed acute lymphoblastic leukemia in the pediatric population," *Blood*, vol. 136, no. 16, pp. 1803–1812, 2020.

[16] M. Labib Salem, A. A. Zidan, R. Ezz El-Din El-Naggar et al., "Myeloid-derived suppressor cells and regulatory T cells share common immunoregulatory pathways-related microRNAs that are dysregulated by acute lymphoblastic leukemia and chemotherapy," *Human Immunology*, vol. 82, no. 1, pp. 36–45, 2021.

[17] M. Delia, P. Carluccio, A. Mestice et al., "The impact of graft CD3 cell/regulatory T cell ratio on acute graft-versus-host disease and post-transplantation outcome: a prospective multicenter study of patients with acute leukemia undergoing allogeneic peripheral blood stem cell transplantation," *Transplantation and Cellular Therapy*, vol. 27, no. 11, pp. 918.e1–918.e9, 2021.

[18] N. Pang, X. Alimu, R. Chen et al., "Activated galectin-9/Tim3 promotes Treg and suppresses Th1 effector function in chronic lymphocytic leukemia," *The FASEB Journal*, vol. 35, no. 7, article e21556, 2021.

[19] Z. E. Niu, D. X. Jing, and C. Y. Xu, "Clinical effect of Bazhen decoction combined with sequential treatment of chemotherapy on acute lymphoblastic leukemia patients with deficiency

of qi and yin," *Zhongguo Shi Yan Xue Ye Xue Za Zhi*, vol. 30, no. 1, pp. 119–125, 2022.

[20] C. Duault, A. Kumar, A. Taghi Khani et al., "Activated natural killer cells predict poor clinical prognosis in high-risk B- and T-cell acute lymphoblastic leukemia," *Blood*, vol. 138, no. 16, pp. 1465–1480, 2021.

[21] J. Cheng, H. Z. Ma, and H. Zhang, "Detection and analysis of T lymphocyte subsets and B lymphocytes in patients with acute leukemia," *Zhongguo Shi Yan Xue Ye Xue Za Zhi*, vol. 27, no. 2, pp. 327–330, 2019.

[22] V. S. Sheth and J. Gauthier, "Taming the beast: CRS and ICANS after CAR T-cell therapy for ALL," *Bone Marrow Transplantation*, vol. 56, no. 3, pp. 552–566, 2021.

[23] A. V. Hirayama and C. J. Turtle, "Toxicities of CD19 CAR-T cell immunotherapy," *American Journal of Hematology*, vol. 94, no. S1, pp. S42–S49, 2019.

[24] P. Strati, A. Varma, S. Adkins et al., "Hematopoietic recovery and immune reconstitution after axicabtagene ciloleucel in patients with large B-cell lymphoma," *Haematologica*, vol. 106, no. 10, pp. 2667–2672, 2021.

[25] A. Cordeiro, E. D. Bezerra, A. V. Hirayama et al., "Late events after treatment with CD19-targeted chimeric antigen receptor modified T cells," *Biology of Blood and Marrow Transplantation*, vol. 26, no. 1, pp. 26–33, 2020.

Hindawi

Research Article

Silencing of NLRP3 Sensitizes Chemoresistant Ovarian Cancer Cells to Cisplatin

Weijia Li [ID],[1] **Xibo Zhao** [ID],[2] **Rujian Zhang** [ID],[3] **Jiabin Xie** [ID],[3] and **Guangmei Zhang** [ID][2]

[1]*Department of Gynecology, Harbin Medical University, Harbin, 150081 Heilongjiang, China*
[2]*Department of Gynecology, The First Affiliated Hospital of Harbin Medical University, Harbin, 150081 Heilongjiang, China*
[3]*Department of Gynecology, Southern Medical University Affiliated Maternal and Child Health Hospital of Foshan, Foshan, 528000 Guangdong, China*

Correspondence should be addressed to Guangmei Zhang; guangmeizhang@126.com

Background. Ovarian cancer is a fatal gynecological malignancy. The resistance to chemotherapy in ovarian cancer treatment has been a thorny issue. This study is aimed at probing the molecular mechanism of cisplatin (DDP) resistance in ovarian cancer. *Methods.* Bioinformatics analysis was conducted to examine the role of Nod-like receptor protein 3 (NLRP3) in ovarian cancer. The NLRP3 level in DDP-resistant ovarian cancer tumors and cell lines (SKOV3/DDP and A2780/DDP) was evaluated by applying immunohistochemical staining, western blot, and qRT-PCR. Cell transfection was conducted to regulate the NLRP3 level. Cell abilities to proliferate, migrate, invade, and apoptosis were measured employing colony formation, CCK-8, wound healing, transwell, and TUNEL assays, respectively. Cell cycle analysis was completed via flow cytometry. Corresponding protein expression was measured by western blot. *Results.* NLRP3 was overexpressed in ovarian cancer, correlated with poor survival, and upregulated in DDP-resistant ovarian cancer tumors and cells. NLRP3 silencing exerted antiproliferative, antimigrative, anti-invasive, and proapoptotic effects in A2780/DDP and SKOV3/DDP cells. Additionally, NLRP3 silencing inactivated NLRPL3 inflammasome and blocked epithelial-mesenchymal transition via enhancing E-cadherin and lowering vimentin, N-cadherin, and fibronectin. *Conclusion.* NLRP3 was overexpressed in DDP-resistant ovarian cancer. NLRP3 knockdown hindered the malignant process of DDP-resistant ovarian cancer cells, providing a potential target for DPP-based ovarian cancer chemotherapy.

1. Introduction

Ovarian cancer, well-prevalent gynecological oncology, is one of the main contributors to deaths associated with cancer in females worldwide [1, 2]. It is estimated that the new ovarian cancer cases may rise to 371000, and the number of deaths will be 254000 by 2035 [3]. Early ovarian cancer is not easily diagnosed due to ineffective screening means, [4] resulting in its development to an advanced stage when diagnosed. Surgical resection combined with cisplatin- (DDP-) based chemotherapy is the mainstay of ovarian cancer treatment. Nevertheless, 70%-90% of the patients relapse, and most develop resistance to the DPP challenge, which takes

the main responsibility for the treatment failure and the poor 5-year survival rate below 40% [5, 6]. Thus, clarifying the potential mechanism of chemoresistance and developing effective strategies for reducing DDP resistance in ovarian cancer are quite essential.

Nod-like receptor protein 3 (NLRP3) inflammasome is a complex consisting of NLRP3, the adaptor apoptosis-associated speck-like protein (ASC), and the effector pro-caspase1. NLRP3 inflammasome activation facilitates the formation of active caspase-1 and contributes to the maturity and production of interleukin (IL)-18 and IL-1β, eventually leading to inflammation [7–9]. As a crucial constituent of the innate immune system, the NLRP3 inflammasome frequently

responds to cellular damage and microbial infection [10]. Recently, emerging evidence revealed that NLRP3 inflammasome was dysregulated during tumor development. For example, NLRP3 was overexpressed in colon cancer cells and linked to the poor survival of patients [11, 12]; NLRP3 inflammasome was activated in gastric cancer, which was beneficial in promoting tumorigenesis [13]. On the contrary, NLRP3 inflammasome was downregulated in human hepatocellular carcinoma, and the absent NLRP3 was linked to advanced stages [14]. Thus, attributed to the dual role in different types of malignant tumor, NLRP3 inflammasome was regarded as a double-edged sword in tumorigenesis [15]. Of note, NLRP3 was reported to have an aberrantly high expression in ovarian cancer, and NLRP3 inflammasome participated in the development of ovarian cancer [16, 17]. However, a knowledge gap exists concerning the impacts of NLRP3 inflammasome on ovarian cancer with DPP resistance.

Here, we aimed to assess the expression level of NLRP3 in ovarian cancer with DDP resistance, clarify its potential regulatory role, and offer new therapeutic strategies for the advancement of chemoresistance in ovarian cancer. The graphical flow chart has been illustrated in Scheme 1.

2. Methods and Materials

2.1. Bioinformatics Analysis.
Gene Expression Omnibus (GEO; https://www.ncbi.nlm.nih.gov/geo/) database includes experimental data for genomic DNA and proteins and data from single- and dual-channel determination of mRNA expression. Five expression profiling datasets (GSE26712, GSE53963, GSE51088, GSE66957, and GSE135886) were obtained from the GEO database. The expression data of NLRP3 in ovarian cancer were analyzed using GEO2R online. The figure construction was carried out, adopting R package software 4.0.3. A total of 381 ovarian cancer cases and 71 normal cases were downloaded from The Cancer Genome Atlas (TCGA) database (http://www.cancer.gov/tcga). The expression of NLRP3 in ovarian cancer tumor tissues and normal tissues was analyzed according to the downloaded data. The clinical profile of 381 ovarian cancer patients was obtained from the TCGA database, and the survival analysis was conducted using the Kaplan-Meier method. The patients with missing clinical data about tumor stages were excluded from this study. A total of 377 samples (23 at stage II, 296 at stage III, and 58 at stage IV) were examined for NLRP3 level at different tumor stages. Moreover, a single-variable Cox proportional risk regression assay was conducted to explore the risk factors that were remarkably correlated with overall survival in TCGA ovarian cancer dataset. In addition, Tumor Immunization Estimation Resource (TIMER; http://timer.cistrome.org), a comprehensive database to assess the relationship between immune infiltrating cells and overall survival of cancers, was applied to estimate the infiltration of CD8^{+} T cells, CD4^{+} T cells, B cells, neutrophils, macrophage, and myeloid dendritic cells related to NLRP3 level in ovarian cancer patients.

2.2. Tissue Samples.
A total of 36 ovarian cancer specimens were collected from patients receiving oophorectomies from 2022.1 to 2022.10 at Foshan Women and Children Hospital. Among these specimens, 18 were harvested from DDP-resistant patients suffering from recurrent or persistent disease within 6 months following DDP-based chemotherapy. The other was collected from DDP-sensitive (nonresistant) patients without recurrence or with recurrence beyond 6 months. The patient's clinical information is listed in Table 1. The study was approved by the Ethics Committees of Foshan Women and Children Hospital (Approval number: FSFY-MEC-2021-145), and written consent was acquired from all patients.

2.3. Immunohistochemical Staining.
The tissue was fixed in 4% paraformaldehyde for 24 h, embedded in paraffin, and sliced to a thickness of 5 μm. Subsequently, the slices were deparaffinized and rehydrated, followed by heating in 0.01 M citric buffer for 15 min. Before probing overnight at 4°C with anti-NLRP3 antibody (ab263899, Abcam), the slices were impeded in 3% H_2O_2 for 20 min and then with 5% normal serum for 30 min. Thereafter, the slices were probed with horseradish peroxidase- (HRP-) conjugated secondary antibody (ab6721, Abcam) for 30 min, diaminobenzidine (DAB) stained (ZSGB-BIO, Beijing, China) for 5 min followed by hematoxylin counterstaining for 30 s. Eventually, the images were obtained utilizing a light microscope (Olympus, Tokyo, Japan).

2.4. Quantitative Real-Time Polymerase Chain Reaction (qRT-PCR).
RNA content was exacted from the tumor tissues adopting Trizol (Thermo Fisher Scientific, CA, USA). The concentration and purity of the total RNA were checked using NanoDrop 3000 (Thermo Fisher Scientific Inc., Waltham, MA, USA). The RNA content was reversely transcribed into complementary DNA (cDNA) adopting a cDNA synthesis kit (Thermo Fisher Scientific Inc.), followed by qRT-PCR analysis utilizing SYBR Green Master Mix (Takara, Shiga, Japan). The primers of PCR are listed in Table 2. $2^{-\triangle\triangle Ct}$ method was utilized for calculating gene expressions using β-actin as an internal reference.

2.5. Western Blot.
RIPA lysis buffer (Bolingkewei, Beijing, China) was applied to homogenize the tissues. The whole protein was extracted and quantified using a bicinchoninic acid (BCA) protein assay kit (Pierce, Rockford, IL, USA). The protein (35 μg/lane) was isolated through 12% SDS-PAGE gels, followed by transferring onto polyvinylidene difluoride (PVDF) membranes (Millipore, MA, USA). After 1 h incubation with 5% defatted milk, membranes were probed at 4°C overnight against the following antibodies: NLRP3 (ab263899, Abcam), IL-18 (ab243091, Abcam), cleaved caspase-1 (orb126550, Biorbyt), IL-1β (ab216995, Abcam), N-cadherin (ab76011, Abcam), E-cadherin (ab40772, Abcam), fibronectin (ab2413, Abcam), vimentin (ab92547, Abcam), and β-actin (ab8226, Abcam). On the following day, membranes were exposed to goat anti-mouse (ab6789, Abcam) or goat anti-rabbit (ab6721, Abcam) HRP-conjugated secondary antibodies for 2 h at room temperature. Eventually, the signals were

Table 1: Clinical characteristics of ovarian carcinoma patients.

Pathological parameters	Nonresistant	DDP-resistant
Age		
<50	7	9
≥50	11	9
Stage		
I+II	13	9
III+IV	5	9
Lymph node metastasis		
Negative	17	17
Positive	1	1
Histologic subtype		
Serous	7	14
Others	11	4

Table 2: Primer of the target gene for real-time PCR.

Genes		Sequences (5′-3′)
NLRP3	Forward	5′-CTCTAGCTGTTCCTGAGGCTG-3′
	Reverse	5′-TTAGGCTTCGGTCCACACAG-3′
β-Actin	Forward	5′-AGCGAGCATCCCCCAAAGTT-3′
	Reverse	5′-GGGCACGAAGGCTCATCATT-3′

developed with an enhanced chemiluminescence system (Millipore, USA), followed by quantification with ImageJ software (NIH, Bethesda, Maryland, USA).

2.6. Cell Culture and Treatment. A2780 and SKOV3, two human ovarian cancer cell lines, were provided by BeNa Culture Collection (Beijing, China). SKOV3 cells were cultivated in McCoy's 5a medium. In contrast, A2780 cells were cultivated in RPMI-1640 medium (Hyclone, Logan, UT, USA) in a 5% CO_2 environmental incubator at 37°C, supplemented with 10% fetal bovine serum (FBS; Gibco, USA) with 0.1 mg/mL streptomycin and 100 U/mL penicillin (Gibco, USA). DDP-resistant SKOV3/DDP and A2780/DDP cells were constructed as previously reported [18]. 0.5 μg/L of DDP was added for SKOV3/DDP and A2780/DDP cells to retain the resistance to DDP.

2.7. Cell Transfection. Short hairpin RNA (shRNA) targeting NLRP3 (sh-NLRP3) was designed and synthesized by Ribo-Bio (Guangzhou, China). Cells transfection using sh-NLRP3 and sh-vector (negative control) was implemented utilizing a Lipofectamine 3000 Transfection reagent (Invitrogen, CA, USA) strictly in line with its guidelines. Subsequent experiments were carried out 48 h posttransfection.

2.8. Cell Counting Kit-8 (CCK-8) Assay. 5×10^3 cells were cultivated into 96-well plates. CCK-8 reagent (Dojindo Molecular Technologies, Gaithersburg, MD) was added to the plates at indicated times (20 l), and the plates were incubated for 2

hours. The absorbance was tested at 450 nm with the help of a microplate reader (Bio-Rad Laboratories, Hercules, CA).

2.9. Colony Formation Assay. 2×10^3 cells were plated in 6-well plates and then cultivated for ten days. During this period, the medium was replaced every three days. 4% paraformaldehyde was employed to immobilize the colonies for 20 min. Eventually, cells underwent staining with 0.1% crystal violet for 30 min, followed by observation and counting.

2.10. Wound-Healing Assay. 5×10^4 cells were cultivated into 6-well plates in a 5% CO_2 incubator at 37°C. Upon achieving 100% confluence, a sterile pipette tip was adopted to create liner scratches. PBS washed the plates carefully to discard the floating cells. 24 h later, the healing of the scratches was observed and photographed employing a light microscope (Olympus, Tokyo, Japan).

2.11. Transwell Assay. A 24-well insert transwell chamber (Millipore, MA, USA) was coated with 200 mg/ml Matrigel (BD Biosciences, NY, USA). 5×10^4 cells were resuspended in serum-free medium and placed into the upper transwell chamber, while 500 μl medium with 10% FBS was put into the lower chamber. 24 h later, after wiping out the noninvasive cells, the cells got a fixation with 4% paraformaldehyde, followed by 0.5% crystal violet staining. Images of invaded cells were photographed by a light microscope (Olympus, Tokyo, Japan).

2.12. Terminal Deoxynucleotidyl Transferase-Mediated dUTP Nick End Labeling (TUNEL) Staining. 4% paraformaldehyde was utilized to fix cells. 20 min later, cells underwent permeabilization using 0.1% Triton X-100 for 30 minutes and inactivated endogenous peroxidase by 0.3% H2O2 for 20 minutes. Afterward, the TUNEL mixture solution (Beyotime and Biotechnology, Shanghai, China) was added, and the cells were incubated for 1 h at 37°C in the darkness. 4′, 6-diamidino-2-phenylindole (DAPI) solution was added to stain cells. The images were captured adopting an Olympus IX70 inverted microscopy (Olympus, Tokyo, Japan).

2.13. Flow Cytometry Analysis. Cells were washed with precooled PBS at 4°C, followed by fixation in 70% ethanol overnight at 4°C. After that, cells were stained with 50 μg/mL propidium iodide (PI) containing RNase (Beyotime and Biotechnology, Shanghai, China) for 30 min in the darkness. The cell cycle was measured adopting flow cytometry (FACSCalibur, Becton-Dickinson) and analyzed using FlowJo software (Leonard Herzenberg, Stanford University, USA).

2.14. Statistical Analysis. All data analyzed by GraphPad Prism 8.0 (GraphPad, CA, USA) were presented as mean ± standard deviation. Group comparisons were evaluated by adopting a one-way analysis of variance (ANOVA) with Tukey's post hoc test. $p < 0.05$ meant statistically significant.

3. Results

3.1. NLRP3 Is Overexpressed in Ovarian Cancer and Linked to Poor Prognosis. Based on the indicated role of NLRP3 in

malignant diseases, we analyzed the expression profile of NLRP3 in ovarian cancer depending on GEO and TCGA databases. As shown in Figure 1(a), the public data from the GEO data portal revealed that NLRP3 expression was upregulated in tumor tissues of ovarian cancer, compared to the normal, which was concordant with the findings from the TCGA database (Figure 1(b)). Meanwhile, the expression level of NLRP3 was increasing from stage II to stage IV of ovarian cancer patients (Figure 1(c)), suggesting that NLRP3 was positively linked to the deterioration of ovarian cancer. The survival assay followed by Cox regression analysis revealed that patients with a higher level of NLRP3 had a poorer survival probability, and NLRP3 might act as an independent prognostic gene in ovarian cancer (Figures 1(d) and 1(e)). Finally, immune infiltration analysis using TIMER2 found that NLRP3 expression levels were significantly positively linked to the proportions of T cells, neutrophils, macrophages, and myeloid dendritic cells in ovarian cancer tissues (Figure 1(f)).

3.2. NLRP3 Is Upregulated in DPP-Resistant Ovarian Cancer.

To understand the role of NLRP3 in DDP-resistant ovarian cancer, we first detected NLRP3 levels in patients with DPP resistance. As shown in Figure 2(a), the NLRP3 level in DDP-resistant tumor tissues was greatly higher than that in nonresistant tissues. Subsequently, three unpaired tumor tissues from DDP-resistant and non-resistant patients were randomly measured, employing immunohistochemical staining and western blot. It was observable that the NLRP3 level was remarkably upregulated in resistant tissues (Figures 2(b) and 2(c)). Furthermore, we evaluated the NLRP3 level in ovarian cancer cell lines (A2780 and SKOV3) and their DDP-resistant forms and found that NLRP3 was upregulated in A2780/DDP and SKOV3/DDP cells (Figures 2(d) and 2(e)).

3.3. Silencing of NLRP3 Retard Cell Proliferation and Cell Cycle Progression in DDP-Resistant Ovarian Cancer Cells.

Next, a series of cellular biological activities were measured to assess the regulation of NLRP3 in DDP-resistant ovarian cancer. A2780/DDP and SKOV3/DDP cells were transfected with sh-NLRP3 to knock down NLRP3. Attributed to a relatively high transfection efficacy, sh-NLRP3-1 was selected in the following experiments (Figure 3(a)). The findings, as shown in Figure 3(b), revealed that the cell viability in the sh-NLRP3 group was significantly reduced in A2780/DDP and SKOV3/DDP cells compared to the sh-vector group. Meanwhile, the colonies were also lessened following NLRP3 knockdown (Figures 3(c) and 3(d)). In addition, flow cytometry analysis exhibited an elevated cell cycle arrest in G0/G1 phase, accompanied by a reduced cell proportion in the S phase after NLRP3 knockdown in both A2780/DDP and SKOV3/DDP cells (Figures 3(e) and 3(f)), suggesting that the cell cycle progression was blocked by NLRP3 knockdown in DPP-resistant ovarian cancer cells.

3.4. Silencing of NLRP3 Represses Cell Invasion and Migration While Promoting Apoptosis in DDP-Resistant Ovarian Cancer Cells.

Subsequently, a series of cellular behaviors were examined to assess cell migration, invasiveness, and apoptosis changes after NLRP3 silencing. As presented in Figures 4(a) and 4(b), the healing of the scratch was hindered in the sh-NLRP3 group compared to the sh-vector group in both SKOV3/DPP cells and A2780/DDP cells, suggesting that the migration ability of these DDP-resistant cells was weakened upon following NLRP3 knockdown. Meanwhile, the less invasive cells observed in the sh-NLRP3 group in Figure 4(c) indicate that NLRP3 silencing weakened the invasive ability of DDP-resistant ovarian cancer cells. Afterward, Figure 4(e) revealed that the silencing of NLRP3 caused a remarkable elevation of TUNEL-positive cells in SKOVE/DDP cells but not A2780/DDP cells.

3.5. Silencing of NLRP3 Inactivates NLRP3 Inflammasome in DDP-Resistant Ovarian Cancer Cells.

As NLRP3 is a crucial component of the NLRP3 inflammasome, we examined the impact of NLRP3 silencing on the NLRP3 inflammasome. Figure 5 shows that the expression level of NLRP3, IL-18, IL-1β, and cleaved caspase-1 was significantly reduced following NLRP3 knockdown in both SKOVE/DDP cells and A2780/DDP cells, demonstrating that silencing of NLRP3 inactivated NLRP3 inflammasome in DDP-resistant ovarian cancer cells.

3.6. Silencing of NLRP3 Suppresses Epithelial-Mesenchymal Transition (EMT) in DDP-Resistant Ovarian Cancer Cells.

EMT is an early event of tumor invasion and metastasis [19]; hence, we examined the impacts of NLRP3 knockdown on EMT markers. As exhibited in Figure 6, the epithelial marker E-cadherin was significantly upregulated following NLRP3 silencing, but the expression level of N-cadherin, fibronectin, and vimentin, the mesenchymal markers, were markedly lowered following NLRP3 knockdown, indicating that NLRP3 knockdown reversed EMT in DDP-resistant ovarian cancer cells.

4. Discussion

Ovarian cancer is a fatally gynecological malignant tumor. Attributed to drug resistance, it is hard to completely cure, leading to recurrences, metastasis, and poor survival rate of ovarian cancer [20]. Hence, it is essential to elucidate the drug-resistance mechanism and to prevent drug resistance in ovarian cancer. Here, it is the first time to be verified that NLRP3 serves a vital role in DDP-based chemoresistance of ovarian cancer. The findings revealed that NLRP3 was overexpressed in response to DDP-resistant ovarian cancer. NLRP3 knockdown could effectively block cell proliferation, invasion, and EMT, while it promotes apoptosis in ovarian cancer cells with DDP resistance. Collectively, the data revealed that NLRP3 knockdown and the inactivation of NLRP3 inflammasome might weaken the malignant phenotype of ovarian cancer with DDP resistance and regulate the chemoresistance of ovarian cancer cells to DDP-based therapy.

The involvement of NLRP3 inflammasome in tumor initiation and development of different types of cancer has been widely addressed, especially its dual role in cancers as aforementioned. As drug resistance strictly limits the therapeutic

(a)

(b)

(c)

(d)

(e)

(f)
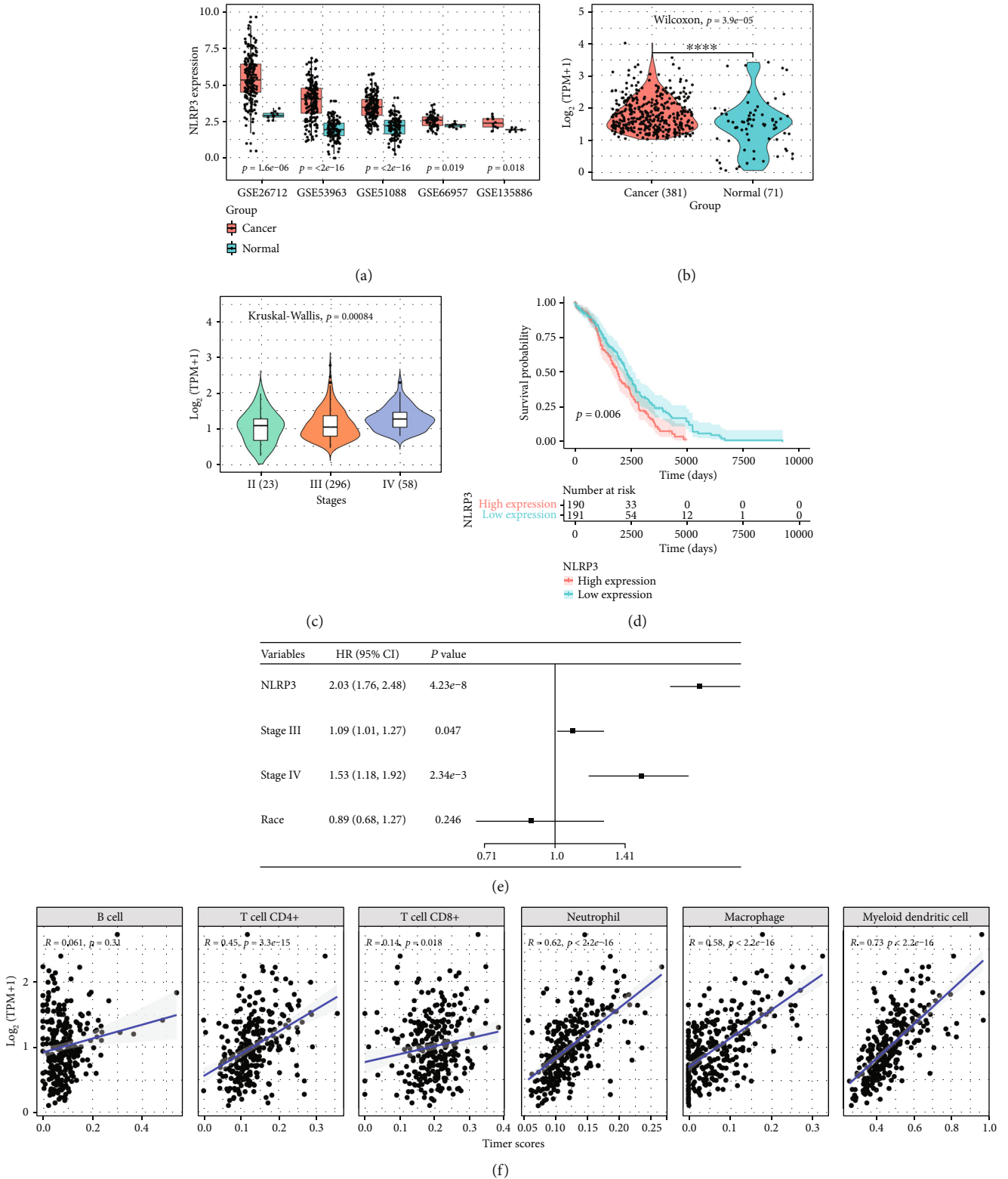
Figure 1: NLRP3 is overexpressed in ovarian cancer and linked to poor prognosis. (a) The gene expression data for ovarian cancer patients with NLRP3 expression information (GSE26712, GSE53963, GSE51088, GSE66957, and GSE135886) were obtained from the NCBI GEO database. (b) The expression profile of NLRP3 in ovarian cancer from TCGA database. (c) NLRP3 level in different clinical stages of patients with ovarian cancer. (d) The survival rate analysis of NLRP3 level and ovarian cancer patients. (e) Cox regression analysis of NLRP3 in ovarian cancer. (f) TIMER database was adopted to assess the association between NLRP3 level and immune infiltrates' abundances in ovarian cancer.

(a)

(b)

(c)

(d)

(e)
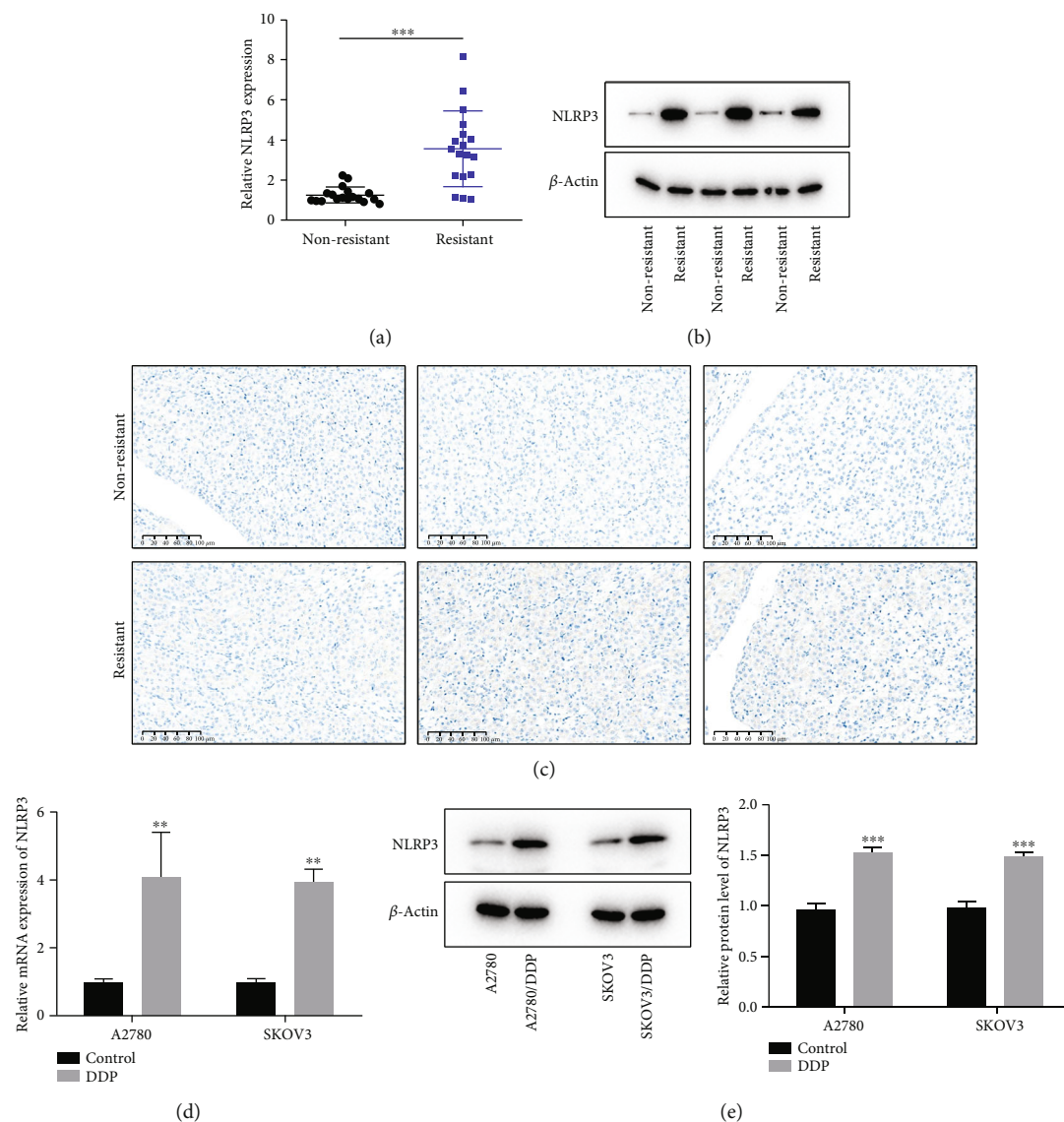
FIGURE 2: NLRP3 is upregulated in DPP-resistant ovarian cancer. (a) The tumor tissues from ovarian cancer patients with DDP resistance or not were collected, and the mRNA level of NLRP3 in tumor tissues was assessed by qRT-PCR. (b) The NLRP3 expression in tumor tissues was assessed using a western blot. (c) The NLRP3 expression in tumor tissues was observed using immunohistochemical staining. (d) The NLRP3 level in A2780 and SKOV3 and the DDP-resistant ovarian cancer cells was assessed, adopting qRT-PCR. (e) The NLRP3 expression in A2780 and SKOV3 and the DDP-resistant ovarian cancer cells was assessed adopting a western blot. $^{**}p < 0.01$, and $^{***}p < 0.001$.

efficacy of chemotherapy and seriously harms patients' health and life, increasing attention has been paid to whether NLRP3 can also regulate the malignant processes against drug resistance in cancer. For instance, the activated NLRP3 inflammasome facilitated leukemia cell proliferation and improved chemotherapy resistance, while the inactivation of NLRP3 exerted the opposite effects, demonstrating the promotive effects of NLRP3 on cancer development and chemotherapy resistance in acute myeloid leukemia [21]. Meanwhile, NLRP3 was reported to enhance gemcitabine-based resistance in triple-negative breast cancer cells [22]. In addition, it was proved that NLRP3 inflammasome could promote resistance of 5-fluorouracil to oral squamous cell carcinoma [23]. The existing evidence suggested that NLRP3

inflammasome might be an effective target for the adjuvant chemotherapy of multiple types of cancer. Regarding ovarian cancer, it was only reported by Alrashed et al. that NLRP3 could improve the gemcitabine sensitivity in gemcitabine-resistant ovarian cancer cell lines [20], but whether NLRP3 inflammasome also exerted critical effects on DDP resistance in ovarian cancer remained unclear. Here, a high level of NLRP3 was found in DPP-resistant ovarian tumors, whereas NLRP3 silencing can suppress cell proliferation, invasion, and migration and promote apoptosis of SKOV3/DPP and A2780/DPP cells. The abovementioned findings suggest that downregulation of NLRP3 repressed the malignant processes of DPP-resistant ovarian cancer cells, which might be beneficial to improve the

(a)

(b)

(c)

(d)

(e)

(f)
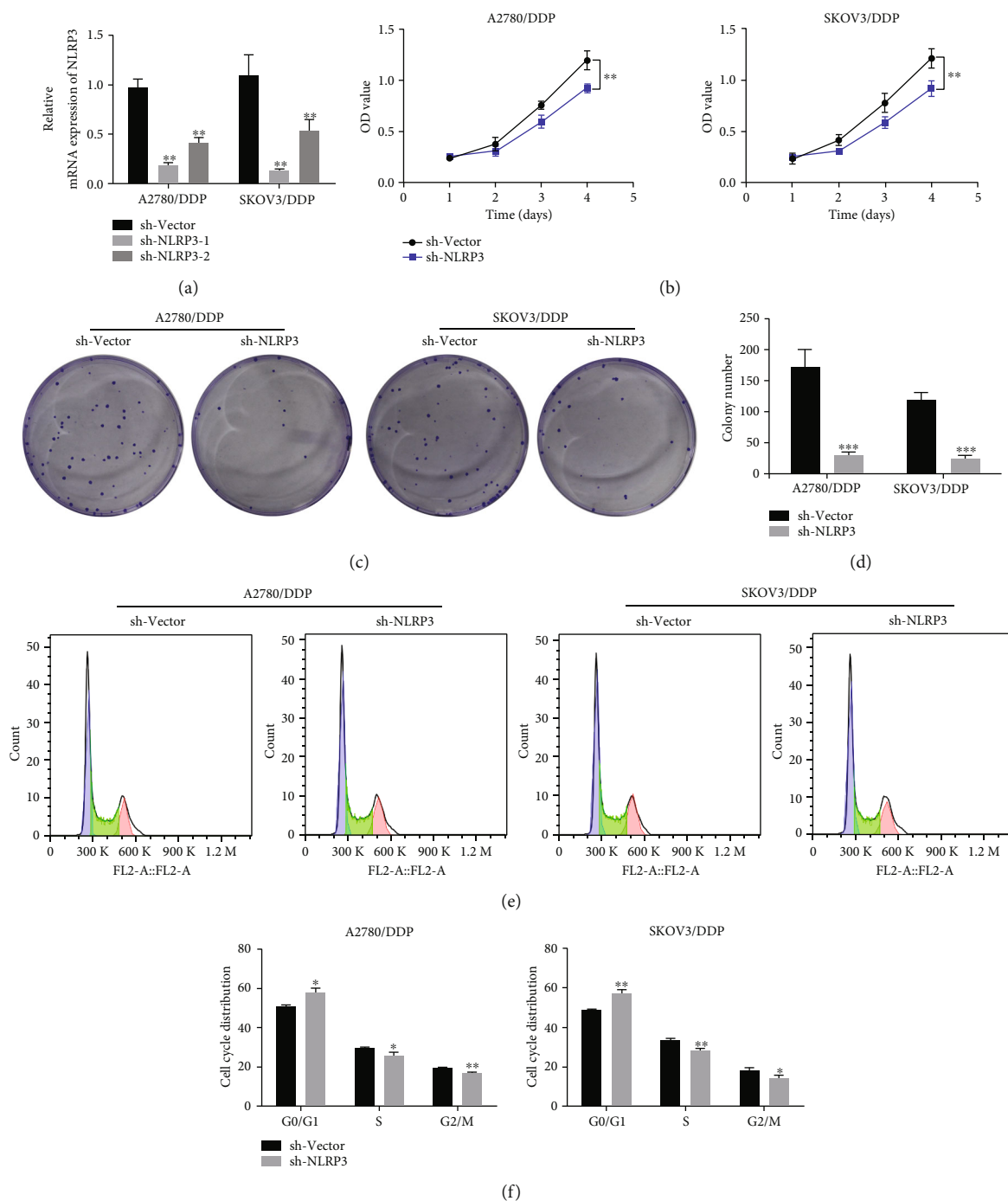
Figure 3: Silencing of NLRP3 suppressed cell proliferation and cell cycle progression in DDP-resistant ovarian cancer cells. (a) Both A2780/DDP and SKOV3/DDP cells received transfection using sh-NLRP3-1 and sh-NLRP3 to knock down NLRP3, and the mRNA level of NLRP3 was detected using qRT-PCR. (b) The cell viability was assessed, adopting CCK-8 assay. (c, d) Colony formation assay was conducted to examine cell proliferation. (e, f) Cell cycle was assessed using flow cytometry. $^*p < 0.05$, $^{**}p < 0.01$, and $^{***}p < 0.001$.

antitumor effects of DDP against DDP-resistant patients with ovarian cancer.

EMT, an early event of tumor invasion and metastasis [19], is a fundamental developmental process wherein epithelial cells lose their polarity and gain invasiveness, eventually leading to the transformation into mesenchymal cells, which has been recognized as a major approach to propagating tumor dissemination. Therefore, along with this condition, the classical epithelial marker E-cadherin was downregulated, while mesenchymal markers, including fibronectin, vimentin, and N-cadherin, were upregulated [24–26]. Currently, EMT is considered a crucial indicator for not only cancer development but also drug resistance. Resistance to DDP-based chemotherapy in ovarian cancer

(a)

(b)

(c)

(d)

(e)
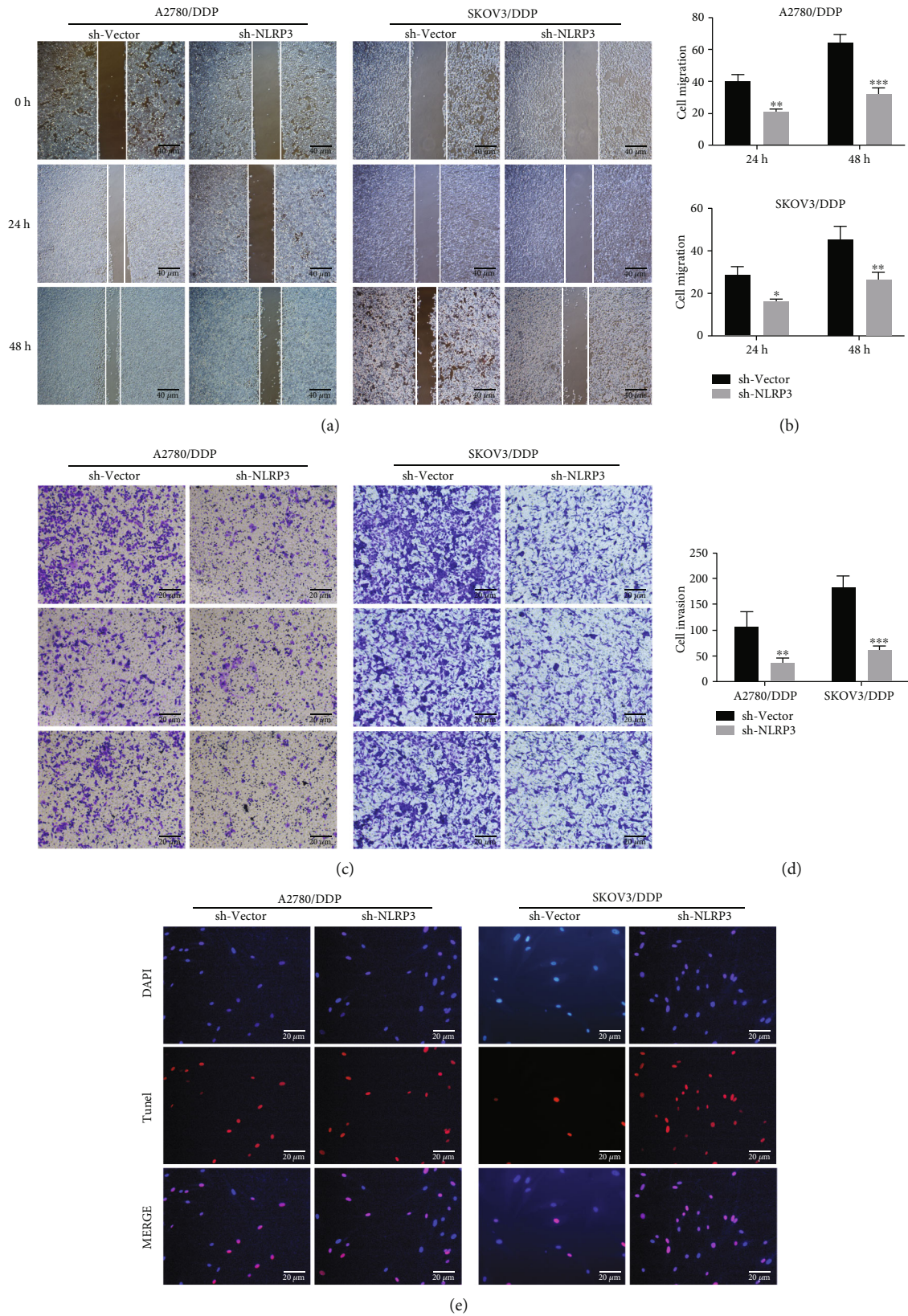
Figure 4: Silencing of NLRP3 repressed cell invasion and migration while facilitated apoptosis in DDP-resistant ovarian cancer cells. (a, b) Cell ability to migrate was assessed, adopting a wound-healing assay. (c, d) Cell ability to invade was assessed, adopting transwell assay. (e) TUNEL assay was carried out to detect cell apoptosis and apoptosis. $^*p < 0.05$, $^{**}p < 0.01$, and $^{***}p < 0.001$.
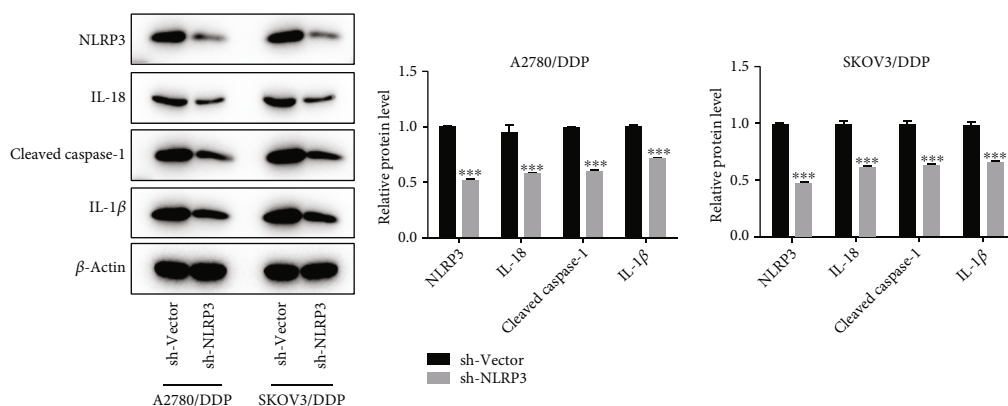
FIGURE 5: Silencing of NLRP3 inactivated NLRP3 inflammasome in DDP-resistant ovarian cancer cells. The protein expression of NLRP3, IL-18, IL-1β, and cleaved caspase-1 was assessed, adopting a western blot. ***$p < 0.001$.
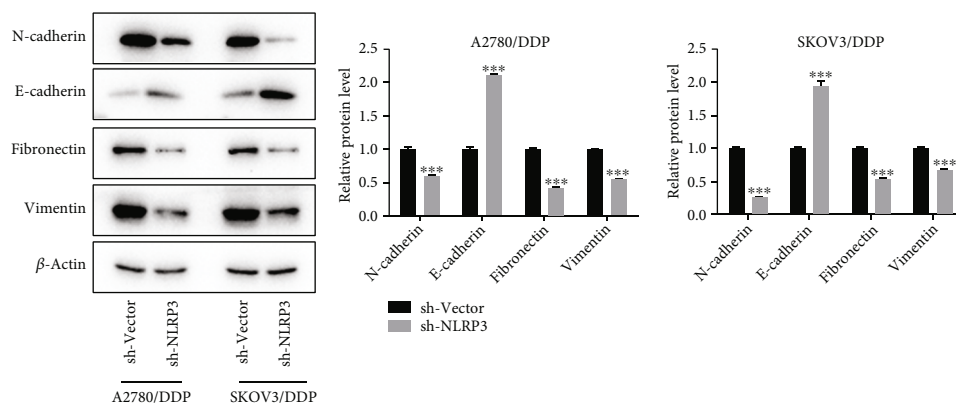
FIGURE 6: Silencing of NLRP3 suppressed EMT in DDP-resistant ovarian cancer cells. The protein expression of vimentin, fibronectin, N-cadherin, and E-cadherin was assessed, adopting a western blot. ***$p < 0.001$.

was linked to EMT [27]. Blocking PI3K/Akt/mTOR signaling pathway attenuates ovarian cancer chemoresistance to DDP through reversing EMT [28]. Consistently, we also observed a restoration of EMT following NLRP3 silencing in DDP-resistant ovarian cancer cells in this study, as proved by the elevated level of E-cadherin and the reduced level of N-cadherin, vimentin, and fibronectin, suggesting that NLRP3 knockdown might alleviate resistance towards ovarian cancer via reversing EMT.

However, some limitations still exist in the present study. First, *in vivo* assay may be beneficial to validate the current findings *in vitro*. Secondly, this study preliminarily explored the molecular mechanism of NLRP3 in DDP-resistant ovarian cancer, and the in-depth research focusing on its potential mechanism is deserved to be conducted in our future work.

5. Conclusion

Taken together, the current research highlights the specific role of NLRP3 in DDP-resistant ovarian cancer. Silencing of NLRP3 can weaken drug resistance through repressing cell proliferation, invasion, and EMT in DDP-resistant ovar-

ian cancer cells. NLRP3 is suggested to be a target for monitoring DDP resistance in ovarian cancer and improving therapeutic outcomes.

Abbreviations

DDP: Cisplatin
NLRP3: Nod-like receptor protein 3
qRT-PCR: Quantitative real-time PCR
EMT: Epithelial-mesenchymal transition
IL-18: Interleukin-18
DAB: Diaminobenzidine
PVDF: Polyvinylidene difluoride
TBST: Tris-buffered saline and Tween-20
sh-NLRP3: Short hairpin RNA targeting NLRP3
sh-vector: Empty vector
CCK-8: Cell counting kit-8
OD: Optical density
TUNEL: Terminal deoxynucleotidyl transferase-mediated dUTP nick end labeling
DAPI: 4′,6-Diamidino-2-phenylindole
SD: Standard deviation
ANOVA: One-way analysis of variance.

Data Availability

All data can be obtained from the corresponding author on reasonable request.

Conflicts of Interest

The authors declare that there is no potential interest.

Acknowledgments

Supplementary Materials

Scheme 1. Inhibition of NLRP3 enhances the susceptibility of cisplatin-resistant ovarian cancer cells to cisplatin treatment. NLRP3 was overexpressed in DDP-resistant ovarian cancer and activated the assembly of NLRP3 inflammasome. NLRP3 inflammasome could promote cell proliferation, invasion, and metastasis of DDP-resistant ovarian cancer and inhibit apoptosis of DDP-resistant ovarian cancer. (Supplementary Materials)

References

[1] M. R. Mirza, R. L. Coleman, A. González-Martín et al., "The forefront of ovarian cancer therapy: update on PARP inhibitors," *Annals of Oncology*, vol. 31, no. 9, pp. 1148–1159, 2020.

[2] B. M. Reid, J. B. Permuth, and T. A. Sellers, "Epidemiology of ovarian cancer: a review," *Cancer Biology & Medicine*, vol. 14, no. 1, pp. 9–32, 2017.

[3] F. B. N. Reid and A. Jones, *The World Ovarian Cancer Coalition Atlas-Global Trends in Incidence, Mortality and Survival*, World Ovarian Cancer Coalition, 2018.

[4] B. Orr and R. P. Edwards, "Diagnosis and treatment of ovarian cancer," *Hematology/Oncology Clinics of North America*, vol. 32, no. 6, pp. 943–964, 2018.

[5] X. Ju, H. Yu, D. Liang et al., "LDR reverses DDP resistance in ovarian cancer cells by affecting ERCC-1, Bcl-2, survivin and caspase-3 expressions," *Biomedicine & Pharmacotherapy*, vol. 102, pp. 549–554, 2018.

[6] E. L. Christie and D. D. L. Bowtell, "Acquired chemotherapy resistance in ovarian cancer," *Annals of Oncology*, vol. 28, suppl_8, p. viii13-viii5, 2017.

[7] J. P. Ting, R. C. Lovering, E. S. Alnemri et al., "The NLR gene family: a standard nomenclature," *Immunity*, vol. 28, no. 3, pp. 285–287, 2008.

[8] A. M. Janowski, R. Kolb, W. Zhang, and F. S. Sutterwala, "Beneficial and detrimental roles of NLRs in carcinogenesis," *Frontiers in Immunology*, vol. 4, p. 370, 2013.

[9] S. S. Faria, S. Costantini, V. C. C. de Lima et al., "NLRP3 inflammasome-mediated cytokine production and pyroptosis cell death in breast cancer," *Journal of Biomedical Science*, vol. 28, no. 1, p. 26, 2021.

[10] M. Moossavi, N. Parsamanesh, A. Bahrami, S. L. Atkin, and A. Sahebkar, "Role of the NLRP3 inflammasome in cancer," *Molecular Cancer*, vol. 17, no. 1, p. 158, 2018.

[11] H. Wang, Y. Wang, Q. du et al., "Inflammasome-independent NLRP3 is required for epithelial-mesenchymal transition in colon cancer cells," *Experimental Cell Research*, vol. 342, no. 2, pp. 184–192, 2016.

[12] J. Ungerbäck, D. Belenki, A. Jawad ul-Hassan et al., "Genetic variation and alterations of genes involved in NFκB/TNFAIP3- and NLRP3-inflammasome signaling affect susceptibility and outcome of colorectal cancer," *Carcinogenesis*, vol. 33, no. 11, pp. 2126–2134, 2012.

[13] S. Li, X. Liang, L. Ma et al., "MiR-22 sustains NLRP3 expression and attenuates _H. pylori_ -induced gastric carcinogenesis," *Oncogene*, vol. 37, no. 7, pp. 884–896, 2018.

[14] Q. Wei, K. Mu, T. Li et al., "Deregulation of the NLRP3 inflammasome in hepatic parenchymal cells during liver cancer progression," *Laboratory Investigation*, vol. 94, no. 1, pp. 52–62, 2014.

[15] S. Hamarsheh and R. Zeiser, "NLRP3 inflammasome activation in cancer: a double-edged sword," *Frontiers in Immunology*, vol. 11, p. 1444, 2020.

[16] H. Wu, J. Liu, Y. Zhang, Q. Li, Q. Wang, and Z. Gu, "miR-22 suppresses cell viability and EMT of ovarian cancer cells via NLRP3 and inhibits PI3K/AKT signaling pathway," *Clinical & Translational Oncology*, vol. 23, no. 2, pp. 257–264, 2021.

[17] X. Wang, Y. Yin, W. Qian et al., "Citric acid of ovarian cancer metabolite induces pyroptosis via the caspase-4/TXNIP-NLRP3-GSDMD pathway in ovarian cancer," *The FASEB Journal*, vol. 36, no. 6, article e22362, 2022.

[18] D. Y. Wang, N. Li, and Y. L. Cui, "Long non-coding RNA CCAT1 sponges miR-454 to promote chemoresistance of ovarian cancer cells to cisplatin by regulation of surviving," *Cancer Research and Treatment*, vol. 52, no. 3, pp. 798–814, 2020.

[19] J. P. Thiery and J. P. Sleeman, "Complex networks orchestrate epithelial-mesenchymal transitions," *Nature Reviews Molecular Cell Biology*, vol. 7, no. 2, pp. 131–142, 2006.

[20] M. M. Alrashed, H. Alharbi, A. S. Alshehry, M. Ahmad, and M. S. Aloahd, "miR-624-5p enhances NLRP3 augmented gemcitabine resistance via EMT/IL-1β/Wnt/β-catenin signaling pathway in ovarian cancer," *Journal of Reproductive Immunology*, vol. 150, article 103488, 2022.

[21] C. Zhong, R. Wang, M. Hua et al., "NLRP3 inflammasome promotes the progression of acute myeloid leukemia via IL-1β pathway," *Frontiers in Immunology*, vol. 12, article 661939, 2021.

[22] Q. Zheng, D. Yao, Y. Cai, and T. Zhou, "NLRP3 augmented resistance to gemcitabine in triple-negative breast cancer cells via EMT/IL-1β/Wnt/β-catenin signaling pathway," *Bioscience Reports*, vol. 40, no. 7, 2020.

[23] X. Feng, Q. Luo, H. Zhang et al., "The role of NLRP3 inflammasome in 5-fluorouracil resistance of oral squamous cell carcinoma," *Journal of Experimental & Clinical Cancer Research*, vol. 36, no. 1, p. 81, 2017.

[24] J. Antony, J. P. Thiery, and R. Y. Huang, "Epithelial-to-mesenchymal transition: lessons from development, insights into cancer and the potential of EMT-subtype based therapeutic intervention," *Physical Biology*, vol. 16, no. 4, article 041004, 2019.

[25] Y. Wu and B. P. Zhou, *Epithelial–mesenchymal transition in development and diseases*, Cancer Drug Discovery and Development, 2010.

[26] V. G. Keshamouni and W. P. Schiemann, "Epithelial-mesenchymal transition in tumor metastasis: a method to the madness," *Future Oncology*, vol. 5, no. 8, pp. 1109–1111, 2009.

[27] S. Marchini, R. Fruscio, L. Clivio et al., "Resistance to platinum-based chemotherapy is associated with epithelial to mesenchymal transition in epithelial ovarian cancer," *European Journal of Cancer*, vol. 49, no. 2, pp. 520–530, 2013.

[28] J. Deng, X. Bai, X. Feng et al., "Inhibition of PI3K/Akt/mTOR signaling pathway alleviates ovarian cancer chemoresistance through reversing epithelial-mesenchymal transition and decreasing cancer stem cell marker expression," *BMC Cancer*, vol. 19, no. 1, p. 618, 2019.

Research Article

Focusing on scRNA-seq-Derived T Cell-Associated Genes to Identify Prognostic Signature and Immune Microenvironment Status in Low-Grade Glioma

Jiayu Wen,[1,2,3] **Qiaoyi Huang,**[2,3] **Jiuxiu Yao,**[4] **Wei Wei,**[1] **Zehui Li** ⓘ**,**[3] **Huiqin Zhang,**[3] **Surui Chang** ⓘ**,**[3] **Hui Pei,**[3] **Yu Cao** ⓘ**,**[3] **and Hao Li** ⓘ[1]

[1]*Wangjing Hospital of China Academy of Chinese Medical Sciences, Beijing 100020, China*
[2]*Graduate College, Beijing University of Chinese Medicine, Beijing 100020, China*
[3]*Department of Geriatrics, Xiyuan Hospital, China Academy of Chinese Medical Sciences, Beijing 100089, China*
[4]*First Clinical College, Shandong University of Traditional Chinese Medicine, Jinan 250011, China*

Correspondence should be addressed to Yu Cao; yu.cao-xiyuan@outlook.com and Hao Li; xyhplihao1965@126.com

Background. The clinical outcomes of low-grade glioma (LGG) are associated with T cell infiltration, but the specific contribution of heterogeneous T cell types remains unclear. *Method.* To study the different functions of T cells in LGG, we mapped the single-cell RNA sequencing results of 10 LGG samples to obtain T cell marker genes. In addition, bulk RNA data of 975 LGG samples were collected for model construction. Algorithms such as TIMER, CIBERSORT, QUANTISEQ, MCPCOUTER, XCELL, and EPIC were used to depict the tumor microenvironment landscape. Subsequently, three immunotherapy cohorts, PRJEB23709, GSE78820, and IMvigor210, were used to explore the efficacy of immunotherapy. *Results.* The Human Primary Cell Atlas was used as a reference dataset to identify each cell cluster; a total of 15 cell clusters were defined and cells in cluster 12 were defined as T cells. According to the distribution of T cell subsets (CD4+ T cell, CD8+ T cell, Naïve T cell, and Treg cell), we selected the differentially expressed genes. Among the CD4+ T cell subsets, we screened 3 T cell-related genes, and the rest were 28, 4, and 13, respectively. Subsequently, according to the T cell marker genes, we screened six genes for constructing the model, namely, RTN1, HERPUD1, MX1, SEC61G, HOPX, and CHI3L1. The ROC curve showed that the predictive ability of the prognostic model for 1, 3, and 5 years was 0.881, 0.817, and 0.749 in the TCGA cohort, respectively. In addition, we found that risk scores were positively correlated with immune infiltration and immune checkpoints. To this end, we obtained three immunotherapy cohorts to verify their predictive ability of immunotherapy effects and found that high-risk patients had better clinical effects of immunotherapy. *Conclusion.* This single-cell RNA sequencing combined with bulk RNA sequencing may elucidate the composition of the tumor microenvironment and pave the way for the treatment of low-grade gliomas.

1. Introduction

In the brain and other parts of the central nervous system, gliomas are the most common primary malignant tumors [1]. According to the World Health Organization, gliomas were mainly classified into four levels and the higher grade notified the poor prognosis [2]. According to routine histopathology, low-grade gliomas are less malignant, usually in WHO grade 2 and 3 patients [3]. The characteristics of low-grade gliomas were their highly invasive nature, their

difficulty in surgical resection, their recurrence, and their rapid progression to malignancy [4]. Several biomarkers were widely used to define a subtype which was correlated to a great prognosis like IDH1 and IDH2 [5]. LGG with both mutation of IDH1 and IDH2 and deficiency of chromosome of arms 1p and 19q have better therapeutic effect to radio-chemotherapy than other LGG without these mutations [6]. Although more and more LGG-like biomarkers have been widely explored and applied in clinical practice, common biomarkers are still unable to effectively delineate the

heterogeneity of tumor microenvironment [7]. Immuno-therapy still has limited clinical benefits in LGG patients. Therefore, it is important to find an effectively prognostic biomarker or therapy target for the therapy of LGG patients.

TME were composed of numerous cell types including cancer cells, bone marrow-derived inflammatory cells, lymphocytes, blood vessels, and the extracellular matrix which were made up of collagen and proteoglycans [8]. The components of TME play an important role in the progression and invasion of tumors [9]. The alterations of TME not only impact the development of tumor but also could become biomarkers for prognosis and immunotherapy [10]. T cells, a subtype of immune cells, play an important role in innate immune and adaptive immune systems [11]. In the progression of cancer, the interactions between TME and T cells have a great influence on the development of tumors [12]. Poor vascular differentiation and cancer cell metabolism in the TME, which contribute to hypoxia, accumulation of metabolic waste, and insufficient energy supply, lead to the anergy of effector T cells to recognize and kill cancer cells [13]. T cells are also one of the important targets for immunotherapy. Stromal cells of TME mediate the coexistence of T cells and cancer cells which results in the immune escape of cancer cells and reduces the effect of immunotherapy [14]. Therefore, the study for T cells in TME is of great significance for the future search of tumor therapy.

Several immune cell populations in the TME can now be revealed molecularly through single-cell RNA sequencing (scRNA-seq) technology [15]. Previous studies have shown that screening immune cell subsets for relevant molecular signals based on RNA-seq data can help predict clinical outcomes and implement personalized medicine [16]. The aim of this study is to predict the T cell marker genes, construct a prognostic model, and evaluate the immunotherapy effect in patients with LGG.

2. Method

2.1. Data Collection. A total of 983 samples were enrolled in our investigation. Ten LGG tissues with scRNA-seq data were obtained from GSE138794 in GEO database, which were used to identify the T cell markers of LGG. The Cancer Genome Atlas (TCGA) transcriptome matrix (FPKM format) and clinical information of 481 LGG samples were obtained from the TCGA-LGG cohort to construct prognostic signatures. In addition, CGGA693 and CGGA325 cohorts were collected from the Chinese Glioma Genome Atlas (CGGA) database. The cohorts contained 332 and 162 patients, respectively, which were used as external validation cohorts to verify the prognostic model. In addition, GSE16011 was also included in this research to verify the accuracy of the model. As in our previous study, the microarray data was processed [17]. To make comparisons between samples easier, TCGA RNA sequencing data were converted to transcripts per kilobasemillion (TPM) values. To eliminate differences between batches, we used the "sva" package in R software for normalization. To ensure the availability and reliability of the data, strict inclusion and exclusion criteria were established for this study. Inclu-

sion criteria were as follows: (1) the pathological results showed glioma, (2) complete genomic expression level data were included, and (3) clear reporting of pathological conditions and follow-up. Exclusion criteria were as follows: (1) other pathological types and (2) concurrent primary tumors from other sites. In addition, three immunotherapy cohorts (PRJEB23709, GSE78820, IMvigor210) were used to explore the immune treatment effect.

2.2. Identification of T Cell Marker Genes by scRNA-seq Analysis. scRNA-seq data were preprocessed, and three cells were excluded with less than 200 genes and gene expression only in individual cells. The different scRNA-seq datasets were corrected by the Harmony algorithm. The FindNeighbors function is used to distinguish cell subsets. The T-SNE function is used to show the distribution of cell subsets, and the single R package is used to annotate cell subsets. T cell marker genes were determined by screening criteria of adjusted $p < 0.05$ and $|\log 2FC| > 1$.

2.3. Construction of the Prognostic Model of T Cell Marker Genes. The transcriptional profiles of T cell marker genes were obtained based on single-cell data. LASSO algorithm was used to reduce the correlation between T cell marker genes and play a role in defitting. Subsequently, the multivariate Cox regression analysis algorithm was used to assign the coefficient of each gene to construct the prognosis model of T cell marker genes, in which the TCGA cohort was used as the training group and the CGGA cohort was used as the validation group. The risk values of key genes in the prognostic model are presented by dendrogram.

2.4. Tumor Microenvironment Landscape. To observe the overall landscape of immune cells in different T cell subsets, we used a variety of machine learning algorithms, including TIMER, CIBERSORT, QUANTISEQ, MCPCOUTER, XCELL, and EPIC. These algorithms can predict the content of immune cells based on transcriptome expression levels and find regularities through simulation of different algorithms to explain that T cell-related genes' change in the proportion of immune cells in TME. Expression levels of immune regulators and HLA family genes in different T cell subsets were examined to calculate the correlation between RNAss, DNAss, and risk scores.

2.5. Evaluation of Immunotherapy Effect. Risk scores were assigned to each patient in the three immunotherapy cohorts mentioned earlier based on the formula of the model construction. Compare the risk scores of immunotherapy responders and nonresponders to determine whether the risk model can be used to evaluate the effect of immunotherapy. In addition, the bar graph shows the AUC values used to predict the expression of individual cell subsets or molecules.

2.6. Statistics. All data analysis was analyzed with R software. GSEA algorithm was used to calculate the abundance of immune cell infiltration. Student's *t*-test was used to compare the differences between the two groups, and all statistical data were normally distributed. The PCA
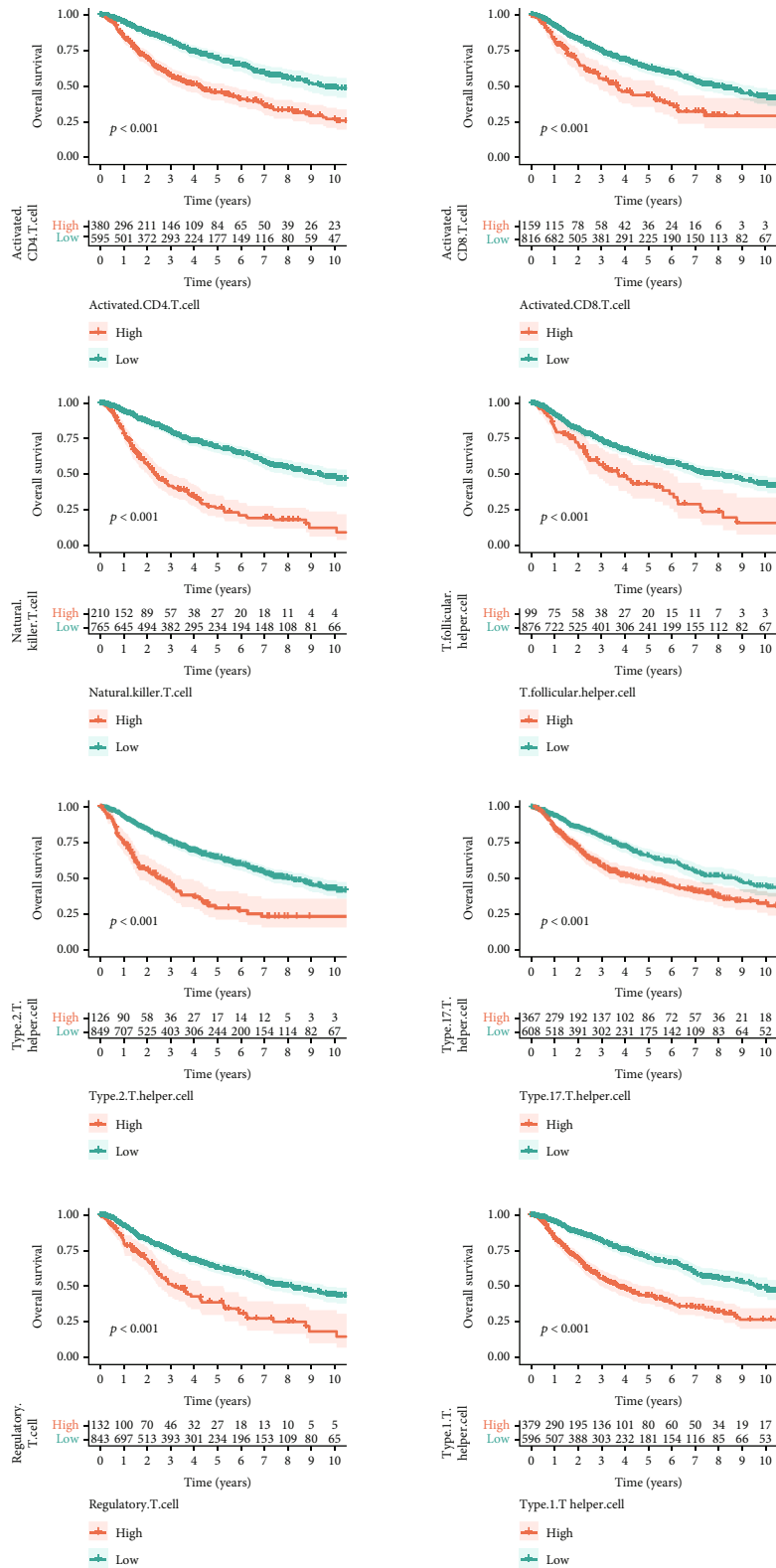
Figure 1: K-M survival analysis.

(a)

(b)

(c)

(d)
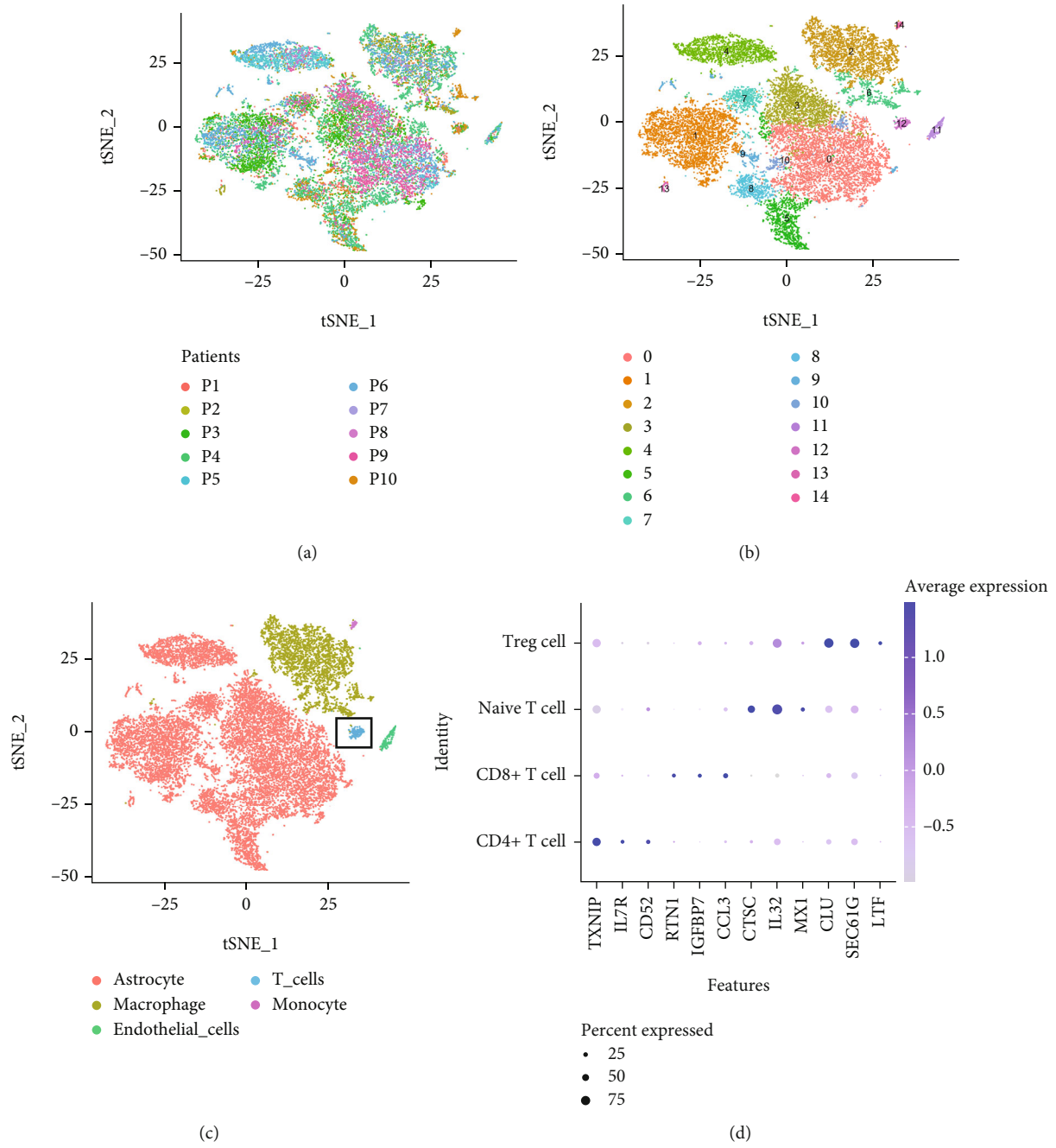
FIGURE 2: Continued.
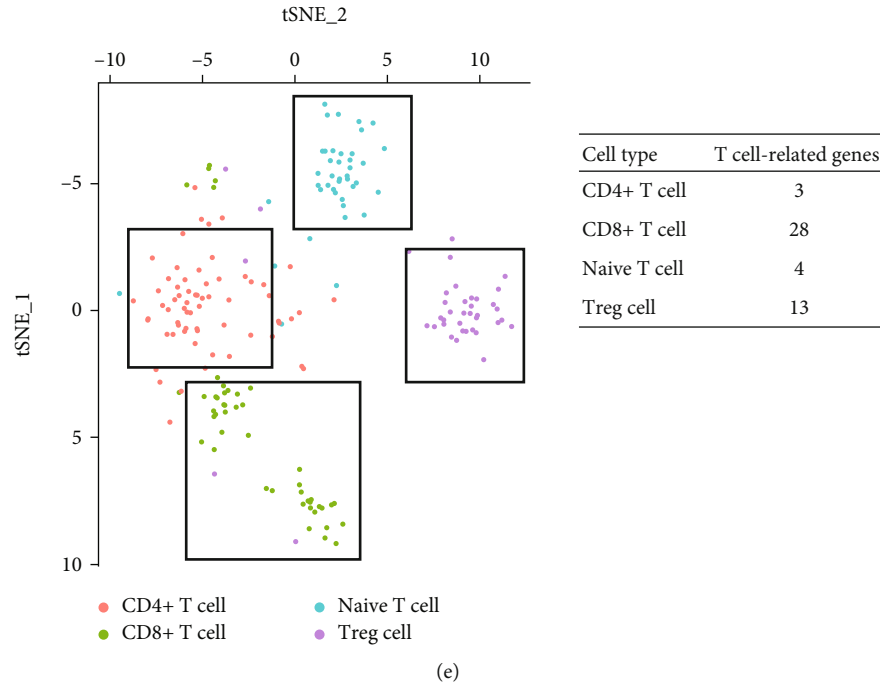
FIGURE 2: Identification of T cell marker gene. (a) The T-SNE showed the distribution of cell in ten patients. (b) 15 cell subsets were presented by T-SNE algorithm. (c) According to the expression level of marker genes, T-SNE algorithm drew 5 cell subsets. (d) T cell-related gene expression in four T cell subsets were plotted. (e) The T-SNE plot shows the cell distribution after reannotation of T cell subsets.

algorithm was used to render individual distribution. $p < 0.05$ was considered significant.

3. Results

3.1. Identification of T Cell Marker Gene Expression Profiles. We calculated the immune cell infiltration score according to the ssGSEA algorithm and divided the patients into high and low immune cell infiltration groups according to the median immune cell infiltration score. The K-M results suggested that the infiltration level of T cell subsets had a great impact on the clinical outcome of patients (Figure 1). In addition, we calculated the content of immune cell subsets in different WHO grades and found that T cell subsets differed significantly in G2 and G3 grades. Cell distribution profiles of scRNA-seq data from GSE138794 are shown in Figure 2(a). To reduce the dimension, the top 1500 variable genes were selected and PCA was performed. A total of 15 cell clusters were identified, and cells in cluster 12 were defined as T cells by the Human Primary Cell Atlas (Figures 2(b) and 2(c)). Figure 2(d) shows the expression of specific markers in various T cell subsets. TXNIP was mainly expressed in CD4+ T cells; CTSC and IL32 were mainly expressed in Naïve T cells; and CLU and SEC61G were mainly expressed in Treg T cells. In the CD4+ T cell subtype, there were 3 genes associated with T cell, and the remaining subsets were 28, 4, and 13, respectively, which were defined as T cell marker genes for subsequent analysis.

3.2. Prognostic Model. PCA results showed that the three cohorts had batch effects distributed in different regions.

As shown in Figure 3(a), after the batch effect was removed, data of three cohorts were at a consistent level. After the LASSO regression analysis, 10 genes were finally obtained. A multivariate Cox regression analysis screened candidate genes for model construction and calculated coefficient (Figure 3(b)). According to the expression values of candidate genes and corresponding coefficient, the model formula was constructed as follows:

$$\text{Riskscore} = 0.257 * \text{MX1} + 0.127 * \text{SEC61G} + 0.168 * \text{HOPX}$$
$$+ 0.199 * \text{CHI3L1} - 0.222 * \text{RTN1}$$
$$- 0.590 * \text{HERPUD1}.$$

$$(1)$$

The tree map shows the risk values of candidate genes, in which RTN1 and HERPUD1 are protective factors and MX1, SEC61G, HOPX, and CHI3L1 are risk factors (Figure 3(c)). The heatmap shows the expression levels of candidate genes between the high- and low-risk groups. RTN1 is highly expressed in the low-risk group, but MX1, SEC61G, HOPX, and CHI3L1 are highly expressed in the high-risk group. The expression trend of candidate genes in TCGA and CGGA cohorts is consistent in Figure 3(d). The dot plot shows the distribution of risk scores and clinical outcomes for each patient. With increase of the risk score, the mortality rate increases.

The K-M survival curve shows that patients in the high-risk group has a shorter survival time than those in the low-risk group (Figures 3(e) and 3(f)). The ROC curve shows that the prediction ability of the prognostic model at 1, 3,

PCA for combined expression profile before ComBat

PCA for combined expression profile after ComBat

CGGA325
CGGA325
TCGA

(a)

(b)

FIGURE 3: Continued.

(c)

(d)

FIGURE 3: Continued.

(e)

(f)

(g)

(h)
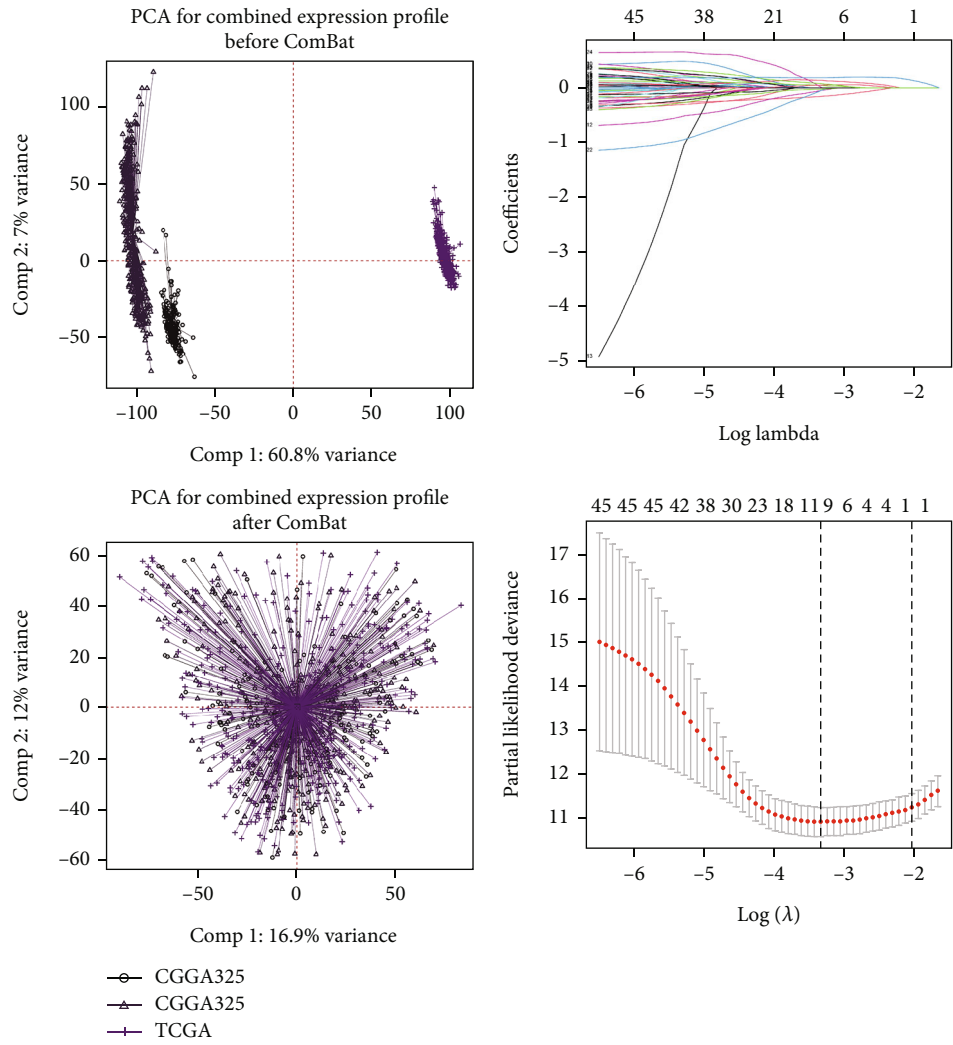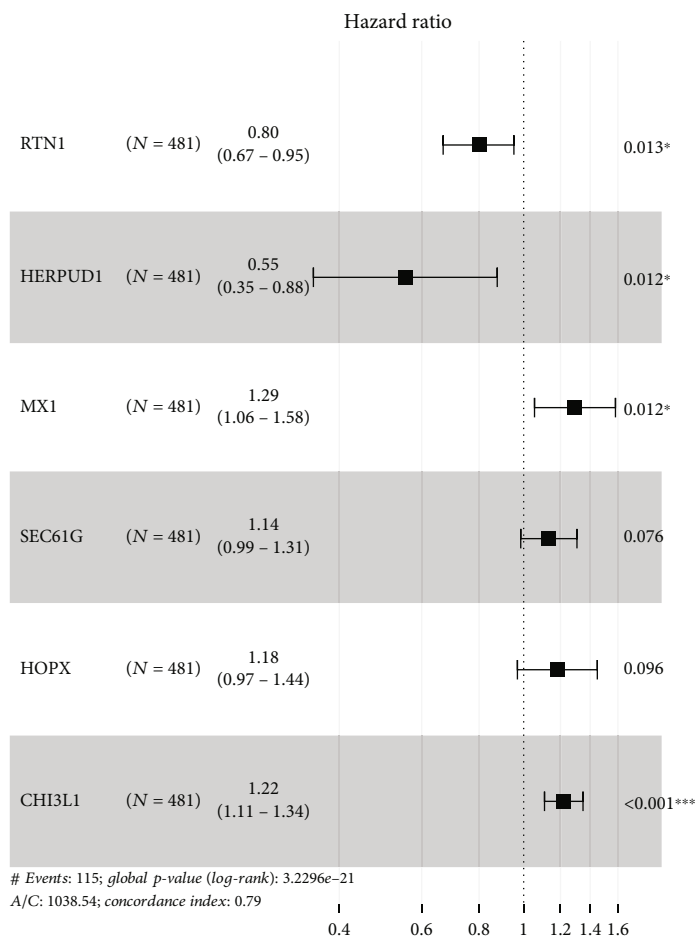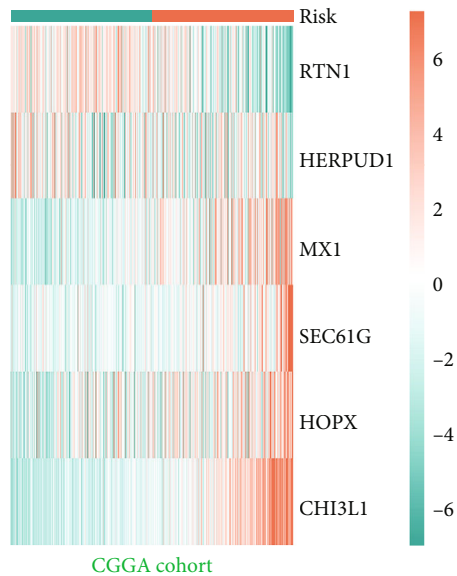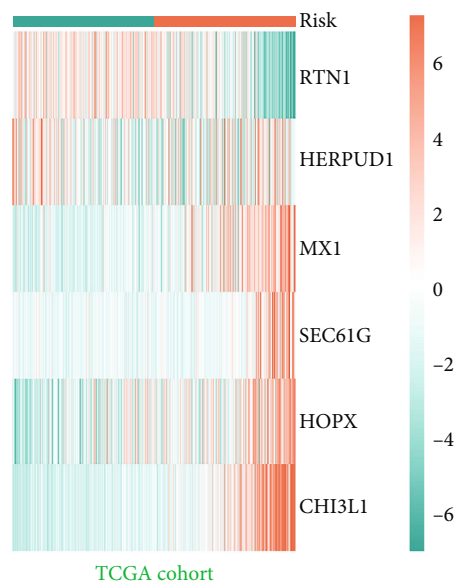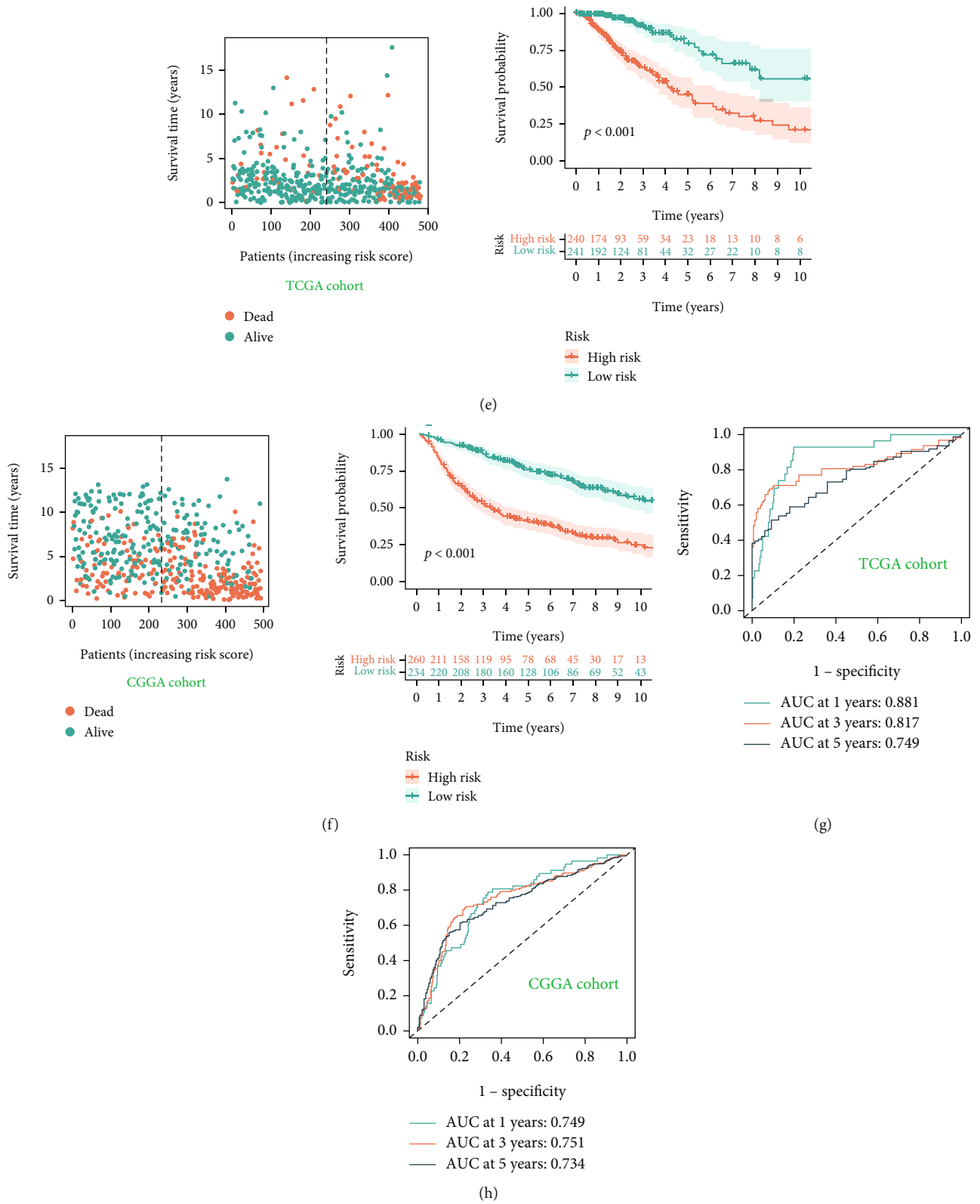
Figure 3: T cell-related model construction. (a) The PCA showed the distribution of patients in each cohort. (b) The LASSO algorithm for screening candidate genes. (c) The tree diagram shows the genes used to construct the prognostic model and their hazard values. (d) Heatmaps show the expression of prognostic genes in different risk groups. (e) Risk score and prognostic status of patients in the TCGA cohort. (f) Risk score and prognostic status of patients in the CGGA cohort. (g) The ROC curve for this model in the TCGA cohort. (h) The ROC curve for this model in the CGGA cohort.

(a)

(b)

Figure 4: Continued.

(c)

(d)

(e)
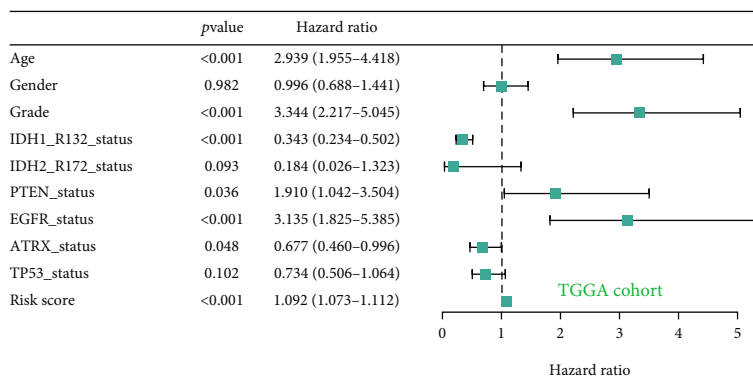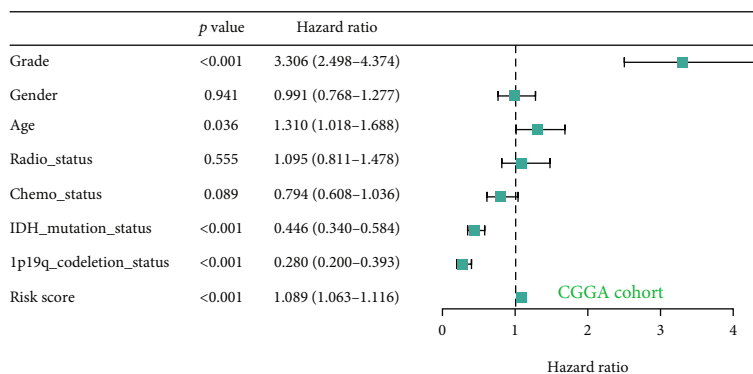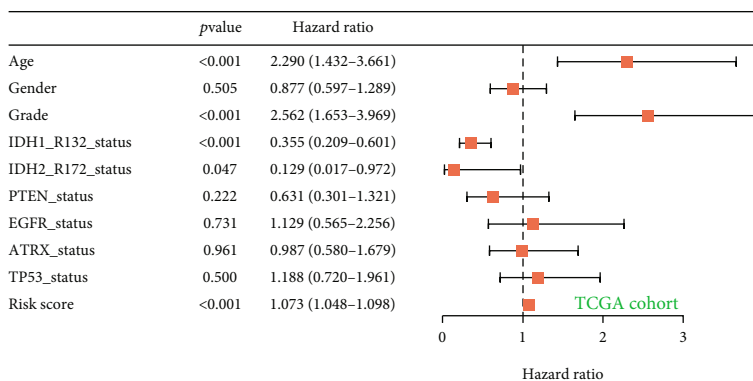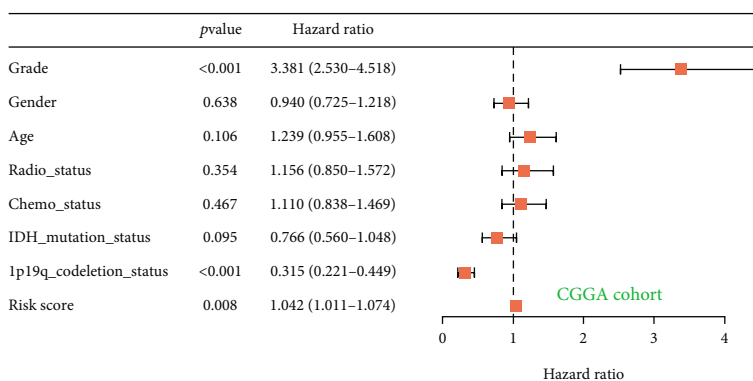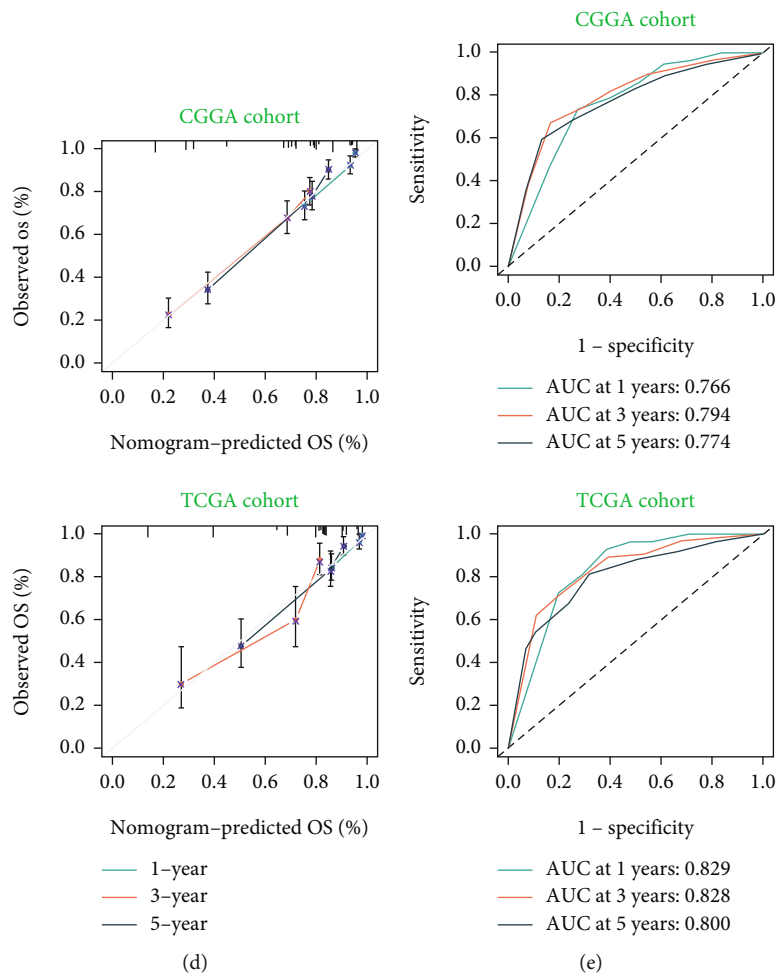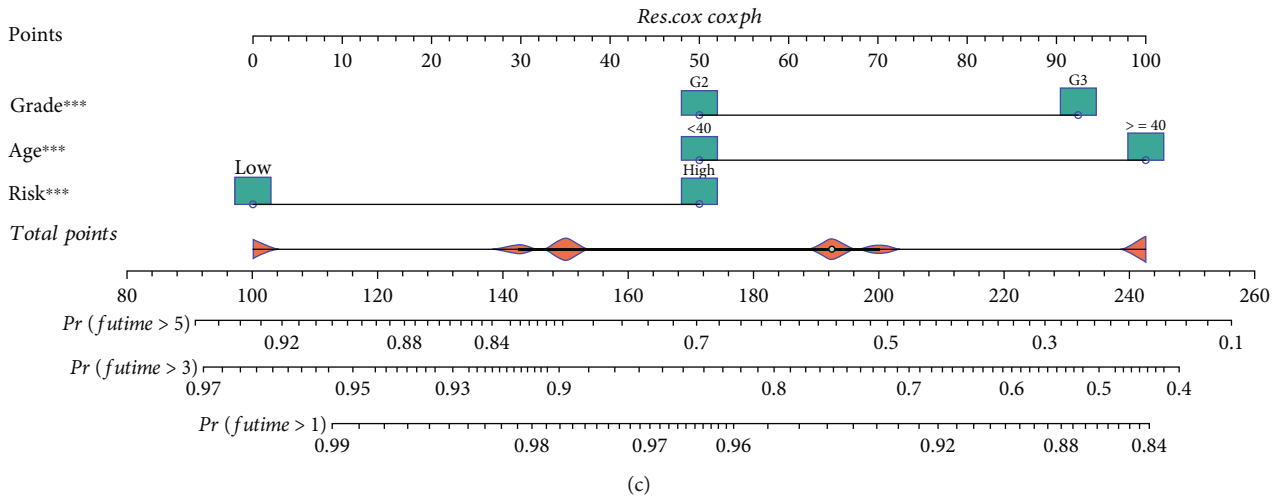
FIGURE 4: Nomogram model construction and verification. (a) The univariate regression analysis verified the predictive performance of the prognostic model. (b) The multivariate regression analysis verified the predictive performance of the prognostic model. (c) Construction of the nomogram model, including grade, age, and risk score. (d) The decision curve analysis was used to evaluate the predictive performance of the nomogram model. (e) The ROC curve was used to evaluate the predictive ability of the nomogram model for 1-, 3-, and 5-year survival prognosis.

and 5 years in the TCGA cohort is 0.881, 0.817, and 0.749, respectively, and the prediction ability at 1, 3, and 5 years in the CGGA cohort is 0.749, 0.751, and 0.734, respectively (Figures 3(g) and 3(h)). In addition, we selected GSE16011

to further verify our prognostic model, and the results showed that it was consistent with the above, with the predictive power of up to 0.903, 0.818, and 0.776 at 1, 3, and 5 years, respectively (Figure S1).

(a)

(b)

(c)

Figure 5: Continued.

(d)

(e)

(f)
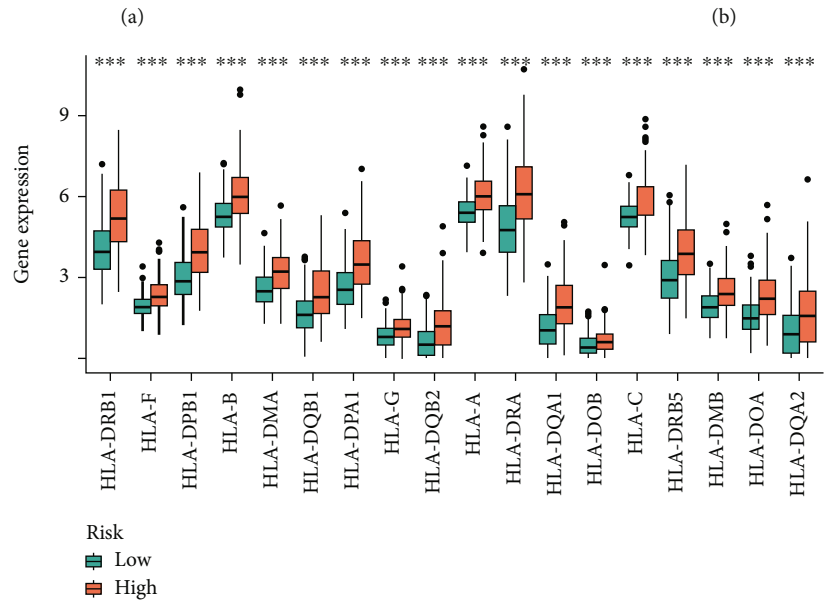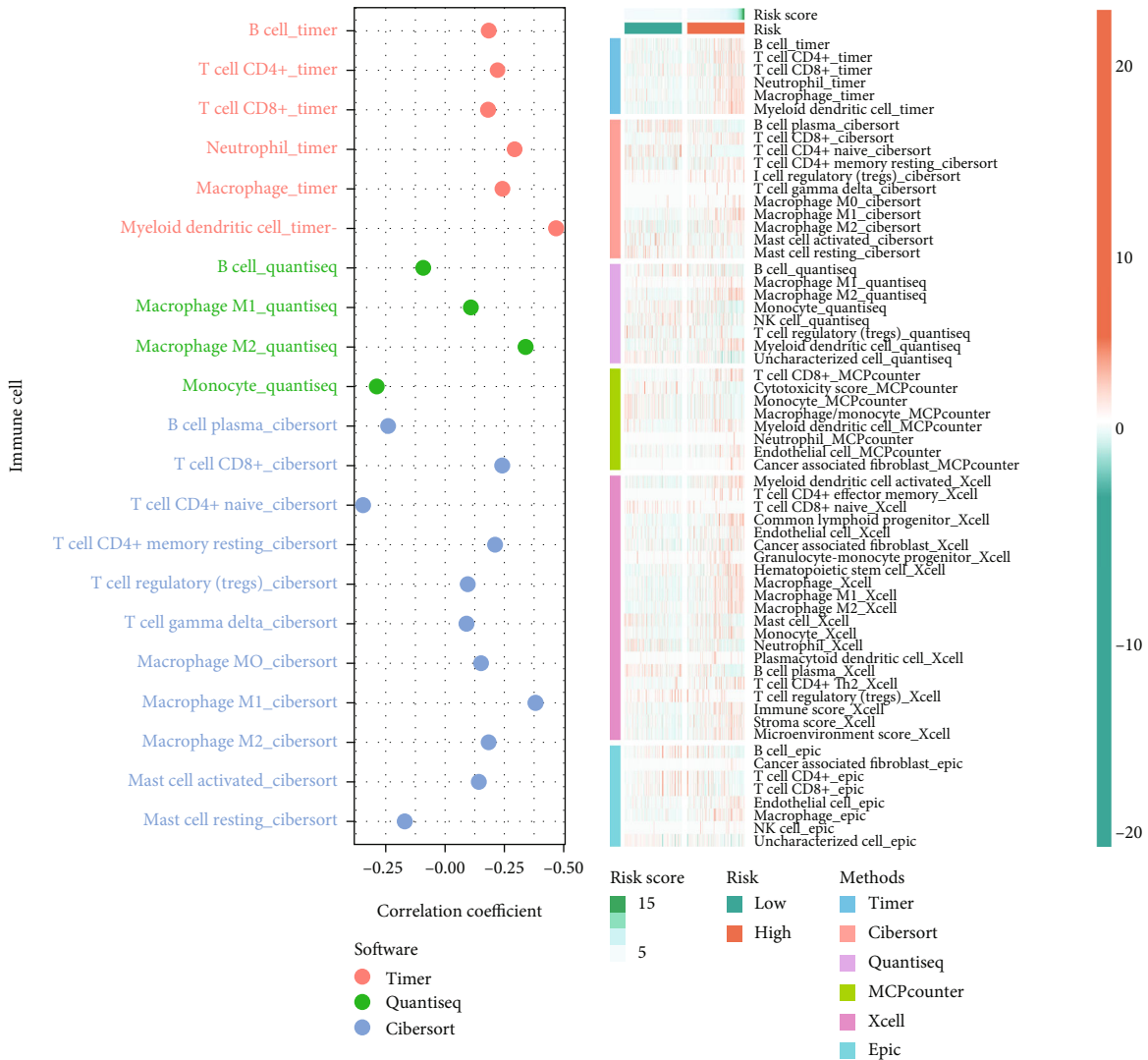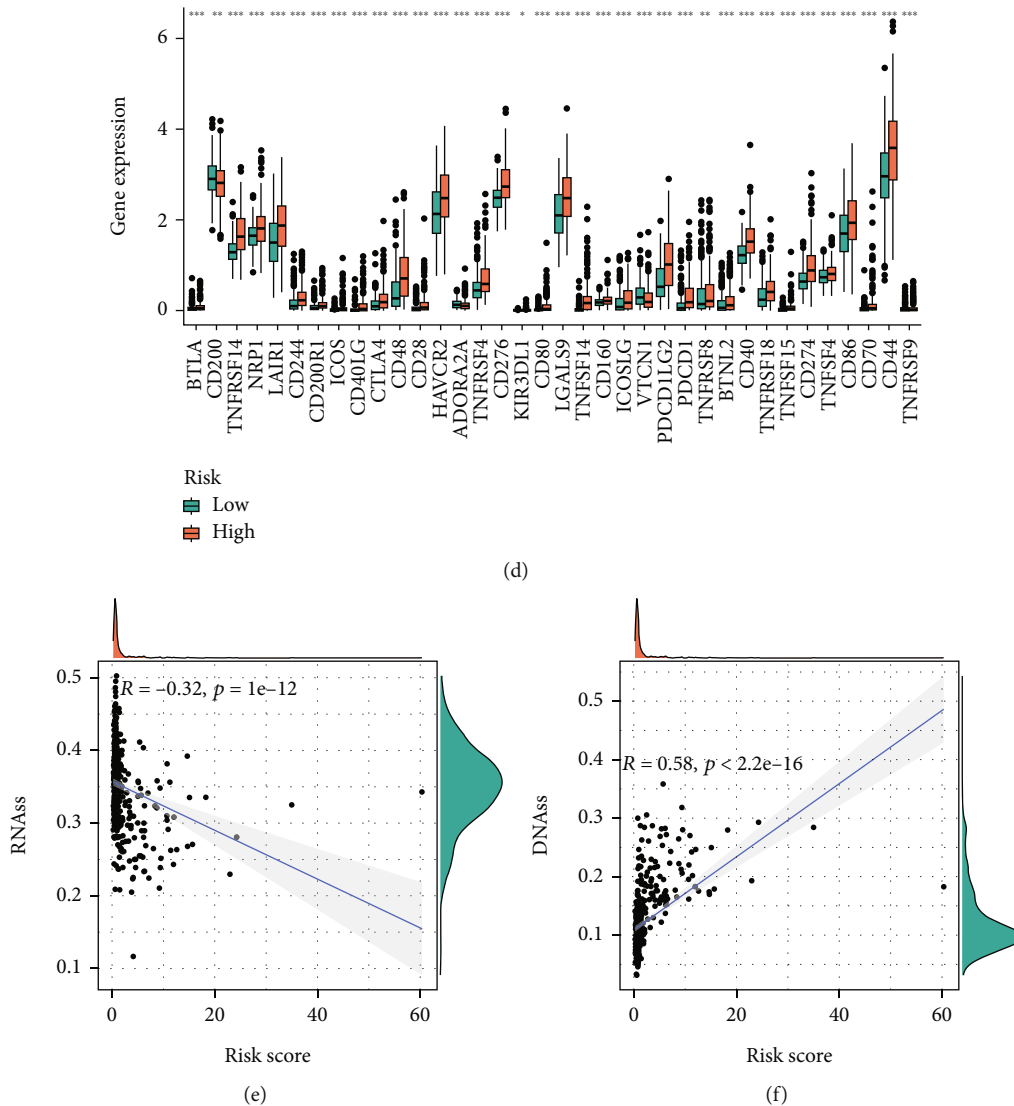
Figure 5: Tumor microenvironment assessment. (a) Correlation between risk score and immune cell infiltration. Algorithms: TIMER, QUANTISEQ, and CIBERSORT. (b) Heatmap shows the infiltration of immune cells in the high- and low-risk groups. Algorithms: TIMER, CIBERSORT, QUANTISEQ, MCPCOUNTER, XCELL, and EPIC. (c) The expression level of HLA gene family in the high- and low-risk groups. (d) Expression level of immunomodulator in the high- and low-risk groups. (e, f) The correlation between risk score and RNAss and DNAss scores.

Univariate and multivariate Cox regression analysis showed that the risk score model was an independent prognostic factor (Figures 4(a) and 4(b)). Multiple factors could be used to predict clinical outcomes. A nomogram model was constructed with risk score, grade, and AGE to predict clinical outcomes of patients (Figure 4(c)). Figure 4(d) shows the relationship between the expected results and the actual observed values. The angle close to 45% represents a high accuracy. The ROC curve shows that the prediction ability of the prognostic model at 1, 3, and 5 years in the TCGA cohort is 0.829, 0.828, and 0.800, respectively, and the prediction ability at 1, 3, and 5 years in the CGGA cohort is 0.766, 0.794, and 0.774, respectively. The prediction performance was significantly improved (Figure 4(e)).

3.3. Correlation between Prognostic Models and TME. As shown in Figure 5(a), the risk score is positively correlated with effector cells such as B cell and T cell, as well as M2 macrophages, but it is difficult to judge whether risk score exerted antitumor immunity or inhibited tumor immunity. The heatmap shows higher levels of immune cell infiltration in the high-risk group than those in the low-risk groups (Figure 5(b)). The expression of immunomodulators such as CD276, CTLA4, and HLA family molecules was higher in the high-risk group than that in the low-risk group (Figures 5(c) and 5(d)). The stemness index scores of RNAss were obtained based on transcriptome expression data, while those of DNAss were obtained based on methylation data. The risk score was negatively correlated with RNAss and positively correlated with DNAss (Figures 5(e) and 5(f)).
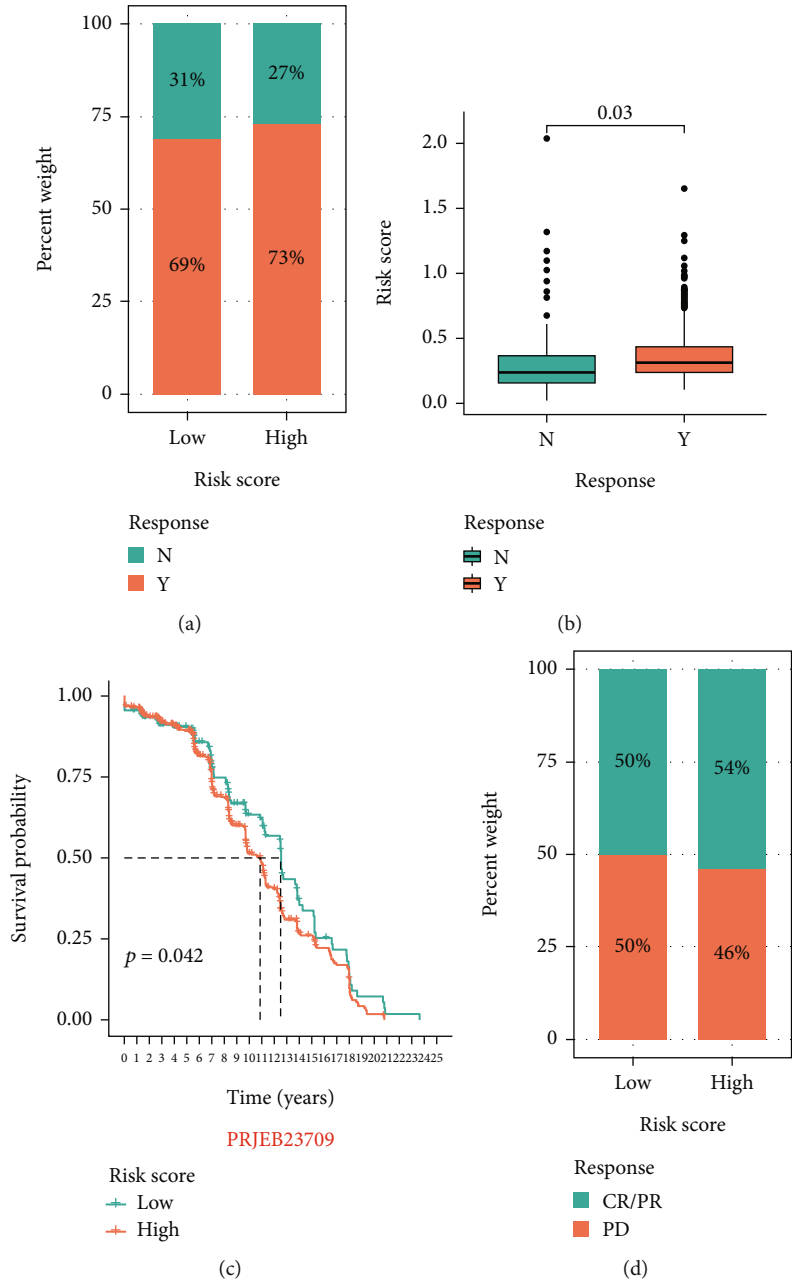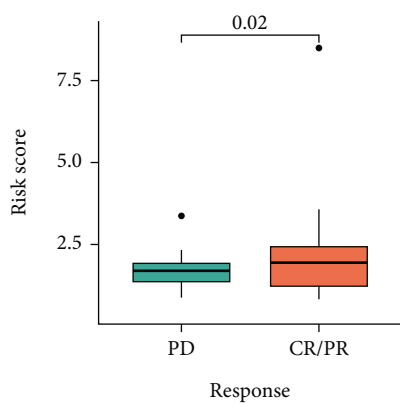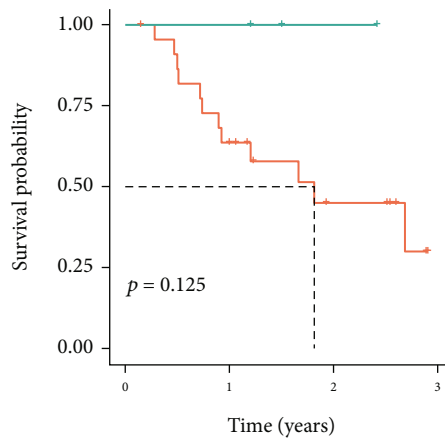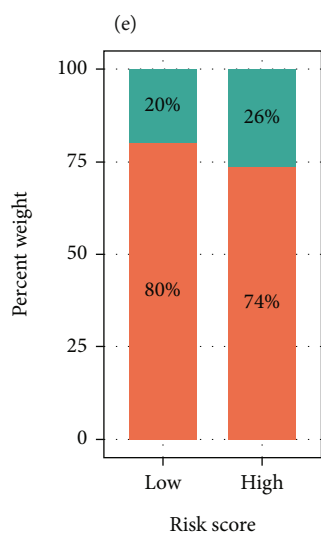
(a)

(b)

PRJEB23709

(c)

(d)

FIGURE 6: Continued.

(e)

GSE78820

(f)

(g)

(h)

FIGURE 6: Continued.

(i)

(j)
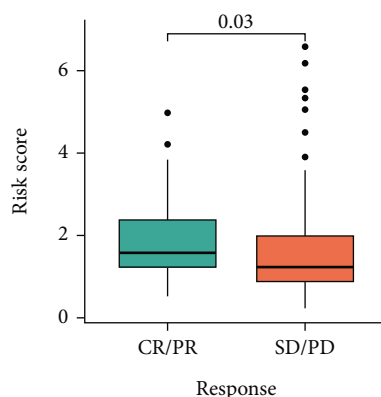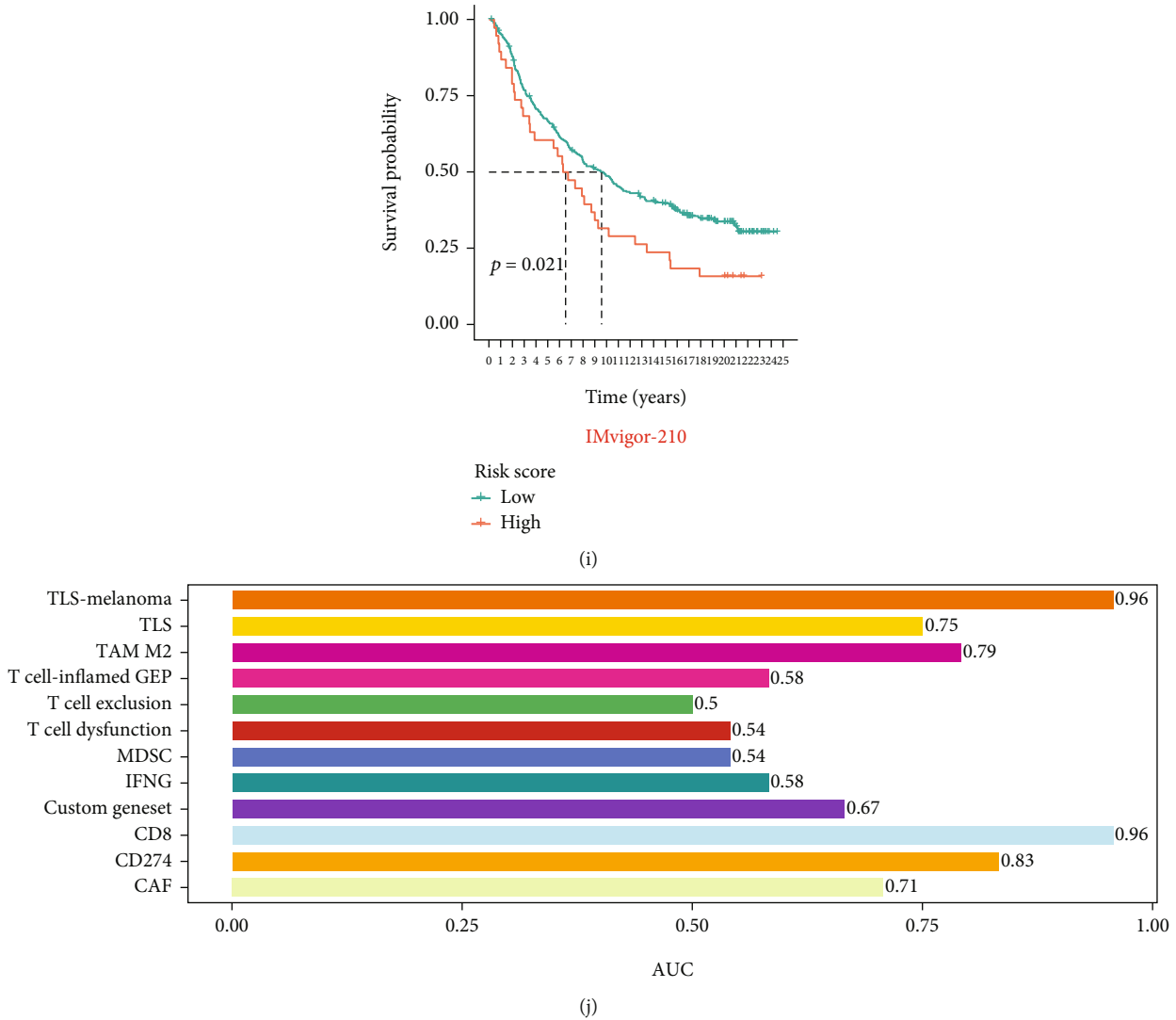
FIGURE 6: Evaluation of immunotherapy effect. (a–c) In the PRJEB23709 cohort, the bar chart shows the proportion of patients in the high- and low-risk groups who responded to immunotherapy. The box plot shows the risk score for different immunotherapy effects. The K-M survival analysis shows the clinical outcome of the high- and low-risk groups. (d–i) In the GSE78820 and IMvigor-210 cohorts. The bar chart shows the proportion of patients in the high- and low-risk groups who responded to immunotherapy. The box plot shows the risk score for different immunotherapy effects. The K-M survival analysis shows the clinical outcome of the high- and low-risk groups. (j) The bar chart shows the AUC values for each biomarker used to predict immunotherapy.

3.4. Immunotherapy Performance in Prognostic Models. In the three immunotherapy cohorts of PRJEB23709, GSE78820, and IMvigor210, it was found that high-risk patients had better clinical effects on immunotherapy, and the median risk value of patients who responded to immunotherapy was higher than that of patients who did not respond to immunotherapy. Moreover, K-M curves showed that the overall survival time of high-risk patients was shorter than that of low-risk patients (Figures 6(a)–6(i)). Figure 6(j) shows that the prediction performance of our prognostic model for immunotherapy response was 0.67 (Custom Geneset), which was lower than that of the immunodetection point (CD274) but higher than that of other T cells.

4. Discussion

scRNA-seq can precisely and rapidly determine the gene expression patterns of tens of thousands of individual cells [18]. Traditional bulk RNA-seq technology can only reflect the average expression level of genes in the population cells, which is difficult to mask the expression heterogeneity among different cells [19]. With scRNA-seq technology, all genes in a genome can be examined at the single-cell level, which is very helpful for studying cell expression heterogeneity [20]. In this study, scRNA-seq was used to process and analyze the glioma data in the public database, and the role of T cell marker gene in LGG was deeply explored. Based on the selected T cell marker genes, we constructed

a prognostic model to predict clinical outcome and immunotherapy effect, and its prediction performance in 1, 3, and 5 years was 0.881, 0.817, and 0.749, respectively. In general, for healthy tissues and organs, the higher the degree of immune cell infiltration, the better the effect of antitumor and targeted killing [21]. The brain has a blood-brain barrier, which makes it difficult for immune cells to enter the brain [22]. Therefore, only low-grade gliomas have the good prognosis, but high-grade gliomas may destroy the blood-brain barrier and infiltrate more immune cells, directly leading to the poor prognosis of high-grade gliomas. Meanwhile, in low-grade gliomas, a high degree of immune cell infiltration is associated with poor clinical outcomes. This study found that LGG patients with high-risk scores had a higher degree of immune cell infiltration, and patients with high-risk scores had poorer clinical outcomes. T cell marker genes may serve as biomarkers to predict disease progression.

Another popular approach in immunotherapy is immune checkpoint blockade (ICB), which makes unprecedented advance in cancer treatment [23]. Interactions between ligands and receptors regulate ICBs in the immune system [24, 25]. In addition to regulating the duration and amplitude of physiological immune responses, it also maintains autoimmune tolerance. As a result, the immune system will not damage and destroy normal tissue [26, 27]. With the advent of immune checkpoint inhibitors (ICIs), mainly anti-programmed cell death protein 1/programmed cell death ligand 1 (PD-1/PD-L1) and anticytotoxic T-lymphocyte-associated antigen-4 (CTLA-4) monoclonal antibodies have made great progress in the field of research related to certain types of cancer [28]. Both activated cytotoxic T lymphocytes to enhance antitumor response [29]. There is increasing evidence that molecule inhibitors that target carcinogenesis play a role far beyond the biological behavior of tumors [30, 31]. Our study found that the expression levels of immune modulators (such as PD-1 and PD-L1) and HLA family in the high-risk group were higher than those in the low-risk group. Based on three immunotherapy cohorts, the proportion of patients in the high-risk group who responded to immunotherapy was higher than that in the low-risk group. It is conceivable that a combination of T cell-based marker gene inhibitors and immune checkpoint inhibitors may benefit patients with LGG. In addition, bioinformatics methods were used to analyze the expression and prognosis of T cell marker genes in glioma.

In our investigation, we first performed a comprehensive study of scRNA-seq of patients with LGG to identify prognostic signatures and immune environment status. We identified T cell marker gene signature (TCMGS) to establish a survival model to evaluate the progression of LGG. Besides, based on the expression of TCMGS, we validated our prognostic model in an independent cohort which was downloaded from the Gene Expression Omnibus (GEO) database. Our study identifies that TCMGS may become the new target for the prognosis and treatment of LGG progression in the future.

There are some limitations in the study. First of all, our research is based on the mining of existing public databases with artificial bias. Secondly, possible pathogenic pathways are only proposed in this study, which requires further experimental verification. Finally, animal experiments are needed to test the hypothesis of drug combination before applying it to patients. Future studies of the relationship between T cell marker genes and cancer development and progression may focus on more discoveries of significant prognostic and even therapeutic value.

Data Availability

Data were obtained from CGGA, TCGA, and GEO, as detailed in the methodology section.

Ethical Approval

All the information of patients was obtained from the public database.

Conflicts of Interest

The authors declare that there are no conflicts of interest regarding the publication of this study.

Authors' Contributions

Wen-Jiayu was responsible for the conceptualization, methodology, and writing and the original draft preparation. Li-Hao and Cao-Yu reviewed the manuscript. All authors have read and agreed to the published version of the manuscript.

Acknowledgments

Supplementary Materials

Figure S1: external cohort validation (GSE16011). (A) The K-M survival analysis showed the clinical outcome of the high- and low-risk groups. (B) The ROC curve was used to evaluate the predictive ability of the nomogram model for the 1-, 3-, and 5-year survival prognosis. (Supplementary Materials)

References

[1] P. Śledzińska, M. G. Bebyn, J. Furtak, J. Kowalewski, and M. A. Lewandowska, "Prognostic and predictive biomarkers in gliomas," International Journal of Molecular Sciences, vol. 22, no. 19, article 10373, 2021.

[2] P. Wesseling and D. Capper, "Classification of gliomas," Neuropathology and Applied Neurobiology, vol. 44, no. 2018, pp. 139–150, 2016.

[3] D. Doig, C. Kachramanoglou, M. Dumba et al., "Characterisation of isocitrate dehydrogenase gene mutant WHO grade 2 and 3 gliomas: MRI predictors of 1p/19q co-deletion and tumour grade," Clinical Radiology, vol. 76, no. 785, pp. e9–785.e16, 2021.

[4] G. Youssef and J. J. Miller, "Lower grade gliomas," *Current Neurology and Neuroscience Reports*, vol. 20, no. 7, p. 21, 2020.

[5] H. Yan, D. W. Parsons, G. Jin et al., "IDH1 and IDH2 mutations in gliomas," *The New England Journal of Medicine*, vol. 360, no. 8, pp. 765–773, 2009.

[6] L. M. Dittmann, A. Danner, J. Gronych et al., "Downregulation of *PRDX1* by promoter hypermethylation is frequent in 1p/19q-deleted oligodendroglial tumours and increases radio- and chemosensitivity of Hs683 glioma cells in vitro," *Oncogene*, vol. 31, no. 29, pp. 3409–3418, 2012.

[7] S. Gong, C. Wu, F. Köhler, J. Meixensberger, N. Schopow, and S. Kallendrusch, "Procollagen-lysine, 2-oxoglutarate 5-dioxygenase family: novel prognostic biomarkers and tumor microenvironment regulators for lower-grade glioma," *Frontiers in Cellular Neuroscience*, vol. 16, article 838548, 2022.

[8] K. Liu, A. Huang, J. Nie et al., "IL-35 regulates the function of immune cells in tumor microenvironment," *Frontiers in Immunology*, vol. 12, article 683332, 2021.

[9] D. F. Quail and J. A. Joyce, "Microenvironmental regulation of tumor progression and metastasis," *Nature Medicine*, vol. 19, no. 11, pp. 1423–1437, 2013.

[10] D. C. Hinshaw and L. A. Shevde, "The tumor microenvironment innately modulates cancer progression," *Cancer Research*, vol. 79, no. 18, pp. 4557–4566, 2019.

[11] C. Dong, "Cytokine regulation and function in T cells," *Annual Review of Immunology*, vol. 39, no. 1, pp. 51–76, 2021.

[12] W. Xuan, W. H. Hsu, F. Khan et al., "Circadian regulator CLOCK drives immunosuppression in glioblastoma," *Cancer Immunology Research*, vol. 10, no. 6, pp. 770–784, 2022.

[13] Y. Gu, X. Wu, J. Zhang et al., "The evolving landscape of N^6-methyladenosine modification in the tumor microenvironment," *Molecular Therapy*, vol. 29, no. 5, pp. 1703–1715, 2021.

[14] M. B. Schaaf, A. D. Garg, and P. Agostinis, "Defining the role of the tumor vasculature in antitumor immunity and immunotherapy," *Cell Death & Disease*, vol. 9, no. 2, p. 115, 2018.

[15] A. Sathe, S. M. Grimes, B. T. Lau et al., "Single-cell genomic characterization reveals the cellular reprogramming of the gastric tumor microenvironment," *Clinical Cancer Research*, vol. 26, no. 11, pp. 2640–2653, 2020.

[16] H. W. Lee, W. Chung, H. O. Lee et al., "Single-cell RNA sequencing reveals the tumor microenvironment and facilitates strategic choices to circumvent treatment failure in a chemorefractory bladder cancer patient," *Genome Medicine*, vol. 12, no. 1, p. 47, 2020.

[17] J. Yao, W. Wei, J. Wen, Y. Cao, and H. Li, "The efficacy and mechanism of berberine in improving aging-related cognitive dysfunction: a study based on network pharmacology," *Frontiers in Neuroscience*, vol. 17, article 1093180, 2023.

[18] C. Ziegenhain, B. Vieth, S. Parekh et al., "Comparative analysis of single-cell RNA sequencing methods," *Molecular Cell*, vol. 65, no. 4, pp. 631–643.e4, 2017.

[19] B. Hwang, J. H. Lee, and D. Bang, "Single-cell RNA sequencing technologies and bioinformatics pipelines," *Experimental & Molecular Medicine*, vol. 50, no. 8, pp. 1–14, 2018.

[20] X. Chen, Y. Chen, X. Chen et al., "Single-cell RNA sequencing reveals intra-tumoral heterogeneity of glioblastoma and a pro-tumor subset of tumor-associated macrophages characterized by *EZH2* overexpression," *Biochimica et Biophysica Acta (BBA) - Molecular Basis of Disease*, vol. 1868, no. 12, article 166534, 2022.

[21] N. D. Mathewson, O. Ashenberg, I. Tirosh et al., "Inhibitory CD161 receptor identified in glioma-infiltrating T cells by single- cell analysis," *Cell*, vol. 184, no. 5, pp. 1281–1298.e26, 2021.

[22] P. T. Ronaldson and T. P. Davis, "Regulation of blood-brain barrier integrity by microglia in health and disease: a therapeutic opportunity," *Journal of Cerebral Blood Flow and Metabolism*, vol. 40, 1 Supplement, pp. S6–s24, 2020.

[23] G. Morad, B. A. Helmink, P. Sharma, and J. A. Wargo, "Hallmarks of response, resistance, and toxicity to immune checkpoint blockade," *Cell*, vol. 184, no. 21, pp. 5309–5337, 2021.

[24] Y. Q. Jiang, Z. X. Wang, M. Zhong et al., "Investigating mechanisms of response or resistance to immune checkpoint inhibitors by analyzing cell-cell communications in tumors before and after Programmed Cell Death-1 (PD-1) targeted therapy: an integrative analysis using single-cell RNA and bulk-RNA sequencing data," *Oncoimmunology*, vol. 10, article 1908010, 2021.

[25] S. Sadreddini, B. Baradaran, A. Aghebati-Maleki et al., "Immune checkpoint blockade opens a new way to cancer immunotherapy," *Journal of Cellular Physiology*, vol. 234, no. 6, pp. 8541–8549, 2019.

[26] L. Lee, M. Gupta, and S. Sahasranaman, "Immune checkpoint inhibitors: an introduction to the next-generation cancer immunotherapy," *Journal of Clinical Pharmacology*, vol. 56, no. 2, pp. 157–169, 2016.

[27] P. G. Holder, S. A. Lim, C. S. Huang et al., "Engineering interferons and interleukins for cancer immunotherapy," *Advanced Drug Delivery Reviews*, vol. 182, article 114112, 2022.

[28] S. Qin, L. Xu, M. Yi, S. Yu, K. Wu, and S. Luo, "Novel immune checkpoint targets: moving beyond PD-1 and CTLA-4," *Molecular Cancer*, vol. 18, no. 1, p. 155, 2019.

[29] S. L. Topalian, J. M. Taube, R. A. Anders, and D. M. Pardoll, "Mechanism-driven biomarkers to guide immune checkpoint blockade in cancer therapy," *Nature Reviews Cancer*, vol. 16, no. 5, pp. 275–287, 2016.

[30] J. M. M. Levy, C. G. Towers, and A. Thorburn, "Targeting autophagy in cancer," *Nature Reviews Cancer*, vol. 17, no. 9, pp. 528–542, 2017.

[31] A. M. K. Law, F. Valdes-Mora, and D. Gallego-Ortega, "Myeloid-derived suppressor cells as a therapeutic target for cancer," *Cell*, vol. 9, no. 3, p. 561, 2020.

Research Article

TMEM33 as a Prognostic Biomarker of Cervical Cancer and Its Correlation with Immune Infiltration

Hui Zhang, Jun Wang, Ji Yang, Qingwen He, Sanli Guan, Minxia Qiao, Jian Zhao, and Xiu Wang [iD]

Department of Ultrasound, Xi'an People's Hospital (Xi'an Fourth Hospital), Xi'an, China

Correspondence should be addressed to Xiu Wang; 3137119239@qq.com

In women all over the world, cervical cancer (CC) ranks as the fourth most common form of cancer to be diagnosed. It was previously reported that transmembrane protein 33(TMEM33) could report a poor prognosis in several cancers. The current study is aimed at investigating the potential prognostic value of TMEM33 and its relevance to the tumor microenvironment in CC in a comprehensive manner. In this study, CC specimens presented noticeably higher TMEM33 expression level in comparison to nontumor specimens. In pan-cancer assays, it was found that TMEM33 was present at a high level in many different kinds of tumors. We found that patients with CC patients who had a high TMEM33 expression presented worse overall survival (OS) and disease-free survival (DFS) relative to patients who had a low TMEM33 expression. According to the results of a multivariate analysis, a high level of TMEM33 expression can significantly and independently predict the prognosis of CC. The levels of TMEM33 were found to have a negative correlation with resting dendritic cells, resting mast cells, plasma cells, T cells CD8, T cells regulatory, and regulatory T cells. Finally, we confirmed that TMEM33 was overexpressed in CC cells, and its knockdown distinctly suppressed the proliferation and invasion of CC cells. Overall, we provided evidences that TMEM33 could be used as a potential biomarker to assess the prognosis and the level of immune infiltration in CC.

1. Introduction

Cervical cancer (CC) is a representative disease and the third leading cause of death related to cancers among females [1]. In 2018, there were about 570,000 newly diagnosed CC cases worldwide, leading to 311,000 death cases among females [2]. It is well known that infection with the human papilloma virus (HPV) is a common cause of the carcinogenesis of CC in populations with high risks [3, 4]. However, approximately 90% of CC developed in low- and middle-income countries lack screening and HPV vaccination [5]. Patients diagnosed with cervical cancer typically undergo one of two treatment modalities, either surgery or a chemotherapy-radiotherapy combination [6, 7]. The cancer, on the other hand, is almost certainly incurable for the patient. There is a high risk that cervical cancer will progress from an early stage to a more advanced stage if it has not been treated [8, 9]. As a result, diagnosis and treatment at an early stage are extremely important. Future researches are suggested to understand the processes leading to CC development and to locate novel biomarkers capable of aiding in the early diagnosis and treatment of the disease.

Growing evidences suggest that both the intrinsic characteristics exhibited by the tumor cells and components in the tumor microenvironment (TME) can determine the cancer malignancy degree [10]. These components include endothelial cells, immune cells, inflammatory mediators, mesenchymal cells, and extracellular matrix molecules [11]. There is an increasing body of evidence suggesting that the characteristics exhibited by tumor-infiltrating immune cells (TIICs) can impact cancer onset and development [12, 13]. TIIC type and density can predict patients' survival and impact the responses of tumors to treatment [14]. Hence, TIICs can promisingly serve as clinical biomarkers targeting cancers and other malignancy types. Tumor-associated neutrophils (TANs) are the most common type of immune cell.

They eliminate pathogens and prevent the host from being infected by microorganism. Additionally, TANs have been shown to present a positive relevance to poorer prognosis in gastric cancer and breast cancer. In addition, tumor-associated macrophages (TAMs) are capable of inhibiting antitumor immunity and promoting tumor progression, as well as having a negative correlation with the prognosis of patients with CC [15, 16]. Also, the TME could impact the gene expression in tumor tissues and contribute to the clinical outcome. All these elucidated the relationship of TME with cancer progression, which opened the door to the possibility of improving the treatment of tumors.

Transmembrane protein 33 (TMEM33) has been conserved throughout the course of evolution. Previous studies found that TMEM33 was a downstream effector of PKM2 and that it regulated the activation of SREBP and lipid metabolism [17]. The depletion of PKM2 resulted in increased TMEM33 expression, which, in turn, promoted SCAP degradation through its interactions with the ubiquitin ligase RNF5. On the other hand, there was limited information regarding the possible function of TMEM33 in tumors. The study was the first one to hypothesize that TMEM33 might be a novel prognostic biomarker involved in TME in CC patients.

2. Materials and Methods

2.1. Raw Data. TMEM33 expression data together with clinical information was gathered from the TCGA public database (http://cancergenome.nih.gov). This data set included 3 normal tissues and 306 cancerous tissue samples. An HTseq tool was used to compute the level 3 HTSeq-fragments per kilobase per million (FPKM) samples, and these results were then converted to transcripts per million (TPM) units. In addition, we acquired publicly accessible transcript data from the Genotype-Tissue Expression (GTEx) database. This data was consistently maintained by the Toil process from UCSC Xena (https://xenabrowser.net/datapages/). In addition, 292 CC patients were included for survival assays.

2.2. TMEM33 Expression Pattern in Human Pan-Cancer. The data of normal tissues from the GTEx database were combined with the data from TCGA in order to investigate the TMEM33 dysregulation that occurs between different cancer types and normal tissues. The TCGA database provided access to the RNA sequencing data and the clinical follow-up information of patients who suffered from 33 different cancer types. All expression data were normalized via log2 conversion.

2.3. Survival Analysis. Both the survminer and the survival packages (version 0.4.6; http://cran.r-project.org/) by R software were utilized in the survival analysis that was conducted. We screened out 292 tumor samples out of 309 CC cases considering the following conditions: (i) eliminate samples with a predicted lifespan of less than one month; (ii) eliminate normal samples; (iii) eliminate samples of which the clinical information were incomplete. The

Kaplan-Meier method served for generating a survival curve. The log-rank test assisted in determining the statistical significance, and a p value cutoff of 0.05 served as the significant threshold.

2.4. TICs Profile. CIBERSORT is an algorithm that has applications for discovering biological biomarkers and potential therapeutic targets. It has the capability of discriminating between 22 human immune cell morphologies in a manner that is both extremely sensitive and specific. Chen et al. revealed that by using the support regression vector-based machine learning approach, they were able to show that CIBERSORT efficiently resolves cell subtypes that have comparable gene expression patterns through the use of benchmarking analysis [18]. CIBERSORT was used to estimate the TIC abundance profile in each and every tumor sample [19]. For the subsequent analyses, we only considered those patients eligible whose CIBERSORT p values were less than 0.05. The total number of immune cell type fractions estimated for each sample was added up to 1 after being summed.

2.5. Cell Lines and Cell Cultures. The human normal epithelial cell line HaCaT and the CC cell lines HeLa, SiHa, C-33A, and CaSKi came from the cell bank of the Chinese Academy of Sciences. These cell lines were used to study CC. These cells were grown in a high-glucose DMEM medium with 10% fetal bovine serum(FBS) in an atmosphere that contained 5% carbon dioxide and humidified at 37 degrees Celsius.

2.6. Cell Transfection. Small interfering RNAs (siRNAs) against TMEM33 were provided by Shanghai GenePharma, as were control siRNAs (si-NC). The indicated siRNAs were transfected into cells by using the Lipofectamine 2000 reagent(Invitrogen; Thermo Fisher Scientific, Inc.).

2.7. Quantitative RT-PCR. In order to conduct the experiments, RNAse-free water was required. cDNA was synthesized using an RT2 first-strand kit that was purchased from Qiagen in China. After adding and mixing 1 microgram (μg) of RNA and 2 microliters (μl) of genomic DNA elimination mix, the mixture then underwent 5 min of incubation at 42 degrees Celsius, after which it was rapidly transferred to ice-cold water for one minute. Following the addition of the reverse transcription mix, which included a 5 buffer and a reverse transcriptase enzyme, the mixture underwent 15 min of incubation at a temperature of 42 degrees. When the incubation period ended, the tube that contained the reaction mixture was heated to 95 degrees Celsius for terminating the reaction. All of the genes were identified by utilizing probes manufactured by Qiagen. The GAPDH gene served as an internal control to help standardize the results. Primers used for RT-RCR are presented as follows: TMEM33-F: ATGGCAGATACGACCCCGAA, TMEM33-R: GAAAGCCACATTGCCGTGTC. GAPDH-F: 5′-CTGGGCTACACTGAGCACC-3′, GAPDH-R: 5′-AAGTGG TCGTTGAGGGCAATG-3′.

2.8. Cell Proliferation Assays. To perform the CCK-8 assays, each well of 96-well plates contained cultured CC cells that
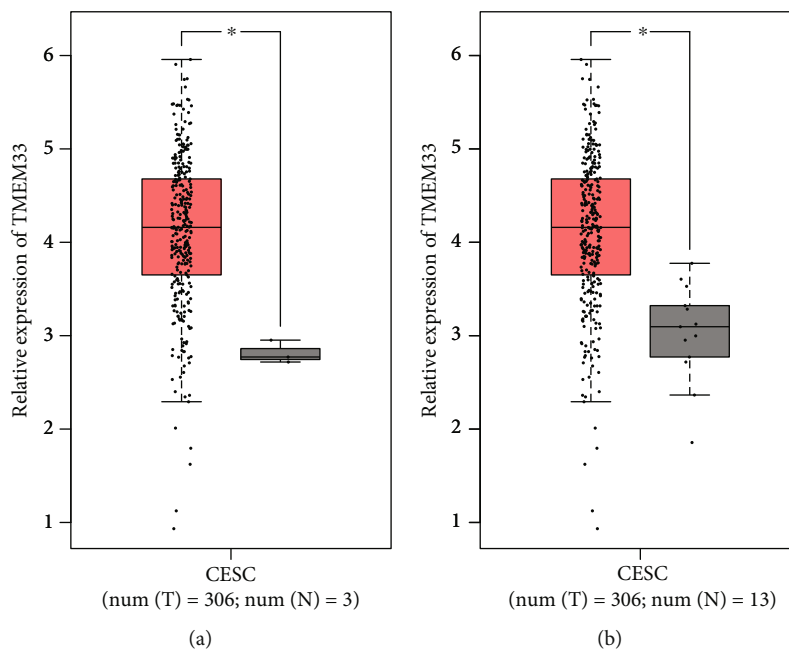
FIGURE 1: TMEM33 expression in CC tissues and nontumor specimens from (a) TCGA datasets or (b) TCGA datasets and GTEx data.

had been transfected by either a silencing or control sequence of TMEM33. The total number of cells used was $N = 1 \times 10^4$. In order to determine the health of the cells, a 10% CCK-8 working solution (Dojindo, Japan) was formulated, and then $100\,\mu l$ of it was injected into each well to receive 2 h of incubation at 37 degrees Celsius. For determining the relative cell viability, the absorbance at 450 nm was utilized.

2.9. Cell Clone Formation Experiment. In order to get started with the experiment, HeLa and SiHa cells were transfected and then plated in a 6-well plate at a density of 1×10^3 cells per well. Following a transfection process that lasted for 24 hours, the cells were put into a complete medium and given the chance to develop for 14 days. After the allotted time for incubation had passed, the cells were stained with 0.1% crystal violet and then fixed in paraformaldehyde at a concentration of 4%. After that, a microscope was used to count the colonies, each of which had to have at least 50 cells.

2.10. 5-Ethynyl-2′-deoxyuridine (EdU) Assay. After a transfection that lasted for 48 hours, HeLa and SiHa cells were seeded at a density of 1×10^4 cells per well in 96-well plates. These cells were then tagged with the BeyoClickTM EdU cell proliferation kit (Beyotime, Shanghai, China). The 4′,6-diamidino-2-phenylindole (DAPI) staining solution was utilized in order to see the nuclei of the cells. Using a fluorescent microscope(Olympus, Tokyo, Japan), it was possible to see cells that had been positively tagged. In order to guarantee the accuracy of the findings, the experiment was repeated three times with no overlap between the runs.

2.11. Transwell Assay. A transwell test was carried out in order to measure the capacity of the cells to invade. In this particular experiment, cells were seeded into the top chambers of 24-well plates that had been precoated with Matrigel (Millipore, MA, USA) and then cultured for 48 hours in serum-free media. Following incubation, the invasive cells were fixed with 4% paraformaldehyde and then stained for 20 minutes with a crystal violet solution containing 0.25% crystal violet (Sigma-Aldrich Co., St. Louis, MO, USA). Following this step, stained cells were seen and counted using an inverted microscope manufactured by Nikon in Japan. Five distinct microscopic images were then chosen at random for examination. With the use of this technology, we were able to evaluate the capability of cells to infiltrate through a barrier, which gives important insight into the metastatic potential of the cells.

2.12. Western Blot Analysis. As the first stage in the process of obtaining protein lysates, we utilized RIPA buffer. After that, the total protein samples were separated using SDS-PAGE at a 12.5% concentration and then deposited onto PVDF membranes (Thermo Fisher, IL, USA). Before the membranes were probed with primary antibodies against the target proteins at 4°C for a whole night, they were first treated with 5% nonfat milk for the purpose of preventing any nonspecific binding. Secondary antibodies against TMEM33 and GAPDH (Abcam) were added to the membranes after they had been washed three times with PBS. The membranes were then left to incubate in the dark at room temperature for one hour. A chemiluminescence device was utilized in order to carry out the protein concentration measurement study.

2.13. Statistical Analysis. Using the R programming language (R version: 3.6.1), each and every piece of data was analyzed. A *t*-test with two independent hypotheses served for data analysis. The Kaplan-Meier method served for the actuarial calculations needed to determine overall survival rates. The

(a)

(b)
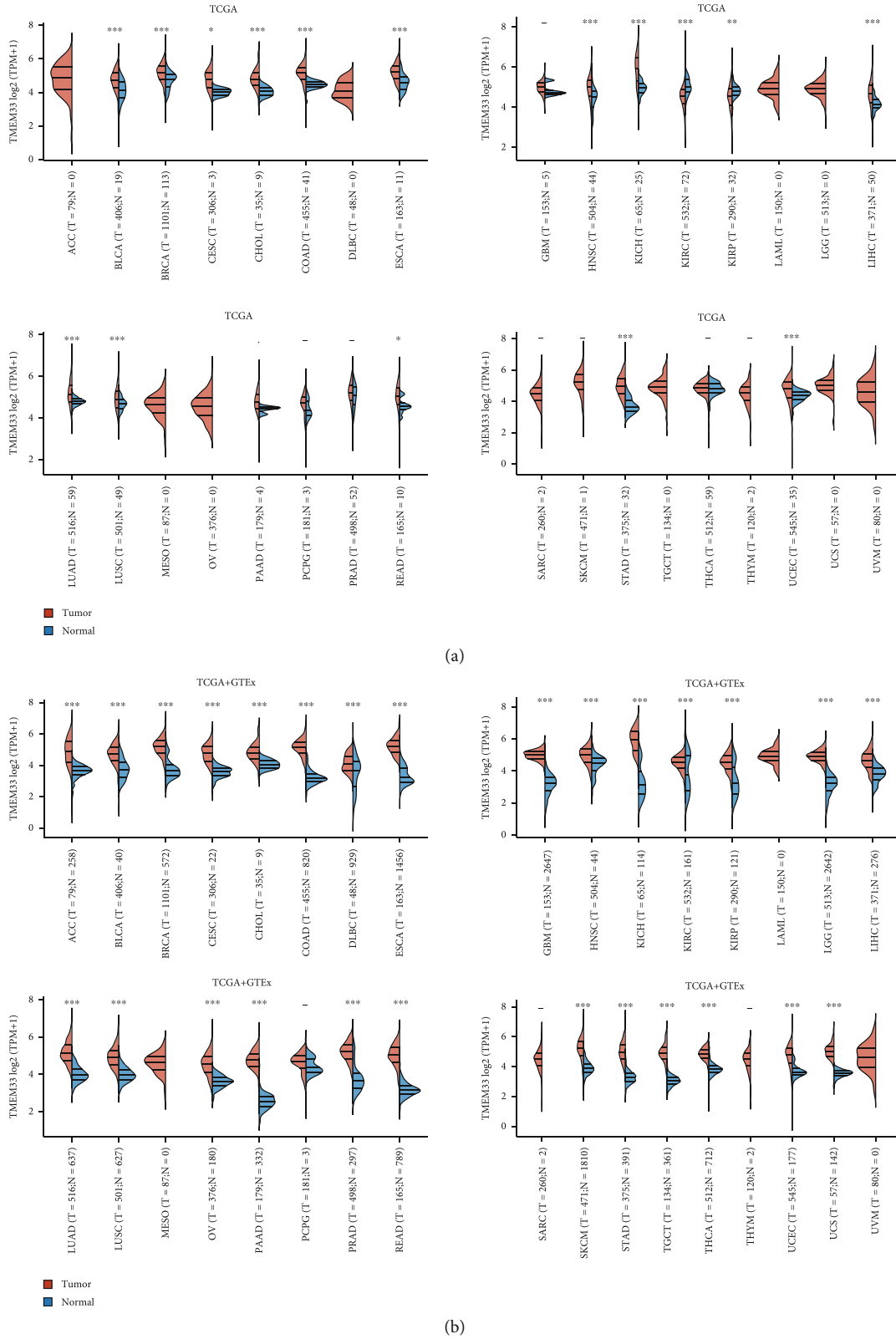
FIGURE 2: The differential expression of TMEM33 in 33 types of tumors and the nontumor tissues from (a) TCGA datasets or (b) TCGA datasets and GTEx data.
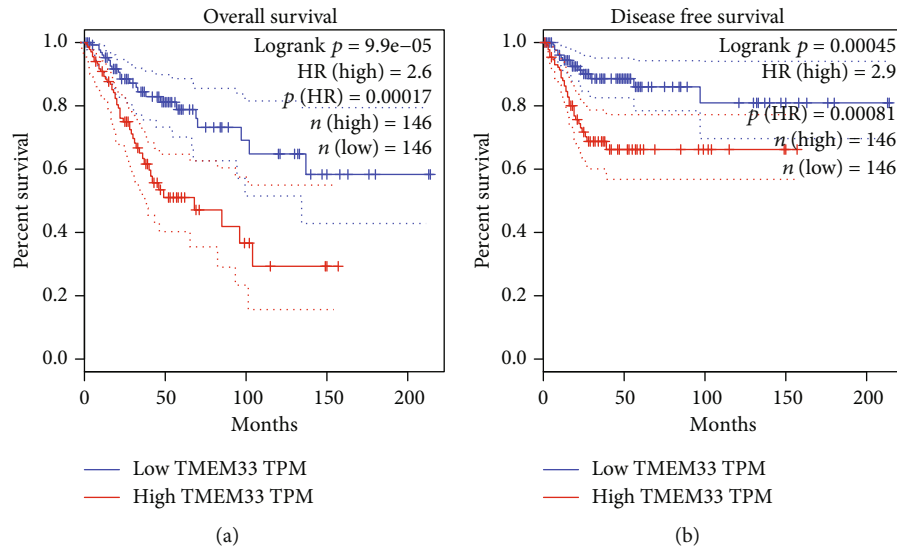
FIGURE 3: Kaplan-Meier curves of (a) OS and (b) DFS between the TMEM33-high and -low expression cohorts.

Cox proportional hazard regression model determined the independent prognostic factors. In order to be considered statistically significant, the two-tailed p value needed to be lower than 0.05.

3. Results

3.1. TMEM33 Expression Was Overexpressed in CC and Its Pan-Cancer Analysis. Firstly, we examined the expression of TMEM33 in CC using data from TCGA datasets and GTEx. When compared with nontumor specimens, CC samples presented noticeably higher TMEM33 expression level relative to nontumor samples. This was illustrated in Figures 1(a) and 1(b). After that, we conducted pan-cancer assays and found that TMEM33 was present at a high level in many different kinds of tumors, including ACC, LUAD, and PRAD (Figure 2). Based on our findings, TMEM33 may function as an oncogene in a variety of tumors.

3.2. The Prognostic Value of TMEM33 in CC and Pan-Cancer. In order to explore the prognostic value of TMEM33 expression in CC, we manually divided CC patients into two groups (high group and low group) based on the mean expression of TMEM33 in CC. The Kaplan-Meier survival analysis was applied to evaluate the prognostic value of TMEM33 expression in patients with CC. We discovered that patients with CC patients with high TMEM33 expression presented a shorter OS (Figure 3(a)) and DFS (Figure 3(b)) relative to CC patients with low TMEM33 expression. A univariate Cox analysis was carried out for the purpose of determining the degree of prognostic significance that clinicopathological factors have for survival rates. Both clinical stage ($p = 0.001$) and TMEM33 expression ($p = 0.022$) had a significant correlation with an individual patient's overall survival (Figure 4(a)). According to the additional multivariate analysis, high TMEM33 expression could significantly and independently predict CC patients' poor OS (hazard ratio [HR] = 1.964, confidence interval [CI

] = 1.237 − 2.004) (Figure 4(b)). In addition, the findings of pan-cancer survival assays suggested that TMEM33 expression was linked to the prognosis of patients who were diagnosed with KIRC, SKCM, and CC (Figure S1).

3.3. Correlation of TMEM33 with the Proportion of TICs. To more deeply validate that TMEM33 expression was positively correlated with the immune microenvironment, the CIBERSORT algorithm determined the percentage of immune subsets that had infiltrated the tumor. 21 distinct immune cell profiles were generated from CC tissue samples (Figures 5(a) and 5(b)). According to the difference and correlation analyses, 8 kinds of TICs showed a relevance to TMEM33 expression (Figure 6). Thereinto, 3 kinds of TICs presented a positive relevance to TMEM33 expression, including macrophages M0, mast cells activated, and T cells CD4 memory resting; 5 kinds of TICs presented a negative relevance to TMEM33 expression, namely, dendritic cells resting, mast cells resting, plasma cells, T cells CD8, and T cells regulatory (Tregs). All these further proved the impact of TMEM33 levels on TEM immune activity.

3.4. The Impact of TMEM33 Knockdown on CC Cell Proliferation and Invasion. In order to investigate whether or not TMEM33 was expressed in CC, we utilized RT-PCR and western blot on a number of CC cells. In comparison to the HaCaT cells, all four of the CC cells exhibited remarkably higher TMEM33 expression(Figure 7(a)). HeLa and SiHa cells were transfected by small interfering RNAs against TMEM33 (si-TMEM33) for examining the functional roles that TMEM33 plays in CC. Then, RT-PCR and western blot demonstrated that siRNAs had the ability to effectively suppress TMEM33 expression in both HeLa and SiHa cells (Figure 7(b)). According to the CCK-8 assays, TMEM33 siRNA-transfected HeLa and SiHa cells presented remarkably lower optical density (OD 450 nm) relative to cells transfected with si-NC (Figures 7(c) and 7(d)). In addition, the results of EdU staining proved that repressing

(a)

(b)
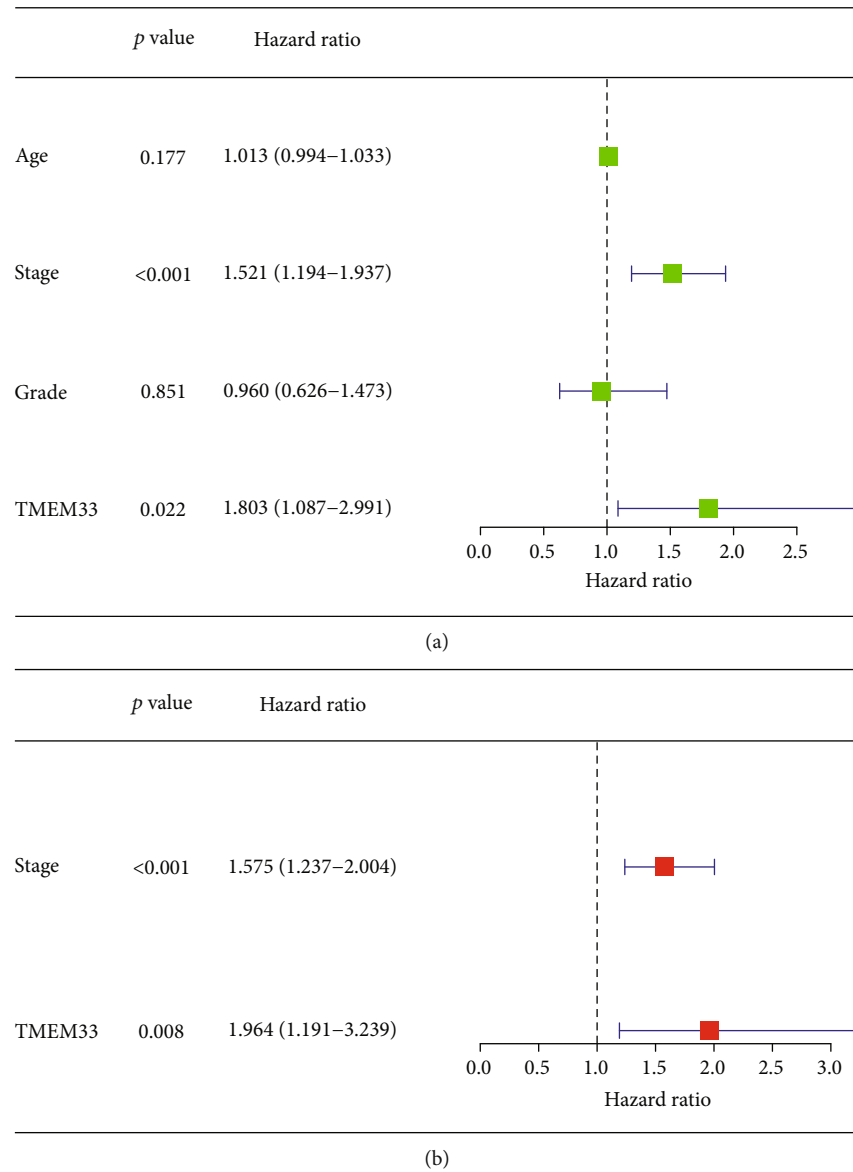
FIGURE 4: (a) Univariate and (b) multivariate Cox regression analyses of OS in CC patients.

TMEM33 levels markedly reduced the number of proliferative CC cells (Figure 7(e)). Moreover, clonogenic assays revealed that the clone formation abilities were also attenuated upon TMEM33 knockdown (Figure 7(f)). Finally, we also found that the knockdown of TMEM33 distinctly suppressed the invasion of CC cells (Figure 7(g)).

4. Discussion

CC is primarily brought on by an infection with high-risk HPV (hrHPV), and it is the fourth most common cancer type among females around the world [20, 21]. Squamous cell carcinoma (SCC) and adenocarcinoma take up 80-85% and 15-20%, respectively, of all pathological types of cancer that are classified as CC [22, 23]. Even though surgery, chemotherapy, radiation therapy, etc. are available today, recurrence rate and metastasis rate for patients suffering late-stage CC are up to 40.3% and 31%, respectively [24, 25]. Patients who have metastatic CC continue to have a poor prognosis, and the median survival time ranges from 8 to 13 months. As a result, it is of the utmost importance to discover reliable prognostic biomarkers and molecular mechanisms that can impact CC prognosis, which may lead to the discovery of more effective predictive and therapeutic targets.

During our investigation of pan-cancer, we discovered that TMEM33 was overexpressed in two of the tumors. After further investigation, it was found that a higher level of TMEM33 expression reported poorer OS and DFS in patients with CC. In addition, both univariate and multivariate Cox analyses suggested that TMEM33 was a factor that could be considered independent when attempting to forecast the prognosis of patients. All of these results, which have been discussed previously, point to the
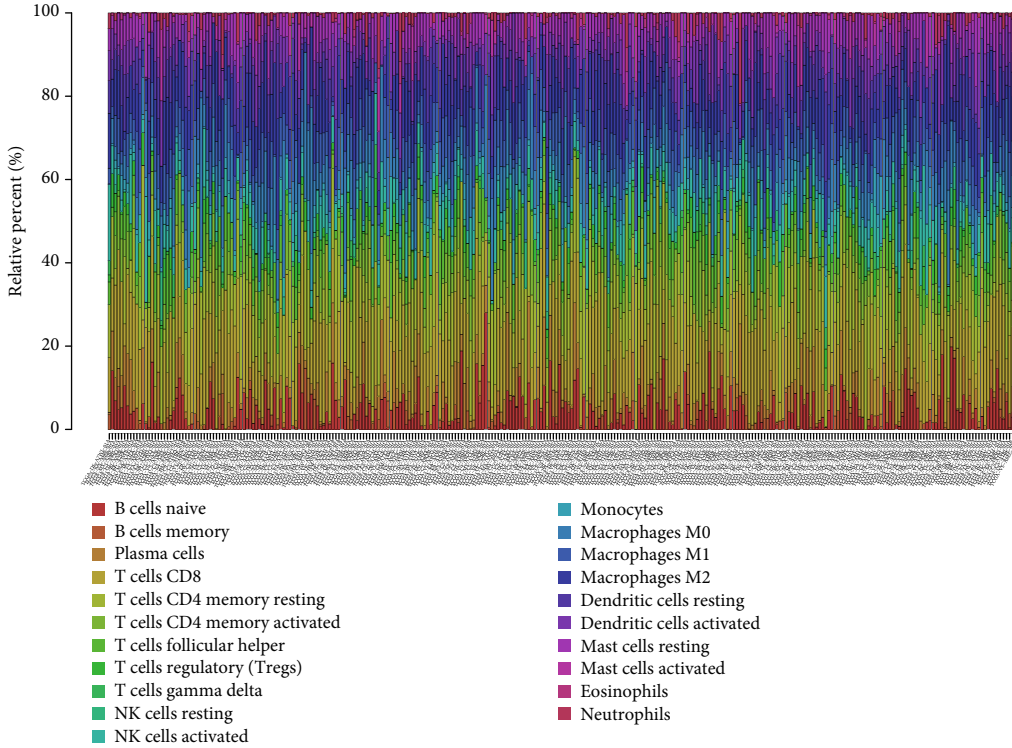
(a)
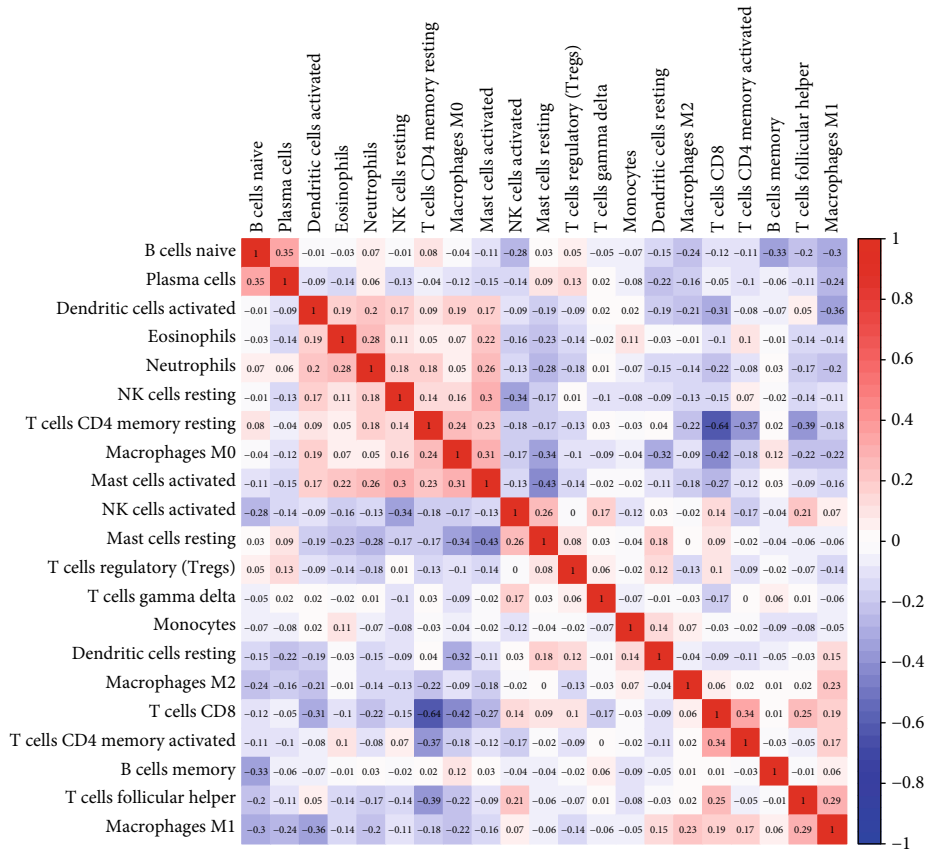
(b)

FIGURE 5: TIC profile in tumor samples together with correlation analysis. (a) Barplot that illustrates the proportion of 21 kinds of TICs in CC tumor samples. (b) Heatmap that illustrates the association of 21 kinds of TICs with numeric in each tiny box.
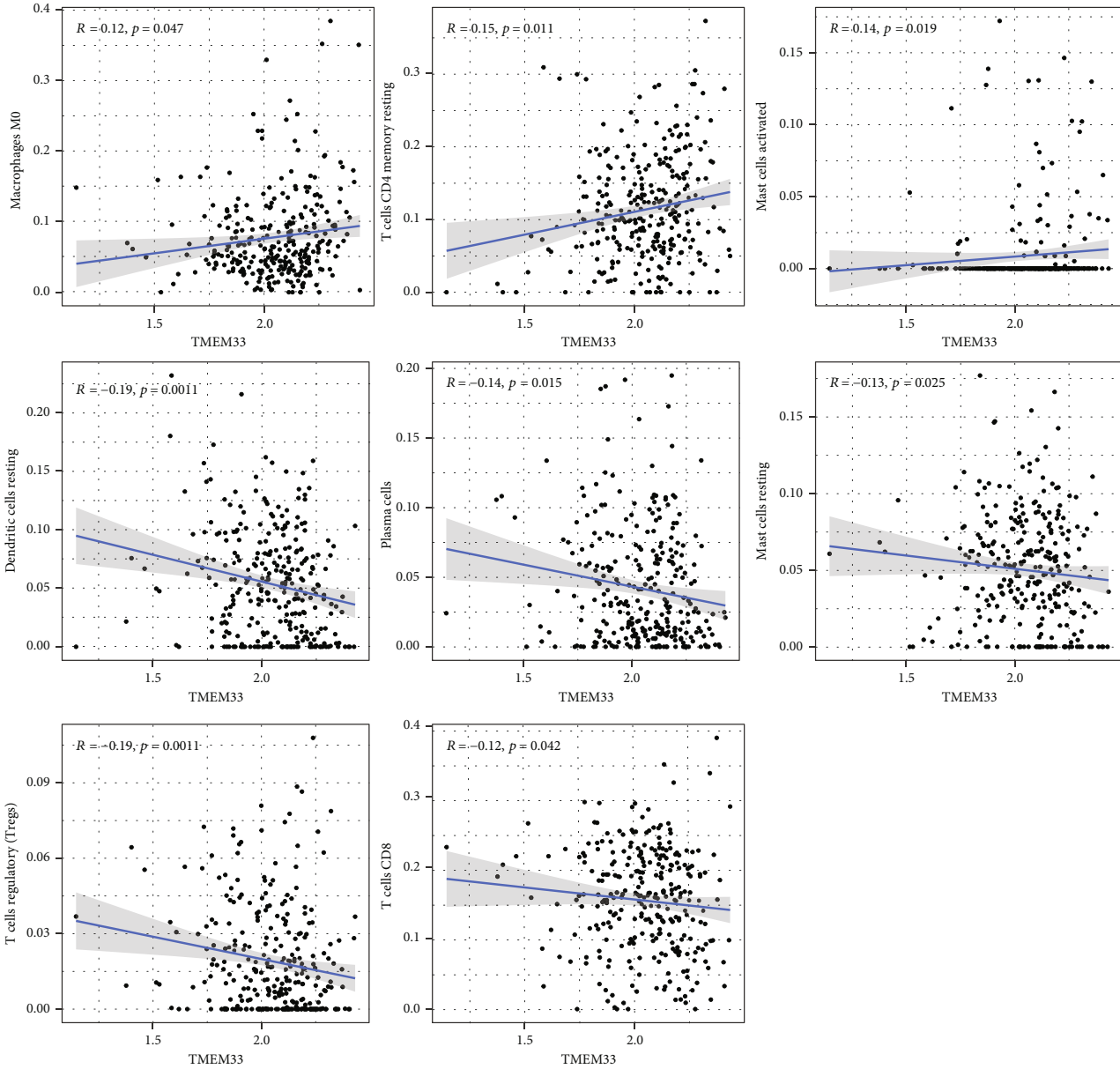
FIGURE 6: Scatter plot that demonstrates the association between 8 kinds of TICs proportion and the TMEM33 expression.

possibility that TMEM33 is a promising prognostic bio-marker for CC patients. In addition, we carried out RT-PCR, which provided further evidence that the level of TMEM33 expression was noticeably elevated in CC cells. According to the results of functional assays, knockdown of TMEM33 suppressed the proliferation and invasion of CC cells. Although a previous study has reported the prognostic value of TMEM33 in CC patients, we firstly provided evidences that TMEM33 may be involved in the progression of metastasis [26]. Our finding suggested TMEM33 as an oncogene in CC progression.

Immunotherapy has only relatively recently been rec-ognized as a potential new treatment option for cancer patients suffering from CC [27, 28]. The tumor microenvi-ronment (TME), which consists of tumor vasculature,

stroma cells, the ECM, and various cells of the immune system, has been confirmed to stimulate the developments of various tumors [29]. It is common knowledge that immunosuppressive cells can cause the occurrence of immune escape in TME, that in turn, can promote tumor progression and metastasis [30]. There is evidence that the number of regulatory T cells, or Tregs, a typical immuno-suppressive cell type, is correlated with patients' prognosis. This suggests the Treg count as a useful marker for the prognosis of CC. It has been hypothesized that the TME remarkably impacts CC development. TIICs make up the majority of the nontumor components that can effectively assist in assessing CC prognosis. Therefore, it is of the utmost importance to work toward increasing the efficacy of immunotherapy in CC by methodically evaluating the

(a)

(b)

(c)

(d)

(e)
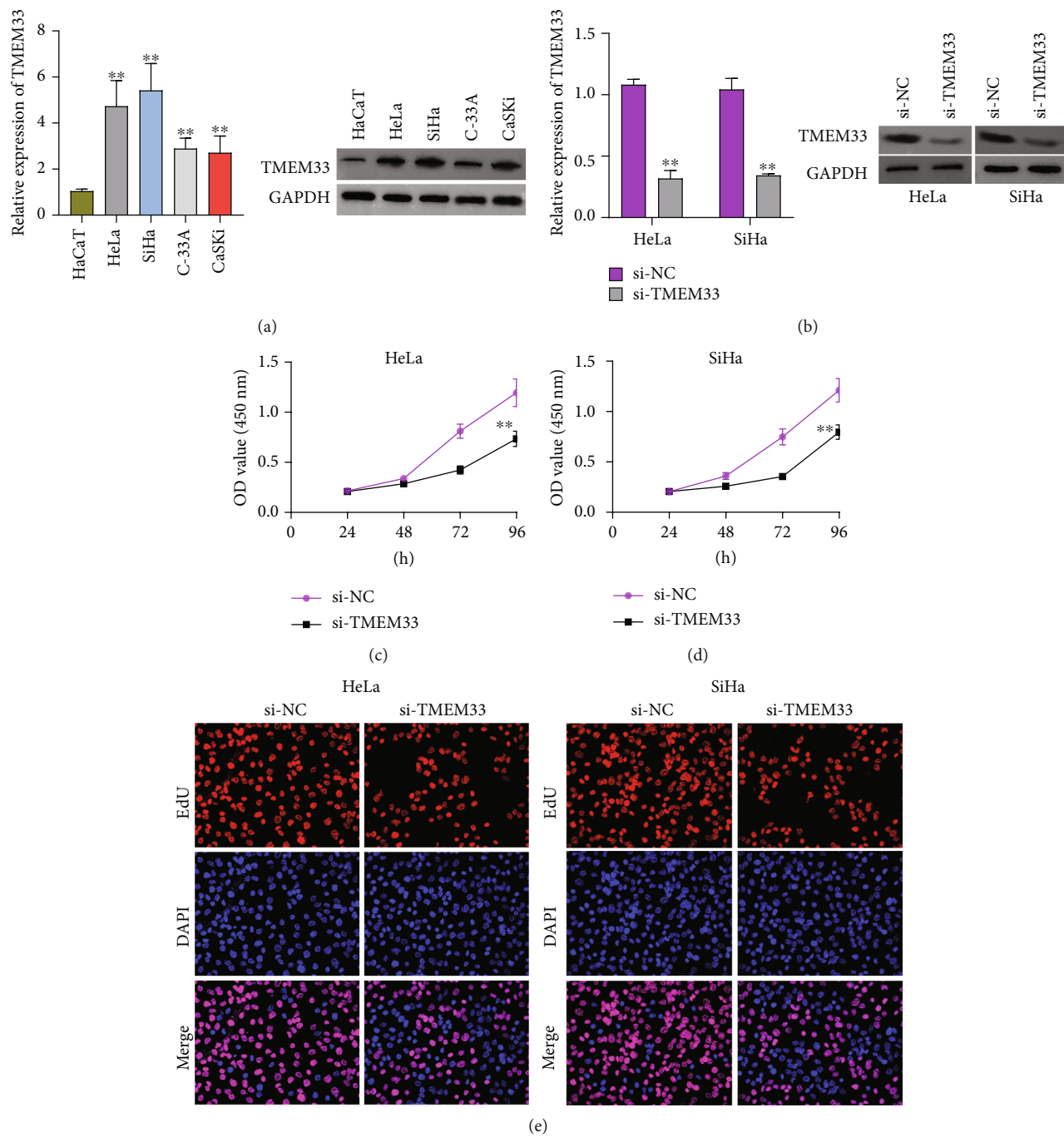
Figure 7: Continued.

(f)

(g)
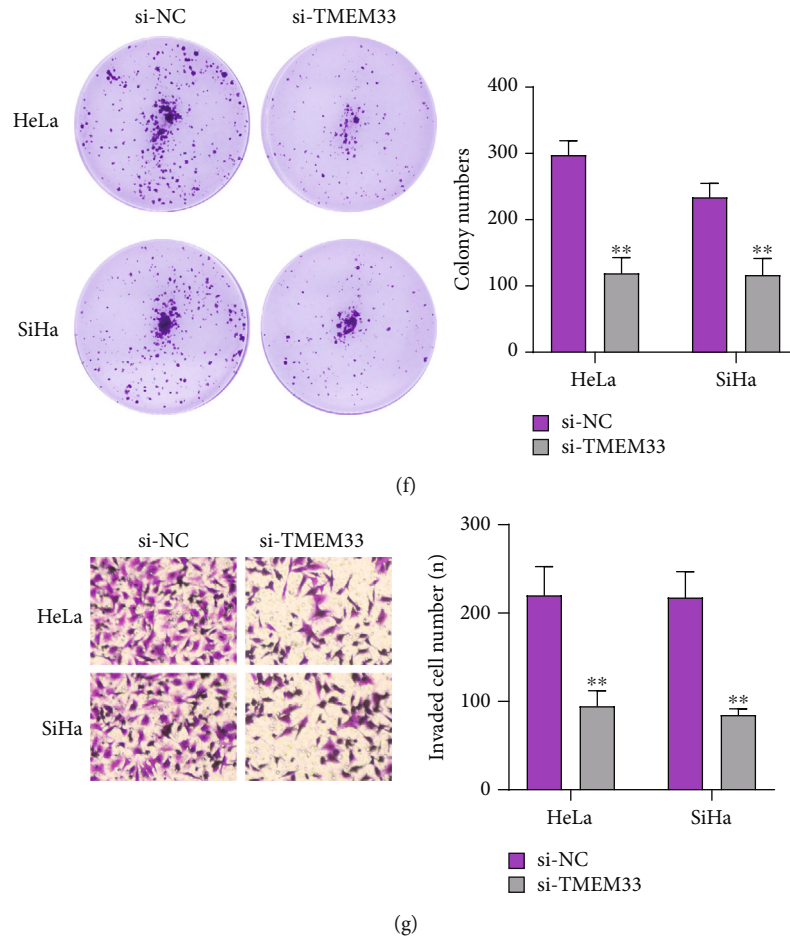
FIGURE 7: TMEM33 knockdown inhibited CC cell proliferation and invasion. (a) Relative expression of TMEM33 in CC cell lines (HeLa, SiHa, C-33A, and CaSKi) and HaCaT cell line using RT-PCR and western blot. (b) RT-PCR and western blot detected the changes of TMEM33 expressing levels in CC cells after transfection with TMEM33 siRNA. (c, d) CCK8 assays were employed to determine the growth curves of CC cells at 24 h, 48 h, 72 h, and 96 h. (e) EdU immunofluorescence staining assays for HeLa and SiHa cells. (f) Clone formation assays were used to detect cell proliferation in HeLa and SiHa cells. (g) The effect of TMEM33 knockdown1 on the invasion of HeLa and SiHa was determined by transwell assays.

immune properties of the TME and determining the distribution and functions of TIIC. In this study, the TMEM33 expression presented a positive relevance to three different types of TICs, including macrophages M0, activated mast cells, and resting T cells CD4 memory. On the other hand, TMEM33 expression was negatively correlated with five different types of TICs, including resting dendritic cells, resting mast cells, resting plasma cells, resting T cells CD8, and resting T cells regulatory, suggesting TMEM33 may inhibit the infiltration and activation of these immune cells in the tumor microenvironment. This could potentially contribute to tumor immune evasion and promote tumor growth. On the other hand, inhibition of TMEM33 expression could potentially enhance the infiltration and activation of these immune cells, leading to improved antitumor immunity. This suggests that TMEM33 may be a potential therapeutic target for cancer immunotherapy. One potential clinical application related to TMEM33 and immunotherapy is the development of small molecule inhibitors or monoclonal antibodies targeting TEM33. These could be used to enhance

the infiltration and activation of immune cells in the tumor microenvironment, potentially improving the efficacy of existing immunotherapies.

The present study has some limitations. First, the clinical information from the TCGA databases was scant and lacked essential details. No in-depth analysis was performed on the information pertaining to neuroimaging, the extent of the resection, radiotherapy, or chemotherapy. Second, additional validation of the prognostic value of TMEM33 expression in patients with CC is required through multicenter, large-scale clinical trials and prospective studies.

5. Conclusion

Our research demonstrated that TMEM33 was a candidate biomarker that can predict the outcome of treatment and the patient's prognosis in patients with CC. To elucidate the biological effects and underlying mechanisms of TMEM33, further experimental validation is required.

Data Availability

Some or all data generated or used during the study can be obtained from the corresponding author upon request.

Conflicts of Interest

The authors have declared that there are no conflicts of interest.

Authors' Contributions

Hui Zhang, Jun Wang, and Ji Yang wrote the manuscript, critically revised the manuscript, and contributed in data analysis; Hui Zhang, Jun Wang, and Ji Yang designed and supervised the research and analyzed the data; Qingwen He, Sanli Guan, Minxia Qiao, and Jian Zhao contributed in the conduction of the research; Hui Zhang and Xiu Wang contributed in the design and supervision of the study.

Supplementary Materials

Figure S1: pan-cancer survival analysis of TMEM33 based on TCGA datasets. (Supplementary Materials)

References

[1] E. Ward, C. DeSantis, A. Robbins, B. Kohler, and A. Jemal, "Childhood and adolescent cancer statistics, 2014," *CA: a Cancer Journal for Clinicians*, vol. 64, no. 2, pp. 83–103, 2014.

[2] L. A. Torre, R. L. Siegel, E. M. Ward, and A. Jemal, "Global cancer incidence and mortality rates and trends—an update," *Cancer Epidemiology, Biomarkers & Prevention : a Publication of the American Association for Cancer Research, cosponsored by the American Society of Preventive Oncology*, vol. 25, no. 1, pp. 16–27, 2016.

[3] Z. Hu and D. Ma, "The precision prevention and therapy of HPV-related cervical cancer: new concepts and clinical implications," *Cancer Medicine*, vol. 7, no. 10, pp. 5217–5236, 2018.

[4] Y. Yuan, X. Cai, F. Shen, and F. Ma, "HPV post-infection microenvironment and cervical cancer," *Cancer Letters*, vol. 497, pp. 243–254, 2021.

[5] S. L. Bedell, L. S. Goldstein, A. R. Goldstein, and A. T. Goldstein, "Cervical cancer screening: past, present, and future," *Sexual Medicine Reviews*, vol. 8, no. 1, pp. 28–37, 2020.

[6] A. Buskwofie, G. David-West, and C. A. Clare, "A review of cervical cancer: incidence and disparities," *Journal of the National Medical Association*, vol. 112, no. 2, pp. 229–232, 2020.

[7] H. Li, X. Wu, and X. Cheng, "Advances in diagnosis and treatment of metastatic cervical cancer," *Journal of Gynecologic Oncology*, vol. 27, no. 4, article e43, 2016.

[8] M. Vu, J. Yu, O. A. Awolude, and L. Chuang, "Cervical cancer worldwide," *Current Problems in Cancer*, vol. 42, no. 5, pp. 457–465, 2018.

[9] S. Shen, S. Zhang, P. Liu, J. Wang, and H. Du, "Potential role of microRNAs in the treatment and diagnosis of cervical cancer," *Cancer Genetics*, vol. 248-249, pp. 25–30, 2020.

[10] D. Chen, X. Zhang, Z. Li, and B. Zhu, "Metabolic regulatory crosstalk between tumor microenvironment and tumor-associated macrophages," *Theranostics*, vol. 11, no. 3, pp. 1016–1030, 2021.

[11] T. Du, J. Gao, P. Li et al., "Pyroptosis, metabolism, and tumor immune microenvironment," *Clinical and Translational Medicine*, vol. 11, no. 8, article e492, 2021.

[12] R. Tang, J. Xu, B. Zhang et al., "Ferroptosis, necroptosis, and pyroptosis in anticancer immunity," *Journal of Hematology & Oncology*, vol. 13, no. 1, p. 110, 2020.

[13] S. S. Wang, W. Liu, D. Ly, H. Xu, L. Qu, and L. Zhang, "Tumor-infiltrating B cells: their role and application in antitumor immunity in lung cancer," *Cellular & Molecular Immunology*, vol. 16, no. 1, pp. 6–18, 2019.

[14] A. Tanaka and S. Sakaguchi, "Targeting Treg cells in cancer immunotherapy," *European Journal of Immunology*, vol. 49, no. 8, pp. 1140–1146, 2019.

[15] Y. Pan, Y. Yu, X. Wang, and T. Zhang, "Tumor-associated macrophages in tumor immunity," *Frontiers in Immunology*, vol. 11, article 583084, 2020.

[16] P. Pathria, T. L. Louis, and J. A. Varner, "Targeting tumor-associated macrophages in cancer," *Trends in Immunology*, vol. 40, no. 4, pp. 310–327, 2019.

[17] F. Liu, M. Ma, A. Gao,,,, et al., "PKM2-TMEM33 axis regulates lipid homeostasis in cancer cells by controlling SCAP stability," *The EMBO Journal*, vol. 40, no. 22, article e108065, 2021.

[18] B. Chen, M. S. Khodadoust, C. L. Liu, A. M. Newman, and A. A. Alizadeh, "Profiling tumor infiltrating immune cells with CIBERSORT," *Methods in Molecular Biology (Clifton, NJ)*, vol. 1711, pp. 243–259, 2018.

[19] A. M. Newman, C. L. Liu, M. R. Green et al., "Robust enumeration of cell subsets from tissue expression profiles," *Nature Methods*, vol. 12, no. 5, pp. 453–457, 2015.

[20] D. H. Moore, "Cervical cancer," *Obstetrics and Gynecology*, vol. 107, no. 5, pp. 1152–1161, 2006.

[21] A. Fernandes, D. Viveros-Carreño, J. Hoegl, M. Ávila, and R. Pareja, "Human papillomavirus-independent cervical cancer," *International Journal of Gynecological Cancer : Official Journal of the International Gynecological Cancer Society*, vol. 32, no. 1, pp. 1–7, 2022.

[22] M. Saleh, M. Virarkar, S. Javadi, S. B. Elsherif, F. S. de Castro, and P. Bhosale, "Cervical cancer: 2018 revised International Federation of Gynecology and Obstetrics Staging System and the role of imaging," *AJR American Journal of Roentgenology*, vol. 214, no. 5, pp. 1182–1195, 2020.

[23] G. Marquina, A. Manzano, and A. Casado, "Targeted agents in cervical cancer: beyond bevacizumab," *Current Oncology Reports*, vol. 20, no. 5, p. 40, 2018.

[24] L. Wang, Y. Zhao, Y. Wang, and X. Wu, "The role of galectins in cervical cancer biology and progression," *BioMed Research International*, vol. 2018, Article ID 2175927, 11 pages, 2018.

[25] S. Karim, T. Souho, M. Benlemlih, and B. Bennani, "Cervical cancer induction enhancement potential of chlamydia trachomatis: a systematic review," *Current Microbiology*, vol. 75, no. 12, pp. 1667–1674, 2018.

[26] H. Chen, X. Zhao, Y. Li et al., "High expression of TMEM33 predicts poor prognosis and promotes cell proliferation in cervical cancer," *Frontiers in Genetics*, vol. 13, article 908807, 2022.

[27] L. B. Kennedy and A. K. S. Salama, "A review of cancer immunotherapy toxicity," *CA: a Cancer Journal for Clinicians*, vol. 70, no. 2, pp. 86–104, 2020.

[28] R. S. Riley, C. H. June, R. Langer, and M. J. Mitchell, "Delivery technologies for cancer immunotherapy," *Nature Reviews Drug Discovery*, vol. 18, no. 3, pp. 175–196, 2019.

[29] K. G. K. Deepak, R. Vempati, G. P. Nagaraju et al., "Tumor microenvironment: challenges and opportunities in targeting metastasis of triple negative breast cancer," *Pharmacological Research*, vol. 153, article 104683, 2020.

[30] X. Tian, H. Shen, Z. Li, T. Wang, and S. Wang, "Tumor-derived exosomes, myeloid-derived suppressor cells, and tumor microenvironment," *Journal of Hematology & Oncology*, vol. 12, no. 1, p. 84, 2019.

Hindawi

Research Article

GATA6-AS1 via Sponging miR-543 to Regulate PTEN/AKT Signaling Axis Suppresses Cell Proliferation and Migration in Gastric Cancer

Yi Jin and Daqing Jiang ⓘ

Department of Breast Surgery, Cancer Hospital of China Medical University, Liaoning Cancer Hospital & Institute, Shenyang, 110001 Liaoning, China

Correspondence should be addressed to Daqing Jiang; yulaishan2322@163.com

Gastric cancer (GC) is one of the most common and lethal cancers worldwide. In view of the prominent roles of long noncoding RNAs (lncRNAs) in cancers, we investigated the specific role and underlying mechanism of GATA binding protein 6 antisense RNA 1 (GATA6-AS1) in GC. Quantitative real-time polymerase chain reaction (qRT-PCR) detected GATA6-AS1 expression in GC cell lines. Functional assays were conducted to explore the role of GATA6-AS1 in GC. Furthermore, mechanism investigations were implemented to uncover the interaction among GATA6-AS1, microRNA-543 (miR-543), and phosphatase and tensin homolog (PTEN). In the present study, it was found that GATA6-AS1 expression is significantly downregulated in GC cell lines. Functionally, GATA6-AS1 markedly suppresses GC cell growth and migration *in vitro* and *in vivo* tumorigenesis. Besides tumor suppressor, GATA6-AS1 serves as a miR-543 sponge. Specifically speaking, GATA6-AS1 acts as a competing endogenous RNA (ceRNA) of miR-543 to upregulate the expression of PTEN, thus inactivating AKT signaling pathway to inhibit GC progression. In conclusion, this study has manifested that GATA6-AS1 inhibits GC cell proliferation and migration as a sponge of miR-543 by regulating PTEN/AKT signaling axis, offering new perspective into developing novel GC therapies.

1. Introduction

Gastric cancer (GC) is the fifth most prevalent malignancy globally with high morbidity and mortality [1]. The risk factors like atrophic gastritis and intestinal metaplasia contribute to the occurrence of GC. In the past few years, the strategies of reducing the incidence of GC have been developed [2]. For instance, Helicobacter pylori (H. pylori) eradication therapy is effective for GC prevention [3]. In addition, apatinib is approved in the treatment of advanced GC [4]. Furthermore, there are an increasing number of scientific researches, reports, and findings about the molecular mechanism of lncRNAs, contributing to the development of targeted therapies for GC.

Long noncoding RNAs (lncRNAs) refer to transcripts with over 200 nucleotides and without the capacity to code

proteins [5]. Multiple lncRNAs have been reported to be involved with the pathogenesis and progression of various cancers [6]. GC is no exception. Some lncRNAs exert cancer-promoting functions in GC. For instance, HOTAIR overexpression was manifested to enhance GC cell proliferation and metastasis and shortening overall survival of GC patients [7]. ATB expedites tumor growth in GC [8]. At the same time, some lncRNAs serve as tumor suppressors in GC. For instance, MEG3 was found to target p53 signaling pathway to attenuate the proliferation and metastasis of GC cells [9].

lncRNA GATA binding protein 6 antisense RNA 1 (GATA6-AS1) acts as a tumor suppressor in several cancers [10]. For example, GATA6-AS1 overexpression was confirmed to indicate poor prognosis of lung squamous cell carcinoma [11, 12]. More importantly, Li et al. have elucidated

ENSG00000266010.1 gene expression from GTEx (release V6)

(a)

(b)

(c)
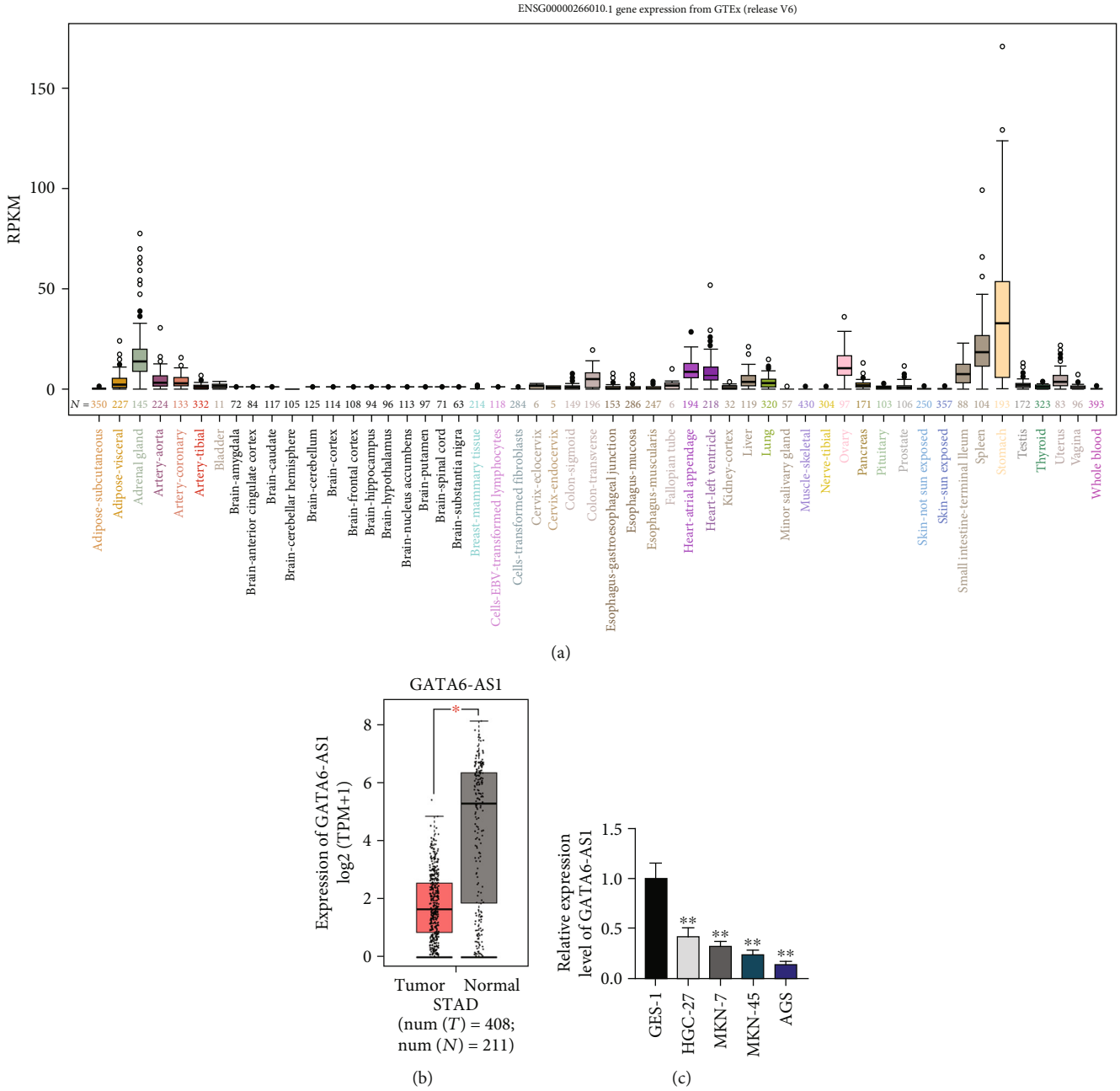
Figure 1: GATA6-AS1 is lowly expressed in the GC tissues and cell lines. (a) UCSC database displayed the level of GATA6-AS1 in human normal tissues. GATA6-AS1 expression level was significantly elevated in normal stomach tissues. (b) GEPIA analysis displayed the GATA6-AS1 expression in tumor (T; $n = 408$) and normal (N; $n = 211$) tissues. (c) GATA6-AS1 expression in GES-1 and HGC-27, MKN-7, MKN-45, and AGS cell lines was detected by qRT-PCR. One-way ANOVA and Dunnett's test. $^{**}P < 0.01$ and $^{*}P < 0.05$.

that overexpressed GATA6-AS1 could inhibit LNM and EMT via FZD4 in GC cells by targeting the Wnt/β-catenin pathway [13]. It was worth noting that in their report, GATA6-AS1 was located in the nucleus and participated in the regulation of GC at the transcriptional level. However, it was unclear whether GATA6-AS1 regulates the progression of GC via acting as a competing endogenous RNA (ceRNA) at the posttranscription level.

In recent years, ceRNA mechanism has been one of the most popular regulation mechanisms concerning lncRNA,

and ceRNA is a new type of gene expression regulation mode [14]. Previous reports have indicated that lncRNA could sponge microRNA (miRNA) to regulate the expression of messenger RNA (mRNA) as a ceRNA, so as to take part in the progression of cancers [15]. For example, XLOC_006390 could promote cervical tumorigenesis by serving as a ceRNA to target miR-331-3p and miR-338-3p [16]. FAL1 was proved to accelerate the proliferative and migratory capacities of hepatocellular carcinoma cells *in vitro* through ceRNA mode with miR-1236 [17].

(a)

(b)

Figure 2: Continued.

(c)

(d)

Figure 2: Continued.

(e)

(f)   (g)   (h)
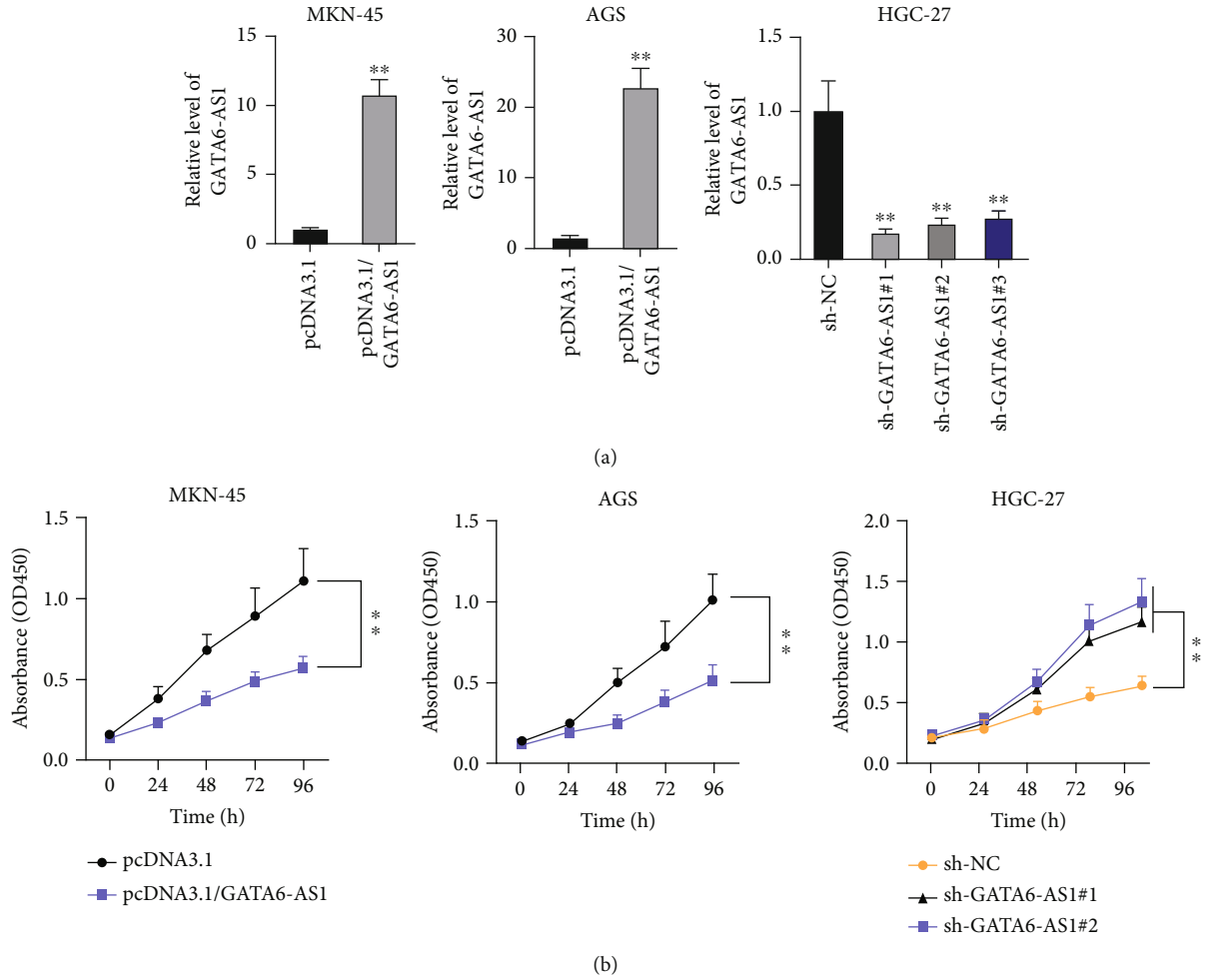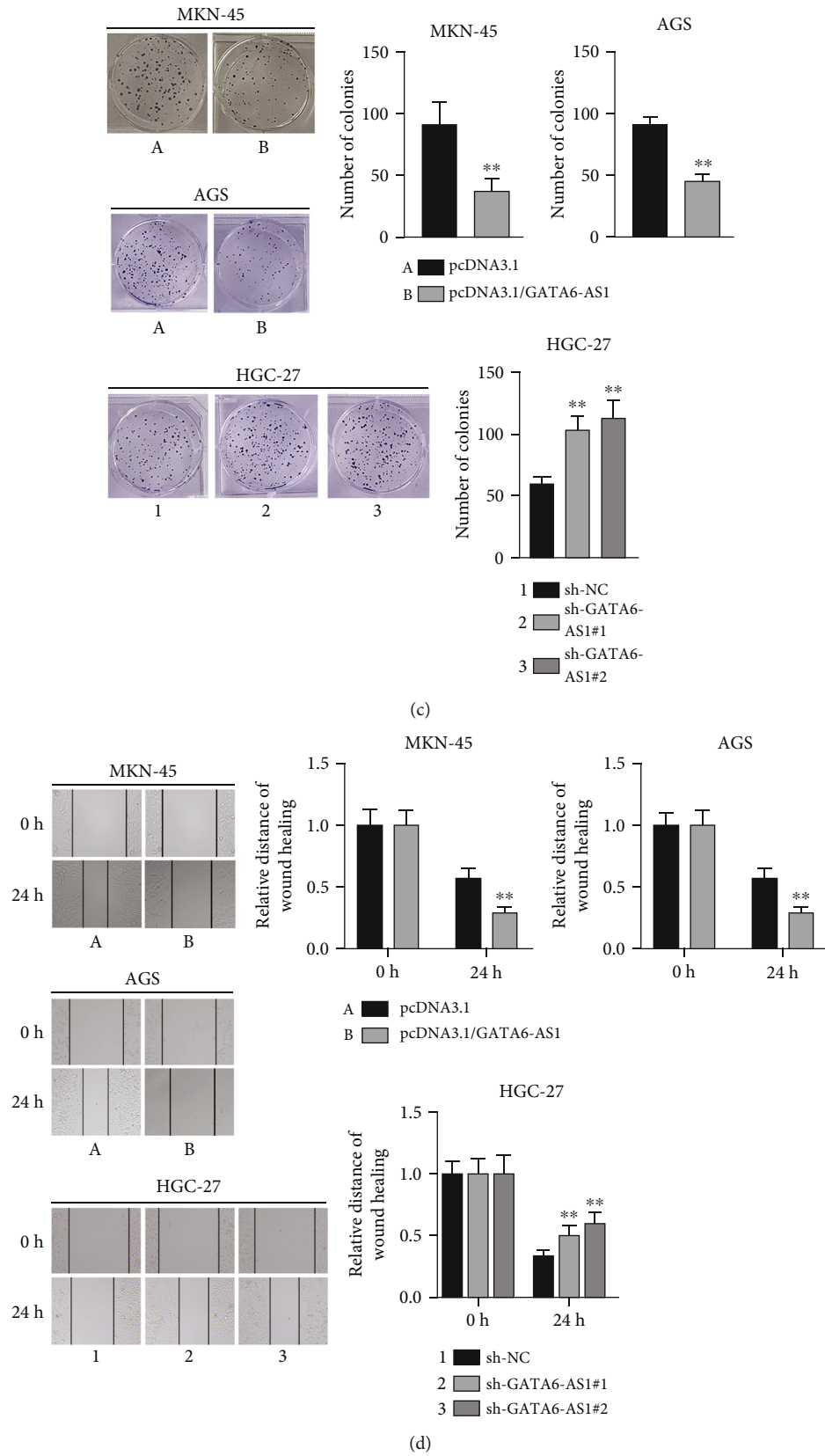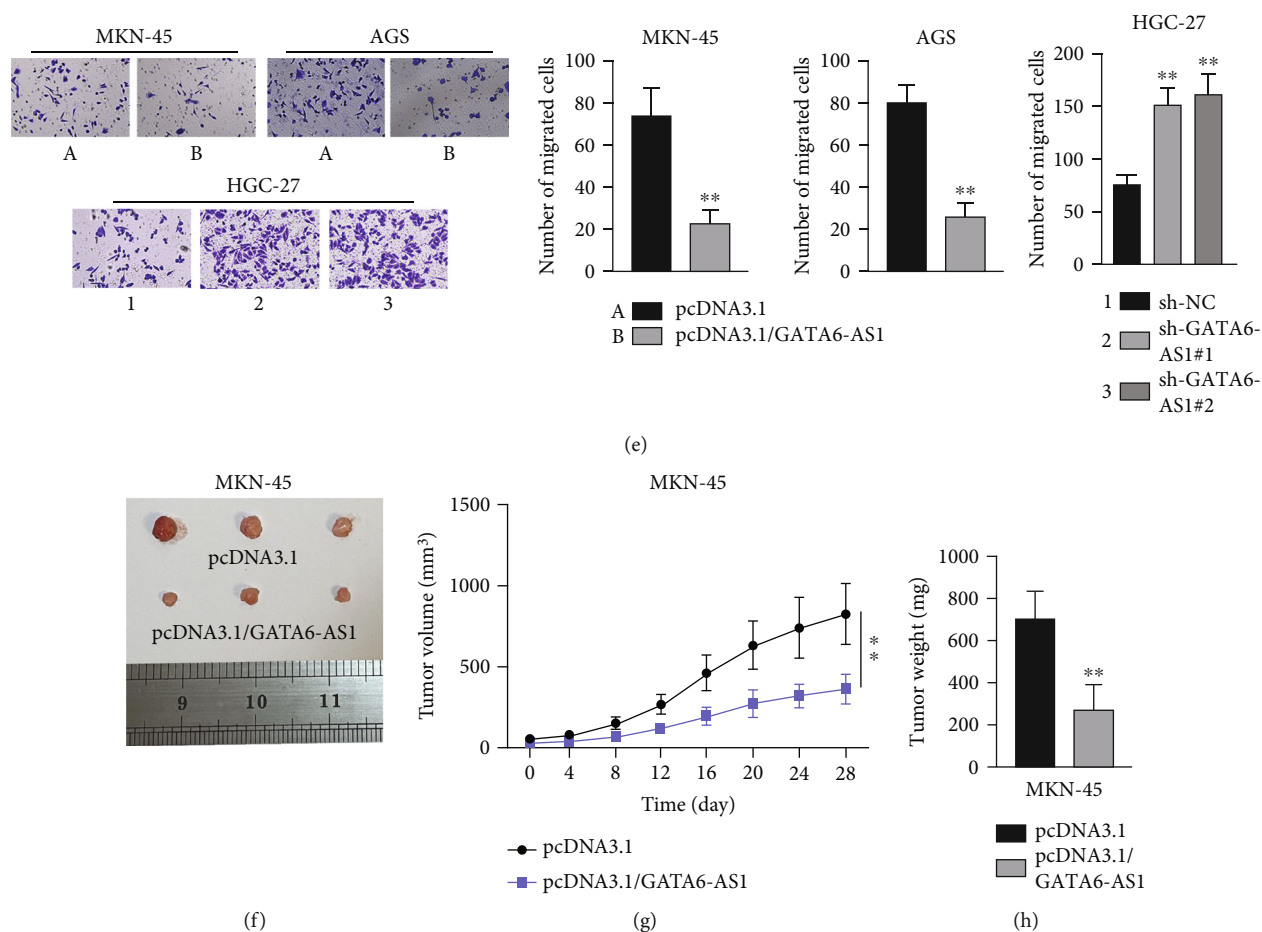
FIGURE 2: GATA6-AS1 represses cell proliferation and migration in GC. (a) QRT-PCR was used to analyze the overexpression efficiency of pcDNA3.1/GATA6-AS1 in transfected MKN-45 and AGS cells and interference efficiency of sh-GATA6-AS1#1/#2/#3 in transfected HGC-27 cells. (b) CCK-8 assays were applied to access the cell viability when GATA6-AS1 was overexpressed or inhibited in GC cells. (c) Colony formation assays were performed to assess cell proliferation when GATA6-AS1 was upregulated or silenced in GC cells. (d) The migration ability of GC cells was assessed by wound healing assays in the indicated cells. (e) Transwell assays were further conducted to evaluate cell migration after the overexpression or deficiency of GATA6-AS1 in GC cells. (f–h) Representative image, tumor growth curve, and tumor weight at the end points of xenografted tumors formed by subcutaneous injection of MKN-45 cells stably transfected with pcDNA3.1 or pcDNA3.1/GATA6-AS1 into nude mice. The number of nude mice used in each group is 3. Student's t-test for overexpression studies and one-way ANOVA and Dunnett's test for knockdown studies. $^{**}P < 0.01$.

In this study, we intended to explore whether GATA6-AS1 affects GC progression in terms of ceRNA regulatory mode.

2. Materials and Methods

2.1. Cell Lines and Reagent. Human gastric mucosa cell line (GES-1) used in this study was procured from BeNa Culture Collection (Beijing, China). Human GC cell lines (HGC-27, AGS) were bought from Cell Bank of the Chinese Academy of Sciences (Shanghai, China); both MKN-7 and MKN-45 cell lines were obtained from Procell Life Science & Technology Co., Ltd. (Wuhan, China). RPMI-1640 commercially acquired from Thermo Fisher Scientific (Waltham, MA) was used to culture GES-1, HGC-27, MKN-7, and MKN-45 cells under 37°C and 5% CO_2. AGS cells were cultivated in F12K medium (Gibco). In addition, 10% fetal bovine serum (FBS; Gibco) and 1% penicillin-streptomycin (Gibco)

both served as medium supplements. SF1670 ($1\,\mu$M), an inhibitor of PTEN (phosphatase and tensin homolog), was purchased from MedChemExpress (South Brunswick, NJ).

2.2. Total RNA Isolation and Quantitative Real-Time Polymerase Chain Reaction (qRT-PCR). TRIzol reagent purchased from Invitrogen (Carlsbad, CA) was used to isolate total RNAs from the cultured cells. Reverse transcription of RNA into cDNA was conducted via the implementation of PrimeScript™ RT reagent kit (Takara, Shiga, Japan) as per the instructions of manufacturer. Power SYBR® Green Master Mix bought from Applied Biosystems (Carlsbad, CA) was then employed for PCR on the StepOne™ Real-Time PCR System from Applied Biosystems. Relative gene expression was calculated by $2^{-\Delta\Delta Ct}$ method. GAPDH or U6 was used as the internal reference. Each experiment was undertaken in triplicate, with three technical replicates for each biorepeat.

(a)

(b)

(c)

FIGURE 3: Continued.

(d)

(e)

GATA6-AS1-WT: 5'-CCTAACGAGGGAATGGGTAGTGAATGTTG-3'

miR-543: 3'-TTCTTCACGTGGCGCTTACAAA-5'

GATA6-AS1-Mut: 5'-CCTAACGTGCGTAACGGTACTCTTACAAG-3'

(f)

(g)

FIGURE 3: Continued.

(h)

(i)
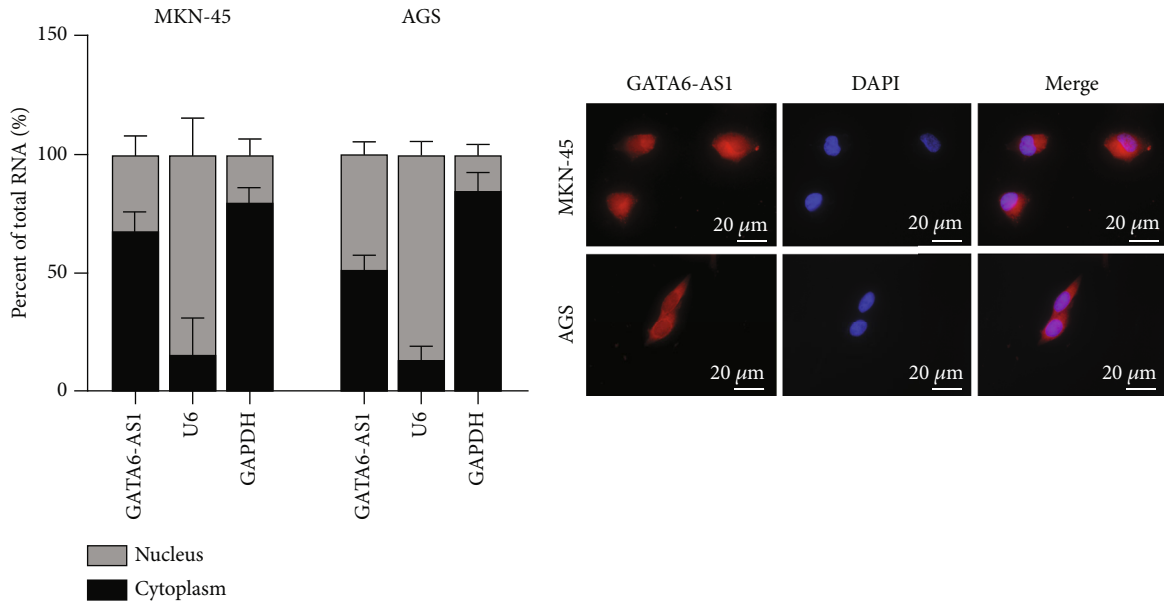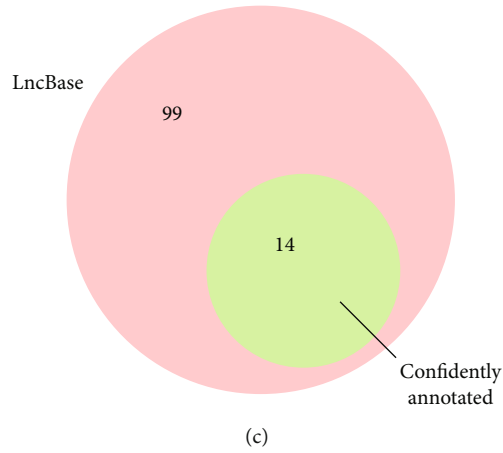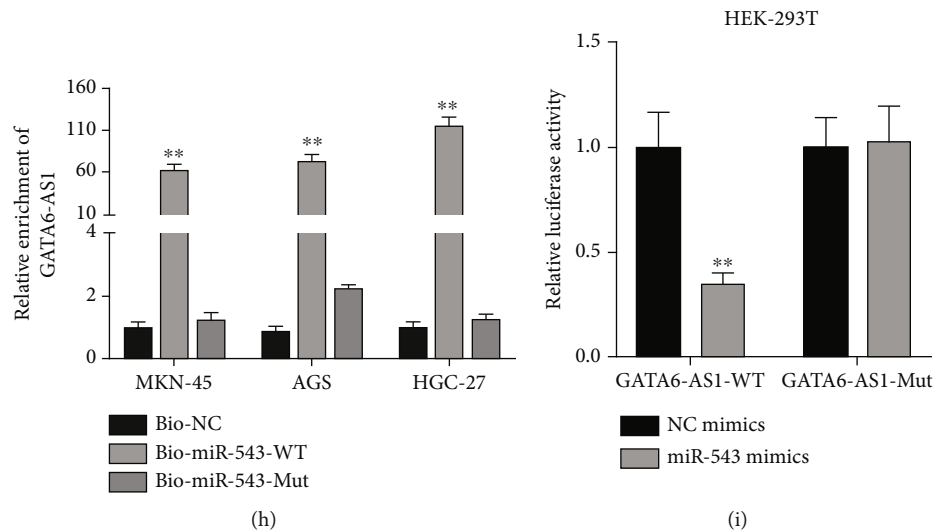
FIGURE 3: GATA6-AS1 binds to miR-543 in GC cells. (a, b) Cytoplasmic/nuclear fractionation and FISH assays were performed to detect the subcellular distribution of GATA6-AS1 in MKN-45 and AGS cells. U6 and GAPDH were used as control. Scale bar = 20 μm. (c) LncBase database was used to screen out 14 putative target miRNAs which possibly bind to GATA6-AS1 and are confidently annotated. (d) The levels of 14 candidate miRNAs in GATA6-AS1-knockdown HGC-27 cells were detected by qRT-PCR. (e) miR-543 level in GATA6-AS1-overexpression MKN-45 and AGS cells was detected via qRT-PCR. (f) The starBase predicted the potential binding site between GATA6-AS1 and miR-543. The sequence of GATA6-AS1 was mutated based on the miR-543 binding site to obtain the GATA6-AS1-Mut plasmid. (g) The enrichment of GATA6-AS1 and miR-543 in anti-Ago2 bound complex was detected by RIP assays. (h) RNA pull-down assays followed by qRT-PCR analysis were carried out to detect the expression of GATA6-AS1 in the complexes pulled down by wild-type biotinylated miR-543 (Bio-miR-543-WT) or mutant biotinylated miR-543 (Bio-miR-543-Mut). (i) Luciferase reporter assays were conducted to further verify the interaction of GATA6-AS1 and miR-543. Luciferase activity of reporter vector containing wild-type GATA6-AS1 (GATA6-AS1-WT) or mutant type (GATA6-AS1-Mut) was detected post cotransfection with miR-543 mimics or NC mimics into HEK-293T cells. Student's t-test was used in (d), (e), (g), and (i) and one-way ANOVA and Dunnett's test for (h). $^*P < 0.05$ and $^{**}P < 0.01$.

2.3. Plasmid Transfection.

The pcDNA3.1/GATA6-AS1 and negative control pcDNA3.1 were available from Gene-Pharma (Shanghai, China) for 48 h transfection into GC cell samples using Lipofectamine 3000 (Invitrogen). For the sake of silencing GATA6-AS1 and PTEN, the short hairpin RNAs (shRNAs) and negative controls of shRNAs (sh-NCs) were also specifically designed by and purchased from Gene-Pharma. In addition, microRNA-543 (miR-543) mimics were transfected into GC cells to overexpress miR-543, while miR-543 inhibitors for silencing miR-543. In this study, miR-543 mimics, miR-543 inhibitors, and corresponding negative controls (NC mimics/NC inhibitors) were purchased from RiboBio (Guangzhou, China) for plasmid transfection.

2.4. Cell Counting Kit-8 (CCK-8).

Transfected GC cells were harvested and seeded into 96-well plates. A total of 10 μL CCK-8 (Dojindo Laboratories, Kumamoto, Japan) was then added into each well of the plates for 1 h under culture condition. The absorbance at 450 nm was monitored with a microplate reader. Independent experiment was done in triplicate, with three technical replicates for each biorepeat.

2.5. Colony Formation.

MKN-45, AGS, and HGC-27 cells were collected at log phase of growth post transfection and subsequently seeded into 6-well plates at a density of 500 cells each well. After 14-day incubation, cells were fixed with 4% paraformaldehyde and then dyed by 0.1% crystal violet.

Finally, the colonies in three separately conducted assays were manually counted. Independent experiments were performed in triplicate. Three technical replicates were performed for each biorepeat.

2.6. Wound Healing.

The processed cell samples were cultured in 96-well plates with culture medium with no serum. After reaching the required confluence, the samples were scratched by pipette tips and photographed immediately (0 h). With the rinse in phosphate-buffered saline (PBS), the wounds were observed 24 h later and photographed by microscopy (Olympus, Tokyo, Japan). Each experiment was carried out in triplicate, with three technical replicates for each biorepeat.

2.7. Transwell Migration Assay.

Totally, 1×10^5 transfected cell samples were inoculated into the upper part of transwell chamber (Corning, NY). Serum-free medium was added to cultivate the cells in the upper chamber. The complete medium was added to the lower chamber. Prior to 24-hour incubation at 37°C, the migrated cells to the lower chamber were fixed and dyed by 0.5% crystal violet. Inverted microscope (Olympus) was employed to count the stained cells in 5 random fields. Separate experiment was undertaken in triplicate, with three technical replicates for each biorepeat.

2.8. RNA Pull-Down Assay.

For RNA pull-down assay, specific miR-543 probe was synthesized and biotinylated,

(a)

(b)

(c)

(d)
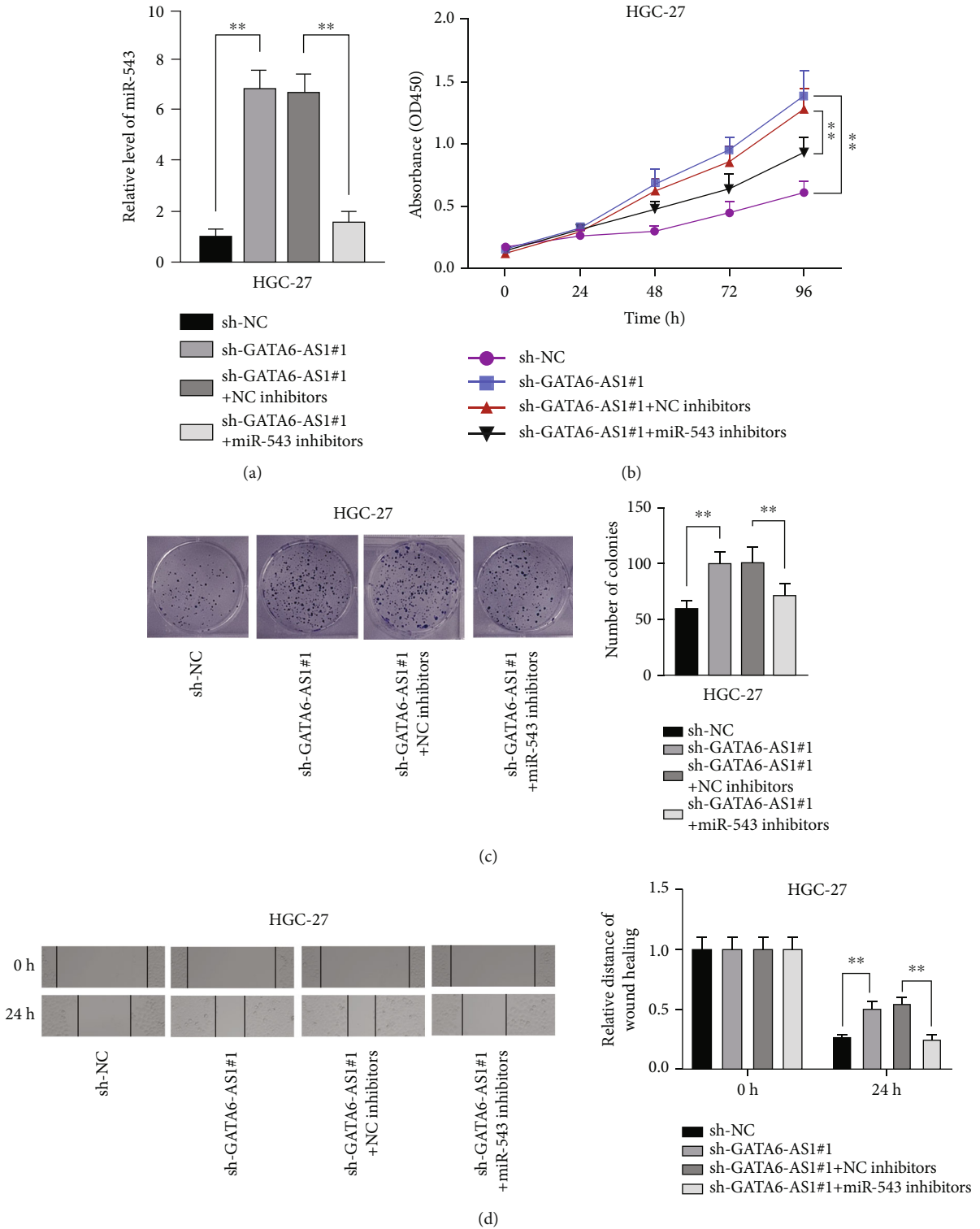
Figure 4: Continued.
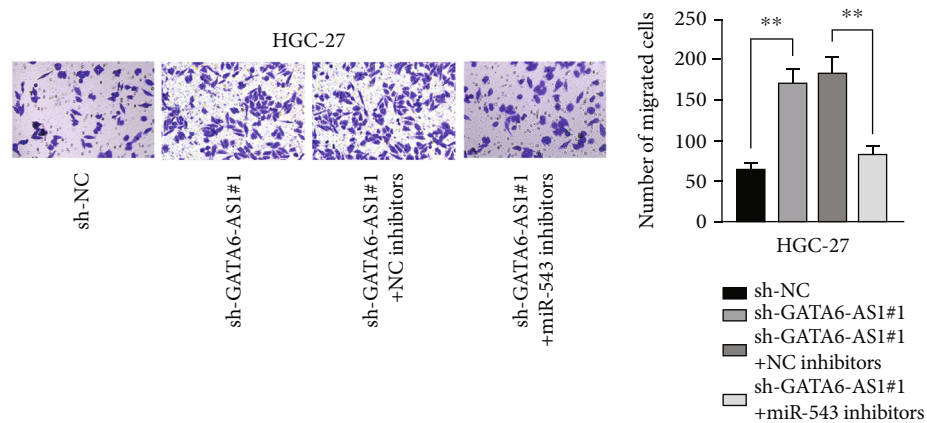
(e)

Figure 4: GATA6-AS1 represses cell growth and migration by regulating miR-543 in GC. (a) QRT-PCR was applied to estimate miR-543 level in HGC-27 cells transfected with sh-GATA6-AS1#1 and miR-543 inhibitors. (b) GC cell proliferation was estimated by CCK-8 assays when GATA6-AS1 and miR-543 were silenced. (c) Colony formation assays measured cell proliferation when GATA6-AS1 and miR-543 were knocked down. (d, e) The migratory capacity was assessed by wound healing and transwell assays when GATA6-AS1 and miR-543 were inhibited. One-way ANOVA and Dunnett's test. $^{**}P < 0.01$.

forming wild-type and mutant Bio-miR-543 probes (Bio-miR-543-WT/Mut). Bio-miR-543-WT/Mut probes were then incubated with the protein extracts from GC cells along with magnetic beads. Subsequent to RNA isolation, the purified RNA from the collected pull-down complex was assayed using qRT-PCR to detect relative RNA enrichment. Each experiment was undertaken in triplicate, with three technical replicates for each biorepeat.

2.9. RNA-Binding Protein Immunoprecipitation (RIP). RNA interaction was examined by RIP assay in GC cells using Magna RIP™ RNA-Binding Protein Immunoprecipitation Kit (Millipore, Billerica, MA) in line with the supplier's suggestions. Subsequent to the lysis in RIP lysis buffer, cell lysates were treated with human Argonaute2 (Ago2) antibody (anti-Ago2, 1/1,000–1/2,000, ab186733; Abcam, Cambridge, MA) or control immunoglobulin G antibody (anti-IgG, 1/1,000–1/10,000, ab133470; Abcam). Followed by the addition of magnetic beads, qRT-PCR was performed after RNA purification and RNA extraction. Each experiment was undertaken three times, with three technical replicates for each biorepeat.

2.10. Western Blot. Cell protein samples extracted from cultured cells were prepared for the electrophoresis separation using 12% sodium dodecyl sulphate-polyacrylamide gel electrophoresis (SDS-PAGE). Subsequently, the samples were shifted onto polyvinylidene fluoride (PVDF) membranes. The diluted primary antibodies against PTEN (1 : 10,000, ab32199; Abcam) and loading control GAPDH (1 : 1,000, ab8245; Abcam) were incubated with the blocked membranes overnight at 4°C. After washing in tris-buffered saline-tween (TBST), the membranes were subjected to incubation with the secondary antibodies tagged with horseradish peroxidase (1 : 5,000, ab7090; Abcam). ECL luminous liquid bought from Pierce (Rockford, IL) was applied for the detection of proteins on western blots. Each experiment was

undertaken in triplicate, with three technical replicates for each biorepeat.

2.11. Subcellular Fractionation Assay. The subcellular fractionation assay was performed with the application of PARIS™ kit acquired from Ambion (Austin, TX) following the guidebook. AGS and MKN-45 cells (1×10^6 cells) were harvested and placed on ice after PBS washing. The precooled cell fractionation buffer was added to cell samples for 10 min incubation. Following centrifugation for 5 min, cytoplasmic and nuclear fractions were separated. GATA6-AS1 expression was detected by qRT-PCR analysis. Each experiment was undertaken in triplicate, with three technical replicates for each biorepeat.

2.12. Fluorescence In Situ Hybridization (FISH). The specific probe for GATA6-AS1 was designed and synthesized by RiboBio for FISH assay. GC cells were fixed for 20 min, followed by the treatment with protease K for 10 min. After being washed in PBS, the probe and hybridization buffer were added to cell samples overnight at 42°C. The fluorescence detection was undertaken with Olympus fluorescence microscope. Each experiment was undertaken in triplicate, with three technical replicates for each biorepeat.

2.13. Luciferase Reporter Assay. The wild-type and mutant GATA6-AS1 or PTEN-3′ untranslated region (3′-UTR) fragments containing the potential sites for the binding of miR-543 were acquired and inserted into luciferase vector pmirGLO, establishing luciferase reporter vectors including GATA6-AS1-WT/Mut and PTEN-3′-UTR-WT/Mut. The acquired constructs were then cotransfected into HEK-293T cells (ATCC, Manassas, VA) with indicated plasmids for 48 h. At length, Luciferase Reporter Assay System (Promega, Madison, WI) was employed for examining the luciferase intensity as instructed. Each experiment was

(a)

(b)

(c)

(d)

(e)
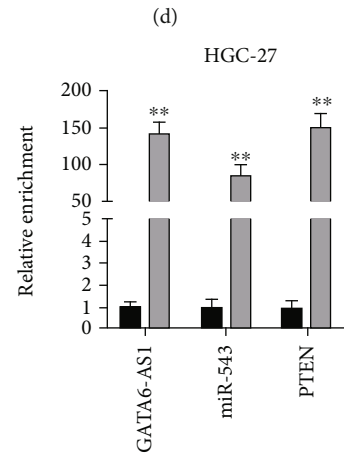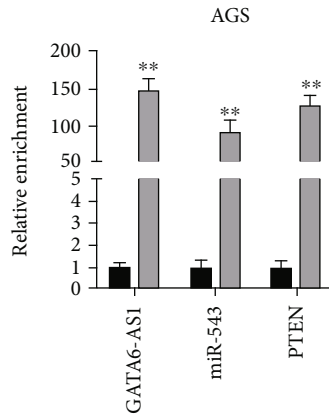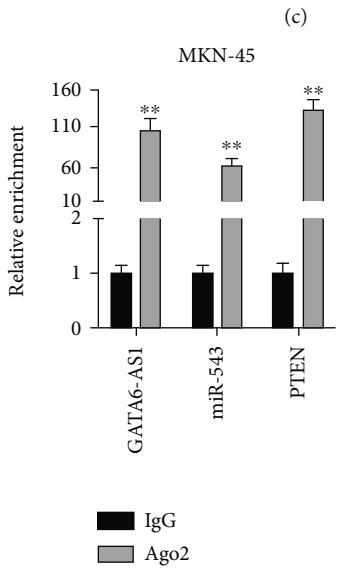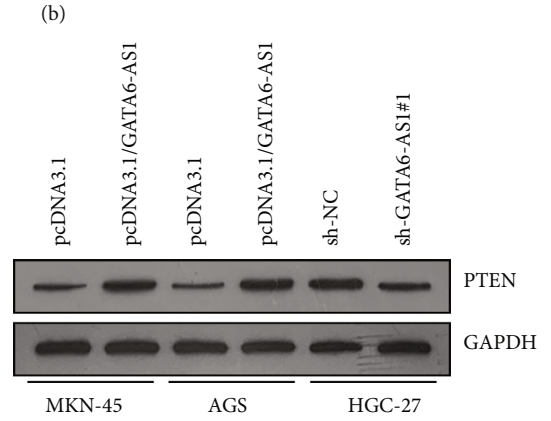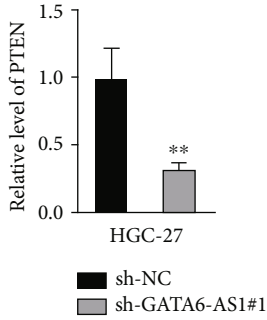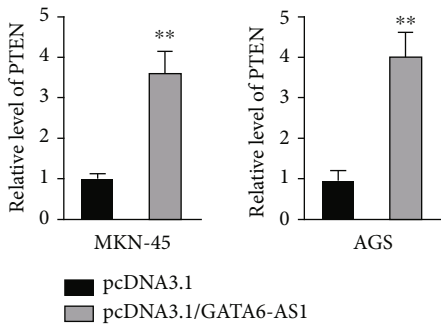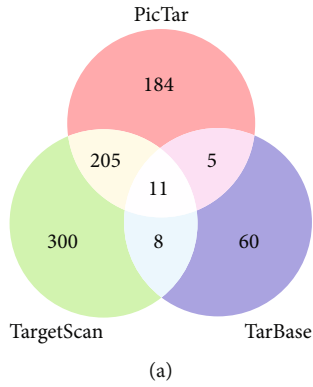
FIGURE 5: Continued.

(f)

(g)
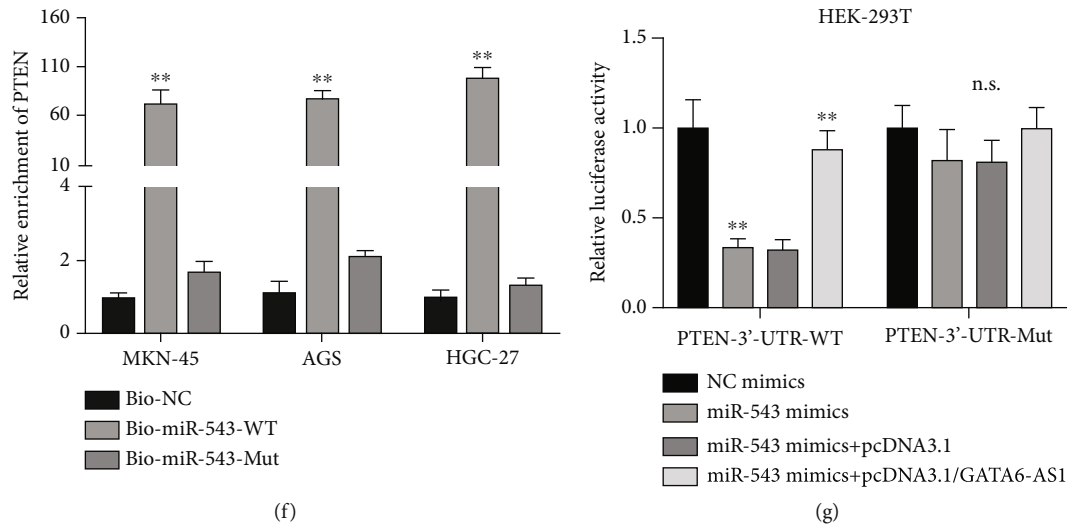
Figure 5: PTEN is the target gene of miR-543 in GC cells. (a) Venn diagram represented the overlap of miR-543 targets based on three algorithms (PicTar, TargetScan, and TarBase). 11 predicted miR-543 targets are TWIST1, DYNC1LI2, PTEN, HERPUD1, FNDC3B, FOXP1, ANKRD13C, BTBD3, CDH11, ZNF281, and COPS2. (b) The starBase was utilized to predict the potential binding site between miR-543 and PTEN-3′-UTR. The sequence of PTEN-3′-UTR-WT containing miR-543-binding site was mutated to obtain PTEN-3′-UTR-Mut plasmid. (c) The level of PTEN in the indicated GC cells after the upregulation or depletion of GATA6-AS1 was assessed via qRT-PCR. (d) Western blot analysis was utilized to measure the protein level of PTEN in the transfected cells after the overexpression and downregulation of GATA6-AS1. (e) RIP assays were conducted to analyze the association of GATA6-AS1, miR-543, and PTEN in GC cells. (f) RNA pull-down assays verified the binding between miR-543 and PTEN. (g) Luciferase activity of PTEN-3′-UTR was detected. Student's t-test was used in (c)–(e) and one-way ANOVA followed by Dunnett's test for (f) and (g). $**P < 0.01$. n.s.: no significance.

undertaken in triplicate, with three technical replicates for each biorepeat.

2.14. In Vivo Experiments. A total of 15 BALB/c nude mice (6 weeks old, male) purchased from Model Animal Research Center of Nanjing University were prepared for the animal experiments. Animal study was approved by the Institutional Animal Care and Use Committee of Cancer Hospital of China Medical University. GATA6-AS1-overexpressed or GATA6-AS1-overexpressed+PTEN-silenced MKN-45 cells were used to treat nude mice with subcutaneous injection. The mice treated with pcDNA3.1-transfected cells were used as negative controls. The volume of tumors was examined every 4 days. Four weeks post subcutaneous injection, the nude mice were sacrificed, and the xenografted tumors were resected for the measurement.

2.15. Statistical Analysis. Each assay in the study was biorepeated in triplicate. The experimental data were expressed as the mean ± standard deviation (S.D.) and processed by Prism 6 (GraphPad, San Diego, CA). The P value below 0.05 was defined as significant difference for the statistical analyses. Student's t-test or analysis of variance (one-way/two-way ANOVA) was used for comparing differences between groups.

3. Results

3.1. GATA6-AS1 Is Lowly Expressed in GC Tissues and Cell Lines. To detect the biological function of GATA6-AS1 in

GC, we analyzed GATA6-AS1 expression in normal tissues and tumor tissues through UCSC and TCGA databases. UCSC database (http://genome.ucsc.edu/) showed that GATA6-AS1 expression was the highest in the normal stomach tissues compared with the other normal tissues (Figure 1(a)). In addition, TCGA database (http://gepia2.cancer-pku.cn/#index) displayed that GATA6-AS1 was significantly underexpressed in stomach adenocarcinoma (STAD) tissues compared with that in normal tissues (Figure 1(b)). Besides, qRT-PCR was applied to measure the GATA6-AS1 expression in GC cell lines (HGC-27, MKN-7, MKN-45, and AGS) relative to normal cell line. The results elucidated that the GATA6-AS1 was expressed at low level in GC cell lines versus that in GES-1 (Figure 1(c)). We also found that GATA6-AS1 expression was relatively higher in HGC-27 cell line but relatively lower in AGS and MKN-45 cell lines, so we chose these three cells for subsequent experiments. Taken together, GATA6-AS1 is underexpressed in GC tissues and cell lines.

3.2. GATA6-AS1 Represses Cell Proliferation and Migration in GC and Suppresses In Vivo Tumorigenesis. Next, we knocked down GATA6-AS1 in HGC-27 cells and overexpressed GATA6-AS1 in MKN-45 and AGS cells. After the transfection of pcDNA3.1/GATA6-AS1 into or the transfection of sh-GATA6-AS1#1/#2/#3 into GC cells, qRT-PCR analysis was applied to test the overexpression efficiency of pcDNA3.1/GATA6-AS1 or silencing efficiency of sh-GATA6-AS1#1/2/3. The results demonstrated that GATA6-AS1 expression was efficiently increased by

(a)

(b)

(c)
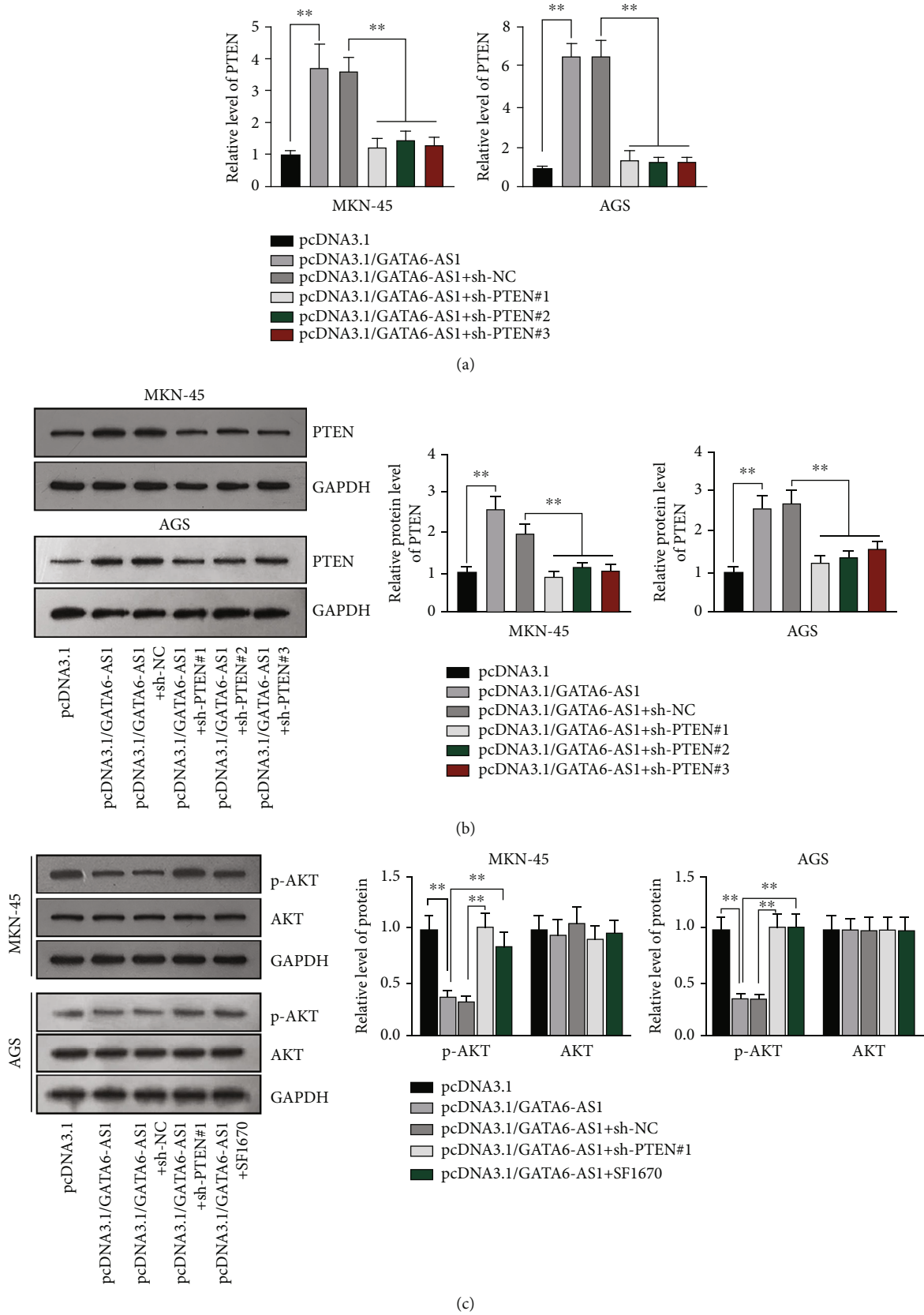
Figure 6: Continued.

(d)

(e)

(f)

Figure 6: Continued.

(g)
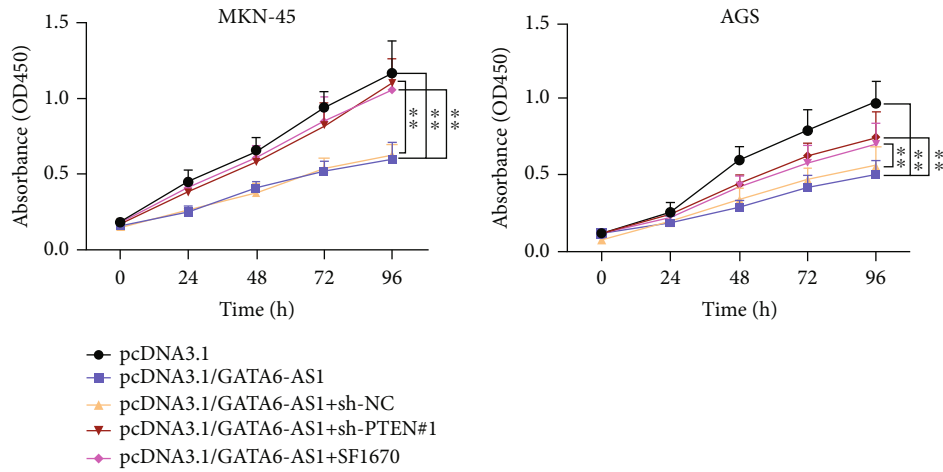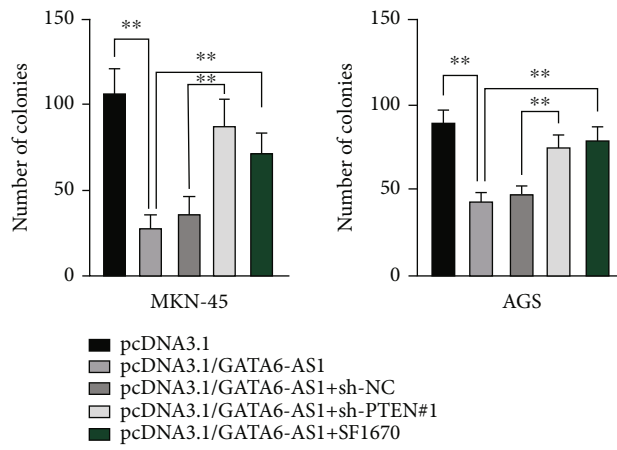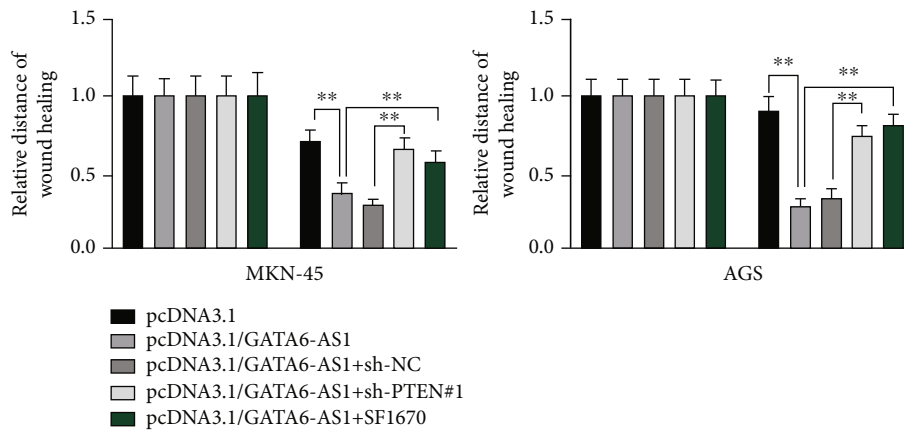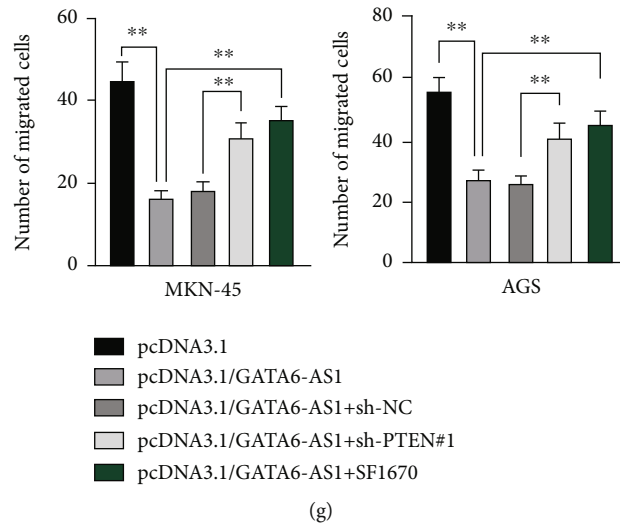
FIGURE 6: GATA6-AS1 suppresses the progression of GC by regulating PTEN/AKT signaling axis. (a) QRT-PCR was implemented to detect PTEN level in GC cells transfected with pcDNA3.1/GATA6-AS1 and sh-PTEN#1/#2/#3. (b) Western blot was applied to evaluate the protein level of PTEN in GC cells after the transfection with pcDNA3.1/GATA6-AS1 and sh-PTEN#1/#2/#3 (left panels). Quantification of western blot results was shown in the bar graphs (right panels). (c) Western blot was applied to detect the protein level of AKT and phosphorylated AKT (p-AKT) in the transfected cells with overexpressed GATA6-AS1 and inhibited PTEN or added with SF1670 (left panels). Quantification of western blot results was shown in the bar graphs (right panels). (d) Cell viability of GC cells in different groups was assessed by CCK-8. (e) Cell proliferation in different groups was evaluated by colony formation assays. (f) Wound healing assays were conducted to assess the migratory capacity of GC cells in different groups. (g) The evaluation of cell migration in different groups through transwell assays was displayed. One-way ANOVA followed by Dunnett's test. $^{**}P < 0.01$.

pcDNA3.1/GATA6-AS1 in comparison with control (Figure 2(a), left panels). The level of GATA6-AS1 was obviously diminished by the transfection of sh-GATA6-AS1#1/#2/#3 into HGC-27 cells (Figure 2(a), right panel). Particularly, sh-GATA6-AS1#1 and sh-GATA6-AS1#2 presented a relatively higher knockdown efficiency (Figure 2(a), right panel). Subsequently, we chose pcDNA3.1/GATA6-AS1 and sh-GATA6-AS1#1/#2 for the following investigations.

For further study on the effects of GATA6-AS1 on the malignant progression of GC, we designed functional assays to assess the function of GATA6-AS1 in GC cells. With CCK-8 and colony formation assays examining the proliferation of GC cells, we discovered that the absorbance at 450 nm in GC cells was markedly declined after the transfection with pcDNA3.1/GATA6-AS1 in comparison with negative control (Figure 2(b), left panels), while that was significantly increased in the HGC-27 cells transfected with sh-GATA6-AS1#1 and sh-GATA6-AS1#2 compared with the sh-NC group (Figure 2(b), right panel), indicating that overexpressed GATA6-AS1 restrains cell viability while GATA6-AS1 depletion promotes that in GC. Besides, colony formation assay displayed that overexpression of GATA6-AS1 reduced the number of colonies but knockdown of GATA6-AS1 increased that, which indicated that upregulation of GATA6-AS1 hampers GC cell proliferation (Figure 2(c), upper panels) but downregulation of GATA6-AS1 enhances that (Figure 2(c), lower panels). In addition, wound healing and transwell assays were implemented to assess the capacity of GC cells to migrate. The results of wound healing assays presented that the relative distance of wound healing at 24 h in the pcDNA3.1/GATA6-AS1

group was evidently narrower versus the control group (Figure 2(d), upper panels), while that in the sh-GATA6-AS1#1/#2 groups at 24 h was wider versus the control group (Figure 2(d), lower panels), indicating that GATA6-AS1 overexpression inhibits cell migration while GATA6-AS1 knockdown propels that. The results of transwell assay also verified this finding as overexpression of GATA6-AS1 effectively decreased the number of migrated cells (Figure 2(e), upper left panels and middle panels) while knockdown of GATA6-AS1 increased the number of migrated cells (Figure 2(e), lower left panels and right panel). Consistently, the injection of pcDNA3.1/GATA6-AS1 transfected cells resulted in a marked decrease in the growth of xenografted tumors (Figures 2(f)–2(h)).

Overall, GATA6-AS1 represses the abilities of GC cells to proliferate and migrate *in vitro* and suppresses *in vivo* tumorigenesis.

3.3. GATA6-AS1 Binds to miR-543 in GC Cells. Next, we investigated the regulatory mechanism of GATA6-AS1 in GC. Previous studies have reported that lncRNAs participate in the biological processes via regulating downstream target genes [18] and some sponge miRNAs to regulate mRNA expression by acting as a ceRNA [14]. ceRNA network is a posttranscriptional regulatory mechanism concerning cytoplasmic lncRNA [19]. Thus, we firstly detected the subcellular localization of GATA6-AS1 in GC cells. Through subcellular fractionation assays, we discovered that GATA6-AS1 is localized in both cytoplasm and nucleus of GC cells (Figure 3(a)). FISH assay also detected GATA6-AS1 fluorescence (red) in both nucleus and cytoplasm

(Figure 3(b)). Given that, we hypothesized that GATA6-AS1 might regulate the development of GC at the transcriptional and posttranscriptional levels. Considering that the transcriptional regulation of GATA6-AS1 in GC has been uncovered [13], we decided to explore its posttranscriptional regulation mechanism in terms of ceRNA network. As Figure 3(c) presented, ninety-nine downstream miRNAs of GATA6-AS1 were screened out on the LncBase database via DIANA (http://carolina.imis.athena-innovation.gr/diana_tools/web/index.php?r=lncbasev2%2Findex-predicted). Notably, fourteen miRNAs have been confidently annotated and have been studied by other researchers before. To further determine the most suitable target miRNA of GATA6-AS1 in GC cells, qRT-PCR was applied to test the levels of candidate miRNAs in the HGC-27 cells transfected with sh-GATA6-AS1#1. The results revealed that the level of miR-543 was the most upregulated among candidate miRNAs (Figure 3(d)). Thus, we selected miR-543 as a potential target of GATA6-AS1 for the follow-up exploration. To further determine the association between GATA6-AS1 and miR-543, we detected miR-543 level in GATA6-AS1-overexpression GC cells via qRT-PCR analysis. It showcased that the level of miR-543 was downregulated in GATA6-AS1-overexpression GC cells (Figure 3(e)), indicating that GATA6-AS1 negatively regulates miR-543 expression. Further, we performed mechanism investigation to verify whether GATA6-AS1 binds to miR-543 in GC cells. As Figure 3(f) presented, the starBase database (https://starbase.gene.com/) predicted the potential binding sites between GATA6-AS1 and miR-543. The results of RIP displayed that GATA6-AS1 and miR-543 were both overtly enriched in the Anti-Ago2 groups versus that in Anti-IgG controls in GC cells (Figure 3(g)), indicating the existence of GATA6-AS1 and miR-543 in RNA-induced silencing complex (RISC) as Ago2 is the main component of RISC. Additionally, RNA pull-down assay further uncovered that GATA6-AS1 was highly enriched in the Bio-miR-543-WT groups while GATA6-AS1 had no marked abundance in the Bio-miR-543-Mut groups relative to controls (Figure 3(h)), indicating that GATA6-AS1 binds to miR-543 in GC cells. Moreover, the luciferase reporter assays further verified this finding as overexpression of miR-543 led to a remarkable decline of luciferase activity in the GATA6-AS1-WT groups compared to the NC mimics groups, while no marked changes were found in the GATA6-AS1-Mut groups (Figure 3(i)). All in all, GATA6-AS1 binds to miR-543 in GC cells.

3.4. GATA6-AS1 Represses Cell Growth and Migration by Regulating miR-543 in GC. To further study the effect of GATA6-AS1-miR-543 interaction on GC cell behaviors, we performed several relevant functional assays along with rescue experiments. Before that, we applied qRT-PCR to detect the level of miR-543 in HGC-27 cells transfected with sh-NC, sh-GATA6-AS1#1, sh-GATA6-AS1#1+NC inhibitors, or sh-GATA6-AS1#1+miR-543 inhibitors. The results showed that miR-543 level was conspicuously upregulated in GATA6-AS1-knockdown HGC-27 cells and dramatically decreased by the additional transfection of miR-543 inhibi-

tors (Figure 4(a)). CCK-8 assays revealed that the increase in cell viability caused by GATA6-AS1 deficiency could be fully reversed by cotransfection with miR-543 inhibitors (Figure 4(b)), indicating that miR-543 reversed the increase in cell viability induced by GATA6-AS1 knockdown and miR-543 silencing represses cell viability in GC cells. Likewise, the number of colonies was increased by GATA6-AS1 depletion but reduced by miR-543 silencing (Figure 4(c)), which indicated that cell proliferation was enhanced by inhibited GATA6-AS1 but reversed by silenced miR-543. Furthermore, via wound healing assay, we discovered that the relative distance of wound healing was increased in the sh-GATA6-AS1#1 groups compared to control and then altered by the inhibition of miR-543 (Figure 4(d)), indicating that miR-543 inhibition reverses the promoting effect of silenced GATA6-AS1 on the migratory ability of GC cells. Besides, transwell assay also indicated that downregulation of miR-543 could offset the promoting function of inhibited GATA6-AS1 on cell migration (Figure 4(e)). On the whole, GATA6-AS1 represses the capacities of GC cell to proliferate and migrate via modulating miR-543.

3.5. PTEN Is the Target Gene of miR-543 in GC Cells. To further probe into the regulatory mechanism of GATA6-AS1 in GC, we utilized bioinformatics to predict potential targets of miR-543. The putative mRNAs of miR-543 were obtained according to the combined prediction of PicTar, TargetScan, and TarBase databases (Figure 5(a)). Among 11 putative mRNAs, PTEN has been extensively reported to exert tumor-suppressive function in multiple cancers [20–22]. Thereby, PTEN was chosen for the follow-up investigations. Further, starBase was utilized to predict the potential binding sites, which suggested that miR-543 had the potential to bind to PTEN-3′-UTR (Figure 5(b)). In addition, we investigated the regulatory relationship between GATA6-AS1 and PTEN via qRT-PCR analysis of PTEN levels in GC cells after the overexpression or depletion of GATA6-AS1. The results showed that PTEN level was apparently enhanced by GATA6-AS1 overexpression in GC cells relative to controls (Figure 5(c), upper panel and left panel) but markedly declined by GATA6-AS1 deficiency (Figure 5(c), right panel), indicating that GATA6-AS1 positively regulates PTEN expression in GC cells. Western blot analysis also verified this finding as PTEN protein level was notably increased in GATA6-AS1-overexpression MKN-45 and AGS cells but reduced in GATA6-AS1-silence HGC-27 cells (Figure 5(d)). RIP assays were conducted to analyze the interaction among GATA6-AS1, miR-543, and PTEN in GC cells. It displayed that GATA6-AS1, miR-543, and PTEN were all significantly abundant in the Anti-Ago2 groups versus those in Anti-IgG controls (Figure 5(e)), suggesting that GATA6-AS1, miR-543, and PTEN coexist in Ago2-RISC. Then, RNA pull-down assays were conducted to further prove the interaction between miR-543 and PTEN. The results showed that PTEN was obviously enriched in the Bio-miR-543-WT groups while the Bio-miR-543-Mut groups had no significant abundance of PTEN compared with controls (Figure 5(f)), suggesting

that miR-543 could bind to PTEN in GC cells. Subsequently, luciferase reporter assay was employed to detect the interaction between GATA6-AS1, miR-543, and PTEN. The results showed the decline on the luciferase activity of PTEN-3′-UTR-WT by miR-543 mimics and then recovered by over-expressed GATA6-AS1 (Figure 5(g)). However, the PTEN-3′-UTR-Mut groups had no remarkable change (Figure 5(g)). Taken together, PTEN serves as a direct target of miR-543 in GC cells.

3.6. GATA6-AS1 Suppresses the Progression of GC by Regulating PTEN/AKT Signaling Axis. Finally, we assessed the effect of PTEN-GATA6-AS1 interaction in GC cells. Based on qRT-PCR results, PTEN expression was increased after the overexpression of GATA6-AS1 and downregulated after the knockdown of PTEN in GC cells (Figure 6(a)). Additionally, western blot also indicated that PTEN protein levels were elevated when GATA6-AS1 was overexpressed and declined after the additional transfection with sh-PTEN#1/#2/#3 (Figure 6(b)). Afterwards, western blot analyses were implemented to determine whether PTEN knockdown activates AKT function. The phosphorylated AKT (p-AKT) level was reduced after the overexpression of GATA6-AS1 but upregulated by the silence of PTEN or addition of SF1670 (Figure 6(c)). SF1670 was a specific PTEN inhibitor, which could also accelerate the phosphorylation of AKT indirectly. In this assay, we also discovered that the repressed phosphorylation of AKT was activated by SF1670 (Figure 6(c)). According to CCK8 assays, it was found that enhanced GATA6-AS1 suppressed cell viability, while silencing PTEN or adding SF1670 could recover cell viability in GC (Figure 6(d)). Then, colony formation assays showed that colonies were reduced by upregulated GATA6-AS1, but this was reversed by silenced PTEN or addition of SF1670, which indicated that cell proliferation could be restrained by GATA6-AS1 overexpression but reversed by the depletion of PTEN or addition of SF1670 (Figure 6(e)). Moreover, wound healing assays assessed cell migration in GC. The outcomes suggested that the relative distance of wound healing was decreased by GATA6-AS1 overexpression but then increased by PTEN depletion or addition of SF1670 (Figure 6(f)). Finally, transwell assays also verified that the decreased number of migrated cells caused by GATA6-AS1 upregulation could be offset by the ablation of PTEN or addition of SF1670 (Figure 6(g)). Taken together, GATA6-AS1 could suppress cell proliferation and migration in GC by regulating PTEN/AKT signaling axis.

3.7. GATA6-AS1 Represses In Vivo GC Tumorigenesis via Regulating PTEN. Besides *in vitro* assays, *in vivo* experiments were performed to verify this molecular mechanism. Xenograft mouse model was established by subcutaneous injection of GATA6-AS1-overexpressed or GATA6-AS1-overexpressed+PTEN-inhibited MKN-45 cells into nude mice, with those injected with pcDNA3.1 as controls. It was found that the volume and weight of xenografts were significantly reduced in the pcDNA3.1/GATA6-AS1 group versus the control group but cotransfection of sh-PTEN#1 altered the suppressive effect of GATA6-AS1 overexpression

on tumor growth (Figure S1A-C). Further, it was found that GATA6-AS1 positively regulates PTEN expression *in vivo* (Figure S1D-E). To conclude, GATA6-AS1 represses *in vivo* GC tumor growth via regulating PTEN.

4. Discussion

lncRNAs, associated with different types of cancers, regulate gene expression via modulating transcription and chromatin modification [23]. Besides the promoting effects, lncRNAs have the suppressive effects on cancer progression [24]. Previous studies have reported that upregulated GATA6-AS1 predicts poor prognosis of lung squamous cell carcinoma [11, 12]. GATA6-AS1 impedes the progression of non-small-cell lung cancer [1]. Moreover, GATA6-AS1 has been found to be lowly expressed in GC, and upregulated GATA6-AS1 has been elucidated to suppress the progression of GC by downregulating FZD4 expression to inactivate the Wnt/β-catenin signaling pathway [13]. With the induction of GATA6-AS1 depletion, miR-582 facilitated liver and lung metastasis of GC via downregulating FOXO3 expression and promoting the activity of PI3K/AKT/Snail pathway [25]. Apart from the regulation of cancer development, GATA6-AS1 also exerts function in normal tissues. For instance, GATA6-AS1 facilitates human endoderm differentiation through upregulating GATA6 expression by promoting SMAD2/3-mediated GATA6 transcriptional activation [26].

In the present study, we discovered that GATA6-AS1 expression was aberrantly underexpressed in GC cell lines. After the validation of GATA6-AS1 expression in GC, we silenced and overexpressed GATA6-AS1 in GC cells separately to evaluate its loss-of-function and gain-of-function effects on cell viability, proliferation, and migration in GC. Through functional assays, we discovered that overexpressed GATA6-AS1 restrained cell proliferation and migration. In contrast, knockdown of GATA6-AS1 has the promoting effects in the progression of GC. Thus, we confirmed that GATA6-AS1 acts as a tumor suppressor in GC. In normal tissues, this tumor suppressor gene might prevent GC by slowing or stopping cell growth.

Interestingly, GATA6-AS1 was proved to be located in the nucleus and exerted its regulatory function at the transcriptional level in GC [13]. In our study, we discovered that GATA6-AS1 was distributed in both nucleus and cytoplasm through subcellular fractionation and FISH assays. Thus, we speculated that GATA6-AS1 could regulate GC progression through the ceRNA network. In recent years, emerging researches have proven that ceRNA networks play critical roles in the regulation of various cancers [15, 27]. Also, lncRNAs have been confirmed to modulate cancers via acting as a ceRNA of miRNA and regulate mRNA expression at the posttranscriptional level [19].

As a kind of endogenous small noncoding RNA, miRNAs feature 19~26 nucleotides in length [28]. Increasing studies have indicated that lncRNAs combine with miRNAs to regulate cellular progression in cancers. Herein, our study, for the first time, verified and confirmed miR-543 as the target of GATA6-AS1 in GC.

As for miR-543, it has been extensively studied in a number of different human cancers previously. For example, miR-543 was proved to accelerate the proliferation and metastasis of colorectal cancer by targeting KLF4 [29]. Additionally, miR-543 targets RKIP to accelerate cell proliferation and EMT in prostate cancer [30]. Besides, miR-543 can motivate the proliferative and invasive abilities of non-small-cell lung cancer cells [31]. Remarkably, miR-543 has also been validated to promote gastric tumorigenesis [32, 33]. In our research, rescue assays demonstrated that GATA6-AS1 regulates GC cell proliferation and migration via miR-543. Accordingly, this study verified that miR-543 serves as an oncogene in GC.

Moreover, PTEN has been elucidated as the downstream target of miR-543 in multiple cancers, such as colorectal cancer [34, 35]. Herein, our study firstly identified PTEN as a target of miR-543 in GC. PTEN is a dual phosphatase featuring both protein and lipid phosphatase activities and is taken as a tumor suppressor [36]. PTEN exhibits its inhibitory effect on both heritable and sporadic cancers [22]. Besides, the mutation/depletion of PTEN was considered as a negative regulator of the AKT signaling pathway [37]. Also, it was reported that PTEN inhibits PTK6 oncogenic signaling in prostate cancer [38]. In addition, mammary carcinogenesis was confirmed to be associated with PTEN loss of activity rather than loss of expression [39]. Furthermore, some therapeutic strategies targeting PTEN-deficient cancers are under development [40]. In our study, the positive correlation between PTEN and GATA6-AS1 in GC was identified. According to the previous study, AKT signaling pathway is crucial in regulating GC [41, 42]. In our research, western blot indicated that phosphorylated AKT level was reduced by the overexpression of GATA6-AS1 but upregulated by the downregulation of PTEN or addition of SF1670 (PTEN inhibitor). In addition, rescue assays demonstrated that GATA6-AS1 regulates GC progression through the regulation of PTEN/AKT signaling pathway axis.

When it comes to the future research focus in the further studies, the upstream mechanism of GATA6-AS1 in GC will be investigated. For instance, the future investigation will be centered on potential mechanisms underlying the interaction between GATA6-AS1 and its transcription factors since the inactivation of GATA6-AS1 transcription might result in the downregulation of GATA6-AS1 in GC cells. For the downstream mechanism of GATA6-AS1 in GC, other increased miRNAs upon knockdown of GATA6-AS1 as shown in Figure 3(d), such as miR-525-5p, miR-3121-3p, and miR-4424, deserve to be studied to determine whether they are potential targets and how they exert their functions.

Taken together, the current study proved that GATA6-AS1 is lowly expressed in GC tissues and cell lines. More importantly, GATA6-AS1 can repress cell viability, proliferation, and migration in GC by sponging miR-543 and regulating the PTEN/AKT signaling axis. Thus, GATA6-AS1 can act as a potential target for GC treatment, which might provide novel insight into developing effective treatment strategies for patients with GC.

Data Availability

The data used to support the findings of this study are included within the article.

Conflicts of Interest

The authors declare that they have no competing interest.

Supplementary Materials

Figure S1: (A–C) representative image, tumor growth curve, and tumor weight at the end points of xenografted tumors formed by hypodermic injection of stably transfected GC cells into the nude mice. The number of nude mice used in each group is 3. (D) The expression of GATA6-AS1/miR-543/PTEN in xenografted tumor was displayed. (E) The protein expression of PTEN in xenografted tumor was shown. GAPDH was used as an internal reference. One-way ANOVA followed by Dunnett's test. **$P < 0.01$. n.s.: no significance. (*Supplementary Materials*)

References

[1] Y. J. Choi and N. Kim, "Gastric cancer and family history," *The Korean Journal of Internal Medicine*, vol. 31, no. 6, pp. 1042–1053, 2016.

[2] H. Yoon and N. Kim, "Diagnosis and management of high risk group for gastric cancer," *Gut and Liver*, vol. 9, no. 1, pp. 5–17, 2015.

[3] I. J. Choi, "Helicobacter pylori eradication therapy and gastric cancer prevention," *The Korean Journal of Gastroenterology*, vol. 72, no. 5, pp. 245–251, 2018.

[4] R. Geng and J. Li, "Apatinib for the treatment of gastric cancer," *Expert Opinion on Pharmacotherapy*, vol. 16, no. 1, pp. 117–122, 2015.

[5] S. Jathar, V. Kumar, J. Srivastava, and V. Tripathi, "Technological developments in lncRNA biology," *Advances in Experimental Medicine and Biology*, vol. 1008, pp. 283–323, 2017.

[6] A. Ahadi, "Functional roles of lncRNAs in the pathogenesis and progression of cancer," *Genes & Diseases*, vol. 8, no. 4, pp. 424–437, 2021.

[7] X. H. Liu, M. Sun, F. Q. Nie et al., "Lnc RNA HOTAIR functions as a competing endogenous RNA to regulate HER2 expression by sponging miR-331-3p in gastric cancer," *Molecular Cancer*, vol. 13, no. 1, p. 92, 2014.

[8] K. Lei, X. Liang, Y. Gao et al., "Lnc-ATB contributes to gastric cancer growth through a MiR-141-3p/TGFβ2 feedback loop," *Biochemical and Biophysical Research Communications*, vol. 484, no. 3, pp. 514–521, 2017.

[9] G. H. Wei and X. Wang, "lncRNA MEG3 inhibit proliferation and metastasis of gastric cancer via p53 signaling pathway," *European Review for Medical and Pharmacological Sciences*, vol. 21, no. 17, pp. 3850–3856, 2017.

[10] Z. Li, S. Hong, and Z. Liu, "LncRNA LINC00641 predicts prognosis and inhibits bladder cancer progression through miR-197-3p/KLF10/PTEN/PI3K/AKT cascade," *Biochemical and Biophysical Research Communications*, vol. 503, no. 3, pp. 1825–1829, 2018.

[11] Y. Xiong, X. Zhang, Z. Lin et al., "SFTA1P, LINC00968, GATA6-AS1, TBX5-AS1, and FEZF1-AS1 are crucial long

non-coding RNAs associated with the prognosis of lung squamous cell carcinoma," *Oncology Letters*, vol. 18, no. 4, pp. 3985–3993, 2019.

[12] W. J. Chen, R. X. Tang, R. Q. He et al., "Clinical roles of the aberrantly expressed lncRNAs in lung squamous cell carcinoma: a study based on RNA-sequencing and microarray data mining," *Oncotarget*, vol. 8, no. 37, pp. 61282–61304, 2017.

[13] Z.-T. Li, X. Zhang, D.-W. Wang et al., "Retracted: Overexpressed lncRNA GATA6-AS1 inhibits LNM and EMT via FZD4 through the Wnt/β-catenin signaling pathway in GC," *Molecular Therapy - Nucleic Acids*, vol. 19, pp. 827–840, 2019.

[14] Y. Tay, J. Rinn, and P. P. Pandolfi, "The multilayered complexity of ceRNA crosstalk and competition," *Nature*, vol. 505, no. 7483, pp. 344–352, 2014.

[15] X. Qi, D. H. Zhang, N. Wu, J. H. Xiao, X. Wang, and W. Ma, "ceRNA in cancer: possible functions and clinical implications," *Journal of Medical Genetics*, vol. 52, no. 10, pp. 710–718, 2015.

[16] X. Luan and Y. Wang, "LncRNA XLOC_006390 facilitates cervical cancer tumorigenesis and metastasis as a ceRNA against miR-331-3p and miR-338-3p," *Journal of Gynecologic Oncology*, vol. 29, no. 6, article e95, 2018.

[17] B. Li, R. Mao, C. Liu, W. Zhang, Y. Tang, and Z. Guo, "LncRNA FAL1 promotes cell proliferation and migration by acting as a CeRNA of miR-1236 in hepatocellular carcinoma cells," *Life Sciences*, vol. 197, pp. 122–129, 2018.

[18] M. D. Paraskevopoulou and A. G. Hatzigeorgiou, "Analyzing MiRNA-LncRNA interactions," *Methods in Molecular Biology*, vol. 1402, pp. 271–286, 2016.

[19] C. L. Smillie, T. Sirey, and C. P. Ponting, "Complexities of post-transcriptional regulation and the modeling of ceRNA crosstalk," *Critical Reviews in Biochemistry and Molecular Biology*, vol. 53, no. 3, pp. 231–245, 2018.

[20] Y. Qi, J. Liu, J. Chao et al., "PTEN suppresses epithelial-mesenchymal transition and cancer stem cell activity by downregulating Abi1," *Scientific Reports*, vol. 10, no. 1, p. 12685, 2020.

[21] K. Cui and G. Zhu, "LncRNA CTBP1-AS2 regulates miR-216a/PTEN to suppress ovarian cancer cell proliferation," *Journal of Ovarian Research*, vol. 13, no. 1, p. 84, 2020.

[22] Y. R. Lee, M. Chen, and P. P. Pandolfi, "The functions and regulation of the PTEN tumour suppressor: new modes and prospects," *Nature Reviews Molecular Cell Biology*, vol. 19, no. 9, pp. 547–562, 2018.

[23] T. R. Mercer, M. E. Dinger, and J. S. Mattick, "Long noncoding RNAs: insights into functions," *Nature Reviews Genetics*, vol. 10, no. 3, pp. 155–159, 2009.

[24] J. E. Wilusz, H. Sunwoo, and D. L. Spector, "Long noncoding RNAs: functional surprises from the RNA world," *Genes & Development*, vol. 23, no. 13, pp. 1494–1504, 2009.

[25] T. Xie, D. Wu, S. Li et al., "microRNA-582 potentiates liver and lung metastasis of gastric carcinoma cells through the FOXO3-mediated PI3K/Akt/snail pathway," *Cancer Management and Research*, vol. 12, pp. 5201–5212, 2020.

[26] J. Yang, P. Lu, M. Li, C. Yan, T. Zhang, and W. Jiang, "GATA6-AS1 regulates GATA6 expression to modulate human endoderm differentiation," *Stem Cell Reports*, vol. 15, no. 3, pp. 694–705, 2020.

[27] Z. Zhang, W. Qian, S. Wang et al., "Analysis of lncRNA-associated ceRNA network reveals potential lncRNA biomarkers in human colon adenocarcinoma," *Cellular Physiology and Biochemistry*, vol. 49, no. 5, pp. 1778–1791, 2018.

[28] Y. Cai, X. Yu, S. Hu, and J. Yu, "A brief review on the mechanisms of miRNA regulation," *Genomics, Proteomics & Bioinformatics*, vol. 7, no. 4, pp. 147–154, 2009.

[29] F. Zhai, C. Cao, L. Zhang, and J. Zhang, "miR-543 promotes colorectal cancer proliferation and metastasis by targeting KLF4," *Oncotarget*, vol. 8, no. 35, pp. 59246–59256, 2017.

[30] Y. Du, X. H. Liu, H. C. Zhu, L. Wang, J. Z. Ning, and C. C. Xiao, "MiR-543 promotes proliferation and epithelial-mesenchymal transition in prostate cancer via targeting RKIP," *Cellular Physiology and Biochemistry*, vol. 41, no. 3, pp. 1135–1146, 2017.

[31] P. Zhang, H. X. Zhou, M. X. Yang et al., "WITHDRAWN: miR-543 promotes proliferation and invasion of non-small cell lung cancer cells by inhibiting PTEN," *Biochemical and Biophysical Research Communications*, vol. S0006-291X, no. 16, p. 30478-8, 2016.

[32] J. Li, G. Dong, B. Wang, W. Gao, and Q. Yang, "miR-543 promotes gastric cancer cell proliferation by targeting SIRT1," *Biochemical and Biophysical Research Communications*, vol. 469, no. 1, pp. 15–21, 2016.

[33] H. Zhao, C. Diao, X. Wang et al., "MiR-543 promotes migration, invasion and epithelial-mesenchymal transition of esophageal cancer cells by targeting phospholipase A2 group IVA," *Cellular Physiology and Biochemistry*, vol. 48, no. 4, pp. 1595–1604, 2018.

[34] Y. Liang, D. Zhu, L. Zhu et al., "Dichloroacetate overcomes oxaliplatin chemoresistance in colorectal cancer through the miR-543/PTEN/Akt/mTOR pathway," *Journal of Cancer*, vol. 10, no. 24, pp. 6037–6047, 2019.

[35] G. Liu, J. Zhou, and M. Dong, "Down-regulation of miR-543 expression increases the sensitivity of colorectal cancer cells to 5-fluorouracil through the PTEN/PI3K/AKT pathway," *Bioscience Reports*, vol. 39, no. 3, 2019.

[36] C. Y. Chen, J. Chen, L. He, and B. L. Stiles, "PTEN: tumor suppressor and metabolic regulator," *Frontiers in Endocrinology*, vol. 9, p. 338, 2018.

[37] Y. Y. Cao, J. Yu, T. T. Liu et al., "Plumbagin inhibits the proliferation and survival of esophageal cancer cells by blocking STAT3-PLK1-AKT signaling," *Cell Death & Disease*, vol. 9, no. 2, p. 17, 2018.

[38] D. J. Wozniak, A. Kajdacsy-Balla, V. Macias et al., "PTEN is a protein phosphatase that targets active PTK6 and inhibits PTK6 oncogenic signaling in prostate cancer," *Nature Communications*, vol. 8, no. 1, p. 1508, 2017.

[39] P. Kechagioglou, R. M. Papi, X. Provatopoulou et al., "Tumor suppressor PTEN in breast cancer: heterozygosity, mutations and protein expression," *Anticancer Research*, vol. 34, no. 3, pp. 1387–1400, 2014.

[40] L. M. Dillon and T. W. Miller, "Therapeutic targeting of cancers with loss of PTEN function," *Current Drug Targets*, vol. 15, no. 1, pp. 65–79, 2014.

[41] X. Zheng, F. Jiang, M. Katakowski, Z. G. Zhang, Q.-e. Lu, and M. Chopp, "ADAM17 promotes breast cancer cell malignant phenotype through EGFR-PI3K-AKT activation," *Cancer Biology & Therapy*, vol. 8, no. 11, pp. 1045–1054, 2009.

[42] X. Huo, H. Wang, N. Jiang et al., "Long Non-Coding RNA GATA6-AS1 inhibits proliferation and promotes apoptosis of lung adenocarcinoma through sponging miR-331-3p and regulating SOCS1/JAK2/STAT3 pathway.

Research Article

Comprehensive Analysis to Reveal Amino Acid Metabolism-Associated Genes as a Prognostic Index in Gastric Cancer

Gangjun Zhao,[1] Mi Wu,[2,3] and Qiuwen Yan [2,3,4]

[1]*Affiliated Xiaoshan Hospital, Hangzhou Normal University, Hangzhou, China*
[2]*Ningbo Medical Center Lihuili Hospital, Ningbo, China*
[3]*The Affiliated Lihuili Hospital, Ningbo University, Ningbo, China*
[4]*Medical School of Ningbo University, Ningbo, China*

Correspondence should be addressed to Qiuwen Yan; 2111101029@nbu.edu.cn

Background. Amino acid metabolism (AAM) is related to tumor growth, prognosis, and therapeutic response. Tumor cells use more amino acids with less synthetic energy than normal cells for rapid proliferation. However, the possible significance of AAM-related genes in the tumor microenvironment (TME) is poorly understood. *Methods.* Gastric cancer (GC) patients were classified into molecular subtypes by consensus clustering analysis using AAMs genes. AAM pattern, transcriptional patterns, prognosis, and TME in distinct molecular subtypes were systematically investigated. AAM gene score was built by least absolute shrinkage and selection operator (Lasso) regression. *Results.* The study revealed that copy number variation (CNV) changes were prevalent in selected AAM-related genes, and most of these genes exhibited a high frequency of CNV deletion. Three molecular subtypes (clusters A, B, and C) were developed based on 99 AAM genes, which cluster B had better prognosis outcome. We developed a scoring system (AAM score) based on 4 AAM gene expressions to measure the AAM patterns of each patient. Importantly, we constructed a survival probability prediction nomogram. The AAM score was substantially associated with the index of cancer stem cells and sensitivity to chemotherapy intervention. *Conclusion.* Overall, we detected prognostic AAM features in GC patients, which may help define TME characteristics and explore more effective treatment approaches.

1. Introduction

Globally, gastric cancer (GC) ranks among the deadliest gastrointestinal disorders, accounting for 5.7% of all cancer diagnoses and causing more than a million cases annually; increases among people under 40 years of age [1, 2]. The current treatment for GC is surgical resection followed by fluorouracil and platinum-based chemotherapy. Unfortunately, GC is characterized by mild initial symptoms, a high degree of heterogeneity, distinct molecular kinds, and a range of biological characteristics. Most patients with GC are diagnosed late due to clinical relapse, distant metastases, inadequate treatment, and a poor prognosis. Chemotherapy-targeted drugs and immunotherapy are frequently employed to increase the survival rates of these patients. However, substantial systemic

toxicity and rapidly developing drug resistance significantly reduce treatment efficacy [3]. Recently, the characterization of novel tumor subtypes based on expression profiling has contributed to a better understanding of molecular features and tumor heterogeneity in GC, such as the four molecular subtypes identified by a comprehensive molecular evaluation: the Epstein-Barr virus-positive tumors, unsteady microsatellite tumors, genomically secure lesions, and chromosomally unstable growths [4]; the three subtypes to describe the molecular and genetic characteristics of gastric adenocarcinoma [5]; the two molecular subtypes of metastatic gastric adenocarcinoma [6]; and three subtypes based on the altered proteome [7]. However, these molecular subtypes still face significant challenges in distinguishing patient prognosis and guiding personalized gastric adenocarcinoma treatment regimens.

Tumor cell metabolism is a key pathway that drives cancer stem cell survival, tumor cell transformation, immune evasion, drug resistance, and disease recurrence. Targeting tumor cell metabolism can enhance treatment responses to drug-resistant cancers and mitigate treatment-related toxicity by reducing the need for genotoxic drugs. Therefore, targeting tumor cell metabolism is a popular form of cancer treatment, especially amino acid consumption therapy, which has been the focus of recent research [8]. The categories of amino acid metabolism KEGG components include proline and aromatic amino acid metabolism and branched and branched-chain amino acid metabolism. A combination of signaling pathways and transcription factors often changes amino acid metabolic pathways in tumor cells [9, 10]. Cancer cells rely on foreign amino acid supply and meet increasing demand by upregulating the expression of the amino acid transporter. Interfering with amino acid availability is the Achilles heel unique to cancer [11]. Amino acids are also critical elements for immunological cells. T cells can upregulate amino acid transporter expression during proliferation, differentiation, and immunological response, increasing amino acid absorption and improving immune function [12, 13].

Regarding drug resistance, amino acids support cancer cells against therapy by maintaining biosynthetic processes, maintaining redox homeostasis, regulating epigenetic modifications, and providing metabolic intermediates for energy production [14]. For example, leucine or branched-chain amino acid therapy increases cisplatin sensitivity in cancer cells by suppressing cisplatin- or bcat1-mediated autophagy and promoting mTOR signaling [15].

In this study, our aim was to investigate the characteristics of AAM-related genes in GC systematically and comprehensively. First, we used TCGA-STAD and GSE84337, which were obtained from the Cancer Genome Atlas (TCGA) database and GEO database, to analyze that the genome associated with amino acid metabolism (AAM) could divide GC into different subgroups. We then evaluated molecular signatures and infiltrative immune cell strength to identify AAM clusters. In addition, risk profiles based on four genes were confirmed as independent prognostic factors for gastric cancer, suggesting an association between amino acid metabolism-related genes and prognosis. Finally, we determined an AAM score that significantly predicted clinical outcomes and medication therapy effects in patients with gastric cancer. These findings might open up new avenues for GC study and customized therapy.

2. Materials and Methods

2.1. Data Collection and Collation. TCGA-STAD tool (https://portal.gdc.cancer.gov) was used to retrieve information on RNA expression, somatic mutations, copy number variation (CNV) files, and related GC clinicopathology., Moreover, GSE84337 from the GEO archive (https://www.ncbi.nlm.nih.gov/geo/) was used to obtain clinical parameters and normalized gene expression data. Two datasets were combined, and batch effects were eliminated by applying the "Combat" algorithm [16]. A total of 101 AAM genes were

discovered in older research in addition to the amino acid and derivative metabolic process gene list in the Molecular Signatures Database (MSigDB) (https://www.gsea-msigdb.org/gsea/index.jsp) (Table S1). STRING analysis (https://string-db.org/) was utilized to illustrate interactions between AAM-correlating genes.

2.2. Differential Expression and Mutation Analysis of AAM Genes. Differential expression AAM genes were identified in TCGA-STAD dataset by the limma package in R software [17]. The landscape of AAM gene mutations was illustrated by the maltools package's waterfall graph, while changes in CNV placements of AAM genes on chromosomes were mapped by the RCircos program [18].

2.3. Consensus Clustering. The different AAM correlation modes were defined by the ConsensusClusterPlus package [19] and the K-means method. These steps have been performed 1000 times to guarantee the stability of the categories. Then, the clustering results were validated using principal component analysis (PCA) [20]. The clinical significance of the clusters was determined by evaluating molecular patterns, clinical variables, and patient outcomes. Additionally, GSVA enrichment analysis was performed in the heatmaps using the GSVA program to evaluate if the verified gene sets differed significantly across three clusters [21]. Additionally, a single-sample gene set enrichment analysis (ssGSEA) was applied to examine the differences in immune cell infiltration proportions between subgroups.

2.4. Differentially Expressed Genes (DEGs). Package "limma" in R [17] was used to identify DEGs between different AAM molecular subtypes, with the criterion of $|\log 2FC| > 0.585$ and false discovery rate (FDR) < 0.05. Genes that intersect or do not intersect between subgroups were visualized using Venn diagrams.

2.5. Development of a Risk Signature Based on Clusters of AAM. AAM score was constructed to quantify amino acid metabolism in GC patients. Intersect genes were chosen based on DEGs expression data in various clusters of AAM across GC samples. The 65 intersect genes associated with prognosis were screened and analyzed by univariate Cox regression. Genes linked with AAM were scored using PCA through the following technique: AAM score $= \Sigma(\text{Expi} \times \text{coefi})$. Then, TCGA-STAD and GSE84437 cohorts were used for further analysis. A nomogram was created from risk scores and clinical data using the rms program [22] to predict the overall survival (OS) of patients with GC at one, three, and five years. The stromal, immunological, and ESTIMATE scores were examined using the ESTIMATE algorithm [23] to determine the relationship between the risk score and the tumor immune microenvironment.

2.6. Chemotherapy Sensitivity Prediction. To explore differences in chemotherapy sensitivity between groups, we evaluated the highest half-maximal inhibitory concentration of chemotherapy drugs (IC50) by R-package "pRRophetic" [24].

(a)

(b)

(c)
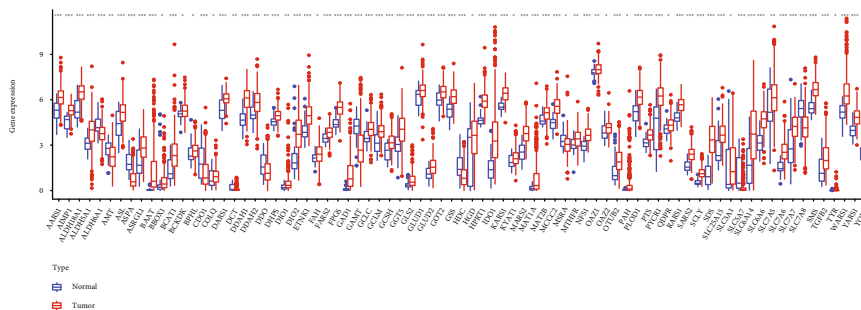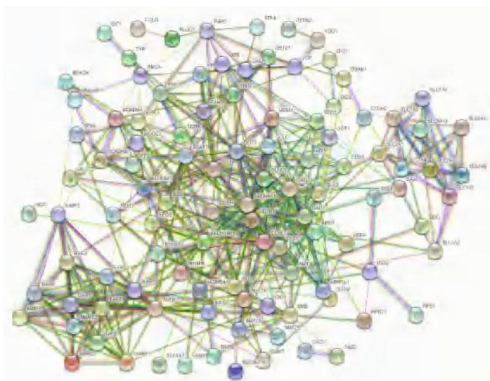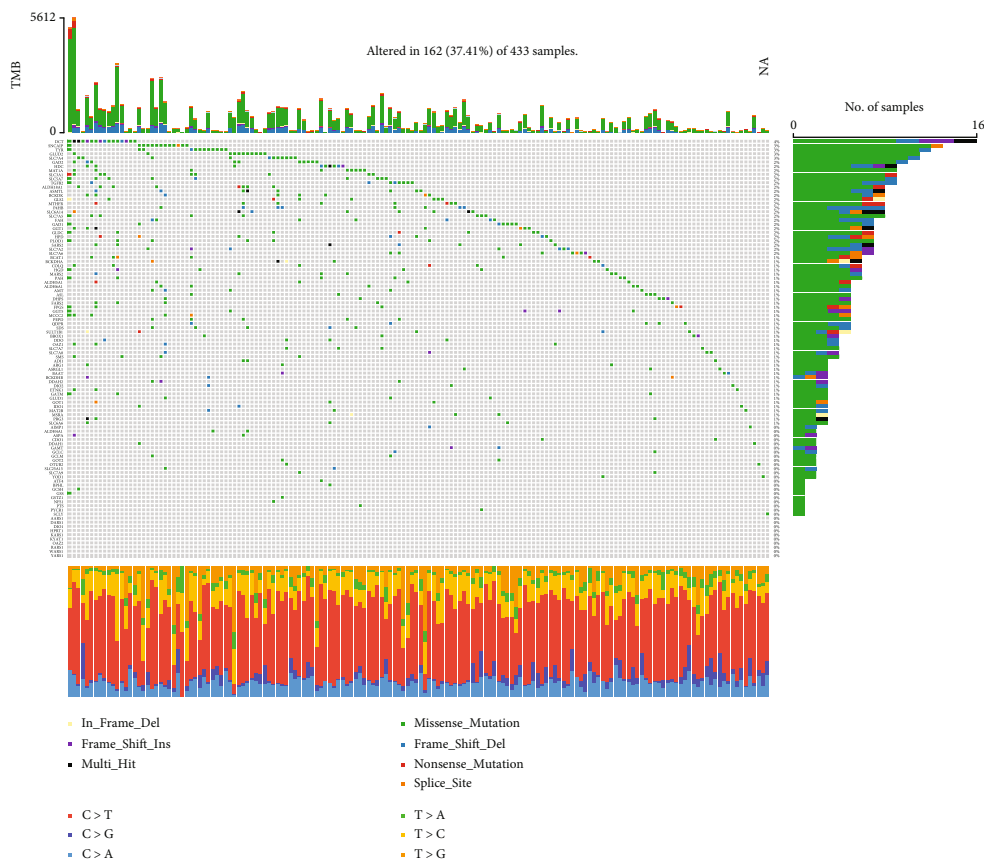
Figure 1: Continued.
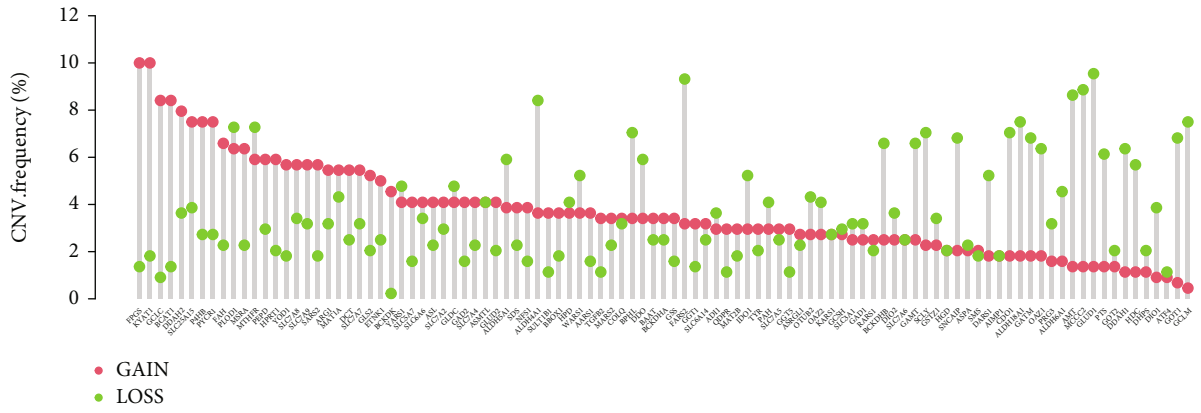
(d)
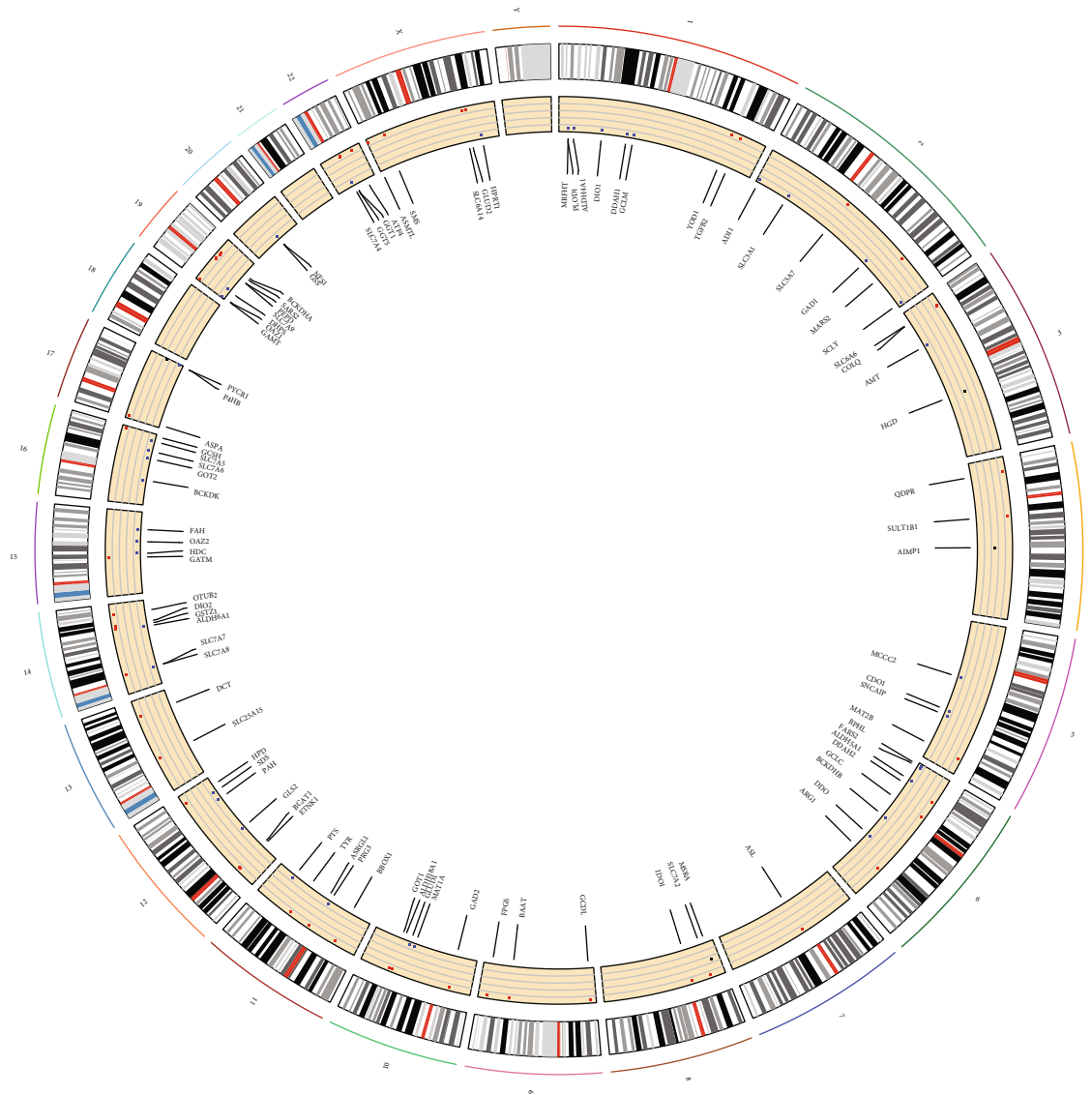
(e)

FIGURE 1: Genetic mutational landscape of AAMs in GC. (a) Expression distributions of DEGs between GC and normal tissues. (b) The PPI network acquired from the STRING database among the DEGs. (c) Genetic alteration on a query of *AAMs*. (d) Frequencies of CNV gain, loss, and non-CNV among AAMs. (e) Circus plots of chromosome distributions of AAMs. (*$P < 0.05$; **$P < 0.01$; ***$P < 0.001$).

(a)

FIGURE 2: Continued.

Consensus matrix *k* = 3

□ 1
■ 2
□ 3

(b)

AAM cluster
● A
● B
● C

(c)

(d)

FIGURE 2: Continued.

(e)
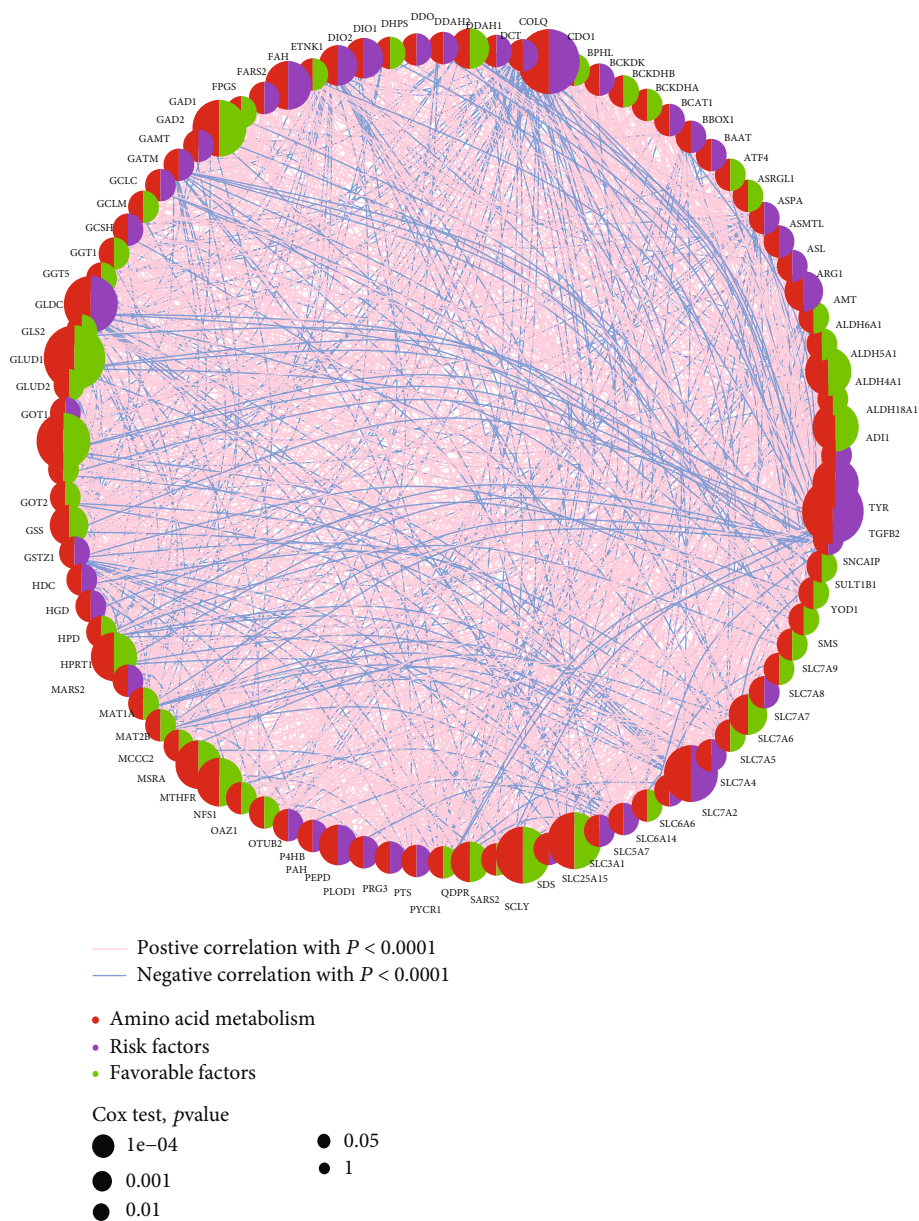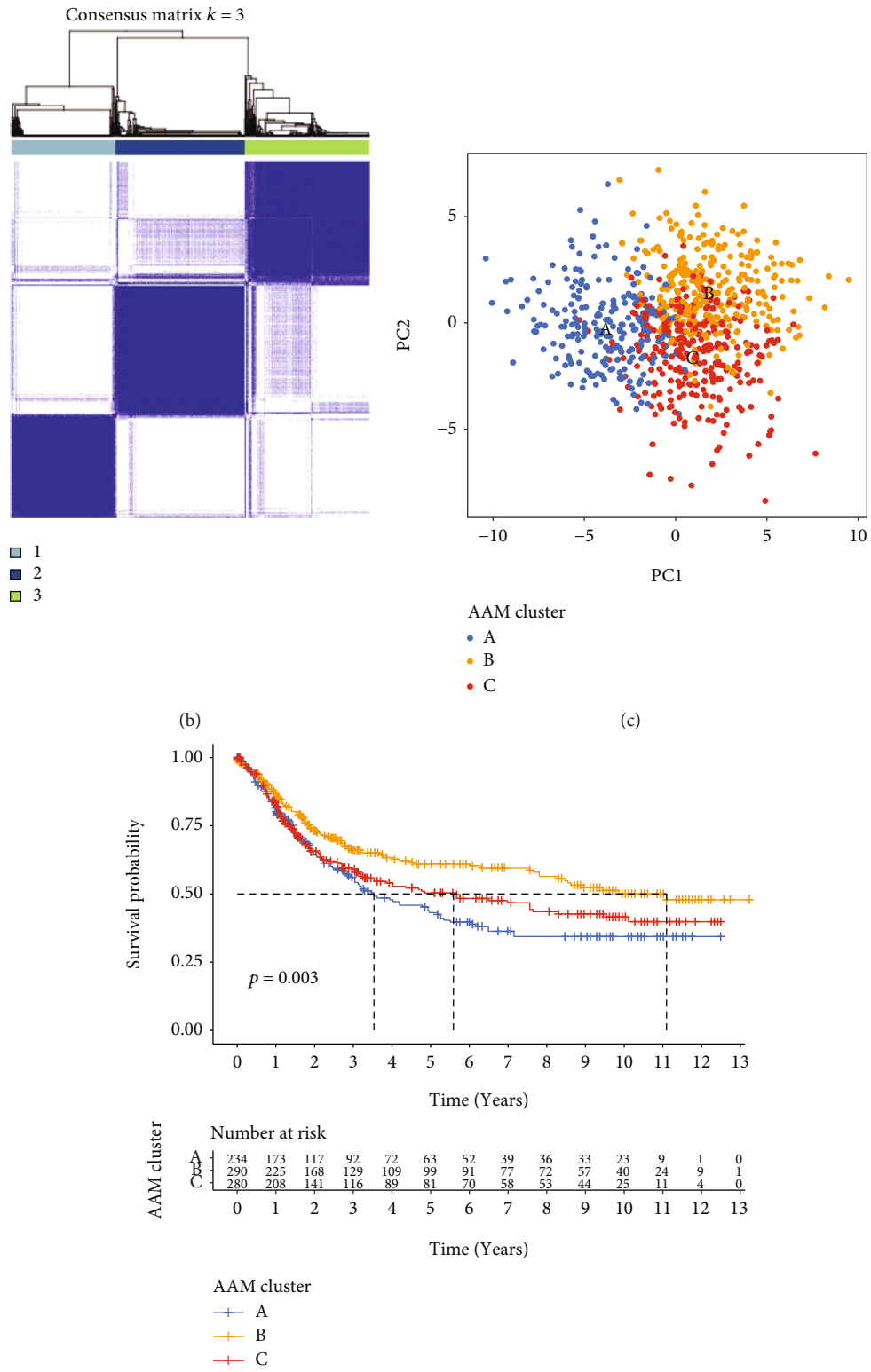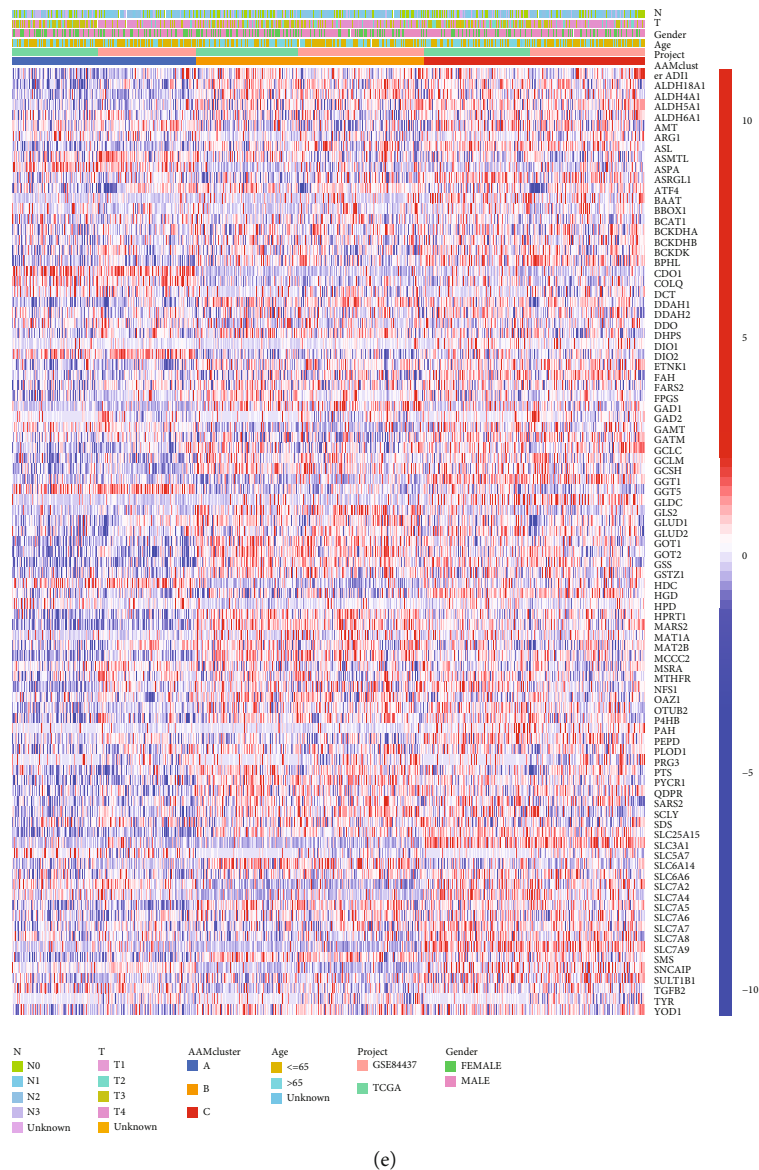
FIGURE 2: AAM subgroups and clinicopathological and biological characteristics of three distinct subtypes of samples divided by consistent clustering. (a) A network of correlations including AAMs in the TCGA cohort. (b) Consensus matrix heatmap defining three clusters and their correlation area. (c) PCA analysis indicating an obvious difference in transcriptomes among the three subgroups. (d) Univariate analysis showing three distinct subtypes correlated with OS. (e) Differences in clinicopathologic characteristics and expression levels of AAMs among the three distinct subgroups.

2.7. Statistical Analysis. All statistical tests were performed using R software, version 4.2.0, and the relevant feature packages. Differences between different datasets were determined using the Chi-square test. Two groups were compared using the Wilcoxon test. The log-rank test was applied to determine the Kaplan-Meier (KM) survival analysis. P values below 0.05 were classified as statistically significant ($^*P < 0.05$; $^{**}P < 0.01$; $^{***}P < 0.001$).

3. Results

3.1. AAM Gene Expression Analysis and Mutation Analysis in STAD. We examined 101 AAM gene expressions in tumor and normal tissue samples using the TCGA-STAD dataset. 79 AAM genes were either up or downregulated in

STAD (Figure 1(a)). At the protein level, the interactions between the 101 AAM gene proteins were analyzed using STRING and mapped the PPI network (Figure 1(b)) The incidence of somatic mutations and CNVs of AAM-related genes in GC patients was assessed. Only 163 of 433 samples contained mutations in AAM-related genes, with a mutation frequency of 37.41%, and the data implicated DCT as the gene with the highest mutation frequency (4%) (Figure 1(c)). Missense mutations are the most common type of gene alteration. We also discovered that at the CNV level, the focus was mostly on CNV loss. FPGS and KYAT1 have a broad rate of CNV gain (Figure 1(d)). Additionally, we discovered alterations in 95 AAM genes with chromosomal CNV characteristics (Figure 1(e)).

(a)

(b)

FIGURE 3: Continued.

(c)
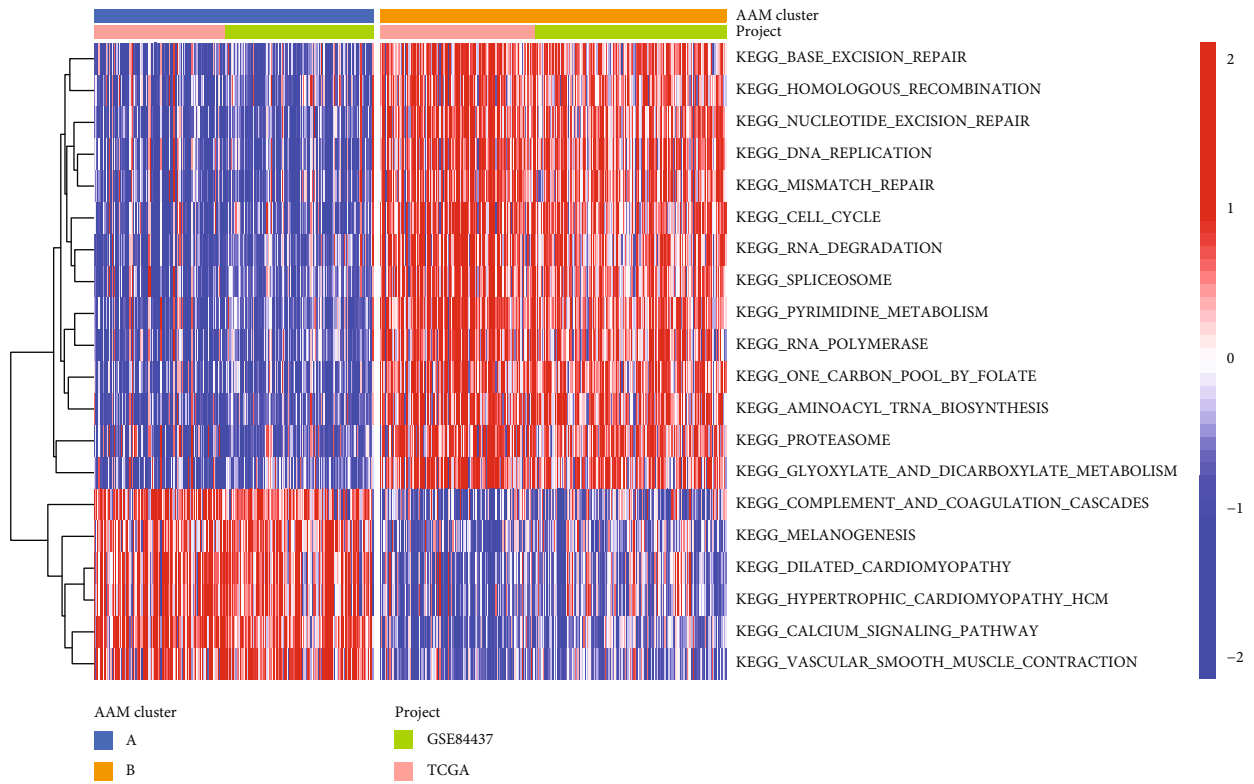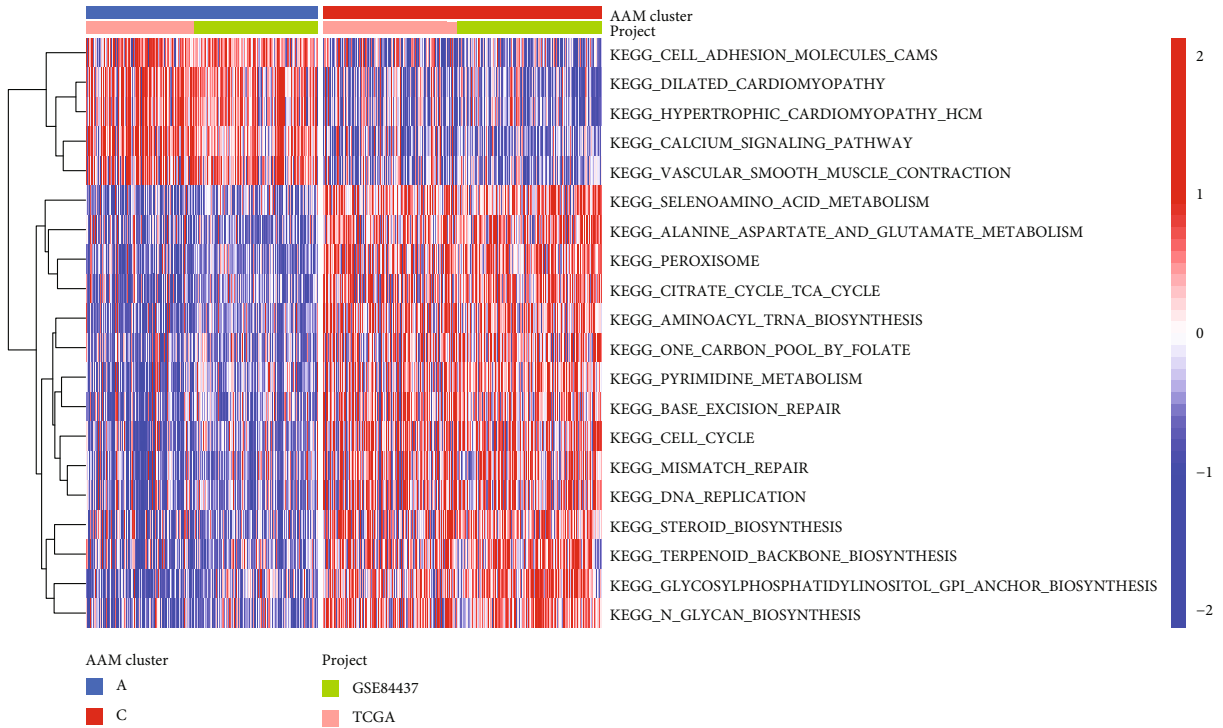
(d)
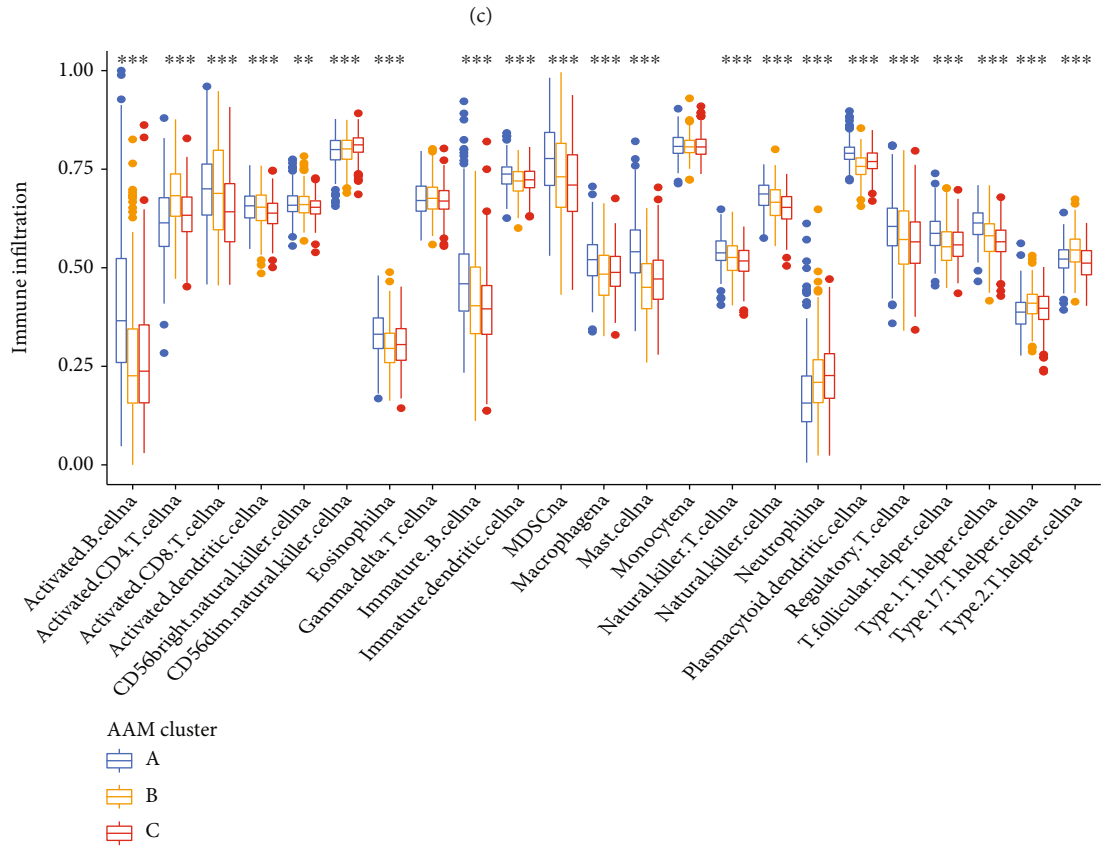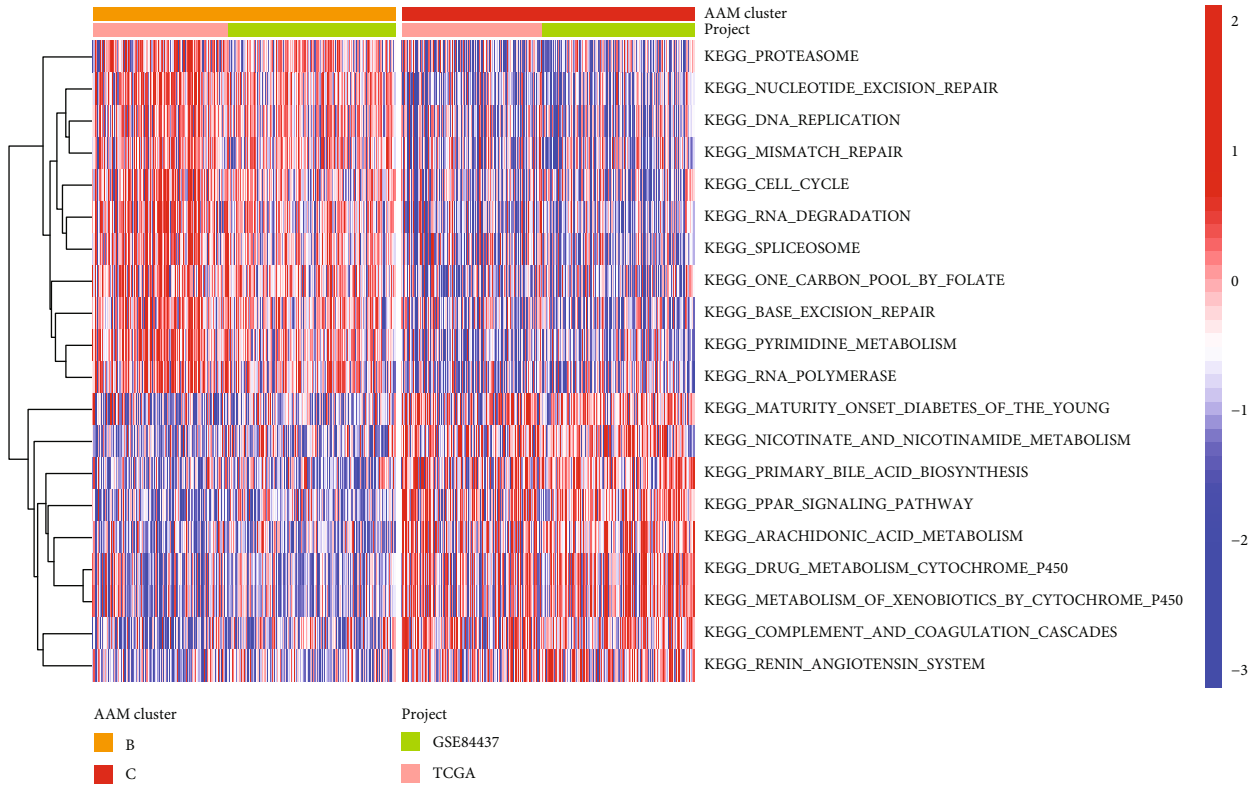
FIGURE 3: Different clusters' TME characteristics. (a–c) GSVA of biological pathways among three distinct subgroups. (d) The abundance of each TME infiltrating cell in three AAM clusters.

(a)

(b)

(c)

(d)

FIGURE 4: Continued.

(e)

N
- N0
- N1
- N2
- N3
- Unknown

T
- T1
- T2
- T3
- T4
- Unknown

Gender
- FEMALE
- MALE

Age
- < = 65
- > 65
- Unknown

Project
- GSE84437
- TCGA

AAMcluster
- A
- B
- C

geneCluster
- A
- B

(f)
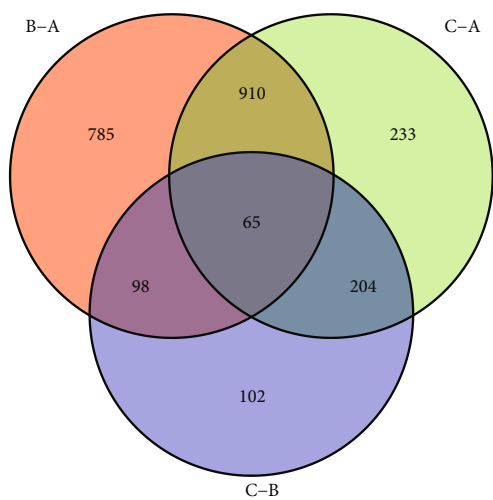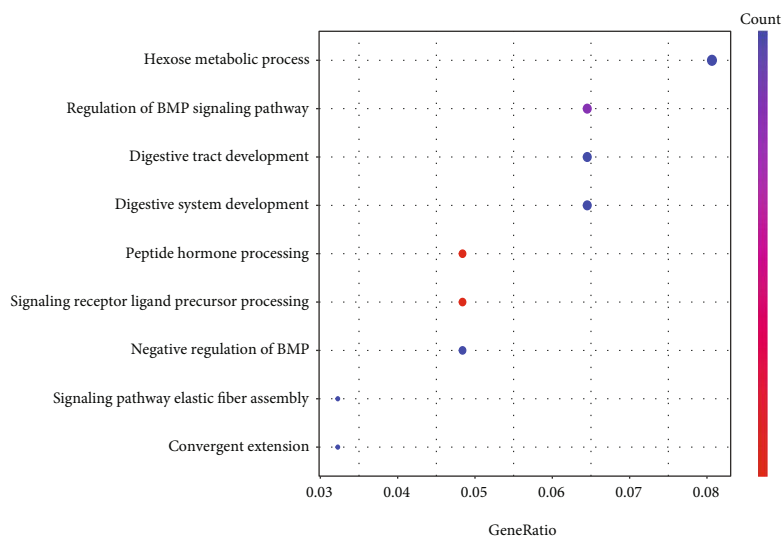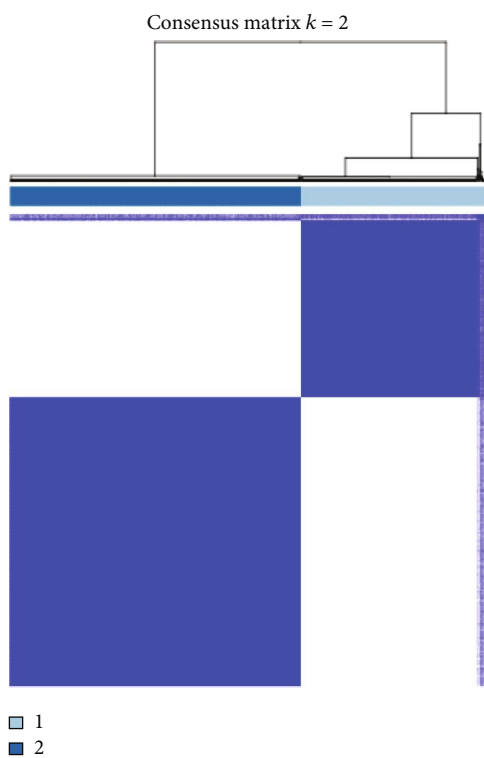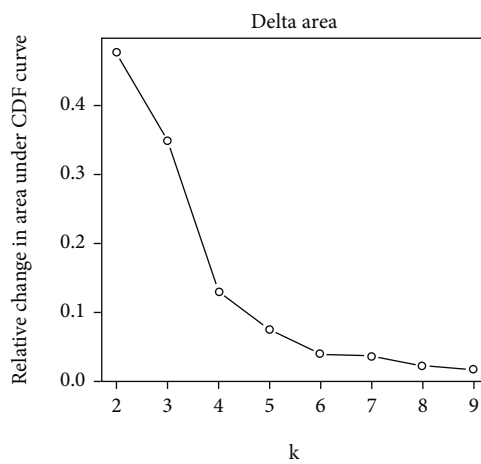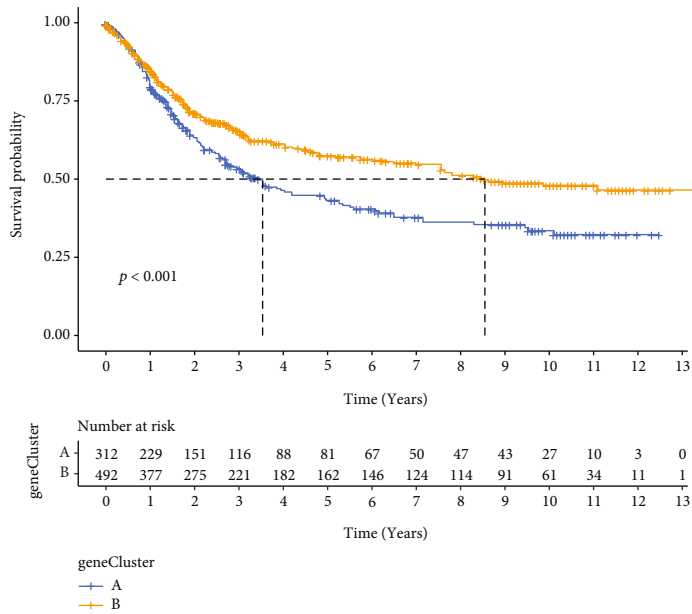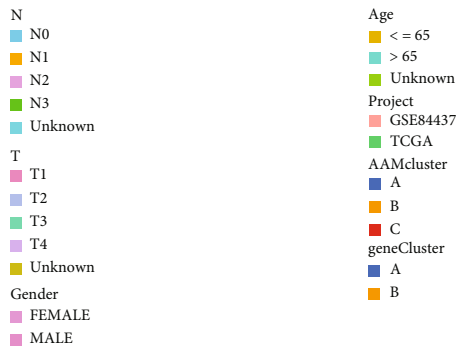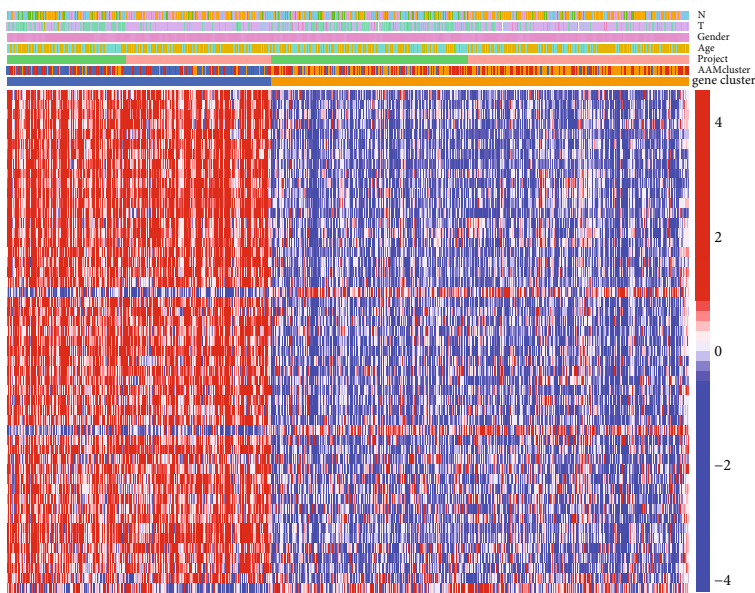
FIGURE 4: Continued.
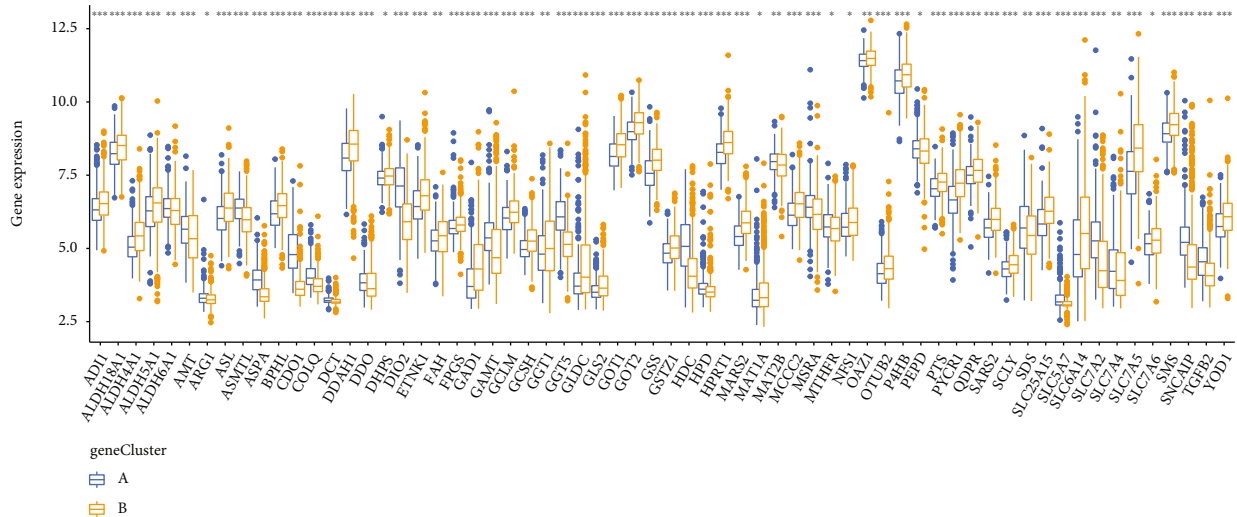
(g)

FIGURE 4: Generation of AAMs signatures. (a) Venn diagram showing overlapping genes of three distinct subgroups. (b) Results of GO enrichment. (c, d) Consensus matrix heatmap defining two gene clusters and their correlation area. (e) Kaplan–Meier curves showing the overall survival of gene clusters. (f) Heatmap of the clinical relevance of three AAM clusters and two geneClusters. (g) Gene expression levels of AAM-related genes in two geneClusters.

3.2. AAM Patterns in GC. We combined TCGA-STAD and GSE84337 transcriptome data and retrieved the mRNA expression data for 101 AAM genes; Table S2 lists the OS statistics and clinical details for these subjects. Table S2 provides information on these subjects. Ninety-one genes in GC have prognostic scores determined using univariate Cox regression analysis and KM analysis (Table S3). The regulator network illustrated the entire landscape of 91 gene connections, regulator relationships, and their prognosis for GC patients (Figure 2(a)). The above data showed that AAM might significantly characterize TME cell infiltration within specific tumors. Patients were categorized using the ConsensusClusterPlus R package based on the expression of the 91 AAM genes. The unsupervised clustering technique divided the data into three distinct groups: 234 cases of model A, 291 cases of model B, and 282 cases of model C (Figure 2(b)). PCA analysis also showed a good distribution among groups (Figure 2(c)). The cluster B model provided a significant health benefit (Figure 2(d)). Moreover, Figure 2(e) shows that both cluster's genomic expression and clinic pathological factors were compared, revealing a significant difference in AAM gene expression and clinical characteristics.

3.3. Different Clusters' TME Characteristics. GSVA enrichment analysis revealed that cluster A was greatly elevated in cardiovascular pathways, including vascular smooth muscle contraction, dilated cardiomyopathy, and hypertrophic cardiomyopathy (Figure 3(a)). Cluster C described the enrichment mechanisms for metabolism. These included the alanine, aspartate, glutamate, arachidonic acid metabolisms, toxic substances metabolism by cytochrome P450, and nicotinate and nicotinamide metabolisms (Figure 3(c)). Cluster B was significantly associated with nucleic acid anabolism (Figure 3(b)).

Furthermore, we analyzed the immune cell infiltration of three clusters using the ssGSEA technique. Cluster A contained a significantly high number of innate immune cells, such as activated B cells, activated CD4 T cells, activated CD8 T cells, activated dendritic cells (DC), eosinophils, immature B cells, immature DC, MDSCs, macrophages, mast cells, natural killer T (NKT) cells, natural killer (NK) cells, plasmacytoid DC, regulatory T cells, and T helper cells (Figure 3(d)).

3.4. Generation of AAM-Related Gene Signatures. We discovered 65 overlapped genes in the three groups to further investigate the possible biological properties of AAM-related genes (Figure 4(a)). GO enrichment analysis revealed that these cluster-related genes were primarily enriched in biological processes associated with metastasis (Figure 4(b)). Afterward, we performed a uniCox analysis to determine the importance of these genes for survival. 51 genes were considered for the next analysis because they met $P < 0.05$ criteria (Table S4). Individuals were separated into 2 gene clusters (clusters A and B) based on prognostic genes to investigate this regulatory regime (Figures 4(c) and 4(d)). We identified that the OS time for cluster A patients was the shortest, while the OS time for cluster B patients was the best (Figure 4(e)). Figure 4(f) shows a heatmap of the correlation between clusters and clinicopathological symptoms. The AAM gene clusters showed significant differences in the AAM gene expression, as predicted by the AAM subgroups (Figure 4(g)).

3.5. Prognostic AAM Score Construction and Validation. The AAM score was derived from DEGs connected with clusters. The GC participants were randomly divided into two groups: a training group ($n = 402$) and a test group ($n = 402$) with a ratio of 1 : 1. LASSO Cox regression analysis built a prognostic gene

(a)

(b)

(c)

AAMcluster   geneCluster   Risk   Fustat

FIGURE 5: Continued.

(d)

(e)

(f)

(g)

(h)

(i)

FIGURE 5: Continued.

(j)

(k)

Figure 5: Continued.

(l)
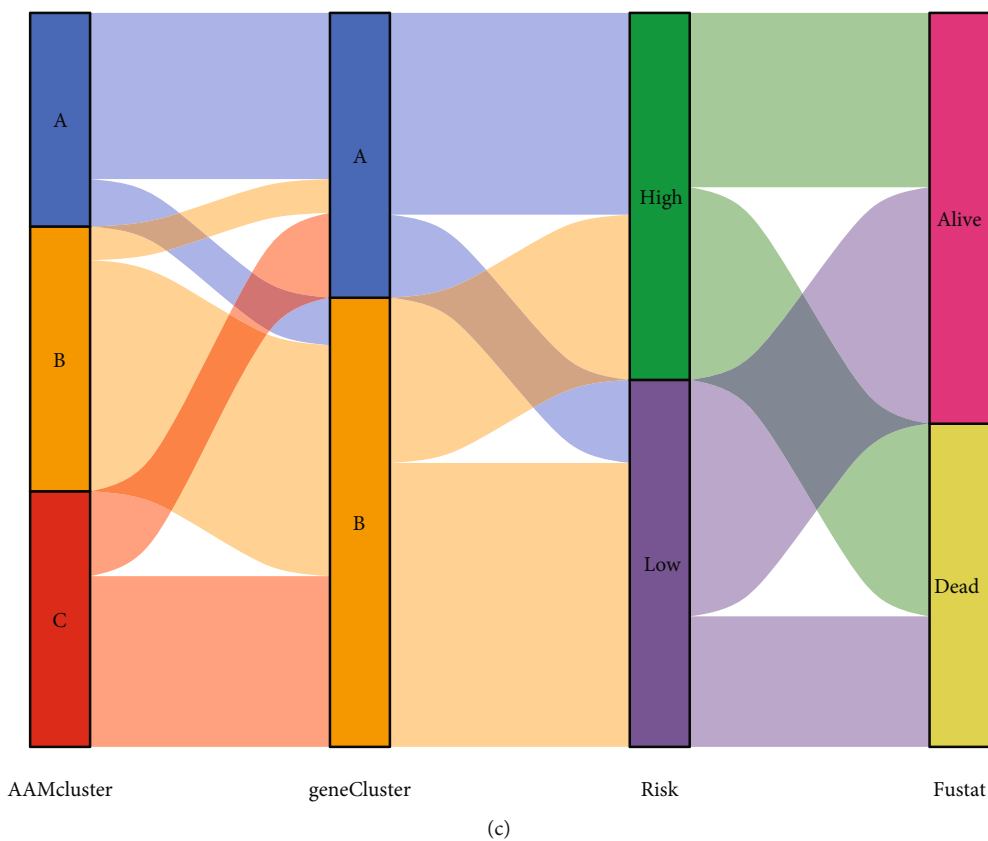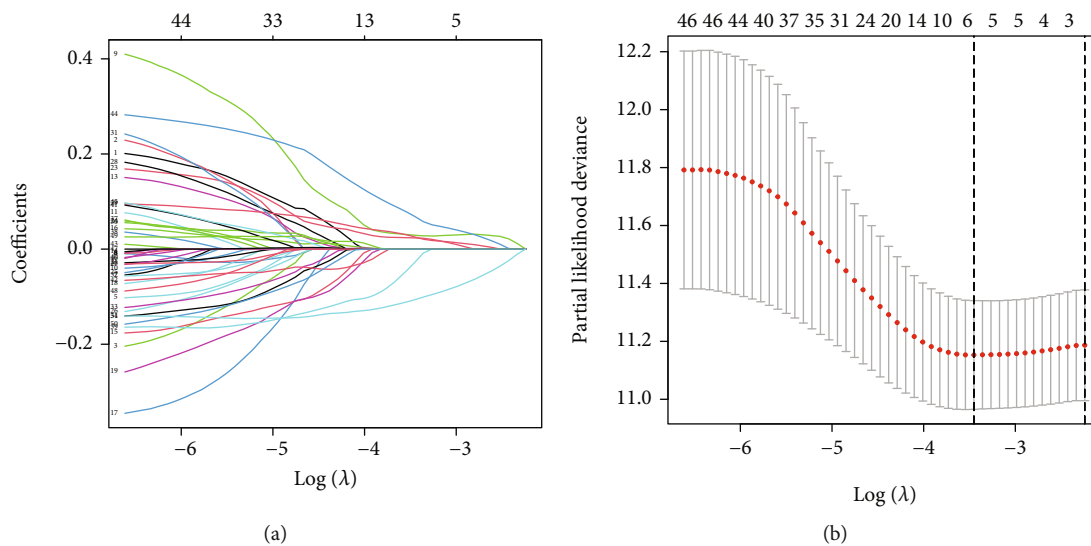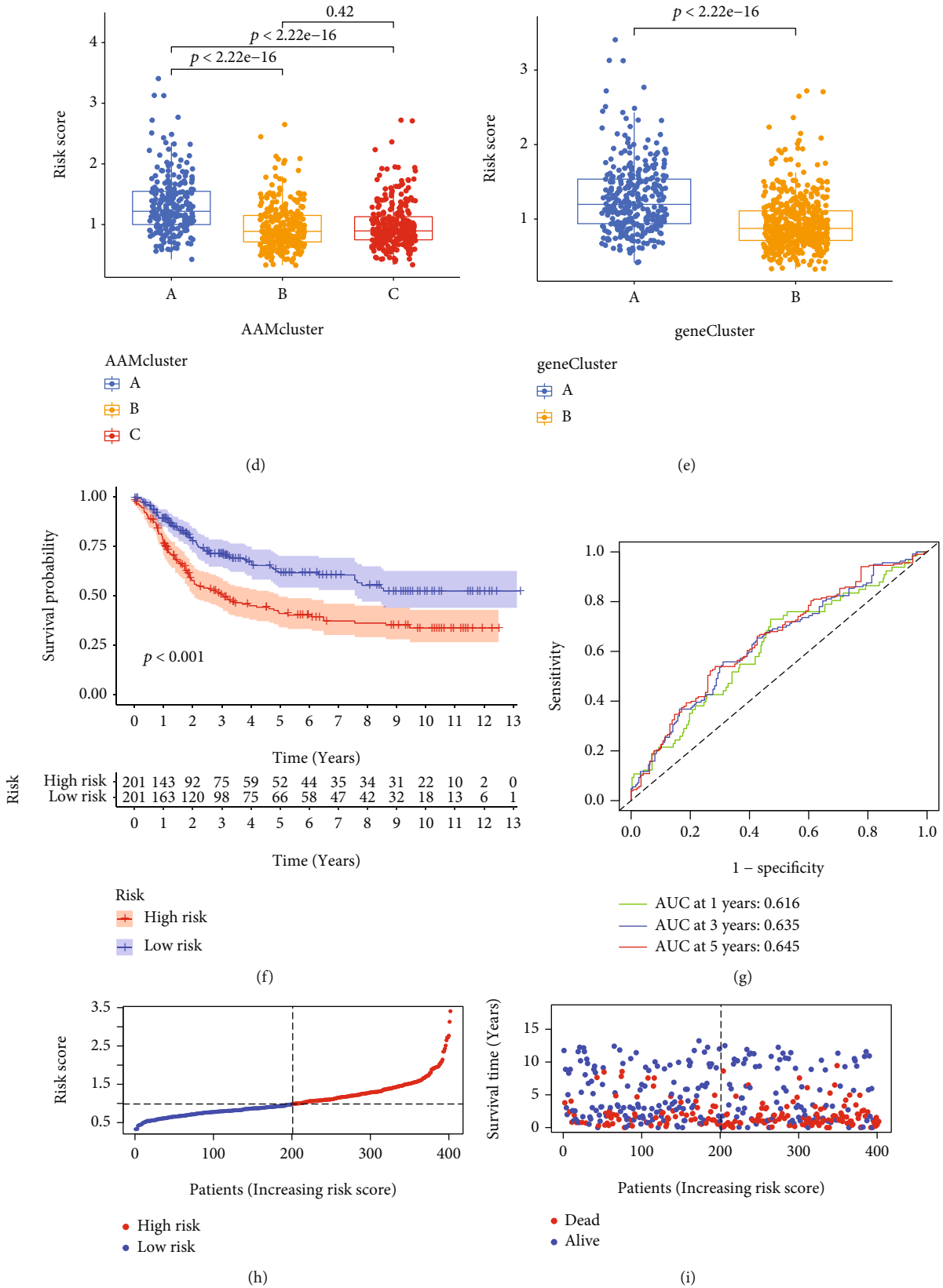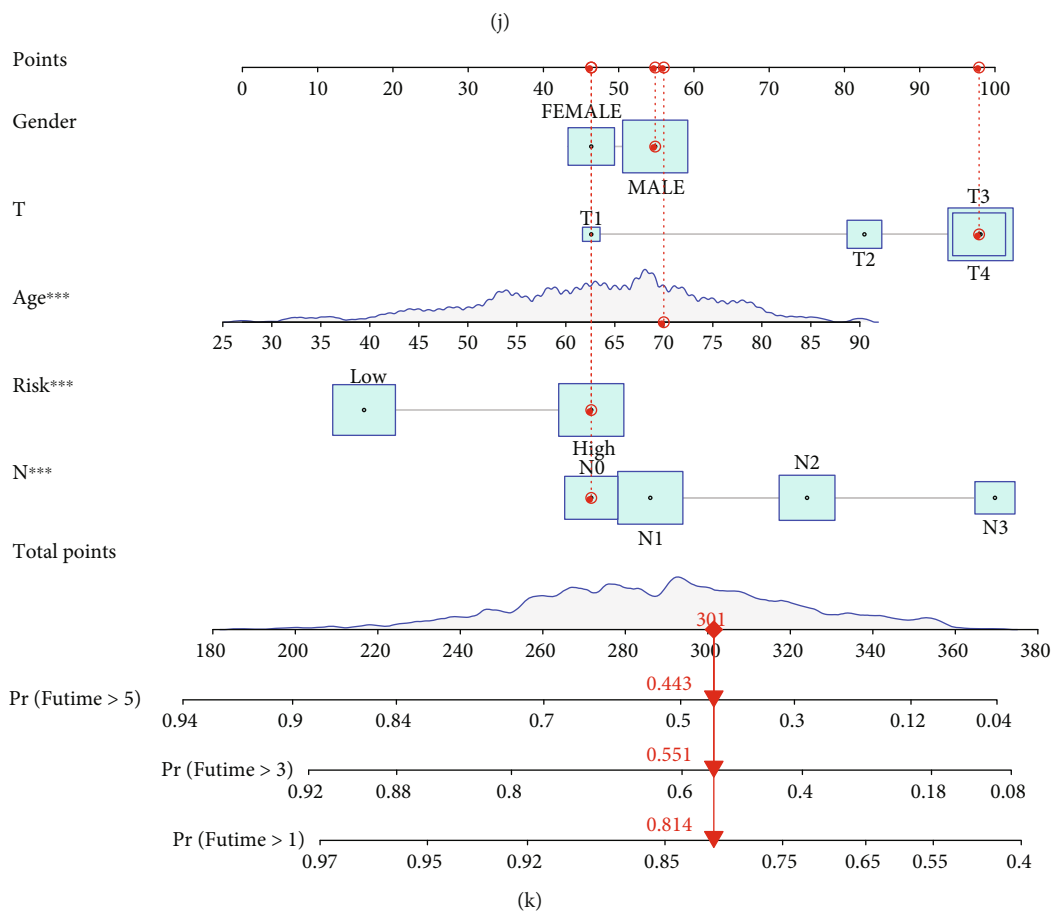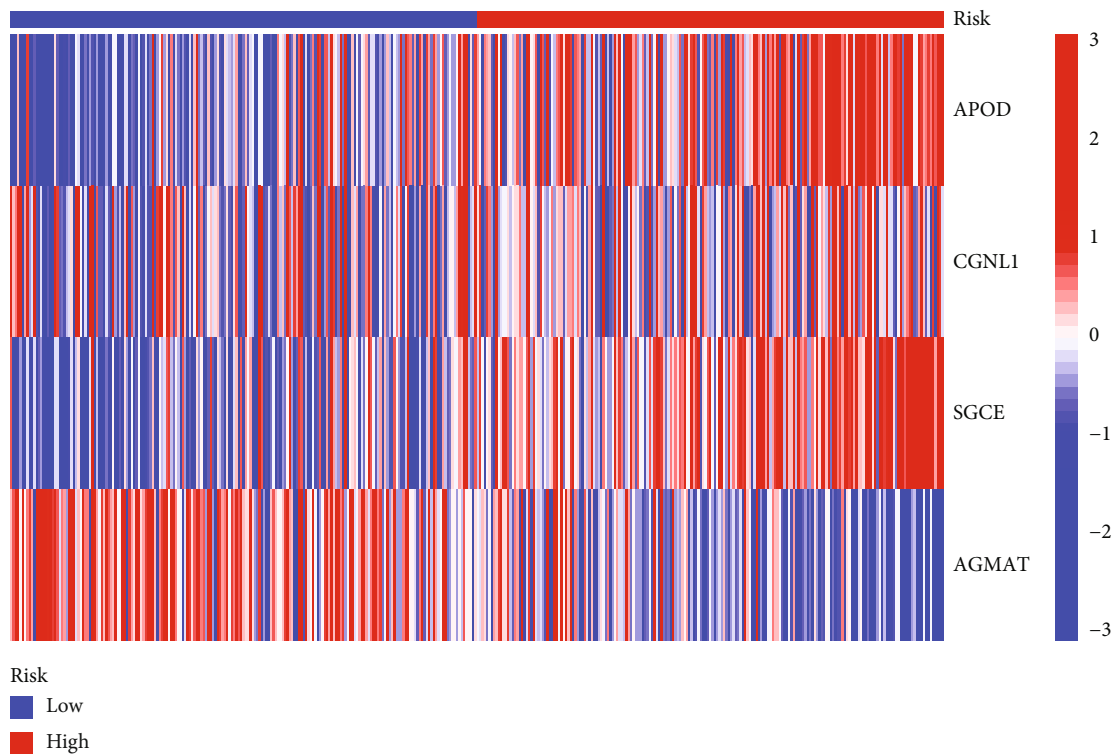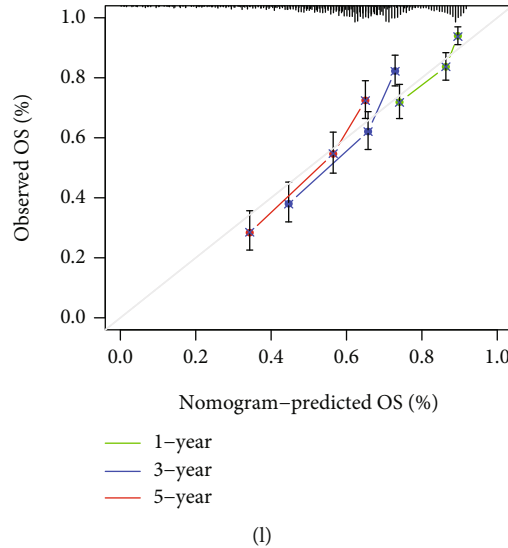
FIGURE 5: Four gene-based prognostic models were constructed using Lasso-Cox regression analysis. (a, b) The distribution of partial likelihood deviation of the Lasso coefficient preserves 4 variables when partial likelihood deviation reaches the minimum. (c) Alluvial diagram showing the connection between AAM clusters, gene clusters, and AAM score. (d) The level of the risk score in different AAM cluster subgroups. (e) The level of AAM score in different gene clusters. (f) The overall survival of AAM score. (g) ROC curves to predict the sensitivity and specificity of 1-, 3-, and 5-year survival according to the AAM score. (h, i) Ranked dot and scatter plots showing the AAM score distribution and patient survival status. (j) Heatmap showing four gene expression signatures in GC. (k, l) Establishment of nomogram and its performance verification.

model based on the 4 prognostic AAM genes (Figures 5(a) and 5(b)). This is the risk score: $(0.099 \times$ expression APOD) + $(0.236 \times$ expression CGNL1) + $(0.213 \times$ expression SGCE) + $(0.164 \times$ expression AGMAT). Figure 5(c) shows the distribution of patients among the three subtypes of AAM, two gene subtypes, and two AAM score groups. Moreover, each gene cluster A (Figure 5(a)) and AAM cluster A (Figure 5(e)) had a high AAM score, whereas both gene cluster A (Figure 4(e)) and AAM cluster A (Figure 2(d)) had a poor prognosis. In the training sample, KM survival analysis revealed that OS rates were considerably lower in the high-score group than in the low-score group (log-rank test, $P < 0.001$) (Figure 5(f)). The ROC findings show AUC scores of 0.616, 0.635, and 0.645 for one, three, and five years, respectively, revealing that the signature's accuracy was adequate (Figure 5(g)). This finding also confirmed the results of our analysis. The hazard plot of the AAM value revealed that as the AAM score increased, OS time decreased, and death rates increased (Figures 5(h) and 5(i)). Figure 5(j) also shows a heatmap of the chosen genes. Then, the nomogram plot showed that the AAM score might be a good tool for predicting long-term survival (Figure 5(k)). Calibration maps demonstrated that the nomogram technique was remarkably accurate, indicating that it can predict a patient's prognosis (Figure 5(l)).

3.6. AAM Score Association with TME, TMB, MSI, and CSC Score. We used the estimate package to determine the relationship between the AAM score and immune and stromal results. High AAM scores were closely linked to elevated immune scores, and high AAM scores were linked to increased stromal results (Figure 6(a)). The association between the four genes in the suggested model and the num-

ber of immune cells was also evaluated. Most immune cells were strongly linked to these genes (Figure 6(b)).

The "maftools" R software showed the distinctions in somatic mutation patterns between the higher and lower AAM score groups (Figures 7(a) and 7(b)). We discovered that TTN, TP53, and MUC16 mutation occurrences in GC patients in two risk categories were higher than or equivalent to 20%. Additionally, our results showed that the TMB was greater in the low-risk groups compared to the high-risk groups (Figure 7(c)), indicating that immunotherapy may be more beneficial for low-risk patients. Spearman's correlation analysis also demonstrated a negative relation between the AAM score and TMB (Figure 7(d)). We also performed a survival study across several TMB subgroups to examine the effect of TMB status on prognosis in GC patients. Individuals with elevated TMB had a better prognosis than those with reduced TMB (Figure 7(e)).

Moreover, correlation analysis revealed a significant relationship between a lower AAM score and the MSI-H condition, while a higher AAM score was associated with the microsatellite constant (MSS) condition (Figures 7(f) and 7(g)). We also integrated the AAM score and CSC index values to analyze any potential link between the AAM score and CSC in GC. Figure 7(h) presents the findings of the linear correlation between the AAM score and the CSC index. We discovered that the AAM scoring was negatively related to the CSC index $(R = 0.49, P < 2.2e - 16)$, indicating that GC cells with a lower AAM score exhibited stem cell features and a lower degree of cell differentiation.

3.7. Drug Sensitivity Testing. The IC_{50} of 98 drugs was measured in TCGA-STAD patients to determine the significance

(a)

(b)
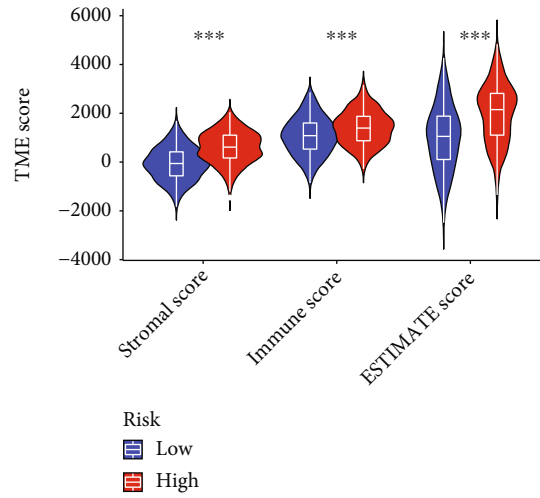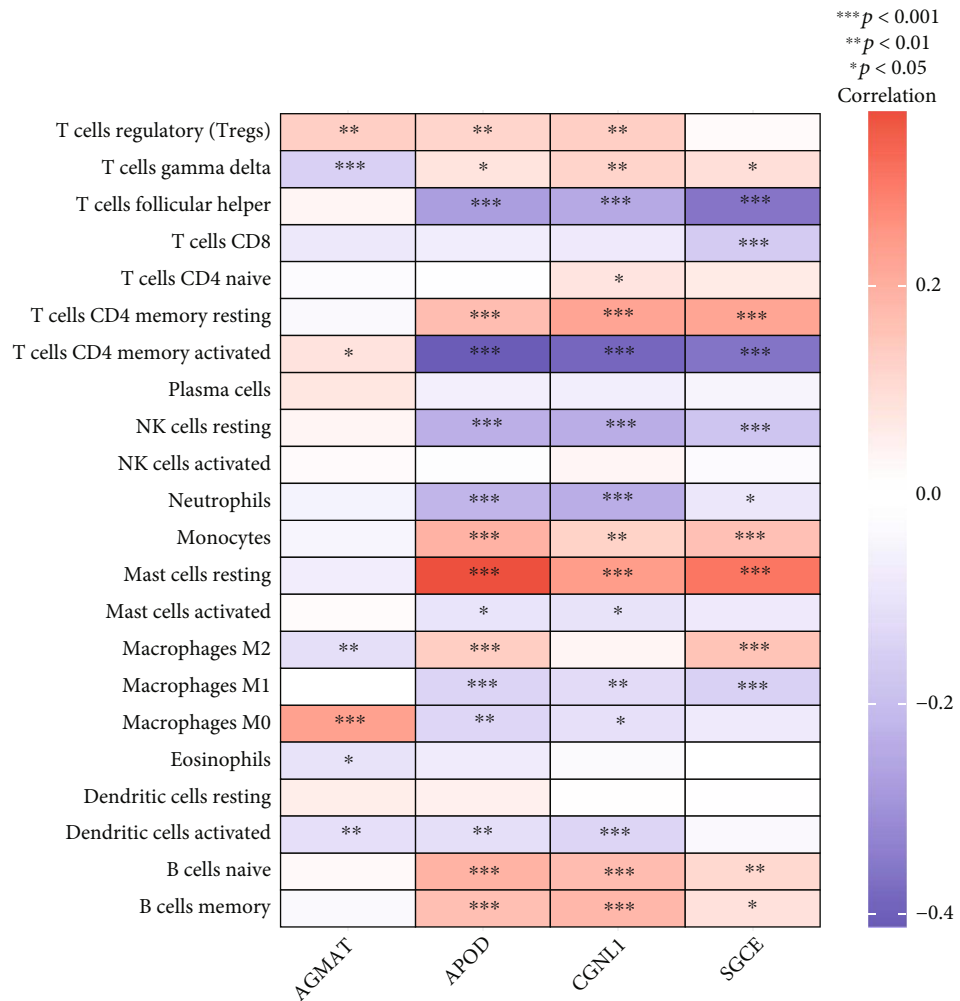
FIGURE 6: Evaluation of the TME between the two groups. (a) Correlations between AAM score and both immune and stromal scores. (b) Correlations between the abundance of immune cells and four genes in the proposed model.

of the AAM value as an indicator of therapy response in GC patients. We found that individuals with high AAG scores may respond well to bexarotene and several tar-

geted therapy agents, such as axitinib, sunitinib, dasatinib, lapatinib, imatinib, and pazopanib (Figures 8(a)). In contrast, individuals with low AAM scores may react better

(a)

(b)
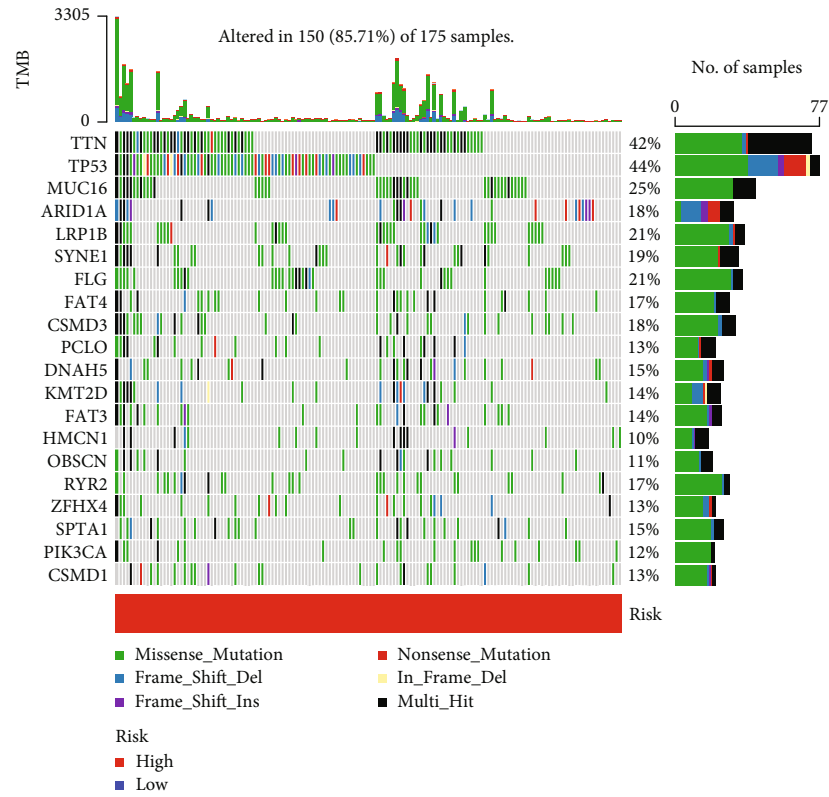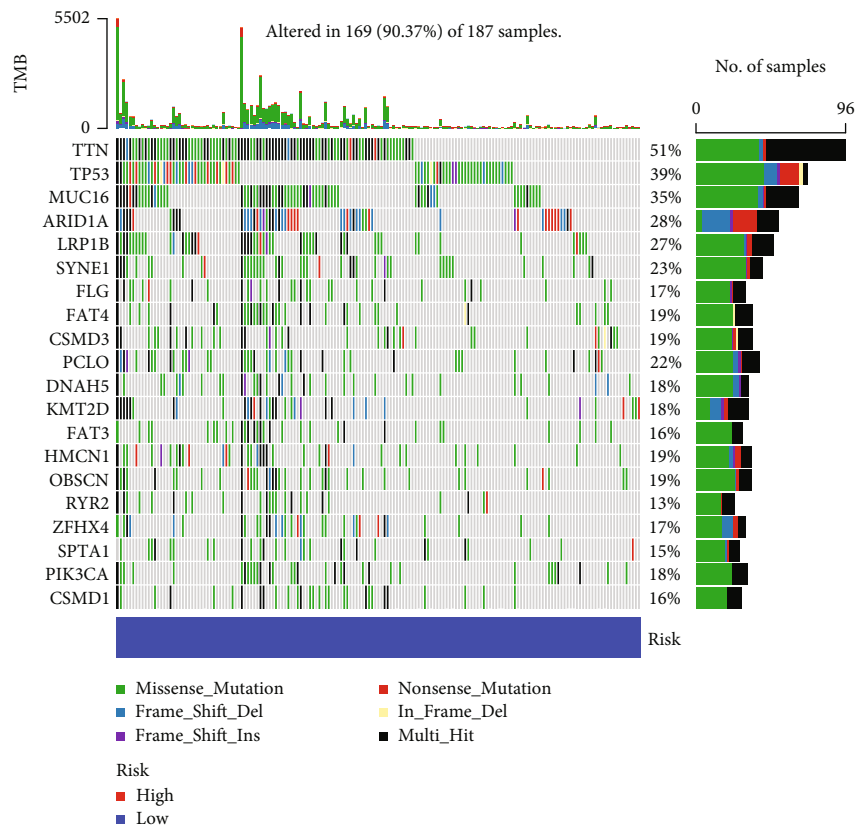
Figure 7: Continued.

(c)

(d)

(e)

(f)

FIGURE 7: Continued.

(g)

(h)
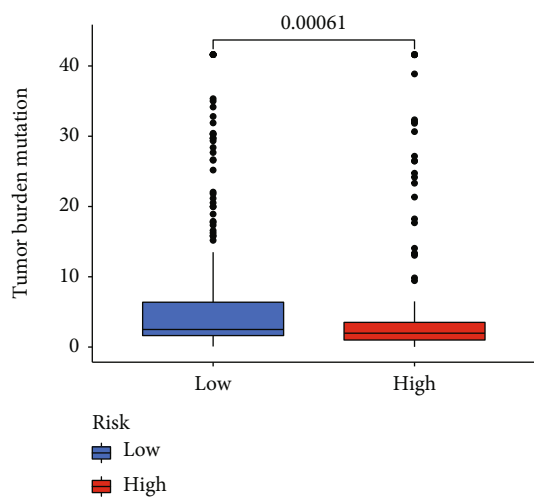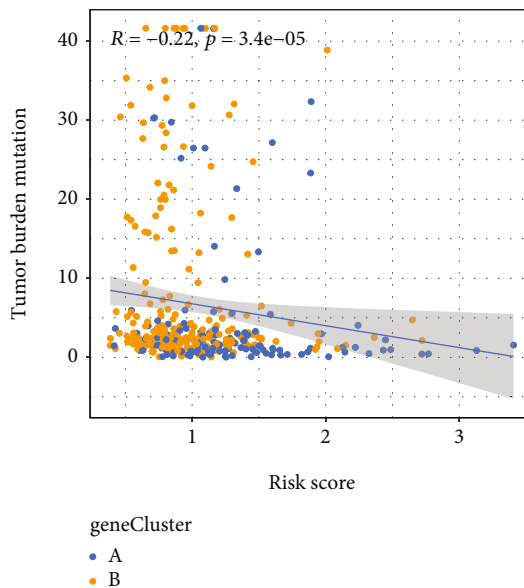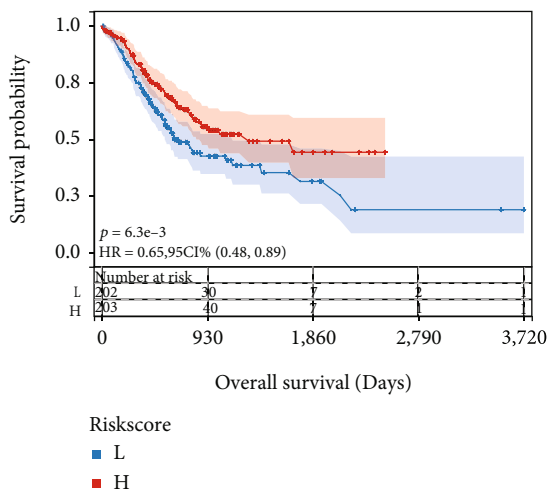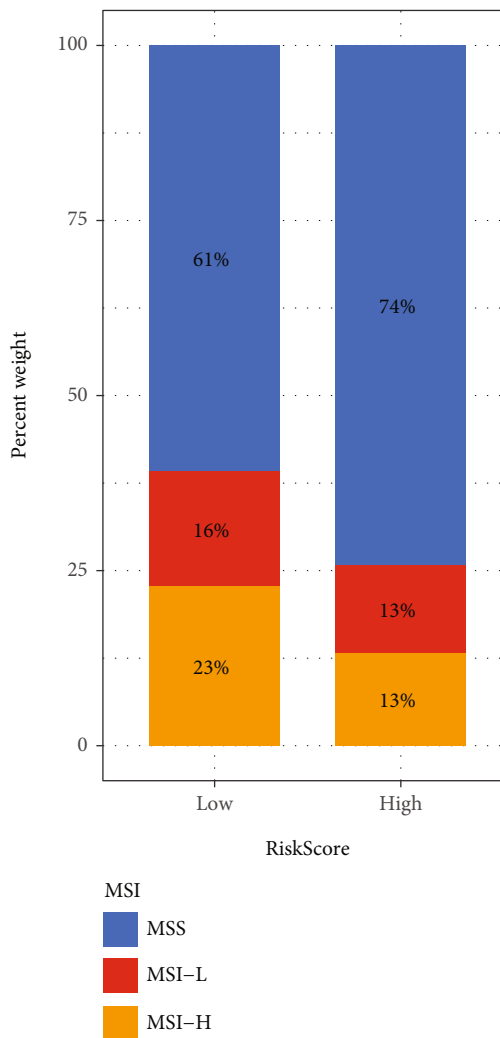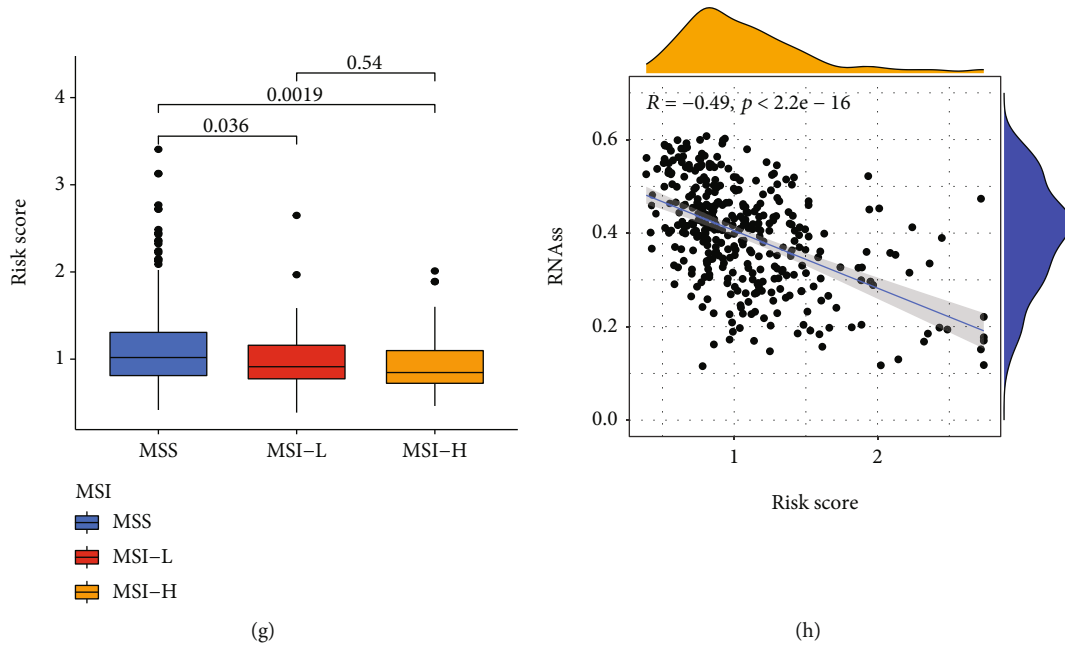
Figure 7: Comprehensive analysis of the AAM Score in GC. (a, b) The waterfall plot of somatic mutation features established with high and low AAM scores. (c) TMB in different AAM score groups. (d) Spearman's correlation analysis of the AAM score and TMB. (e) The Kaplan–Meier curves were used to perform survival analyses for patients with low and high TMB. (f, g) Relationships between AAM score and MSI. (h) Spearman's correlation analysis of the AAM score and RNAss. MSI: microsatellite instability; CSC: cancer stem cell; TMB: tumor mutation burden.

to metformin, vorinostat, methotrexate, and sorafenib (Figures 8(b)).

4. Discussion

GC is a highly heterogeneous malignant tumor that develops through the synergistic action of multiple mechanisms. Currently, the most common treatments for GC include surgery combined with immunotherapy, radiotherapy, chemotherapy, and targeted therapy [25]. However, survival outcomes for this cancer are far from satisfactory because of high recurrence and metastasis rates. Numerous studies have shown the essential function of amino acid metabolism in innate immunity and antitumor responses [26]. Additionally, most research has concentrated on a particular gene related to amino acid metabolism or a specific cell type in the TME. Therefore, the overall effect mediated by the combined action of multiple genes and the infiltration properties of the TME remains unknown. Moreover, our study can provide valuable information for the in-depth investigation. The outcomes of this research demonstrate alterations in transcription and AAM variations at the genetic level in GC.

Our study initially investigated the genetic alterations and AAM-related gene expressions using data from the TCGA-STAD and GSE84437 cohorts. While AAM gene mutation rates were lower, most prognosis-related genes were higher in GC patients. Then, we employed an unsupervised clustering approach to classify GC patients into three AAM subgroups. We found that clinical outcomes, immune infiltration, and function differed significantly among the

three subgroups. Patients with subtype A exhibited a shorter OS and greater levels of immune cell infiltration than subtypes B and C. However, subtype A was considerably elevated in metastasis-related pathways. AAM cluster A was significantly enriched in innate immune cell infiltration, including activated B cells, activated CD4 T cells, activated CD8 T cells, activated DC, eosinophils, immature B cells, immature DC, MDSCs, macrophages, mast cells, NKT cells, NK cells, plasmacytoid DC cells, regulatory T cells, and T helper cells. Similar to the AAM clustering results, two genomic groupings with distinct clinical characteristics, immunological activities, and functions were discovered based on AAM-related genes. The AAM subgroups were quantified using LASSO Cox regression and the AAM score. Cluster A and gene cluster A, with the worst outcome measures, had the highest AAM value out of the three AAM clusters and two gene clusters. Amino acids can supply nitrogen and carbon for rapid tumor cell development and biosynthesis [27].

The AAM score was substantially related to the clinic pathological characteristics of GC. After adjusting for various factors, the results demonstrated that the AAM score was an independent predictor of survival outcomes in GC patients. ROC validated its predictive robustness over one, three, and five years of OS. Recently, risk scores associated with AAM have established clinical outcomes in GC patients. Moreover, the AAM score may provide useful prognostic information for patients. The aggregation of gene mutations leads to tumor development related to metabolic changes. According to our research, there are substantial variations between genetic modifications of individuals with

(a)

(b)
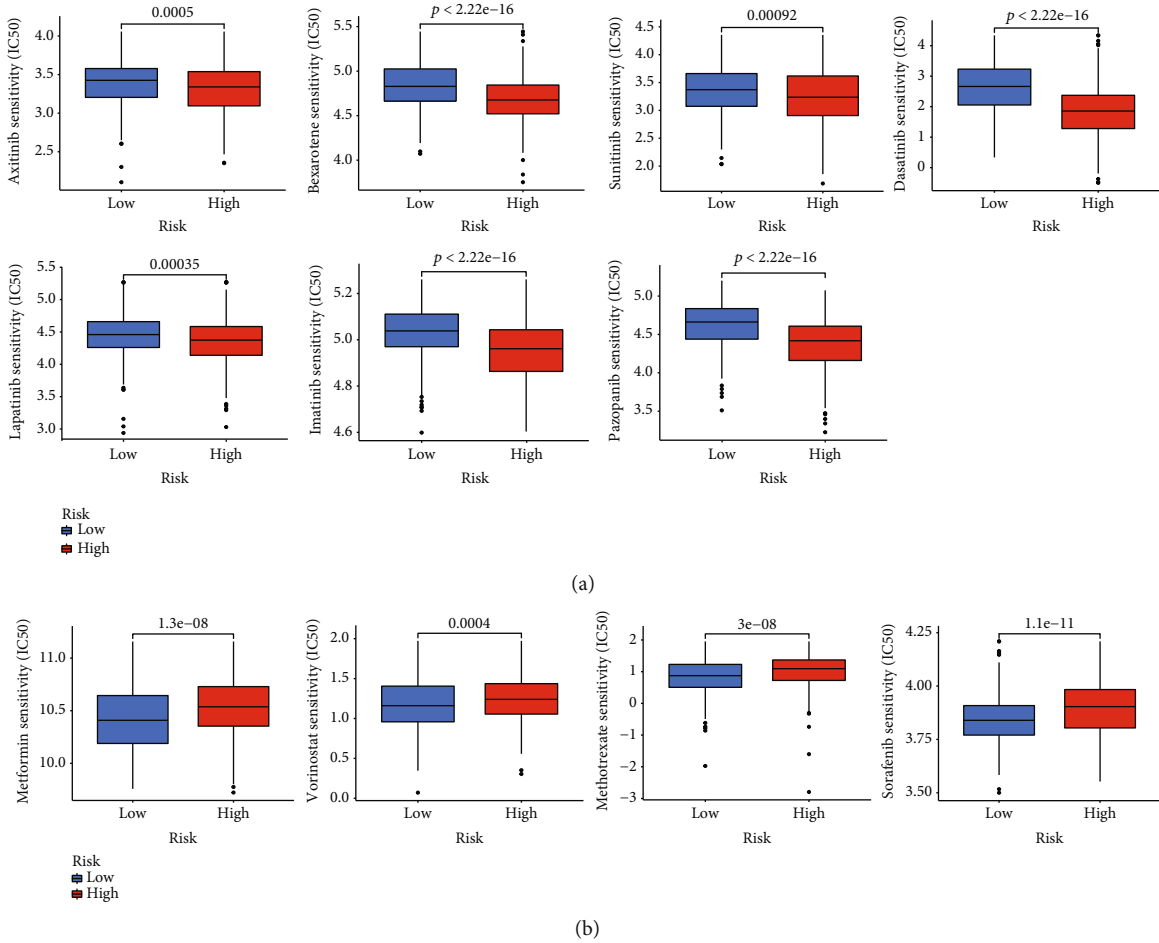
FIGURE 8: Relationships between AAM score and chemotherapeutic sensitivity. High IC50 of indicated chemotherapeutics drugs in low (a) and low (b) AAM score groups, respectively.

low and high AAM scores. Elevated TMB was correlated with a better prognosis in GC patients, which is consistent with our results [28]. Clinical outcomes were substantially better in the low AAM score group compared to the low TMB group, indicating that the AAM score was a reliable predictor of immunotherapy performance. Immune check-point inhibitor treatment markedly enhanced outcomes in a comparatively higher percentage of MSI-H cancers than MSI-L/MSS tumors, providing significant and long-lasting reactions and survival advantages [29]. In this investigation, more MSI-H patients were found in the groups with a low AAM score and a better prognosis. AAM meets the cellular demands for maintaining redox homeostasis, energy generation, and biomass production and has been recognised as a key determinant of drug resistance in tumors [30, 31]. There is growing evidence that drug resistance in cancer cells can be overcome by suppressing or enhancing AAM and by depleting or supplementing amino acid availability [11, 32]. Currently, GC is slowly developing chemotherapeutics resistance. Finally, we explored the relationship between AAM score and chemotherapeutic drugs, which identified a novel insight for exploring tumor therapy treatment and avoiding the resistance of GC. The study identified drugs

that may be effective for patients in various AAM score groups. Combining these drugs with the targeted AAM score may help reduce drug resistance and enhance clinical results. Our work uncovered the potential for repurposing "stale" chemotherapy drugs for new oncology indications.

We acknowledge that our research has several limitations. The first one was that all studies relied only on data obtained from public sources, and all samples were acquired retroactively in this research. The second limitation was that most datasets lacked data on crucial clinical characteristics like surgery, neoadjuvant chemotherapy, and chemoradiotherapy. The third was that more experimental studies should be conducted to confirm our findings.

5. Conclusion

In this study, we researched and identified several AAM genes that regulate TME, clinicopathological aspects, and prognosis. We also developed an AAM score to anticipate the prognosis and treatment sensitivity of GC patients, which assisted the development of more effective therapy regimens and paved the pathway for further research on the relationship between AAM-related genes and GC.

Data Availability

The datasets analyzed for this study can be found in the TCGA-STAD project (http://www.cancer.gov/tcga) and GSE84337 from the GEO archive (https://www.ncbi.nlm.nih.gov/geo/).

Conflicts of Interest

The authors report no conflict of interest.

Authors' Contributions

GZ, MW, and BL conceived the project. MW, BL, XXW, SZF, and JZY contributed to data acquisition, analysis and interpretation, and manuscript writing. XXW, SZF, and JZY performed the experiments and revised the manuscript. All authors read and approved the submitted manuscript.

Supplementary Materials

Table S1: 101 amino acid metabolism-related denes. Table S2: clinical information of 871 gastric cancer patients. Table S3: univariate Cox regression analysis and the Kaplan–Meier analysis of 91 AAM genes associated with OS in GC patients. Table S4: univariate Cox regression analysis of 51 AAM genes associated with OS in GC patients. (Supplementary Materials)

References

[1] M. C. S. Wong, J. Huang, P. S. F. Chan et al., "Global incidence and mortality of gastric cancer, 1980-2018," *JAMA Network Open*, vol. 4, no. 7, article e2118457, 2021.

[2] E. C. Smyth, M. Nilsson, H. I. Grabsch, N. C. T. van Grieken, and F. Lordick, "Gastric cancer," *Lancet*, vol. 396, no. 10251, pp. 635–648, 2020.

[3] J. A. Ajani, T. A. D'Amico, D. J. Bentrem et al., "Gastric cancer, version 2.2022, NCCN clinical practice guidelines in oncology," *Journal of the National Comprehensive Cancer Network*, vol. 20, no. 2, pp. 167–192, 2022.

[4] A. J. Bass, V. Thorsson, I. Shmulevich, and The Cancer Genome Atlas Research Network, "Comprehensive molecular characterization of gastric adenocarcinoma," *Nature*, vol. 513, no. 7517, pp. 202–209, 2014.

[5] Z. Lei, I. B. Tan, K. Das et al., "Identification of molecular subtypes of gastric cancer with different responses to PI3-kinase inhibitors and 5-fluorouracil," *Gastroenterology*, vol. 145, no. 3, pp. 554–565, 2013.

[6] R. Wang, S. Song, K. Harada et al., "Multiplex profiling of peritoneal metastases from gastric adenocarcinoma identified novel targets and molecular subtypes that predict treatment response," *Gut*, vol. 69, no. 1, pp. 18–31, 2020.

[7] S. Ge, X. Xia, C. Ding et al., "A proteomic landscape of diffuse-type gastric cancer," *Nature Communications*, vol. 9, no. 1, p. 1012, 2018.

[8] Y. Tabe, P. L. Lorenzi, and M. Konopleva, "Amino acid metabolism in hematologic malignancies and the era of targeted therapy," *Blood*, vol. 134, no. 13, pp. 1014–1023, 2019.

[9] C. L. Jones, B. M. Stevens, A. D'Alessandro et al., "Inhibition of amino acid metabolism selectively targets human leukemia stem cells," *Cancer Cell*, vol. 34, no. 5, pp. 724–740.e4, 2018.

[10] Z. Li and H. Zhang, "Reprogramming of glucose, fatty acid and amino acid metabolism for cancer progression," *Cellular and Molecular Life Sciences*, vol. 73, no. 2, pp. 377–392, 2016.

[11] M. Butler, L. T. van der Meer, and F. N. van Leeuwen, "Amino acid depletion therapies: starving cancer cells to death," *Trends in Endocrinology and Metabolism*, vol. 32, no. 6, pp. 367–381, 2021.

[12] Y. Bian, W. Li, D. M. Kremer et al., "Cancer SLC43A2 alters T cell methionine metabolism and histone methylation," *Nature*, vol. 585, no. 7824, pp. 277–282, 2020.

[13] S. K. Biswas, "Metabolic reprogramming of immune cells in cancer progression," *Immunity*, vol. 43, no. 3, pp. 435–449, 2015.

[14] H. C. Yoo and J. M. Han, "Amino acid metabolism in cancer drug resistance," *Cell*, vol. 11, no. 1, p. 140, 2022.

[15] L. Luo, W. Sun, W. Zhu et al., "BCAT1 decreases the sensitivity of cancer cells to cisplatin by regulating mTOR-mediated autophagy *via* branched-chain amino acid metabolism," *Cell Death & Disease*, vol. 12, no. 2, p. 169, 2021.

[16] C. K. Stein, P. Qu, J. Epstein et al., "Removing batch effects from purified plasma cell gene expression microarrays with modified ComBat," *BMC Bioinformatics*, vol. 16, no. 1, p. 63, 2015.

[17] M. E. Ritchie, B. Phipson, D. Wu et al., "Limma powers differential expression analyses for RNA-sequencing and microarray studies," *Nucleic Acids Research*, vol. 43, no. 7, article e47, 2015.

[18] H. Zhang, P. Meltzer, and S. Davis, "RCircos: an R package for Circos 2D track plots," *BMC Bioinformatics*, vol. 14, no. 1, 2013.

[19] M. D. Wilkerson and D. N. Hayes, "ConsensusClusterPlus: a class discovery tool with confidence assessments and item tracking," *Bioinformatics*, vol. 26, no. 12, pp. 1572-1573, 2010.

[20] A. Camargo, "PCAtest: testing the statistical significance of principal component analysis in R," *PeerJ*, vol. 10, article e12967, 2022.

[21] S. Hänzelmann, R. Castelo, and J. Guinney, "GSVA: gene set variation analysis for microarray and RNA-seq data," *BMC Bioinformatics*, vol. 14, no. 1, 2013.

[22] L. Zhu, Y. Sun, X. Wang et al., "Survival stratification in childhood rhabdomyosarcoma of the extremities: a derivation and validation study," *Scientific Reports*, vol. 10, no. 1, p. 5684, 2020.

[23] K. Yoshihara, M. Shahmoradgoli, E. Martínez et al., "Inferring tumour purity and stromal and immune cell admixture from expression data," *Nature Communications*, vol. 4, no. 1, p. 2612, 2013.

[24] P. Geeleher, N. Cox, and R. S. Huang, "pRRophetic: an R package for prediction of clinical chemotherapeutic response from tumor gene expression levels," *PLoS One*, vol. 9, no. 9, article e107468, 2014.

[25] Z. Song, Y. Wu, J. Yang, D. Yang, and X. Fang, "Progress in the treatment of advanced gastric cancer," *Tumour Biology*, vol. 39, no. 7, 2017.

[26] E. Ananieva, "Targeting amino acid metabolism in cancer growth and anti-tumor immune response," *World Journal of Biological Chemistry*, vol. 6, no. 4, pp. 281–289, 2015.

[27] N. Liu, F. Shi, L. Yang, W. Liao, and Y. Cao, "Oncogenic viral infection and amino acid metabolism in cancer progression: molecular insights and clinical implications," *Biochimica et*

Biophysica Acta (BBA) - Reviews on Cancer, vol. 1877, no. 3, article 188724, 2022.

[28] J. Cao, X. Yang, S. Chen et al., "The predictive efficacy of tumor mutation burden in immunotherapy across multiple cancer types: a meta-analysis and bioinformatics analysis," *Translational Oncology*, vol. 20, article 101375, 2022.

[29] M. J. M. van Velzen, S. Derks, N. C. T. van Grieken, N. Haj Mohammad, and H. W. M. van Laarhoven, "MSI as a predictive factor for treatment outcome of gastroesophageal adenocarcinoma," *Cancer Treatment Reviews*, vol. 86, article 102024, 2020.

[30] E. L. Lieu, T. Nguyen, S. Rhyne, and J. Kim, "Amino acids in cancer," *Experimental & Molecular Medicine*, vol. 52, no. 1, pp. 15–30, 2020.

[31] N. Muhammad, H. M. Lee, and J. Kim, "Oncology therapeutics targeting the metabolism of amino acids," *Cell*, vol. 9, no. 8, p. 1904, 2020.

[32] E. Pranzini, E. Pardella, P. Paoli, S. M. Fendt, and M. L. Taddei, "Metabolic reprogramming in anticancer drug resistance: a focus on amino acids," *Trends Cancer*, vol. 7, no. 8, pp. 682–699, 2021.

Hindawi

Research Article

The Underlying Mechanism Involved in Gefitinib Resistance and Corresponding Experiment Validation in Lung Cancer

Puwei Song [1,2] Jianghui Zhou,[3] Kaiqin Wu [1], Wenli Wang [1], and Shaorui Gu [1]

[1]*Department of Thoracic Surgery, Shanghai Tongji Hospital, School of Medicine, Tongji University, Shanghai, China*
[2]*Department of Cardiothoracic Surgery, Children's Hospital of Nanjing Medical University, Nanjing, China*
[3]*Department of Thoracic Surgery, Northern Jiangsu People's Hospital Affiliated to Yangzhou University, Yangzhou, China*

Correspondence should be addressed to Kaiqin Wu; kailchin@163.com, Wenli Wang; anderson840913@163.com, and Shaorui Gu; gsr@alumni.tongji.edu.cn

Background. Gefitinib resistance remains a major problem in the treatment of lung cancer. However, the underlying mechanisms involved in gefitinib resistance are largely unclear. *Methods.* Open-accessed data of lung cancer patients were downloaded from The Cancer Genome Atlas Program and Gene Expression Omnibus databases. CCK8, colony formation, and 5-ethynyl-2′-deoxyuridine assays were utilized to evaluate the cell proliferation ability. Transwell and wound-healing assays were utilized to evaluate the cell invasion and migration ability. Quantitative real-time PCR was utilized to detect the RNA level of specific genes. *Results.* Here, we obtained the expression profile data of wild and gefitinib-resistant cells. Combined with the data from the TCGA and GDSC databases, we identified six genes, RNF150, FAT3, ANKRD33, AFF3, CDH2, and BEX1, that were involved in gefitinib resistance in both cell and tissue levels. We found that most of these genes were expressed in the fibroblast of the NSCLC microenvironment. Hence, we also comprehensively investigated the role of fibroblast in the NSCLC microenvironment, including its biological effect and cell interaction. Ultimately, CDH2 was selected for further analysis for its prognosis correlation. In vitro experiments presented the cancer-promoting role of CDH2 in NSCLC. Moreover, cell viability detection showed that the inhibition of CDH2 could significantly decrease the IC50 of gefitinib in NSCLC cells. GSEA showed that CDH2 could significantly affect the pathway activity of PI3K/AKT/mTOR signaling. *Conclusions.* This study is aimed at investigating the underlying mechanism involved in gefitinib resistance to lung cancer. Our research has improved researchers' understanding of gefitinib resistance. Meanwhile, we found that CDH2 could lead to gefitinib resistance through PI3K/AKT/mTOR signaling.

1. Introduction

Lung cancer remains the most prevalent and dangerous malignant tumor worldwide, resulting in over one million related death cases per year [1]. Lung cancer is a multifactorial disease, and its specific mechanism is still unclear, but current research has found that the incidence of lung cancer is often related to environmental factors, lifestyle, genomic differences, and so on [2]. For now, patients at the early stage of the disease can often obtain long-term treatment benefits and a satisfactory prognosis from radical surgery [3]. Unfortunately, many lung cancer patients have already reached the late stages of the disease when they are diagnosed [4]. Lung

cancers that have advanced are mostly treated with chemotherapy. Nonetheless, the effectiveness of chemotherapy is often limited, coupled with cytotoxicity and side effects, which exacerbate the patients' medical burden and quality of life [5].

Gefitinib is suitable for the treatment of locally advanced or metastatic non-small cell lung cancer (NSCLC) that has received chemotherapy or is not appropriate for chemotherapy [6]. Gefitinib can effectively improve the prognosis of patients with advanced NSCLC, and it has also been reported that when combined with chemotherapy, gefitinib can improve the therapy effect on lung cancer patients [7]. In clinical application, gefitinib may have acquired drug

resistance, thus reducing its therapeutic effect [8]. Research has begun to focus on the biological mechanisms involved in gefitinib resistance. Chen et al. noticed that the lncRNA CASC9 could affect gefitinib resistance by epigenetically suppressing DUSP1 [9]. Liu et al. found that METTL3, an m6A methyltransferase, could regulate the gefitinib resistance by inducing autophagy and affecting β-elemene [10]. Cheng and Tong revealed that in NSCLC, the interaction between FLNA and ANXA2 could lead to the resistance of gefitinib through activating Wnt signaling [11]. Hence, exploring the factors influencing gefitinib resistance from the internal biological mechanism of tumors can provide a prospective reference for clinical application.

Here, we obtained the expression profile data of wild and gefitinib-resistant cells. Combined with the data from the TCGA and GDSC databases, we identified six genes, RNF150, FAT3, ANKRD33, AFF3, CDH2, and BEX1, that were involved in gefitinib resistance in both cell and tissue levels. We found that most of these genes were expressed in the fibroblast of the NSCLC microenvironment. Hence, we also comprehensively investigated the role of fibroblast in the NSCLC microenvironment, including its biological effect and cell interaction. Ultimately, CDH2 was selected for further analysis for its prognosis correlation. In vitro experiments presented the cancer-promoting role of CDH2 in NSCLC. Moreover, cell viability detection showed that the inhibition of CDH2 could significantly decrease the IC50 of gefitinib in NSCLC cells. We noticed that CDH2 could lead to gefitinib resistance through PI3K/AKT/mTOR signaling.

2. Methods

2.1. Download and Collection of Public Data from The Cancer Genome Atlas Program (TCGA). The TCGA database provides the gene expression data and clinical information of NSCLC patients, which was downloaded for the analysis (524 samples from TCGA-LUAD and 503 samples from TCGA-LUSC). The initial gene expression data of a single sample was in STAR counts format and was summarized in R language and converted to TPM. Clinical data are organized by a Perl script written by the author. Before data analysis, data preprocessing is used to improve data quality. Its brief process includes annotation of the ENSG id, data standardization, and log2 conversion. The IC50 data of gefitinib was obtained from the Genomics of Drug Sensitivity in Cancer (GDSC) database [12].

2.2. Public Data from Gene Expression Omnibus (GEO) Database. The GSE123066 project was selected, and its data was obtained from the GEO database. GSE123066 provides the total RNA data sequenced from wild and gefitinib-resistant NSCLC cell lines. Data were directly downloaded from the "Series Matrix File(s)" link. Further patient information including gender, age, stage, and survival data is provided in Supplemental Table 1.

2.3. Differentially Expression Gene (DEGs) Analysis. We used the limma package for DEG analysis based on the detailed threshold [13].

2.4. Investigation of the Biological Aspect. Gene Ontology (GO) and Kyoto Encyclopedia of Genes and Genomes (KEGG) were conducted for biological investigation [14]. Gene set enrichment analysis (GSEA) was utilized to identify the biological differences between the two groups based on the hallmark pathway set [15].

2.5. Prognosis Evaluation. The evaluation of patient prognosis was completed using the Kaplan-Meier (KM) survival curves.

2.6. Single-Cell Analysis. The expression pattern of specific genes at the single-cell level and potential cell interactions was evaluated using the TSICH [16].

2.7. Cell Culture. The cell lines used include BEAS-2B, H441, H1299, and A549. All these cells were cultured in the DMEM culture medium under standard conditions.

2.8. Quantitative Real-Time PCR (qRT-PCR). The whole process of qRT-PCR was conducted following the standard protocol [17]. The primers used were as follows: CDH2, forward primer, 5′-TCAGGCGTCTGTAGAGGCTT-3′, reverse primer, 5′-ATGCACATCCTTCGATAAGACTG-3′.

2.9. Cell Transfection. The whole process of cell transfection was conducted following the standard protocol [17]. The sh-CDH2 and control plasmids were obtained from Genechem, Shanghai, China.

2.10. Cell Proliferation Assays. Cell proliferation ability was evaluated using the CCK8, colony formation, and 5-ethynyl-2′-deoxyuridine (EdU) assays. The whole process of qRT-PCR was conducted following the standard protocol [18, 19].

2.11. Transwell Assay. The whole process of transwell assay was conducted following the standard protocol [20].

2.12. Wound-Healing Assay. The whole process of the wound-healing assay was conducted following the standard protocol [20].

2.13. Detection of Cell Viability. The whole process of cell viability detection was conducted following the standard protocol [18].

2.14. Statistical Analysis. The statistical analysis was conducted in R, GraphPad Prism 8, and SPSS software. The 0.05 was set as the statistical threshold. For the comparison of two groups using Wilcoxon's rank-sum tests and the comparison between continuous variables using Wilcoxon's rank-sum tests, Wilcoxon's test was used to examine statistical significance.

3. Results

3.1. Identification of the Genes Contributing to Gefitinib Resistance and Their Biological Role. Through the limma package, we identified the DEGs between the wild and gefitinib-resistant NSCLC cell lines, which are shown in Figure 1(a). Totally, 476 downregulated and 322 upregulated
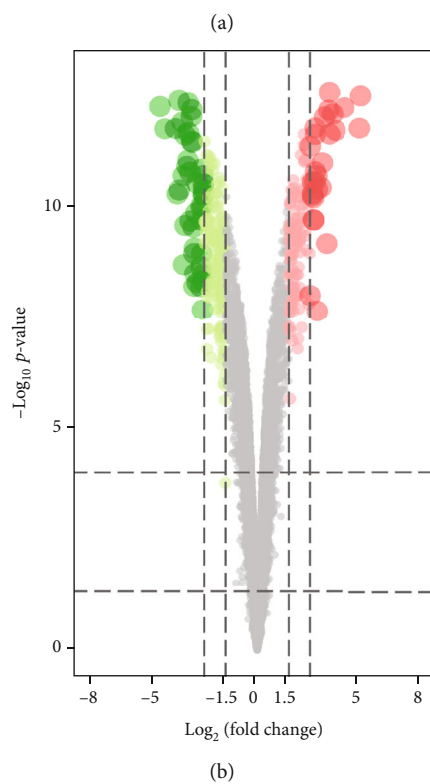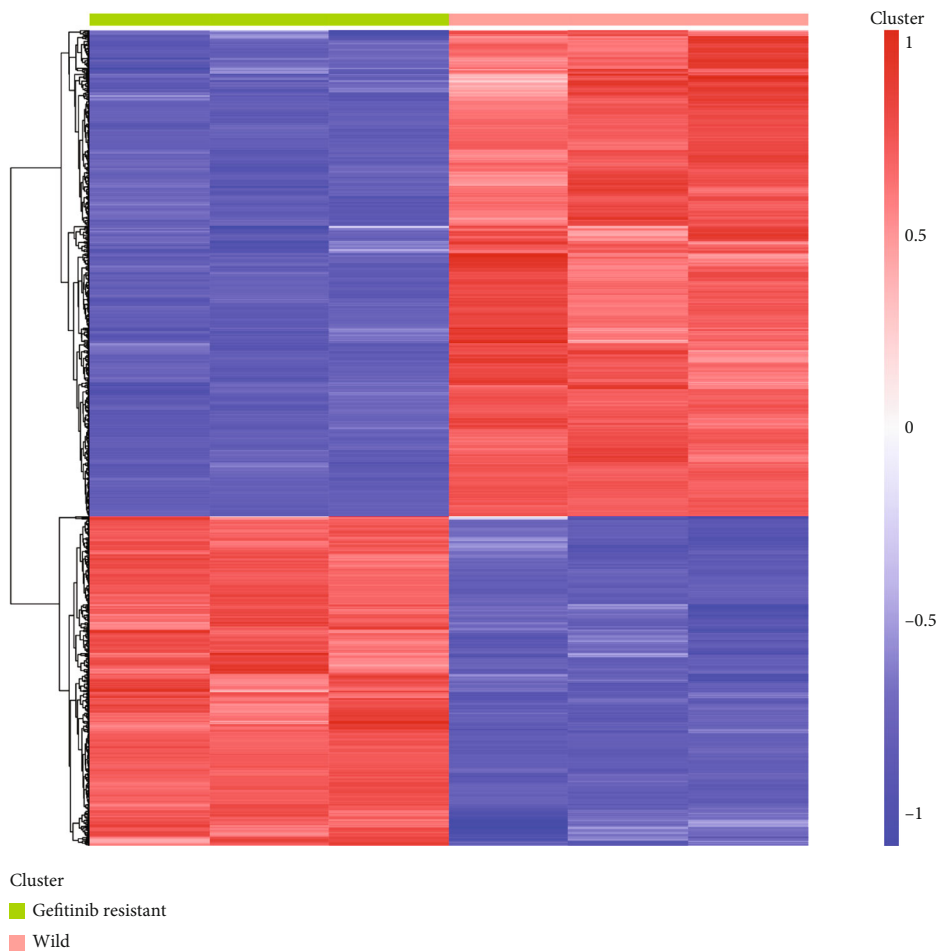
(a)

(b)

Figure 1: Continued.
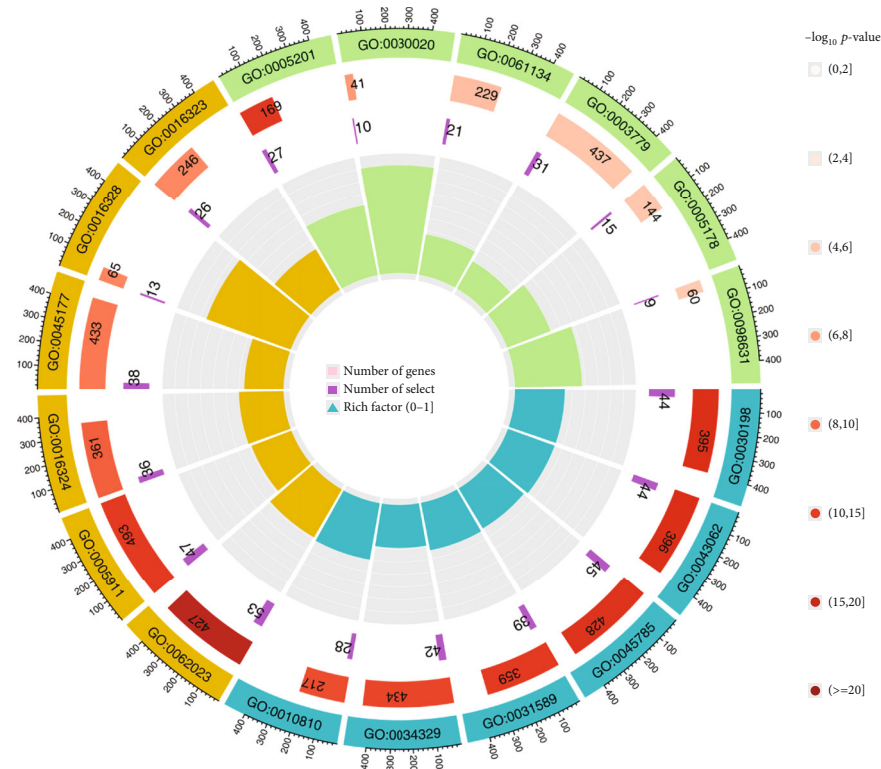
(c)
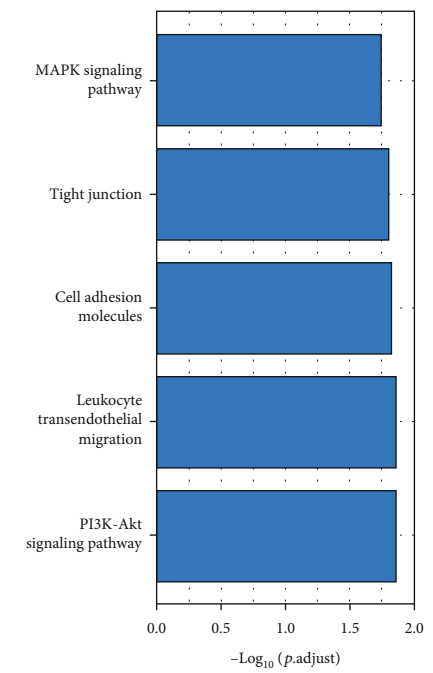
(d)

FIGURE 1: Collection of the molecules involved in gefitinib resistance. Notes: (a) Heatmap was used to present the expression pattern of DEGs between the wild and gefitinib-resistant NSCLC cell lines. (b) 476 downregulated and 322 upregulated molecules were identified as involved in the gefitinib resistance in the cell level. (c) GO analysis of these DEGs. (d) KEGG analysis of these DEGs.

(a)

(b)

(c)

Figure 2: Continued.

(d)

(e)

FIGURE 2: Continued.

ANKRD33

log (TPM/10+1)

	CD4Tconv	Treg	Tprolif	CD8T	CD8Tex	NK	B	Plasma	DC	Mono/Macro	Mast	Neutrophils	Endothelial	Fibroblasts	Epithelial	Malignant	Oligodendrocyte	Alveolar
NSCLC_GSE127465	0.01				0	0.03	0	0.01	0.01	0.01	0.03	0.01	0.03	0.01		0.01		
NSCLC_GSE131907	0			0	0		0	0	0	0	0		0	0	0		0	
NSCLC_GSE148071			0	0			0		0				0	0	0	0		0
NSCLC_GSE99254	0	0.01	0	0	0					0.5								

(f)

CDH2

log (TPM/10+1)

	CD4Tconv	Treg	Tprolif	CD8T	CD8Tex	NK	B	Plasma	DC	Mono/Macro	Mast	Endothelial	Fibroblasts	Myofibroblasts	Epithelial	Malignant	Alveolar
NSCLC_EMTAB6149	0	0		0	0		0	0		0	0	0	0			0	0
NSCLC_GSE127465	0			0	0	0	0	0	0	0	0	0	0.02			0	
NSCLC_GSE131907	0			0	0		0	0.03	0	0	0	0.01	0.01		0.02		
NSCLC_GSE139555	0	0	0	0	0	0	0	0	0	0							
NSCLC_GSE146100	0	0		0		0	0		0.02	0	0	0	0.06		0.01		
NSCLC_GSE148071			0	0			0		0		0	0.01			0	0	0
NSCLC_GSE149655				0				0	0	0	0.01	0				0	
NSCLC_GSE153935			0	0	0		0		0	0	0	0	0.04	0		0	
NSCLC_GSE162498	0	0	0	0	0	0	0		0						0		
NSCLC_GSE176021_aPD1	0	0	0	0	0	0.1	0		0								
NSCLC_GSE99254	0	0	0	0	0					0.03							

(g)

Figure 2: Continued.

BEX1   log (TPM/10+1)

	CD4Tconv	Treg	Tprolif	CD8T	CD8Tex	NK	B	Plasma	DC	Mono/Macro	Mast	Endothelial	Fibroblasts	Myofibroblasts	Epithelial	Malignant	Alveolar
NSCLC_EMTAB6149	0	0		0	0		0	0		0	0	0	0			0	0
NSCLC_GSE127465	0.02			0.01	0		0.02	0	0.02	0.03	0.07	0.03	0.02			0.03	
NSCLC_GSE131907	0.02			0.01	0.02		0.02	0.07	0.04	0.04	0.02	0.19	0.05		0.14		
NSCLC_GSE139555	0.01	0.02	0.02	0	0	0	0.01	0	0	0.02							
NSCLC_GSE146100	0.01	0		0		0	0		0.02	0.01	0	0	0.06		0.02		
NSCLC_GSE148071			0.02	0				0		0.02	0	0	0.04		0	0.13	0
NSCLC_GSE149655					0.01					0	0.04	0.33	0	0.32			0.03
NSCLC_GSE150660	0			0.01	0.01			0		0.02					0		
NSCLC_GSE153935			0.13	0.05	0.04			0.1		0.04	0.03	0.03	0.02	0.14	0.01		0.12
NSCLC_GSE162498	0.01	0.01	0.02	0.01		0.01				0.02					0.07		
NSCLC_GSE176021_aPD1	0.01	0.01	0.02	0.01	0	0	0.01		0.02								
NSCLC_GSE179373	0.01			0.01	0												
NSCLC_GSE99254	0.01	0.01	0.04	0	0.01					0.27							

Scale: 0 – 0.1 – 0.2 – 0.3 – 0.4

(h)

FAT3   log (TPM/10+1)

	CD4Tconv	Treg	Tprolif	CD8T	CD8Tex	NK	B	Plasma	DC	Mono/Macro	Mast	Endothelial	Fibroblasts	Myofibroblasts	Epithelial	Malignant	Alveolar
NSCLC_EMTAB6149	0	0		0	0		0	0		0	0	0	0.01			0	0
NSCLC_GSE127465	0				0	0.01	0	0	0	0	0	0	0			0	
NSCLC_GSE131907	0			0			0	0	0	0	0	0	0.01		0		
NSCLC_GSE146100	0	0		0		0	0		0	0	0	0	0.04		0		
NSCLC_GSE148071			0	0				0		0		0	0		0	0	0
NSCLC_GSE149655					0					0	0	0	0.03	0.01			0
NSCLC_GSE153935			0	0	0			0		0	0	0	0	0	0		0
NSCLC_GSE162498	0	0	0	0		0				0					0		
NSCLC_GSE176021_aPD1	0	0	0	0	0	0	0		0								
NSCLC_GSE99254	0	0	0	0	0					0.03							

Scale: 0 – 0.01 – 0.02 – 0.03 – 0.04

(i)

Figure 2: Continued.

RNF150

log (TPM/10+1)

	CD4Tconv	Treg	Tprolif	CD8T	CD8Tex	NK	B	Plasma	DC	Mono/Macro	Mast	Endothelial	Fibroblasts	Myofibroblasts	Epithelial	Malignant	Alveolar
NSCLC_EMTAB6149	0	0		0	0		0	0		0	0	0	0			0	0
NSCLC_GSE127465	0			0	0	0	0	0	0	0.01	0	0	0.02			0.01	
NSCLC_GSE131907	0			0			0	0	0	0		0	0.01		0		
NSCLC_GSE146100	0	0		0		0	0	0.01	0	0	0	0.07		0.01			
NSCLC_GSE148071		0	0				0		0		0	0.01		0	0	0	
NSCLC_GSE149655				0					0	0	0	0.01	0.02			0	
NSCLC_GSE153935			0	0			0		0	0	0	0	0.01	0.01		0	
NSCLC_GSE162498	0	0	0	0		0			0				0				
NSCLC_GSE176021_aPD1	0	0	0	0	0	0	0		0								
NSCLC_GSE99254	0	0	0	0	0				0.01								

0.075 — 0.05 — 0.025 — 0

(j)

FIGURE 2: Identification of the hub genes. Notes: (a) DEG analysis between the top 50 patients with the highest or the lowest IC50 (LUAD). (b) DEG analysis between the top 50 patients with the highest or the lowest IC50 (LUSC). (c) The intersection of GSE123066, TCGA-LUAD, and TCGA-LUAD identified six genes. (d) The expression level of RNF150, FAT3, ANKRD33, AFF3, CDH2, and BEX1 in wild and gefitinib resistance cells. (e–j) The single-cell level of RNF150, FAT3, ANKRD33, AFF3, CDH2, and BEX1.

molecules were identified as involved in the gefitinib resistance in the cell level (Figure 1(b)). GO analysis revealed that these DEGs were mainly associated with GO:0005201, GO:0030020, GO:0061134, GO:0003779, GO:0005178, GO:0098631, GO:0030198, GO:0043062, GO:0045785, GO:0031589, GO:0034329, GO:0010810, GO:0062023, GO:0005911, GO:0016324, GO:0045177, GO:0016328, and GO:0016323 (Figure 1(c)), and all the results of GO analysis were provided in Supplemental Table 2. KEGG analysis indicated that these DEGs were primarily enriched in the MAPK signaling pathway, PI3K/AKT signaling pathway, leukocyte transendothelial migration, cell adhesion molecules, and tight junction (Figure 1(d)).

3.2. RNF150, FAT3, ANKRD33, AFF3, CDH2, and BEX1 Were Correlated with Gefitinib Resistance in Both Cell and Tissue Levels. We next obtained the IC50 data of gefitinib in the GDSC database (lung cancer). Then, we performed a DEG analysis between the top 50 patients with the highest or lowest IC50. Finally, 1711 upregulated genes were identified in LUAD (Figure 2(a)) and 2302 upregulated genes were identified in LUSC (Figure 2(b)). The intersection of GSE123066, TCGA-LUAD, and TCGA-LUAD identified six genes, RNF150, FAT3, ANKRD33, AFF3, CDH2, and BEX1, indicating that these genes were involved in gefitinib resistance in both cell and tissue levels (Figure 2(c)). Results indicated that all these genes were overexpressed in the gefitinib-resistant cells (Figure 2(d)). Single-cell analysis revealed that AFF3 was primarily expressed in B and endothe-lial cells (Figure 2(e)); ANKRD33 was primarily expressed in mono/macrocells (Figure 2(f)); CDH2 was primarily expressed in fibroblast cells (Figure 2(g)); BEX1 was primarily expressed in mono/macrocells (Figure 2(h)); FAT3 was primarily expressed in mono/macro and fibroblast cells (Figure 2(i)); RNF150 was primarily expressed in fibroblast l cells (Figure 2(j)).

3.3. Role of Fibroblast in NSCLC Microenvironment. Considering that most of these six genes were expressed in fibroblast, following this, we investigated the role of fibroblasts in the NSCLC microenvironment. In the EMTAB-6149 cohort, we found that in KEGG analysis, fibroblast was correlated with upregulated focal adhesion, ECM receptor interaction, dilated cardiomyopathy, and B cell receptor signaling pathway while downregulating ribosome, cell adhesion molecules (CAMs), leishmania infection, and some immune-related pathway activities (Figures 3(a) and 3(b)). As for the hallmark pathway, we noticed that fibroblast was positively correlated with UV response DN, adipogenesis, epithelial_mesenchymal_transition (EMT), angiogenesis, myogenesis, coagulation, and hypoxia (Figure 3(c)), while negatively correlated with mTORC signaling, E2F targets, allograft rejection, and the interferon alpha response (Figure 3(d)). Cell interaction analysis showed that the fibroblast could interact with malignant and endothelial cells (Figure 3(e)). In the LUAD-GSE146100 cohort, fibroblasts were positively correlated with focal adhesion, ECM receptor interaction, dilated cardiomyopathy, complement, and

(a)

Figure 3: Continued.

(b)
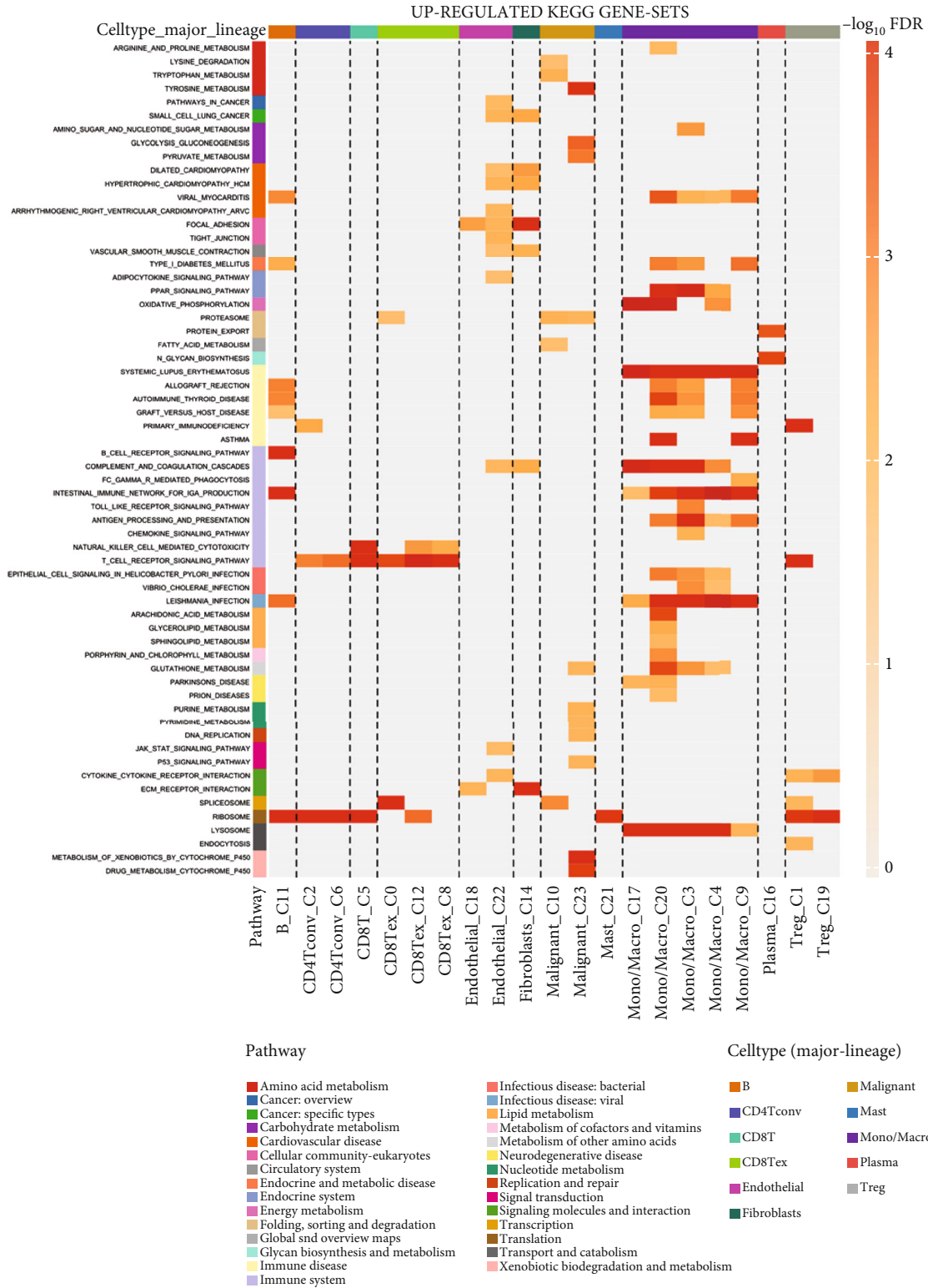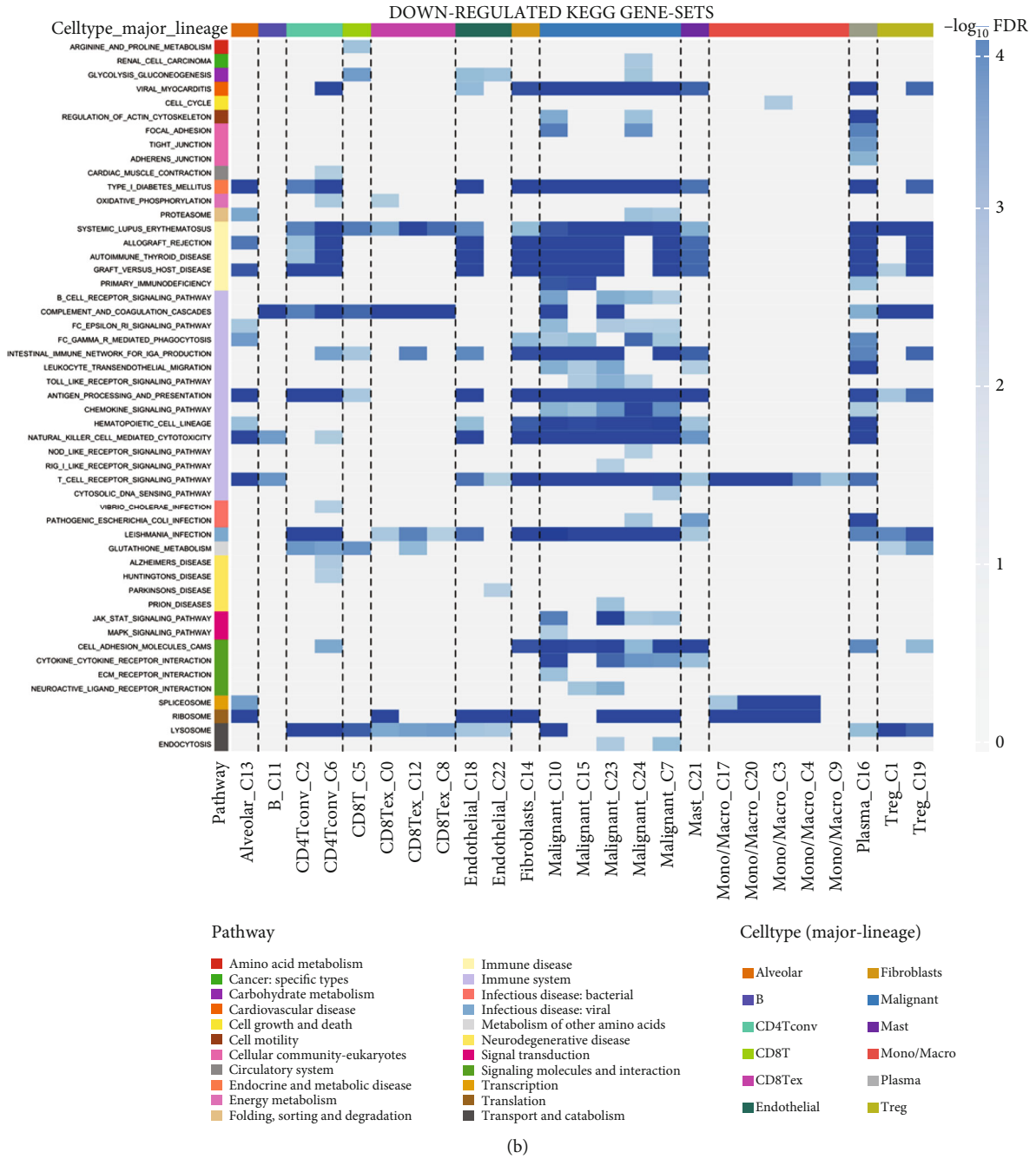
FIGURE 3: Continued.

(c)
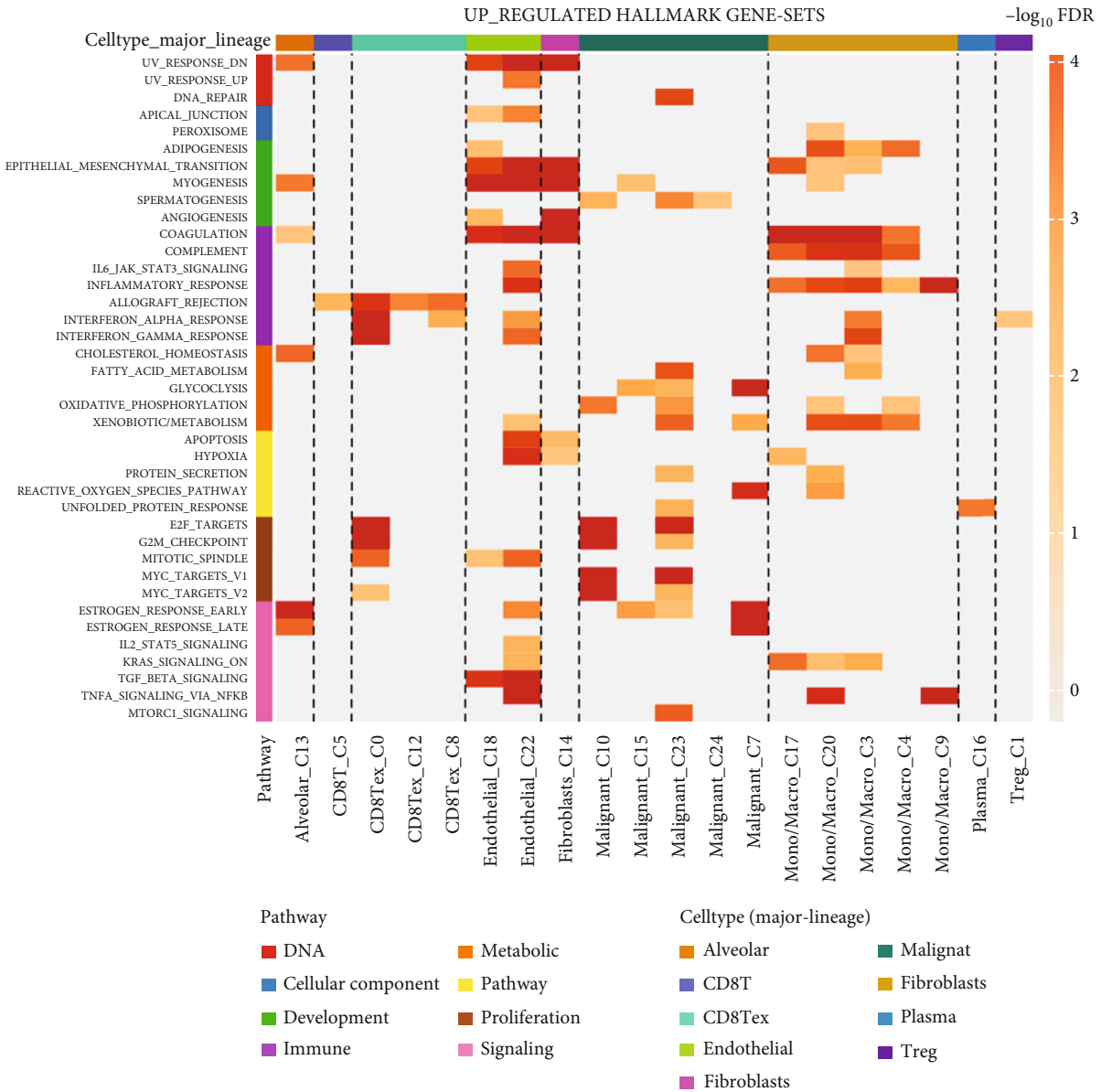
FIGURE 3: Continued.

(d)
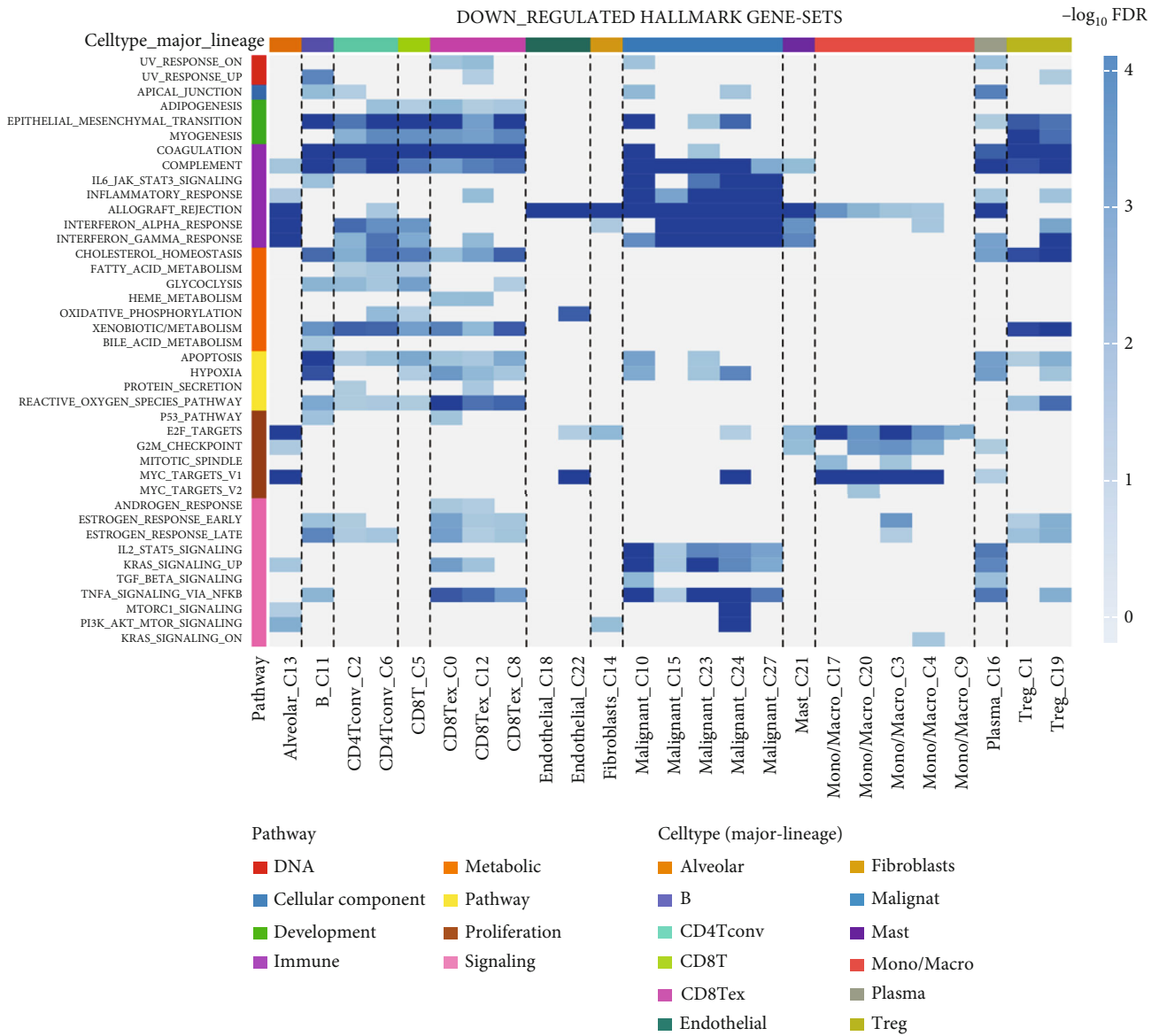
Figure 3: Continued.

(e)

FIGURE 3: Continued.

(f)
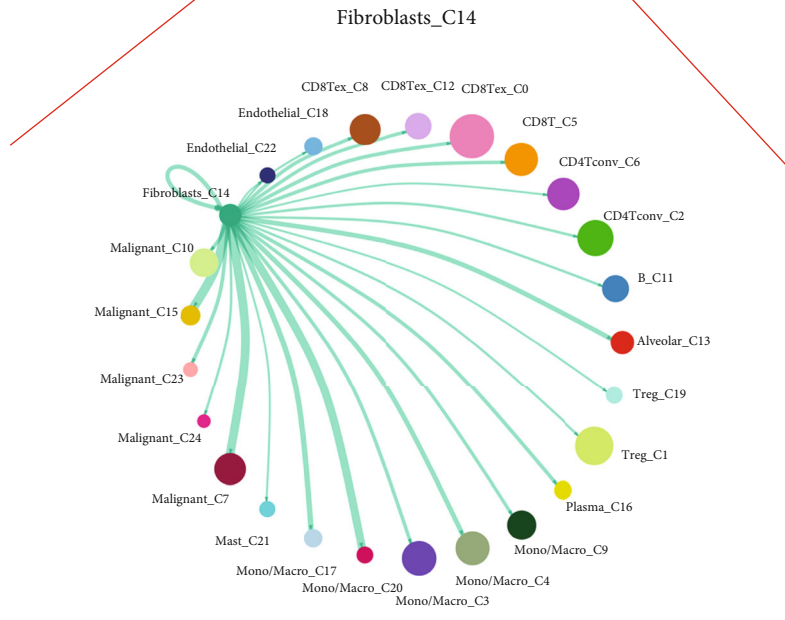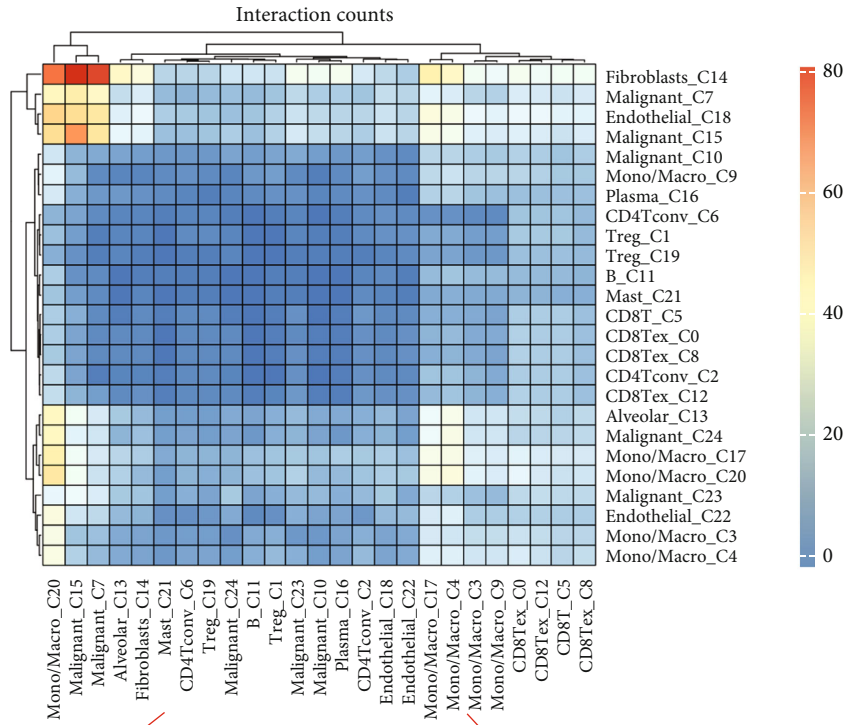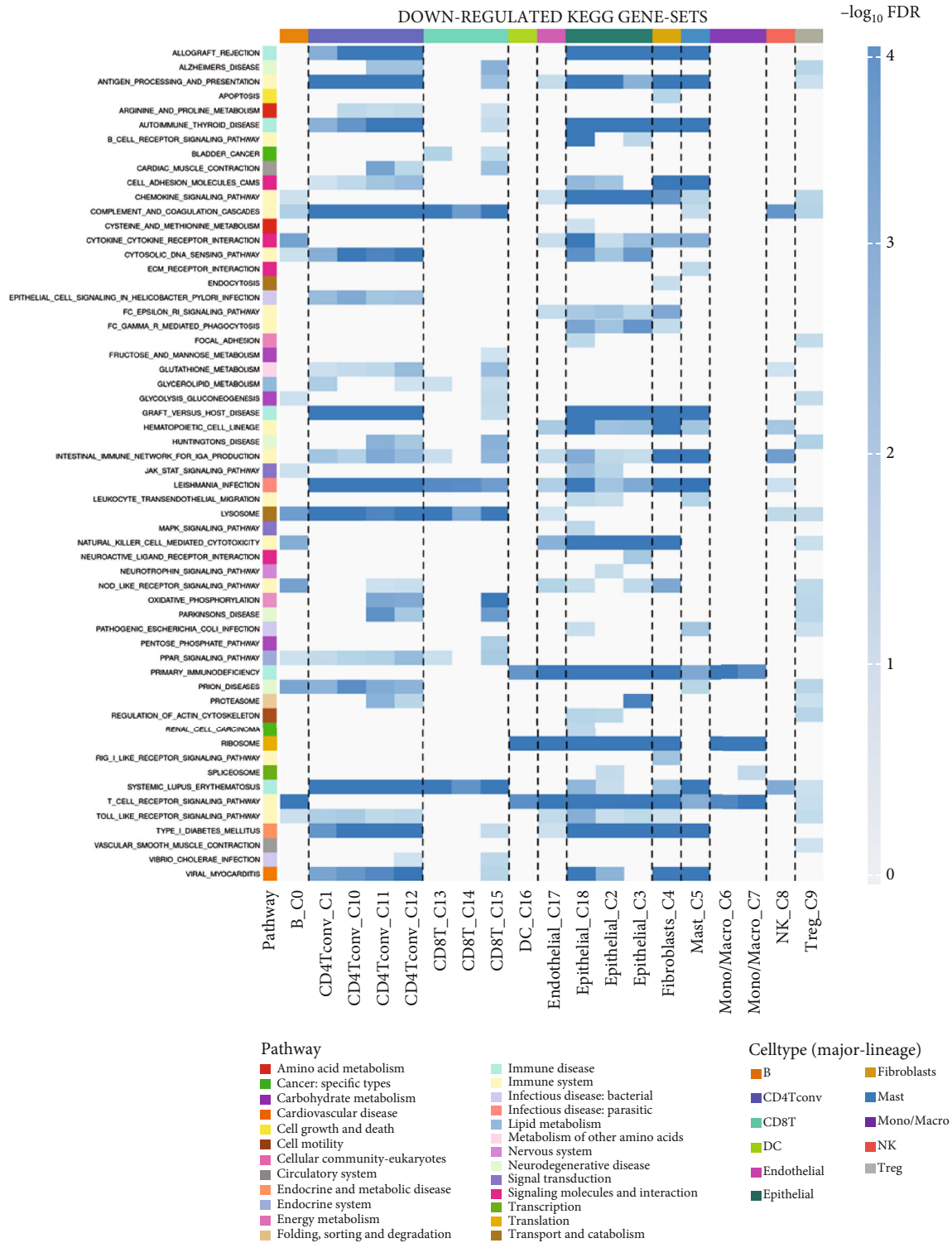
Figure 3: Continued.

FIGURE 3: Continued.

(h)

Figure 3: Continued.

(i)
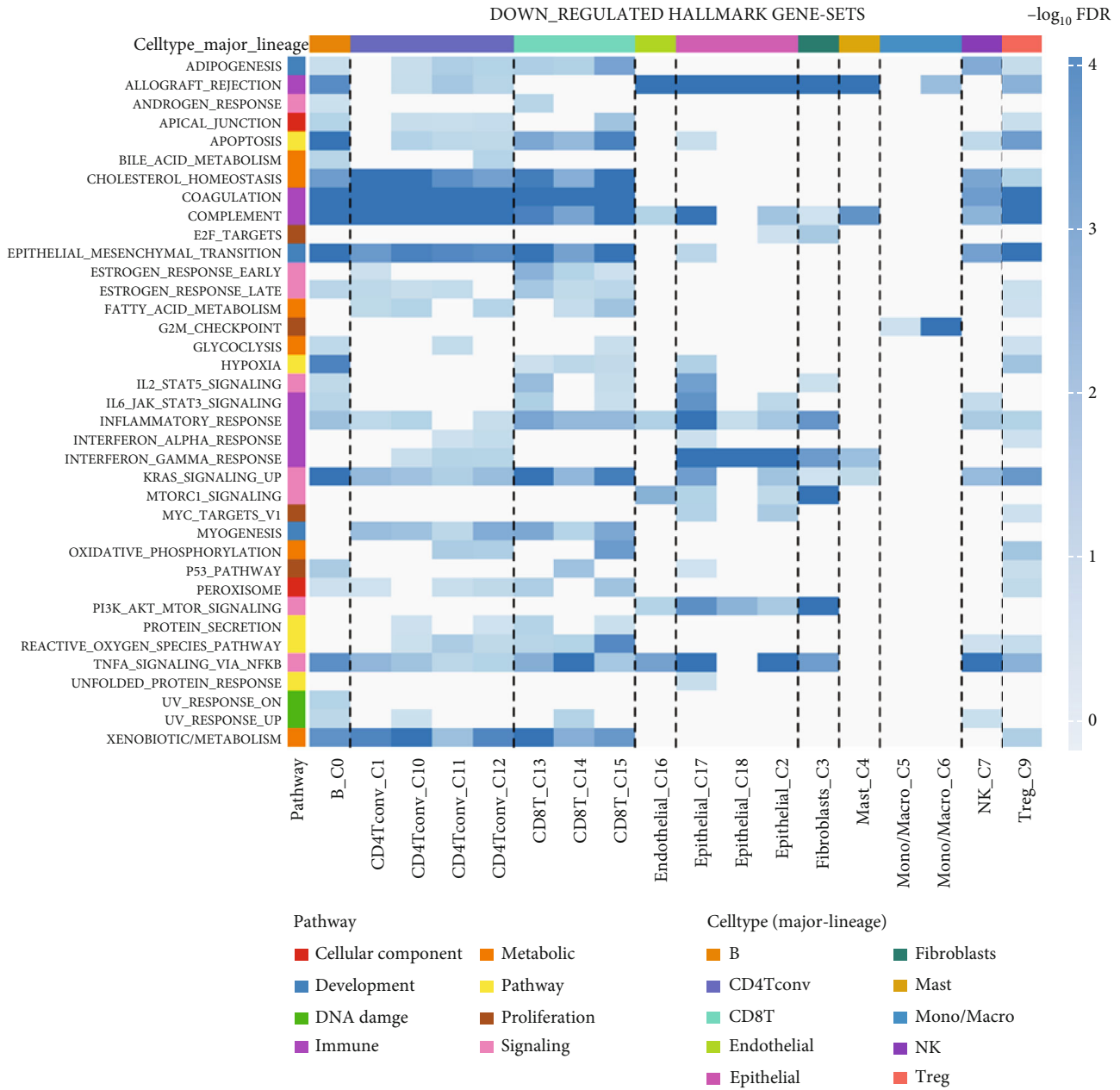
FIGURE 3: Continued.
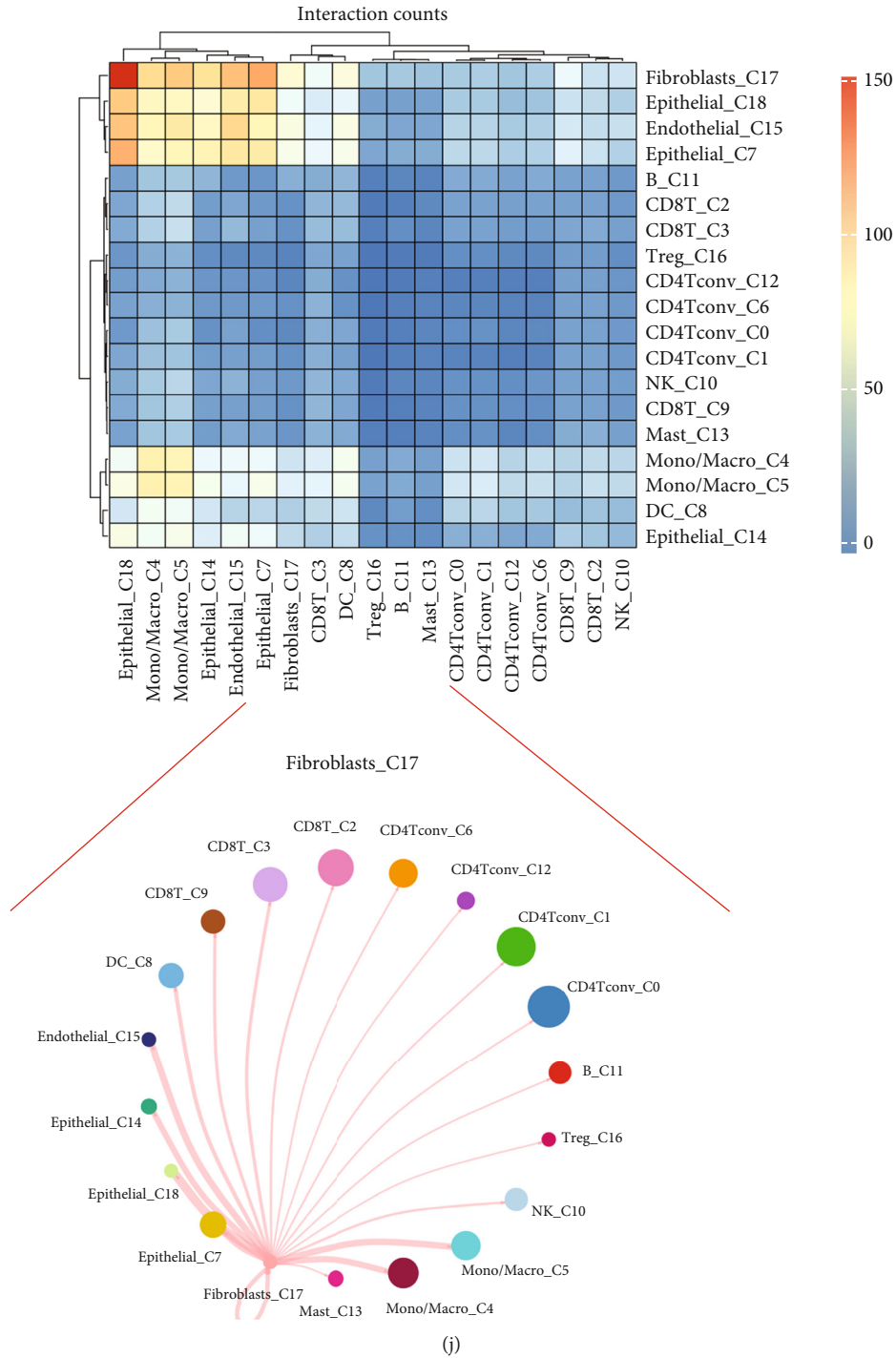
Figure 3: Role of CAFs in NSCLC microenvironment. Notes: (a) The upregulated KEGG terms regulated by CAFs (EMTAB-6149 cohort). (b) The downregulated KEGG terms regulated by CAFs (EMTAB-6149 cohort). (c) The upregulated hallmark terms regulated by CAFs (EMTAB-6149 cohort). (d) The downregulated KEGG terms regulated by CAFs (EMTAB-6149 cohort). (e) Cell interaction in EMTAB-6149 cohort. (f) The upregulated KEGG terms regulated by CAFs (LUAD-GSE146100 cohort). (g) The downregulated KEGG terms regulated by CAFs (LUAD-GSE146100 cohort). (h) The upregulated hallmark terms regulated by CAFs (LUAD-GSE146100 cohort). (i) The downregulated KEGG terms regulated by CAFs (LUAD-GSE146100 cohort). (j) Cell interaction in EMTAB-6149 cohort.

coagulation cascades while negatively correlated with many immune-related pathways (Figures 3(f) and 3(g)). For hallmark analysis, fibroblasts were positively correlated with angiogenesis, apical junction, apoptosis, coagulation, EMT, myogenesis, and UV response DN, yet negatively correlated with allograft rejection, IL2/STAT5 signaling, complement, mTORC1 signaling, and PI3K/AKT/mTOR signaling (Figures 3(h) and 3(i)). Cell interaction analysis

(a)

(b)

(c)

(d)

(e)

Figure 4: Continued.

(f)
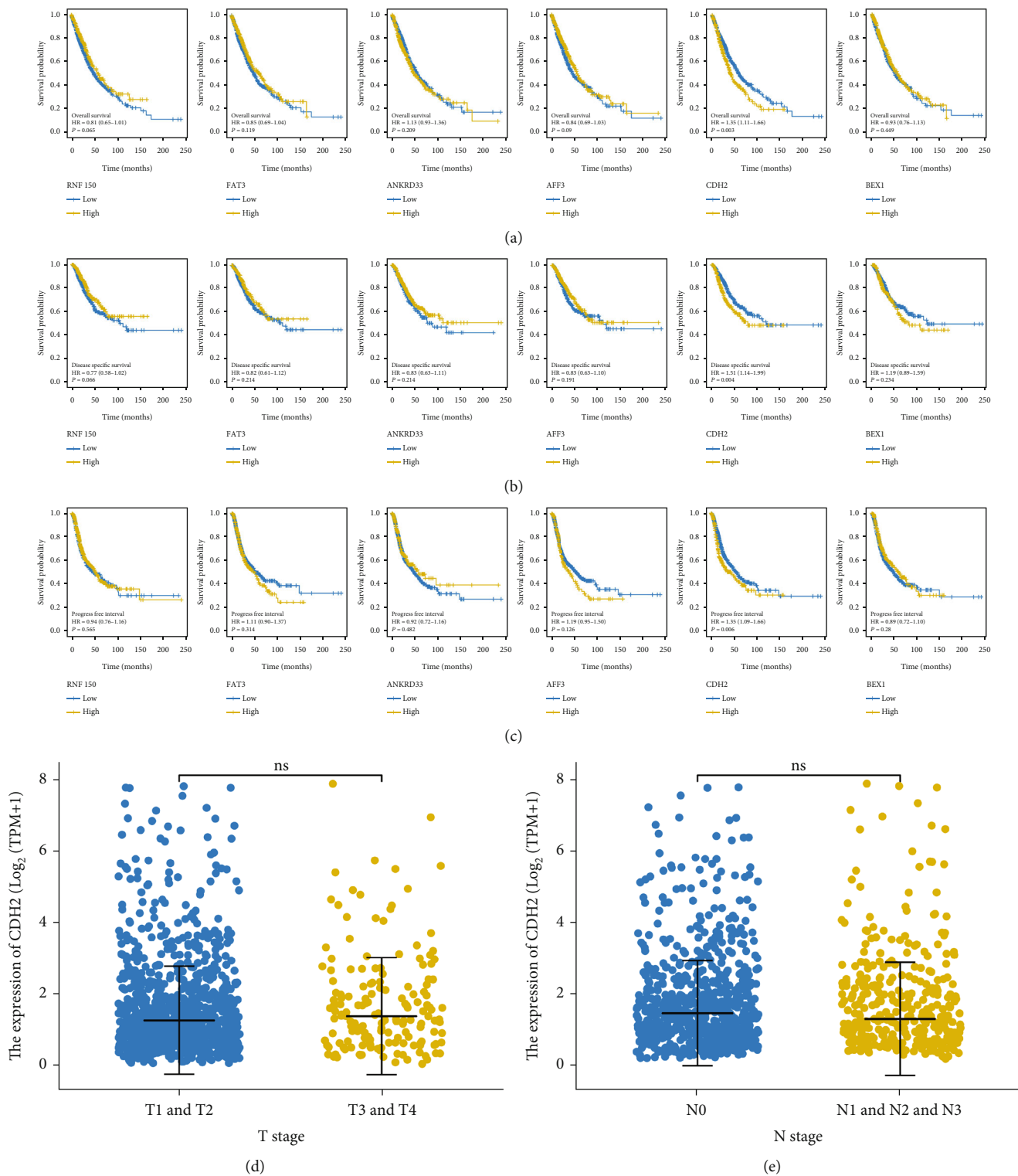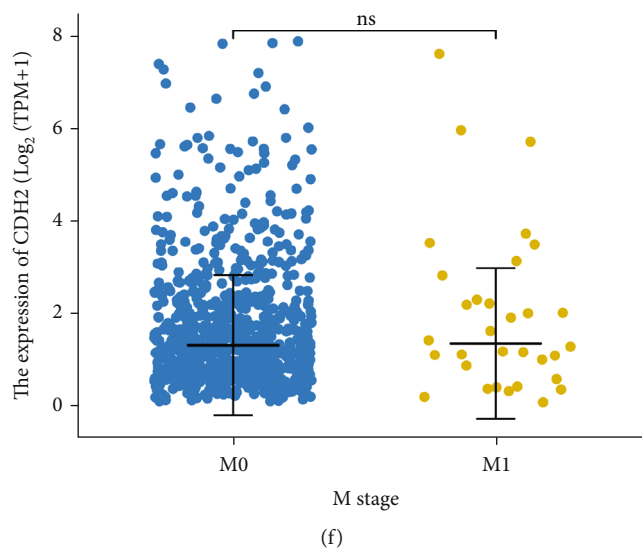
FIGURE 4: Prognosis analysis. Notes: (a) Performance of overall survival of RNF150, FAT3, ANKRD33, AFF3, CDH2, and BEX1. (b) Performance of disease free survival of RNF150, FAT3, ANKRD33, AFF3, CDH2, and BEX1. (c) Performance of progression free survival of RNF150, FAT3, ANKRD33, AFF3, CDH2, and BEX1. (d–f) Expression level of CDH2 in patients with different clinical features.

indicated that in the LUAD-GSE146100 cohort, fibroblasts mainly interacted with epithelial and endothelial cells (Figure 3(j)).

3.4. Prognosis Analysis of RNF150, FAT3, ANKRD33, AFF3, CDH2, and BEX1.

Then, we tried to explore the clinical value of RNF150, FAT3, ANKRD33, AFF3, CDH2, and BEX1. KM survival curves indicated that only CDH2 significantly affects patient survival (Figure 4(a), overall survival, HR = 1.35; Figure 4(b), disease-free survival, HR = 1.51; Figure 4(c), progression-free survival, HR = 1.35). However, no significant difference was found in patients with better or worse clinical features (Figures 4(d)–4(f)).

3.5. CDH2 Facilitates the Malignant Biological Behaviors of NSCLC Cells.

We next investigated the influence of CDH2 on NSCLC biological behaviors. Data of TCGA indicated that CDH2 was overexpressed in NSCLC tissue (Figure 5(a)). Also, in the cell level, the NSCLC cell lines had a higher CDH2 expression compared to the normal cell line (Figure 5(b)). The result of qRT-PCR demonstrated that the knockdown efficiency of sh#2 might have the best performance, therefore it was selected for further analysis (Figure 5(c)). The CCK8 assay indicated that the suppression of CDH2 in NSCLC cells could inhibit the proliferation ability (Figures 5(d) and 5(e)). The same result was also observed through colony formation and EdU assay (Figures 5(f) and 5(g)). A transwell assay was applied to evaluate the invasion and migration abilities of NSCLC cells. Results indicated that the inhibition of CDH2 could remarkably reduce the invasion and migration cells per filled compared to the control group (Figure 6(a)). The wound-healing assay showed that the inhibition of CDH2 could significantly hamper the cell mobility of NSCLC cells (Figure 6(b)).

3.6. CDH2 Lead to Gefitinib Resistance through PI3K/AKT/mTOR Signaling.

We next added gefitinib to the CDH2-inhibited and control cells. Cell viability detection showed that the inhibition of CDH2 could significantly decrease the IC50 of gefitinib in both A549 and H1299 cells (Figure 7(a): A549, sh#ctl, IC50 = 18.46, sh#2, IC50 = 13.70; Figure 7(b): H1299, sh#ctl, IC50 = 18.46, sh#2, IC50 = 13.70). GSEA showed that CDH2 could significantly affect the pathway activity of PI3K/AKT/mTOR signaling (Figure 7(c)). The previous study indicated that the PI3K/AKT/mTOR pathway could affect the gefitinib resistance. Therefore, we tried to evaluate whether CDH2 could affect the pathway activity of PI3K/AKT/mTOR signaling.

4. Discussion

Although the reform of medical technology has brought high-quality medical services, lung cancer is still facing the threat of a high incidence rate and mortality [21]. In clinical practice, early detection often enables patients to undergo radical surgery at the early stage of the disease and obtain long-term treatment benefits [22]. However, since the early symptoms are not obvious, many lung cancer patients have already had disease progression at the time of initial diagnosis and lost the best opportunity for surgery [23]. Gefitinib can improve the prognosis of advanced NSCLC patients, but it is still limited by acquired drug resistance. For several years now, a crucial role has been played in bioinformatics analysis in cancer research [24–26]. The objective of this study was to determine the underlying mechanism behind lung cancer resistance to gefitinib through bioinformatics analysis and corresponding experiment validation.

Here, we obtained the expression profile data of wild and gefitinib-resistant cells. Combined with the data from the

(a)

(b)

(c)

FIGURE 5: Continued.

(d)

(e)

(f)

Figure 5: Continued.

(g)
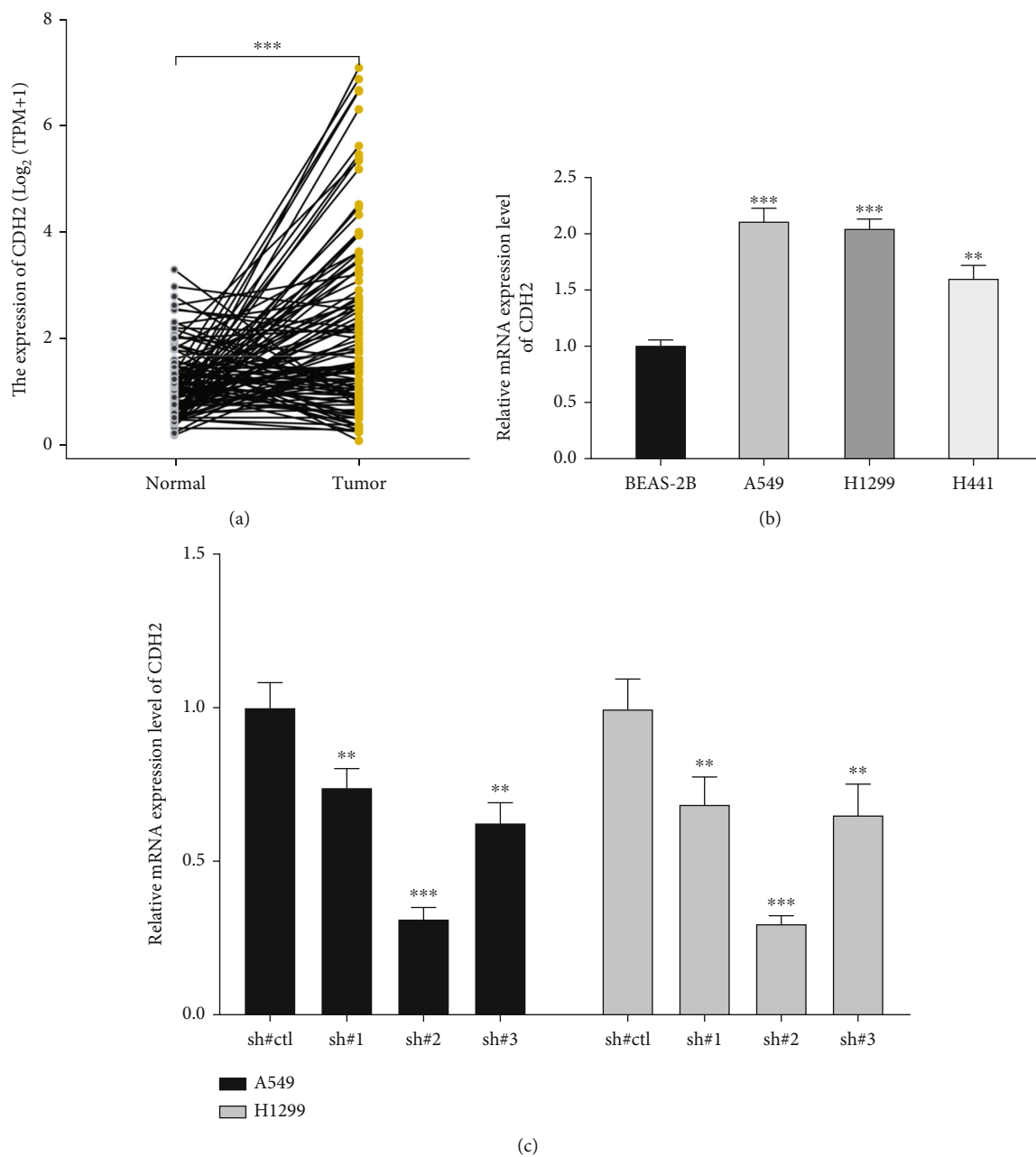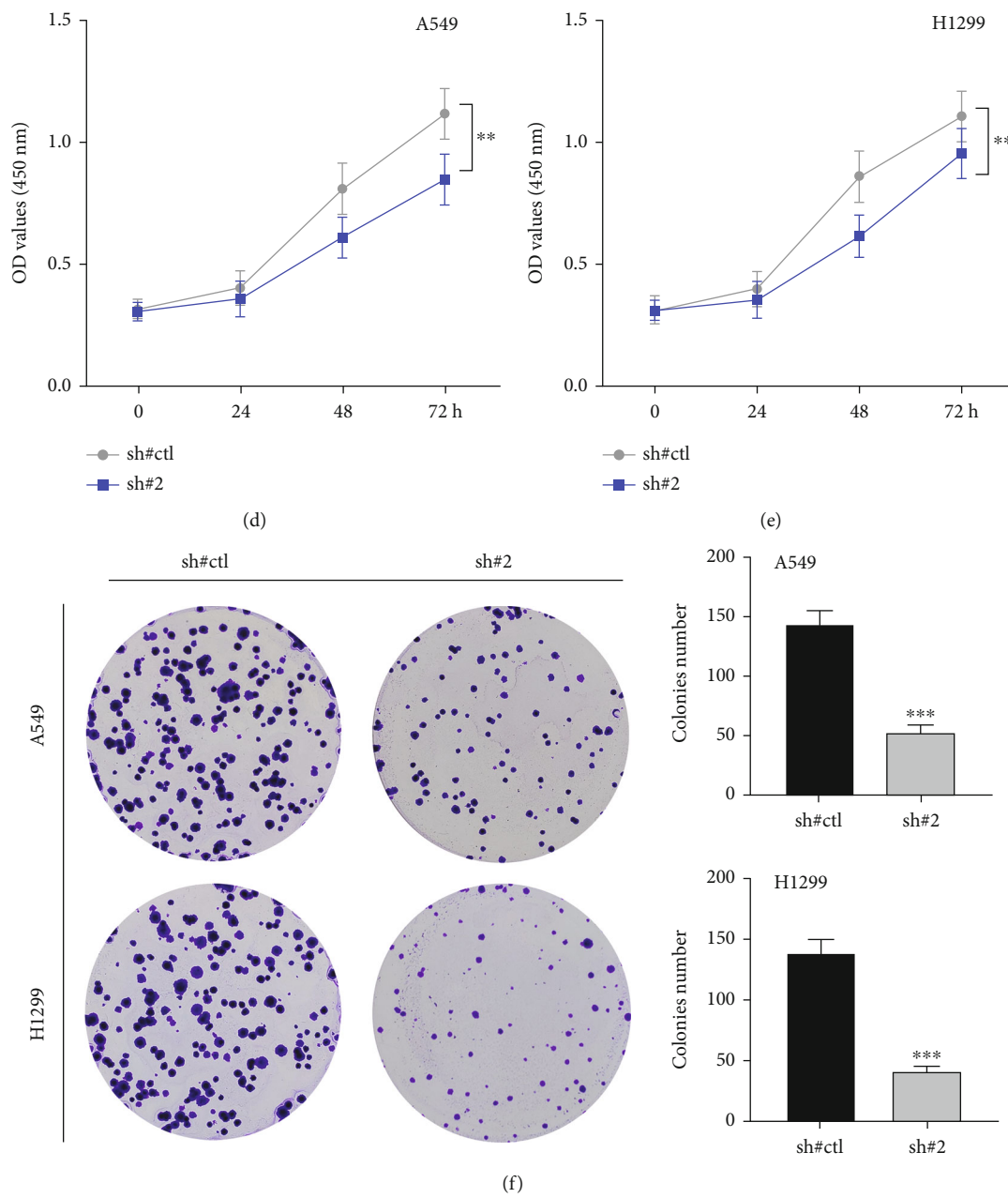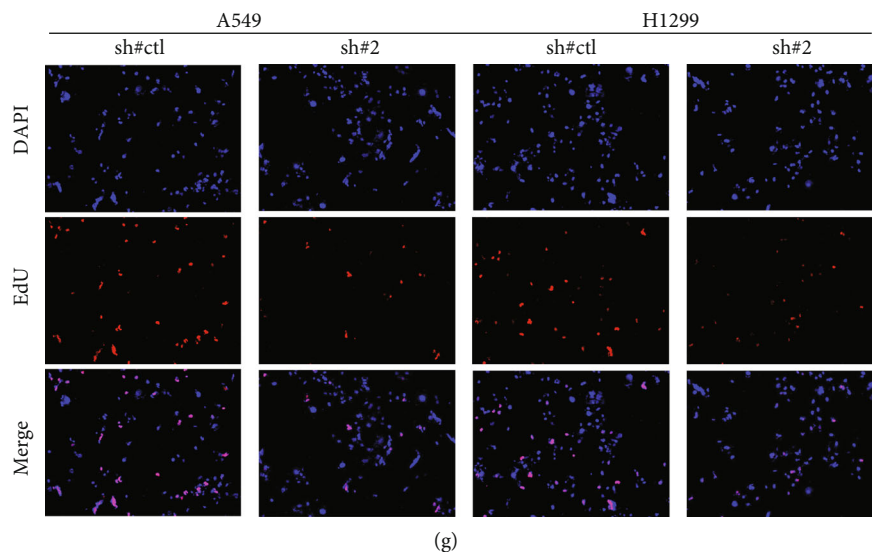
FIGURE 5: CDH2 promotes the cell proliferation of NSCLC. Notes: (a) The expression level of CDH2 in paired NSCLC tissue. (b) Expression level of CDH2 in NSCLC cells. (c) Knockdown efficiency of CDH2. (d, e) CCK8 assay was performed in sh-CDH2 and control cells. (f) Colony formation assay was performed in sh-CDH2 and control cells. (g) EdU assay was performed in sh-CDH2 and control cells.

(a)

(b)
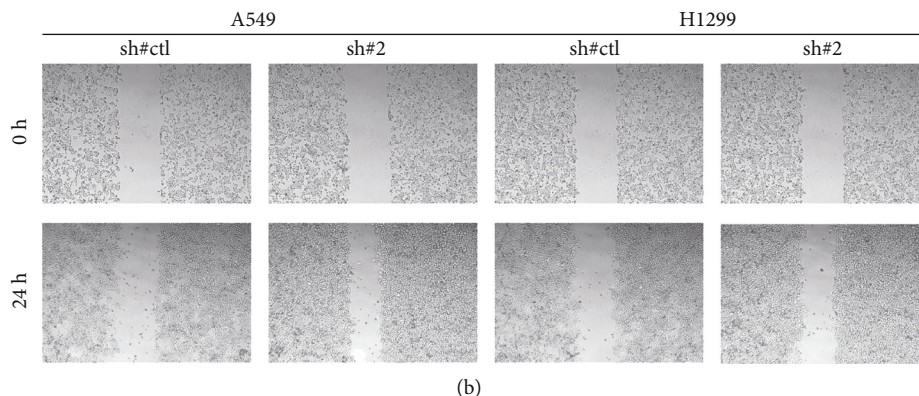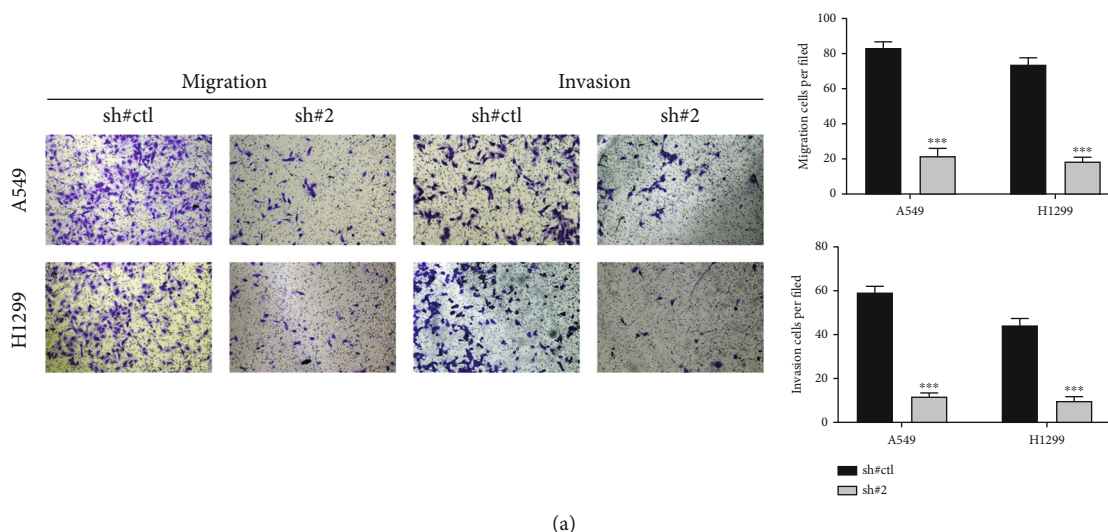
FIGURE 6: CDH2 facilitates the invasion and migration of NSCLC cells. Notes: (a) Transwell assay was performed in sh-CDH2 and control cells. (b) Wound-healing assay was performed in sh-CDH2 and control cells.
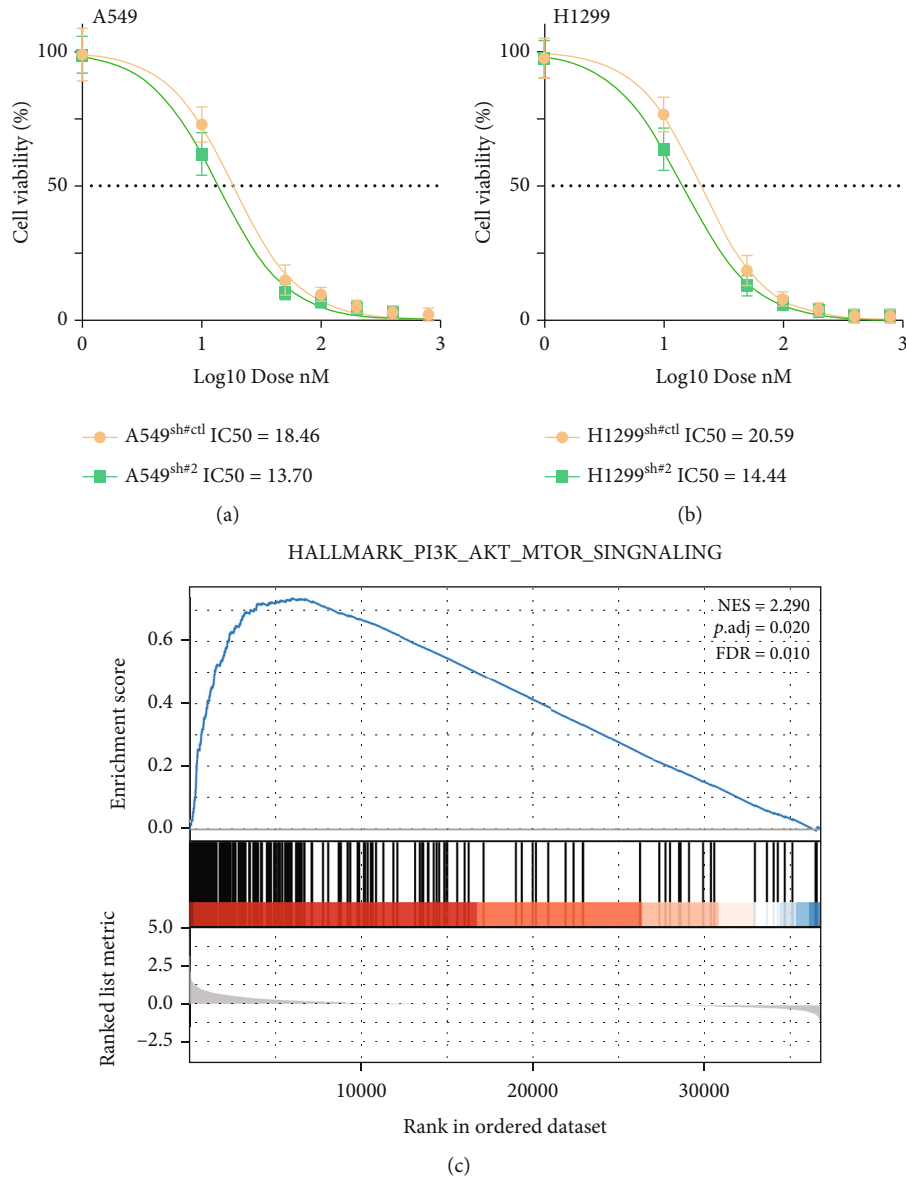
FIGURE 7: CDH2 could lead to gefitinib resistance through PI3K/AKT/mTOR signaling. Notes: (a, b) Cell viability detection in sh-CDH2 and control cells. (c) GSEA showed that CDH2 significantly affect the pathway activity of PI3K/AKT/mTOR signaling.

TCGA and GDSC databases, we identified six genes, RNF150, FAT3, ANKRD33, AFF3, CDH2, and BEX1, that were involved in gefitinib resistance in both cell and tissue levels. We found that most of these genes were expressed in the fibroblast of the NSCLC microenvironment. Hence, we also comprehensively investigated the role of fibroblast in the NSCLC microenvironment, including its biological effect and cell interaction. Ultimately, CDH2 was selected for further analysis for its prognosis correlation. In vitro experiments presented the cancer-promoting role of CDH2 in NSCLC. Moreover, cell viability detection showed that the inhibition of CDH2 could significantly decrease the IC50 of gefitinib.

We noticed that the DEGs were primarily enriched in the MAPK signaling pathway, PI3K/AKT signaling pathway, leukocyte transendothelial migration, cell adhesion mole-

cules, and tight junction. Some previous studies have begun to explore the relationship between the above pathways and gefitinib. AlAsmari et al. revealed that MAPK/NF-κB signaling could significantly lighten the cardiotoxicity induced by gefitinib [27]. Lu et al. found that in NSCLC, the trans-3,5,4′-trimethoxystilbene could inhibit the MAPK/Akt/Bcl-2 axis by upregulating miR-345 and miR-498, further reducing gefitinib resistance [28]. Zheng et al. found that polyphyllin II could regulate the gefitinib resistance by affecting the PI3K/Akt/mTOR signaling [29]. These results indicated that the activation of the above pathways may promote the development of gefitinib resistance under the influence of specific factors.

Our results also found that RNF150, FAT3, ANKRD33, AFF3, CDH2, and BEX1 were involved in gefitinib resistance in both cell and tissue levels. The role of these genes in

cancer has also been reported. Guo et al. found that FAT3 was correlated with the prognosis of esophageal cancer patients [30]. In breast cancer, Shi et al. found that FAT3 was associated with resistance to tamoxifen [31]. Wang et al. revealed that the BEX1 methylation regulated by DNMT1 could contribute to liver cancer stemness and tumorigenicity [32]. Lee et al. found that BEX1 could promote glioblastoma progression by activating the YAP/TAZ signaling [33]. In NSCLC, cancer-associated fibroblasts might exert an important role. Yi et al. noticed that the CAFs could lead to EMT and the resistance of EGFR-TKI by mediating the HGF/IGF-1/ANXA2 signaling axis [34].

The arrival of the big data era has produced massive data. On this basis, the secondary analysis of open data or research can facilitate researchers and draw valuable conclusions. Based on high-quality data and analysis process, our research has improved researchers' understanding of gefitinib resistance. Nevertheless, some limitations should be noted. Firstly, most of the populations included in the study are from Western countries. There are biological differences between populations of different races, which may reduce the reliability of our conclusions. Secondly, some patients have incomplete clinical baseline data, which may lead to sample bias to some extent.

Data Availability

The data that support the findings of this study are available from the corresponding authors upon reasonable request.

Conflicts of Interest

The authors declare no conflicts of interest.

Authors' Contributions

Puwei Song and Jianghui Zhou are co-first authors.

Acknowledgments

Supplementary Materials

Supplementary 1. Supplemental Table 1: the detailed clinicopathological parameters of patient.

Supplementary 2. Supplemental Table 2: all the results of GO analysis of the genes contributing to gefitinib resistance.

References

[1] F. Nasim, B. F. Sabath, and G. A. Eapen, "Lung Cancer," *The Medical Clinics of North America*, vol. 103, no. 3, pp. 463–473, 2019.

[2] D. Rodescu, "Lung cancer," *The Medical Clinics of North America*, vol. 61, no. 6, pp. 1205–1218, 1977.

[3] F. R. Hirsch, G. V. Scagliotti, J. L. Mulshine et al., "Lung cancer: current therapies and new targeted treatments," *The Lancet*, vol. 389, no. 10066, pp. 299–311, 2017.

[4] J. S. Donington, C. W. Koo, and M. S. Ballas, "Novel therapies for non-small cell lung cancer," *Journal of Thoracic Imaging*, vol. 26, no. 2, pp. 175–185, 2011.

[5] A. Rossi and M. Di Maio, "Platinum-based chemotherapy in advanced non-small-cell lung cancer: optimal number of treatment cycles," *Expert Review of Anticancer Therapy*, vol. 16, no. 6, pp. 653–660, 2016.

[6] W. Z. Zhong, Q. Wang, W. M. Mao et al., "Gefitinib versus vinorelbine plus cisplatin as adjuvant treatment for stage II-IIIA (N1-N2) EGFR-mutant NSCLC: final overall survival analysis of CTONG1104 phase III trial," *Journal of Clinical Oncology : Official Journal of the American Society of Clinical Oncology*, vol. 39, no. 7, pp. 713–722, 2021.

[7] Y. Hosomi, S. Morita, S. Sugawara et al., "Gefitinib alone versus Gefitinib plus chemotherapy for non-small-cell lung cancer with mutated epidermal growth factor receptor: NEJ009 study," *Journal of Clinical Oncology : Official Journal of the American Society of Clinical Oncology*, vol. 38, no. 2, pp. 115–123, 2020.

[8] Z. Liu, N. Shah, K. L. Marshall et al., "Overcoming the acquired resistance to gefitinib in lung cancer brain metastasis in vitro and in vivo," *Archives of Toxicology*, vol. 95, no. 11, pp. 3575–3587, 2021.

[9] Z. Chen, Q. Chen, Z. Cheng et al., "Long non-coding RNA CASC9 promotes gefitinib resistance in NSCLC by epigenetic repression of DUSP1," *Cell Death & Disease*, vol. 11, no. 10, p. 858, 2020.

[10] S. Liu, Q. Li, G. Li et al., "The mechanism of m^6A methyltransferase METTL3-mediated autophagy in reversing gefitinib resistance in NSCLC cells by β-elemene," *Cell Death & Disease*, vol. 11, no. 11, p. 969, 2020.

[11] L. Cheng and Q. Tong, "Interaction of FLNA and ANXA2 promotes gefitinib resistance by activating the Wnt pathway in non-small-cell lung cancer," *Molecular and Cellular Biochemistry*, vol. 476, no. 10, pp. 3563–3575, 2021.

[12] W. Yang, J. Soares, P. Greninger et al., "Genomics of drug sensitivity in Cancer (GDSC): a resource for therapeutic biomarker discovery in cancer cells," *Nucleic Acids Research*, vol. 41, no. Database issue, pp. D955–D961, 2013.

[13] M. E. Ritchie, B. Phipson, D. Wu et al., "Limma powers differential expression analyses for RNA-sequencing and microarray studies," *Nucleic Acids Research*, vol. 43, no. 7, p. e47, 2015.

[14] G. Yu, L. G. Wang, Y. Han, and Q. Y. He, "clusterProfiler: an R package for comparing biological themes among gene clusters," *Omics : a Journal of Integrative Biology*, vol. 16, no. 5, pp. 284–287, 2012.

[15] A. Subramanian, P. Tamayo, V. K. Mootha et al., "Gene set enrichment analysis: a knowledge-based approach for interpreting genome-wide expression profiles," *Proceedings of the National Academy of Sciences of the United States of America*, vol. 102, no. 43, pp. 15545–15550, 2005.

[16] D. Sun, J. Wang, Y. Han et al., "TISCH: a comprehensive web resource enabling interactive single-cell transcriptome visualization of tumor microenvironment," *Nucleic Acids Research*, vol. 49, no. D1, pp. D1420–D1430, 2021.

[17] J. Pan, S. Fang, H. Tian et al., "lncRNA JPX/miR-33a-5p/ Twist1 axis regulates tumorigenesis and metastasis of lung

cancer by activating Wnt/β-catenin signaling," *Molecular Cancer*, vol. 19, no. 1, p. 9, 2020.

[18] Y. Wei, X. Chen, X. Ren et al., "Identification of MX2 as a novel prognostic biomarker for Sunitinib resistance in clear cell renal cell carcinoma," *Frontiers in Genetics*, vol. 12, article 680369, 2021.

[19] C. Xie, X. Zhou, C. Liang et al., "Apatinib triggers autophagic and apoptotic cell death via VEGFR2/STAT3/PD-L1 and ROS/Nrf2/p62 signaling in lung cancer," *Journal of Experimental & Clinical Cancer Research : CR*, vol. 40, no. 1, p. 266, 2021.

[20] J. W. Song, J. Zhu, X. X. Wu et al., "GOLPH3/CKAP4 promotes metastasis and tumorigenicity by enhancing the secretion of exosomal WNT3A in non-small-cell lung cancer," *Cell Death & Disease*, vol. 12, no. 11, p. 976, 2021.

[21] H. A. Hamann, E. S. Ver Hoeve, L. Carter-Harris, J. L. Studts, and J. S. Ostroff, "Multilevel opportunities to address lung cancer stigma across the cancer control continuum," *Journal of Thoracic Oncology : Official Publication of the International Association for the Study of Lung Cancer*, vol. 13, no. 8, pp. 1062–1075, 2018.

[22] A. G. Pallis and K. N. Syrigos, "Lung cancer in never smokers: disease characteristics and risk factors," *Critical Reviews in Oncology/Hematology*, vol. 88, no. 3, pp. 494–503, 2013.

[23] T. Sethi, "Lung cancer * Introduction," *Thorax*, vol. 57, no. 11, pp. 992-993, 2002.

[24] D. Zhang, X. Xu, Y. Wei et al., "Prognostic role of DNA damage response genes mutations and their association with the sensitivity of olaparib in prostate cancer patients," *Cancer Control : Journal of the Moffitt Cancer Center*, vol. 29, 2022.

[25] T. Zhang, X. Zhou, X. Zhang et al., "Gut microbiota may contribute to the postnatal male reproductive abnormalities induced by prenatal dibutyl phthalate exposure," *Chemosphere*, vol. 287, Part 1, article 132046, 2022.

[26] X. Zhang, T. Zhang, X. Ren, X. Chen, S. Wang, and C. Qin, "Pyrethroids toxicity to male reproductive system and offspring as a function of oxidative stress induction: rodent studies," *Frontiers in Endocrinology*, vol. 12, article 656106, 2021.

[27] A. F. AlAsmari, N. Ali, F. AlAsmari et al., "Liraglutide attenuates gefitinib-induced cardiotoxicity and promotes cardioprotection through the regulation of MAPK/NF-κB signaling pathways," *Saudi Pharmaceutical Journal : SPJ : the Official Publication of the Saudi Pharmaceutical Society*, vol. 28, no. 4, pp. 509–518, 2020.

[28] M. Lu, B. Liu, H. Xiong, F. Wu, C. Hu, and P. Liu, "Trans-3,5,4′-trimethoxystilbene reduced gefitinib resistance in NSCLCs via suppressing MAPK/Akt/Bcl-2 pathway by upregulation of miR-345 and miR-498," *Journal of Cellular and Molecular Medicine*, vol. 23, no. 4, pp. 2431–2441, 2019.

[29] R. Zheng, H. Jiang, J. Li, X. Liu, and H. Xu, "Polyphyllin II restores sensitization of the resistance of PC-9/ZD cells to gefitinib by a negative regulation of the PI3K/Akt/mTOR signaling pathway," *Current Cancer Drug Targets*, vol. 17, no. 4, pp. 376–385, 2017.

[30] Z. Guo, X. Yan, C. Song et al., "FAT3 mutation is associated with tumor mutation burden and poor prognosis in esophageal cancer," *Frontiers in Oncology*, vol. 11, article 603660, 2021.

[31] Y. Shi, Y. Zhao, Y. Zhang et al., "AFF3 upregulation mediates tamoxifen resistance in breast cancers," *Journal of Experimental & Clinical Cancer Research : CR*, vol. 37, no. 1, p. 254, 2018.

[32] Q. Wang, N. Liang, T. Yang et al., "DNMT1-mediated methylation of BEX1 regulates stemness and tumorigenicity in liver cancer," *Journal of Hepatology*, vol. 75, no. 5, pp. 1142–1153, 2021.

[33] S. Lee, H. Kang, E. Shin, J. Jeon, H. Youn, and B. Youn, "BEX1 and BEX4 induce GBM progression through regulation of actin polymerization and activation of YAP/TAZ signaling," *International Journal of Molecular Sciences*, vol. 22, no. 18, 2021.

[34] Y. Yi, S. Zeng, Z. Wang et al., "Cancer-associated fibroblasts promote epithelial-mesenchymal transition and EGFR-TKI resistance of non-small cell lung cancers via HGF/IGF-1/ANXA2 signaling," *Biochimica et Biophysica acta Molecular Basis of Disease*, vol. 1864, no. 3, pp. 793–803, 2018.

Research Article

Identification of WD-Repeat Protein 72 as a Novel Prognostic Biomarker in Non-Small-Cell Lung Cancer

Guanglin Shi [1,2] **Qinggan Ni** [3] **Yuqing Miao,**[2] **Hua Huang,**[4] **Zhongbo Yin,**[5] **Weirong Shi,**[6] **and Minhua Shi** [1]

¹*Department of Respiratory and Critical Care Medicine, Second Affiliated Hospital of Soochow University, Suzhou, Jiangsu 215004, China*
²*Department of Respiratory Diseases, The Sixth People's Hospital of Nantong (Affiliated Nantong Hospital of Shanghai University), Nantong, Jiangsu 226011, China*
³*Department of Burns and Plastic Surgery, Yancheng Clinical College of Xuzhou Medical University, The First People's Hospital of Yancheng, Yancheng 224000, China*
⁴*Department of Pathology, Affiliated Hospital of Nantong University, Nantong, Jiangsu 226011, China*
⁵*Department of Pathology, The Sixth People's Hospital of Nantong (Affiliated Nantong Hospital of Shanghai University), Nantong, Jiangsu 226011, China*
⁶*Department of Thoracic Surgery, The Sixth People's Hospital of Nantong (Affiliated Nantong Hospital of Shanghai University), Nantong (Affiliated Nantong Hospital of Shanghai University), Jiangsu 226011, China*

Correspondence should be addressed to Minhua Shi; shiminhua@163.com

WD-repeat protein 72 (WDR72; OMIM*613214), a scaffolding protein lacking intrinsic enzymatic activity, produces numerous β-propeller blade formations, serves as a binding platform to assemble protein complexes and is critical for cell growth, differentiation, adhesion, and migration. Despite evidence supporting a basic role of WDR72 in the tumorigenesis of particular cancers, the value of WDR72 in non-small-cell lung cancer (NSCLC), the tumor with the highest mortality rate globally, is undocumented. We investigated the prognostic value of WDR72 in NSCLC and studied its potential immune function and its correlation with ferroptosis. According to The Cancer Genome Atlas, Cancer Cell Line Encyclopedia, Genotype-Tissue Expression, and Gene Set Cancer Analysis, we used multiple bioinformatic strategies to investigate the possible oncogenic role of WDR72, analyze WDR72 and prognosis, and immune cell infiltration in different tumors correlation. WDR72 exhibited a high expression in NSCLC and a positive association with prognosis. WDR72 expression was related to immune cell infiltration and tumor immune microenvironment in NSCLC. Finally, we validated WDR72 in human NSCLC; it has a predictive value in NSCLC related to its function in tumor progression and immunity. The significance of our study is that WDR72 can be used as a potential indicator of lung cancer prognosis. Helping physicians more accurately predict patient survival and risk of disease progression.

1. Introduction

Lung cancer is a deadly malignancy widespread worldwide, and non-small-cell lung cancer (NSCLC) represents approximately 85% of all lung cancers [1]. NSCLC onset is devious, with invisible clinical manifestations in the early stages, making early diagnosis hard. Furthermore, due to the highly aggressive nature of NSCLC, many patients have distant metastases at diagnosis [2]. Despite recent advances, early detection and treatment of NSCLC remain inadequate [3]. Gene mutation and aberrant expression lead to malignant alteration of airway epithelial cells, eventually leading to lung

TABLE 1: All data sources.

	Data sources	Website
1	TCGA	http://portal.gdc.cancer.gov/
2	NCBI	http://www.ncbi.nlm.nih.gov/
3	GEO2R	http://www.ncbi.nlm.nih.gov/geo/geo2r
4	CIBERSORT	https://cibersortx.stanford.edu/
5	GSE19804	https://www.ncbi.nlm.nih.gov/geo/query/acc.cgi?acc=GSE19804
6	GSE118370	https://www.ncbi.nlm.nih.gov/geo/query/acc.cgi?acc=GSE118370
7	GSE19188	https://www.ncbi.nlm.nih.gov/geo/query/acc.cgi?acc=GSE19188
8	GSE27262	https://www.ncbi.nlm.nih.gov/geo/query/acc.cgi?acc=GSE27262
9	GSE33532	https://www.ncbi.nlm.nih.gov/geo/query/acc.cgi?acc=GSE33532

cancer [4]. Discovering new markers and driver genes is essential for the early detection, diagnosis, targeted treatment, and prognosis assessment of NSCLC.

WD-repeat protein 72(WDR72 ; OMIM*613214) is a scaffold lacking intrinsic enzymatic activity. It produces several β-propeller blade formations, acting as binding platforms to assemble protein complexes and form tooth enamel, as well as causing autosomal recessive developmental defects [5]. Ibrahim-Verbaas et al. [6] identified a significant genome-wide association between a single nucleotide polymorphism (SNP) in the WDR72 gene (chromosome 15) and a cognitive test comparable to the Stroop interference test, demonstrating that at the level of executive function, WDR72 gene is also related to renal function. Howles et al. [7] demonstrated that WDR72 could involve in clathrin-mediated endocytosis, a critical process to persist intracellular CaSR signaling. WDR72 has a significant role in clear renal cell carcinoma [8], esophageal cancer [9], and colorectal cancer [10] but undetected in NSCLC. Accordingly, this paper intended to further analyze the specific mechanism of WDR72 and NSCLC.

Ferroptosis is a sort of controlled necrosis that performs a part in neurodegenerative cancers. Lipid peroxidation inhibitors, lipophilic antioxidants, and iron chelators can prevent ferroptosis [11]. Initially, ferroptosis was only recognized as erastin-induced death; however, additional studies revealed its function in various pathophysiological processes and diseases. Since certain oncogenically mutated tumor cells are more susceptible to ferroptosis, ferroptosis can be triggered, and ferroptosis-sensitive tumor cells may have significant therapeutic potential [12–14]. Therefore, modulation of ferroptosis may offer therapeutic potential for certain disorders associated with ferroptosis. Many key targets are important mediators of ferroptosis induction; however, the relationship between WDR72 and ferroptosis is still unclear. Herein, we further study whether WDR72 is sensitive to ferroptosis-induced cell death. Studies have shown that excessive iron overload may suppress the function of the immune system, thereby increasing the risk of infection and tumor development [15]. Immune infiltration refers to the presence of immune cells (T cells, B cells, macrophages, natural killer cells, etc.) in tumor tissues [16]. The immune infiltration of lung cancer patients is closely related to the survival and prognosis of patients [17]. Immune cells can

slow the growth and spread of tumors by attacking tumor cells [18]. However, studies have also shown that tumor cells can evade the attack of immune cells through different mechanisms, thereby suppressing the immune response [19]. Overall, immune infiltration and ferroptosis are associated with the prognosis and survival of lung cancer patients, but more studies are needed to confirm the direct relationship between the two.

2. Materials and Methods

2.1. Gene Expression and Clinical Data Collection. First, we downloaded gene expression and clinical transcriptome profiling information for NSCLC patients from The Cancer Genome Atlas (TCGA) website (http://portal.gdc.cancer.gov/). The R tool "limma" was utilized to normalize raw gene expression information. GSE19804 [20, 21], GSE118370 [22], GSE19188 [23], GSE27262 [24, 25], and GSE33532 [26] were obtained from the GEO database GPL570 platform ([HG-U133_Plus_2] Affymetrix Human Genome U133 Plus 2.0 Array) through the "GEOquery" package for subsequent analysis (Table 1).

2.2. Identification DEGS. The selected datasets above were compared and examined utilizing the NCBI (https://www.ncbi.nlm.nih.gov/) toolGEO2R (http://www.ncbi.nlm.nih.gov/geo/geo2r). We applied adjusted (adj.) p values and thresholds to the Benjamini and Hochberg false discovery rates (FDR) are utilized to develop a balance between the statistical thresholds of finding significant genes and false positives. Probe sets without matching gene symbols or genes with several probe sets were excluded or averaged accordingly. Log fold change (FC) > 1.2 and adj < 0.01 indicated statistical significance.

2.3. Analysis of Association between WDR72 and Prognosis of Patients with Small-Cell Lung Cancer (SCLC). In the TCGA database, a Kaplan-Meier (KM) analysis was conducted to examine the overall survival (OS), disease-specific survival (DSS), disease-free survival (DFS), and progression-free survival (PFI) of patients with NSCLC. To show the connection between WDR72 expression and survival in NSCLC, a Cox regression analysis was done utilizing the R tools "survival" and "forest plot."

(a)

(b)

(c)

(d)
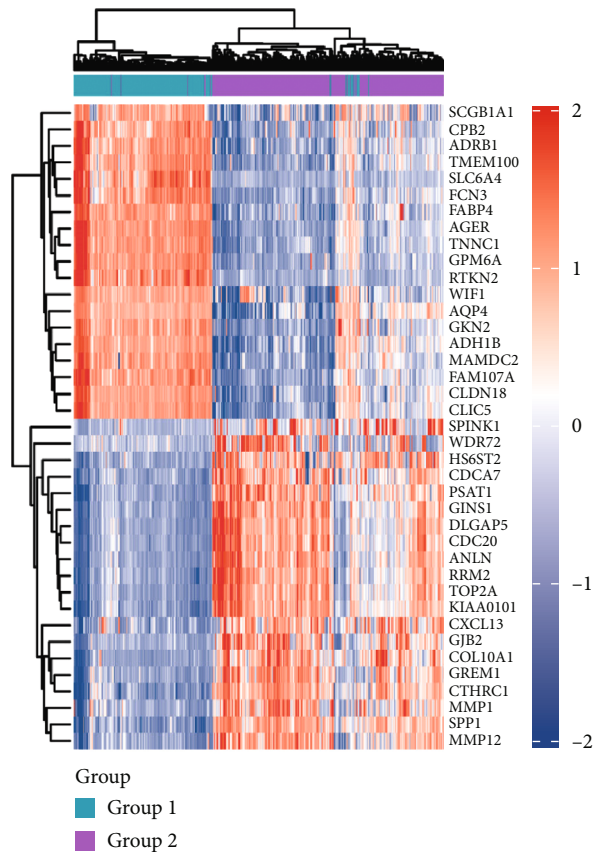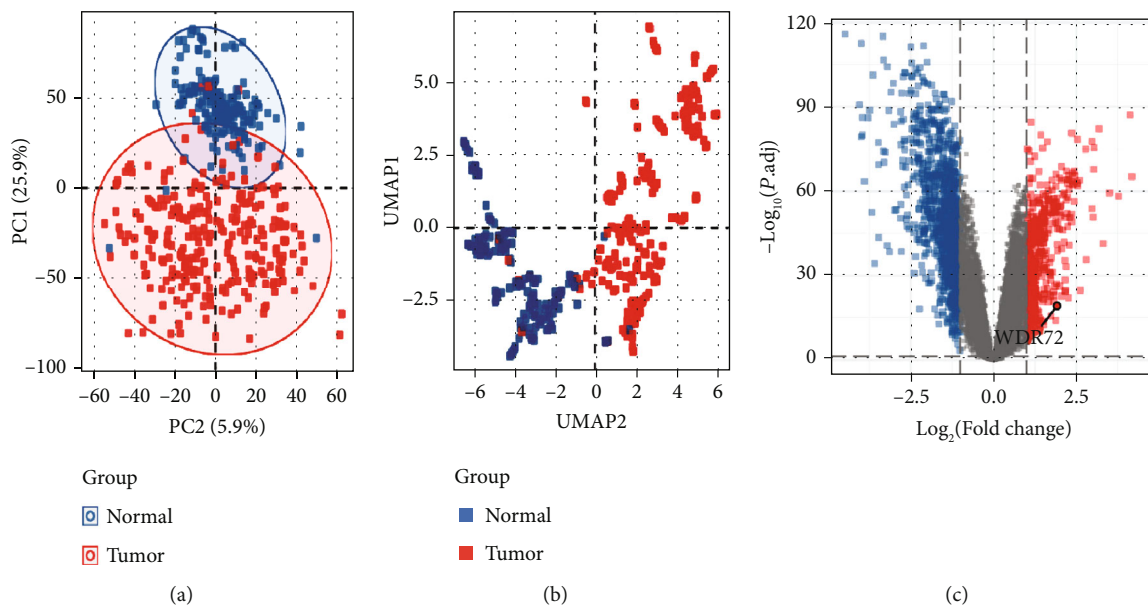
Figure 1: Continued.
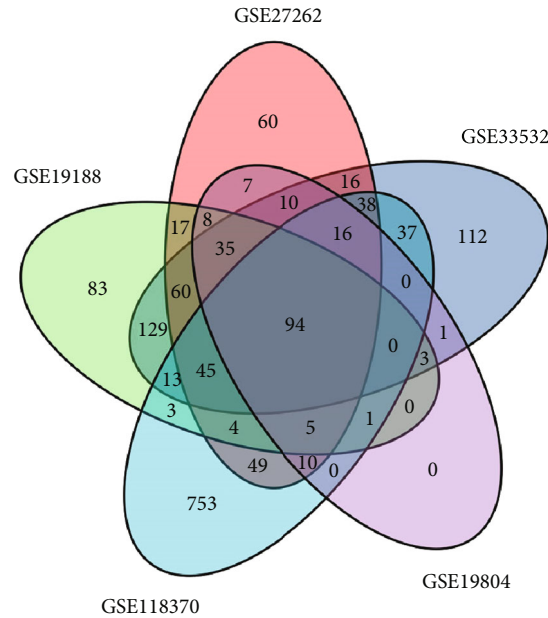
(e)

Figure 1: Five datasets of GPL570 platform in GEO database: GSE19804, GSE118370, GSE19188, GSE27262, and GSE33532. It can be seen from the PC graph and UMAP graph that the samples of the two groups are separated (a, b). Using the ggplot2 package of classical difference analysis-volcano plot to mark the location of WDR72 (c). (d) Visualizing the expression profile of the ComplexHeatmap package, the high and low expressions of each top 20 gene is shown. Venn diagram of (e) plots the crossover genes of the 5 datasets, showing that there are 94 crossover genes in the datasets.

2.4. Association between WDR72 Expression and Immunity. Employing the ESTIMATE algorithm, immune and stromal scores of NSCLC samples were measured to investigate the association between WDR72 expression and TME (tumor microenvironment). The relationship between WDR72 expression and score was assessed utilizing the R tools "estimate" and "limma" based on the degree of immune infiltration. We downloaded the TCGA immune cell infiltration value from the CIBERSORT database (https://cibersortx .stanford.edu/) and calculated the relative score of 24 immune cells in NSCLC utilizing the CIBERSORT algorithm. Then, the Spearman rank correlation coefficient was employed to assess the association between the level of WDR72 and the infiltration level of each immune cell in NSCLC. R tools "limma," "reshape2," and "RColorBrewer" were utilized to present the visualizations.

2.5. Gene Set Enrichment Analysis. Gene Ontology (GO) and Kyoto Encyclopedia of Genes and Genomes (KEGG) gene sets were downloaded from the Gene Set Enrichment Analysis (GSEA) website. The biological role of WDR72 in NSCLC was investigated using the GSEA method. Both analyses were performed using the R "Cluster Profiler" tool.

2.6. Clinical Samples. We should be confirmed non-small-cell lung cancer at Nantong University from 2012 to 2020. A total of 158 matched NSCLC and paracancerous tissues were obtained through radical resection in the Affiliated Hospital of Nantong University. All diagnoses were con-

firmed by histopathological examination. For further study, the specimens were frozen in a -80°C freezer after surgery. All 158 patients had signed written informed consent and underwent a standardized ethnic review.

2.7. Reverse Transcription-Polymerase Chain Reaction (RT-qPCR). Four matched lung adenocarcinoma and paracancerous tissues were randomly selected to extract total RNA. RNA was reverse transcript into cDNA utilizing a reverse transcription kit (transgene Biotech, China). Nano-Drop 2000 (Thermo Fisher Scientific, Waltham, USA) was utilized to detect its fluorescent expression. GAPDH (glyceraldehyde-3-phosphate dehydrogenase) served as an internal control. WDR72 relative expression was computed employing the $2^{-\Delta\Delta}$CT approach.WDR72 F:GCAACTCAAACTCGGC AAACTTCC, R:GGCTCACCTGGACTCTCAGACTC.

2.8. Immunohistochemistry Staining Analysis. Paraffin-embedded NSCLC tissue sections were deparaffinized, hydrated, antigen retrieved, and goat serum blocked. Therefore, samples were incubated overnight at 4°C with an anti-WDR72 antibody (thermofisher PA5-63780 1 : 200) and species-specific secondary antibody for 30 min at 37°C. The immunosignal of the samples was observed utilizing a DAB solution and double-stained with hematoxylin in turn. A light microscope was used to obtain representative immunohistochemical (IHC) staining images.

2.9. Western Blot Analysis. Protein specimens from NSCLC and paracancerous tissue were isolated and transmitted to

(a)

(b)

(c)

Figure 2: Continued.

(d)

(e)

(f)
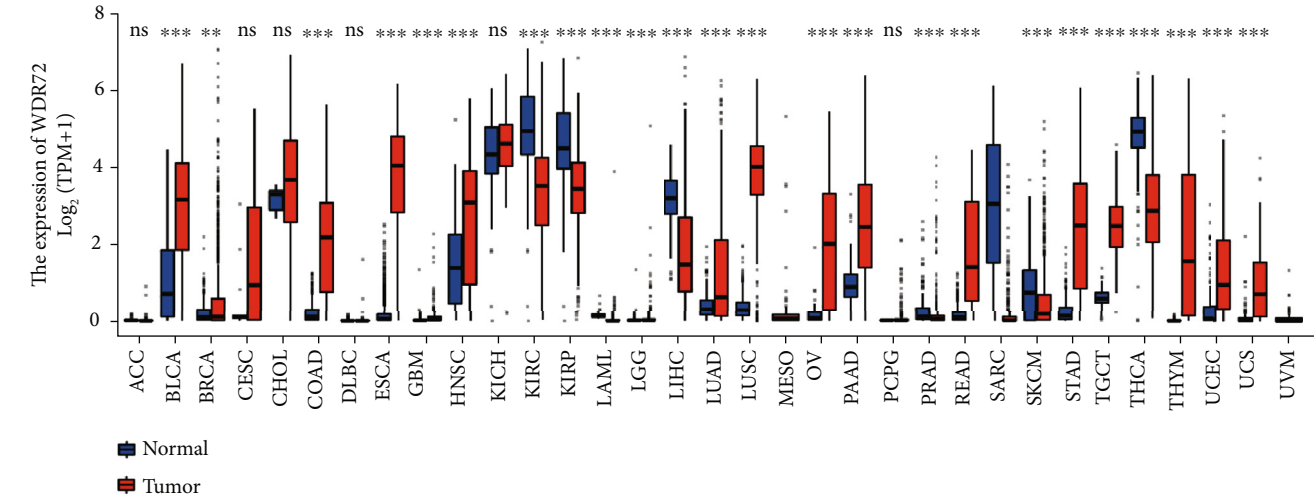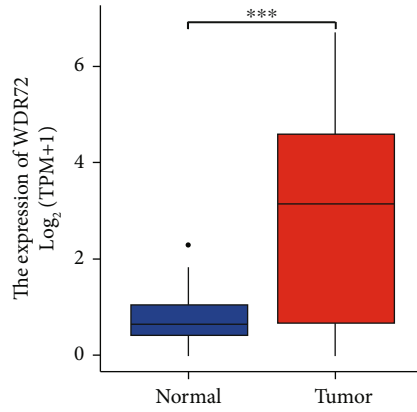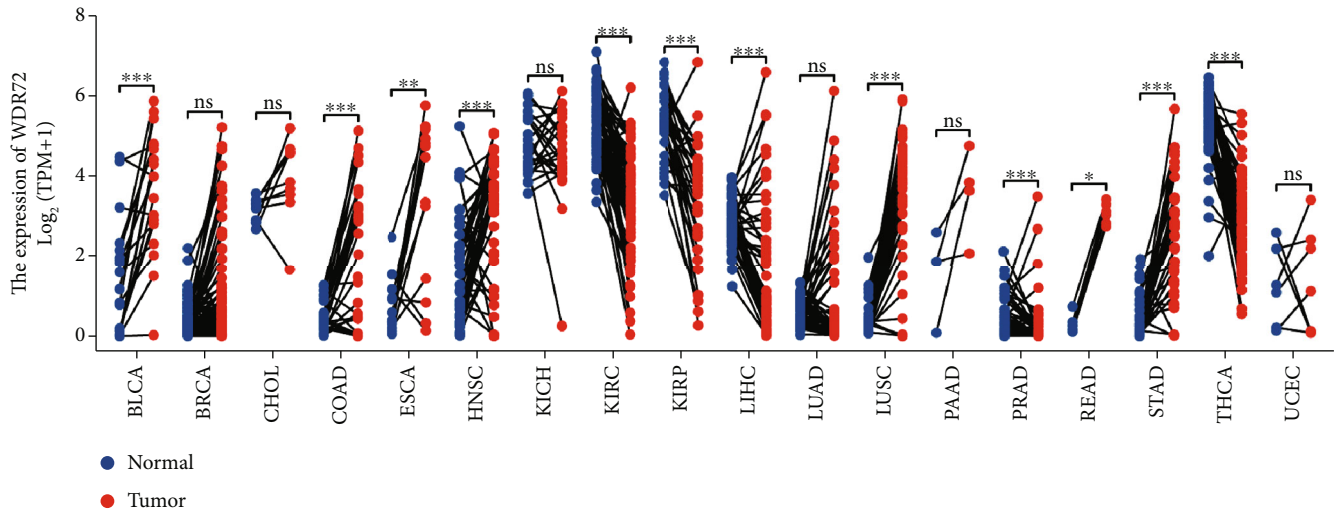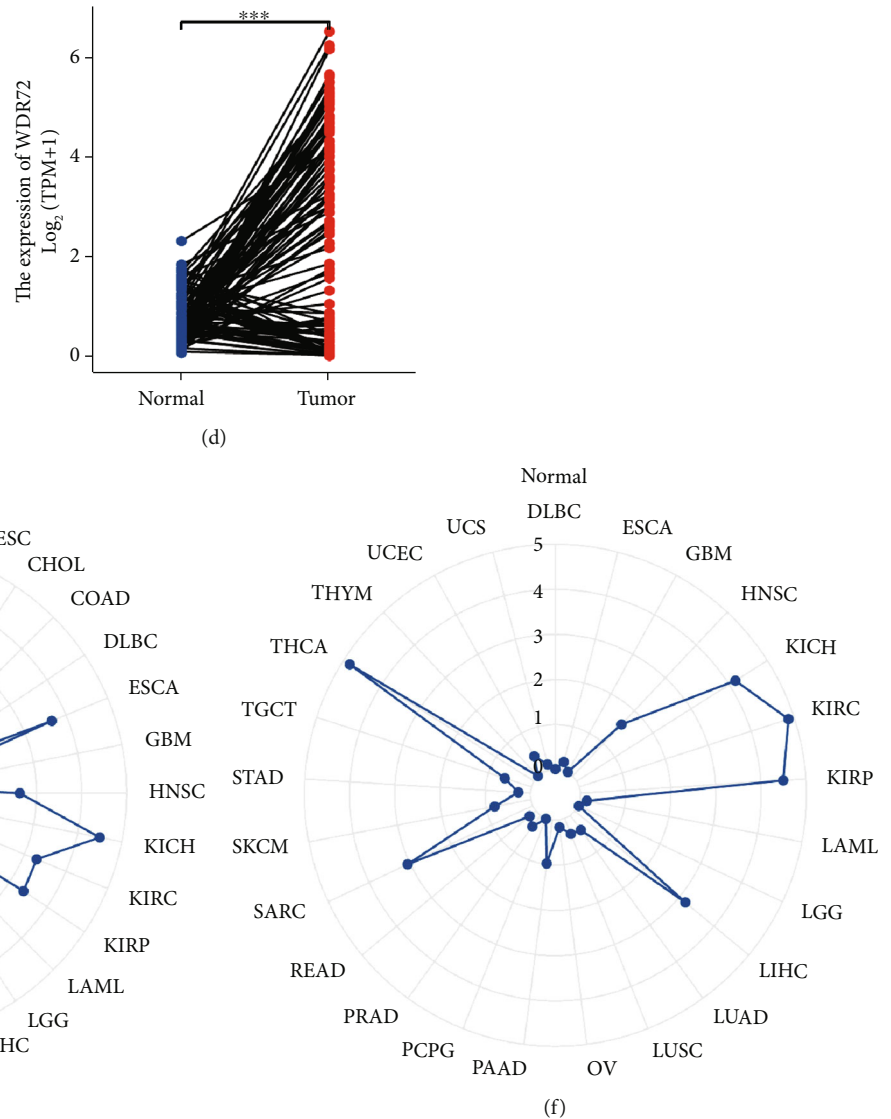
FIGURE 2: Differential expression of WDR72 in pan-cancer tissues and corresponding adjacent tissues and between paired and unpaired non-small-cell lung cancer tissues and corresponding adjacent tissues were analyzed using the package "ggplot2," ns; $p \geq 0.05$; $^*p \leq 0.05$; $^{**}p \leq 0.01$; $^{***}p \leq 0.001$ (a–d). Expression of WDR72 in pancreatic cancer tissues was analyzed using radar visualization in the "ggradar" and "ggplot2" software packages. (e) The expression of WDR72 in normal tissues adjacent to pan-cancer tumors (f).

polyvinylidene fluoride (PVDF) membranes for the next steps. Following blocking with 5% BSA, PVDF membranes were incubated overnight at 4°C with primary antibodies to WDR72 (Thermo Fisher PA5-637801:2000) and GAPDH (1:1000) and then were incubated at room temperature (15-25°C) with HRP-labeled secondary antibodies for 1 h (1:1000) 2000). ECL (enhanced chemiluminescence) is used to capture images. GAPDH was chosen as the internal control.

2.10. Statistical Analyses. All data were normalized on gene expression using log2 transformation. Analyses of the correlation between two variables were carried out utilizing Spearman or Pearson test. $p < 0.05$ was judged statistically significant. Differences between adjacent tissues and cancerous tissues were conducted employing the Wilcox test.

$p < 0.05$ was judged statistically significant. Kaplan-Meier curves and Cox proportional hazards regressions were employed for all survival analyses. R program (Ver. 4.1.2) was used to process the statistical significance of bioinformatic results, and GraphPad Prism (Ver. 9) was used to analyze the statistical importance of the in vitro data.

3. Results

3.1. Differential Expression of WDR72 between NSCLC Tumor and Normal Tissue Samples. We selected five datasets of GPL570 platform in GEO database, GSE19804, GSE118370, GSE19188, GSE27262, and GSE33532; "limma" R package; and "umap" R package. By drawing the PC and

(a)

(b)

(c)

(d)

(e)

(f)

(g)

(h)
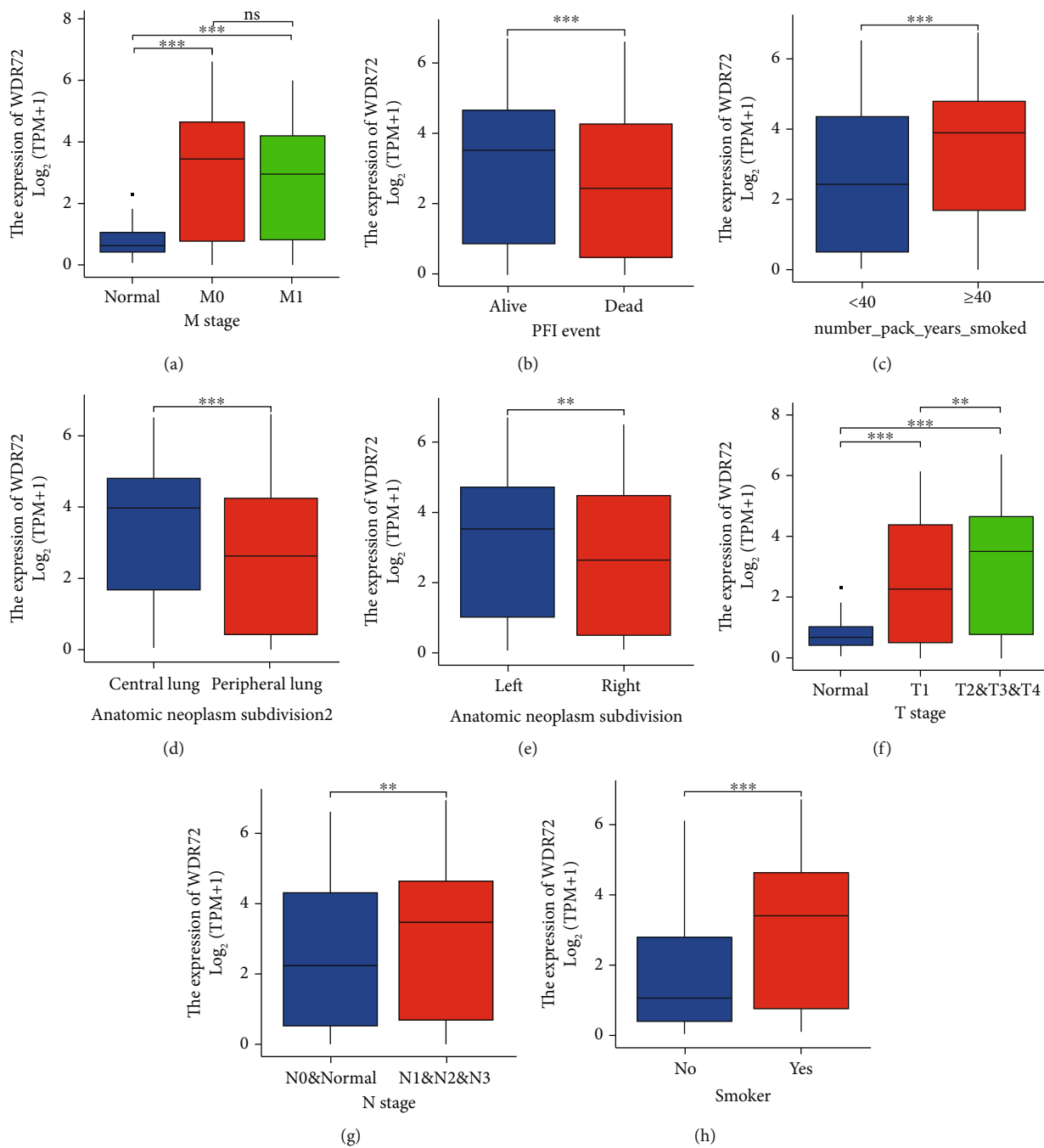
Figure 3: Continued.
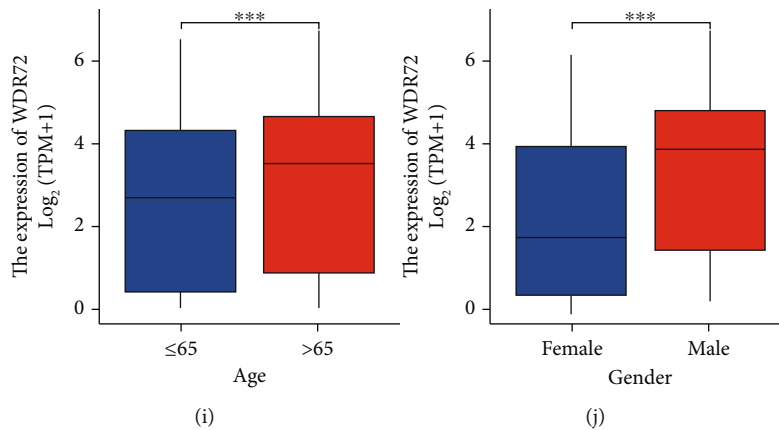
FIGURE 3: Correlation analysis between WDR72 and clinic. M grade correlation (a). PFI event correlation (b). Smoking year correlation (c). Tumor distribution (central or peripheral) correlation (d). Tumor distribution (left lung or right lung) correlation (e). T grade correlation (f). N grade correlation (g). Smoking correlation (h). Age correlation (i). Gender correlation (j). significance indicator: ns; $p \geq 0.05$; $^*p \leq 0.05$; $^{**}p \leq 0.01$; $^{***}p \leq 0.001$.

UMAP graphs, the samples of the two groups were separated, showing a significant variation between the two groups. The subsequent difference analysis may have more meaningful results (Figures 1(a) and 1(b)). Using the ggplot2 package of classical difference analysis-volcano plot, the threshold was selected as $|logFC| \geq 1.2$, p value < 0.05. The figure is highlighted in blue or red, and the location of WDR72 is highlighted (Figure 1(c)). Figure 1(d) depicts the visual expression profile of the ComplexHeatmap package and shows the expression of each top 20 genes with high and low expressions. Concurrently, the Venn diagram of Figure 1(e) plots the intersecting genes of the five datasets, showing 94 intersecting genes. Then, we evaluated the expression degrees of WDR72 in 33 cancers from TCGA data. The "ggplot2" package was utilized to examine the differential expression of WDR72 in pan-cancer tissues and corresponding adjacent tissues and the expression in paired and unpaired NSCLC tissues and corresponding adjacent tissues, ns, $p \geq 0.05$, $^*p \leq 0.05$; $^{**}p \leq 0.01$; $^{***}p \leq 0.001$ (Figures 2(a)–2(d)). Radar visualization using the "ggradar" and "ggplot2" packages was utilized to identify WDR72 expression in pan-cancer tissues (Figure 2(e)) and adjacent pan-cancer tissues (Figure 2(f)). WDR72 was differentially expressed in 27 tumors except ACC, CESC, CHOL, DLBC, KICH, and PCPG.

3.2. Correlation Analysis of WDR72 with Clinical Factors in TCGA Database.
RNAseq and clinical data in level 3 HTSeq-FPKM form in the TCGA (https://portal.gdc.cancer.gov/), LUAD (lungadenocarcinoma) and LUSC (lung squamous cell carcinoma) (lung cancer) experiments were excluded from control/normal (unapplied in projects without control/normal)+retained after clinical data availability. R package "ggplot" (Ver. 3.6.3) was used to evaluate the clinical correlations. Clinical analysis showed that the expression of WDR72 gene was related to whether smoking, age, lesion location, and TNM stage. M grade correlation is pre-

sented in Figure 3(a). PFI event correlation is presented in Figure 3(b). Smoking years correlation is presented in Figure 3(c). Tumor distribution (central or peripheral) correlation is presented in Figure 3(d). Tumor distribution (left lung or right lung) correlation is presented in Figure 3(e). T grade correlation is presented in Figure 3(f). N grade correlation is presented in Figure 3(g). Smoking correlation is presented in Figure 3(h). Age correlation is presented in Figure 3(i). Gender correlation is presented in Figure 3(j). Significance indicator: ns, $p \geq 0.05$; $^*p \leq 0.05$; $^{**}p \leq 0.01$; $^{***}p \leq 0.001$; Figure 4(a) is the survival analysis of WDR72 in NSCLC on the Kaplan-Meier Plotter website (https://kmplot.com/analysis). The 5-year survival rate was significantly decreased for higher WDR72 expression patients compared to those with lower WDR72 expression. Control/normal (unapplied in projects without control/normal) was removed, and the clinical data was retained. Figure 1(d) shows genes with higher expression differences in the heat map employing the R (ver. 3.6.3) "glmnet" tool (ver. 4.1-2) and survival tool (ver. 3.2-10) to draw the LASSO analysis utilizing the RMS tool (Ver. 6.2-0) and the survival package (Ver. 3.2-10) in R (ver. 3.6.3, Figure 4(b)). The COX statistical method incorporated TMN and WDR72 parameters to visualize the prognosis calibration analysis (Figure 4(c)).

3.3. PPI Network Map, GO/KEGG, and GSEA Enrichment Analysis of WDR72-Related Differential Genes.
TCGA (https://portal.gdc.cancer.gov/) was utilized to obtain RNAseq information in level 3 HTSeq-Counts formed in the LUAD-LUSC (lung cancer) experiment after eliminating controls/normals (unapplied in projects without control/normal) using R (3.6.3 ver.) and "DESeq2" (ver. 1.26.0, Love MI et al. 2014) packages to target the molecule WDR72 [ENSG00000166415] in NSCLC by the reduce expression group: 0–50% and the increased expression group: 50–100% with analysis of differential genes of
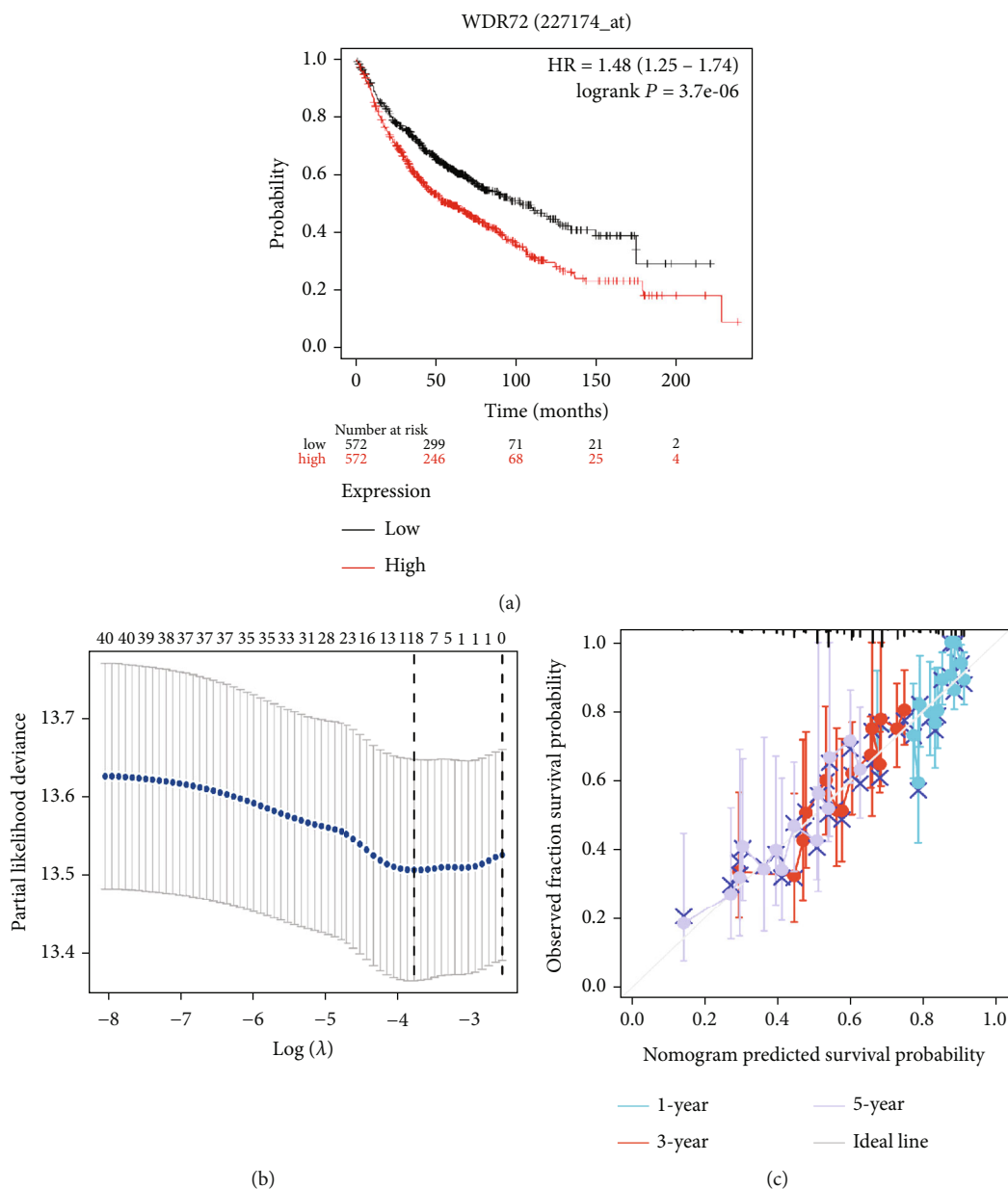
FIGURE 4: (a) Survival analysis of WDR72 non-small-cell lung cancer using the Kaplan-Meier plotter (http://kmplot.com/analysis). (b) The "glmnet" package was used to draw a LASSO variable trajectory was also drawn. (c) The calibration visualization. The abscissa is the survival probability predicted by the model, the ordinate is the actual observed survival probability, and the gray diagonal line is the ideal line.

high correlation with WDR72. R (ver. 3.6.3) "ggplot2" tool (Ver. 3.3.3) was employed for visualization, and "cluster-Profiler" package (Ver. 3.14.3) was used for WDR72 differential genes data analysis. (Figures 5(a) and 5(b)) show GO/KEGG enrichment analysis and protein interaction network, respectively. Figure 5(c) depicts the GSEA mountain map, while Figures 5(d)–5(f) depict the GSEA enrichment analysis map. KEGG/GO and PPI analyses were shown in adrenergic signaling in cardiomyocytes, cytokine–cytokine receptor interaction, organelle fission, extracellular structure organization, biomineral tissue development, odontogenesis spindle, apical part of the cell, collagen–containing extracellular matrix, glycosaminogly-can binding, enzyme inhibitor activity, amide binding, receptor-ligand activity, protein digestion, absorption, and mitotic nuclear. GSEA enrichment analysis showed enrichment in reactome mitotic metaphase, anaphase, reactome RHO GTPase effectors, reactome RHO GTPases activate formins, reactome cell cycle checkpoints, reactome mitotic prometaphase, reactome mitotic spindle checkpoint, reactome separation of sister chromatids, reactome M phase, reactome signaling by RHO GTPases, reactome cell cycle mitotic, reactome resolution of sister chromatid cohesion, reactome cell cycle, reactome innate immune system, reactome rna polymerase II transcription, and reactome extracellular matrix organization.

(a)

(b)

Figure 5: Continued.

(c)

(d)

(e)

FIGURE 5: Continued.

REACTOME_RESOLUTION_OF_SISTER_CHROMATID_COHESION
REACTOME_CELL_CYCLE
REACTOME_INNATE_IMMUNE_SYSTEM
REACTOME_RNA_POLYMERASE_II_TRANSCRIPTION
REACTOME_EXTRACELLULAR_MATRIX_ORGANIZATION

(f)

FIGURE 5: Data analysis of WDR72 differential genes (a, b) are, respectively, the GO/KEGG enrichment analysis diagram and protein interaction network diagram. (c) is the GSEA mountain map. (d–f) is the GSEA enrichment analysis map.

3.4. Coexpression of WDR72 and Ferroptosis-Related Genes in NSCLC.
TCGA (https://portal.gdc.cancer.gov/) was utilized to acquire RNAseq data in level 3 HTSeq-FPKM form in the LUADLUSC (lung cancer) experiment after removing control/normal (unapplied in projects without control/normal) using R (ver. 3.6.3) in the "ggplot2" package to analyze the target molecule: WDR72 (ENSG00000166415) coexpression heat map of ferroptosis-related genes in NSCLC, significance indicator: ns, $p \geq 0.05$; $^*p \leq 0.05$; $^{**}p \leq 0.01$; $^{***}p \leq 0.001$ (Figures 6(a)–6(m)).

3.5. Association of WDR72 with 24 Types of Immune Cells in NSCLC.
It is well known that there are typical 24 types of immune infiltrating cells, namely, aDC cells, B cells, CD8 cells, T cells, cytotoxic cells, DC cells, eosinophils cells, iDC cells, macrophages cells, mast cells, neutrophils cells, NK CD56 bright cells, NK CD56dim cells, NK cells, pDC cells, T cells, T helper cells, Tcm cells, Tem cells, TFH cells, Tgd cells, Th1 cells, Th17 cells, Th2 cells, and TReg cells. TCGA (https://portal.gdc.cancer.gov/) was employed to recover RNAseq information in level 3 HTSeq-FPKM form in LUAD-LUSC (lung cancer) experiment after removing control/normal (unapplied in projects without control/normal) using R software (GSVA package ver. 3.6.3) to examine the immune infiltration method: ssGSEA (the built-in method of the GSVA) grouped WDR72 (ENSG00000166415) by the median and calculated the higher and lower expression of WDR72 and 24 forms of immunity cells, significant threshold: ns; $p \geq 0.05$; $^*p \leq 0.05$; $^{**}p \leq 0.01$; $^{***}p \leq 0.001$. Except for Tcm and NK CD56, 24 immune cells had a nonsignificant correlation, while the p values of the other 22 cells were significant (Figures 7(a)–7(m)).

3.6. Clinical Correlation of WDR72 in NSCLC.
WDR72 was upregulated in NSCLC. To further validate the results of the previous analysis, we found the RNA and protein expressions of WDR72 in NSCLC. (Figures 8(a) and 8(b)) show a significantly greater level of WDR72 expression in NSCLC tissues compared to the matching normal tissues. Immunohistochemistry verified that WDR72 was strongly produced in NSCLC tissue proteins (Figures 9(a) and 9(b)). The results demonstrated that WDR72 expression level was greater in NSCLC tissues than in surrounding normal tissues. We collected clinical reports of 158 patients with NSCLC and discovered that patients with higher WDR72 levels had a poor prognosis (Figure 9(c)). Similarly, we found that WDR72 expression and smoking, tumor size, TNM staging, tumor grade, and metastasis were correlated ($p < 0.05$, Table 2). Multivariate analysis revealed that tumor size, TNM staging, tumor grade, and metastasis were associated with the expression of WDR72 ($p < 0.05$, Table 3).

(a)

(b)

(c)

(d)

FIGURE 6: Continued.

(e)

(f)

(g)

(h)

Figure 6: Continued.

(i)

(j)

(k)

(l)
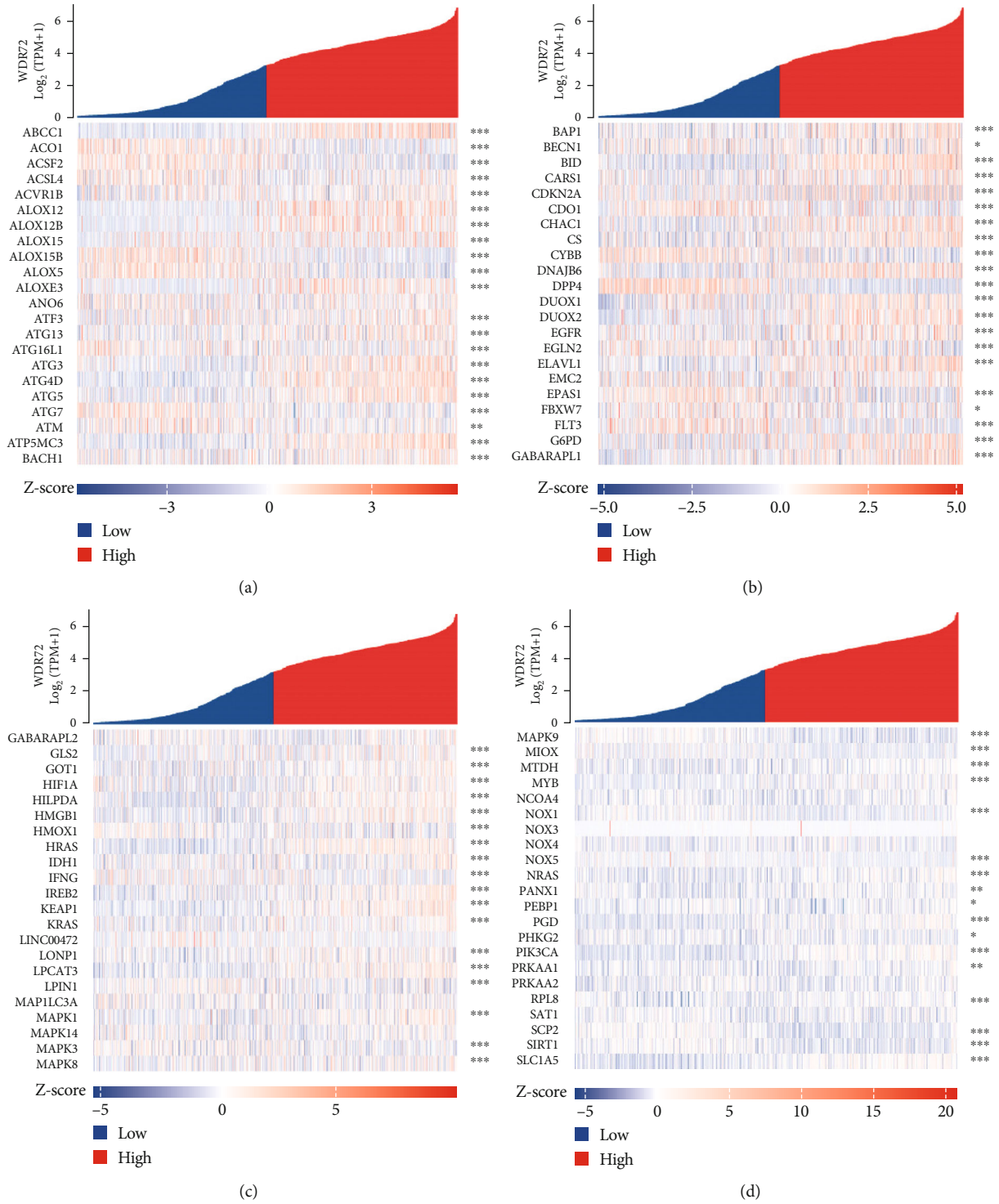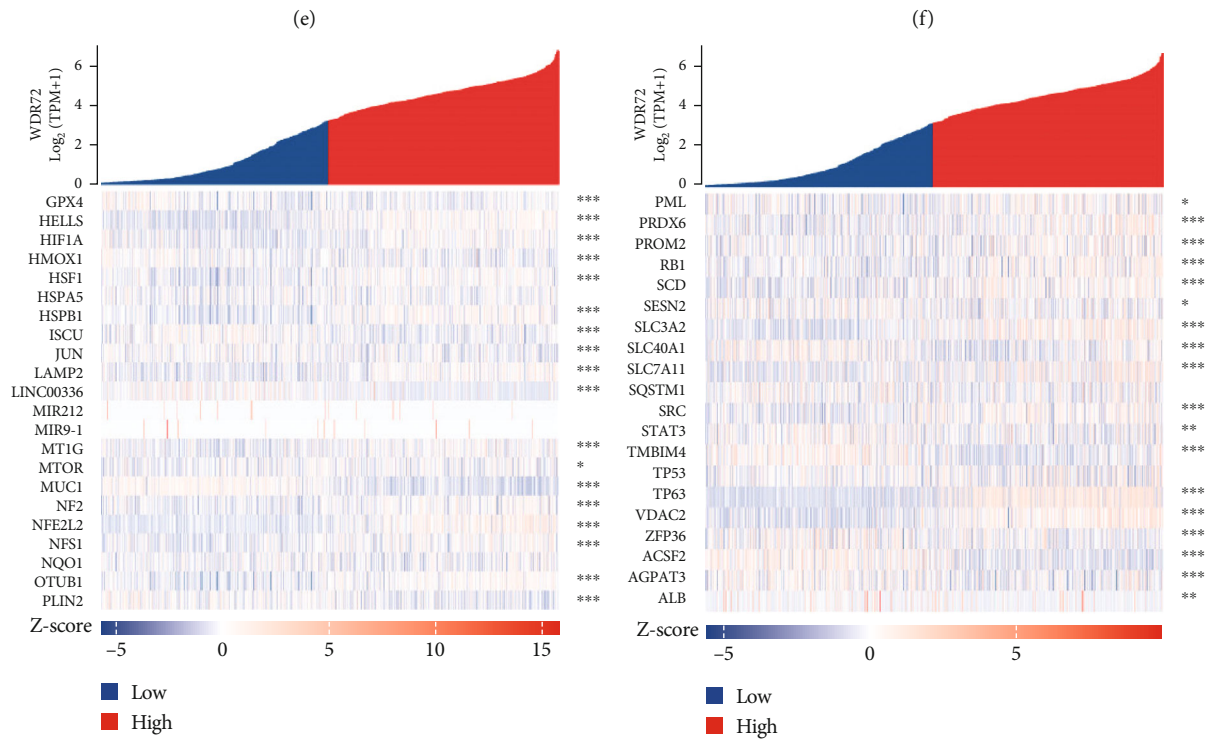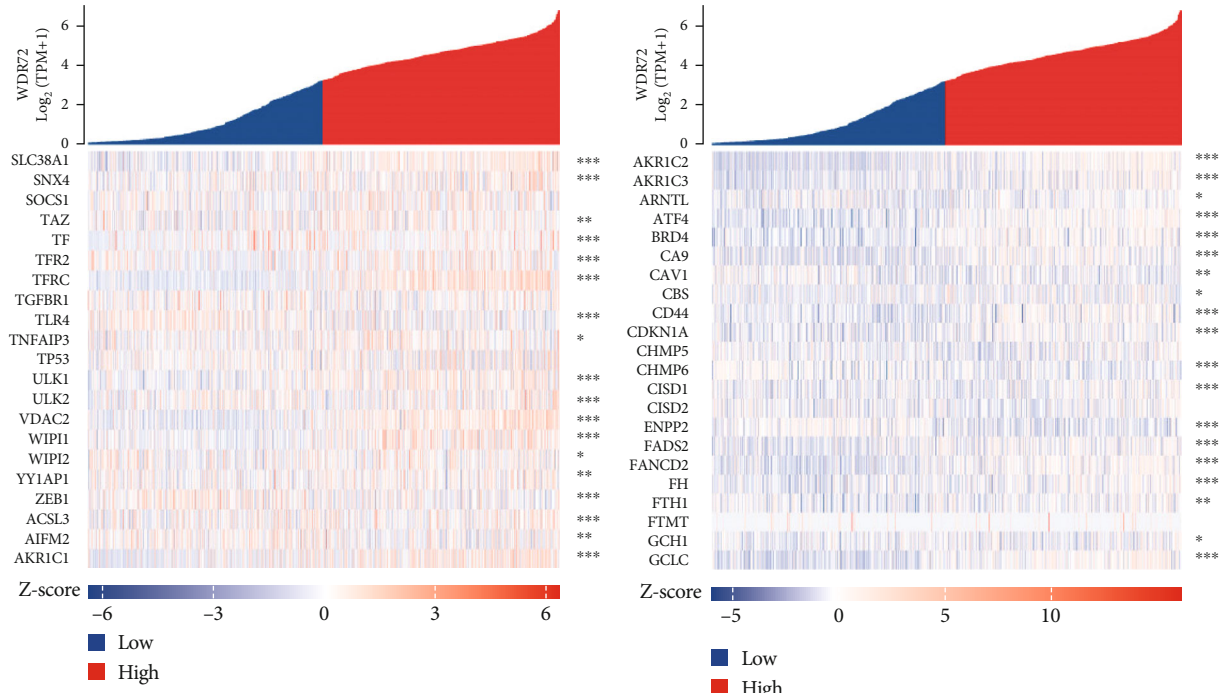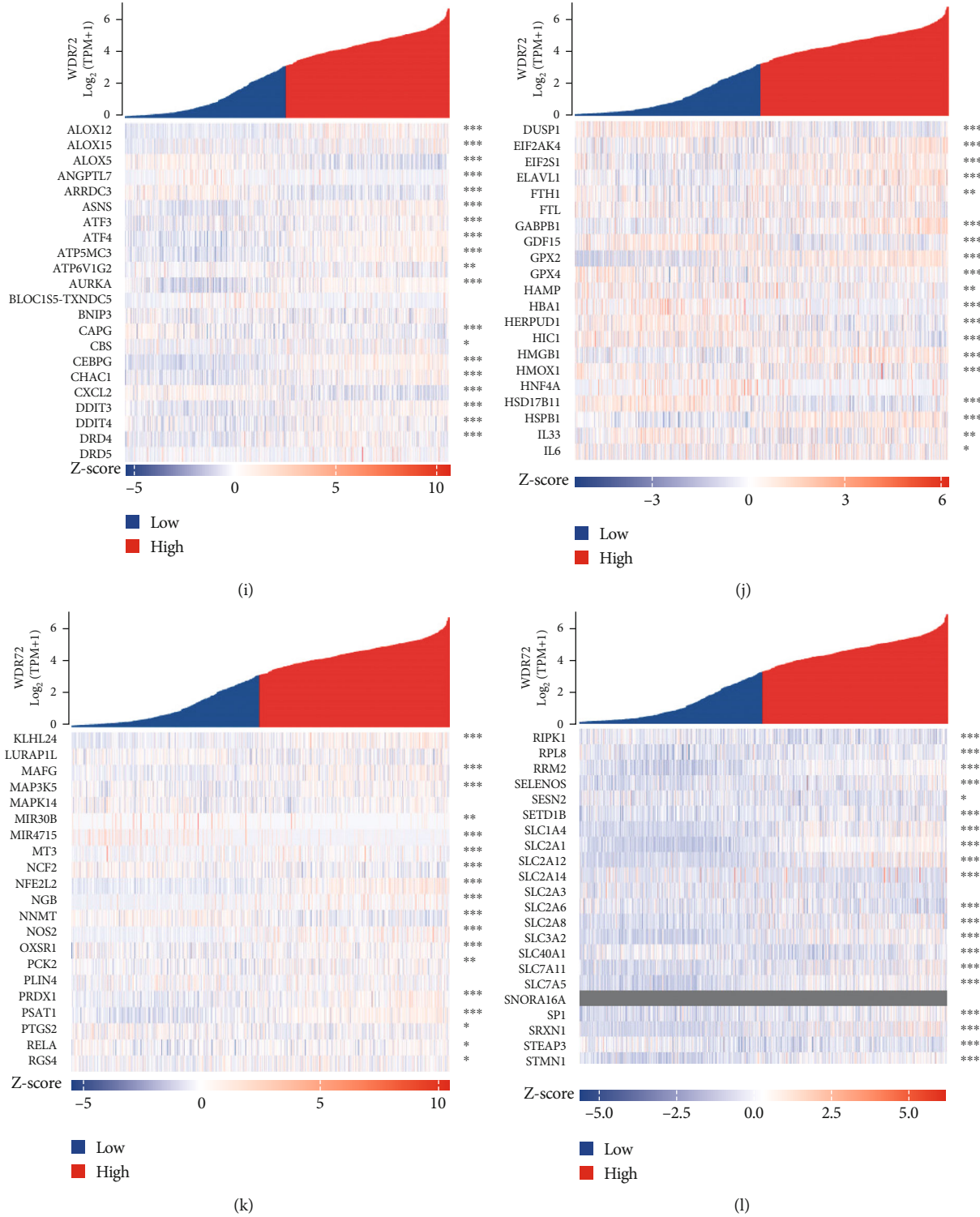
FIGURE 6: Continued.

(m)
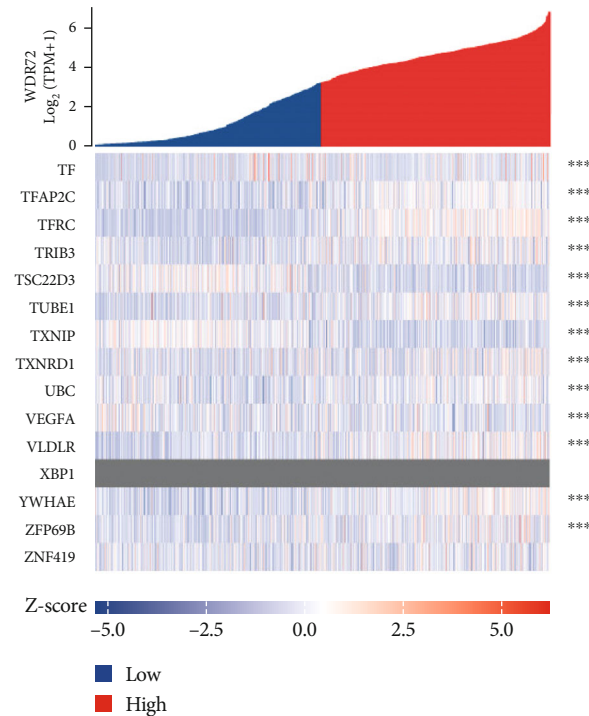
FIGURE 6: (a–m) TCGA (https://portal.gdc.cancer.gov/) removed target molecules in element LUADLUSC (lung cancer) and analyzed control/normal (not all elements have control/normal). Then use R (version 3.6.; 3) with the ggplot2 package: WDR72[ENSG00000166415] coexpression heat map of ferroptosis-related genes in non-small cell-lung cancer. Significance indicator: ns; $p \geq 0.05$; $^*p < 0.05$; $^{**}p < 0.01$; $^{***}p < 0.001$.

4. Discussion

Lung cancer has two major histological forms: small-cell and non-small-cell. Genomic alterations have been found in LUSC and SCC. Lung cancer causes the greatest cancer-related deaths among males and females and inflammation and environmental risk factors such as smoking significantly contribute to lung cancer progression [27]. We analyzed the clinical significance of WDR72 in NSCLC data from the TCGA database WDR72. We discovered a close correlation with smoking, and the duration of smoking in years is also positively related to WDR72 expression. Concurrently, we used our clinical data to conduct univariate and multivariate analysis and found consistent results with the bioinformatic analysis; accordingly, WDR72 can be used as an NSCLC-target gene.

Ferroptosis was first identified as erastin-induced death and found to be involved in various pathophysiological processes and diseases. Since certain oncogenically mutated tumor cells have increased susceptibility to ferroptosis, ferroptosis can be triggered, and ferroptosis-sensitive tumor cells may also have significant therapeutic potential. Therefore, modulation of ferroptosis may have clinical potential in disorders related to ferroptosis [28]. The high-iron concentration of cancer cells and their increased susceptibility to developing ferroptosis are promising for cancer therapy [29]. Herein, we analyzed the correlation between WDR72

and ferroptosis-related genes using the R language and found that WDR72 was related to most ferroptosis-related genes. It is speculated that WDR72 may affect non-small-cells through the ferroptosis pathway of lung cancer progression.

TME is critical in cancer development, and different microenvironment signals have tumor-promoting and tumor-suppressing effects [30]. In TME, injury-related signals can influence the phenotype and activation condition of tumor cells and infiltrate immune cells [31]. The connection between the inflammatory microenvironment and tumors is bidirectional and dynamic and has both tumor-promoting and tumor-suppressing properties that it is not only the basis for the onset and progression of tumors [32]. Correlation analysis was performed in the NSCLC data, except for NK CD56dim cells and Tcm. In contrast, the other 22 cells were related, so we confirmed that WDR72 changes the TME through immune infiltration and impacts the progression of NSCLC.

Finally, our enrichment analysis indicated that WDR72 might be enriched through the cell cycle, immune system, RNA polymerase II transcription, and extracellular matrix organization. This suggested that it may affect tumor growth and metastasis through these pathways. Moreover, we conducted a series of tests to examine WDR72 expression in NSCLC tissues. WDR72 was elevated in NSCLC tissues relative to surrounding normal tissue.

(a)

(b)

(c)

(d)

(e)

(f)

(g)

Figure 7: Continued.

(h)

(i)

(j)

(k)

(l)

(m)
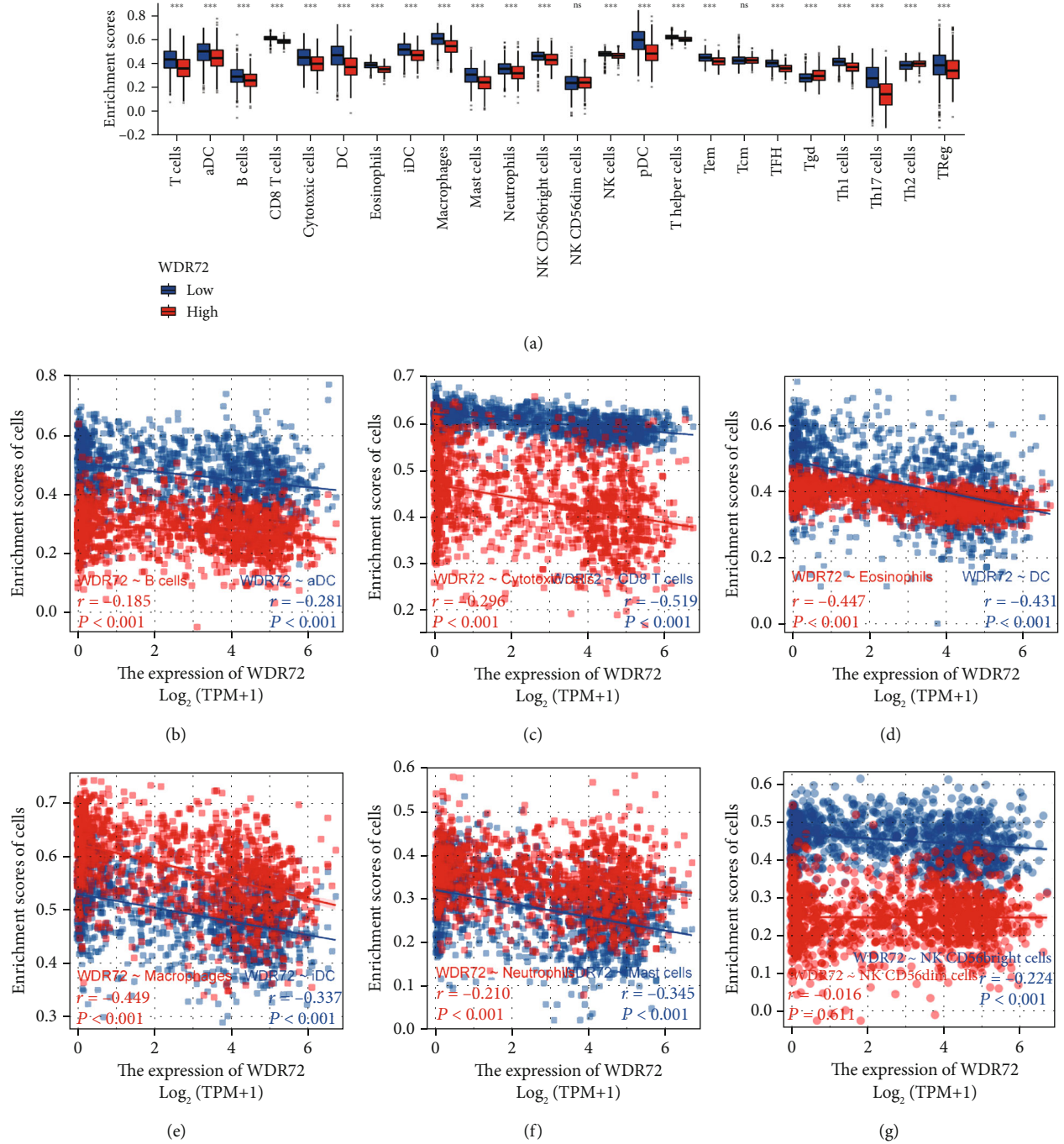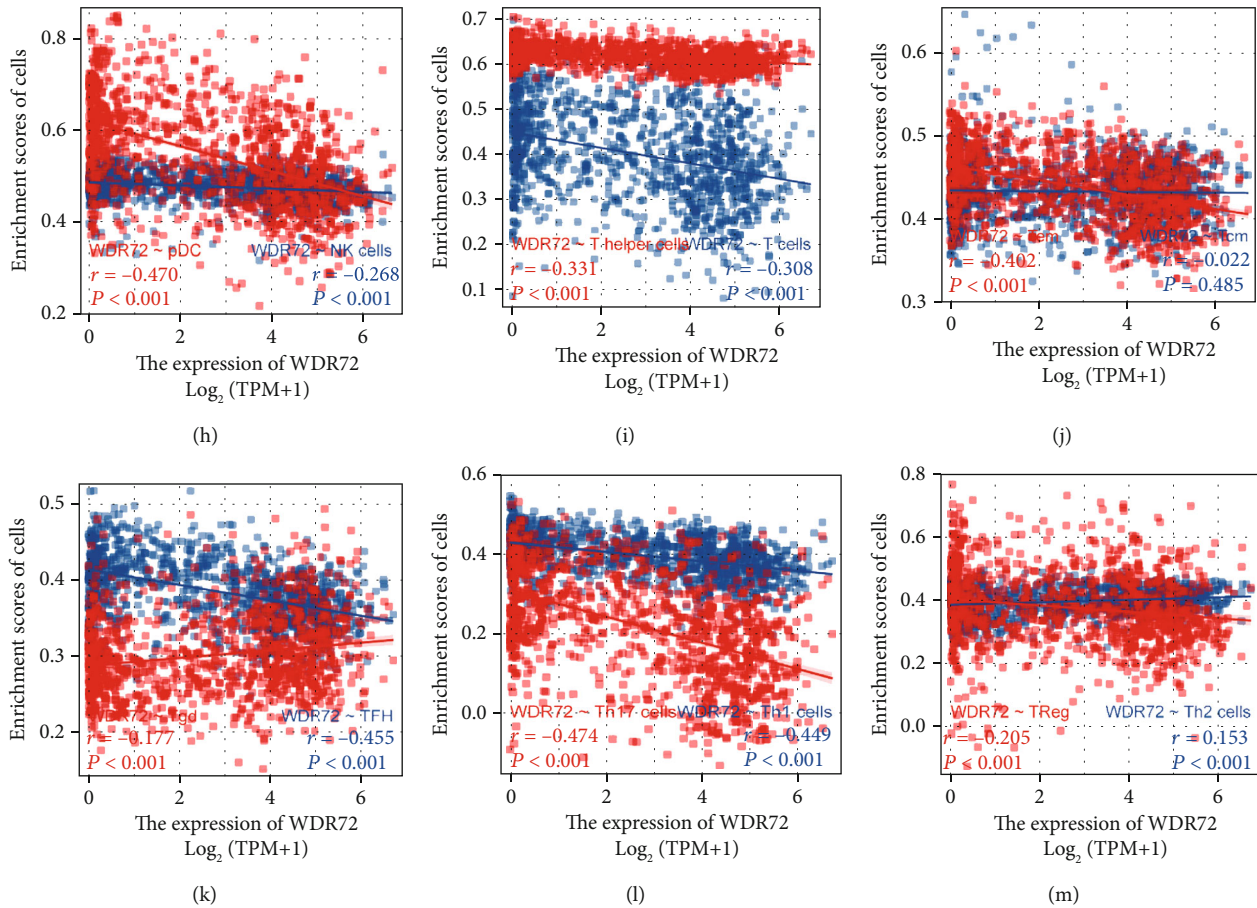
FIGURE 7: (a–m) TCGA (https://portal.gdc.cancer.gov/) RNAseq data in level 3 HTSeq-FPKM format in LUADLUSC (lung cancer) project after removing control/normal (not all projects have control/normal) using software: R (The GSVA package in version 3.6.3) has undergone the immune infiltration algorithm: ssGSEA (the built-in algorithm of the GSVA package) grouped WDR72 [ENSG00000166415] by the median and calculated the high and low expressions of WDR72 and 24 types of immune cells. Significant sign: ns; $p \geq 0.05$; $^{*}p < 0.05$; $^{**}p < 0.01$; $^{***}p < 0.001$.

(a)

(b)
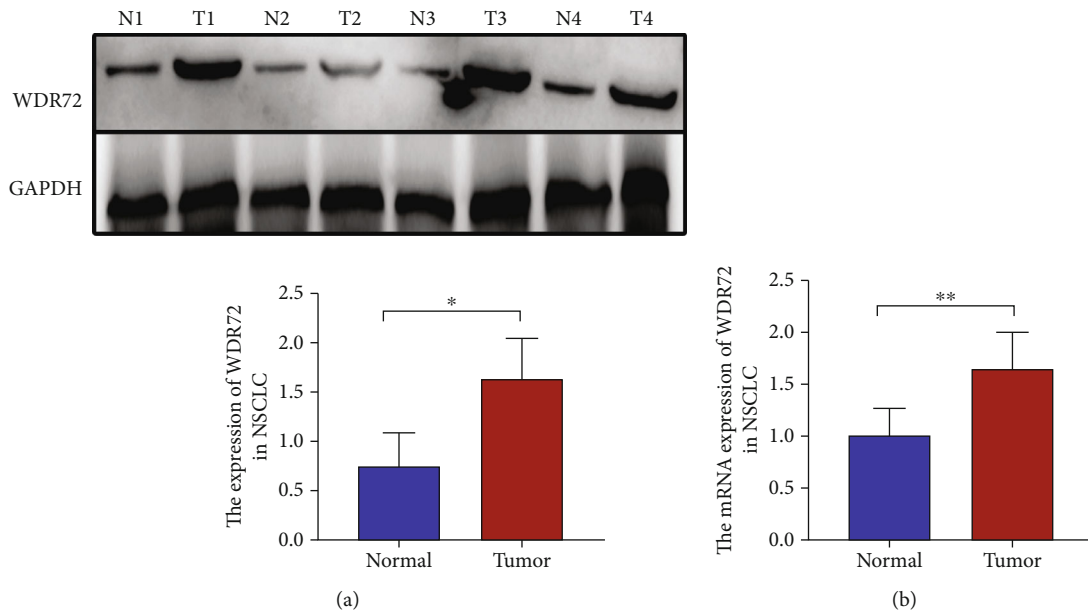
FIGURE 8: Expression of WDR72 in non-small-cell lung cancer (NSCLC). (a) Western blot analysis was used to detect the expression level of WDR72 in NSCLC tissues. (b) The expression level of WDR72 mRNA in NSCLC tissues was detected by qRT-PCR. $^{*}p < 0.05$; $^{**}p < 0.01$. N stands for normal tissue; T stands for tumor.

(a)   (b)

(c)
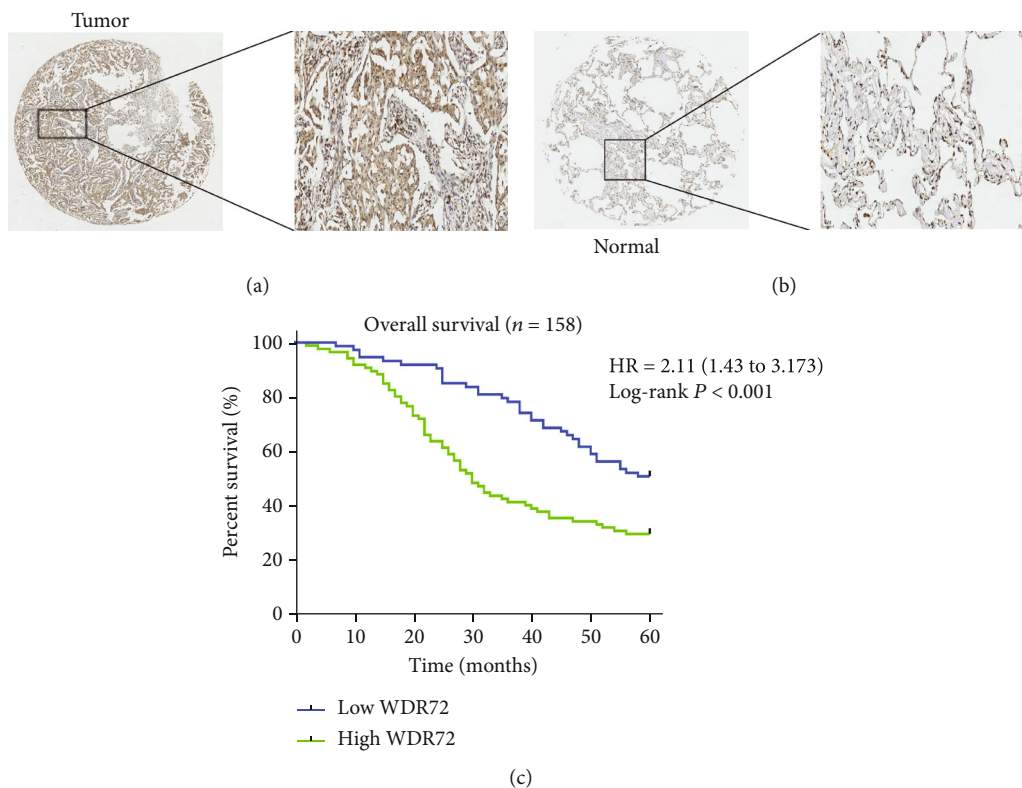
Figure 9: Expression of WDR72 in non-small-cell lung cancer (NSCLC). (a, b) Representative images of different IHC staining intensities of WDR72 in NSCLC tissues and corresponding adjacent normal tissues. (Tumor staining intensity score: 5)(Normal staining intensity score: 2) Magnification: x100 and x400. (c) Prognostic and survival analysis of 158 clinical NSCLC patients.

Table 2: Relationship between WDR72 expression and clinicopathologic features of NSCLC patients.

| Characteristics | Number | Expression of WDR72 | | P value[a] |
		Low (N = 73)	High (N = 85)	
Age				0.425
≤60	72	36	36	
>60	86	37	49	
Gender				0.202
Female	77	40	37	
Male	81	33	48	
Smoke				0.025*
No	75	42	33	
Yes	83	31	52	
Tumor size				0.038*
≤3 cm	72	40	32	
>3 cm	86	33	53	
TNM stage				0.032*
I and II	114	59	55	
III and IV	44	14	30	
Histology stage				0.037*
Well	122	62	60	
Poorly	36	11	25	
Metastasis				0.016*
Negative	85	47	38	
Positive	73	26	47	

[a]Chi-square test.*$p < 0.05$.

TABLE 3: Univariate and multivariate analysis of prognostic factors of 5-year overall survival in WDR 72 patients.

Characteristic	Univariate analysis			Multivariate analysis		
	HR	95% CI	P	HR	95% CI	P
WDR72 expression						
Low vs. high	0.478	0.328~0.752	<0.001**	0.624	0.404~0.963	0.033*
Gender						
Male vs. female	0.706	0.471~1.057	0.091			
Age (years)						
≤60 vs. >60	0.925	0.617~1.386	0.705			
Smoking						
No vs. yes	0.605	0.402~0.910	0.016*	0.885	0.546~1.432	0.618
Tumor size (cm)						
≤3 vs. >3	0.342	0.220~0.530	<0.001**	0.827	0.495~1.381	0.468
TNM stage						
I/II vs. III/VI	0.219	0.144~0.332	<0.001**	0.416	0.263~0.660	<0.001**
Histology stage						
Well vs. poorly	0.356	0.232~0.548	<0.001**	0.417	0.257~0.677	<0.001**
Metastasis						
No vs. yes	0.192	0.124~0.298	<0.001**	0.240	0.149~0.387	<0.001**

HR: hazard ratio; CI: confidence interval; $*P < 0.05$; $**P < 0.001$.

Our study has some limitations. First, in vitro cell experiments are required to study WDR72 expression and function further. Second, our data suggest that WDR72 can act as a prognostic factor in NSCLC, which needs additional validation. Third, the presence of WDR72 on the TME and immunotherapy requires in vitro and in vivo experimental and clinical validation. Fourth, although we confirmed WDR72 expression in human NSCLC tissues, its exact regulatory mechanism remains unclear. WDR72 can participate in some biological processes in cells, including cell death, cell division, protein synthesis, and membrane transport. Ferroptosis is also a kind of programmed death. According to our research and analysis, WDR72 has a high correlation with many molecules of the ferroptosis pathway. Is it possible that WDR72 affects NSCLC through the ferroptosis pathway? In the next study, we will focus on the mechanism research.

5. Conclusion

Herein, the analysis of WDR72 suggested that WDR72 may be a prognostic factor in NSCLC, which was expressed at the mRNA and protein levels among NSCLC tumors and normal tissues. We initially revealed the association between WDR72 and ferroptosis and immune infiltration. Furthermore, WDR72 expression was linked to MSI, TMB, and immune cell infiltration in NSCLC. These findings may elucidate the aim of WDR72 in the incidence and growth of NSCLC and provide a reference for future patients with NSCLC to receive more accurate and personalized immunotherapy.

Data Availability

The utilized and examined datasets (Table 1) are available upon reasonable request from the corresponding author.

Ethical Approval

The ethics committee of The Sixth People's Hospital of Nantong and Affiliated Hospital of Nantong University, Jiangsu, China, approved the research. All human research was done following the most recent iteration of the Declaration of Helsinki.

Consent

Participants provided an informed permission before this research.

Conflicts of Interest

These authors declare no conflict of interest.

Authors' Contributions

Guanglin Shi did the experiments and wrote the document. Hua Huang and Zhongbo Yin greatly contributed to pathological specimens and immunohistochemistry examination. Qinggan Ni helped significantly with the analysis and document preparation. Yuqing Miao helped with the analysis with productive discussions and contributed reagents and materials. Weirong Shi did the data analyses. Minhua Shi designed the experiments. All researchers read and approved

References

[1] A. Amatu, A. Sartore-Bianchi, K. Bencardino, E. G. Pizzutilo, F. Tosi, and S. Siena, "Tropomyosin receptor kinase (TRK) biology and the role of NTRK gene fusions in cancer," Annals of Oncology, vol. 30, Supplement 8, pp. viii5–viii15, 2019.

[2] Y. J. Jeon, T. Kim, D. Park et al., "miRNA-mediated TUSC3 deficiency enhances UPR and ERAD to promote metastatic potential of NSCLC," Nature Communications, vol. 9, no. 1, p. 5110, 2018.

[3] M. C. Schwaederlé, S. P. Patel, H. Husain et al., "Utility of genomic assessment of blood-derived circulating tumor DNA (ctDNA) in patients with advanced lung adenocarcinoma," Clinical Cancer Research, vol. 23, no. 17, pp. 5101–5111, 2017.

[4] T. Koo, A. R. Yoon, H. Y. Cho, S. Bae, C. O. Yun, and J. S. Kim, "Selective disruption of an oncogenic mutant allele by CRISPR/Cas9 induces efficient tumor regression," Nucleic Acids Research, vol. 45, no. 13, pp. 7897–7908, 2017.

[5] H. Zhang, M. Koruyucu, F. Seymen et al., "WDR72 mutations associated with amelogenesis imperfecta and acidosis," Journal of Dental Research, vol. 98, no. 5, pp. 541–548, 2019.

[6] C. A. Ibrahim-Verbaas, J. Bressler, S. Debette et al., "GWAS for executive function and processing speed suggests involvement of the CADM2 gene," Molecular Psychiatry, vol. 21, no. 2, pp. 189–197, 2016.

[7] S. A. Howles, A. Wiberg, M. Goldsworthy et al., "Genetic variants of calcium and vitamin D metabolism in kidney stone disease," Nature Communications, vol. 10, no. 1, p. 5175, 2019.

[8] Y. Wu, X. Zhang, X. Wei et al., "Development of an individualized ubiquitin prognostic signature for clear cell renal cell carcinoma," Frontiers in Cell and Development Biology, vol. 22, no. 9, article 684643, 2021.

[9] U. Warnecke-Eberz, R. Metzger, A. H. Hölscher, U. Drebber, and E. Bollschweiler, "Diagnostic marker signature for esophageal cancer from transcriptome analysis," Tumour Biology, vol. 37, no. 5, pp. 6349–6358, 2016.

[10] Z. Zhang, Q. Wang, M. Zhang et al., "Comprehensive analysis of the transcriptome-wide m6A methylome in colorectal cancer by MeRIP sequencing," Epigenetics, vol. 16, no. 4, pp. 425–435, 2021.

[11] L. Cao and W. Mu, "Necrostatin-1 and necroptosis inhibition: pathophysiology and therapeutic implications," Pharmacological Research, vol. 163, article 105297, 2021.

[12] P. H. Chen, J. Wu, C. C. Ding et al., "Kinome screen of ferroptosis reveals a novel role of ATM in regulating iron metabolism," Cell Death and Differentiation, vol. 27, no. 3, pp. 1008–1022, 2020.

[13] Y. Zou, M. J. Palte, A. A. Deik et al., "A GPX4-dependent cancer cell state underlies the clear-cell morphology and confers sensitivity to ferroptosis," Nature Communications, vol. 10, no. 1, 2019.

[14] X. Sui, R. Zhang, S. Liu et al., "RSL3 drives ferroptosis through GPX4 inactivation and ROS production in colorectal cancer," Frontiers in Pharmacology, vol. 22, no. 9, 2018.

[15] D. Stefanova, A. Raychev, J. Arezes et al., "Endogenous hepcidin and its agonist mediate resistance to selected infections by clearing non-transferrin-bound iron," Blood, vol. 130, no. 3, pp. 245–257, 2017.

[16] J. K. Sa, S. H. Kim, J. K. Lee et al., "Identification of genomic and molecular traits that present therapeutic vulnerability to HGF-targeted therapy in glioblastoma," Neuro-Oncology, vol. 21, no. 2, pp. 222–233, 2019.

[17] H. Kadara, M. Choi, J. Zhang et al., "Whole-exome sequencing and immune profiling of early-stage lung adenocarcinoma with fully annotated clinical follow-up," Annals of Oncology, vol. 28, no. 1, pp. 75–82, 2017.

[18] N. Nagarsheth, M. S. Wicha, and W. Zou, "Chemokines in the cancer microenvironment and their relevance in cancer immunotherapy," Nature Reviews Immunology, vol. 17, no. 9, pp. 559–572, 2017.

[19] M. Poggio, T. Hu, C. C. Pai et al., "Suppression of Exosomal PD-L1 induces systemic anti-tumor immunity and memory," Cell, vol. 177, no. 2, pp. 414–427.e13, 2019.

[20] T. P. Lu, M. H. Tsai, J. M. Lee et al., "Identification of a novel Biomarker,SEMA5A, for non-small cell lung carcinoma in nonsmoking women," Cancer Epidemiology, Biomarkers & Prevention, vol. 19, no. 10, pp. 2590–2597, 2010.

[21] T.-P. Lu, C. K. Hsiao, L.-C. Lai et al., "Identification of regulatory SNPs associated with genetic modifications in lung adenocarcinoma," BMC Research Notes, vol. 8, no. 1, 2015.

[22] L. Xu, C. Lu, Y. Huang et al., "SPINK1 promotes cell growth and metastasis of lung adenocarcinoma and acts as a novel prognostic biomarker," BMB Reports, vol. 51, no. 12, pp. 648–653, 2018.

[23] J. Hou, J. Aerts, B. den Hamer et al., "Gene expression-based classification of non-small cell lung carcinomas and survival prediction," PLoS One, vol. 5, no. 4, article e10312, 2010.

[24] T. Y. Wei, C. C. Juan, J. Y. Hisa et al., "Protein arginine methyltransferase 5 is a potential oncoprotein that upregulates G1 cyclins/cyclin-dependent kinases and the phosphoinositide 3-kinase/AKT signaling cascade," Cancer Science, vol. 103, no. 9, pp. 1640–1650, 2012.

[25] T. Y. Wei, J. Y. Hsia, S. C. Chiu et al., "Methylosome protein 50 promotes androgen- and estrogen-independent tumorigenesis," Cellular Signalling, vol. 26, no. 12, pp. 2940–2950, 2014.

[26] K. Quek, J. Li, M. Estecio et al., "DNA methylation intratumor heterogeneity in localized lung adenocarcinomas," Oncotarget, vol. 8, no. 13, pp. 21994–22002, 2017.

[27] T. D. O'Brien, P. Jia, N. E. Caporaso, M. T. Landi, and Z. Zhao, "Weak sharing of genetic association signals in three lung cancer subtypes: evidence at the SNP, gene, regulation, and pathway levels," Genome Medicine, vol. 10, no. 1, 2018.

[28] J. Li, F. Cao, H. L. Yin et al., "Ferroptosis: past, present and future," Cell Death & Disease, vol. 11, no. 2, p. 88, 2020.

[29] P. P. Yee, Y. Wei, S. Y. Kim et al., "Neutrophil-induced ferroptosis promotes tumor necrosis in glioblastoma progression," Nature Communications, vol. 11, no. 1, 2020.

[30] O. Iriondo, Y. Liu, G. Lee et al., "TAK1 mediates microenvironment-triggered autocrine signals and promotes

triple-negative breast cancer lung metastasis," *Nature Communications*, vol. 9, no. 1, 2018.

[31] A. G. Alvarado, P. S. Thiagarajan, E. E. Mulkearns-Hubert et al., "Glioblastoma cancer stem cells evade Innate immune suppression of self-renewal through reduced TLR4 expression," *Cell Stem Cell*, vol. 20, no. 4, pp. 450–461.e4, 2017.

[32] N. N. Pavlova, J. Zhu, and C. B. Thompson, "The hallmarks of cancer metabolism: still emerging," *Cell Metabolism*, vol. 34, no. 3, pp. 355–377, 2022.

Research Article

High Expression of Ten Eleven Translocation 1 Is Associated with Poor Prognosis in Hepatocellular Carcinoma

Haopeng Wen,[1] Tengfei Ji,[2] Liteng Lin,[3] Nan Cheng,[1] Kangshun Zhu,[3] and Liangqi Cao [1]

[1]*Department of Hepatobiliary Surgery, The Second Affiliated Hospital of Guangzhou Medical University, Guangzhou 510260, China*
[2]*Department of Hepatobiliary Surgery, Affiliated Huadu Hospital, Southern Medical University (People's Hospital of Huadu District), Guangzhou 510000, China*
[3]*Department of Minimally Invasive Interventional Radiology, The Second Affiliated Hospital of Guangzhou Medical University, Guangzhou 510260, China*

Correspondence should be addressed to Liangqi Cao; clq0829@163.com

Haopeng Wen and Tengfei Ji contributed equally to this work.

Background. DNA methylation patterns have been found to be distinct between tumor and normal patients. However, the effect of DNA demethylation enzymes, ten eleven translocation (TET) proteins, has not been comprehensively characterized in liver cancer. In this research, we sought to unravel the linkage of TET proteins with prognosis, immune characteristics and biological pathways in hepatocellular carcinoma (HCC). *Materials and Methods.* Four independent datasets with gene expression data and clinical data of HCC samples were downloaded from public databases. CIBERSORT, single sample Gene Set Enrichment Analysis (ssGSEA), MCP-counter, and TIMER were implemented to evaluate immune cell infiltration. limma was employed to screen differentially expressed genes (DEGs) between two groups. The demethylation-related risk model was established by using univariate Cox regression analysis, the least absolute shrinkage and selection operator (LASSO), and stepwise Akaike information criterion (stepAIC). *Results.* TET1 was significantly higher expressed in tumor samples than that in normal samples. HCC patients with advanced stages (III+IV) and grades (G3+G4) had higher TET1 expression compared to early stages (I+II) and grades (G1+G2). HCC samples with high TET1 expression had worse prognosis than that with low expression. High and low TET1 expression groups had distinct immune cell infiltration and response to immunotherapy and chemotherapy. We identified 90 DEGs related to DNA demethylation in high vs. low TET1 expression groups. Furthermore, we established a risk model based on 90 DEGs containing seven key prognostic genes (SERPINH1, CDC20, HACD2, SPHK1, UGT2B15, SLC1A5, and CYP2C9) with effectiveness and robustness in predicting HCC prognosis. *Conclusions.* Our study suggested TET1 as a potential indicator in HCC progression. TET1 was closely involved in immune infiltration and activation of oncogenic pathways. The DNA demethylation-related risk model was potential to be applied for predicting HCC prognosis in clinics.

1. Introduction

Liver cancer contributes to a proportion of 4.7% new cancer cases and 8.3% new cancer deaths worldwide according to the global cancer statistics in 2020 [1]. Hepatocellular carcinoma (HCC) is the most common histological type, comprising of approximately 75% of liver cancer patients [2]. The incidence of liver cancer in male populations are almost two times of that in female populations, as shown in 2020 cancer data [1]. Strikingly, liver cancer contributes to the second cancer death in male populations (10.5% of cancer deaths) [1]. Metastatic liver cancer patients have a poor overall survival, in spite of the treatment with molecular drugs, which results from the unavoidable drug resistance in most of the patients [3]. Also, due to the intratumor heterogeneity of liver cancer, the development of targeted therapies becomes even challenging [4]. Therefore, understanding the molecular mechanisms during liver cancer progression is of

great importance for facilitating the exploration of novel therapeutic targets.

It is knowledgeable that the variations of tumor suppressor genes or protumor genes are the key inducers of cancer. In addition to solid genetic mutations, the alterations of epigenetic modifications are also a crucial factor in the onset process of cancer. Bulk of evidences have illustrated that DNA methylation profiles are distinct between normal and cancer genomes [5–7]. DNA methylation is under controlled by two classes of enzymes, methylation enzymes (DNMT3a and DNMT3b) [8] and demethylation enzymes (ten eleven translocation (TET) family) [9]. TET enzymes, consisting of consists of TET1, TET2, and TET3, are capable to reverse DNA methylation by oxidizing 5-methylcytosine (5mC) to 5-hydroxymethylcytosine (5hmC), 5-formylcytosine (5fC), and 5-carboxylcytosine (5caC) [10]. It has been shown that the aberrant expression and mutations of TET proteins are not rare in cancer patients [11, 12]. The expression levels of TET proteins are associated with tumor progression and metastasis, which offers a potential of TET proteins as markers in cancer prognosis and diagnosis [13, 14].

In this study, we focused on the effect of TET1 in HCC patients and sought to elucidate the potential crosstalk of TET1 with immune microenvironment in HCC. In addition, we identified key prognostic genes by extracting the TET1 and DNA methylation-related genes and established a risk model for predicting HCC prognosis. We demonstrated the potential of DNA methylation-related genes as prognostic markers in HCC patients.

2. Materials and Methods

2.1. Data Acquisition. TCGA-LIHC dataset (abbreviated as TCGA dataset) containing RNA sequencing (RNA-seq) data and clinical information was downloaded from Genomic Data Commons Data Portal (https://portal.gdc.cancer.gov/projects/TCGA-LIHC) through TCGA GDC API [15]. ICGC-LIRI-JP dataset (abbreviated as ICGC dataset) was downloaded from hepatocellular carcinoma database [16] (HCCDB, http://lifeome.net/database/hccdb/home.html). GSE14520 and GSE76427 datasets with microarray data were obtained from Gene Expression Omnibus (GEO) database [17] (https://www.ncbi.nlm.nih.gov/geo/query/acc.cgi?acc=GSE14520, https://www.ncbi.nlm.nih.gov/geo/query/acc.cgi?acc=GSE76427).

2.2. Data Preprocessing. For TCGA dataset, the HCC samples with survival time (over than 30 days and less than 10 years) and survival status were retained. Ensembl ID was transferred to gene symbol. The median value of gene expression was selected when the gene had multiple Ensembl IDs. After preprocessing, 334 HCC samples and 50 paracancerous (normal) samples were included in TCGA dataset. For two microarray datasets (GSE14520 and GSE76427), the probes were matched to the gene symbols according to the annotation file of microarray platform. The probes matching to multiple gene symbols were excluded, and the median expression level was used when there were multiple probes of one gene. A total of 221 and

115 HCC samples were included in GSE14520 and GSE76427 datasets, respectively. ICGC dataset included 212 HCC samples and 177 normal samples, and no preprocessing was performed for the ICGC data.

2.3. Immune Analysis. CIBERSORT, single sample gene set enrichment analysis (ssGSEA), Microenvironment Cell Populations-counter (MCP-counter), and Tumor IMmune Estimation Resource (TIMER) were employed to assess immune cell infiltration. CIBERSORT [18] (http://cibersort.stanford.edu/) is able to estimate the proportion of 22 immune cells from tumor mix based on a validated leukocyte gene signature matrix (LM22). MCP-counter [19] allows to detect the abundance of 10 cell populations including immune cell and stromal cell populations from the transcriptome of tumor tissues. SsGSEA [20] is a widely used methodology for evaluating the absolute enrichment score of a gene set for each sample. The gene sets of 28 immune cells were obtained from a previous study [21], and the ssGSEA scores of the immune cells were measured through GSVA R package [22]. TIMER [23] (http://timer.cistrome.org/) provides the interpretation of six major immune modules and visualizes the estimated proportion of tumor-infiltrated immune cells. TIDE [24] (http://tide.dfci.harvard.edu/) tool can predict the response to immune checkpoint inhibitors (ICIs) through estimating T cell status (exclusion and dysfunction) and infiltration of immunosuppressive cells including myeloid-derived suppressor cells (MDSCs), cancer-associated fibroblasts (CAFs), and M2 tumor-associated macrophages (TAMs).

2.4. Functional Enrichment Analysis of Biological Pathways. Gene set enrichment analysis (GSEA) software [25] was applied to identify enriched pathways with an ordered gene set. Kyoto Encyclopedia of Genes and Genomes (KEGG) pathways "c2.cp.kegg.v7.5.1.symbols.gmt" and hallmark pathways "h.all.v7.5.1.symbols.gmt" were downloaded from Molecular Signature Database (MSigDB, https://www.gsea-msigdb.org/gsea/msigdb/).

2.5. Differential Analysis. Differentially expressed genes (DEGs) between two groups were identified by limma R package [26] based on their gene expression profiles. False discovery rate (FDR) < 0.05 and |log2 fold change (FC)| > 1 were set as thresholds to screen significant DEGs. ClusterProfiler R package [27] was implemented to annotate the significantly enriched Gene Ontology (GO) terms and KEGG pathways of DEGs.

2.6. Construction of a Risk Model for Predicting HCC Prognosis. The gene sets of two DNA demethylation-related biological processes (BPs) GOBP_DNA_METHYLATION_OR_DEMETHYLATION and GOBP_POSITIVE_REGULATION_OF_DNA_DEMETHYLATION were downloaded from MSigDB. The enrichment score of the two BPs was calculated by ssGSEA via GSVA R package. Pearson correlation analysis was performed between DEGs and TET1 and DEGs and the ssGSEA score of BPs by using Hmisc R package (https://cran.r-project.org/web/packages/Hmisc/index.html). The DEGs with significant correlations both with TET1 and BPs were screened under $|R| > 0.2$ and $P < 0.05$. Next, the DEGs were further screened by univariate Cox regression

(a)

(b)

(c)

(d)

(e)

FIGURE 1: Continued.

TCGA-LIHC
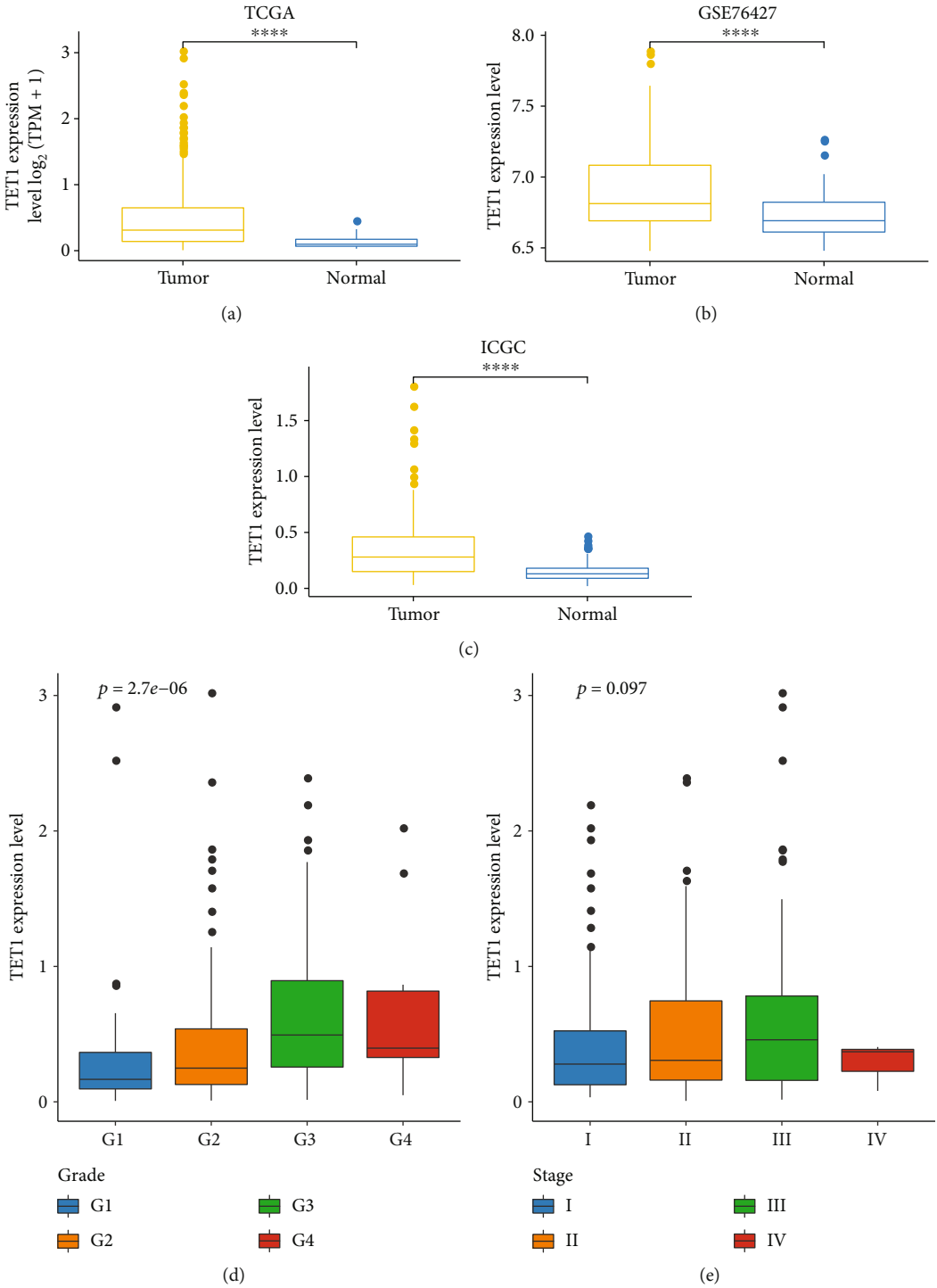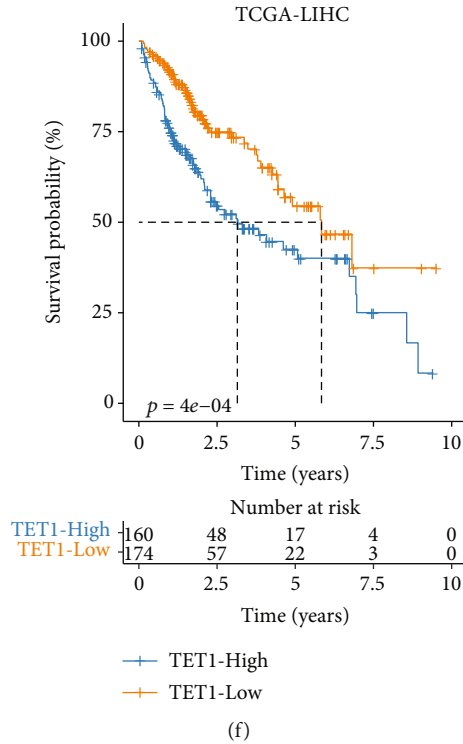
FIGURE 1: TET1 expression was associated with HCC progression and survival. (a–c) The expression level of TET1 in normal and tumor samples in three datasets. Wilcoxon test was performed. (d, e) The expression level of TET1 in different grades and stages in TCGA dataset. ANOVA test was conducted. (f) Kaplan-Meier survival analysis of TET1-high and TET1-low groups in TCGA dataset. Log-rank test was performed. ****$P < 0.0001$.

analysis, least absolute shrinkage and selection operator (LASSO) [28], and stepwise Akaike information criterion (stepAIC) [29]. Finally, the risk model was constructed with gene expression and Lasso coefficients. Risk score = $\Sigma(\text{Exp } i * \text{beta } i)$. Exp indicates the expression levels of genes (i), and beta indicates the LASSO coefficients of corresponding genes. The effectiveness and efficiency of the risk model were validated by Kaplan-Meier survival analysis and receiver operating characteristic (ROC) curve analysis.

2.7. Statistical Analysis. The statistical analysis used in this study was performed in R software (v4.2.0). Wilcoxon test was used to measure the difference between two groups. ANOVA test was conducted to detect the difference among four groups. $P < 0.05$ was determined as statistically significant. The visualization of analyzed results was supported by the Sangerbox platform [30] (http://sangerbox.com/).

3. Results

3.1. TET1 Expression Was Correlated with the Prognosis and Clinical Characteristics in HCC. To evaluate the TET alteration in HCC, we assessed the expression levels of TET1, TET2, and TET3 in three independent datasets (TCGA, GSE76427, and ICGC). As a result, only TET1 was differently expressed between tumor and normal samples in TCGA, GSE76427, and ICGC datasets ($P < 0.0001$, Figures 1(a)–1(c)). An upregulated expression level of TET1 was observed in HCC samples compared with normal

samples. In addition, the samples with late grades or stages showed higher TET1 expression (Figures 1(d) and 1(e)), suggesting that high expression of TET1 may be a risk factor of HCC progression. To examine the performance of TET1 as a prognostic biomarker in HCC, we divided HCC samples into high TET1 expression (TET1-high) and low TET expression (TET1-low) groups according to the median value. Not surprisingly, samples in TET1-low group had obviously longer overall survival than that in TET1-low group ($P = 4e - 04$, Figure 1(f)). Moreover, the distribution of clinical characteristics showed significant differences between TET1-low and TET1-high groups (Figure 2). The proportion of samples with early stages (T1, stage I, and G1) was higher in TET1-low group than that in TET1-high group. Conversely, TET1-high group had a higher proportion of late stages than TET1-low group. In accordant with the above observations, dead samples were more accumulated in TET1-high group compared with TET1-low group. The significant difference of clinical characteristics and prognosis in two TET1 groups indicated that TET1 was importantly involved in HCC progression.

3.2. Immune Characteristics and Biological Analysis in Two TET1 Groups. Evidence has shown that TET proteins play a regulatory role in immune cell development and orchestrate cell differentiation in tumorigenesis [31]. We compared the immune cell infiltration in two TET1 groups through multiple strategies including CIBERSORT, ssGSEA, MCP-counter, and TIMER. The results presented that multiple
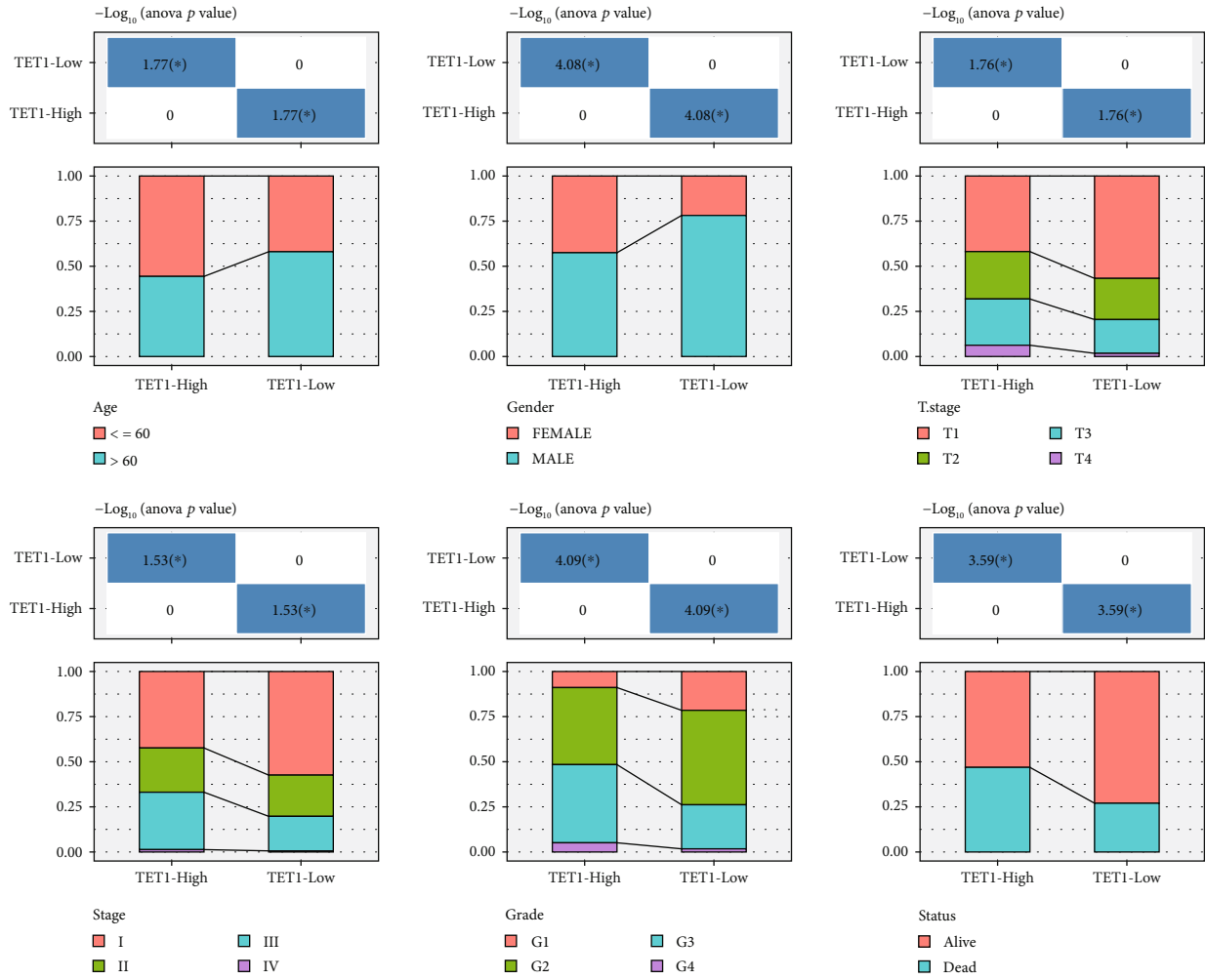
FIGURE 2: TET1-high and TET1-low groups had different distribution of clinical characteristics including age, gender, T stage, stages I-IV, grade, and survival status in TCGA dataset.

types of immune cells were differently enriched in TET1-high and TET1-low groups, such as macrophages, CD8 T cells, and natural killer (NK) cells (Figures 3(a)–3(d)). In the response to immunotherapy, TET1-high group showed higher TIDE score than TET1-low group, which suggested higher immune evasion of TET1-high group possibly resulting from T cell exclusion and infiltration of MDSC (Figure 3(e)). Furthermore, we assessed 10 oncogenic pathways in two TET1 groups and found that 9 oncogenic pathways had distinct enrichment scores between two groups ($P < 0.01$, Figure 3(f)). TET1-high group had higher enrichment score of most oncogenic pathways such as Hippo, Notch, TGF-beta, cell cycle, TP53, and Wnt signaling pathways than TET1-low group. GSEA results showed that metabolic pathways fatty acid metabolism and retinol metabolism were more activated in TET1-low group compared with TET-high group (Figure 3(g)).

To further explore the difference of activated biological pathways in two TET1 groups, we performed differential analysis and identified a total of 516 DEGs between two groups. We identified 404 upregulated DEGs and 112 downregulated DEGs in TET1-high group (Figures 4(a) and 4(b)).

Functional analysis on the upregulated DEGs revealed that cell cycle and DNA repair-related pathways were strikingly enriched (Figure 4(c)). The above results suggested that TET1 may serve as an important role in immune cell orchestration and tumorigenesis.

3.3. Construction and Verification of a Risk Model Related to TET1 and Demethylation-Related Genes. TET1 proteins serve an important role in DNA demethylation. Therefore, we tried to obtain the DEGs associated with both TET1 and DNA demethylation. To reach this goal, we accessed DNA demethylation-related BPs from MsigDB database (GOBP_DNA_METHYLATION_OR_DEMETHYLATION and GOBP_POSITIVE_REGULATION_OF_DNA_DEME THYLATION). Correlation analysis was conducted between DEGs and TET1 or the two demethylation-related BPs, and a total of 90 DEGs were screened to be significantly correlated with both TET1 and the ssGSEA score of two BPs ($|R| > 0.2$; $P < 0.05$, Figure 5(a)). The 90 DEGs were used as a basis for constructing a risk model. Subsequently, we performed a series of methodologies to screen key DEGs for reaching the optimal model. First of all, univariate Cox

(a)

(b)

(c)
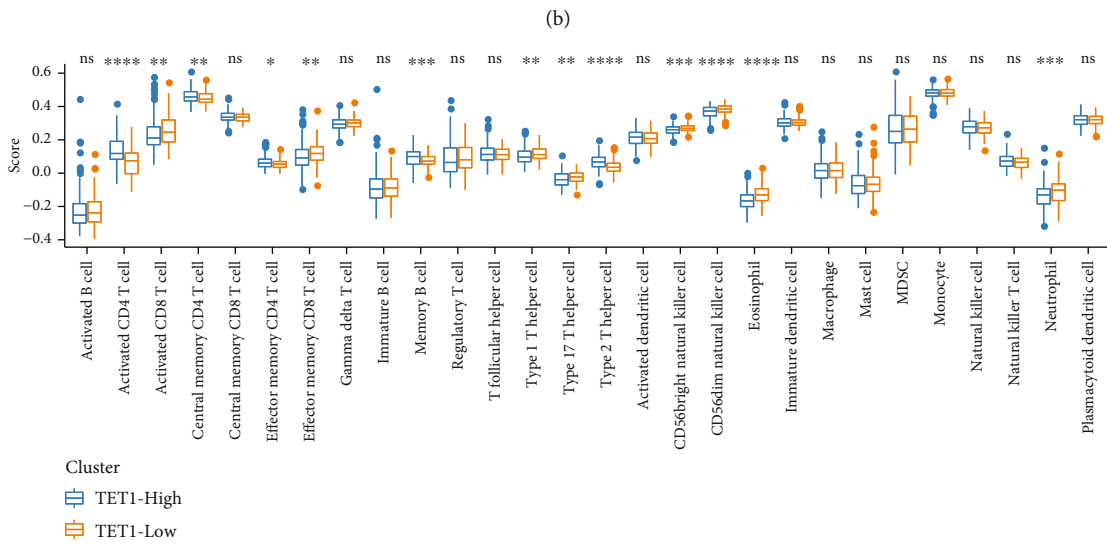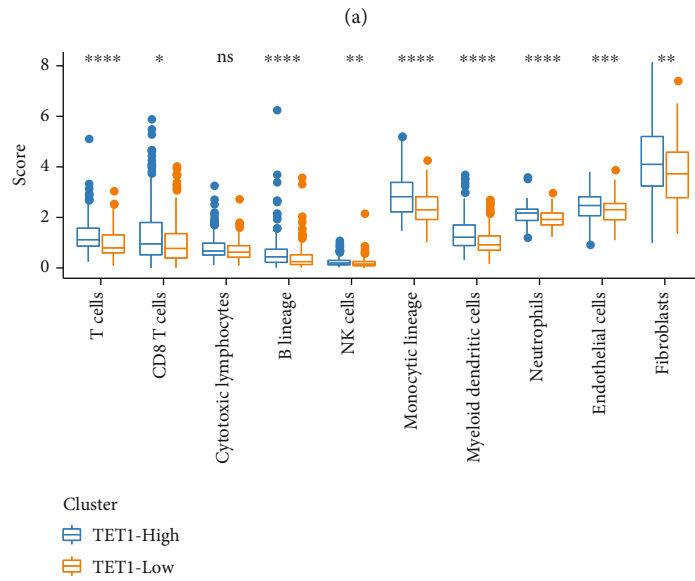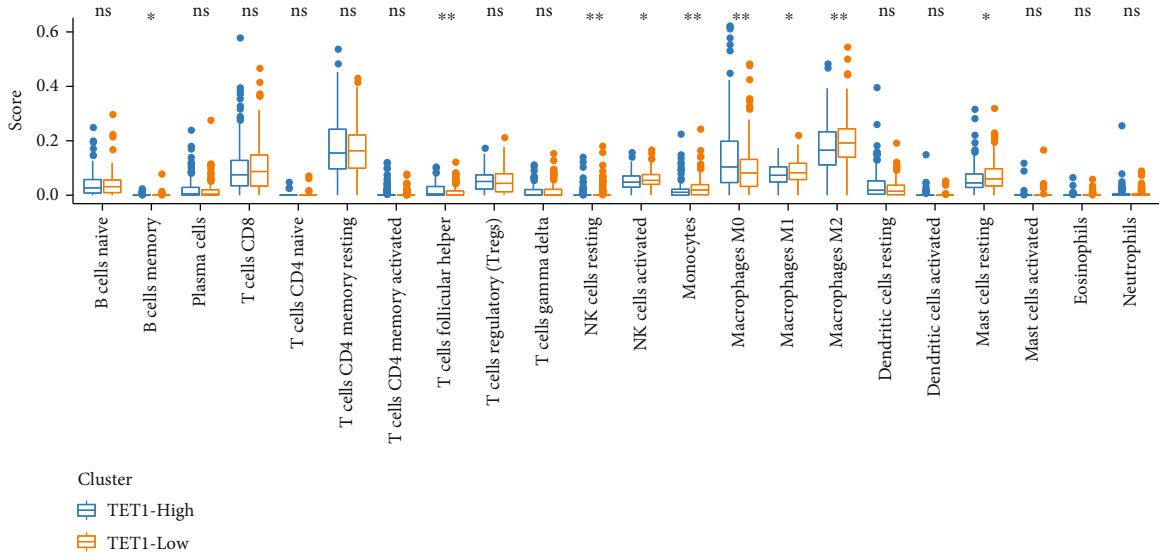
FIGURE 3: Continued.

(d)

(e)

(f)
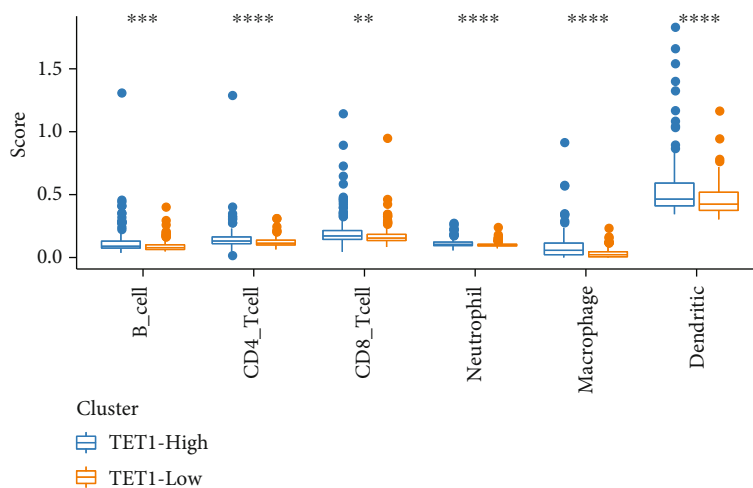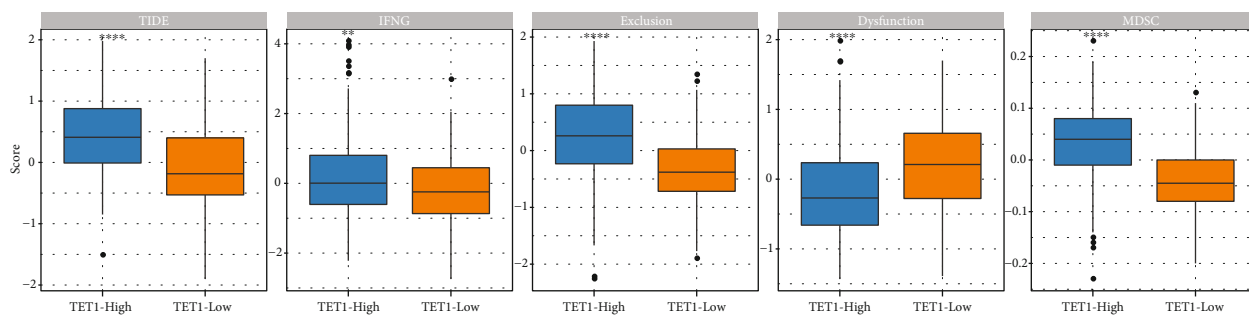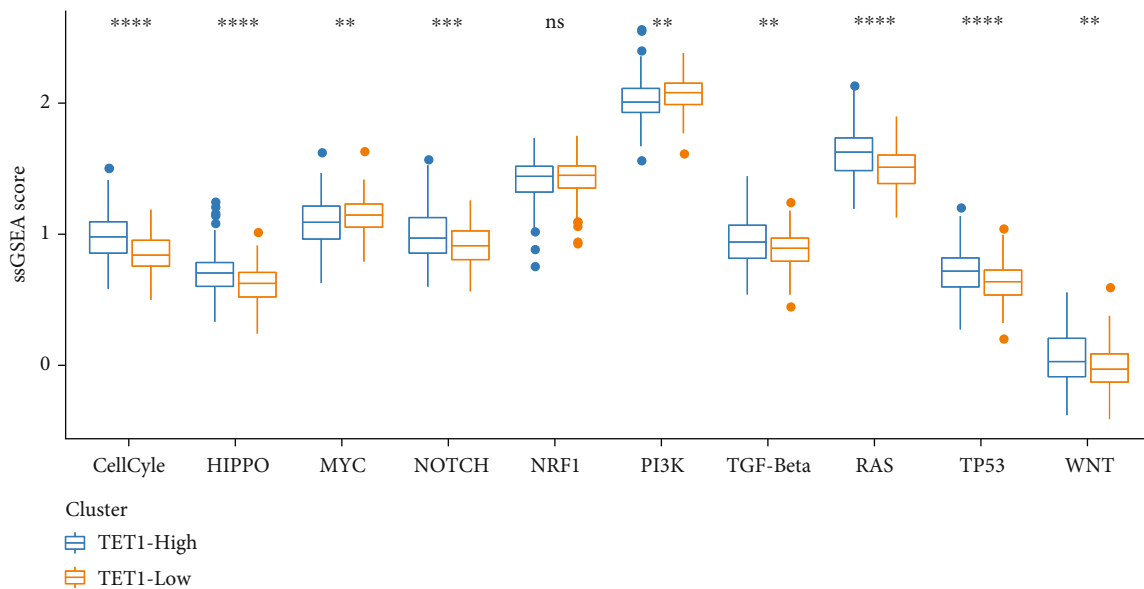
Figure 3: Continued.
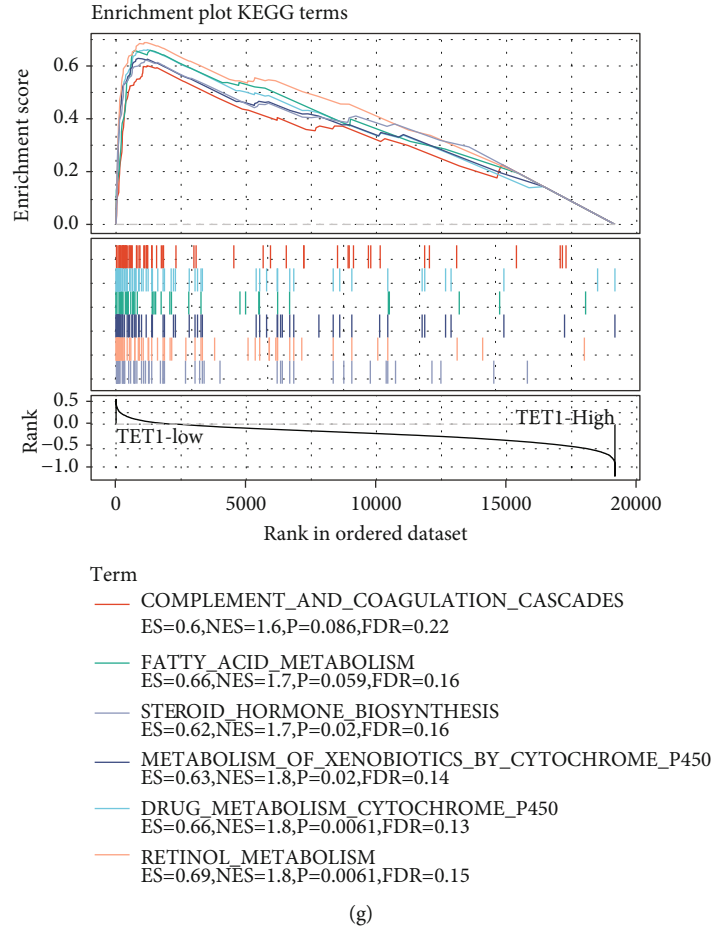
FIGURE 3: Immune characteristics and biological pathways in TET1-high and TET-low groups in TCGA dataset. (a–d) The estimated enrichment of immune cells analyzed by CIBERSORT, MCP-counter, ssGSEA, and TIMER. (e) TIDE analysis on TET1-high and TET-low groups. (f) The ssGSEA score of 10 oncogenic pathways. (g) GSEA on TET1-high vs. TET1-low groups. Wilcoxon test was conducted. ns: not significant. $^*P < 0.05$; $^{**}P < 0.01$; $^{***}P < 0.001$; $^{****}P < 0.0001$.

regression analysis identified the genes significantly associated with overall survival (defined as prognostic genes) in TCGA dataset. Then, the number of prognostic genes were compressed by LASSO and stepAIC. LASSO analysis identified 10 prognostic genes when the lambda and the model reached the optimal (lambda = 0.0294) (Figure S1). Lastly, stepAIC confirmed the 7 prognostic genes as the final genes for constructing the risk model defined as follows (Figure 5(b)):

$$
\begin{aligned}
\text{Risk score} = {} & -0.351 * \text{SERPINH1} + 0.271 * \text{CDC20} \\
& + 0.313 * \text{HACD2} - 0.149 * \text{SPHK1} \\
& - 0.089 * \text{UGT2B15} + 0.324 * \text{SLC1A5} \\
& - 0.084 * \text{CYP2C9}.
\end{aligned}
\tag{1}
$$

The risk model was verified in four independent datasets. Each sample obtained a risk score and two groups (high-risk and low-risk groups) were determined according to the median value of risk score. Kaplan-Meier survival analysis carried out significant differences on the overall

survival between two risk groups in four independent datasets ($P < 0.05$, Figures 5(c), 5(e), 5(g), and 5(i)). Moreover, ROC curve analysis verified that the risk score was efficient to predict 1- to 5-year survival (Figures 5(d), 5(f), 5(h), and 5(j)), indicating the risk model was effective and reliable in predicting prognosis for HCC patients.

3.4. The Linkage of Risk Score with Clinical Characteristics, Immune Characteristics and Biological Pathways. In the relation between risk score and clinical characteristics, we observed that there were evident differences on the risk score between different genders, stages, and grades. Strikingly, the risk score increased with the advancing stages and grades (Figure 6(a)). We also analyzed the association of TET1 with the risk score, and the result shown that TET1-high group had markedly higher risk score than TET1-low group ($P < 0.0001$, Figure 6(a)), implying that the 7 prognostic genes in the risk model may be involved in the regulation of TET1.

We investigated the immune microenvironment of two risk groups by CIBERSORT, MCP-counter, ssGSEA, and TIMER. Some immune cells were differently enriched

(a)

(b)

FIGURE 4: Continued.

(c)
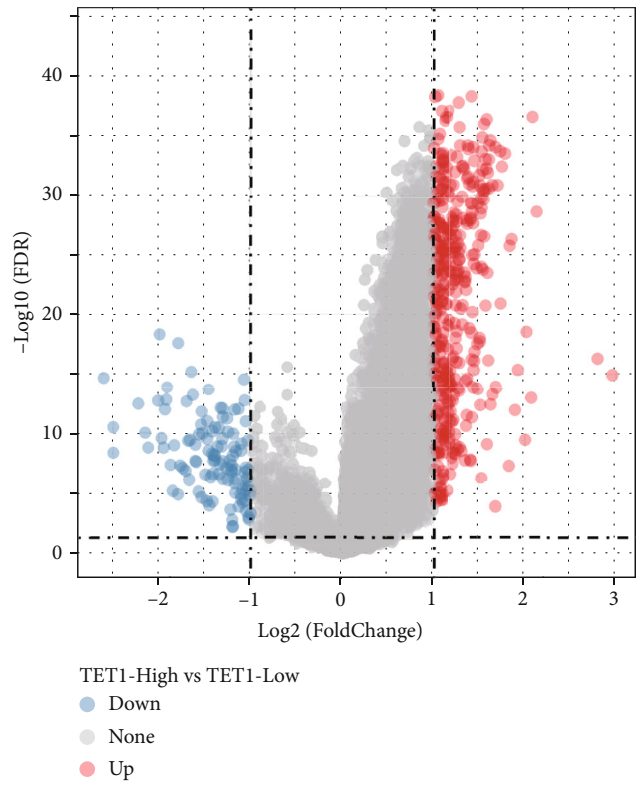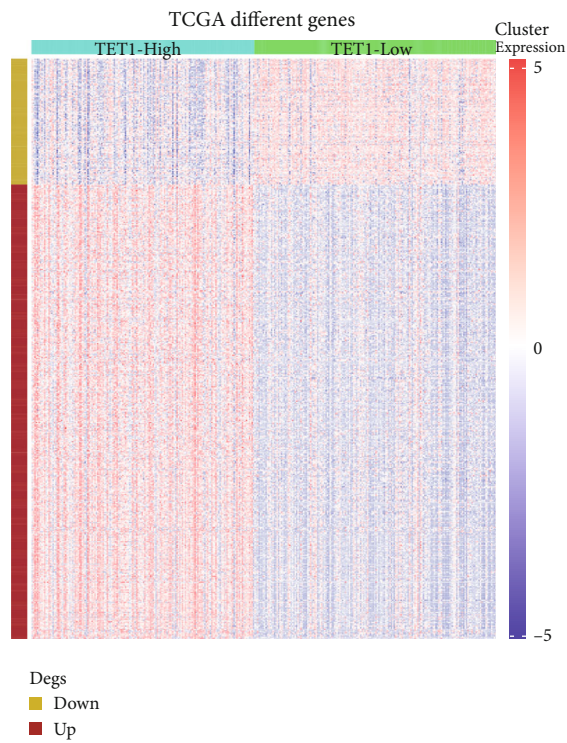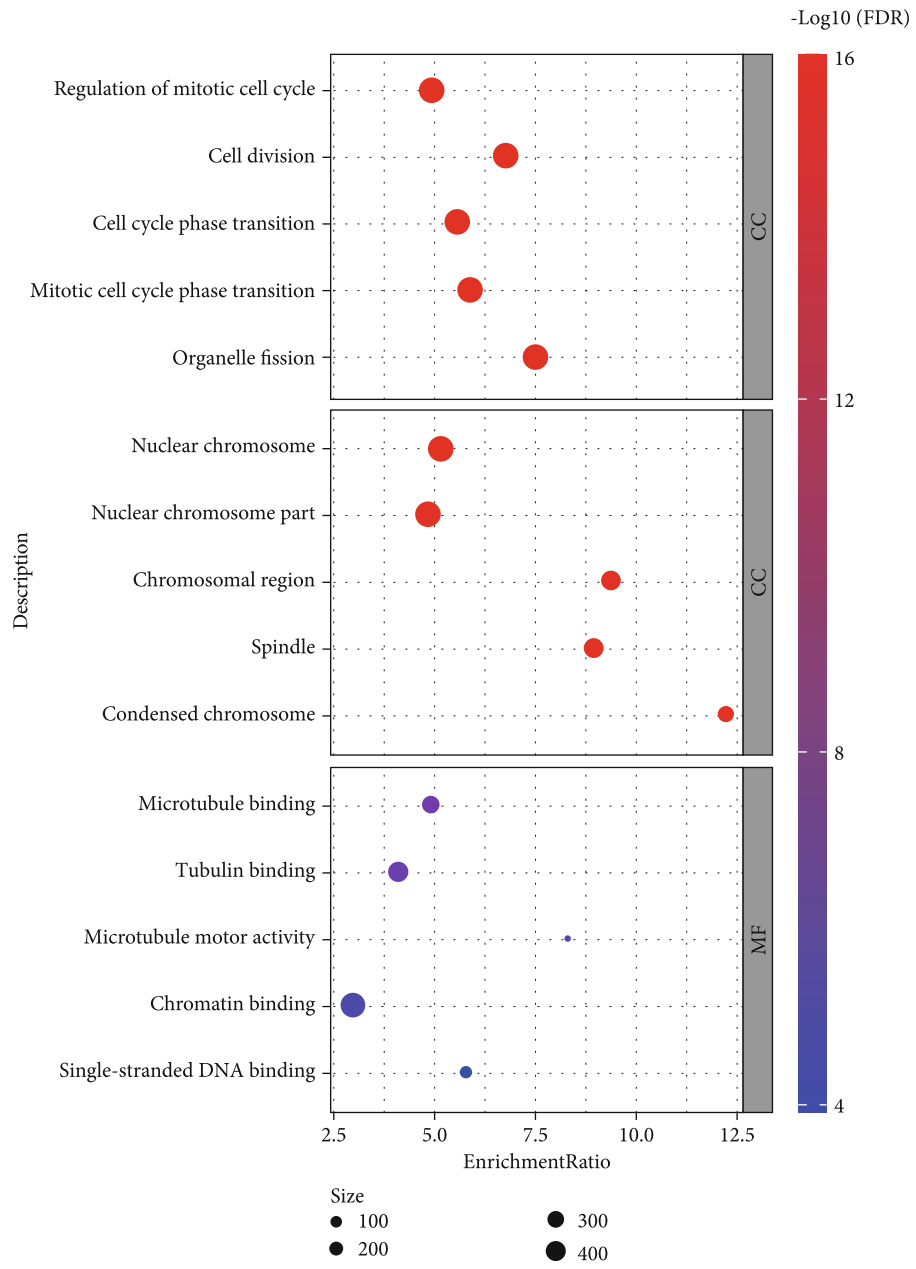
Figure 4: Continued.

(d)
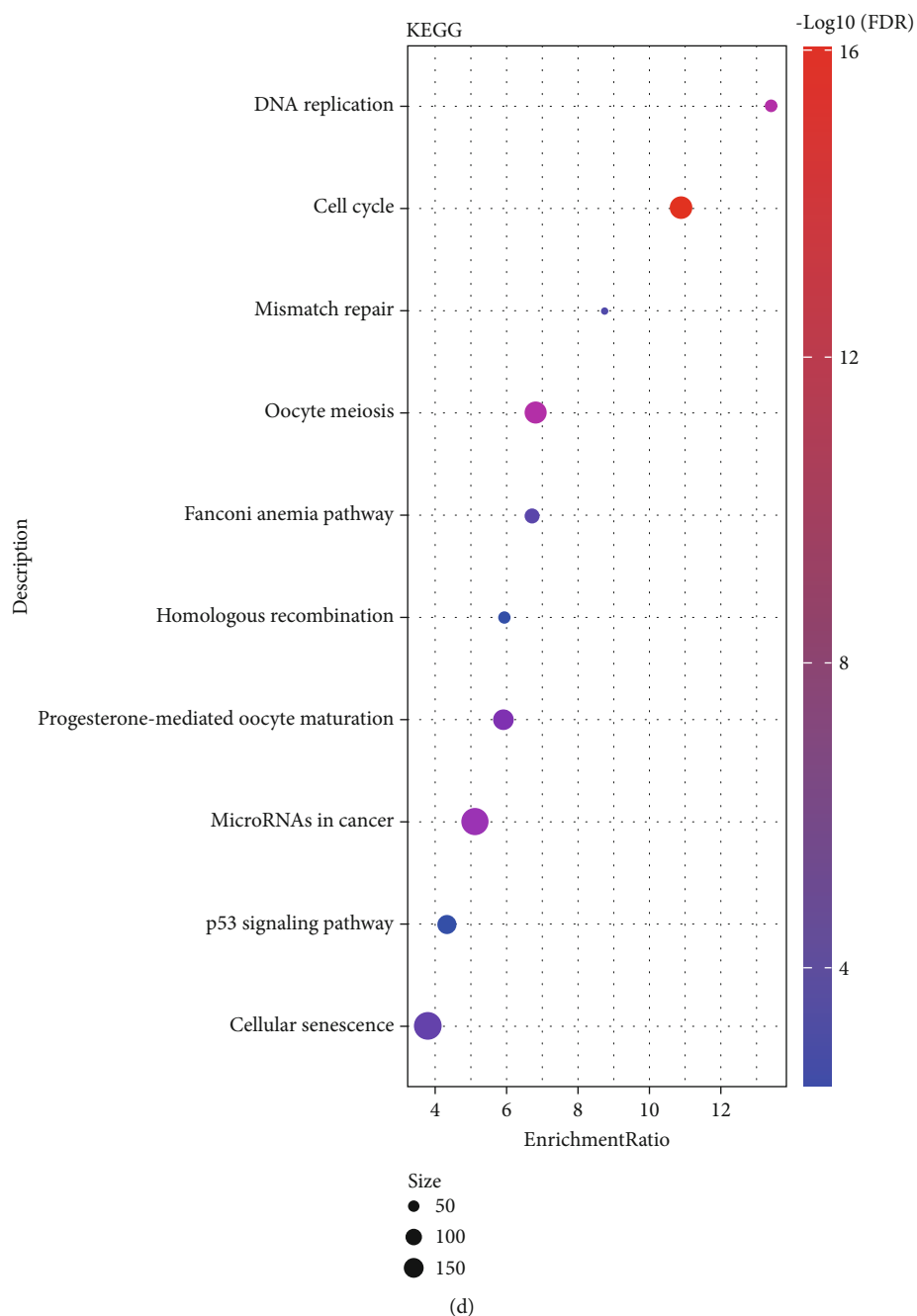
Figure 4: Differential analysis between TET1-high and TET1-low groups in TCGA dataset. (a) Volcano plot of DEGs between TET1-high and TET1-low groups. (B) Heat map of the expression of DEGs. (c) GO enrichment analysis showed the top five enriched biological pathways (BP), cellular components (CC), and molecular function (MF). (D) KEGG pathway analysis showed the top 10 enriched pathways. FDR: false discovery rate. BP: biological process. CC: cellular component. MF: molecular function.

between two risk groups, such as macrophages, memory CD4 T cells, and dendritic cells (Figure S2). Notably, significant correlations were observed between risk score and M0 macrophages, type 2 helper T cells, monocytic lineage, and activated CD4 T cells (Figure 6(b)). TIDE analysis predicted that high-risk group was easier to escape from immunotherapy due to its high T cell exclusion and high infiltration of MDSCs (Figure 6(c)). However, high-risk group may benefit more from chemotherapeutic drugs

than low-risk groups, because the estimated IC50 of cisplatin, sunitinib, MG-132, paclitaxel, and cyclopamine were lower in high-risk group (Figure 6(d)).

To explore whether two risk groups had different biological activities, we included all hallmark pathways downloaded from MSigDB and calculated the ssGSEA score for each pathway in TCGA dataset. By comparing the ssGSEA score in two risk groups, we identified a total of 25 pathways markedly differently activated between two groups (Figure 7(a)).

(a)

(b)

FIGURE 5: Continued.

(c)

(d)

(e)

(f)

Figure 5: Continued.

(g)

(h)

(i)

(j)
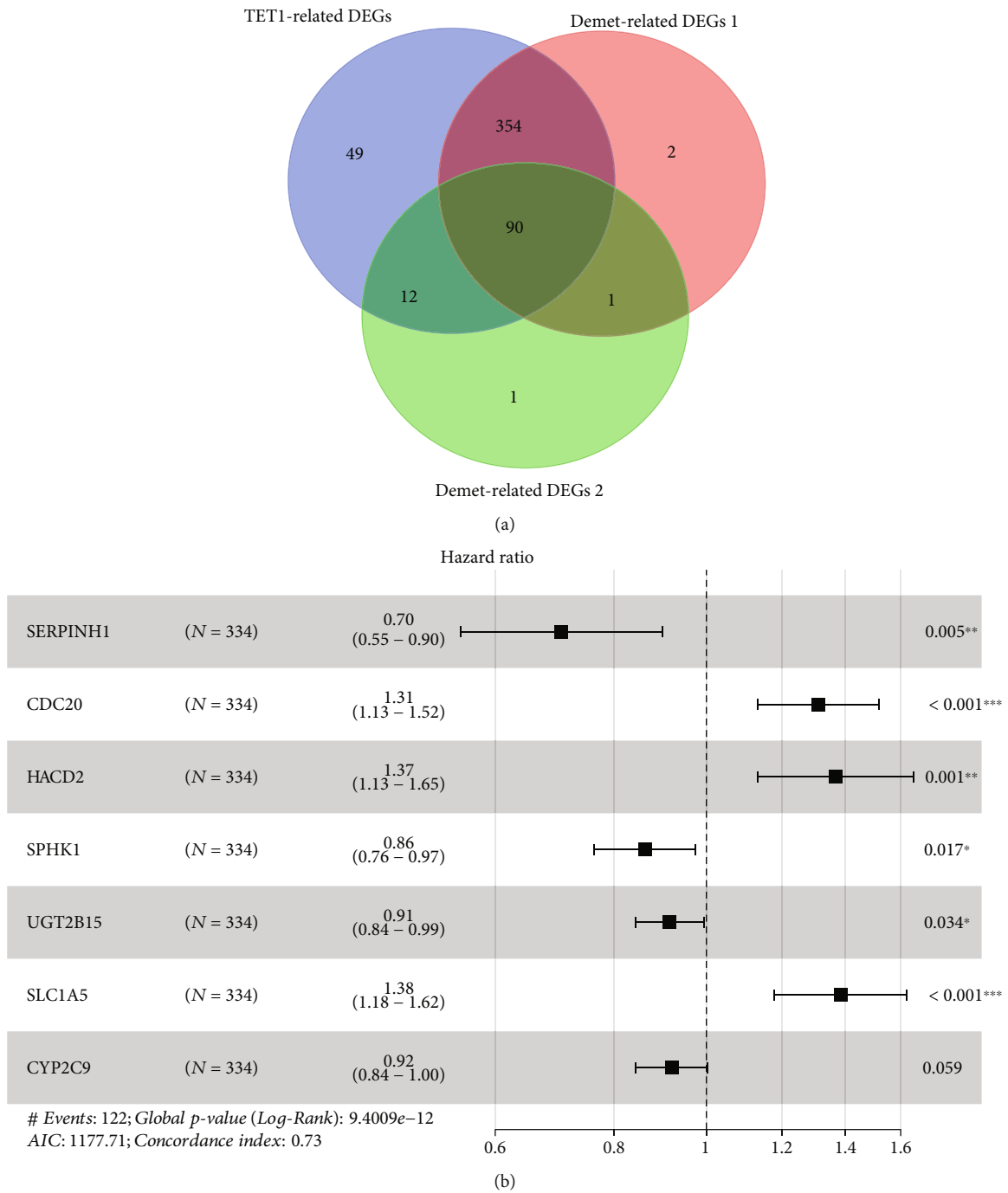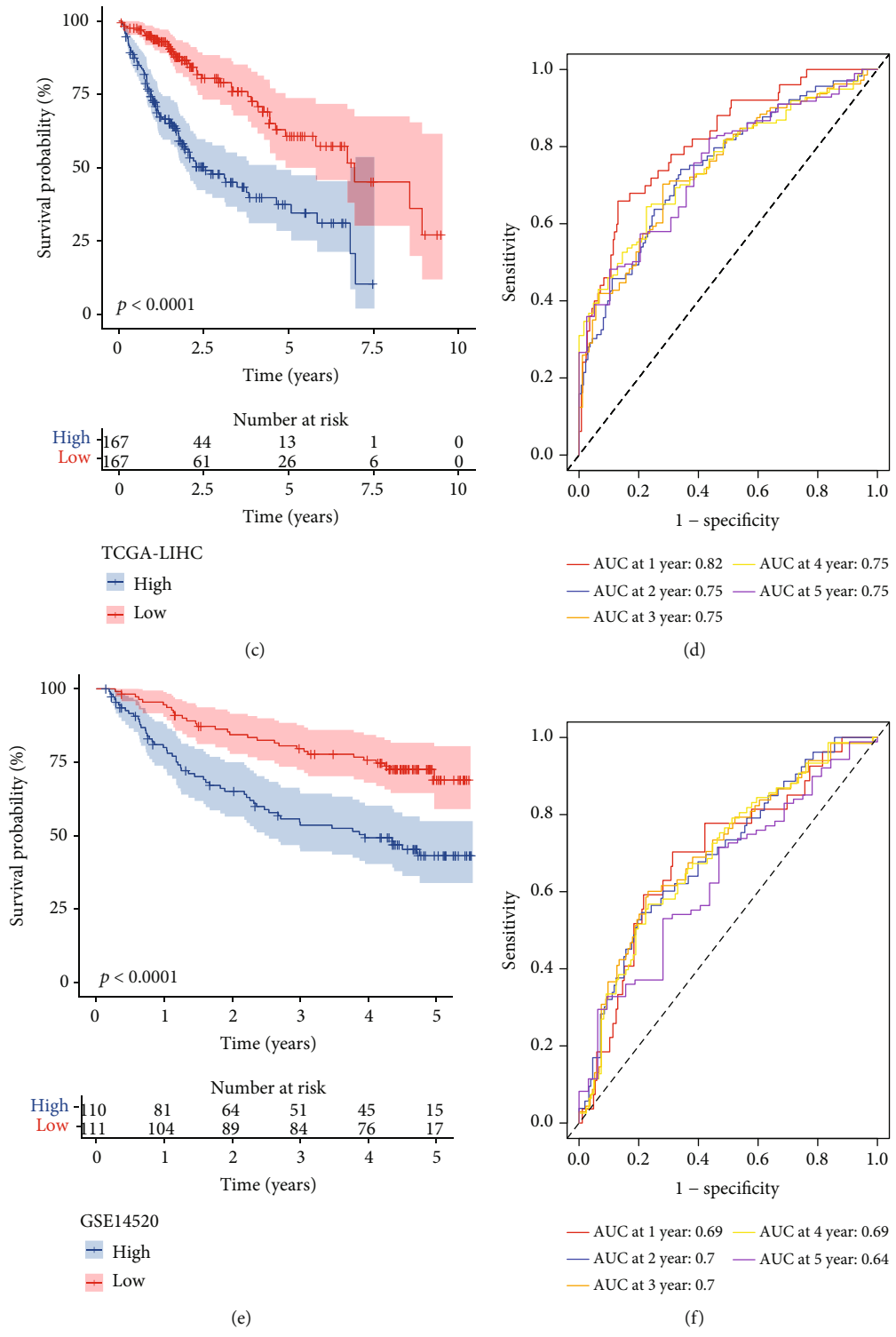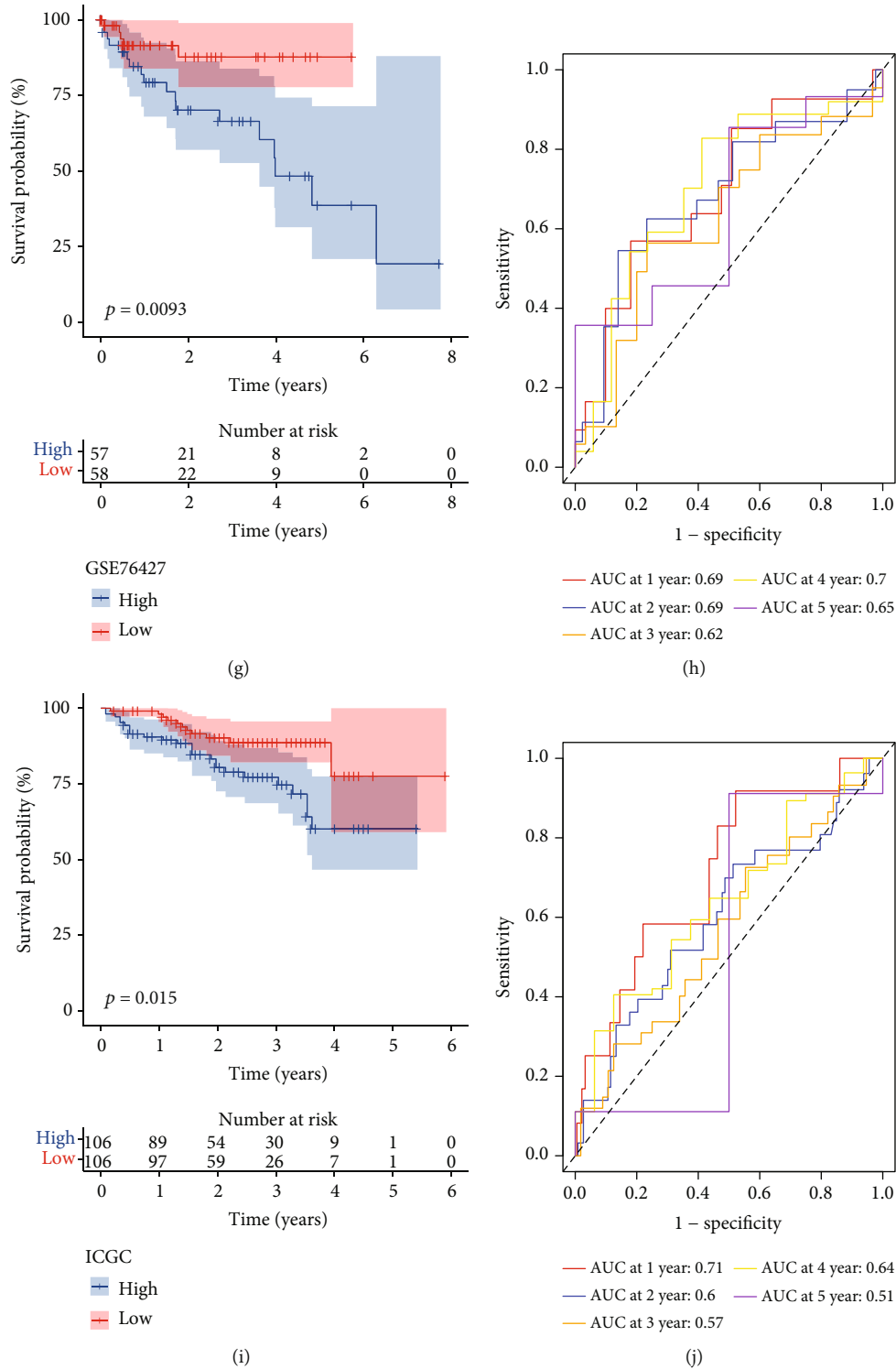
Figure 5: Construction and verification of TET1 and demethylation-related risk model. (a) Venn plot of TET1-related DEGs and demethylation-related DEGs. (b) Hazard ratio of the 7 prognostic genes determined by stepAIC. Kaplan-Meier survival curves of high-risk and low-risk groups in TCGA (c), GSE14520 (e), GSE76427 (g), and ICGC (i) datasets. ROC curves of the risk model in predicting 1- to 5-year survival in TCGA (d), GSE14520 (f), GSE76427 (h), and ICGC (j) datasets.

Clustering results of these pathways presented that two risk groups had distinct patterns of activated pathways. Cell cycle-related pathways such as E2F targets, MYC target V1, MYC target V2, G2M checkpoint, and DNA repair were evi-

dently activated in high-risk group, while metabolism-related pathways were significantly activated in low-risk group such as adipogenesis, fatty acid metabolism, heme metabolism, xenobiotic metabolism, and bile acid metabolism. In

(a)

(b)

Figure 6: Continued.

(c)
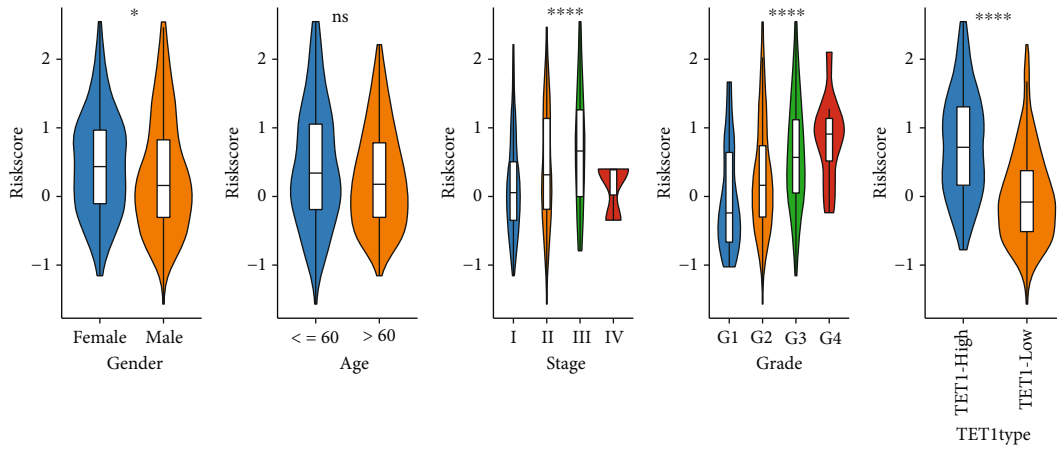
(d)
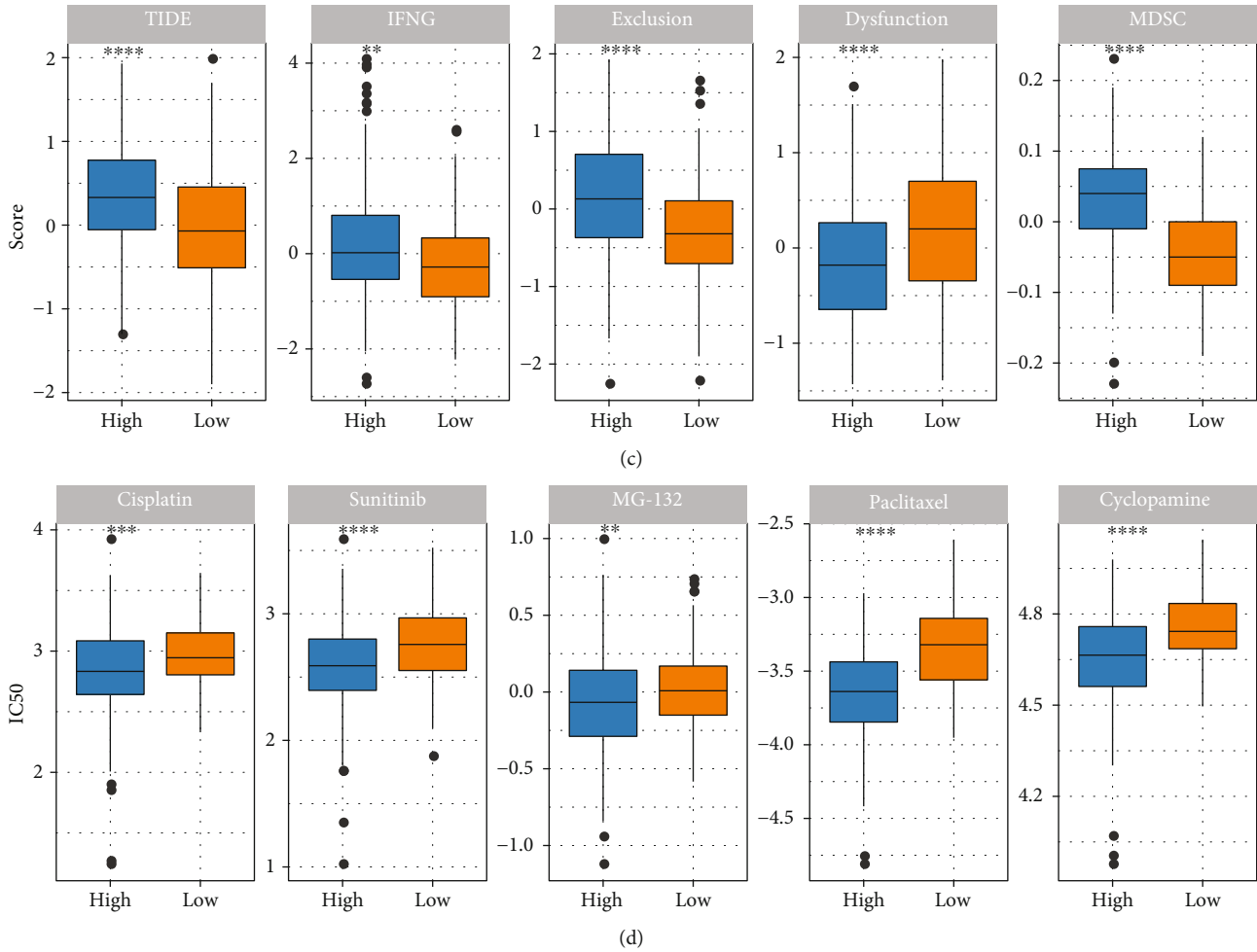
FIGURE 6: The relation of risk score with clinical characteristics, immune characteristics, and chemotherapeutic drugs. (a) The risk score in different genders, ages, stages, grades, and TET1 groups. (b) Correlation analysis between risk score and immune cell infiltration. (c) TIDE analysis of two risk groups. (d) The estimated IC50 of chemotherapeutic drugs in two risk groups. Wilcoxon test was performed between two groups, and ANOVA was performed among four groups. ns: not significant. $^*P < 0.05$; $^{**}P < 0.01$; $^{***}P < 0.001$; $^{****}P < 0.0001$.

addition, glycolysis, PI3K Akt mTOR signaling, and unfolded protein response were also found to be more enriched in high-risk group. In the relation of risk score with the above pathways, consistent results were outputted that a positive correlation was shown between cell cycle-related pathways and risk score, while a negative correlation was shown between metabolic pathways and risk score (Figure 7(b)).

3.5. Optimizing the Clinical Application of Risk Score. To make the risk score more conveniently used in clinical situations, we introduced a nomogram system involving all prognostic factors. Cox regression was applied to determine the variables involved in the nomogram. As a result, only stage and risk score were independent risk factors with hazard ratio (HR) of 2.369 and 2.690, respectively, in multivariate regression (Figures 8(a) and 8(b)). Therefore, stage and risk score were used to construct the nomogram for predicting the 1-year, 3-year, and 5-year survivals (Figure 8(c)). The predicted 1-year, 3-year, and 5-year overall survivals by the nomogram were almost overlapped with the actual ones (Figure 8(d)), indicating that the nomogram was reliable.

Moreover, decision curve analysis (DCA) demonstrated that the nomogram had the best net benefit that the patients could obtain from (Figure 8(e)).

4. Discussion

Previous studies have discovered that the aberrant DNA methylation patterns with global hypomethylation are associated with cancer progression in HCC [32, 33]. In the demethylation process, TET proteins are responsible for the removal of methylation and the alteration of DNA methylation patterns. To further understand the role of TET proteins and DNA demethylation-related genes in HCC, this study characterized the linkage of demethylation with survival, clinical characteristics, tumor microenvironment (TME), and biological pathways using various strategies of bioinformatics analysis. We emphasized the importance of TET proteins in HCC progression and the response to clinical treatment.

First of all, we compared the expression levels of TET proteins between tumor and normal samples and found that

(a)

Figure 7: Continued.

(b)
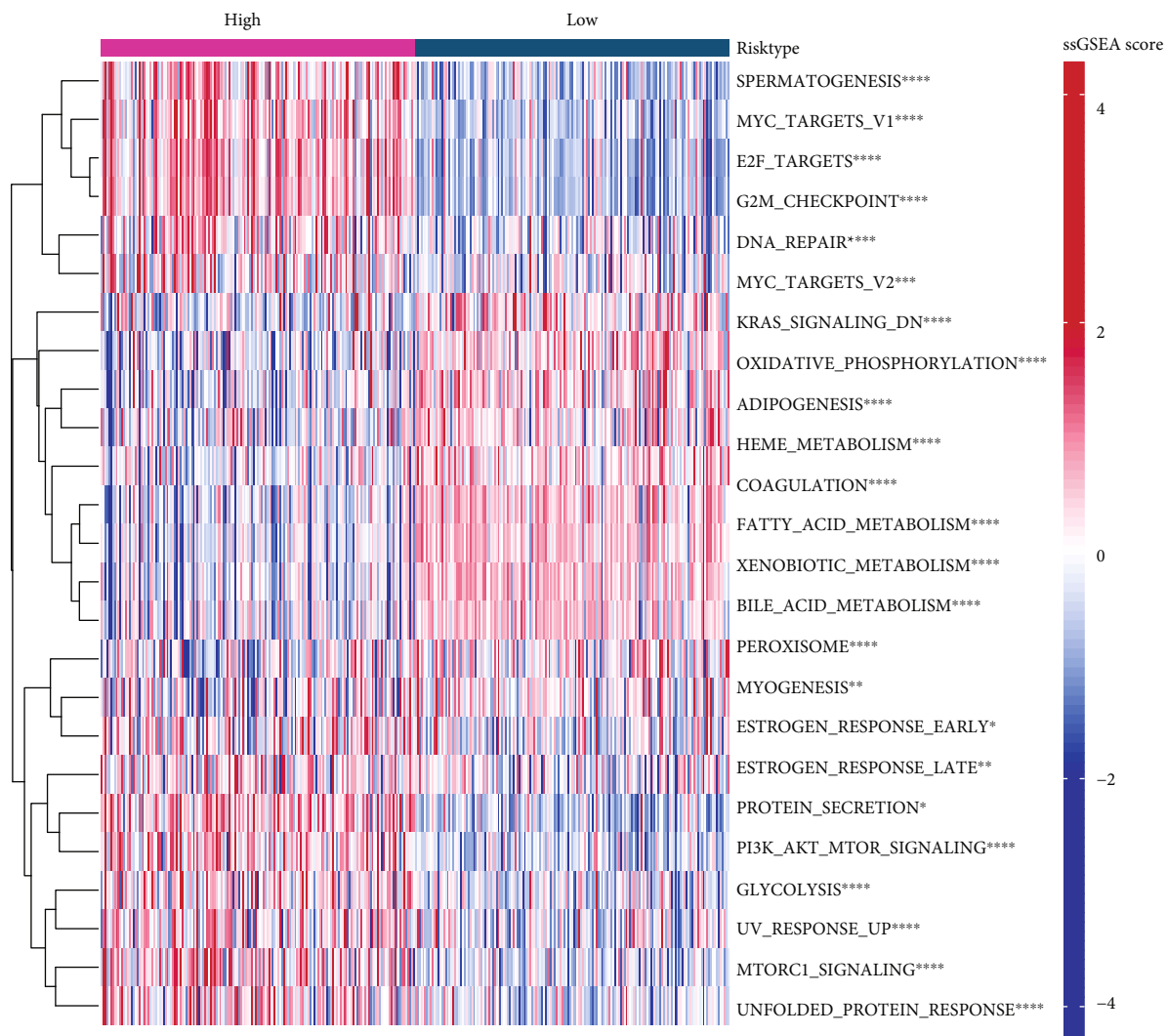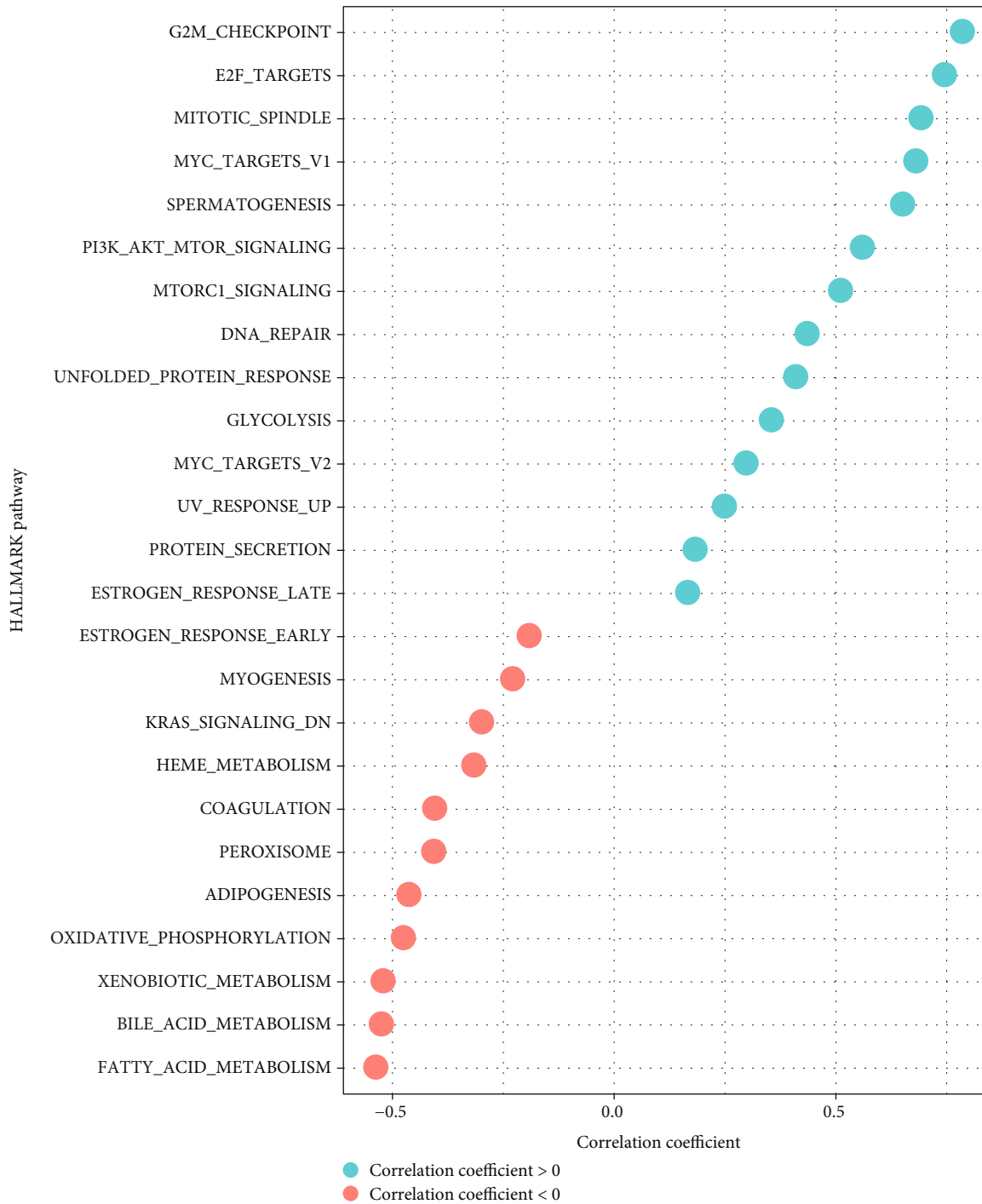
FIGURE 7: Pathway analysis of two risk groups. (a) Heat map of differently enriched pathways in two risk groups. Wilcoxon test was performed. Red and blue indicate relatively activated and suppressed, respectively. (b) Correlation analysis between risk score and hallmark pathways. Red and green indicate negative and positive correlations, respectively.

only TET1 had an elevated expression level in HCC samples compared with the normal samples in three independent datasets. The HCC samples with late grades (G2-G4) and stages (II-IV) had higher TET1 expression than that with the early grade (G1) and stage (I), suggesting a linkage between TET1 expression and prognosis. To demonstrate the speculation, we stratified HCC samples into two groups by the median cut-off of TET1 expression. Not surprisingly, TET1-high group showed evidently shorter overall survival than TET1-low group. High expression level of TET1 may

	pvalue	Hazard ratio
Age	0.349	1.007 (0.993–1.021)
Gender	0.315	0.829 (0.574–1.196)
Stage	< 0.001	2.937 (2.003–4.308)
Grade	0.963	1.009 (0.693–1.469)
RiskScore	< 0.001	2.718 (2.139–3.455)

Hazard ratio

(a)

	pvalue	Hazard ratio
Age	0.185	1.010 (0.995–1.025)
Gender	0.801	1.054 (0.701–1.583)
Stage	< 0.001	2.369 (1.589–3.533)
Grade	0.200	0.766 (0.510–1.151)
RiskScore	< 0.001	2.690 (2.054–3.523)

Hazard ratio
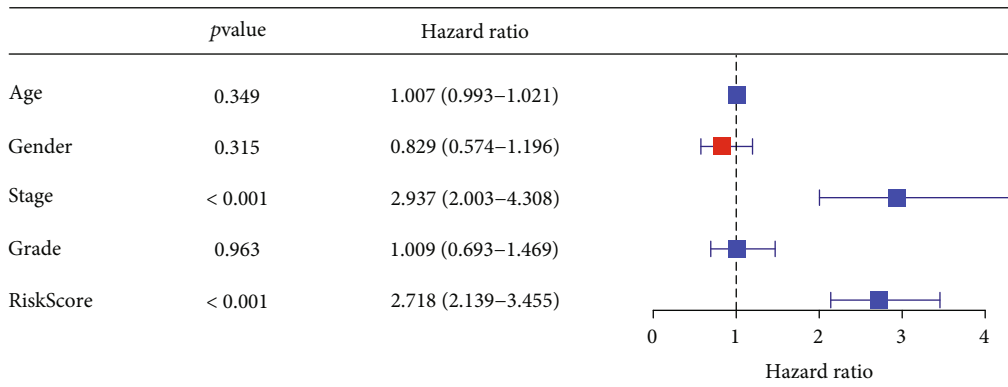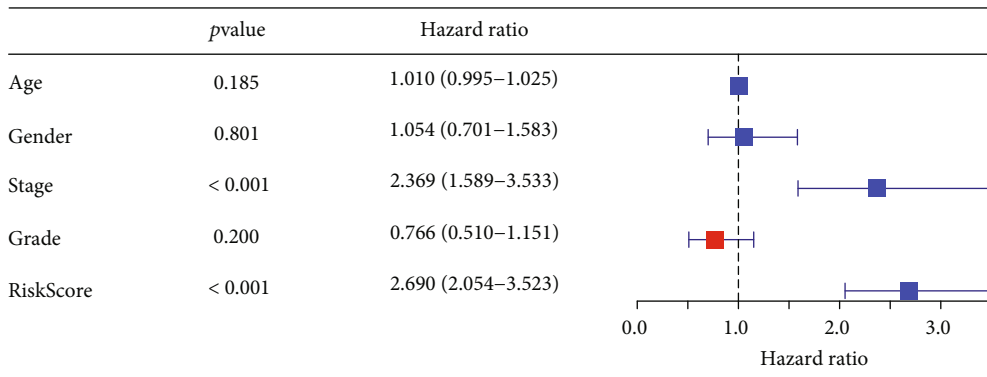
(b)
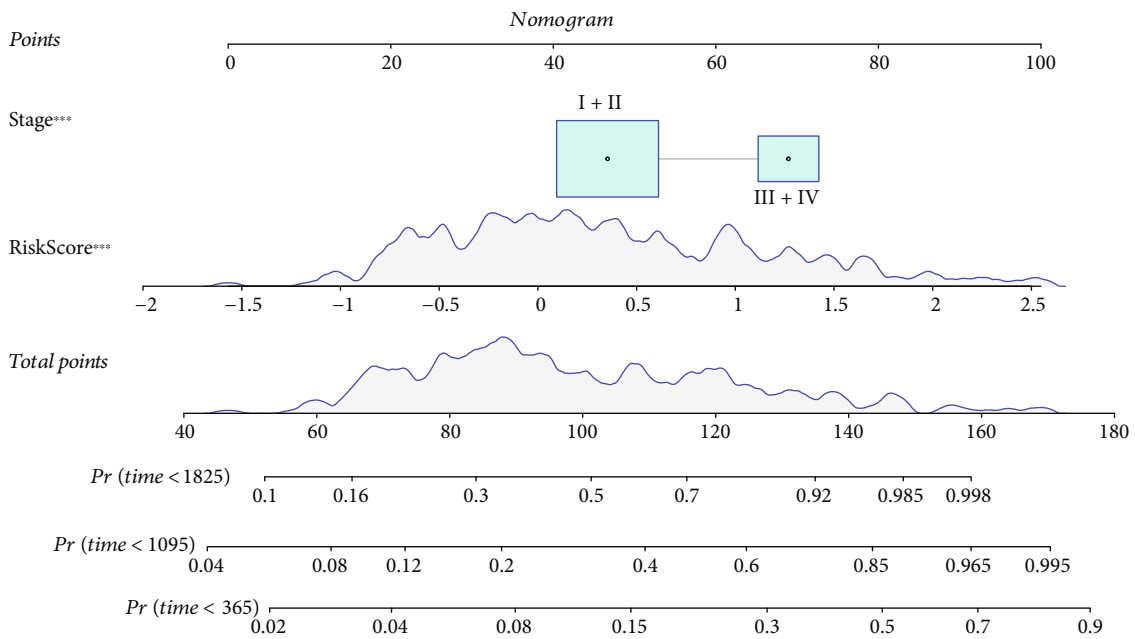
(c)

FIGURE 8: Continued.

(d)

(e)
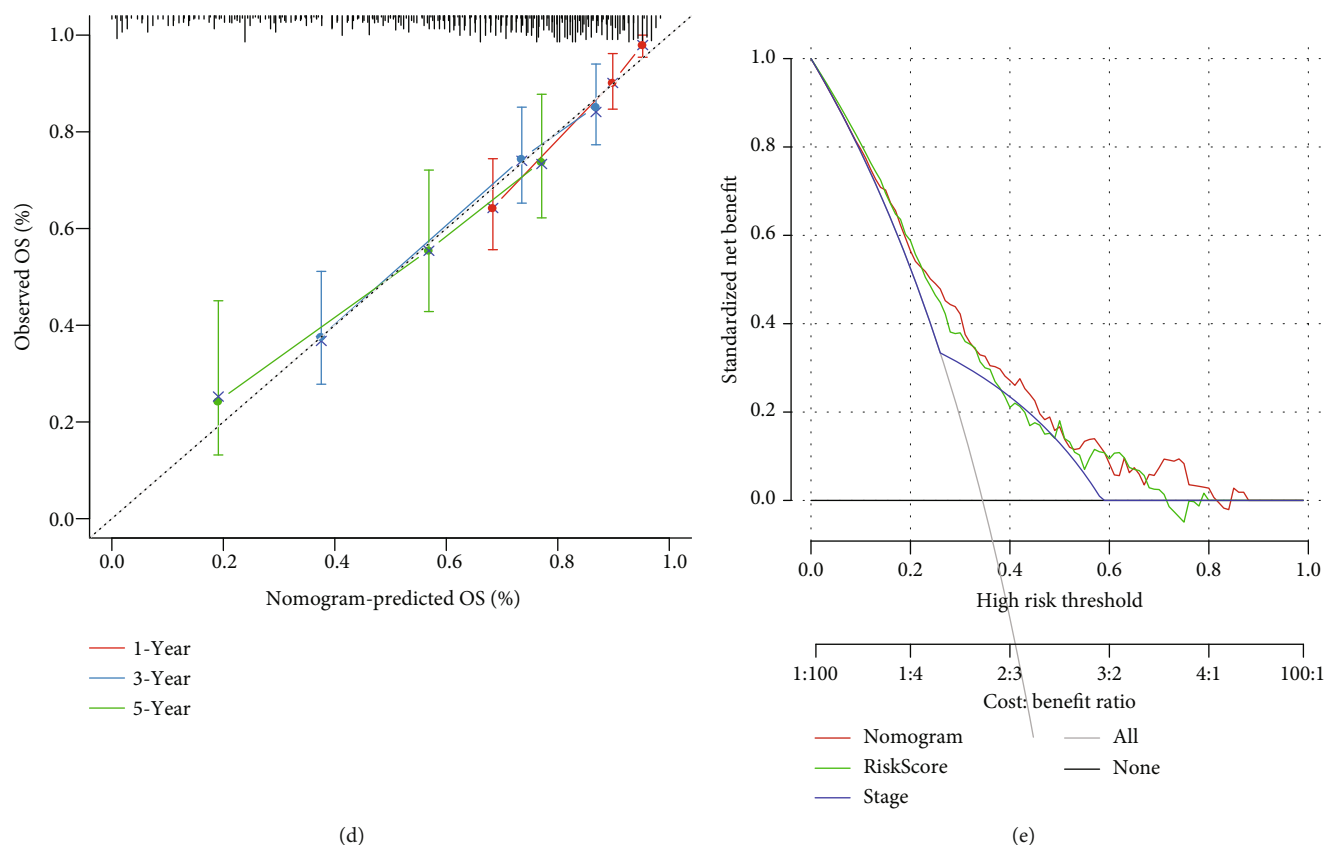
FIGURE 8: Construction of a nomogram based on risk score and clinical characteristics. (a) Univariate Cox regression analysis of risk score and clinical characteristics. (b) Multivariate Cox regression analysis of risk score and clinical characteristics. (c) The nomogram based on risk score and stage. (d) Calibration curve of the predicted OS and the observed OS. (e) DCA curve of risk score, nomogram, and stage. OS: overall survival. $***P < 0.001$.

lead to high activity of demethylation process, which supported that the downregulated methylations were associated with poor prognosis.

TME is a critical component affecting cancer invasion, metastasis, and even the efficiency of immunotherapy and chemotherapy [34]. To understand the potential effect of TET1 in TME, we assessed the relation of two TET1 expression groups with immune infiltration through multiple methodologies. As a result, some immune cells were found to be differently enriched in two TET1 groups, indicated that DNA methylation may function an effect in TME regulation. Lines of studies have found that DNA methylation patterns had an influence in immune characteristics in various cancer types. For example, Mitra et al. identified three immune methylation-based clusters showing different immune cell infiltration and prognosis in metastatic melanoma [35]. Meng et al. delineated a landscape of DNA methylation regulators in gastric cancer and found the extensive dysregulation of the regulators [36]. Moreover, the expression of DNA methylation regulators was closely related to immune cell infiltration, where TET1 expression was related to the enrichment of activated dendritic cells, neutrophils, and type 17 T helper cells [36]. In our results, TET1-high and TET1-low groups showed different enrichment of multiple immune cells such as macrophages, natural killer cells, and

neutrophils. It could be implied that TET1 was involved in the crosstalk with immune microenvironment. Strikingly, TET1-high group was easier to escape from immunotherapy than TET1-low group, suggesting that TET1 had a potential to serve as an indicator for guiding immunotherapy in HCC.

To reveal the interplay of TET1 with biological pathways, we assessed oncogenic pathway and KEGG pathway in TET1-high and TET1-low groups. Of 10 oncogenic pathways, it was remarkable that 9 of them were differentially enriched in two TET1 groups, supporting that TET1 expression was related to the activation of oncogenic pathways. Specifically, TET1-high group had significantly higher enrichment of most of oncogenic pathways such as cell cycle, Hippo, Notch, TGF-β, TP53, and Wnt signaling pathways. Evidence has shown that there is a substantial difference on DNA methylation of oncogenic pathways such as Hippo and Wnt between HCC and normal samples [37]. We speculated that the demethylation effect resulting from high TET1 expression activated the expression of genes involved in the oncogenic pathways. In addition, KEGG enrichment analysis on the DEGs between two TET1 groups unveiled that cell cycle-related and DNA repair-related pathways were more activated in the upregulated DEGs of TET1-high group. The results further sustained the important role of TET1 in regulating oncogenic pathways.

Due to the close relation of TET1 with survival and oncogenic pathways, we dug out a bulk of genes related to TET1 and DNA demethylation process for constructing a risk model. Based on TET1 and DNA demethylation-related genes, we identified seven key prognostic genes including SERPINH1, CDC20, HACD2, SPHK1, UGT2B15, SLC1A5, and CYP2C9 for the model construction. The risk model manifested superior prediction efficiency of HCC prognosis in four independent datasets. Notably, TET1-high group had extraordinarily higher risk score than TET1-low group. The risk score increased with the advancing stages and grades, which was consistent with the observation regarding TET1 expression. Therefore, the seven key prognostic genes may be closely involved in the TET1-mediated demethylation. Increased expression of CDC20 was reported to be associated with HCC progression through promoting cell proliferation and inhibiting apoptosis [38, 39]. SPHK1 was found to be upregulated in HCC and could induce epithelial-mesenchymal transition (EMT) process [40]. Few studies have reported the other five prognostic genes on their molecular mechanisms in HCC.

However, our study only relied on the bioinformatics analysis, the mechanism of TET1 in HCC development and progression needed verification in molecular experiments. We did not simultaneously compare the DNA methylation patterns relating TET1 expression. In addition, the seven-gene risk model should be further validated in clinical samples, and the potential mechanisms of the seven key prognostic genes in TET1-mediated demethylation needed to be clarified in future study.

5. Conclusions

In conclusion, our study confirmed the overexpression of TET1 in HCC patients and unveiled the relation of TET1 expression with survival, clinical stages, immune cell infiltration, the response to immunotherapy and chemotherapy, and oncogenic pathways. We identified seven key prognostic genes related to TET1 and DNA demethylation and established a nomogram for effectively predicting HCC prognosis.

Data Availability

The data used to support the findings of this study are included within the article.

Conflicts of Interest

The authors declare that they have no competing interest.

Authors' Contributions

All authors contributed to this present work. HPW and TFJ designed the study. LTL acquired the data. NC drafted the manuscript. KSZ and LQC revised the manuscript. All authors read and approved the manuscript. Haopeng Wen and Tengfei Ji contributed equally to this work and the co-first authors.

Supplementary Materials

Supplementary 1. Figure S1: LASSO regression of the prognostic genes. (A) The coefficients of prognostic genes with the changing lambda values. Red dotted line indicates lambda = 0.0294. (B) Partial likelihood deviance of different lambda values. Red dot indicates lambda = 0.0294.

Supplementary 2. Figure S2: the enrichment score of immune cells analyzed by CIBERSORT (A), MCP-counter (B), ssGSEA (C), and TIMER (D). The Wilcoxon test was conducted. ns: not significant. $^{*}P < 0.05$; $^{**}P < 0.01$; $^{***}P < 0.001$; $^{****}P < 0.0001$.

References

[1] H. Sung, J. Ferlay, R. L. Siegel et al., "Global cancer statistics 2020: GLOBOCAN estimates of incidence and mortality worldwide for 36 cancers in 185 countries," *CA: A Cancer Journal for Clinicians*, vol. 71, no. 3, pp. 209–249, 2021.

[2] J. L. Petrick and K. A. McGlynn, "The changing epidemiology of primary liver cancer," *Current Epidemiology Reports*, vol. 6, no. 2, pp. 104–111, 2019.

[3] A. Villanueva, "Hepatocellular carcinoma," *The New England Journal of Medicine*, vol. 380, no. 15, pp. 1450–1462, 2019.

[4] B. Losic, A. J. Craig, C. Villacorta-Martin et al., "Intratumoral heterogeneity and clonal evolution in liver cancer," *Nature Communications*, vol. 11, no. 1, p. 291, 2020.

[5] K. Skvortsova, C. Stirzaker, and P. Taberlay, "The DNA methylation landscape in cancer," *Essays in Biochemistry*, vol. 63, no. 6, pp. 797–811, 2019.

[6] A. Koch, S. C. Joosten, Z. Feng et al., "Analysis of DNA methylation in cancer: location revisited," *Nature Reviews Clinical Oncology*, vol. 15, no. 7, pp. 459–466, 2018.

[7] S. Saghafinia, M. Mina, N. Riggi, D. Hanahan, and G. Ciriello, "Pan-cancer landscape of aberrant DNA methylation across human tumors," *Cell Reports*, vol. 25, no. 4, pp. 1066–1080.e8, 2018.

[8] M. Okano, D. W. Bell, D. A. Haber, and E. Li, "DNA methyltransferases Dnmt3a and Dnmt3b are essential for de novo methylation and mammalian development," *Cell*, vol. 99, no. 3, pp. 247–257, 1999.

[9] S. Ito, A. C. D'Alessio, O. V. Taranova, K. Hong, L. C. Sowers, and Y. Zhang, "Role of Tet proteins in 5mC to 5hmC conversion, ES-cell self-renewal and inner cell mass specification," *Nature*, vol. 466, no. 7310, pp. 1129–1133, 2010.

[10] S. Ito, L. Shen, Q. Dai et al., "Tet proteins can convert 5-methylcytosine to 5-formylcytosine and 5-carboxylcytosine," *Science*, vol. 333, no. 6047, pp. 1300–1303, 2011.

[11] Y. Huang and A. Rao, "Connections between TET proteins and aberrant DNA modification in cancer," *Trends in Genetics*, vol. 30, no. 10, pp. 464–474, 2014.

[12] L. Scourzic, E. Mouly, and O. A. Bernard, "TET proteins and the control of cytosine demethylation in cancer," *Genome Medicine*, vol. 7, no. 1, p. 9, 2015.

[13] X. Hao, H. Luo, M. Krawczyk et al., "DNA methylation markers for diagnosis and prognosis of common cancers," *Proceedings of the National Academy of Sciences*, vol. 114, no. 28, pp. 7414–7419, 2017.

[14] J. Shekhawat, K. Gauba, S. Gupta et al., "Ten-eleven translocase: key regulator of the methylation landscape in cancer," *Journal of Cancer Research and Clinical Oncology*, vol. 147, no. 7, pp. 1869–1879, 2021.

[15] K. Tomczak, P. Czerwińska, and M. Wiznerowicz, "The cancer genome atlas (TCGA): an immeasurable source of knowledge," *Współczesna Onkologia*, vol. 19, no. 1A, pp. 68–77, 2015.

[16] Q. Lian, S. Wang, G. Zhang et al., "HCCDB: a database of hepatocellular carcinoma expression atlas," *Genomics, Proteomics & Bioinformatics*, vol. 16, no. 4, pp. 269–275, 2018.

[17] E. Clough and T. Barrett, "The gene expression omnibus database," *Methods in Molecular Biology*, vol. 1418, pp. 93–110, 2016.

[18] B. Chen, M. S. Khodadoust, C. L. Liu, A. M. Newman, and A. A. Alizadeh, "Profiling tumor infiltrating immune cells with CIBERSORT," *Methods in Molecular Biology*, vol. 1711, pp. 243–259, 2018.

[19] E. Becht, N. A. Giraldo, L. Lacroix et al., "Estimating the population abundance of tissue-infiltrating immune and stromal cell populations using gene expression," *Genome Biology*, vol. 17, no. 1, p. 218, 2016.

[20] D. A. Barbie, P. Tamayo, J. S. Boehm et al., "Systematic RNA interference reveals that oncogenic *KRAS*-driven cancers require TBK1," *Nature*, vol. 462, no. 7269, pp. 108–112, 2009.

[21] P. Charoentong, F. Finotello, M. Angelova et al., "Pan-cancer Immunogenomic analyses reveal genotype-Immunophenotype relationships and predictors of response to checkpoint blockade," *Cell Reports*, vol. 18, no. 1, pp. 248–262, 2017.

[22] S. Hänzelmann, R. Castelo, and J. Guinney, "GSVA: gene set variation analysis for microarray and RNA-seq data," *BMC Bioinformatics*, vol. 14, no. 1, 2013.

[23] T. Li, J. Fu, Z. Zeng et al., "TIMER2.0 for analysis of tumor-infiltrating immune cells," *Nucleic Acids Research*, vol. 48, no. W1, pp. W509–W514, 2020.

[24] P. Jiang, S. Gu, D. Pan et al., "Signatures of T cell dysfunction and exclusion predict cancer immunotherapy response," *Nature Medicine*, vol. 24, no. 10, pp. 1550–1558, 2018.

[25] A. Subramanian, P. Tamayo, V. K. Mootha et al., "gene set enrichment analysis: a knowledge-based approach for interpreting genome-wide expression profiles," *Proceedings of the National Academy of Sciences*, vol. 102, no. 43, pp. 15545–15550, 2005.

[26] M. E. Ritchie, B. Phipson, D. Wu et al., "limma powers differential expression analyses for RNA-sequencing and microarray studies," *Nucleic Acids Research*, vol. 43, no. 7, article e47, 2015.

[27] G. Yu, L. G. Wang, Y. Han, and Q. Y. He, "clusterProfiler: an R package for comparing biological themes among gene clusters," *OMICS: A Journal of Integrative Biology*, vol. 16, no. 5, pp. 284–287, 2012.

[28] J. Friedman, T. Hastie, and R. Tibshirani, "Regularization paths for generalized linear models via coordinate descent," *Journal of Statistical Software*, vol. 33, no. 1, pp. 1–22, 2010.

[29] Z. Zhang, "Variable selection with stepwise and best subset approaches," *Annals of Translational Medicine*, vol. 4, no. 7, p. 136, 2016.

[30] W. Shen, Z. Song, X. Zhong et al., "Sangerbox: a comprehensive, interaction-friendly clinical bioinformatics analysis platform," *iMeta*, vol. 1, no. 3, article e36, 2022.

[31] N. J. Tsiouplis, D. W. Bailey, L. F. Chiou, F. J. Wissink, and A. Tsagaratou, "TET-mediated epigenetic regulation in immune cell development and disease," *Frontiers in Cell and Development Biology*, vol. 8, article 623948, 2021.

[32] H. Hernandez-Vargas, M.-P. Lambert, F. Le Calvez-Kelm et al., "Hepatocellular carcinoma displays distinct DNA methylation signatures with potential as clinical predictors," *PLoS One*, vol. 5, no. 3, article e9749, 2010.

[33] R. A. Hlady, D. Zhou, W. Puszyk, L. R. Roberts, C. Liu, and K. D. Robertson, "Initiation of aberrant DNA methylation patterns and heterogeneity in precancerous lesions of human hepatocellular cancer," *Epigenetics*, vol. 12, no. 3, pp. 215–225, 2017.

[34] C. Roma-Rodrigues, R. Mendes, P. V. Baptista, and A. R. Fernandes, "Targeting tumor microenvironment for cancer therapy," *International Journal of Molecular Sciences*, vol. 20, no. 4, p. 840, 2019.

[35] S. Mitra, M. Lauss, R. Cabrita et al., "Analysis of DNA methylation patterns in the tumor immune microenvironment of metastatic melanoma," *Molecular Oncology*, vol. 14, no. 5, pp. 933–950, 2020.

[36] Q. Meng, Y. X. Lu, D. Y. Ruan et al., "DNA methylation regulator-mediated modification patterns and tumor microenvironment characterization in gastric cancer," *Molecular Therapy–Nucleic Acids*, vol. 24, pp. 695–710, 2021.

[37] J. Lu, P. Wilfred, D. Korbie, and M. Trau, "Regulation of canonical oncogenic signaling pathways in cancer via DNA methylation," *Cancers*, vol. 12, no. 11, p. 3199, 2020.

[38] J. Li, J. Z. Gao, J. L. Du, Z. X. Huang, and L. X. Wei, "Increased CDC20 expression is associated with development and progression of hepatocellular carcinoma," *International Journal of Oncology*, vol. 45, no. 4, pp. 1547–1555, 2014.

[39] S. Zhao, Y. Zhang, X. Lu et al., "CDC20 regulates the cell proliferation and radiosensitivity of P53 mutant HCC cells through the Bcl-2/Bax pathway," *International Journal of Biological Sciences*, vol. 17, no. 13, pp. 3608–3621, 2021.

[40] M. Maceyka, T. Rohrbach, S. Milstien, and S. Spiegel, "Role of sphingosine kinase 1 and Sphingosine-1-phosphate axis in hepatocellular carcinoma," *Handbook of Experimental Pharmacology*, vol. 259, pp. 3–17, 2020.

Hindawi

Research Article

STK24 Promotes Progression of LUAD and Modulates the Immune Microenvironment

Yadong Li,[1] Yanhu Liu,[2] Kun Wang,[3] Dong Xue,[2] Yiqin Huang,[2] Zhenguo Tan,[2] and Yijiang Chen [1]

[1]*Department of Thoracic and Cardiovascular Surgery, The First Affiliated Hospital of Nanjing Medical University, Nanjing, China*
[2]*Department of Thoracic and Cardiovascular Surgery, The Second Affiliated Hospital of Nanjing Medical University, Nanjing, China*
[3]*The Affiliated Anning First People's Hospital, Kunming University of Science and Technology, Kunming, China*

Correspondence should be addressed to Yijiang Chen; yijiangchen@njmu.edu.cn

Objective. Recent studies have shown that serine/threonine-protein kinase 24 (STK24) plays an important role in cancer development. However, the significance of STK24 in lung adenocarcinoma (LUAD) remains to be determined. This study is aimed at investigating the significance of STK24 in LUAD. *Methods.* STK24 was silenced and overexpressed by siRNAs and lentivirus, respectively. Cellular function was assessed by CCK8, colony formation, transwell, apoptosis, and cell cycle. mRNA and protein abundance was checked by qRT-PCR and WB assay, respectively. Luciferase reporter activity was evaluated to examine the regulation of KLF5 on STK24. Various public databases and tools were applied to investigate the immune function and clinical significance of STK24 in LUAD. *Results.* We found that STK24 was overexpressed in lung adenocarcinoma (LUAD) tissues. High expression of STK24 predicted poor survival of LUAD patients. In vitro, STK24 enhanced the proliferation and colony growth ability of A549 and H1299 cells. STK24 knockdown induced apoptosis and cell cycle arrest at G0/G1 phase. Furthermore, Krüppel-like factor 5 (KLF5) activated STK24 in lung cancer cells and tissues. Enhanced lung cancer cell growth and migration triggered by KLF5 could be reversed by silencing of STK24. Finally, the bioinformatics results showed that STK24 may be involved in the regulation of the immunoregulatory process of LUAD. *Conclusion.* KLF5 upregulation of STK24 contributes to cell proliferation and migration in LUAD. Moreover, STK24 may participate in the immunomodulatory process of LUAD. Targeting KLF5/STK24 axis may be a potential therapeutic strategy for LUAD.

1. Introduction

Lung adenocarcinoma (LUAD) is one of the common malignant tumors in China [1]. During the past decades, a large amount of efforts, including whole genome sequencing, RNA sequencing, and proteomics, have been made to dissect the molecular drivers for this deadly malignancy. Genetic alterations, such as EGFR-activating mutations, are identified as the essential promoter of lung cancer development [2]. Lung cancer patients harboring EGFR activation benefit from the targeted therapies of gefitinib, a specific EGFR inhibitor [3]. However, there are still some of the patients exhibiting no effectiveness when using gefitinib. Therefore, novel drug targets triggering lung cancer are constantly in need.

In recent years, immunotherapy based on immune checkpoint inhibitors (ICIs) has gradually become the focus of cancer treatment. To date, a variety of ICIs have been applied in the treatment of LUAD patients [4]. However, only a minority of patients benefit from immunotherapy [5]. Numerous evidences indicate that the leukocyte infiltration status within the tumor immune microenvironment is closely related to the response to immunotherapy [6, 7]. Therefore, the exploration and identification of novel LUAD immune-related genes are crucial for the development of LUAD treatment strategies.

STK24, which is also named as MST3, is one of the members of the mammalian sterile twenty (MST) kinase family of proteins [8]. The role of STK24 in cancers is a limited report. While STK24 plays an oncogenic role in gastric cancer growth [9], it can serve as a tumor suppressor in colorectal cancer [10]. STK24 also contributes to breast cancer development by regulating VAV2/Rac1 signaling cascade [11]. Nevertheless, the significance of STK24 in LUAD growth and migration is poorly elucidated.

Herein, we explored the role of STK24 in LUAD by analyzing its clinical significance based on TCGA database, by exploring its function on LUAD cell proliferation, cell cycle, apoptosis, migration, and immunoregulatory.

2. Materials and Methods

2.1. Cell Lines and Regents. A549 and H1299 cells were obtained from American Type Culture Collection (Manassas, USA). Dulbecco's modified eagle (DMEM), 1640 cell culture medium, and antibiotics were from Corning. Fetal bovine serum (FBS) was purchased from Gibco (California, USA). Antibodies against KLF5, STK24, β-actin, and all of the secondary antibodies were from Proteintech (Wuhan, China). siRNAs against negative control, STK24, and KLF5 were obtained from GenePharma (Shanghai, China). TRIzol reagent was from Invitrogen (Carlsbad, USA). The RT-for-PCR kit was from Clontech. SYBR Green qPCR mix was from Takara (Japan). Protease and phosphatase inhibitors were purchased from Roche (Basel, Switzerland).

2.2. Bioinformatic Analyses. In this study, we used multiple public databases and tools to investigate the biological function of STK24 in LUAD. A total of 515 cancer samples and 59 normal samples were downloaded from TCGA database. The expression of STK24 and the correlation between STK24 and PCNA, between STK24 and KLF5, and survival data were analyzed from TCGA-LUAD cohort. For survival analysis, LUAD patients were cut off by quartile.

Tumor Immune Estimation Resource 2.0 (TIMER2.0) is a web service database that can be used to systematically analyze immune cell infiltration in various cancers. This database provides a variety of analytical functions, including gene, survival, SCNA, Diff Exp, correlation, and estimation to analyze tumor immune function [12]. In the present study, we analyzed the relationship between STK24 and immune cells by somatic copy number variation (SCNV).

In this study, we applied the Cell type Identification by Estimating Relative Subsets of RNA Transcripts (CIBERSORT) algorithm to analyze the relationship between STK24 and immune cells [13]. The method relies on a matrix file called LM22 to analyze immune cells in tissues.

Tumor Immune Dysfunction and Exclusion (TIDE) is an algorithm for evaluating tumor immune escape potential via gene expression profiling in cancer samples [14]. We analyzed the relationship of STK24 and T cell dysfunction and potential regulators of tumor immune escape by this web tool.

2.3. Cell Culture. A549 and H1299 cells were cultured in DMEM culture medium, which contained 10% FBS and 1%

antibiotics. All cells were cultured in a 37°C incubator with the constant CO_2.

2.4. Real-Time Quantitative Polymerase Chain Reaction (RT-qPCR). Lung cancer cells were lased in TRIzol, and RNA was extracted from the cells based on the manufacturer's protocols. mRNA was reversely transcribed into cDNA by using RT-for-PCR kit. Detection of indicated cDNA level was performed by using SYBR Green qPCR mix. The primer sequences were as follows: STK24 forward, 5′-AGGCATTGACAATCGGACT CA-3′, and reverse, 5′-CTGACTCAGCACTGTGATTTCT-3′. β-actin forward, 5′-GAGCTGCGTGTGGCTCCC-3′, and reverse, 5′-CCAGAGGCGTACAGGGATAGCA-3′.

2.5. Immunoblotting. Cells were lased in lysis buffer, and protein amount was detected by using BCA kit. After being boiled, proteins with loading buffer were loaded onto SDS-PAGE gels. After 1-2 hours of separation, the proteins on gels were transferred onto PVDF membranes, which were activated by methanol. After blocking with 5% skim milk and incubating with primary and secondary antibodies, protein expression was detected by using chemiluminescence reagent.

2.6. Cell Proliferation. CCK8 kit was used to investigate cell proliferation. At indicated time after seeding lung cancer cells in 96-well plates, 10% of CCK8 regent was added into each well, and the plates were maintained at 37°C for 3-4 hours. OD450 was then checked, and cell proliferation was normalized to day 1.

2.7. Colony Formation. A549 and H1299 were seeded at the concentration of 1000 cells per well. 8-12 days later, colonies were fixed by methanol and viewed by crystal violet.

2.8. Transwell Assay. Cell migration was examined by transwell assay. 30000 of A549 cells and 4000 of H1299 cells in 200 ul DMEM medium without FBS were plated onto the upper surface of the transwell chamber. 24 hours later, cells attached on the lower surface of the transwell chamber were fixed by methanol and viewed by crystal violet.

2.9. Cell Cycle. Cell cycle was detected by staining the cells with PI. Cells were washed with PBS and incubated with 70% iced alcohol overnight. Then, the cells were stained with PI, and the cell cycle was analyzed on flow cytometry.

2.10. Apoptosis. Trypsin without EDTA was used to trypsinize the cells when analyzing cell apoptosis. Then, the cells were stained with PI and annexin V, and apoptosis was analyzed on flow cytometry.

2.11. Dual Luciferase Reporter Activity. The promoter sequence of STK24 was inserted into pGL3.basic vectors. The CDS sequence of KLF5 was cloned into pCDNA3.1 vectors. After cotransfecting expressing vectors, luciferase pGL3.basic vectors, and internal control pCMV-RL-TK vectors into A549 cells, the dual luciferase activity was assessed. Luciferase activity was normalized to TK activity.

2.12. Statistical Analysis. Statistical data were analyzed using GraphPad Prism software. Student's *t*-test was applied to
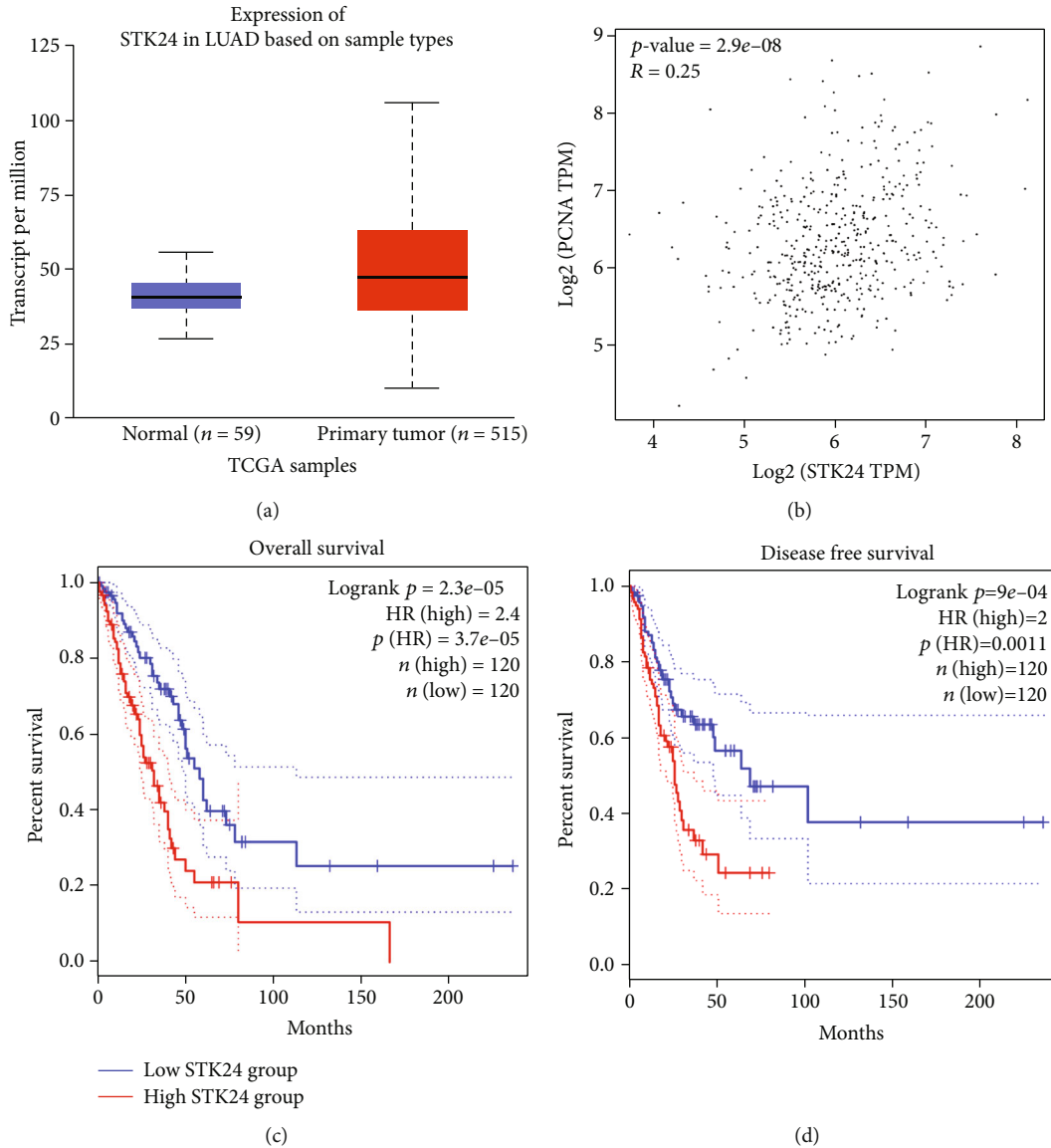
FIGURE 1: STK24 overexpression confers poor prognosis of LUAD patients. (a) Analysis of STK24 transcript in LUAD ($n = 515$) and normal tissues ($n = 59$). (b) Spearman correlation between STK24 and PCNA. (c, d) Overall and disease-free survival of LUAD patients who were divided into STK24 high expression ($n = 120$) and low expression ($n = 120$) groups. $p < 0.01$.

analyze the difference between the two groups. $p < 0.05$ was considered statistically significant.

3. Results

3.1. STK24 Is Overexpressed in LUAD Patients.
We initially analyzed the expression of STK24 in LUAD patients based on the public TCGA database. STK24 was upregulated in LUAD samples compared with normal tissues (Figure 1(a)). Spearman association analysis found that STK24 was positively correlated with PCNA (Figure 1(b)). Then, we analyzed the survival of LUAD patients who were divided into STK24 high-expression and low-expression groups. Both overall and disease-free survival of LUAD patients who had high expression of STK24 were shorter than that in STK24 lowly expressed patients

(Figures 1(c) and 1(d)). These results strongly suggested that STK24 and LUAD are closely related to prognosis.

3.2. STK24 Plays a Pivotal Role in the Proliferation of LUAD.
To explore the function of STK24, we silenced STK24 in A549 and H1299 cells. STK24 mRNA and protein expression were efficiently reduced by siRNAs (Figure 2(a)). STK24 downregulation led to reduced proliferation of A549 and H1299 cells (Figure 2(a)). Furthermore, STK24 was upregulated after incubating with Leti-STK24 for 48 hours (Figure 2(b)). Cell proliferation ability was enhanced after STK24 ectopic expression in A549 and H1299 cells (Figure 2(b)). Colony formation results showed that STK24 downregulation suppressed the colony growth in A549 and H1299 cells (Figure 2(c)). On the contrary, STK24 overexpression potentiated the proliferation and growth ability of both cells (Figure 2(d)). Thus, our findings

(a)

(b)

(c)

(d)
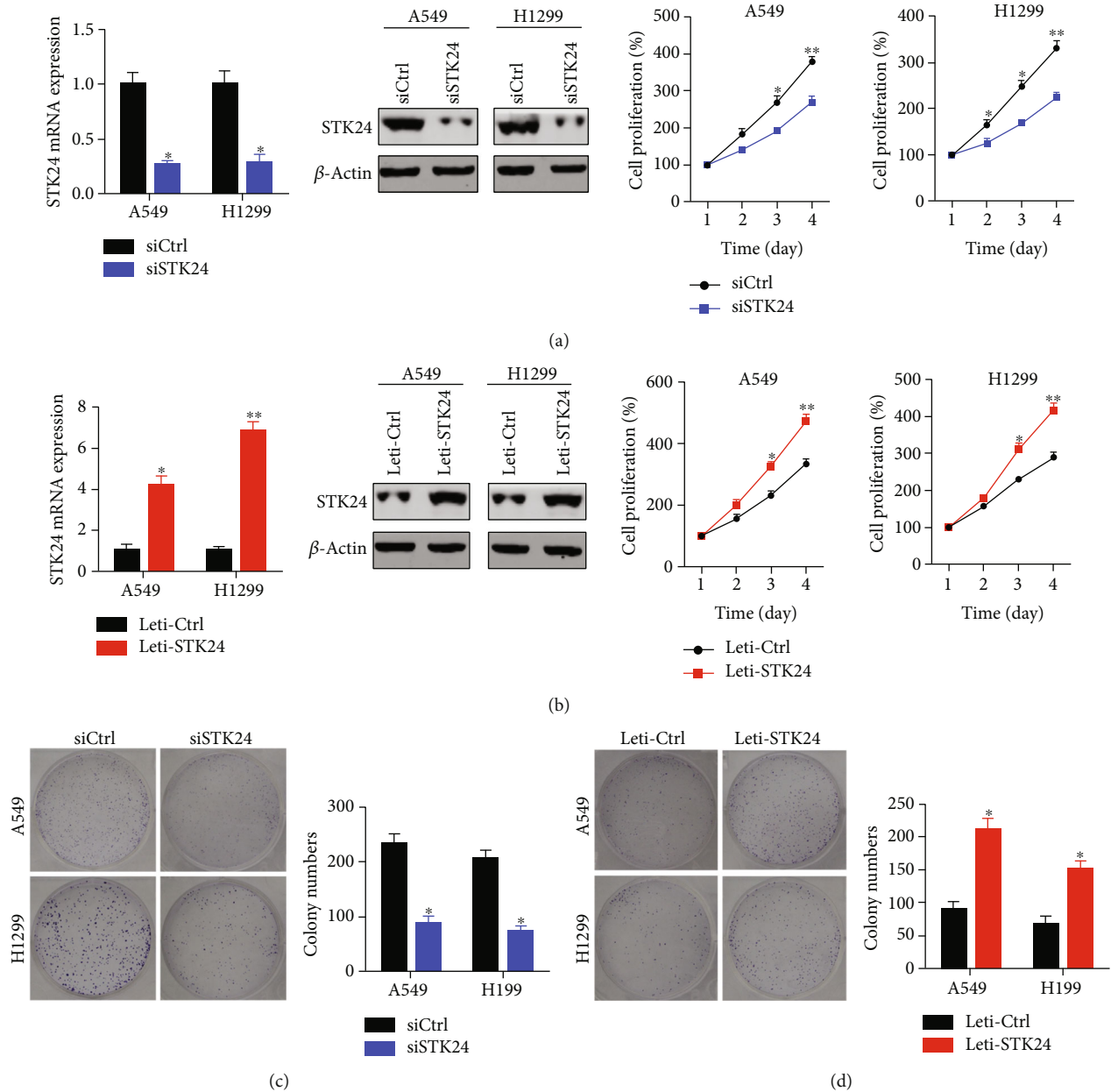
FIGURE 2: STK24 accelerates LUAD cell proliferation. (a) siCtrl and siSTK24 A549 and H1299 cells were subjected to qRT-PCR detection of STK24 mRNA level, immunoblotting detection of STK24 protein abundance, and CCK8 analysis of cell viability. (b) Leti-Ctrl and Leti-STK24 A549 and H1299 cells were subjected to qRT-PCR detection of STK24 mRNA level, immunoblotting detection of STK24 protein abundance, and CCK8 analysis of cell viability. (c, d) Colony growth was assessed. $^{*}p < 0.05$. $^{**}p < 0.01$.

suggest that STK24 has an oncogenic function for lung cancer cell proliferation and growth.

3.3. Downregulation of STK24 Induces LUAD Apoptosis and Cell Cycle Arrest.
We next investigated whether STK24 regulated cell apoptosis and cell cycle progression by staining the cell with PI/annexin V and PI, respectively. We found that STK24 downregulation resulted in a reduction of early apoptosis but a dramatic enhancement of late apoptosis in the A549 and H1299 cells. Total apoptosis, which included early and late apoptosis, was increased after STK24 knockdown in the cells (Figures 3(a) and 3(b)). Cell cycle analysis found

that STK24 downregulation increased the cells at G0/G1 phase but decreased the cells at S phase. Cells at G2/M phase were slightly increased in A549 cells, while they were decreased in H1299 cells (Figures 3(c) and 3(d)). These results generally indicate that STK24 silencing promotes cell apoptosis and cell cycle arrest at G0/G1 phase.

3.4. A Positive Regulation between KLF5 and STK24 Exists in Lung Cancer Cells and Patients.
KLF5 belongs to the Krüppel-like factor family and has transcription activity. Dysregulation of KLF5 is involved in cancer development. To assess the relationship between KLF5 and STK24, we overexpressed and
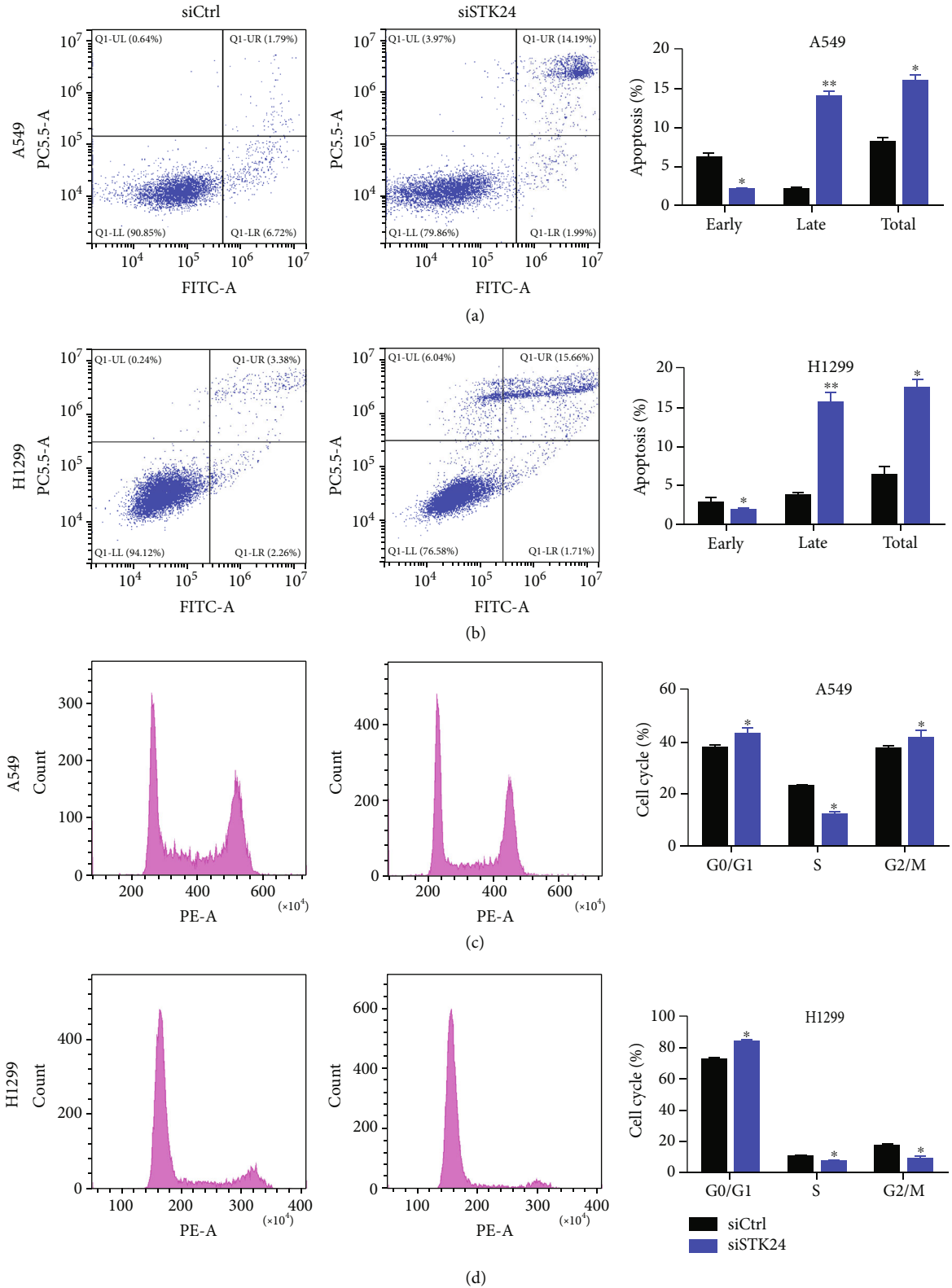
Figure 3: STK24 regulates apoptosis and cell cycle of LUAD. (a, b) Cell apoptosis was detected by PI/annexin V staining. (c, d) Cell cycle was detected by PI staining. $^{*}p < 0.05$. $^{**}p < 0.01$.

(a)

(b)

(c)

(d)
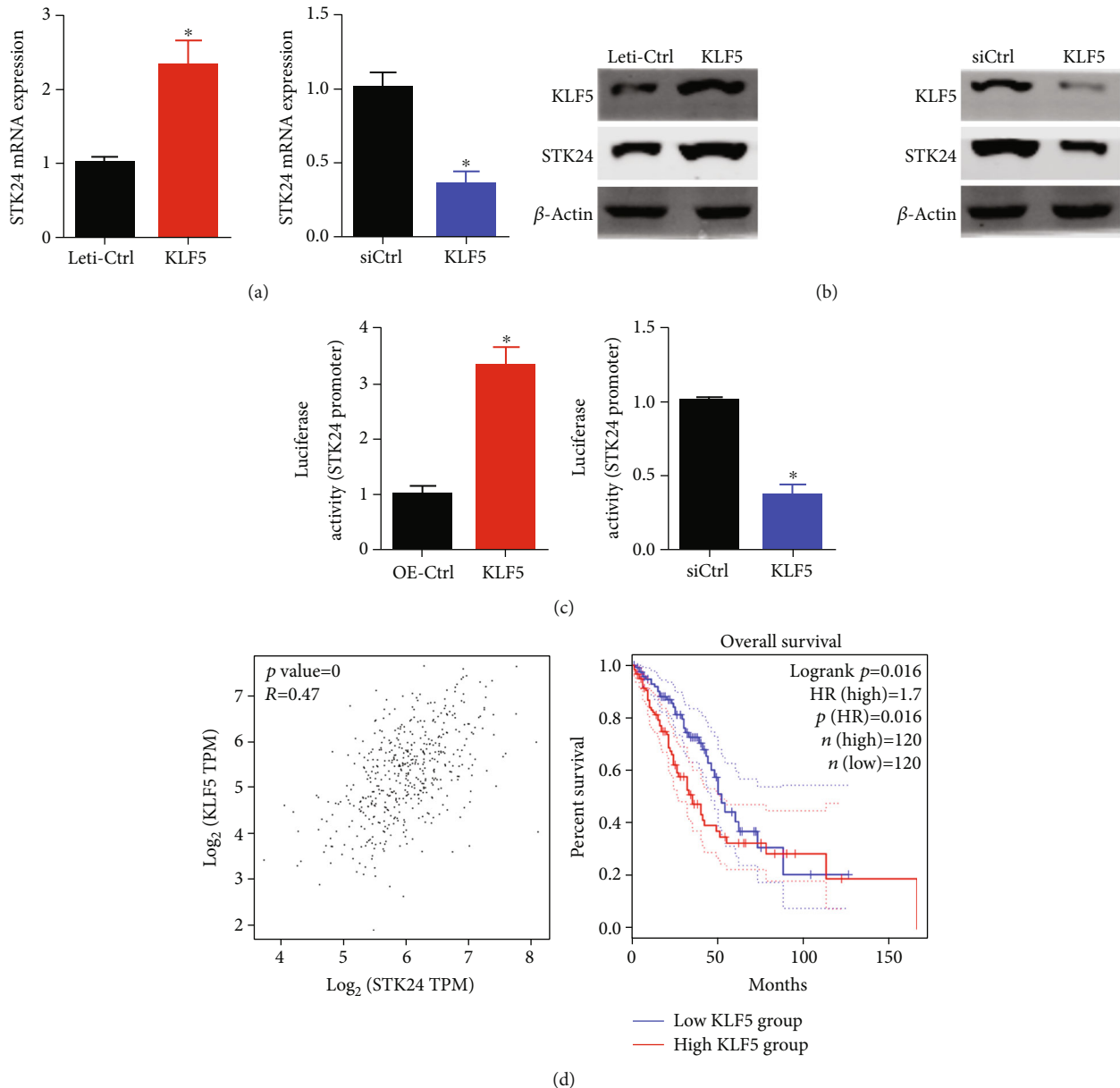
FIGURE 4: KLF5 promotes the expression of STK24 at transcription level. (a) mRNA expression of STK24 was assessed in KLF5 overexpressed and knockdown A549 cells. (b) Immunoblotting detection of KLF5 and STK24 protein abundance was assessed in KLF5 overexpressed and knockdown A549 cells. (c) Luciferase reporter activity of STK24 promoter was determined in A549 cells after KLF5 overexpression and knockdown. (d) Spearman correlation between KLF5 and STK24 in LUAD samples. Overall survival analysis of LUAD patients who were divided into KLF5 high expression ($n = 120$) and low expression ($n = 120$) groups. $^*p < 0.05$.

knocked down KLF5 in A549 cells and checked the expression of STK24. qRT-PCR and immunoblotting results showed that STK24 mRNA and protein expression were upregulated after KLF5 overexpression and downregulated after KLF5 knockdown in A549 cells (Figures 4(a) and 4(b)). Luciferase reporter assay confirmed that KLF5 positively regulated the luciferase activity of STK24 promoter (Figure 4(c)). Analyzing from TCGA data, we found that there was a positive correlation between KLF5 transcript and STK24 transcript in LUAD samples. KLF5 highly expressed patients exhibited shorter overall survival than patients who had low expression of KLF5

(Figure 4(d)). Therefore, KLF5 upregulation of STK24 may contribute to the progression of lung cancer in both cells and patients.

3.5. KLF5 Upregulation of STK24 Promotes Lung Cancer Cell Proliferation and Migration. Above results promoted us to further illustrate the function of KLF5/STK24 axis in lung cancer cell function. We then constructed negative control (Ctrl), KLF5 overexpressed (KLF5), and KLF5 overexpressed with silenced STK24 (KLF5 + siSTK24) A549 and H1299 cells. Immunoblotting results confirmed that we successfully

(a)

(b)

(c)
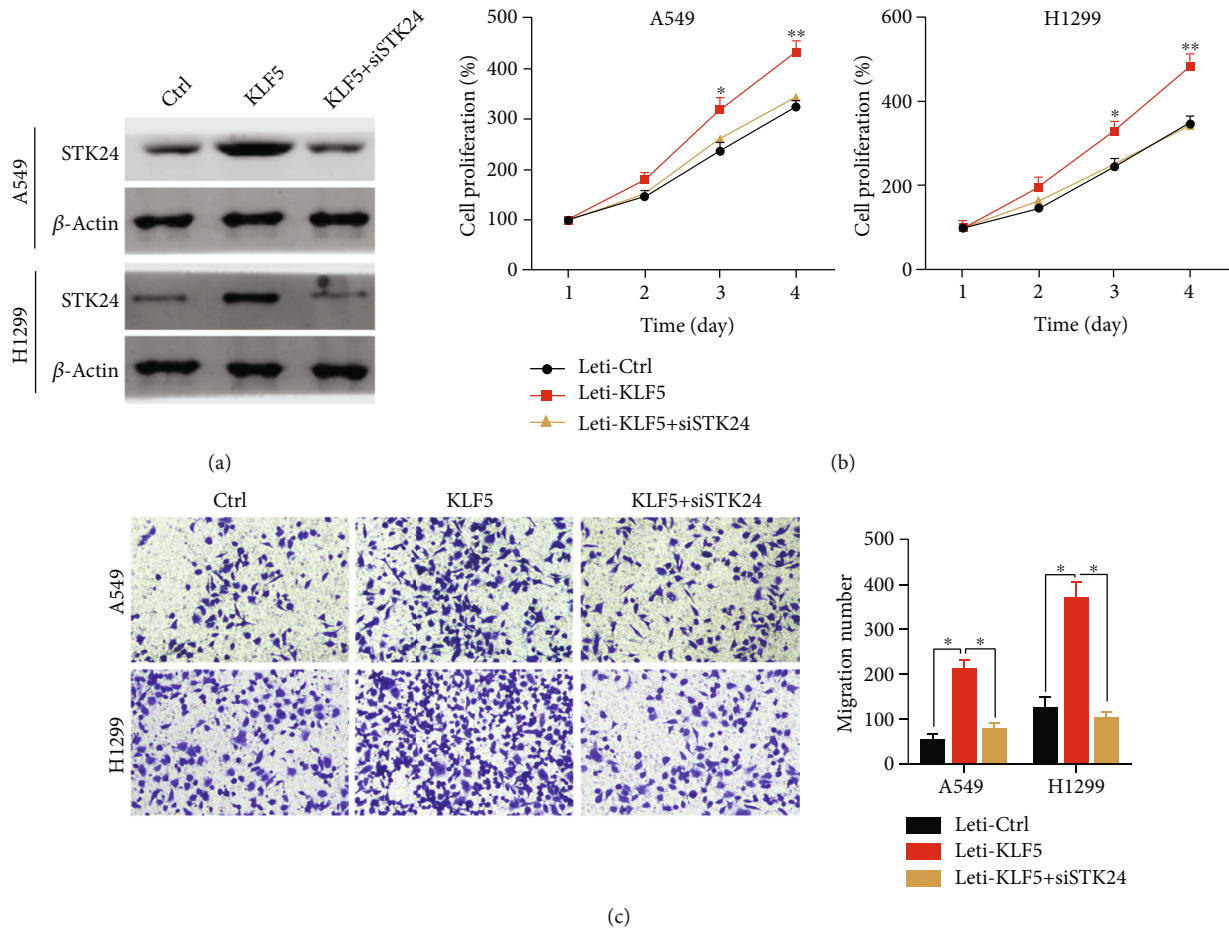
FIGURE 5: KLF5 promotes cell proliferation and migration through SKT24. (a) Immunoblotting analysis of STK24 in Ctrl, KLF5, KLF5 + siSTK24 A549, and H1299 cells. (b) CCK8 assay was performed in Ctrl, KLF5, KLF5 + siSTK24 A549, and H1299 cells. (c) Cell migration was examined in Ctrl, KLF5, KLF5 + siSTK24 A549, and H1299 cells. $^*p < 0.05$. $^{**}p < 0.01$.

constructed the indicated cells (Figure 5(a)). As shown by CCK8 results, we demonstrated that KLF5 overexpression enhanced the proliferation ability of A549 and H1299 cells, which could be reversed by STK24 downregulation (Figure 5(b)). Transwell assay indicated that KLF5 promoted the migration capacity of A549 and H1299 cells, which could also be reduced by STK24 knockdown (Figure 5(c)). Collectively, KLF5 promotes lung cancer cell proliferation and migration and promotes STK24 expression. Inhibition of STK24 expression decreased the ability of KLF5 to promote tumor proliferation and metastasis. KLF5 promotes the proliferation and metastasis of lung cancer cells by promoting the expression of STK24.

3.6. STK24 Expression Mediates the Immunomodulatory Function of LUAD. Dysregulation of tumor immune function is a key step in tumorigenesis and development [15]. It has been previously reported that STK24 promotes the expansion of myeloid-derived suppressor cells in gastric cancer. Therefore, in this study, we further explored the relationship between STK24 and tumor immunity. As shown in Figures 6(a) and 6(b), through the analysis of the TIMER database, we found that the deletion of the copy number of STK24 significantly increased the number of CD8 cells, and conversely, the ampli-

fication of the copy number of STK24 decreased the number of myeloid dendritic cells. Next, the CIBERSORT algorithm showed that the expression of STK24 was negatively correlated with monocytes, activated NK cells, and resting mast cells (Figure 6(c)). In addition, we further analyzed the relationship between STK24 expression and various immune checkpoints. The results showed that STK24 was positively correlated with PDCD1LG2 and CD276 but negatively correlated with TNFRSF14, IDO2, and TNFRSF18 (Figure 6(d)). Finally, we used the TIDE algorithm to analyze LUAD. The T cell dysfunction score was positive for STK24. Patients with high STK24 expression had poor prognosis and low cytotoxic T lymphocyte infiltration, while patients with low STK24 expression had the opposite prognosis and cytotoxic T lymphocyte infiltration (Figure 6(e)).

4. Discussion

LUAD is the most common subtype of lung cancer [16]. In this study, we found that STK24 was highly expressed in LUAD samples based on TCGA data. High expression of STK24 conferred poorer overall and disease-free survival of LUAD patients. Loss-of-function and gain-of-function experiments demonstrated that STK24 expression in lung cancer

(a)

(b)

(c)

(d)

(e)
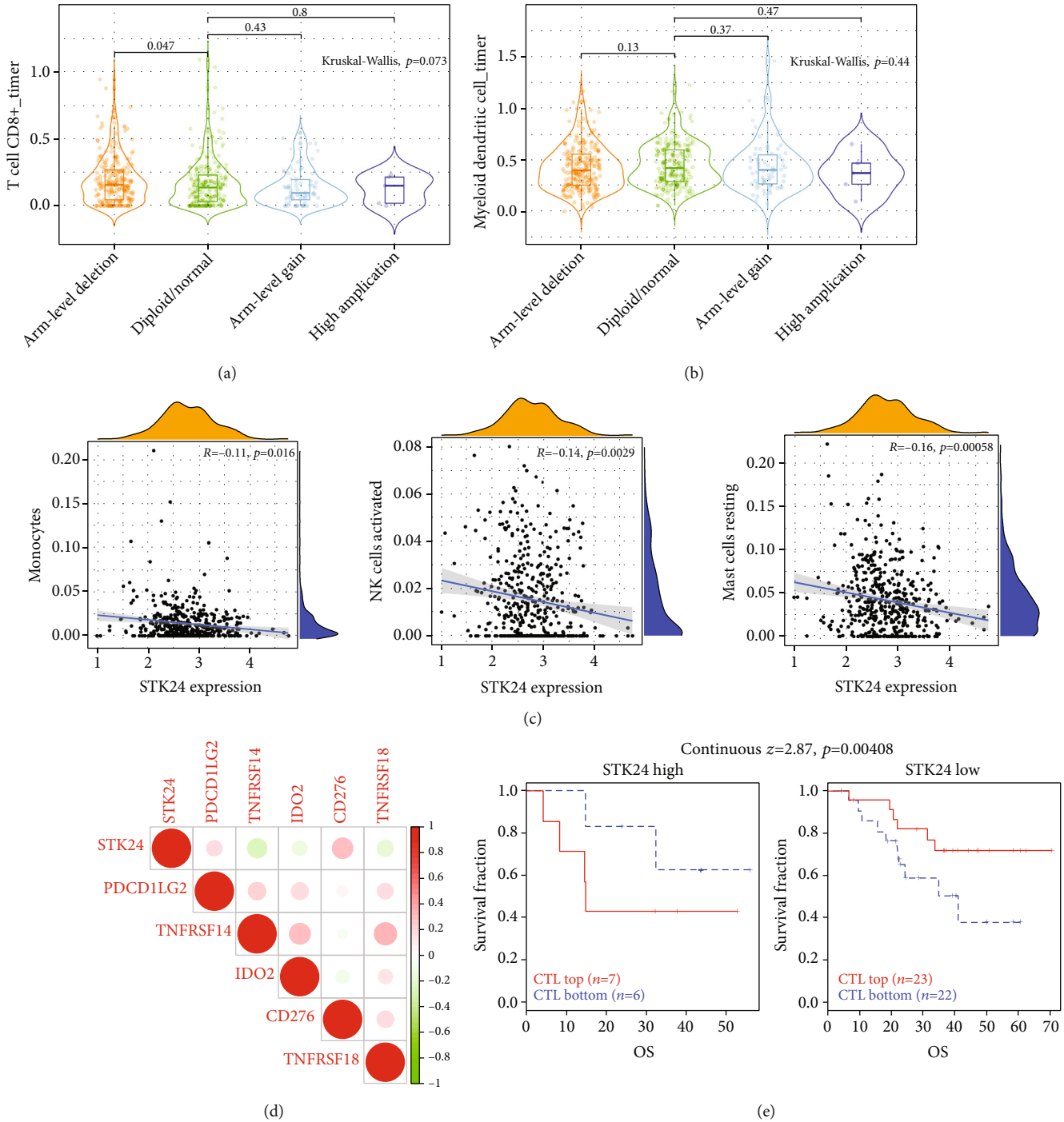
Figure 6: STK24 expression mediates the immunity of LUAD. (a) Relationship between sCNV of STK24 and CD8$^+$ T cells. (b) Relationship between sCNV of STK24 and myeloid dendritic cells. (c) The CIBERSORT algorithm analyzed the correlation of STK24 expression with monocytes, activated NK cells and resting mast cells. (d) The relationship between STK24 expression levels and immuneC checkpoints. (e) The TIDE algorithm concluded that different STK24 expression levels and cytotoxic T lymphocyte infiltration weDre associated with LUAD prognosis.

cells A549 and H1299 was essential to sustain cell growth and proliferation. Cell cycle arrest at G0/G1 and apoptosis were also induced by STK24 knockdown. Thus, STK24 acts as a proliferation inducer for lung cancer.

Protein kinases and phosphatases are important factors in regulating mammals' physiological and pathological functions.

Protein kinases promote or suppress the activity of downstream substrate by increasing the phosphorylation of the proteins. The most well-known kinases are PI3K/AKT/mTOR signaling family, the activation of which contributes to the development of a wide variety of malignancies [17–19]. Recently, serine/threonine-protein kinase family attracts

oncologists' attention because dysregulation of these proteins participates in cancer development. By knowing that MST1/STK4 mainly functions as a tumor suppressor, while MST2/STK3 can act as an oncogene [20], the role of MST3/STK24 in carcinogenesis should be determined. Although STK24 has been identified as an oncogene in breast cancer [11], it suppresses colon cancer growth [10]. One literature showed that STK24 was highly expressed in LUAD tissues and might be a potential biomarker for LUAD diagnosis [21], whereas the function of STK24 remains to be investigated. Thus, our evidences that STK24 overexpression promoted lung cancer cell proliferation and its knockdown-suppressed cancer cell growth revealed that STK24 acts as an oncogene in lung cancer. We also showed the important role of STK24 in regulating cell cycle progression and apoptosis.

Krüppel-like factor 5 (KLF5) is an important transcription factor. KLF5 overexpression enhances the malignancy of gastric cancer via modulating cell cycle proteins p21 and CDK4 [22]. Overexpression of KLF5 is inversely correlated with the prognosis of colon cancer patients [23]. In prostate cancer, KLF5 interacts with androgen receptor (AR) and contributes to cancer development stimulated by AR signaling [24]. These studies highlight the important role of KLF5 in cancer development. Nevertheless, the downstream effectors of KLF5 need intensive studies. Here, we showed that KLF5 positively regulated the expression of STK24 at transcription level. There was also a positive relationship between KLF5 expression and STK24 expression in LUAD samples. KLF5 overexpression was also inversely correlated with patients' survival. Interestingly, when KLF5 overexpression promoted lung cancer cell proliferation and migration, the knockdown of STK24 significantly blocked the oncogenic role of KLF5.

Immune escape is a key link in tumor metastasis, and changes in the immune microenvironment play a pivotal role in this process [25]. The tumor immune microenvironment is regulated by many factors, such as the tumor itself, and various immune and stromal cells [26]. It has been reported that tumor cells can suppress the immune microenvironment by secreting various cytokines [27]. In this study, we preliminarily found that STK24 has an inhibitory effect on the immune microenvironment by bioinformatics analysis, but we failed to investigate its phenotype and mechanism through in vitro and in vivo experiments. We intend to investigate further in subsequent studies.

In conclusion, KLF5 upregulation of STK24 promotes lung cancer growth and migration. Our findings not only illustrated the important role of STK24 in LUAD but also revealed a possible mechanism that STK24 was upregulated by KLF5 in lung cancer patients. Notably, we also predicted that STK24 might also be involved in the immunomodulatory function of LUAD. Based on these findings, we proposed that targeting STK24 might be a potential therapy for lung cancer patients with highly expressed KLF5.

Data Availability

The data generated or analyzed in this study are available from the corresponding author for reasonable request.

Ethical Approval

The study was conducted in accordance with the Declaration of Helsinki, and the protocol was approved by the Ethics Committee of The First Affiliated Hospital of Nanjing Medical University.

Conflicts of Interest

The authors declared no conflict of interest.

Authors' Contributions

Yadong Li and Yanhu Liu contributed equally to this work.

Acknowledgments

References

[1] L. A. Torre, F. Bray, R. L. Siegel et al., "CA cancer," *Jornal dos Clinicos*, vol. 65, no. 2015, pp. 87–108, 2012.

[2] Z. Piotrowska and L. V. Sequist, "Treatment ofEGFR-Mutant lung cancers after progression in patients receiving first-line EGFR tyrosine kinase inhibitors," *JAMA Oncology*, vol. 2, no. 7, pp. 948–954, 2016.

[3] K. Arbour and G. J. Riely, "Systemic therapy for locally advanced and metastatic non-small cell lung cancer," *JAMA*, vol. 322, no. 8, pp. 764–774, 2019.

[4] M. Santarpia, A. Aguilar, I. Chaib et al., "Non-small-cell lung cancer signaling pathways, metabolism, and PD-1/PD-L1 antibodies," *Cancers*, vol. 12, no. 6, p. 1475, 2020.

[5] M. Spella and G. T. Stathopoulos, "Immune resistance in lung adenocarcinoma," *Cancers*, vol. 13, no. 3, p. 384, 2021.

[6] V. Kurbatov, A. Balayev, A. Saffarzadeh et al., "Digital inference of immune microenvironment reveals low-risk subtype of early lung adenocarcinoma," *The Annals of Thoracic Surgery*, vol. 109, no. 2, pp. 343–349, 2020.

[7] X. Liu, S. Wu, Y. Yang, M. Zhao, G. Zhu, and Z. Hou, "The prognostic landscape of tumor-infiltrating immune cell and immunomodulators in lung cancer," *Biomedicine & Pharmacotherapy*, vol. 95, pp. 55–61, 2017.

[8] C. Pombo, C. Iglesias, M. Sartages, and J. B. Zalvide, "MST kinases and metabolism," *Endocrinology*, vol. 160, no. 5, pp. 1111–1118, 2019.

[9] K. Lee, C. Chang, C. Li, H. Song, Y. Shan, and M. Lai, "The oncogenic role of MST3 in human gastric cancer," *American Journal of Cancer Research*, vol. 8, no. 10, pp. 2130–2139, 2018.

[10] F. Luo, J. Zhou, S. Wang, Z. Sun, Q. Han, and C. Bai, "microRNA-222 promotes colorectal cancer cell migration and invasion by targeting MST3," *FEBS Open Bio*, vol. 9, no. 5, pp. 901–913, 2019.

[11] C. Cho, K. Lee, W. Chen et al., "MST3 promotes proliferation and tumorigenicity through the VAV2/Rac1 signal axis in breast cancer," *Oncotarget*, vol. 7, no. 12, pp. 14586–14604, 2016.

[12] T. Li, J. Fan, B. Wang et al., "TIMER: a web server for comprehensive analysis of tumor-infiltrating immune cells," *Cancer Research*, vol. 77, no. 21, pp. e108–e110, 2017.

[13] K. E. Craven, Y. Gokmen-Polar, and S. S. Badve, "CIBERSORT analysis of TCGA and METABRIC identifies subgroups with better outcomes in triple negative breast cancer," *Scientific Reports*, vol. 11, no. 1, p. 4691, 2021.

[14] J. Fu, K. Li, W. Zhang et al., "Large-scale public data reuse to model immunotherapy response and resistance," *Genome Medicine*, vol. 12, no. 1, p. 21, 2020.

[15] H. Gonzalez, C. Hagerling, and Z. Werb, "Roles of the immune system in cancer: from tumor initiation to metastatic progression," *Genes & Development*, vol. 32, no. 19-20, pp. 1267–1284, 2018.

[16] G. Lambe, M. Durand, A. Buckley, S. Nicholson, and R. McDermott, "Adenocarcinoma of the lung: from BAC to the future," *Insights Into Imaging*, vol. 11, no. 1, p. 69, 2020.

[17] G. Hoxhaj and B. D. Manning, "The PI3K-AKT network at the interface of oncogenic signalling and cancer metabolism," *Nature Reviews. Cancer*, vol. 20, no. 2, pp. 74–88, 2020.

[18] F. Janku, T. Yap, and F. Meric-Bernstam, "Targeting the PI3K pathway in cancer: are we making headway?," *Clinical Oncology*, vol. 15, no. 5, pp. 273–291, 2018.

[19] G. Liu and D. M. Sabatini, "mTOR at the nexus of nutrition, growth, ageing and disease," *Nature Reviews. Molecular Cell Biology*, vol. 21, no. 4, pp. 183–203, 2020.

[20] J. Park, G. H. Kim, J. Lee et al., "MST2 silencing induces apoptosis and inhibits tumor growth for estrogen receptor alpha-positive MCF-7 breast cancer," *Toxicology and Applied Pharmacology*, vol. 408, p. 115257, 2020.

[21] N. Huang, W. Lin, X. Shi, and T. Tao, "STK24 expression is modulated by DNA copy number/methylation in lung adenocarcinoma and predicts poor survival," *Future Oncology*, vol. 14, no. 22, pp. 2253–2263, 2018.

[22] P. Chen, X. Qian, Y. Zhang, X. Sun, X. Shi, and Y. Gao, "KLF5 promotes proliferation in gastric cancer via regulating p21 and CDK4," *European Review for Medical and Pharmacological Sciences*, vol. 24, no. 8, pp. 4224–4231, 2020.

[23] Y. Takagi, N. Sakai, H. Yoshitomi et al., "High expression of Krüppel-like factor 5 is associated with poor prognosis in patients with colorectal cancer," *Cancer Science*, vol. 111, no. 6, pp. 2078–2092, 2020.

[24] J. Li, B. Zhang, M. Liu et al., "KLF5 is crucial for androgen-AR signaling to transactivate genes and promote cell proliferation in prostate cancer cells," *Cancers*, vol. 12, no. 3, p. 748, 2020.

[25] A. Osipov, M. T. Saung, L. Zheng, and A. G. Murphy, "Small molecule immunomodulation: the tumor microenvironment and overcoming immune escape," *Journal for Immunotherapy of Cancer*, vol. 7, no. 1, p. 224, 2019.

[26] X. Mao, J. Xu, W. Wang et al., "Crosstalk between cancer-associated fibroblasts and immune cells in the tumor microenvironment: new findings and future perspectives," *Molecular Cancer*, vol. 20, no. 1, p. 131, 2021.

[27] A. J. Ozga, M. T. Chow, and A. D. Luster, "Chemokines and the immune response to cancer," *Immunity*, vol. 54, no. 5, pp. 859–874, 2021.

Research Article

Analysis of the Influencing Factors of Tumor Volume, Body Immunity, and Poor Prognosis after ^{125}I Particle Therapy for Differentiated Thyroid Cancer

Liling Tan,[1] Zhijun Chen [2] Wenjun Wang,[2] Yu Su,[2] Zhen Wu,[2] Ling Yi,[2] and Zhipeng Zheng[2]

[1]*Department of Nuclear Medicine, The Second Affiliated Hospital, Nanchang University, Nanchang, Jiangxi, China*
[2]*Department of Nuclear Medicine, Jiangxi Tumor Hospital, Nanchang, Jiangxi, China*

Correspondence should be addressed to Zhijun Chen; csoodbs@163.com

Objective. To analyze the influencing factors of tumor volume, body immunity, and poor prognosis after ^{125}I particle therapy for differentiated thyroid cancer. *Methods*. A total of 104 patients with differentiated TC who were treated with ^{125}I particles during January 2020 to January 2021 was picked. These subjects were graded as low-dose group (80Gy-110Gy) and high-dose group (110Gy-140Gy) according to the minimum dose received by 90% of the target volume (D90) after surgery. The tumor volume before and after treatment was compared, and fasting venous blood was collected before and after treatment. The content of thyroglobulin (Tg) was detected by electrochemiluminescence immunoassay. The levels of absolute lymphocyte count (ALC), lymphocytes, neutrophils, and monocytes were detected on automatic blood cell analyzer. The lymphocyte to monocyte ratio (LMR), neutrophil to lymphocyte ratio (NLR) and platelet to lymphocyte ration (PLR) were calculated. The changes in the condition of patients were closely observed, and the occurrence of adverse reactions in the two groups were compared. The risk factors influencing the efficacy of ^{125}I particle therapy for differentiated TC were analyzed through multivariate logistic regression analysis. *Results*. The total effective rate of patients in the low- and high-dose groups was 78.85% and 82.69%, respectively ($P > 0.05$). Compared with the pretreatment period, the tumor volume and Tg level in both groups were much lower ($P < 0.05$), and the differences in tumor volume and Tg level had no statistically significant difference between the two groups before and after treatment ($P > 0.05$). At 1 week of the treatment, the total incidence of adverse reactions such as nausea, radiation gastritis, radiation parotitis, and neck discomfort was obviously higher in the high-dose group than in the low-dose group ($P < 0.05$). At 1 month of treatment, the incidence of adverse reactions such as nausea was markedly higher in the high-dose group than in the low-dose group ($P < 0.05$). After treatment, serum NLR and PLR contents were memorably elevated and LMR level was sharply decreased in both groups, and serum NLR and PLR contents were higher and LMR content was lower in the high-dose group than in the low-dose group ($P < 0.05$). Multivariate logistic regression analysis showed that the pathological type of follicular adenocarcinoma, tumor size ≥ 2 cm, clinical stage of III~IV, distant metastasis, and high TSH level before ^{125}I particle treatment were all risk factors related to the efficacy of ^{125}I particle treatment of TC ($P < 0.05$). *Conclusion*. The efficacy of low-dose and high-dose ^{125}I particles in the treatment of differentiated thyroid cancer is comparable, among which low-dose ^{125}I particles have fewer adverse effects and have less impact on the immunity of the body, which is well tolerated by patients and can be widely used in clinical practice. In addition, the pathological type of follicular adenocarcinoma, tumor size ≥ 2 cm, clinical stage III~IV, distant metastasis, and high TSH level before ^{125}I particle treatment are all risk factors that affect the poor effect of ^{125}I particles on thyroid cancer treatment, and early monitoring of the above index changes can help evaluate the prognosis.

1. Introduction

Thyroid cancer (TC) is one of the most common malignant tumors in the endocrine system, accounting for more than 90% of all endocrine malignant tumors. In recent years, the incidence rate of TC is increasing year by year, which has a certain relationship with region, race, and gender [1]. Previous studies suggested that the incidence of TC was closely related to excessive iodine diet, radiation, abnormal secretion of sex hormones, and thyroid stimulating hormones [2]. With the acceleration of life rhythm and the increase of life pressure in recent years, the number of patients with TC has increased year by year, and most of them are differentiated TC, which accounts for more than 90% of TC. Differentiated TC includes papillary TC and follicular TC, of which papillary TC accounts for about 75%, with slow growth, low malignancy, and high 10-year survival rate. Follicular TC is highly malignant and can metastasize to bone and lung through blood with poor prognosis and the 10-year survival rate of less than 40%. Therefore, effective therapy for differentiated TC is the focus of thyroid related research [3, 4].

^{125}I particle is a radioactive particle with wide clinical application at present, which can continuously emit γ-ray for a long time to suppress the reproduce ability of tumor cells, thus inhibiting tumor progression. At present, ^{125}I particle has a good effect in the treatment of prostate cancer, lung cancer, pancreatic cancer, and other solid tumors [5, 6]. Some scholars found that ^{125}I particle therapy could alleviate the clinical symptoms related to lymph node metastasis in patients with refractory differentiated TC with effective and safe local control effect in tumor for short term [7]. However, there are few studies on the effects of different ^{125}I particle treatment dose parameters on the patients.

In this study, 104 patients with differentiated TC admitted in our hospital during January 2020 to January 2021 were picked as the subjects to analyze the factors influencing tumor volume, body immunity, and poor prognosis after ^{125}I particle therapy for differentiated TC.

2. Materials and Methods

2.1. General Materials.
A total of 104 patients with differentiated TC admitted in our hospital during January 2020 to January 2021 was picked. Inclusive criteria are as follows: (1) all patients were diagnosed as differentiated TC by preoperative pathological examination [8] and underwent total thyroidectomy or subtotal thyroidectomy. (2) All patients received ^{125}I particle therapy after operation. (3) The patients and their family members signed the informed consent form and could cooperate with the examination and treatment with good compliance. Exclusion criteria are as follows: (1) the patients with serious functional disorder of important organs. (2) The patients with ^{125}I contraindication. (3) The patients complicated with endocrine metabolism and immune system diseases. (4) The patients with predicted survival time of less than 6 months. (5) The patients combined with other malignant tumors. (6) The patient in lactating or pregnant period. These subjects were
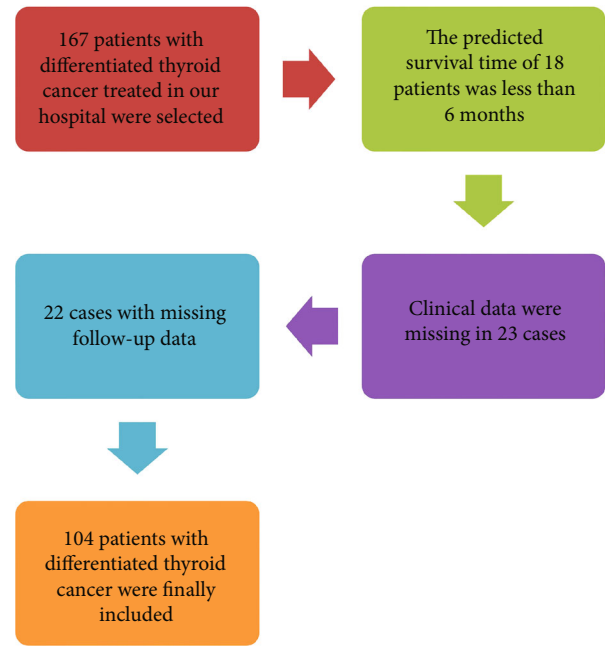
FIGURE 1: The inclusion process of the general data of 104 patients.

graded as low-dose group (80Gy-110Gy) and high-dose group (110Gy-140Gy) according to the minimum dose received by 90% of the target volume (D90) after surgery. 52 patients (23 males and 29 females) were graded as the low-dose group, with an average age of (44.85 ± 5.96) years, an average BMI of (21.12 ± 1.45) kg/m^2, and an average course of disease of (4.52 ± 1.23) years. 52 patients (21 males and 31 females) were graded as the high-dose group, with an average age of (45.15 ± 6.10) years, an average BMI of (20.85 ± 1.33) kg/m^2, and an average course of disease of (4.33 ± 1.28) years. There existed no significant difference in age, gender, BMI, and other general data between the groups $(P > 0.05)$. This experiment was approved by the Ethics Committee of our hospital.

2.2. Methods.
All patients were treated with ^{125}I particle therapy after total or subtotal thyroidectom. (1) Preoperative preparation: blood routine test, biochemical test, thyroid function test, CT, ECG, and ^{131}I whole body imaging were performed before operation. Fasting and water deprivation for 4 hours before operation and venous channels were established. (2) Three-dimensional treatment planning system (TPS) plan: this plan is currently an important tool for radiation therapy for oncology, and the planning system can meet the requirements of conventional radiation therapy. The radioactive particle implantation treatment plan through image pictures was designed, and the gross tumor volume (GTV) and planning target volume (PTV) were outlined. The ^{125}I particles with an activity of 14.8-25.9 MBq was selected, and the prescription dose was set as 100-150Gy. The quantity, distribution, and puncture needle layout of ^{125}I particles were reasonably designed. ^{125}I particle was implanted under the guidance of CT, and the CT images were observed after operation for verification. (3) Operation: the patient was guided to take a comfortable position. The

TABLE 1: Comparison of curative effect (cases, %).

Groups	CR	PR	NC	PD	Total effective rate
Low-dose group ($n = 52$)	29 (55.77)	6 (11.54)	6 (11.54)	11 (21.15)	41 (78.85)
High-dose group ($n = 52$)	31 (59.61)	7 (13.46)	5 (9.62)	9 (17.31)	43 (82.69)
χ^2					0.248
P					0.619
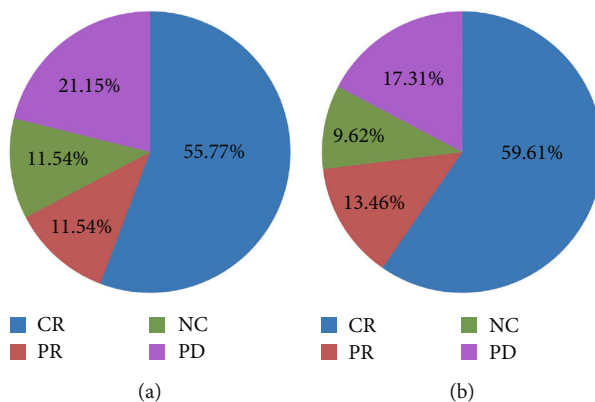
FIGURE 2: Pie chart analysis of comparison of curative effect between two groups. (a) Low-dose group. (b) High-dose group. Note: CR: complete response; PR: partial response; NC: no change; PD: progression.

puncture point was marked and routine disinfection was conducted. Sterile sheet was paved and local anesthesia was performed using 2% lidocaine. The position of puncture needle was confirmed through CT after puncture. Implantation was conducted with particle spacing of 0.5-1.0 cm and row spacing of 1.0 cm. After CT reexamination and confirmation of correct position, pressure bandage was performed, and antibiotics were routinely used after operation.

2.3. Outcome Measures

2.3.1. Efficacy. The efficacy was graded as complete response (CR), partial response (PR), no change (NC), and progression (PD). The lesions disappeared completely, and only strip shadow or no abnormality in imaging were CR. PR referred to the reduction of lesion volume $\geq 50\%$ compared with that before treatment. NC referred to that the lesion volume reduced by <50% or increased by <25% compared with that before treatment. The volume of lesion increased by $\geq 25\%$ than that before treatment or new lesion appeared was PD. Total effective = CR + PR + NC.

2.3.2. Tumor Volume. Cervical ultrasound was performed before and 3 months after treatment to measure the longitude of thyroid tissue before and after treatment, and the thyroid volume was calculated by Brunn's formula.

2.3.3. Serum Index. The fasting venous blood in the morning before treatment and 3 months after the treatment was collected and centrifuged at 3000 r/min for 10 minutes. The serum was carefully collected and stored at -40°C to avoid repeated freezing and thawing. The content of thyro-globulin (Tg) was detected by electrochemiluminescence immunoassay. The levels of absolute lymphocyte count (ALC), lymphocytes, neutrophils, and monocytes were detected on automatic blood cell analyzer. The lymphocyte to monocyte ratio (LMR), neutrophil to lymphocyte ratio (NLR), and platelet to lymphocyte ration (PLR) were calculated.

2.3.4. Adverse Reactions. The changes in the condition of patients were closely observed, and the occurrence of adverse reactions such as nausea, radiation gastritis, radiation mumps, and neck discomfort in two groups were compared.

2.3.5. Collection of Clinical Characteristics. The indicators such as the patients' age (<45 years old, ≥ 45 years old), gender (male, female), pathological type (papillary adenocarcinoma, follicular adenocarcinoma), tumor size (<2 cm, ≥ 2 cm), number of lesions (single, multiple), invasion (no invasion of capsule, membrane invasion, slight invasion outside the thyroid, and obvious invasion outside the thyroid), clinical stage (I~II, III~IV), distant metastasis (yes, no), and the level of thyroid stimulating hormone (TSH) before ^{125}I particle therapy (<30 mIU/L, 30-59 mIU/L, 60-89 mIU/L, and ≥ 90 mIU/L) were collected.

2.4. Statistical Analysis. The experimental data were analyzed by SPSS20.0 software. NLR, PLR, LMR, and other measurement data were expressed in ($\bar{x} \pm s$) and were compared using t-test between groups; The enumeration data of curative effect and adverse reaction were expressed in (%) and were compared by χ^2 text. The risk factors related to the efficacy of ^{125}I particle therapy for differentiated TC were analyzed by multivariate logistic regression analysis.

TABLE 2: Changes of tumor volume ($\bar{x} \pm s$).

Time	Groups	Tumor volume (cm^3)	Tg (μg/L)
Before treatment	Low-dose group ($n = 52$)	7.15 ± 2.46	57.46 ± 14.29
	High-dose group ($n = 52$)	7.08 ± 1.85	57.82 ± 13.96
t		0.164	0.130
P		0.870	0.897
After treatment	Low-dose group ($n = 52$)	1.96 ± 0.52[a]	38.59 ± 12.48[a]
	High-dose group ($n = 52$)	1.86 ± 0.26[a]	36.59 ± 15.49[a]
t		1.240	0.725
P		0.218	0.470

Note: [a]$P < 0.05$ compared with the same group before treatment; Tg: thyroglobulin.

$P < 0.05$ indicated that the statistical results were statistically significant.

3. Results

3.1. General Data of 104 Patients. There were 167 cases of differentiated TC included, and 104 patients were finally included after screening according to the inclusion and exclusion criteria. The specific process was shown in Figure 1.

3.2. Comparison of Curative Effect. The proportions of CR patients in low- and high-dose groups were 55.77% and 59.62%, PR patients of 11.54% and 13.46%, and NC patients of 11.54%, 9.62%, respectively. The total effective rate of patients in the low- and high-dose groups was 78.85% and 82.69%, respectively ($P > 0.05$; Table 1 and Figure 2).

3.3. Changes of Tumor Volume. Compared with the pretreatment period, the tumor volume and Tg level in both groups were much lower ($P < 0.05$), and the differences in tumor volume and Tg level had no statistically significant difference between the two groups before and after treatment ($P > 0.05$; Table 2 and Figure 3).

3.4. Comparison of Adverse Reactions. At 1 week of treatment, the total incidence of adverse reactions such as nausea, radiation gastritis, radiation parotitis, and neck discomfort was obviously higher in the high-dose group than in the low-dose group ($P < 0.05$). At 1 month of treatment, the incidence of adverse reactions such as nausea was markedly higher in the high-dose group than in the low-dose group ($P < 0.05$) but there existed no significant difference in the probability of adverse reactions such as radiation gastritis, radiation mumps, and neck discomfort ($P > 0.05$). At 3 months of treatment, there existed no significant difference in the probability of adverse reactions such as nausea, radiation gastritis, radiation mumps, and neck discomfort between two groups ($P > 0.05$; Table 3 and Figure 4).

3.5. Comparison of Immune Function. There existed no significant difference in serum ALC, NLR, LMR, and PLR levels between the two groups before treatment ($P > 0.05$). After treatment, serum NLR and PLR content was memorably elevated and LMR level was sharply decreased in both
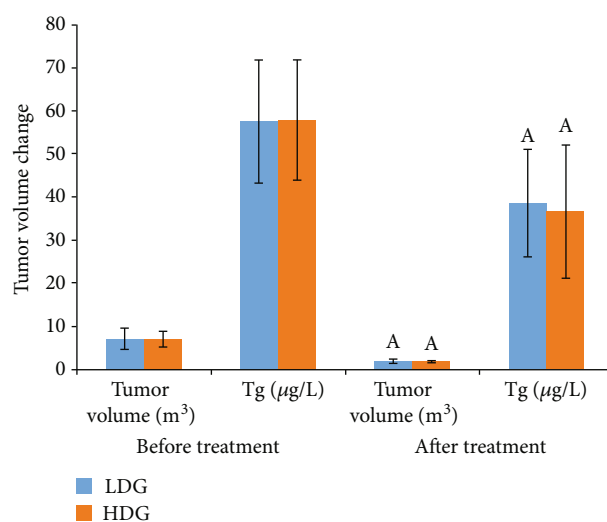
FIGURE 3: The tumor volume changed after different radiation doses in the two groups. Note: [A]$P < 0.05$ compared with the same group before treatment.

groups, and serum NLR and PLR contents were higher and LMR content was lower in the high-dose group than in the low-dose group ($P < 0.05$; Table 4).

3.6. Univariate Analysis of Factors Influencing the Efficacy of ^{125}I Particle Therapy for Differentiated TC. As shown in Table 5, the univariate analysis showed that there existed statistically significant differences between the effective group and the ineffective group in terms of pathological type, tumor size, clinical stage, distant metastasis, and TSH level before ^{125}I particle therapy ($P < 0.05$; Table 5).

3.7. Risk Factors Related to the Efficacy of ^{125}I Particle Treatment Analyzed by Multivariate Logistic Regression Analysis. The indicators with statistical significance in Table 5 were included into the multivariate logistic regression analysis. The results showed that the pathological type of follicular adenocarcinoma, tumor size ≥2 cm, clinical stage of III~IV, distant metastasis, and high TSH level before ^{125}I particle treatment were all risk factors related to the efficacy of ^{125}I particle treatment of TC ($P < 0.05$; Table 6).

Table 3: Comparison of adverse reactions between the two groups (cases, %).

Time	Groups	Nausea	Radiation gastritis	Radiation parotitis	Neck discomfort
1 week after treatment	Low-dose group ($n = 52$)	6 (11.54%)	2 (3.85%)	3 (5.77%)	8 (15.38%)
	High-dose group ($n = 52$)	15 (28.85%)	9 (17.31%)	10 (19.23%)	17 (32.69%)
χ^2		4.833	4.981	4.308	4.265
P		0.028	0.026	0.038	0.039
1 month after treatment	Low-dose group ($n = 52$)	2 (3.85%)	1 (1.92%)	2 (3.85%)	5 (9.62%)
	High-dose group ($n = 52$)	8 (15.38%)	2 (3.85%)	3 (5.77%)	8 (15.38%)
χ^2		3.983	0.343	0.210	0.791
P		0.046	0.558	0.647	0.374
3 months after treatment	Low-dose group ($n = 52$)	1 (1.92%)	1 (1.92%)	0 (0.00%)	2 (3.85%)
	High-dose group ($n = 52$)	2 (3.85%)	3 (5.77%)	1 (1.92%)	3 (5.77%)
χ^2		0.343	1.040	1.010	0.210
P		0.558	0.308	0.315	0.647

(a)

(b)

(c)
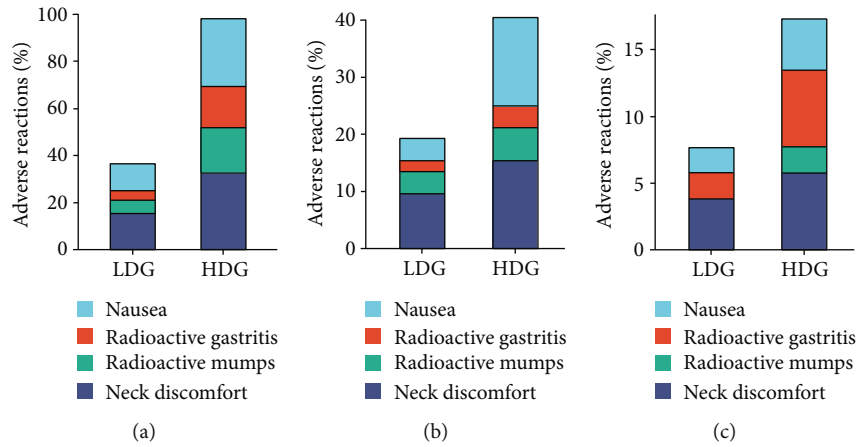
Figure 4: Comparison of the incidence of adverse reactions after different radiotherapy in the two groups. (a) 1 week after treatment. (b) 1 month after treatment. (c) 3 months after treatment.

4. Discussion

Differentiated TC is the TC with the highest incidence rate at present, which has the characteristics of high differentiation, low malignancy, and better surgical treatment. However, different clinical manifestations of patients, including tumor size, extraglandular invasion, cervical lymph node metastasis, and distant metastasis, will lead to different prognosis of patients. In addition, due to the complex anatomical structure of the thyroid region in the neck, the incidence of early thyroid infiltration or invasion of surrounding tissues is high, and there may be residual thyroid cancer tissue after surgery [9]. Therefore, differentiated TC has a high rate of recurrence, local or distant metastasis. Statistics show that 10%-30% of patients are accompanied by recurrence and metastasis after surgery. If the lung metastasis of thyroid cancer could be diagnosed early and treated effectively, the 10-year survival rate of lung metastasis could be as high as 90% [10]. Therefore, how to reduce the recurrence and

metastasis rate of differentiated TC after surgery has become the research focus of medical scholars.

[125]I particle therapy is a new radiation therapy technology in recent years, which effectively protects parathyroid gland, recurrent laryngeal nerve, and other important organs by implanting ^{125}I particle into the focus by minimally invasive method without surgical incision and suture. At the same time, ^{125}I particles have the characteristics of high local dose and high dose of surrounding normal tissues in brachytherapy, which can effectively reduce the impact on normal thyroid tissues while ensuring the efficacy [11, 12]. At present, ^{125}I particles have achieved good efficacy in the treatment of TC, non-small-cell lung cancer and other malignant tumors [13, 14], but there is no formal research report on dosage application. There are few studies on the effects of different doses on the efficacy, adverse reactions, and immunity of differentiated TC. It was found that compared with before treatment, the lymph node metastasis was much smaller; the Tg level and postoperative dose

TABLE 4: Comparison of immune function ($\bar{x} \pm s$).

Time	Groups	ALC (10^9/L)	NLR	LMR	PLR
Before treatment	Low-dose group ($n = 52$)	1.85 ± 1.26	2.43 ± 1.85	3.63 ± 2.15	152.63 ± 35.85
	High-dose group ($n = 52$)	1.82 ± 1.38	2.40 ± 1.26	3.81 ± 2.45	148.67 ± 46.33
t		0.116	0.096	0.398	0.488
P		0.908	0.923	0.691	0.627
After treatment	Low-dose group ($n = 52$)	0.91 ± 0.46[a]	3.59 ± 2.15[a]	2.48 ± 1.26[a]	225.46 ± 102.53[a]
	High-dose group ($n = 52$)	0.81 ± 0.37[a]	6.36 ± 5.12[a]	1.69 ± 1.05[a]	316.48 ± 142.03[a]
t		1.222	3.597	3.473	3.747
P		0.225	0.001	0.001	<0.001

Note: [a]$P < 0.05$ compared with the same group before treatment; ALC: absolute lymphocyte count; NLR: neutrophil to lymphocyte ratio; LMR: lymphocyte to monocyte ratio; PLR: platelet to lymphocyte ration.

TABLE 5: Univariate analysis of factors influencing the efficacy of ^{125}I particle therapy for differentiated TC.

Related factors	Effective group ($n = 85$)	Ineffective group ($n = 19$)	χ^2	P
Gender				
Male	33 (38.82)	11 (57.89)	2.314	0.128
Female	52 (61.18)	8 (42.11)		
Age				
<45 years old	47 (55.29)	7 (36.84)	2.118	0.146
≥45 years old	38 (44.71)	12 (63.16)		
Pathological type				
Papillary adenocarcinoma	51 (60.00)	5 (26.32)	7.090	0.008
Follicular adenocarcinoma	34 (40.00)	14 (73.68)		
Tumor size				
<2 cm	63 (74.18)	7 (36.84)	9.806	0.002
≥2 cm	22 (25.88)	12 (63.16)		
Number of lesions				
Single	27 (31.76)	9 (47.38)	1.671	0.196
Multiple	58 (68.24)	10 (52.63)		
Invasion				
No invasion of capsule	30 (35.29)	5 (26.32)	0.974	0.808
Membrane invasion	27 (31.76)	8 (42.11)		
Slight invasion outside the thyroid	16 (18.82)	3 (15.79)		
Obvious invasion outside the thyroid	12 (14.12)	3 (15.79)		
Clinical stage				
I~II stage	60 (70.59)	8 (42.11)	5.566	0.018
III~IV stage	25 (29.41)	11 (57.89)		
Distant metastasis				
Yes	30 (35.29)	13 (68.42)	7.027	0.008
No	55 (64.71)	6 (31.58)		
TSH level before ^{125}I particle therapy (mIU/L)				
<30	1 (1.18)	2 (10.53)	7.896	0.048
30~59	37 (43.53)	4 (21.05)		
60~89	24 (28.24)	5 (26.32)		
≥90	23 (27.06)	8 (42.11)		

Note: TSH: thyroid-stimulating hormone.

TABLE 6: Risk factors related to the efficacy of ^{125}I particle treatment analyzed by multivariate logistic regression analysis.

Factors	B	SE	Wald	P	OR	95% CI
Follicular adenocarcinoma	0.985	0.263	12.218	0.001	2.718	1.469~4.852
Tumor size ≥ 2 cm	1.236	0.318	5.006	0.001	3.421	2.052~5.526
Clinical stage of III~IV	1.181	0.283	6.775	0.001	3.283	1.562~6.571
Distant metastasis	0.860	0.363	5.136	0.002	2.359	1.182~4.203
TSH level ≥ 90	0.952	0.413	5.750	0.001	2.523	1.409~4.853

Note: TSH: thyroid-stimulating hormone.

parameters were much lower after treatment when ^{125}I radioactive particles were implanted for refractory differentiated TC treatment [15], suggesting that ^{125}I radioactive particle implantation could achieve the expected dose distribution and effectively control tumor progression. In this study, the total effective rate of patients in the low- and high-dose groups was 78.85% and 82.69%, respectively. Compared with the pretreatment period, the tumor volume and Tg level in both groups were much lower. The results of this study suggested that ^{125}I particles with D90 in the range of 80Gy-140Gy were effective in the treatment of differentiated TC, which could effectively inhibit tumor progression. The effects of low dose and high dose after surgery were similar.

Radiotherapy treats tumors using radiation, usually accompanied by side effects such as nausea, vomiting, and gastrointestinal dysfunction, which not only increases the pain of patients but also has a certain impact on their lives. Long term adverse reactions further reduce the patient's tolerance [16, 17]. Therefore, how to reduce the side effects of radiotherapy and increase the confidence of patients to overcome the disease are also important options for selecting treatment plans. Radiotherapy can not only inhibit the proliferation of tumor cells but also inhibit the immune function of the body. NLR and PLR are commonly used clinical immune indicators, and the increased content of NLR and PLR usually indicates that the body is in an immunosuppressive state [18]. LMR is a marker of inflammatory immune response, and decreased level of LMR indicates the malignant progress of tumor. In this experiment, the high-dose group had much higher probability of nausea, radiation gastritis, radiation mumps, and neck discomfort than the low-dose group at 1 week after treatment. At the first month after treatment, the probability of nausea in the high-dose group was markedly higher than that in the low-dose group. After treatment, serum NLR and PLR content was higher and LMR content was lower in the high-dose group than in the low-dose group. Hammad et al. [19] showed that radiotherapy could reduce lymphocyte count, and lymph nodes were the key to regulating tumor immune response as peripheral immune organs. The results in the study showed that the pathological type of follicular adenocarcinoma, tumor size ≥2 cm, clinical stage of III~IV, distant metastasis, and high TSH level before ^{125}I particle treatment were all risk factors related to the efficacy of ^{125}I particle treatment of TC ($P < 0.05$). Therefore, our study suggested that the increase of immunotoxicity related to the increase of radiotherapy dose might be an important factor leading to tumor progression. It is of great significance to limit the radiation dose to minimize the damage of the immune system for improving the survival of patients.

In general, the efficacy of low-dose and high-dose ^{125}I particles in the treatment of differentiated thyroid cancer is comparable, among which low-dose ^{125}I particles have fewer adverse effects and have less impact on the immunity of the body, which is well tolerated by patients and can be widely used in clinical practice. In addition, the pathological type of follicular adenocarcinoma, tumor size ≥ 2 cm, clinical stage III~IV, distant metastasis, and high TSH level before ^{125}I particle treatment are all risk factors that affect the poor effect of ^{125}I particles on thyroid cancer treatment, and early monitoring of the above index changes can help evaluate the prognosis. However, due to the limited time of this study, and for patients undergoing radiotherapy and chemotherapy at the same time, the peripheral blood immune indicators may be affected by the radiotherapy. How to control the metrological parameters after ^{125}I particle therapy and how to reduce the impact on the body immunity while ensuring the efficacy will be further explored in the following study.

Data Availability

The datasets used and/or analyzed during the current study are available from the corresponding author on reasonable request.

Conflicts of Interest

The authors declare that they have no competing interests.

References

[1] P. Kumar, N. A. Damle, S. Agarwala, S. N. Dwivedi, and C. Bal, "Individualized dosimetry in children and young adults with differentiated thyroid cancer undergoing iodine-131 therapy," *Journal of Pediatric Endocrinology and Metabolism*, vol. 33, no. 8, pp. 1031–1044, 2020.

[2] J. N. Taylor, K. Mochizuki, K. Hashimoto et al., "High-resolution Raman microscopic detection of follicular thyroid cancer cells with unsupervised machine learning," *Journal of Physical Chemistry B*, vol. 123, no. 20, pp. 4358–4372, 2019.

[3] N. Fukuda, K. Toda, A. Ohmoto et al., "Baseline tumour size as a prognostic factor for radioiodine-refractory differentiated thyroid cancer treated with lenvatinib," *Anticancer Research*, vol. 41, no. 3, pp. 1683–1691, 2021.

[4] B. Kahramangil, E. Kose, M. Donmez et al., "Thyroglobulin washout from cervical lymph node fine needle aspiration biopsies in patients with differentiated thyroid cancer: an analysis of different expressions to use in post-total thyroidectomy follow-up," *Surgery*, vol. 167, no. 1, pp. 34–39, 2020.

[5] Y. Niu, Z. Ding, X. Deng et al., "A novel multimodal therapy for anaplastic thyroid carcinoma: ^{125}I seed implantation plus apatinib after surgery," *Frontiers in Endocrinology*, vol. 11, p. 207, 2020.

[6] Y. Wang, L. Zhu, X. Lin et al., "Therapeutic effect of CT-guided ^{125}I seed Implantation on advanced lung cancer and pulmonary metastatic carcinoma," *Zhongguo Fei Ai Za Zhi*, vol. 23, no. 6, pp. 424–428, 2020.

[7] R. Sánchez Sánchez, A. D. González Jiménez, A. C. Rebollo Aguirre et al., "^{125}I radioactive seed localization for non-palpable lesions in breast cancer," *Revista Espanola de Medicina Nuclear e Imagen Molecular (English Edition)*, vol. 38, no. 6, pp. 343–347, 2019.

[8] K. A. Araque, S. Gubbi, and J. Klubo-Gwiezdzinska, "Updates on the management of thyroid cancer," *Hormone and Metabolic Research*, vol. 52, no. 8, pp. 562–577, 2020.

[9] X. Zhang, D. S. Liu, Z. S. Luan et al., "Efficacy of radioiodine therapy for treating 20 patients with pulmonary metastases from differentiated thyroid cancer and a meta-analysis of the current literature," *Clinical and Translational Oncology*, vol. 20, no. 7, pp. 928–935, 2018.

[10] M. T. Parisi, H. Khalatbari, S. R. Parikh, and A. Alazraki, "Initial treatment of pediatric differentiated thyroid cancer: a review of the current risk-adaptive approach," *Pediatric Radiology*, vol. 49, no. 11, pp. 1391–1403, 2019.

[11] T. Cambil, J. A. Terrón, C. Marín, and T. Martín, "^{125}I radioactive seed localization (RSL) in surgery of cervical metastasis of thyroid cancer," *Revista Espanola de Medicina Nuclear e Imagen Molecular (English Edition)*, vol. 39, no. 3, pp. 140–145, 2020.

[12] R. Sharma, N. S. Sagoo, A. S. Haider et al., "Iodine-125 radioactive seed brachytherapy as a treatment for spine and bone metastases: a systematic review and meta-analysis," *Surgical Oncology*, vol. 38, article 101618, 2021.

[13] G. S. Zhao, S. Liu, L. Yang et al., "Evaluation of radioactive ^{125}I seed implantation for the treatment of refractory malignant tumours based on a CT-guided 3D template-assisted technique: efficacy and safety," *BMC Cancer*, vol. 20, no. 1, p. 718, 2020.

[14] M. J. Dryden, B. E. Dogan, P. Fox et al., "Imaging factors that influence surgical margins after preoperative ^{125}I radioactive seed localization of breast lesions: comparison with wire localization," *American Journal of Roentgenology*, vol. 206, no. 5, pp. 1112–1118, 2016.

[15] W. Chen, Y. K. Luo, Y. Zhang, Q. Song, and J. Tang, "Ultrasound-guided implantation of radioactive ^{125}I seed in radioiodine refractory differentiated thyroid carcinoma," *BMC Cancer*, vol. 21, no. 1, p. 834, 2021.

[16] L. Facs, "Making resistance futile: how targeted therapies may improve existing treatments in conventional, differentiated thyroid cancer," *Surgery*, vol. 167, no. 1, pp. 64-65, 2020.

[17] M. Zoltek, T. M.-L. Andersson, C. Hedman, C. Ihre-Lundgren, and C. Nordenvall, "Cardiovascular incidence in 6900 patients with differentiated thyroid cancer: a Swedish nationwide study," *World Journal of Surgery*, vol. 44, no. 2, pp. 436–441, 2020.

[18] M. Yokota, H. Katoh, H. Nishimiya et al., "Lymphocyte-Monocyte Ratio Significantly Predicts Recurrence in Papillary Thyroid Cancer," *Journal of Surgical Research*, vol. 246, pp. 535–543, 2020.

[19] R. Hammad, M. A. E. L. R. Eldosoky, S. H. Fouad et al., "Circulating cell-free DNA, peripheral lymphocyte subsets alterations and neutrophil lymphocyte ratio in assessment of COVID-19 severity," *Innate Immunity*, vol. 27, no. 3, pp. 240–250, 2021.

Hindawi

Research Article

INKA2-AS1 Is a Potential Promising Prognostic-Related Biomarker and Correlated with Immune Infiltrates in Hepatocellular Carcinoma

Wenke Li,[1] Guoqing Hong,[2] and Xing Lai [2]

[1]Department of Hepatobiliary Surgery, Yongchuan Hospital of Chongqing Medical University, Chongqing, China
[2]Department of Hepatobiliary Surgery, Tongnan District People's Hospital, Chongqing, China

Correspondence should be addressed to Xing Lai; lx8243495@163.com

Hepatocellular carcinoma (HCC) is a malignancy with one of the worst prognoses. Long noncoding RNAs (lncRNAs) may be important in cancer development and may serve as new biomarkers for the diagnosis and treatment of various tumors, according to mounting research. The purpose of this study was to investigate the expression of INKA2-AS1 and clinical importance in HCC patients. The TCGA database was used to obtain the human tumor samples, while the TCGA and GTEx databases were used to gather the human normal samples. We screened differentially expressed genes (DEGs) between HCC and nontumor tissues. Investigations were made into the statistical significance and clinical significance of INKA2-AS1 expression. A single-sample gene set enrichment analysis (ssGSEA) was used to examine potential relationships between immune cell infiltration and INKA2-AS1 expression. In this investigation, we found that HCC specimens had considerably greater levels of INKA2-AS1 expression than nontumor specimens. When utilizing the TCGA datasets and the GTEx database, high INKA2-AS1 expression showed an AUC value for HCC of 0.817 (95% confidence interval: 0.779 to 0.855). Pan-cancer assays revealed that numerous tumor types had dysregulated levels of INKA2-AS1. Gender, histologic grade, and pathologic stage were all substantially correlated with high INKA2-AS1 expression. A survival study indicated that HCC patients with high INKA2-AS1 expression have shorter OS, DSS, and PFI than those with low INKA2-AS1 expression. Multivariate analysis indicated that INKA2-AS1 expression was an independent prognostic factor for OS of patients with HCC. According to immune analysis, the expression of INKA2-AS1 was favorably correlated with T helper cells, Th2 cells, macrophages, TFH, and NK CD56bright cells and negatively correlated with Th17 cells, pDC, cytotoxic cells, DC, Treg, Tgd, and Tcm. The results of this study collectively suggest that INKA2-AS1 has the potential to be a novel biomarker for predicting the prognosis of HCC patients as well as a significant immune response regulator in HCC.

1. Introduction

Liver cancer ranks sixth in terms of incidence among malignancies and is the fourth leading cause of tumor-related death worldwide [1, 2]. Over 782,000 individuals lose their lives to cancer annually, with over 841,000 new cases being diagnosed [3]. Hepatocellular carcinoma (HCC), the most prevalent kind of primary liver cancer, has been connected to several recognized risk factors, including a history of

chronic HBV or HCV infection, excessive alcohol consumption, nonalcoholic fatty liver disease, and exposure to food toxins like aflatoxins [4, 5]. Even if a number of creative management strategies have demonstrated considerable effects on the diagnosis of HCC, the high rate of metastasis leads to poor overall survival (OS) of patients with HCC [6, 7]. The prognosis of patients is severely impacted by the fact that over 70% of HCC patients who have surgical resection or ablation will experience a tumor recurrence

(a)

(b)

(c)

(d)
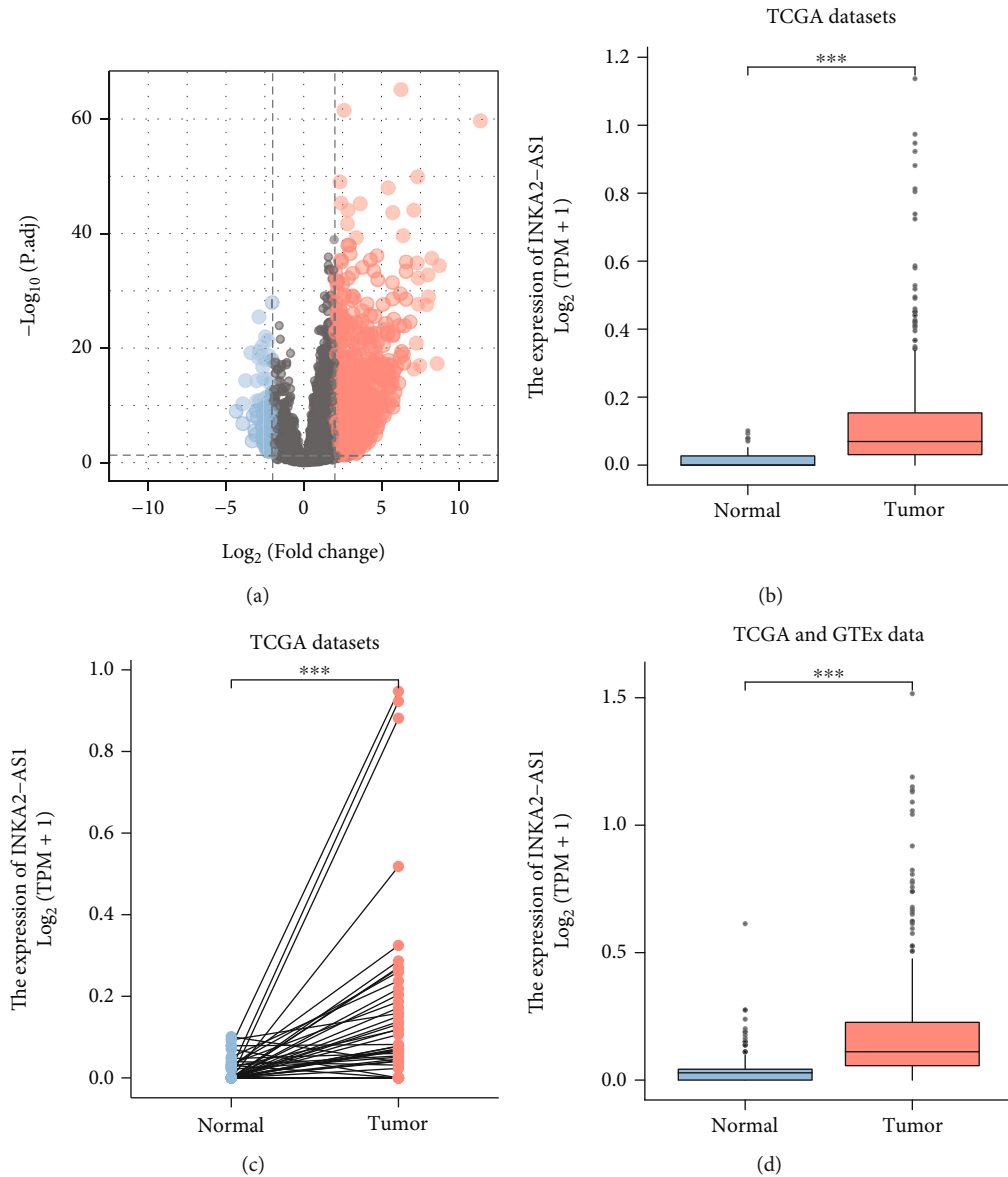
FIGURE 1: In HCC patients, INKA2-AS1 expression was noticeably elevated. (a) A volcano map displayed the DEGs between HCC and nontumor specimens. (b–d) The expression pattern of INKA2-AS1 in HCC specimens and nontumor specimens from the TCGA datasets or the TCGA datasets plus GTEx data.

within five years [8, 9]. Accurately predicting the prognosis may help select an appropriate customized treatment and, as a result, increase the survival time for patients with HCC. The identification of novel biomarkers that can assess the prognosis of HCC cases is, therefore, crucial.

The term "long non-coding RNA" (lncRNA) refers to RNAs that are longer than 200 nucleotides yet cannot code for proteins [10]. In the past, lncRNAs were considered to be "transcriptional noise" since they did not take part in the process of creating proteins [11, 12]. As a result, it was believed that lncRNAs did not have any biological purpose. However, recent research has shown that lncRNAs have a biological function [13, 14]. The role of lncRNAs in several biological processes, including the silencing of X chromosome genes, chromatin modification, and transcription activity, has come under greater scrutiny in recent years [15, 16]. Recent research

has identified a large number of lncRNAs as being improperly expressed in a variety of malignancies, which either inhibits the growth of these tumors or causes them to worsen [17, 18]. According to reports, several lncRNAs are crucial in the development of HCC [19, 20]. For instance, Hu et al. reported that in HCC, there was an increase in the level of expression of the lncRNA GSTM3TV2. The downregulation of lncRNA GSTM3TV2 via the miR-597/FOSL2 axis led to a considerable inhibition of cell proliferation and invasion [21]. When coupled with surrounding normal liver tissue samples and normal liver cell lines, Wang et al. found that the expression of the lncRNA MIR210HG was considerably greater in HCC tissue samples and cells [22]. Because of this, MIR210HG is a great marker for separating HCC tissues from normal tissues. Significant tumor growth, vascular invasion, an advanced clinical stage, and unfavorable histological differentiation have all been
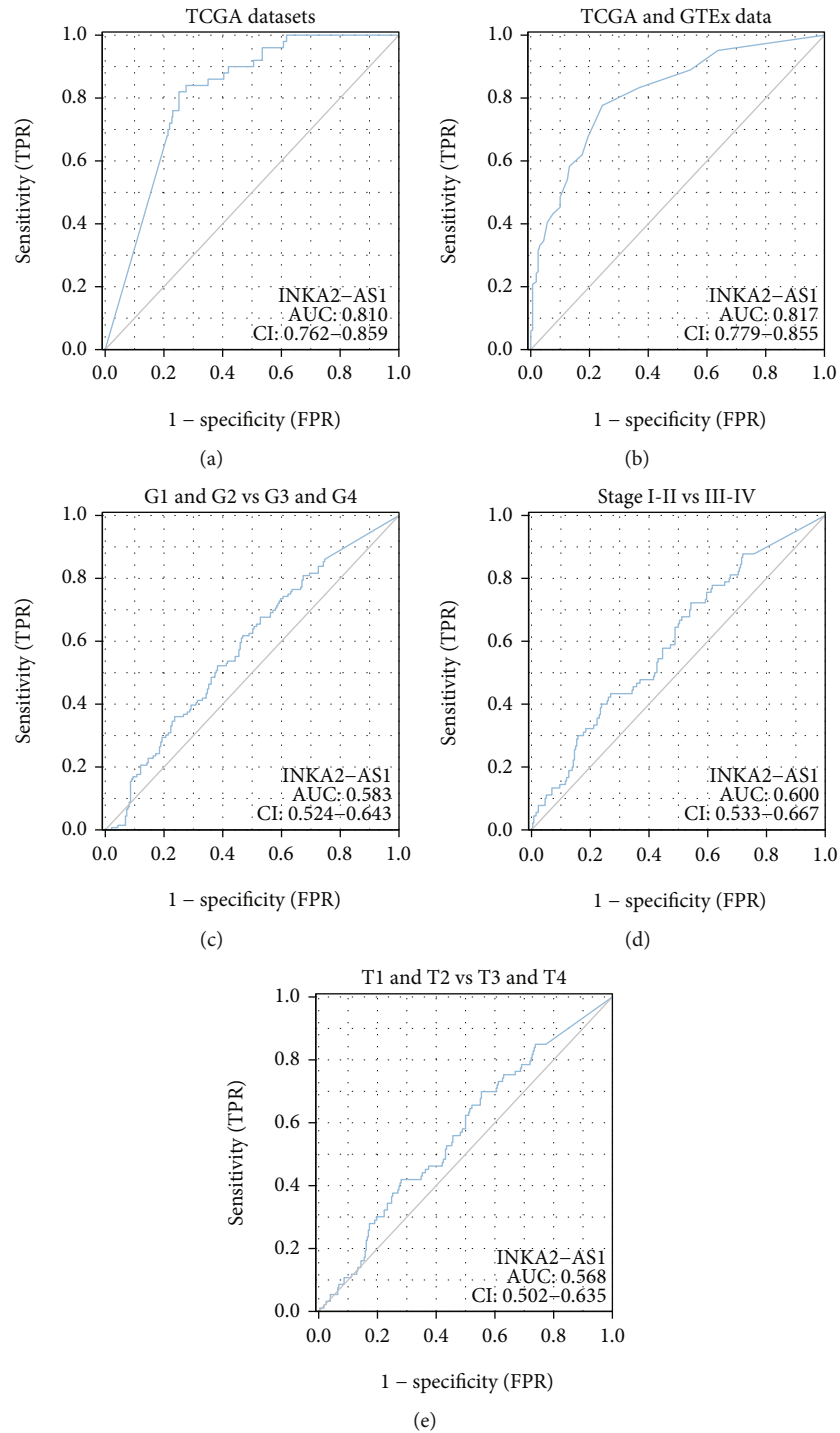
FIGURE 2: ROC analyses for the INKA2-AS1 expression in HCC's diagnostic value. (a, b) HCC specimens vs. normal specimens. (c) G1 and G2 vs. G3 and G4. (d) stage I-II vs. III-IV. (e) T1 and T2 vs. T3 and T4.

demonstrated to be related to high levels of MIR210HG expression. The survival research results showed that patients with high levels of MIR210HG expression had a considerably worse prognosis than patients with low levels of MIR210HG expression, both in their cohort and the TCGA cohort. HCC cells' ability to proliferate, migrate, and invade was decreased when MIR210HG was expressed less. These results indicated that novel diagnostic and prognostic lncRNAs for HCC patients

hold substantial promise. On the other hand, it has not been investigated how many lncRNAs function. In this study, we discovered a new lncRNA called INKA2-AS1 that is associated with HCC and found that it is substantially expressed in HCC. Then, in addition to examining its connection to immune cell infiltration, we analyzed its diagnostic and prognostic relevance in more details. The findings of our study suggested that INKA2-AS1 may be a novel diagnostic and predictive

TCGA datasets

(a)

TCGA and GTEx data

(b)
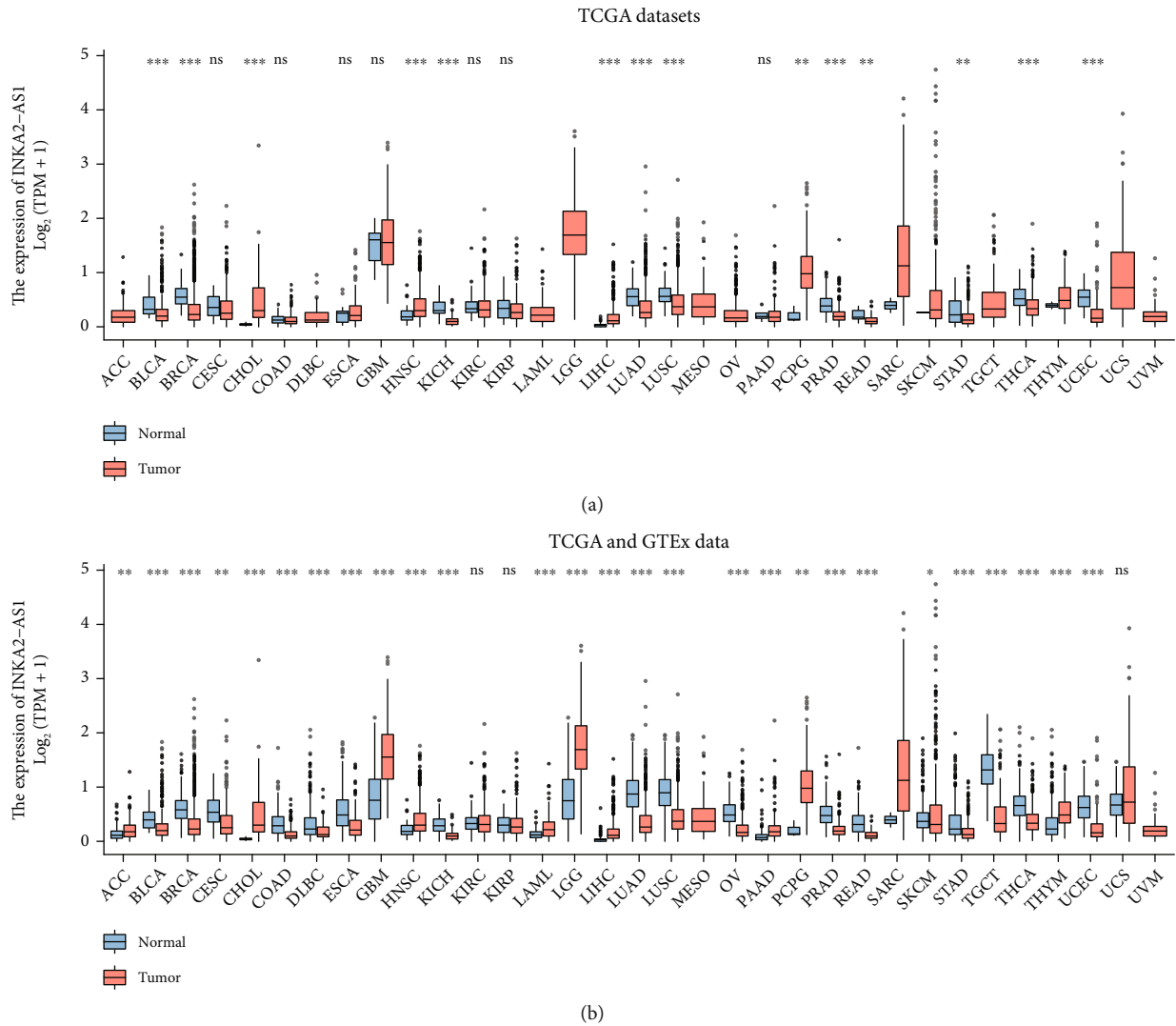
Figure 3: The expressions of INKA2-AS1 in various cancer types by analyzing (a) TCGA and (b) GTEx data and TCGA datasets.

biomarker for HCC patients, as well as a possible immune-related biomarker for HCC patients' treatment.

2. Methods

2.1. Microarray Data and RNA Sequencing Data.

By clicking the URL (https://xenabrowser.net/datapages/), one can access the original mRNA expressions for the TCGA HCC data and GTEx from the UCSC XENA database. Human tumor samples came from the TCGA database, while normal human samples came from both the GTEx and TCGA databases. 374 liver cancer tissues and 160 healthy liver tissues collectively provided the data for the mRNA sequencing. 33 distinct cancers' RNA-seq transcriptome data were found by searching the TCGA database (https://portal.gdc.cancer.gov/). Included were the following 33 cancer types: ACC, BRCA, BLCA, COAD, ESCA, DLBC, HNSC, GBM, KICH, KIRC, KIRP, LGG, LIHC, LUAD, LAML, LUSC, OV, READ, PAAD, THCA, SKCM, UCEC, STAD, TGCT, THYM, PRAD, and UCS. We applied the Limma R package

to screen the differentially expressed genes (DEGs) between HCC specimens and nontumor specimens. The cut-off value was determined to be log2FC greater than 2 and FDR less than 0.05 (FC, fold change; FDR, false discovery rate). It was not necessary for this study to get ethical approval or informed consent because the data on the TCGA databases are accessible to the general public.

2.2. General Enrichment Analysis.

For the differential INKA2-AS1 obtained between single INKA2-AS1 high-/low-expression groups, additional GO enrichment analysis was performed. In addition, a KEGG signaling pathway analysis was carried out in order to determine which signaling pathways were engaged in the regulatory process. "ClusterProfiler" was used to carry out these two enrichment studies [23]. A false discovery rate (FDR) of 0.25 was chosen as the threshold for the statistical difference between the two enrichment analyses. Alternatively, the Metascape screening conditions were applied, and significant differences were

(a)

(b)

(c)

(d)
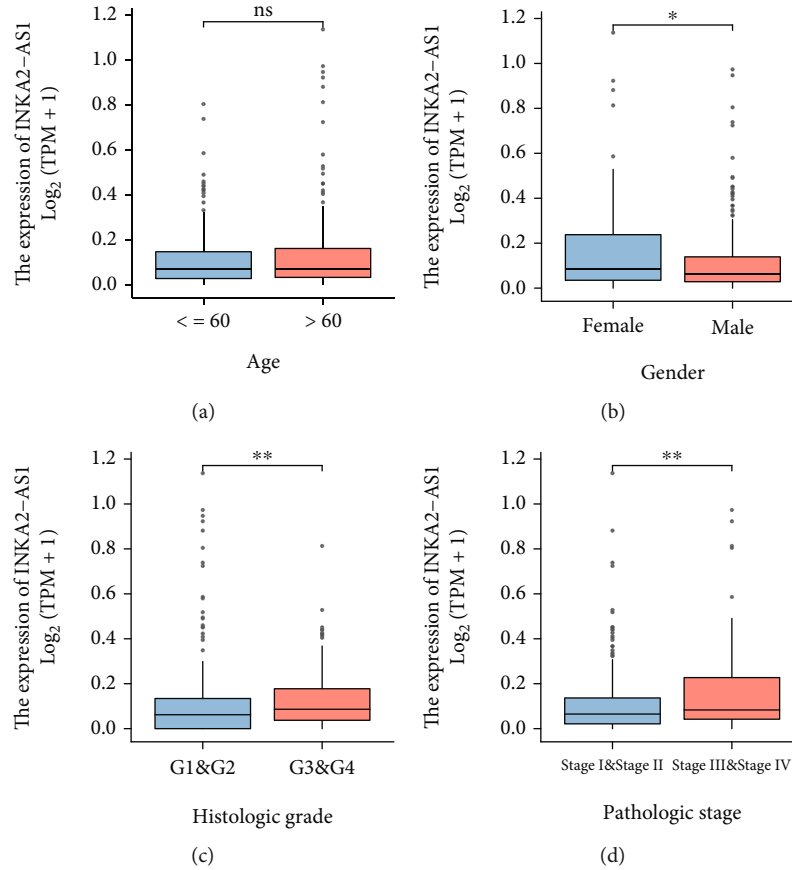
FIGURE 4: Relationship between clinicopathological traits such as (a) age, (b) gender, (c) histological grade, and (d) pathological stage and INKA2-AS1 expression.

defined by a P value of less than 0.05, a minimum count of 3, and an enrichment factor larger than 1.

2.3. Study of Immune Infiltration Using a Single-Sample Gene Set Enrichment Analysis (ssGSEA). Using the ssGSEA method using the R package "sparcl," 24 distinct kinds of immune cells discovered in tumor samples were examined for their immune infiltration of HCC [24]. The gene expression profile of each tumor sample was used to calculate the relative enrichment scores of each immune cell based on the marker genes of 24 distinct kinds of immune cells identified in the research literature. Both the correlation between immune cell infiltration and the groups with high and low levels of INKA2-AS1 expression and the correlation between immune cell infiltration and the groups with high and low levels of INKA2-AS1 expression were examined.

2.4. Statistical Analysis. Statistical analysis was performed using R (v.3.5.1) (R Core Team, 2018). Comparison of the expression of INKA2-AS1 between HCC specimens and nontumor specimens was carried out by the use of Wilcoxon rank sum tests. We separated patients into two groups: those whose gene expression was more than the median value and those whose gene expression was less than the median value. The relationship between clinical pathologic features and INKA2-AS1 was examined using the Kruskal-Wallis test or the Wilcoxon rank sum test in addition to logistic regression. The clinicopathological variables associated with 10-year overall survival (OS), progression-free interval (PFI), and disease-specific survival (DSS) in TCGA patients were identified using the Kaplan-Meier methods and Cox regression analysis. P values were two-sided, and a statistically significant difference was defined as one with a P value less than 0.05.

3. Results

3.1. INKA2-AS1 Expression Status in HCC Patients. In this work, information from 374 HCC and 50 nontumor specimens from TCGA databases was retrospectively examined. 938 DEGs include 859 strongly upregulated and 79 significantly downregulated genes (Figure 1(a)). Among the 938 DEGs, INKA2-AS1 caught our attention. We discovered that INKA2-AS1 expression was noticeably higher in HCC tissues compared to nontumor specimens, as illustrated in Figures 1(b)–1(d).

3.2. The Diagnostic Value of INKA2-AS1 Expression for HCC. The diagnostic utility of INKA2-AS1 for patients with HCC was then investigated. Using the TCGA datasets, the ROC assays determined that HCC had high INKA2-AS1 expression, with an AUC value of 0.810 (95% CI: 0.762 to

TABLE 1: Correlation of INKA2-AS1 expression with clinicopathological features of HCC.

Characteristic	Low expression of INKA2-AS1	High expression of INKA2-AS1	P
n	187	187	
Age (n, %)			0.874
≤60	90 (24.1%)	87 (23.3%)	
>60	97 (26%)	99 (26.5%)	
Gender (n, %)			0.015
Female	49 (13.1%)	72 (19.3%)	
Male	138 (36.9%)	115 (30.7%)	
Histologic grade (n, %)			0.036
G1	36 (9.8%)	19 (5.1%)	
G2	91 (24.7%)	87 (23.6%)	
G3	52 (14.1%)	72 (19.5%)	
G4	6 (1.6%)	6 (1.6%)	
Vascular invasion (n, %)			0.217
No	113 (35.5%)	95 (29.9%)	
Yes	51 (16%)	59 (18.6%)	
Residual tumor (n, %)			0.220
R0	168 (48.7%)	159 (46.1%)	
R1	6 (1.7%)	11 (3.2%)	
R2	1 (0.3%)	0 (0%)	
Pathologic stage (n, %)			0.023
Stage I	100 (28.6%)	73 (20.9%)	
Stage II	37 (10.6%)	50 (14.3%)	
Stage III	35 (10%)	50 (14.3%)	
Stage IV	2 (0.6%)	3 (0.9%)	
T stage (n, %)			0.030
T1	105 (28.3%)	78 (21%)	
T2	39 (10.5%)	56 (15.1%)	
T3	35 (9.4%)	45 (12.1%)	
T4	5 (1.3%)	8 (2.2%)	
M stage (n, %)			1.000
M0	133 (48.9%)	135 (49.6%)	
M1	2 (0.7%)	2 (0.7%)	
N stage (n, %)			0.122
N0	129 (50%)	125 (48.4%)	
N1	0 (0%)	4 (1.6%)	
Age (median, IQR)	61 (52, 69)	62 (51, 68)	0.492

0.859) (Figure 2(a)). The AUC value for high INKA2-AS1 expression in HCC was 0.817 (95% CI: 0.779 to 0.855) in the TCGA datasets and GTEx database (Figure 2(b)). Then, we performed subgroup assays, and the result is not ideal for histologic grade, pathologic stage, and T stage (Figures 2(c)–2(e)).

3.3. INKA2-AS1 Expression Analysis in Pan-Cancer. Then, we examined the expression of INKA2-AS1 in the TCGA and GTEx databases. The findings indicated that high INKA2-AS1 expression was found in 14 tumors, including ACC, CHOL, GBM, HNSC, LAML, LGG, PAAD, PCPG, SARC, and THYM (Figures 3(a) and 3(b)). In contrast, low

INKA2-AS1 expression was found in eleven tumors, including BLCA, COAD, BRCA, DLBC, CESC, KICH, ESCA, LUAD, LUSC, OV, and PRAD (Figures 3(a) and 3(b)). Our research indicated that INKA2-AS1 was crucial for the development of tumors.

3.4. Upregulation of INKA2-AS1 Associates with Advanced Clinicopathological Features of HCC. We separated the 374 HCC patients into two groups based on the median INKA2-AS1 expression level, a high-expression group (n = 187) and a low-expression group (n = 187), to study further the clinicopathological importance of INKA2-AS1 levels in HCC patients. We observed that INKA2-AS1
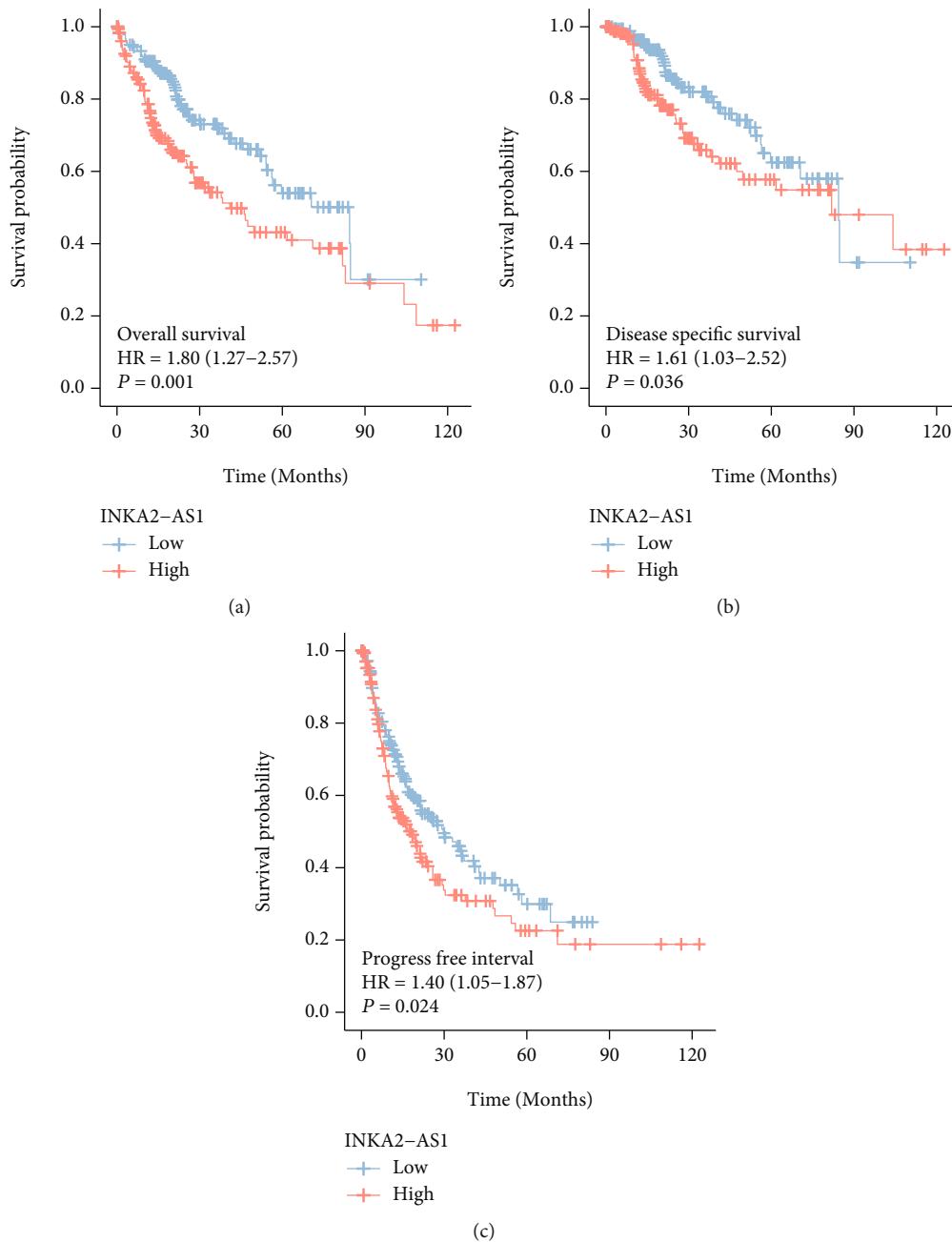
FIGURE 5: Kaplan-Meier survival curves contrasting HCC with high and low INKA2-AS1 expression. Survival curves of HCC patients with high and low INKA2-AS1 levels for (a) OS, (b) DSS, and (c) PFI.

expression was not related to age (Figure 4(a)) but was associated with gender, histologic grade, and pathologic stage (Figures 4(b)–4(d)). Additionally, the outcomes of the chi-square test supported the conclusions mentioned above (Table 1).

3.5. The Prognostic Value of INKA2-AS1 Expression in HCC Patients. We also performed a Kaplan-Meier analysis and a log-rank test to investigate the predictive significance of INKA2-AS1 expression in HCC. The findings revealed that HCC patients with high INKA2-AS1 expression had shorter OS (Figure 5(a), $P = 0.001$), DSS (Figure 5(b), $P = 0.036$),

and PFI (Figure 5(c), $P = 0.024$) than those with low INKA2-AS1 expression. Then, we performed a Cox proportional hazard regression analysis. In patients with HCC, INKA2-AS1 expression was shown to be a standalone predictive factor for OS (Table 2, $P = 0.005$), according to multivariate analysis. However, neither the DSS (Table 3, $P = 0.093$) nor the PFI (Table 4, $P = 0.075$) of HCC patients showed evidence of INKA2-AS1 expression as an independent prognostic factor.

3.6. Functional Enrichment Analysis and DEG Profiles. Based on the median value of INKA2-AS1 expression, we split the

TABLE 2: Univariate and multivariate Cox regression analyses for overall survival.

Characteristics	Total (N)	Univariate analysis Hazard ratio (95% CI)	P value	Multivariate analysis Hazard ratio (95% CI)	P value
Gender	373				
Female	121	Reference			
Male	252	0.793 (0.557-1.130)	0.200		
Age	373				
≤60	177	Reference			
>60	196	1.205 (0.850-1.708)	0.295		
Histologic grade	368				
G1 and G2	233	Reference			
G3 and G4	135	1.091 (0.761-1.564)	0.636		
Pathologic stage	349				
Stage I and stage II	259	Reference			
Stage III and stage IV	90	2.504 (1.727-3.631)	<0.001	2.352 (1.618-3.419)	<0.001
INKA2-AS1	373				
Low	187	Reference			
High	186	1.804 (1.268-2.568)	0.001	1.722 (1.180-2.514)	0.005

TABLE 3: Univariate and multivariate Cox regression analyses for disease-specific survival.

Characteristics	Total (N)	Univariate analysis Hazard ratio (95% CI)	P value	Multivariate analysis Hazard ratio (95% CI)	P value
Gender	365				
Female	118	Reference			
Male	247	0.813 (0.516-1.281)	0.373		
Age	365				
≤60	174	Reference			
>60	191	0.846 (0.543-1.317)	0.458		
Histologic grade	360				
G1 and G2	227	Reference			
G3 and G4	133	1.086 (0.683-1.728)	0.726		
Pathologic stage	341				
Stage I and stage II	254	Reference			
Stage III and stage IV	87	3.803 (2.342-6.176)	<0.001	3.637 (2.233-5.924)	<0.001
INKA2-AS1	365				
Low	186	Reference			
High	179	1.612 (1.032-2.520)	0.036	1.529 (0.932-2.507)	0.093

HCC patient population from the TCGA database into low- and high-expression groups to better understand the biological processes connected to the DEGs. There were 430 DEGs found in all. According to the findings of the GO tests, 430 DEGs were mostly linked to the growth of the epidermis, the skin, digestion, synapses, transmembrane transporters, channels, and hormone function (Figure 6(a)). According to KEGG assays, the primary enrichment areas for 430 DEGs were nicotine addiction and neuroactive ligand-receptor interaction (Figure 6(b)).

3.7. Immune Cell Invasion and INKA2-AS1 Expression Were Related. To ascertain the extent of immune cell infiltration,

the transcriptomes of the TCGA HCC cohort were examined using the ssGSEA approach. The number of immune cells present in a tumor's microenvironment was quantified in the research using 24 immune-related genes. We found that the expression of INKA2-AS1 was favorably correlated with T helper cells, Th2 cells, macrophages, TFH, and NK CD56bright cells and negatively associated with Th17 cells, pDC, cytotoxic cells, DC, Treg, Tgd, and Tcm (Figure 7).

4. Discussion

HCC continues to be one of the most aggressive forms of solid malignancy found anywhere in the world [25]. The

TABLE 4: Univariate and multivariate Cox regression analyses for progression-free interval.

Characteristics	Total (N)	Univariate analysis Hazard ratio (95% CI)	P value	Multivariate analysis Hazard ratio (95% CI)	P value
Gender	373				
Female	121	Reference			
Male	252	0.982 (0.721-1.338)	0.909		
Age	373				
≤60	177	Reference			
>60	196	0.960 (0.718-1.284)	0.783		
Histologic grade	368				
G1 and G2	233	Reference			
G3 and G4	135	1.152 (0.853-1.557)	0.355		
Pathologic stage	349				
Stage I and stage II	259	Reference			
Stage III and stage IV	90	2.201 (1.591-3.046)	<0.001	2.123 (1.531-2.944)	<0.001
INKA2-AS1	373				
Low	187	Reference			
High	186	1.398 (1.045-1.870)	0.024	1.321 (0.972-1.795)	0.075

discovery of prognostic factors in HCC is critical for determining the most effective therapy options and predicting patients' survival rates [26]. To this point, a wide variety of biological markers have been reported. Growing studies have suggested that the abnormal expressions of antioncogene or tumor promotors played a vital role in the tumor growth and invasion of HCC [27, 28]. lncRNAs are the subject of increasing investigation as a possible new class of biomarker. In addition, several studies have discussed the potential of lncRNAs as predictive or diagnostic biomarkers for cancer [29, 30].

Several researches published in recent years have shown that lncRNAs have a role in the development of HCC and may serve as new biomarkers for HCC patients. For instance, Zhou et al. found that the expression of the lncRNA ID2-AS1 reduced in metastatic HCC cell lines and in HCC tissues. This lowered expression was associated with a poorer overall survival rate in HCC patients. lncRNA ID2-AS1 significantly reduced the motility, invasion, and metastasis of HCC cells in vitro and in vivo in HCC patients via activating the HDAC8/ID2 pathway [31]. Li et al. demonstrated that HCC tissues and HCC cells expressed the lncRNA DCST1-AS1 at a high levels. High expression of the lncRNA DCST1-AS1 was significantly correlated with a bad outcome. In addition, the absence of the lncRNA DCST1-AS1 led to a reduction in cell proliferation and an acceleration of apoptosis in HCC cells, as well as an activation of cycle arrest, a reduction in cell migration, and an increase in autophagy. These effects were mediated by the AKT and mTOR signaling pathways [32]. We discovered the HCC-related lncRNA INKA2-AS1 in this investigation. The expression of INKA2-AS1 was noticeably elevated in HCC patients, as we initially observed. In TCGA datasets, the diagnostic utility of INKA2-AS1 was also established. Furthermore, we discovered that poor prognosis and advanced stage were linked to increased expression of INKA2-AS1. It is significant to note that multivariate analysis revealed that INKA2-AS1 expression was a standalone predictive factor for OS in HCC patients. Our research indicated that INKA2-AS1 could be a new diagnostic and predictive biomarker for people with HCC.

Immunotherapy, which works by boosting patients' natural defenses against disease, has been successful in treating a variety of malignancies and converting them into illnesses that can be healed [33, 34]. Immune-based treatment methods have been shown to offer survival improvements for patients with HCC in a significant amount of preclinical and clinical researches [35, 36]. Additionally, it is envisaged that shortly a combination of immunotherapy and other therapeutic modalities may be a workable alternative for treating HCC. Additionally, recent studies have shown that tumor-infiltrating lymphocytes, including regulatory T cells and tumor-associated macrophages, play a critical part in the immune evasion that occurs during the progression of HCC [37, 38]. Because of the depletion of follicular helper T cells caused by intratumoral PDL1, poor B cell function was produced, which aided in the advancement of advanced HCC. In this work, we found that the expression of INKA2-AS1 was favorably correlated with T helper cells, Th2 cells, macrophages, TFH, and NK CD56bright cells and negatively associated with Th17 cells, pDC, cytotoxic cells, DC, Treg, Tgd, and Tcm. Our research revealed that INKA2-AS1 might be crucial for immune infiltrate cells to be recruited and regulated in HCC.

However, there are several limitations in our study. First, given the small sample size, thorough clinical testing will be required. Second, even though the bioinformatics study gave us some relevant insights of INKA2-AS1 in HCC, to validate our results and increase their therapeutic significance, we still need to perform biological research, either in vitro or

(a)

(b)
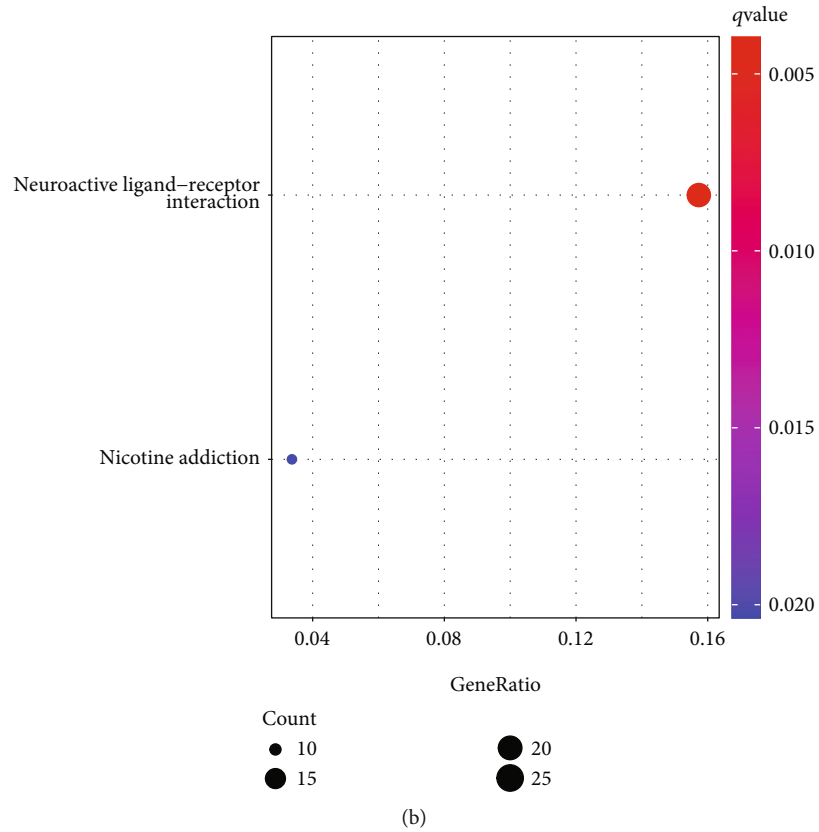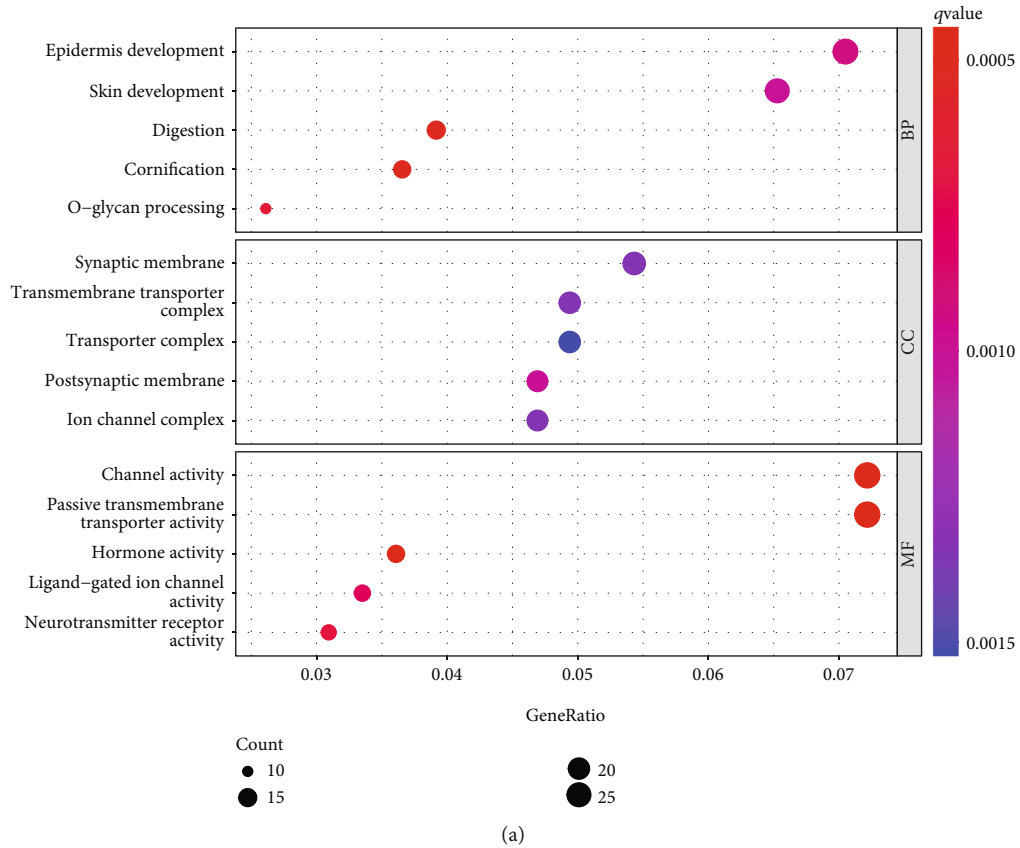
FIGURE 6: Functional enrichment analysis of DEGs comparing groups with high and low INKA2-AS1 expression levels. (a) DEGs with significantly enhanced GO terms. (b) Important KEGG pathway.
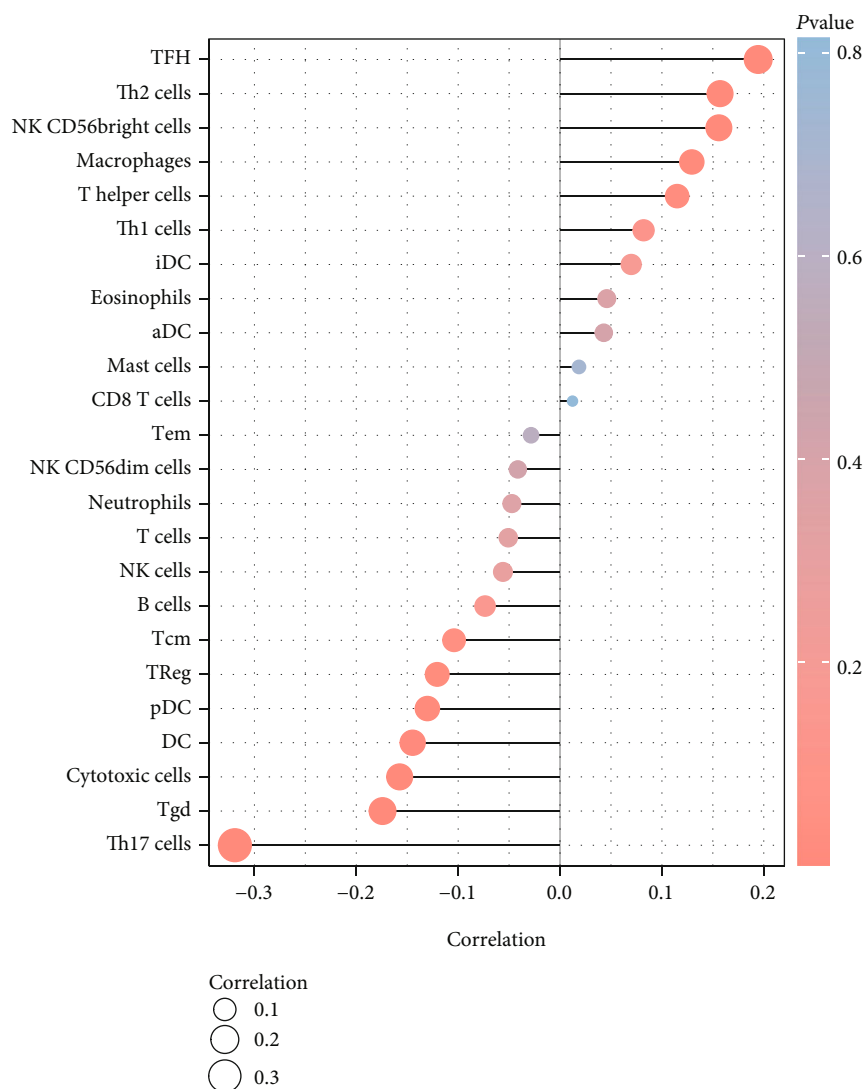
Figure 7: Immune cell infiltration was linked to INKA2-AS1 expression.

in vivo. To further understand the function of INKA2-AS1 on both the molecular and cellular levels, additional research into its mechanistic studies is required.

5. Conclusion

We firstly provided evidence that demonstrated a considerably elevated expression level of INKA2-AS1 in HCC patients. As a predictive biomarker for HCC, INKA2-AS1 may function as a tumor promoter and predict prognosis as well as immune infiltration.

Data Availability

The analyzed datasets generated during the study are available from the corresponding author on reasonable request.

Conflicts of Interest

The authors declare that they have no conflicts of interests.

Acknowledgments

References

[1] K. D. Miller, M. Fidler-Benaoudia, T. H. Keegan, H. S. Hipp, A. Jemal, and R. L. Siegel, "Cancer statistics for adolescents and young adults," *CA: a Cancer Journal for Clinicians*, vol. 70, no. 6, pp. 443–459, 2020.

[2] A. Vogel, T. Meyer, G. Sapisochin, R. Salem, and A. Saborowski, "Hepatocellular carcinoma," *Lancet*, vol. 400, no. 10360, pp. 1345–1362, 2022.

[3] C. E. DeSantis, C. C. Lin, A. B. Mariotto et al., "Cancer treatment and survivorship statistics," *CA: a Cancer Journal for Clinicians*, vol. 64, no. 4, pp. 252–271, 2014.

[4] A. Forner, M. Reig, and J. Bruix, "Hepatocellular carcinoma," *Lancet*, vol. 391, no. 10127, pp. 1301–1314, 2018.

[5] J. Hartke, M. Johnson, and M. Ghabril, "The diagnosis and treatment of hepatocellular carcinoma," *Seminars in Diagnostic Pathology*, vol. 34, no. 2, pp. 153–159, 2017.

[6] H. W. Sim and J. Knox, "Hepatocellular carcinoma in the era of immunotherapy," *Current Problems in Cancer*, vol. 42, no. 1, pp. 40–48, 2018.

[7] E. Cho, H. A. Cho, C. H. Jun, H. J. Kim, S. B. Cho, and S. K. Choi, "A review of hepatocellular carcinoma in elderly patients focused on management and outcomes," *In Vivo*, vol. 33, no. 5, pp. 1411–1420, 2019.

[8] J. Rubin, N. Ayoub, F. Kaldas, and S. Saab, "Management of recurrent hepatocellular carcinoma in liver transplant recipients: a systematic review," *Experimental and Clinical Transplantation*, vol. 10, no. 6, pp. 531–543, 2012.

[9] T. Kumagi, Y. Hiasa, and G. M. Hirschfield, "Hepatocellular carcinoma for the non-specialist," *BMJ*, vol. 339, no. dec04 2, article b5039, 2009.

[10] T. Nojima and N. J. Proudfoot, "Mechanisms of lncRNA biogenesis as revealed by nascent transcriptomics," *Nature Reviews. Molecular Cell Biology*, vol. 23, no. 6, pp. 389–406, 2022.

[11] P. J. Batista and H. Y. Chang, "Long noncoding RNAs: cellular address codes in development and disease," *Cell*, vol. 152, no. 6, pp. 1298–1307, 2013.

[12] J. B. Pierce, H. Zhou, V. Simion, and M. W. Feinberg, "Long noncoding RNAs as therapeutic targets," *Advances in Experimental Medicine and Biology*, vol. 1363, pp. 161–175, 2022.

[13] P. Grote and R. A. Boon, "LncRNAs coming of age," *Circulation Research*, vol. 123, no. 5, pp. 535–537, 2018.

[14] A. B. Herman, D. Tsitsipatis, and M. Gorospe, "Integrated lncRNA function upon genomic and epigenomic regulation," *Molecular Cell*, vol. 82, no. 12, pp. 2252–2266, 2022.

[15] Z. Xu, Y. Chen, L. Ma et al., "Role of exosomal non-coding RNAs from tumor cells and tumor-associated macrophages in the tumor microenvironment," *Molecular Therapy*, vol. 30, no. 10, pp. 3133–3154, 2022.

[16] Y. B. Zuo, Y. F. Zhang, R. Zhang et al., "Ferroptosis in cancer progression: role of noncoding RNAs," *International Journal of Biological Sciences*, vol. 18, no. 5, pp. 1829–1843, 2022.

[17] E. G. Park, S. J. Pyo, Y. Cui, S. H. Yoon, and J. W. Nam, "Tumor immune microenvironment lncRNAs," *Briefings in Bioinformatics*, vol. 23, no. 1, 2022.

[18] G. St Laurent, C. Wahlestedt, and P. Kapranov, "The landscape of long noncoding RNA classification," *Trends in Genetics*, vol. 31, no. 5, pp. 239–251, 2015.

[19] C. M. Wong, F. H. Tsang, and I. O. Ng, "Non-coding RNAs in hepatocellular carcinoma: molecular functions and pathological implications," *Nature Reviews Gastroenterology & Hepatology*, vol. 15, no. 3, pp. 137–151, 2018.

[20] Z. Huang, J. K. Zhou, Y. Peng, W. He, and C. Huang, "The role of long noncoding RNAs in hepatocellular carcinoma," *Molecular Cancer*, vol. 19, no. 1, p. 77, 2020.

[21] Y. Hu, W. Qiu, Z. Kong et al., "LncRNA GSTM3TV2 promotes cell proliferation and invasion via miR-597/FOSL2 Axis in hepatocellular carcinoma," *BioMed Research International*, vol. 2021, Article ID 3445970, 10 pages, 2021.

[22] Y. Wang, W. Li, X. Chen, Y. Li, P. Wen, and F. Xu, "MIR210HG predicts poor prognosis and functions as an oncogenic lncRNA in hepatocellular carcinoma," *Biomedicine & Pharmacotherapy*, vol. 111, pp. 1297–1301, 2019.

[23] G. Yu, L. G. Wang, Y. Han, and Q. Y. He, "clusterProfiler: an R package for comparing biological themes among gene clusters," *OMICS*, vol. 16, no. 5, pp. 284–287, 2012.

[24] S. Hänzelmann, R. Castelo, and J. Guinney, "GSVA: gene set variation analysis for microarray and RNA-seq data," *BMC Bioinformatics*, vol. 14, no. 1, p. 7, 2013.

[25] T. Flecken, H. C. Spangenberg, and R. Thimme, "Immunobiology of hepatocellular carcinoma," *Langenbeck's Archives of Surgery*, vol. 397, no. 5, pp. 673–680, 2012.

[26] Z. Y. Tang, "Hepatocellular carcinoma surgery-review of the past and prospects for the 21st century," *Journal of Surgical Oncology*, vol. 91, no. 2, pp. 95-96, 2005.

[27] J. D. Yang, P. Hainaut, G. J. Gores, A. Amadou, A. Plymoth, and L. R. Roberts, "A global view of hepatocellular carcinoma: trends, risk, prevention and management," *Nature Reviews. Gastroenterology & Hepatology*, vol. 16, no. 10, pp. 589–604, 2019.

[28] Q. M. Anstee, H. L. Reeves, E. Kotsiliti, O. Govaere, and M. Heikenwalder, "From NASH to HCC: current concepts and future challenges," *Nature Reviews. Gastroenterology & Hepatology*, vol. 16, no. 7, pp. 411–428, 2019.

[29] C. Xing, S. G. Sun, Z. Q. Yue, and F. Bai, "Role of lncRNA LUCAT1 in cancer," *Biomedicine & Pharmacotherapy*, vol. 134, article 111158, 2021.

[30] J. J. Chan and Y. Tay, "Noncoding RNA:RNA regulatory networks in cancer," *International Journal of Molecular Sciences*, vol. 19, no. 5, p. 1310, 2018.

[31] Y. Zhou, L. Huan, Y. Wu et al., "LncRNA ID2-AS1 suppresses tumor metastasis by activating the HDAC8/ID2 pathway in hepatocellular carcinoma," *Cancer Letters*, vol. 469, pp. 399–409, 2020.

[32] J. Chen, D. Wu, Y. Zhang, Y. Yang, Y. Duan, and Y. An, "LncRNA DCST1-AS1 functions as a competing endogenous RNA to regulate FAIM2 expression by sponging miR-1254 in hepatocellular carcinoma," *Clinical Science (London, England)*, vol. 133, no. 2, pp. 367–379, 2019.

[33] L. B. Kennedy and A. K. S. Salama, "A review of cancer immunotherapy toxicity," *CA: a Cancer Journal for Clinicians*, vol. 70, no. 2, pp. 86–104, 2020.

[34] J. M. Llovet, F. Castet, M. Heikenwalder et al., "Immunotherapies for hepatocellular carcinoma," *Nature Reviews. Clinical Oncology*, vol. 19, no. 3, pp. 151–172, 2022.

[35] B. Sangro, P. Sarobe, S. Hervás-Stubbs, and I. Melero, "Advances in immunotherapy for hepatocellular carcinoma," *Nature Reviews. Gastroenterology & Hepatology*, vol. 18, no. 8, pp. 525–543, 2021.

[36] J. M. Llovet, T. De Baere, L. Kulik et al., "Locoregional therapies in the era of molecular and immune treatments for hepatocellular carcinoma," *Nature Reviews. Gastroenterology & Hepatology*, vol. 18, no. 5, pp. 293–313, 2021.

[37] B. Ruf, B. Heinrich, and T. F. Greten, "Immunobiology and immunotherapy of HCC: spotlight on innate and innate-like immune cells," *Cellular & Molecular Immunology*, vol. 18, no. 1, pp. 112–127, 2021.

[38] Y. Fu, S. Liu, S. Zeng, and H. Shen, "From bench to bed: the tumor immune microenvironment and current immunotherapeutic strategies for hepatocellular carcinoma," *Journal of Experimental & Clinical Cancer Research*, vol. 38, no. 1, p. 396, 2019.

Research Article

Identification of a New m6A Regulator-Related Methylation Signature for Predicting the Prognosis and Immune Microenvironment of Patients with Pancreatic Cancer

Tianle Zou,[1,2] **Dan Shi,**[1] **Weiwei Wang,**[3] **Guoyong Chen,**[3] **Xianbin Zhang,**[1] **Yu Tian** [ID][1,4] **and Peng Gong** [ID][1]

[1]*Department of General Surgery and Integrated Chinese and Western Medicine, Institute of Precision Diagnosis and Treatment of Gastrointestinal Tumors, Carson International Cancer Center, Shenzhen University General Hospital, Shenzhen University, Shenzhen, Guangdong 518060, China*
[2]*College of Nursing, Shenzhen University Medical School, Shenzhen University, Shenzhen, Guangdong 518060, China*
[3]*Hepatobiliary Surgery, People's Hospital of Zhengzhou University and Henan Provincial People's Hospital, Zhengzhou, Henan, China*
[4]*School of Public Health, Benedictine University, Lisle, USA*

Correspondence should be addressed to Yu Tian; tianyu4710199@163.com and Peng Gong; doctorgongpeng@szu.edu.cn

Pancreatic cancer (PC) is a malignant tumor of the digestive system that has a bad prognosis. N6-methyladenosine (m6A) is involved in a wide variety of biological activities due to the fact that it is the most common form of mRNA modification in mammals. Numerous research has accumulated evidence suggesting that a malfunction in the regulation of m6A RNA modification is associated with various illnesses, including cancers. However, its implications in PC remain poorly characterized. The methylation data, level 3 RNA sequencing data, and clinical information of PC patients were all retrieved from the TCGA datasets. Genes associated with m6A RNA methylation were compiled from the existing body of research and made available for download from the m6Avar database. The LASSO Cox regression method was used to construct a 4-gene methylation signature, which was then used to classify all PC patients included in the TCGA dataset into either a low- or high-risk group. In this study, based on the set criteria of $|cor| > 0.4$ and p value < 0.05. A total of 3507 gene methylation were identified to be regulated by m6A regulators. Based on the univariate Cox regression analysis and identified 3507 gene methylation, 858 gene methylation was significantly associated with the patient's prognosis. The multivariate Cox regression analysis identified four gene methylation (PCSK6, HSP90AA1, TPM3, and TTLL6) to construct a prognosis model. Survival assays indicated that the patients in the high-risk group tend to have a worse prognosis. ROC curves showed that our prognosis signature had a good prediction ability on patient survival. Immune assays suggested a different immune infiltration pattern in patients with high- and low-risk scores. Moreover, we found that two immune-related genes, CTLA4 and TIGIT, were downregulated in high-risk patients. We generated a unique methylation signature that is related to m6A regulators and is capable of accurately predicting the prognosis for patients with PC. The findings might prove useful for therapeutic customization and the process of making medical decisions.

1. Introduction

Pancreatic cancer (PC) is among the deadliest malignancies, with a mortality rate that ranks among the top four worldwide [1]. At the moment, less than 10% of patients with PC are diagnosed in the early stage of the disease [2, 3]. Due to the fact that most patients are detected at a later stage, they are unable to undergo surgical therapy because this treatment option is not available [4, 5]. The high death rate is mostly attributable to a number of factors, including,

but not limited to, the medical history of the family, genetics, the intake of cigarettes, and chronic pancreatitis [6]. PC has continued to have a poor clinical prognosis due to its late presentation with vague symptoms and its early metastatic tendency, despite the breakthroughs in cancer treatments that have occurred during the past few decades [7, 8]. When compared to all other types of solid tumors, the probability of surviving PC for five years is the lowest, at 8% [9, 10]. Therefore, in order to better the prognosis for patients with PC, there is an urgent need to discover new biomarkers for early diagnosis and prospective therapeutic strategies to combat the progression of cancer.

Previous research has demonstrated that mutated genes are the primary cause of cancerous growths. Epigenetic modifications like DNA methylation, histone acetylation, and RNA modification have all been proven to play a role in the development and progression of tumors [11, 12]. These epigenetic modifications have been recognized as new treatment and prognostic targets as a result of the expansion of research into the subject. To this day, researchers have discovered an increasing number of posttranscriptional changes of RNA. It was not until the 1970s that researchers discovered N6-methyladenosine, also known as m6A, which is now thought to be the most common and prolific posttranscriptional modification found in eukaryotic mRNA [13, 14]. Although just 0.1-0.4% of all adenosine in mammals is methylated as a result of m6A RNA, this type of RNA is responsible for around 50% of all methylation ribonucleotides. The alteration of m6A is involved in virtually every stage of the RNA metabolic process, from splicing to decay [15, 16]. There is a growing body of research that acknowledges the significant role that m6A alteration plays in the progression of a variety of disorders, including hypertension, cardiovascular diseases, and acute myeloid leukemia, among others [17, 18]. Emerging research suggests that m6A regulators may be able to mediate gene expression levels in a variety of biological processes, such as the formation, progression, invasion, and metastasis of cancer, and may also be able to function as prognostic indicators [19–22]. In addition, a study demonstrated that there are four distinct types of RNA modification writers, each of which may play an important part in the tumor microenvironment (TME), targeted therapy, and immunotherapy in PC [23, 24]. However, it is not yet known how important the m6A-related genes are in PC from a functional standpoint.

Gene expression profiles have been utilized as a means of locating prognostic genes as novel biomarkers for many types of cancer since the emergence of genome sequencing and screening tools [25, 26]. Several research over the past several years have established a variety of predictive models based on m6A-related genes, m6A-related lncRNAs, and m6A-related eRNAs [27, 28]. RNA methylation is an important epigenetic modification that is involved in the regulation of gene expression in a variety of biological processes [29, 30]. This regulation takes place without any alterations to the fundamental nucleotide sequence. In carcinogenesis, aberrant RNA methylation takes place, and numerous methylation biomarkers have been exploited to predict the prognosis of patients with PC [31, 32]. RNA methylation profiles can be used to provide an accurate prediction as well as

suggest potential treatments for cancers. Therefore, research into the predictive significance of m6A-related epigenetic characteristics such as DNA methylation in PC is required.

2. Methods

2.1. Data Preparation. The level 3 RNA sequencing data, methylation data, and clinical information of pancreatic cancer patients were downloaded from TCGA datasets (TCGA-PAAD, https://portal.gdc.cancer.gov/). m6A RNA methylation-related genes were collected from the known literature and were downloaded from the m6Avar database (http://m6avar.renlab.org/). The m6Avar database was a collection of information pertaining to functional variants that were involved in the m6A alteration process. For the purpose of measuring the DNA methylation data, an Illumina Human Methylation 450 Beadchip (450 K array), was utilized. Across the entirety of the genome, a total of 482,421 CpG sites are going to be analyzed. The association of mean methylation and expression of specific genes in pancreatic cancer was compared via MEXPRESS (https://mexpress.be/).

2.2. Identification of m6A Regulator-Related Methylation. To identify methylation regulated by m6A regulators, Pearson's test was performed to examine the correlation between gene methylation value and m6A regulator expression. Pearson's $R > 0.3$ was considered to be statistically significant.

2.3. Differentially Expressed Gene (DEG) Analysis. DEG analysis was performed based on the limma package in R software with the set standards.

2.4. Gene Set Enrichment Analysis (GSEA). We tested for the overrepresentation of differentially methylated genes or genes linked with differential methylation risk scores by using gene sets from the Molecular Signatures Database version 6.2 (MSigDB). The reference gene sets were Hallmark, Gene Ontology (GO), and Kyoto Encyclopedia of Genes and Genomes (KEGG). GSEA was carried out with the help of the fgsea package (version 1.4.1), and 10,000 permutations were used in order to locate enriched pathways that were shared by the high-risk group and the low-risk group. |NES| values greater than one and a false discovery rate of less than 0.05 percent were regarded as statistically significant.

2.5. Prognosis Model Construction. Firstly, for the input gene methylation data, univariate assays were utilized to identify the gene methylation tightly correlated with patient survival. Then, LASSO Cox regression of overall survival (OS) was carried out to identify survival-related gene methylation. Multivariate assays were used for prognosis model construction (Risk score = Methylation level of gene $A \times$ coef A + Methylation level of gene $B \times$ coef $B + \cdots +$ Methylation level of gene $N \times$ coef N), and the risk score of each sample in all the datasets was calculated based on the signature. For survival analysis, the samples were divided into a high-risk group and a low-risk group based on the median cutoff value of the risk score. Kaplan-Meier (KM) and receiver operating characteristic (ROC) curves were used to explore the prognostic significance of the prognosis signature.

(a)

(b)

(c)

(d)

Figure 1: Continued.

(e)
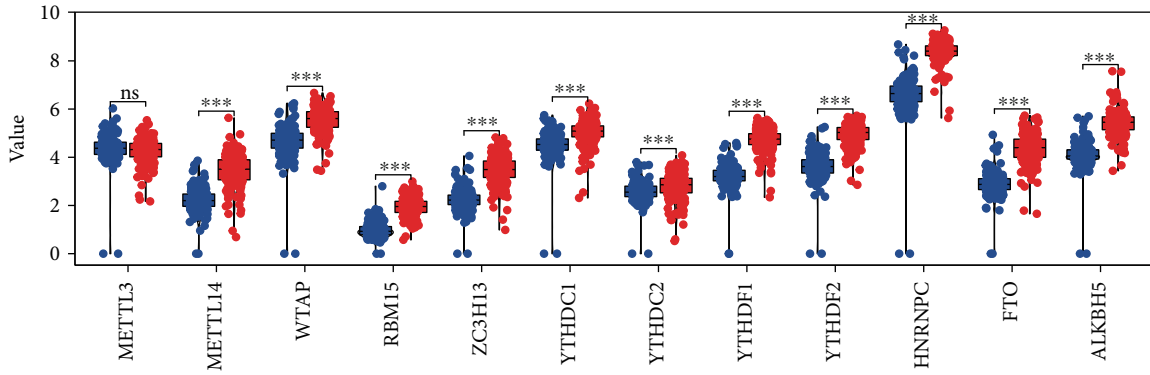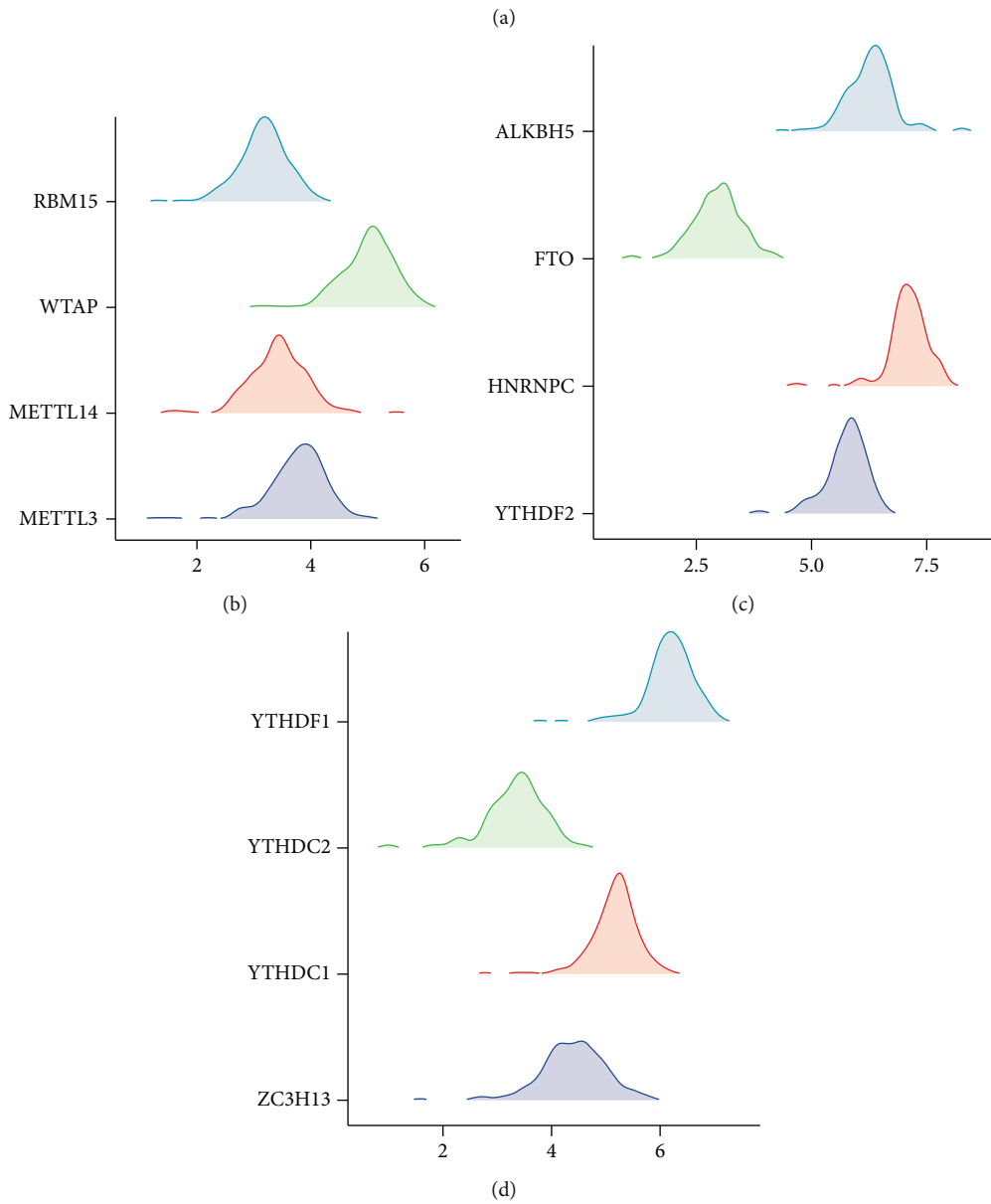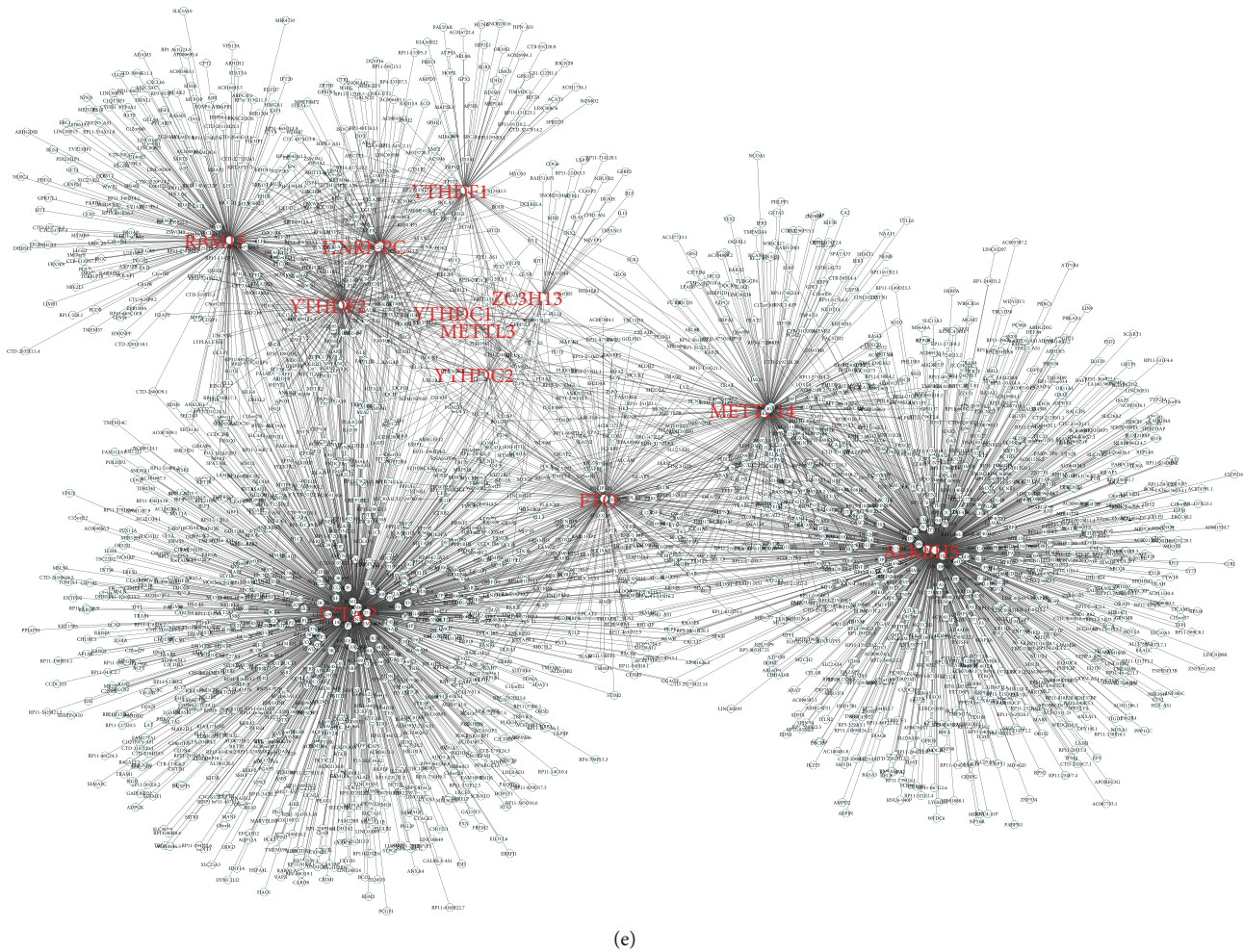
Figure 1: Identification of the gene methylation regulated by m6A regulators. (a) The expression level of the m6A regulator in pancreatic cancer and normal tissue; (b–d) the expression level of m6A regulators in TCGA-PAAD; (e) the gene methylation regulated by the m6A regulators. $^{***}p < 0.001$, $^{**}p < 0.01$, $^{*}p < 0.05$.

2.6. Immune-Related Analysis. Comparisons were made between the CIBERSORT, ESTIMATE, MCPcounter, EPIC, Xcell, and TIMER algorithms in order to evaluate the differences in cellular components or cellular immune responses between the high-risk group and the low-risk group based on the prognostic signature [33–36]. A heatmap was used to uncover the changes in the immune response that occurred under the influence of several algorithms. In addition, the potential response of patients to immunotherapy was inferred by the tumor immune dysfunction and exclusion (TIDE) score. Generally, a lower TIDE score indicates a better response to immunotherapy, in which the patients with TIDE score < 0 were regarded as immunotherapy responders, otherwise, nonresponders. For the purpose of quantifying the differences in tumor-infiltrating immune cell subgroups between the two groups, the single sample gene set enrichment analysis (ssGSEA) algorithm was utilized.

2.7. Statistical Analysis. Data were analyzed using Bioconductor packages in R software(version 4.0.2, R Core Team, Massachusetts, USA). The differences between clinical tis-

sues were tested by Student's t-test. Log-rank test and Kaplan-Meier analysis were used to compare the OS between groups. The Cox proportional hazards model was used to examine the independent significance of relevant clinical factors. A $p < 0.05$ was considered statistically significant.

3. Results

3.1. Identification of m6A Regulators in PC. It has been confirmed that the dysregulation of m6A methylation was involved in the progression of various tumors. Thus, our group extracted the expressions of identified m6A regulator, including METTL3, METTL14, WTAP, RBM15, ZC3H13, ALKBH5, FTO, HNRNPC, YTHDF2, YTHDF1, YTHDC2, and YTHDC1. The result indicated that all these m6A regulators showed an aberrant expression pattern in pancreatic cancer (Figure 1(a)). The expression distribution of all these m6A regulators was shown in Figures 1(b)–1(d). Based on the set criteria of |cor| > 0.4 and p value < 0.05. A total of 3507 gene methylation were identified to be regulated by m6A regulators (Figure 1(e)).

Subgroup	*p*value
RP11-24D15.1	8.63E-05
DDX21	9.71E-05
HMOX2	0.000109
GALM	0.000131
AC096649.3	0.000139
ITM2B	0.000142
HSP90AA1	0.000192
ARPC5L	0.000219
SET	0.00024
RP11-285E18.2	0.000242
MAPK1	0.000273
RP11-474P2.4	0.000285
LYSMD4	0.000321
HCG27	0.000333
H1F0	0.000381
ANP32B	0.000397
TTLL6	0.000397
RP11-57G10.8	0.000398
RPP25	0.000414
TBC1D30	0.00043
AC018816.3	0.000474
RP11-152K4.2	0.000484
POLR2L	0.000489
TPM3	0.000497
CYP4F11	0.000503
RP11-372M18.2	0.000509
PLD3	0.000517
AOX3P	0.000561
RP13-516M14.2	0.000571
GPR157	0.000575
C15orf57	0.000597
KIFAP3	0.000645
REC8	0.000696
PCSK6	0.0007
PLD1	0.000721
RPS18	0.00073
SSBP4	0.000759
RAPGEF3	0.000766
RP11-114B7.6	0.000776
ZNF710	0.000776
LINC01252	0.000781
NUDT4	0.000802
RP1-249H1.2	0.000823
NT5C2	0.000829
TACC2	0.000875
RP11-523L20.1	0.000892
ADIRF	0.000914
RP11-95P2.3	0.000936
NCK1	0.00098
B3GNT8	0.000987

Log2 (hazard ratio (95%CI))

(a)

Figure 2: Continued.

(b)

(c)

(d)

FIGURE 2: Screening of prognosis-related gene methylation. (a) The top 50 gene methylation tightly correlated with patients' prognosis; (b, c) LASSO regression analysis; (d) multivariate Cox regression analysis. $^{**}p < 0.01$, $^{*}p < 0.05$.

3.2. Prognosis Model Construction.

Based on the univariate assays and identified 3507 gene methylation, 858 gene methylation was distinctly related to the clinical outcome of PC patients. Among which, the top 50 prognosis-related gene methylations were selected for visualization and further analysis (Figure 2(a)). LASSO regression algorithm was used for data dimension reduction (Figures 2(b) and 2(c)). Finally,

the multivariate assays identified four gene methylation to construct a prognosis model with the formula of Risk score = Methylation level of PCSK6 × 11.54 + Methylation level of HSP90AA1 × −12.68 + Methylation level of TPM3 × −7.24 + Methylation level of TTLL6 × −17.35 (Figure 2(d)). The overview of our prognosis signature was shown in Figure 3(a), in which a higher percentage of dead cases was observed in the

(a)

(b)

(c)

(d)

(e)

(f)
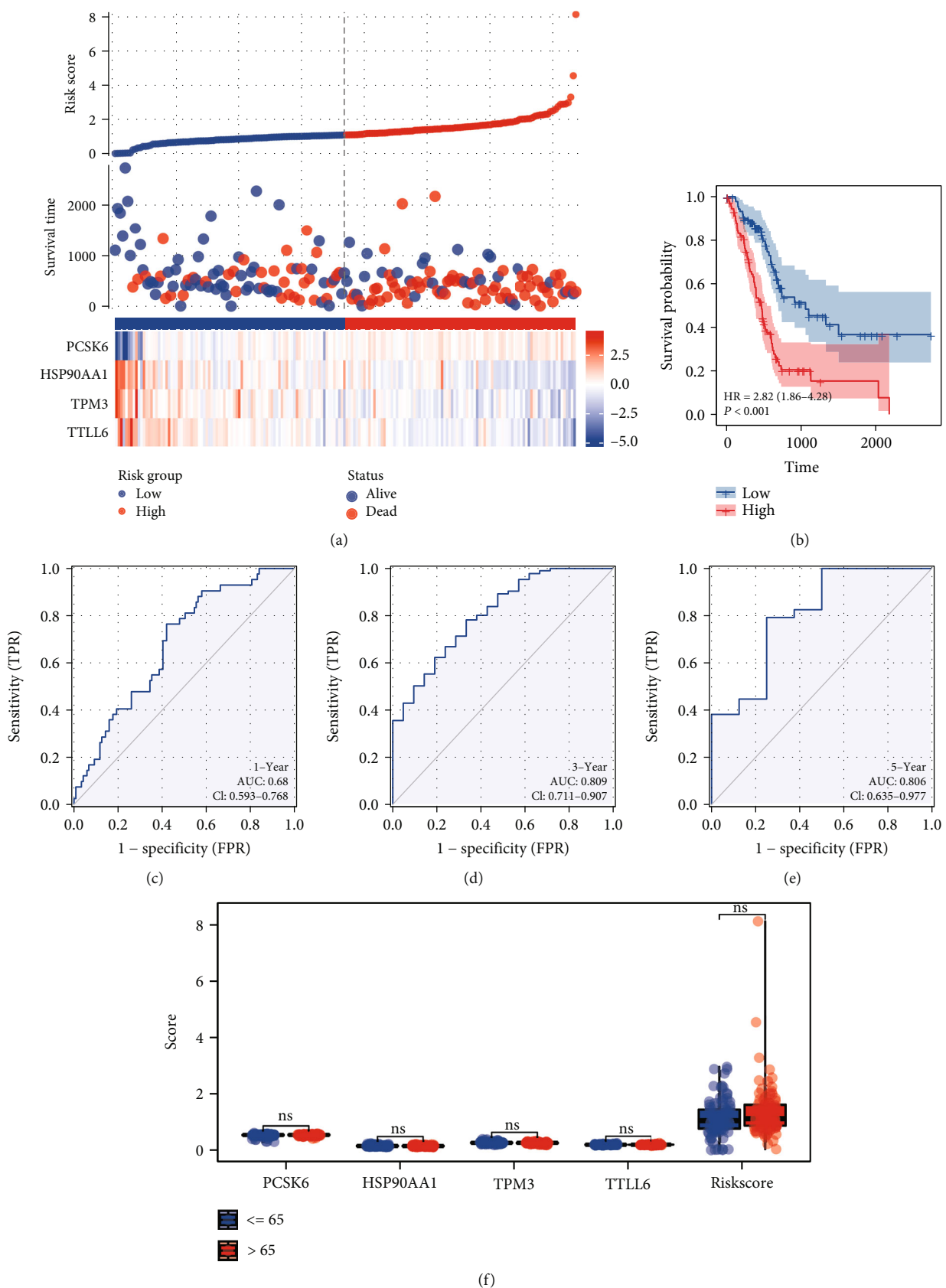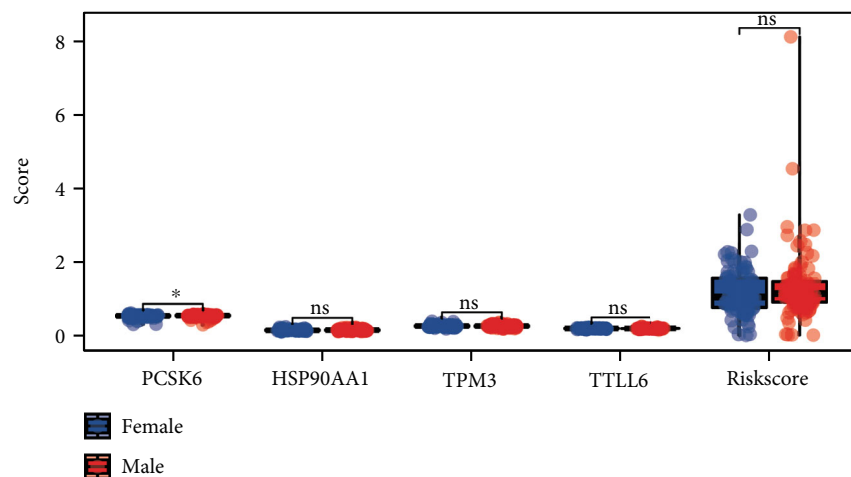
FIGURE 3: Continued.

(g)
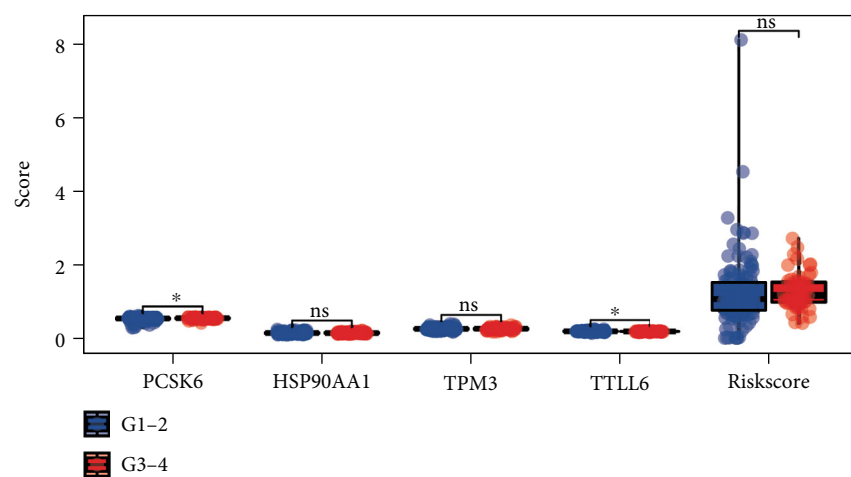
(h)

(i)

Figure 3: Continued.

(j)

(k)
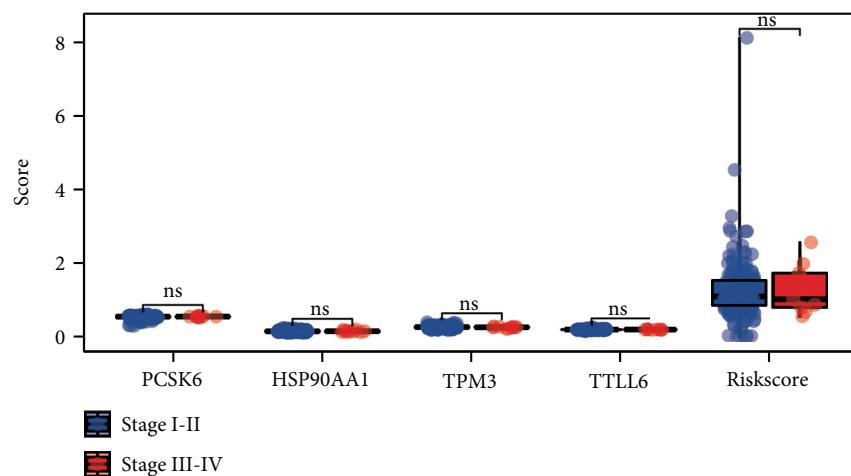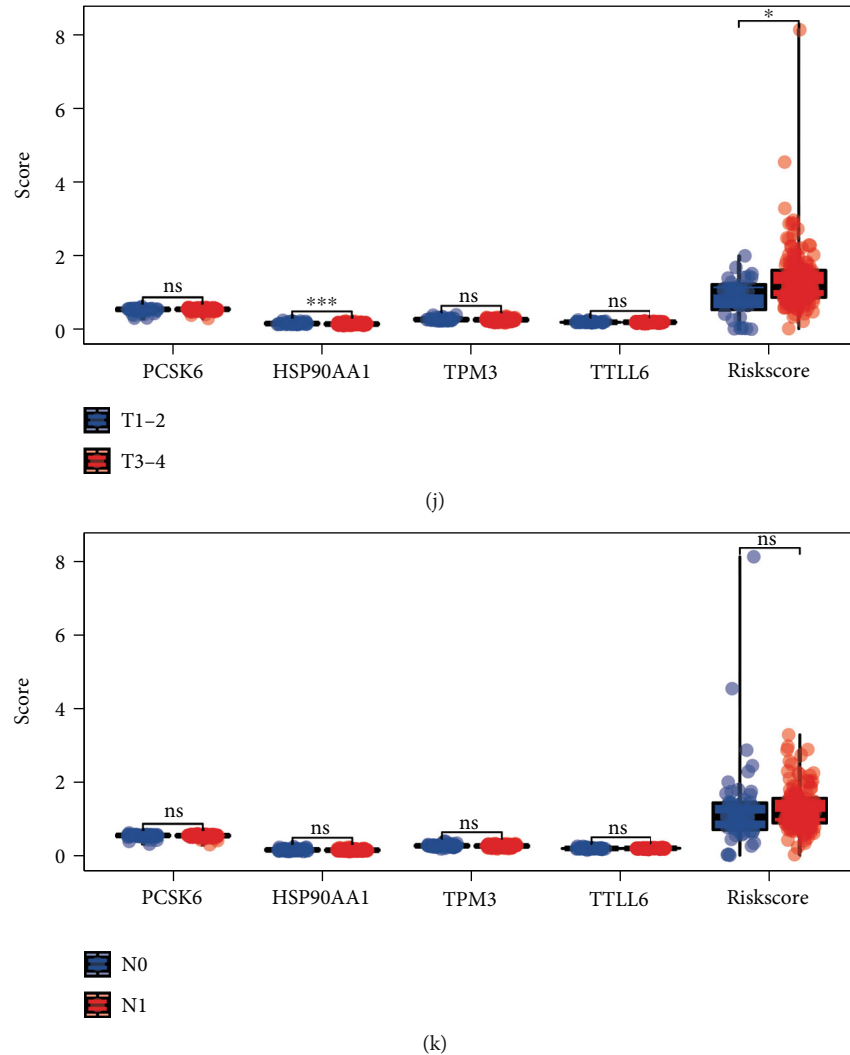
FIGURE 3: Prognosis signature. (a) The overview of the prognosis model; (b) KM survival curve of high- and low-risk patients; (c–e) the ROC curve of 1-, 3-, and 5-year survival; (f–k) clinical correlation of model gene methylation and risk score.

high-risk group. Survival assays indicated that the patients in the high-risk group tend to have a worse prognosis (Figure 3(b), HR = 2.82, $p < 0.001$). ROC curves showed that our prognosis signature had a good prediction ability on patient survival (Figures 3(c)–3(e)) (1-year AUC = 0.68, 3-year AUC = 0.809, and 5-year AUC = 0.806).

3.3. *Clinical Correlation Analysis.* To better understand the prognosis differences between high- and low-risk patients, we then performed a clinical correlation analysis. Results indicated that no significant differences were observed in patients with different ages (Figure 3(f)); PCSK6 was upregulated in female patients (Figure 3(g)); PCSK6 was overexpressed in G1-2 patients (Figure 3(h)); no significant differences were observed in patients with different clinical stages (Figure 3(i)); the T3-4 patients tend to have a lower HSP90AA1, while a higher risk score level compared to the T1-2 patients (Figure 3(j)); no significant differences were observed in patients with different N stages (Figure 3(k)).

Finally, we evaluated the roles of the novel model and other clinicopathologic parameters on the prognosis of PC with univariate and multivariate assays. As shown in Figures 4(a) and 4(b), we confirmed that the novel prognostic model was an independent prognostic factor for overall survival in PC patients.

3.4. *Biological Enrichment Analysis.* Underlying biological pathway difference can lead to different prognosis performance. For the GSEA analysis based on GO, the terms positive regulation of chromosome segregation, cysteine-type endopeptidase inhibitor activity, structural constituent of chromatin, phosphatidylserine metabolic process, and positive regulation of chromosome separation were the top five enriched terms (Figure 5(a)). For the GSEA analysis based on KEGG analysis, the cell cycle, systemic lupus erythematosus, base excision repair, DNA replication, and ether lipid metabolism were the top five enriched terms (Figure 5(b)). For the GSEA analysis based on the Hallmark gene set, the

	*p*value	Hazard ratio
Age	0.023	1.024 (1.003–1.045)
Gender	0.311	0.812 (0.542–1.215)
Grade	0.036	1.354 (1.020–1.798)
Stage	0.222	1.256 (0.871–1.811)
T	0.079	1.505 (0.954–2.375)
N	0.002	2.218 (1.325–3.712)
Riskscore	< 0.001	1.484 (1.272–1.732)

(a)

	*p*value	Hazard ratio
Age	0.168	1.014 (0.994–1.035)
Gender	0.325	0.811 (0.536–1.230)
Grade	0.178	1.223 (0.913–1.639)
Stage	0.803	0.925 (0.501–1.708)
T	0.741	1.115 (0.584–2.128)
N	0.005	2.271 (1.278–4.036)
Riskscore	< 0.001	1.566 (1.298–1.888)

(b)

FIGURE 4: Prognostic factors for overall survival by univariate (a) and multivariate (b) analysis.

terms interferon alpha response, MYC targets, mTORC1 signaling, oxidative phosphorylation, and Notch signaling were the top five enriched terms (Figure 5(c)).

3.5. Immune-Related Analysis. The tumor immune microenvironment plays an important role in tumor progression. We next quantified the tumor immune microenvironment based on multiple algorithms, including CIBERSORT, ESTIMATE, MCPcounter, EPIC, Xcell, and TIMER. The result indicated a different immune infiltration pattern in patients with high- and low-risk scores (Figure 6(a)). Moreover, we found that two immune-related genes CTLA4 and TIGIT were downregulated in high-risk patients (Figure 6(b)). Also, we explored the underlying effect of risk score on TIDE, immune dysfunction, and immune exclusion, while no significant difference was found (Figures 6(c)–6(e)).

4. Discussion

PC is one of the most dangerous types of malignant tumors [37]. According to the latest statistics on cancer in 2019, the incidence and mortality rates of pancreatic cancer are only second to those of colorectal cancer among malignancies

that affect the digestive tract [38, 39]. Studies conducted in clinical settings have indicated that resistance to chemotherapy is the single most important factor that restricts treatment options for pancreatic cancer. This factor also adds to the disease's low survival rate and bad prognosis [40, 41]. The TNM staging system is typically applied in practice for the purposes of classifying cancer patients and choosing appropriate treatments for them [42]. Yet, due to the wide variety of cancers, even those at the same stage may respond differently to therapy. High-throughput sequencing has grown increasingly prevalent in cancer diagnosis and treatment in recent years. In addition, there has been a significant number of research conducted on the process by which RNA is altered in cancer. The various m6A signatures have been identified as predictive prognosis models in many cancers, such as hepatocellular carcinoma, renal cell carcinoma, lung adenocarcinoma, breast cancer, and glioma [43–45].

DNA methylation, as a major epigenetic alteration, has been implicated in the regulation of gene expression by DNA methyltransferase (DNMT) [46, 47]. In addition, the importance of DNA methylation in the development and progression of cancers has been established beyond a reasonable doubt. The prognosis of patients with PC has been

(a)

(b)

Figure 5: Continued.

Pathway	NES	pval	padj
HALLMARK_INTERFERON_ALPHA_RESPONSE	2.26	9.3e−03	2.3e−01
HALLMARK_MYC_TARGETS_V1	1.46	9.1e−02	9.1e−01
HALLMARK_MTORC1_SIGNALING	1.14	1.2e−01	9.1e−01
HALLMARK_OXIDATIVE_PHOSPHORYLATION	1.19	1.2e−01	9.1e−01
HALLMARK_NOTCH_SIGNALING	1.25	1.3e−01	9.1e−01
HALLMARK_E2F_TARGETS	1.81	2.0e−01	1.0e+00
HALLMARK_G2M_CHECKPOINT	2.03	2.0e−01	1.0e+00
HALLMARK_MITOTIC_SPINDLE	1.15	2.0e−01	1.0e+00
HALLMARK_UNFOLDED_PROTEIN_RESPONSE	1.03	3.9e−01	1.0e+00
HALLMARK_GLYCOLYSIS	1.10	4.0e−01	1.0e+00
HALLMARK_ANGIOGENESIS	−0.83	7.6e−01	1.0e+00
HALLMARK_PEROXISOME	−0.89	7.5e−01	1.0e+00
HALLMARK_IL2_STAT5_SIGNALING	−0.92	7.3e−01	1.0e+00
HALLMARK_MYOGENESIS	−1.01	4.9e−01	1.0e+00
HALLMARK_HEDGEHOG_SIGNALING	−1.06	4.0e−01	1.0e+00
HALLMARK_BILE_ACID_METABOLISM	−1.11	2.7e−01	1.0e+00
HALLMARK_ALLOGRAFT_REJECTION	−1.09	2.5e−01	1.0e+00
HALLMARK_KRAS_SIGNALING_DN	−1.11	2.2e−01	1.0e+00
HALLMARK_SPERMATOGENESIS	−1.25	5.6e−02	9.1e−01
HALLMARK_PANCREAS_BETA_CELLS	−1.51	4.9e−03	2.3e−01

(c)

Figure 5: Biological enrichment analysis. (a) GSEA analysis based on the GO gene set; (b) GSEA analysis based on the KEGG gene set; (c) GSEA analysis based on the Hallmark gene set.

predicted using a variety of methylation indicators. In PC, the prognostic prediction model that was based on the DNA methylation site demonstrated greater prediction effectiveness. In a previous study, an unsupervised consistent clustering approach was used to identify two PAAD methylation subtypes, which were dubbed Cluster1 and Cluster2. Cluster2 was shown to be linked with a more favorable prognosis than Cluster1, which was found to be more common. Fourteen methylation genes that are exclusive to each PAAD subtype were found, and these genes might be used as molecular markers to describe the different methylation patterns that are associated with the two PAAD subtypes [48]. However, the DNA methylation signature of m6A regulators has not been investigated in the prognostic prediction of PC. In this study, based on the set criteria of $|cor| > 0.4$ and p value < 0.05. A total of 3507 gene methylation were identified to be regulated by m6A regulators. The LASSO regression algorithm was used for data dimension reduction. Finally, the multivariate Cox regression analysis identified four gene methylation(PCSK6, HSP90AA1, TPM3, and TTLL6) to construct a prognosis model. Survival analysis indicated that the patients in the high-risk group tend to have a worse prognosis. ROC curves showed that our prognosis signature had a good prediction ability on patients' survival. Our findings highlighted the potential of the novel model used as a novel prognostic biomarker for PC patients.

Immunotherapy has only very recently been recognized as a potential new treatment for PC [49]. The extracellular matrix (ECM), stromal cells, tumor vasculature, and numerous immune system cells all contribute to the TME, which is what encourages the development and progression of cancer [50, 51]. It is common knowledge that immune-suppressing cells might play a role in the development of immune eva-

sion in the TME, which in turn helps tumor spread and progression. Tregs are a well-known kind of immunosuppressive cells, and it has been demonstrated that their number is connected with the prognosis of patients [52, 53]. This suggested that the number of Tregs may be an efficient marker for determining the clinical outcome of patients with PC. Immune suppression is one of the most recognizable symptoms of PC, which is caused by the oncogenic drivers. Because of the metabolic reprogramming of tumor cells, which allows them to facilitate the aerobic glycolysis process in order to adapt to their heterogeneous microenvironment, the majority of solid tumors depend heavily on aerobic glycolysis as a source of energy production [54]. TME consists of more than just the tumor cells themselves; it also contains the immune cells, fibroblasts, and fibroblasts that surround the tumor [55]. PC cells are difficult to penetrate and exist in a low-perfusion environment, both of which favor metabolic rearrangement in the PC [56]. This is because the PC is composed of dense connective tissue and has a vascular milieu. Then, we found a different immune infiltration pattern in patients with high- and low-risk scores. In addition, we discovered that macrophage M0 cells were significantly different between high-risk and low-risk signatures. This suggests that macrophage M0 cells might be directly associated to the signature; however, the mechanism behind this relationship has to be researched in more depth. Thus, we came to the conclusion that the tumor immunosuppressive microenvironment might be to blame for the dismal prognosis that high-risk PC patients experience.

In addition, the expression and control of immune checkpoint molecules (such as PD-1, PD-L1, PD-L2, and CTLA-4) also play a vital role in the regulation of the immune response [57]. This is accomplished by inhibiting the activation of protective immune cells and enhancing

(a)

(b)

(c)

(d)

Figure 6: Continued.

(e)
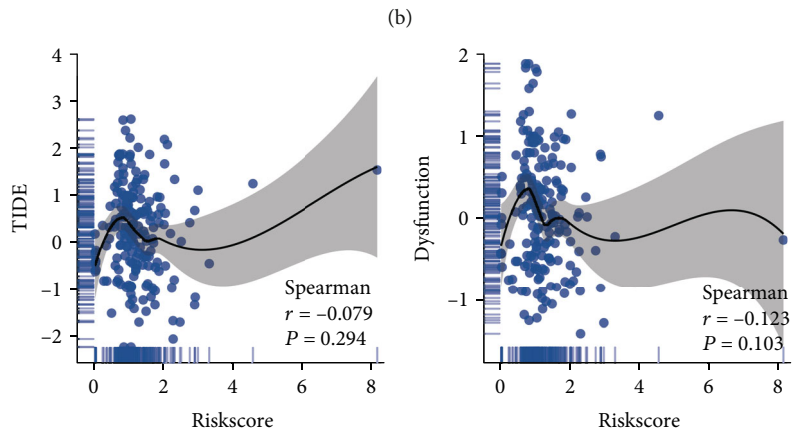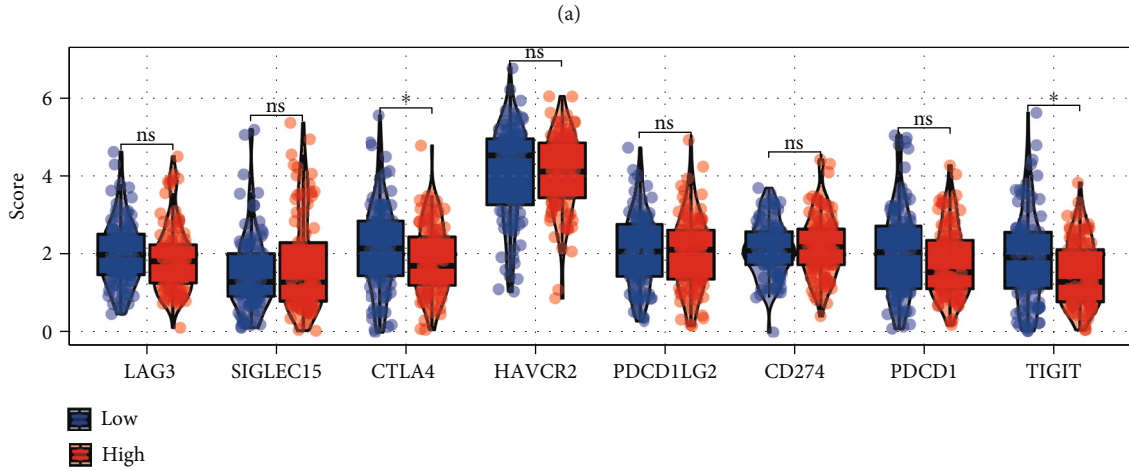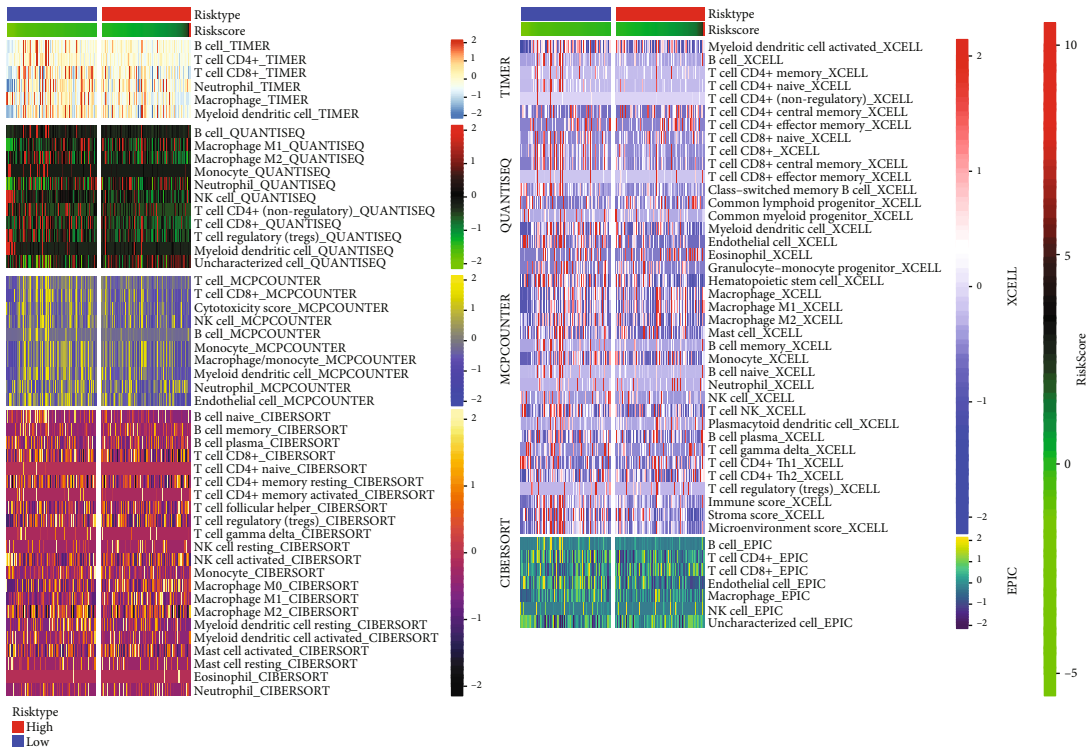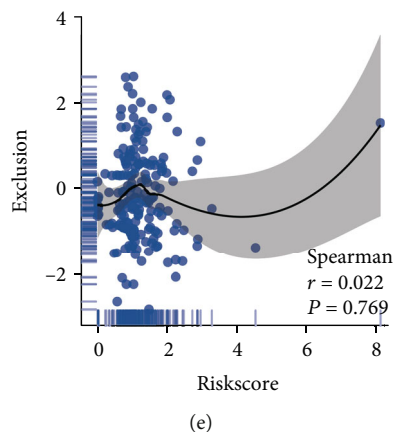
FIGURE 6: Immune-related analysis. (a) Immune infiltration analysis based on multiple algorithms; (b) several immune checkpoint genes in high- and low-risk groups; (c–e) correlation of risk score with TIDE, dysfunction, and exclusion. $^*p < 0.05$.

immune surveillance [58]. Thus, it is not difficult to comprehend why the expression of immune checkpoint molecules was found to be higher in the high-risk group in our study. Immune checkpoint drugs are typically more effective in cases with higher expression of immune checkpoint molecules (ICIs) [59, 60]. In this study, we found two immune-related genes CTLA4 and TIGIT were downregulated in high-risk patients. The results need to be further studied. I suggested that the function of CTLA4 and TIGIT in advanced PC may be different from patients with early stage.

Several limitations exist in this study. Firstly, the clinical data that was obtained from the TCGA databases was scant and lacked essential details. Secondly, this was a retrospective study, and therefore, it lacked novel clinical samples and data.

5. Conclusion

We generated a unique methylation signature that is related to m6A regulators and is capable of accurately predicting patients' prognoses when they have PC. This model can be used to aid doctors in the selection of the therapy that is most appropriate for different individuals, and it can, thus, optimize the clinical outcome for patients' PC.

Data Availability

The datasets used and/or analyzed during the current study are available from the corresponding author on reasonable request.

Conflicts of Interest

The authors declare no conflict of interest regarding the publication of this paper.

Authors' Contributions

Tianle Zou, Yu Tian, and Peng Gong conceived and designed the research. Dan Shi and Weiwei Wang acquired the data. Guoyong Chen and Xianbin Zhang analyzed and interpreted the data. Tianle Zou and Dan Shi carried out statistical analysis. Tianle Zou drafted the manuscript. All authors read and approved the final manuscript.

References

[1] R. L. Siegel, K. D. Miller, H. E. Fuchs, and A. Jemal, "Cancer statistics, 2022," *CA: a Cancer Journal for Clinicians*, vol. 72, no. 1, pp. 7–33, 2022.

[2] Z. Zhao and W. Liu, "Pancreatic cancer: a review of risk factors, diagnosis, and treatment," *Technology in Cancer Research & Treatment*, vol. 19, 2020.

[3] J. P. Neoptolemos, J. Kleeff, P. Michl, E. Costello, W. Greenhalf, and D. H. Palmer, "Therapeutic developments in pancreatic cancer: current and future perspectives," *Nature Reviews Gastroenterology & Hepatology*, vol. 15, no. 6, pp. 333–348, 2018.

[4] D. Ansari, B. Tingstedt, B. Andersson et al., "Pancreatic cancer: yesterday, today and tomorrow," *Future Oncology*, vol. 12, no. 16, pp. 1929–1946, 2016.

[5] H. Zhu, T. Li, Y. Du, and M. Li, "Pancreatic cancer: challenges and opportunities," *BMC Medicine*, vol. 16, no. 1, p. 214, 2018.

[6] E. S. Lee and J. M. Lee, "Imaging diagnosis of pancreatic cancer: a state-of-the-art review," *World Journal of Gastroenterology*, vol. 20, no. 24, pp. 7864–7877, 2014.

[7] A. P. Klein, "Pancreatic cancer epidemiology: understanding the role of lifestyle and inherited risk factors," *Nature Reviews Gastroenterology & Hepatology*, vol. 18, no. 7, pp. 493–502, 2021.

[8] S. Heinrich and H. Lang, "Neoadjuvant therapy of pancreatic cancer: definitions and benefits," *International Journal of Molecular Sciences*, vol. 18, no. 8, p. 1622, 2017.

[9] J. Cai, H. Chen, M. Lu et al., "Advances in the epidemiology of pancreatic cancer: trends, risk factors, screening, and prognosis," *Cancer Letters*, vol. 520, pp. 1–11, 2021.

[10] C. J. Halbrook and C. A. Lyssiotis, "Employing metabolism to improve the diagnosis and treatment of pancreatic cancer," *Cancer Cell*, vol. 31, no. 1, pp. 5–19, 2017.

[11] L. D. Moore, T. Le, and G. Fan, "DNA methylation and its basic function," *Neuropsychopharmacology*, vol. 38, no. 1, pp. 23–38, 2013.

[12] M. Kulis and M. Esteller, "DNA methylation and cancer," *Advances in Genetics*, vol. 70, pp. 27–56, 2010.

[13] H. Hashimoto, P. M. Vertino, and X. Cheng, "Molecular coupling of DNA methylation and histone methylation," *Epigenomics*, vol. 2, no. 5, pp. 657–669, 2010.

[14] H. Zhang and J. Gelernter, "Review: DNA methylation and alcohol use disorders: progress and challenges," *The American Journal on Addictions*, vol. 26, no. 5, pp. 502–515, 2017.

[15] S. Oerum, V. Meynier, M. Catala, and C. Tisné, "A comprehensive review of m6A/m6Am RNA methyltransferase structures," *Nucleic Acids Research*, vol. 49, no. 13, pp. 7239–7255, 2021.

[16] T. Sun, R. Wu, and L. Ming, "The role of m6A RNA methylation in cancer," *Biomedicine & Pharmacotherapy*, vol. 112, article 108613, 2019.

[17] X. Jiang, B. Liu, Z. Nie et al., "The role of m6A modification in the biological functions and diseases," *Signal Transduction and Targeted Therapy*, vol. 6, no. 1, p. 74, 2021.

[18] Z. X. Liu, L. M. Li, H. L. Sun, and S. M. Liu, "Link between m6A modification and cancers," *Frontiers in Bioengineering and Biotechnology*, vol. 6, p. 89, 2018.

[19] L. He, H. Li, A. Wu, Y. Peng, G. Shu, and G. Yin, "Functions of N6-methyladenosine and its role in cancer," *Molecular Cancer*, vol. 18, no. 1, p. 176, 2019.

[20] Z. Ma and J. Ji, "N6-methyladenosine (m6A) RNA modification in cancer stem cells," *Stem Cells*, vol. 38, no. 12, pp. 1511–1519, 2020.

[21] X. Guo, K. Li, W. Jiang et al., "RNA demethylase ALKBH5 prevents pancreatic cancer progression by posttranscriptional activation of PER1 in an m6A-YTHDF2-dependent manner," *Molecular Cancer*, vol. 19, no. 1, p. 91, 2020.

[22] J. Xiong, J. He, J. Zhu et al., "Lactylation-driven METTL3-mediated RNA m^{6}A modification promotes immunosuppression of tumor-infiltrating myeloid cells," *Molecular Cell*, vol. 82, no. 9, pp. 1660–1677.e10, 2022.

[23] B. Arneth, "Tumor microenvironment," *Medicina (Kaunas, Lithuania)*, vol. 56, no. 1, p. 15, 2020.

[24] I. Vitale, G. Manic, L. M. Coussens, G. Kroemer, and L. Galluzzi, "Macrophages and metabolism in the tumor microenvironment," *Cell Metabolism*, vol. 30, no. 1, pp. 36–50, 2019.

[25] C. Peng, L. Li, G. Luo, S. Tan, R. Xia, and L. Zeng, "Integrated analysis of the M2 macrophage-related signature associated with prognosis in ovarian cancer," *Frontiers in Oncology*, vol. 12, article 986885, 2022.

[26] P. Jiang, F. Yang, C. Zou et al., "The construction and analysis of a ferroptosis-related gene prognostic signature for pancreatic cancer," *Aging*, vol. 13, no. 7, pp. 10396–10414, 2021.

[27] Y. Wu, C. Zhou, and Q. Yuan, "Role of DNA and RNA N6-adenine methylation in regulating stem cell fate," *Current Stem Cell Research & Therapy*, vol. 13, no. 1, pp. 31–38, 2018.

[28] M. M. Mahfouz, "RNA-directed DNA methylation: mechanisms and functions," *Plant Signaling & Behavior*, vol. 5, no. 7, pp. 806–816, 2010.

[29] S. Oerum, C. Dégut, P. Barraud, and C. Tisné, "m1A posttranscriptional modification in tRNAs," *Biomolecules*, vol. 7, no. 4, p. 20, 2017.

[30] M. Zhang, J. Song, W. Yuan, W. Zhang, and Z. Sun, "Roles of RNA methylation on tumor immunity and clinical implications," *Frontiers in Immunology*, vol. 12, article 641507, 2021.

[31] Y. Yang, X. Su, K. Shen et al., "PUM1 is upregulated by DNA methylation to suppress antitumor immunity and results in poor prognosis in pancreatic cancer," *Cancer Research*, vol. 10, no. 5, pp. 2153–2168, 2021.

[32] X. Yin, L. Kong, and P. Liu, "Identification of prognosis-related molecular subgroups based on DNA methylation in pancreatic cancer," *Clinical Epigenetics*, vol. 13, no. 1, p. 109, 2021.

[33] B. Chen, M. S. Khodadoust, C. L. Liu, A. M. Newman, and A. A. Alizadeh, "Profiling tumor infiltrating immune cells with CIBERSORT," *Methods in Molecular Biology*, vol. 1711, pp. 243–259, 2018.

[34] Y. W. Wang and C. Ané, "KIMGENS: a novel method to estimate kinship in organisms with mixed haploid diploid genetic systems robust to population structure," *Bioinformatics*, vol. 38, no. 11, pp. 3044–3050, 2022.

[35] A. M. Newman, C. L. Liu, M. R. Green et al., "Robust enumeration of cell subsets from tissue expression profiles," *Nature Methods*, vol. 12, no. 5, pp. 453–457, 2015.

[36] T. Li, J. Fan, B. Wang et al., "TIMER: a web server for comprehensive analysis of tumor-infiltrating immune cells," *Cancer Research*, vol. 77, no. 21, pp. e108–e110, 2017.

[37] G. Ercan, A. Karlitepe, and B. Ozpolat, "Pancreatic cancer stem cells and therapeutic approaches," *Anticancer Research*, vol. 37, no. 6, pp. 2761–2775, 2017.

[38] C. Lu, C. F. Xu, X. Y. Wan, H. T. Zhu, C. H. Yu, and Y. M. Li, "Screening for pancreatic cancer in familial high-risk individuals: a systematic review," *World Journal of Gastroenterology*, vol. 21, no. 28, pp. 8678–8686, 2015.

[39] D. S. Zuckerman and D. P. Ryan, "Adjuvant therapy for pancreatic cancer," *Cancer*, vol. 112, no. 2, pp. 243–249, 2008.

[40] J. D. Mizrahi, R. Surana, J. W. Valle, and R. T. Shroff, "Pancreatic cancer," *Lancet*, vol. 395, no. 10242, pp. 2008–2020, 2020.

[41] C. Springfeld, D. Jäger, M. W. Büchler et al., "Chemotherapy for pancreatic cancer," *Presse Médicale*, vol. 48, no. 3, pp. e159–e174, 2019.

[42] X. D. Liu, Z. W. Zhang, H. W. Wu, and Z. Y. Liang, "A new prognosis prediction model combining TNM stage with MAP2K4 and JNK in postoperative pancreatic cancer patients," *Pathology, Research and Practice*, vol. 217, article 153313, 2021.

[43] L. Li, R. Xie, and G. Lu, "Identification of m6A methyltransferase-related lncRNA signature for predicting immunotherapy and prognosis in patients with hepatocellular carcinoma," *Bioscience Reports*, vol. 41, no. 6, 2021.

[44] J. Zhou, J. Wang, B. Hong et al., "Gene signatures and prognostic values of m6A regulators in clear cell renal cell carcinoma - a retrospective study using TCGA database," *Aging*, vol. 11, no. 6, pp. 1633–1647, 2019.

[45] J. Zheng, Z. Zhao, J. Wan et al., "N-6 methylation-related lncRNA is potential signature in lung adenocarcinoma and influences tumor microenvironment," *Journal of Clinical Laboratory Analysis*, vol. 35, no. 11, article e23951, 2021.

[46] X. Sui, A. Klungland, and L. Gao, "RNA m6A modifications in mammalian gametogenesis and pregnancy," *Reproduction*, vol. 165, no. 1, pp. R1–R8, 2023.

[47] Z. Ma, X. Gao, Y. Shuai, X. Xing, and J. Ji, "The m6A epitranscriptome opens a new charter in immune system logic," *Epigenetics*, vol. 16, no. 8, pp. 819–837, 2021.

[48] X. Li, X. Zhang, X. Lin, L. Cai, Y. Wang, and Z. Chang, "Classification and prognosis analysis of pancreatic cancer based on

DNA methylation profile and clinical information," *Genes*, vol. 13, no. 10, p. 1913, 2022.

[49] D. M. Geynisman, C. R. Chien, F. Smieliauskas, C. Shen, and Y. C. Shih, "Economic evaluation of therapeutic cancer vaccines and immunotherapy: a systematic review," *Human Vaccines & Immunotherapeutics*, vol. 10, no. 11, pp. 3415–3424, 2014.

[50] O. Demaria, L. Gauthier, G. Debroas, and E. Vivier, "Natural killer cell engagers in cancer immunotherapy: next generation of immuno-oncology treatments," *European Journal of Immunology*, vol. 51, no. 8, pp. 1934–1942, 2021.

[51] J. J. Wang, K. F. Lei, and F. Han, "Tumor microenvironment: recent advances in various cancer treatments," *European Review for Medical and Pharmacological Sciences*, vol. 22, no. 12, pp. 3855–3864, 2018.

[52] B. Farhood, M. Najafi, and K. Mortezaee, "CD8+ cytotoxic T lymphocytes in cancer immunotherapy: a review," *Journal of Cellular Physiology*, vol. 234, no. 6, pp. 8509–8521, 2019.

[53] M. Najafi, N. Hashemi Goradel, B. Farhood et al., "Macrophage polarity in cancer: a review," *Journal of Cellular Biochemistry*, vol. 120, no. 3, pp. 2756–2765, 2019.

[54] W. J. Ho, E. M. Jaffee, and L. Zheng, "The tumour microenvironment in pancreatic cancer – clinical challenges and opportunities," *Nature Reviews Clinical Oncology*, vol. 17, no. 9, pp. 527–540, 2020.

[55] E. Hessmann, S. M. Buchholz, I. E. Demir et al., "Microenvironmental determinants of pancreatic cancer," *Physiological Reviews*, vol. 100, no. 4, pp. 1707–1751, 2020.

[56] A. N. Ariston Gabriel, F. Wang, Q. Jiao et al., "The involvement of exosomes in the diagnosis and treatment of pancreatic cancer," *Molecular Cancer*, vol. 19, no. 1, p. 132, 2020.

[57] J. M. Michot, C. Bigenwald, S. Champiat et al., "Immune-related adverse events with immune checkpoint blockade: a comprehensive review," *European Journal of Cancer*, vol. 54, pp. 139–148, 2016.

[58] Y. Zhang and J. Zheng, "Functions of immune checkpoint molecules beyond immune evasion," *Advances in Experimental Medicine and Biology*, vol. 1248, pp. 201–226, 2020.

[59] S. Qin, L. Xu, M. Yi, S. Yu, K. Wu, and S. Luo, "Novel immune checkpoint targets: moving beyond PD-1 and CTLA-4," *Molecular Cancer*, vol. 18, no. 1, p. 155, 2019.

[60] X. He and C. Xu, "Immune checkpoint signaling and cancer immunotherapy," *Cell Research*, vol. 30, no. 8, pp. 660–669, 2020.

Research Article

An Inflammation-Associated Prognosis Model for Hepatocellular Carcinoma Based on Adenylate Uridylate- (AU-) Rich Element Genes

Li Song ,[1] Xiangzheng Su ,[2] Yao Lu ,[2] Dongliang Hua ,[1] and Ziren Gao [3]

[1]*Academy of Advanced Interdisciplinary Studies, Qilu University of Technology (Shandong Academy of Sciences), Jinan 250353, China*
[2]*Department of Tissue Repair and Regeneration, The First Medical Center of Chinese PLA General Hospital, Beijing 100853, China*
[3]*Xiyuan Hospital, China Academy of Chinese Medical Sciences, Beijing 100091, China*

Correspondence should be addressed to Dongliang Hua; huadl@sdas.org and Ziren Gao; songli14@mails.ucas.ac.cn

Hepatocellular carcinoma (HCC) is a typical inflammation-driven cancer and ranks sixth in the incidence rate worldwide. The role of adenylate uridylate- (AU-) rich element genes (AREGs) in HCC remains unclear. HCC-related datasets were acquired from The Cancer Genome Atlas (TCGA) database and Gene Expression Omnibus (GEO) database. Differentially expressed AREGs (DE-AREGs) between HCC samples and healthy controls were identified. The univariate Cox and LASSO analyses were performed to determine the prognostic genes. Furthermore, a signature and corresponding nomogram were configured for the clinical prediction of HCC. The potential signature-related biological significance was explored using functional and pathway enrichment analysis. Additionally, immune infiltration analysis was also performed. Finally, the expression of prognostic genes was verified using real-time quantitative polymerase chain reaction (RT-qPCR). A total of 189 DE-AREGs between normal and HCC samples were identified, wherein CENPA, TXNRD1, RABIF, UGT2B15, and SERPINE1 were selected to generate an AREG-related signature. Moreover, the prognostic accuracy of the AREG-related signature was also confirmed. Functional analysis indicated that the high-risk score was related to various functions and pathways. Inflammation and immune-related analyses indicated that the difference of T cell and B cell receptor abundance, microvascular endothelial cells (MVE), lymphatic endothelial cells (lye), pericytes, stromal cells, and the six immune checkpoints was statistically significant between the different risk groups. Similarly, RT-qPCR outcomes of these signature genes were also significant. In conclusion, an inflammation-associated signature based on five DE-AREGs was constructed, which could act as a prognostic indicator of patients with HCC.

1. Introduction

Hepatocellular carcinoma (HCC) is one of the most common cancers and has the second-highest mortality rates worldwide [1]. Currently, the standard treatment for HCC includes resection, local therapies such as ablation and radiotherapy, and liver transplantation. However, owing to the high recurrence and mortality rates, the prognosis of patients with HCC remains unsatisfactory [2, 3].

As an essential cis-acting short sequence in the $3'$UTR, adenylate uridylate- (AU-) rich element (ARE) has a signif-

icant effect on mRNA stability and translation and is closely related to mRNA decay [4, 5]. Chen and Shyu reported three classes (class I, class II, and class III) of ARE, which were based on the presence of an AUUUA motif in the U-rich region [6]. Specifically, among U- or AU-rich sequences and repeated sequences of AUUUA or non-AUUU overlapping pentamers determined as ARE sequences, the latter two forms are considered to be the least functional ARE sequences [4, 7]. Moreover, the AU-rich binding factor 1 (AUF1) is a well-known ARE-specific RNA-binding protein (ARE-BPs). Zhang et al. reported a novel role of AUF1 in

promoting the development and drug resistance of HCC [8] Furthermore, if the degradation of ARE-mRNAs was destroyed, chronic inflammation will be induced. For example, IL-17, a mediator implicated in chronic and severe inflammatory diseases, can enhance the production of proinflammatory mediators by attenuating the decay of ARE-mRNAs [9]. Similarly, the correlation of the biomarkers relevant to inflammatory response disorder and HCC prognosis was explored by Xing et al., wherein an inflammation-related gene (IRG) risk model comprising six IRGs that could identify tumors with low immune levels and also indicate the efficacy of immunotherapy was constructed [10].

HCC is a typical inflammation-driven carcinoma with progressive chronic nonresolving inflammation [11]. In addition, owing to the disruption of the degradation progress of ARE-mRNA, chronic inflammation and cancer are considered potential outcomes [12]. For example, the ARE gene uPA is upregulated in various cancers and stimulates angiogenesis, providing tumor cells with abundant nutrition and oxygen [13]. COX-2 in ARE genes contributes to angiogenesis, metastasis, and other tumor-related mechanisms in colon cancer [14]. Additionally, AUBPs contain typical sequences that are rich in AU bases (AREs) and can rapidly regulate $3'$-UTR harbouring ARE-binding motifs of liver disease-related cytokines and proinflammatory molecules. AUBPs could also be considered effective factors in HCC progression [15]. Therefore, ARE genes are speculated to be closely related to tumors and have promising potential prognostic value as a new target for tumor therapy.

This study is aimed at demonstrating the prognostic value of the ARE genes for the first time in HCC using bioinformatics analysis and exploring its potential therapeutic agents. This study is also aimed at aiding in the theoretical guidance for the treatment of HCC.

2. Materials and Methods

2.1. Data Source. The TCGA-LIHC datasets were downloaded from The Cancer Genome Atlas (TCGA) database (https://portal.gdc.cancer.gov/), including 374 samples with HCC and 50 controls. A total of 421 non-formalin-soaked tumor tissues and normal tissues (50 normal samples, 371 HCC samples) were selected for differential expression analysis. Moreover, 363 samples were retained for constructing a prognostic model based on extracted complete survival status and clinical information. The GSE14520 dataset was downloaded from the Gene Expression Omnibus (GEO) database (https://www.ncbi.nlm.nih.gov/gds/) for external validation, wherein 221 case samples had complete survival information. Furthermore, the GSE54236 dataset containing 81 HCC tissue samples and 80 adjacent nontumor samples was utilized for gene expression analysis. Additionally, 4884 AREGs were downloaded from the Adenylate Uridylate-Rich Element Database (ARED, https://brp.kfshrc.edu.sa/ared).

2.2. Differential Expression Analysis. Limma within R was applied to select differentially expressed genes (DEGs) ($p < 0.05$ and $|Log2FC| > 1$) between the HCC and healthy groups in the TCGA-LIHC datasets [16]. Following this,

TABLE 1: Primers for real-time quantitative polymerase chain reaction (RT-qPCR).

Primer		Sequence
UGT2B15	F	ATTTCTGTTCCCTCCTTCC
UGT2B15	R	AACTGGTCCCACTTCTTCA
SERPINE1	F	ACCCACCGCCGCCTCTTC
SERPINE1	R	CCACCGTGCCACTCTCGT
RABIF	F	GGACCGCTCTCTTCTCTC
RABIF	R	AACTTGATGTTGCCCACG
CENPA	F	TCGTGGTGTGGACTTCAAT
CENPA	R	GCTTCTGCTGCCTCTTGTA
TXNRD1	F	ATAAATGAAAAGACTGGAAAAA
TXNRD1	R	GCCAAAAGTAACTATGGTAAAC
Internal reference H-GAPDH	F	CCCATCACCATCTTCCAGG
Internal reference H-GAPDH	R	CATCACGCCACAGTTTCCC

TBtools were used to intersect DEGs and ARE genes to obtain differentially expressed AREGs (DE-AREGs) [17].

2.3. Functional and Pathway Enrichment Analysis of DE-AREGs. The Gene Ontology (GO) and the Kyoto Encyclopedia of Genes and Genomes (KEGG) enrichment scores of DE-AREGs were further analysed using "clusterProfiler," with p.adj < 0.05 and q value cutoff = 0.2 determining statistical significance [18].

2.4. Construction and Validation of the DE-AREG Signature. A total of 363 HCC samples with complete survival and clinical information were used as the training set to construct an AREG-related signature. Moreover, prognostic DE-AREGs were screened using univariate Cox and LASSO regression methods, which were performed using the survival and glmnet package, respectively [19, 20]. Subsequently, the multivariate Cox regression was used to construct the DE-AREG signature. The risk score was calculated as follows: Risk score = $h0(t) * \exp (\beta 1X1 + \beta 2X2 + \cdots + \beta nXn)$. Following this, the training set was classified into high- and low-risk groups based on the median value among risk scores of patients of HCC. Kaplan-Meier (K-M) curves were plotted using the survminer package [21]. The receiver operating characteristic (ROC) curve and the area under the curve (AUC) were drawn using the R package survival ROC [22]. Finally, the GSE14520 dataset was used to validate the prognostic performance of the signature.

2.5. Independent Prognostic Analysis. The wilcox.test function in R was used to evaluate the clinical relevance of the risk model based on the clinical data of HCC samples. Using the univariate and multivariate Cox regression models, the independent prognostic factors and relevant clinical parameters (p-value < 0.05) were used to establish the prognostic nomogram.

2.6. Functional Enrichment Analysis. To further investigate the functions related to the DE-AREG signature, gene set enrichment analysis (GSEA) was conducted using the gene
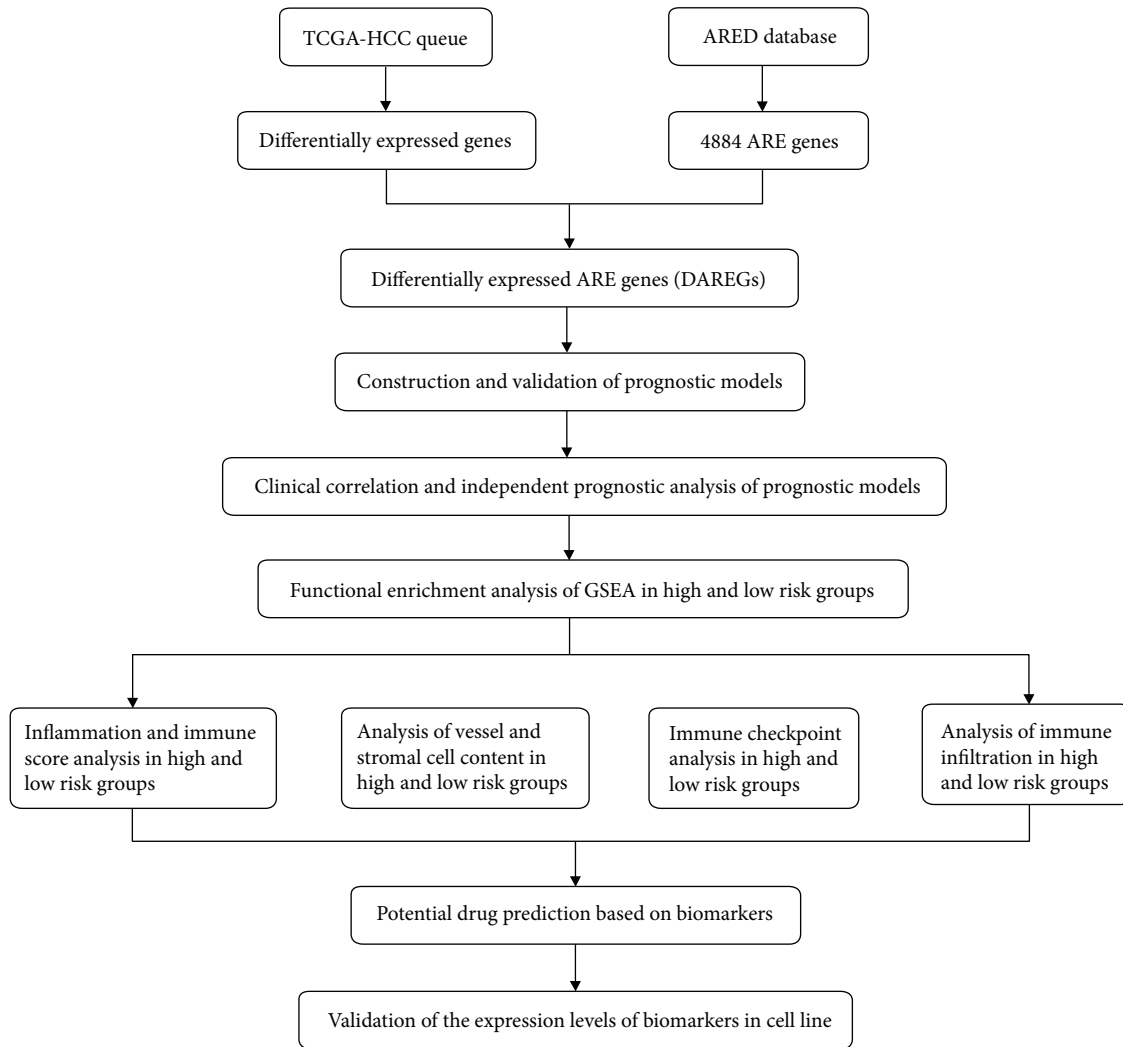
FIGURE 1: Workflow of the study on AREG prognostic signatures for HCC.

expression data extracted from the two risk groups. c5.go.v7.4.symbols.gmt (GO) and c2.cp.kegg.v7.4.symbols.gmt (KEGG) were selected as reference gene sets. The pathways and GO terms with $|NES| > 1$, NOM p value < 0.05, and FDR $q$value < 0.25 were extracted for further analysis.

2.7. Inflammatory and Immune-Related Analyses. The differences in inflammation-related factors, cytolytic score (CYT), antigen presentation mechanism (APM), infiltration of vascular cells, and immune checkpoints were interpreted in the two risk groups using xCell [23]. Additionally, the single sample GSEA (ssGSEA) algorithm was used to estimate the relative abundance of 28 immune cells for comparison between the risk groups [19]. Correlation analysis was performed to identify the relationship between immune cells and risk score. Next, overlapping immune cells with $r > 0.3$ were obtained that could be associated with different risk groups.

2.8. Prediction of Potential Biomarker-Drug Interactions. The potential drugs for the signature genes were predicted based on the Binding DB database (https://www.bindingdb.org/bind/index.jsp), STRING database (https://cn.string-db.org), and ZINC15 database (https://zinc15.docking.org/). In the Binding DB database, the drugs with affinity value < 50 were selected first, and then, these drugs were screened in the STRING database with a confidence value = 0.85. In the ZINC15 database, the potential drugs with the lowest affinity according to the molecular docking score were selected.

2.9. Real-Time Quantitative Polymerase Chain Reaction (RT-qPCR) Analysis and Validation of the Signature Genes in Cell Lines. Total RNA was collected from the nontumorigenic hepatocyte cell line (WRL68) and three HCC tumor cell lines (Huh-7, HepG2, and Sk-Hep-1) using a TRIzol reagent (Invitrogen, Eugene, OR, USA). The first-strand cDNA was synthesized with superScript RT I First-Strand cDNA Synthesis All-in-One™ First-Strand cDNA Synthesis Kit (Servicebio, Wuhan, China). The 2x Universal Blue Sybr Green qPCR Master Mix (Servicebio, Wuhan, China) was used for RT-qPCR detection. The primers used in this study are presented in Table 1. The $2^{-\Delta\Delta Ct}$ method was used for the expression detection of the signature genes [24].

(a)

(b)
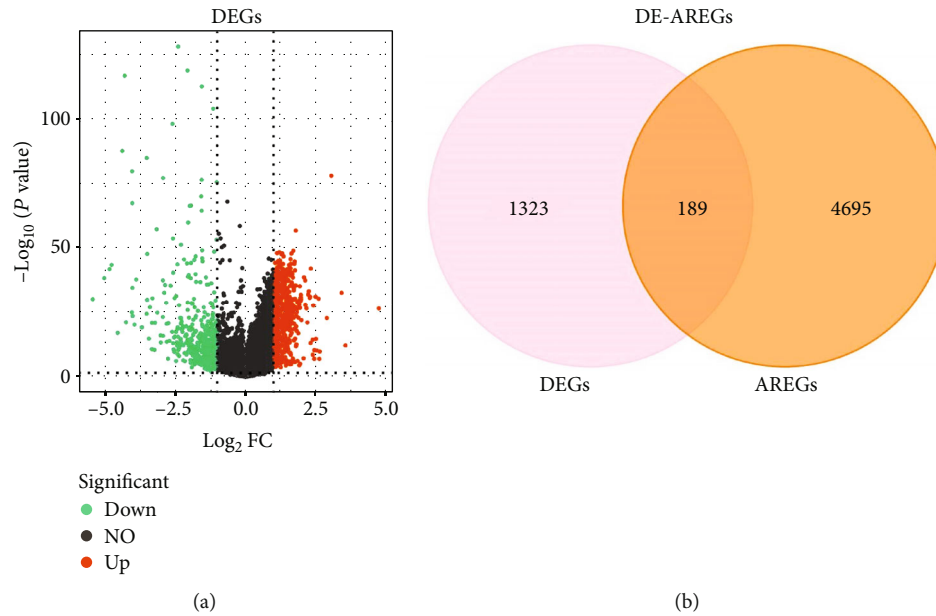
FIGURE 2: A total of 180 DE-AREGs were selected. (a) Volcano plot of 1512 differentially expressed genes (DEGs). Red, upregulation; green, downregulation. (b) Venn diagram of the 189 overlapping genes.

(a)

(b)
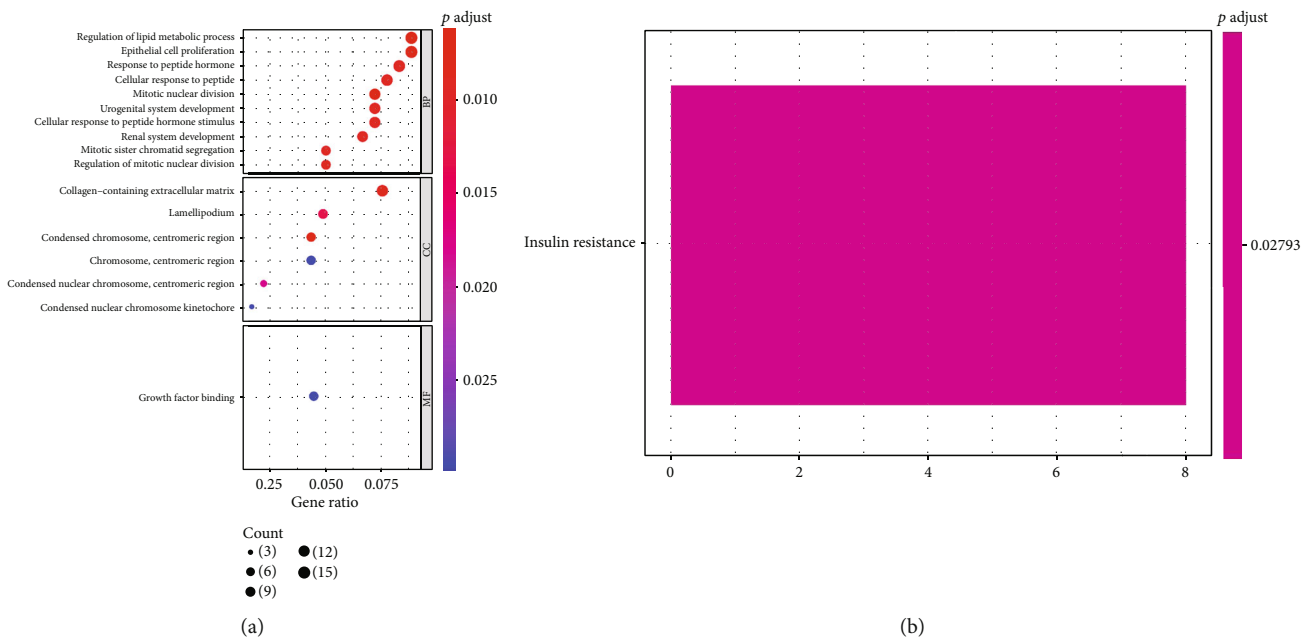
FIGURE 3: Functional enrichment analysis. (a) GO annotation of DE-AREGs with the top 10 enrichment scores. (b) Top 10 KEGG pathways of DE-AREGs.

3. Results

We conducted our study as presented in the workflow (Figure 1). A total of 1512 genes were identified as differently expressed at mRNA level in tumor tissues ($n = 371$) when compared with that of normal tissues ($n = 50$) [25]. More-over, the following software was used in this study: xCell (v.1.1.0), limma (v.3.44.3), ggplot2 (v.3.3.2), TBtools (v.1.098661), clusterProfiler (v.3.16.0), Survival (v.3.2 3),

pROC (v.1.16.2), psych (v.2.0.9), GSVA (v.1.38.2), rms (v.5.4-1), and Vina (v.1.1.2).

3.1. Identification of DE-AREGs.
We identified 1512 DEGs between HCC and normal samples, including 1046 upregulated and 366 downregulated DEGs (Figure 2(a)). Following this, 189 overlapping genes were obtained between 1512 DEGs and 4884 AREGs, which were considered DE-AREGs (Figure 2(b)). Furthermore, the hypergeometric

(a)

(b)

	p value	Hazard ratio
TXNRD1	<0.001	1.344 (1.145–1.577)
CENPA	0.002	1.419 (1.142–1.764)
UGT2B15	0.034	0.914 (0.841–0.993)
SERPINE1	0.125	1.084 (0.978–1.201)
RABIF	0.153	1.281 (0.912–1.801)

(c)
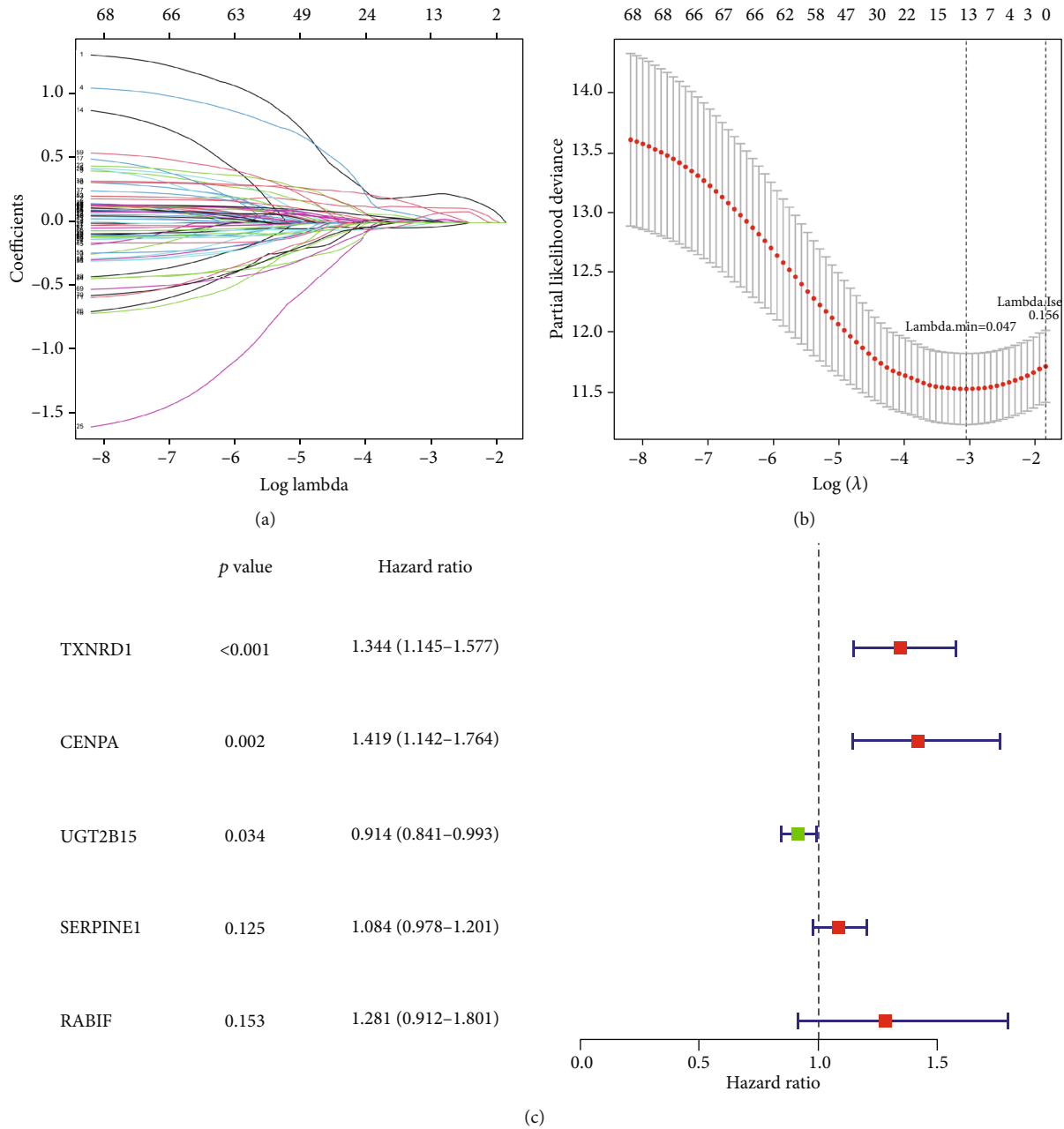
Figure 4: Five signature genes were generated based on the LASSO Cox regression. (a, b) Construction of the LASSO Cox regression model. (c) Forest map of the multivariate Cox results.

Table 2: Top five differentially expressed adenylate uridylate-rich element genes (DE-AREGs) identified using the multivariate Cox regression analysis.

ID	Coef	HR	HR.95L	HR.95H	p value
TXNRD1	0.295306992	1.343538751	1.144714554	1.576896501	0.000301488
CENPA	0.35019523	1.41934462	1.142163909	1.763791637	0.00158281
UGT2B15	0.089964684	0.913963462	0.841185018	0.99303862	0.03358938
SERPINE1	0.080432278	1.08375545	0.977870418	1.201105845	0.125189516
RABIF	0.247936243	1.281378233	0.911795369	1.800766085	0.15326473

(a)

(b)

(c)
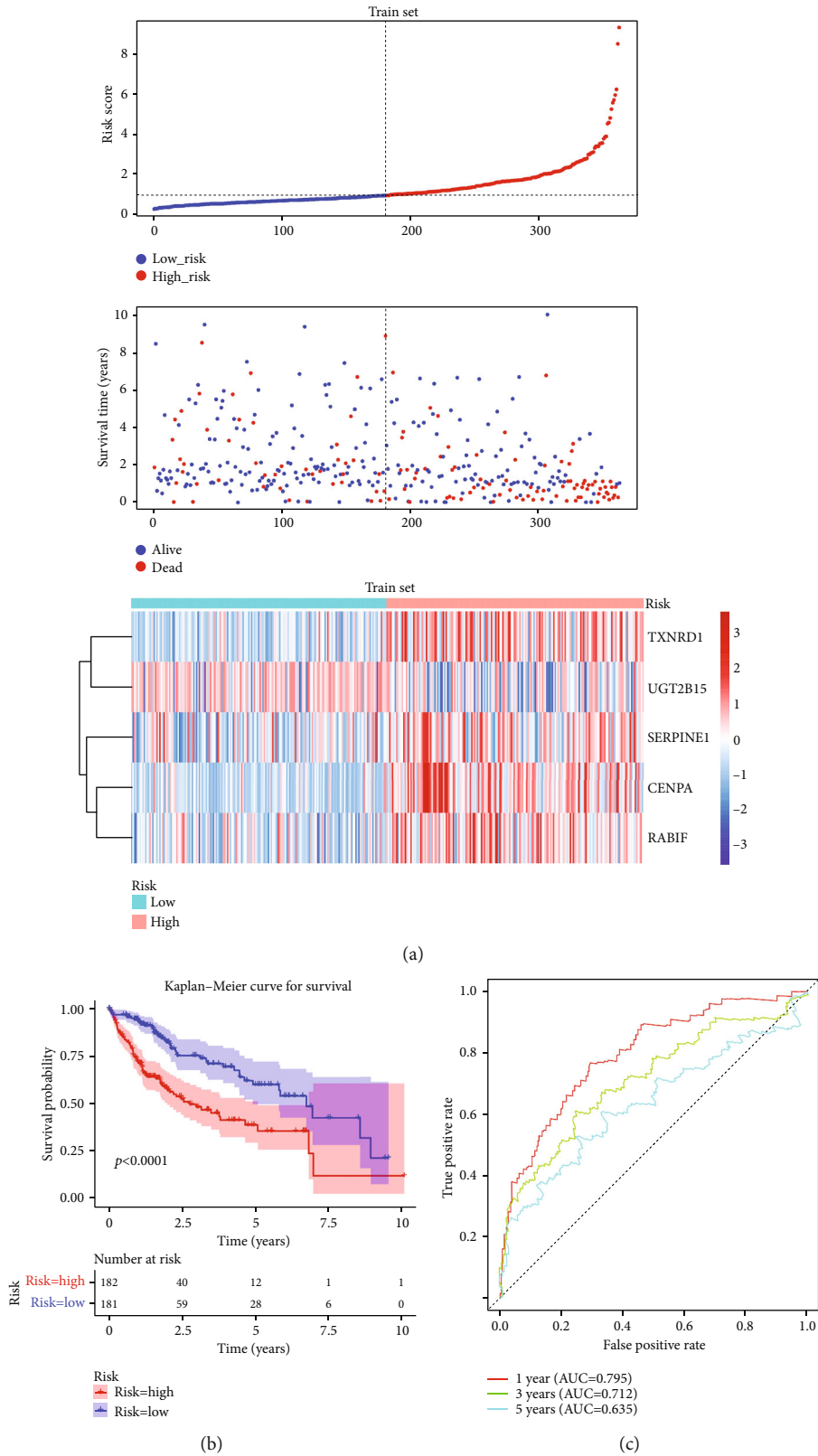
Figure 5: The prognostic value of the five gene signatures in the training set. (a) Distribution of risk score, survival time, and heatmap of the five gene signatures in the training set. (b) Kaplan-Meier curve of patients with HCC having different risk scores ($p < 0.0001$). (c) The receiver operating characteristic (ROC) curve evaluating the validity of the risk model.

(a)

(b)

(c)
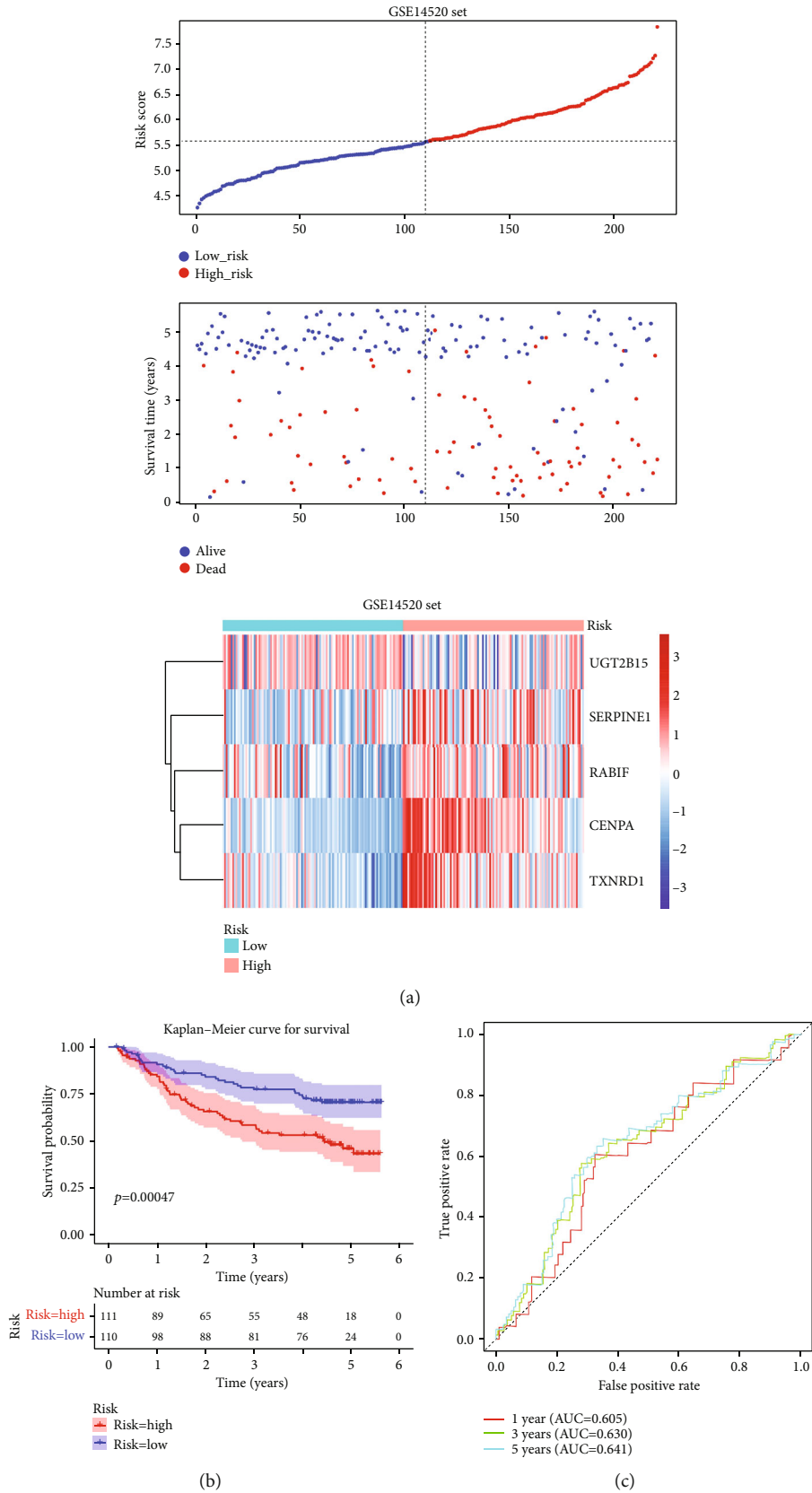
FIGURE 6: Risk model validation is in the GSE14520 dataset. (a) Risk score, survival time, and gene expression heatmaps were plotted in the validation set (GSE14520 dataset). (b) Kaplan-Meier analysis in the validation set (GSE14520 dataset) ($p < 0.001$). (c) The receiver operating characteristic (ROC) curve evaluating the validity of the risk model.

(a)

(b)

(c)
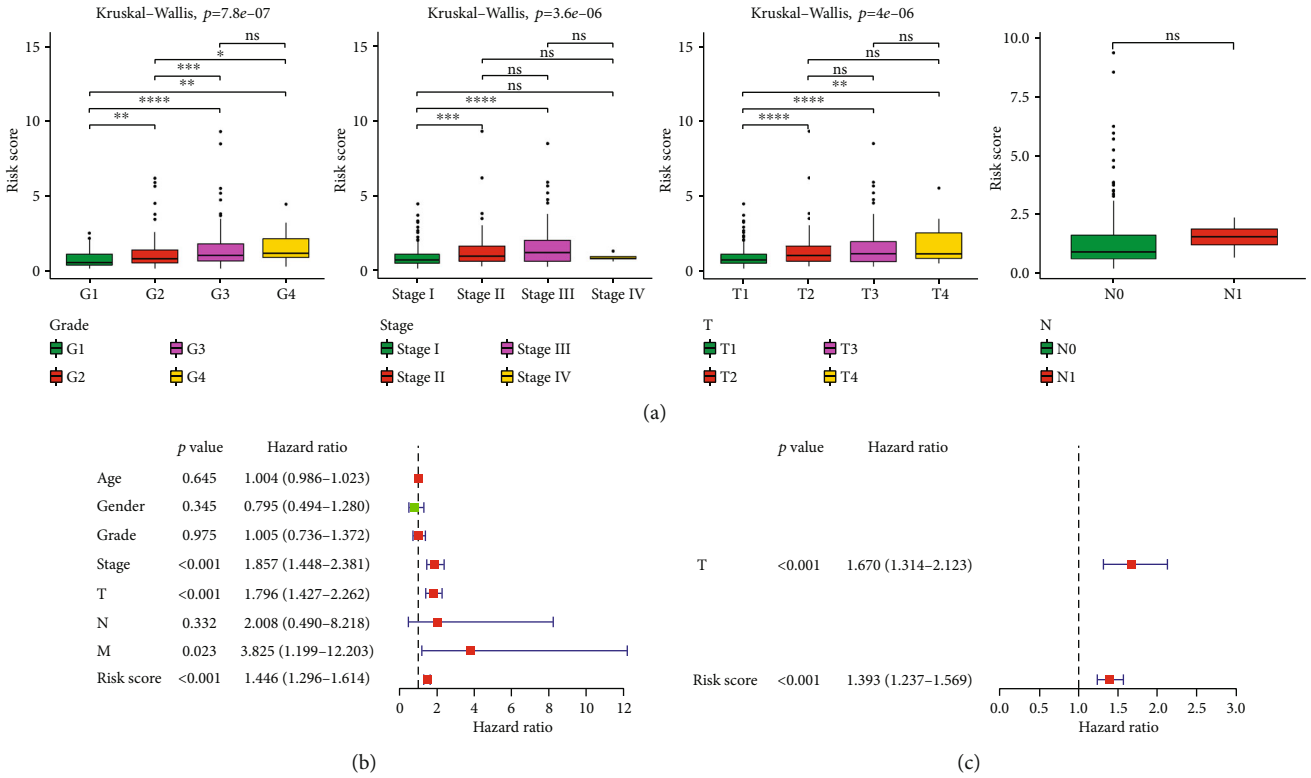
FIGURE 7: Correlation analysis between AREG-related signature and clinicopathological features. (a) Correlation of risk score and clinicopathological features. The abscissa represents clinical traits, and the ordinate represents risk score. $^*p < 0.05$, $^{**}p < 0.01$, $^{***}p < 0.001$, and $^{****}p < 0.0001$. ns: not significant. (b) Forest plots of independent prognostic-univariate Cox results. (c) Forest plots of independent prognostic-multivariate Cox results.

distribution of the intersection data in the Venn graph was analysed using the Phyper function of R language. A significant overlap between the non-DEGs and AREG sets was observed ($p = 2.42e − 46$), indicating that the AREGs tend to be stable between tumor and normal samples.

3.2. Functional and Pathway Enrichment of Different Risk Groups.
From the perspective of the biological roles of the 189 DE-AREGs, a total of 59 GO terms were enriched, including biological process (BP) of 52 terms, cell component (CC) of six terms, and one molecular function (MF) term. GO BP analysis suggested that 189 DE-AREGs were relevant to mitotic nuclear division, regulation of lipid metabolic process, epithelial cell proliferation, etc. (Figure 3(a)). For GO CC analysis, the top three enriched terms were condensed chromosome, centromeric region, and collagen-containing extracellular matrix. For GO MF analysis, 189 DE-AREGs were related to growth factor binding. Furthermore, the KEGG pathway showed enrichment in the insulin resistance pathway (Figure 3(b)).

Furthermore, enrichment analyses of the aforementioned DE-AREGs with different expression trends indicated that the upregulated genes enriched 19 GO terms and downregulated genes enriched two GO terms; however, no KEGG pathway enrichment was observed. Moreover, the downregulated genes annotated in GO terms included core promoter sequence−specific DNA binding and neurotrophin receptor binding of the MF category. The upregulated genes mainly

TABLE 3: Results of independent prognostic-univariate analysis.

ID	HR	HR.95L	HR.95H	p value
Age	1.004326	0.986076	1.022914	0.644558
Gender	0.795005	0.493806	1.279922	0.345073
Grade	1.00493	0.735968	1.372186	0.975314
Stage	1.856679	1.448018	2.380673	0.00000107
T	1.796322	1.42663	2.261814	0.000000629
N	2.007582	0.49043	8.218068	0.332458
M	3.825294	1.199118	12.20303	0.023405
Risk score	1.44637	1.296357	1.613743	0.0000000000395

TABLE 4: Results of independent prognostic-multivariate analysis.

ID	HR	HR.95L	HR.95H	p value
T	1.670126	1.313847	2.123019	0.0000279
Risk score	1.392981	1.237027	1.568598	0.0000000447

enriched in GO terms included epithelial cell proliferation, regulation of lipid metabolic process, response to peptide hormone, urogenital system development, and renal system of BP (Figure S1).

3.3. Construction of an AREG-Related Signature.
The univariate Cox regression analysis was first performed with 189 DE-AREGs, and 72 DE-AREGs were screened (Table S1).

(a)

(b)
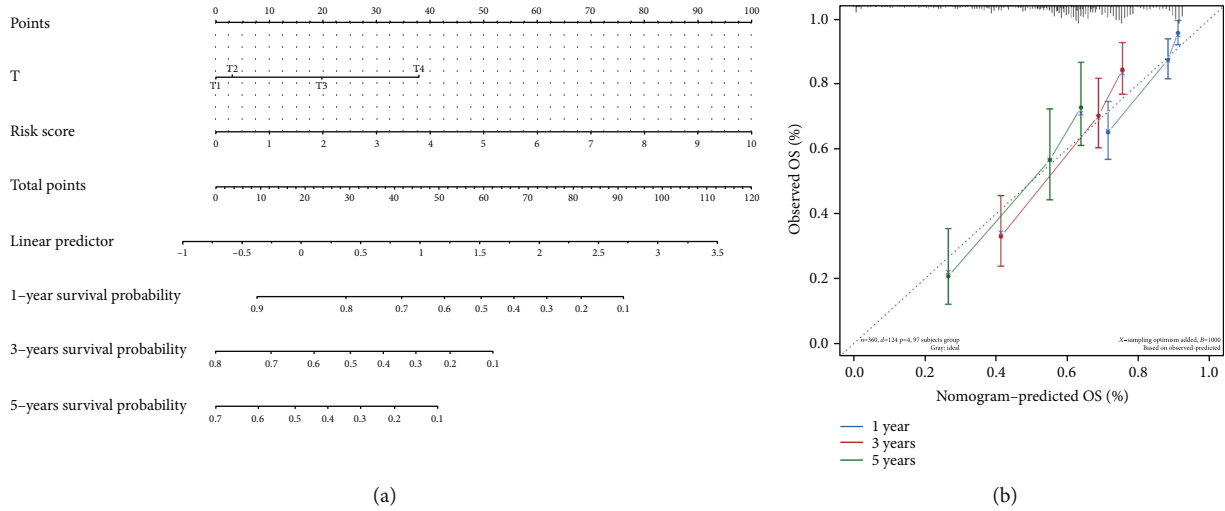
FIGURE 8: Evaluation of the clinical benefit of the risk score. (a) The nomogram to predict the survival rate of patients with hepatocellular carcinoma (HCC). (b) Calibration curves of the nomogram.

(a)

(b)

(c)

(d)
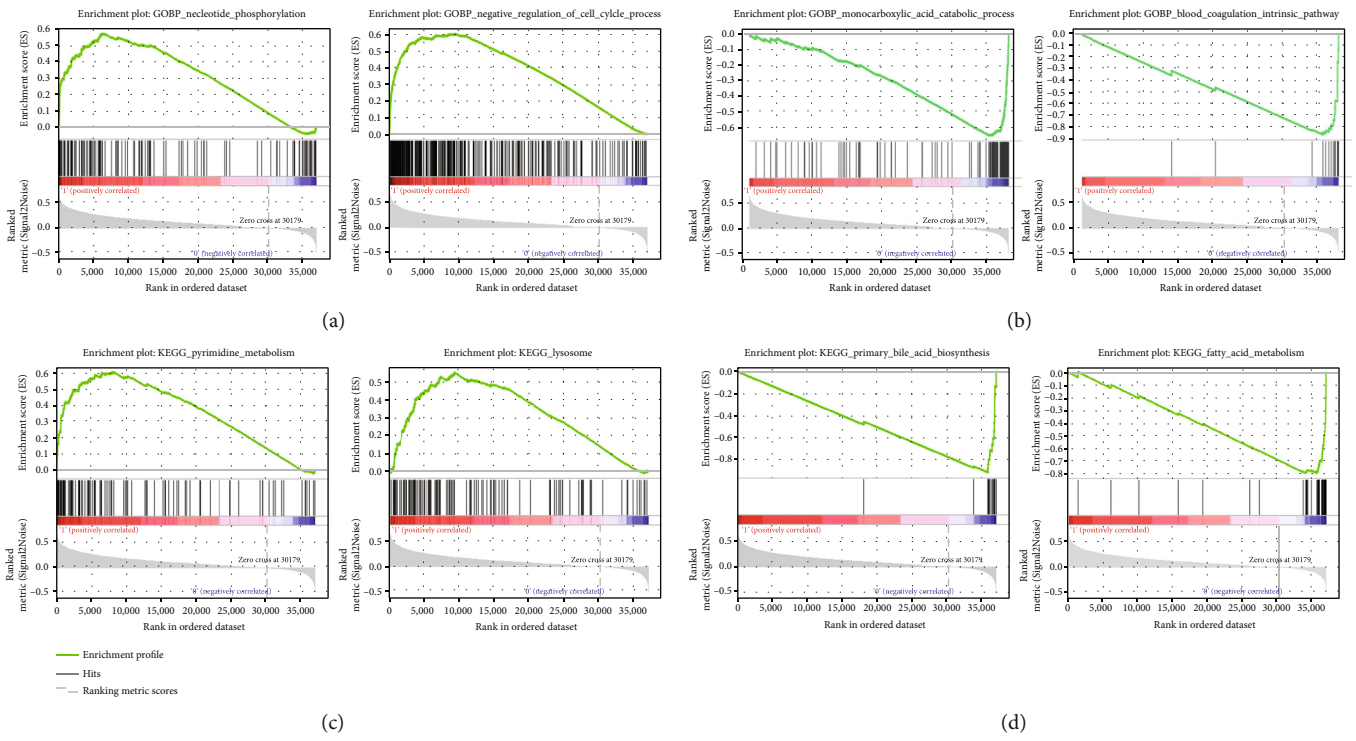
FIGURE 9: Gene set enrichment analysis outcomes in different risk groups. (a) The Top2 GO significant enrichment in the high-risk group. (b) The Top2 GO significant enrichment in the low-risk group. (c) The Top2 KEGG significant enrichment in the high-risk group. (d) The Top2 KEGG significant enrichment in the low-risk group.

Subsequently, the LASSO Cox analysis on the 72 DE-AREGs showed that 13 DE-AREGs were potential prognostic genes at the lambda.min = 0.047 (Figures 4(a) and 4(b)). Moreover, the adopted multivariate Cox analysis identified five 5 signature genes (CENPA, TXNRD1, RABIF, UGT2B15, and SERPINE1) (Table 2 and Figure 4(c)). Furthermore, the five DE-AREG expressions were validated in the GSE14520 and TCGA datasets. The expression levels of *CENPA*, *TXNRD1*, and *RABIF* in the HCC groups were significantly higher than that in the normal groups.

Contrarily, *UGT2B15* and *SERPINE1* were significantly higher in the normal groups compared with the HCC samples (Figure S2).

3.4. Evaluation and Validation of the AREG-Related Signature. Risk score = $0.3501952 \times$ CENPA + $0.295307 \times$ TXNRD1 + $0.2479362 \times$ RABIF + $(-0.0899647) \times$ UGT2B15 + $0.0804323 \times$ SERPINE1. The samples of the training set were divided into the high- (182 HCC samples) and low-risk (181 HCC samples) groups

(a)   (b)

(c)   (d)

(e)

(f)
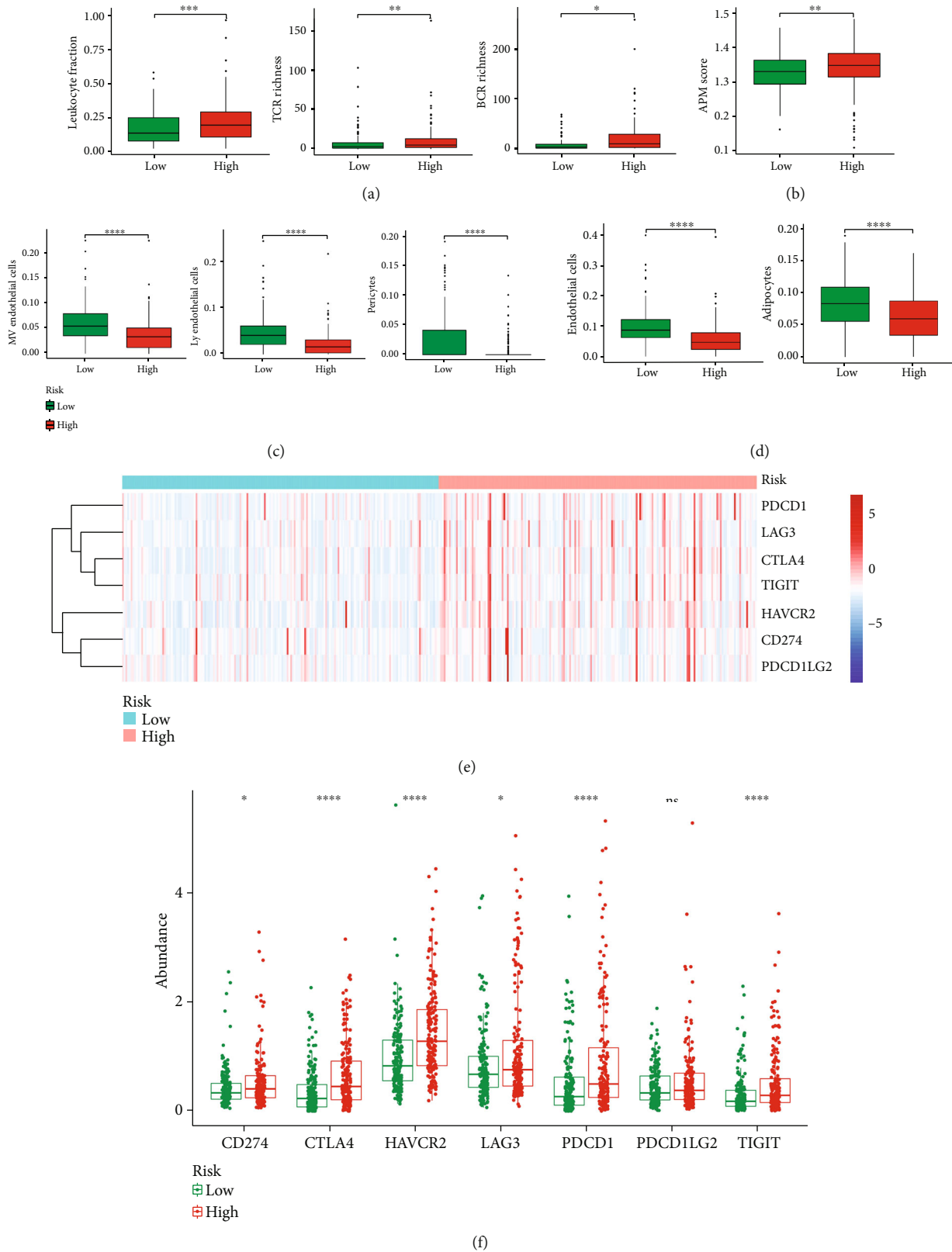
FIGURE 10: Analysis of inflammation and immune response. Differences in inflammatory immune factors (a), APM score (b), vascular cell infiltration (c), and stromal cell infiltration (d) in different risk groups were displayed. (e, f) Heatmap and box plots of immune checkpoint expressions in different risk groups. $^*p < 0.05$, $^{**}p < 0.01$, $^{***}p < 0.001$, and $^{****}p < 0.0001$. ns: not significant.

(a)

(b)

(c)
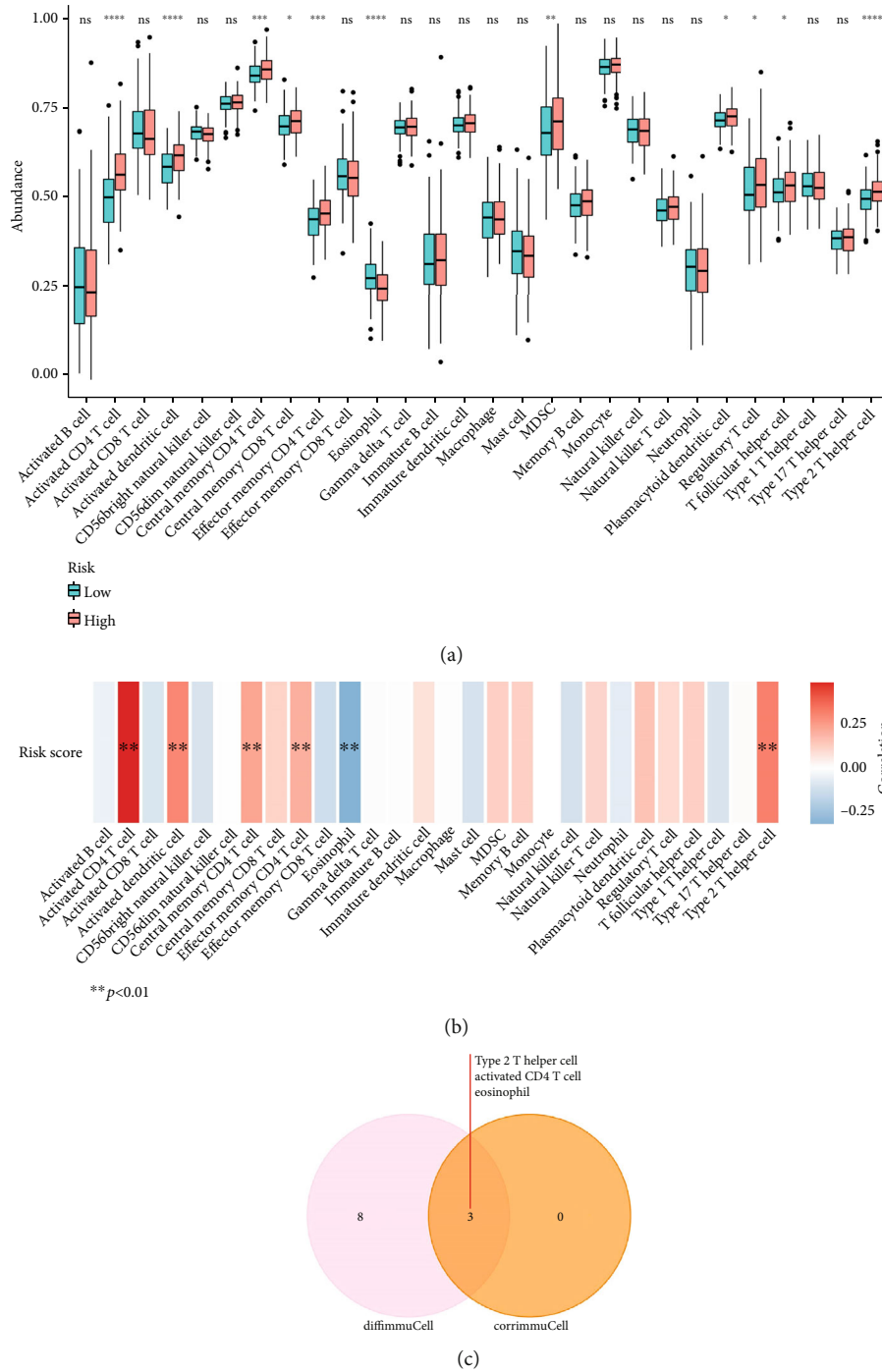
FIGURE 11: Immunoinfiltration analysis. (a) Box plot of the 28 immune cell differences in the two risk groups. (b) Heatmap of immune cell correlation with a risk score. (c) Venn diagram of 11 differentially expressed immune cell types and three immune cell types significantly correlated with risk score ($r > 0.3$). $*p < 0.05$, $**p < 0.01$, $***p < 0.001$, and $****p < 0.0001$. ns: not significant.

(median risk score = 0.9064) (Figure 5(a)). Additionally, the overall survival (OS) of HCC samples showed that a higher risk score was accompanied by poorer OS (Figure 5(b)). Furthermore, the ROC curve revealed that the AUC was greater than 0.6 (Figure 5(c)).

Furthermore, the five DE-AREG prognostic signatures were verified in the GSE14520 dataset. The GSE14520 dataset was also divided into two risk groups (cutoff = 5.581)

(Figure 6(a)). The performance of the K-M analysis and AUC values were per the training set (Figures 6(b) and 6(c)), indicating that the five AREG-related signatures had higher specificity and sensitivity for HCC.

3.5. Independent Prognostic Value of the DE-AREG Prognostic Signature and Construction of a Predictive Nomogram. To estimate the correlations between the

(a)

(b)
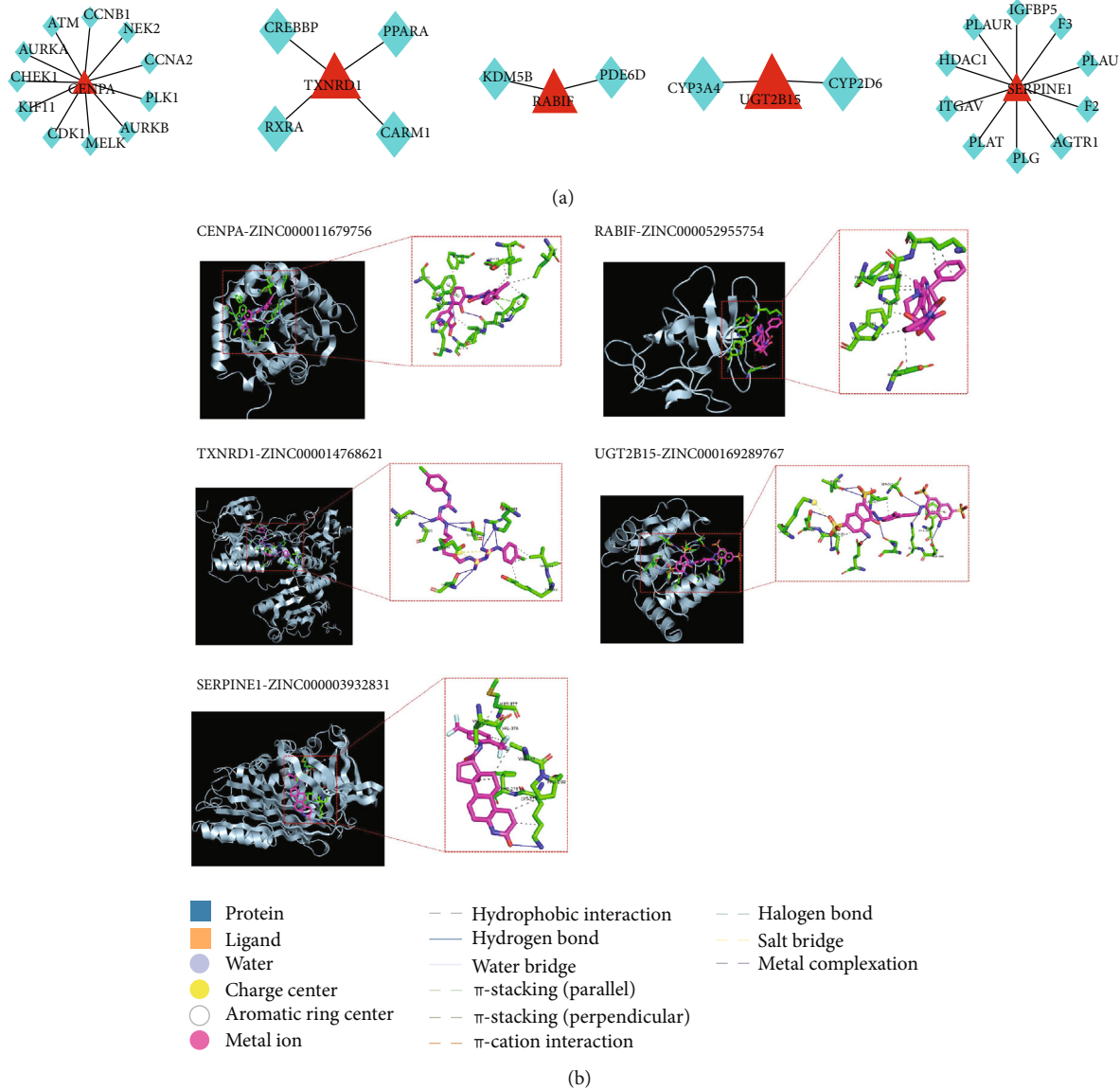
FIGURE 12: Prediction for the potential drugs of biomarkers. (a) Potential drug targets for biomarkers. Red triangles represent biomarkers and green diamonds represent drug targets. (b) Molecular docking complex and element legend.

AREG-related signature and clinicopathological features, the risk score and clinicopathological information were combined. As shown in Figure 7(a), the grade, stage, and T stage were significantly different. Univariate analysis suggested that stage, T/M stage, and risk score were considered essential to the prognosis of HCC ($p < 0.05$) (Table 3 and Figure 7(b)). Additionally, the T stage and risk score had an independent prognostic value for HCC ($p < 0.05$) (Table 4 and Figure 7(c)).

Furthermore, a nomogram was generated with T stage and risk score as the variables (Figure 8(a)), and the C-index of 1, 3, and 5 years indicated that the nomogram performed well (Figure 8(b)).

3.6. GO and KEGG Pathways Enriched in the Two Risk Groups. To explore the biological function of the DEGs between different risk groups, functional and pathway

enrichment was performed. A total of 2242 GO annotations were correlated with high-risk scores (Table S2 and Figure 9(a)), such as nucleotide phosphorylation and negative regulation of the cell cycle process. The low-risk group was found to affect the monocarboxylic acid catabolic process and blood coagulation intrinsic pathway (Table S3 and Figure 9(b)). Moreover, 72 KEGG pathways were enriched in the high-risk group, such as pyrimidine metabolism, cell cycle, and lysosome (Table S4 and Figure 9(c)). A total of 13 KEGG pathways were enriched in the low-risk group, such as primary bile acid biosynthesis, fatty acid metabolism, and retinol metabolism (Table S5 and Figure 9(d)).

3.7. Difference Analyses of Inflammation, Immune, Vascular Cells, and Stromal Cells with Different Risk Scores. Inflammation and immune infiltration were validated to be critical to
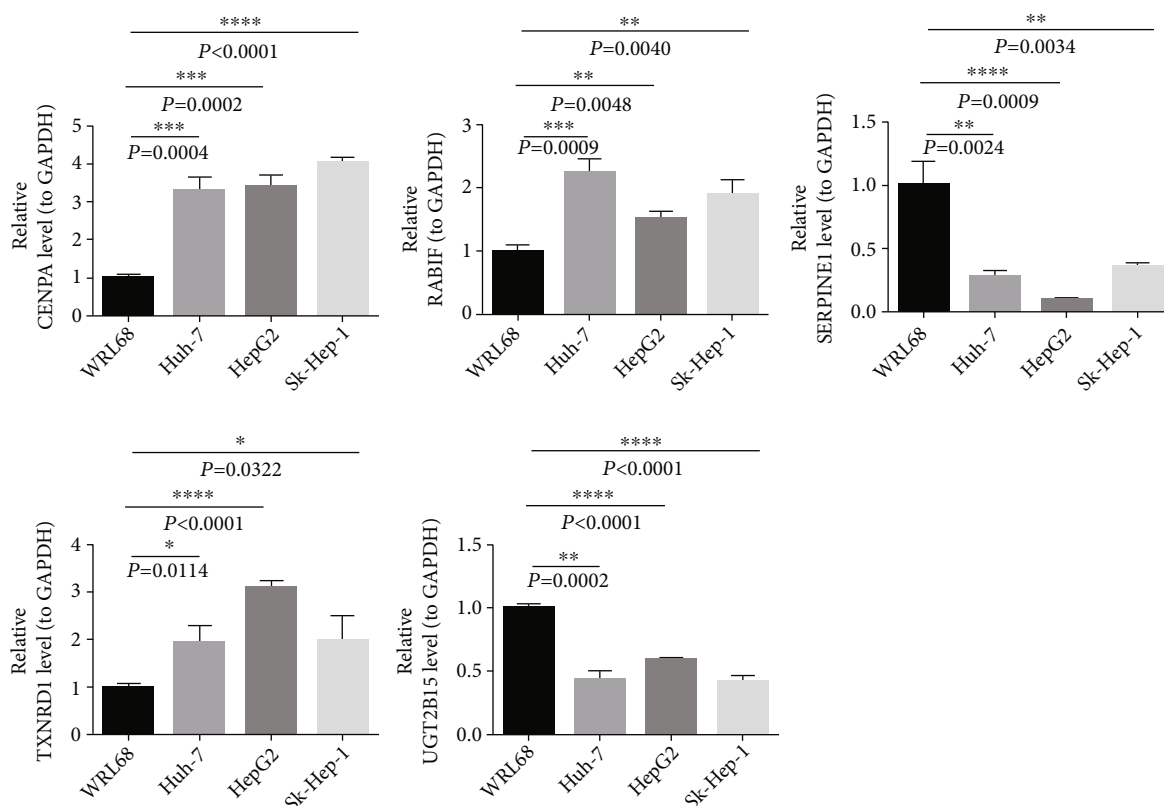
FIGURE 13: Real-time quantitative polymerase chain reaction (RT-qPCR) validation of five signature genes in hepatocellular carcinoma cells and controls.

HCC development. Additionally, T cell and B cell receptor abundance and APM levels were significantly upregulated in the low-risk group (Figures 10(a) and 10(b)). Moreover, in the low-risk group, higher cell infiltrations were observed in microvascular endothelial cells (MVE), lymphatic endothelial cells (lye), pericytes, and stromal cells (Figures 10(c) and 10(d)). The immune checkpoints of PDCD1, CTLA4, HAVCR2, and TIGIT had a significant difference in different risk groups (Figures 10(e) and 10(f)).

Furthermore, the results of immune cell infiltration suggested that 11 immune cells were significantly different such as activated CD4 T cells and eosinophils (Figure 11(a)). Moreover, five cell types, such as activated CD4 T cell and type 2 T helper cell, were positively correlated with risk scores (Figure 11(b)). However, there was a significantly negative correlation between eosinophil and risk score (Figure 11(b)). Finally, activated CD4 T cells, type 2 T helper cells, and eosinophils were identified as key immune cells in different risk groups (Figure 11(c)). Additionally, the hypergeometric distribution of the intersection data in the Venn graph was validated using the Phyper function of R language ($p = 0.05$).

3.8. Potential Drug Prediction. To investigate the potential drugs that regulate signature genes, the predictions were performed based on the Binding DB database and ZINC15 database. In the Binding DB database, 11 drug targets were predicted for CENPA; four drug targets were predicted for

TXNRD1; two drug targets were predicted for RABIF; two drug targets were predicted for UGT2B15; 10 drug targets were predicted for SERPIN1 (Figure 12(a)). In the ZINC15 database, the target drugs of TXNRD1, CENPA, UGT2B15, SERPINE1, and RABIF were ZINC00014768621, ZINC000167289767, ZINC000003932831, and ZINC0000 52955754, respectively (Figure 12(b)).

3.9. Validation of Signature Genes in Cell Lines by Using RT-qPCR. Differences in the expression of the five signature genes between the nontumorigenic hepatocyte cell line (WRL68) and three HCC tumor cell lines (Huh-7, HepG2, and Sk-Hep-1) were compared using RT-qPCR (Figure 13). *UGT2B15* and *SERPINE1* were significantly higher in WRL68 than in HCC cells. However, the mRNA levels of RABIF, CENPA, and TXNRD1 were lower in WRL68 compared with HCC cells.

4. Discussion

Owing to the progressivity of HCC, it is necessary to establish reliable prognostic signatures for HCC diagnosis and treatment. Computational models have recently become an effective adjunct to explore possible carcinogenic factors and biomarkers for HCC [26]. Additionally, several vital proteins were identified that were coded by AU-rich mRNAs, which play a similar role in inflammation and cancer development [4].

For the treatment of HCC, histological grades and gene expression data were utilized to construct a novel signature for the prediction of HCC prognosis [27]. Moreover, immune-related genes and corresponding potential compounds were investigated in HCC [24]. In this study, a five DE-AREG-based prognostic signature was generated and validated. Furthermore, several potential drugs were identified, providing a reference for HCC treatment. Additionally, RT-qPCR results confirmed the expression of the prognostic genes in HCC cell lines.

RNA-seq data in the TCGA-HCC datasets was conducted to investigate biomarkers related to HCC prognosis, wherein a prognostic model comprising CENPA, TXNRD1, RABIF, UGT2B15, and SERPINE1 was constructed. Functional and pathway enrichment analyses of these model genes showed that they could play an important role in the prognosis of patients with HCC using various pathways. Specifically, CENPA (centromere protein A), an essential factor in cell division, acts on centromeres and kinetochores. A study on breast cancer indicated that the functional alteration of the CENPA-related coexpression network can affect and contribute to the development of various cancers by targeting the process of cell cycle progression [28]. Additionally, a study related to HCC prognosis revealed that high expression levels of CENPA were correlated to poor prognosis in patients with HCC [29], which was consistent with this study's findings where CENPA was considered an unfavourable prognostic factor for HCC prognosis. Furthermore, in the current study, the cell cycle-related KEGG pathway was significantly enriched in the high-risk group. The expression of CENPA was also observed to be lower in HCC samples compared to normal samples, indicating that CENPA could play an important role in the prognosis of HCC patients via cell cycle-related pathways. The overexpression of *TXNRD1* (thioredoxin reductase 1) had been reported as a promising therapeutic factor in HCC [30]. Conversely, the lipid peroxidation-related gene *SLC27A5* was found to downregulate TXNRD1 expression and inhibit HCC progression [31]. Notably, the fatty acid metabolism pathway was activated in the low-risk group, indicating that the imbalance between TXNRD1 mRNA expression and fatty acid metabolism regulation could promote poor prognosis in patients with HCC. Furthermore, *RABIF* (RAB interacting factor) was mutated in GTPase Sec4 and was speculated to be involved in cancer cell progression, invasion, and metastasis [32, 33]. The RT-qPCR results also demonstrated the increased expression of RABIF in HCC cell lines. Uridine diphosphate glucuronic acid transferase (UGT) is a crucial phase II metabolism enzyme in the human body, mainly found in liver microsomes. Moreover, studies have demonstrated that the homozygous D85 UGT2B15 (UDP glucuronosyltransferase family 2 member B15) allele genotype could be associated with an increased risk of prostate cancer [34]. In this study, the univariate Cox analysis revealed that UGT2B15 was a favourable prognostic factor. The RT-qPCR analysis also revealed that UGT2B15 mRNA was lower in the three HCC cell lines than that in the control group, indicating the favourable prognostic value of UGT2B15 in HCC. SERPINE1 (serpin family E member 1) could promote the malignant transfor-

mation of chronic hepatitis to HCC by targeting miR-145 [35–37]. Hachim et al. indicated that SERPINE1 is also closely associated with the cell cycle process [38]. Consistently, multivariate Cox results suggested that SERPINE1 was an unfavourable prognostic factor for HCC. Notably, the gene expression results showed that SERPINE1 was expressed lower in HCC samples than in paracancerous tissues, which was contradictory to the multivariate Cox results. Thus, we hypothesised that this phenomenon could be due to the complex mechanism of genes and disease; however, further experimental verification is needed.

Next, we analysed inflammatory and immune-related differences between the risk subgroups associated with the five DE-AREG prognostic models. The results indicated an inconsistent immune microenvironment and inflammatory status between the two risk subgroups. Through ssGSEA analysis of the three essential immune cells, it was revealed that activated CD4 T cell, type 2 T helper cell, and eosinophil have a great relationship with the five DE-AREG prognostic models. First, activated CD4 T cells in HCC could induce the generation of IgG-producing plasma cells with the assistance of macrophages. IgG further inhibited the tumor immune response by producing cytokines [39]. Second, the neddylation pathway was activated in HCC and changed with disease development. Herein, we revealed that an activated neddylation pathway was accompanied by a higher infiltration of Th2 cells. Meanwhile, the immunosuppressive effects of IL-4 and IL-10 secreted by Th2 cells could further regulate tumor growth and metastasis [40, 41]. However, Th2-released cytokines were also influenced by the Th1/Th2 imbalance in patients with HCC [42, 43]. Additionally, it was reported that eosinophils, originally located in the primary cancer cells, could be stimulated by eosinophilic chemokines and transported into the liver to promote cancer development [44, 45]. These findings provided more possibilities by targeting immunotherapy for HCC treatment.

Cui et al. identified five prognosis-related metabolic genes that were involved in the dysregulation of the metabolic microenvironment in the survival prognosis model of patients with HCC, which was constructed using TCGA-LIHC. They also reported on the use of these genes in metabolic therapy [46]. Moreover, based on TCGA-LIHC and GSE14520 datasets, the prognosis model of HCC, which included a nine-gene amino acid metabolism-related risk signature, represented only amino acid metabolisms that cause liver cancer. Meanwhile, amino acid metabolism therapy was also proposed [47]. Shen et al. constructed a ten-immune-related gene risk model to predict the survival of patients with HCC in terms of immune regulation, providing a novel target for the treatment of patients with HCC [48]. In comparison, the five DE-AREG prognostic models in this study present more carcinogenic factors. Additionally, multiangle therapy could be used to guide clinical therapy, such as using multiple types of anticancer drugs based on the five signature gene targets. Moreover, this model could improve the treatment options for patients with HCC.

Currently, the presence of cirrhosis causes a considerable challenge to the surgical treatment of HCC [1, 24]. Liver transplantation has many limitations, such as the lack of

an appropriate liver source or graft rejection [24, 49]. In the treatment of patients with advanced HCC, such as first-line sorafenib and second-line regorafenib, only certain patients exhibited good liver function [50, 51]. Therefore, bioinformatics analysis based on next-generation sequencing is becoming an important method to identify biomarkers and explore therapeutic drugs and pathogenesis. Moreover, ARE genes can reliably predict the OS of patients with HCC, and the prognostic signature was relevant to the inflammation-associated element. However, to provide patients with a better prognosis and aid in personalised targeted therapy, further prospective trials to test the clinical efficacy of the signature should be conducted.

5. Conclusions

Using three cohort profile datasets and integrated bioinformatics analysis, five DE-AREGs were identified and referred to as biomarkers of the inflammation-associated prognostic model in HCC. The novel DE-AREG-based risk scoring system was established for the clinical assessment of patients with HCC.

Data Availability

TCGA-LIHC dataset was downloaded from TCGA database (https://portal.gdc.cancer.gov/), and GSE14520 and GSE54236 were derived from the GEO database (https://www.ncbi.nlm.nih.gov/gds/). 4884 AREGs were downloaded from the Adenylate Uridylate- (AU-) Rich Element Database (ARED, https://brp.kfshrc.edu.sa/ared).

Conflicts of Interest

The authors declare that there are no conflicts of interest regarding the publication of this manuscript.

Acknowledgments

Supplementary Materials

Supplementary 1. Figures S1: Gene Ontology (GO) annotation analysis on the downregulated genes (a) and upregulated genes (b).

Supplementary 2. Figures S2: the gene expression levels of the five DE-AREGs in GSE14520 (a) and TCGA (b) datasets.

Supplementary 3. Table S1: the 72 DE-AREGs were selected using the univariate Cox regression analysis.

Supplementary 4. Table S2: the high-risk top 10 of the Gene Ontology (GO) enrichment analysis.

Supplementary 5. Table S3: the low-risk top 10 of the Gene Ontology (GO) enrichment analysis.

Supplementary 6. Table S4: the high-risk top 10 of the Kyoto Encyclopedia of Genes and Genomes (KEGG) enrichment analysis.

Supplementary 7. Table S5: the low-risk top 10 of the Kyoto Encyclopedia of Genes and Genomes (KEGG) enrichment analysis.

References

[1] J. M. Llovet, A. Burroughs, and J. Bruix, "Hepatocellular carcinoma," *Nature*, vol. 362, no. 9399, pp. 1907–1917, 2003.

[2] R. Mahn, F. Sadeghlar, A. Bartels et al., "Multimodal and systemic therapy with cabozantinib for treatment of recurrent hepatocellular carcinoma after liver transplantation: A case report with long term follow-up outcomes," *Medicine*, vol. 100, no. 38, article e27082, 2021.

[3] D. Dimitroulis, C. Damaskos, S. Valsami et al., "From diagnosis to treatment of hepatocellular carcinoma: an epidemic problem for both developed and developing world," *World Journal of Gastroenterology*, vol. 23, no. 29, pp. 5282–5294, 2017.

[4] K. S. Khabar, "Post-transcriptional control during chronic inflammation and cancer: a focus on AU-rich elements," *Cellular and Molecular Life Sciences*, vol. 67, no. 17, pp. 2937–2955, 2010.

[5] E. Yang, E. van Nimwegen, M. Zavolan et al., "Decay rates of human mRNAs: correlation with functional characteristics and sequence attributes," *Genome Research*, vol. 13, no. 8, pp. 1863–1872, 2003.

[6] C. Y. Chen and A. B. Shyu, "AU-rich elements: characterization and importance in mRNA degradation," *Trends in Biochemical Sciences*, vol. 20, no. 11, pp. 465–470, 1995.

[7] T. Bakheet, M. Frevel, B. R. Williams, W. Greer, and K. S. Khabar, "ARED: human AU-rich element-containing mRNA database reveals an unexpectedly diverse functional repertoire of encoded proteins," *Nucleic Acids Research*, vol. 29, no. 1, pp. 246–254, 2001.

[8] T. Zhang, G. W. Guan, J. Zhang et al., "E2F1-mediated AUF1 upregulation promotes HCC development and enhances drug resistance via stabilization of AKR1B10," *Cancer Science*, vol. 113, no. 4, pp. 1154–1167, 2022.

[9] S. Chowdhury, A. Dijkhuis, S. Steiert, and R. Lutter, "IL-17 attenuates degradation of ARE-mRNAs by changing the cooperation between AU-binding proteins and microRNA16," *PLoS Genetics*, vol. 9, no. 9, article e1003747, 2013.

[10] M. D. Xing, J. Li, M. D. Xing, and J. Li, "A new inflammation-related risk model for predicting hepatocellular carcinoma prognosis," *BioMed Research International*, vol. 2022, Article ID 5396128, 33 pages, 2022.

[11] L. X. Yu, Y. Ling, H. Y. Wang, L. X. Yu, Y. Ling, and H. Y. Wang, "Role of nonresolving inflammation in hepatocellular carcinoma development and progression," *NPJ Precision Oncology*, vol. 2, no. 1, p. 6, 2018.

[12] P. A. Andreasen, R. Egelund, H. H. Petersen, P. A. Andreasen, R. Egelund, and H. H. Petersen, "The plasminogen activation system in tumor growth, invasion, and metastasis," *Cellular and Molecular Life Sciences: CMLS*, vol. 57, no. 1, pp. 25–40, 2000.

[13] M. Schmitt, N. Harbeck, N. Brünner et al., "Cancer therapy trials employing level-of-evidence-1 disease forecast cancer biomarkers uPA and its inhibitor PAI-1," *Expert Review of Molecular Diagnostics*, vol. 11, no. 6, pp. 617–634, 2011.

[14] G. Li, T. Yang, J. Yan, G. Li, T. Yang, and J. Yan, "Cyclooxygenase-2 increased the angiogenic and metastatic potential of

tumor cells," *Biochemical and Biophysical Research Communications*, vol. 299, no. 5, pp. 886–890, 2002.

[15] D. Dolicka, C. Sobolewski, M. Correia de Sousa, M. Gjorgjieva, and M. Foti, "mRNA post-transcriptional regulation by AU-rich element-binding proteins in liver inflammation and cancer," *International Journal of Molecular Sciences*, vol. 21, no. 18, p. 6648, 2020.

[16] G. K. Smyth, "Linear models and empirical Bayes methods for assessing differential expression in microarray experiments," *Statistical Applications in Genetics and Molecular Biology*, vol. 3, no. 1, pp. 1–25, 2004.

[17] C. Chen, H. Chen, Y. Zhang et al., "TBtools: an integrative toolkit developed for interactive analyses of big biological data," *Molecular Plant*, vol. 13, no. 8, pp. 1194–1202, 2020.

[18] G. Yu, L. G. Wang, Y. Han et al., "clusterProfiler: an R package for comparing biological themes among gene clusters," *OMICS*, vol. 16, no. 5, pp. 284–287, 2012.

[19] T. Mosmann, "Rapid colorimetric assay for cellular growth and survival: application to proliferation and cytotoxicity assays," *Journal of Immunological Methods*, vol. 65, no. 1-2, pp. 55–63, 1983.

[20] I. S. Ramsay, S. Ma, M. Fisher et al., "Model selection and prediction of outcomes in recent onset schizophrenia patients who undergo cognitive training," *Schizophrenia Research Cognition*, vol. 11, pp. 1–5, 2018.

[21] J. Wang, J. Yang, J. Wang, and J. Yang, "Identification of significant genes with a poor prognosis in skin cutaneous malignant melanoma based on a bioinformatics analysis," *Annals of Translational Medicine*, vol. 10, no. 8, p. 448, 2022.

[22] P. J. Heagerty, T. Lumley, M. S. Pepe, P. J. Heagerty, T. Lumley, and M. S. Pepe, "Time-dependent ROC curves for censored survival data and a diagnostic marker," *Biometrics*, vol. 56, no. 2, pp. 337–344, 2000.

[23] D. Aran, Z. Hu, A. J. Butte, D. Aran, Z. Hu, and A. J. Butte, "xCell: digitally portraying the tissue cellular heterogeneity landscape," *Genome Biology*, vol. 18, no. 1, p. 220, 2017.

[24] K. J. Livak, T. D. Schmittgen, K. J. Livak, and T. D. Schmittgen, "Analysis of relative gene expression data using real-time quantitative PCR and the 2(-delta delta C(T)) method," *Methods*, vol. 25, no. 4, pp. 402–408, 2001.

[25] G. M. Liu, H. D. Zeng, C. Y. Zhang, and J. W. Xu, "Identification of a six-gene signature predicting overall survival for hepatocellular carcinoma," *Cancer Cell International*, vol. 19, p. 138, 2019.

[26] J. Zhang, G. Chen, J. Zhang, P. Zhang, and Y. Ye, "Construction of a prognostic model based on nine immune-related genes and identification of small molecule drugs for hepatocellular carcinoma (HCC)," *American Journal of Translational Research*, vol. 12, no. 9, pp. 5108–5130, 2020.

[27] H. Zhang, R. Liu, L. Sun et al., "A reliable prognostic model for HCC using histological grades and the expression levels of related genes," *Journal of Oncology*, vol. 2021, Article ID 9512774, 9 pages, 2021.

[28] X. Sun, P. L. Clermont, W. Jiao et al., "Elevated expression of the centromere protein-A(CENP-A)-encoding gene as a prognostic and predictive biomarker in human cancers," *International Journal of Cancer*, vol. 139, no. 4, pp. 899–907, 2016.

[29] Y. Zhang, L. Yang, J. Shi, Y. Lu, X. Chen, and Z. Yang, "The oncogenic role of CENPA in hepatocellular carcinoma development: evidence from bioinformatic analysis," *BioMed Research International*, vol. 2020, Article ID 3040839, 8 pages, 2020.

[30] S. Hua, Y. Quan, M. Zhan, H. Liao, Y. Li, and L. Lu, "miR-125b-5p inhibits cell proliferation, migration, and invasion in hepatocellular carcinoma via targeting TXNRD1," *Cancer Cell International*, vol. 19, no. 1, p. 203, 2019.

[31] Q. Z. Gao, G. J. Zhang, Y. Q. Zheng et al., "SLC27A5 deficiency activates NRF2/TXNRD1 pathway by increased lipid peroxidation in HCC," *Cell Death and Differentiation*, vol. 27, no. 3, pp. 1086–1104, 2020.

[32] J. L. Burton, M. E. Burns, E. Gatti, G. J. Augustine, and P. De Camilli, "Specific interactions of Mss4 with members of the Rab GTPase subfamily," *The EMBO Journal*, vol. 13, no. 23, pp. 5547–5558, 1994.

[33] P. Thaw, N. J. Baxter, A. M. Hounslow, C. Price, J. P. Waltho, and C. J. Craven, "Structure of TCTP reveals unexpected relationship with guanine nucleotide-free chaperones," *Nature Structural Biology*, vol. 8, no. 8, pp. 701–704, 2001.

[34] S. L. MacLeod, S. Nowell, J. Plaxco, and N. P. Lang, "An allele-specific polymerase chain reaction method for the determination of the D85Y polymorphism in the human UDP-glucuronosyltransferase 2B15 gene in a case-control study of prostate cancer," *Annals of Surgical Oncology*, vol. 7, no. 10, pp. 777–782, 2000.

[35] K. Matsuzaki, M. Murata, K. Yoshida et al., "Chronic inflammation associated with hepatitis C virus infection perturbs hepatic transforming growth factor beta signaling, promoting cirrhosis and hepatocellular carcinoma," *Hepatology*, vol. 46, no. 1, pp. 48–57, 2007.

[36] A. Boye, H. Kan, C. Wu et al., "MAPK inhibitors differently modulate TGF-β/Smad signaling in HepG2 cells," *Tumour Biology*, vol. 36, no. 5, pp. 3643–3651, 2015.

[37] L. M. Li, C. Chen, R. X. Ran et al., "Loss of TARBP2 drives the progression of hepatocellular carcinoma via miR-145-SERPINE1 axis," *Frontiers in Oncology*, vol. 11, article 620912, 2021.

[38] M. Y. Hachim, N. M. Elemam, R. K. Ramakrishnan et al., "Derangement of cell cycle markers in peripheral blood mononuclear cells of asthmatic patients as a reliable biomarker for asthma control," *Scientific Reports*, vol. 11, article 11873, 2021.

[39] Y. Wei, X. M. Lao, X. Xiao et al., "Plasma cell polarization to the immunoglobulin g phenotype in hepatocellular carcinomas involves epigenetic alterations and promotes hepatoma progression in mice," *Gastroenterology*, vol. 156, no. 6, pp. 1890–904.e16, 2019.

[40] A. Mantovani, P. Allavena, A. Sica, and F. Balkwill, "Cancer-related inflammation," *Nature*, vol. 454, no. 7203, pp. 436–444, 2008.

[41] H. L. Lee, J. W. Jang, S. W. Lee et al., "Inflammatory cytokines and change of Th1/Th2 balance as prognostic indicators for hepatocellular carcinoma in patients treated with transarterial chemoembolization," *Scientific Reports*, vol. 9, no. 1, p. 3260, 2019.

[42] L. Ji, J. Gu, L. Chen et al., "Changes of Th1/Th2 cytokines in patients with primary hepatocellular carcinoma after ultrasound-guided ablation," *International Journal of Clinical and Experimental Pathology*, vol. 10, no. 8, pp. 8715–8720, 2017.

[43] L. Zhou, L. Zhang, S. Chen et al., "Elevated neddylation pathway promotes Th2 cells infiltration by transactivating STAT5A in hepatocellular carcinoma," *Frontiers in Oncology*, vol. 11, article 709170, 2021.

[44] S. I. Wasserman, E. J. Goetzl, L. Ellman et al., "Tumor-associated eosinophilotactic factor," *The New England Journal of Medicine*, vol. 290, no. 8, pp. 420–424, 1974.

[45] H. S. Kwak, Y. M. Han, J. M. Lee, H. S. Kwak, Y. M. Han, and J. M. Lee, "Focal eosinophilic infiltration of the liver mimicking hepatocellular carcinoma: case reports," *Clinical Imaging*, vol. 28, no. 1, pp. 36–39, 2004.

[46] L. J. Cui, H. A. Xue, Z. T. Wen, Z. H. Lu, Y. F. Liu, and Y. Zhang, "Prognostic roles of metabolic reprogramming-associated genes in patients with hepatocellular carcinoma," *Aging*, vol. 12, no. 21, pp. 22199–22219, 2020.

[47] Y. J. Zhao, J. L. Zhang, S. H. Wang, Q. Q. Jiang, and K. S. Xu, "Identification and validation of a nine-gene amino acid metabolism-related risk signature in HCC," *Frontiers in Cell and Development Biology*, vol. 9, article 731790, 2021.

[48] B. Shen, G. Zhang, Y. Liu, J. Wang, and J. Jiang, "Identification and analysis of immune-related gene signature in hepatocellular carcinoma," *Genes*, vol. 13, p. 1834, 2022.

[49] V. Mazzaferro, E. Regalia, R. Doci et al., "Liver transplantation for the treatment of small hepatocellular carcinomas in patients with cirrhosis," *The New England Journal of Medicine*, vol. 334, no. 11, pp. 693–700, 1996.

[50] J. M. Llovet, S. Ricci, V. Mazzaferro et al., "Sorafenib in advanced hepatocellular carcinoma," *The New England Journal of Medicine*, vol. 359, no. 4, pp. 378–390, 2008.

[51] N. Mir, A. Jayachandran, B. Dhungel, R. Shrestha, and J. C. Steel, "Epithelial-to-mesenchymal transition: a mediator of sorafenib resistance in advanced hepatocellular carcinoma," *Current Cancer Drug Targets*, vol. 17, no. 8, pp. 698–706, 2017.

Research Article

Comprehensive Analysis of the Expression, Prognostic Value, and Immune Infiltration Activities of GABRD in Colon Adenocarcinoma

Fakun Huang,[1] Zhengyang Wang,[2] Liyue Zhu,[2] Changqing Lin,[2] and Jia-xing Wang [1]

[1]*Department of Gastrointestinal Surgery, The First Affiliated Hospital of Fujian Medical University, Fujian, China*
[2]*Fujian Medical University, Fuzhou, Fujian, China*

Correspondence should be addressed to Jia-xing Wang; wjs581026@sina.com

Colon adenocarcinoma (COAD) is one of the tumors with the highest mortality rates. It is of the utmost significance to make an accurate prognostic assessment and to tailor one's treatment to the specific needs of the patient. Multiple lines of evidence point to the possibility that genetic variables and clinicopathological traits are connected to the onset and development of cancer. In the past, a number of studies have revealed that gamma-aminobutyric acid type A receptor subunit delta (GABRD) plays a role in the advancement of a number of different cancers. However, its function in COAD was rarely reported. In this study, we analyzed TCGA datasets and identified 29 survival-related differentially expressed genes (DEGs) in COAD patients. In particular, GABRD expression was noticeably elevated in COAD specimens. There was a correlation between high GABRD expression and an advanced clinical stage. According to the results of the survival tests, patients whose GABRD expression was high had a lower overall survival time and progression-free survival time than those whose GABRD expression was low. GABRD expression was found to be an independent predictive predictor for overall survival, as determined by multivariate COX regression analysis. Additionally, the predictive nomogram model can accurately predict the fate of individuals with COAD. In addition, we observed that GABRD expressions were positively associated with the expression of T cells regulatory (Tregs), macrophages M0, while negatively associated with the expression of T cells CD8, T cells follicular helper, macrophages M1, dendritic cells activated, eosinophils, and T cells CD4 memory activated. The IC50 of BI-2536, bleomycin, embelin, FR-180204, GW843682X, LY317615, NSC-207895, rTRAIL, and VX-11e was higher in the GABRD high-expression group. In conclusion, we have shown evidence that GABRD is a novel biomarker that is connected with immune cell infiltration in COAD and may be utilized to predict the prognosis of COAD patients.

1. Introduction

Colon adenocarcinoma (COAD) ranks third and fourth place in the rankings of cancer incidence and mortality all over the world, respectively [1]. It is well known that variables such as dietary choices, age, obesity, smoking, and a lack of physical activity are risk factors for COAD [2, 3]. The prevalence of COAD varies greatly from nation to nation. It is believed that a number of different causes are responsible for this variation in occurrence [4, 5]. To be more specific, among other things, socioeconomic status is important, with a poor socioeconomic level being related

to an increased risk of developing COAD [6, 7]. The death rate associated with COAD has declined by around 35% from 1990 to 2007, and it is presently down approximately 50% from its highest mortality rate. This decline can be attributed to effective screening techniques, early interventions, and improved treatment choices. However, it is important to highlight that the decrease in overall mortality from COAD may have obscured the death rate for young adult patients with COAD [8, 9]. Despite the fact that target therapies, chemotherapy, and surgery have considerably improved the overall survival of COAD patients, around half of all COAD patients will eventually develop distant

metastases, which is also the most common reason why treatments do not work [10, 11]. If the tumor has metastasized to other organs, the 5-year mortality rate declines drastically to 8.1%. Biomarkers, such as the microsatellite instability state, the BRAF mutation state, and the RAS mutation state, have been utilized to assist in the identification of patients who are at an increased risk of the progression or recurrence of their tumors [12, 13]. As a consequence of this, one of the primary focuses of COAD research has shifted to the identification of molecular abnormalities in COAD patients.

The process of tumorigenesis is intimately connected to the properties of cancer cells in and of themselves, and it is an essential component of the immune system [14, 15]. Immune cells serve a vital function in immune surveillance and are critical components of the tumor microenvironment (TME) [16]. Tumor-infiltrating lymphocytes (TILs), myeloid-derived suppressor cells (MDSCs), tumor-associated macrophages (TAMs), and regulatory T cells (Tregs) are all components of the immunosuppressive microenvironment that have recently been shown to predict poorer outcomes in solid tumors like melanoma, breast, lung, ovarian, bladder, prostate, and renal cancer [17, 18]. Immunotherapy is currently considered a typical component of treatment for a variety of solid tumors. This is due to the fact that the immune system shows a different status in tumor patients and is inexorably related to the formation of tumors. High levels of stromal cells and immune cell infiltration are present in COAD at an early stage. Monoclonal antibodies, checkpoint inhibitors, therapeutic vaccines, adoptive cell therapy, adjuvant immunotherapy, and cytokines and oncolytic virus treatments are the six groups that make up anticancer immunotherapeutic methods [19, 20]. However, the inadequate immune response has been a problem for a long time, particularly for checkpoint inhibitors targeting PD-1 and PD-L1s in COAD [21, 22]. This is especially true in COAD. In particular, the use of ICIs, which have been shown to have little to no therapeutic efficacy in the majority of patients with metastatic COAD, in view of the fact that there are presently no drugs that have been proven to be successful and the fact that COAD is related to low rates of survival, immunosuppressive mechanisms that occur inside the tumor microenvironment may offer intriguing targets for future immunotherapy [23, 24]. This is especially relevant when considering the context of the current situation. Therefore, defining the immunophenotype of tumor-immune interactions and finding novel indicators and therapeutic options for COAD are both essential.

Gamma-aminobutyric acid type A receptor subunit delta (GABRD) is a ligand-gated ion channel-type receptor that has been linked to a wide range of neurological and psychiatric disease-related symptoms as well as the progression of cancer [25]. Recent research has shed light on the potential functional functions that GABRD played in the development of malignancies. For instance, Zhang et al. reported that patients who have IDH WT low-grade glioma and have GABRD expression on their tumors could benefit from its use as a possible independent prognostic marker. During this time, its expression was shown to have a negative corre-

lation with the degree of TIM, which may assist to explain the beneficial conclusion of the survival analysis. It is possible that Cg13916816 is an important CpG site that influences GABRD expression in IDH wild-type low-grade gliomas [26]. Sawaki et al. reported that having a high level of GABRD mRNA expression in primary human gastric cancer tissue was related to a poor prognosis. In comparison to the expression of control siRNA, the expression of siGABRD in gastric cancer cells resulted in a considerable reduction of cellular proliferation and invasion, as well as an increase in apoptosis. The growth of gastric cancer cells was suppressed in vitro by anti-GABRD polyclonal antibodies, which also led to a reduction in the size of peritoneal tumor nodules in the mouse xenograft model. It has been suggested that GABRD may be a viable therapeutic target for gastric cancer since its expression is increased in gastric cancer tissue and it is related to a poor prognosis [27]. In colorectal cancer, GABRD has been hypothesized to have a role similar to that of a tumor promoter in a previous study [28]. On the other hand, the clinical relevance of GABRD and its connection with TME were only infrequently recorded.

2. Materials and Methods

2.1. Patient Samples.
The TCGA website was accessed in order to retrieve the mRNA expression data as well as the pertinent clinical information for COAD patients. It is now being gathered that there are 41 normal tissues and 480 COAD tissues. Patients from the TCGA who were included in later research but lacked necessary clinical information were excluded. The following clinicopathological features of patients were recorded: age, gender, and stage.

2.2. Pan-Cancer Analysis.
The ONCOMINE database is an integrated online data-mining platform that offers a comprehensive examination of the expression of the genome across various tumor samples as well as normal control samples. In the course of our research, we compared the levels of GABRD transcription found in COAD samples to those found in normal neighboring tissues. The level of statistical significance was determined to be attained when p was less than 0.05, the fold change (FC) was fixed at 2, and the cutoff for statistical significance was established at 10%.

2.3. Differential Expression Analysis.
In order to examine the gene expression matrix for differences between COAD samples and normal colon samples, the limma software was utilized. $|\log 2(FC)| > 2$ and a false discovery rate (FDR) of less than 0.05 were required in order to classify genes as differentially expressed genes (DEGs).

2.4. Survival Assays according to GABRD Expressions in COAD.
After classifying TCGA-COAD patients into high-expression and low-expression groups according to the levels of each GABRD, the differences were analyzed using the Kaplan-Meier methods, taking into consideration the survival information revealed by the "Surv_cutpoint" function in the survminer R package [29]. An investigation into whether or not there was a link exists between the OS

features of COAD patients and the expressions of each GABRD was carried out by employing the "survival" package to conduct univariate assays. In order to determine whether or not these variables may be considered independent predictors of OS, multivariate assays were carried out with the "survival" package.

2.5. Functional Enrichment Analysis. Patients diagnosed with COAD who participated in the TCGA were classified into high and low GABRD expression groups, respectively, based on the median expression of GABRD expression. The DEG analysis between these two groups was carried out with the help of the R software DESeq2, and the criterion for DEGs was determined to be an adjusted p value of less than 0.05 and a log2-fold-change (FC) of more than 1. Spearman's correlation analysis was utilized to examine the degree of overlap that exists between the expression of the top 10 DEGs and GABRD. The "GOplot R" program was used to carry out functional enrichment studies on the DEGs. These analyses included Gene Ontology (GO) and Kyoto Encyclopedia of Genes and Genomes (KEGG) analyses. The GSEA was performed with the R package cluster-Profiler, and statistically substantially enriched function or pathway words were considered to have an adjusted p value of less than 0.05 and a false discovery rate of less than 0.25 [30].

2.6. Nomogram Construction. Combining the findings of the genetic risk score model with clinical characteristics led to the development of a nomogram that was able to accurately forecast the 3- and 5-year OS of COAD. The calibration plot was used to evaluate the nomogram's ability to make accurate predictions. The area under the curve (AUC) was used to analyze the time-dependent sensitivities and specificities of the nomogram for both the 3-year and 5-year OS ROC curves. R was the statistical program of choice for all of the statistical studies that were conducted. The rms package was used to create the nomogram and calibration plots, and the timeROC package was used to conduct the analysis of the time-dependent ROC curve. Both packages are part of the R program. The Hmisc package of the R program was used to conduct comparisons of the C-index between the nomogram and the staging systems developed by the American Joint Committee on Cancer. If the p values were lower than 0.05, then the null hypothesis that there was no difference was rejected.

2.7. Analysis of the Relative Proportions of Tumor-Infiltrating Immune Cells (TIICs) in COAD Tissues. The CIBERSORT deconvolution technique was utilized in order to evaluate the TIICs present in COAD samples that were taken from the TCGA cohort [31]. Using the CIBERSORT platform, we were able to derive the gene expression signature matrix, consisting of 22 TIICs. The matrix data of gene expression levels were compared with those of the signature matrix of 22 TIICs from the CIBERSORT platform. This p value serves as a measure of confidence in the data that was collected. Inferred proportions of TIICs were evaluated by CIBERSORT, and when the criterion of $p < 0.05$ was met, the find-

ings of those evaluations were deemed to be accurate. Because of this, the only samples that were considered eligible for further analysis were those with a CIBERSORT p value of less than 0.05. In addition to that, the default setting for the signature matrix's number of permutations was set to 100.

2.8. Immunoassay. We analyzed the link between GABRD expression and TILs by using the data from TIMER and TCGA. This allowed us to evaluate whether or not there was a connection between GABRD and TILs. In order to further investigate the impact that GABRD has on TILs, the interaction between GABRD and immunological checkpoints in each of the three groups was investigated. The tumor immune dysfunction and exclusion (TIDE) method was used to provide a prediction on the potential ICI response.

2.9. Drug Sensitivity Prediction. For the purpose of predicting the IC50 of chemotherapeutic medications, the "pRRo-phetic" R package was utilized. The IC50 is a figure that reflects how efficient a substance is at blocking particular biological or biochemical processes.

2.10. Statistical Analysis. Statistical analyses were performed using R software v3.5.0 (R Foundation for Statistical Computing, Vienna, Austria) and GraphPad Prism v7.00 (GraphPad Software Inc., USA). The data were put through several statistical tests that are considered to be conventional. The FDR approach was used to make adjustments for the multiple testing. p values were two-sided, and a value of less than 0.05 was regarded as statistically significant.

3. Results

3.1. Identification of the Survival-Related DEGs in COAD Patients. Firstly, we compared the DEGs of COAD specimens and nontumor specimens against one another. As can be seen in Figure 1(a), we identified 2088 DEGs in COAD specimens, comprising 1000 genes with a downregulation and 1088 genes with an upregulation. After that, we carried out survival tests and located 309 genes associated with the process of survival. A Venn diagram was used to display the genes that overlapped one another (Figure 1(b)). The heat map displayed the expression pattern of 29 genes that overlapped one another (Figure 1(c)). To further explore the potential function of the critical 29 genes, we performed GO analysis, and the results indicated that 29 genes were mainly enriched in muscle contraction, muscle system process, acto-myosin structure organization, synaptic vesicle, sarcomere, exocytic vesicle, receptor-ligand activity, signaling receptor activator activity, and G protein-coupled receptor binding (Figure 1(d)). KEGG assays suggested that 29 genes were mainly associated with epithelial cell signaling in *Helicobacter pylori* infection (Figure 1(e)). Moreover, we performed DO assays and found that 29 genes were mainly associated with obstructive lung disease, lung disease, preeclampsia, allergic rhinitis, and nasal cavity disease (Figure 1(f)).
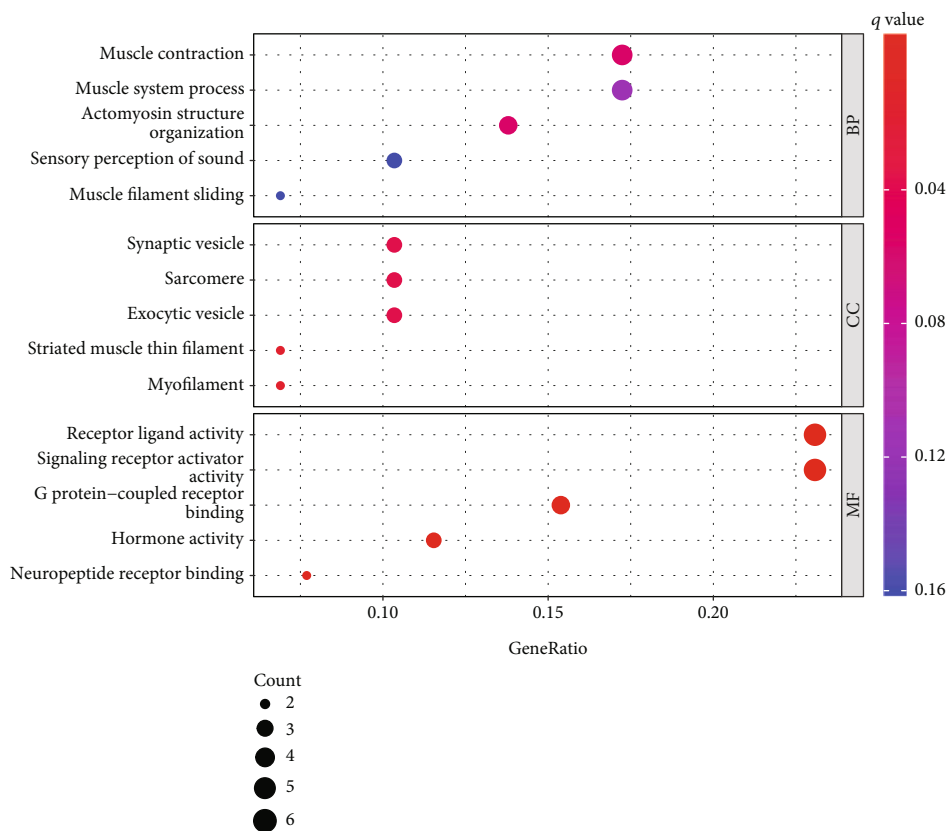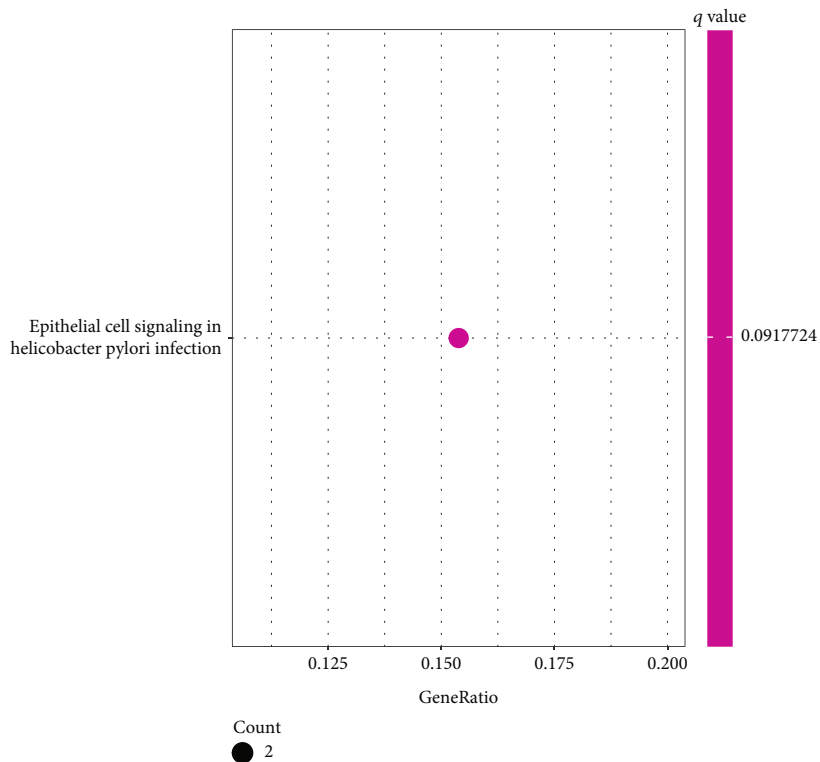
(a)

(b)

(c)

Figure 1: Continued.

(d)

(e)

Figure 1: Continued.

(f)
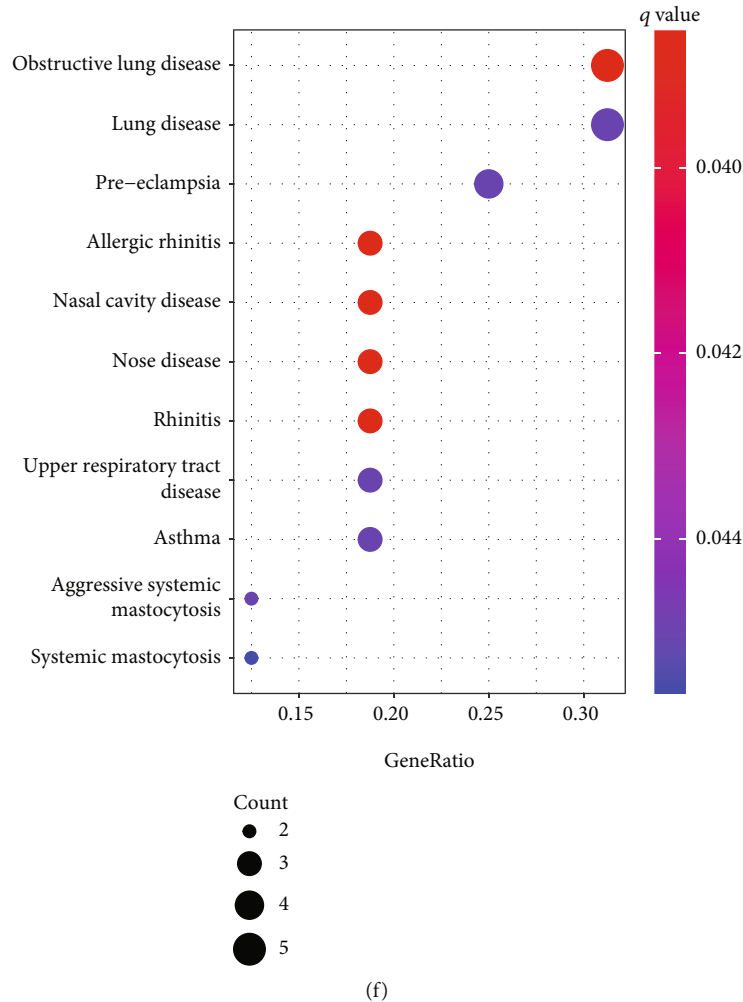
FIGURE 1: Identification of the survival-related DEGs in COAD patients. (a) Volcano plot of 2088 DEGs in COAD specimens, including 1000 downregulated genes and 1088 upregulated genes. (b) Venn diagram showed 29 survival-related DEGs in COAD. (c) The expressing pattern of 29 survival-related DEGs in COAD shown in heat map. (d) Bubble graph for GO enrichments. (e) Barplot graph for KEGG pathways. (f) Disease ontology enrichment analysis of the 29 survival-related DEGs in COAD.

3.2. GABRD Expression in COAD and Normal Tissues. Then, we used those 29 genes to do a search in the database known as "PubMed," and we discovered that several of those genes had been investigated in the context of a variety of malignancies, including COAD. On the other hand, very little information on the expression and function of GABRD in COAD has been documented. As a result, we concentrated on GABRD. To begin, we carried out pan-cancer tests and discovered that GABRD displayed a dysregulated level in a wide variety of cancers. This led us to hypothesize that it may play a role in the growth of malignancies as a regulator (Figure 2(a)). Importantly, we showed that GABRD expression was markedly elevated in COAD tissues compared with nontumor specimens (Figures 2(b) and 2(c)). The purpose of this study was to investigate the diagnostic utility of GABRD expression in COAD patients. To do so, we carried out an ROC curve analysis, which revealed that GABRD was a potential indicator for distinguishing COAD specimens from nontumor specimens, with an area under the curve (AUC) of 0.969 (Figure 2(d)).

3.3. The Prognostic Value of GABRD Expression in COAD Patients. To determine the relevance of GABRD expression to clinical practice, we analyzed associations between GABRD levels and other clinical factors in COAD patients. We discovered that COAD patients above the age of 65 had significantly higher levels of GABRD expression than COAD patients under the age of 65 (Figure 3(a)). On the other hand, we did not find any discernible differences in the GABRD expression of male patients compared to female patients (Figure 3(b)). Importantly, we identified a correlation between high GABRD expression and advanced clinical stage in COAD patients (Figures 3(c)–3(f)). The use of a heat map was utilized in order to demonstrate the relationship between GABRD expression and several clinical variables (Figure 3(g)). The prognostic value of GABRD expression in COAD patients was investigated further, and the results of the Kaplan-Meier survival curves indicated that patients with high GABRD expression showed poorer overall survival (Figure 4(a) $p = 0.002$) and progression-free survival (Figure 4(b) $p = 0.002$) than patients with low
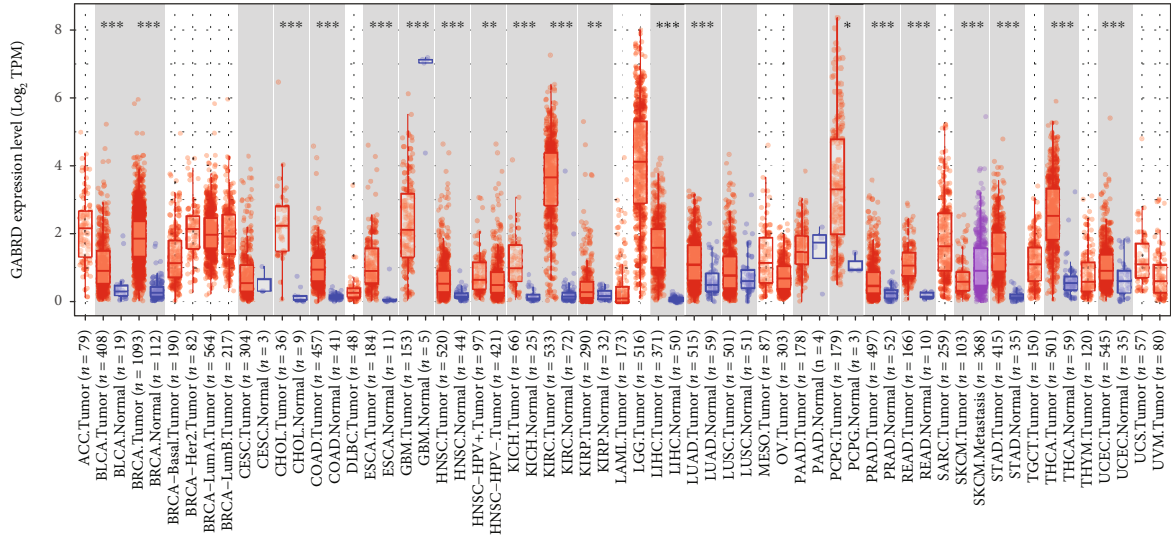
(a)
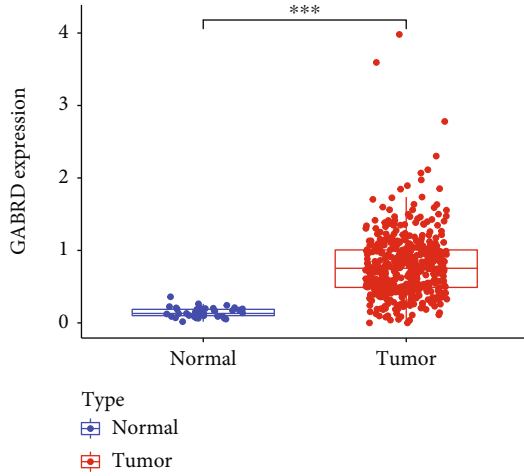
(b)
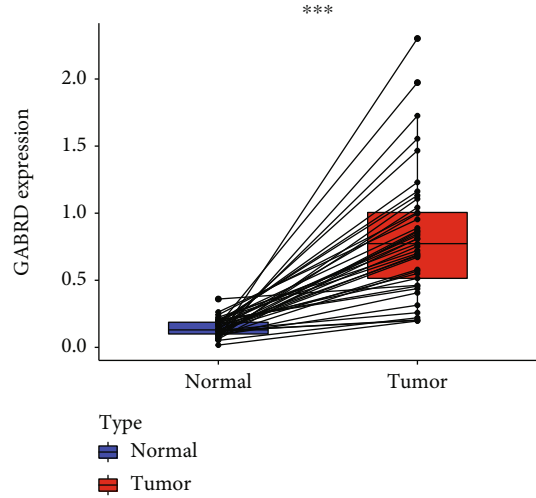
(c)
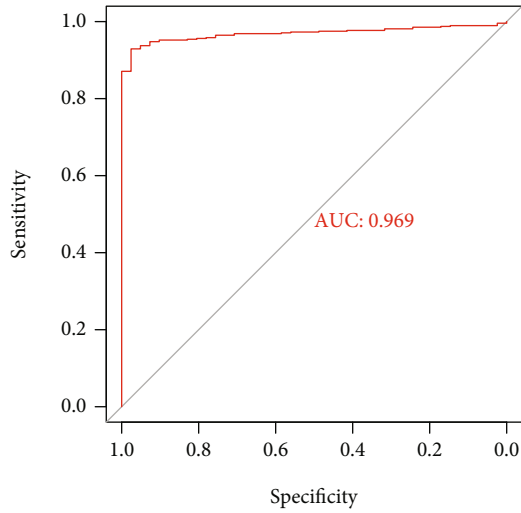
(d)

Figure 2: GABRD was highly expressed in COAD patients. (a) Pan-cancer assays of GABRD expression based on TCGA datasets. (b, c) A high expression of GABRD was observed in COAD specimens compared with nontumor specimens. (d) The diagnostic values of GABRD expression were confirmed in screening COAD specimens from normal specimens based on TCGA datasets. $^{**}p < 0.01$, $^{***}p < 0.001$.

(a)

(b)

(c)

(d)

(e)

(f)

Figure 3: Continued.

(g)
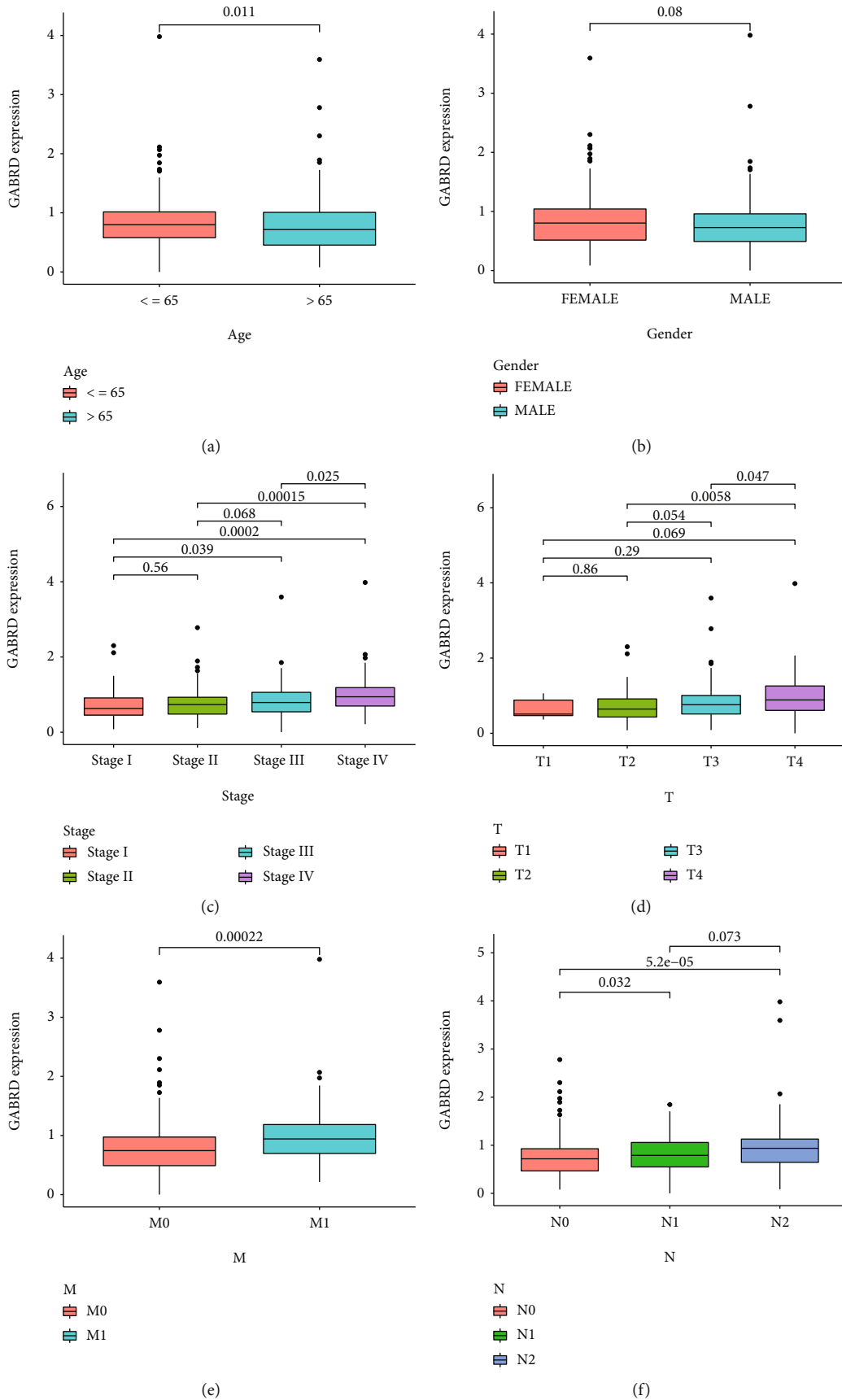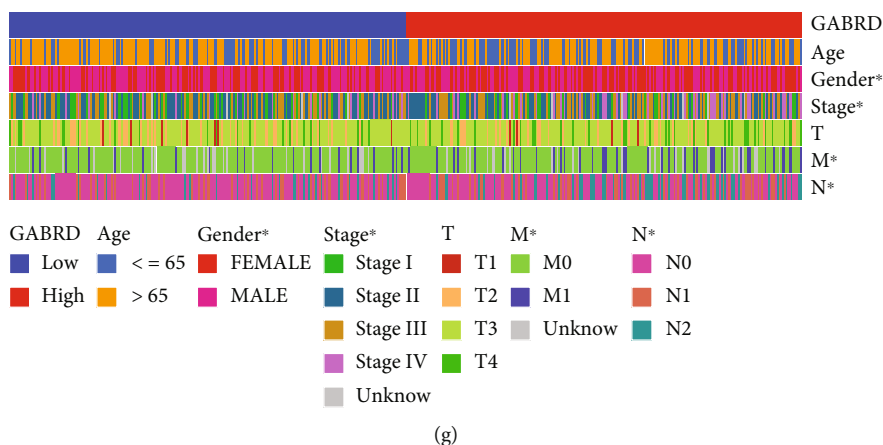
Figure 3: Association between the expression of GABRD and clinical characteristics in COAD patients. (a) Age, (b) gender, (c) clinical stage, (d) T stage, (e) M stage, (f) N stage. (g) The association between GABRD expression and different clinical factors was shown using heat map. $^*p < 0.05$.

GABRD expression. According to the findings of TCGA, the area under the curve (AUC) for GABRD expression was 0.658, which indicated that GABRD has a significant predictive potential for the survival of COAD patients (Figure 4(c)). According to the findings of a univariate Cox regression analysis, the overall survival rate was significantly affected by age ($p = 0.005$), stage ($p < 0.001$), and GABRD expression ($p < 0.001$) (Figure 4(d)). Additionally, the multivariate COX regression analysis demonstrated that GABRD expression was an independent predictive predictor for overall survival (Figure 4(e)). A quantitative strategy for predicting the chance of overall survival at 1, 3, and 5 years for COAD patients is provided by the expression level of GABRD, which is an independent prognostic risk factor (Figures 5(a) and 5(b)). Our findings suggested GABRD as a novel prognostic biomarker for COAD patients.

3.4. The Biological Functions of GABRD in COAD. A total of 236 DEGs were screened (Figure 6(a)). Functional annotation was conducted. GO assays revealed that GABRD-associated DEGs were mainly involved in the muscle system process, skin development, muscle contraction, perikaryon, dendrite membrane, cornified envelope, heparin binding, glycosaminoglycan binding, and sulfur compound binding (Figures 6(b) and 6(c)). Meanwhile, KEGG pathway analysis showed that GABRD-associated DEGs were mainly involved in the PPAR signaling pathway (Figure 6(d)). Since the level of GABRD expression was shown to be connected with the grade of the tumor and the prognosis of COAD patients, we formed the hypothesis that an increased level of GABRD expression accelerates the growth of tumors. Our group carried out GSEA and found that hallmarks of tumors such as ACUTE_MYELOID_LEUKEMIA, GLYCOSAMINOGLY-CAN_BIOSYNTHESIS_CHONDROITIN_SULFAT, and _MTOR_SIGNALING_PATHWAY, NOTCH_SIGNAL-ING_PATHWAY were dynamically correlated with the high GABRD expression, while OLFACTORY_TRANSDUC-TION was significantly enriched in the low GABRD expression group (Figure 6(e)).

3.5. Distribution of Tumor-Infiltrating Immune Cells. Through the application of the CIBERSORT approach, we investigated the pattern of immune cells. Figures 7(a) and 7(b), respectively, showed the makeup of it on COAD samples as well as the relationships among immune cells. A number of studies have demonstrated that immune cells have the potential to act as independent markers of survival rates and the efficacy of immunotherapy in COAD. The next step was to determine definitively whether or not the actions of GABRD were linked to immune cells. Importantly, we observed that GABRD showed a dysregulated level in several immune cells, including T cells regulatory (Tregs), T cells follicular helper, T cells CD4 memory activated, T cells CD8, macrophages M0, dendritic cells activated, mast cells resting, and eosinophils (Figure 8(a)). In addition, our group showed that GABRD expressions were positively related to the expressions of T cells regulatory (Tregs) and macrophages M0, while negatively associated with the expression of T cells CD8, T cells follicular helper, macrophages M1, dendritic cells activated, eosinophils, and T cells CD4 memory activated (Figures 8(b) and 8(c)).

3.6. Relationship between GABRD Expression and Immune Checkpoints in COAD. Immune checkpoint genes (ICGs) are fundamental to the field of immunotherapy and have a role in both the onset and development of COAD. ICGs were shown to have a connection to both the beginning and the development of cancer by researchers. Additionally, it has been suggested that the ICGs have the potential to be therapeutic targets for ICB treatment. The examination of the clinical information and expression data on the many combinations of ICGs that are now accessible can be of assistance in finding targets for individualized treatment and in improving the efficacy of the present therapeutic approaches. Then, we found that GABRD expression was positively associated with CD40, TNFSF14, LAIR1, TNFRSF4, TNFRSF18, CD40LG, TNFRSF25, TNFRSF8, NRP1, CD27, and CD276 while negatively associated with HHLA2 and CD44 (Figures 9(a) and 9(b)). The tumor mutation burden (TMB) refers to the total
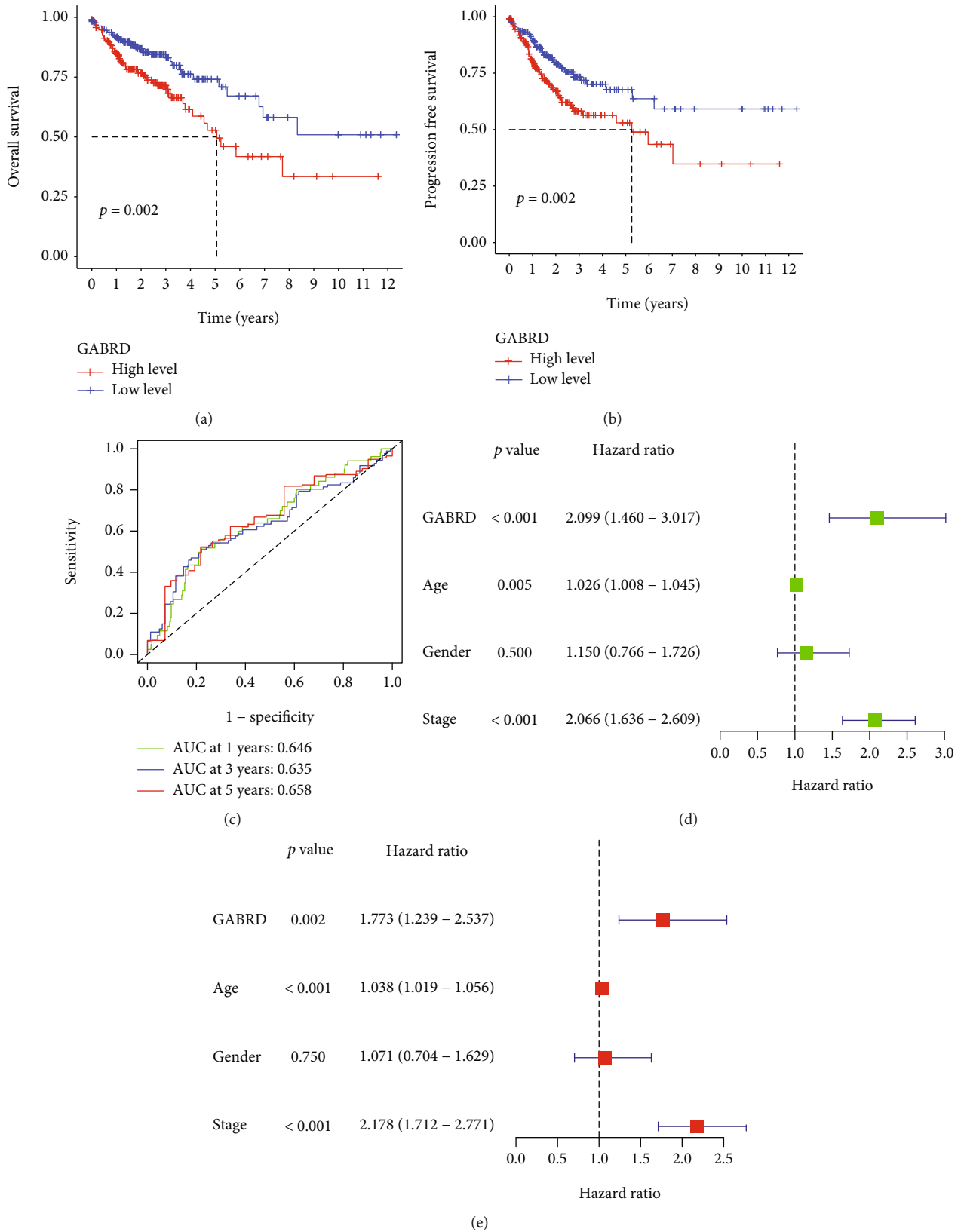
FIGURE 4: Correlation between GABRD expression and the long-term survival of COAD patients. (a, b) The Kaplan-Meier survival curves between groups with high GABRD expression and groups with low GABRD expression. (c) ROC curves drawn using TCGA data. (d, e) Univariate Cox analysis and multivariate Cox regression analysis of the risk factors related to the survival of COAD.

(a)

(b)
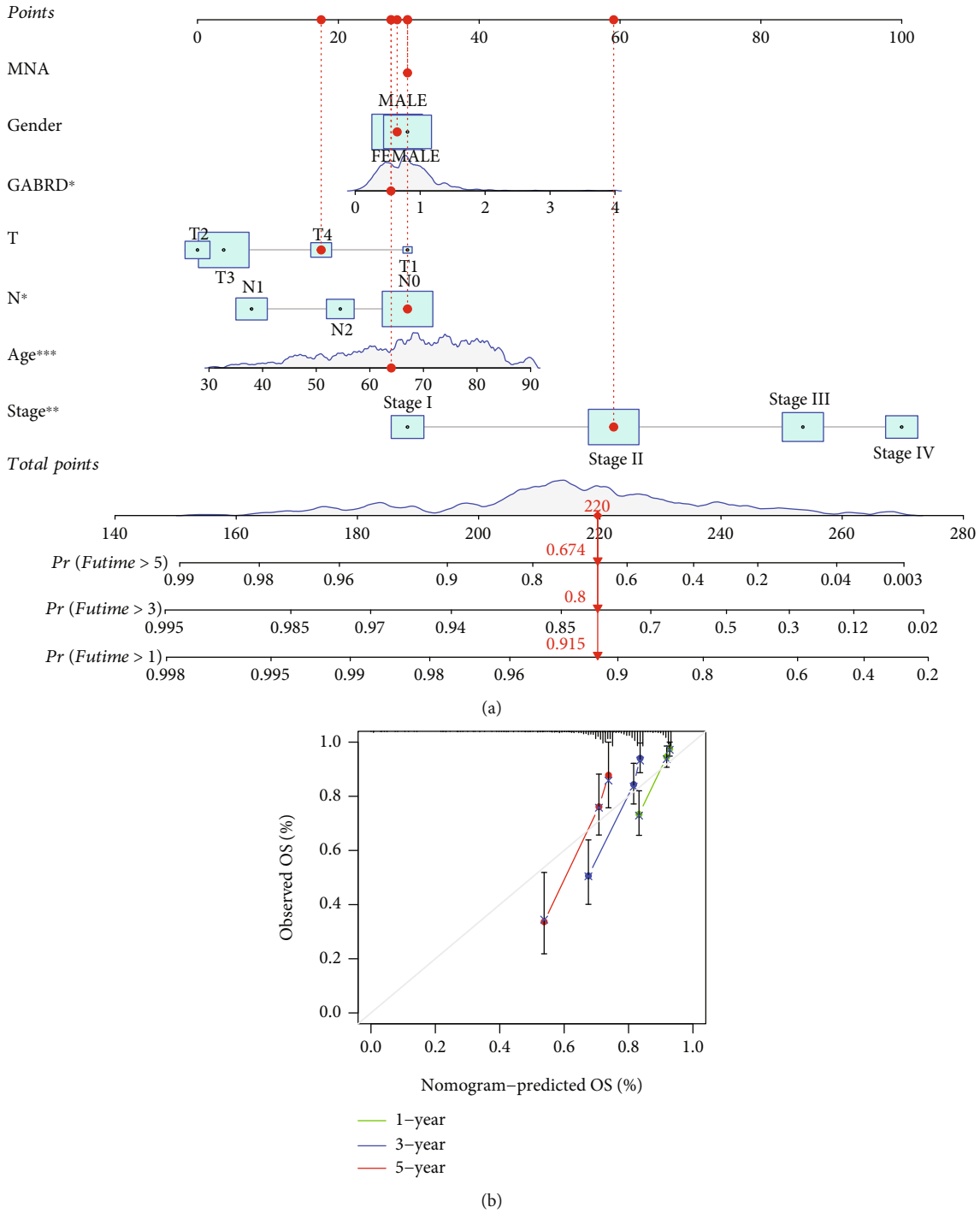
Figure 5: Validation of the nomogram for determining the overall survivals of COAD patients using data from the TCGA. (a) A prognostic nomogram for COAD patients that predicts their overall survival rate at one, two, and three years. (b) The ideal nomogram is represented by the dashed diagonal line on the calibration curve for the OS nomogram model. $^*p < 0.05$, $^{**}p < 0.01$, $^{***}p < 0.001$.

number of somatic gene variations found per million bases of genomic DNA. These variants might be base substitutions, insertions, or deletions. At the genetic level, tumor cells are capable of producing a large number of specific mutations. Every 150 nonsynonymous mutations have the potential to produce one to two neoantigens. These neoantigens are able to be recognized by the autoimmune system, which in turn

activates T cells and causes an immune response. We also found that GABRD expression was negatively associated with TMB (Figure 9(c)).

3.7. IC50 Score. When trying to assess how well patients may react to targeted pharmacological therapy, the IC50 is an important statistic that has to be employed. We were able

(a)

(b)

Figure 6: Continued.

(c)

(d)

Fᴵɢᴜᴿᴱ 6: Continued.

KEGG_ACUTE_MYELOID_LEUKEMIA
KEGG_GLYCOSAMINOGLYCAN_BIOSYNTHESIS_CHONDROITIN_SULFA
KEGG_MTOR_SIGNALING_PATHWAY
KEGG_NOTCH_SIGNALING_PATHWAY
KEGG_OLFACTORY_TRANSDUCTION

(e)
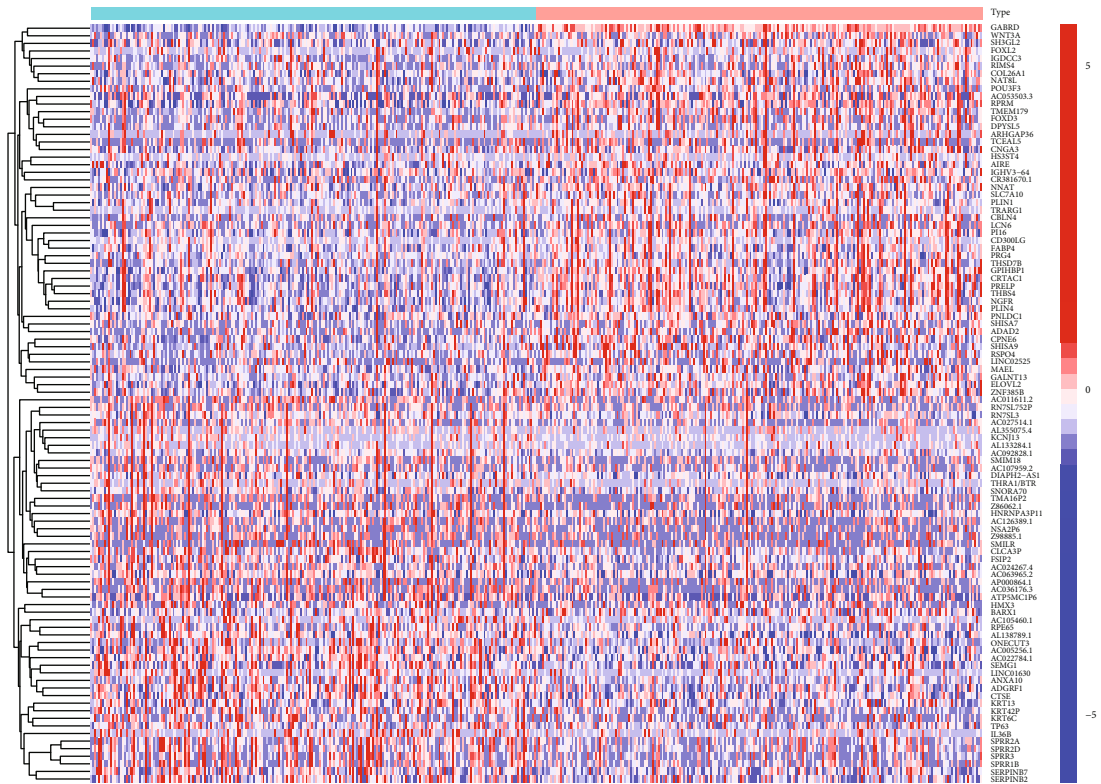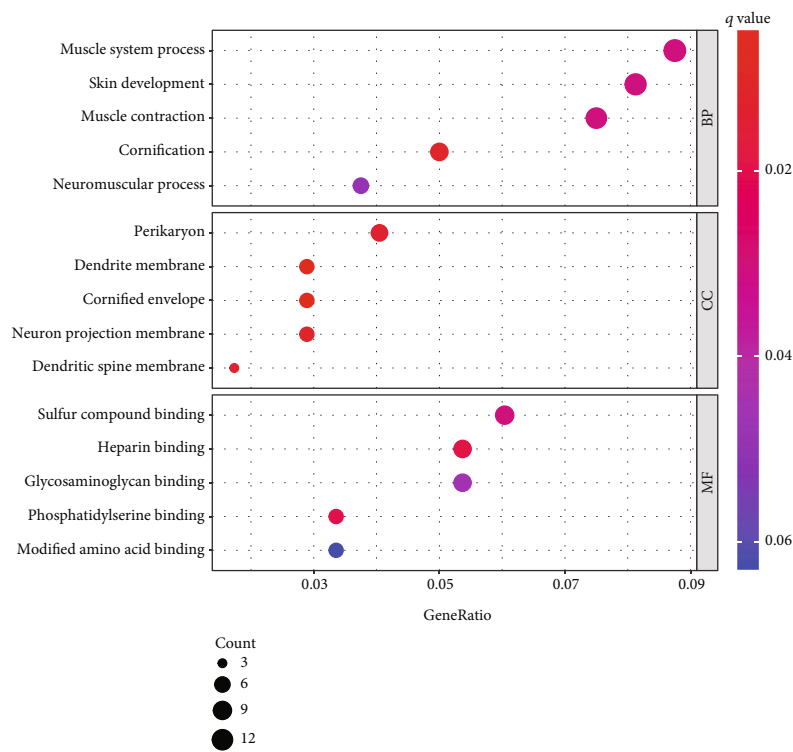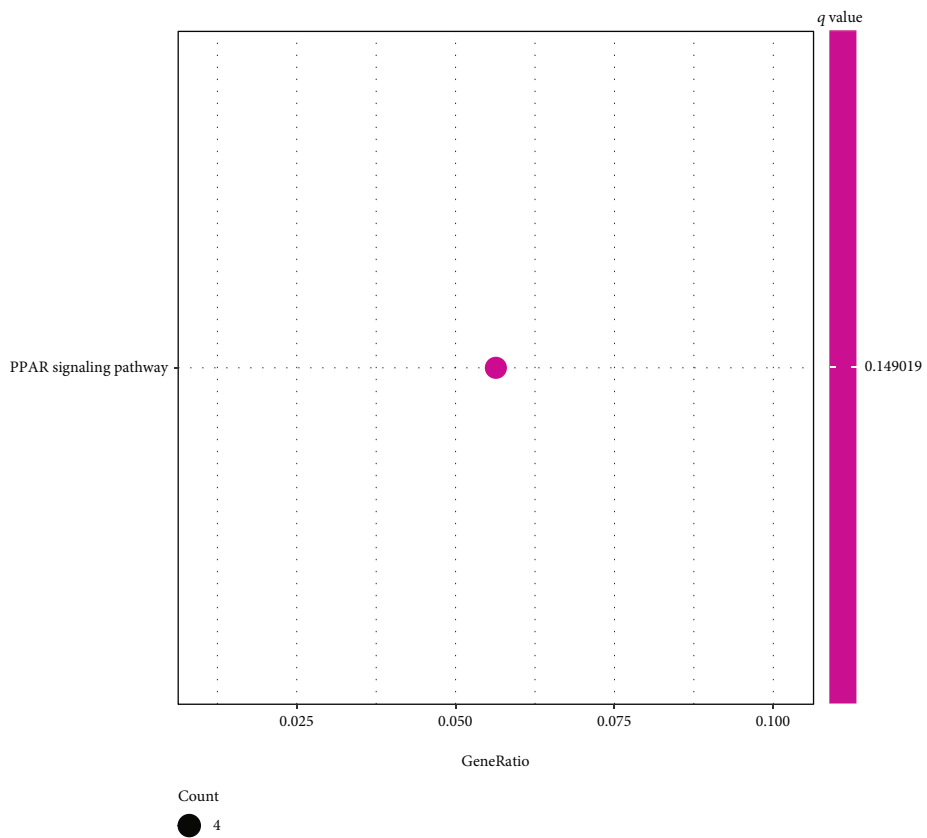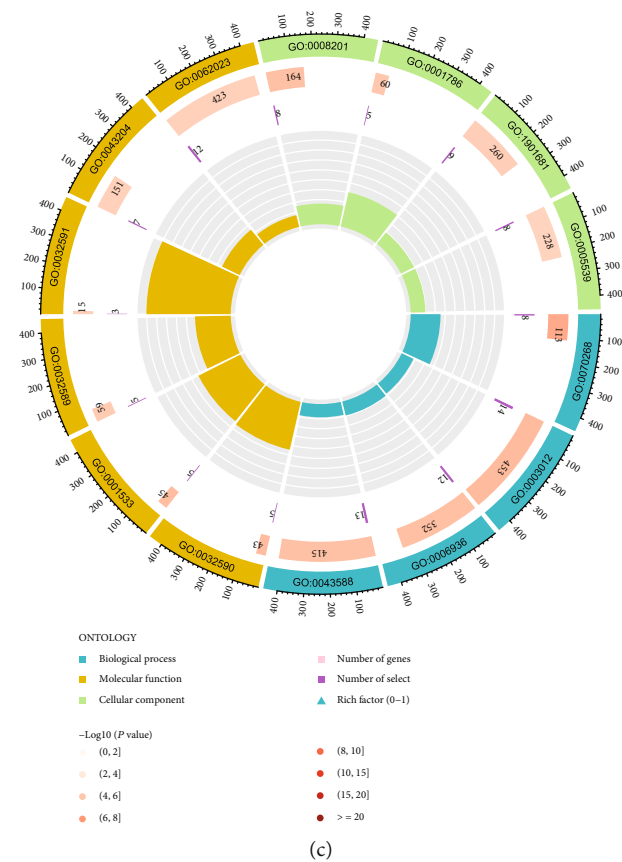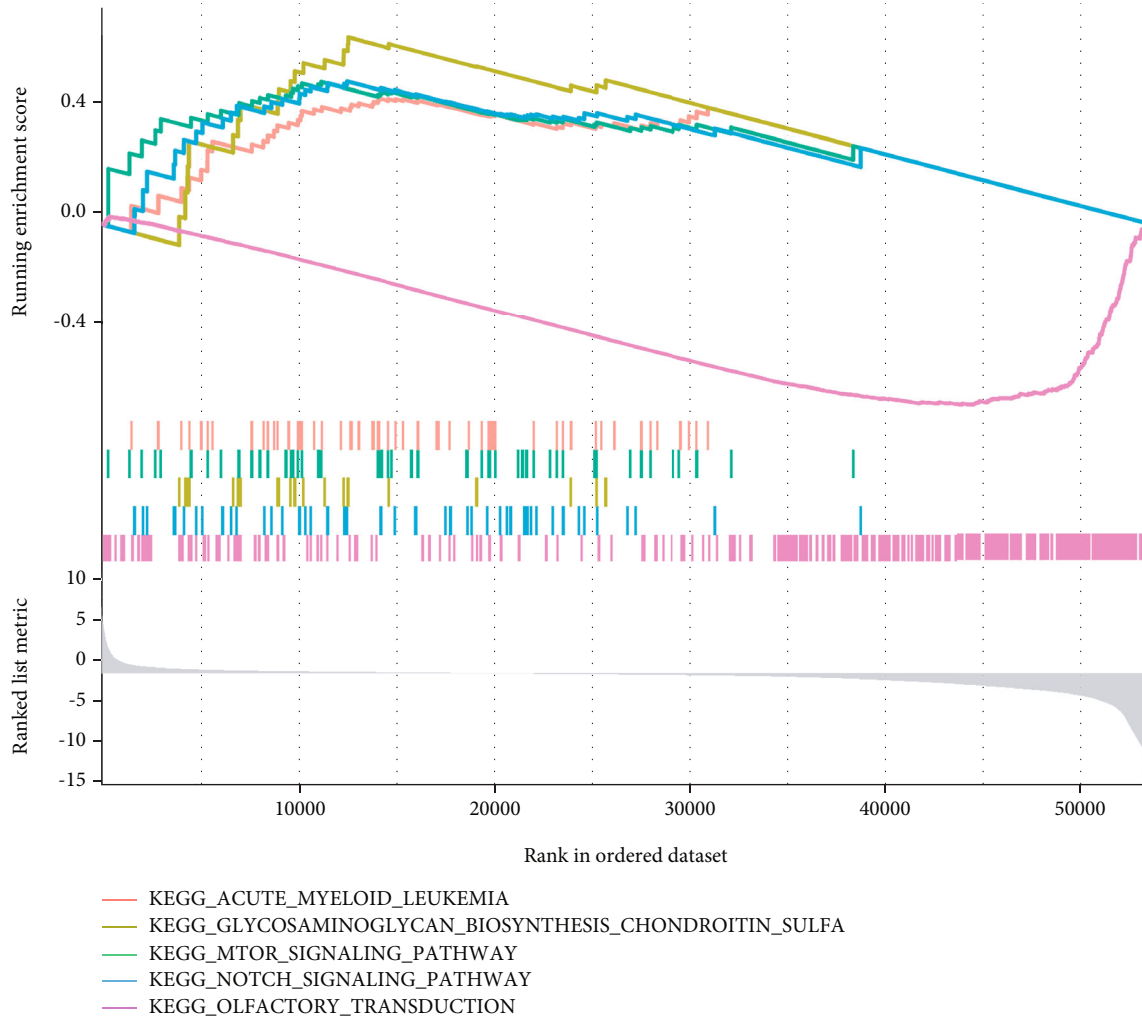
FIGURE 6: The function assays of GABRD-associated DEGs in COAD. (a) The representative DEGs associated with GABRD were shown in heat map. (b, c) Bubble graph for GO enrichment. (d) Barplot graph for KEGG pathways. (e) Gene set enrichment analysis.

to estimate probable alterations in the IC50 values of chemotherapeutic medications across the various GABRD expression groups by making use of the information that was supplied by the GDSC. The IC50 of BI-2536, bleomycin, embelin, FR-180204, GW843682X, LY317615, NSC-207895, rTRAIL, and VX-11e was higher in the GABRD high-expression group (Figure 10). As a consequence of this, the results showed that there was a significant distinction between the various GABRD expression groups in terms of the distribution of IC50 values for drugs that are specifically targeted.

3.8. Identification of GABRD Protein Expression in COAD Specimens. In addition, in order to evaluate the expression of GABRD in terms of the protein level, we requested immunohistochemistry pictures from the HPA database. It is obvious that the protein expression of COAD was significantly higher in tumor specimens than in normal specimens (Figures 11(a) and 11(b)).

4. Discussion

In recent years, COAD has emerged as an increasingly serious hazard to human health all over the world and has imposed a significant burden on society [32]. Even with recent advancements in surgery, radiation, chemotherapy, and immunotherapy, COAD still has a high propensity to spread and a dismal overall survival rate [33, 34]. In addition, the traditional TNM classification method determines a patient's stage of cancer based not on the patient themselves but rather on the location and size of the tumor [35, 36]. It is challenging to individually identify the result of a patient's condition. Therefore, discovering molecular prognostic indicators to estimate the risks and prognoses of individuals with COAD is vital for the purpose of directing treatment.

The development of throughput sequencing technology has helped shed light on illness-causing genes, expanded our knowledge of disease etiology, led to the discovery of new biomarkers, and fundamentally altered our perspective
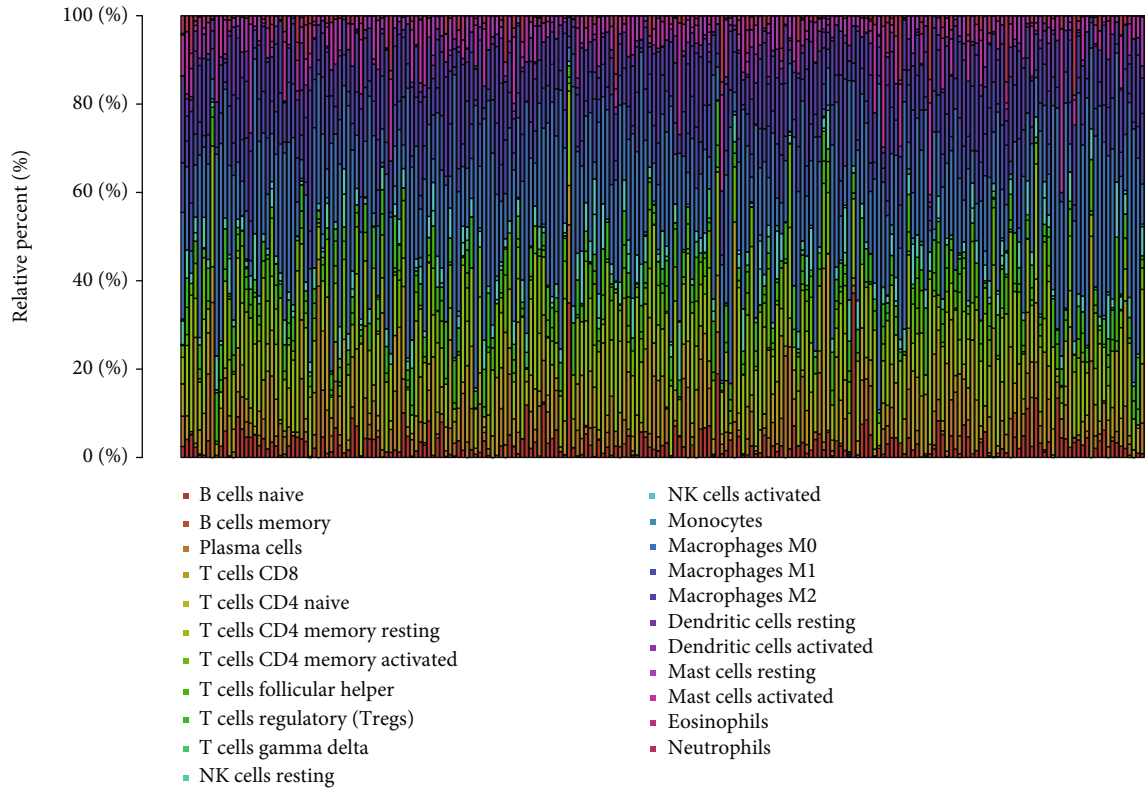
(a)
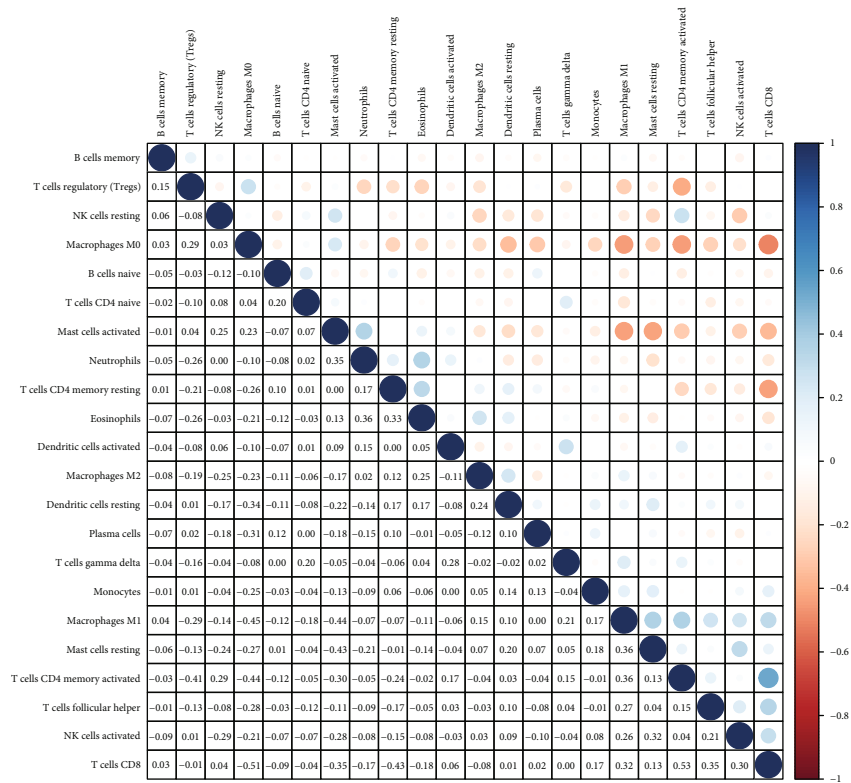
(b)

FIGURE 7: TIC profiles in tumor samples and correlation analysis. (a) A barplot illustrating the percentage of 21 different TIC types found in COAD tumor samples The names of the plot's columns were sample IDs. (b) A heat map displaying the association between 22 different types of TICs, with a number in each very small box representing the level of statistical significance of the link between the two types of cells.

(a)

(b)

Figure 8: Continued.

(c)
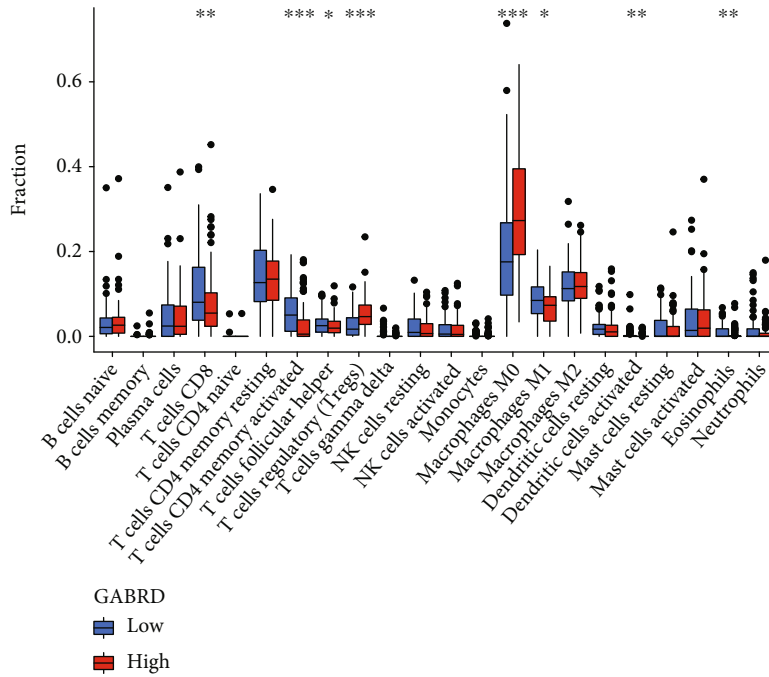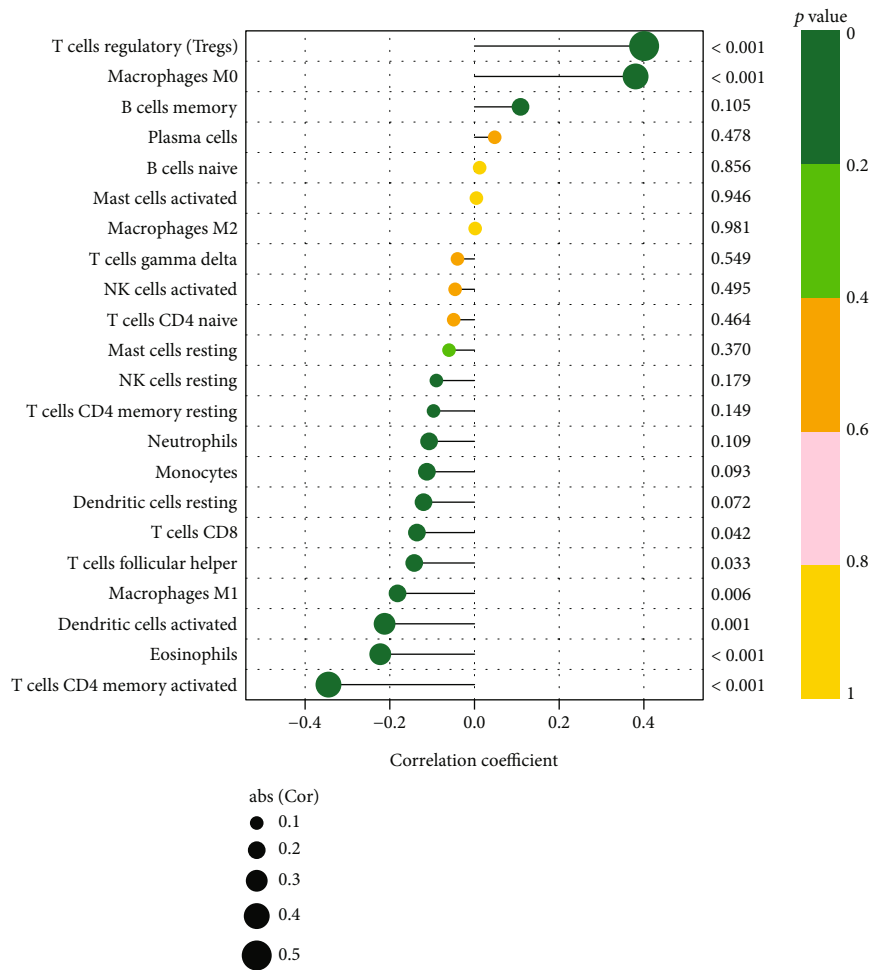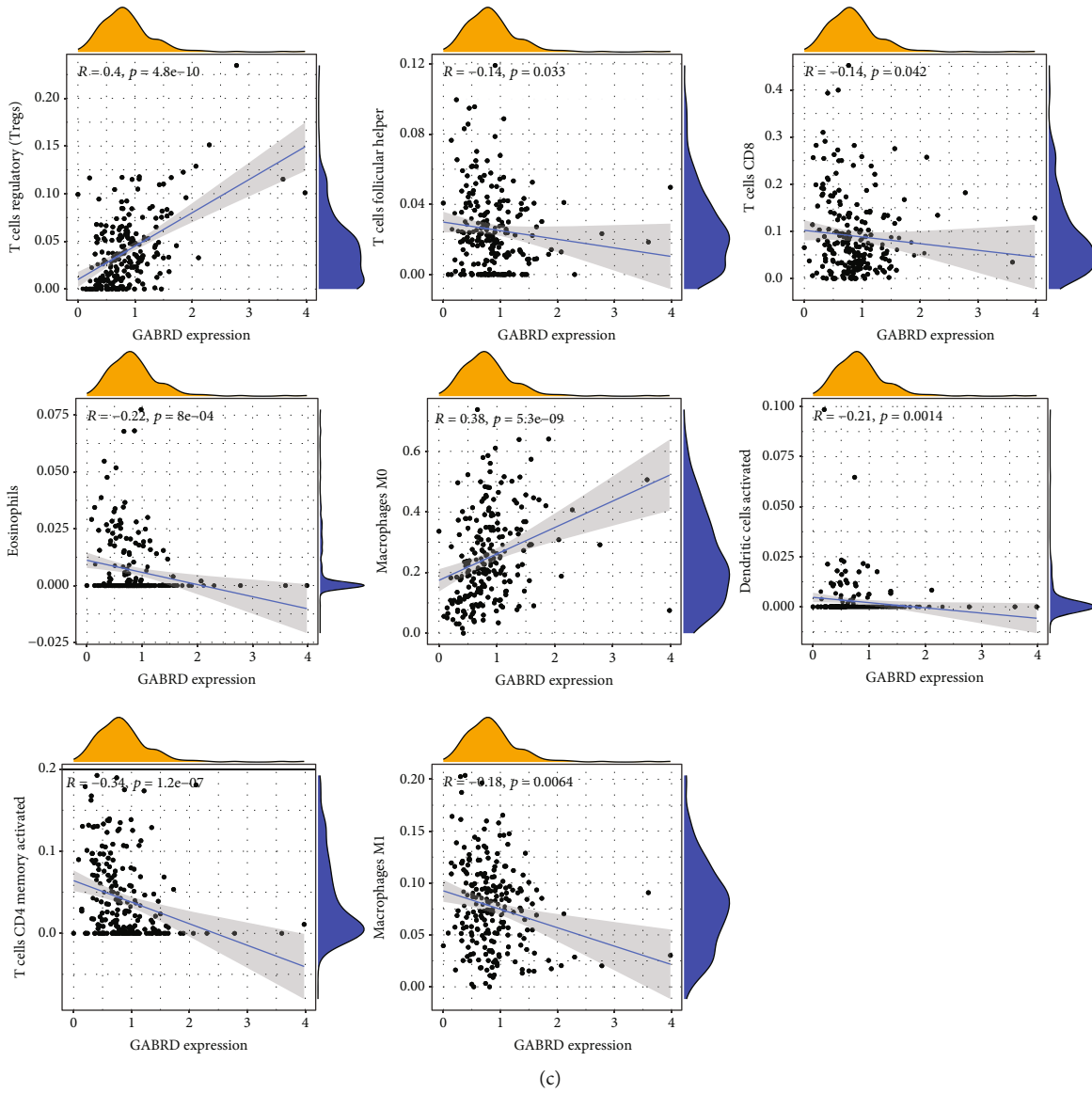
FIGURE 8: Correlation of TIC proportion with GABRD expression. (a) The ratio differentiation of 22 distinct types of immune cells was shown using a violin plot, and it was compared to the median level of BTK expression. This was done using COAD tumor samples with low or high GABRD expression levels. (b, c) Correlation between GABRD and infiltrating immune cells in COAD. $^*p < 0.05$, $^{**}p < 0.01$, $^{***}p < 0.001$.

on the variety of human life [37, 38]. Researchers have identified a large number of genes connected to tumors that, when combined with genomic information, provide an accurate prediction of whether or not a patient's prognosis risk is high [39, 40]. By mining data on gene expression, a number of researchers have examined and evaluated numerous biomarkers connected to COAD [41, 42]. In this study, we performed a comprehensive analysis and identified 29 survival-related DEGs. Among them, our attention focused on GABRD, which was highly expressed in many types of tumors, including COAD. In addition, we also confirmed its diagnostic value in screening COAD specimens from nontumor specimens. Then, we analyzed its clinical significance and found that high GABRD expression was associated with an advanced clinical stage and a poor prognosis.

More importantly, multivariate COX regression analysis confirmed that GABRD expression was an independent prognostic factor for overall survival. Our findings suggested GABRD as a novel biomarker for COAD patients.

The TME is made up of cancer cells, stromal cells, immune cells, and extracellular matrix, all of which have a substantial impact on the progression of cancer [43]. The TME contains cancer cells that can invade surrounding tissues either directly or indirectly through blood and lymphatic vessels [44]. These infiltrated cells have the ability to stimulate an immune response by cytokine receptors, releasing cytokines and other elements that influence the progression of the tumor. In recent years, fresh research has demonstrated that TME considerably alters the course of tumors and has shown a possible prognostic value for cancer
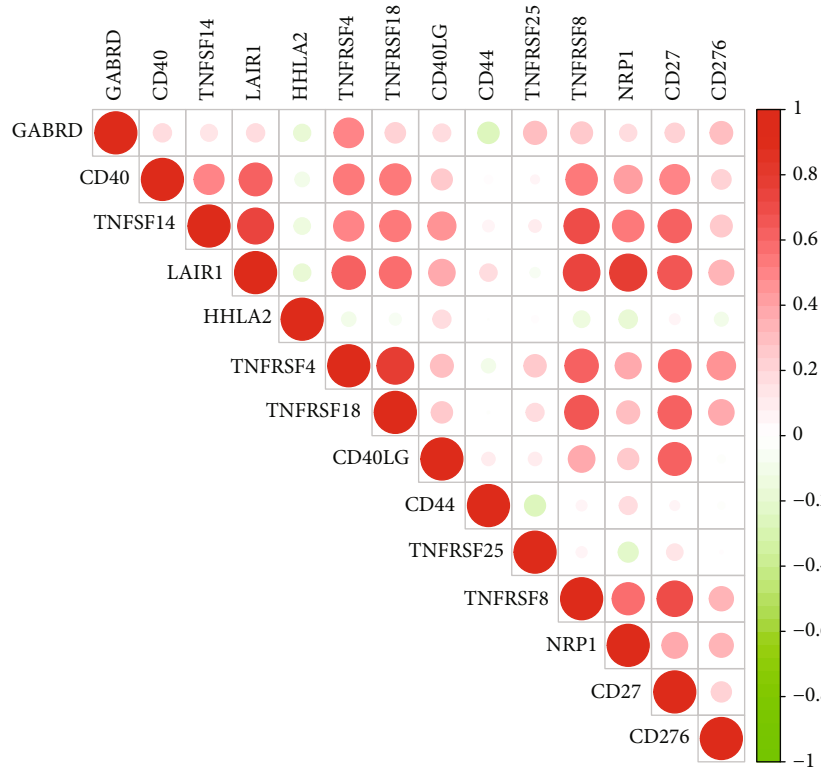
(a)

(b)

FIGURE 9: Continued.

(c)
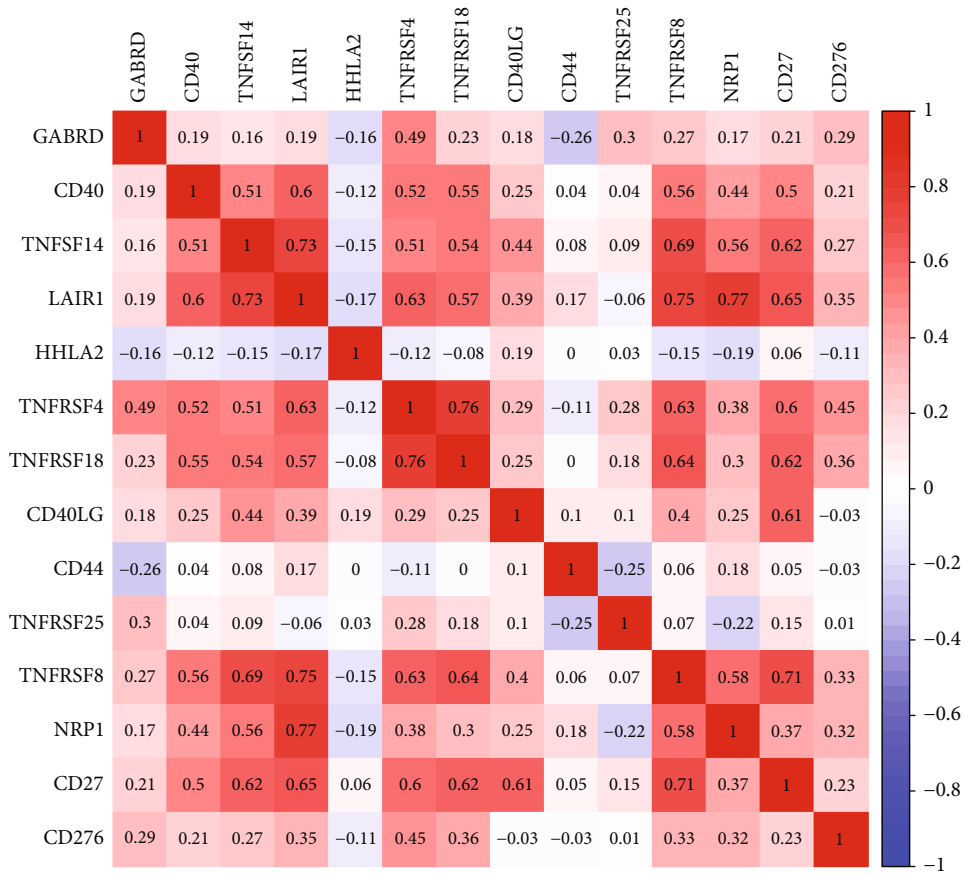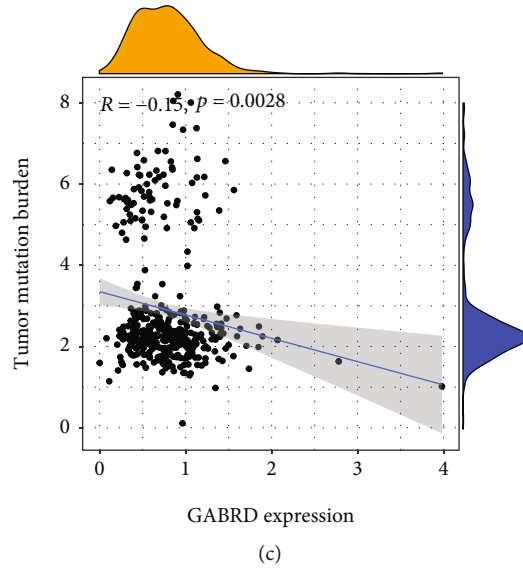
FIGURE 9: (a, b) The association between GABRD expression and immune checkpoints in COAD patients. (c) GABRD expression was negatively associated with tumor mutation burden.
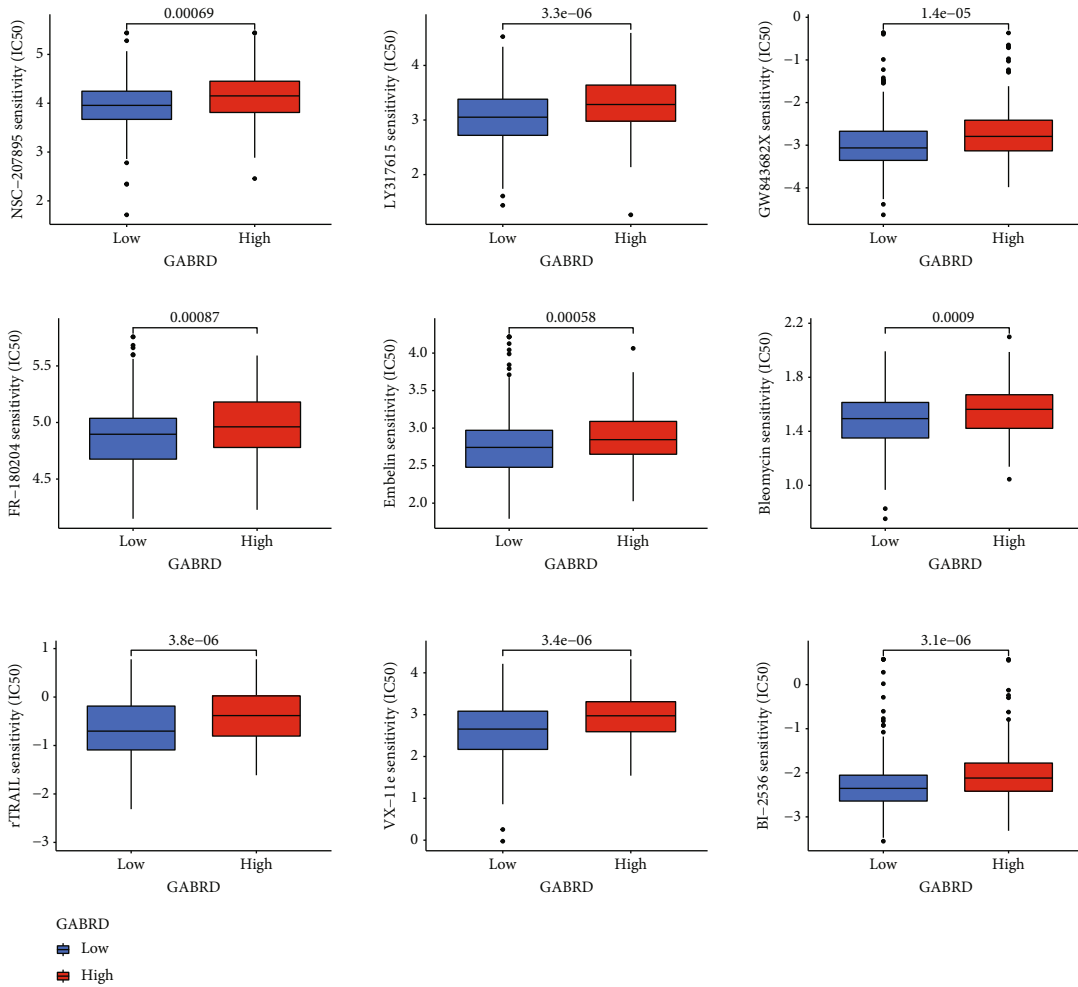
FIGURE 10: A breakdown of the IC50 values for several targeted medicines across the various GABRD expression groups.

Normal   Normal

(a)

Tumor   Tumor

(b)
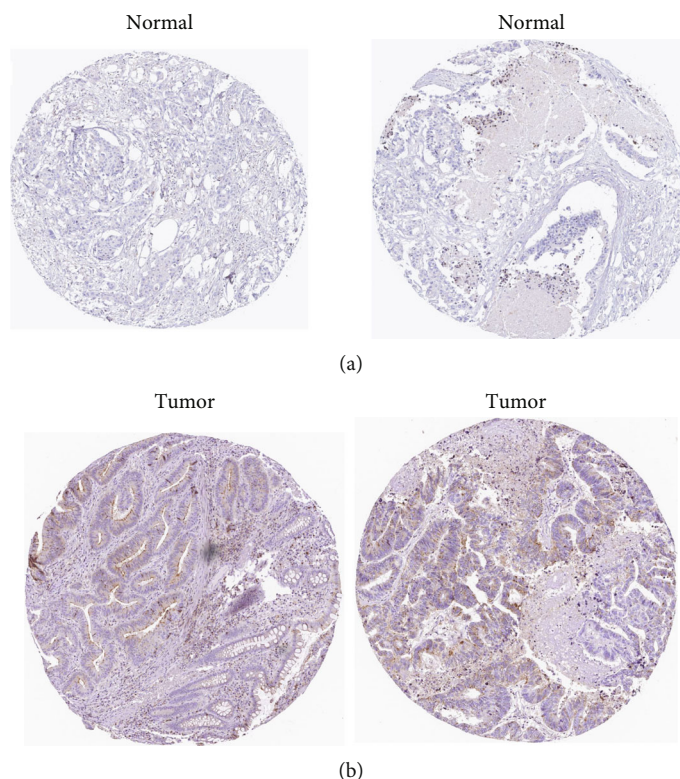
FIGURE 11: Images from the Human Protein Atlas, showing representative examples of immunohistochemistry staining for GABRD in normal tissues as well as COAD tissues: (a) normal tissues; (b) malignant tissues.

prognosis, including COAD [45, 46]. These findings are now available to the general public. The fast growth of precision medicine has led to an increase in the number of studies in which researchers use statistical algorithms to investigate novel diagnostic and therapeutic targets. This homeostatic system contributes to the progression and recurrence of cancer, and it has significant ramifications for chemoresistant disease and immunotherapy. In addition to this, the therapeutic response is also affected by the nonimmune cellular components of the TME [47, 48]. For instance, the tumor treatment effect is proportional to the depth of stromal cell invasion since TGF synthesis by fibroblasts can cause immune cell efflux or resistance to chemotherapeutic medicines. Therefore, gene expression patterns in tumor tissue can be used to show the link between the tumor microenvironment and patient prognosis. TCGA delivered genomic profiles as well as clinical data, which made it feasible to study the association between genomic features and clinical as well as prognostic aspects. In this study, we observed that GABRD expression was positively associated with the expression of T cells regulatory (Tregs), macrophages M0, while negatively associated with the expression of T cells CD8, T cells follicular helper, macrophages M1, dendritic cells activated, eosinophils, and T cells CD4 memory activated. Based on our findings, it appeared as though GABRD may play a significant part in the TME. In light of these findings, we conducted additional research to investigate the possible connections between GABRD and immunological checkpoints, immunosuppressive genes, chemokines, and

chemokine receptors. We found that GABRD expression was positively associated with CD40, TNFSF14, LAIR1, TNFRSF4, TNFRSF18, CD40LG, TNFRSF25, TNFRSF8, NRP1, CD27, and CD276, while negatively associated with HHLA2 and CD44. Based on these findings, GABRD appears to have a tight connection with the regulation of the immune system. Patients with tumors that have high GABRD expression levels could develop an immunosuppressive condition.

We evaluated the connection between GABRD expression and IC50 values of anticancer therapies using data from the GDSC database in order to investigate the possible role that GABRD plays as an indicator in the process of selecting anticancer medications. We found that the IC50 values of BI-2536, bleomycin, embelin, FR-180204, GW843682X, LY317615, NSC-207895, rTRAIL, and VX-11e increased in the high-GABRD group. Based on these findings, it appeared that individuals who had high levels of GABRD expression may be unable to benefit from the therapies provided by the aforementioned medications.

In the end, we must clarify the limitations of this research. Firstly, the sample size is not particularly huge; therefore, it is important to conduct extensive clinical tests. Secondly, we did not assess the expression profiles of GABRD in the serum samples taken from COAD patients. Investigating the serum biomarkers might be an effective way to evaluate treatment responses in real-time. Thirdly, there is a lack of information on the function of GABRD in the control of COAD carcinogenesis on both the cellular and molecular levels.

5. Conclusions

Overall, the findings of our research showed that the GABRD expression level in COAD patient tissues was significantly higher than that in normal tissues. In addition to that, GABRD may be a novel prognostic biomarker for COAD patients. The nomogram model can effectively predict patient survival in clinical practice. In addition to this, one of the benefits of our research was that it was the first study to investigate whether or not there is a connection between GABRD expression and TME.

Data Availability

Some or all data generated or used during the study can be obtained from the corresponding author upon request.

Conflicts of Interest

The authors have declared that there are no conflicts of interest.

Authors' Contributions

Fakun Huang and Jia-xing Wang conceived and designed the research. Fakun Huang, Zhengyang Wang, and Liyue Zhu acquired the data. Liyue Zhu and Changqing Lin analyzed and interpreted the data. Fakun Huang and Liyue Zhu carried out the statistical analysis. Fakun Huang and Jia-xing Wang drafted the manuscript. All authors read and approved the final manuscript.

Acknowledgments

References

[1] R. L. Siegel, K. D. Miller, and A. Jemal, "Cancer statistics, 2020," *CA: a Cancer Journal for Clinicians*, vol. 70, no. 1, pp. 7–30, 2020.

[2] K. W. Jasperson, T. M. Tuohy, D. W. Neklason, and R. W. Burt, "Hereditary and familial colon cancer," *Gastroenterology*, vol. 138, no. 6, pp. 2044–2058, 2010.

[3] E. M. Stoffel and C. C. Murphy, "Epidemiology and mechanisms of the increasing incidence of colon and rectal cancers in young adults," *Gastroenterology*, vol. 158, no. 2, pp. 341–353, 2020.

[4] S. J. O'Keefe, "Diet, microorganisms and their metabolites, and colon cancer," *Nature Reviews Gastroenterology & Hepatology*, vol. 13, no. 12, pp. 691–706, 2016.

[5] R. Gupta, L. K. Bhatt, T. P. Johnston, and K. S. Prabhavalkar, "Colon cancer stem cells: potential target for the treatment of colorectal cancer," *Cancer Biology & Therapy*, vol. 20, no. 8, pp. 1068–1082, 2019.

[6] T. R. Lannagan, R. Jackstadt, S. J. Leedham, and O. J. Sansom, "Advances in colon cancer research: _in vitro_ and animal models," *Current Opinion in Genetics & Development*, vol. 66, pp. 50–56, 2021.

[7] H. Birgisson, E. J. Olafsdottir, A. Sverrisdottir, S. Einarsson, A. Smaradottir, and L. Tryggvadottir, "Screening for cancer of the colon and rectum a review on incidence, mortality, cost and benefit," *Læknablaðið*, vol. 107, no. 9, pp. 398–405, 2021.

[8] H. Ruan, B. J. Leibowitz, L. Zhang, and J. Yu, "Immunogenic cell death in colon cancer prevention and therapy," *Molecular Carcinogenesis*, vol. 59, no. 7, pp. 783–793, 2020.

[9] J. Li, X. Ma, D. Chakravarti, S. Shalapour, and R. A. DePinho, "Genetic and biological hallmarks of colorectal cancer," *Genes & Development*, vol. 35, no. 11-12, pp. 787–820, 2021.

[10] I. Mármol, C. Sánchez-de-Diego, A. Pradilla Dieste, E. Cerrada, and M. J. Rodriguez Yoldi, "Colorectal carcinoma: a general overview and future perspectives in colorectal cancer," *International Journal of Molecular Sciences*, vol. 18, no. 1, p. 197, 2017.

[11] K. Simon, "Colorectal cancer development and advances in screening," *Clinical Interventions in Aging*, vol. 11, pp. 967–976, 2016.

[12] N. A. Johdi and N. F. Sukor, "Colorectal cancer immunotherapy: options and strategies," *Frontiers in Immunology*, vol. 11, p. 1624, 2020.

[13] A. L. Zygulska and P. Pierzchalski, "Novel diagnostic biomarkers in colorectal cancer," *International Journal of Molecular Sciences*, vol. 23, no. 2, p. 852, 2022.

[14] P. Darvin, S. M. Toor, V. Sasidharan Nair, and E. Elkord, "Immune checkpoint inhibitors: recent progress and potential biomarkers," *Experimental & Molecular Medicine*, vol. 50, no. 12, pp. 1–11, 2018.

[15] M. C. Sellars, C. J. Wu, and E. F. Fritsch, "Cancer vaccines: building a bridge over troubled waters," *Cell*, vol. 185, no. 15, pp. 2770–2788, 2022.

[16] D. C. Hinshaw and L. A. Shevde, "The tumor microenvironment innately modulates cancer progression," *Cancer Research*, vol. 79, no. 18, pp. 4557–4566, 2019.

[17] I. Vitale, G. Manic, L. M. Coussens, G. Kroemer, and L. Galluzzi, "Macrophages and metabolism in the tumor microenvironment," *Cell Metabolism*, vol. 30, no. 1, pp. 36–50, 2019.

[18] Y. Xiao and D. Yu, "Tumor microenvironment as a therapeutic target in cancer," *Pharmacology & Therapeutics*, vol. 221, article 107753, 2021.

[19] P. Dey, A. C. Kimmelman, and R. A. DePinho, "Metabolic codependencies in the tumor microenvironment," *Cancer Discovery*, vol. 11, no. 5, pp. 1067–1081, 2021.

[20] S. Peng, F. Xiao, M. Chen, and H. Gao, "Tumor-microenvironment-responsive nanomedicine for enhanced cancer immunotherapy," *Advanced Science*, vol. 9, no. 1, article e2103836, 2022.

[21] A. J. McFarlane, F. Fercoq, S. B. Coffelt, and L. M. Carlin, "Neutrophil dynamics in the tumor microenvironment," *The Journal of Clinical Investigation*, vol. 131, no. 6, 2021.

[22] M. Taki, K. Abiko, M. Ukita et al., "Tumor immune microenvironment during epithelial-mesenchymal transition," *Cancer Research*, vol. 27, no. 17, pp. 4669–4679, 2021.

[23] A. Aponte-López and S. Muñoz-Cruz, "Mast cells in the tumor microenvironment," *Advances in Experimental Medicine and Biology*, vol. 1273, pp. 159–173, 2020.

[24] D. E. A. Komi and F. A. Redegeld, "Role of mast cells in shaping the tumor microenvironment," *Clinical Reviews in Allergy & Immunology*, vol. 58, no. 3, pp. 313–325, 2020.

[25] A. Arslan, "Extrasynaptic δ-subunit containing GABA (A) receptors," *Journal of Integrative Neuroscience*, vol. 20, no. 1, pp. 173–184, 2021.

[26] H. Zhang, L. Zhang, Y. Tang et al., "Systemic screening identifies *GABRD*, a subunit gene of GABAA receptor as a prognostic marker in adult IDH wild-type diffuse low-grade glioma," *Biomedicine & Pharmacotherapy*, vol. 118, article 109215, 2019.

[27] K. Sawaki, M. Kanda, H. Baba et al., "Gamma-aminobutyric acid type a receptor subunit delta as a potential therapeutic target in gastric cancer," *Annals of Surgical Oncology*, vol. 30, no. 1, pp. 628–636, 2023.

[28] G. Niu, L. Deng, X. Zhang et al., "GABRD promotes progression and predicts poor prognosis in colorectal cancer," *Open Medicine*, vol. 15, no. 1, pp. 1172–1183, 2020.

[29] S. Li, S. Chen, B. Wang, L. Zhang, Y. Su, and X. Zhang, "A robust 6-lncRNA prognostic signature for predicting the prognosis of patients with colorectal cancer metastasis," *Frontiers in Medicine*, vol. 7, p. 56, 2020.

[30] G. Yu, L. G. Wang, Y. Han, and Q. Y. He, "clusterProfiler: an R package for comparing biological themes among gene clusters," *OMICS*, vol. 16, no. 5, pp. 284–287, 2012.

[31] B. Chen, M. S. Khodadoust, C. L. Liu, A. M. Newman, and A. A. Alizadeh, "Profiling tumor infiltrating immune cells with CIBERSORT," in *Cancer Systems Biology. Methods in Molecular Biology, vol 1711*, L. Stechow, Ed., Humana Press, New York, NY, 2018.

[32] P. Wrobel and S. Ahmed, "Current status of immunotherapy in metastatic colorectal cancer," *International Journal of Colorectal Disease*, vol. 34, no. 1, pp. 13–25, 2019.

[33] Z. Dai, J. Zhang, Q. Wu et al., "The role of microbiota in the development of colorectal cancer," *International Journal of Cancer*, vol. 145, no. 8, pp. 2032–2041, 2019.

[34] D. Ding, S. Han, H. Zhang, Y. He, and Y. Li, "Predictive biomarkers of colorectal cancer," *Computational Biology and Chemistry*, vol. 83, article 107106, 2019.

[35] A. Pakiet, J. Kobiela, P. Stepnowski, T. Sledzinski, and A. Mika, "Changes in lipids composition and metabolism in colorectal cancer: a review," *Lipids in Health and Disease*, vol. 18, no. 1, p. 29, 2019.

[36] M. Jin and W. L. Frankel, "Lymph node metastasis in colorectal cancer," *Surgical Oncology Clinics of North America*, vol. 27, no. 2, pp. 401–412, 2018.

[37] M. G. Best, P. Wesseling, and T. Wurdinger, "Tumor-educated platelets as a noninvasive biomarker source for cancer detection and progression monitoring," *Cancer Research*, vol. 78, no. 13, pp. 3407–3412, 2018.

[38] R. Almufti, M. Wilbaux, A. Oza et al., "A critical review of the analytical approaches for circulating tumor biomarker kinetics during treatment," *Medical Oncology*, vol. 25, no. 1, pp. 41–56, 2014.

[39] H. Fang, S. Sheng, B. Chen et al., "A pan-cancer analysis of the oncogenic role of cell division cycle-associated protein 4 (CDCA4) in human tumors," *Frontiers in Immunology*, vol. 13, article 826337, 2022.

[40] A. Fäldt Beding, P. Larsson, K. Helou, Z. Einbeigi, and T. Z. Parris, "Pan-cancer analysis identifies BIRC5 as a prognostic biomarker," *BMC Cancer*, vol. 22, no. 1, p. 322, 2022.

[41] Y. Cao, N. Jiao, T. Sun et al., "CXCL11 correlates with antitumor immunity and an improved prognosis in colon cancer," *Frontiers in Cell and Development Biology*, vol. 9, article 646252, 2021.

[42] R. Cao, F. Yang, S. C. Ma et al., "Development and interpretation of a pathomics-based model for the prediction of microsatellite instability in colorectal cancer," *Theranostics*, vol. 10, no. 24, pp. 11080–11091, 2020.

[43] L. Bejarano, M. J. C. Jordão, and J. A. Joyce, "Therapeutic targeting of the tumor microenvironment," *Cancer Discovery*, vol. 11, no. 4, pp. 933–959, 2021.

[44] O. Meurette and P. Mehlen, "Notch signaling in the tumor microenvironment," *Cancer Cell*, vol. 34, no. 4, pp. 536–548, 2018.

[45] Y. Liu, Q. Zhang, B. Xing et al., "Immune phenotypic linkage between colorectal cancer and liver metastasis," *Cancer Cell*, vol. 40, no. 4, pp. 424–437.e5, 2022.

[46] S. Kamali Zonouzi, P. S. Pezeshki, S. Razi, and N. Rezaei, "Cancer-associated fibroblasts in colorectal cancer," *Clinical & Translational Oncology*, vol. 24, no. 5, pp. 757–769, 2022.

[47] S. AlMusawi, M. Ahmed, and A. S. Nateri, "Understanding cell-cell communication and signaling in the colorectal cancer microenvironment," *Clinical and Translational Medicine*, vol. 11, no. 2, article e308, 2021.

[48] M. Nenkov, Y. Ma, N. Gaßler, and Y. Chen, "Metabolic reprogramming of colorectal cancer cells and the microenvironment: implication for therapy," *International Journal of Molecular Sciences*, vol. 22, no. 12, p. 6262, 2021.

Research Article

A Model of Basement Membrane-Associated Gene Signature Predicts Liver Hepatocellular Carcinoma Response to Immune Checkpoint Inhibitors

Jiajia Shen ⬡,[1] Zhihong Wei ⬡,[1] Lizhi Lv ⬡,[1] Jingxiong He ⬡,[1] Suming Du ⬡,[1] Fang Wang ⬡,[1] Ye Wang,[1] Lin Ni ⬡,[2] Xiaojin Zhang ⬡,[1] and Fan Pan ⬡[1]

[1]*Department of Hepatobiliary Surgery, 900th Hospital of Joint Logistics Support Force (Fuzong Clinical Medical College) (Former Fuzhou General Hospital), Fuzhou, Fujian, China*
[2]*Department of General Surgery, 900th Hospital of Joint Logistics Support Force (Fuzong Clinical Medical College) (Former Fuzhou General Hospital), Fuzhou, Fujian, China*

Correspondence should be addressed to Xiaojin Zhang; zxjin72@126.com and Fan Pan; pdsg@163.com

Liver hepatocellular carcinoma (LIHC) is a highly lethal malignant tumor originating from the digestive system, which is a serious threat to human health. In recent years, immunotherapy has shown significant therapeutic effects in the treatment of LIHC, but only for a minority of patients. The basement membrane (BM) plays an important role in the occurrence and development of tumors, including LIHC. Therefore, this study is aimed at establishing a risk score model based on basement membrane-related genes (BMRGs) to predict patient prognosis and response to immunotherapy. First, we defined three patterns of BMRG modification (C1, C2, and C3) by consensus clustering of BMRG sets and LIHC transcriptome data obtained from public databases. Survival analysis showed that patients in the C2 group had a better prognosis, and Gene Set Variation Analysis (GSVA) revealed that the statistically significant pathways were mainly enriched in the C2 group. Moreover, we performed Weighted Correlation Network Analysis (WGCNA) on the above three subgroups and obtained 179 intersecting genes. We further applied function enrichment analyses, and the results demonstrated that they were mainly enriched in metabolism-related pathways. Furthermore, we conducted the LASSO regression analysis and obtained 4 BMRGs (MPV17, GNB1, DHX34, and MAFG) that were significantly related to the prognosis of LIHC patients. We further constructed a prognostic risk score model based on the above genes, which was verified to have good predictive performance for LIHC prognosis. In addition, we analyzed the correlation between the risk score and the tumor immune microenvironment (TIM), and the results showed that the high-risk scoring group tended to be in an immunosuppressed status. Finally, we investigated the relationship between the risk score and LIHC immune function. The results demonstrated that the risk score was closely related to the expression levels of multiple immune checkpoints. Patients in the low-risk group had significantly higher IPS scores, and patients in the high-risk group had lower immune escape and TIDE score. In conclusion, we established a novel risk model based on BMRGs, which may serve as a biomarker for prognosis and immunotherapy in LIHC.

1. Introduction

Liver cancer is a highly lethal malignant tumor that seriously threatens human physical and mental health. Liver hepatocellular carcinoma (LIHC) is the most common pathological type of liver cancer, accounting for more than 90% of all

cases [1]. Currently, the most common treatment options for LIHC are surgery, ablation, microwave ablation, cryotherapy ablation, percutaneous ethanol injection, and noncatheter-based therapies, but the 5-year survival rate is less than 20% [2–4]. It is now widely recognized that the poor prognosis of LIHC is due to the lack of appropriate

prognostic biomarkers [5]. Therefore, it is crucial to develop a model to identify high-risk patients and enable personalized medicine for LIHC patients.

In recent years, with the deepening understanding of the pathogenesis of the tumor, a variety of immune checkpoint inhibitors (ICIs) based on immune checkpoints have gradually become the focus of LIHC treatment. At present, the PD1/PD-L1 antibody is widely used in the immunotherapy of LIHC and has achieved significant treatment effects [6]. It has been confirmed that the tumor immune environment (TIM) is key to the immunotherapeutic effect of ICIs [7]. Therefore, it is particularly critical to clarify the specific regulation mechanism of regulating the TIM of LIHC.

The structure of the basement membrane (BM) plays a key role in the occurrence and development of malignant tumors [8–10]. Under normal physiological conditions, the BM is a sheet-like structure under the epithelial cells, of which laminin and type IV collagen are its main structural components [11]. The BM not only resists mechanical stress and maintains tissue shape but also regulates the adhesion and migration of various cells, including immune cells [12]. However, under tumor conditions, the structure of the BM is destroyed, resulting in the loss of its original shape and function, which in turn causes abnormal migration of tumor cells and various immune cells [8, 10, 13]. Epithelial-mesenchymal transition (EMT) of the basement membrane promotes the transfer of tumor cells through the lymphatic vasculature in an intravasation and extravasation manner [14]. The products of tumor metabolism can induce changes in the structural components of the BM, thereby enhancing the metastatic ability of tumors [15]. Other studies have confirmed that the migration ability of T cells in the dense collagen matrix area around the tumor nest is significantly reduced, and the reduction of the collagen matrix density in the BM will enhance the infiltration of T cells in the tumor [16]. Although this change has little effect on tumor growth, it does improve response to anti-PD1 therapy [17, 18]. In 2022, Jayadev et al. applied bioinformatics and in vivo experiments to define more than 200 genes related to BM, such as LAMA5, MPZL2, and MATN2 [19]. Therefore, a better understanding of the role of the basement membrane may lead to new and promising treatments for LIHC.

In this study, we first obtained the transcriptome data of LIHC from the TCGA database and then further analyzed and screened 4 basement membrane-related genes (BMRGs) that were significantly associated with the prognosis of LIHC. Furthermore, we constructed a prognostic risk model by screening the BMRGs and confirmed that the model has good predictive capacity for the prognosis of LIHC patients. Finally, we further evaluated the differences in the risk score of this model for immune cell infiltration and immunotherapy response. Our study provides a novel research direction for the monitoring of prognosisand evaluation of immunotherapy in LIHC.

2. Materials and Methods

2.1. Identification of BMRGs and Collection of LIHC Transcriptome Data.
First, we obtained 222 basement membrane-related gene sets from previous studies. Next, we used the public database TCGA to download the LIHC transcriptome information. The survival information of the LIHC samples was merged with the transcriptome data, and finally, 342 LIHC samples with survival information were obtained.

2.2. Construction of Risk Scoring Model.
We obtained the basement membrane-related gene sets associated with patient prognosis by the LASSO Cox regression analysis. The risk score for each LIHC patient was calculated according to an established formula. Risk score = $(\beta_i{}^* \mathrm{Exp}_i)$, where Exp_i represents the expression level of each gene and β_i represents the coefficient of each gene [20]. ROC curves were used to evaluate the accuracy of the predictive power of each dataset.

2.3. Consensus Clustering of 222 Basement Membrane-Related Genes by NMF Algorithm.
We applied the NMF algorithm for consensus clustering to identify different classification patterns based on the expression of 222 BMRGs. Then, the optimal number of clusters is selected according to the cooccurrence coefficient, dispersion coefficient, and silhouette coefficient [21].

2.4. Analysis of Immune Cell Infiltration in LUAD.
We applied CIBERSORT to assess the correlation between the high- and low-risk scores and the proportion of immune cell infiltration. CIBERSORT relies on a gene expression matrix file (named LM22), which can specifically identify specific genes in immune cells. The expression of this specific gene can analyze immune cells in tissues and identify human hematopoietic cell phenotypes [22].

2.5. IPS, ESTIMATE, and TIDE.
The immunophenoscore (IPS) is a predictor of response to anti-CTLA-4 and anti-PD1 therapy by quantifying tumor immunogenicity, immunomodulators, effector cells, and suppressor cells. This method obtains the final IPS score by the weighted quantification of the above components [23]. ESTIMATE (estimation of stromal and immune cells in malignant tumor organizations using expression data) is a novel algorithmic algorithm that infers tumor cell structure and distinct infiltrating normal cells from uniquely characterized genes in the transcriptional profile of cancer tissues [24]. In this study, by using the ESTIMATE algorithm, we calculated the immune and stromal scores to predict the correlation of risk scores with immune and stromal levels. The tumor immune dysfunction and exclusion (TIDE) is an algorithm used to predict response to immune checkpoint inhibitors. Low TIDE scores represent weaker immune evasion, and these patients may show a stronger response to immunotherapy, while high TIDE scores represent strong immune evasion, and these patients are less responsive to immunotherapy [25].

2.6. Statistics.
In this study, gene expression data from TCGA database were analyzed using Student's t-test. Correlation analysis of Spearman and Pearson was used to assess in the TISdb database. The expression of ADAR1 was correlated with the abundance scores of immune cells assessed using Spearman's correlation analysis. All analyses were performed

(a)

(b)

Figure 1: Continued.

(c)
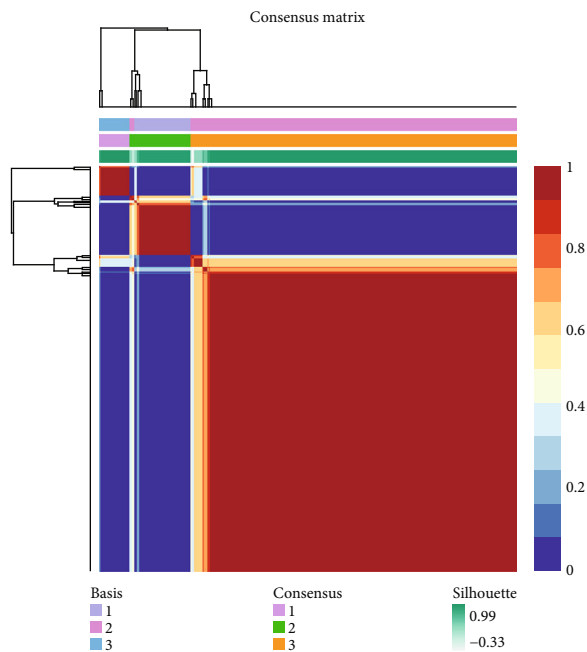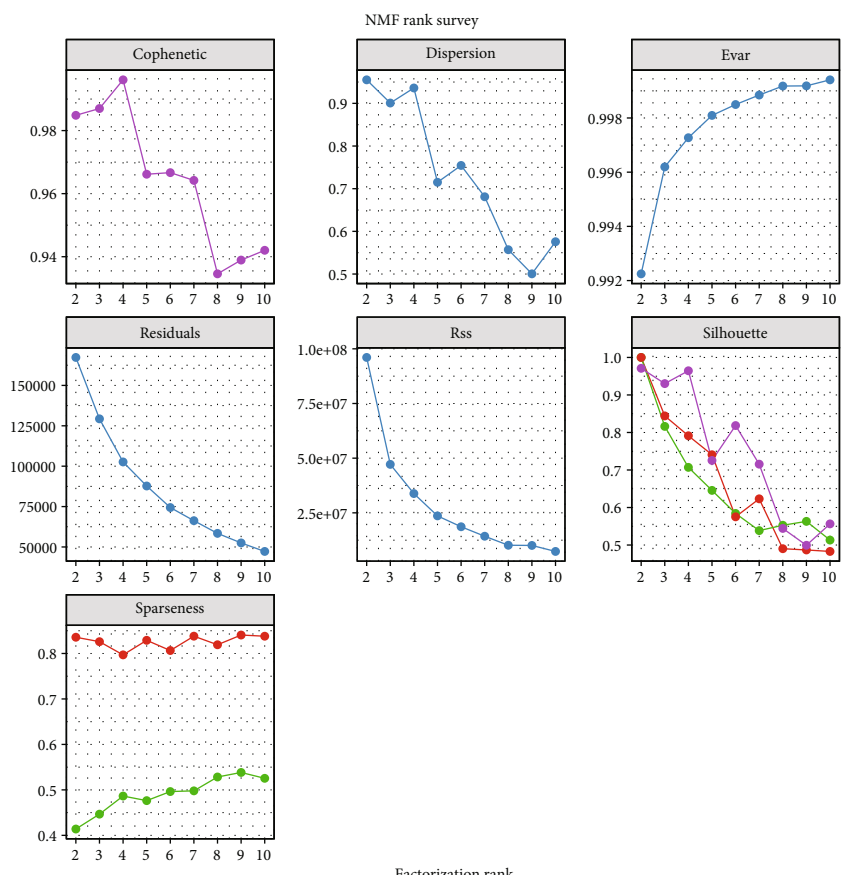
(d)
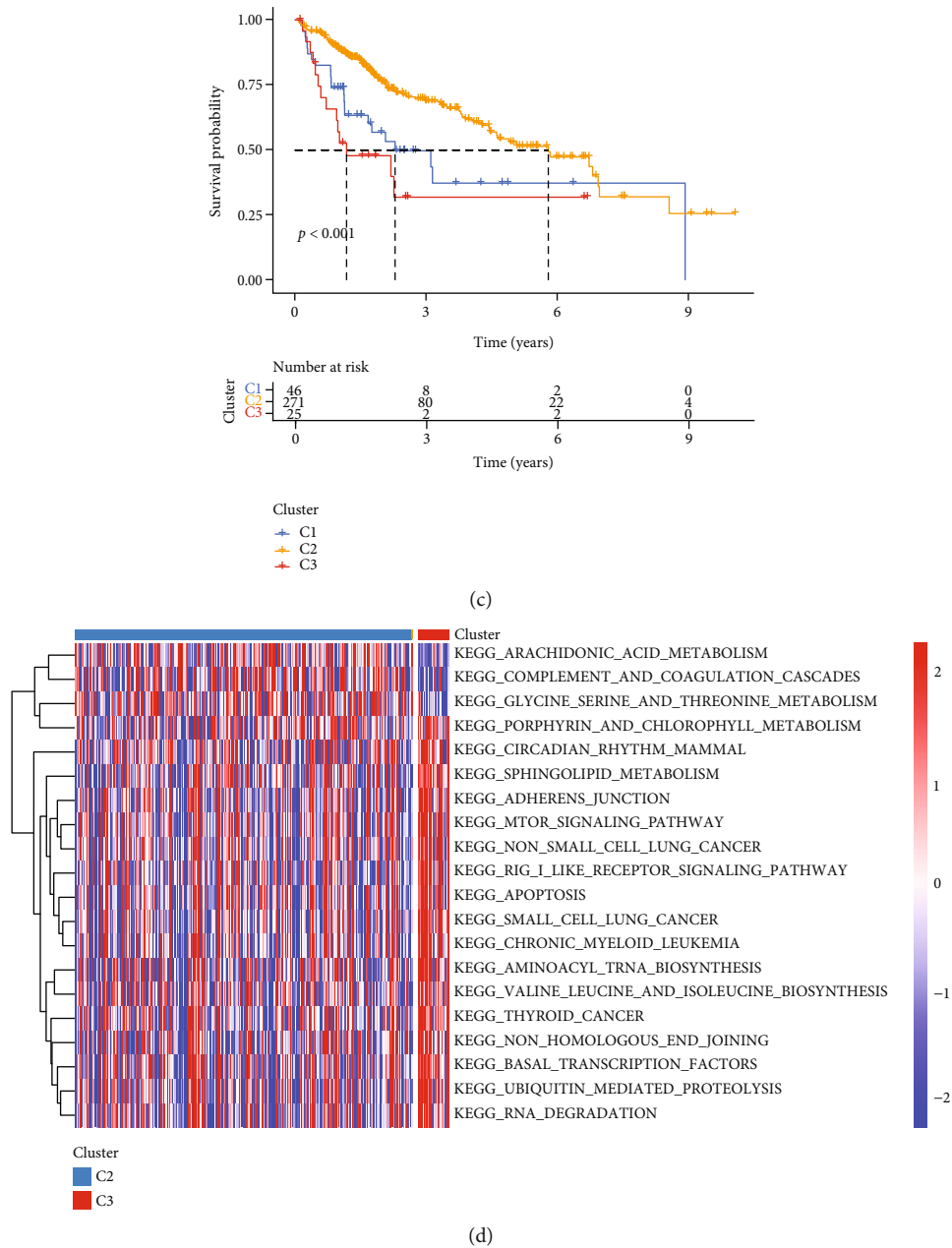
FIGURE 1: BMRG consensus cluster and relevant biological pathway. (a) Nonnegative matrix factorization (NMF) clustering was conducted, and three subgroups were identified as the optimal value for consensus clustering. (b) Factorization rank for k = 2-10. (c) The Kaplan-Meier curves of overall survival (OS) for 342 LIHC patients in TCGA cohort with different BMRG clusters. The numbers of C1, C2, and C3 patients are 46, 271, and 25, respectively (log-rank test). (d) GSVA analysis heatmap for different clusters.

with the R software (version 4.1.1, http://www.r-project.org) loaded with the R packages ("ggplot2," "ggpubr," "limma," "survival," "survminer," "clusterProfiler," "ESTIMATE," "enrichplot," and "forestplot"), and the results were visualised. p value < 0.05 was considered statistically significant.

3. Results

3.1. Consensus Clustering Analysis of BMRGs in LIHC by NMF Algorithm. The structure of the BM regulates the migration of tumor and immune cells in a variety of malignancies [26, 27]. First, we applied the consensus clustering analysis of the NMF algorithm to stratify 222 basement membrane-related genes into 9 subtypes (Supplementary Figure 1). As seen in the cophenetic, the curve decline was most pronounced when all samples were separated into type 3, so we identified three distinct clusters of modification modes. The three different patterns of cluster distribution were cluster 1 (146 cases, named C1), cluster 2 (271 cases, named C2), and cluster 3 (25 cases, named C3) (Figures 1(a)

(a)

(b)
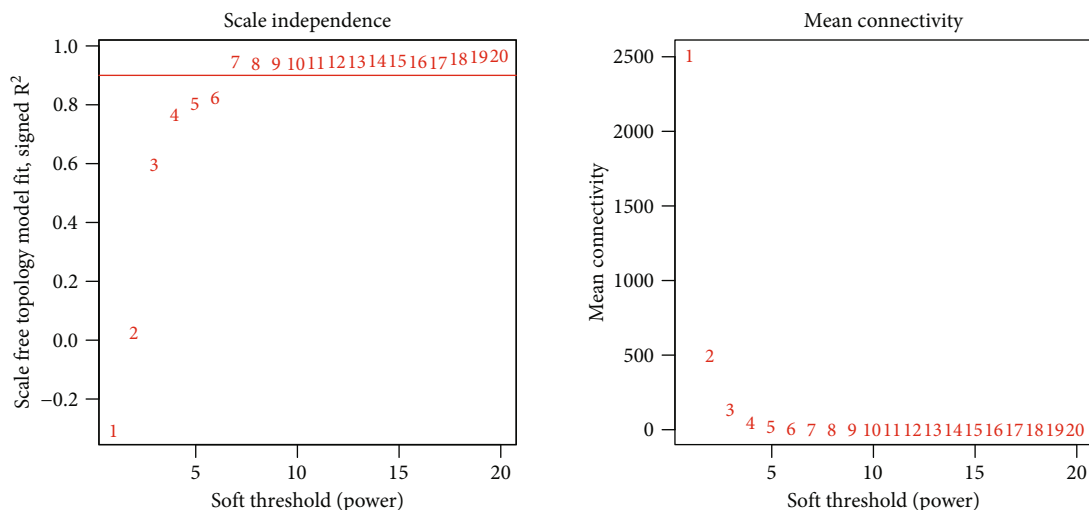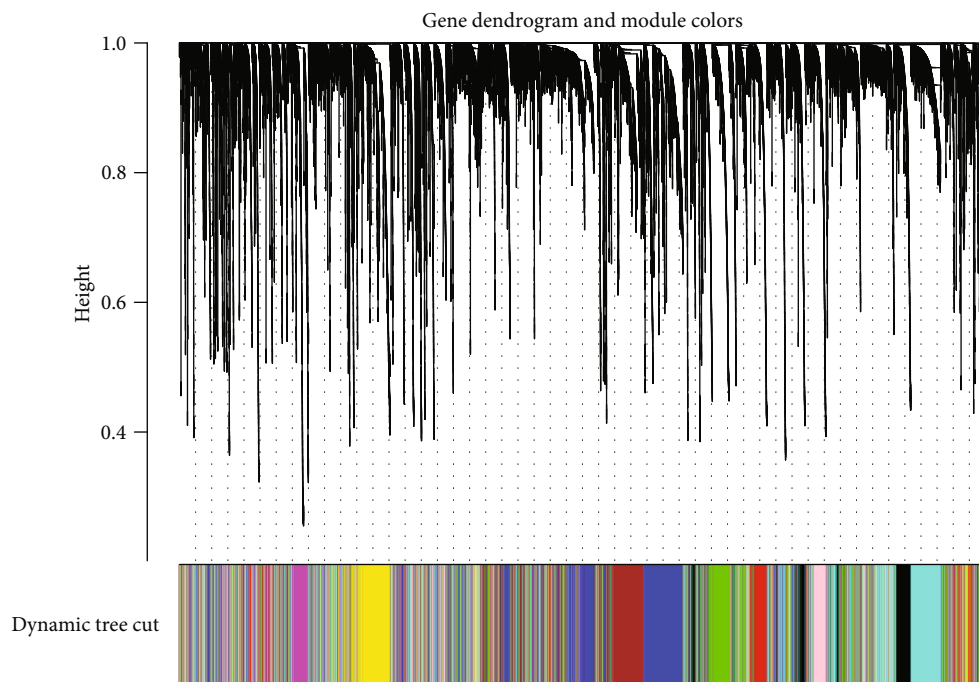
FIGURE 2: Continued.

Figure 2: Continued.

Module membership vs. gene significance
cor = 0.52, $p = 1.8e-152$

(d)

Module membership vs. gene significance
cor = 0.85, $p < 1e-200$
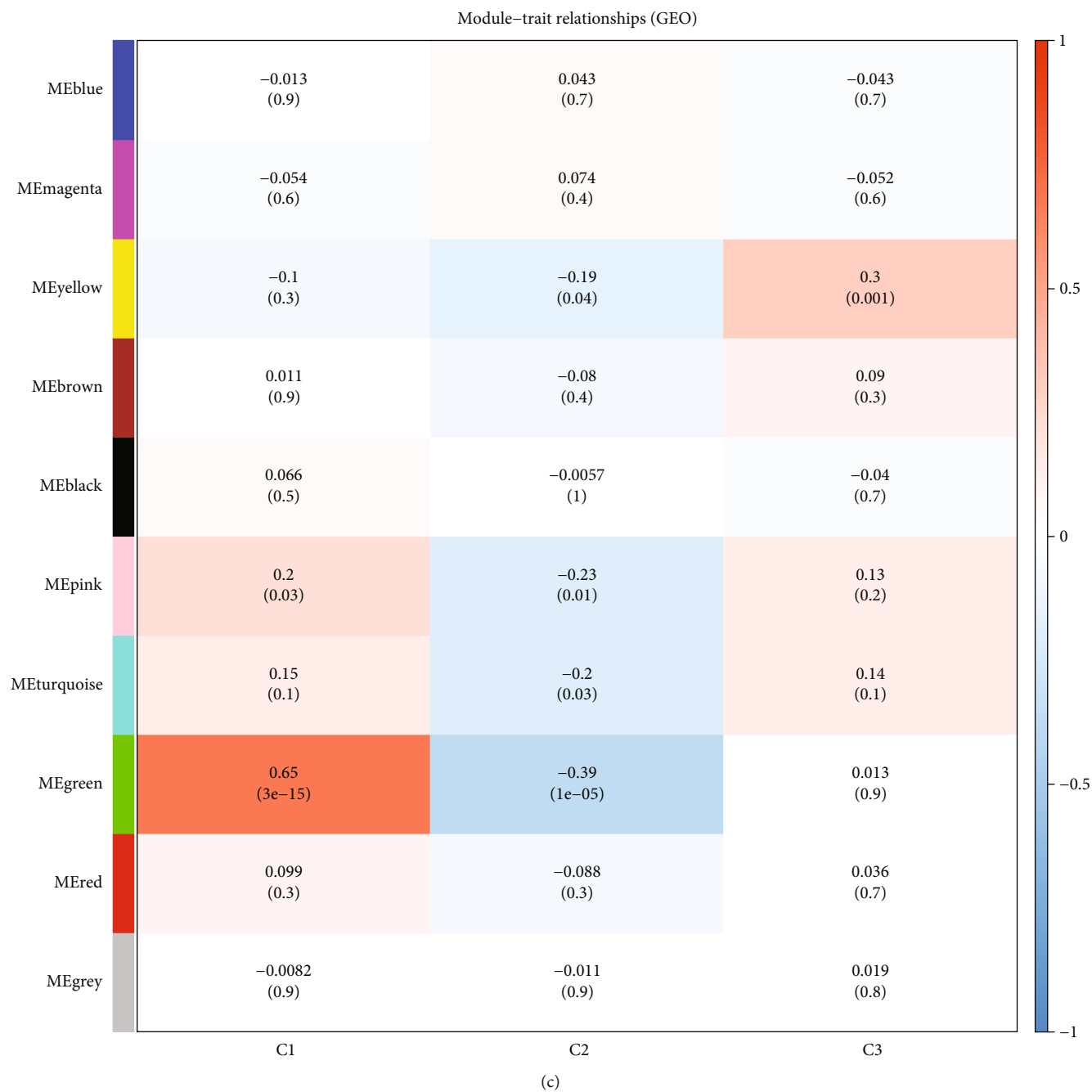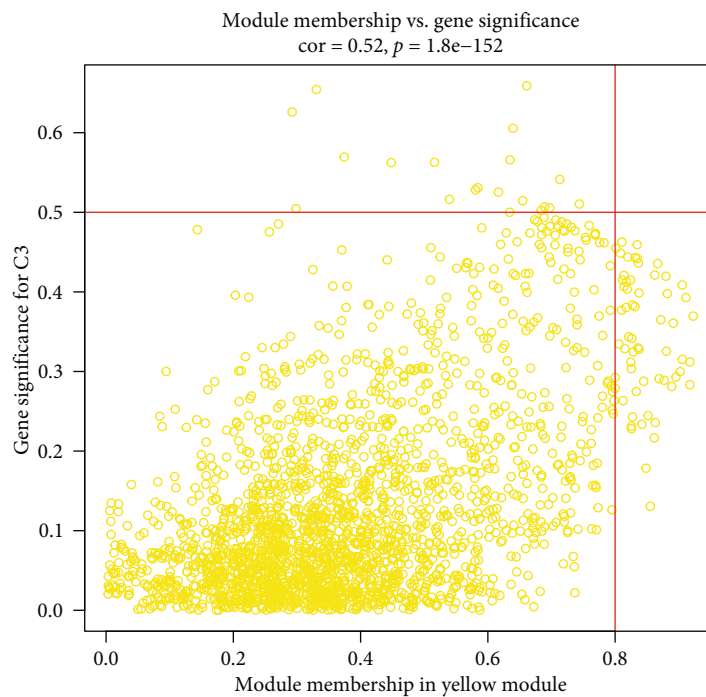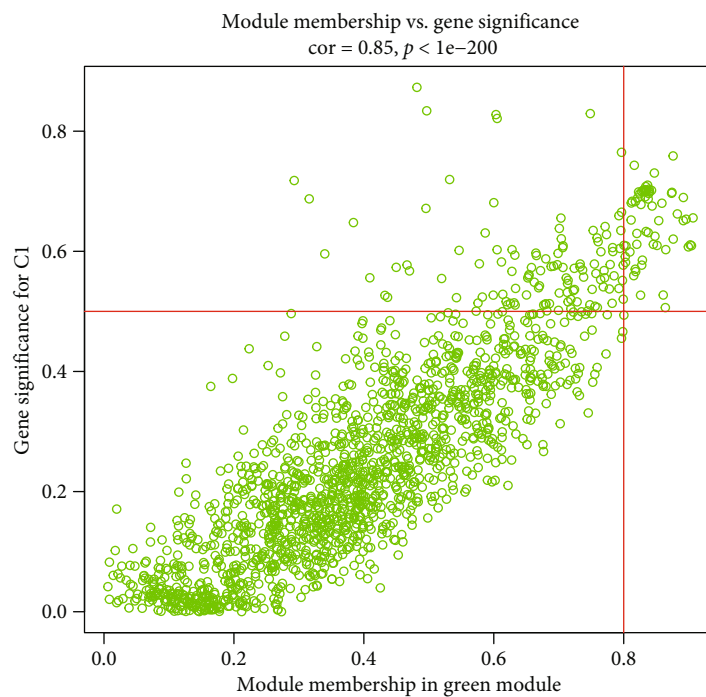
(e)

FIGURE 2: The WGCNA of the NMF phenotypes of BM. (a, b) Detailed results of the weighted gene coexpression network analysis. (c) The relationship of module features with the consensus subgroups was assessed by ten gene modules obtained from WGCNA. (d) The results of module-feature relationship analysis between the yellow module and the consensus subgroup C3. (e) The results of module-feature relationship analysis between the green module and the consensus subgroup C1.

and 1(b)). Next, we performed survival analysis, which showed that C2 had a better survival prognosis, whereas C3 had the worst prognosis (Figure 1(c)). In addition, we further conducted the GSVA on C2 and C3, and the results showed that a variety of pathways were abnormally enriched in the samples of C3 (Figure 1(d)).

(a)

(b)

(c)
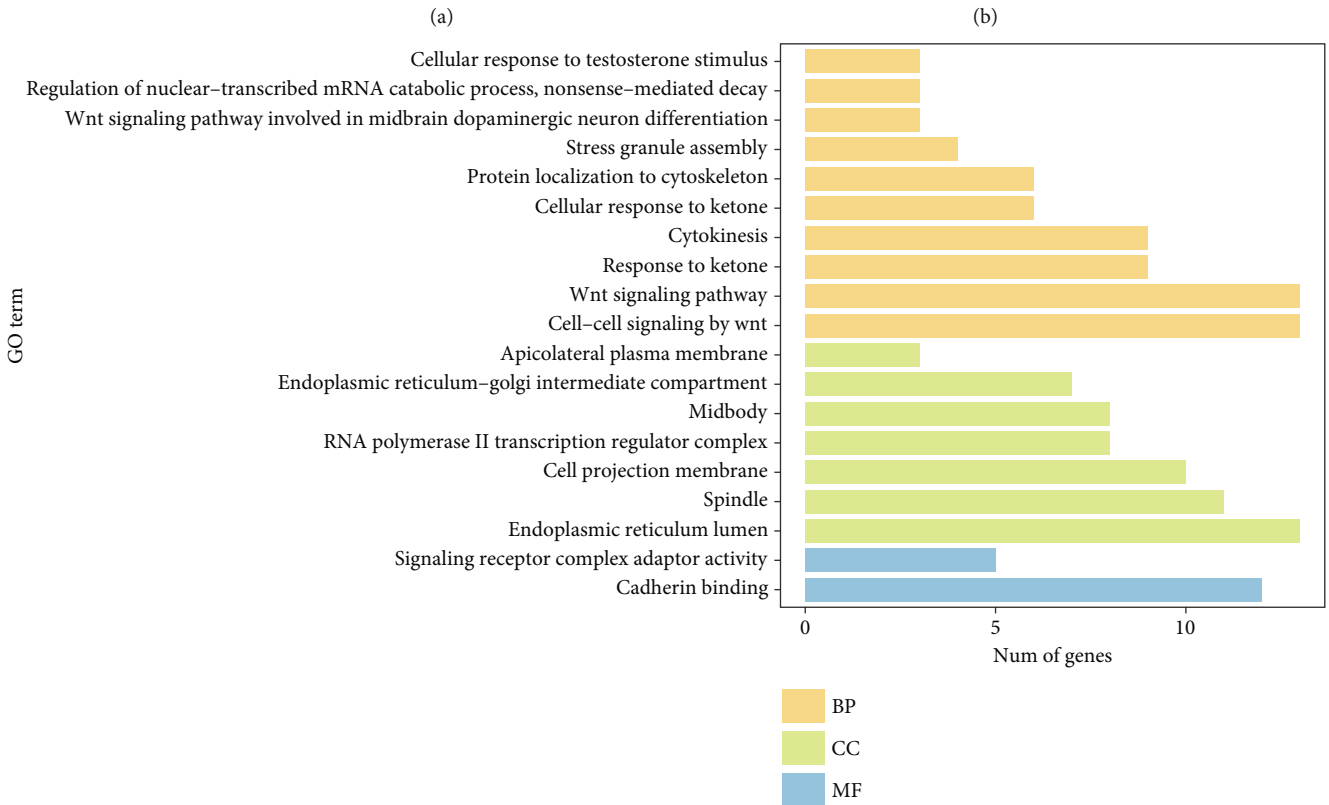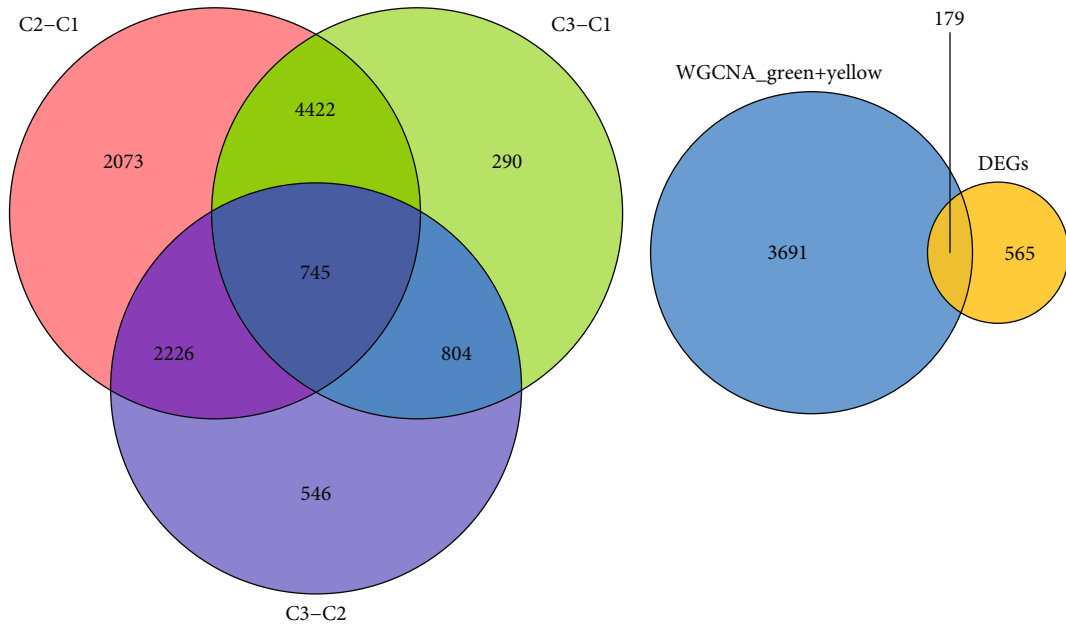
FIGURE 3: Continued.
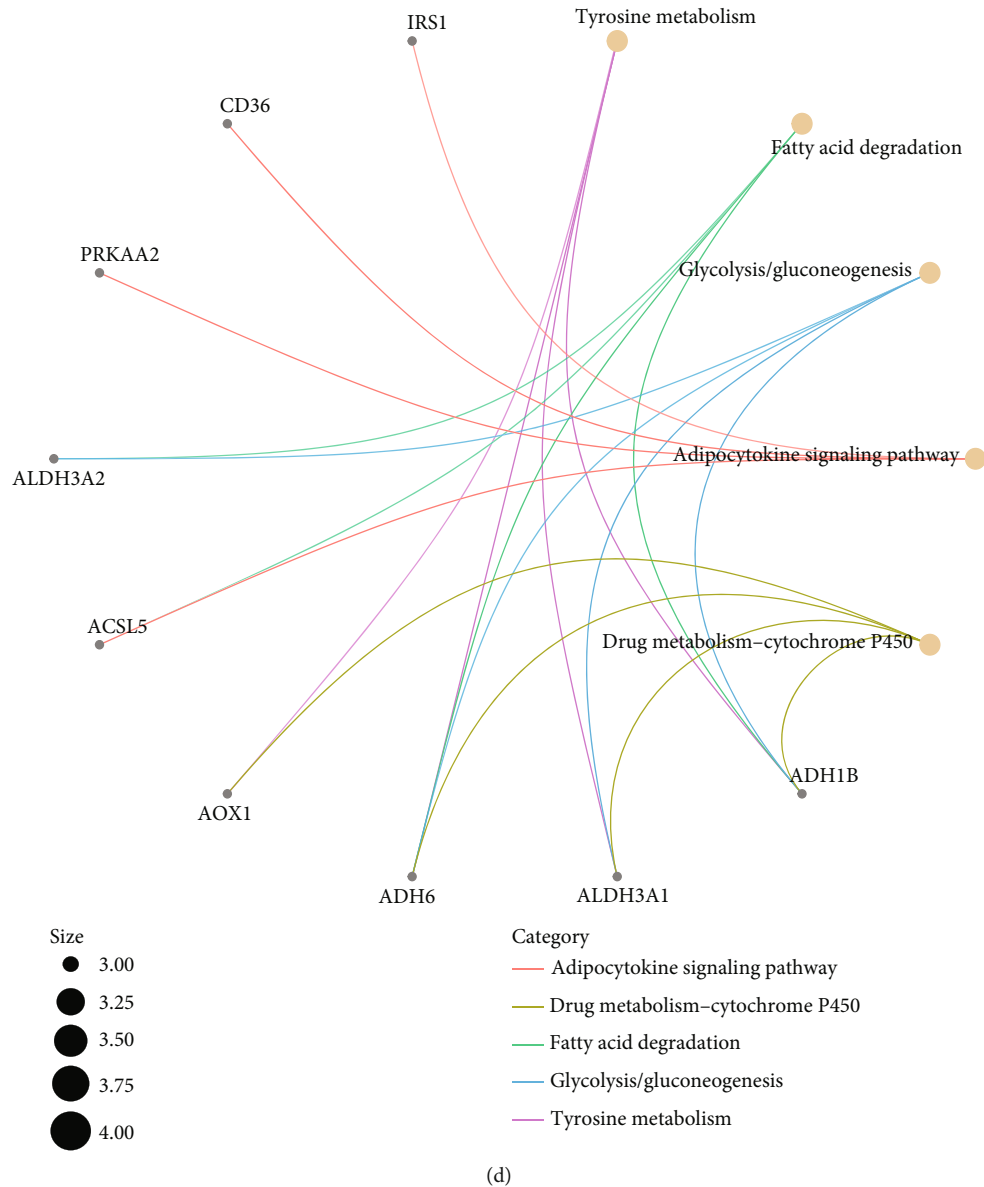
FIGURE 3: Identification and functional analysis of BMRGs. (a) Differential genes for the three molecular clusters of NMF. (b) Venn diagram of WGCNA module genes with differential genes. (c) GO functional analysis of intersecting genes. (d) KEGG functional analysis of intersecting genes.

3.2. WGCNA and Difference Analysis Based on Different Typing of BMRGs in LIHC. Given the obtained 3 different subtypes of LIHC based on BMRGs, we applied the weighted gene coexpression network analysis (WGCNA) to analyze the above subtypes. In this study, we chose 6 as the optimal threshold (Figure 2(a)). Based on the WGCNA results, we obtained 10 coexpressed gene modules (Figure 2(b)). The yellow module was significantly correlated with the worst prognosis C3, and the green module was closely correlated with the worst prognosis C1 (Figure 2(c)). As shown in Figures 2(d) and 2(e), there was a significant correlation between the gene sets within these two modules and the signatures in each type. In addition, we performed the differentially expressed genes (DEGs) analysis on each of the three

subgroups C1, C2, and C3 and obtained a total of 745 genes with statistical significance (Figure 3(a)). Furthermore, based on the 3770 coexpressed genes obtained by the green and yellow modules, we took the intersection with the above-mentioned differential genes and finally obtained a total of 179 intersecting genes (Figure 3(b)). Finally, we applied GO and KEGG enrichment analyses on these 179 genes, and the results showed that they were mainly enriched in related metabolic pathways, such as tyrosine metabolism, fatty acid metabolism glycolysis, and adipokine signaling pathway (Figures 3(c) and 3(d)).

3.3. Construction and Validation of BMRG Risk Scoring Model. We first performed the LASSO regression analysis

(a)

(b)

(c)

(d)

Figure 4: Continued.

(e)

(f)

(g)

(h)
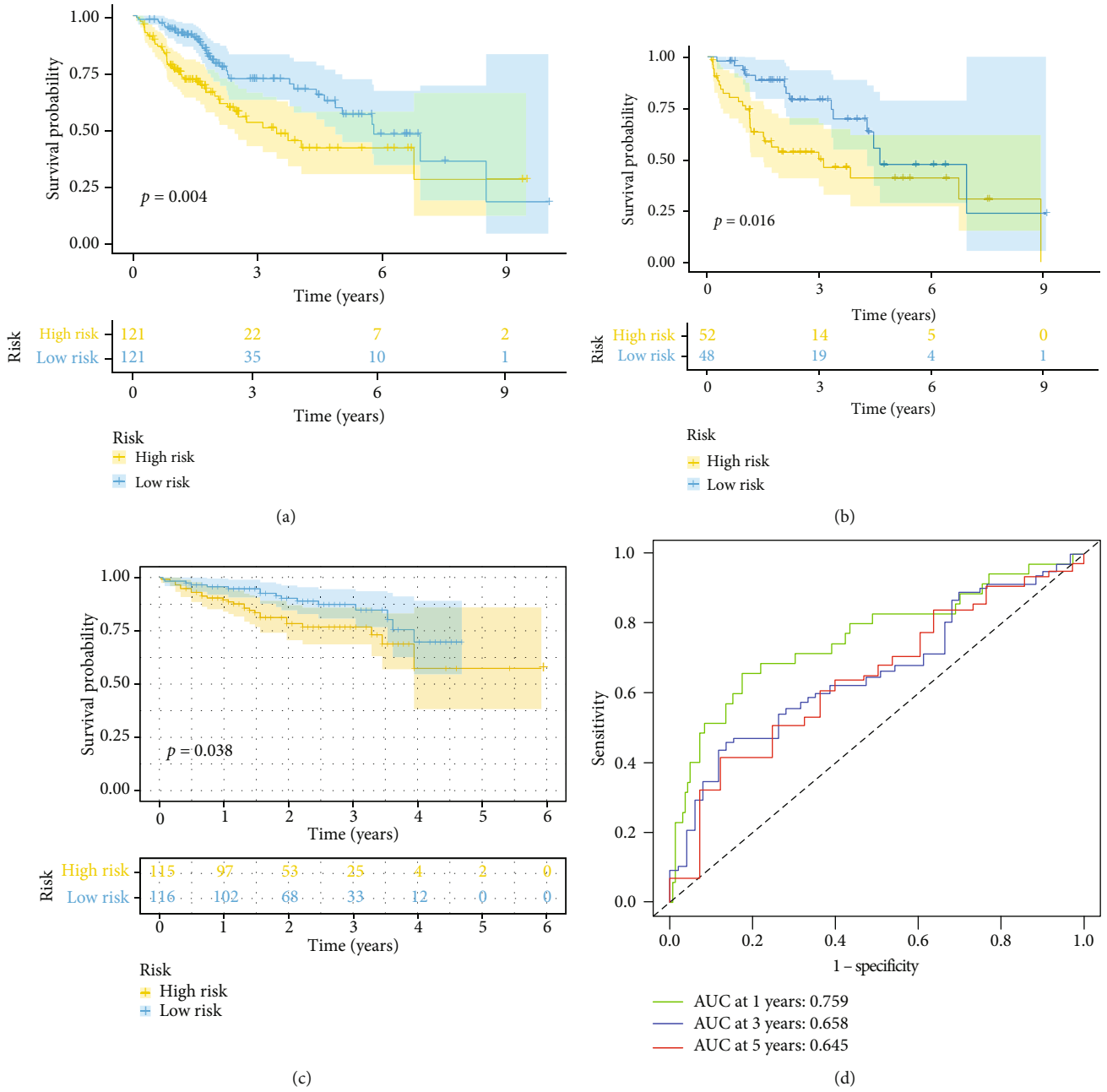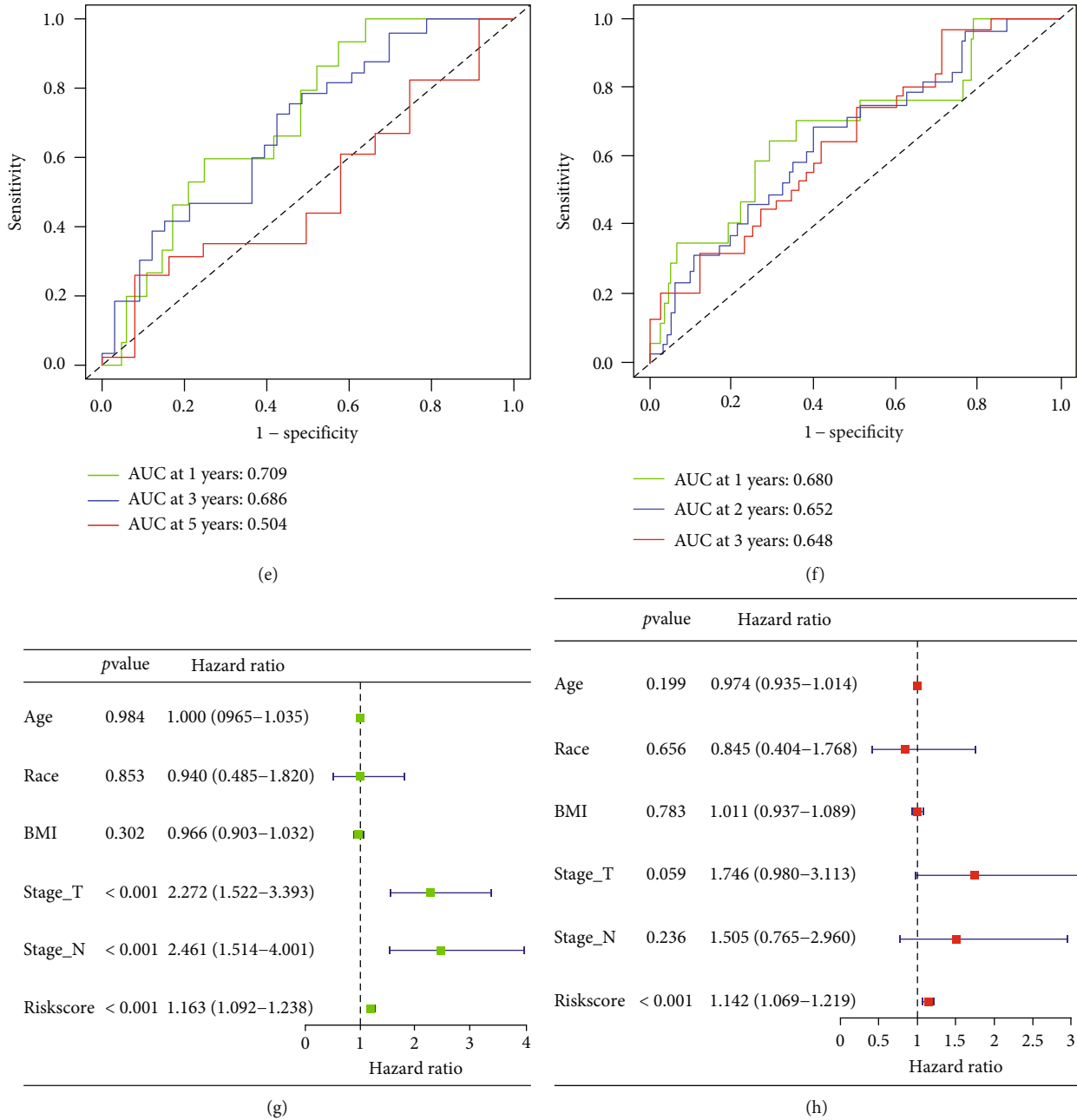
FIGURE 4: Construction and verification of the BMRG risk model by LASSO Cox regression analysis. (a–c) The Kaplan-Meier curves for patients with the high- and low-BMRG subgroups: (a) train cohort, (b) test cohort, and (c) ICGC cohort. (d–f) ROC curves showing the predictive efficiency of the BMRG risk scores for 1-year, 3-year, and 5-year survival: (d) train set, (e) test set, and (f) ICGC validation set. (g) Univariate analysis of risk scores of BMRGs and clinicopathological characteristics of LIHC. (h) Multivariate analysis of risk scores of BMRGs and clinicopathological characteristics of LIHC.

on the obtained 179 genes and screened 4 basement membrane-related genes (Supplementary Figure 2). Next, we randomly divided the LIHC samples in TCGA into two cohorts, namely, the training cohort and the validation cohort, at a ratio of 7 : 3, while using the ICGC-LIHC cohort as the external validation cohort. Furthermore, we constructed a LIHC risk prognostic model with basement membrane characteristics using the four genes obtained above. In the training, validation, and external validation

cohorts, high-risk patients had significantly worse outcomes than low-risk patients (Figures 4(a)–4(c) and Supplementary Figure 3). In addition, we used ROC curves to evaluate the predictive power of the BMRG risk model, and the results showed that the AUCs of each cohort at 1, 3, and 5 years were 0.759, 0.658, and 0.645 (training cohort); 0.709, 0.686, and 0.504 (validation cohort); and 0.680, 0.680, 0.652, and 0.648 (external validation cohort) (Figures 4(d)–4(f)), and these results show that the model
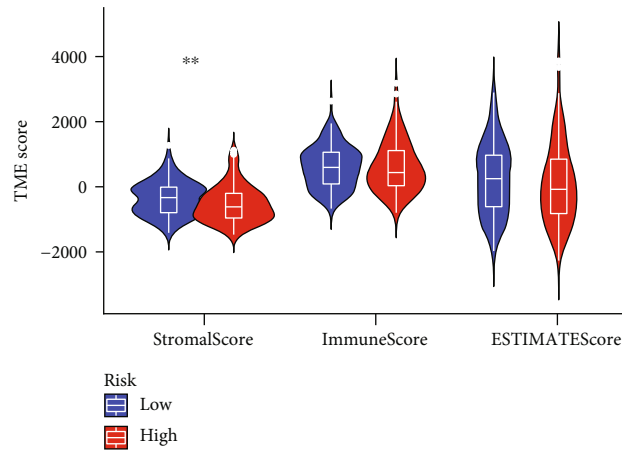
(a)
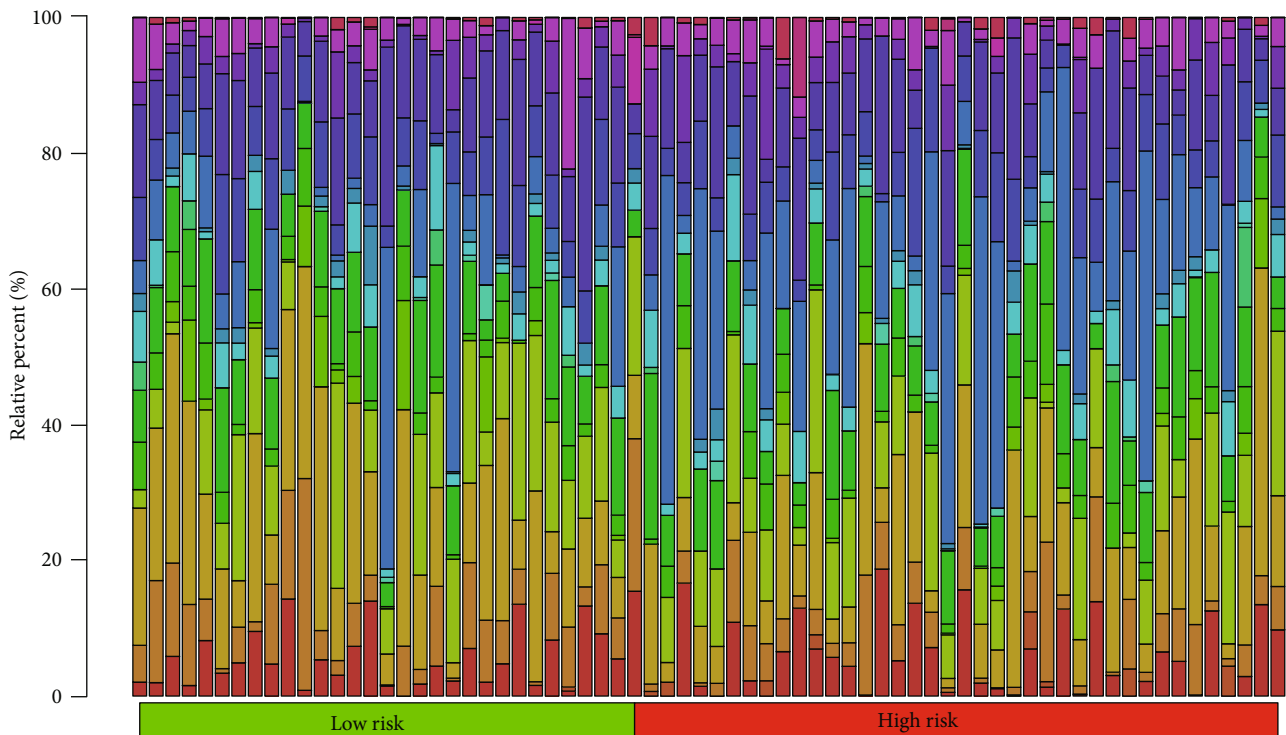
(b)

FIGURE 5: Continued.

(c)

FIGURE 5: Continued.

(d)

(e)

(f)

(g)
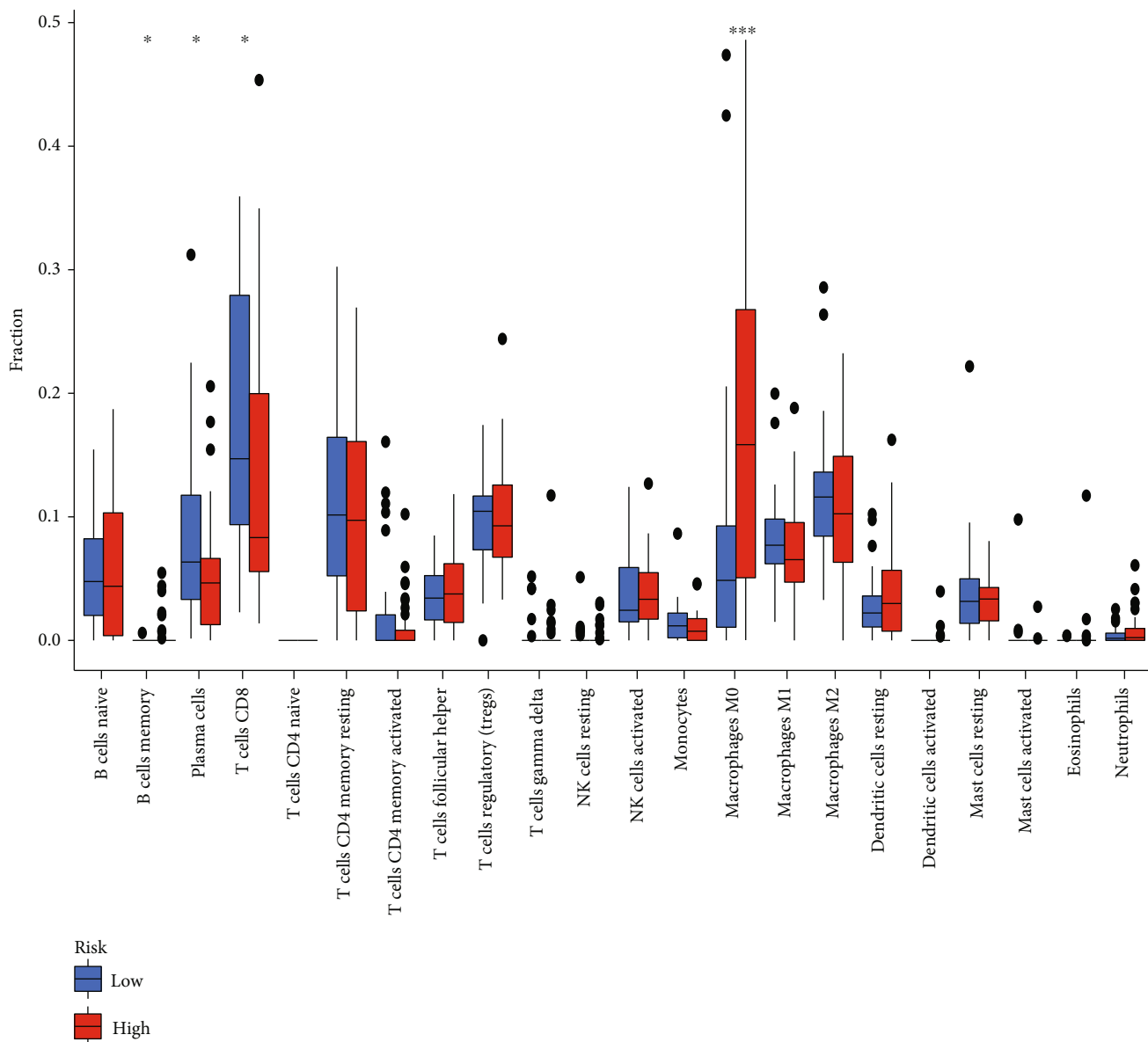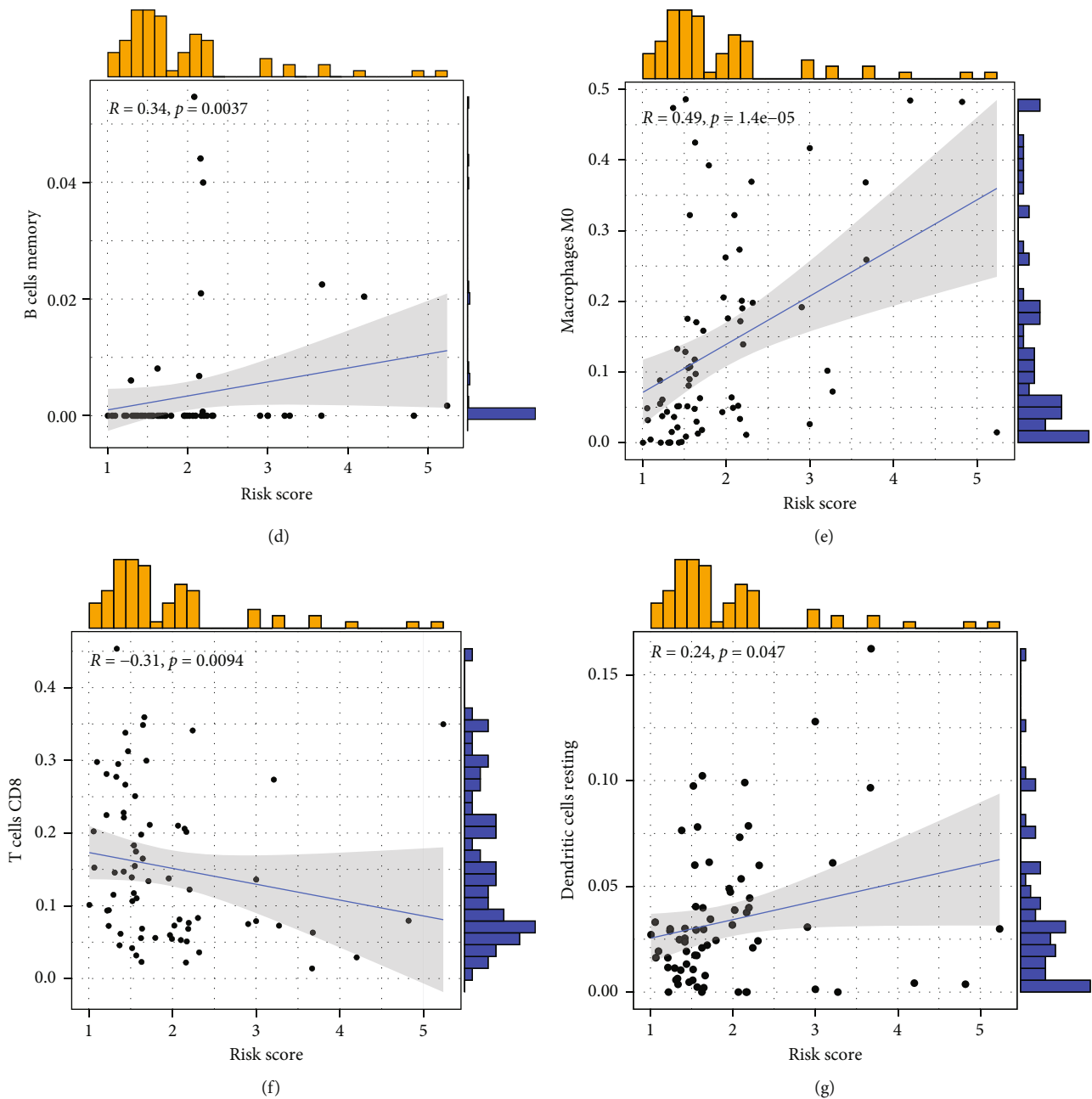
FIGURE 5: The relationship between the BMRG risk score and the TIM in LIHC. (a) Correlation between the BMRG risk score and the TME score. (b) The proportion of tumor-infiltrating immune cells in the BMRG high- and low-risk cohort via the CIBERSORT algorithm. (c) Comparison of different immune cell infiltrations under high and low risk scores. (d–g) Linear relationship between BMRG risk score and immune cells.

has good predictive performance. Finally, we applied the univariate and multivariate Cox regression analyses on the risk score combined with each clinical feature, and the results revealed that the risk prognostic model based on BMRG could be used as an independent prognostic factor (Figures 4(g) and 4(h)).

3.4. Correlation Analysis between BMRG Risk Score and LIHC Immune Microenvironment. The TIM is closely related to tumor immune escape. To clarify their complex relationship, we evaluated the TIM of LIHC by the ESTI-MATE algorithm and observed that the low-risk cohort

had significantly higher stromal scores than the high-risk cohort (Figure 5(a)). Next, we assessed the correlation between the infiltration abundance of immune cells and the risk score by the CIBERSORT algorithm and presented them in the form of heatmaps and boxplots. The results showed that the infiltrating abundance of CD8^{+} T cells and plasma cells was higher in the low-risk cohort than in the high-risk group (Figures 5(b) and 5(c)). As shown in Figures 5(d)–5(g), we further analyzed the correlation between the risk score and the degree of immune cell infil-tration, and the results showed that memory B cells, M0 macrophages, and dendritic cells were positively associated

(a)

*** $p < 0.001$
** $p < 0.01$
* $p < 0.05$

(b)

(c)

(d)

Figure 6: Continued.

(e)

(f)
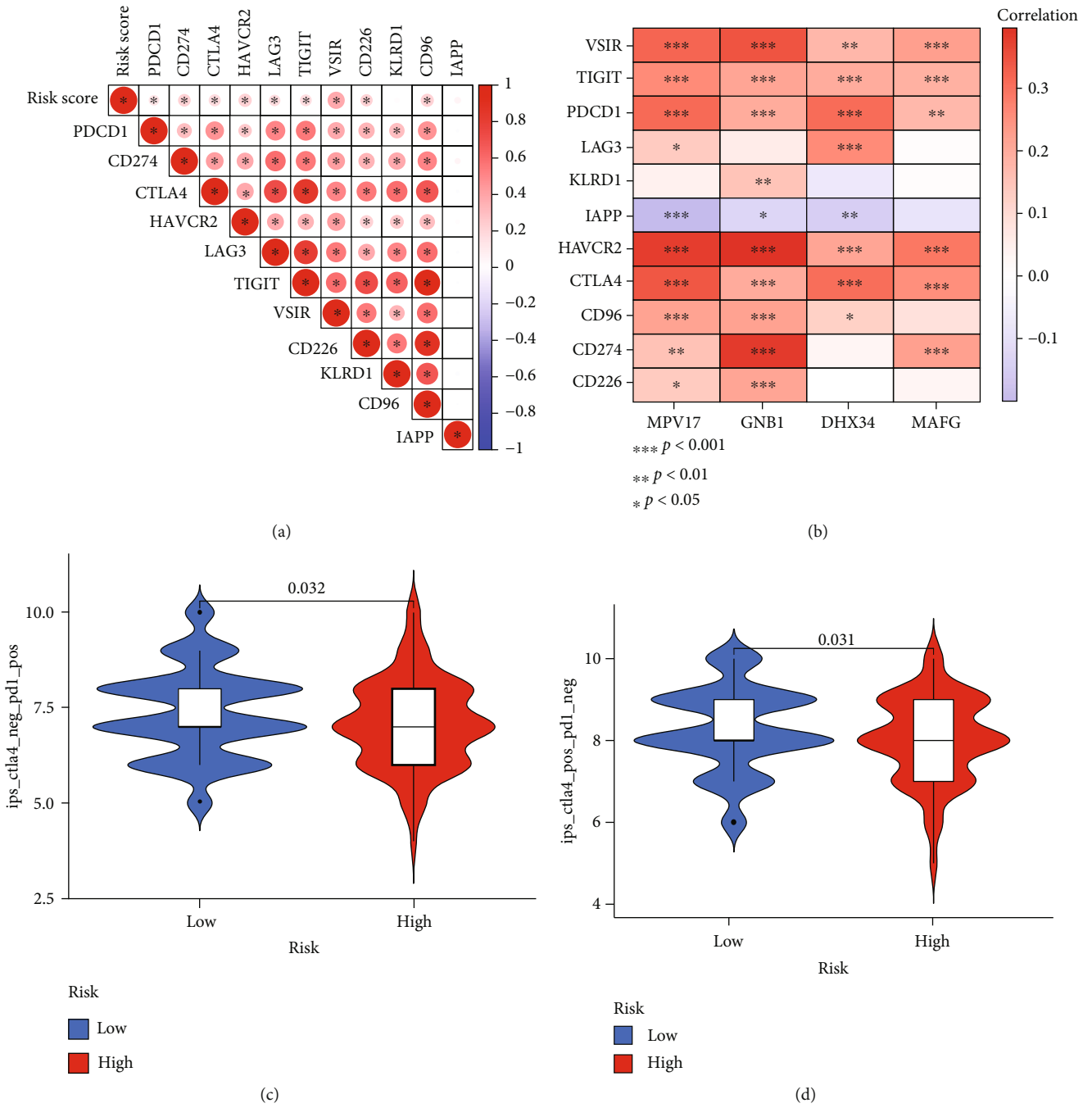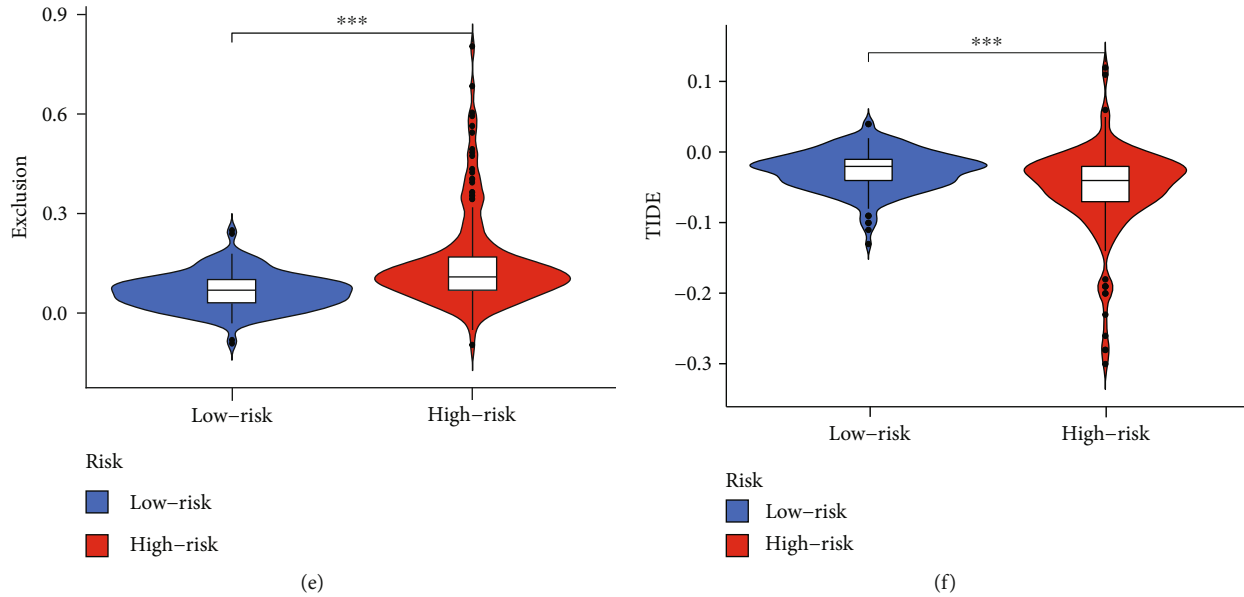
Figure 6: The BMRG risk score predicts immunotherapeutic benefits. (a) Association of BMRG risk scores with immune checkpoints. (b) Association of four BMRGs with eleven immune checkpoints. (c, d) The proportion of patients with clinical response to anti-PD1 and anti-CTLA4 immunotherapy in the low- or high-BMRG-risk group. (e) Differences in immune escape score between the high- and low-risk groups. (f) Differences in TIDE scores between the high- and low-risk groups.

with the risk score, while CD8$^+$ was negatively associated with the risk score. The above results strongly suggested that the risk score of this model is closely related to the TIM of LIHC patients.

3.5. The Role of the BMRG Risk Score in Predicting Response to Immunotherapy.

Immune checkpoints are important receptors that regulate immune cell function and are important predictors for evaluating immunotherapy response [28] Therefore, we evaluated the association of 11 immune checkpoints with risk scores of BMRGs, and the results showed that risk scores were positively correlated with multiple immune checkpoints (Figure 6(a)). Next, we analyzed the relationship between the 4 BMRGs in the model and immune checkpoints, and the results demonstrated that IAPP was negatively correlated with these genes, while other immune checkpoints were positively correlated with 4 genes (Figure 6(b)). Given the strong correlation between BMRG scores and immune checkpoints, we further investigated whether the risk scores of BMRGs could predict the response of LIHC patients to ICIs. The IPS scoring system is widely applied to assess response to immunotherapy at present. In this study, we found that the IPS scores of PD1-positive and CTLA4-positive patients were significantly elevated in the low-risk group, and the IPS scores of PD1-negative and CTLA4-positive patients were also significantly elevated in the low-risk group (Figures 6(c) and 6(d)). Finally, we demonstrated that high-risk patients had stronger immune evasion and worse TIDE scores (Figures 6(e) and 6(f)). These findings indirectly indicated that risk scoring models based on BMRGs can be used to assess response to immunotherapy.

3.6. GSEA of BMRG Risk Model.

Our previous data suggested that the BMRG risk score is closely related to the TIM of LIHC. To further elucidate the underlying mechanism, we performed GSEA by differentially expressed genes between the high- and low-risk cohorts. The results of the KEGG enrichment analysis showed that the high-risk cohorts were mainly enriched in cytokine receptor interaction, extracellular matrix receptor interaction, and neuroligand-receptor interaction pathways (Figure 7(a)). Meanwhile, the enrichment results of the immune gene set showed that the high-risk cohort was mainly enriched in B cells, CD8$^+$ T cells, NK cells, and monocytes (Figure 7(b)).

4. Discussion

Recurrence and metastasis are the main causes of treatment failure in LICH. Different from traditional treatments, immunotherapy is a promising treatment for LIHC. BM structure plays an important role in immune cell migration and is closely related to prognosis [29, 30]. In this study, we first performed consensus clustering of BMRGs using the NMF algorithm to classify all samples into three patterns. In addition, through WGCNA and differential gene analysis, the intersection between the two was further taken to obtain a differential gene set. Moreover, LASSO regression analysis was performed on the obtained differential gene set, and a prognostic risk score model based on BMRGs was constructed. Its predictive ability was further verified. Finally, we found that a risk score model based on BMRGs could have good predictive power for the immune microenvironment and immunotherapy.

(a)

Figure 7: Continued.

Enriched in high risk group

GSE13547_CTRL_VS_ANTI_IGM_STIM_BCELL_12H_UP

GSE15750_DAY6_VS_DAY10_TRAF6KO_EFF_CD8_TCELL_UP

HOWARD_NK_CELL_INACT_MONOV_INFLUENZA_A_INDONESIA_05_2005_H5N1_AGI

VAN_DEN_BIGGELAAR_PBMC_PREVNAR_9MO_INFANT_STIMULATED_VS_UNSTIMULATED_8MO_UP

VAN_DEN_BIGGELAAR_PBMC_PREVNAR_9MO_INFANT_STIMULATED_VS_UNSTIMULATED_9MO_UP

(b)
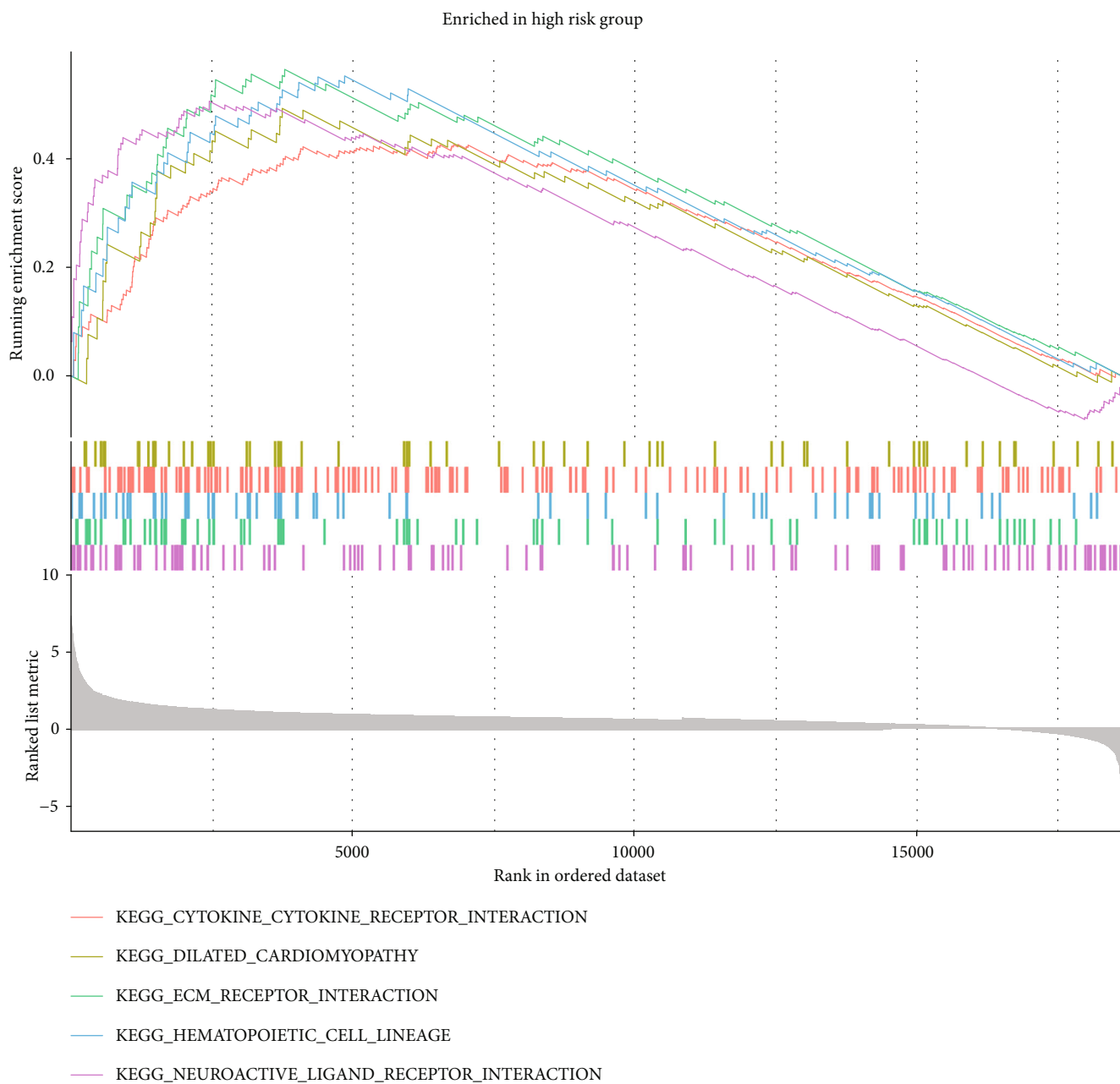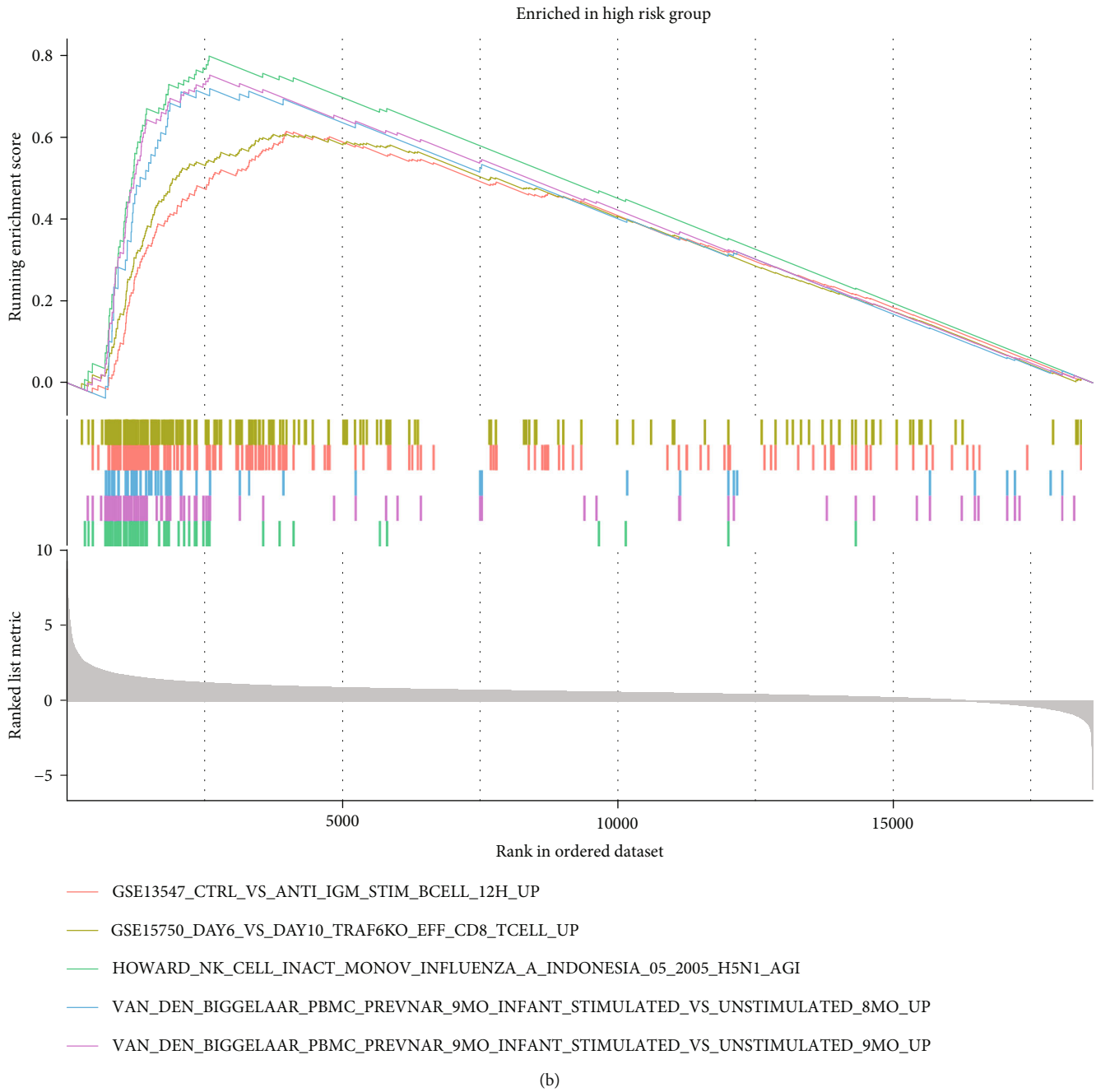
FIGURE 7: GSEA of BMRGs. (a) GSEA of KEGG gene set for the high- and low-risk cohorts of BMRGs. (b) GSEA of immune gene set for the high- and low-risk cohorts of BMRGs.

In recent years, a variety of prognostic risk models based on cell-related functional genes have been developed, which provide favorable help for the prognosis assessment of various malignant tumors. Luo et al. analyzed the expression of ferroptosis-related genes in LIHC from public databases and constructed a corresponding prognostic model. The AUC areas for the model at 1, 3, and 5 years were 0.6838, 0.694, and 0.559, respectively [31]. Yu et al. constructed a prognostic model with good predictive ability by extracting the pyroptotic genes in LIHC. The AUC areas for 1, 3, and 5 years were 0.748, 0.732, and 0.603, respectively [32]. In this study, the AUC of our prognostic model was 0.759, 0.658, and 0.654 at 1, 3, and 5 years, respectively. Compared with previous related functional gene set models, the model established in this study has higher predictive performance.

The BM plays an important role in both physiological and pathological states, so the set of genes involved in regulating the structure of the basement membrane is particularly important. In this study, we found that the risk model based on BMRGs was closely related to the immune cell

infiltration of LIHC. Meanwhile, we also found that the high-risk score of this model suggested low responsiveness to tumor immunotherapy. These evidences strongly indicated that the BMRGs not only regulate the infiltration of leukocytes but may also be related to the checkpoint function of multiple immune cells. For these surprising findings, we intend to further develop in vitro and in vivo use in follow-up studies to support the above inferences.

In this study, we revealed the important role of BMRGs in LIHC, which also provides new directions for the treatment of LIHC, but there are still many shortcomings. First, all LIHC data in this study was derived from public databases and lacked validation in vivo and in vitro. In addition, the biological molecular mechanism of various genes in BMRGS has not been explored, which greatly limits its accuracy.

In conclusion, our study revealed that BM is closely related to LIHC progression. We provided a novel BMRG risk model to predict LIHC patients' survival. In addition, our established model can provide guidance on the immune microenvironmental status of LIHC and the efficacy of immunotherapy. We firmly believe that the model based on BMRGs has excellent application prospects after further verification.

Data Availability

All data and result in this study are available from the corresponding author for reasonable request.

Conflicts of Interest

All authors in this study declare that they have no conflict of interest.

Authors' Contributions

Jiajia Shen, Zhihong Wei, and Lizhi Lv contributed equally to this work. All authors read and approved the final manuscript.

Acknowledgments

Supplementary Materials

Supplementary Figure 1: nonnegative matrix decomposition (NMF) clustering was performed, showing a total of eight subgroups to determine the best values for consensus clustering. Supplementary Figure 2: construction of the BM-related risk model by the LASSO Cox regression analysis. (A) The partial likelihood deviations of the variables revealed by the LASSO regression model. The red dots indicate the partial likelihood of the deviation values, the gray line indicates the standard error (SE), and the two vertical dashed lines on the left and right represent the minimum standard and the optimal value of the 1-SE standard, respectively. (B) Coefficient profiles of the 179 prognosis-related BM-related genes via LASSO Cox regression analysis. Supplementary Figure 3: distribution of risk curves and number of patients in BMRG risk score. (A, B) Train set and (C, D) test set. *(Supplementary Materials)*

References

[1] J. M. Llovet, R. K. Kelley, A. Villanueva et al., "Hepatocellular carcinoma," *Nature Reviews Disease Primers*, vol. 7, no. 1, p. 6, 2021.

[2] Y. Sugawara and T. Hibi, "Surgical treatment of hepatocellular carcinoma," *Bioscience Trends*, vol. 15, no. 3, pp. 138–141, 2021.

[3] C. A. Arciero and E. R. Sigurdson, "Liver-directed therapies for hepatocellular carcinoma," *Journal of the National Comprehensive Cancer Network*, vol. 4, no. 8, pp. 768–774, 2006.

[4] F. Chino, S. J. Stephens, S. S. Choi et al., "The role of external beam radiotherapy in the treatment of hepatocellular cancer," *Cancer*, vol. 124, no. 17, pp. 3476–3489, 2018.

[5] J. C. Nault and A. Villanueva, "Biomarkers for hepatobiliary cancers," *Hepatology*, vol. 73, Supplement 1, pp. 115–127, 2021.

[6] F. Xu, T. Jin, Y. Zhu, and C. Dai, "Immune checkpoint therapy in liver cancer," *Journal of Experimental & Clinical Cancer Research*, vol. 37, no. 1, p. 110, 2018.

[7] X. Lei, Y. Lei, J. K. Li et al., "Immune cells within the tumor microenvironment: biological functions and roles in cancer immunotherapy," *Cancer Letters*, vol. 470, pp. 126–133, 2020.

[8] X. Liu, Y. Qiao, J. Chen, and G. Ge, "Basement membrane promotes tumor development by attenuating T cell activation," *Journal of Molecular Cell Biology*, vol. 14, no. 2, 2022.

[9] D. S. Grant, M. C. Kibbey, J. L. Kinsella, M. C. Cid, and H. K. Kleinman, "The role of basement membrane in angiogenesis and tumor growth," *Pathology, Research and Practice*, vol. 190, no. 9-10, pp. 854–863, 1994.

[10] V. P. Terranova, E. S. Hujanen, and G. R. Martin, "Basement membrane and the invasive activity of metastatic tumor cells," *Journal of the National Cancer Institute*, vol. 77, no. 2, pp. 311–316, 1986.

[11] M. J. Randles, M. J. Humphries, and R. Lennon, "Proteomic definitions of basement membrane composition in health and disease," *Matrix Biology*, vol. 57-58, pp. 12–28, 2017.

[12] A. Srivastava, J. C. Pastor-Pareja, T. Igaki, R. Pagliarini, and T. Xu, "Basement membrane remodeling is essential for drosophila disc eversion and tumor invasion," *Proceedings of the National Academy of Sciences of the United States of America*, vol. 104, no. 8, pp. 2721–2726, 2007.

[13] R. Hallmann, X. Zhang, J. Di Russo et al., "The regulation of immune cell trafficking by the extracellular matrix," *Current Opinion in Cell Biology*, vol. 36, pp. 54–61, 2015.

[14] S. Banerjee, W. C. Lo, P. Majumder et al., "Multiple roles for basement membrane proteins in cancer progression and EMT," *European Journal of Cell Biology*, vol. 101, no. 2, article 151220, 2022.

[15] D. Niu, T. Luo, H. Wang, Y. Xia, and Z. Xie, "Lactic acid in tumor invasion," *Clinica Chimica Acta*, vol. 522, pp. 61–69, 2021.

[16] D. W. Kowalczyk, A. P. Wlazlo, M. Blaszczyk-Thurin, Z. Q. Xiang, W. Giles-Davis, and H. C. Ertl, "A method that allows easy characterization of tumor-infiltrating lymphocytes," *Journal of Immunological Methods*, vol. 253, no. 1-2, pp. 163–175, 2001.

[17] D. H. Peng, B. L. Rodriguez, L. Diao et al., "Collagen promotes anti-PD-1/PD-L1 resistance in cancer through LAIR1-

dependent CD8$^+$ T cell exhaustion," *Nature Communications*, vol. 11, no. 1, p. 4520, 2020.

[18] S. Mariathasan, S. J. Turley, D. Nickles et al., "TGFβ attenuates tumour response to PD-L1 blockade by contributing to exclusion of T cells," *Nature*, vol. 554, no. 7693, pp. 544–548, 2018.

[19] R. Jayadev, M. Morais, J. M. Ellingford et al., "A basement membrane discovery pipeline uncovers network complexity, regulators, and human disease associations," *Science Advances*, vol. 8, no. 20, article eabn2265, 2022.

[20] J. Y. Liang, D. S. Wang, H. C. Lin et al., "A novel ferroptosis-related gene signature for overall survival prediction in patients with hepatocellular carcinoma," *International Journal of Biological Sciences*, vol. 16, no. 13, pp. 2430–2441, 2020.

[21] T. Wang, N. Dang, G. Tang et al., "Integrating bulk and single-cell RNA sequencing reveals cellular heterogeneity and immune infiltration in hepatocellular carcinoma," *Molecular Oncology*, vol. 16, no. 11, pp. 2195–2213, 2022.

[22] K. W. Bi, X. G. Wei, X. X. Qin, and B. Li, "BTK has potential to be a prognostic factor for lung adenocarcinoma and an indicator for tumor microenvironment remodeling: a study based on TCGA data mining," *Frontiers in Oncology*, vol. 10, p. 424, 2020.

[23] J. Wu, L. Li, H. Zhang et al., "A risk model developed based on tumor microenvironment predicts overall survival and associates with tumor immunity of patients with lung adenocarcinoma," *Oncogene*, vol. 40, no. 26, pp. 4413–4424, 2021.

[24] Q. Ma, Y. Chen, F. Xiao et al., "A signature of estimate-stromal-immune score-based genes associated with the prognosis of lung adenocarcinoma," *Translational Lung Cancer Research*, vol. 10, no. 3, pp. 1484–1500, 2021.

[25] Q. Wang, M. Li, M. Yang et al., "Analysis of immune-related signatures of lung adenocarcinoma identified two distinct subtypes: implications for immune checkpoint blockade therapy," *Aging*, vol. 12, no. 4, pp. 3312–3339, 2020.

[26] T. M. Sweeney, M. C. Kibbey, M. Zain, R. Fridman, and H. K. Kleinman, "Basement membrane and the SIKVAV laminin-derived peptide promote tumor growth and metastases," *Cancer Metastasis Reviews*, vol. 10, no. 3, pp. 245–254, 1991.

[27] E. J. Hagedorn and D. R. Sherwood, "Cell invasion through basement membrane: the anchor cell breaches the barrier," *Current Opinion in Cell Biology*, vol. 23, no. 5, pp. 589–596, 2011.

[28] B. Li, H. L. Chan, and P. Chen, "Immune checkpoint inhibitors: basics and challenges," *Current Medicinal Chemistry*, vol. 26, no. 17, pp. 3009–3025, 2019.

[29] R. M. Bremnes, T. Donnem, S. Al-Saad et al., "The role of tumor stroma in cancer progression and prognosis: emphasis on carcinoma-associated fibroblasts and non-small cell lung cancer," *Journal of Thoracic Oncology*, vol. 6, no. 1, pp. 209–217, 2011.

[30] W. L. Grzelczyk, J. Szemraj, and M. Jozefowicz-Korczynska, "The matrix metalloproteinase in larynx cancer," *Postępy Higieny i Medycyny Doświadczalnej*, vol. 70, pp. 1190–1197, 2016.

[31] L. Luo, X. Yao, J. Xiang, F. Huang, and H. Luo, "Identification of ferroptosis-related genes for overall survival prediction in hepatocellular carcinoma," *Scientific Reports*, vol. 12, no. 1, article 10007, 2022.

[32] H. Yu, X. Bai, and W. Zheng, "Identification of the pyroptosis-related prognosis gene signature and immune infiltration in hepatocellular carcinoma," *Disease Markers*, vol. 2022, Article ID 9124216, 16 pages, 2022.

Hindawi

Research Article

Study on Clinicopathological Features and Risk Factors of Patients with Multiple Primary Breast Cancers and Thyroid Disease

Jie Li [D],[1] Yonghong Liu,[1] Jian Jin,[1] Qingfeng Shi,[1] Yanting Ji,[1] Bo Zhang,[1] and Pengfei Hu[2]

[1]*Cangzhou Central Hospital, Cangzhou 061000, China*
[2]*Hebei Medical University, Shijiazhuang 050017, China*

Correspondence should be addressed to Jie Li; lijiezxyy@163.com

Objective. To explore the clinicopathological features and risk factors of patients with multiple primary breast cancers and thyroid disease. *Method*. An analytic approach of the reviewing method was adopted to analyze the clinical data of 80 breast cancer patients who were admitted to our hospital from January 2020 to January 2022. They were divided into an observation group (breast cancer with thyroid lesions) and a control group (simple breast cancer) according to whether the clinical data were accompanied with thyroid lesions to compare the clinical characteristics, pathological types, staging characteristics, and molecular biological characteristics of the two groups and to research the risk factors of the two groups. *Result*. (1) In the comparison of clinical data, the number of people aged ≥60 in the observation group was higher than that in the control group, and there was significant difference between the groups in the menopausal status data ($P < 0.05$). There was no statistical difference between the observation group and the control group in the comparison of clinical data of the body mass index, pregnancy frequency, labor frequency, and abortion history ($P > 0.05$). (2) In the comparison of pathological type and staging data, there was no statistical difference in the comparison of data on the pathological type, histological grade, T staging, N staging, and TNM staging between the observation group and the control group ($P > 0.05$). (3) In the comparison of data on molecular biology characteristics, there was a statistical difference in the nuclear proliferation antigen data between the observation group and the control group ($P < 0.05$). There was no statistical difference in the comparison of data on the estrogen receptor, progesterone receptor, human epidermal growth factor receptor-2, and molecular typing between the observation group and the control group ($P > 0.05$). (4) Logistic regression analysis showed that age, menopausal status, and nuclear proliferation antigen index were the high-risk inflammatory factors for combined thyroid lesions ($P < 0.05$). *Conclusion*. For patients with simple breast cancer, age, menopausal status, and nuclear proliferation antigen index are risk factors for combined thyroid lesions. Therefore, clinical attention should be paid to the above factors in the process of clinical treatment, and early-risk screening should be performed to achieve the purpose of improving the prognosis to the greatest extent.

1. Introduction

With the continuous development of social lifestyle, more and more factors will affect people's physical and mental health [1, 2]. Among them, the most obvious factors are biological genetic factors, environment, and lifestyle, which have also led to the increasing incidence and mortality of cancer in recent years. However, the form of cancer prevention and treatment all over the word is not very ideal. According to some research reports [3, 4], the tumor burden

in China keeps increasing, and the number of deaths from cancer exceeds 2.3 million throughout the year. Just from the perspective of breast cancer, the number of new breast cancer cases in China is 280,000 in recent years, and the patients are mainly aged 45–55 years old. Compared with other European and American countries, the onset time in China is about ten years ahead of schedule. Therefore, breast cancer has become one of the most common cancer types among women in China, and it is also an important cause of death for women in our country, and the incidence has

TABLE 1: Comparison of clinical characteristics between the two groups (%).

Index		Observation group ($n = 40$)	Control group ($n = 40$)	χ^2	P
Age	≤35 years old	3 (7.50)	10 (25.00)		
	35–60 years	9 (22.50)	12 (30.00)	6.372	0.041
	≥60 years old	28 (70.00)	18 (45.00)		
Body mass index	<24.0 kg/m^2	10 (25.00)	9 (22.50)		
	24.0 kg/m^2–28.0 kg/m^2	12 (30.00)	13 (32.50)	0.0926	0.954
	≥28.0 kg/m^2	18 (45.00)	18 (45.00)		
Pregnancy times	≤2 times	20 (50.00)	21 (52.50)	0.050	0.823
	>2 times	20 (50.00)	19 (47.50)		
Production number	≤2 times	21 (52.50)	19 (47.50)	0.200	0.655
	>2 times	19 (47.50)	21 (52.50)		
Abortion history	Without	21 (52.50)	20 (50.00)	0.050	0.823
	Have	19 (47.50)	20 (50.00)		
Menopausal status	No menopause	2 (5.00)	10 (25.00)	6.275	0.012
	Menopause	38 (95.00)	30 (75.00)		
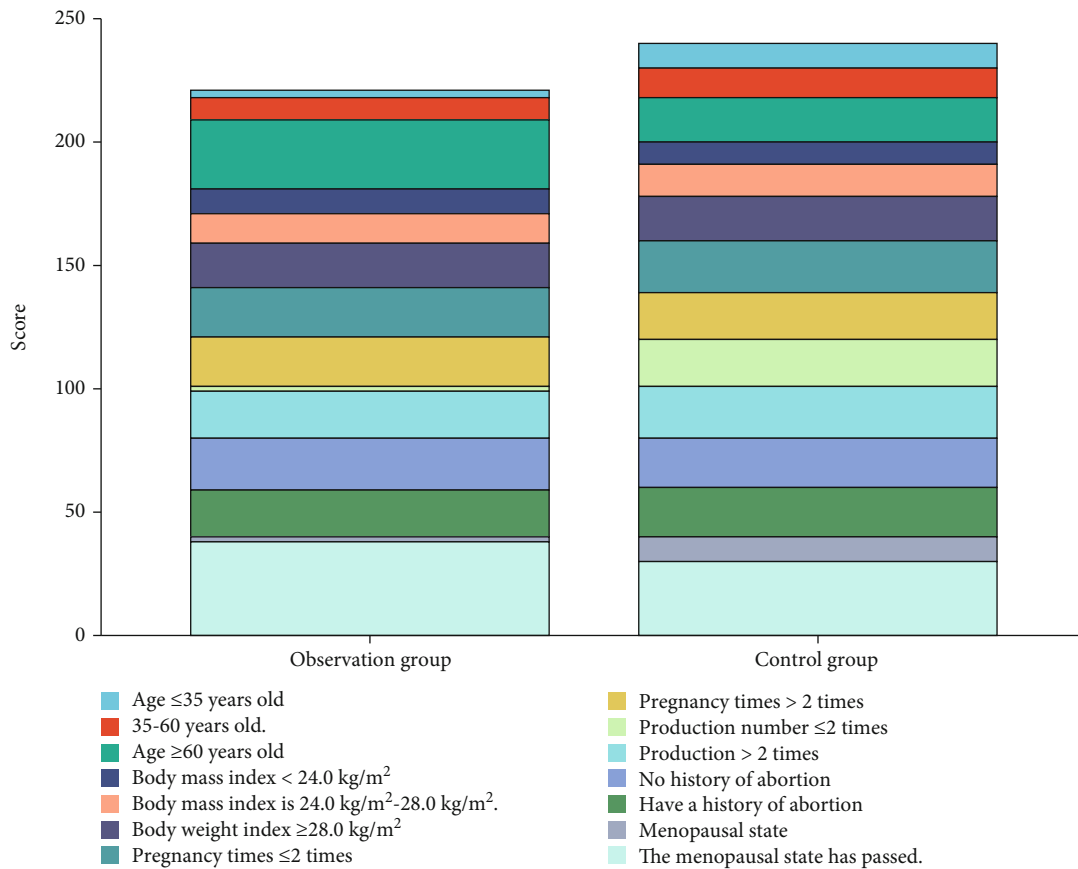
FIGURE 1: Comparison of clinical features between the two groups.

been rising every year. However, there is no unified specific cause of breast cancer, and most of the medical researchers believe that it is related to heredity, age, body mass index, and living habits [5, 6]. Nowadays, the levels of medical diagnosis and treatment have been developed in China, but breast cancer still seriously affects the physical and mental health of female residents, so it is particularly important to improve the diagnosis and treatment technology for breast cancer and its related complications. Thyroid diseases mainly include hyperthyroidism, hypothyroidism, thyroiditis, and

TABLE 2: Comparison of pathological types and stages between the two groups (%).

Index		Observation group ($n = 40$)	Control group ($n = 40$)	χ^2	P
Pathological type	Invasive ductal carcinoma	21 (52.50)	20 (50.00)	0.050	0.823
	Other cancers	19 (47.50)	20 (50.00)		
Histological grade	I–II	10 (25.00)	9 (22.50)	0.085	0.958
	III	15 (37.50)	16 (40.00)		
	Unknown	15 (37.50)	15 (37.50)		
T staging	T0-2	20 (50.00)	21 (52.50)	0.050	0.823
	T3-4	20 (50.00)	19 (47.50)		
N staging	N0	21 (52.50)	19 (47.50)	0.200	0.655
	N1-3	19 (47.50)	21 (52.50)		
TNM staging	0+I+II	22 (55.00)	19 (47.50)	0.450	0.502
	III+IV	18 (45.00)	21 (52.50)		
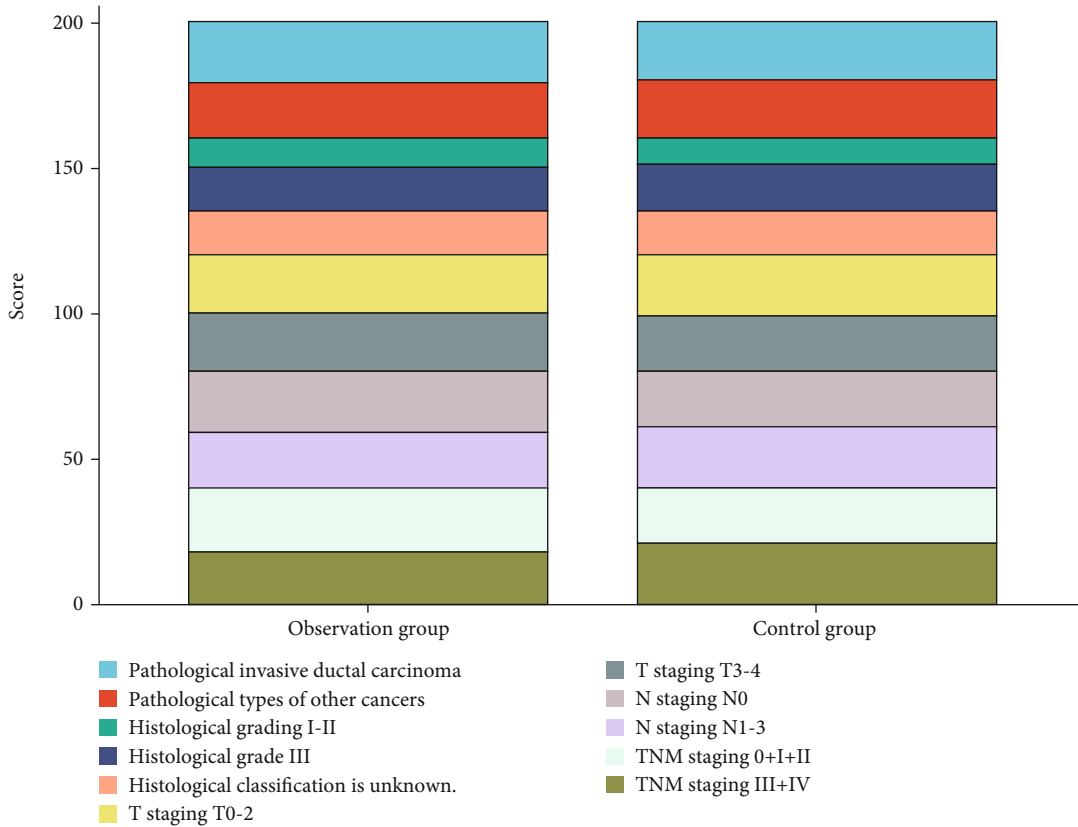
FIGURE 2: Comparison of pathological types and stages between the two groups.

thyroid tumor, which often occur in the female population. Among them, the thyroid nodular lesion is a very common hyperplastic disease clinically. Data [7] shows that the incidence of thyroid disease is closely related to gender, age, heredity, iodine intake, etc. Both the thyroid and breast belong to hormone-responsive organs, and they are regulated by the hypothalamic and pituitary systems, so it can be deduced that the endocrine function changes of the body are closely related to the occurrence and development of these two diseases. Estrogen and thyroid hormones can lead to interaction and influence on breast cancer and thyroid disease. For example, estrogen can affect physiological and pathological changes of the thyroid, thus leading to thyroid disease. The thyroid hormone, in turn, can also increase the risk of breast cancer. Medical studies on the relationship between breast cancer and the thyroid gland are increasing in recent years, and the specific conclusions obtained are inconsistent [8, 9]. Therefore, this study intended to explore the clinicopathologic features and risk factors of patients with multiple primary breast cancers and thyroid disease, by mainly analyzing the clinical data of 80 breast cancer patients who were admitted to our hospital from January 2020 to January 2022. The reports are as follows.

TABLE 3: Comparison of molecular biological characteristics between the two groups (%).

Index		Observation group ($n = 40$)	Control group ($n = 40$)	χ^2	P
Estrogen receptor	Negative	22 (55.00)	19 (47.50)	0.450	0.502
	Positive	18 (45.00)	21 (52.50)		
Progesterone receptor	Negative	19 (47.50)	18 (45.00)	0.050	0.823
	Positive	21 (52.50)	22 (55.00)		
Human epidermal growth factor receptor-2	Negative	22 (55.00)	19 (47.50)	0.450	0.502
	Positive	18 (45.00)	21 (52.50)		
Nuclear proliferation antigen	<14%	2 (5.00)	8 (20.00)	4.114	0.043
	≥14%	38 (95.00)	32 (80.00)		
Molecular typing	Breast cancer cell type A	10 (25.00)	9 (22.50)	0.100	0.992
	Breast cancer cell type B	10 (25.00)	10 (25.00)		
	Human epidermal growth factor receptor-2 overexpression	10 (25.00)	11 (27.50)		
	Three negative types	10 (25.00)	10 (25.00)		

2. Data and Methods

2.1. General Data.
An analytic approach of the reviewing method was adopted to analyze the clinical data of 80 breast cancer patients who were admitted to our hospital from January 2020 to January 2022. They were divided into an observation group (breast cancer with thyroid lesions) and a control group (simple breast cancer) according to whether the clinical data were accompanied with thyroid lesions.

2.1.1. Inclusion Criteria.
The inclusion criteria are as follows: (1) primary breast cancer is confirmed through clinical diagnosis and laboratory tests; (2) there is no treatment history of chemotherapy, radiotherapy, endocrine therapy, and thyroid disease treatment; (3) thyroid diseases include nodular goiter, thyroid adenoma, and thyroid cancer; and (4) complete clinical and pathological data are available.

2.1.2. Exclusion Criteria.
The exclusion criteria are as follows: (1) patients with nonprimary breast cancer; (2) patients who lack some relevant imaging data such as B ultrasound of the thyroid or CT; and (3) patients with unclear consciousness and who could not cooperate with the study.

2.1.3. Included Case Data.
Strict investigation was conducted on the inclusion and exclusion criteria in this study. A total of 80 patients were involved in this study, and all of them were female, aged from 24 to 79, with an average age of 47.11 ± 10.11 years. Among them, there were 40 cases of breast cancer combined with a thyroid lesion, accounting for 50.00%, aged from 25 to 79, with the average age of 50.99 ± 10.11 years; there were 40 patients (50.00%) with simple breast cancer, aged from 24 to 78 years old, with an average age of 46.33 ± 10.11 years.

Analyses of specific conditions of patients with breast cancer combined with thyroid lesion are as follows: (1) at the beginning of admission, 40 patients with breast cancer coexisting with thyroid lesion were found, and 35 cases were benign and 5 cases were malignant according to the results of the B ultrasound and CT examination; (2) during the follow-up period, there were 15 cases of thyroid lesions, and 14 cases were benign and 1 case was malignant according to the results of the B ultrasound and CT examination.

2.2. Relevant Definitions and Standards.
Nodular lesion changes of thyroid lesions are as follows: it is mainly about the morphology description of the thyroid goiter, which can be divided into two types according to the relevant diagnostic criteria—thyroid nodules with malignant signs and benign thyroid nodules. The malignant risk of the malignant signs of thyroid nodules involved this time is between 5% and 90%: (1) Ultrasound examination shows that the edges are irregular; i.e., there are infiltrations, lobulations, and burrs; microcalcification; invasion of thyroid capsule; interrupted marginal calcification; and aspect ratio > 1. (2) The components in the solid nodules/cystic solid nodules are manifested as hypoechoic or solid partial eccentricity.

Body weight index: it is also known as the body mass index, which is an evaluation standard currently used internationally to judge the degree of obesity and the health of adult groups. The body mass index could be divided into four types: low body weight is when the body mass index is less than $18.5 \, kg/m^2$, normal body weight is when the body mass index is between $18.5 \, kg/m^2$ and $24.0 \, kg/m^2$, overweight is when the body mass index is between $24.0 \, kg/m^2$ and $28.0 \, kg/m^2$, and obesity is when the body mass index is more than $28.0 \, kg/m^2$.

Pathological classification of breast cancer: it is mainly divided according to the WHO pathological definition of breast cancer and its related classification criteria.

The stages of breast cancer are divided according to the specific tumor size, axillary lymph node metastasis, and presence of distant metastasis.

Immunohistochemistry and molecular typing of breast cancer: (1) When estrogen receptor and progesterone receptor were positive, the tumor nucleus staining was greater
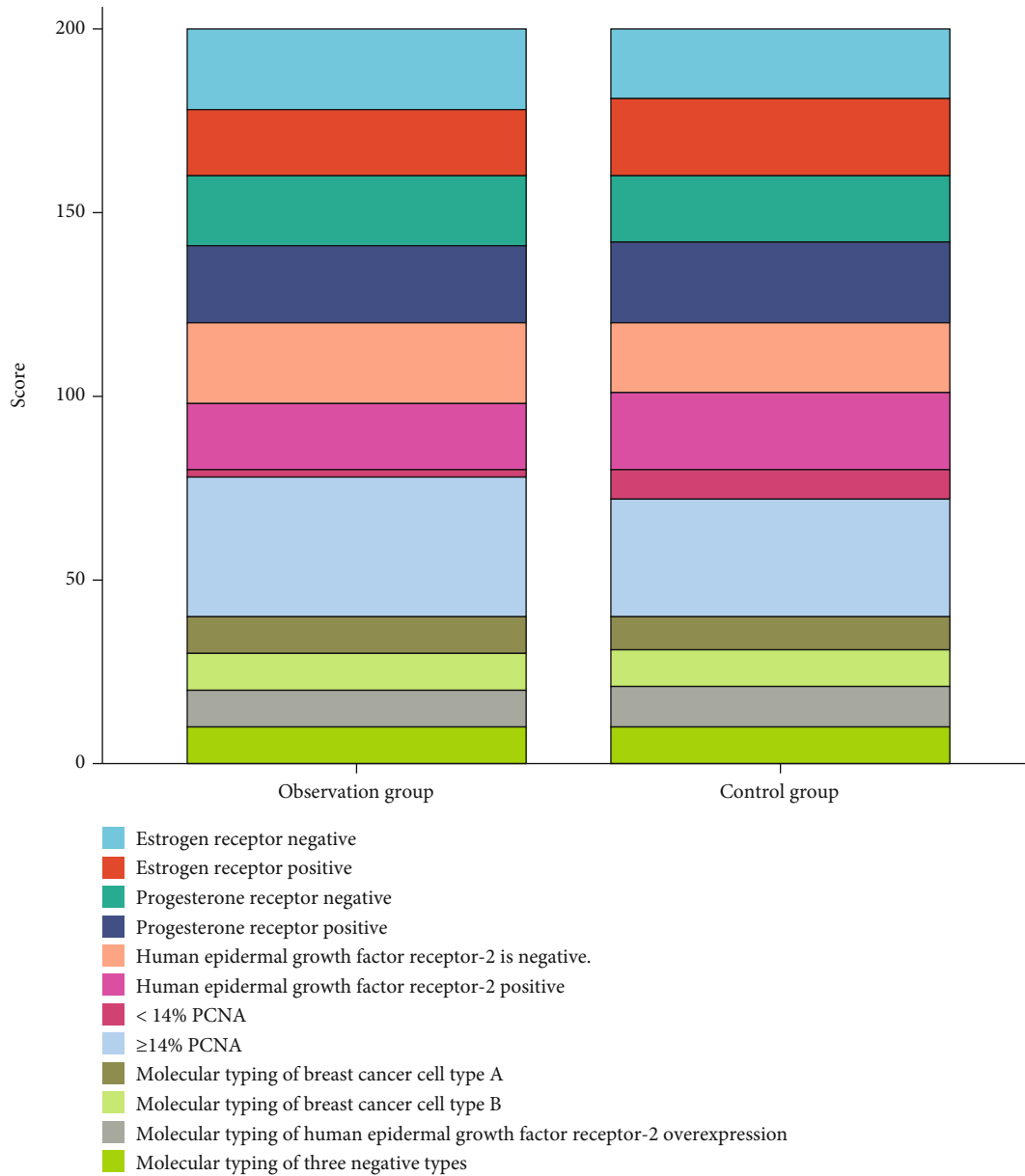
Figure 3: Comparison of molecular biological characteristics between the two groups.

Table 4: Variable assignment of influencing factors for multiple primary breast cancers complicated with thyroid lesions.

Variable	Assignment
Dependent variable	
Breast cancer	Simple breast cancer = 0; combined thyroid lesions = 1
Independent variable	
Age	≤35 years old, ≥60 years old = 0; 35–60 years = 1
Menopausal status	No menopause = 0; menopause = 1
Nuclear proliferation antigen index	Positive = 0; negative = 1

than or equal to 1%; based on the positive internal reference condition, the tumor nucleus staining less than 1% was considered to be negative; uncertainty is determined if normal epithelial cells are stained but tumor nuclei are not stained in the same specimen, or tumor nucleus staining did not exist after multiple inspections in the same specimen. (2) *Nuclear proliferation antigen*: the cells with brown granules in the nucleus were considered to be positive, and a high expression was when the nuclear proliferation antigen was more than or equal to 14%, and the low expression was when the nuclear proliferation antigen was less than 14%. (3) *Human epidermal growth factor receptor-2*: it belongs to the proto-oncogene located on the long arm of human chromosome 17, which needs to be detected by fluorescence in situ hybridization when the result is uncertain. (4) Molecular typing was classified based on the comprehensive

TABLE 5: Multifactor analysis.

Correlative factor	β	Standard deviation	Wald	P	OR	95% CI
Age	1.615	0.597	7.318	0.011	3.217	2.021–6.119
Menopausal status	1.446	0.611	5.601	0.012	3.187	2.077–4.177
Nuclear proliferation antigen index	1.721	0.356	23.370	0.003	2.995	1.336–4.369

expression of the estrogen receptor, progesterone receptor, and nuclear proliferation antigen.

2.3. Statistical Process. SPSS 24.0 software was used for analysis. The measurement data was expressed in the form of $\bar{x} \pm s$, and t was used for the test. The count data was expressed in the form of %, and χ^2 was used for the test. Logistic regression analysis was used for the multifactor. $P < 0.05$ indicated that the difference had statistical significance.

3. Results

3.1. Comparison of Clinical Characteristics between the Two Groups. The number of people aged older than or equal to 60 in the observation group was higher than that in the control group, and there was significant difference in the data of menopausal status between the two groups ($P < 0.05$). There was no statistical difference in the comparison of data, such as body mass index, pregnancy frequency, labor frequency, and abortion history, between the observation group and the control group ($P > 0.05$), as shown in Table 1 and Figure 1.

3.2. Comparison of Pathological Types and Stages between the Two Groups. There was no statistical difference in the data comparison of the pathological type, histological grade, T staging, N staging, and TNM staging between the observation group and the control group ($P > 0.05$), as shown in Table 2 and Figure 2.

3.3. Comparison of Molecular Biological Characteristics between the Two Groups. There was statistical difference in the data comparison of the nuclear proliferation antigen between the observation group and the control group ($P < 0.05$). There was no statistical difference in the data comparison of the estrogen receptor, progesterone receptor, human epidermal growth factor receptor-2, and molecular typing between the observation group and the control group ($P > 0.05$), as shown in Table 3 and Figure 3.

3.4. Multifactor Analysis. Logistic regression analysis showed that age, menopausal status, and nuclear proliferation antigen index were the high-risk factors for combined thyroid lesions ($P < 0.05$), as shown in Tables 4 and 5.

4. Discussion

The concept and research of multiple primary malignant tumors have attracted much attention in the medical field in recent years. It was first proposed in 1989, and the data showed [10] that after the diagnosis and treatment of the patients' first cancer, the chance of developing a second cancer would increase. At present, the specific etiology and pathogenesis of this condition are not very clear, but it is roughly related to many factors, including genetics, environment, and treatment. Breast cancer is a very common kind of female malignant tumor, and it is also the main disease type leading to the death of women, which poses a serious threat to their physical and mental health. With the increasing pace of social life and increasing physical and mental pressure on women, a variety of internal and external factors will affect the endocrine function of the body, and the incidence of endocrine-related thyroid diseases also increases [11]. Both the mammary gland and thyroid gland are closely related to the body hormone levels, while the pituitary gland, ovary, adrenal cortex, etc., which secrete hormones, play an important role in the pathogenesis of breast cancer. Among them, estrogen and progesterone are the most important endocrine hormones that have been proven to influence the pathogenesis of breast cancer based on current research [12, 13]. The thyroid gland is also one of the organs affected by endocrine glands, just like with breast cancer, which is subject to the influence of the hypothalamus-pituitary-gland axis of the human body and the proprioceptive secretion control system, wherein the hypothalamus secretes a thyroid-stimulating hormone-releasing hormone, the pituitary gland secretes a thyroid-stimulating hormone, and the thyroid gland itself secretes hormones to exert effects on the normal morphology of the thyroid gland and its functional maintenance. Thus, the occurrence of breast cancer and thyroid disease may interact with each other, and it is difficult to separate their associations. In the current clinical research data, many researchers have begun to conduct in-depth research on the relationship between breast cancer and thyroid lesions to develop as much research data as possible in order to show the correlation between the two diseases. However, more research is needed to confirm the mechanism behind breast cancer and the thyroid [14, 15].

According to multiple data [16, 17], thyroid nodule lesions occur in 30.7% of males and 39.9% of females, and the incidence will be significantly increased in the female patient population with breast cancer. Among thyroid lesions, compared with the general population, breast cancer patients are more likely to have thyroid lesions that are malignant, generally about seven times that of the general population, which shows that breast cancer patients have a very high risk of thyroid lesions. In this study, there were a total of 40 patients with breast cancer combined with thyroid lesions, including five patients with thyroid lesions of malignant signs. The conclusion of the study was generally consistent with the conclusion in the previous literature. However, the prevalence rate of thyroid cancer in this study

was low, which might be related to a small total number of selections and many other factors. In addition, no puncture biopsy was conducted for patients with malignant signs in this study, so there might be a certain deviation.

According to the data [18, 19], the onset age of breast cancer in Chinese women is mainly between 45 and 55 years old, while, in Western countries, it is mainly around 65 years old. The onset age of breast cancer in China has a tendency to change towards results found in Western countries in recent years. Studies have speculated that in 2030, there may be about 27.0% patients over the age of 65 years old diagnosed with breast cancer in China, which will be higher than in previous years. For the postmenopausal elderly, their ovarian function will decrease, together with the reduction of estrogen and progesterone and the transformation of the normal growth rate of mammary cells, leading to the atrophy of the acinus in the body. In addition, their immune ability will be reduced due to age factors, so they are more likely to develop cancer. Therefore, the elderly are also the high-incidence group of thyroid disease. According to the data [20], compared with the population aged 20–30, the incidence of thyroid lesions in the elderly over 70 years old is four times higher. Thus, breast cancer patients with menopause directly affect the prevalence of thyroid disease. In this study, it was also shown that the differences in the age and menopausal status between the two groups were significant ($P < 0.05$). Besides, multivariate analysis showed that age and menopause were the high-risk factors for breast cancer patients complicated with thyroid lesions; that is, the postmenopausal breast cancer patients aged ≥60 years old have a greater chance of thyroid lesions. Between age and menopausal status factors, the postmenopausal status is more instructive than age because all patients above 60 years old have reached menopausal status, while not all patients who are already postmenopausal have reached 60 years old. On the other hand, the cell proliferation antigen, which is a regulatory factor affecting the cell proliferation and differentiation of the body, is also a nuclear proliferation marker with an extremely high-application value at present, which can effectively reflect the proliferation capacity and invasion of tumor cells, and plays a key role in maintaining cell proliferation. Nowadays, when molecular typing is performed to detect breast cancer, the cell proliferation antigen is also one of the important judgment indicators, because some research data have confirmed that the expression of the cell proliferation antigen is closely related to the pathological differentiation, staging, and axillary lymph metastasis of breast cancer tissue, which can become an important indicator for judging the severity and prognosis of breast cancer patients. In addition, the cell proliferation antigen also has a certain expression in the process of thyroid lesions, especially in thyroid papillary carcinoma, which is closely related to the specific tumor size and thyroglobulin antibody. It is generally believed that the higher the expression level of the cell proliferation antigen is, the higher the recurrence rate of the disease will be, which is an effective biological marker for identifying benign and malignant thyroid lesions. The patients with breast cancer and recurrent thyroid cancer also have the phenomenon of high expression of the cell pro-

liferation antigen. This study also indicates that observation, which shows that the nuclear proliferation antigen index belongs to the risk factor for breast cancer combined with thyroid lesions, which may be related to the degree of thyroid cell proliferation and differentiation affected by the high expression of the nuclear proliferation antigen.

According to the data analysis of this study, among the comparisons of clinical data, the number of people aged ≥60 in the observation group was higher than that in the control group, and there was significant difference between the groups in the menopausal status and nuclear proliferation antigen data ($P < 0.05$). There was no statistical difference in the body mass index, pregnancy frequency, labor frequency, abortion history, pathological type, histological grade, T staging, N staging, TNM staging, estrogen receptor, progesterone receptor, human epidermal growth factor receptor-2, molecular typing, and other data between the observation group and the control group ($P > 0.05$). To sum up, for patients with simple breast cancer, age, menopausal status, and nuclear proliferation antigen index are risk factors for developing combined thyroid lesions. Therefore, clinical attention should be paid to the above factors, and risk screening for the above factors should be conducted in advance in the process of clinical treatment to achieve the purpose of improving the prognosis to the greatest extent. In this study, there are also certain research limitations, such as having no thyroid function inspections for breast cancer patients. Therefore, related inspections should be improved in future research to identify the specific mechanism of occurring thyroid lesions in breast cancer, so as to provide a more accurate theoretical basis for the relevant research on clinicopathologic characteristics and risk factors of patients with multiple primary breast cancers and thyroid disease.

Data Availability

The labeled dataset used to support the findings of this study are available from the corresponding author upon request.

Conflicts of Interest

The authors declare that there are no conflicts of interest.

Funding

References

[1] M. Ralli, D. Angeletti, M. Fiore et al., "Hashimoto's thyroiditis: an update on pathogenic mechanisms, diagnostic protocols, therapeutic strategies, and potential malignant transformation," *Autoimmunity Reviews*, vol. 19, no. 10, article 102649, 2020.

[2] D. T. W. Lui, C. H. Lee, W. S. Chow et al., "Thyroid dysfunction in relation to immune profile, disease status, and outcome

in 191 patients with COVID-19," *The Journal of Clinical Endocrinology and Metabolism*, vol. 106, no. 2, pp. e926–e935, 2021.

[3] C. Kurimoto, H. Inaba, H. Ariyasu et al., "Predictive and sensitive biomarkers for thyroid dysfunctions during treatment with immune-checkpoint inhibitors," *Cancer Science*, vol. 111, no. 5, pp. 1468–1477, 2020.

[4] S. Benvenga, M. Nordio, A. S. Laganà, and V. Unfer, "The role of inositol in thyroid physiology and in subclinical hypothyroidism management," *Frontiers in Endocrinology*, vol. 10, no. 12, article 662582, 2021.

[5] N. P. Tkachuk, "Thyroid and Pseudothyroid dysfunction as a cause that is promoting the relapse of benign focal thyroid pathology," *Journal of Medicine and Life*, vol. 13, no. 3, pp. 426–430, 2020.

[6] M. Rotondi, F. Coperchini, G. Ricci et al., "Detection of SARS-COV-2 receptor ACE-2 mRNA in thyroid cells: a clue for COVID-19-related subacute thyroiditis," *Journal of Endocrinological Investigation*, vol. 44, no. 5, pp. 1085–1090, 2021.

[7] I. I. Kamyshna, L. B. Pavlovych, V. A. Maslyanko, and A. M. Kamyshnyi, "Analysis of the transcriptional activity of genes of neuropeptides and their receptors in the blood of patients with thyroid pathology," *Journal of Medicine and Life*, vol. 14, no. 2, pp. 243–249, 2021.

[8] I. Piga, S. Casano, A. Smith et al., "Update on: proteome analysis in thyroid pathology - part II: overview of technical and clinical enhancement of proteomic investigation of the thyroid lesions," *Expert Review of Proteomics*, vol. 15, no. 11, pp. 937–948, 2018.

[9] M. Barbuti, A. F. Carvalho, C. A. Köhler et al., "Thyroid autoimmunity in bipolar disorder: a systematic review," *Journal of Affective Disorders*, vol. 15, no. 221, pp. 97–106, 2017.

[10] A. Buha, V. Matovic, B. Antonijevic et al., "Overview of cadmium thyroid disrupting effects and mechanisms," *International Journal of Molecular Sciences*, vol. 19, no. 5, p. 1501, 2018.

[11] V. Canini, D. Leni, A. I. Pincelli et al., "Clinical-pathological issues in thyroid pathology: study on the routine application of NIFTP diagnostic criteria," *Scientific Reports*, vol. 9, no. 1, p. 13179, 2019.

[12] R. Ameziane El Hassani, C. Buffet, S. Leboulleux, and C. Dupuy, "Oxidative stress in thyroid carcinomas: biological and clinical significance," *Endocrine-Related Cancer*, vol. 26, no. 3, pp. R131–R143, 2019.

[13] M. T. Stib, I. Pan, D. Merck, W. D. Middleton, and M. D. Beland, "Thyroid nodule malignancy risk stratification using a convolutional neural network," *Ultrasound Quarterly*, vol. 36, no. 2, pp. 164–172, 2020.

[14] B. Uhliarova and A. Hajtman, "Tireoidite de Hashimoto – um fator de risco independente para o carcinoma papilar," *Brazilian Journal of Otorhinolaryngology*, vol. 84, no. 6, pp. 729–735, 2018.

[15] D. Jackson, R. S. Handelsman, J. C. Farrá, and J. I. Lew, "Increased incidental thyroid cancer in patients with subclinical chronic lymphocytic thyroiditis," *The Journal of Surgical Research*, vol. 245, pp. 115–118, 2020.

[16] J. Lee, K. C. Park, H. J. Sul et al., "Loss of primary cilia promotes mitochondria-dependent apoptosis in thyroid cancer," *Scientific Reports*, vol. 11, no. 1, p. 4181, 2021.

[17] J. F. Swietlik, S. C. Mauch, E. A. Knott et al., "Noninvasive thyroid histotripsy treatment: proof of concept study in a porcine model," *International Journal of Hyperthermia*, vol. 38, no. 1, pp. 798–804, 2021.

[18] D. T. W. Lui, C. H. Lee, W. S. Chow et al., "Insights from a prospective follow-up of thyroid function and autoimmunity among COVID-19 survivors," *Journal of the Endocrine Society*, vol. 36, no. 3, pp. 582–589, 2021.

[19] M. Rotondi, A. Carbone, F. Coperchini, R. Fonte, and L. Chiovato, "Diagnosis of endocrine disease: IgG4-related thyroid autoimmune disease," *European Journal of Endocrinology*, vol. 180, no. 5, pp. R175–R183, 2019.

[20] N. M. Dias Lopes, H. H. Mendonça Lens, A. Armani, P. C. Marinello, and A. L. Cecchini, "Thyroid cancer and thyroid autoimmune disease: a review of molecular aspects and clinical outcomes," *Pathology, Research and Practice*, vol. 216, no. 9, article 153098, 2020.

Hindawi

Research Article

RTP4, a Biomarker Associated with Diagnosing Pulmonary Tuberculosis and Pan-Cancer Analysis

Hao Li [1], **Qin Zhou** [2], **ZhiXiang Ding**,[1] **and QingHai Wang**[1]

[1]*Department of Infectious Diseases, The First People's Hospital of Changde City, Changde, China*
[2]*Intensive Care Unit, The First People's Hospital of Changde City, Changde, China*

Correspondence should be addressed to Hao Li; 13721056589@163.com

Background. Pulmonary tuberculosis (PTB) is a global epidemic of infectious disease; the purpose of our study was to explore new potential biomarkers for the diagnosis of pulmonary tuberculosis and to use the biomarkers for further pan-cancer analysis. *Methods*. Four microarray gene expression sets were downloaded from the GEO public databases and conducted for further analysis. Healthy control (HC) samples and samples of pulmonary tuberculosis (PTB) were calculated with enrichment scores in folate biosynthesis pathways. The scores acted as a new phenotype combined with clinical information (control or PTB) for subsequent analysis. Weight gene coexpression network analysis (WGCNA) was used to seek the modules mostly related to PTB and folate biosynthesis in training sets. Twenty-nine coexistence genes were screened by intersecting the genes in the green-yellow module of GSE28623 and the brown module of GSE83456. We used the protein-protein interaction network analysis to narrow the gene range to search for hub genes. Then, we downloaded the unified and standardized pan-cancer data set from the UCSC database for correlations between biomarkers and prognosis and tumor stage differences. *Results*. Eventually, RTP4 was selected as a biomarker. To verify the reliability of this biomarker, an area under the ROC (AUC) was calculated in gene sets (GSE28623, GSE83456, and GSE34608). Lastly, to explore the difference in RTP4 expression before and after antituberculosis treatment, the GSE31348 gene set was enrolled to compare the expressions in weeks 0 and 26. The results showed significant differences between these two time points ($p < 0.001$). RTP4 was significantly upregulated in the pulmonary tuberculosis group compared to the healthy control group in three gene sets and downregulated after antituberculosis therapy in one gene set. These results suggest that RTP4 can be used as a potential biomarker in diagnosing tuberculosis. The results of pan-cancer analysis showed that high expression of RTP4 in 4 tumor types was positively correlated with poor prognosis and high expression of RTP4 in 6 tumor types was negatively correlated with poor prognosis. We found significant differences in the expression of the RTP4 gene at different stages in 5 types of tumors. *Conclusion*. RTP4 might be a new potential biomarker for diagnosing pulmonary tuberculosis.

1. Introduction

Mycobacterium tuberculosis (MTB) is one of the significant causes of tuberculosis. According to the World Health Organization, about 5.8 million people worldwide were infected with TB in 2020 [1]. Mycobacterium tuberculosis infection has become a global public problem, especially in developing countries [2].

MTB can escape immune surveillance and kill by inhibiting oxidative stress, autophagy, and apoptosis of cells. It also can affect antigen presentation of antigen-presenting cells (APC) by inhibiting the synthesis of histocompatibility complex molecules [3]. There are many clinical trials used to test for diagnosing TB, such as tuberculin skin test (TST), T-SPOT, smear microscope, the culture of Mycobacterium tuberculosis, and chest X-ray [4, 5]. But as a slow-growing intracellular parasitic bacteria [6], the above clinical test methods have certain false negative and hysteresis.

To search for sensitive indicators in Mycobacterium tuberculosis infection, we use bioinformatics methods to compare and analyze the spectrum of gene expression

spectrum of pulmonary tuberculosis and healthy people, hoping to find genes that play a significant role in the pathogenesis of PTB as potential biomarkers for diagnosing pulmonary tuberculosis and further explore the relationship between biomarkers and tumor prognosis and stage through pan-cancer analysis.

2. Materials and Methods

2.1. Data Acquisition and Processing. We downloaded the GSE28623 (GPL4133, Agilent-014850 Whole Human Genome Microarray), GSE83456 (GPL10558, Illumina HumanHT-12 V4.0 expression beadchip), GSE34608 (GPL6480, Agilent-014850 Whole Human Genome U133 Microarray), and GSE31348 (GPL570, Affymetrix Human Genome U133 Plus) from Gene Expression Omnibus (GEO, https://www.ncbi.nlm.nih.gov/geo/) by "GEOquery" R-package and extracted each expression profile information and Clinical phenotype of these gene sets. There were 46 pulmonary tuberculosis samples and 37 healthy control samples in GSE28623 and 45 pulmonary tuberculosis samples and 61 healthy control samples in GSE83456. Finally, 189 blood samples were enrolled as training sets. There were 8 pulmonary tuberculosis samples and 16 healthy control samples in GSE34608 and 135 pulmonary tuberculosis samples in GSE31348. In the end, 159 blood samples were enrolled as validation sets. After that, we downloaded the unified and standardized pan-cancer data set from the UCSC (https://xenabrowser.net/) database, TCGA Pan-cancer (PANCAN, $N = 10535$, $G = 60499$), extracted expression data of the RTP4 gene (ENSG00000136514) in each sample, and carried out a log2 $(x + 0.001)$ transformation, and finally, we also eliminated cancer types with fewer than 3 samples in a single cancer type and finally obtained the expression data of 26 cancer types.

2.2. KEGG and Gene Set Variation Analysis. The KEGG was a set of databases that included information about biological mechanisms, cellular processes, chemical substances, and diseases [7]. Gene set variation analysis (GSVA) was applied to explore different activity variations of the KEGG pathway (c2.cp.kegg v7.5.1, http://www.gsea-msigdb.org/) in GSE28623 and GSE83456 by using "GSVA" R package [8]. "limma" R package was used to determine the significant differences in GSVA enrichment between the healthy control (HC) group and pulmonary tuberculosis (PTB) group. After setting the threshold value (PTB versus HC, log 2FC > 0.25, adjust p value < 0.05) and taking the intersection of the training set (GSE28623 and GSE83456), we selected the folate biosynthesis pathway enrichment scores for further analysis with clinical phenotype.

2.3. Identification of Significant Modules and Weight Gene Coexpression Network Analysis. Data selected in training sets were processed using the "WGCNA" R package [9]. After obtaining the gene expression matrix of GSE28623 and GSE83456 gene sets, we chose the genes that variance in the top quartile and used the hierarchical agglomerative

clustering (average link) to distinguish the outliers of each gene set. Then, we set each threshold to construct a scale-free network. After setting an approximate scale-free topology fit index above 0.85, we built an adjacency matrix and constructed the topological overlap matrix for searching the coexpression modules, which is a collection of genes with high topological overlap similarity and containing at least 30 genes. Genes in the same module usually have a higher degree of coexpression. The module eigengene (ME) represents the first principal component of modules and reflects the expression pattern of modules in each sample. After merging modules whose similarities were higher than 75%, 8 modules in GSE28623 and 13 modules in GSE83456 were identified according to the average hierarchical clustering and dynamic tree clipping algorithm. The green-yellow module of GSE28623 and brown module of GSE83456 were most relevant to the clinical phenotype and folate biosynthesis pathway enrichment.

2.4. Hub Gene Identification and PPI Network. The coexisting genes in both modules were considered essential and uploaded to the Search Tool for the Retrieval of Interacting Genes (STRING) online database (http://string-db.org; version 11.5). A confidence score > 0.70 was set as significant. After obtaining the protein-protein interaction (PPI) network data, we used the Cytoscape (version 3.9.1) to visualize the results. In order to verify the effectiveness of the hub genes, "pROC" and "ggplot2" were used to calculate and plot the area under curve (AUC) [10, 11].

2.5. Pan-Cancer Analysis. We used R software to calculate the expression difference between normal samples and tumor samples in each tumor to analyze the significance of the difference. The "Coxph" function of "survival" R package (version 3.4.0) was used to establish a Cox proportional hazard regression model to analyze the relationship between gene expression and prognosis in each tumor. After that, we calculated the expression difference of genes in different clinical stage samples in each tumor to explore the correlations between them.

2.6. Statistical Analysis. This study's statistical analyses were carried out by R (version 4.1.0). Linear fitting and empirical Bayes, implemented in the "limma" R package, were used to test the difference between the HC and PTB groups [12]. Weight gene coexpression network analysis was used to allocate genes with similar expression patterns into different modules. The Pearson correlation analysis was applied to find correlations between the selected modules and clinical phenotype. The receiver operating characteristic (ROC) curve was used to evaluate the reliability of candidate biomarkers. It was considered statistically significant if the area under curve (AUC) was greater than 0.70. Student's t-test was used to estimate the different expressions of RTP4 before and after antituberculosis therapy. All $p < 0.05$ (bilateral) was considered statistically significant. The logarithmic ranking test was to obtain the tumor prognostic significance. The unpaired Student's t-test was used for analyzing
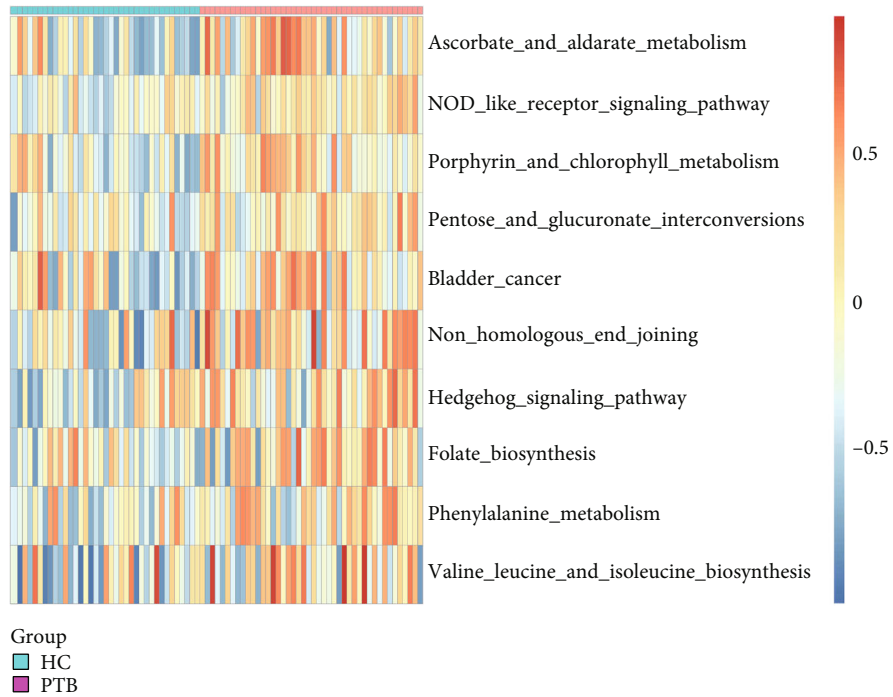
(a) GSE28623: the different activated levels of Kyoto Encyclopedia of Genes and Genomes gene set between the healthy control and pulmonary tuberculosis groups. Turquoise and red lines represented the control group and pulmonary tuberculosis group, respectively
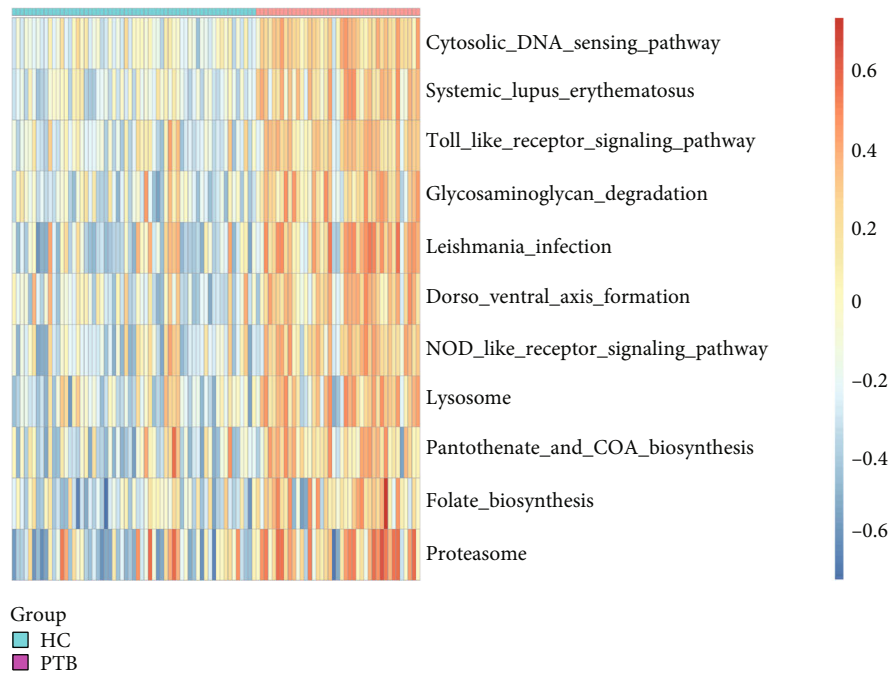
(b) GSE83456: the different activated levels of Kyoto Encyclopedia of Genes and Genomes gene set between the healthy control and pulmonary tuberculosis groups. Turquoise and red lines represented the control group and pulmonary tuberculosis group, respectively

FIGURE 1: Enrichment of differential KEGG pathway gene sets of training gene sets.

difference between each type of tumor groups. The unpaired Wilcoxon rank sum and signed rank tests were used to explore the significance of the difference between normal and tumor samples in each tumor type.

3. Results

3.1. Folate Biosynthesis Pathway Gene Set Scores and WGCNA.
The gene expression of GSE28623 (19172 genes) and
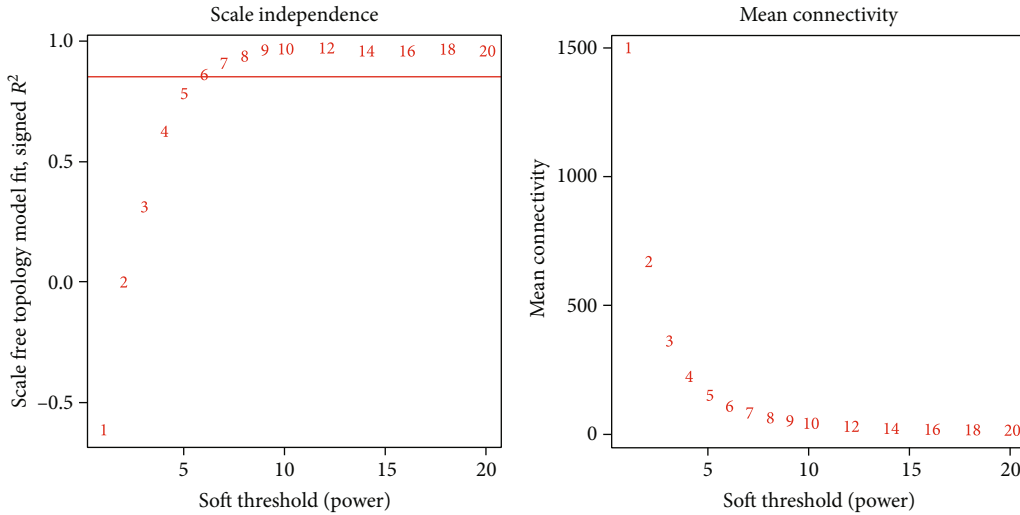
(a) Analysis of the scale-free index and mean connectivity for various soft threshold powers in GSE28623
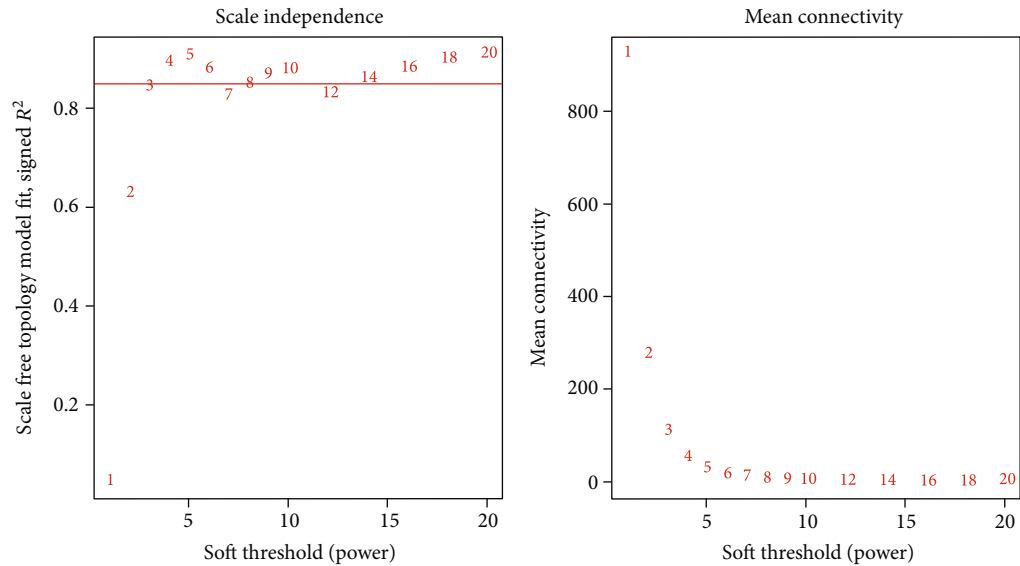
(b) Analysis of the scale-free index and mean connectivity for various soft threshold powers in GSE83456

FIGURE 2: Determination of soft threshold power in the WGCNA.

GSE83456 (20937 genes) was obtained after data preprocessing. After excluding latent tuberculosis, extrapulmonary tuberculosis, and sarcoid samples, we had 83 samples left in GSE28263 and 106 samples in GSE83456. We used an agglomerative hierarchical clustering algorithm to exclude 2 PTB samples of GSE28623 and 4 PTB samples of GSE83456 because there were outliers. Subsequently, the top quartile variance genes were selected (GSE28623, 4982 genes; GSE83456, 5234 genes). Through gene set variation analysis, we found that the KEGG pathways activated in GSE28623 (PTB group versus HC group) were mainly associated with ascorbate and aldarate metabolism, NOD-like receptor signaling, porphyrin and chlorophyll metabolism, pentose and glucuronate interconversions, bladder cancer, nonhomologous and joining, hedgehog signaling, folate biosynthesis, phenylalanine metabolism, valine leucine, and isoleucine biosynthesis. However, the main KEGG pathways

activated in GSE83456 (PTB group versus HC group) were cytosolic DNA sensing, systemic lupus erythematosus, toll-like receptor signaling, glycosaminoglycan degradation, leishmania infection, dorso-ventral axis formation, NOD-like receptor signaling, lysosome, pantothenate and CoA biosynthesis, folate biosynthesis, and proteasome. We observed the same activation trend both in GSE28623 ($\log 2FC = 0.286$, adj.$p < 0.001$) and GSE83456 ($\log 2FC = 0.325$, adj.$p < 0.001$) of folate biosynthesis pathway. The differential KEGG pathway gene set enrichment results were depicted by a heat map (Figure 1). We set the threshold power at 6 (GSE28623, $R^2 = 0.850$) and 4 (GSE83456, $R^2 = 0.895$) respectively based on an approximate scale-free topology fit index of above 0.85 for each gene set. This network conforms to the power-law distribution closer to the real biological network state (Figures 2(a) and 2(b)). Gene dendrograms and module colors of the training sets are shown in Figure 3. After

Cluster dendrogram

(a) GSE28623: gene clustering tree obtained by hierarchical clustering of adjacency-based dissimilarity

Cluster dendrogram

(b) GSE83456: gene clustering tree obtained by hierarchical clustering of adjacency-based dissimilarity
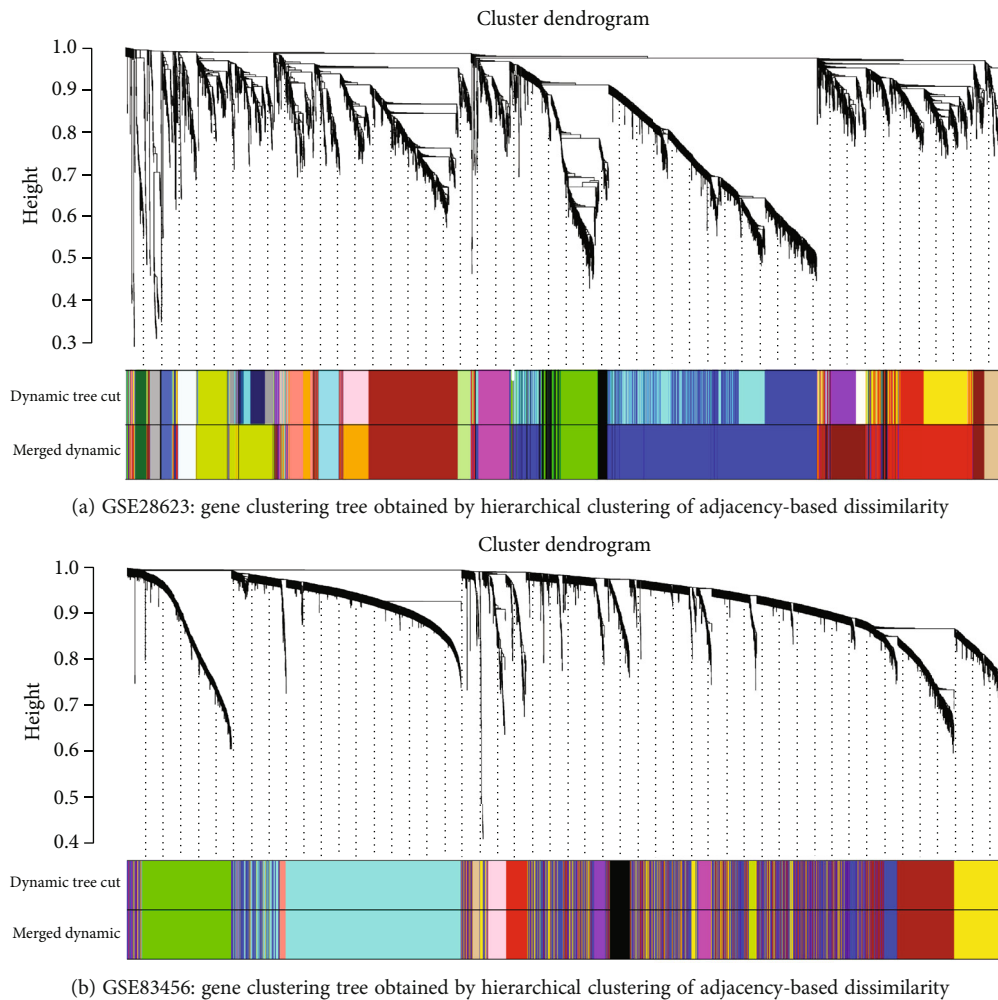
FIGURE 3: Dendrogram of all differentially expressed genes clustered based on the measurement of dissimilarity (1-TOM). The color band shows the results obtained from the automatic single-block analysis. Each color band of dynamic tree cut represents a cluster of a collection of genes with high topological overlap similarity and has minimal genes of 30. Merged dynamic represents the merged modules of dynamic tree cut, in which the dissimilarity degree is below 75%.

obtaining the different modules, we screened out that the most associated with pulmonary tuberculosis. After that, we selected the most relevant folate biosynthesis pathway of them. By carefully comparing, we found that the green-yellow module in GSE28623 and the brown module in GSE83456 were highly related to pulmonary tuberculosis and the folate biosynthesis pathway. Finally, we selected these two modules for further analysis (Figure 4).

3.2. PPI Network Analysis and Hub Gene Identification. In the intersection of the two modules, we obtained 29 coexisting genes, which were illustrated by the Veen map (Figure 5). After using the STRING online database, eight nodes and sixteen edges were observed. Six genes (OAS2, SAMD9L, RSAD2, RTP4, CD151, and BATF) were filtered in the PPI network complex based on the setting confidence score (Figure 6).

We then screen one (RTP4) of them according to the area under curve both in training sets (GSE28623, AUC = 0.719; GSE83456, AUC = 0.964, Figures 7(a) and 7(b)) and

the validation cohort (GSE34608, AUC = 0.903 Figure 7(c)) as the hub gene. To make the outcome persuasive, we chose the gene set (GSE31384) to validate diversity expression before and after antituberculosis therapy and compare the differential expression of RTP4 between the HC and PTB groups in GSE28623 and GSE83456. As shown in Figure 8, the expression of RTP4 was significantly downregulated after 26 weeks of antituberculosis treatment. We also found that there were significantly upregulated in the PTB group (Figures 9 and 10).

3.3. Pan-Cancer Analysis. In the expression difference between normal samples and tumor samples in each tumor, we found that RTP4 was significantly upregulated in 13 types of tumor tissues such as GBM (tumor: 2.22 ± 1.14, normal: 0.3 ± 0.44, $p = 5.4e - 4$), GBMLGG (tumor: 1.70 ± 1.09, normal: 0.35 ± 0.44, $p = 3.2e - 3$), LGG (tumor: 1.54 ± 1.02, normal: 0.35 ± 0.44, $p = 5.5e - 3$), ESCA (tumor: 2.78 ± 1.49, normal: 1.00 ± 1.39, $p = 1.5e - 4$), STES (tumor: 2.87 ± 1.24, normal: 1.63 ± 1.20, $p = 1.7e - 10$), KIRP

(a) The module-trait relationships of the GSE28623 gene set

(b) The module-trait relationships of the GSE83456 gene set
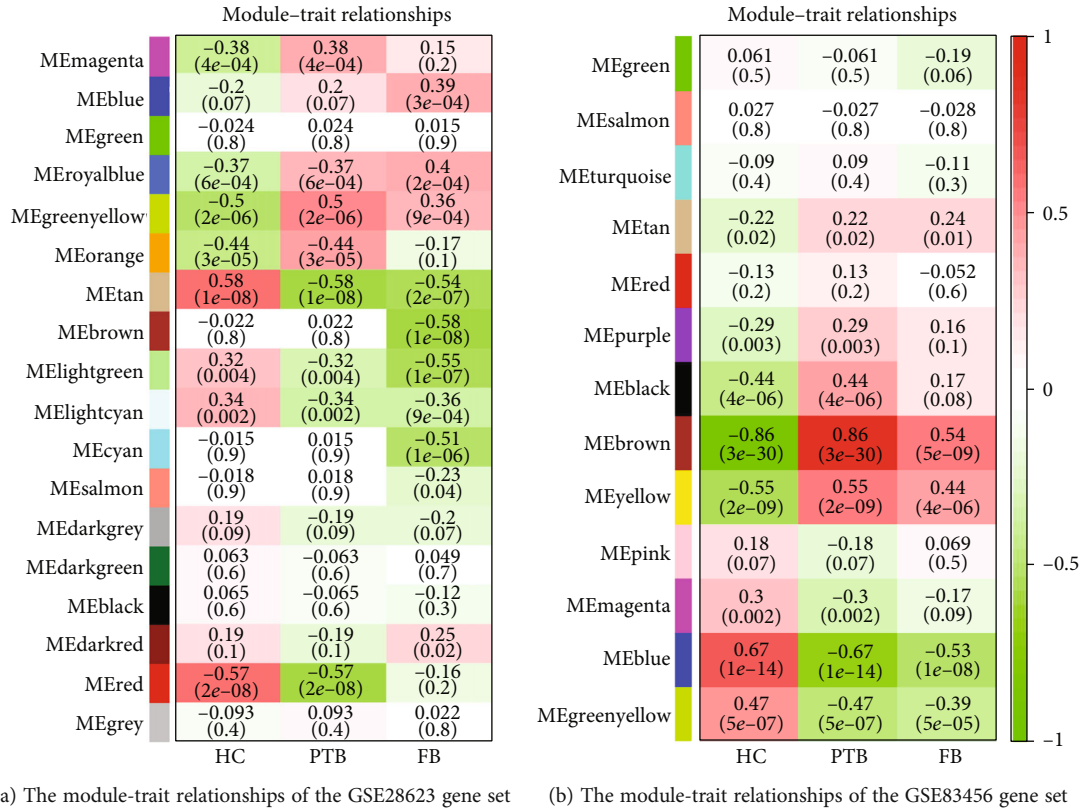
Figure 4: Each row corresponds to the module eigengene column to a clinical trait. Each cell contains the corresponding correlation and p value, red for positive and green for negative correlations.

(tumor: 2.78 ± 1.34, normal: 2.00 ± 0.76, $p = 4.2e - 13$), KIPAN (tumor: 3.15 ± 1.27, normal: 2.00 ± 0.76, $p = 7.1e - 28$), STAD (tumor: 2.91 ± 1.12, normal: 1.86 ± 1.06, $p = 1.1e - 7$), HNSC (tumor: 3.07 ± 1.50, normal: 1.34 ± 1.51, $p = 6.5e - 11$), KIRC (tumor: 3.44 ± 1.10, normal: 2.00 ± 0.76, $p = 6.7e - 37$), LIHC (tumor: 2.29 ± 1.29, normal: 1.50 ± 1.19, $p = 1.3e - 6$), KICH (tumor: 2.47 ± 1.48, normal: 2.00 ± 0.76, $p = 2.8e - 3$), and CHOL (tumor: 3.66 ± 1.28, normal: 1.25 ± 0.56, $p = 6.0e - 7$) and significantly downregulated in 4 types of tumor tissues such as LUAD (tumor: 2.19 ± 1.22, normal: 2.71 ± 0.56, $p = 1.9e - 6$), COAD (tumor: 2.08 ± 1.13, normal: 2.51 ± 0.57, $p = 0.02$), COADREAD (tumor: 2.02 ± 1.10, normal: 2.50 ± 0.55, $p = 2.1e - 3$), and PRAD (tumor: 1.50 ± 1.27, normal: 2.22 ± 0.75, $p = 1.7e - 6$) (Figure 11) [13].

In the analysis process of the relationship between expression level and tumor prognosis, we found that the poor prognosis of 4 tumors was positively correlated with the high expression of RTP4 (GBMLGG ($N = 619$, $p = 1.5e - 13$, HR = 1.58 (1.40, 1.78)), LGG ($N = 474$, $p = 2.5e - 5$, HR = 1.49 (1.24, 1.79)), LAML ($N = 144$, $p = 1.2e - 3$, HR = 1.30 (1.11, 1.53)), and PAAD ($N = 172$, $p = 8.8e - 4$, HR = 1.44 (1.16, 1.78))), and the poor prognosis of 6 tumors was positively correlated with the low expression of RTP4 (SARC ($N = 254$, $p = 9.7e - 8$, HR = 0.72 (0.64, 0.81)), KIRC ($N = 515$, $p = 3.2e - 3$, HR = 0.82 (0.72, 0.94)), THCA ($N = 501$, $p = 0.01$, HR = 0.43 (0.23, 0.83)), MESO ($N = 84$, $p = 6.1e - 6$, HR = 0.68 (0.58, 0.81)), SKCM-M
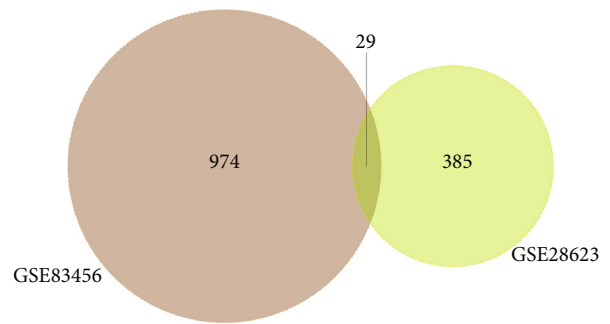
Figure 5: Coexisting genes exist in yellow-green modules (GSE28623) and brown modules (GSE83456). The intersection of the two modules.

($N = 347$, $p = 1.1e - 3$, HR = 0.85 (0.78, 0.94)), and SKCM ($N = 444$, $p = 4.2e - 3$, HR = 0.88 (0.80, 0.96))) (Figures 12 and 13).

After exploring the expression difference of the RTP4 gene in different clinical stages in each type of tumor, we found significant differences among the 5 types of tumors. (HNSC (stage I = 27, II = 82, III = 93, IV = 316) ($p = 0.03$), LIHC (stage I = 169, II = 86, III = 85, IV = 5) ($p = 0.04$), THCA (stage I = 283, II = 52, III = 112, IV = 55) ($p = 2.7e - 3$), PAAD (stage I = 21, II = 147, III = 3, IV = 4) ($p = 0.02$), and BLCA (stage II = 130, III = 140, IV = 133) ($p = 0.02$)) (Figure 14).
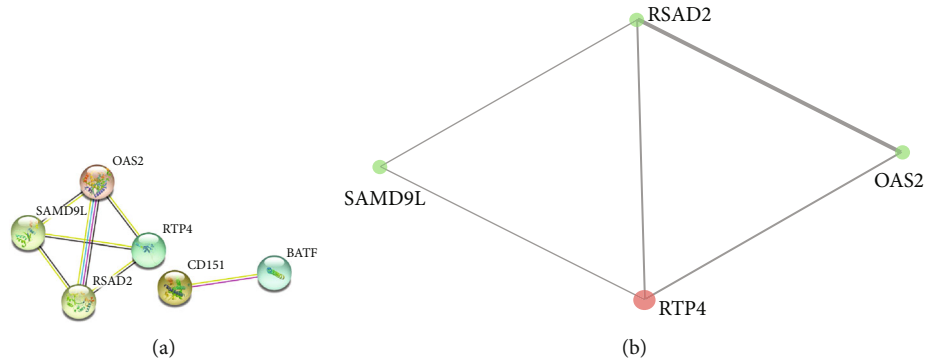
FIGURE 6: PPI network. (a) The interaction between 6 intersections coexisted; only 4 genes had the interaction. (b) The interaction between hub genes.
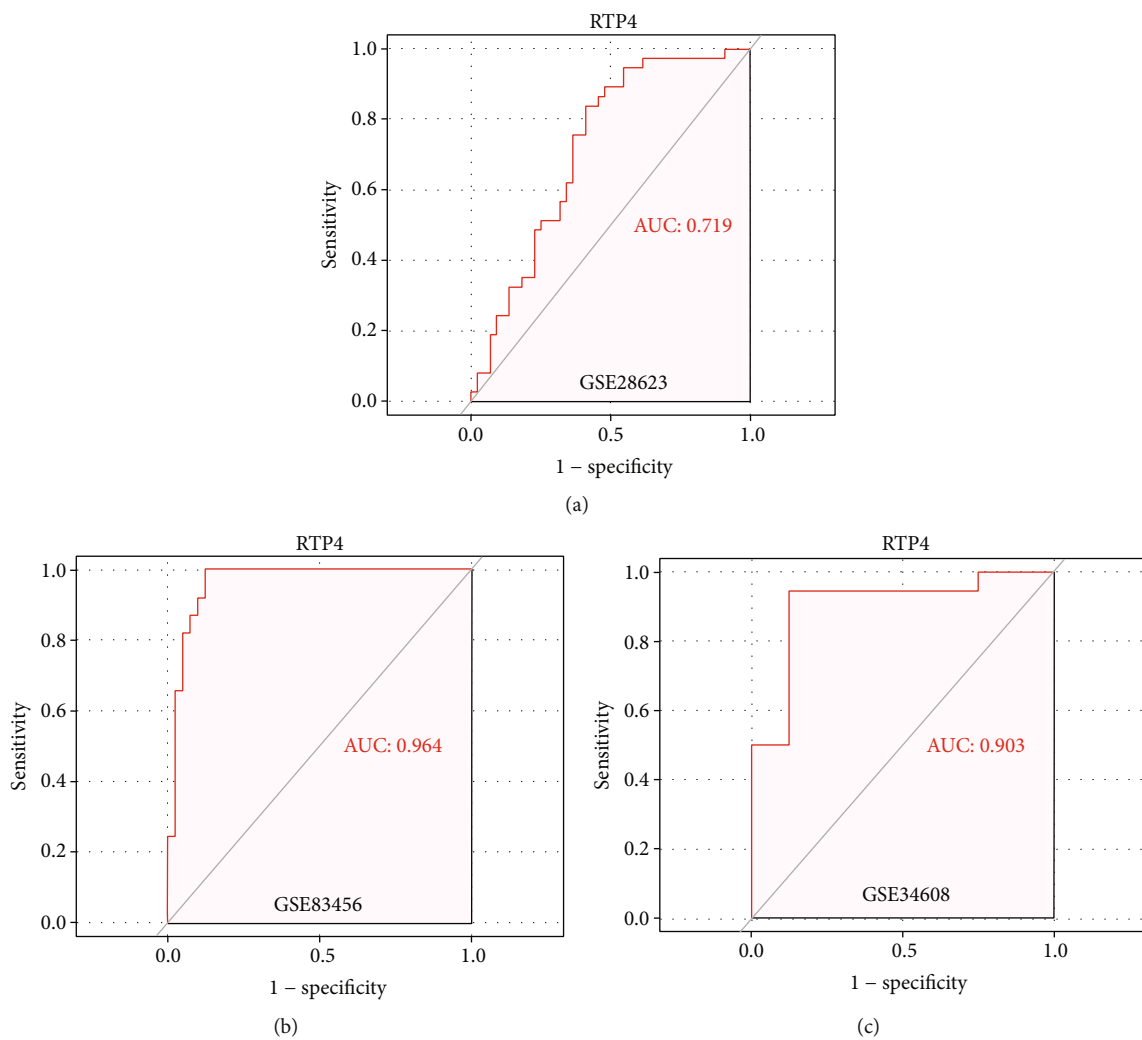
FIGURE 7: The different AUCs of RTP4 expression. AUC plot of RTP4 expression in GSE28623, GSE83456, and GSE34608, respectively.

4. Discussion

MTB can infect many tissues and organs of the human body, causing various tuberculosis-related diseases, such as primary and secondary tuberculosis, tuberculous enteritis, osteoarticular tuberculosis, tuberculous pleurisy, tubercular meningitis, and tuberculous lymphadenitis. Some diseases can be fatal because of delays in diagnosis and treatment.

Tuberculosis is a common infectious disease in developing countries. There are some clinical tests in diagnosing this
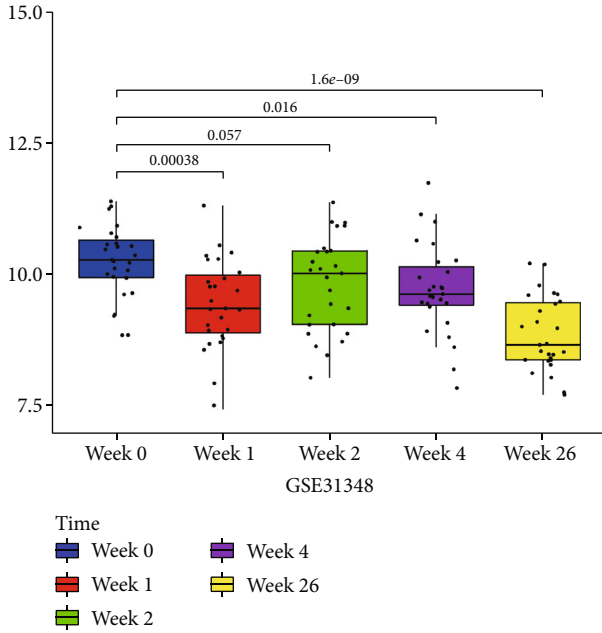
FIGURE 8: Diversity expression of RTP4 before and after antituberculosis therapy (five time points). RTP4 expression of different time points (week 0, week 1, week 2, week 4, and week 26) in GSE31348.
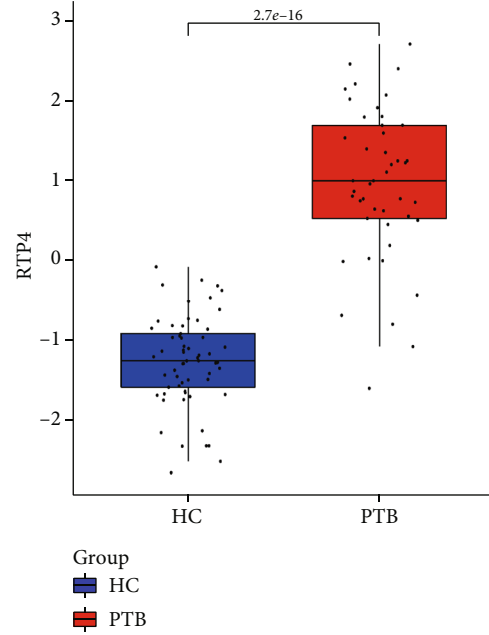
FIGURE 10: The different expressions of RTP4 between the HC group and PTB group in GSE83456.
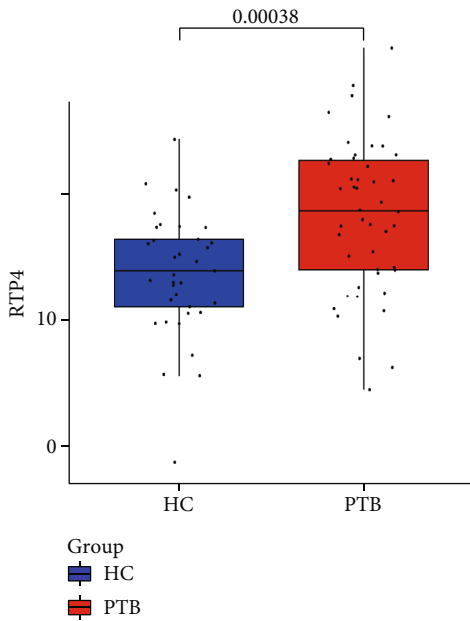
FIGURE 9: The different expressions of RTP4 between the HC group and PTB group in GSE28623.
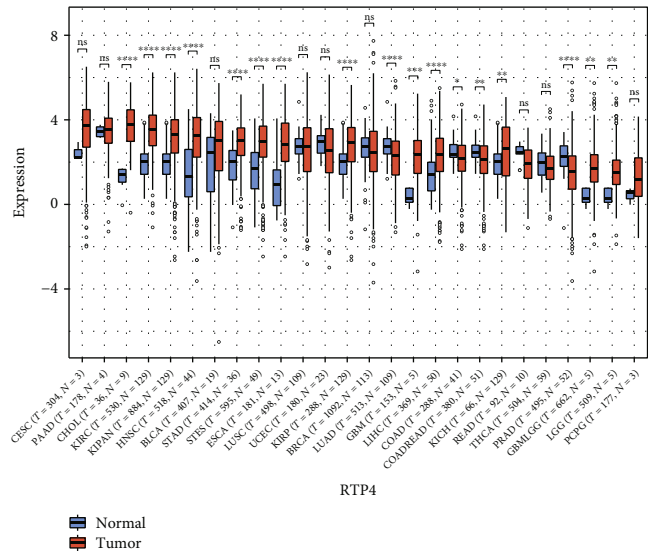
FIGURE 11: The different expressions of RTP4 in 26 types of tumors between normal samples and tumor samples. *0.05, **0.01, *** 0.001, and ****0.0001. Red: tumor group. Blue: normal group.

disease, but those ways have somehow false negatives [14–16]. The histopathologic biopsy is an excellent method to diagnose tuberculosis infection. Due to the difficulty of sampling, some tissues in vivo and patients cannot tolerate the discomfort during the sampling process, so this method is not often used in clinical diagnosis. Sputum culture is considered the gold standard for diagnosing PTB infections.

However, as a slow-growing bacteria, clinical doctors may be able to get results in 2-3 months. We conducted this study to reduce the time of diagnosing and improve the diagnostic accuracy of PTB.

Several previous researchers have reported some potential biomarkers for tuberculosis [17, 18]. Our study is aimed at investigating new biomarkers for diagnosing pulmonary tuberculosis related to folate synthesis, and RTP4 was finally identified in training and validated in the validation set.

(a)

(b)
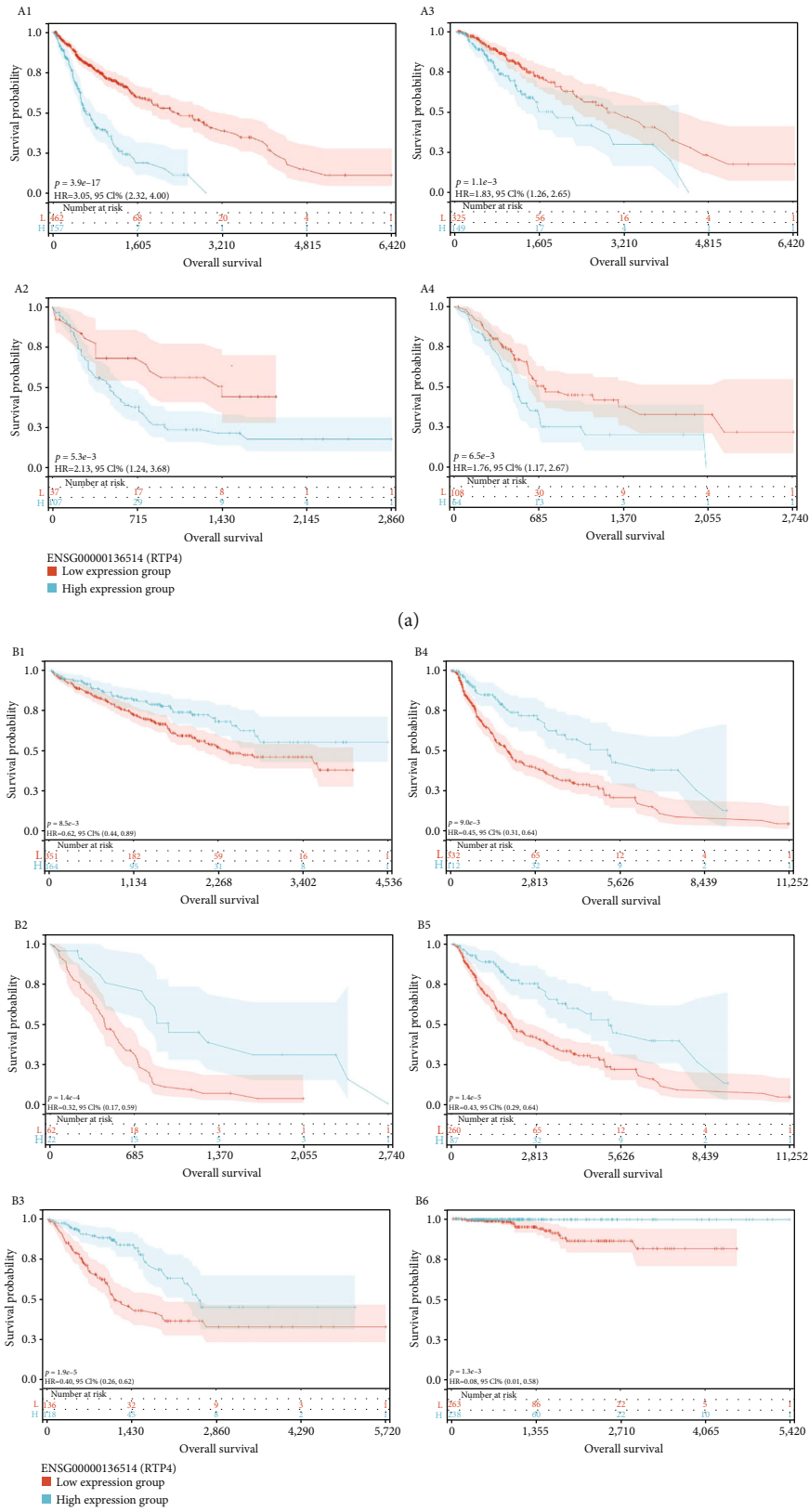
Figure 12: (A1–A4) The survival probability of the RTP4 low expression group and high expression group in GBMLGG, LAMA, LGG, and PAAD. (B1–B6) The survival probability of RTP4 low expression group and high expression group in KIRC, MESO, SARC, SKCM. Red: low expression group. Blue: high expression group.

Cancer code	p value		Hazard ratio (95% CI)
TCGA-GBMLGG ($N = 619$)	1.5e−13		1.58 (1.40, 1.78)
TCGA-LGG ($N = 474$)	2.5e−5		1.49 (1.24, 1.79)
TCGA-PAAD ($N = 172$)	8.0e−4		1.44 (1.16, 1.78)
TCGA-LAML ($N = 144$)	1.2e−3		1.30 (1.11, 1.53)
TCGA-TGCT ($N = 128$)	0.06		3.75 (0.85, 16.65)
TCGA-THYM ($N = 117$)	0.13		1.82 (0.86, 3.89)
TCGA-UCEC ($N = 166$)	0.14		1.19 (0.95, 1.48)
TCGA-COAD ($N = 278$)	0.47		1.08 (0.87, 1.35)
TCGA-SKCM-P ($N = 97$)	0.51		1.11 (0.81, 1.53)
TCGA-LUAD ($N = 490$)	0.52		1.04 (0.92, 1.17)
TCGA-UVM ($N = 74$)	0.56		1.13 (0.74, 1.74)
TCGA-GBM ($N = 144$)	0.63		1.04 (0.89, 1.22)
TCGA-COADREAD ($N = 368$)	0.66		1.05 (0.86, 1.28)
TCGA-PCPG ($N = 170$)	0.69		1.15 (0.59, 2.23)
TCGA-KICH ($N = 64$)	0.99		1.00 (0.63, 1.60)
TCGA-SARC ($N = 254$)	9.7e−8		0.72 (0.64, 0.81)
TCGA-MESO ($N = 84$)	6.1e−6		0.68 (0.58, 0.81)
TCGA-SKCM-M ($N = 347$)	1.1e−3		0.85 (0.78, 0.94)
TCGA-KIRCN ($N = 515$)	3.2e−3		0.82 (0.72, 0.94)
TCGA-SKCM ($N = 444$)	4.2e−3		0.88 (0.80, 0.96)
TCGA-THCA ($N = 501$)	0.01		0.43 (0.23, 0.83)
TCGA-OV ($N = 407$)	0.09		0.93 (0.86, 1.01)
TCGA-BLCA ($N = 398$)	0.09		0.94 (0.87, 1.01)
TCGA-CHOL ($N = 33$)	0.19		0.78 (0.53, 1.14)
TCGA-KIPAN ($N = 855$)	0.23		0.94 (0.85, 1.04)
TCGA-BRCA ($N = 1044$)	0.26		0.94 (0.85, 1.05)
TCGA-LIHC ($N = 341$)	0.26		0.92 (0.80, 1.06)
TCGA-CESC ($N = 273$)	0.30		0.92 (0.80, 1.07)
TCGA-STES ($N = 547$)	0.32		0.95 (0.86, 1.05)
TCGA-STAD ($N = 372$)	0.38		0.94 (0.82, 1.08)
TCGA-DLCB ($N = 44$)	0.41		0.79 (0.45, 1.40)
TCGA-KIRP ($N = 276$)	0.42		0.92 (0.74, 1.13)
TCGA-ACC ($N = 77$)	0.44		0.93 (0.76, 1.13)
TCGA-READ ($N = 90$)	0.46		0.82 (0.49, 1.38)
TCGA-PRAD ($N = 492$)	0.48		0.83 (0.51, 1.38)
TCGA-UCS ($N = 55$)	0.54		0.94 (0.78, 1.14)
TCGA-LUSC ($N = 468$)	0.84		0.99 (0.91, 1.08)
TCGA-HNSC ($N = 509$)	0.86		0.99 (0.91, 1.08)
TCGA-ESCA ($N = 175$)	0.88		0.99 (0.85, 1.15)

$$-2.0 \quad -1.5 \quad -1.0 \quad -0.5 \quad 0.0 \quad 0.5 \quad 1.0 \quad 1.5 \quad 2.0 \quad 2.5 \quad 3.0 \quad 3.5 \quad 4.0$$

Log$_2$ (hazard ratio (95% CI))

Figure 13: The relationship between RTP4 gene expression and prognosis in 39 types of tumors.

Folate acid is known as vitamin B9. It is necessary for the body to yield amino acids, RNA, and DNA [19]. It has previously been reported that lacking folic acid may lead to neuropathy and neoplastic diseases [20–22]. Folic acid is also an element for M. tuberculosis. It is believed that folate can affect the synthesis of purines and thymidine by regulating one-carbon transfer reactions as an essential factor, which is vital for bacteria [23, 24]. In recent years, there has been renewed interest in synthesizing antifolic acid drugs due to the increase in clinical drug-resistant tuberculosis cases [25, 26].

The RTP4 is known as a member of the receptor transport protein (RTP), which participates in exporting odorant and taste receptors to the cell surface [27, 28]. Previous studies have suggested that RTP4 helps the GPCR oligomer properly assemble in the endoplasmic reticulum, promotes the dimerization of receptors in the Golgi apparatus, and decreases the ubiquitination of the heterodimers [29]. Other studies have shown that the RTP4 was overexpressed in some connective tissue disorders and parasitic infections [30, 31] and correlated with some cancers [32, 33]. That RTP4 induced by IFN-I could explain this phenomenon and is associated with immune responses.
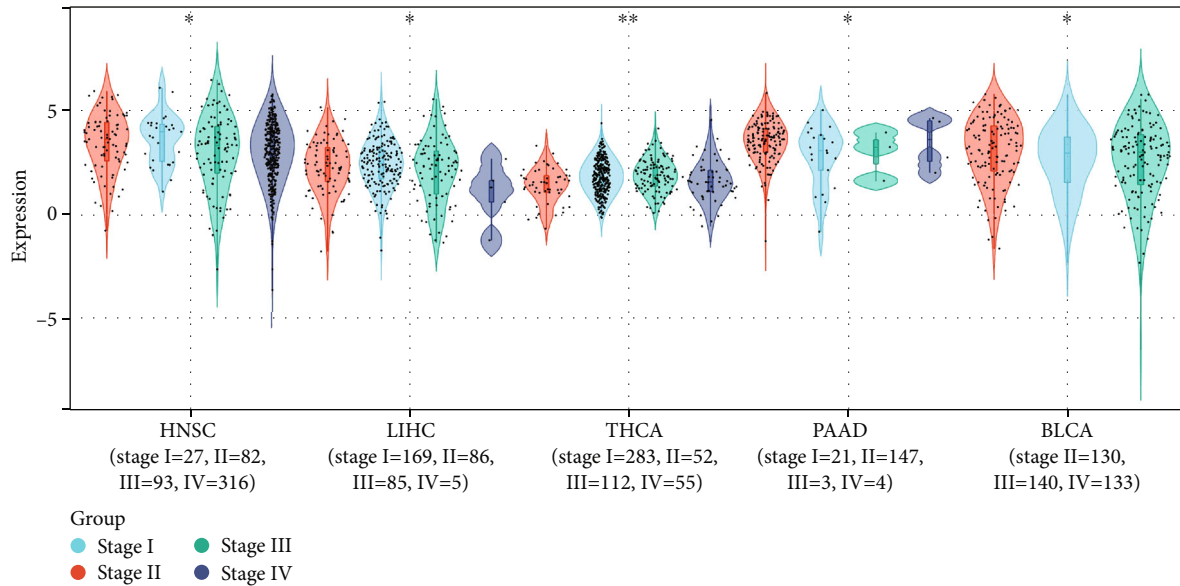
FIGURE 14: Differences in the expression of RTP4 in different stages in 5 types of tumors. *0.05, **0.01, ***0.001, and ****0.0001.

In our research, we also found several other enriched signaling pathways related to complications of PTB. Previous studies have implicated the NOD-like signaling pathway and Toll-like receptor signaling pathways in idiopathic pulmonary fibrosis [34]. The Hedgehog signaling pathway was reported to be associated with lung cancer. Abnormal activation of this pathway is thought to be related to the development of lung cancer and promotes malignant lung cancer progression with poor prognostic outcomes [35, 36]. These may explain some PTB patients' clinical progression of pulmonary fibrosis and lung cancer. However, in this study, we only found that the folate biosynthesis singling pathways were most associated with the PTB group in training gene sets.

Some previous articles have reported a correlation between the RTP4 gene and certain characteristics of tumors. For example, methylated RTP4 can be considered as a new biomarker for precise diagnosis and treatment of prostate cancer [37] and RTP4 can be considered as an independent indicator to judge the prognosis of oral cancer [38]. RTP4 has also been reported that it is significantly associated with immune cell infiltration and immune checkpoint encoding genes (PDCD1, TIM-3, and LAG3) in melanoma [33].

We worked on seeking the different genes as biomarkers of diagnosing PTB infection through four GEO databases and used a method combing gene set variation analysis with weight gene coexpression network analysis. There were some limitations in this study. Firstly, the validated samples were less than the training samples, and more gene chip samples of patients with TB were validated from the experimental verification. To further explore the relationship between the expression of RTP4 and tumors, we performed a pan-cancer analysis based on TCGA database. It was also found that RTP4 expression was different between some tumor and normal tissues, and it was correlated with the overall survival time and stage of some tumors.

To conclude, our results suggest that RTP4 can be used as a biomarker to identify tuberculosis infection, providing a new perspective on TB diagnosis in clinical.

Abbreviations

PTB:	Pulmonary tuberculosis
HC:	Healthy control
WGCNA:	Weight gene coexpression network analysis
ROC:	Receiver operating characteristic
GSVA:	Gene set variation analysis
PPI:	Protein-protein interaction network
MTB:	Mycobacterium tuberculosis
APC:	Antigen-presenting cells
TST:	Tuberculin skin test
STRING:	Search Tool for the Retrieval of Interacting Genes
AUC:	Area under curve
KEGG:	Kyoto Encyclopedia of Genes and Genomes
ACC:	Adrenocortical carcinoma
BLCA:	Bladder urothelial carcinoma
BRCA:	Breast invasive carcinoma
CESC:	Cervical squamous cell carcinoma and endocervical adenocarcinoma
CHOL:	Cholangiocarcinoma
COAD:	Colon adenocarcinoma
COADREAD:	Colon adenocarcinoma/rectum adenocarcinoma esophageal carcinoma
DLBC:	Lymphoid neoplasm diffuse large B-cell lymphoma
ESCA:	Esophageal carcinoma
FPPP:	FFPE pilot phase II
GBM:	Glioblastoma multiforme
GBMLGG:	Glioma
HNSC:	Head and neck squamous cell carcinoma
KICH:	Kidney chromophobe
KIPAN:	Pan-kidney cohort (KICH+KIRC+KIRP)

KIRC: Kidney renal clear cell carcinoma
KIRP: Kidney renal papillary cell carcinoma
LAML: Acute myeloid leukemia
LGG: Brain lower grade glioma
LIHC: Liver hepatocellular carcinoma
LUAD: Lung adenocarcinoma
LUSC: Lung squamous cell carcinoma
MESO: Mesothelioma
OV: Ovarian serous cystadenocarcinoma
PAAD: Pancreatic adenocarcinoma
PCPG: Pheochromocytoma and paraganglioma
PRAD: Prostate adenocarcinoma
READ: Rectum adenocarcinoma
SARC: Sarcoma
STAD: Stomach adenocarcinoma
SKCM: Skin cutaneous melanoma
STES: Stomach and esophageal carcinoma
TGCT: Testicular germ cell tumors
THCA: Thyroid carcinoma
THYM: Thymoma
UCEC: Uterine corpus endometrial carcinoma
UCS: Uterine carcinosarcoma
UVM: Uveal melanoma.

Data Availability

Data can be obtained from GEO (https://www.ncbi.nlm.nih.gov/geo/) and TCGA (https://www.cancer.gov/ccg/research/genome-sequencing/tcga).

Ethical Approval

This study was approved by the Ethics Committee of The First People's Hospital of Changde City.

Consent

Written informed consent for publication was obtained from all participants.

Disclosure

The authors are accountable for all aspects of the work in ensuring that questions related to the accuracy or integrity of any part of the work are appropriately investigated and resolved.

Conflicts of Interest

The authors have no conflicts of interest to declare.

Authors' Contributions

LH and ZQ performed analyses and drafted the manuscript. LH searched and downloaded the original gene sets from GEO. LH and ZQ contributed to statistical analyses. LH, DZX, and WQH edited the pictures. LH conceived and supervised the study. All authors contributed to writing the manuscript. All authors reviewed and approved the final manuscript. Hao Li and Qin Zhou contributed equally to this work.

Supplementary Materials

Supplementary materials The difference in gene expression between the PTB group and the HC group are shown in supplementary Figure 1, Figure 2, and Figure 3 (supplementary Figure 1: GSE28623, supplementary Figure 2: GSE83456, and supplementary Figure 3: GSE 34608). (Supplementary 1)

References

[1] Organization, W H, Global Tuberculosis Report, World health organization, 2021.

[2] A. D. Harries and A. M. V. Kumar, "Challenges and progress with diagnosing pulmonary tuberculosis in low- and middle-income countries," Diagnostics (Basel), vol. 8, no. 4, p. 78, 2018.

[3] S. Chauhan, M. A. Mandell, and V. Deretic, "Mechanism of action of the tuberculosis and Crohn disease risk factor IRGM in autophagy," Autophagy, vol. 12, no. 2, pp. 429–431, 2016.

[4] S. Toonkomdang, P. Phinyo, B. Phetsuksiri, J. Patumanond, J. Rudeeaneksin, and W. Klayut, "Pragmatic accuracy of an in-house loop-mediated isothermal amplification (LAMP) for diagnosis of pulmonary tuberculosis in a Thai community hospital," PLoS One, vol. 15, no. 7, article e0236496, 2020.

[5] S. E. Murthy, F. Chatterjee, A. Crook et al., "Pretreatment chest X-ray severity and its relation to bacterial burden in smear positive pulmonary tuberculosis," BMC Medicine, vol. 16, no. 1, p. 1, 2018.

[6] S. Cole, R. Brosch, J. Parkhill et al., "Deciphering the biology of Mycobacterium tuberculosis from the complete genome sequence," Nature, vol. 393, no. 6685, pp. 537–544, 1998.

[7] M. Kanehisa and S. Goto, "KEGG: Kyoto Encyclopedia of Genes and Genomes," Nucleic Acids Research, vol. 28, no. 1, pp. 27–30, 2000.

[8] S. Hanzelmann, R. Castelo, and J. Guinney, "GSVA: gene set variation analysis for microarray and RNA-seq data," BMC Bioinformatics, vol. 14, no. 1, p. 7, 2013.

[9] P. Langfelder and S. Horvath, "WGCNA: an R package for weighted correlation network analysis," BMC Bioinformatics, vol. 9, no. 1, p. 559, 2008.

[10] X. Robin, N. Turck, A. Hainard et al., "pROC: an open-source package for R and S+ to analyze and compare ROC curves," BMC Bioinformatics, vol. 12, no. 1, 2011.

[11] H. Wickham, ggplot2: Elegant Graphics for Data Analysis, Springer-Verlag, New York, 2016.

[12] M. E. Ritchie, B. Phipson, D. Wu et al., "Limma powers differential expression analyses for RNA-sequencing and microarray studies," Nucleic Acids Research, vol. 43, no. 7, article e47, 2015.

[13] S. Yu, H. Wang, T. Liu, C. Liang, and J. Luo, "A knowledge-driven network for fine-grained relationship detection between miRNA and disease," Briefings in Bioinformatics, vol. 23, no. 3, article bbac058, 2022.

[14] L. Di and Y. Li, "The risk factor of false-negative and false-positive for T-SPOT.TB in active tuberculosis," *Journal of Clinical Laboratory Analysis*, vol. 32, no. 2, article e22273, 2018.

[15] P. D. Davies and M. Pai, "The diagnosis and misdiagnosis of tuberculosis," *The International Journal of Tuberculosis and Lung Disease*, vol. 12, no. 11, pp. 1226–1234, 2008.

[16] C. M. Bauer, A. Schmahl, and M. Kreuter, "Imaging and laboratory diagnostics for tuberculosis," *Klinische Monatsblätter für Augenheilkunde*, vol. 233, no. 5, pp. 587–593, 2016.

[17] S. Natarajan, M. Ranganathan, L. E. Hanna, and S. Tripathy, "Transcriptional profiling and deriving a seven-gene signature that discriminates active and latent tuberculosis: an integrative bioinformatics approach," *Genes (Basel)*, vol. 13, no. 4, p. 616, 2022.

[18] Z. Wen, L. Wu, L. Wang et al., "Comprehensive genetic analysis of tuberculosis and identification of candidate biomarkers," *Frontiers in Genetics*, vol. 13, article 832739, 2022.

[19] M. Fenech, "Folate (vitamin B9) and vitamin B12 and their function in the maintenance of nuclear and mitochondrial genome integrity," *Mutation Research*, vol. 733, no. 1-2, pp. 21–33, 2012.

[20] R. J. Berry, "Lack of historical evidence to support folic acid exacerbation of the neuropathy caused by vitamin B12 deficiency," *The American Journal of Clinical Nutrition*, vol. 110, no. 3, pp. 554–561, 2019.

[21] J. R. Rees, C. B. Morris, J. L. Peacock et al., "Unmetabolized folic acid, tetrahydrofolate, and colorectal adenoma risk," *Cancer Prevention Research (Philadelphia, Pa.)*, vol. 10, no. 8, pp. 451–458, 2017.

[22] J. M. Gong, Y. Shen, W. W. Shan, and Y. X. He, "The association between MTHFR polymorphism and cervical cancer," *Scientific Reports*, vol. 8, no. 1, p. 7244, 2018.

[23] M. R. Nixon, K. W. Saionz, M. S. Koo et al., "Folate pathway disruption leads to critical disruption of methionine derivatives in Mycobacterium tuberculosis," *Chemistry & Biology*, vol. 21, no. 7, pp. 819–830, 2014.

[24] Z. B. Li, L. Y. Shi, Y. S. Han et al., "Pyridoxal phosphate, pyridoxamine phosphate, and folic acid based on ceRNA regulatory network as potential biomarkers for the diagnosis of pulmonary tuberculosis," *Infection, Genetics and Evolution*, vol. 99, article 105240, 2022.

[25] K. A. Wolff and L. Nguyen, "Strategies for potentiation of ethionamide and folate antagonists against Mycobacterium tuberculosis," *Expert Review of Anti-Infective Therapy*, vol. 10, no. 9, pp. 971–981, 2012.

[26] Y. Minato, J. M. Thiede, S. L. Kordus, E. J. McKlveen, B. J. Turman, and A. D. Baughn, "Mycobacterium tuberculosis folate metabolism and the mechanistic basis for para-aminosalicylic acid susceptibility and resistance," *Antimicrobial Agents and Chemotherapy*, vol. 59, no. 9, pp. 5097–5106, 2015.

[27] M. Behrens, J. Bartelt, C. Reichling, M. Winnig, C. Kuhn, and W. Meyerhof, "Members of RTP and REEP gene families influence functional bitter taste receptor expression," *The Journal of Biological Chemistry*, vol. 281, no. 29, pp. 20650–20659, 2006.

[28] H. Saito, M. Kubota, R. W. Roberts, Q. Chi, and H. Matsunami, "RTP family members induce functional expression of mammalian odorant receptors," *Cell*, vol. 119, no. 5, pp. 679–691, 2004.

[29] F. M. Decaillot, R. Rozenfeld, A. Gupta, and L. A. Devi, "Cell surface targeting of mu-delta opioid receptor heterodimers by RTP4," *Proceedings of the National Academy of Sciences of the United States of America*, vol. 105, no. 41, pp. 16045–16050, 2008.

[30] G. Chen, L. Che, X. Cai, P. Zhu, and J. Ran, "Bioinformatic analysis identifies biomarkers and treatment targets in primary Sjogren's syndrome patients with fatigue," *BioMed Research International*, vol. 2022, Article ID 7697558, 10 pages, 2022.

[31] X. He, A. W. Ashbrook, A. Du et al., "RTP4 inhibits IFN-I response and enhances experimental cerebral malaria and neuropathology," *Proceedings of the National Academy of Sciences of the United States of America*, vol. 117, no. 32, pp. 19465–19474, 2020.

[32] Y. Peng, C. Liu, M. Li et al., "Identification of a prognostic and therapeutic immune signature associated with hepatocellular carcinoma," *Cancer Cell International*, vol. 21, no. 1, p. 98, 2021.

[33] Y. Li, J. Qi, and J. Yang, "RTP4 is a novel prognosis-related hub gene in cutaneous melanoma," *Hereditas*, vol. 158, no. 1, p. 22, 2021.

[34] H. Wang, Q. Xie, W. Ou-Yang, and M. Zhang, "Integrative analyses of genes associated with idiopathic pulmonary fibrosis," *Journal of Cellular Biochemistry*, vol. 120, no. 5, p. 8648, 2019.

[35] C. Ma, K. Hu, I. Ullah, Q. K. Zheng, N. Zhang, and Z. G. Sun, "Molecular mechanisms involving the sonic hedgehog pathway in lung cancer therapy: recent advances," *Frontiers in Oncology*, vol. 12, article 729088, 2022.

[36] S. Huang, L. Yang, Y. An et al., "Expression of hedgehog signaling molecules in lung cancer," *Acta Histochemica*, vol. 113, no. 5, pp. 564–569, 2011.

[37] N. Xu, Y. P. Wu, Z. B. Ke et al., "Identification of key DNA methylation-driven genes in prostate adenocarcinoma: an integrative analysis of TCGA methylation data," *Journal of Translational Medicine*, vol. 17, no. 1, p. 311, 2019.

[38] A. Reyimu, Y. Chen, X. Song, W. Zhou, J. Dai, and F. Jiang, "Identification of latent biomarkers in connection with progression and prognosis in oral cancer by comprehensive bioinformatics analysis," *World Journal of Surgical Oncology*, vol. 19, no. 1, p. 240, 2021.

Research Article

Cancer-Associated Fibroblast Risk Model for Prediction of Colorectal Carcinoma Prognosis and Therapeutic Responses

Yan Wang ,[1] **Zhengbo Chen** ,[2] **Gang Zhao** ,[2] **and Qiang Li** [1]

[1]*Department of Anesthesiology, State Key Laboratory of Oncology in South China, Sun Yat-sen University Cancer Center, Guangzhou, 510060 Guangdong, China*
[2]*Department of Vascular and Plastic Surgery, Guangdong Provincial People's Hospital (Guangdong Academy of Medical Sciences), Southern Medical University, Guangzhou, 510080 Guangdong, China*

Correspondence should be addressed to Qiang Li; liqiang@sysucc.org.cn

Colorectal carcinoma (CRC) is a malignant tumor of the digestive system. Cancer-associated fibroblasts (CAFs) are important cellular elements in the tumor microenvironment of CRC, which contribute to CRC progression and immune escape. To predict the survival outcome and therapeutic responses of CRC patients, we identified genes connected with stromal CAF and generated a risk model. In this study, we used multiple algorithms to reveal CAF-related genes in the Gene Expression Omnibus and The Cancer Genome Atlas datasets and construct a risk model composed by prognostic CAF-associated genes. Then, we evaluated whether the risk score could predict CAF infiltrations and immunotherapy in CRC and confirmed the expression of the risk model in CAFs. Our results showed that CRC patients with high CAF infiltrations and stromal score had worse prognosis than those with low-CAF infiltrations and stromal score. We obtained 88 stromal CAF-associated hub-genes and generated a CAF risk model consisting of ZNF532 and COLEC12. Compared with low-risk group, the overall survival in high-risk group was shorter. The relationship between risk score, ZNF532 and COLEC12, and stromal CAF infiltrations and CAF markers was positive. In addition, the effect of immunotherapy in the high-risk group was not as good as that in the low-risk group. Patients with the high-risk group were enriched in chemokine signaling pathway, cytokine-cytokine receptor interaction, and focal adhesion. Finally, we confirmed that the expressions of ZNF532 and COLEC12 in risk model were widely distributed in fibroblasts of CRC, and the expression levels were higher in fibroblasts than CRC cells. In conclusion, the prognostic CAF signature of ZNF532 and COLEC12 can be applied not only to predict the prognosis of CRC patients but also to evaluate the immunotherapy response in CRC patients, and these findings provide the possibility for further development of individualized treatment for CRC.

1. Introduction

As a common malignant tumor, the risk of colorectal carcinoma (CRC) is related to individual characteristics or habits such as age, history of chronic diseases, and lifestyle [1]. Currently, there are various screening methods for CRC, such as colonoscopy, fecal occult blood test, multitarget stool DNA test, and fecal immunochemical test [2]. Although early screening can improve the curability of CRC, it is necessary to improve the screening methods and accuracy of CRC because of its slow growth and easy to be confused with other cancers [3, 4]. As a consequence, identification new

markers of tumor metastasis are important for improving CRC diagnosis and prognosis.

Tumor microenvironment is the cellular environment in which cancer cells exist, including fibroblasts, immune cells, and extracellular matrix (ECM) [5]. The acquisition and maintenance of tumor markers depend on the role of tumor microenvironment to varying degrees. There are a large number of tumor-associated fibroblasts in the tumor microenvironment, which actively participate in cancer progression through complex interactions with other cell types [6]. Clinically, cancer-associated fibroblast (CAF) markers are associated with poor prognosis in many types of cancer
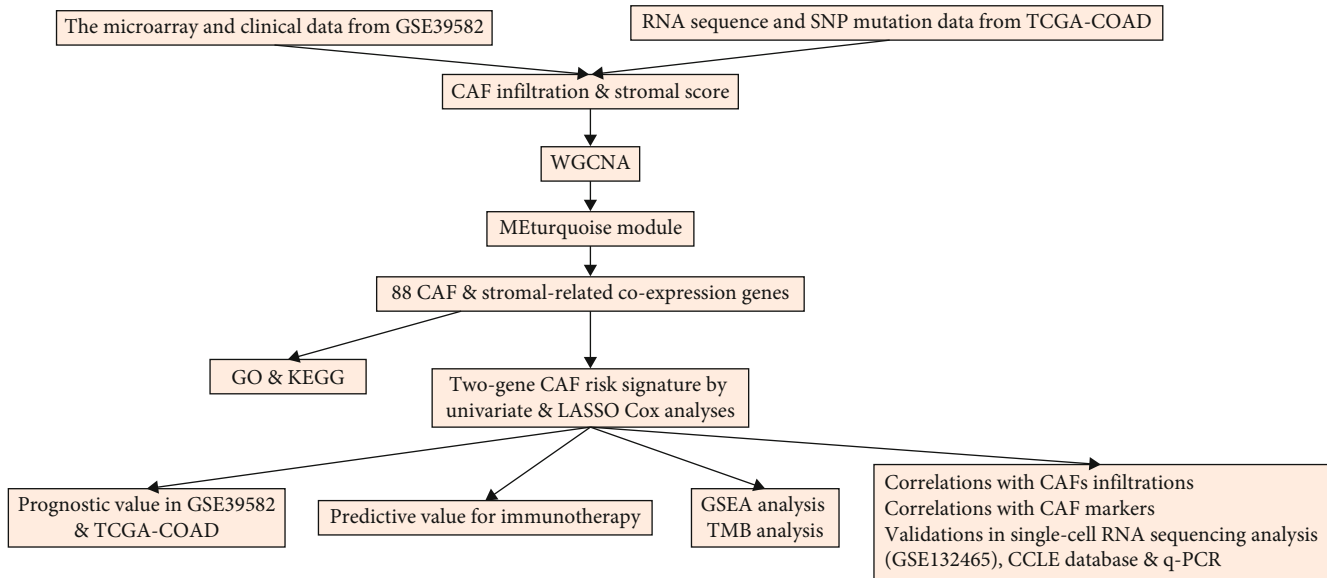
Figure 1: The schematic diagram of the workflow.

[7]. Researchers have identified the heterogeneity of CAFs in breast cancer by single-cell RNA sequencing, and the identification of CAF-specific markers provides support for the development of drugs targeting CAFs [8]. Nowadays, CAF-derived key genes have diagnostic efficacy for gastric cancer [9]. Factors secreted by CAFs can promote the progression of CRC [10]. However, whether stromal CAF-related gene expression signatures could predict clinical outcomes of CRC remains unknown.

Herein, we collected stromal CAF-related factors datasets from the Gene Expression Omnibus (GEO) and The Cancer Genome Atlas (TCGA) databases. Next, we performed weighted gene coexpression network analysis (WGCNA) for identifying the hub-genes of stromal CAFs and construct a risk model composed ZNF532 and COLEC12 by univariate and the least absolute shrinkage and selection operator (LASSO) Cox regression to predict CRC prognosis and treatment effects. Our results offer new markers and therapeutic approaches for the diagnosis and prognosis of CRC.

2. Materials and Methods

2.1. Data Acquisition and Preprocessing.
The microarray and clinical data were obtained from GEO database (GSE39582, 566 tumor samples). The RNA sequence and single-nucleotide polymorphism (SNP) mutation data were obtained from TCGA COAD database (TCGA-COAD, 476 tumor samples). We picked GSE39582 as the training cohort, and TCGA-COAD was chosen for validation cohort. Additionally, the single-cell RNA sequencing data was obtained from GSE132465 from the GEO database.

2.2. CAF and Stromal Score Calculation, Survival Analysis.
According to other reports [11–14], "EPIC," "MCPcounter" and "xCell" R packages, and "TIDE" algorithm (http://tide.dfci.harvard.edu/) were applied to evaluate CAF abundances in tumor samples. The "estimate" package was

utilized to evaluate the stromal score. Survival analysis of tumor patients was using "survminer" R package based on CAF and stromal scores.

2.3. WGCNA.
According to previous report [9], the weighted coexpression analysis was performed using the "WGCNA" package to analyze the coexpression modules associated with CAF and stroma. The hub-genes were selected from the most relevant modules according to the threshold criteria (module membership > 0.8 and gene significance > 0.4) (Figure S1A and B).

2.4. Functional Enrichment Analysis of Hub-Genes.
The "clusterProfiler" package was utilized to analyze functional enrichment information of hub-genes. The graphics were drawn using "enrichplot" package.

2.5. Risk Model Construction and Validation.
Univariate Cox analysis was utilized to identify prognostic genes. Next, the risk model was built by LASSO Cox regression analysis. Then, the patient's risk score was calculated. The "survminer" R package was utilized to analyze the survival outcomes of different risk groups.

2.6. Association Analysis between Risk Score and CAF Score.
The Cor function was utilized to calculate the correlation between risk score and CAF score, and the "GGally" package was utilized to analyze the pairwise correlation map. The "Pheatmap" package was utilized to analyze the cluster maps of risk genes and CAF known marker genes. The Cor function was utilized to calculate the relationship between risk genes, risk scores, and CAF marker genes.

2.7. Immunotherapy Prediction.
The effect of each sample tumor immunotherapy was predicted by the TIDE algorithm. The pROC package was utilized to identify the accuracy of the model's predictions.

(a)

(b)

FIGURE 2: Continued.

(c)
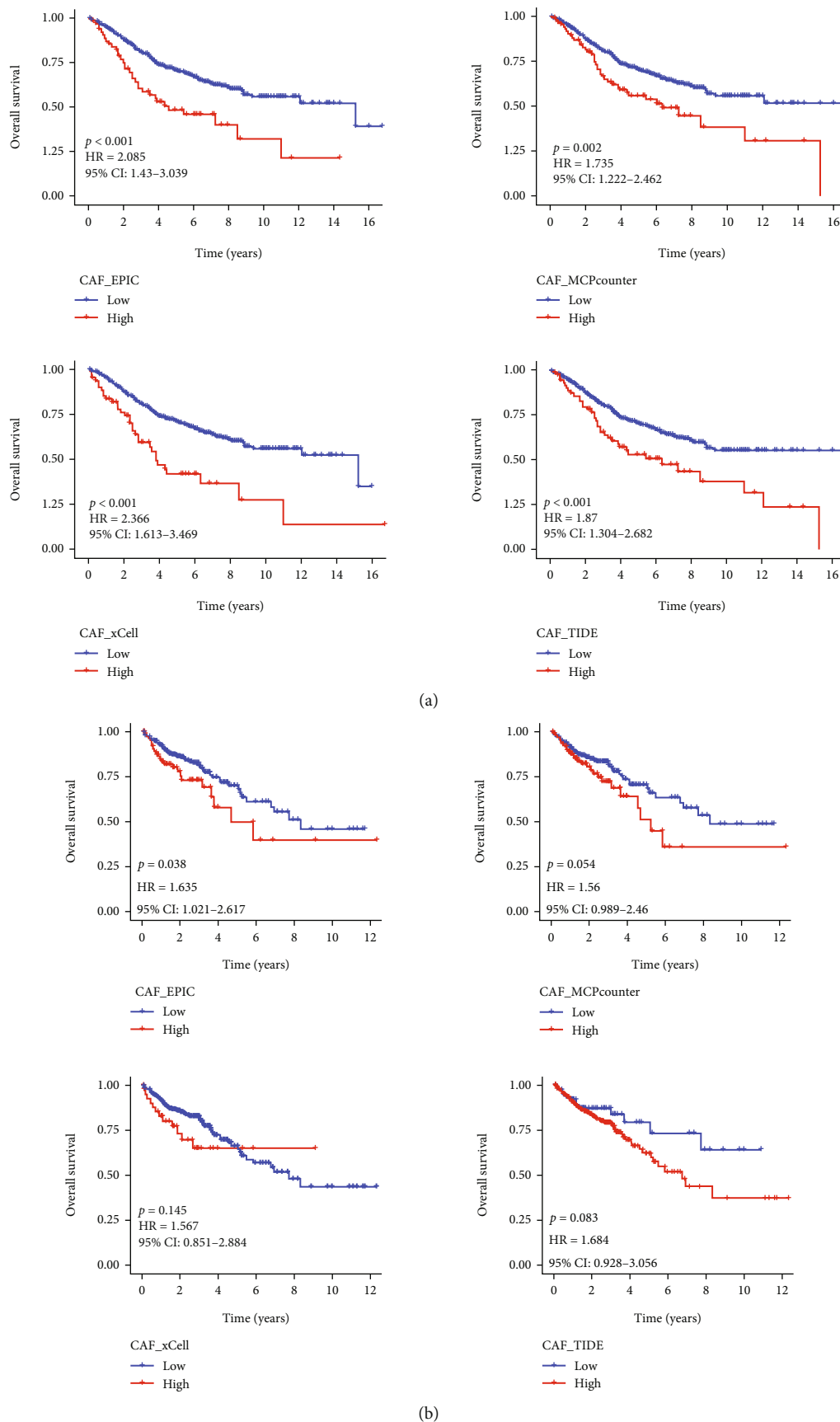
(d)
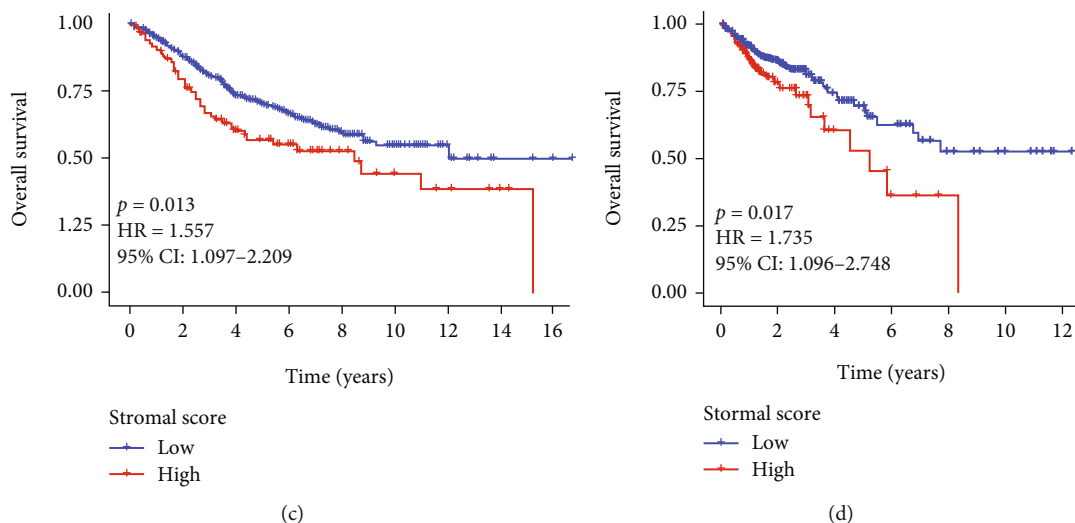
FIGURE 2: High CAF and stromal scores in CRC had a bad prognosis. High CAF immune infiltration level was associated with poor prognosis in GSE39582 (a) and TCGA-COAD (b) cohorts. High stromal score was associated with poor prognosis in GSE39582 (c) and TCGA-COAD (d) cohorts.

2.8. Gene Set Enrichment Analysis (GSEA). The GSEA was utilized to analyze the pathways enriched in different risk groups by the "clusterProfiler" package.

2.9. SNP Analysis. The "Maftools" package was applied to analyze high- and low-risk mutant genes, mutation types, and maps waterfalls and then compare whether there was a difference in tumor mutation burden (TMB) between the high- and low-risk groups.

2.10. Single-Cell RNA Sequencing Analysis. In this study, the CRC single-cell sequencing dataset was obtained from the GEO database (GSE132465, 10 normal samples and 23 tumor samples). The effect of cell cycle on subsequent results was removed using the SCTransform function. A standardized "SCT" method was used to integrate different samples to eliminate batch effects. Cells were reduced in dimension by principal component analysis (PCA), and then, cell clustering was displayed by uniform manifold approximation and projection (UMAP) method. Cells were then annotated by BlueprintEncodeData dataset and known cell markers in the singleR and celldex packages. The gene set variation analysis (GSVA) R package was used to assess potential changes in pathway activity in each CAF subcluster.

2.11. Validation of ZNF532 and COLEC12 Expression on CAFs. The mRNA expressions of the Cancer Cell Line Encyclopedia (CCLE) database were used to analyze the expression of ZNF532 and COLEC12 in fibroblasts and CRC cells. Human colorectal fibroblast CCD-18-co was purchased from ATCC (Manassas, UAS), and SW480 cells were provided by the Shanghai Academy of Biological Sciences. Cells were cultured in DMEM medium with 10% fetal bovine serum. Total RNA was extracted by TRIzol reagent (Invitrogen, USA). Then, cDNA was prepared using the PrimeScript RT kit (Takara, Nanjing, China). AceQ Universal SYBR qPCR Master Mix (Vazyme, Nanjing, China)

was used on an ABI StepOnePlus™ real-time quantitative PCR (q-PCR) instrument (Applied Biosystems, CA, USA) for q-PCR. Primer information was given in Table S1. GAPDH was the internal parameters of q-PCR.

2.12. Statistical Analysis. The overall survival (OS) of high- and low-risk groups was displayed by Kaplan–Meier curves. GraphPad Prism 8.0 was performed for statistical analyses. Student's *t*-test was used for comparison between two groups. Statistical significance was regarded as *p* values < 0.05.

3. Results

3.1. Higher CAF Infiltrations and Stromal Scores Had Poor OS in Patients with CRC. Figure 1 displayed the work chart of our study. We used the EPIC, MCP-counter, xCell, and TIDE methods to evaluate the infiltration of CAFs in tumor microenvironment, and the stromal score was a displayed estimate algorithm. Subsequently, the prognostic values of CAFs on CRC were predicted by Kaplan-Meier curves. As depicted in Figure 2(a), high CAF infiltrations had a shorter OS in patients with CRC in GSE39582 cohort compared with low CAF infiltrations. Similar results were obtained in TCGA-COAD (Figure 2(b)). Additionally, the prognosis of CRC patients with high stromal score was bad both in GSE39582 and TCGA-COAD cohorts (Figures 2(c) and 2(d)). Collectively, the above information highlighted the importance of the relationship between CAF infiltration and CRC prognosis.

3.2. WGCNA Analysis Performed for Identifying the Hub-Genes of CAFs. To filtrate the key genes related to stromal CAFs, we performed WGCNA analysis. We used the soft threshold power of 5 in GSE39582 (Figure 3(a)) and 6 in TCGA-COAD (Figure 3(b)) to construct a scale-free topology network. For GSE39582, 17 coexpression models were clustered by hierarchical clustering tree (Figure 3(c)), and

(a)

(b)

(c)

(d)

(e)

(f)

(g)
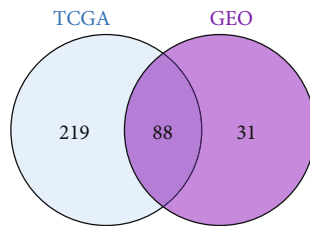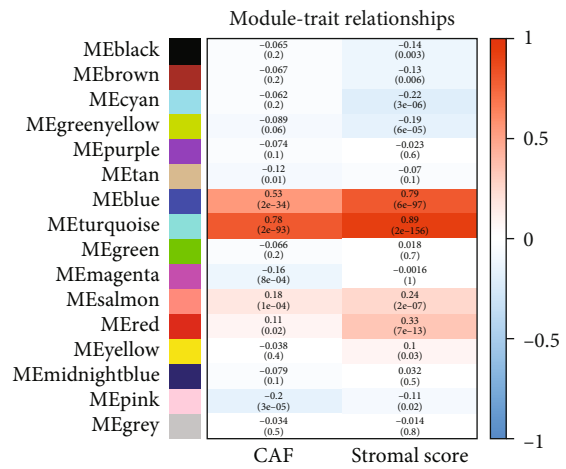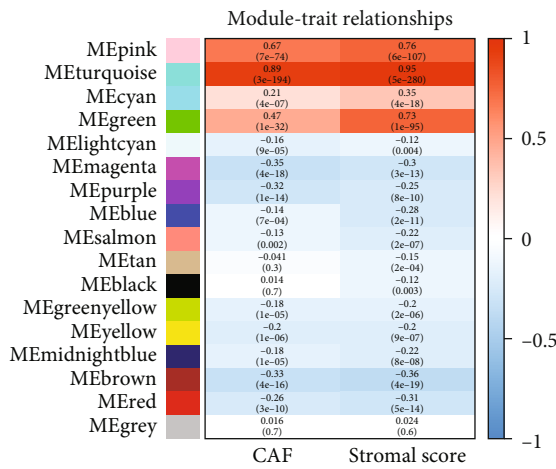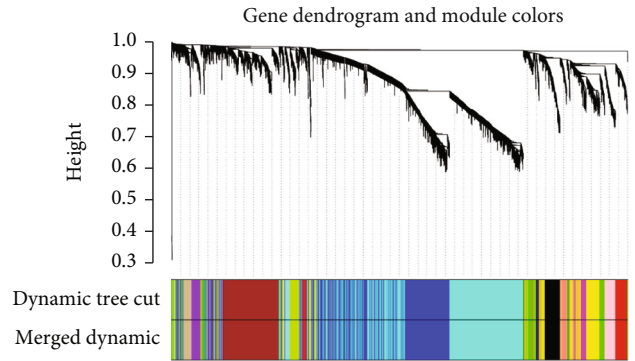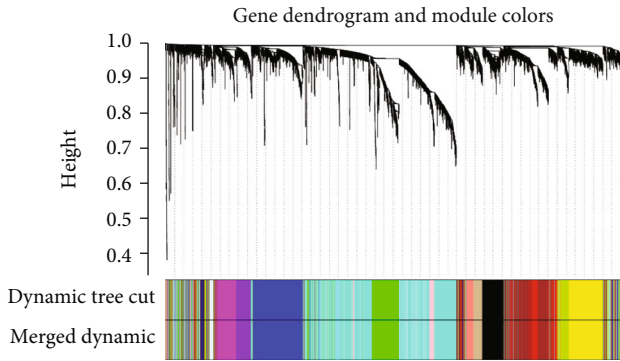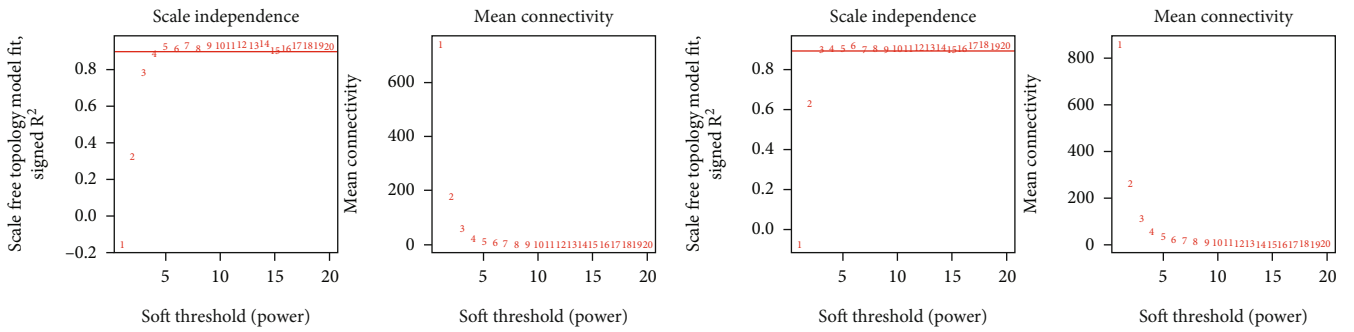
FIGURE 3: Continued.
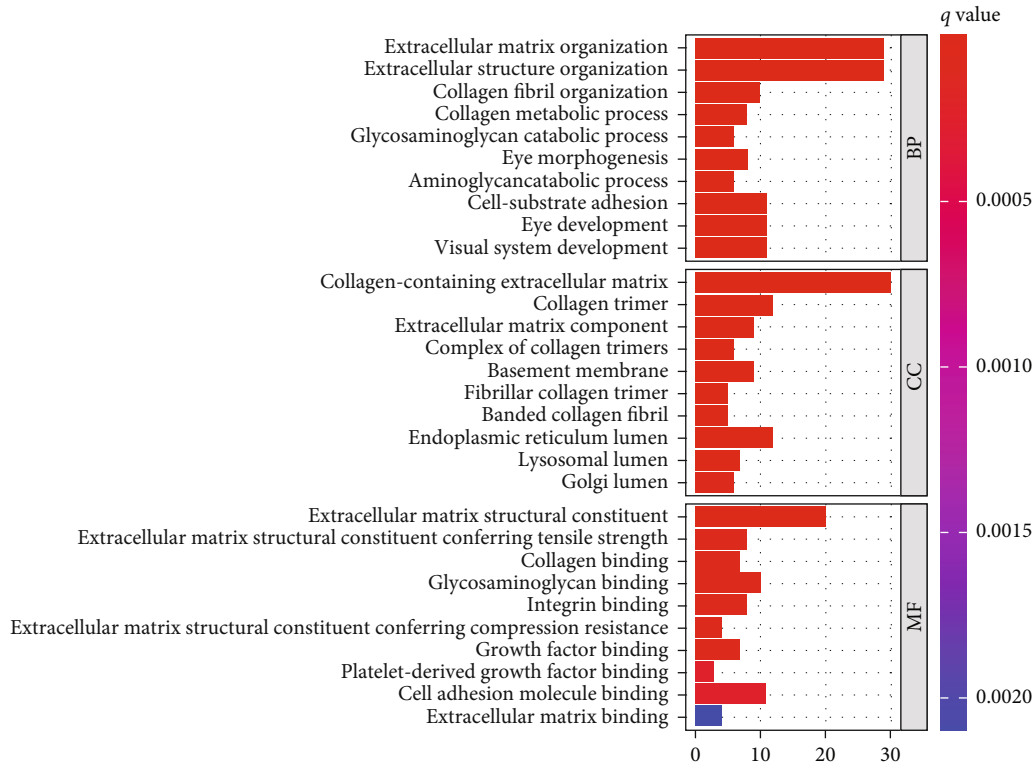
(h)
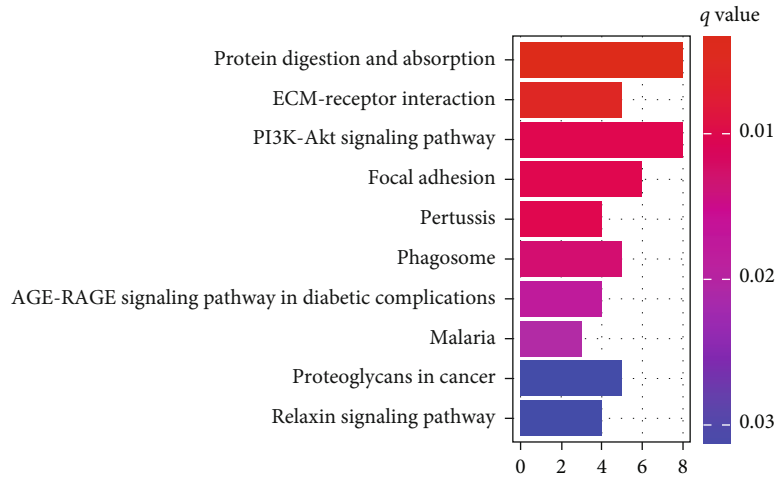
(i)

Figure 3: WGCNA was used to explore stromal CAF-related hub-genes and perform functional enrichment analysis. The soft-thresholding power in GSE39582 (a) and TCGA-COAD (b) cohorts. Clustering dendrograms exhibiting hub-genes with alike expression profiles were converged into coexpression modules in GSE39582 (c) and TCGA-COAD (d) cohorts. MEturquoise module was most closely connected with the CAF proportion and stromal score in GSE39582 (e) and TCGA-COAD (f) cohorts. (g) Venn diagram showed the shared hub-genes in GSE39582 and TCGA-COAD cohorts. (h) GO enrichment analysis of 88 shared hub-genes. (i) KEGG enrichment analysis of 88 shared hub-genes.

the MEturquoise module was significantly positively associated with the CAF proportion (Correlation = 0.89, $p = 3e - 194$) and stromal score (Correlation = 0.95, $p = 5e - 280$) (Figure 3(e)). There were 16 coexpression models in TCGA-COAD (Figure 3(d)), in which the MEturquoise module was positively associated with the CAF propor-

tion (Correlation = 0.78, $p = 2e - 93$) and stromal score (Correlation = 0.89, $p = 2e - 156$) (Figure 3(f)). Thus, a total of 119 and 307 hub-genes, which have the highest correlation with CAF and stromal scores, were screened out in the MEturquoise module of GSE39582 and TCGA-COAD, respectively.

(a)

(b)

FIGURE 4: Continued.

(c)
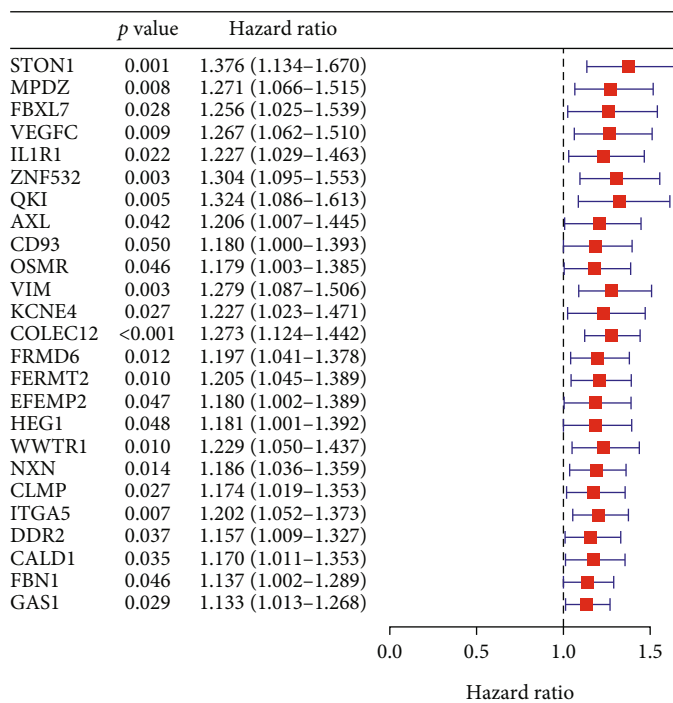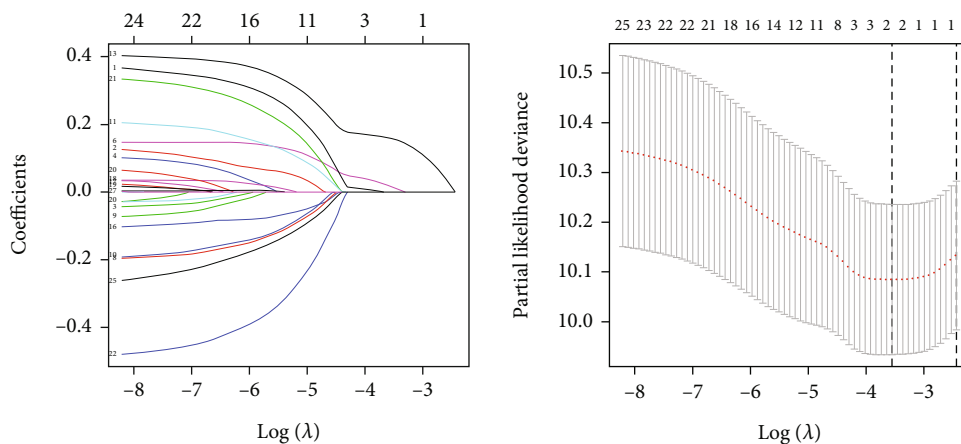
(d)
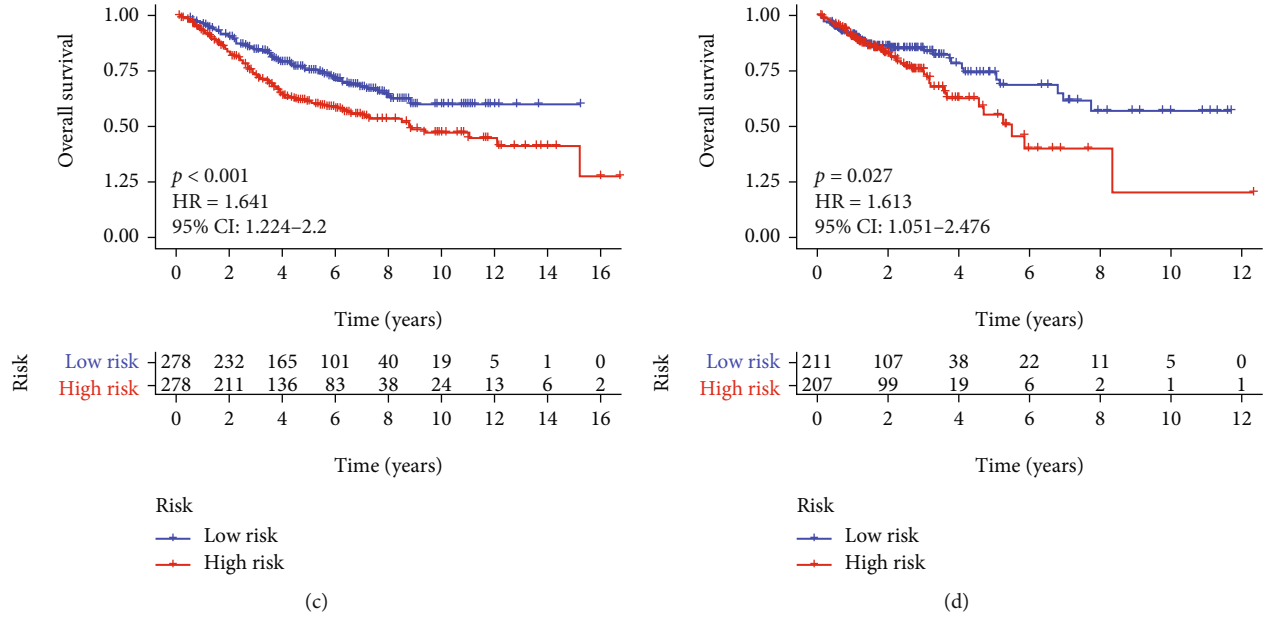
FIGURE 4: Construction of the prognostic model. (a) Univariate Cox analysis. (b) LASSO Cox regression analysis. (c) Survival analysis in GSE39582 cohort. (d) Survival analysis in TCGA-COAD cohort.

3.3. Functional Enrichment Analysis.

Eighty-eight hub-genes were acquired by taking the intersection of 2 hub-gene sets from GSE39582 and TCGA-COAD (Figure 3(g)). Subsequently, we performed functional enrichment analysis of these common hub-genes. Gene Ontology (GO) term analysis demonstrated that "extracellular matrix organization," "collagen-containing extracellular matrix," and "extracellular matrix structural constituent" were the noteworthy terms in biological process (BP), cellular component (CC), and molecular function (MF), respectively (Figure 3(h)). Moreover, Kyoto Encyclopedia of Genes and Genomes (KEGG) pathways exhibited that these common hub-genes were mainly focused on "ECM-receptor interaction" and "PI3K-Akt signaling pathway" (Figure 3(i)). Studies have shown that the ECM acts as a physical barrier that contributes to cancer cell invasion, inhibits the infiltration of antitumor immune cells, and ultimately promotes tumor deterioration and treatment resistance [5, 15]. In addition, the PI3K-Akt signaling pathway promotes tumorigenesis by regulating cell metabolic reprogramming and invasion and metastasis [16]. Together, these results indicated that these hub-genes have a correlation with tumor progression and immune escape.

3.4. Generation of a Stromal CAF-Related Gene (CAFG) Predictive Model.

First, univariate Cox regression analysis was performed to study the relationship between the 88 hub-genes and prognosis and obtained that 25 prognostic hub-genes were finally selected in GSE39582 (Figure 4(a)). Next, LASSO Cox analysis was utilized to generate a risk model with 2 genes (ZNF532 and COLEC12) (Figure 4(b)). Then, we figured the risk score as follows: risk score = expression of ZNF532* 0.017205958 + expression of COLEC 12* 0.158665214. The CRC patients were separated into high- and low-risk groups depending on the median risk

score. The OS of patients in the high-risk group was shorter in the GSE39582 cohort than that of low-risk group ($p < 0.001$; Figure 4(c)). This is equally true of TCGA-COAD cohort ($p = 0.027$; Figure 4(d)). These results suggested that the signature of stromal CAFGs was as prognostic marker in CRC.

3.5. Stromal CAFGs Have a Strong Correlation with CAF Infiltrations and CAF Markers.

To further verify whether our CAF model could predict CAF infiltration, we performed Spearman's correlation analyses. As depicted in Figure 5(a), the risk score was significantly positively associated with the CAF infiltrations and stromal score in GSE39582 cohort, which was similar to those in TCGA-COAD cohort (Figure 5(b)). Meanwhile, the expressions of CAF markers in high-risk group were increased comparing to low-risk group both in GSE39582 (Figure 5(c)) and TCGA-COAD (Figure 5(d)) cohorts. Furthermore, all CAF markers were positively associated with the risk core, ZNF532, and COLEC12 in GSE39582 ($p < 0.001$; Figure 5(e)), as well as in TCGA-COAD cohort ($p < 0.001$; Figure 5(f)). Overall, the predictive model composed of ZNF532 and COLEC12 may predict the state of CAF infiltrations in tumor microenvironment.

3.6. The Relationship between Risk Score and Immunotherapy.

Due to the complexity of tumor immune microenvironment, the effect of immunotherapy in CRC patients is relatively poor [17]. Therefore, we further evaluated whether the risk score could be used as a predictor of immunotherapy in CRC patients. For GSE84437, the high-risk group (28%) was less sensitive to immunotherapy than low-risk group (69%) ($p < 0.001$; Figure 6(a)); compared with low-risk group, the CAF score was elevated in the high-risk group (Figure 6(b)); the area under curve (AUC) value of rick score was 0.770

(a)

(b)

(c)

(d)

(e)

(f)
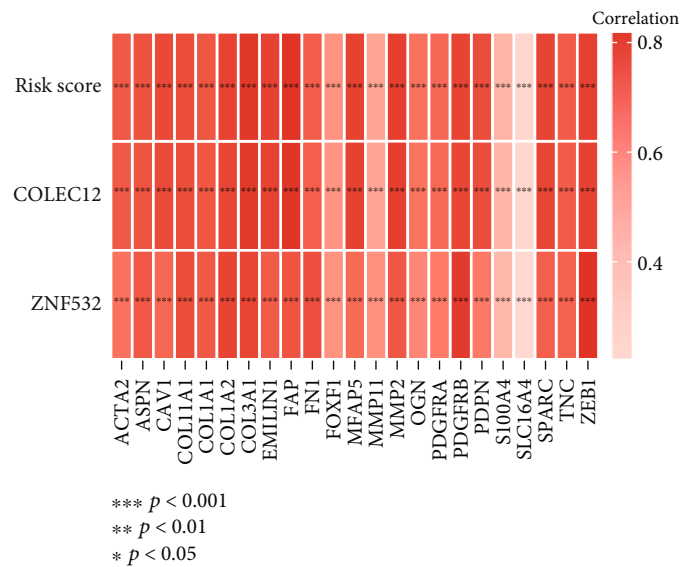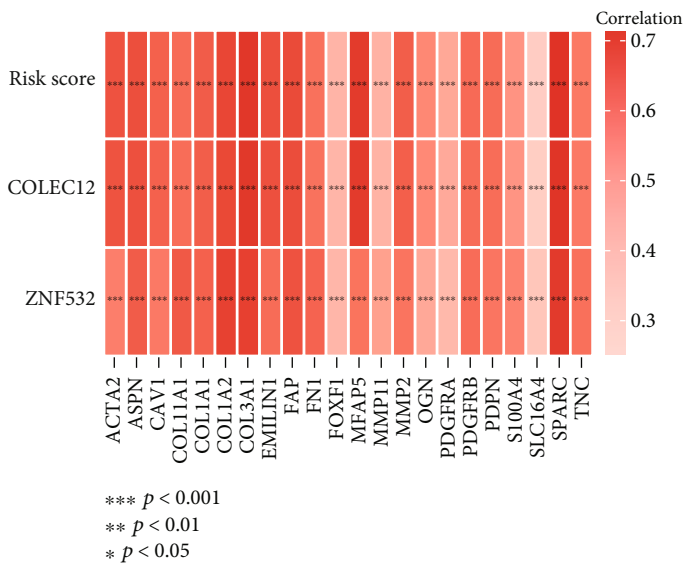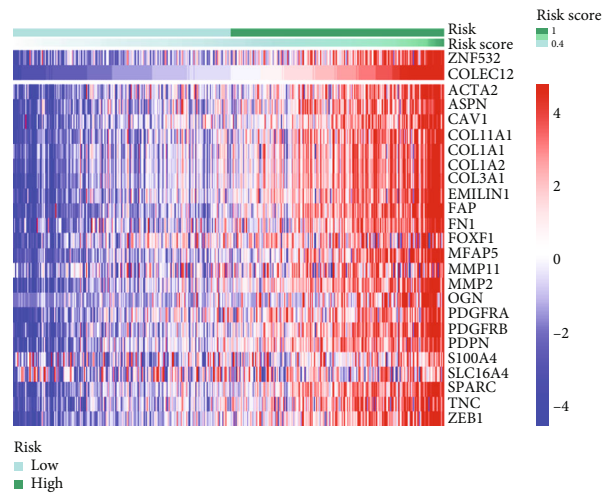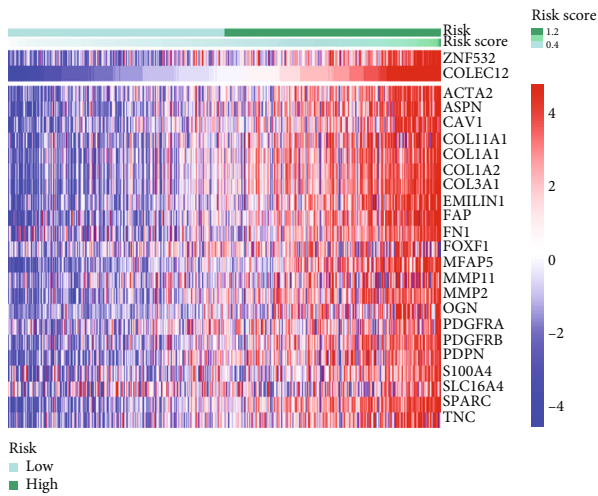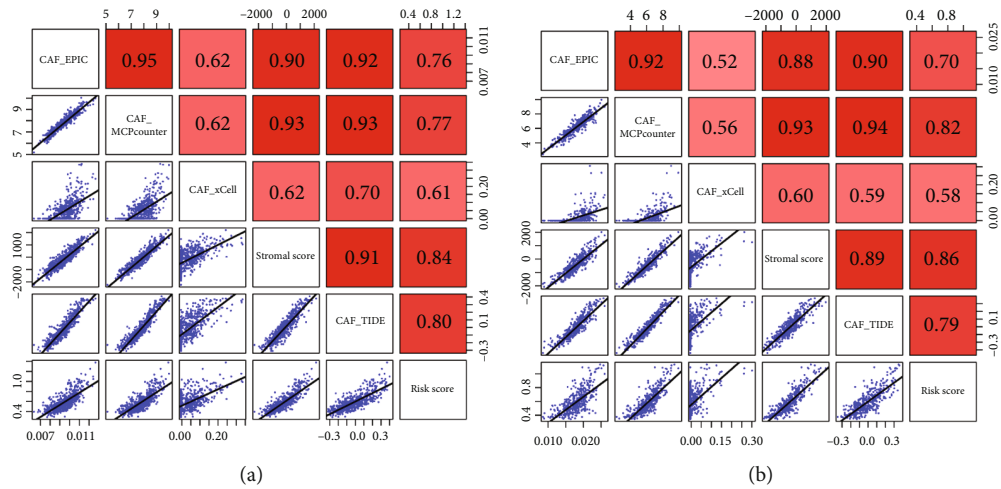
FIGURE 5: Risk score was positively connected with CAF infiltrations and CAF markers. Risk score was positively associated with CAF abundances in GSE39582 (a) and TCGA-COAD (b) cohorts. CAF markers, ZNF532 and COLEC12, were highly expressed in high-risk group, both in GSE39582 (c) and TCGA-COAD (d) cohorts. CAF markers were positively connected with risk score, ZNF532, and COLEC12 in GSE39582 (e) and TCGA-COAD (f) cohorts.

(a)   (b)   (c)

(d)   (e)   (f)
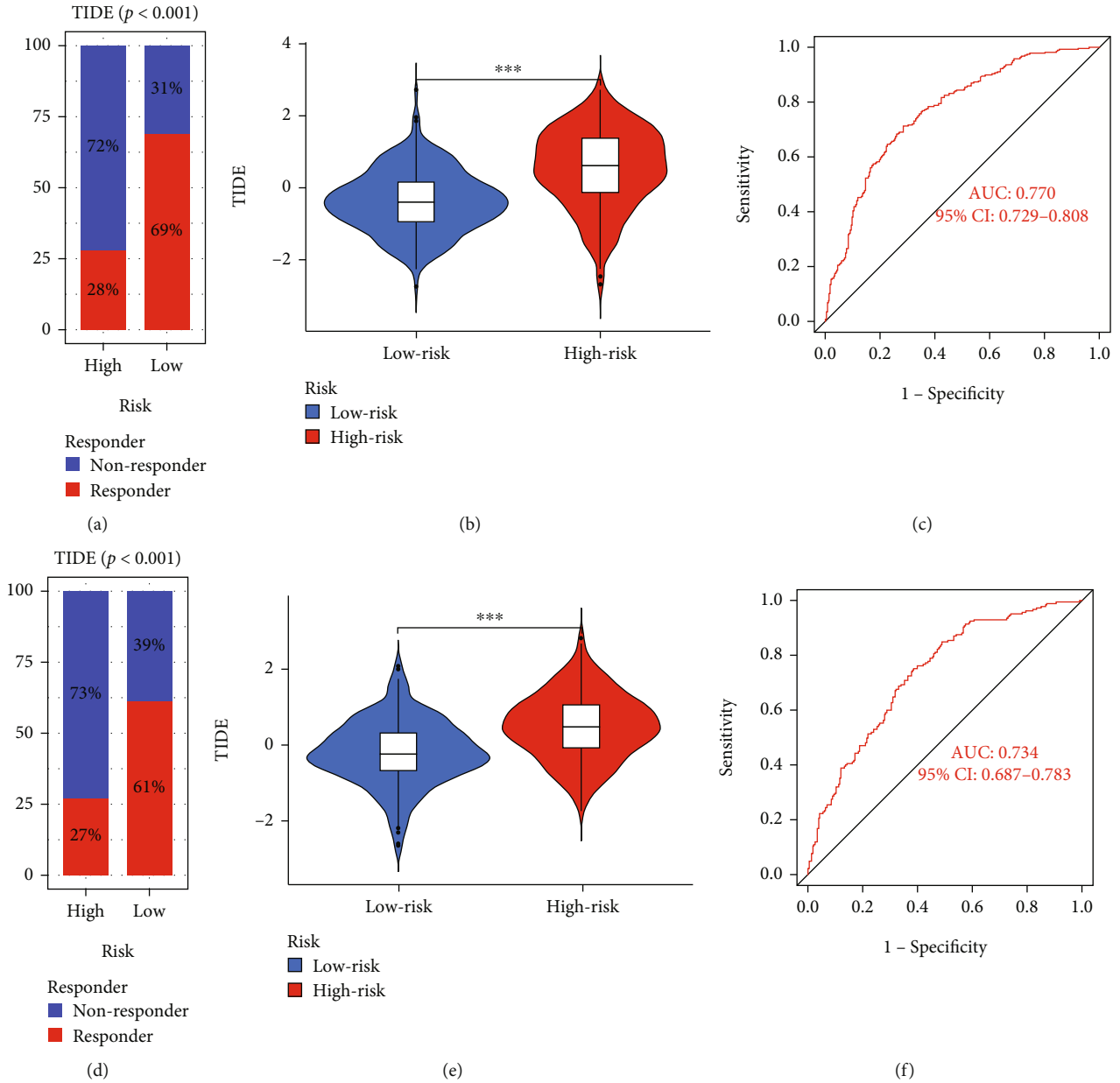
FIGURE 6: Multidimensional validation for risk score. Comparison of the effect of immunotherapy between the high- and low-risk groups in GSE39582 (a) and TCGA-COAD (d) cohorts. Comparison of the TIDE level between the high-and low-risk groups in GSE39582 (b) and TCGA-COAD (e) cohorts. Receiver-operating characteristic curves of the risk score in forecasting treatment effects in GSE39582 (c) and TCGA-COAD (f) cohorts.

(95% CI: 0.729–0.808) (Figure 6(c)). For TCGA-COAD, these results were the same as for GEO (Figures 6(d)–6(f)). Briefly, our prognostic model has predictive power for immunotherapy of CRC.

3.7. GSEA Enrichment Analysis. As shown in Figure 7(a), the high-risk group was mainly focused on cytokine-cytokine receptor interaction, chemokine signaling pathway, and focal adhesion. The low-risk group was mainly focused on aminoacyl tRNA biosynthesis, DNA replication, and retinol metabolism (Figure 7(b)).

3.8. Correlation between Risk Score and TMB. The waterfall plots have displayed top 20 genes with the highest mutational frequencies in the high- (Figure 8(a)) and low-risk (Figure 8(b)) groups, respectively. Surprisingly, these continual mutational genes were shared in the two risk groups. Besides, the risk score has a positive correlation with the TMB value (correlation = 0.13, $p = 0.0098$, Figure 8(c)). Meanwhile, the TMB values were upregulated in the high-risk group compared with low-risk group ($p = 0.0045$; Figure 8(d)). Thus, patients in the high-risk group may benefit more from immune microenvironment with high TMB.

(a)

(b)
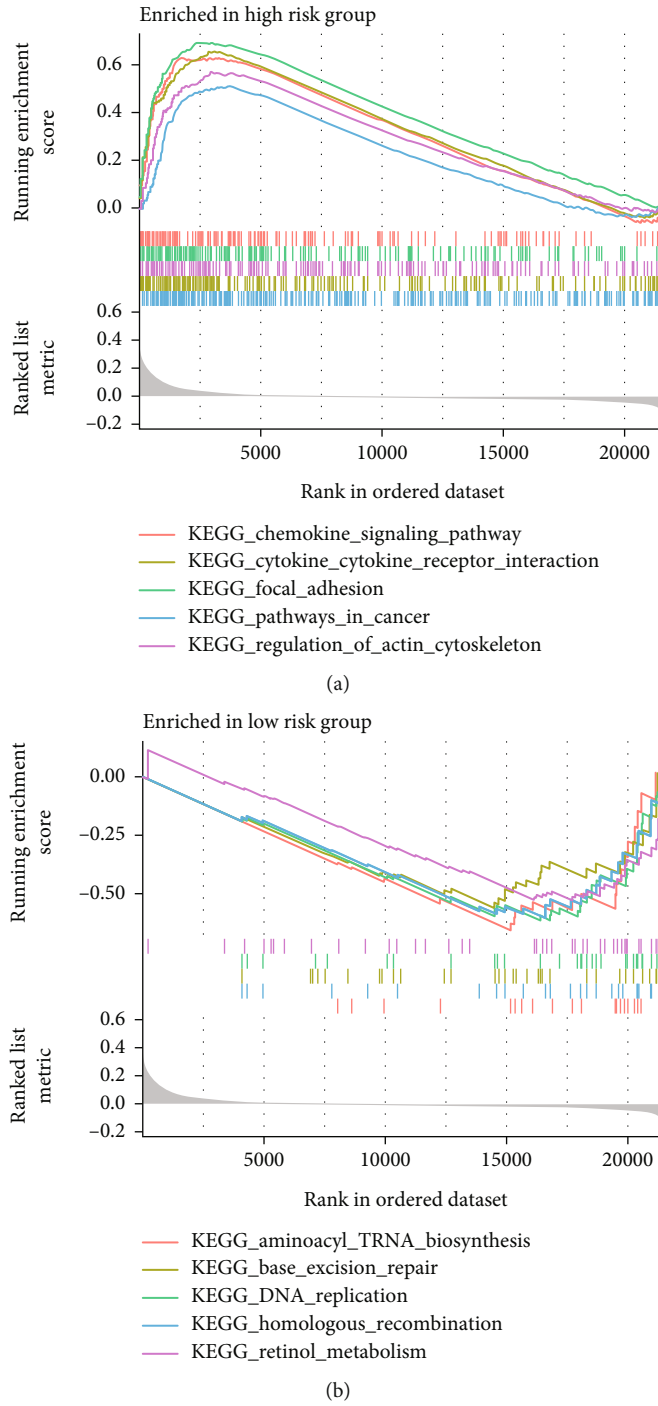
Figure 7: GSEA showing possible associations between high- (a) and low-risk (b) groups and disease phenotypes.

3.9. ZNF532 and COLEC12 Identified in Single-Cell Gene Expression Patterns of Fibroblasts. To describe the expression of ZNF532 and COLEC12 at fibroblasts, we collected single-cell RNA sequencing data from patients with CRC. After preliminary quality control confirmation, 62,716 cells can be used for subsequent analysis. As shown in Figure 9(a), there were 23 kinds of cell clusters in CRC patients, which were mainly divided into B cells, CD4+/8 + T cells, dendritic cells (DC), fibroblasts, mast cells, endothelial cells,

macrophages, epithelial cells, monocytes, and plasma cells (Figure 9(b)), according to the expression level of marker genes (Figure S2). Not surprisingly, ZNF532 and COLEC12 were highly expressed in fibroblasts (Figure 9(c)). In addition, ZNF532 was distributed in endothelial cells, while COLEC12 also belonged to macrophage, speculating CAF signature affecting tumor progression by regulating tumor matrix formation and immune infiltration of CRC. Next, we explored the expression of ZNF532 and COLEC12

(a)

(b)

Figure 8: Continued.

(c)
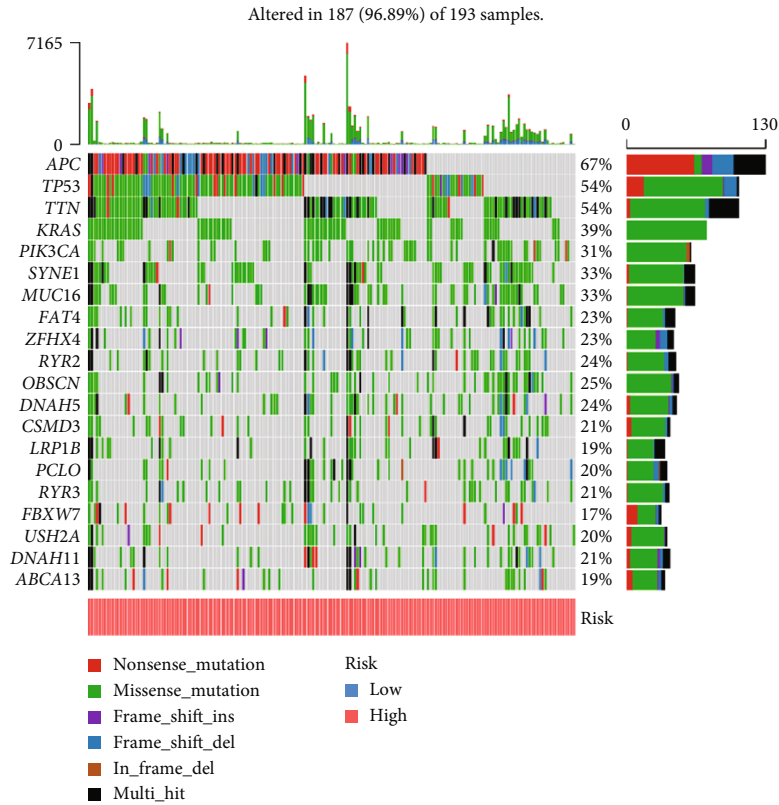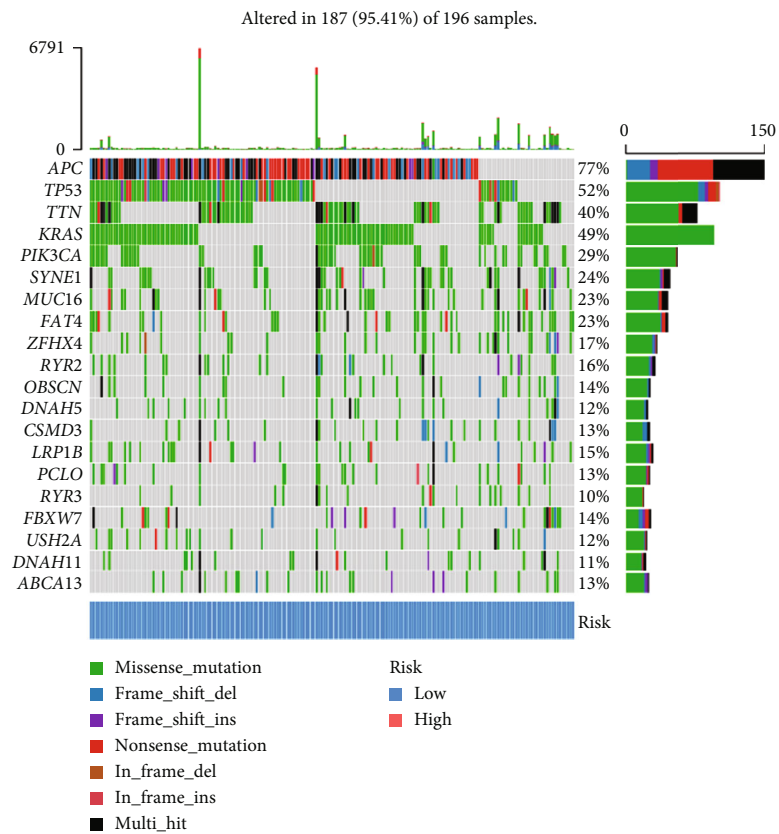
(d)
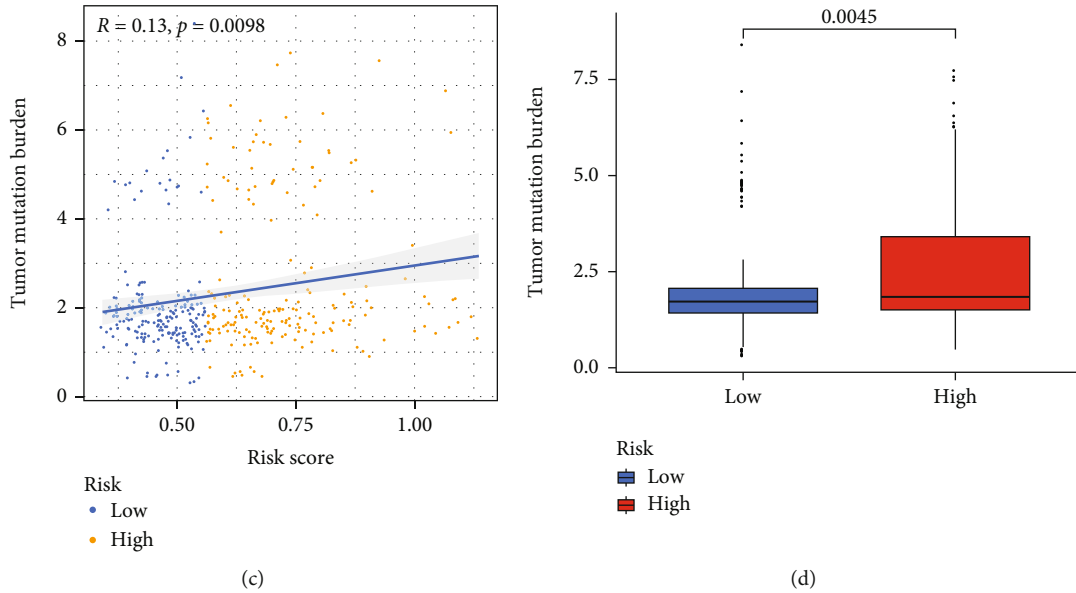
FIGURE 8: SNP analysis. The top 20 mutational genes in high- (a) and low-risk (b) groups. (c) Analysis of correlation between TMB and the risk groups. (d) Comparison of TMB value between the high- and low-risk groups.

in fibroblast subpopulations. There were 8 subpopulations of fibroblasts (Figure 9(d)), including cluster 0 (high expressed genes: CTHRC1 and COL1A1), cluster 1 (CCL13), cluster 2 (MGP), cluster 3 (NDUFA4L2), cluster 4 (PLP1), cluster 5 (FRZB), cluster 6 (TK1), and cluster 7 (ACTG2) (Figure 9(e)). GSVA analysis showed that clusters 5 and 6 were mainly enriched in pathways regulating the tumor microenvironment, such as oxidative phosphorylation, TNF-α signaling via NF-Kβ, and endothelial-mesenchymal transition (Figure 9(f)). Furthermore, ZNF532 was mainly distributed in cluster 6, and COLEC12 was mainly distributed in cluster 5 (Figure 9(g)), which that suggested cluster 6 and cluster 5 in fibroblasts were mainly involved in tumor progression and immunotherapy of CRC.

3.10. Validation of ZNF532 and COLEC12 in Fibroblasts and CRC Cells. Both ZNF532 and COLEC12 were highly expressed in fibroblasts compared to large intestine (Figures 10(a) and 10(b)). To further validate this result, we performed q-PCR validation. Consistently, the mRNA expressions of ZNF532 and COLEC12 were highly expressed in fibroblasts than those in CRC cell line (SW480) (Figure 10(c)). These results indicated that ZNF532 and COLEC12 might be CAF-specific markers.

4. Discussion

CRC, as the third cancer incidence rate in worldwide, has yet to be successfully and completely treated with multiple therapeutic options [18, 19]. In the tumor microenvironment, CAFs were the most abundant stromal cells, which regulated the malignant progression and immunotherapy resistance of CRC by secreting cytokines to control cell proliferation and ECM deposition and remodeling [15, 20]. However, limited studies have investigated the function of stromal CAF-

related factors on CRC. Here, we found that high levels of CAF and stromal score lead to poor prognosis in CRC. Subsequently, we generated a prognostic CAF model including 2 genes (ZNF532 and COLEC12). Patients in the high-risk group in this model had shorter OS, low sensitivity to immunotherapy, and high levels of TMB. Besides, the risk genes were high expressed in fibroblasts.

CAFs are the major cellular component of desmoplastic stroma characteristic that contribute to tumor progression and immune escape [21]. Consistently, we confirmed that higher CAF and stroma scores were interrelated with worse prognosis in CRC. However, whether CAFGs could be as novel treatment targets in CRC is still unknown. Studies have reported that risk signature composed CAF-secreted cytokines can predict the clinical prognosis of breast cancer patients [22]. CAF-related genes had great and prognostic value for hepatocellular carcinoma prognosis [23]. Consistently, we constructed a CAFG prognostic model of CRC by applying WGCNA and univariate and LASSO Cox regression methods. Based the risk score of each patient, CRC patients with high-risk scores had OS survival than CRC patients with low-risk scores. The signature of high CAF score with poor OS can be used to predict the prognosis of patients with gastric cancer [9]. In view of this, our CAF model had good value for applying to predict CRC prognostic.

In addition to the interaction between CAF and cancer cells, the intricate crosstalk between CAFs and tumor immune microenvironment (TIME) is also the key to promote tumor progression [24]. Infiltrated CAFs interact with other immune cells in TIME to promote the formation of immunosuppressive tumor microenvironment, thereby allowing cancer cells to evade the surveillance of the immune system [25]. In the risk model, CAF abundances in tumor microenvironment were positively connected with the risk score and the levels of ZNF532 and COLEC12. Besides,

(a)

(b)

(c)

(d)

(e)
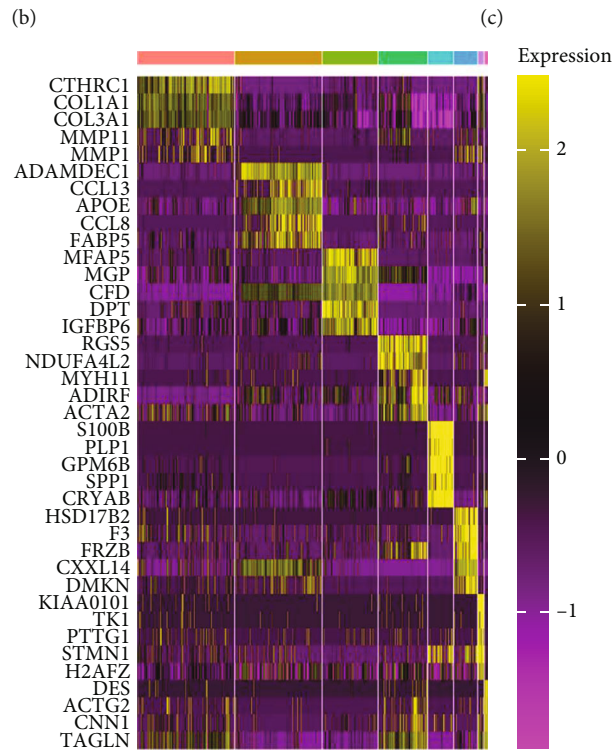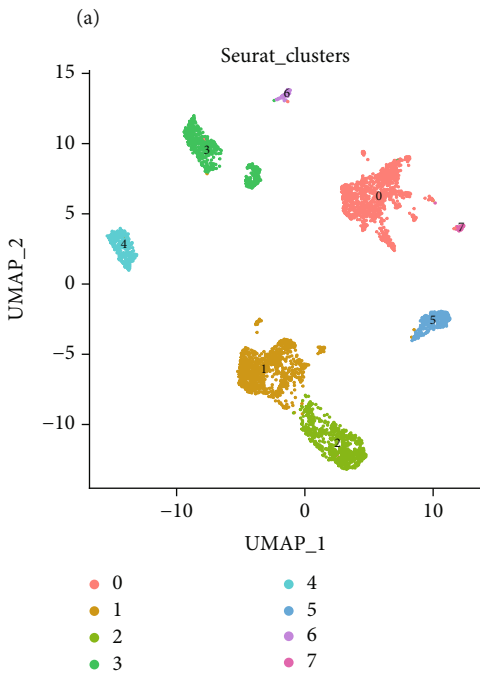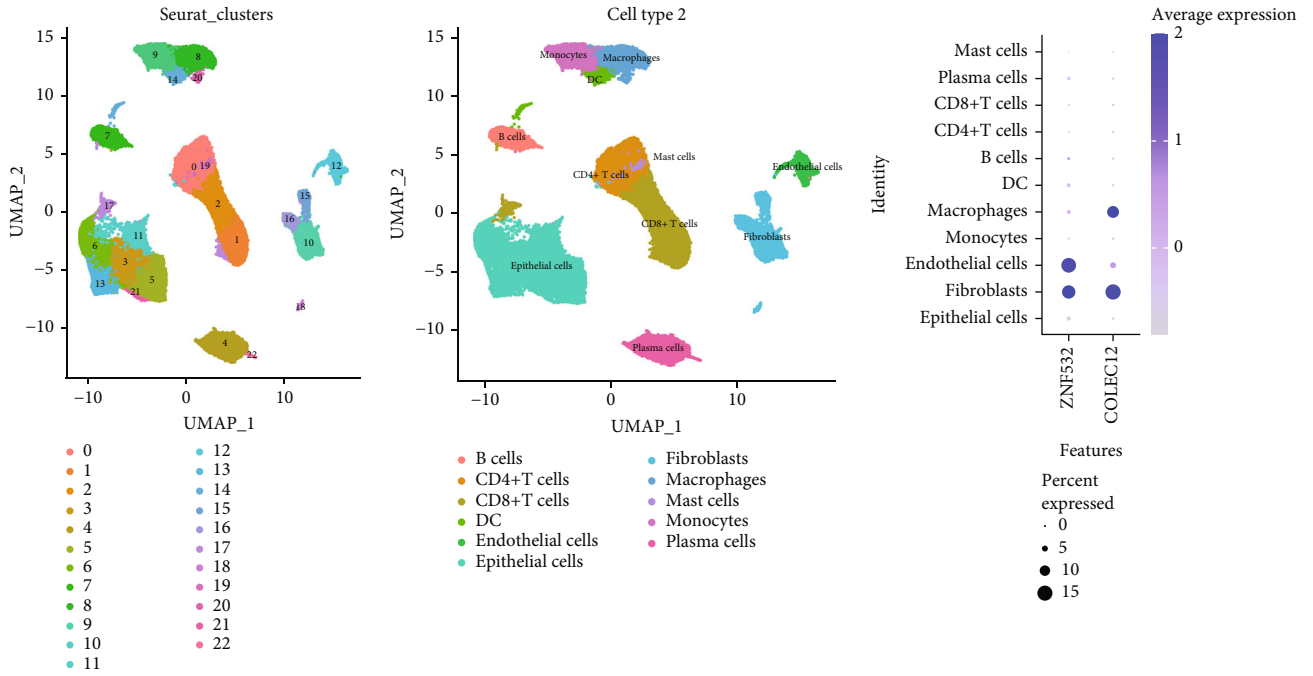
Figure 9: Continued.
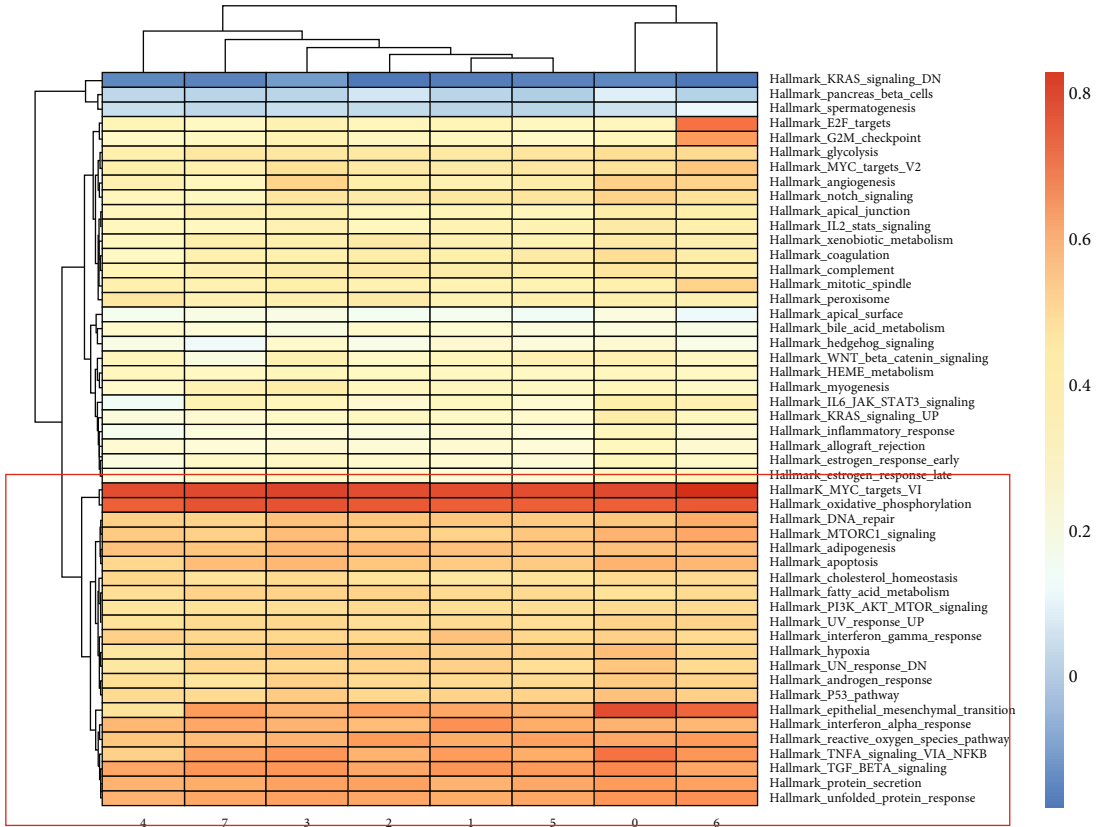
(f)
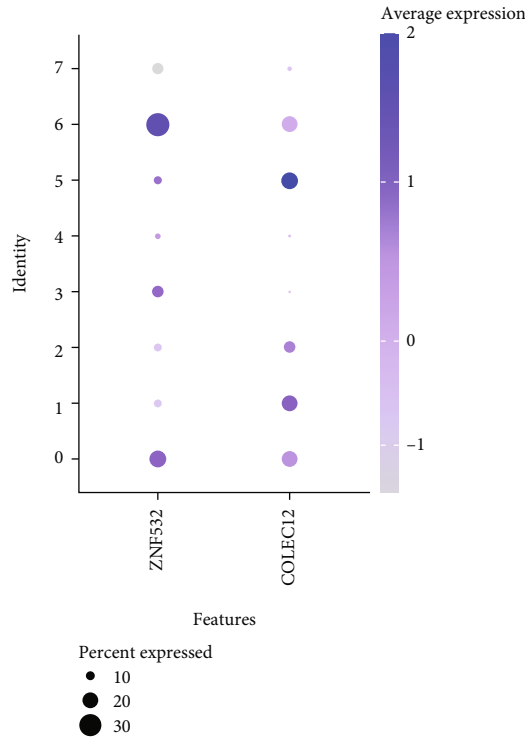
(g)

FIGURE 9: Single-cell RNA sequencing analysis of CRC. UMAP map of cell clusters (a) and types (b). (c) Distribution of ZNF532 and COLEC12 in each cell type. (d) Fibroblasts were divided into 8 subpopulations. (e) The expression of top 5 genes in each fibroblast subpopulation. (f) GSVA analysis of fibroblast subpopulations. (g) Distribution of ZNF532 and COLEC12 in each fibroblast subpopulation.

(a)

(b)

(c)
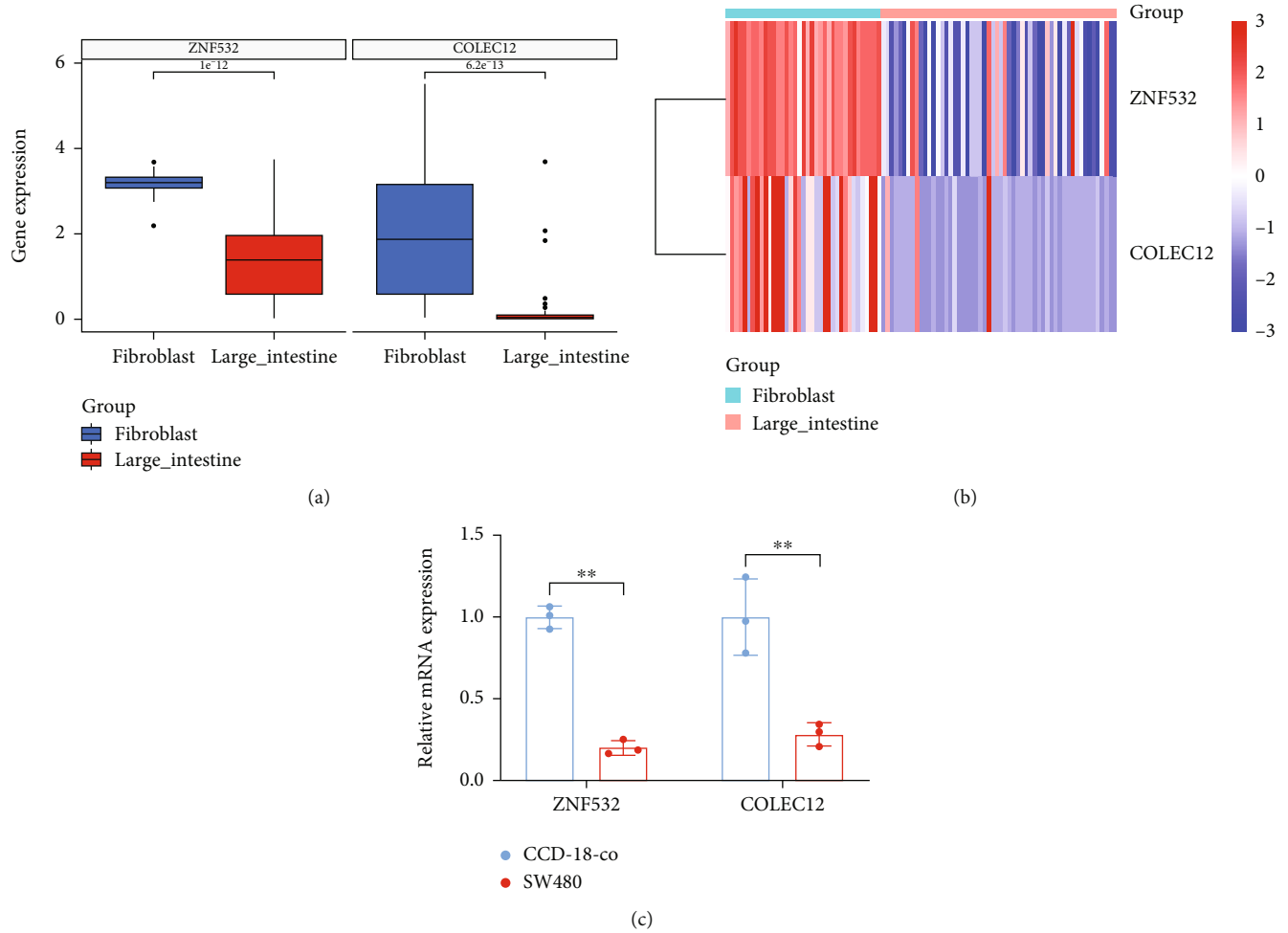
FIGURE 10: Multidimensional expression validation. The levels of ZNF532 and COLEC12 in the fibroblasts and large intestine were compared by Wilcoxon analysis (a) and exhibited in the heat map (b). (c) q-PCR was applied to verify the expression of ZNF532 and COLEC12 in fibroblasts and SW480. $^{**}p < 0.01$.

patients with high-risk scores had lower sensitivity to immunotherapy than patients with low-risk scores. Referring to other similar studies, this means that our CAF risk score has an important predictive effect on immune infiltration of CAF and may regulate the formation of immunosuppressive tumor microenvironment [26]. Meanwhile, the levels of ZNF532 and COLEC12 were increased in fibroblasts compared to CRC cells. These results indicated that ZNF532 and COLEC12 can be CAF-specific markers for CRC, and the CAF risk model can evaluate the level of CAF infiltration in tumor microenvironment.

With respect to ZNF532 and COLEC12 in the model, elevated expression of COLEC12 had a worse prognostic outcome and increased inflammation in osteosarcoma [27]. Moreover, COLEC12 as a cancer stemness-related signature could predict colon adenocarcinoma prognosis [28]. At an epithelial cellular level, activation of ZNF532 could promote the epithelial-to-mesenchymal transition in laryngeal squamous cell carcinoma cells [29]. We observed that COLEC12 and ZNF532 were highly expressed in macrophages and endothelial cells, respectively, which was consistent with the findings that

COLEC12 expression was correlated with immune-related molecules [30], and ZNF532 altered the biological activity of endothelial cells [31]. However, their function in CAFs of CRC remains unclear, so further studies of the mechanisms of these CAF markers are needed to explore the progression, resistance, and immunosuppression of CRC.

5. Conclusion

In conclusion, higher infiltration of stromal CAFs in tumor microenvironment was associated with poor prognosis in CRC, and ZNF532 and COLEC12 could be as novel prognostic CAF biomarkers by producing the prediction model. Our CAF prediction model could forecast CRC prognosis, CAF infiltrations, and treatment effects, which might offer new targets and potential treatment strategies of CRC.

Data Availability

The datasets analyzed in this study could be found in GSE39582, TCGA-COAD, and GSE132465.

Ethical Approval

The data of this study were obtained from the public databases, and no ethical approval was required.

Conflicts of Interest

The authors report that there are no competing interests to declare.

Authors' Contributions

Yan Wang designed the study, analyzed the data, and wrote the manuscript. Zhengbo Chen performed the experiments and participated in data analysis. Gang Zhao analyzed the data and interpreted the data. Qiang Li provided the methodology and managed the project. All authors read and approved the final manuscript.

Supplementary Materials

Supplementary 1. Figure S1: scatter plots of the MEturquoise module in GSE39582 (A) and TCGA-COAD (B).

Supplementary 2. Figure S2: UMAP plots of markers for each cell type in CRC.

Supplementary 3. Supplementary Table 1: the primer information of genes.

References

[1] I. Mármol, C. Sánchez-de-Diego, A. Pradilla Dieste, E. Cerrada, and M. J. Rodriguez Yoldi, "Colorectal carcinoma: a general overview and future perspectives in colorectal cancer," *International Journal of Molecular Sciences*, vol. 18, no. 1, p. 197, 2017.

[2] K. Simon, "Colorectal cancer development and advances in screening," *Clinical Interventions in Aging*, vol. 11, pp. 967–976, 2016.

[3] M. D. Mathey, C. L. Pennella, and P. Zubizarreta, "Colorectal carcinoma in children and adolescents," *Archivos argentinos de pediatria*, vol. 119, no. 5, pp. e487–e498, 2021.

[4] X. Li, D. Song, S. Su et al., "Critical role of guanylate binding protein 5 in tumor immune microenvironment and predictive value of immunotherapy response," *Frontiers in Genetics*, vol. 13, article 984615, 2022.

[5] P. Gamradt, C. De La Fouchardière, and A. Hennino, "Stromal protein-mediated immune regulation in digestive cancers," *Cancers*, vol. 13, no. 1, p. 146, 2021.

[6] Y. A.-O. Chen, K. A.-O. McAndrews, and R. Kalluri, "Clinical and therapeutic relevance of cancer-associated fibroblasts," *Clinical Oncology*, vol. 18, no. 12, pp. 792–804, 2021.

[7] G. Comito, E. Giannoni, C. P. Segura et al., "Cancer-associated fibroblasts and M2-polarized macrophages synergize during prostate carcinoma progression," *Oncogene*, vol. 33, no. 19, pp. 2423–2431, 2014.

[8] M. A.-O. X. Bartoschek, N. Oskolkov, M. A.-O. Bocci et al., "Spatially and functionally distinct subclasses of breast cancer-associated fibroblasts revealed by single cell RNA sequencing," *Nature Communications*, vol. 9, no. 1, p. 5150, 2018.

[9] H. Zheng, H. Liu, H. Li, W. Dou, and X. Wang, "Weighted gene co-expression network analysis identifies a cancer-associated fibroblast signature for predicting prognosis and therapeutic responses in gastric cancer," *Frontiers in Molecular Biosciences*, vol. 8, article 744677, 2021.

[10] X. Dai, Y. Xie, and M. A.-O. Dong, "Cancer-associated fibroblasts derived extracellular vesicles promote angiogenesis of colorectal adenocarcinoma cells through miR-135b-5p/FOXO1 axis," *Cancer Biology & Therapy*, vol. 23, no. 1, pp. 76–88, 2022.

[11] D. Aran, Z. Hu, and A. J. Butte, "xCell: digitally portraying the tissue cellular heterogeneity landscape," *Genome Biology*, vol. 18, no. 1, p. 220, 2017.

[12] J. A.-O. Racle, K. de Jonge, P. Baumgaertner, D. E. Speiser, and D. Gfeller, "Simultaneous enumeration of cancer and immune cell types from bulk tumor gene expression data," *eLife*, vol. 6, article e26476, 2017.

[13] E. Becht, N. A. Giraldo, L. Lacroix et al., "Estimating the population abundance of tissue-infiltrating immune and stromal cell populations using gene expression," *Genome Biology*, vol. 17, no. 1, p. 218, 2016.

[14] P. A.-O. Jiang, S. Gu, D. Pan et al., "Signatures of T cell dysfunction and exclusion predict cancer immunotherapy response," *Nature Medicine*, vol. 24, no. 10, pp. 1550–1558, 2018.

[15] A. A.-O. Kaur, B. L. Ecker, S. M. Douglass et al., "Remodeling of the collagen matrix in aging skin promotes melanoma metastasis and affects immune cell motility," *Cancer Discovery*, vol. 9, no. 1, pp. 64–81, 2019.

[16] A. A.-O. Lin, T. A.-O. Gu, X. A.-O. Hu, J. A.-O. Zhang, and P. A.-O. Luo, "Comprehensive analysis identifies PI3K/Akt pathway alternations as an immune-related prognostic biomarker in colon adenocarcinoma patients receiving immune checkpoint inhibitor treatment," *Journal of Immunology Research*, vol. 2022, Article ID 8179799, 14 pages, 2022.

[17] X. Zhang, H. Zhao, X. Shi, X. Jia, and Y. Yang, "Identification and validation of an immune-related gene signature predictive of overall survival in colon cancer," *Aging*, vol. 12, no. 24, pp. 26095–26120, 2020.

[18] M. Zeng, L. Zhu, L. Li, and C. Kang, "miR-378 suppresses the proliferation, migration and invasion of colon cancer cells by inhibiting SDAD1," *Cellular & Molecular Biology Letters*, vol. 22, no. 1, p. 12, 2017.

[19] V. Karpisheh, A. Nikkhoo, M. Hojjat-Farsangi et al., "Prostaglandin E2 as a potent therapeutic target for treatment of colon cancer," *Prostaglandins & Other Lipid Mediators*, vol. 144, article 106338, 2019.

[20] D. Unterleuthner, P. Neuhold, K. Schwarz et al., "Cancer-associated fibroblast-derived WNT2 increases tumor angiogenesis in colon cancer," *Angiogenesis*, vol. 23, no. 2, pp. 159–177, 2020.

[21] D. von Ahrens, T. D. Bhagat, D. Nagrath, A. Maitra, and A. Verma, "The role of stromal cancer-associated fibroblasts in pancreatic cancer," *Journal of Hematology & Oncology*, vol. 10, no. 1, p. 76, 2017.

[22] C. Sun, S. Wang, Y. Zhang et al., "Risk signature of cancer-associated fibroblast-secreted cytokines associates with clinical outcomes of breast cancer," *Frontiers in Oncology*, vol. 11, article 628677, 2021.

[23] W. Dong, Y. Xie, and H. Huang, "Prognostic value of cancer-associated fibroblast-related gene signatures in hepatocellular carcinoma," *Frontiers in Endocrinology*, vol. 13, article 884777, 2022.

[24] M. A.-O. Song, J. He, Q. Z. Pan et al., "Cancer-associated fibroblast-mediated cellular crosstalk supports hepatocellular carcinoma progression," *Hepatology*, vol. 73, no. 5, pp. 1717–1735, 2021.

[25] X. Mao, J. Xu, W. Wang et al., "Crosstalk between cancer-associated fibroblasts and immune cells in the tumor microenvironment: new findings and future perspectives," *Molecular Cancer*, vol. 20, no. 1, p. 131, 2021.

[26] S. Feng, Y. Xu, Z. Dai, H. Yin, K. Zhang, and Y. Shen, "Integrative analysis from multicenter studies identifies a WGCNA-derived cancer-associated fibroblast signature for ovarian cancer," *Frontiers in Immunology*, vol. 13, 2022.

[27] G. A.-O. Li, J. F. Deng, Y. Z. Qi, R. Liu, and Z. X. Liu, "COLEC12 regulates apoptosis of osteosarcoma through Toll-like receptor 4–activated inflammation," *Journal of Clinical Laboratory Analysis*, vol. 34, no. 11, article e23469, 2020.

[28] W. Wang, C. Xu, Y. Ren et al., "A novel cancer stemness-related signature for predicting prognosis in patients with colon adenocarcinoma," *Stem Cells International*, vol. 2021, Article ID 7036059, 23 pages, 2021.

[29] L. Fan, J. Wang, P. Deng et al., "Foxhead box D1 promotes the partial epithelial-to-mesenchymal transition of laryngeal squamous cell carcinoma cells via transcriptionally activating the expression of zinc finger protein 532," *Bioengineered*, vol. 13, no. 2, pp. 3057–3069, 2022.

[30] H. Huang, Y. Hu, L. Guo, and Z. Wen, "Integrated bioinformatics analyses of key genes involved in hepatocellular carcinoma immunosuppression," *Oncology Letters*, vol. 22, no. 6, p. 830, 2021.

[31] Q. Jiang, C. Liu, C. P. Li et al., "Circular RNA-ZNF532 regulates diabetes-induced retinal pericyte degeneration and vascular dysfunction," *The Journal of Clinical Investigation*, vol. 130, no. 7, pp. 3833–3847, 2020.

Hindawi

Research Article

Identification and Validation of NK Marker Genes in Ovarian Cancer by scRNA-seq Combined with WGCNA Algorithm

Xin He [ID] and Weiwei Feng [ID]

Department of Obstetrics and Gynecology, Ruijin Hospital, Shanghai Jiao Tong University School of Medicine, 197 Ruijin 2nd Road, Huangpu District, Shanghai 200025, China

Correspondence should be addressed to Weiwei Feng; fww12066@rjh.com.cn

Background. As an innate immune system effector, natural killer cells (NK cells) play a significant role in tumor immunotherapy response and clinical outcomes. *Methods*. In our investigation, we collected ovarian cancer samples from TCGA and GEO cohorts, and a total of 1793 samples were included. In addition, four high-grade serous ovarian cancer scRNA-seq data were included for screening NK cell marker genes. Weighted gene coexpression network analysis (WGCNA) identified core modules and central genes associated with NK cells. The "TIMER," "CIBERSORT," "MCPcounter," "xCell," and "EPIC" algorithms were performed to predict the infiltration characteristics of different immune cell types in each sample. The LASSO-COX algorithm was employed to build risk models to predict prognosis. Finally, drug sensitivity screening was performed. *Results*. We first scored the NK cell infiltration of each sample and found that the level of NK cell infiltration affected the clinical outcome of ovarian cancer patients. Therefore, we analyzed four high-grade serous ovarian cancer scRNA-seq data, screening NK cell marker genes at the single-cell level. The WGCNA algorithm screens NK cell marker genes based on bulk RNA transcriptome patterns. Finally, a total of 42 NK cell marker genes were included in our investigation. Among which, 14 NK cell marker genes were then used to develop a 14-gene prognostic model for the meta-GPL570 cohort, dividing patients into high-risk and low-risk subgroups. The predictive performance of this model has been well-verified in different external cohorts. Tumor immune microenvironment analysis showed that the high-risk score of the prognostic model was positively correlated with M2 macrophages, cancer-associated fibroblast, hematopoietic stem cell, stromal score, and negatively correlated with NK cell, cytotoxicity score, B cell, and T cell CD4+Th1. In addition, we found that bleomycin, cisplatin, docetaxel, doxorubicin, gemcitabine, and etoposide were more effective in the high-risk group, while paclitaxel had a better therapeutic effect on patients in the low-risk group. *Conclusion*. By utilizing NK cell marker genes in our investigation, we developed a new feature that is capable of predicting patients' clinical outcomes and treatment strategies.

1. Introduction

In terms of incidence, ovarian cancer (OV) ranks second only to cervical cancer and uterine cancer among female reproductive system tumors [1]. OV has a very high recurrence rate and mortality, which seriously threatens women's health. Due to the lack of effective screening tools and early diagnosis difficulties, 80% of OV patients are diagnosed at an advanced stage, 50-70% of patients will relapse within 2 years after treatment, and a 5-year poor survival rate of 30% [2]. Despite recent improvements in treatment,

improvements in 5-year survival rates were minimal. A new therapeutic target is needed to improve the clinical outcomes of OV patients in light of the limitations of OV treatment [3]. For this reason, the development of predictive models and the identification of new biomarkers are crucial for predicting clinical outcomes and the effects of therapeutic interventions.

In response to tumor growth, a complex microenvironment surrounds tumor cells, including stromal cells, extracellular matrix molecules, and cytokines [4]. Accumulated evidence suggested that tumor microenvironment (TME)

components were thought to play a vital role in tumorigenesis and progression. Moreover, abnormal changes in TME can serve as biomarkers for immunotherapy in addition to affecting patients' prognoses [5]. Antitumor immunity has focused mainly on adaptive T cell responses, without adequate attention being given to innate immune cells. Cancer cells are rapidly recognized and killed by innate immune cells, known as NK cells [6]. As NK cells interact with target cells, their antitumor effect depends entirely on the balance between their inhibitory and activating receptors [7]. In the early stages of tumor growth, NK cells can suppress tumor invasiveness by directly destroying tumor cells and promoting adaptive T cell responses to contribute to antitumor immunity [8]. Tumor progression is controlled by both NK and T cells, which indicates that these immunocytes play a vital role in shaping antitumor immunity. NK cells in peripheral blood are reduced, which increases the risk of malignant tumors [9, 10]. Furthermore, higher numbers of tumor microenvironment NK cells component are significantly associated with better outcomes. In view of the important role of NK cells in immune antitumor, cumulative studies have explored the molecular characteristics of NK cells in cancer [11], but little was known about the comprehensive molecular mechanism of NK cells in OV patients. With the advent of single-cell RNA sequencing (scRNA-seq) technology and related analytical methods, the possibility of identifying the molecular profiles of different immune cell subsets in TME has become a reality [12]. Previous investigations have demonstrated that investigating tranomscriptome characteristics based on the molecular profile of immunocytes extracted from scRNA-seq information may be an effective weapon for predicting clinical outcomes and immunotherapy response [13]. Here, we investigated the comprehensive molecular mechanisms of NK cells from OV patients based on scRNA-seq data.

WGCNA is a technique for examining the variations in gene expression among several samples. The association between modules and clinical profiles can also be analyzed by clustering genes according to similar transcriptome profiles in modules (such as the immune score of patients) [14]. According to the WGCNA algorithm, this study assumed that the gene expression network obeyed the scale-free distribution and constructed the gene coexpression network. Therefore, we calculated dissimilarity coefficients between nodes in order to construct a hierarchical clustering tree. The modules were further visualized by assigning corresponding genes to different modules based on gene similarity. In our study, we investigated the expression profiles of signature genes of NK cells based on single-cell sequencing data to identify their biomarker genes and to identify core module genes associated with NK cells by WGCNA public expression analysis. Next, prediction models were developed based on these factors to predict the clinical outcome of OV by combining bulk RNA-seq datasets. In addition, the performance of the prediction model was validated with four independent cohorts, and the relationship between the prediction model and the response to chemotherapy in OV patients was investigated. These results will help us to better understand the molecular mechanisms of ovarian cancer progression.

2. Materials and Methods

2.1. Data Collection. An analysis of The Cancer Genome Atlas (TCGA) database was conducted in order to obtain RNA sequencing (RNA-seq) fragments per kilobase million (FPKM) and complete follow-up information on 372 samples. Somatic mutation data came from TCGA database. Using the "tmb" algorithm in the maftools package, each sample's tumor mutation burden (TMB) value was calculated. We performed log2 [(TPM)+1] conversion on the above raw data. In addition, we included three GPL platforms (GPL570: GSE19829, GSE18520, GSE9891, GSE26193, GSE30161, and GSE63885; GPL96: GSE3149, GSE23554, GSE26712, and GSE14764; and GPL7759: GSE13876). A total of 11 GEO cohorts and 1793 samples were included in our investigation.

Single-cell transcriptional profiling data and clinical information from ovarian cancer patients were obtained from the GEO website under accession number GSE184880, and scRNA-seq data from a total of four high-grade serous ovarian cancer samples were included.

2.2. Identification of NK Cell Marker Genes Based on the scRNA-seq Database. For single-cell data, we filtered cells with unique feature counts >5000 or <200 and cells with mitochondrial counts >5%. Then, the feature-expression measurements for each cell were normalized by the total expression using the default parameters of the Seurat "NormalizeData" function. Finally, all cell data were fed into a combined Seurat object via the Harmony package. Then, variable genes were scaled and the principal component (PC) was analyzed. Via "RunUMAP" function min. (Dist = 0.2 and neighbors = 20) and the "FindClusters" function (resolution = 0.5) using significant pc (top 15) for UMAP analysis and clustering. For identifying cell types, we employed automated annotation; SingleR is an automated annotation method for single-cell RNA sequencing (scRNA-seq) data [15]. Given a sample reference dataset (single cell or batch size) with known labels, it marks new units in the test dataset based on similarity to the reference. Thus, for reference datasets, the burden of manually interpreting clusters and defining marker genes only needs to be done once, while this biological knowledge can spread to new datasets in an automated manner. Differentially expressed genes (DEGs) were calculated for each cell subgroup using Wilcoxon-Mann–Whitney test in FindAllMarkers function. NK cells were calculated using three methods: EPIC algorithm, xCell algorithm, and MCPcounter algorithm, which were performed based on the "IOBR" package [16]. Adjusted p values < 0.01 and |log 2 (fold change)| > 1 were identified as NK cell marker genes.

2.3. WGCNA Network Construction and Module Identification. Subsequently, we made R "WGCNA" package for coexpression network analysis of NK cell marker genes. WGCNA can be used to find clusters (modules) of highly correlated genes, summarize such clusters using module signature genes or hub genes within nodules, associate modules with each other and external sample traits (using signature
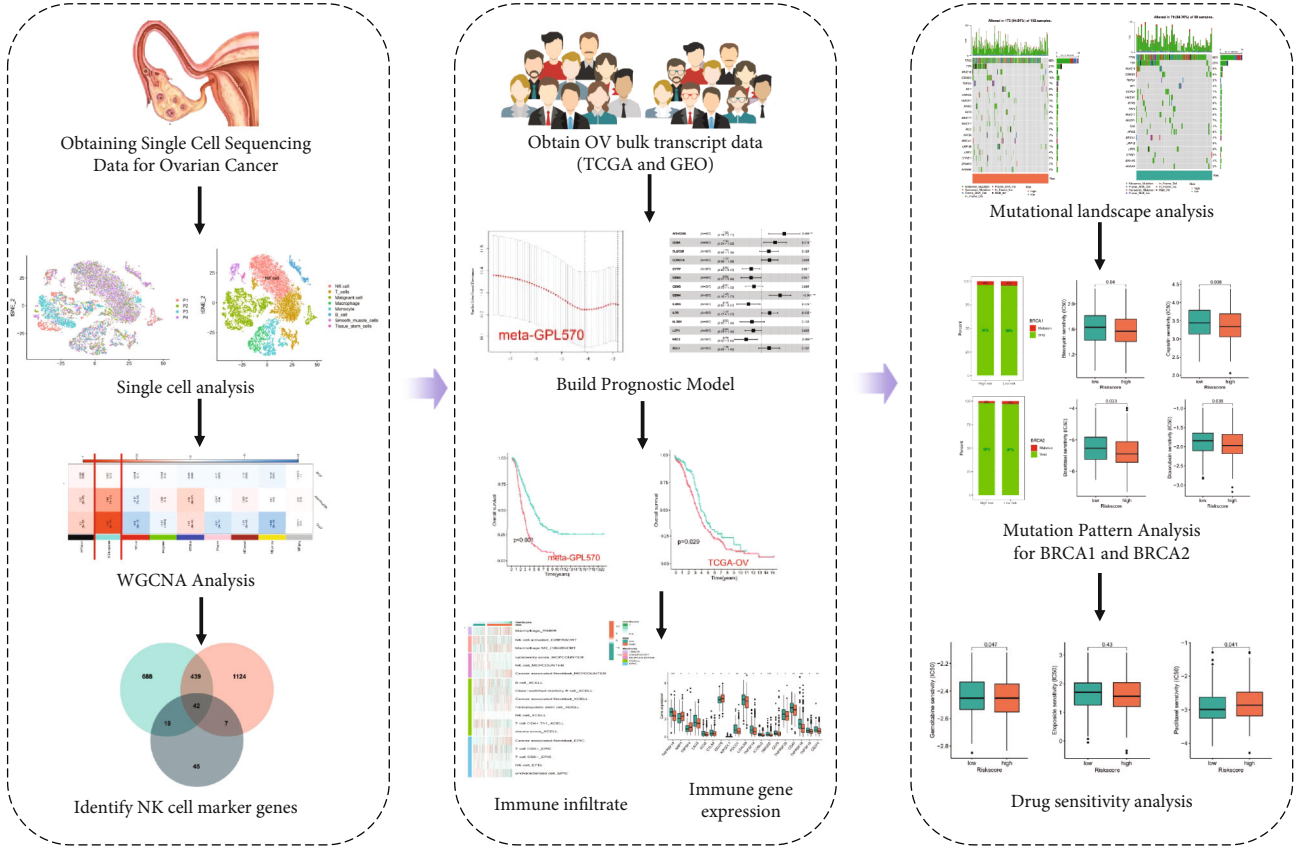
FIGURE 1: Flowchart.

gene network methods), and calculate module membership metrics [14]. Associated networks facilitate network-based gene screening methods that can be used to identify candidate biomarkers or therapeutic targets [14]. Our first step was to cluster the samples in order to determine if there were any outliers. Secondly, the coexpression network was constructed by using the automatic network construction function. The soft threshold power was calculated with the R function "pickSoftThreshold" and the coexpression similarity for adjacency calculations was increased. Third, clustering and dynamic tree-cutting functions were used to detect modules using hierarchical clustering. As a fourth step, the significance of genes and the membership of modules were calculated in order to correlate them with immune features. To further analyze the module gene information, the corresponding module gene information was extracted. Finally, we visualize the feature gene network.

2.4. Construction and Verification of Prognostic Model Based on NK Cell Marker Genes.
Subsequently, we developed a prognostic model based on the NK cell standard genes selected by WGCNA. To minimize overfitting, prognostic genes were evaluated by LASSO Cox proportional hazards regression using the "glmnet" package [17]. LASSO is a popular high-dimensional predictive regression method widely used for survival analysis of Cox proportional hazards regression models [18]. In order to select the best model,

10-fold cross-validation was performed using the function "cv." Finally, we used multivariate Cox regression analysis to calculate the prognostic value of specific genetic characteristics based on genes provided by LASSO Cox regression analysis. Risk models were constructed based on gene mRNA expression and risk coefficients. Risk scores were calculated using the following formula:

$$
\begin{aligned}
\text{riskScore} = \text{Coef}_1 \times \text{gene expression}_1 + \text{Coef}_2 \\
\times \text{gene expression}_2 + \cdots \text{Coef}_n \\
\times \text{gene expression}_{n.}
\end{aligned}
\tag{1}
$$

Coef represents the prognostic value of each gene in multivariate Cox regression analysis. Gene expression values represent the expression values of the corresponding model genes. Patients were divided into low-risk and high-risk groups according to the median cut-off of their risk score. R "survival" software package is a tool for statistical analysis and visualization of survival data and is widely used in scientific research work [19]. The performance of the prognostic model was validated using survival analysis on four datasets using the R package "survminer."

2.5. Pathway and Functional Enrichment Analysis.
According to the whole genome annotation package (org.Hs.eg.db), GO and KEGG enrichment analyses were employed to explore the obtained NK cell marker genes. Through the

(a)

(b)

(c)

(d)

(e)

(f)

(g)

(h)

(i)

(j)
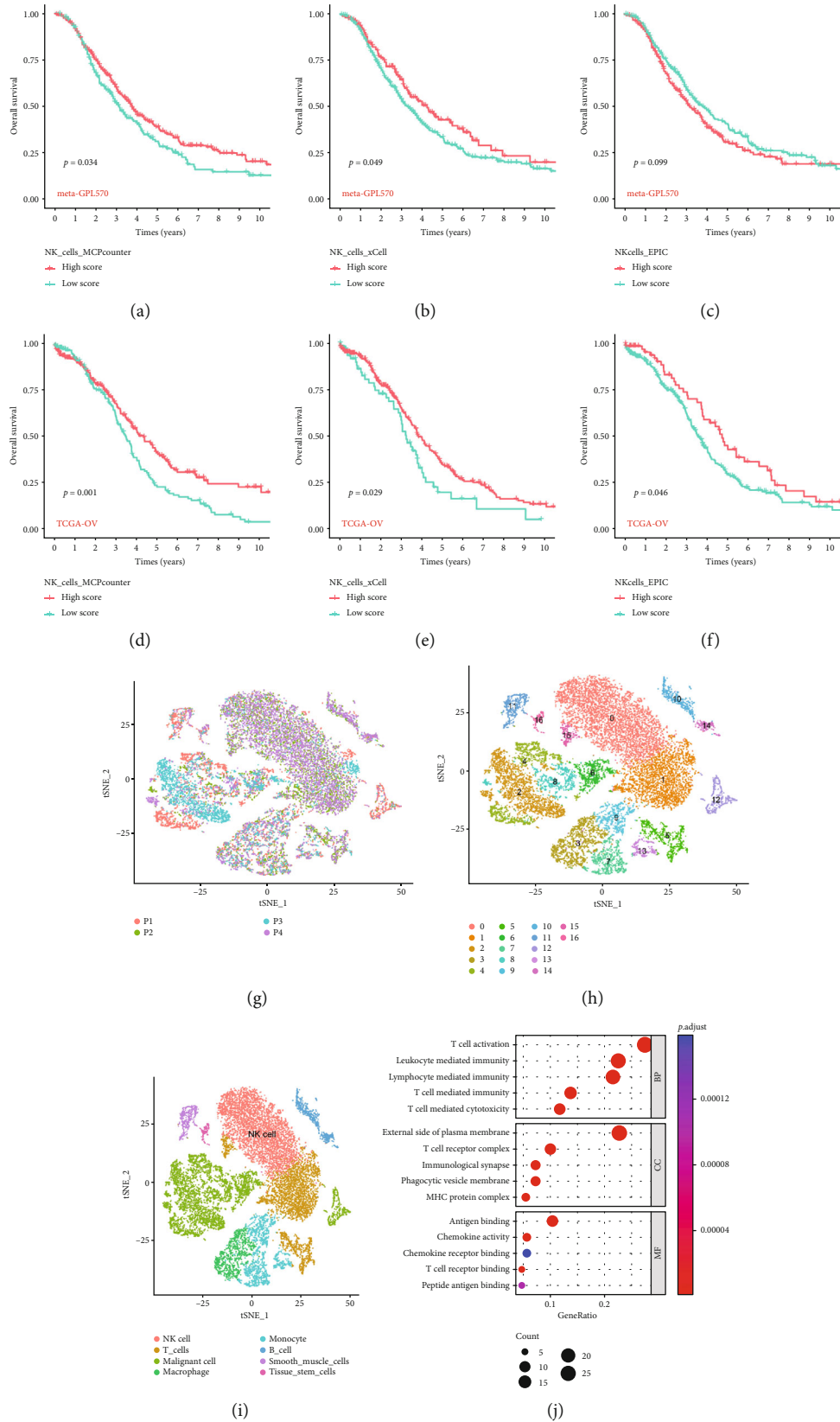
FIGURE 2: The single-cell RNA sequencing analysis identifies NK cell marker genes. (a–f) K-M survival curves suggest a prognostic role for NK cell-related scores assessed based on MCPcount, xCell, and EPIC algorithms. (g) The T-SNE algorithm demonstrated the distribution of cell subsets in four high-grade serous ovarian cancers. (h) The cell types identified by marker genes. (i) T-SNE plot colored by various cell clusters. (j) Histogram of GO analysis based on NK cell marker genes.

(a)

(b)

(c)

(d)

(e)

(f)

Figure 3: Continued.

(g)
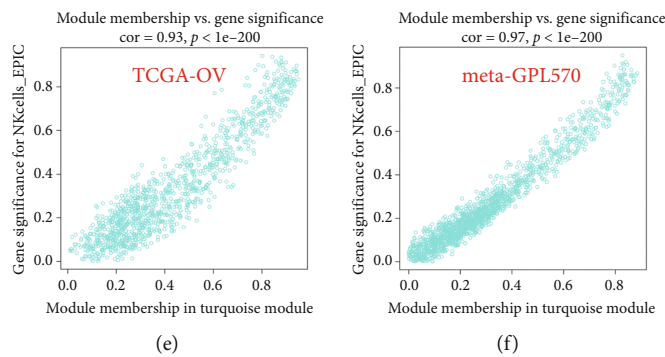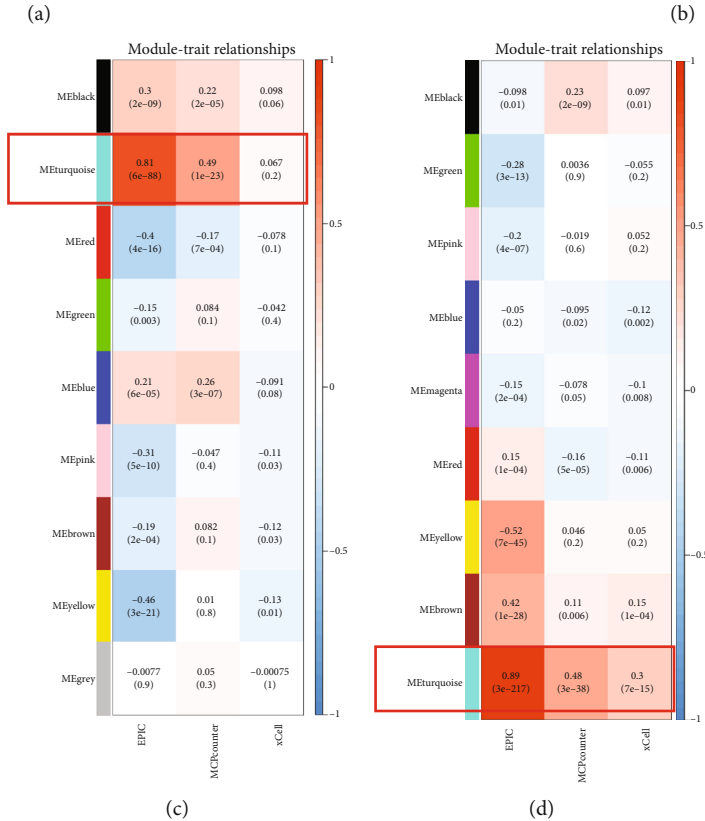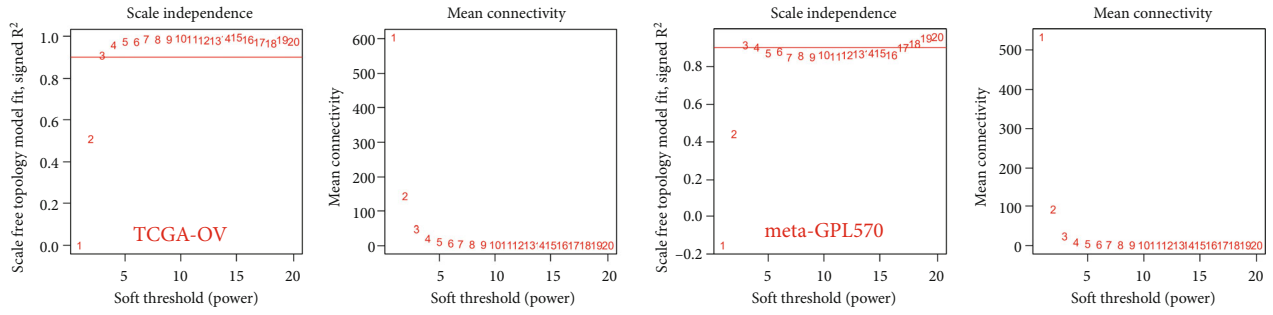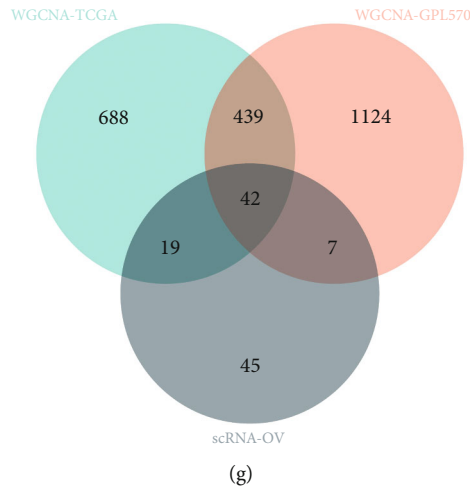
FIGURE 3: The WGNCA algorism identified NK cell marker genes (a, b) Scale-free exponent analysis and average connectivity analysis of soft threshold powers. (c, d) The heat map displayed the correlation between module characteristic genes and NK cell marker genes. (e, f) The correlation between module characteristic genes and NK cell EPIC. (g) The venn diagram showed overlapping genes for three screening datasets. A total of 42 genes were identified as NK cell-related marker genes.

latest online KEGG database, "ClusterProfiler" function obtained pathway data and performs functional analysis [20]. $p < 0.05$ was considered significant.

2.6. Enrichment Analysis of Immune Cell Infiltration. The "TIMER," "CIBERSORT," "MCPcounter," "xCell," and "EPIC" algorithms are all favorable tools for machine learning and are used to assess cell abundance and cell-type-specific gene expression patterns from a large number of tissue transcriptome profiles, quantify the tumor immune background through the type and density of tumor-infiltrating immune cells, and are widely used in scientific research work [21–24]. In addition, the "ESTIMATE" algorithm was used to calculate the proportion of stromal components and immune components in each sample microenvironment. The levels of immunomodulators in each risk group were presented by box plot.

2.7. Statistical Analysis. In order to compare categorical variables between different risk groups, Wilcoxon t-test was used. The significance threshold was set at 0.05. For data analysis and graphic generation, R tool (version 3.6.2) was conducted.

3. Results

The flowchart for this article is shown in Figure 1.

3.1. Screening of NK Cell Marker Genes Profile. First, we used MCPcounter, xCell, and EPIC algorithms to calculate the NK cell index (NK score) of each sample. Based on the median score, patients were classified into high-score and low-score groups. In the meta-GPL570 cohort, NK cell infiltration contributed to the longer survival times of the high-score group than the low-score group (Figures 2(a)–2(c)). In the TCGA-OV queue, the trend is consistent with the meta-GPL570 queue (Figures 2(d)–2(f)). Based on the GSE184880 scRNA-seq data, we included four high-grade serous ovarian

cancer scRNA-seq data for further investigation (Figure 2(g)). We used the first 1,500 variable genes for PCA to reduce dimensionality and then identified 17 cell clusters (Figure 2(i)). Annotating each cluster using the human primary cell map reference data set, cluster 0 was identified as NK cells using the reference data set (Figure 2(h)). There was also a difference in gene expression profiles within the cluster, and the differentially expressed genes (DEGs) for each cell subset were calculated using the Wilcoxon-Mann–Whitney test in the FindAllMarkers function. Functional enrichment showed that NK cell marker genes were mainly related to T cell immune characteristics, such as T cell activation, T cell-mediated immunity, and T cell receptor binding (Figure 2(j)).

3.2. Construction of Gene Coexpression Module. The WGCNA network was built by first calculating the soft threshold power and then improving the coexpression similarity for the adjacency calculations. A topology analysis of the network is undertaken using the pickSoftThreshold function in the R package "WGCNA". Based on the scale independence reaching 0.9 and the average connectivity being relatively high in both TCGA-OV and meta-GPL570 cohorts, the soft threshold power was set at 3 (Figures 3(a) and 3(b)).

In the TCGA-OV and meta-GPL570 cohorts, we associate the modules with the immune infiltration algorithm and search for the most important associations. The results of this analysis showed that the module turquoise was significantly associated with NK cell infiltration (Figures 3(c) and 3(d)). In addition, the NK cell EPIC score we constructed was positively correlated with the turquoise module, which was 0.93, 0.97 in TCGA-OV, and meta-GPL570 cohorts, respectively (Figures 3(e) and 3(f)). Subsequently, we intersected the NK cell marker genes obtained based on the single-cell transcriptome data analysis with the NK cell marker genes obtained based on the WGCNA algorithm to

(a)

(b)

(c)

(d)

(e)

(f)

FIGURE 4: Continued.

(g)

(h)
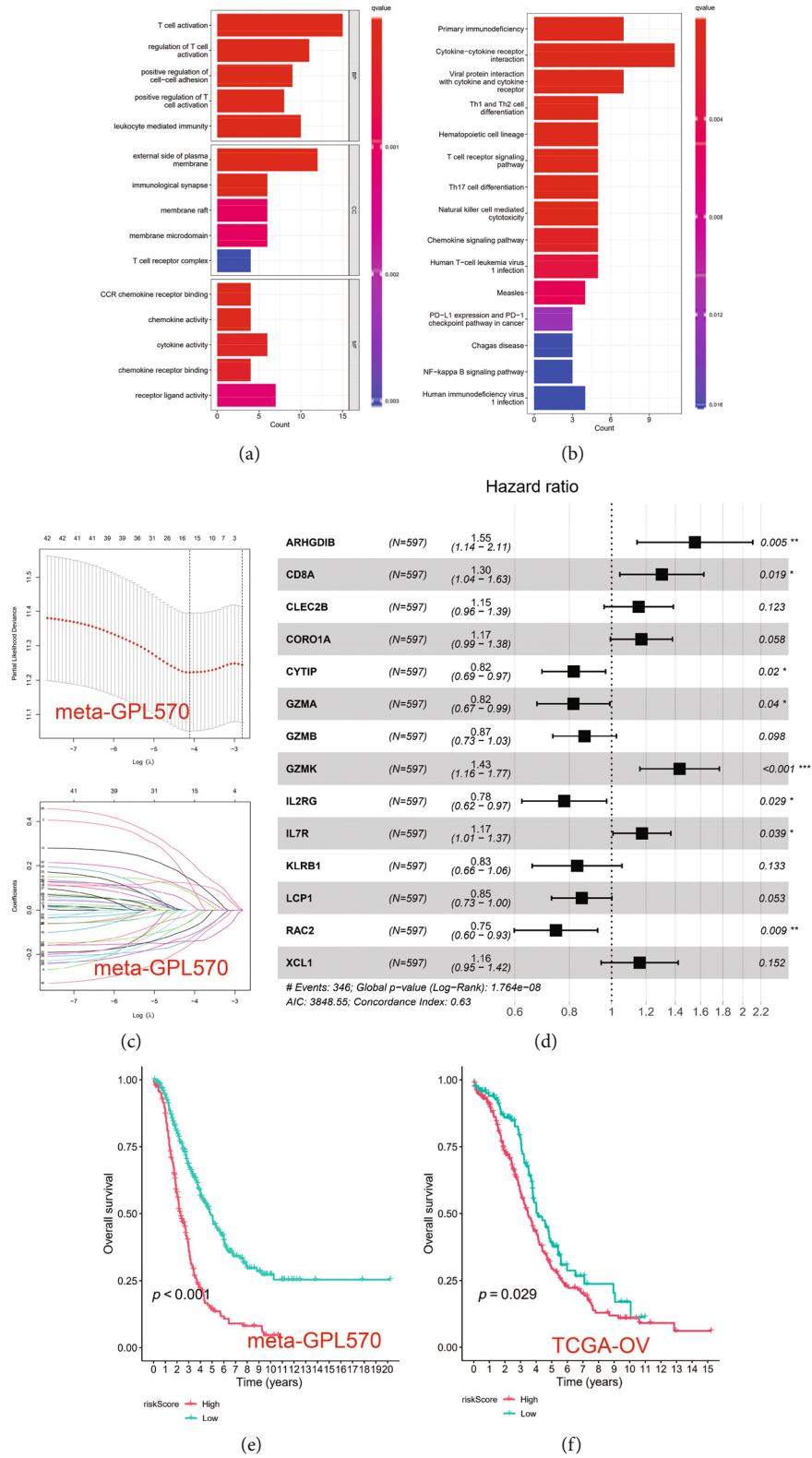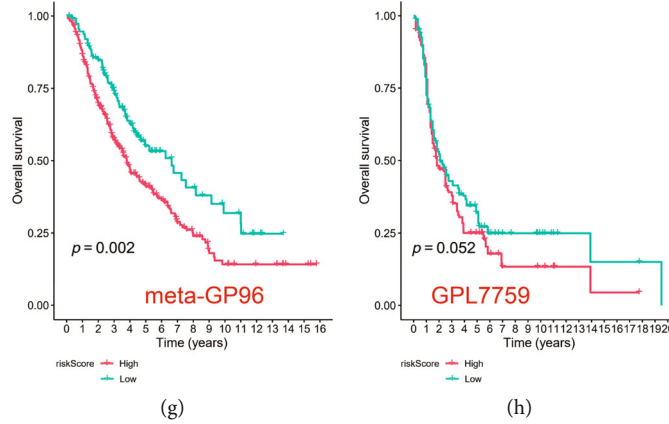
FIGURE 4: Construction of prognostic model based on the NK cell maker genes. (a, b) The GO and KEGG analyses of 42 NK cell marker genes. (c) The LASSO regression was used to reduce gene dimension, and 16 genes were screened for further analysis. (d) The multivariate COX regression analysis was used to obtain the coefficient of 14 genes in prognostic model. (e–h) K-M survival analysis of the prognostic model in different cohorts.

obtain a total of 42 NK cell-related marker genes (Figure 3(g)). We performed pathway enrichment analysis on the 42 NK cell-related marker genes. GO analysis revealed NK cell-associated genes associated with T cell activation, leukocyte-mediated immunity, and immunological immunology (Figure 4(a)). KEGG analysis revealed these genes' enrichment in primary immunodeficiency, Th1 and Th2 cell differentiations, and natural killer cell-mediated cytotoxicity signal pathway (Figure 4(b)).

3.3. Establishment of Prognostic Model Based on 14 NK Cell Marker Genes.
In order to predict the survival for each patient, we constructed a prognostic analysis based on 42 NK cell marker genes. We first used the meta-GPL570 cohort as a training set for LASSO regression analysis and screened 16 genes for further analysis (Figure 4(c)). Finally, we conducted the multivariate Cox regression analysis to optimize prognostic features, including only 14 of the most predictive genes (Figure 4(d)).

$$
\begin{aligned}
\text{Risk score} = {}& 0.44 \times \text{ARHGDIB} + 0.27 \times \text{CD8A} + 0.14 \\
& \times \text{CLEC2B} + 0.16 \times \text{CORO1A} - 0.20 \\
& \times \text{CYTIP} - 0.20 \times \text{GZMA} - 0.14 \times \text{GZMB} \\
& + 0.36 \times \text{GZMK} - 0.25 \times \text{IL2RG} + 0.16 \\
& \times \text{IL7R} - 0.18 \times \text{KLRB1} - 0.16 \times \text{LCP1} - 0.29 \\
& \times \text{RAC2} + 0.15 \times \text{XCL1}.
\end{aligned}
\tag{2}
$$

By ranking risk scores from high to low, patients were divided into low-risk and high-risk groups (low risk : score < median, high risk : score > median). Patients with a high-risk score had significantly shorter OS than patients with a low-risk score, according to Kaplan-Meier analysis (Figure 4(e)). Subsequently, TCGA-OV, meta-GP96, and GPL7759 external cohorts were used to verify the feasibility of the constructed predictive model (Figures 4(f)–4(h)).

3.4. Correlation between Risk Score and Tumor Microenvironment.
Since NK cells play an important role in antitumor immunity, we explored the relationship between the different risk based on the prognostic model and immune cell infiltration in OV patients. We employed TIMER, CIBERSORT, MCPcounter, xCell, and EPIC immune infiltration assessment algorithms to predict the proportion of immune cell infiltration in patients with high- and low-risk groups. M2 macrophages, cancer-associated fibroblast, hematopoietic stem cell, and stromal score were highly infiltrated in the high-risk group. NK cell, cytotoxicity score, B cell, and T cell CD4+Th1 were highly infiltrated in low-risk patients (Figure 5(a)). By using the ESTIMATE algorithm, we found that the risk score was positively correlated with StromalScore and negatively correlated with ImmuneScore (Figure 5(b)). Subsequently, we examined the expression of immunoregulators in patients with high- and low-risk groups. We found that immunoregulators and HLA families were generally highly expressed in the low-risk score group, while NRP1, TNFSF4, and CD276 were the opposite (Figures 5(c) and 5(d)). Therefore, we speculate that there were differences in immune cell infiltration and tumor mutation load between the two groups. For this reason, we divided patients into H-TMB and L-TMB according to tumor mutation burden (TMB). Medium TMB was 1.736842. Result turned out that patients with H-TMB had better survival outcomes than patients with L-TMB (Figure 5(e)). Figures 4(f) and 4(g) show that the frequency of mutation in patients with high-risk score (94.51%) was higher than that in patients with low-risk score (88.76%).

3.5. Predictive Model for Drug Sensitivity in OV Patients.
We detected the mutation frequency of BRCA1 and BRCA2 between the high- and low-risk subgroups and found no difference between the two groups (Figures 6(a) and 6(b)). Subsequently, we performed drug prediction for patients in the high- and low-risk groups. We found that bleomycin, cisplatin, docetaxel, doxorubicin, gemcitabine, and etoposide were more effective in the high-risk group. Paclitaxel had a

(a)

(b)

(c)

Figure 5: Continued.

(d)

(e)

(f)

Figure 5: Continued.

(g)
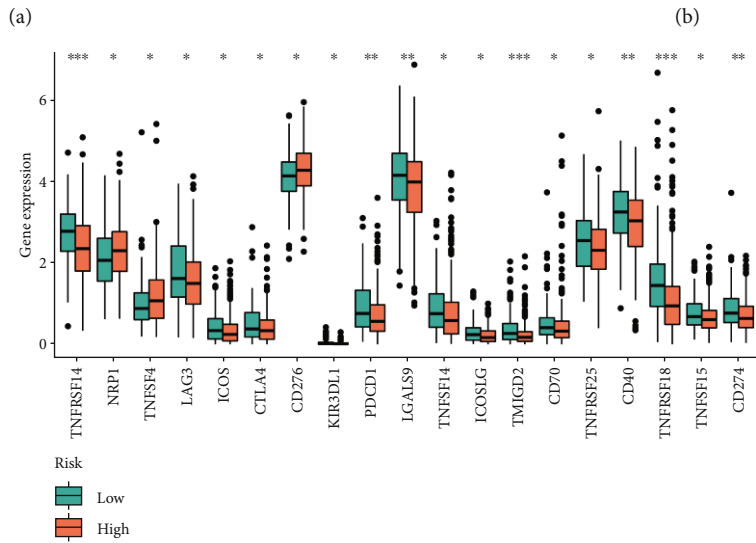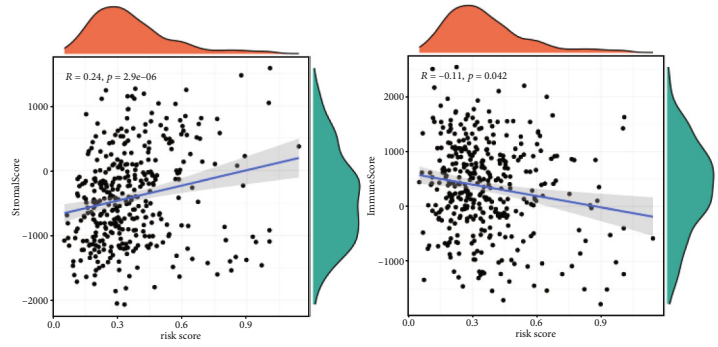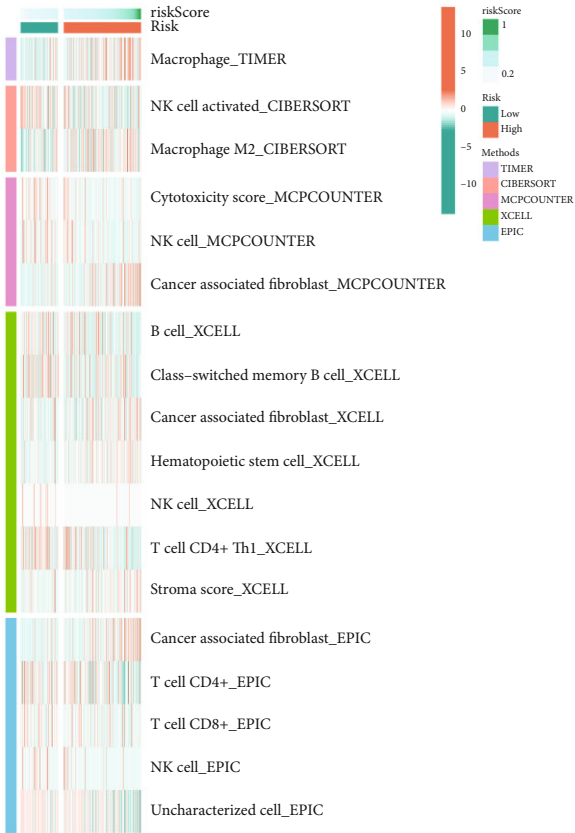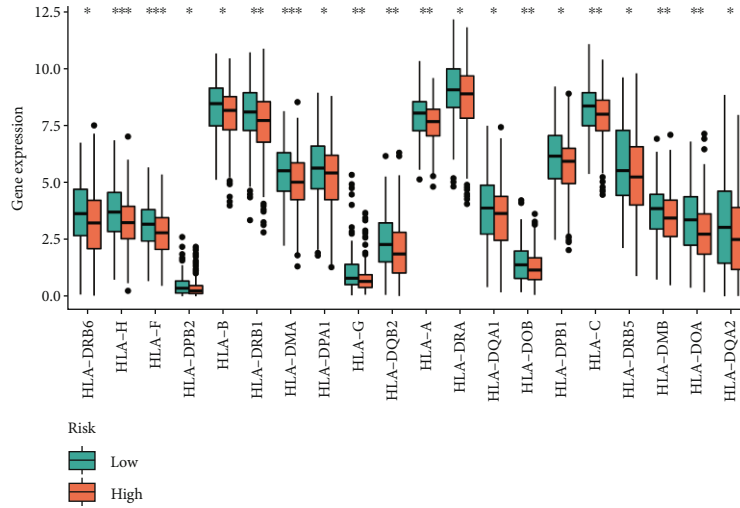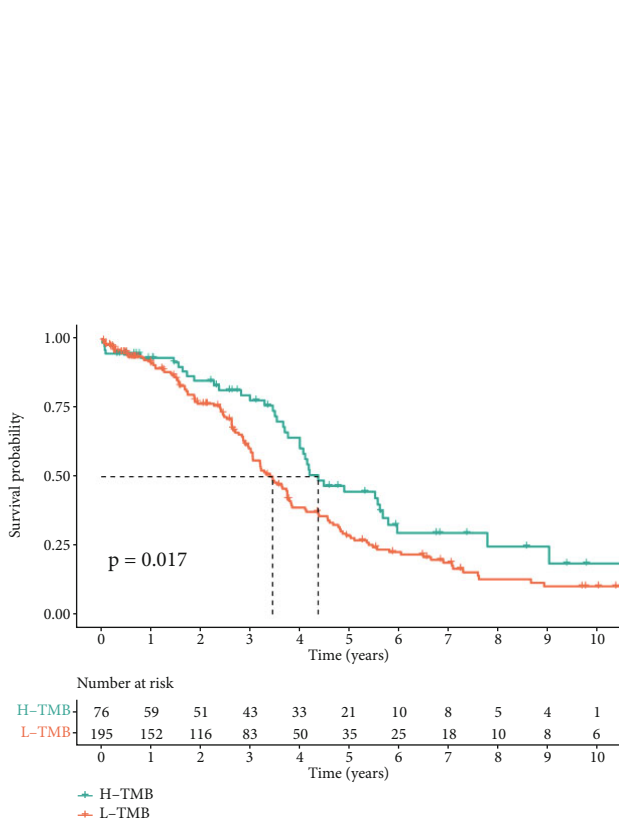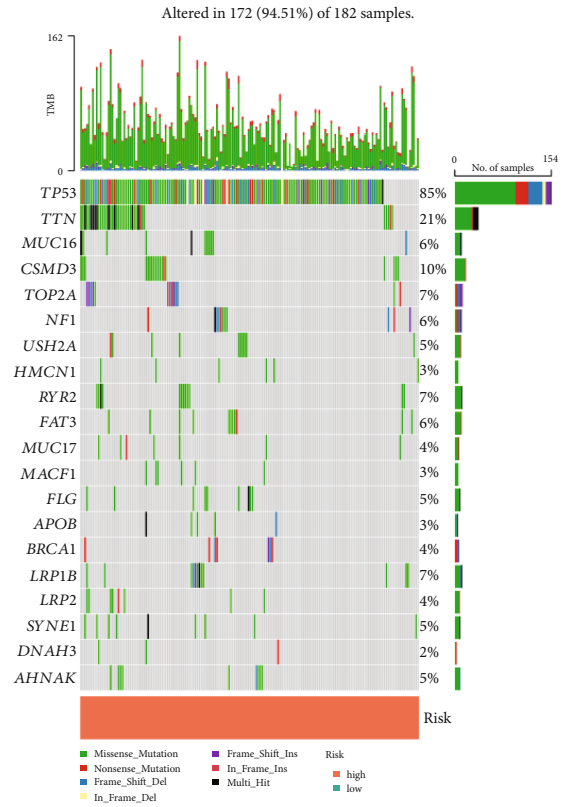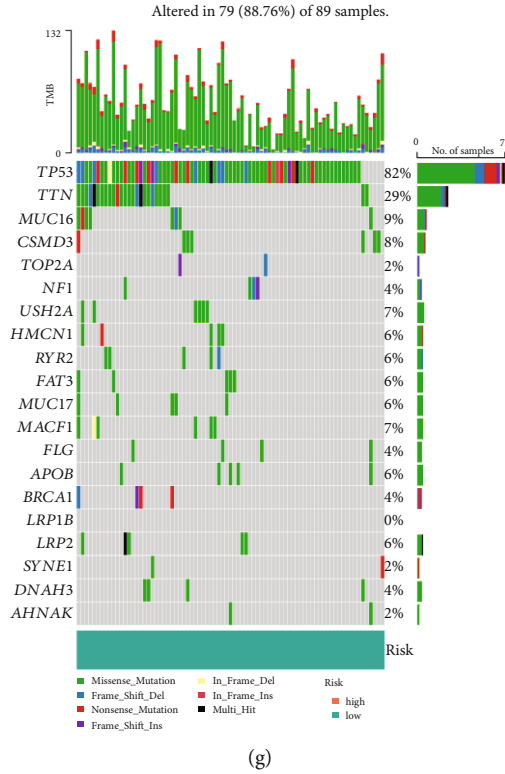
FIGURE 5: Tumor microenvironment assessment in different risk groups based on prognostic model. (a) Heat map showing/depicting immune cell infiltration landscape in high- and low-risk groups based on 5 algorithms. (b) Scatterplots showed the association of risk scores with StromalScore and ImmuneScore. (c, d) The boxplots showed the expression levels of immune regulators in the high- and low-risk groups. (e) K-M survival curves showed a survival difference between patients with high TMB and patients with low TMB. (f, g) The mutation landscape of high- and low-risk groups.

better therapeutic effect on patients in the low-risk group (Figures 6(c)–6(i)). Overall, these findings promoted a prognostic model as a biomarker for predicting individual drug sensitivity.

4. Discussion

As scRNA-seq technology developed rapidly, researchers began to focus more on the molecular characteristics of immune cells that infiltrate tumors. Despite that, most of the current research focuses on adaptive immune cells, ignoring the role of innate immune cells, which may have significant effects on clinical outcomes and immunotherapy response. Tumor-infiltrating NK cells were closely related to prognosis in patients with different solid tumors [25]. In the recent study by Shimasaki et al., NK cell marker genes were used to evaluate the infiltration of NK cells into TME, and the increased NK score significantly stratified the prognosis of patients with metastatic cutaneous melanoma [26]. Under the guidance of the above research, we employed three algorithms to observe the role of the NK cell score for predicting clinical outcomes of patients with ovarian cancer in two data sets and found that the prediction performance according to NK cell score was great. However, due to the algorithm being based on bulK RNA sequencing data, there was a certain deviation. Therefore, we obtained NK cell marker genes by combining scRNA-seq data and bulk RNA-

seq data. Subsequently, we constructed a promising prognostic model based on NK cell marker genes for predicting clinical prognosis and immunotherapy efficacy and verified it in four independent cohorts. The high-risk score of the prognostic model was positively correlated with M2 macrophages, cancer-associated fibroblast, hematopoietic stem cell, and stromal score and negatively correlated with NK cell, cytotoxicity score, B cell, and T cell CD4+Th1. In addition, we found that bleomycin, cisplatin, docetaxel, doxorubicin, gemcitabine, and etoposide were more effective in the high-risk group, while paclitaxel had a better therapeutic effect on patients in the low-risk group.

In our investigation, the predictive prognostic model consisted of 14 NK cell marker genes (ARHGDIB, CD8A, CLEC2B, CORO1A, CYTIP, GZMA, GZMB, GZMK, IL2RG, IL7R, KLRB1, LCP1, RAC2, and XCL1), most of which were associated with prognosis or NK cell activity in OV patients. For example, Lado et al. identified two candidate genes belonging to the innate immune system: FCAR and CLEC2B. The CLEC2B gene was associated with NK cell and stimulated natural killer cells to play an immune defense mechanism [27]. Mace and Orange demonstrated for the first time that CORO1A promoted NK cells to exert cytotoxic functions and immune secretion by regulating F-actin breakdown, thus exerting the function of lytic immune effectors [28]. In addition, NK cells can kill gasdermin B- (GSDMB-) -enriched positive cells in tumor tissues by

(a)

(b)

(c)

(d)

(e)

(f)

FIGURE 6: Continued.

(g)

(h)

(i)
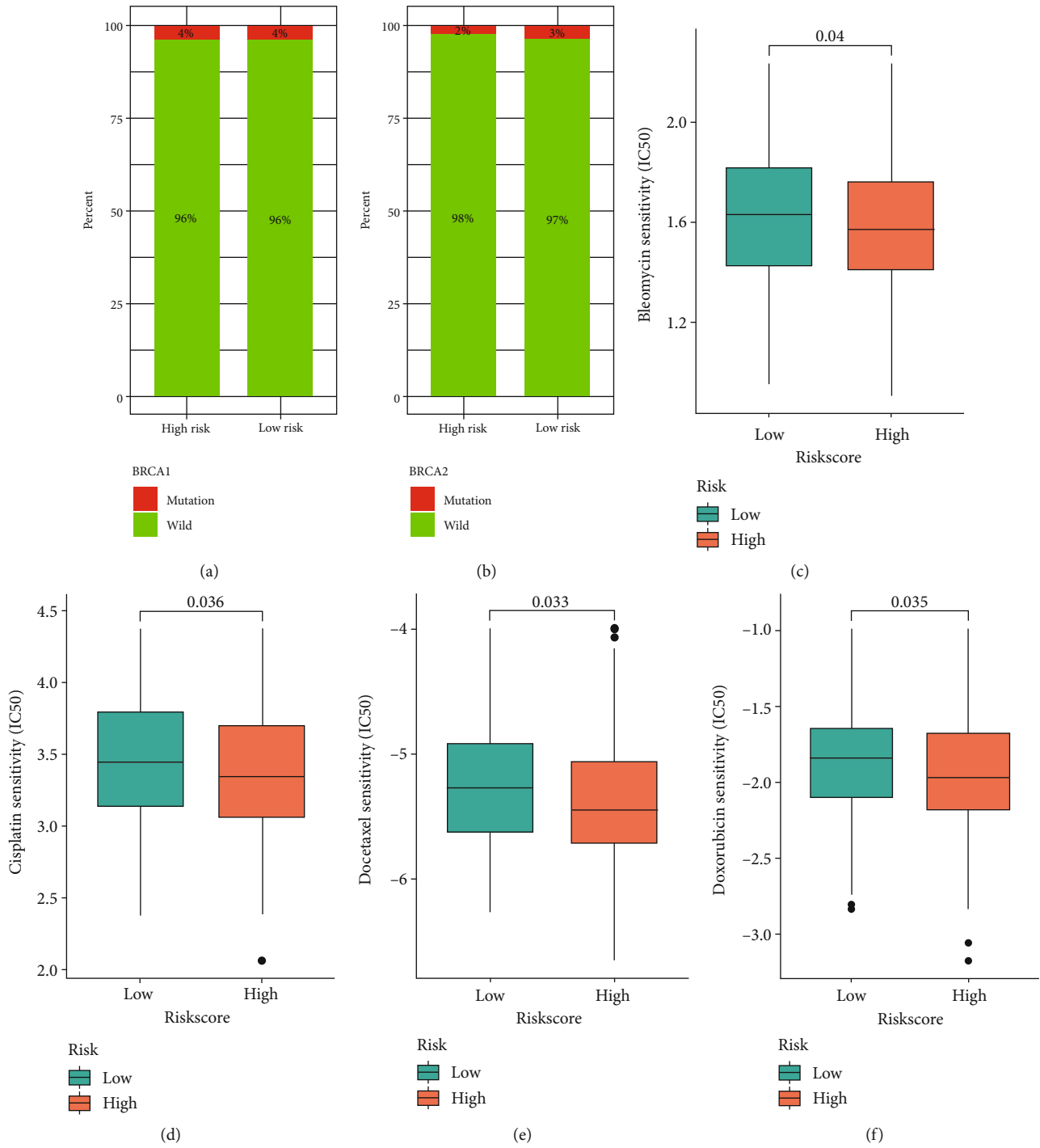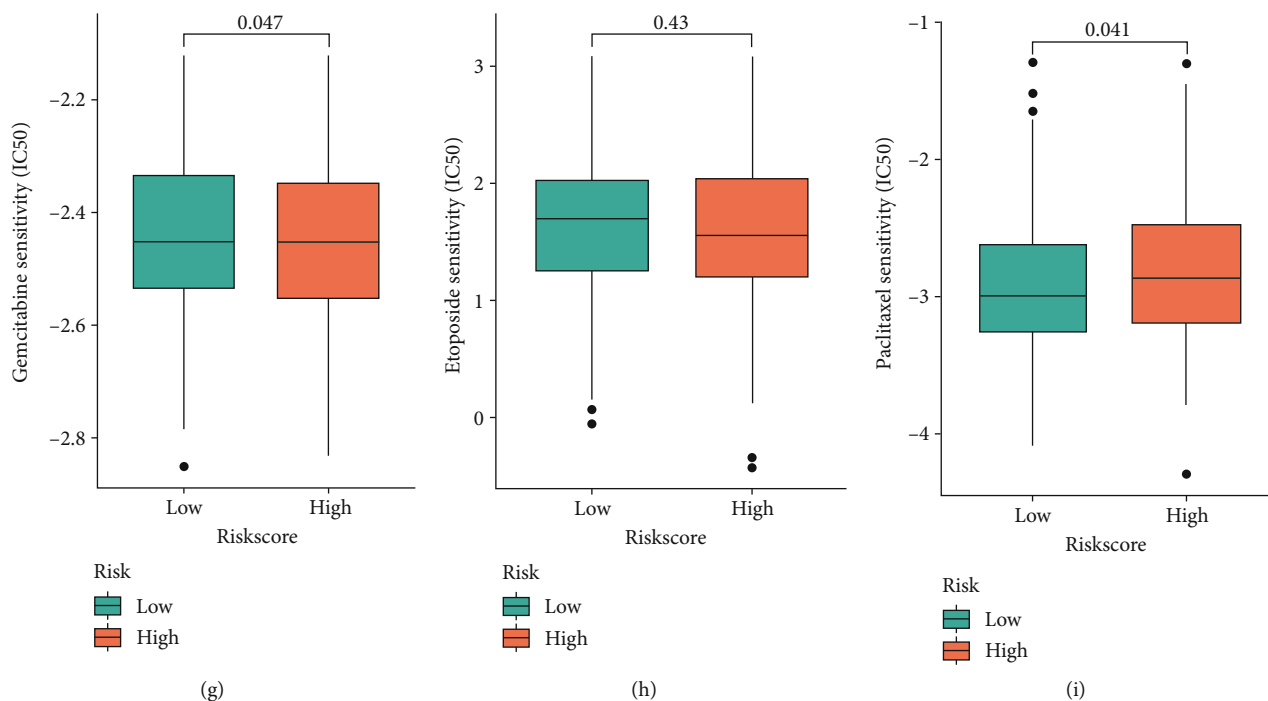
FIGURE 6: Drug sensitivity analysis. (a, b) The mutation patterns of BRCA1 and BRCA2 in high- and low-risk groups. (c–i) The IC_{50} of chemotherapeutic drugs in patients with the high- and low-risk groups.

apoptosis mediated by granzyme A (GZMA), which is transcribed by the GZMA gene [29].To elucidate the molecular mechanisms of OV patients, laboratory experimental designs should focus on genes identified in the prognostic model.

This prognostic model has proven to be powerful predictive tools in training and validation cohorts. The excellent performance of the prognostic model has inspired us to investigate potential mechanisms. We first performed GO and KEGG analyses to explore the enrichment pathway of NK cell marker genes. GO analysis revealed NK cell-associated genes associated with T cell activation, leukocyte-mediated immunity. KEGG analysis revealed these gene enrichment in primary immunodeficiency, Th1 and Th2 cell differentiation, and natural killer cell-mediated cytotoxicity signal pathway. Poor prognosis in high-risk patients may be partly due to abnormal regulation of antitumor immunity, which was closely related to tumor proliferation and progression. Furthermore, tumor-infiltrating immune cells in TME play a crucial role in tumor development and have a significant impact on patient outcome [30]. We then compared ESTIMATE and CIBER-SORT algorithms to determine the abundance of immune cell infiltration in high-risk and low-risk groups. The results showed that the level of immune cell infiltration in high-risk tumors was low, especially T cells and NK cells, suggesting that high-risk samples were called "cold tumors" and their antitumor activity was reduced [31]. The infiltration of immune cells in low-risk tumors can promote tumor cells to evade immune surveillance and promote tumor progression, which may partially explain the significantly reduced survival rate of patients with a high-risk score.

Our study still has some limitations. First, the expression and prognostic role of genes selected for prognostic models at the protein level warrants further investigation. A second limitation of our study is that the candidate genes we observed are all NK cell markers, and there is a high degree of spatial heterogeneity in the tumor immune microenvironment. Thus, the prognostic ability of the signature is restrictive. Finally, all mechanistic analyses in our study are descriptive. Future studies must explore potential mechanisms between prognostic model-associated gene expression and clinical outcome in OV patients. However, in the current prognostic model, our model still has great advantages, and NK cell signature genes also have their immune value. In addition, we used a large number of validation sets, which indicated the reliability and stability of our model.

5. Conclusion

In summary, we identified 14 genetic signatures based on NK cell marker genes and validated their strong predictive power for clinical outcome and response to chemotherapy in patients with OV. It can be used as a prognostic biomarker for clinical decision-making on individualized prediction and help to select suitable patients who can benefit from clinical treatment.

Data Availability

All datasets generated for this study are included in the article material, including TCGA database (https://portal.gdc.cancer.gov/) and the GEO dataset (https://www.ncbi.nlm.nih.gov/gds/).

Conflicts of Interest

The authors declare that they have no conflicts of interest.

Authors' Contributions

He-Xin was a major contributor in the dataset analysis and manuscript writing. Feng-Weiwei is responsible for reviewing the entire article process.

Acknowledgments

References

[1] M. C. Cusimano, S. E. Ferguson, R. Moineddin et al., "Ovarian cancer incidence and death in average-risk women undergoing bilateral salpingo-oophorectomy at benign hysterectomy," *American Journal of Obstetrics and Gynecology*, vol. 226, no. 2, pp. 220.e1–220.e26, 2022.

[2] M. E. Barnard, H. Meeks, E. A. Jarboe, J. Albro, N. J. Camp, and J. A. Doherty, "Familial risk of epithelial ovarian cancer after accounting for gynaecological surgery: a population-based study," *Journal of Medical Genetics*, vol. 60, no. 2, pp. 119–127, 2023.

[3] I. Vergote, A. González-Martín, I. Ray-Coquard et al., "European experts consensus: BRCA/homologous recombination deficiency testing in first-line ovarian cancer," *Annals of Oncology*, vol. 33, no. 3, pp. 276–287, 2021.

[4] A. J. Wiggans, G. K. Cass, A. Bryant, T. A. Lawrie, J. Morrison, and Cochrane Gynaecological, Neuro-oncology and Orphan Cancer Group, "Poly (ADP-ribose) polymerase (PARP) inhibitors for the treatment of ovarian cancer," *Cochrane Database of Systematic Reviews*, vol. 5, 2015.

[5] I. Vitale, G. Manic, L. M. Coussens, G. Kroemer, and L. Galluzzi, "Macrophages and metabolism in the tumor microenvironment," *Cell Metabolism*, vol. 30, no. 1, pp. 36–50, 2020.

[6] O. Meurette and P. Mehlen, "Notch signaling in the tumor microenvironment," *Cancer Cell*, vol. 34, no. 4, pp. 536–548, 2018.

[7] H. Xu, D. Ye, M. Ren, H. Zhang, and F. Bi, "Ferroptosis in the tumor microenvironment: perspectives for immunotherapy," *Trends in Molecular Medicine*, vol. 27, no. 9, pp. 856–867, 2021.

[8] J. Pitt, A. Marabelle, A. Eggermont, J.-C. Soria, G. Kroemer, and L. Zitvogel, "Targeting the tumor microenvironment: removing obstruction to anticancer immune responses and immunotherapy," *Annals of Oncology*, vol. 27, no. 8, pp. 1482–1492, 2016.

[9] J. P. Böttcher, E. Bonavita, P. Chakravarty et al., "NK cells stimulate recruitment of cDC1 into the tumor microenvironment promoting cancer immune control," *Cell*, vol. 172, no. 5, pp. 1022–1037.e14, 2018.

[10] F. Ye, Y. Liang, Z. Cheng et al., "Immunological characteristics of alternative splicing profiles related to prognosis in bladder cancer," *Frontiers in Immunology*, vol. 13, article 911902, 2022.

[11] S. Y. Neo, Y. Yang, J. Record et al., "CD73 immune checkpoint defines regulatory NK cells within the tumor microenvironment," *The Journal of Clinical Investigation*, vol. 130, no. 3, pp. 1185–1198, 2020.

[12] S. Sivori, D. Pende, L. Quatrini et al., "NK cells and ILCs in tumor immunotherapy," *Molecular Aspects of Medicine*, vol. 80, article 100870, 2021.

[13] S.-Y. Wu, T. Fu, Y.-Z. Jiang, and Z.-M. Shao, "Natural killer cells in cancer biology and therapy," *Molecular Cancer*, vol. 19, no. 1, pp. 1–26, 2020.

[14] P. Langfelder and S. Horvath, "WGCNA: an R package for weighted correlation network analysis," *BMC Bioinformatics*, vol. 9, no. 1, p. 559, 2008.

[15] A. Lun, J. M. Andrews, F. Dundar, and D. Bunis, "Using SingleR to annotate single-cell RNA-seq data," *Dim*, vol. 19363, p. 713, 2020.

[16] D. Zeng, Z. Ye, R. Shen et al., "IOBR: multi-omics immuno-oncology biological research to decode tumor microenvironment and signatures," *Frontiers in Immunology*, vol. 12, 2021.

[17] J. H. Friedman, T. Hastie, and R. Tibshirani, "Regularization Paths for Generalized Linear Models via Coordinate Descent," *Journal of Statistical Software*, vol. 33, no. 1, pp. 1–22, 2010.

[18] H. Zou, "The adaptive lasso and its oracle properties," *Journal of the American Statistical Association*, vol. 101, no. 476, pp. 1418–1429, 2006.

[19] D. F. Moore, *Applied Survival Analysis Using R*, vol. 473, Springer, 2016.

[20] G. Yu, L.-G. Wang, Y. Han, and Q. Y. He, "clusterProfiler: an R package for comparing biological themes among gene clusters," *Omics*, vol. 16, no. 5, pp. 284–287, 2012.

[21] B. Chen, M. S. Khodadoust, C. L. Liu, A. M. Newman, and A. A. Alizadeh, "Profiling tumor infiltrating immune cells with CIBERSORT," in *Cancer Systems Biology*, pp. 243–259, Springer, 2018.

[22] T. Li, J. Fan, B. Wang et al., "TIMER: a web server for comprehensive analysis of tumor-infiltrating immune cells," *Cancer Research*, vol. 77, no. 21, pp. e108–e110, 2017.

[23] D. Aran, Z. Hu, and A. J. Butte, "xCell: digitally portraying the tissue cellular heterogeneity landscape," *Genome Biology*, vol. 18, no. 1, pp. 1–14, 2017.

[24] J. Williams, C. Jones, J. Kiniry, and D. A. Spanel, "The EPIC crop growth model," *Transactions of ASAE*, vol. 32, no. 2, pp. 0497–0511, 1989.

[25] H. Song, J. Song, M. Cheng et al., "METTL3-mediated m^{6}A RNA methylation promotes the anti- tumour immunity of natural killer cells," *Nature Communications*, vol. 12, no. 1, pp. 1–15, 2021.

[26] N. Shimasaki, A. Jain, and D. Campana, "NK cells for cancer immunotherapy," *Nature Reviews Drug Discovery*, vol. 19, no. 3, pp. 200–218, 2020.

[27] S. Lado, J. Futas, M. Plasil et al., "Crimean-Congo hemorrhagic fever virus past infections are associated with two innate immune response candidate genes in dromedaries," *Cell*, vol. 11, no. 1, 2021.

[28] E. M. Mace and J. S. Orange, "Lytic immune synapse function requires filamentous actin deconstruction by coronin 1A," *Proceedings of the National Academy of Sciences of the United States of America*, vol. 111, no. 18, pp. 6708–6713, 2014.

[29] Z. Zhou, H. He, K. Wang et al., "Granzyme A from cytotoxic lymphocytes cleaves GSDMB to trigger pyroptosis in target cells," *Science*, vol. 368, no. 6494, 2020.

[30] S. Tao and I. Drexler, "Targeting autophagy in innate immune cells: angel or demon during infection and vaccination?," *Frontiers in Immunology*, vol. 11, p. 460, 2020.

[31] K. Voskarides, "The "cancer-cold" hypothesis and possible extensions for the Nordic populations," *Scandinavian Journal of Public Health*, vol. 47, no. 5, pp. 477–481, 2019.

Hindawi

Research Article

Tumor Necrosis Factor-*α* Promotes the Tumorigenesis, Lymphangiogenesis, and Lymphatic Metastasis in Cervical Cancer via Activating VEGFC-Mediated AKT and ERK Pathways

Xiao Chen [ID],[1] **Luping Lin** [ID],[2] **Qiaoling Wu** [ID],[1] **Sang Li** [ID],[1] **Huihui Wang** [ID],[3] **and Yang Sun** [ID][1]

[1]*Department of Gynecology, Clinical Oncology School of Fujian Medical University, Fujian Cancer Hospital, Fuzhou 350000, China*
[2]*Department of Abdominal Medical Oncology, Clinical Oncology School of Fujian Medical University, Fujian Cancer Hospital, Fuzhou 350000, China*
[3]*Wenzhou Central Hospital, The Second Affiliated Hospital of Shanghai University, China*

Correspondence should be addressed to Yang Sun; doctorsunyang@sina.com

Background. Lymphatic metastasis is a common phenomenon of cervical cancer. Tumor necrosis factor-*α* (TNF-*α*) was found to be closely associated with lymphatic cancer metastasis. However, the mechanism through which TNF-*α* regulates lymphatic metastasis in cervical cancer remains unclear. *Methods.* In this study, cervical cancer cells were cultured in Dulbecco's modified Eagle's medium (DMEM) with or without TNF-*α* for 48 h, and then the corresponding conditional medium (CM-TNF-*α* or CM) was collected. The level of vascular endothelial growth factor (VEGFC) in the corresponding CM was then detected using an enzyme-linked immunosorbent assay (ELISA). Next, human lymphatic endothelial cells (HLECs) were cultured in CM-TNF-*α* or CM for 48 h. Cell viability was measured using the cell counting kit-8 (CCK-8) assay, and angiogenesis was detected using a tube formation assay. Subsequently, the expressions of AKT, p-AKT, ERK, and p-ERK in HLECs were detected using western blotting. In addition, to further investigate the effect of TNF-*α* on the progression of cervical cancer, a C33A subcutaneous xenograft model was established *in vivo*. *Results.* We found that TNF-*α* significantly stimulated cervical cancer cells to secrete VEGFC. Additionally, the CM collected from the TNF-*α*-treated cervical cancer cells notably promoted the proliferation, migration, and angiogenesis of HLECs; however, these changes were reversed by MAZ51, a VEGFR3 inhibitor. Moreover, TNF-*α* obviously elevated D2-40 and VEGFC protein expressions in tumor tissues, promoting lymphangiogenesis and lymphatic metastasis *in vivo*. Meanwhile, TNF-*α* markedly upregulated p-AKT and p-ERK expressions in tumor tissues, whereas these changes were reversed by MAZ51. *Conclusion.* Collectively, TNF-*α* could promote tumorigenesis, lymphangiogenesis, and lymphatic metastasis *in vitro* and *in vivo* in cervical cancer via activating VEGFC-mediated AKT and ERK pathways. These results may provide new directions for the treatment of cervical cancer.

1. Introduction

Cervical cancer remains one of the main cancer in women, particularly in developing countries [1–4]. At present, cervical cancer is the main cause of mortality in women [2, 5, 6]. Lymphatic metastasis has been identified as a risk factor for cervical cancer recurrence [7]. The formation of lymphatic microvessels is the earliest stage of lymphatic metastasis

[8]. At present, clinical treatments for cervical cancer include surgical treatment, radiotherapy, and chemotherapy [9–11]. However, the prognosis of patients with advanced cervical cancer remains relatively poor [12].

Tumor microenvironment (TME) refers to the environment around a tumor, including the surrounding blood vessels, immune cells and son on [13]. A prominent feature of the TME is the recruitment of a large number of inflammatory

cells and the production of inflammatory factors [14]. Inflammatory factors are a double-edged sword for tumors [15–17]. On the one hand, they can directly kill tumor cells or induce immune cells to recognize tumor antigens [18, 19]. On the other hand, they can promote tumor cell invasion and metastasis [20]. Thus, it is necessary to explore the relationships among inflammatory factors, lymphatic microvessel formation, and tumorigenesis in cervical cancer.

The extensively studied pro-inflammatory cytokine, tumor necrosis factor-α (TNF-α) [21], can be secreted by various cells such as adipocytes, activated monocytes, macrophages, B cells, and T cells [22, 23]. Reports have suggested that TNF-α can promote tumor development and metastasis [24] by inducing epithelial-mesenchymal transition (EMT) as demonstrated by Yoshimatsu et al. inoral squamous cell carcinoma [25]. In addition, Fujiki et al. reported that TNF-α was able to facilitate the occurrence and development of gastric cancer [26]. Nevertheless, the relationship among TNF-α, lymphatic microvessel formation, and tumorigenesis in cervical cancer remains unclear. The aim of the present study was therefore to investigate the mechanism through which TNF-α regulates lymphatic microvessel formation in cervical cancer.

2. Materials and Methods

2.1. Cell Culture. HeLa and C33A human cervical cancer cell lines were purchased from the American Type Culture Collection and cultured in DMEM (Thermo Fisher Scientific, Inc.) supplemented with 10% fetal bovine serum (FBS, Thermo Fisher Scientific, Inc.) and 1% penicillin/streptomycin (Thermo Fisher Scientific, Inc.) with 5% CO_2 at 37°C. HLECs were obtained from Procell and cultured in a medium supplemented with 10% FBS, 1% penicillin/streptomycin, and 1% endothelial cell growth supplement (ECGS, CELL RESARCH) [27].

2.2. Conditional Medium (CM). HeLa and C33A cells were stimulated with different concentrations of TNF-α (0, 5, and 10 ng/ml) for 48 h at 37°C, and the corresponding CM (CM-TNF-α) was collected. Meanwhile, in the control group, cervical cancer cell lines were cultured in DMEM for 48 h at 37°C, and the corresponding CM was collected [28]. The CM was supplemented with 1% ECGS. After that, HLECs were cultured in CM with or without MAZ51 treatment.

2.3. ELISA Analysis. The level of VEGFC in the CM was detected using a VEGFC assay kit (cat. no. H046; Nanjing Jiancheng Bioengineering) [29]. The VEGFC inhibitor MAZ51 was purchased from MedChemExpress (cat. no. HY-116624).

2.4. CCK-8 Assay. Cell viability was measured using the CCK-8 assay by culturing HLECs in either CM or CM-TNF-α for 48 h, followed by incubation with 10 μl CCK-8 reagent (cat. no. C0047; Beyotime) for 2 h, and then the absorbance was measured at 450 nm using a microplate reader (Thermo Fisher Scientific) [30].

2.5. 5-Ethynyl-2′-Deoxyuridine (EdU) Staining. Cell proliferation was measured using an EdU staining assay. The EdU detection kit was purchased from Guangzhou RiboBio (cat. no. C10310-1). Firstly, HLECs were cultured in CM or CM-TNF-α for 48 h. Next, HLECs were incubated with 100 μl of 50 μm EdU for 1 h, washed with PBS, and incubated with 1 mg/ml DAPI for 10 min. Next, the EdU-positive HLECs were measured using a fluorescence microscope (IX51; Olympus) [31].

2.6. Tube Formation Assay. The number of tube node formed in the HLECs was observed using a tube formation assay. Matrigel-coated 24-well Transwell® (8 μm pore size) was purchased from Corning, Inc. HLECs were cultured in CM or CM-TNF-α for 48 h. Next, HLECs (1×10^5 cells) were placed in the Matrigel®-coated well at 37°C. Next, the number of tube node of HLECs was observed using a microscope (IX51; Olympus) [32].

2.7. Wound Healing Assay. Cell migration was determined using the wound-healing assay by culturing HLECs (5×10^5/cell) in a 6-well plate overnight, creating a wound in the monolayer using a 200 μl pipette tip, washing the cells with PBS, and then observing the scratch widths using a microscope (IX51; Olympus) after 0 and 24 h [31].

2.8. Transwell Migration Assay. Transwell assay was used by adding HLECs to the upper chamber containing serum-free DMEM andDMEM with 10% FBS t the lower chamber. The cells that had migrated to the lower chamber after24 hours of incubation were stained with crystal violet dye (cat. no. AS1086; ASPEN) and observed using a microscope (IX51; Olympus) [33].

2.9. Western Blotting. The total protein from cells and tumor tissues was extracted, the protein concentration was quantified using a BCA Protein Assay Kit (cat. no. AS1086; Aspen Biosciences) and 40 μg per lane of protein was separated by 10% SDS-PAGE and transferred onto PVDF membranes (EMD Millipore). The membranes were then incubated with primary antibodies: anti-AKT (1 : 1,000; cat. no. AF0836), anti-p-AKT (1 : 1,000; cat. no. 28731-1-AP), anti-ERK (1 : 1,000; cat. no. 11257-1-AP), anti-p-ERK (1 : 1,000; cat. no. 28733-1-AP), and anti-GAPDH (1 : 1,000; cat. no. 60004-1-Ig) overnight at 4°C. GAPDH was used as the internal reference. Next, the membranes were incubated with corresponding HRP-conjugated secondary antibodies for 1 h at room temperature. Finally, an enhanced chemiluminescent substrate kit (cat. no. AS1059; Aspen Biosciences) was used to observe the protein bands [34]. Anti-AKT, anti-p-AKT, anti-ERK, anti-p-AKT, and anti-GAPDH antibodies were obtained from Proteintech Group, Inc. The anti-AKT antibody was provided by Affinity Biosciences.

2.10. Animal Study. BALB/c nude mice (4-6 weeks old) were provided by Charles River Laboratories, Inc. All animals were maintained following the Guide for the Care and Use of Laboratory Animals by the National Institutes of Health. In addition, the experiments of animal study were approved by the Ethics Committee of HY cell biotechnology (No.
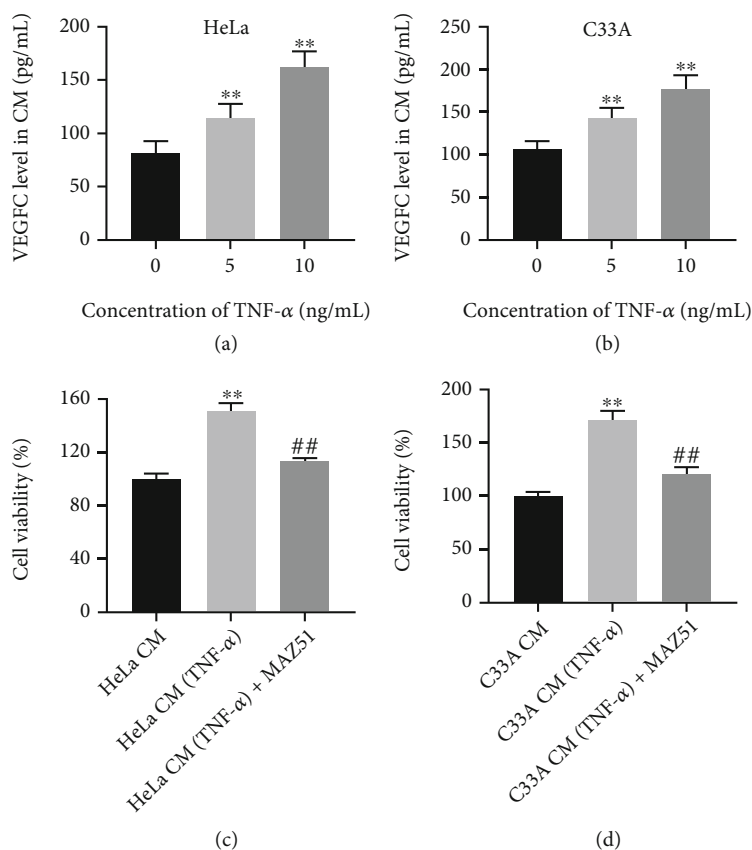
FIGURE 1: TNF-α stimulates cervical cancer cells to secrete VEGFC and promotes HLEC viability. (a, b) Cervical cancer cells (HeLa and C33A) were stimulated with different concentrations of TNF-α (0, 5, or 10 ng/ml) for 48 h, and corresponding CM was collected. Next, the level of VEGFC in the corresponding CM was detected by ELISA. (c, d) HLECs were cultured in CM with or without MAZ51 treatment. HLEC viability was measured by CCK-8 assay. $^{**}P < 0.01$ compared with CM group; $^{\#\#}P < 0.01$ compared with CM-TNF-α group, $n = 3$.

HY2021-33). C33A cells at the density of 1×10^7 cells were subcutaneously injected into the left flank of nude mice. Next, when the tumor volume reached ~200 mm^3, mice were randomly divided into three groups: control, TNF-α, and TNF-α+MAZ251 groups. TNF-α was intraperitoneally injected into mice in TNF-α and TNF-α+MAZ251 groups three times a week at 54 μg/kg for 3 weeks. In addition, MAZ51 was intraperitoneally injected into mice in the TNF-α+MAZ251 group once a day at 8 mg/kg for 15 days. Meanwhile, normal saline was intraperitoneally injected into mice in the control group. The tumor volume was measured weekly according to the following formula: volume = length $\times$ width^2/2 [35]. In 3 weeks, all mice were sacrificed using CO$_2$ (40% volume/min). And the tumors were photographed and weighted. Meanwhile, plasma samples were collected using anticoagulation tubes and then centrifuged for 10 min at 2,000 $\times$ g at 4°C.

2.11. Immunohistochemistry (IHC) Staining. A tumor tissue section was dewaxed with xylene. Antigens from the tumor tissue section were extracted with 0.01 M heated citrate buffers (pH 6.0). Next, 200 μl blocking solution was dropped onto the slices at room temperature for 1 h. The section was then incubated with a primary anti-D2-40 or PDPN antibody overnight at 4°C. Next, the section was washed with

PBS for 3 times. Subsequently, the section was incubated with secondary antibodies for 50 min at room temperature. DAB was then used for chromogenic reactions. In addition, the slices were placed in a hematoxylin solution for redyeing. Finally, the coverslip was placed over the section, and the staining results were observed using a microscope (CX31; Olympus Corporation) [36]. ImageJ software (with IHC Profiler plugins) was used for IHC scoring.

2.12. Real-Time PCR (RT-PCR). The TRIpure Total RNA Extraction Reagent (cat. no. EP013; ELK Biotechnology Co., Ltd.) was used to isolate the RNA from cells. Then, the EnTurbo™ SYBR Green PCR SuperMix kit (cat. no. EQ001; ELK Biotechnology Co., Ltd.) was used to perform RT-PCR. The cycling conditions for qPCR were as follows: 95°C for 3 min, followed by 95°C for 10 s, 58°C for 30 s, and 72°C for 30 s for 40 cycles. The information of primers: GAPDH forward, 5′-CATCATCCCTGCCTCTACTGG-3′ and reverse, 5′-GTGGGTGTCGCTGTTGAAGTC-3′; VEGFC forward, 5′-ACGAGCTACCTCAGCAAGACG-3′ and reverse, 5′-CTCCAGCATCCGAGGAAAAC-3′; D2-40 forward, 5′-CTATAAGTCTGGCTTGACAACTCT-3′ and reverse, 5′-CATCTTTCTCAACTGTTGTCTGTG-3′; VEGFR forward, 5′-GGGCATGTACTGACGATTATGG-3′ and reverse, 5′-
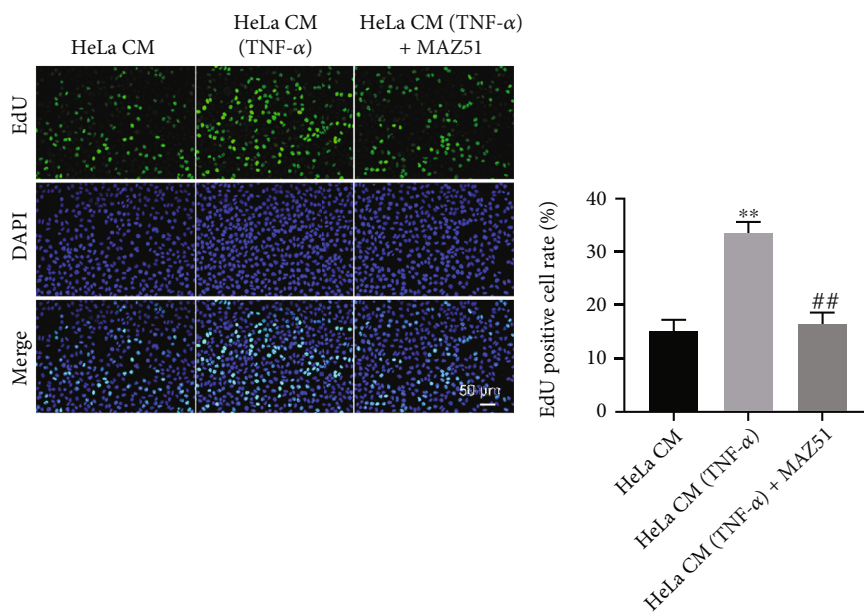
(a)

(b)

FIGURE 2: Continued.

(c)

(d)
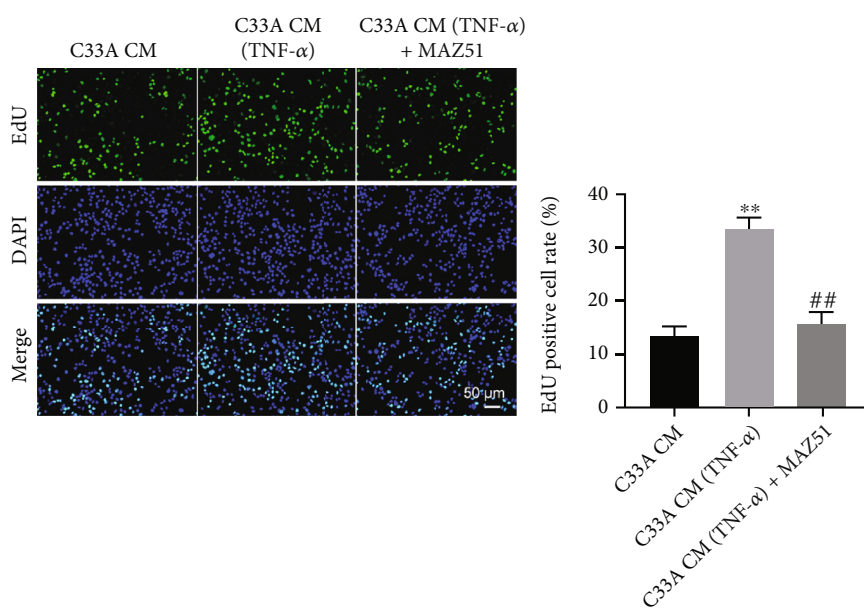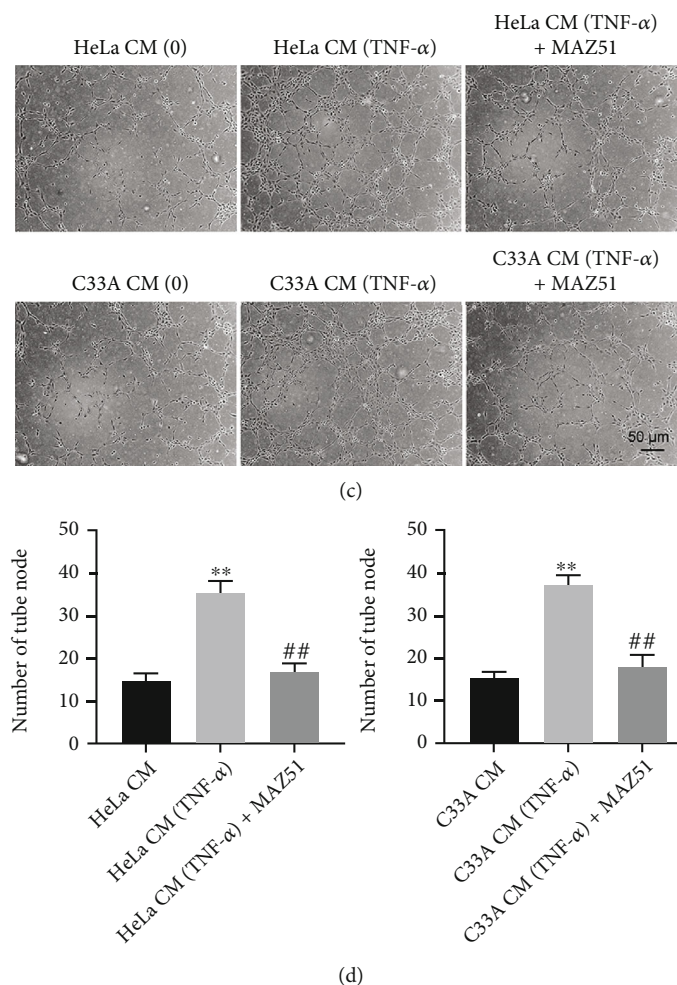
FIGURE 2: CM-TNF-α promotes the proliferation and angiogenesis of HLECs. Cervical cancer cells (HeLa and C33A) were stimulated with 10 ng/ml TNF-α for 48 h, and corresponding CM was collected. Next, HLECs were cultured in CM with or without MAZ51 treatment. (a, b) The proliferation of HLECs was measured by EdU staining assay. (c, d) The number of tube node of HLECs was observed using a microscope. $^{**}P < 0.01$ compared with CM group; $^{##}P < 0.01$ compared with CM-TNF-α group, $n = 3$.

GGAGGAATGGCATAGACCGTA-3$'$. The relative level of VEGFC, D2-40, and VEGFR was calculated using the $2^{-\Delta\Delta Ct}$ method [27, 37].

2.13. Statistical Analysis. The statistical analysis was performed using GraphPad Prism software version 7.0 (GraphPad Software, Inc.). Data are presented as the mean ± standard deviation and analyzed using a one-way analysis of variance and Tukey's post hoc test. $P < 0.05$ indicated a statistically significant difference [30, 38].

3. Results

3.1. TNF-α Promotes the Production of VEGFC in Cervical Cancer Cells. It has been reported that VEGFC is the most representative and important factor promoting the formation of tumor lymphangiogenesis [39, 40]. In addition, TNF-α was found to stimulate cell secretion of VEGF [41]. Our results found that TNF-α obviously upregulated the level of VEGFC in the CM of HeLa and C33A cells in a dose-dependent manner (Figures 1(a) and 1(b)). These

results showed that TNF-α promoted the production of VEGFC in cervical cancer cells.

3.2. CM-TNF-α Promotes HLEC Viability, Proliferation, and Angiogenesis. With the aim of investigating the effect of TNF-α on the formation of lymphangiogenesis in cervical cancer, HLECs were cultured in CM-TNF-α. As indicated in Figures 1(c) and 1(d) and 2(a) and 2(b), CM-TNF-α markedly promoted the viability and proliferation of HLECs. However, these phenomena were reversed in the presence of VEGFR3 inhibitor MAZ51 (Figures 1(c) and 1(d) and 2(a)and 2(b)). Meanwhile, CM-TNF-α significantly increased the number of tube node formed in HLECs, and that effect was notably inhibited by MAZ51 (Figures 2(c) and 2(d)). All these results indicated that CM-TNF-α could promote HLEC proliferation and angiogenesis by upregulating VEGFC.

3.3. CM-TNF-α Increases HLEC Migration. In order to study the role of TNF-α on HLEC migration, wound healing, and transwell assays were conducted. The results showed that CM-TNF-α significantly promoted HLEC migration, but

(a)

(b)

(c)

FIGURE 3: Continued.

(d)
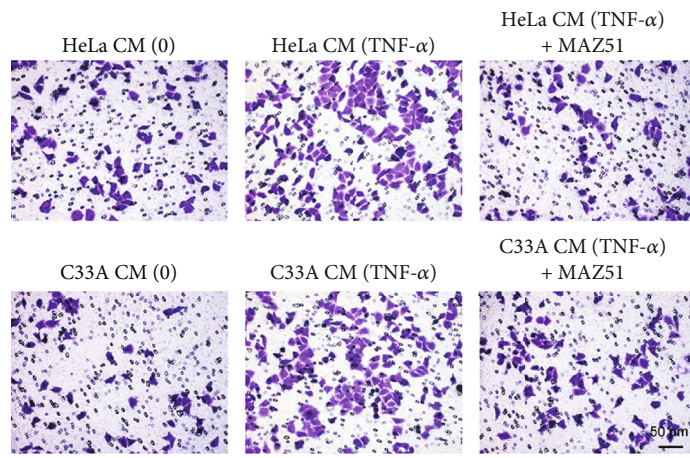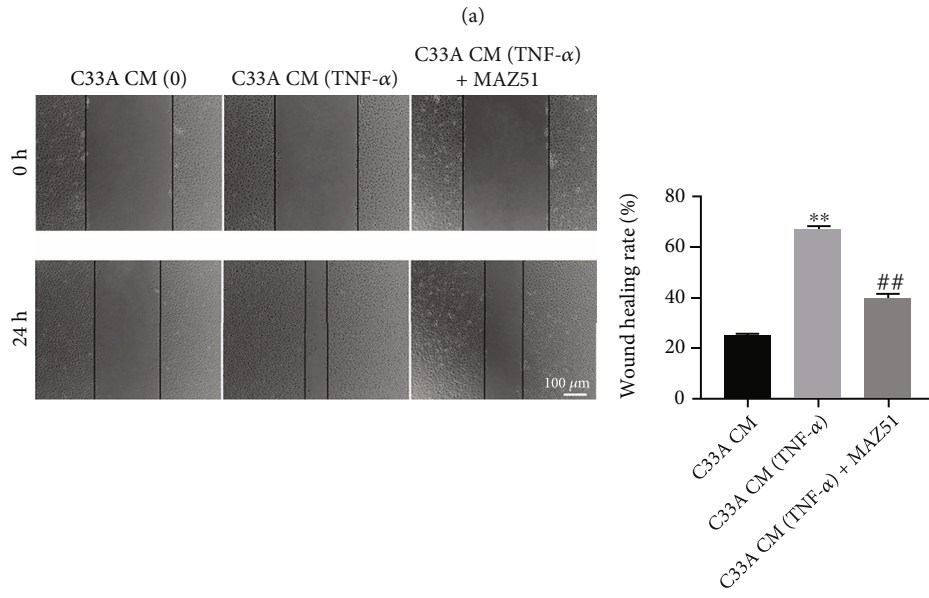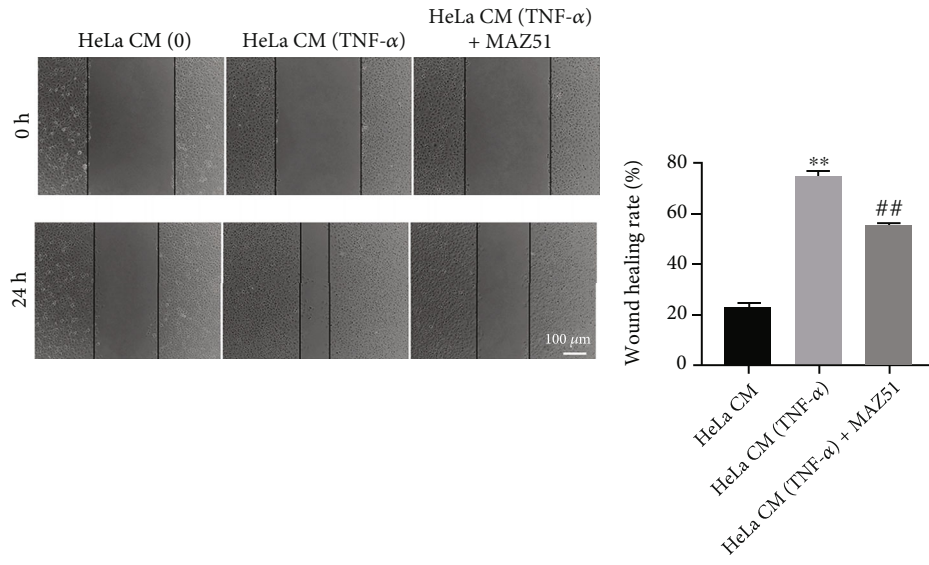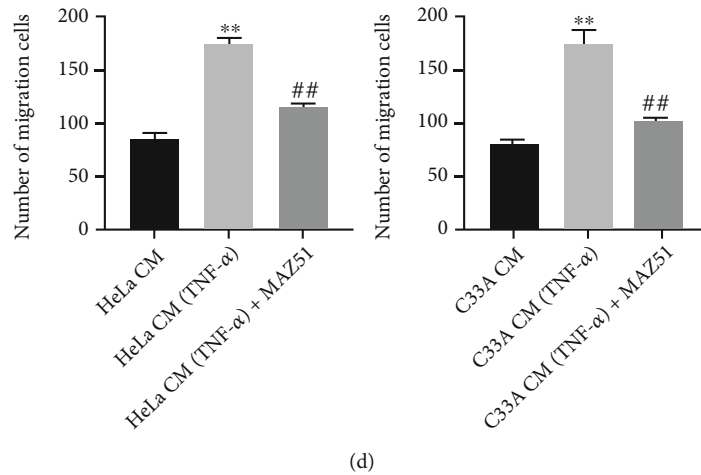
FIGURE 3: CM-TNF-α increases the migration of HLECs. Cervical cancer cells (HeLa and C33A) were stimulated with 10 ng/ml TNF-α for 48 h, and corresponding CM was collected. Next, HLECs were cultured in CM with or without MAZ51 treatment. (a, b) The migration of HLECs was measured by wound healing assay. (c, d) The migration of HLECs was measured by transwell migration assay. $^{**}P < 0.01$ compared with CM group; $^{##}P < 0.01$ compared with CM-TNF-α group, $n = 3$.

(a)   (b)   (c)
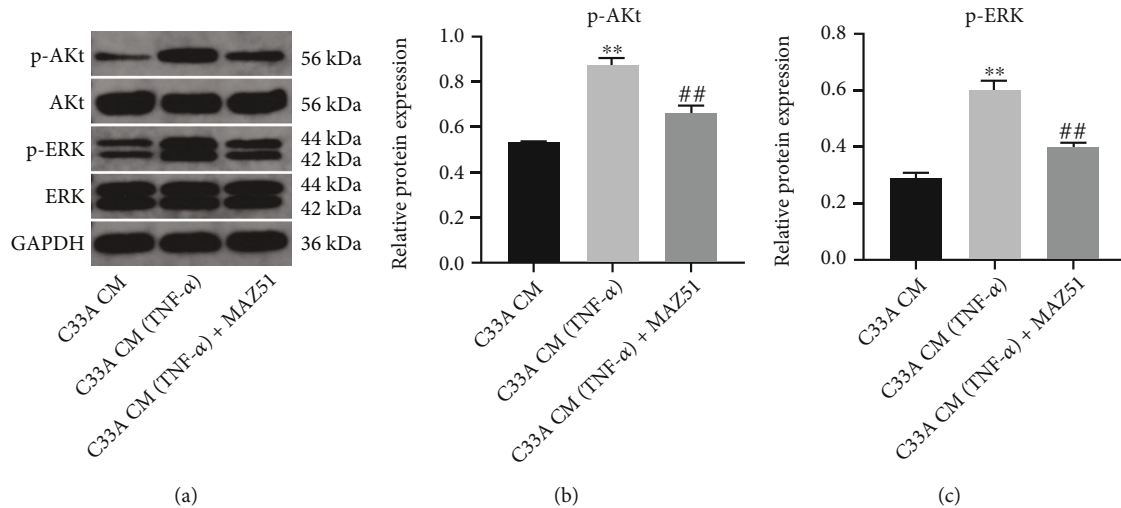
FIGURE 4: CM-TNF-α upregulates the expressions of p-AKT and p-ERK of HLECs. C33A cells were stimulated with 10 ng/ml TNF-α for 48 h, and the CM was collected. Next, HLECs were cultured in CM with or without MAZ51 treatment. (a–c) The levels of AKT, p-AKT, ERK, and p-ERK of HLECs were measured by western blot. $^{**}P < 0.01$ compared with CM group; $^{##}P < 0.01$ compared with CM-TNF-α group, $n = 3$.

MAZ51 clearly inhibited this promotion (Figures 3(a)–3(d)). These results showed that CM-TNF-α could increase HLEC migration by upregulating VEGFC.

3.4. CM-TNF-α Upregulates the Expressions of p-AKT and p-ERK of HLECs.

The AKT and ERK signaling pathways have been reported to play an important role in cervical cancer progression [42, 43]. In order to explore the mechanism by which TNF-α regulates the lymphangiogenesis of HLECs, the expressions of p-AKT and p-ERK were evaluated by western blotting. The results indicated that CM-TNF-α markedly increased the levels of p-AKT and p-ERK in HLECs, and these increases were markedly suppressed by MAZ51 (Figures 4(a)–4(c)). Collectively, CM-TNF-α could

promote the expressions of p-AKT and p-ERK in HLECs by upregulating VEGFC.

3.5. TNF-α Promotes the Tumorigenesis, Lymphangiogenesis, and Lymphatic Metastasis of Cervical Cancer In Vivo.

Finally, to confirm the effect of TNF-α on cervical cancer tumorigenesis and lymph node metastasis, a C33A subcutaneous xenograft model was established *in vivo*. As shown in Figures 5(a)–5(c), TNF-α remarkably promoted tumor volume and weight in C33A subcutaneous xenografts; however, this promotion was clearly inhibited by MAZ51 treatment. In addition, D2-40 has been reported as a specific marker of lymphatic endothelial cells that can be used in the study of lymph node metastasis [44, 45]. The IHC results suggested that TNF-α visibly increased D2-40 and PDPN levels

(a)

(b)

(c)

(d)

(e)

(f)

(g)
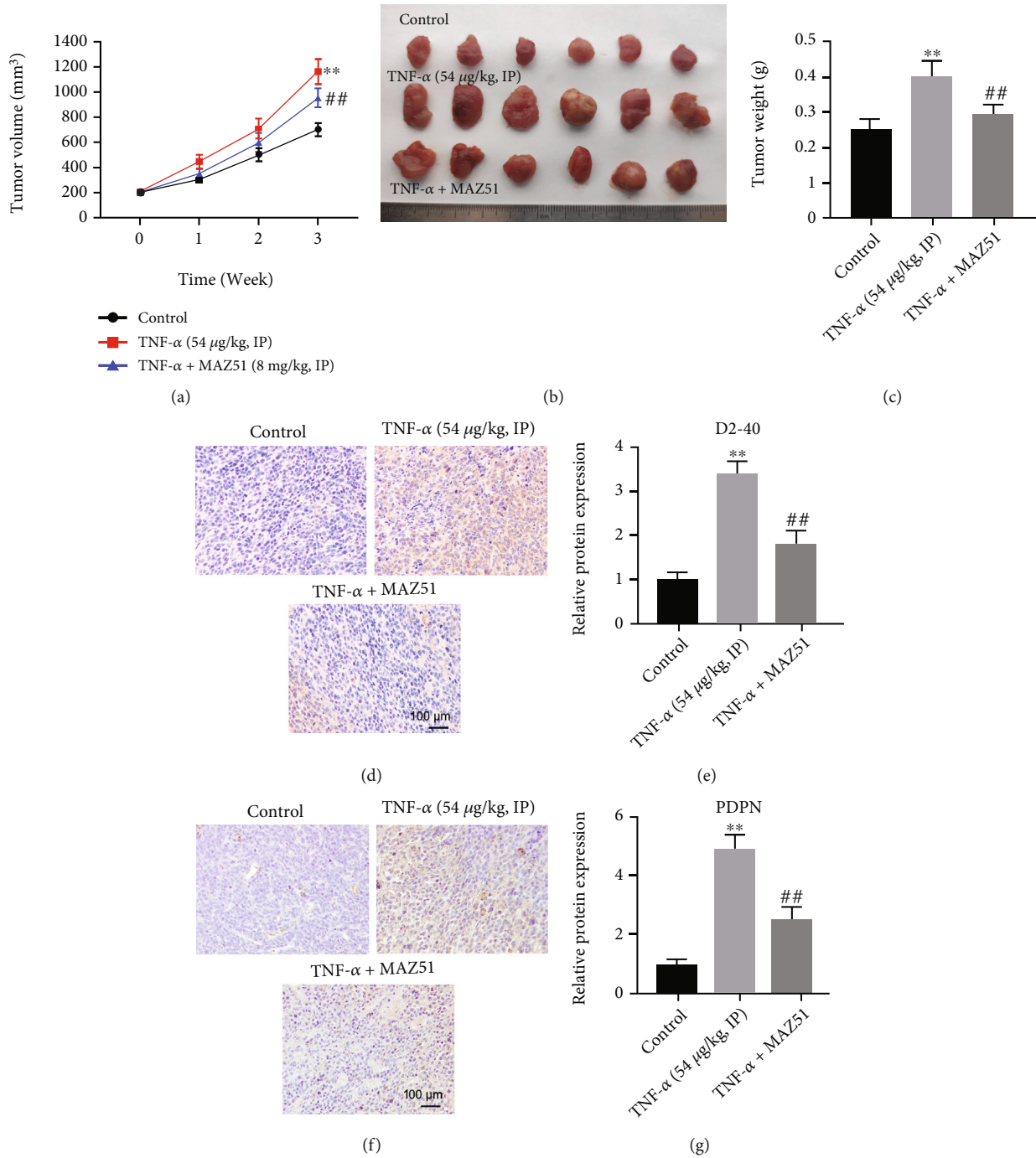
Figure 5: TNF-α promotes the tumorigenesis of cervical cancer *in vivo*. (a) The tumor volume was measured weekly. (b, c) The tumors were photographed and weighted. (d–g) The level of D2-40 or PDPN in tumor tissue was measured by IHC staining assay. $^{**}P < 0.01$ compared with control group; $^{\#\#}P < 0.01$ compared with TNF-α treated group, $n = 3$.

in tumor tissues, and these increases were reversed by MAZ51 (Figures 5(d)–5(g)).

Furthermore, ELISA results suggested that TNF-α significantly increased VEGFC expression in the plasma *in vivo*, which was reversed by MAZ51 (Figure 6(a)). Meanwhile, TNF-α visibly increased p-AKT and p-ERK expressions in tumor tissues, but these increases were reversed by MAZ51 (Figures 6(b)–6(d)). In addition, TNF-α upreg-

ulated the levels of VEGFC and D2-40 in tumor tissues compared with the control group (Figures 6(e) and 6(f)). Meanwhile, compared with the control group, TNF-α had few effects on VEGFR gene expression in tumor tissues (Figure 6(g)). In general, TNF-α could promote cervical cancer tumorigenesis, lymphangiogenesis, and lymphatic metastasis *in vivo* via activating VEGFC-mediated AKT and ERK pathways.

(a)

(b)

(c)

(d)

(e)

(f)

(g)
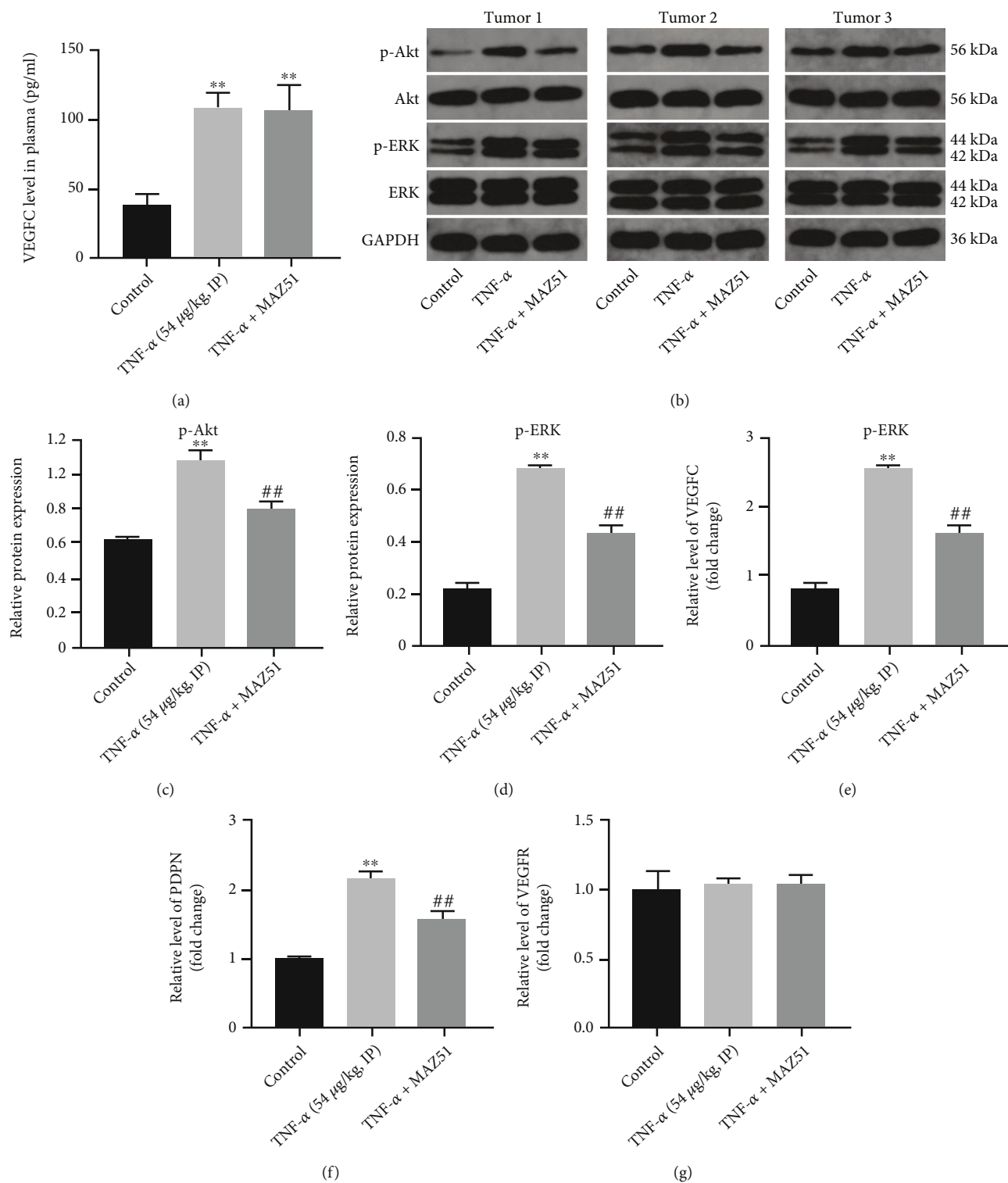
FIGURE 6: TNF-α upregulates p-AKT and p-ERK expression in tumor tissues via mediating VEGFC signaling *in vivo*. (a) The level of VEGFC in the plasma was measured by ELISA. (b–d) The levels of AKT, p-AKT, ERK, and p-ERK in tumor tissue were measured by western blot. (e–g) The levels of VEGFC, D2-40, and VEGFR were detected with RT-qPCR. $^{**}P < 0.01$ compared with control group; $^{##}P < 0.01$ compared with TNF-α treated group, $n = 3$.

4. Discussion

TNF-α is an important regulator of the inflammatory response [46, 47] that can activate neutrophils and lympho-cytes, increase vascular endothelial cell permeability, and regulate cellular and tissues metabolism [46, 48]. Therefore, studying the mechanism of inflammatory factors to promote tumor progression and metastasis has become a research

hotspot in recent years. For instance, TNF-α has been reported to promote tumor development and metastasis [24, 49]. Forkasiewicz et al. found that TNF-α could promote esophageal cancer cell migration [50]. In addition, Liang et al. showed that TNF-α could enhance gastric cancer cell migration and invasion via activating NF-κB signaling [51]. Consistent with that study, the present data indicated that CM-TNF-α could promote the growth of cervical cancer cells in vivo. Furthermore, this study showed that TNF-α could stimulate cervical cancer cells to secrete VEGFC, which in turn promoted the proliferation, migration, and angiogenesis of HLECs. Therefore, this study was the first to explore the effect of TNF-α on the progression of cervical cancer from the perspective of the TME.

The interaction between cancer cells and lymphatic endothelial cells is crucial in promoting tumor growth and metastasis in the TME, as demonstrated by previous studies [52, 53]. One of these studies showed that lymphatic endothelial cells could enhance the proliferation and migration of tumor cells [54], while cancer cells could also accelerate endothelial cell tube formation via activating the PI3K/Akt pathway [55]. Moreover, tumor-induced lymphangiogenesis is known to play a vital role in the initial stages of cancer metastasis [56], and the link between VEGFC and tumor lymphangiogenesis and metastasis has been extensively investigated [57, 58]. Chen et al. found that cancer cell-derived VEGFC could promote lymphangiogenesis in lymph nodes, which in return promotes cancer metastasis [59]. Meanwhile, He et al. showed that VEGFC could promote cervical cancer metastasis [60]. Besides, researchers have found that TNF-α could upregulate VEGFC expression, promoting lymphangiogenesis and lymphatic metastasis in gallbladder cancer [61]. In our study, we observed that the expression of VEGFC was significantly increased in the CM collected from the TNF-α-treated cervical cancer cells. CM collected from these cells also promoted the proliferation, migration, and angiogenesis of HLECs; and these changes were reversed by MAZ51, a VEGFR3 inhibitor. Furthermore, TNF-α elevated D2-40 and VEGFC protein expressions in tumor tissues, indicating that TNF-α could promote lymphangiogenesis and lymphatic metastasis of cervical cancer in vivo. Our findings suggest that TNF-α could be a promising target for cervical cancer treatment, as it promote lymphangiogenesis and lymphatic metastasis by upregulating VEGFC.

TNF-α was found to induce colorectal cancer cell migration and EMT via activating AKT signaling [62]. In addition, TNF-α could promote triple-negative breast cancer cell metastasis through targeting TNFR2-ERK1/2-EZH2 signaling [63]. These findings showed that TNF-α could promote tumor development via modulating AKT and ERK signaling pathways. Additionally, the literature suggested that the AKT and ERK signaling pathways are extensively involved in cervical cancer development [64–66]. For example, exosomal miR-221-3p secreted by cervical squamous cell carcinoma promoted the formation and metastasis of HLECs by upregulating the AKT/ERK pathway [67]. In addition, protein tyrosine phosphatase receptor M can induce lymphangiogenesis and lymph node metastasis through the AKT signaling pathway in a VEGFC-dependent manner [68]. In the present study, the CM collected from the TNF-α-treated cervical cancer cells was found to increase p-AKT and p-ERK expressions in HLECs. Moreover, TNF-α could upregulate p-AKT and p-ERK expressions in tumor tissues. However, inhibition of VEGFR3 obviously reversed these changes. All these data suggested that the AKT and ERK signaling pathways are involved in the lymphangiogenesis in cervical cancer.

In this study, we only determined that TNF-α could inhibit cervical cancer progression by targeting VEGFC-mediated AKT and ERK pathways. Thus, further study is needed to investigate whether TNF-α could affect the progression of cervical cancer via targeting other pathways, such as AMPK/mTOR or the NF-κB signaling pathway [69, 70].

5. Conclusion

To sum up, our study revealed that TNF-α activates VEGFC-mediated AKT and ERK pathways, leading to tumorigenesis, lymphangiogenesis, and lymphatic metastasis in vitro and in vivo in cervical cancer. We hope that our research will provide new directions for the treatment of cervical cancer.

Data Availability

All data, models, and code generated or used during the study are available from the corresponding author upon reasonable request.

Conflicts of Interest

These authors declared no competing interests in this research.

References

[1] M. Vu, J. Yu, O. A. Awolude, and L. Chuang, "Cervical cancer worldwide," Current Problems in Cancer, vol. 42, no. 5, pp. 457–465, 2018.

[2] P. Tsikouras, S. Zervoudis, B. Manav et al., "Cervical cancer: screening, diagnosis and staging," Journal of BUON: Official Journal of the Balkan Union of Oncology, vol. 21, no. 2, pp. 320–325, 2016.

[3] W. Lin, M. Feng, G. Chen, Z. Zhou, J. Li, and Y. Ye, "Characterization of the microRNA profile in early-stage cervical squamous cell carcinoma by next-generation sequencing," Oncology Reports, vol. 37, no. 3, pp. 1477–1486, 2017.

[4] J. Mei, C. Zhu, L. Pan, and M. Li, "MACC1 regulates the AKT/STAT3 signaling pathway to induce migration, invasion, cancer stemness, and suppress apoptosis in cervical cancer cells," *Bioengineered*, vol. 13, no. 1, pp. 61–70, 2022.

[5] P. Olusola, H. N. Banerjee, J. V. Philley, and S. Dasgupta, "Human papilloma virus-associated cervical cancer and health disparities," *Cell*, vol. 8, no. 6, p. 622, 2019.

[6] W. Lin, M. Feng, X. Li et al., "Transcriptome profiling of cancer and normal tissues from cervical squamous cancer patients by deep sequencing," *Molecular Medicine Reports*, vol. 16, no. 2, pp. 2075–2088, 2017.

[7] Y. Zhong, Q. Lu, W. Qiu, and Y. Luo, "LINC00636 promotes lymph node metastasis and cervical cancer through targeting NM23," *Bioscience Reports*, vol. 40, no. 10, 2020.

[8] C. Huang and Y. Chen, "Lymphangiogenesis and colorectal cancer," *Saudi Medical Journal*, vol. 38, no. 3, pp. 237–244, 2017.

[9] P. Cohen, A. Jhingran, A. Oaknin, and L. Denny, "Cervical cancer," *The Lancet*, vol. 393, no. 10167, pp. 169–182, 2019.

[10] D. Vordermark, "Radiotherapy of cervical cancer," *Oncology Research and Treatment*, vol. 39, no. 9, pp. 516–520, 2016.

[11] L. Kumar, P. Harish, P. S. Malik, and S. Khurana, "Chemotherapy and targeted therapy in the management of cervical cancer," *Current Problems in Cancer*, vol. 42, no. 2, pp. 120–128, 2018.

[12] G. Marquina, A. Manzano, and A. Casado, "Targeted agents in cervical cancer: beyond bevacizumab," *Current Oncology Reports*, vol. 20, no. 5, p. 40, 2018.

[13] D. C. Hinshaw and L. A. Shevde, "The tumor microenvironment innately modulates cancer progression," *Cancer Research*, vol. 79, no. 18, pp. 4557–4566, 2019.

[14] N. M. Iyengar, A. Gucalp, A. J. Dannenberg, and C. A. Hudis, "Obesity and cancer mechanisms: tumor microenvironment and inflammation," *Journal of Clinical Oncology: Official Journal of the American Society of Clinical Oncology*, vol. 34, no. 35, pp. 4270–4276, 2016.

[15] A. Rizzo, F. Pallone, G. Monteleone, and M. C. Fantini, "Intestinal inflammation and colorectal cancer: a double-edged sword?," *World Journal of Gastroenterology*, vol. 17, no. 26, pp. 3092–3100, 2011.

[16] H. Chaudhry, J. Zhou, Y. Zhong et al., "Role of cytokines as a double-edged sword in sepsis," *In Vivo (Athens, Greece)*, vol. 27, no. 6, pp. 669–684, 2013.

[17] P. Schreiner and L. Biedermann, "Editorial: anti-TNF therapy—a double-edged sword?," *Alimentary Pharmacology & Therapeutics*, vol. 50, no. 7, pp. 822-823, 2019.

[18] A. Garancher, H. Suzuki, S. Haricharan et al., "Tumor necrosis factor overcomes immune evasion in p53-mutant medulloblastoma," *Nature Neuroscience*, vol. 23, no. 7, pp. 842–853, 2020.

[19] T. Wang, B. Chen, T. Meng, Z. Liu, and W. Wu, "Identification and immunoprofiling of key prognostic genes in the tumor microenvironment of hepatocellular carcinoma," *Bioengineered*, vol. 12, no. 1, pp. 1555–1575, 2021.

[20] E. W. Lin, T. A. Karakasheva, P. D. Hicks, A. J. Bass, and A. K. Rustgi, "The tumor microenvironment in esophageal cancer," *Oncogene*, vol. 35, no. 41, pp. 5337–5349, 2016.

[21] H. J. Patel and B. M. Patel, "TNF-α and cancer cachexia: molecular insights and clinical implications," *Life Sciences*, vol. 170, pp. 56–63, 2017.

[22] S. W. Coppack, "Pro-inflammatory cytokines and adipose tissue," *The Proceedings of the Nutrition Society*, vol. 60, no. 3, pp. 349–356, 2001.

[23] E. Tamburrini, A. De Luca, G. Ventura et al., "Macrophages from healthy adults release TNF-alpha after exposure to Pneumocystis carinii of murine origin. Preliminary study," *Medicina (Florence, Italy)*, vol. 10, no. 4, pp. 393-394, 1990.

[24] D. Cruceriu, O. Baldasici, O. Balacescu, and I. Berindan-Neagoe, "The dual role of tumor necrosis factor-alpha (TNF-α) in breast cancer: molecular insights and therapeutic approaches," *Cellular Oncology (Dordrecht)*, vol. 43, no. 1, pp. 1–18, 2020.

[25] Y. Yoshimatsu, I. Wakabayashi, S. Kimuro et al., "TNF-α enhances TGF-β-induced endothelial-to-mesenchymal transition via TGF-β signal augmentation," *Cancer Science*, vol. 111, no. 7, pp. 2385–2399, 2020.

[26] H. Fujiki and M. Suganuma, "Tumor promoters–microcystin-LR, nodularin and TNF-α and human cancer development," *Anti-Cancer Agents in Medicinal Chemistry*, vol. 11, no. 1, pp. 4–18, 2011.

[27] C. Chen, Y. Luo, W. He et al., "Exosomal long noncoding RNA LNMAT2 promotes lymphatic metastasis in bladder cancer," *The Journal of Clinical Investigation*, vol. 130, no. 1, pp. 404–421, 2020.

[28] Q. Li, L. Liu, Q. Zhang, S. Liu, D. Ge, and Z. You, "Interleukin-17 indirectly promotes M2 macrophage differentiation through stimulation of COX-2/PGE2 pathway in the cancer cells," *Cancer Research and Treatment*, vol. 46, no. 3, pp. 297–306, 2014.

[29] J. Yu, Y. Li, Z. Li et al., "Subconjunctival injections of dimethyl fumarate inhibit lymphangiogenesis and allograft rejection in the rat cornea," *International Immunopharmacology*, vol. 96, article 107580, 2021.

[30] X. Wang, H. Sun, and S. Zhu, "Long non-coding RNA PTAR inhibits apoptosis but promotes proliferation, invasion and migration of cervical cancer cells by binding miR-101," *Bioengineered*, vol. 12, no. 1, pp. 4536–4545, 2021.

[31] G. Shi and F. Yang, "Krüppel-like factor 1 (KLF1) promoted the proliferation, migration and invasion of human lens epithelial cells by enhancing the expression of zinc finger and BTB domain containing 7A (ZBTB7A) and activating Wnt/β-catenin pathway," *Bioengineered*, vol. 12, no. 1, pp. 4374–4384, 2021.

[32] H. Han and X. Xu, "MiR-205 promotes the viability, migration, and tube formation of cervical cancer cells *in vitro* by targeting *GATA3*," *Cancer Biotherapy & Radiopharmaceuticals*, vol. 37, no. 9, pp. 779–791, 2022.

[33] Y. Yang, C. Xiao, K. Liu, L. Song, Y. Zhang, and B. Dong, "Silencing of long noncoding INHBA antisense RNA1 suppresses proliferation, migration, and extracellular matrix deposition in human hypertrophic scar fibroblasts via regulating microRNA-141-3p/myeloid cell leukemia 1 axis," *Bioengineered*, vol. 12, no. 1, pp. 1663–1675, 2021.

[34] X. He, C. Li, H. Yin et al., "Mesenchymal stem cells inhibited the apoptosis of alveolar epithelial cells caused by ARDS through CXCL12/CXCR4 axis," *Bioengineered*, vol. 13, no. 4, pp. 9060–9070, 2022.

[35] S. Y. Zhu, Q. Y. Wu, C. X. Zhang et al., "miR-20a inhibits the killing effect of natural killer cells to cervical cancer cells by downregulating RUNX1," *Biochemical and Biophysical Research Communications*, vol. 505, no. 1, pp. 309–316, 2018.

[36] L. Zan, Q. Chen, L. Zhang, and X. Li, "Epigallocatechin gallate (EGCG) suppresses growth and tumorigenicity in breast cancer cells by downregulation of miR-25," *Bioengineered*, vol. 10, no. 1, pp. 374–382, 2019.

[37] M. Ni, Q. Yan, H. Xue, Y. Du, S. Zhao, and Z. Zhao, "Identification of MYLIP gene and miRNA-802 involved in the growth and metastasis of cervical cancer cells," *Cancer Biomarkers: Section A of Disease Markers*, vol. 30, no. 3, pp. 287–298, 2021.

[38] Y. Shou, X. Wang, Y. Liang, X. Liu, and K. Chen, "Exosomes-derived miR-154-5p attenuates esophageal squamous cell carcinoma progression and angiogenesis by targeting kinesin family member 14," *Bioengineered*, vol. 13, no. 2, pp. 4610–4620, 2022.

[39] M. Raica, A. M. Cimpean, R. Ceausu, and D. Ribatti, "Lymphatic microvessel density, VEGF-C, and VEGFR-3 expression in different molecular types of breast cancer," *Anticancer Research*, vol. 31, no. 5, pp. 1757–1764, 2011.

[40] M. Franc, A. Kachel-Flis, B. Michalski et al., "Lymphangiogenesis in cervical cancer evaluated by expression of the *VEGF-C* gene in clinical stage IB-IIIB," *Menopause Review/Przegląd Menopauzalny*, vol. 14, no. 2, pp. 112–117, 2015.

[41] M. Wang, P. R. Crisostomo, C. Herring, K. K. Meldrum, and D. R. Meldrum, "Human progenitor cells from bone marrow or adipose tissue produce VEGF, HGF, and IGF-I in response to TNF by a p38 MAPK-dependent mechanism," *American Journal of Physiology. Regulatory, Integrative and Comparative Physiology*, vol. 291, no. 4, pp. R880–R884, 2006.

[42] W. Zhang, Q. Zhou, Y. Wei et al., "The exosome-mediated PI3k/Akt/mTOR signaling pathway in cervical cancer," *International Journal of Clinical and Experimental Pathology*, vol. 12, no. 7, pp. 2474–2484, 2019.

[43] H. Ma, F. Han, X. Yan et al., "PBK promotes aggressive phenotypes of cervical cancer through ERK/c-Myc signaling pathway," *Journal of Cellular Physiology*, vol. 236, no. 4, pp. 2767–2781, 2021.

[44] N. Abe, T. Ohtake, K. Saito, K. Kumamoto, T. Sugino, and S. Takenoshita, "Clinicopathological significance of lymphangiogenesis detected by immunohistochemistry using D2-40 monoclonal antibody in breast cancer," *Fukushima Journal of Medical Science*, vol. 62, no. 1, pp. 57–63, 2016.

[45] M. Braun, U. Flucke, M. Debald et al., "Detection of lymphovascular invasion in early breast cancer by D2-40 (podoplanin): a clinically useful predictor for axillary lymph node metastases," *Breast Cancer Research and Treatment*, vol. 112, no. 3, pp. 503–511, 2008.

[46] Y. Wen, N. P. Rudemiller, J. Zhang et al., "TNF-α in T lymphocytes attenuates renal injury and fibrosis during nephrotoxic nephritis," *American Journal of Physiology Renal Physiology*, vol. 318, no. 1, pp. F107–F116, 2020.

[47] F. Yan, D. Wufuer, J. Ding, and J. Wang, "MicroRNA miR-146a-5p inhibits the inflammatory response and injury of airway epithelial cells via targeting TNF receptor-associated factor 6," *Bioengineered*, vol. 12, no. 1, pp. 1916–1926, 2021.

[48] Y. Lu, Z. Lian, H. Yang et al., "TNF-α activates RhoA/ROCK signaling pathway and increases permeability of endothelial cells infected with Listeria monocytogenes," *Xi Bao yu fen zi Mian yi xue za zhi = Chinese Journal of Cellular and Molecular Immunology*, vol. 36, no. 3, pp. 193–197, 2020.

[49] C. W. Hu, Y. C. Chang, C. H. Liu, Y. A. Yu, and K. Y. Mou, "Development of a TNF-α-mediated Trojan horse for bacteria-based cancer therapy," *Molecular Therapy: The Journal of the American Society of Gene Therapy*, vol. 30, no. 7, pp. 2522–2536, 2022.

[50] A. Forkasiewicz, W. Stach, J. Wierzbicki et al., "Effect of LDHA inhibition on TNF-α-induced cell migration in esophageal cancers," *International Journal of Molecular Sciences*, vol. 23, no. 24, p. 16062, 2022.

[51] X. Liang, Z. Feng, R. Yan et al., "Kruppel-like factors 3 regulates migration and invasion of gastric cancer cells through NF-κB pathway," *Alternative Therapies in Health and Medicine*, vol. 29, pp. 64–69, 2022.

[52] E. Lee, N. B. Pandey, and A. S. Popel, "Crosstalk between cancer cells and blood endothelial and lymphatic endothelial cells in tumour and organ microenvironment," *Expert Reviews in Molecular Medicine*, vol. 17, article e3, 2015.

[53] B. S. Lee, J. Y. Jang, C. Seo, and C. H. Kim, "Crosstalk between head and neck cancer cells and lymphatic endothelial cells promotes tumor metastasis via CXCL5-CXCR2 signaling," *FASEB Journal: Official Publication of the Federation of American Societies for Experimental Biology*, vol. 35, no. 1, article e21181, 2021.

[54] M. Van de Velde, M. Ebroin, T. Durré et al., "Tumor exposed-lymphatic endothelial cells promote primary tumor growth via IL6," *Cancer Letters*, vol. 497, pp. 154–164, 2021.

[55] H. W. Cheng, Y. F. Chen, J. M. Wong et al., "Cancer cells increase endothelial cell tube formation and survival by activating the PI3K/Akt signalling pathway," *Journal of Experimental & Clinical Cancer Research : CR*, vol. 36, no. 1, p. 27, 2017.

[56] S. Li and Q. Li, "Cancer stem cells, lymphangiogenesis, and lymphatic metastasis," *Cancer Letters*, vol. 357, no. 2, pp. 438–447, 2015.

[57] W. Lin, L. Jiang, Y. Chen et al., "Vascular endothelial growth factor-D promotes growth, lymphangiogenesis and lymphatic metastasis in gallbladder cancer," *Cancer Letters*, vol. 314, no. 2, pp. 127–136, 2012.

[58] R. C. Ji, "Lymphatic endothelial cells, tumor lymphangiogenesis and metastasis: new insights into intratumoral and peritumoral lymphatics," *Cancer Metastasis Reviews*, vol. 25, no. 4, pp. 677–694, 2006.

[59] J. Y. Chen, Y. S. Lai, P. Y. Chu, S. H. Chan, L. H. Wang, and W. C. Hung, "Cancer-derived VEGF-C increases chemokine production in lymphatic endothelial cells to promote CXCR2-dependent cancer invasion and MDSC recruitment," *Cancers*, vol. 11, no. 8, p. 1120, 2019.

[60] M. He, Y. Cheng, W. Li et al., "Vascular endothelial growth factor C promotes cervical cancer metastasis via up-regulation and activation of RhoA/ROCK-2/moesin cascade," *BMC Cancer*, vol. 10, no. 1, p. 170, 2010.

[61] C. Z. Li, X. J. Jiang, B. Lin et al., "RIP1 regulates TNF-α-mediated lymphangiogenesis and lymphatic metastasis in gallbladder cancer by modulating the NF-κB-VEGF-C pathway," *OncoTargets and Therapy*, vol. 11, pp. 2875–2890, 2018.

[62] H. Wang, H. S. Wang, B. H. Zhou et al., "Epithelial-mesenchymal transition (EMT) induced by TNF-α requires AKT/GSK-3β-mediated stabilization of snail in colorectal cancer," *PLoS One*, vol. 8, no. 2, article e56664, 2013.

[63] X. Y. Mei, J. N. Zhang, W. Y. Jia et al., "Scutellarin suppresses triple-negative breast cancer metastasis by inhibiting TNFα-induced vascular endothelial barrier breakdown," *Acta Pharmacologica Sinica*, vol. 43, no. 10, pp. 2666–2677, 2022.

[64] Y. H. Chen, S. F. Yang, C. K. Yang et al., "Metformin induces apoptosis and inhibits migration by activating the AMPK/p53 axis and suppressing PI3K/AKT signaling in human cervical cancer cells," *Molecular Medicine Reports*, vol. 23, no. 1, 2020.

[65] Y. Che, Y. Li, F. Zheng et al., "TRIP4 promotes tumor growth and metastasis and regulates radiosensitivity of cervical cancer by activating MAPK, PI3K/AKT, and hTERT signaling," *Cancer Letters*, vol. 452, pp. 1–13, 2019.

[66] X. Lu, X. Song, X. Hao et al., "miR-186-3p attenuates the tumorigenesis of cervical cancer via targeting insulin-like growth factor 1 to suppress PI3K-Akt signaling pathway," *Bioengineered*, vol. 12, no. 1, pp. 7079–7092, 2021.

[67] C. F. Zhou, J. Ma, L. Huang et al., "Cervical squamous cell carcinoma-secreted exosomal miR-221-3p promotes lymphangiogenesis and lymphatic metastasis by targeting VASH1," *Oncogene*, vol. 38, no. 8, pp. 1256–1268, 2019.

[68] P. Liu, C. Zhang, Y. Liao et al., "High expression of PTPRM predicts poor prognosis and promotes tumor growth and lymph node metastasis in cervical cancer," *Cell Death & Disease*, vol. 11, no. 8, p. 687, 2020.

[69] X. Zhao, Y. Lin, B. Jiang et al., "Icaritin inhibits lung cancer-induced osteoclastogenesis by suppressing the expression of IL-6 and TNF-a and through AMPK/mTOR signaling pathway," *Anti-Cancer Drugs*, vol. 31, no. 10, pp. 1004–1011, 2020.

[70] A. Mukhopadhyay, S. Shishodia, J. Suttles et al., "Ectopic expression of protein-tyrosine kinase Bcr-Abl suppresses tumor necrosis factor (TNF)-induced NF-κB activation and IκBα phosphorylation," *The Journal of Biological Chemistry*, vol. 277, no. 34, pp. 30622–30628, 2002.

Research Article

Prognostic and Immunological Significance of the Molecular Subtypes and Risk Signatures Based on Cuproptosis in Hepatocellular Carcinoma

Xiaolong Tang [iD],[1,2] **Xiangqing Ren,**[1] **Tian Huang,**[1] **Yandong Miao** [iD],[3] **Wuhua Ha,**[1] **Zheng Li,**[4] **Lixia Yang** [iD],[5] **and Denghai Mi** [iD][1,5]

[1]*The First Clinical Medical College, Lanzhou University, Lanzhou City, Gansu Province, China*
[2]*The Second Department of Gastrointestinal Surgery, Affiliated Hospital of North Sichuan Medical College, Nanchong City, Sichuan Province, China*
[3]*The Second Department of Medical Oncology, Yantai Affiliated Hospital of Binzhou Medical University, The 2nd Medical College of Binzhou Medical University, Yantai City, Shandong Province, China*
[4]*Institute of Modern Physics, Chinese Academy of Sciences, Lanzhou City, Gansu Province, China*
[5]*Gansu Academy of Traditional Chinese Medicine, Lanzhou City, Gansu Province, China*

Correspondence should be addressed to Lixia Yang; yanglixia-415@163.com and Denghai Mi; mi.dh@outlook.com

Background. Hepatocellular carcinoma (HCC) remains a challenging medical problem. Cuproptosis is a novel form of cell death that plays a crucial role in tumorigenesis, angiogenesis, and metastasis. However, it remains unclear whether cuproptosis-related genes (CRGs) influence the outcomes and immune microenvironment of HCC patients. *Method.* From The Cancer Genome Atlas (TCGA) and International Cancer Genome Consortium (ICGC) databases, we obtained the mRNA expression file and related clinical information of HCC patients. We selected 19 CRGs as candidate genes for this study according to previous literature. We performed a differential expression analysis of the 19 CRGs between malignant and precancerous tissue. Based on the 19 CRGs, we enrolled cluster analysis to identify cuproptosis-related subtypes of HCC patients. A prognostic risk signature was created utilizing univariate Cox regression and least absolute shrinkage and selection operator (LASSO) regression analyses. We employed independent and stratification survival analyses to investigate the predictive value of this model. The functional enrichment features, mutation signatures, immune profile, and response to immunotherapy of HCC patients were also investigated according to the two molecular subtypes and the prognostic signature. *Results.* We found that 17 CRGs significantly differed in HCC versus normal samples. Cluster analysis showed two distinct molecular subtypes of cuproptosis. Cluster 1 is preferentially related to poor prognosis, high activity of immune response signaling, high mutant frequency of *TP53*, and distinct immune cell infiltration versus cluster 2. Through univariate and LASSO Cox regression analyses, we created a cuproptosis-related prognostic risk signature containing *LIPT1*, *DLAT*, *MTF1*, *GLS*, and *CDKN2A*. High-risk HCC patients were shown to have a worse prognosis. The risk signature was proved to be an independent predictor of prognosis in both the TCGA and ICGC datasets, according to multivariate analysis. The signature also performed well in different stratification of clinical features. The immune cells, which included regulatory T cells (Treg), B cells, macrophages, mast cells, NK cells, and aDCs, as well as immune functions containing cytolytic activity, MHC class I, and type II IFN response, were remarkably distinct between the high-risk and low-risk groups. The tumor immune dysfunction and exclusion (TIDE) score suggested that high-risk patients had a higher response rate to immune checkpoint inhibitors than low-risk patients. *Conclusion.* This research discovered the potential prognostic and immunological significance of cuproptosis in HCC, improved the understanding of cuproptosis, and may deliver new directions for developing more efficacious therapeutic techniques for HCC patients.

1. Introduction

Primary liver cancer remains a serious threat to global public health in 2020, with over 906,000 new cases and 830,000 fatalities [1]. Most liver cancer cases involve hepatocellular carcinoma (HCC), which accounts for about 90%. Chronic hepatitis B or C virus infection, alcohol abuse, and metabolic syndrome induced by obesity and diabetes are the key risk elements for the occurrence of HCC [2]. Early-stage HCC is remediable through surgery or ablation. Nevertheless, there are very few medicinal choices available for advanced-stage HCC patients due to strong and broad resistance to cyto-toxic chemotherapy [3]. Sorafenib, a multityrosine kinase inhibitor (mTKI) with antiangiogenic and antiproliferative properties, has been the regular first-line treatment for advanced HCC for more than a decade [4, 5]. Nevertheless, it is estimated that only a small ratio of HCC patients responds to sorafenib. Up to now, significant efforts have been dedicated to enhancing the medicinal condition of advanced-stage HCC patients in the past few years, with the approval of four agents: lenvatinib [6] as front-line treatment, ramucirumab [7], cabozantinib [8], and regorafenib [9] as second-line treatment. By utilizing antiprogrammed death protein 1 (PD-1) antibodies, immune checkpoint blockade (ICB) has been licensed to treat HCC in second-line [10, 11]. Despite a marked increase in the choice of systemic therapies, there has been a modest improvement in patient outcomes. Therefore, there is a pressing demand for new molecular biomarkers for HCC patients in order to guide more personalized treatment decisions.

Copper is an essential nutrient for the human body. Meanwhile, copper can cause cell death via cytotoxicity, which is driven by improved mitochondrial-dependent energy metabolism and increased reactive oxygen species (ROS). The phenomenon of cell death because of copper is termed "cuproptosis" [12]. Specifically, cuproptosis is caused by copper in combination with lipidated components of the tricarboxylic acid cycle (TCA). Eventually, proteotoxic pressure and cell death occur as a lack of iron-sulfur cluster proteins and a result of lipoylated protein aggregation. Cuproptosis was classified as a new kind of regulated cell death distinct from the recognized cell death pathway, such as apoptosis, necrosis, autophagy, ferroptosis, and pyroptosis [12]. The process of cell death is inextricably linked to tumor development and the immune microenvironment [13]. The potential role of cuproptosis in clinical outcomes, as well as its immune characterization, warrants further study. As for cancer treatment, ionophores for copper supplementation are the primary current therapeutic approach based on cuproptosis, including disulfiram (DSF) and elesclomol [14–16]. In Wilson's disease, due to ATP7B deletion, a pro-gressive hepatic copper overload may happen in the hepatocytes and lead to liver failure [17]. The improved incidence of HCC in patients with Wilson's disease provides evidence that aberrant copper homeostasis may contribute to HCC development through an unknown mechanism [18]. In both in vitro [19] and in vivo [20], copper excess caused cell death in hepatocytes through the intrinsic pathway. Nevertheless, cuproptosis's contribution to the tumorigenesis and development of HCC has not yet been fully understood.

In our study, we identified a substantial variance in the expression level of cuproptosis-related genes (CRGs) between malignant and precancerous tissue, which may reveal the close relationship between CRGs and HCC development. Next, we performed the consensus cluster analysis and identified two cuproptosis-associated clusters, which were significantly likened to patient survival and immune characterization. We then explored the prognostic value of CRGs for the outcomes of HCC patients and built a prog-nostic risk model containing five CRGs to predict prognosis, somatic mutation signature, immune microenvironment, and response to immunotherapy in HCC. According to multiple datasets, including The Cancer Genome Atlas (TCGA) and International Cancer Genome Consortium (ICGC), this risk model performed high accuracy in evaluating HCC prognoses. These findings can contribute to further insight into the importance of CRGs in HCC development and support further clinical development of cuproptosis for HCC.

2. Materials and Methods

2.1. Data Resources and Preprocessing.
The TCGA (https://portal.gdc.cancer.gov/) provided the somatic mutation information, mRNA expression profile, and matched clinical data for liver hepatocellular carcinoma (LIHC) cases. Through the ICGC (https://dcc.icgc.org/), the project (code: LIRI_JP) on liver cancer was downloaded. R (version 4.2.0) software was enrolled to collate and annotate the somatic mutation and RNA-sequencing data. The TCGA database contained 50 normal tissues and 374 tumor tissues, and the ICGC database contained 202 normal tissues and 243 normal tissues. Then, the mRNA expression files were standardized with fragments per kilobase per million mapped reads (FPKM). To scale data among different databases, we adopted the "scale" function in the "limma" R package [21].

2.2. Exploration of the Differentially Expressed CRGs in HCC.
The cuproptosis-related differentially expressed genes (DEGs) were detected between malignant and precancerous tissue of HCC patients in the TCGA with the "limma" R package. p values <0.05 were regarded as the cutoff values for identifying DEGs. Through the "heatmap" R package [22], we generated a heatmap of cuproptosis-related DEG expression levels between HCC and normal tissue. To better know the connections among CRGs, we examined the relationship between CRGs through Pearson's correlation analysis. The online tool STRING [23] was taken advantage to conduct protein-protein interactions (PPI) network, and the Cytoscape tool was enrolled to picture the network [24].

2.3. Consensus Clustering Analysis.
To further investigate the biological features of CRGs in HCC, with the "ConsensusClusterPlus" R package [25], the patients in TCGA were classified into two clusters according to the 19 CRGs.

2.4. Functional Enrichment Analysis.
To discover the gene functions and biological pathways of the CRGs, we operated Gene Ontology (GO) and Kyoto Encyclopedia of Genes and Genomes (KEGG) pathway enrichment analyses of CRGs utilizing the R packages "limma" and "clusterProfiler" [26].

(a)

(b)

(c)

(d)
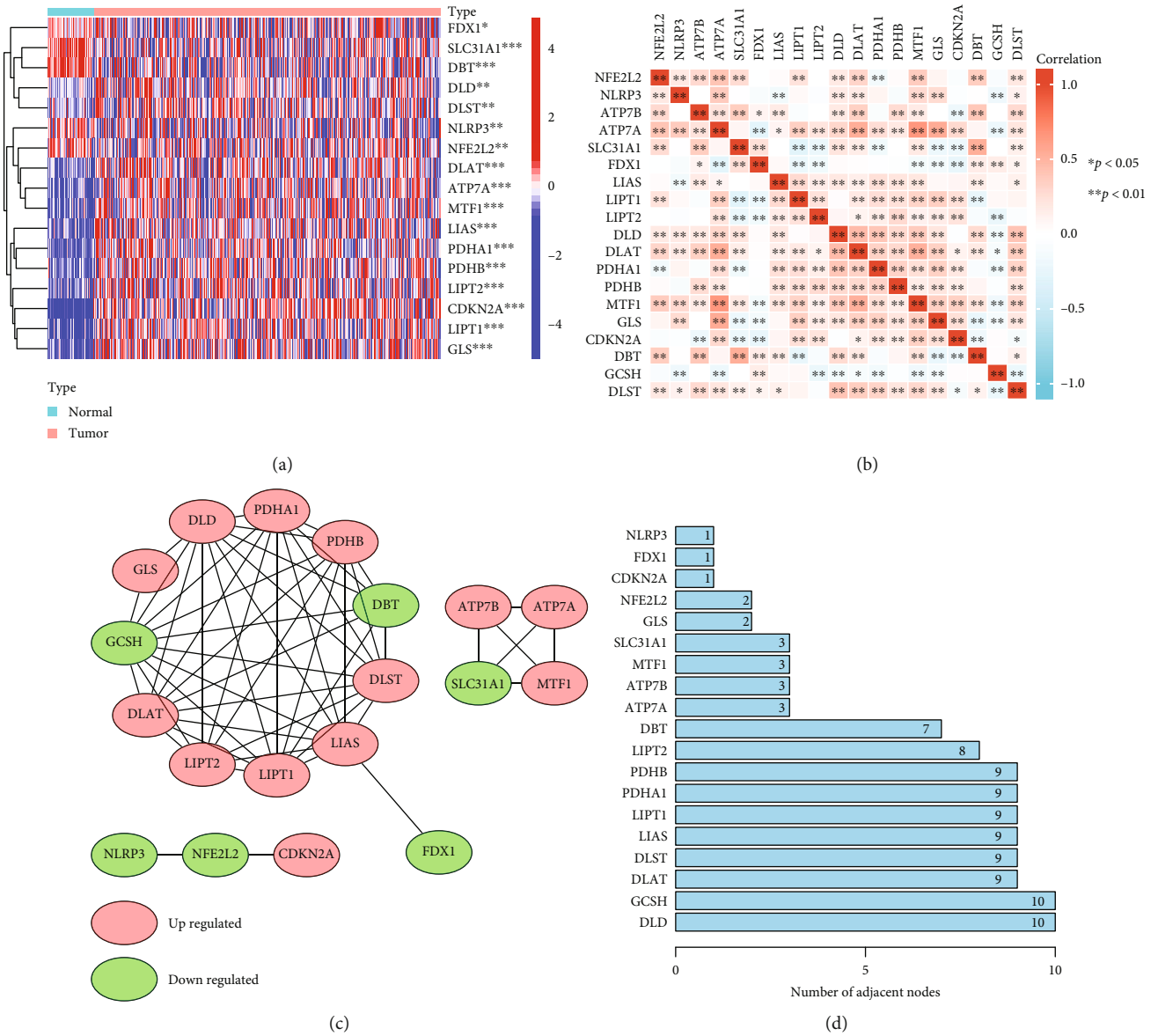
FIGURE 1: Identification of cuproptosis-related DEGs and exploration of the relationship between each CRG in HCC based on the TCGA database. (a) Cuproptosis-related DEGs expression patterns between HCC and normal tissue. The color legend represents the log2 (FPKM) value. (b) Pearson's correlation analysis of each CRG based on the HCC samples. (c) PPI network plot displayed the relationship between each CRG. Red and green nodes indicate up and downregulated genes, respectively. (d) The number of adjacent nodes between each CRG in the PPI network. $^*p < 0.05$, $^{**}p < 0.01$, $^{***}p < 0.001$.

Next, we conducted Gene Set Enrichment Analysis (GSEA) by employing the GSEA tool [27] against gene sets from the MSigDB. To further assess the biological function differences between the groups, GSVA enrichment analysis was performed based on the "GSVA" R package [28].

2.5. Somatic Mutational Hotspot Analysis. Through the GDC data portal at TCGA, we got the somatic mutation data with the Mutation Annotation Format (MAF) for HCC patients. The "Maftools" R package [29] in R software was utilized for summarization and visualization of the mutated genes.

2.6. Construction and Validation of a Novel Prognostic Model Based on CRGs. According to univariate Cox analysis, we

screened out survival-associated genes, and with the least absolute shrinkage and selection operator (LASSO) Cox regression, we formed a risk signature through the "glmnet" and "survival" R packages [30] in the TCGA. The risk score was computed as follows:

$$\text{risk score} = \sum_{j=1}^{n} \text{Coef } j * \text{xj}. \tag{1}$$

xj on behalf of the expression levels of every prognostic CRG and Coef on behalf of the coefficient. According to the median score, HCC patients were categorized into low- and high-risk groups. Kaplan-Meier survival curves were

(a)

(b)

(c)

(d)

Figure 2: Continued.

(e)

(f)
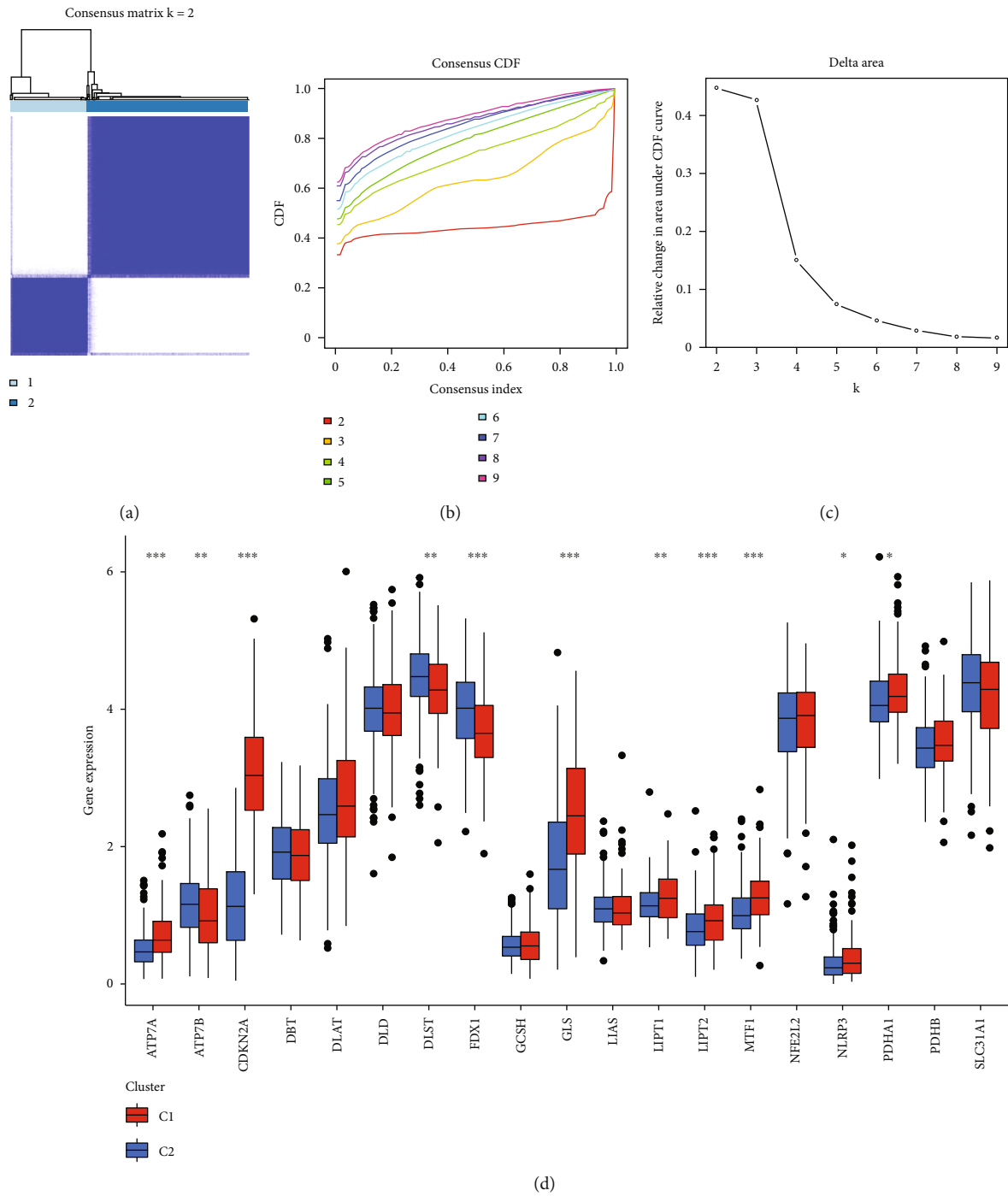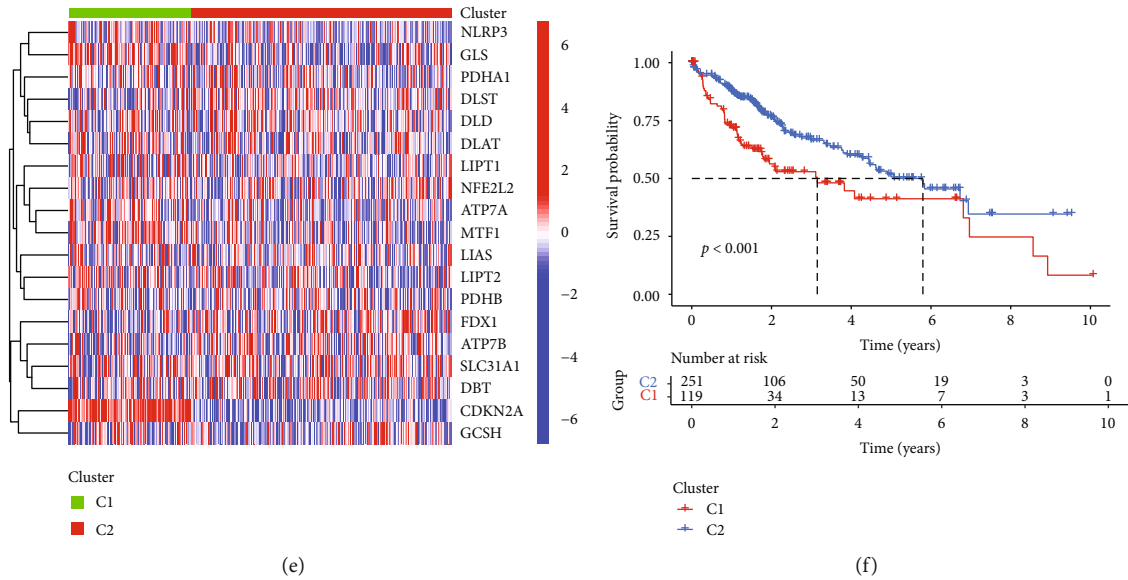
FIGURE 2: Consensus clustering of cuproptosis-associated subtypes and survival analysis in the TCGA. (a) Heatmap represented the consensus clustering solution ($k = 2$) for 19 CRGs among 502 HCC samples. (b, c) The consensus clustering delta area showed the cumulative distribution function area for $k = 2$ to 9. (d) Boxplots represented gene expression profiles for 19 genes in the two clusters. (e) An expression heatmap showed 19 genes grouped into two clusters. The color legend represents the log2 (FPKM) value. Red highlighted the high expression, and blue highlighted the low expression. (f) Kaplan–Meier curves of OS in different clusters. $^*p < 0.05$, $^{**}p < 0.01$, $^{***}p < 0.001$.

utilized to compare the two groups' overall survival (OS) and progression-free survival (PFS). The "timeROC" R package was utilized to calculate the time-dependent receiver operating characteristic (ROC) curve according to the signature's sensitivity and specificity [31]. We employed univariate and multivariate Cox regression analysis to test the risk score's independent prognostic value. Chi-square examinations were utilized to measure the association between risk levels and clinical characteristics. Next, the ICGC database was used to verify the risk score's predictive ability. The same formula used for TCGA patients was enrolled to estimate the risk scores of ICGC patients.

2.7. Kaplan–Meier Survival Curve Analysis. Kaplan-Meier survival curves were adopted for survival analysis with Mantel-Wilcox tests. We conducted a survival analysis of HCC cases in the TCGA database based on gene clusters, risk groups, and clinical features stratification, while HCC patients in the ICGC were analyzed according to risk groups.

2.8. Construction of Prognostic Nomograms. Through the R package "rms" [32], we constructed a nomogram and corresponding calibration map through the risk score and other important clinical traits. The area under the ROC curve (AUC) was utilized to measure the diagnostic power of the nomogram. Univariate and multivariate Cox regressions were employed to assess whether the nomogram was an independent predictor.

2.9. Tumor-Infiltrating Immune Cells Analysis. To comprehensively assess the composition of tumor-infiltrating immune cells, we employed several methods, including TIMER, CIBERSORT, CIBERSORT-ABS, QUANTISEQ,

MCPcounter, XCELL, EPIC, and ssGSEA. Correlation analysis was used to examine the relationship between immune cell infiltration and risk level. Furthermore, eight critical genes involved in immune checkpoint blockade therapy were extracted from each case and compared between different groups, including *TIGIT, PD-L2, PD-L1, PD-1, LAG3, SIGLEC15, TIM-3,* and *CTLA-4.*

2.10. Immunotherapy Response Predictions. Tumor immune dysfunction and exclusion (TIDE) [33] was enrolled to figure out how probable it was that HCC patients' responses to ICB.

3. Results

3.1. Exploration of Differentially Expressed CRGs in HCC. We carefully selected a gene set of 19 genes (*ATP7B, ATP7A, DLD, DLAT, DLST, SLC31A1, FDX1, LIPT1, LIAS, LIPT2, PDHA1, NFE2L2, NLRP3, GLS, MTF1, CDKN2A, GCSH, DBT,* and *PDHB*) which function closely with cuproptosis. The screening criteria of the 19 CRGs were based on the core literature reported by Tsvetkov et al., who first defined the cuproptosis [12]. In the TCGA, compared to normal tissues, 17 genes were differentially expressed in HCC, including *ATP7A, DLD, DLAT, DLST, SLC31A1, FDX1, LIPT1, LIAS, LIPT2, PDHA1, NFE2L2, NLRP3, GLS, MTF1, CDKN2A, DBT,* and *PDHB* (Figure 1(a)). Based on the HCC samples, the relationship between CRGs was then revealed using Pearson's correlation analysis (Figure 1(b)). Next, the PPI network was formed by the web tool STRING and pictured through the Cytoscape program to further reveal the potential connection between the related proteins (Figure 1(c)). In the PPI network, we counted the number of adjacent nodes

(a)

(b)

(c)

(d)

Figure 3: Continued.

(e)

(f)
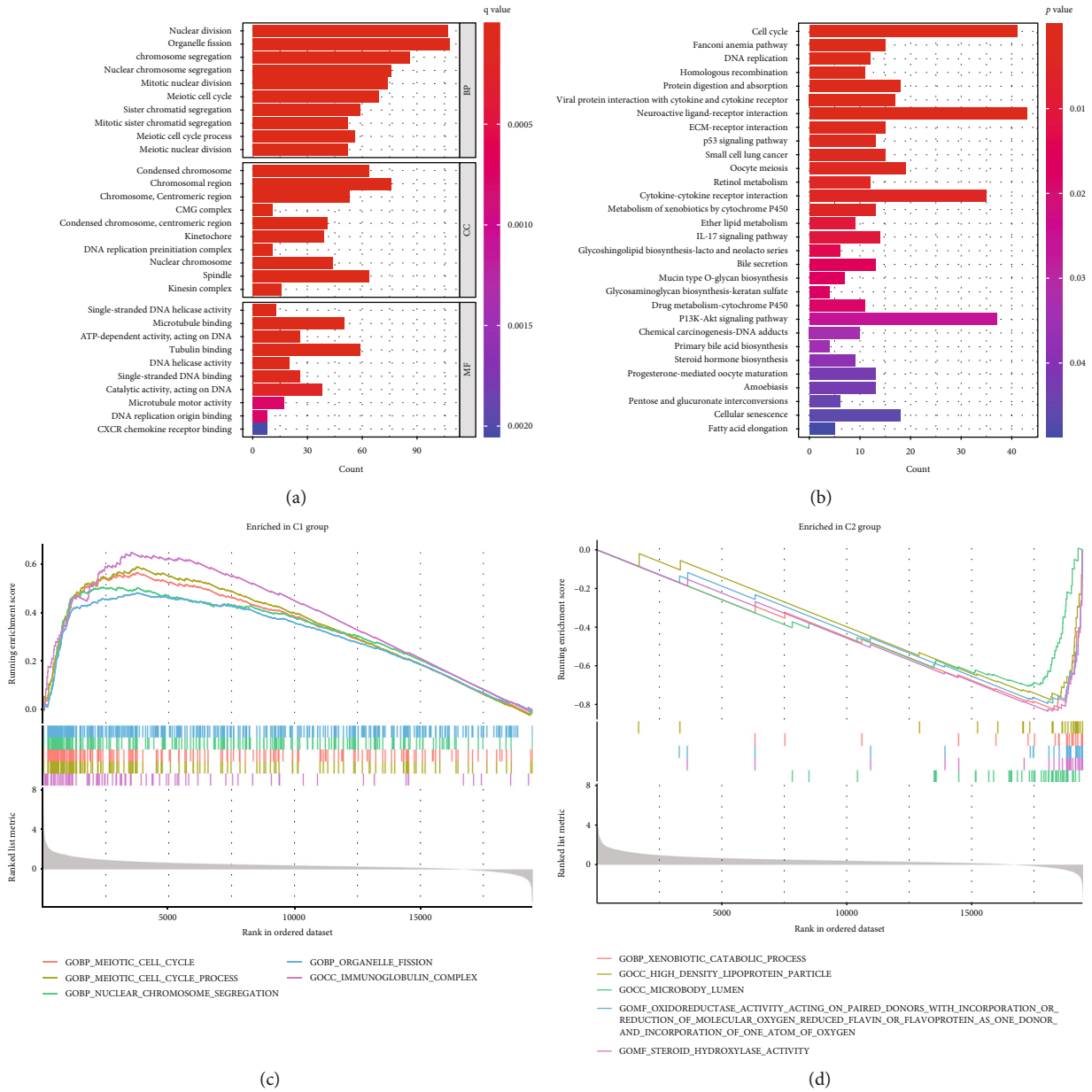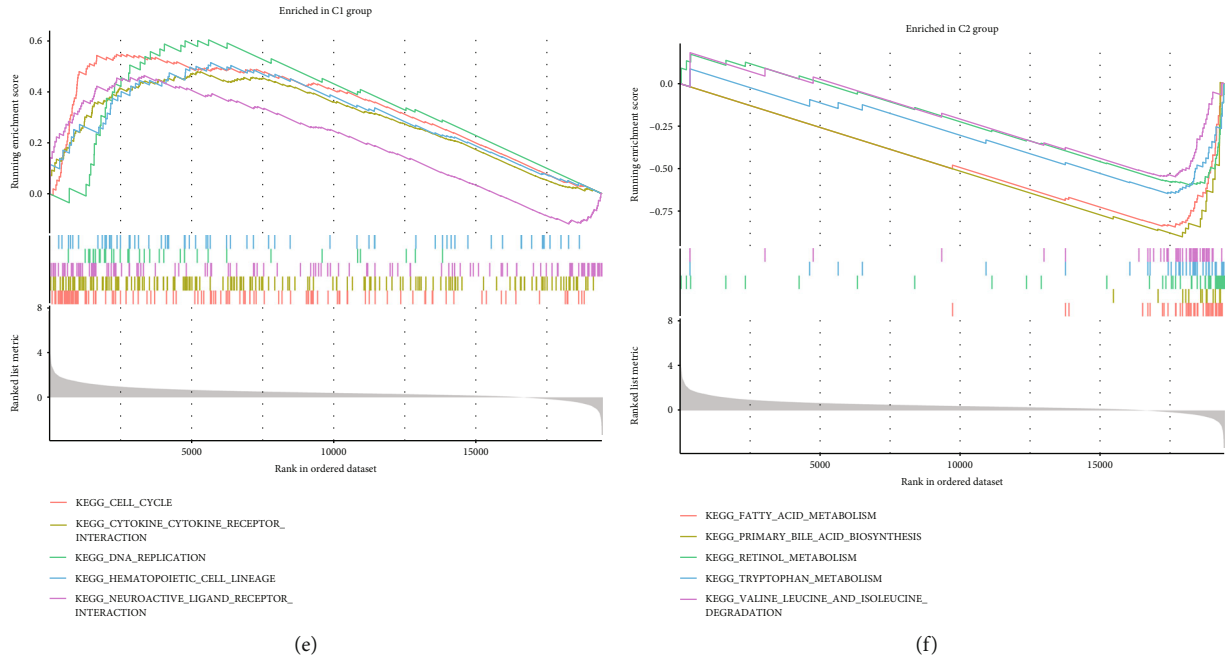
Figure 3: Results of functional enrichment analysis. (a) A list of the top 10 enriched GO terms. Topics contained biological processes (BP), cellular components (CC), and molecular functions (MF). (b) The top 30 most significant enriched KEGG pathways. (c) The top 5 GSEA-GO enrichment in cluster 1. (d) The top 5 GSEA-GO enrichment in cluster 2. (e) The top 5 GSEA-KEGG enrichment in cluster 1. (f) The top 5 GSEA-KEGG enrichment in cluster 2.

(a)

(b)
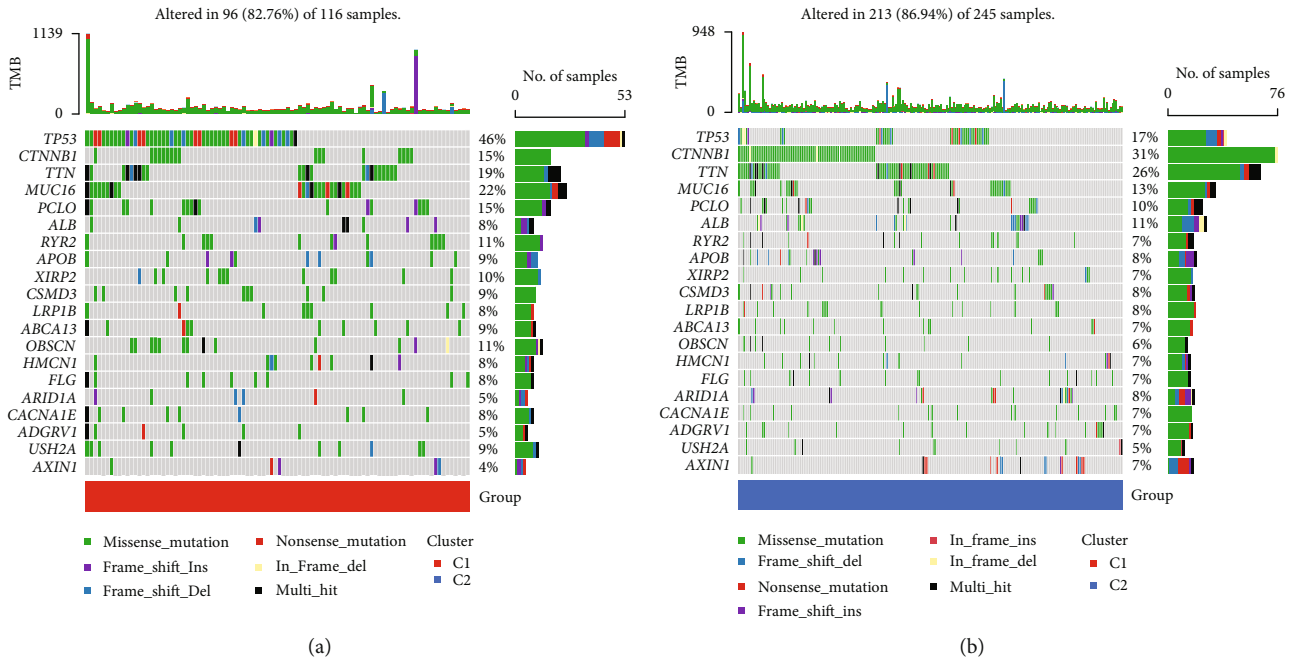
Figure 4: The somatic mutations landscape of two cuproptosis-related clusters. The top ten mutated genes in cluster 1 (a) and cluster 2 (b) were visualized using a waterfall plot.

(Figure 1(d)). We discovered a strong correlation between each CRG in HCC tissues, suggesting that these CRGs may act as a whole and perform a common function of cuproptosis together. These findings demonstrated that CRGs' expression patterns between HCC and normal tissues are remarkably different, indicating that CRGs may perform a significant function in the tumorigenesis and development of HCC.

3.2. Consensus Clustering Identified Two Cuproptosis-Associated Subtypes and Survival Analysis. To reveal the relationship between cuproptosis subtypes and HCC

(a)

(b)

FIGURE 5: Continued.

(c)
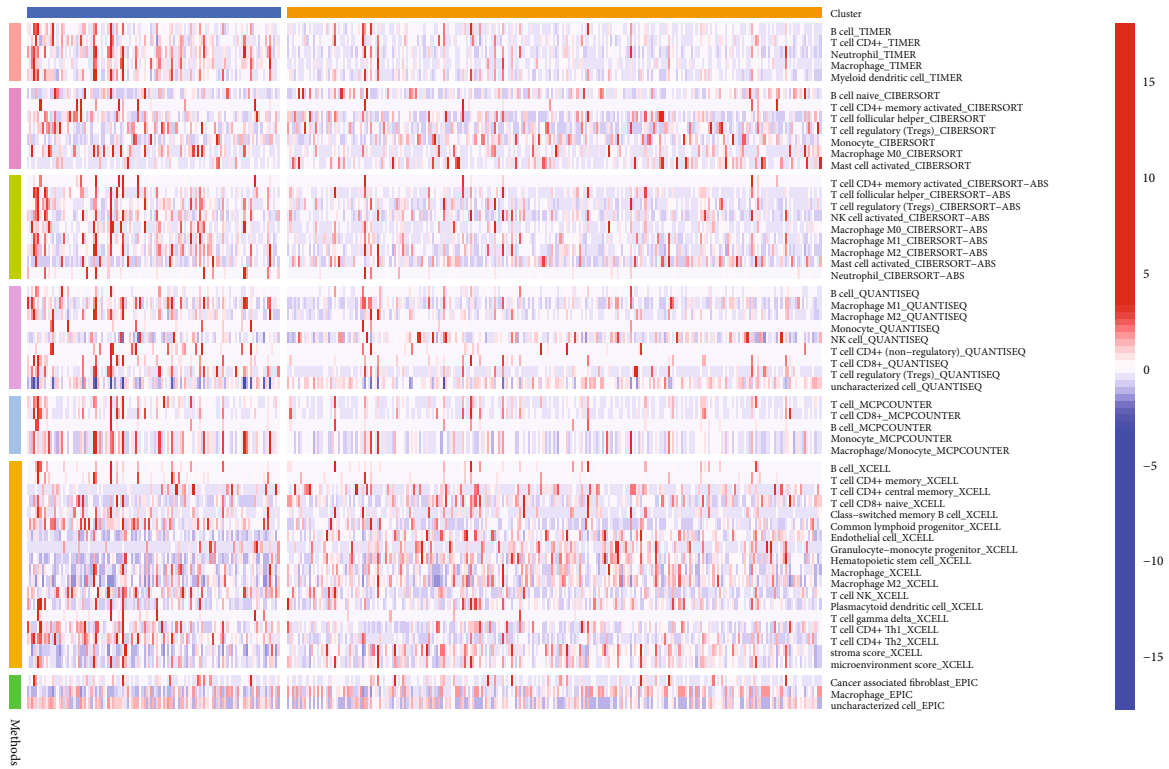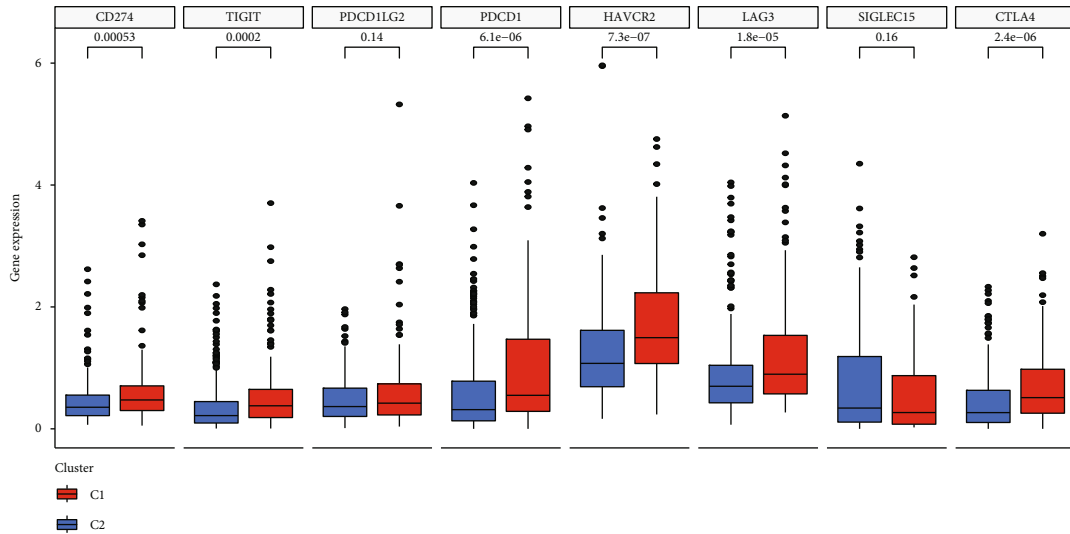
(d)
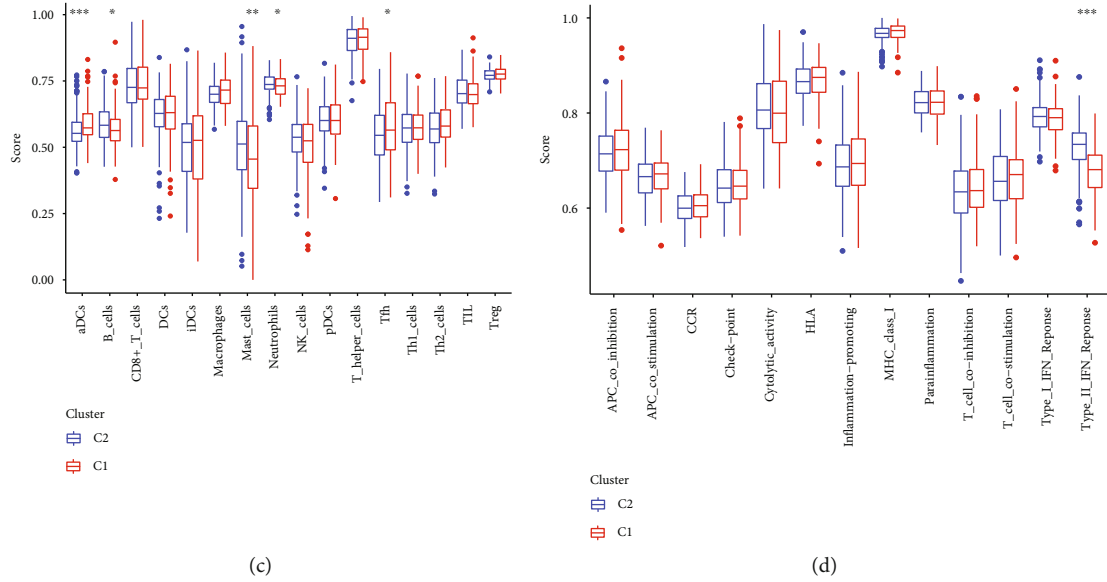
Figure 5: The immune landscape of two cuproptosis-related clusters in HCC. (a) The immune infiltration heatmap between the two clusters using TIMER, CIBERSORT, CIBERSORT-ABS, QUANTISEQ, MCPcounter, XCELL, and EPIC algorithms. (b) The gene expression levels of immune checkpoints for the two clusters. (c) The ssGSEA for examining subpopulation associations in immune cells. (d) The ssGSEA for examining subpopulation associations in immune functions. $^*p < 0.05$, $^{**}p < 0.01$, $^{***}p < 0.001$.

patients' clinical outcomes, we used 19 CRGs to cluster HCC patients in the TCGA database. Through K-means cluster analysis, HCC patients were clustered into two subgroups according to the 19 CRGs with similar expression patterns (Figures 2(a)–2(c)). The gene expression data of 19 CRGs in two clusters showed that a high expression level of *ATP7A*, *CDK2A*, *GLS*, *LIPT1*, *LIPT2*, *MTF1*, *NLRP3*, and *PDHA1* was found in cluster 1, while cluster 2 showed high expression levels of *ATP7B*, *DLST*, and *FDX1* (Figures 2(d), 2(e)). The Kaplan-Meier analysis of survival discovered that the clusters linked with cuproptosis had distinct clinical outcomes. Patients in cluster 1 had poorer clinical results, whereas those in cluster 2 had a more favorable prognosis (Figure 2(f)). These results revealed that there might be a relationship between cuproptosis-associated subtypes and HCC clinical outcomes.

3.3. Functional Enrichment Analysis Based on Clustering. GO, KEGG, and GSEA analyses were conducted on the DEGs between two clusters with cut-off criteria of *p* value <0.05 and |log 2FC| ≥ 1 in order to study the biological function variations of each cluster. We presented the top 10 GO terms, 30 significant enriched KEGG pathways, and the top 5 normalized enrichment scores terms of GSEA. Among GO terms, nuclear division, mitotic nuclear division, condensed chromosomes, and single-stranded DNA helicase activity were significantly enriched (Figure 3(a)). On the KEGG pathway list, DNA replication, cell cycle, p53, and IL-17 signaling pathways are significantly enriched (Figure 3(b)). According to GESA, two clusters had differentially enriched gene sets. Based on GSEA, GO terms in cluster 1 are predominantly associated with cell cycle, nuclear chromosome segregation, organelle fission, and immunoglobulin complex (Figure 3(c)). GO terms in cluster 2 were enriched in xeno-

biotic catabolic processes, high-density lipoprotein particles, and microbody lumens (Figure 3(d)). The KEGG pathways in cluster 1 were predominantly related to DNA replication, cell cycle, and cytokine-cytokine receptor interaction (Figure 3(e)). As for cluster 2, it was enriched in fatty acid metabolism, bile acid production, and retinol production (Figure 3(f)). According to these results, the two clusters differ in biological function, and the differences mainly focus on cell cycle, cell death, and immune-related functions.

3.4. Somatic Mutations and Immune Landscape of Cuproptosis-Related Clusters. In addition, we investigated the mutation profile of cuproptosis-related clusters in HCC patients. *TP53*, *CDKN2A*, *TTN*, *MUC16*, and *FAT1* were the most abundant mutant genes. The relative mutation frequencies differ between the two clusters. A high frequency of *MUC16* and *TP53* mutations was observed in cluster 1, with 46% and 22% of the total, respectively (Figure 4(a)). In cluster 2, *CTNNB1* and *TTN* were the most frequently mutated genes, with 31% and 26% of the total, respectively (Figure 4(b)). The tumor immune microenvironment in the two clusters needs to be investigated further, then TIMER, CIBERSORT, CIBERSORT-ABS, QUANTISEQ, MCPcounter, XCELL, and EPIC algorithms were used to visualize the immune cell infiltration situation (Figure 5(a)). Immune infiltration of various immune cells differed significantly between the two clusters (Supplementary Table 1). We further investigated immune checkpoint gene expression levels in the eight important immune checkpoints across the two clusters. The expression of *CD274*, *TIGIT*, *PDCD1*, *HAVCR2*, *LAG3*, and *CTLA4* was substantially different between the two clusters of HCC patients (Figure 5(b)). Based on ssGSEA analysis, we analyzed immune cell subpopulations and their related functions. The results revealed that aDCs, B cells, mast cells,

(a)

(b)

(c)

(d)

(e)

(f)

(g)

(h)

FIGURE 6: Continued.

(i)

(j)
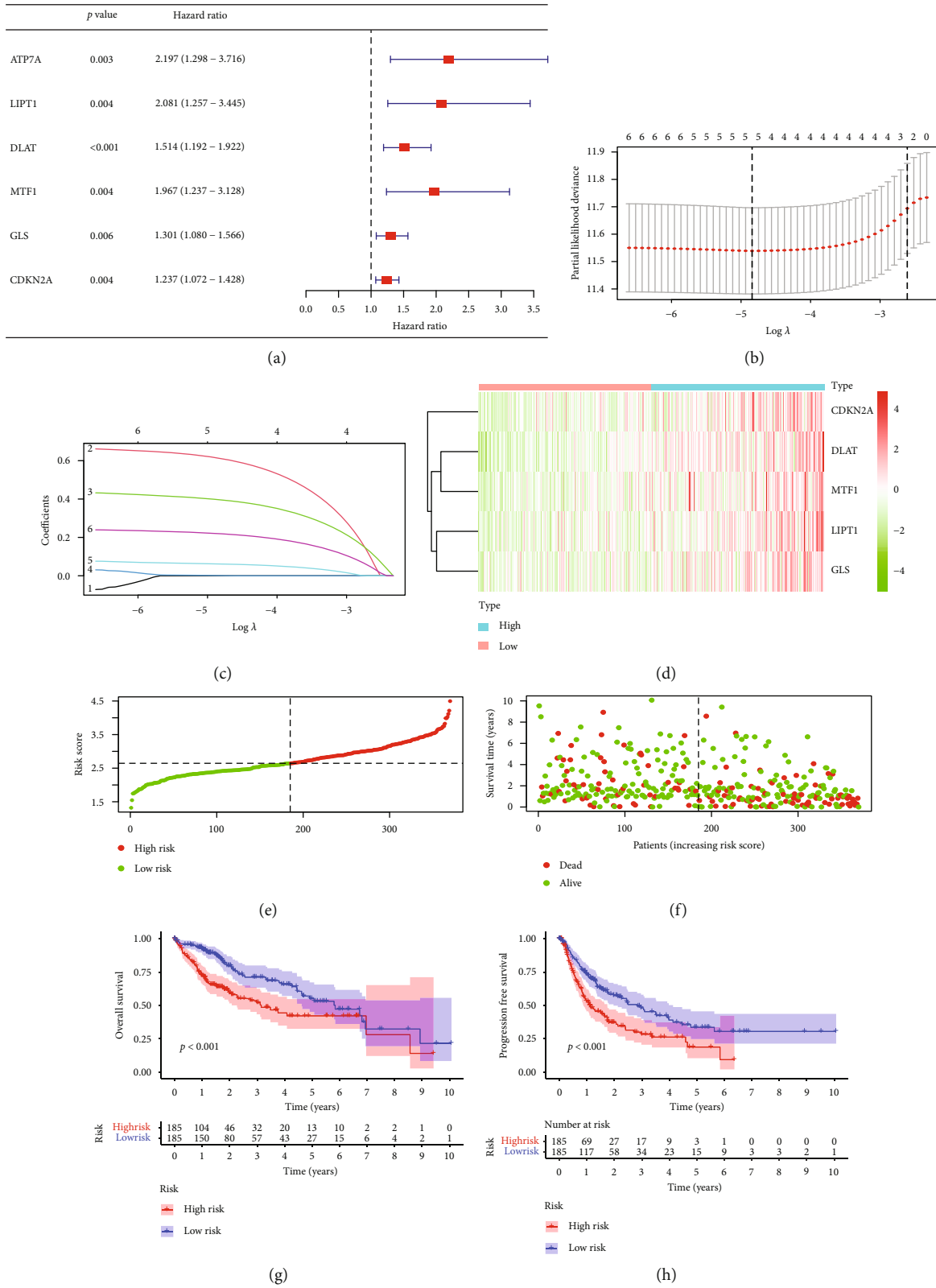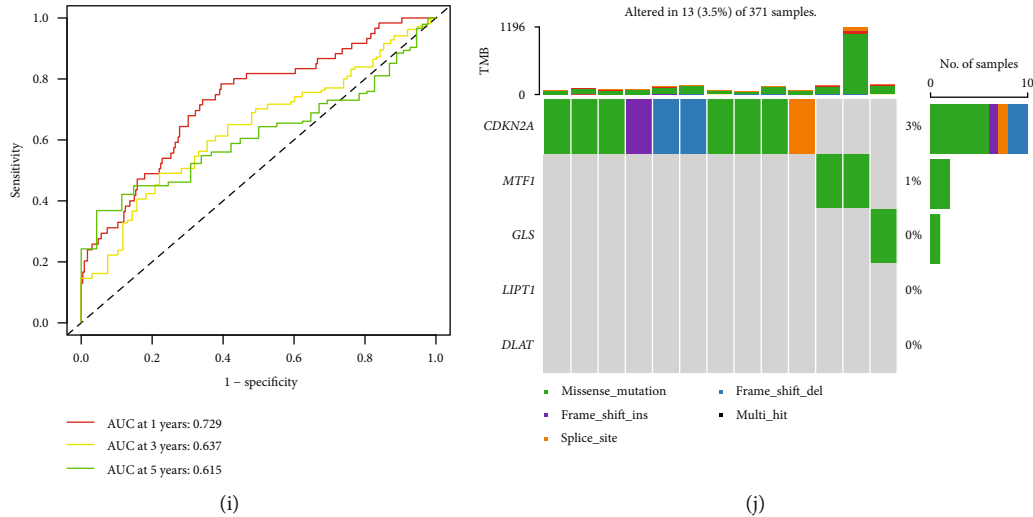
FIGURE 6: Formation of the risk score signature utilizing five CRGs in the TCGA. (a) Univariate Cox regression analysis selected six CRGs. (b, c) Detection of five prognostic CRGs using the LASSO Cox regression analysis. (d) Heatmaps of the five prognostic CRGs according to the distribution of risk scores. The color legend represents the log2 (FPKM) value. (e) The distribution of risk scores. (f) Patients' survival status according to the distribution of risk scores. (g) Kaplan-Meier survival analysis compared the OS between the high-risk and low-risk groups. (h) Kaplan-Meier survival analysis compared the PFS between the high-risk and low-risk groups. (i) The ROC curves for 1, 3, and 5 years of the risk model. (j) Mutation landscape of the five CRGs of the risk model.

neutrophils, Tfh, and type II IFN response significantly differed between the two clusters (Figures 5(c) and 5(d)). According to these findings, there were significant differences between the two cuproptosis-related clusters of HCC in terms of somatic mutations and immune landscape.

3.5. Construction of the Cuproptosis-Related Prediction Model in HCC. To detect the key genes in cuproptosis and explore the possibility of clinical application of cuproptosis-related phenotype, we developed a prognostic model by differentially expressed CRGs in the TCGA database. Through the univariate Cox analysis, we found six CRGs were significantly associated with OS (Figure 6(a)). Then, five genes were selected in the prognostic model with LASSO Cox regression (Figures 6(b) and 6(c)). The risk-score model is formed as the following algorithm: risk score $= (0.6125)^* LIPT1 + (0.3970)^* DLAT + (0.0013)^* MTF1 + (0.0619)^* GLS + (0.2198)^* CDKN2A$. Additionally, according to the distribution of risk scores and survival time, we found higher risk levels were linked to shorter survival times (Figures 6(d)–6(f)). Utilizing Kaplan-Meier analysis, we further assessed the prognostic relevance of this risk profile. A negative correlation was found between risk scores with OS and PFS (Figures 6(g) and 6(h)). Using the ROC curve, we assessed the predictive role of risk score by computing AUC, which was 0.729, 0.637, and 0.615 for the 1-, 3-, and 5-year survival (Figure 6(i)). In addition, we explored the somatic mutation condition of the five model genes. CDKN2A is mutated in 3 percent of HCC patients, MTF1 is mutated in 1 percent of HCC patients, and fewer mutations are found in GLS, LIPT1, and DLAT. The most abundant mutation type is the missense mutation (Figure 6(j)).

3.6. Exploration of the Independent Prognostic Value and Clinical Feature of the Risk Score in HCC. In the TCGA, we conducted both univariate and multivariate Cox regres-

sion analyses to explore whether risk score and other clinical traits were independent prognostic factors. With five parameters (age, gender, stage, grade, and risk score), the risk score obtained by our formula served as an independent predictor of survival for HCC patients ($p < 0.01$, Figures 7(a) and 7(b)). Meanwhile, it was discovered that the risk score was substantially associated with the tumor stage and grade (Supplementary Table 2). Besides, we compared the risk score across different clinical traits. Interestingly, according to the risk score, we found differences were significant between the T1 stage versus T2, T3, and T4 stage ($p < 0.05$, Figure 7(f)) and tumor stage I versus stage II, and stage III ($p < 0.01$, Figure 7(i)). The other clinical characteristics were also compared separately (Figures 7(c)–7(i)). The high-risk group patients had advanced T stage and tumor stage compared with low-risk group patients. These results indicated that the risk model built with these five genes is capable of accurately predicting the prognosis of HCC.

3.7. Implication of Risk Score on the Prognosis of HCC Patients in Different Clinical Parameters Stratification. We carried out a stratified analysis for further data mining (Figures 8(a)–8(h)). Following stratification by age, gender, tumor stage, and tumor grade, the risk score based on five CRGs signature performed as a significant prognostic indicator for age ≤ 65 (Figure 8(b)), male patients with HCC (Figure 8(d)), stages I-II (Figure 8(e)), grades 1-2 (Figure 8(g)), and grades 3-4 (Figure 8(h)).

3.8. Prognosis Model Validation in the ICGC Cohort. We gathered comprehensive clinical information for 232 HCC cases from the ICGC database to serve as an external validation set. The risk score for each patient in the ICGC was computed according to the same formula created in the TCGA. The relationship between risk scores and clinical

(a)

(b)

(c)

(d)

(e)

(f)

Figure 7: Continued.

(g)

(h)

(i)
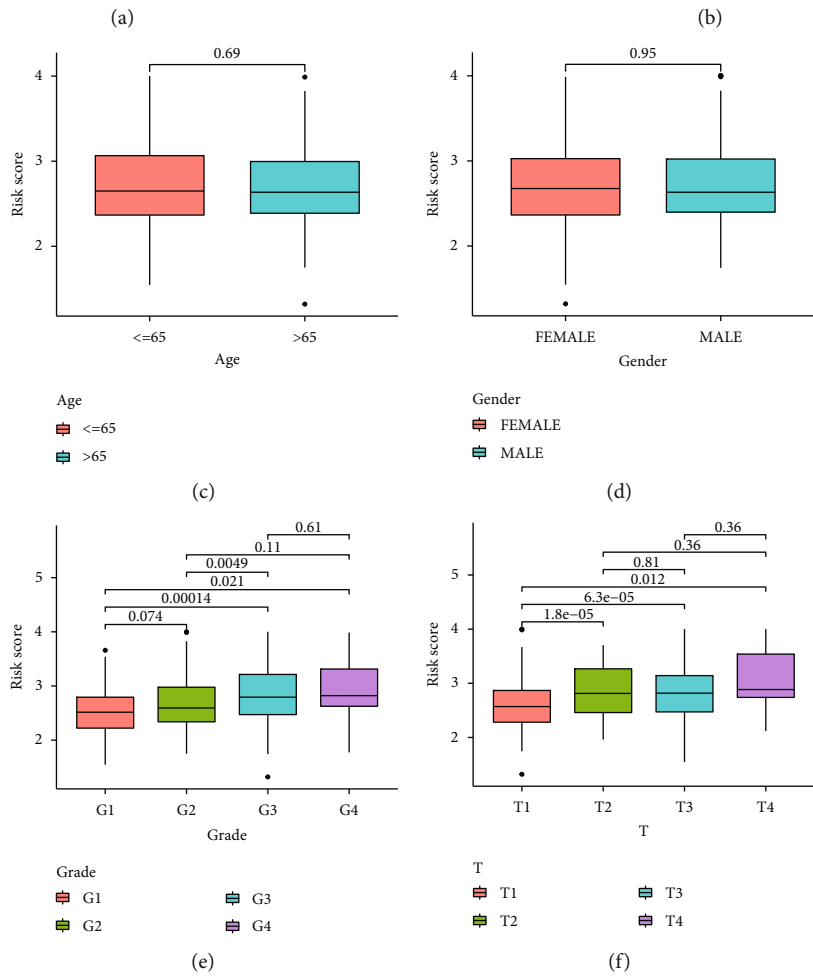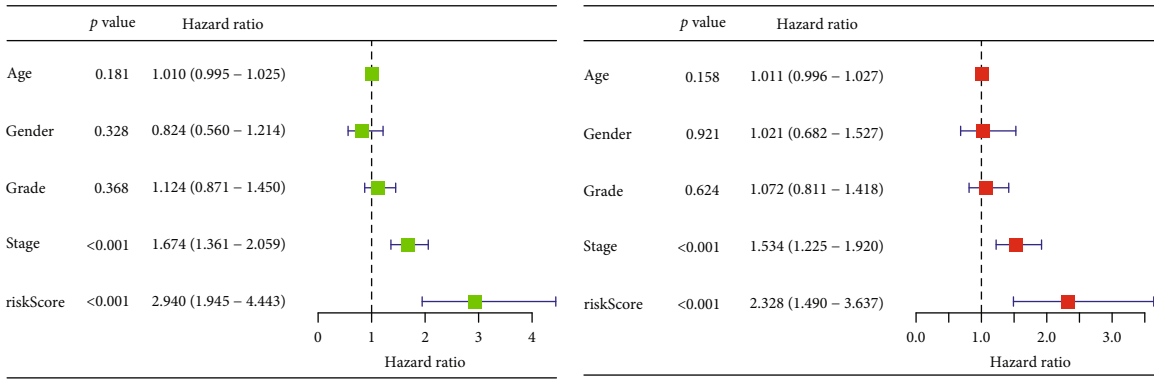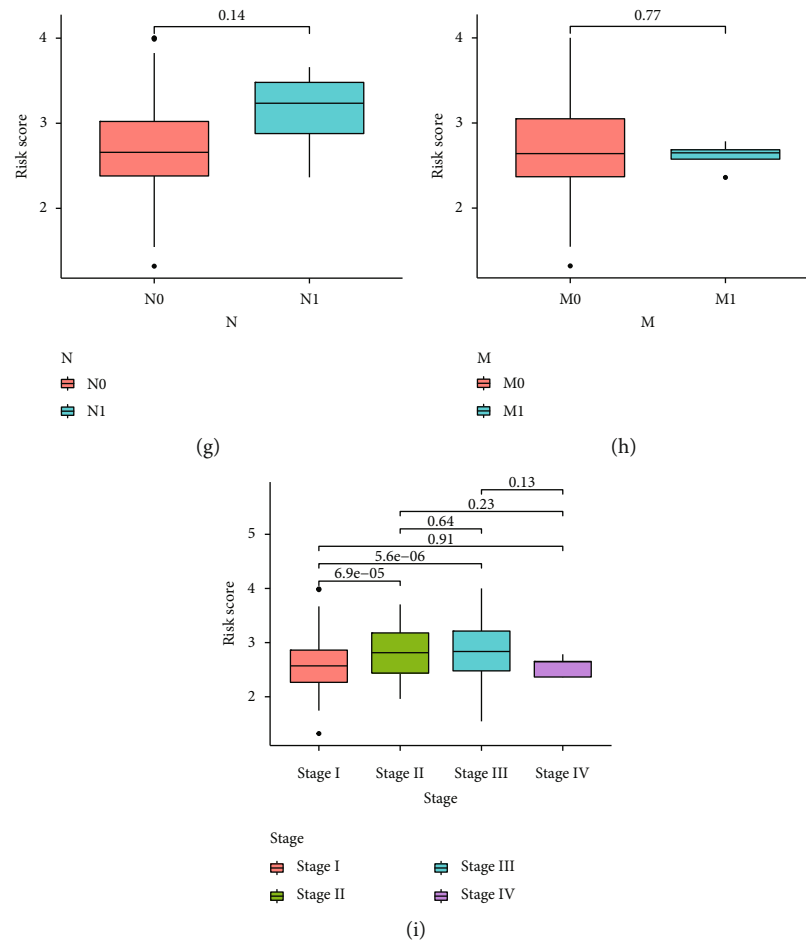
FIGURE 7: Exploration of the independent prognostic value and clinical feature of the risk score in HCC. (a, b) Through univariate and multivariate Cox regression analysis, the risk score was found to be an independent prognostic element for HCC patients. (c–i) The relationship between the risk score and different clinical parameters of HCC.

traits was examined (Supplementary Table 3). The TCGA cohort's median risk score was utilized to separate the ICGC cohort into high-risk and low-risk groups. 101 cases were located in the low-risk group, while the other 131 were in the high-risk group. The distribution diagram of risk scores and survival times displayed that the survival times of HCC patients in the ICGC decreased with rising risk scores, and in the low-risk group, there were more survivors than in the high-risk group (Figures 9(a)–9(c)). According to the Kaplan-Meier survival analysis, the survival time of high-risk patients was shorter than that of low-risk patients ($p = 0.002$, Figure 9(d)). Our risk model was also discovered to be an independent predictor of mortality in the ICGC (Figures 9(e) and 9(f)).

3.9. *Prognostic Nomograms of HCC.* To further elevate the predictive power of our risk model, the nomograms were constructed by utilizing the five significant independent predictors (age, gender, grade, stage, and risk score) in the TCGA (Figure 10(a)). Good consistency between the prediction by nomogram and actual observation of 1-, 3-, and 5-year survival rates (Figure 10(b)) was confirmed by the calibration plot. The nomogram model also showed good pre-

diction accuracy for the 1-, 3-, and 5-year OS rates. The relevant AUC values were 0.758, 0.710, and 0.696. (Figures 10(c)–10(e)). These findings suggest the preferable precision of the nomogram. In addition, the nomogram model could represent an independent risk factor in the TCGA (Figures 10(f) and 10(g)).

3.10. *Function and Pathway Enrichment Analyses Based on Cuproptosis-Related Risk Score.* For the assessment of the mechanisms underlying our risk model, we analyzed DEGs following the criteria: FDR < 0.05 and |log 2FC| ≥ 1. 781 significant DEGs were identified, comprising 724 upregulated genes and 57 downregulated genes in the high-risk group. The GO terms were substantially enriched in chromosome segregation, nuclear division, chromosomal region, spindle, and DNA replication origin binding (Figure 11(a)). The majority of enriched KEGG pathways were cellular senescence, HIF-1 signaling pathway, TNF signaling pathway, apoptosis, cell cycle, and IL-7 signaling pathway (Figure 11(b)). As we could see, both GO terms and KEGG analysis indicated that the functional enrichment of the risk model highly correlated with cell cycle, cell death, and immune response. The results of GSVA revealed that low-

(a)

(b)

(c)

(d)

(e)

(f)

(g)

(h)
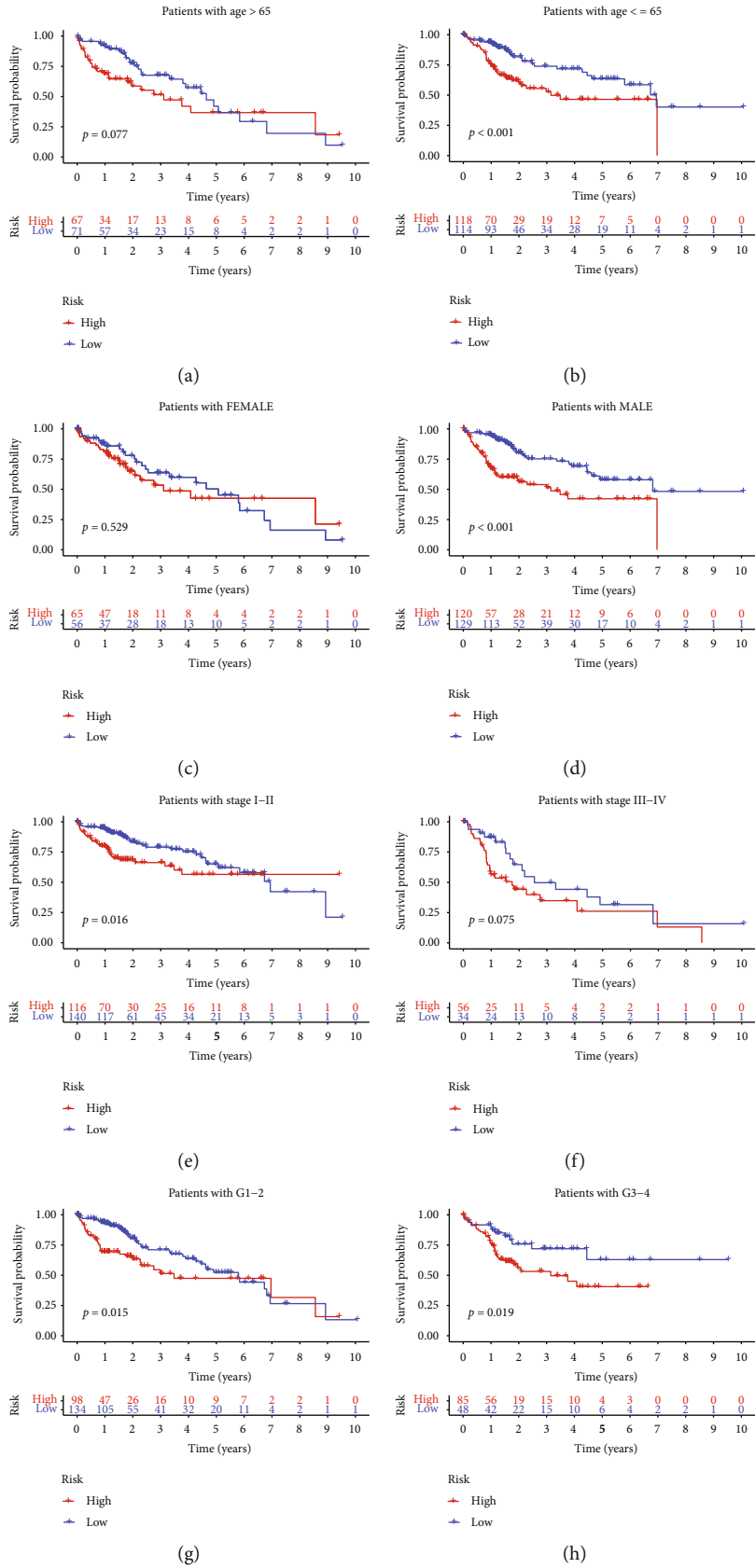
FIGURE 8: Kaplan-Meier analysis of the risk score in different stratifications according to clinicopathological characteristics. (a–h) HCC patients with varying clinical features (age, gender, stage, and grade) were analyzed using the Kaplan-Meier method according to the risk score.

(a)

(b)

(c)

(d)

(e)

(f)
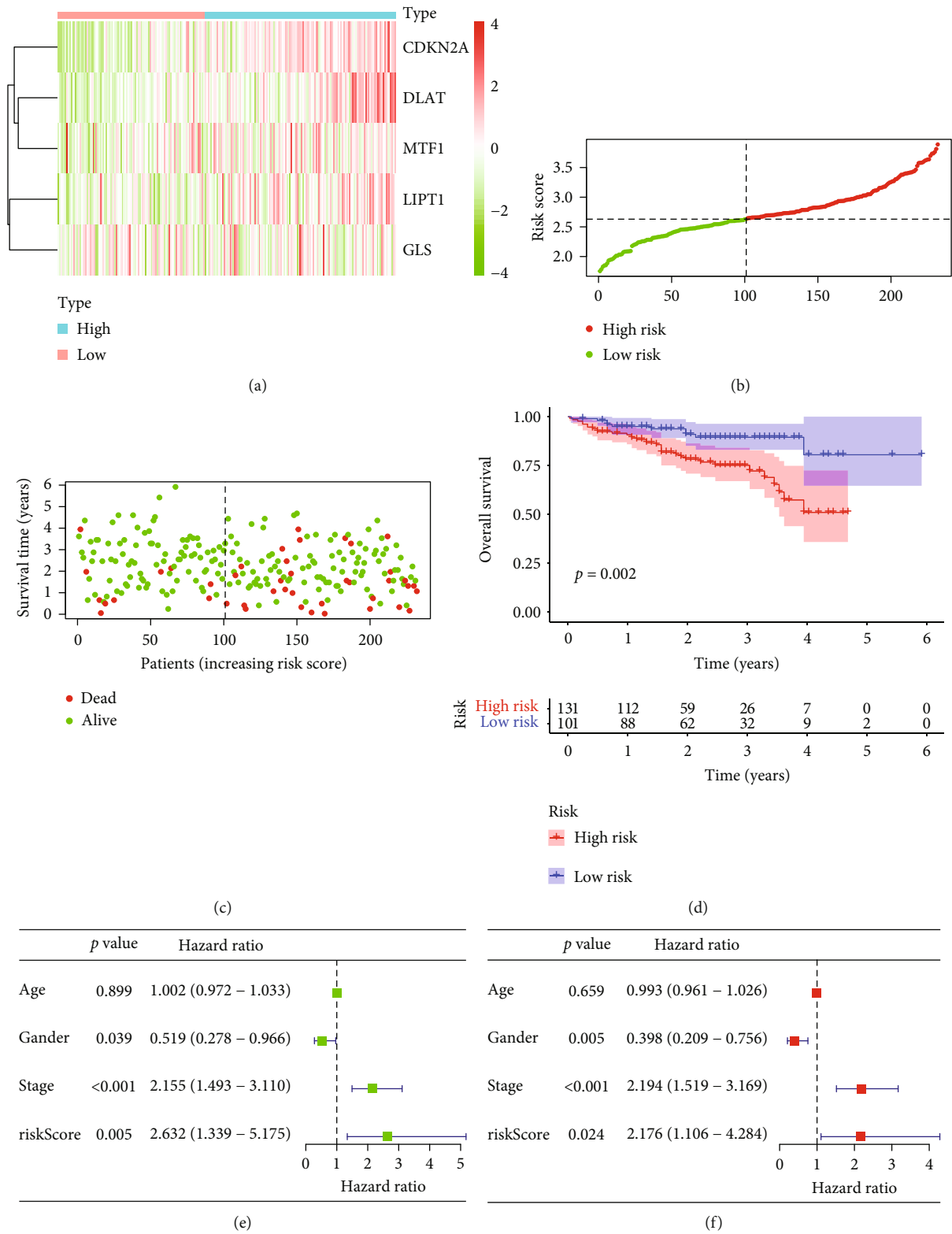
FIGURE 9: Verification of the five CRGs signature in the ICGC cohort. (a) Heatmaps of five prognostic CRGs in the ICGC database according to the risk score distribution. The color legend represents the log2 (FPKM) value. (b) The risk scores distribution. (c) The survival status of each patient is according to the risk score distribution. (d) Kaplan-Meier curves for the OS of HCC patients. (e, f) The independent survival analysis of the risk scores and clinical traits through univariate and multivariate Cox regression analysis.
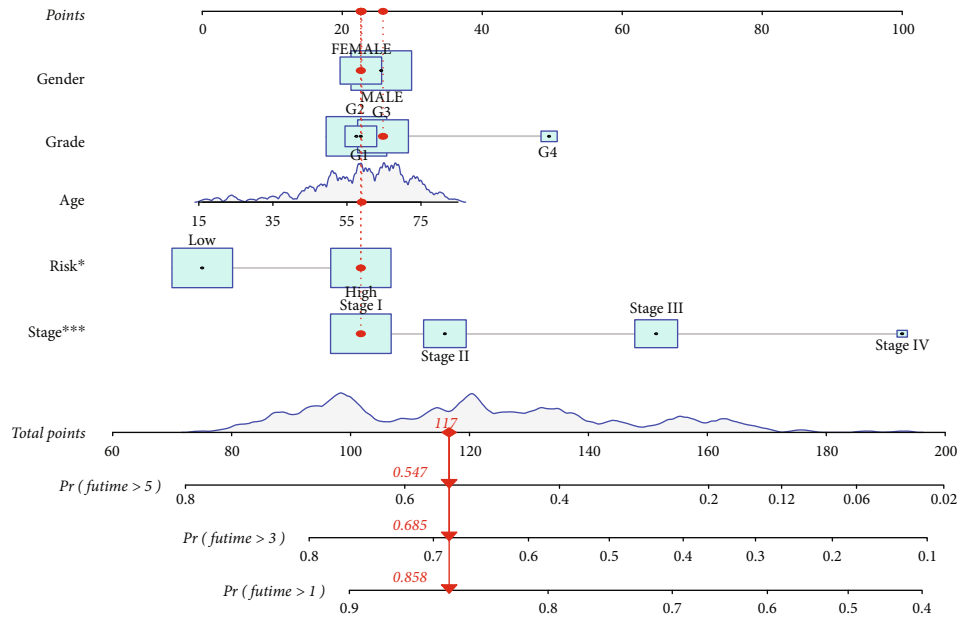
(a)
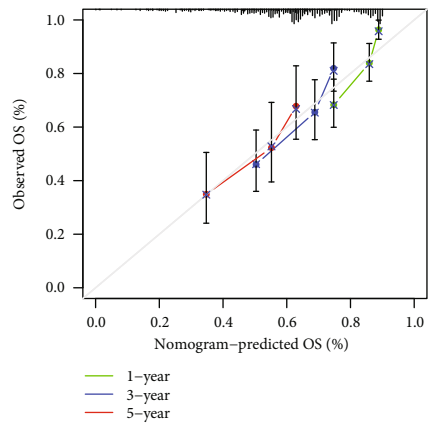
(b)

(c)

(d)

(e)

FIGURE 10: Continued.

	p value	Hazard ratio			p value	Hazard ratio
Age	0.181	1.010 (0.995 – 1.025)		Age	0.421	1.007 (0.991 – 1.023)
Gender	0.328	0.824 (0.560 – 1.214)		Gender	0.873	1.034 (0.688 – 1.554)
Grade	0.368	1.124 (0.871 – 1.450)		Grade	0.503	1.101 (0.832 – 1.457)
Stage	<0.001	1.674 (1.361 – 2.059)		Stage	0.197	1.271 (0.883 – 1.829)
Nomogram	<0.001	1.674 (1.421 – 1.972)		Nomogram	0.046	1.396 (1.006 – 1.938)

(f)   (g)
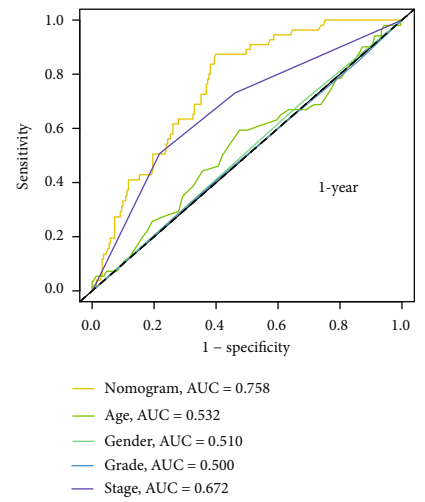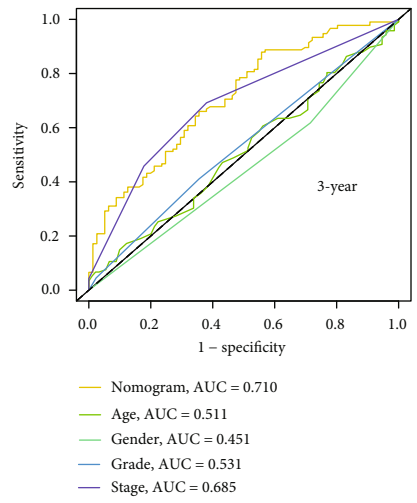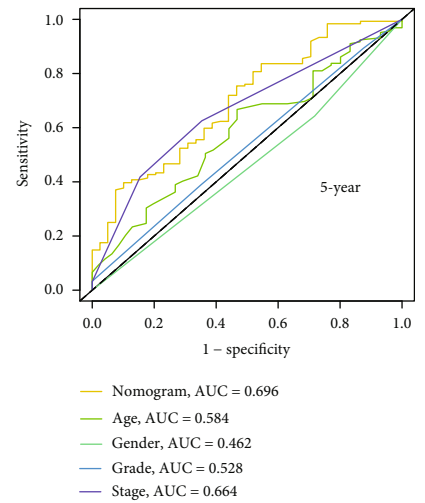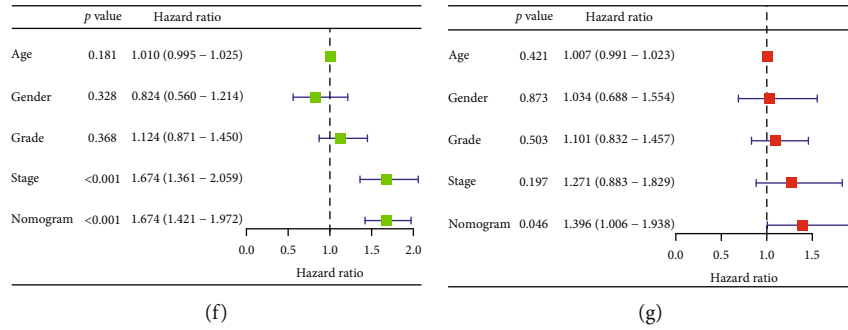
Figure 10: Predicting survival rates for HCC patients after one year, three years, and five years using the nomogram. (a) The nomogram model was formed to predict the survival rates of HCC patients in the TCGA cohorts. (b) Calibration curves of the nomogram. (c–e) The ROC curve explored the prognostic performance of the nomogram model. (f, g) Univariate and multivariate Cox analysis of the nomogram and clinical traits.

risk group patients showed elevated expression levels of multiple metabolism pathways, like arginine and proline, phenylalanine, glycine, serine, and threonine, and high-risk group patients harbored upregulated expression levels of multiple cell cycle and tumorigeneses pathways, such as bladder cancer, notch signaling pathway, p53 signaling pathway, renal cell carcinoma, cell cycle, and DNA replication (Figure 11(c)).

3.11. Immune Characteristics Based on Cuproptosis-Related Risk Score. To further explore the immune landscape of the cuproptosis-related risk model, we calculated the immune responses score through TIMER, CIBERSORT, CIBERSORT-ABS, QUANTISEQ, MCPcounter, XCELL, and EPIC algorithms. Then, the relationship between risk score and tumor immune response score was analyzed by Pearson's correlation. We formed a forest plot to display the detailed correlation coefficient between the immune cell infiltration and risk score (Figure 12(a)). Then, after we performed the ssGSEA method to explore the immune cell subpopulations and related functions, we found that immune cell subpopulations and related functions including aDCs, B cells, macrophages, mast cells, NK cells, Treg, cytolytic activity, MHC class I, and type II IFN response differed between high-risk and low-risk groups (Figures 12(b) and 12(c)). Besides, we further investigated the relationship between the five cuproptosis-related model genes and the ssGSEA result of immune cell subpopulations and related functions in each case (Figure 12(d)). We found some significantly positive correlations, such as the correlation between *MTF1* and MHC class I ($r = 0.49$), and some significantly negative correlations, such as the correlation between CDKN2A and type II IFN response ($r = -0.57$). As a crucial negative regulator of the tumor immune microenvironment, the immune checkpoints act as an essential role in assisting tumor cells in evading immune system attacks. Hence, we examined the expression level of eight important immune checkpoint genes. Between high-risk and low-risk groups, we discovered a significant variance in the expression level of immune checkpoints, including *CD274*, *TIGIT*, *PDCD1*, *HAVCR2*, and *CTLA4* (Figure 12(e)). Following that, a prediction of the immune checkpoint therapy response was made using the TIDE algorithm based on risk scores (Figure 12(f)).

Interestingly, patients in the high-risk group had a higher likelihood of benefiting from immune checkpoint inhibitor therapy, suggesting that the risk score has the potential to predict whether HCC patients will benefit from immune checkpoint therapy.

4. Discussion

Copper overload can cause cuproptosis, which is a novel form of programmed cell death triggered by mitochondrial TCA cycles [12]. The relationship between tumors and copper has long been noted, and in fact, tumor tissue requires higher levels of copper [34]. Copper homeostasis imbalances can result in life-threatening conditions, such as Wilson's disease, in which most patients exhibit chronic liver disease with cirrhosis [35]. Copper overload also can lead to cirrhosis, which is one of the well-known risk factors for HCC [36]. Consequently, a better understanding of cuproptosis in HCC could be meaningful for developing new therapeutics. Here, through a series of analyses, we explored the relationship between cuproptosis and HCC. According to our findings, HCC has a different expression model of CRGs compared with normal liver tissue, and the different cuproptosis subtypes are strongly correlated with the clinical outcome of HCC patients. In addition, a prognostic risk model was created using different expressed CRGs. These findings may have implications for possible new therapeutic approaches to treating HCC.

Based on our study, we found that most of the CRGs are differentially expressed in HCC versus normal liver tissue. This finding is consistent with previous reports. Bian et al. found that most CRGs differ between clear cell renal cell carcinoma and normal renal cell [37]. Another report also indicated that most CRGs are differentially expressed in melanoma [38]. These clues suggested that the CRGs may have different expression patterns in tumors, including HCC, compared with normal tissues. Consensus clustering identified two clusters with significantly different OS based on the expressions of CRGs. We found the function, mutation, and immune analyses were performed differently between the two clusters, suggesting cuproptosis may be broadly related to HCC progression. The higher mutant frequency of *TP53* in cluster 1 and higher mutant frequency of *CTNNB1* in

(a)

(b)

(c)
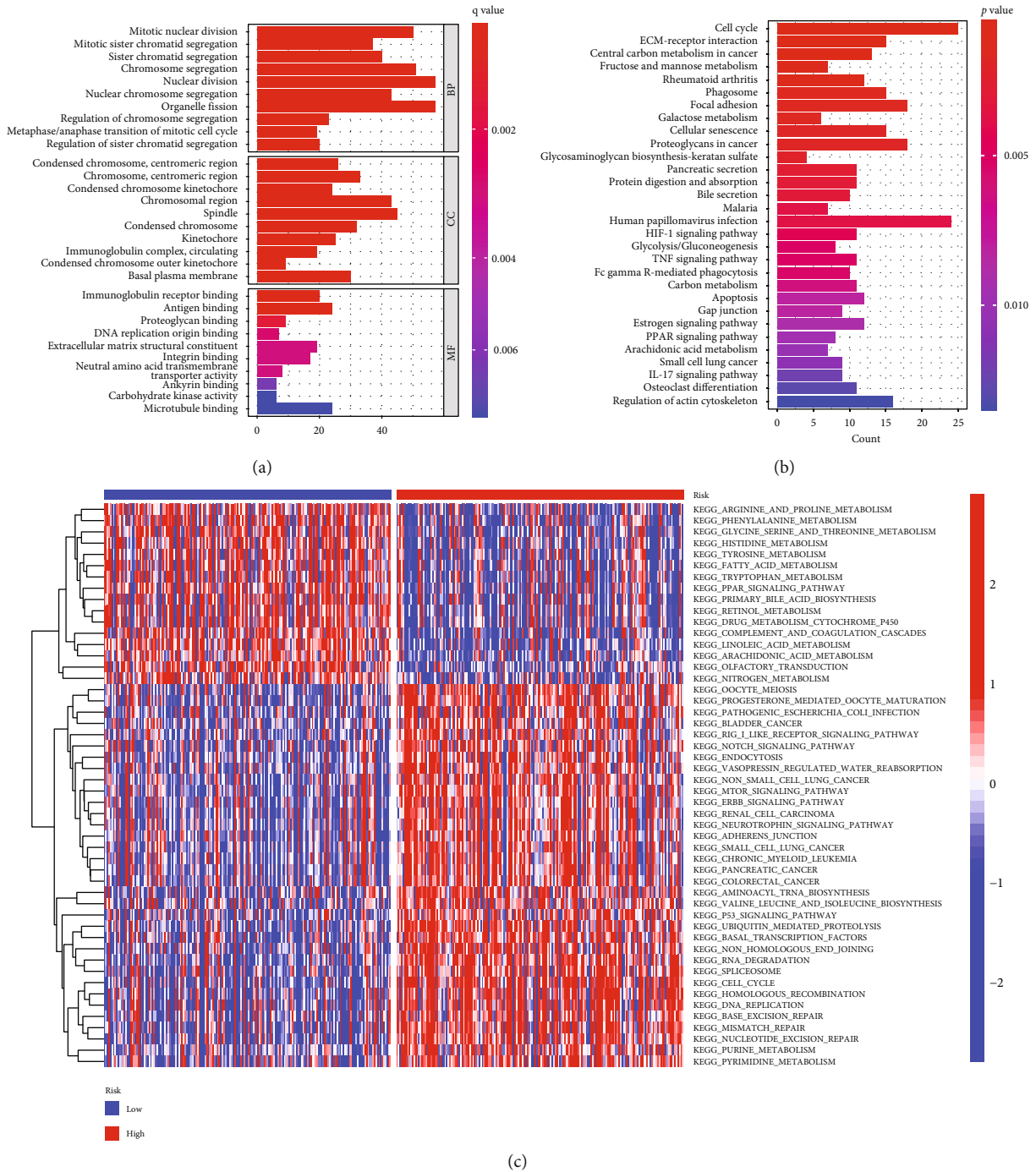
Figure 11: Functional enrichment analysis was performed according to the risk score. (a) A list of the top 10 significantly enriched GO terms. (b) A list of the top 30 most significantly enriched KEGG pathways. (c) The pathway activities scored by GSVA differently for high-risk and low-risk individuals.

cluster 2 could help to elucidate the underlying molecular mechanism of the unique tumor microenvironment. HCC patients with *TP53* mutations have poorer outcomes [39], and the mutation status of *TP53* can be used to predict immune response to immunotherapy in a variety of cancer types [40, 41]. Thus, we showed that CRG expression might be closely related to HCC prognosis and tumor microenvironment.

We next constructed and validated an effective risk model with 5 CRGs (*MTF1*, *DLAT*, *GLS*, *CDKN2A*, *LIPT1*) for separating HCC patients into high-risk and low-risk groups. The model displayed good predictive ability in both the training and validation dataset. We also designed the nomogram to combine the CRGs risk score model and clinical features, and the nomogram showed excellent prediction with good calibration. All these five genes exhibited

(a)

(b)

(c)
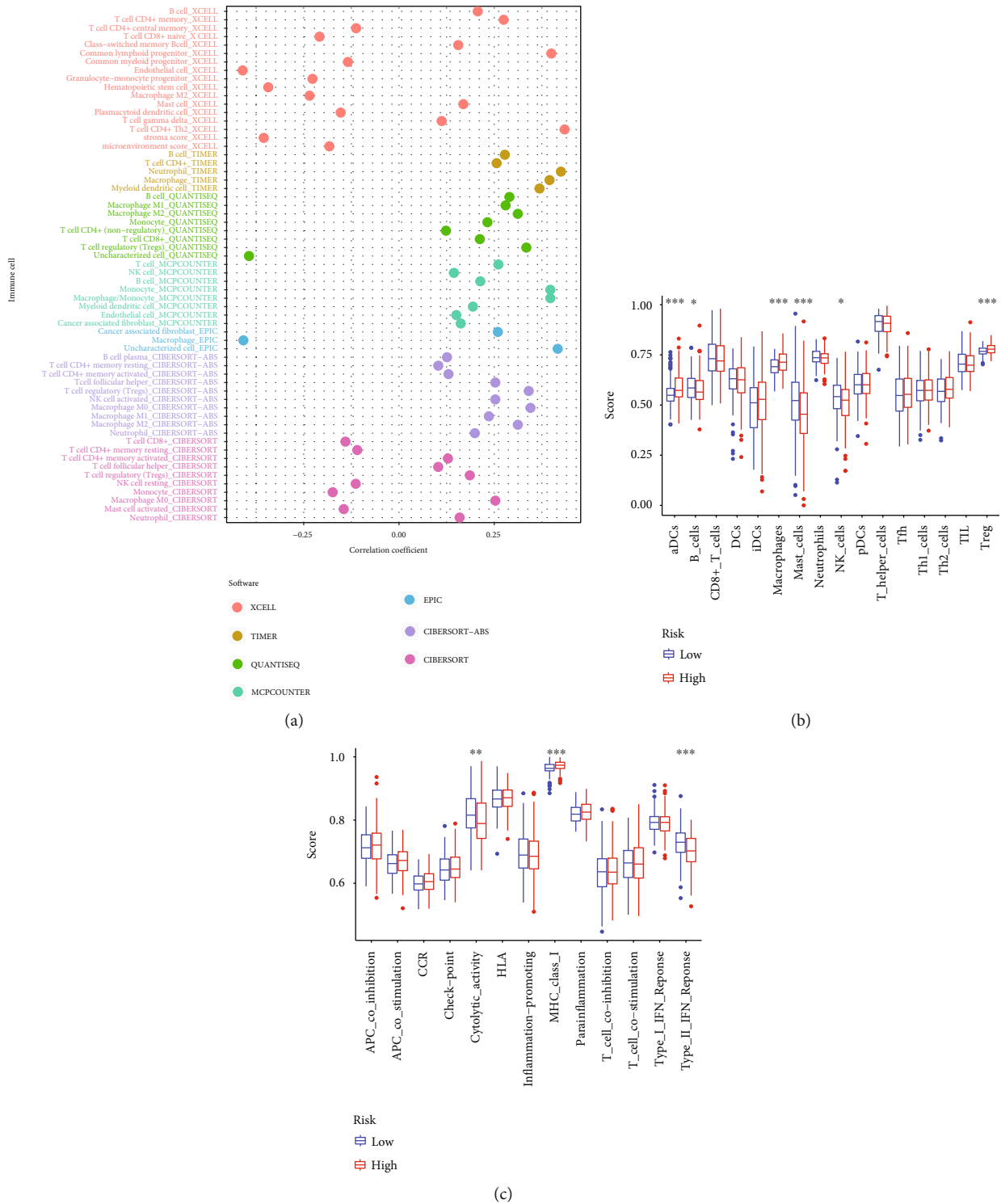
FIGURE 12: Continued.

(d)

(e)

(f)
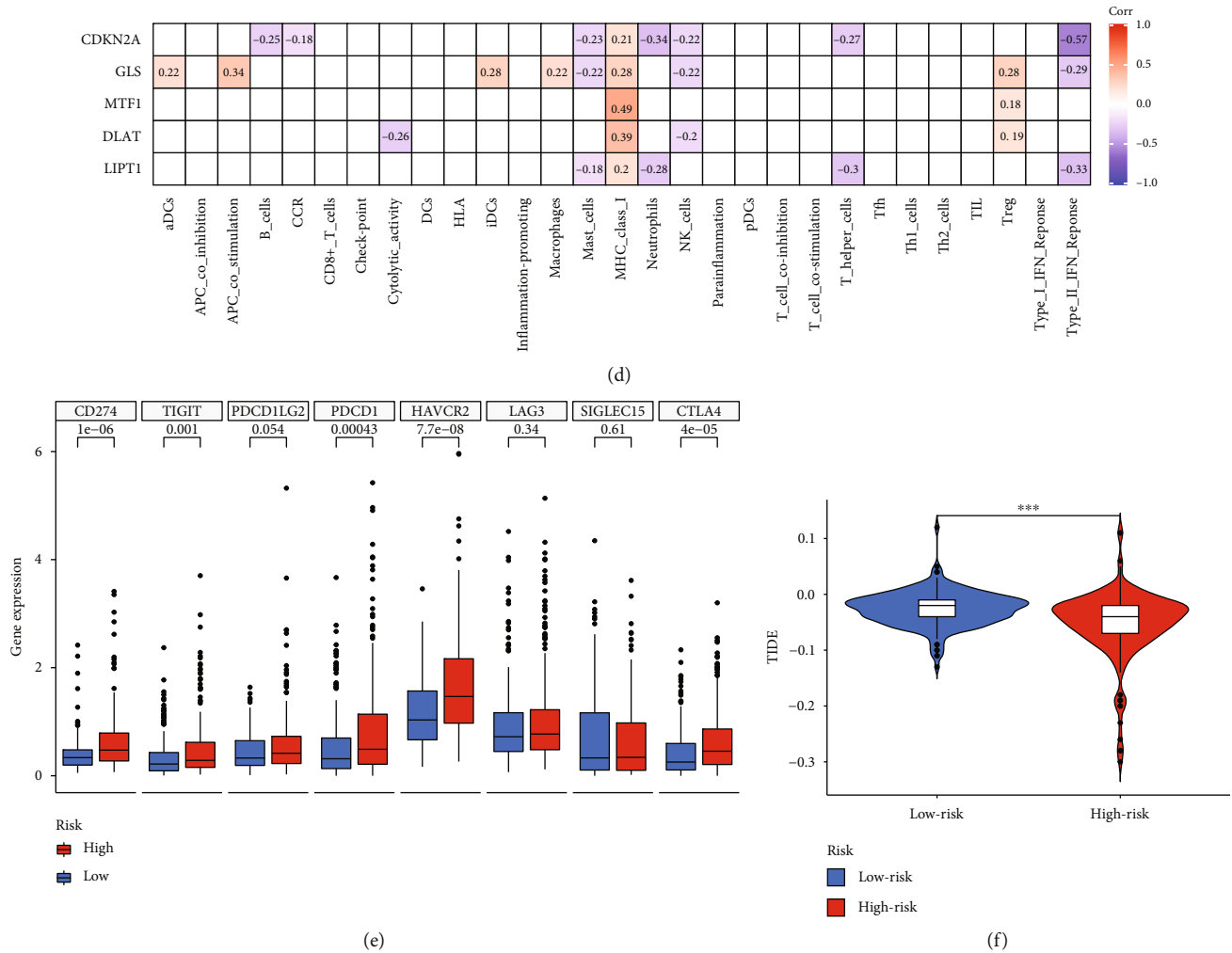
FIGURE 12: The immune landscape of cuproptosis-related risk score in HCC. (a) The forest plot displayed the connection between risk score and immune cell infiltration through TIMER, CIBERSORT, CIBERSORT-ABS, QUANTISEQ, MCPcounter, XCELL, and EPIC algorithms. (b, c) The bar graphs showed the difference in immune cell subpopulations and related functions between high-risk and low-risk groups. (d) The heatmap displayed the relationship of immune cell subpopulations and related functions with the five prognostic genes. (e) Differences in immune checkpoint expression between high-risk and low-risk groups. (f) The violin plots presented the TIDE scores between high-risk and low-risk groups. $^*p < 0.05$, $^{**}p < 0.01$, $^{***}p < 0.001$.

upregulated expression in HCC patients. As a classic metal sensing transcription factor, metal regulatory transcription factor 1 (*MTF1*) stimulates the expression of genes involved in metal homeostasis after exposure to heavy metals, including copper [42]. *MTF1* regulates hepatic *MT1/2* gene expression via a synergistic effect with *SIRT6*. By reducing ROS, inflammation, and tissue injury, *MT1/2* protects the liver from alcoholic liver disease [43]. Dihydrolipoamide S-acetyltransferase (*DLAT*) is one of the limited human proteins which can be lipoylated. Tsvetkov et al. discovered that lipoylated *DLAT* could bind copper and knocking out *DLAT* could prevent copper toxicity for cells [12]. *DLAT* encodes an essential subunit E2 of pyruvate dehydrogenase complex (*PDHC*), which is the critical autoantigen in primary biliary cholangitis (PBC) [44]. Cirrhosis and liver failure are associated with PBC [45]. In a recent study, it was found that posttranslational modifications of *PDHC* and *GLS* are involved in liver cancer metabolism and biogenesis

[46]. There are two main types of *GLS*: kidney glutaminase (*GLS1*) and liver glutaminase (*GLS2*) [47]. The overexpression of *GLS2* in human liver cancer cells induced significant growth, proliferation, ectopic expression, and a G2/M arrest [48]. *CDKN2A* (also known as p16) is a tumor suppressor gene and one of the most frequently deleted genes in cancer genomes [49]. HCCs harboring deletions of *CDKN2A* constitute approximately 8% of cases [50, 51]. *CDKN2A* induces cell cycle arrest at G1 and G2 phases and inhibits the oncogenic effects of *CDK4/6* and *MDM2* [52]. In the TCA cycle, lipoyltransferase 1 (*LIPT1*) activates TCA cycle-associated 2-ketoacid dehydrogenases. The lack of LIPT1 can inhibit the TCA cycle [53]. There is little evidence that *LIPT1* is associated with tumor occurrence and development. Taken together, these five crucial genes, except *LIPT1*, contribute to the progression and development of liver disease or HCC.

Our study found that the phenotype of high-risk patients is more advanced, and the survival time is significantly

shorter (Figures 6(g) and 6(h)). We hypothesized that cuproptosis resistance might be observed in high-risk patients, and cuproptosis might contribute to the poor outcomes of the patients in the high-risk group. *MTF1*, *GLS*, and *CDKN2A* were expressed at higher levels in these patients. Despite the two procuproptosis genes, *LIPT1* and *DLAT* were also upregulated in HCC patients. *LIPT1* is a key upstream regulator of protein lipoylation and a component of the lipoic acid pathway. *DLAT* is one of the protein targets of lipoylation [12]. Lipoylated *DLAT* could bind copper and take part in the regulation of cuproptosis. Thus, *LIPT1* and *DLAT* could regulate cuproptosis through post-translational modifications, not only through the gene expression levels. Secondly, the high-risk patients were not enriched in fatty acid metabolism pathways. The high-risk group patients might therefore show resistance to cuproptosis due to suppressed related proteins of lipoylation.

Cuproptosis might inspire novel insights to treat tumors. Keeping intracellular copper levels within a specific range would be an effective treatment strategy for malignancies [54]. Copper ionophores, such as DSF and elesclomol, are emerging treatment options for cancers and exert their therapeutic effects by inducing cuproptosis. Many studies have demonstrated that, in combination with cupric ions, DSF may be beneficial for treating a variety of cancers in humans [14, 55, 56]. Elesclomol is particularly effective against tumors relying on mitochondrial metabolism [57]. The combination of elesclomol with paclitaxel has been well documented in clinical trials, particularly in advanced melanoma [58–60]. Overall, these findings suggest that copper ionophore-induced cuproptosis could be an effective therapeutic strategy for certain tumors. There is hope that HCC patients with low-risk scores might enjoy the antitumor impact of the copper ionophores. Additionally, we found significant differences in the expression levels of the typical immune checkpoint and TIDE score between the high-risk and low-risk groups, suggesting our risk model may also show good predictability of response to ICB.

Our study has some weaknesses. First, the results may be biased since the small number of patients. Second, although this prognostic model demonstrated robust predictive ability in both TCGA and ICGC databases, there is no clinical data to further validate it, which is urgently warranted in future research. Third, these critical genes of this model require more experiments *in vitro* and *in vivo* to verify, which is underway in our laboratory.

5. Conclusions

In conclusion, CRGs were significantly differentially expressed between HCC and normal liver tissues, and the prognosis of HCC patients is significantly influenced by cuproptosis. A novel prognostic model containing five CRGs has been conducted for HCC prognosis prediction. High-risk HCC patients had a poor prognosis, advanced disease stages, and an enhanced therapeutic response. These results may shed light on new molecular pathways involved in HCC carcinogenesis and enable the prediction of treatment outcomes for HCC patients. Additional *in vitro* and *in vivo* studies to validate these results would be beneficial.

Data Availability

The RNA-seq and clinical data used to support the discoveries of this analysis were collected from the TCGA (https://portal.gdc.cancer.gov/) and ICGC (https://dcc.icgc.org/) databases.

Conflicts of Interest

No potential conflicts of interest were disclosed.

Authors' Contributions

Xiaolong Tang and Xiangqing Ren contributed equally to this work.

Acknowledgments

Supplementary Materials

Description of the three supplementary tables. Supplementary Table 1: immune cell infiltration between the two clusters via various methods. Supplementary Table 2: the relationship between the risk score of cuproptosis and clinicopathologic features in the TCGA database. Supplementary Table 3: the relationship between the risk score of cuproptosis and clinicopathologic features in the ICGC database. *(Supplementary Materials)*

References

[1] H. Sung, J. Ferlay, R. L. Siegel et al., "Global cancer statistics 2020: GLOBOCAN estimates of incidence and mortality worldwide for 36 cancers in 185 countries," *CA: a Cancer Journal for Clinicians*, vol. 71, no. 3, pp. 209–249, 2021.

[2] J. D. Yang, P. Hainaut, G. J. Gores, A. Amadou, A. Plymoth, and L. R. Roberts, "A global view of hepatocellular carcinoma: trends, risk, prevention and management," *Nature Reviews. Gastroenterology & Hepatology*, vol. 16, no. 10, pp. 589–604, 2019.

[3] A. Villanueva, "Hepatocellular carcinoma," *The New England Journal of Medicine*, vol. 380, no. 15, pp. 1450–1462, 2019.

[4] J. M. Llovet, S. Ricci, V. Mazzaferro et al., "Sorafenib in advanced hepatocellular carcinoma," *The New England Journal of Medicine*, vol. 359, no. 4, pp. 378–390, 2008.

[5] A. Huang, X.-R. Yang, W.-Y. Chung, A. R. Dennison, and J. Zhou, "Targeted therapy for hepatocellular carcinoma," *Signal Transduction and Targeted Therapy*, vol. 5, no. 1, p. 146, 2020.

[6] M. Kudo, R. S. Finn, S. Qin et al., "Lenvatinib versus sorafenib in first-line treatment of patients with unresectable

hepatocellular carcinoma: a randomised phase 3 non-inferiority trial," *Lancet*, vol. 391, no. 10126, pp. 1163–1173, 2018.

[7] G. Roviello, N. Sohbani, R. Petrioli, and M. G. Rodriquenz, "Ramucirumab as a second line therapy for advanced HCC: a significant achievement or a wasted opportunity for personalised therapy?," *Investigational New Drugs*, vol. 37, no. 6, pp. 1274–1288, 2019.

[8] G. K. Abou-Alfa, T. Meyer, A.-L. Cheng et al., "Cabozantinib in patients with advanced and progressing hepatocellular carcinoma," *The New England Journal of Medicine*, vol. 379, no. 1, pp. 54–63, 2018.

[9] J. Bruix, S. Qin, P. Merle et al., "Regorafenib for patients with hepatocellular carcinoma who progressed on sorafenib treatment (RESORCE): a randomised, double-blind, placebo-controlled, phase 3 trial," *Lancet*, vol. 389, no. 10064, pp. 56–66, 2017.

[10] A. B. El-Khoueiry, B. Sangro, T. Yau et al., "Nivolumab in patients with advanced hepatocellular carcinoma (CheckMate 040): an open-label, non-comparative, phase 1/2 dose escalation and expansion trial," *Lancet*, vol. 389, no. 10088, pp. 2492–2502, 2017.

[11] A. X. Zhu, R. S. Finn, J. Edeline et al., "Pembrolizumab in patients with advanced hepatocellular carcinoma previously treated with sorafenib (KEYNOTE-224): a non-randomised, open-label phase 2 trial," *The Lancet Oncology*, vol. 19, no. 7, pp. 940–952, 2018.

[12] P. Tsvetkov, S. Coy, B. Petrova et al., "Copper induces cell death by targeting lipoylated TCA cycle proteins," *Science*, vol. 375, no. 6586, pp. 1254–1261, 2022.

[13] A. Strasser and D. L. Vaux, "Cell death in the origin and treatment of cancer," *Molecular Cell*, vol. 78, no. 6, pp. 1045–1054, 2020.

[14] Y. Jiao, B. N. Hannafon, and W.-Q. Ding, "Disulfiram';s anticancer activity: evidence and mechanisms," *Anti-Cancer Agents in Medicinal Chemistry*, vol. 16, no. 11, pp. 1378–1384, 2016.

[15] J. R. Kirshner, S. He, V. Balasubramanyam et al., "Elesclomol induces cancer cell apoptosis through oxidative stress," *Molecular Cancer Therapeutics*, vol. 7, no. 8, pp. 2319–2327, 2008.

[16] P. Tsvetkov, A. Detappe, K. Cai et al., "Mitochondrial metabolism promotes adaptation to proteotoxic stress," *Nature Chemical Biology*, vol. 15, no. 7, pp. 681–689, 2019.

[17] A. Członkowska, T. Litwin, P. Dusek et al., "Wilson disease," *Nature Reviews. Disease Primers*, vol. 4, no. 1, p. 21, 2018.

[18] D. Gunjan, N. Nadda, S. Kedia et al., "Hepatocellular carcinoma: an unusual complication of longstanding Wilson disease," *Journal of Clinical and Experimental Hepatology*, vol. 7, no. 2, pp. 152–154, 2017.

[19] E. V. Polishchuk, A. Merolla, J. Lichtmannegger et al., "Activation of autophagy, observed in liver tissues from patients with wilson disease and from ATP7B-deficient animals, protects hepatocytes from copper- induced apoptosis," *Gastroenterology*, vol. 156, no. 4, pp. 1173–1189.e5, 2019.

[20] J. Guo, J. Cheng, N. Zheng et al., "Copper promotes tumorigenesis by activating the PDK1-AKT oncogenic pathway in a copper transporter 1 dependent manner," *Advanced Science*, vol. 8, no. 18, article e2004303, 2021.

[21] M. E. Ritchie, B. Phipson, D. Wu et al., "Limma powers differential expression analyses for RNA-sequencing and microarray studies," *Nucleic Acids Research*, vol. 43, no. 7, article e47, 2015.

[22] T. Galili, A. O'Callaghan, J. Sidi, and C. Sievert, "Heatmaply: an R package for creating interactive cluster heatmaps for online publishing," *Bioinformatics*, vol. 34, no. 9, pp. 1600–1602, 2018.

[23] A. Franceschini, D. Szklarczyk, S. Frankild et al., "STRING v9.1: protein-protein interaction networks, with increased coverage and integration," *Nucleic Acids Research*, vol. 41, no. D1, pp. D808–D815, 2012.

[24] P. Shannon, A. Markiel, O. Ozier et al., "Cytoscape: a software environment for integrated models of biomolecular interaction networks," *Genome Research*, vol. 13, no. 11, pp. 2498–2504, 2003.

[25] M. D. Wilkerson and D. N. Hayes, "ConsensusClusterPlus: a class discovery tool with confidence assessments and item tracking," *Bioinformatics*, vol. 26, no. 12, pp. 1572-1573, 2010.

[26] G. Yu, L.-G. Wang, Y. Han, and Q.-Y. He, "clusterProfiler: an R package for comparing biological themes among gene clusters," *OMICS*, vol. 16, no. 5, pp. 284–287, 2012.

[27] A. Subramanian, P. Tamayo, V. K. Mootha et al., "Gene Set Enrichment Analysis: a knowledge-based approach for interpreting genome-wide expression profiles," *Proceedings of the National Academy of Sciences of the United States of America*, vol. 102, no. 43, pp. 15545–15550, 2005.

[28] S. Hänzelmann, R. Castelo, and J. Guinney, "GSVA: gene set variation analysis for microarray and RNA-seq data," *BMC Bioinformatics*, vol. 14, no. 1, p. 7, 2013.

[29] A. Mayakonda, D.-C. Lin, Y. Assenov, C. Plass, and H. P. Koeffler, "Maftools: efficient and comprehensive analysis of somatic variants in cancer," *Genome Research*, vol. 28, no. 11, pp. 1747–1756, 2018.

[30] R. Tibshirani, "The lasso method for variable selection in the cox model," *Statistics in Medicine*, vol. 16, no. 4, pp. 385–395, 1997.

[31] P. Blanche, J.-F. Dartigues, and H. Jacqmin-Gadda, "Estimating and comparing time-dependent areas under receiver operating characteristic curves for censored event times with competing risks," *Statistics in Medicine*, vol. 32, no. 30, pp. 5381–5397, 2013.

[32] A. Iasonos, D. Schrag, G. V. Raj, and K. S. Panageas, "How to build and interpret a nomogram for cancer prognosis," *Journal of Clinical Oncology*, vol. 26, no. 8, pp. 1364–1370, 2008.

[33] J. Fu, K. Li, W. Zhang et al., "Large-scale public data reuse to model immunotherapy response and resistance," *Genome Medicine*, vol. 12, no. 1, p. 21, 2020.

[34] S. Blockhuys, E. Celauro, C. Hildesjö et al., "Defining the human copper proteome and analysis of its expression variation in cancers," *Metallomics*, vol. 9, no. 2, pp. 112–123, 2017.

[35] P. Hedera, "Wilson's disease: a master of disguise," *Parkinsonism & Related Disorders*, vol. 59, pp. 140–145, 2019.

[36] C. Gerosa, D. Fanni, T. Congiu et al., "Liver pathology in Wilson's disease: from copper overload to cirrhosis," *Journal of Inorganic Biochemistry*, vol. 193, pp. 106–111, 2019.

[37] Z. Bian, R. Fan, and L. Xie, "A novel cuproptosis-related prognostic gene signature and validation of differential expression in clear cell renal cell carcinoma," *Genes (Basel)*, vol. 13, no. 5, p. 851, 2022.

[38] H. Lv, X. Liu, X. Zeng et al., "Comprehensive analysis of cuproptosis-related genes in immune infiltration and prognosis in melanoma," *Frontiers in Pharmacology*, vol. 13, article 930041, 2022.

[39] P. Zhan, Y.-N. Ji, and L.-K. Yu, "TP53 mutation is associated with a poor outcome for patients with hepatocellular

carcinoma: evidence from a meta-analysis," *Hepatobiliary Surgery and Nutrition*, vol. 2, no. 5, pp. 260–265, 2013.

[40] L. Li, M. Li, and X. Wang, "Cancer type-dependent correlations between *TP53* mutations and antitumor immunity," *DNA Repair*, vol. 88, article 102785, 2020.

[41] F. Skoulidis, M. E. Goldberg, D. M. Greenawalt et al., "STK11/LKB1 mutations and PD-1 inhibitor resistance in KRAS-mutant lung adenocarcinoma," *Cancer Discovery*, vol. 8, no. 7, pp. 822–835, 2018.

[42] C. Tavera-Montañez, S. J. Hainer, D. Cangussu et al., "The classic metal-sensing transcription factor MTF1 promotes myogenesis in response to copper," *The FASEB Journal*, vol. 33, no. 12, pp. 14556–14574, 2019.

[43] H. G. Kim, M. Huang, Y. Xin et al., "The epigenetic regulator SIRT6 protects the liver from alcohol-induced tissue injury by reducing oxidative stress in mice," *Journal of Hepatology*, vol. 71, no. 5, pp. 960–969, 2019.

[44] T. K. Mao, P. A. Davis, J. A. Odin, R. L. Coppel, and M. E. Gershwin, "Sidechain biology and the immunogenicity of PDC-E2, the major autoantigen of primary biliary cirrhosis," *Hepatology*, vol. 40, no. 6, pp. 1241–1248, 2004.

[45] Z. M. Younossi, D. Bernstein, M. L. Shiffman et al., "Diagnosis and management of primary biliary cholangitis," *The American Journal of Gastroenterology*, vol. 114, no. 1, pp. 48–63, 2019.

[46] X. Huang, G. Gan, X. Wang, T. Xu, and W. Xie, "The HGF-MET axis coordinates liver cancer metabolism and autophagy for chemotherapeutic resistance," *Autophagy*, vol. 15, no. 7, pp. 1258–1279, 2019.

[47] D. Baglietto-Vargas, J. F. López-Téllez, I. Moreno-González, A. Gutiérrez, and J. C. Aledo, "Segregation of two glutaminase isoforms in islets of Langerhans," *The Biochemical Journal*, vol. 381, no. 2, pp. 483–487, 2004.

[48] J. Zhang, C. Wang, M. Chen et al., "Epigenetic silencing of glutaminase 2 in human liver and colon cancers," *BMC Cancer*, vol. 13, no. 1, p. 601, 2013.

[49] R. Beroukhim, C. H. Mermel, D. Porter et al., "The landscape of somatic copy-number alteration across human cancers," *Nature*, vol. 463, no. 7283, pp. 899–905, 2010.

[50] K. Schulze, S. Imbeaud, E. Letouzé et al., "Exome sequencing of hepatocellular carcinomas identifies new mutational signatures and potential therapeutic targets," *Nature Genetics*, vol. 47, no. 5, pp. 505–511, 2015.

[51] C. Guichard, G. Amaddeo, S. Imbeaud et al., "Integrated analysis of somatic mutations and focal copy-number changes identifies key genes and pathways in hepatocellular carcinoma," *Nature Genetics*, vol. 44, no. 6, pp. 694–698, 2012.

[52] F. Belinky, N. Nativ, G. Stelzer et al., "PathCards: multi-source consolidation of human biological pathways," *Database*, vol. 2015, article bav006, 2015.

[53] A. Solmonson, B. Faubert, W. Gu et al., "Compartmentalized metabolism supports midgestation mammalian development," *Nature*, vol. 604, no. 7905, pp. 349–353, 2022.

[54] M. A. Kahlson and S. J. Dixon, "Copper-induced cell death," *Science*, vol. 375, no. 6586, pp. 1231-1232, 2022.

[55] Z. Skrott, M. Mistrik, K. K. Andersen et al., "Alcohol-abuse drug disulfiram targets cancer via p97 segregase adaptor NPL4," *Nature*, vol. 552, no. 7684, pp. 194–199, 2017.

[56] D. Chen, Q. C. Cui, H. Yang, and Q. P. Dou, "Disulfiram, a clinically used anti-alcoholism drug and copper-binding agent, induces apoptotic cell death in breast cancer cultures and xenografts via inhibition of the proteasome activity," *Cancer Research*, vol. 66, no. 21, pp. 10425–10433, 2006.

[57] B. Halliwell and J. M. Gutteridge, "Oxygen toxicity, oxygen radicals, transition metals and disease," *The Biochemical Journal*, vol. 219, no. 1, pp. 1–14, 1984.

[58] S. O'Day, R. Gonzalez, D. Lawson et al., "Phase II, randomized, controlled, double-blinded trial of weekly elesclomol plus paclitaxel versus paclitaxel alone for stage IV metastatic melanoma," *Journal of Clinical Oncology*, vol. 27, no. 32, pp. 5452–5458, 2009.

[59] S. J. O'Day, A. M. Eggermont, V. Chiarion-Sileni et al., "Final results of phase III SYMMETRY study: randomized, double-blind trial of elesclomol plus paclitaxel versus paclitaxel alone as treatment for chemotherapy-naive patients with advanced melanoma," *Journal of Clinical Oncology*, vol. 31, no. 9, pp. 1211–1218, 2013.

[60] A. Berkenblit, J. P. Eder, D. P. Ryan et al., "Phase I clinical trial of STA-4783 in combination with paclitaxel in patients with refractory solid tumors," *Clinical Cancer Research*, vol. 13, no. 2, pp. 584–590, 2007.

Research Article

Seven Immune-Related Genes' Prognostic Value and Correlation with Treatment Outcome in Head and Neck Squamous Cell Carcinoma

Rui Mu,[1,2,3] **Yuehong Shen,**[1,2,3] **Chuanbin Guo,**[4] **Xinyun Zhang,**[5] **Hongyu Yang** [1,2,3] **and Huijun Yang** [1,2,3]

[1]*Stomatology Center, The Institute of Stomatology, Peking University Shenzhen Hospital, Shenzhen Peking University-The Hong Kong University of Science and Technology Medical Center, Shenzhen, China*
[2]*Guangdong Provincial High-Level Clinical Key Specialty, Shenzhen, China*
[3]*Guangdong Province Engineering Research Center of Oral Disease Diagnosis and Treatment, Shenzhen, China*
[4]*Department of Oral and Maxillofacial Surgery, Peking University School and Hospital of Stomatology, Beijing, China*
[5]*School of Clinical Medicine, The Zhuhai Campus of the Zunyi Medical University, Zhuhai, China*

Correspondence should be addressed to Hongyu Yang; hyyang192@hotmail.com and Huijun Yang; yanghj8801019@163.com

Background. Head and neck squamous cell carcinoma (HNSCC) is a growing concern worldwide, due to its poor prognosis, low responsiveness to treatment, and drug resistance. Since immunotherapy effectively improves HNSCC patients' survival status, it is important to continuously explore new immune-related predictive factors to accurately predict the immune landscape and clinical outcomes of individuals suffering from HNSCC. *Methods.* The HNSCC transcriptome profiling of RNA-sequencing data was retrieved from TCGA database, and the microarray of GSE27020 was obtained from the GEO database for validation. The differentially expressed genes (DEGs) between HNSCC and normal samples were identified by multiple test corrections in TCGA database. The univariate and multivariate Cox analyses were performed to identify proper immune-related genes (IRGs) to construct a risk model. The Cox regression coefficient was employed for calculation of the risk score (RS) of IRG signature. The median value of RS was utilized as a basis to classify individuals with HNSCC into high- and low-risk groups. The Kaplan-Meier (K-M) survival analysis and receiver operating characteristic (ROC) curves were employed for the identification of the prognostic significance and precision of the IRG signature. The signature was also evaluated based on clinical variables, predictive nomogram, mutation analysis, infiltrating immune cells, immune-related pathways, and chemotherapeutic efficacy. The protein-protein interaction (PPI) network and functional enrichment pathway investigations were utilized to explore possible potential molecular mechanisms. Finally, the hub gene's differential mRNA expression levels were evaluated by means of the Gene Expression Profiling Interactive Analysis (GEPIA), and the Human Protein Atlas (HPA) was utilized for the validation of their translational levels. *Results.* Collectively, 1593 DEGs between HNSCC and normal samples were identified, of which 136 IRGs were differentially expressed. Then, the 136 immune-related DEGs were mostly enriched in the cytokine-related signaling pathways by GO and KEGG analyses. After that, a valuable signature based on seven genes (*DKK1*, *GAST*, *IGHM*, *IL12RB2*, *SLURP1*, *STC2*, and *TNFRSF4*) was designed. The HNSCC patients into the low-risk group and the high-risk group were divided by using the median RS; the HNSCC patients in the high-risk group had a worse survival than those in the low-risk group. The risk signature was verified to be an independent predictive marker for HNSCC patients. Meanwhile, the RS had the largest contribution to survival of these patients based on the predictive nomogram. In addition, the low-risk HNSCC patients exhibited significantly enriched immune cells, along with an association with high chemosensitivity. *Conclusion.* The constructed gene signature can independently function as a predictive indicator for the clinical features of HNSCC patients. The low-risk HNSCC subjects might benefit from immunotherapy and chemotherapy.

1. Introduction

As the sixth most prevalent type of malignancy, head and neck squamous cell carcinoma (HNSCC) is the seventh main cause of cancer-related mortalities globally [1]. A study conducted in the United States predicted that by 2022, approximately 66,470 new HNSCC cases would arise and 15,050 HNSCC-related deaths would occur [2]. Despite steady advancements in relevant medical treatments, like surgery, radiotherapy, and chemotherapy, the five-year survival of individuals with HNSCC has not significantly improved [3]. Therefore, finding new and innovative novel prognostic factors for HNSCC patients is an urgent need.

HNSCC is considered an immunodeficiency disease. The main mechanisms underlying the disease include the induction of immune tolerance, local immune escape, and the destruction of T-cell signals [4]. The immune microenvironment of HNSCC has been widely studied [5, 6]. For instance, the human leukocyte antigen (HLA) is responsible for the vital function of transmitting signals between tumor antigen peptides and killer T cells [7]. A previous study demonstrated that more than 50% of HNSCC patients had low HLA expression, with extensive lymph node metastasis and poor prognosis [8]. HNSCC tumor cells could also release chemical factors, to induce many immunosuppressive hematological cells to enter the immune microenvironment, thus suppressing the immune response [9].

Meanwhile, studying how HNSCC survival is linked to infiltrating immune cell proliferation and function could improve the survival of HNSCC patients [10–12]. Immunotherapy's effect on the clinical outcomes of individuals with HNSCC has also been intensively studied [13–15]. This is why the exploration of immune-related biomarkers to anticipate the clinical features of individuals with HNSCC is imperative. Recent studies demonstrated that immune-related biomarkers could affect the biological behavior of HNSCC as well as the status of patients. For instance, Yao et al.'s model consisted of four immune-related genes (IRGs), including *PVR*, *TNFRSF12A*, *IL21R*, and *SOCS1* [16]; Chen et al. constructed predictive model based on three IRGs (*SFRP4*, *CPXM1*, and *COL5A1*) [17]; and Zhang et al. established a model based on six IRGs (*PLAU*, *STC2*, *TNFRSF4*, *PDGFA*, *DKK1*, and *CHGB*) for the prognostic prediction of HNSCC [18]. Although these studies have constructed a proper model to predict the prognosis of patients with HNSCC, the progression of HNSCC is complexity and uncertainty. Therefore, to date, reliable and predictive biomarkers for identifying HNSCC are still limited; it is essential to continuously look for newly representative biomarkers.

During this research, a risk signature of seven immune-related genes was developed for accurately predicting the clinical outcomes of HNSCC subjects, which may provide an effective treatment strategy for these patients.

2. Methods

2.1. Dataset.
The transcriptome profiling of RNA-sequencing (FPKM) was attained from The Cancer Genome Atlas (TCGA) (https://cancergenome.nih.gov/) containing 502 cancerous and 44 healthy tissues samples, along with the relevant clinical information for 528 HNSCC patients. In total, 2483 IRGs were procured from The ImmPort database (https://immport.niaid.nih.gov/) [19, 20]. Besides, the microarray and clinical information of GSE27020 containing 109 HNSCC samples were provided by the Gene Expression Omnibus (GEO) (https://www.ncbi.nlm.nih.gov/gds/) for authentication.

2.2. Development of the IRG-Based Signature.
The differentially expressed genes (DEGs) between cancerous and healthy samples were identified with the help of TCGA database after multiple test corrections by false discovery rate (FDR) < 0.05 and |log fold change (FC)| > 2 [21]. Then, screening the intersections of these DEGs with IRGs was carried out. Univariate Cox proportional hazards regression analysis was employed for the determination of the predictive ability of IRGs for the overall survival (OS) of individuals with HNSCC with the aid of the "survival" package in R [22]. The genes with a threshold of $P < 0.05$ were subjected to further evaluation using multivariate Cox regression analysis [23]. Then, the expression levels of the hub genes were compared for further exploring their expression features in normal and HNSCC tumor tissues. Subsequently, the calculation of the IRG-based signature-related risk score (RS) was done using the Cox regression coefficient and gene expression formula given below:

$$RS = \sum_{i=1}^{N} (Expi * Co\text{-}eff) \qquad (1)$$

N, Expi, and Co-eff indicate signature gene number, gene expression levels, and regression coefficient values, respectively. Using the median value of RS as a criterion, the individuals with HNSCC were classified into the low- and high-risk groups.

2.3. Prognosis Prediction by the IRG-Based Signature.
For the verification of the IRG-based signature's prognostic performance, the signature's impact on OS in both risk groups was subjected to comparison by Kaplan-Meier (K-M) survival analysis utilizing the "survival" package in R software, followed by the area under the curve (AUC) of the receiver operating characteristic (ROC) curves to assess IRG-based signature's accuracy through the "survival ROC" package in R software [24]. Subsequently, the GEO database (GSE27020) was used for external validation. It was also subjected to K-M survival analysis and ROC curves to identify the signature's prognostic value and precision. The RS distribution and survival status of individuals with HNSCC in TCGA were constructed to further understand the prognostic capability of the signature.

2.4. Correlation Analysis.
The association of IRG-based signature with clinical variables (age, pathological grade, gender, and tumor and TNM stages) was analyzed. Moreover, the clinical factors and robustness of the signature in predicting the OS were demonstrated by employing univariate and multivariate Cox regression analyses.
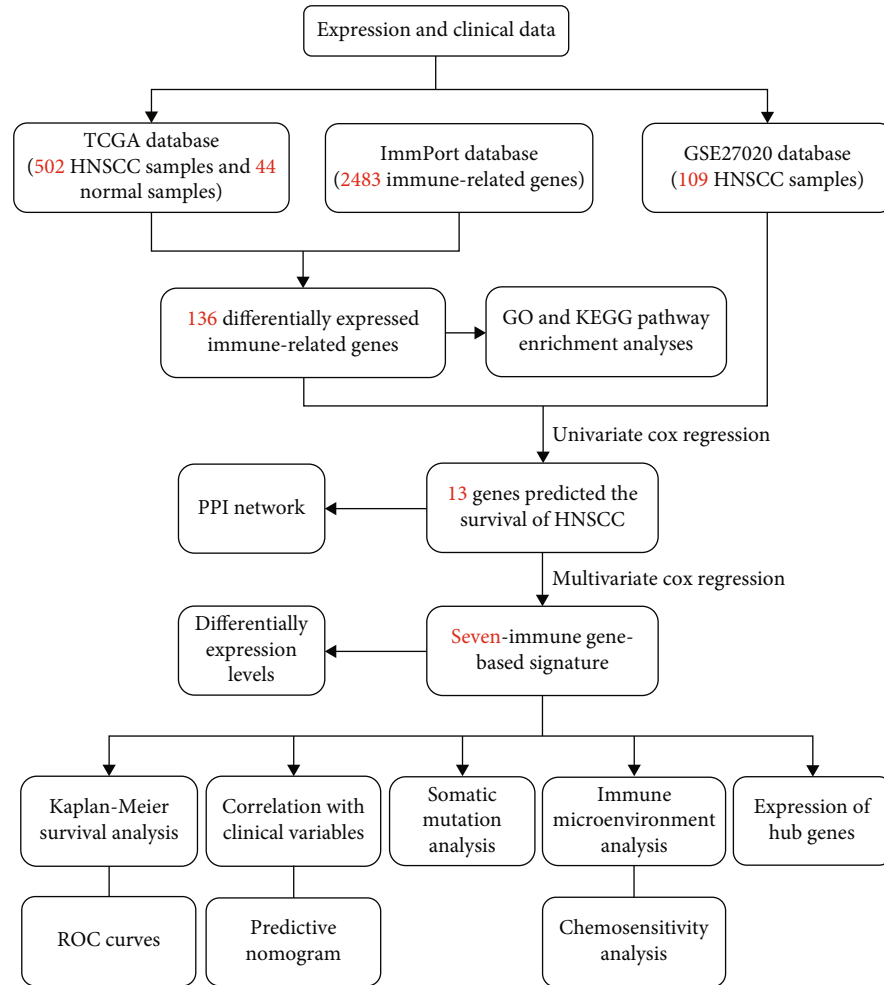
FIGURE 1: The workflow of the present study. TCGA: The Cancer Genome Atlas; HNSCC: head and neck squamous cell carcinoma; PPI: protein-protein interaction; GO: Gene Ontology; KEGG: Kyoto Encyclopedia of Genes and Genomes; ROC: receiver operating characteristic.

2.5. Construction of a Predictive Nomogram. Based on clinical variables, a nomogram was used to establishment a prognostic scoring system for predicting survival in HNSCC patients both in TCGA and GSE27020 databases.

2.6. Somatic Mutation Analysis. We obtained the somatic mutation profiles of all tumor samples from TCGA database and explored the mutation analysis for 528 patients. The R software "maftools" package was utilized to analyzed and visualized for mutation data of the low-risk group and the high-risk group.

2.7. Immune Microenvironment Analysis. Considering the involvement of infiltrating immune cells in the tumor microenvironment, the single-sample gene set enrichment analysis (ssGSEA) algorithm was utilized to evaluate the immune score of each HNSCC sample from TCGA and GSE27020 databases [25]. The different proportions of the infiltrating immune cells between the low- and high-risk groups were assessed by the Wilcoxon test. Moreover, the association between the RS and immune-related biological

functions was performed for further exploring the underlining mechanisms. The gene expression profiles corresponding to samples of TCGA and GSE27020 databases were selected to perform the gene set variation analysis (GSVA).

2.8. Prediction of Clinical Application. The calculation of the half inhibitory concentration (IC50) of common chemotherapeutic agents was done, and the differences in the IC50 across the two risk groups were also evaluated for predicting the clinical application of the IRG-based signature both in TCGA and GSE27020 databases.

2.9. Molecular Mechanism Analysis. The STRING biological database (https://string-db.org/) was applied for extraction of the protein-protein interaction (PPI) network [26] as a mathematical representation of the physical contacts among differentially expressed IRGs linked to HNSCC patient survival. Thereafter, Gene Ontology (GO) and Kyoto Encyclopedia of Genes and Genomes (KEGG) pathway enrichment analyses were employed in determining the potential function of the immune-related DEGs [27].

(a)

(b)

(c)

(d)
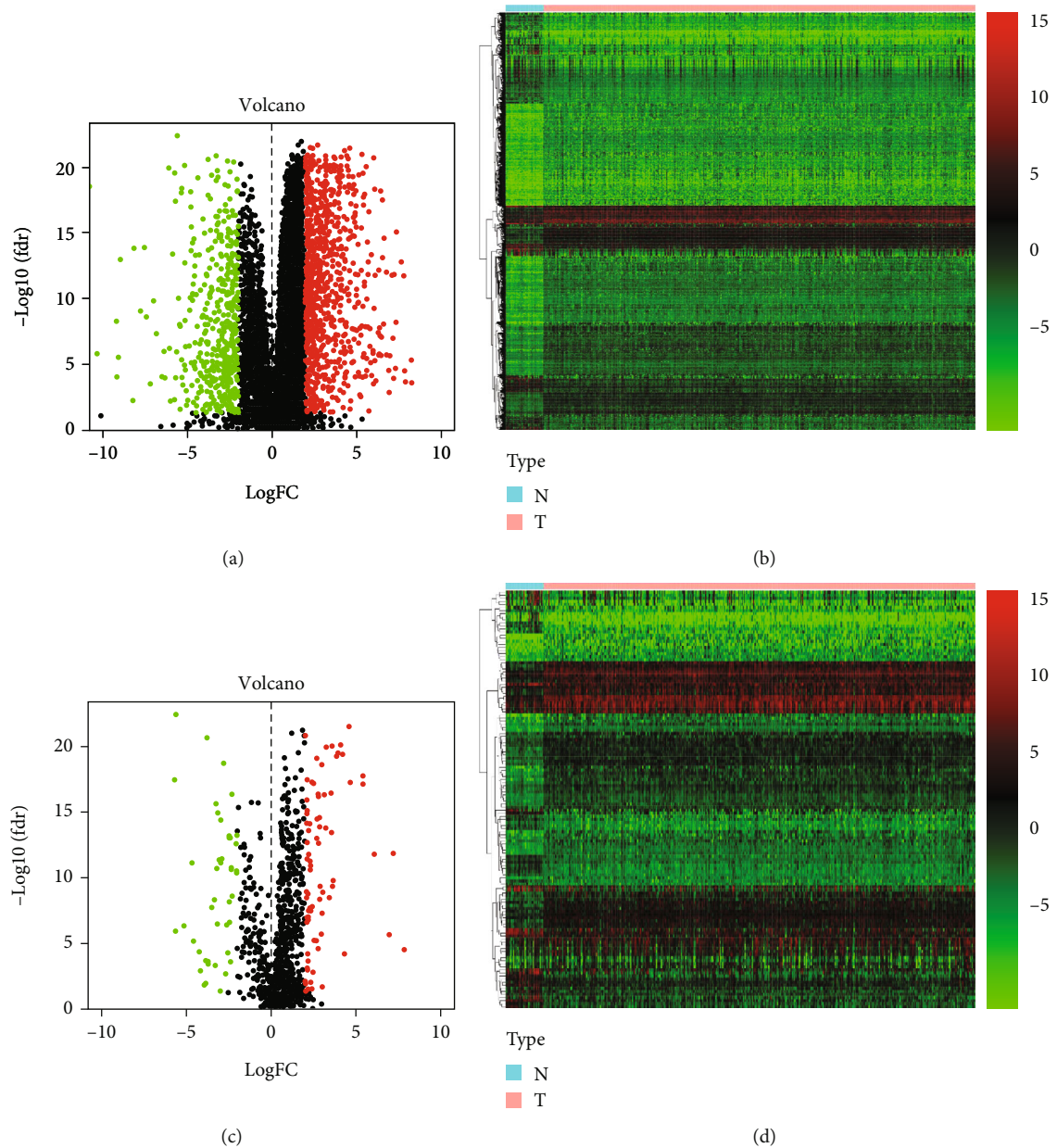
Figure 2: Analysis of differentially expressed genes. (a) Volcano plot of differentially expressed genes in HNSCC. Red dots represent upregulated genes, and green dots represent downregulated genes with statistical significance (FDR < 0.05, |logFC| > 2), while black dots represent the genes without differential significance. (b) Heatmap of differentially expressed genes in HNSCC tumor tissues. The colors from green to red represent differentially expressed genes with low to high expression levels. (c) Volcano plot of differentially expressed immune-related genes in HNSCC tumor tissues. (d) Heatmap of differentially expressed immune-related genes in HNSCC tumor tissues.

2.10. Investigating the Expression of Hub Genes. The Gene Expression Profiling Interactive Analysis (GEPIA) (http://gepia.cancer-pku.cn/) was utilized for the investigation of the differential mRNA expression profiles of the hub genes in the IRG-based signature. Moreover, the Human Protein Atlas (HPA) (https://www.proteinatlas.org/) was employed for the purpose of validating the translational levels of these hub genes.

2.11. Statistical Analysis. R version 3.6.2 was utilized to conduct statistical analysis procedures. DEGs were com-pared with multiple test corrections with FDR < 0.05 and |logFC| > 2 were viewed as being dramatically dysregulated. The survival curves were estimated by using the K-M survival analysis and log-rank test between different groups. Clinico-pathological features were compared by univariate and multivariate Cox regression analyses. The ssGSEA algorithm and Wilcoxon test were used to compare different propor-tions of the infiltrating immune cells between different groups. The *t*-test or Wilcoxon test for comparisons of two variables, and a *P* < 0.05 (two-side) was taken as a statistically significant value.

(a)

(b)

(c)
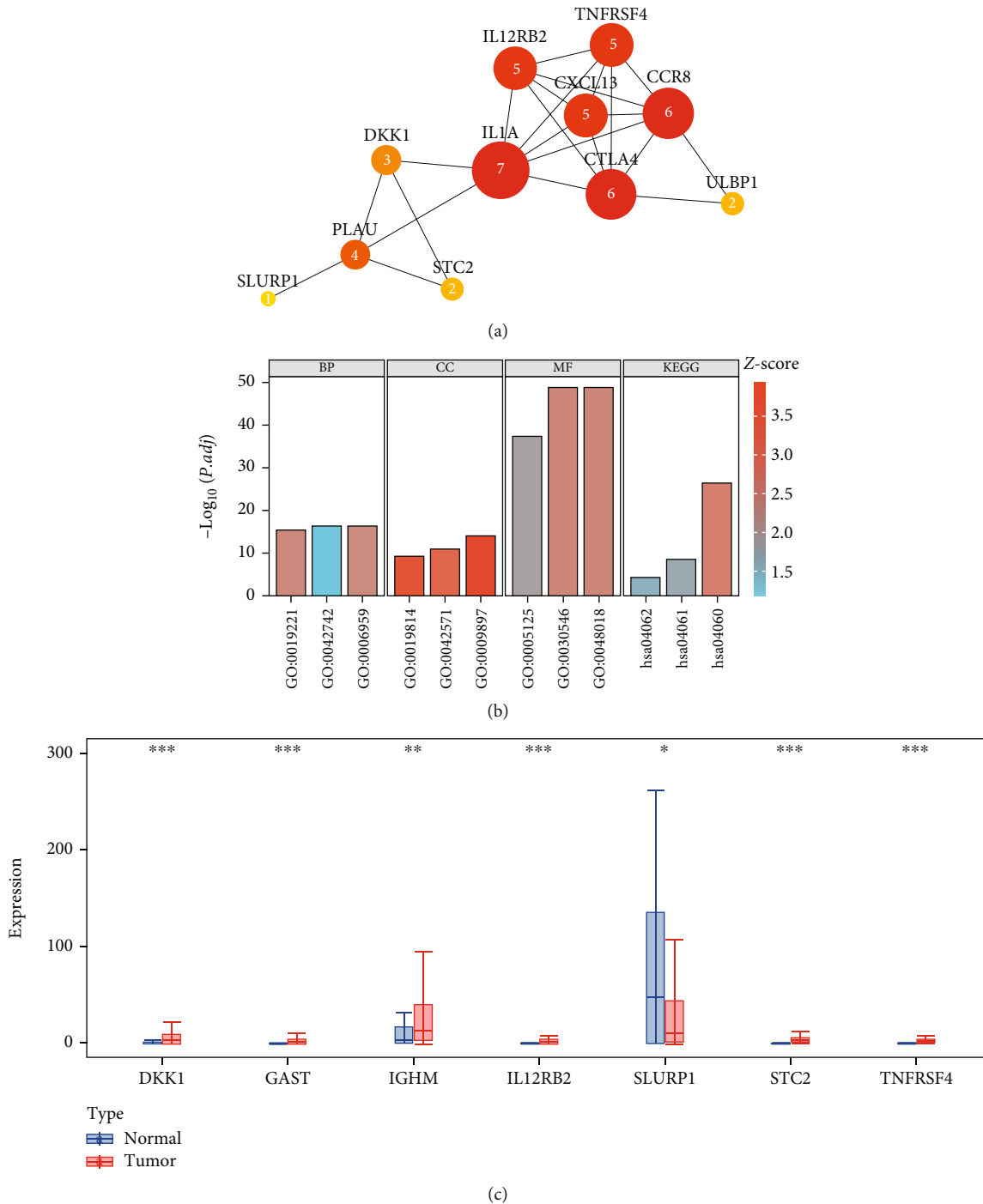
FIGURE 3: Immune-related differentially expressed genes analyzes. (a) PPI network of immune-related differentially expressed genes as predictors of prognosis of HNSCC patients. The Arabic numerals represent the degree of genes. (b) The GO and KEGG pathway analyses based on immune-related differentially expressed genes. (c) Comparison of the expression levels of the seven IRGs between normal tissues and tumor tissues. $^{*}P < 0.05$, $^{**}P < 0.01$, and $^{***}P < 0.001$.

3. Results

3.1. Differential Gene Expression Analysis. TCGA database was employed to retrieve the HNSCC RNA-sequencing data comprising 502 tumor samples and 44 healthy samples. Among these patients, 528 HNSCC subjects with gene

expression profiles and clinical follow-up data were included. The workflow of this research is illustrated in Figure 1. In the differential gene expression analysis, 1593 DEGs between HNSCC and healthy samples were identified (Figures 2(a) and 2(b)), of which 136 IRGs were differentially expressed (Figures 2(c) and 2(d)). Among these genes, 13 genes were

TABLE 1: Comparison of characteristics between TCGA database and the GEO database (GSE27020).

Characteristic	TCGA		GSE27020		P^*
	Frequency	Deaths (%)	Frequency	Deaths (%)	
Total	528	170 (32.20)	109	34 (31.19)	
Age (years)					0.063
≤65	345	99 (28.70)	61	19 (31.15)	
>65	182	71 (39.01)	48	15 (31.25)	
Unknown	1	0			
Sex					—
Male	386	114 (29.53)	—	—	
Female	142	56 (39.44)	—	—	
Grade					0.023
G1-G2	374	120 (32.09)	91	29 (31.87)	
G3-G4	132	43 (32.58)	16	5 (31.25)	
Unknown	22	7 (31.82)	2	0	
Stage					—
Stage I-stage II	120	40 (33.33)	—	—	
Stage III-stage IV	394	130 (32.99)	—	—	
Unknown	14	0			
T					—
T1-T2	189	53 (28.04)	—	—	
T3-T4	323	117 (36.22)	—	—	
Unknown	16	0			
M					—
M0	496	166 (33.47)	—	—	
M1	6	3 (50.00)	—	—	
Unknown	26	1 (3.85)			
N					—
N0	246	88 (35.77)	—	—	
N1-N3	260	81 (31.15)	—	—	
Unknown	22	1 (4.55)			

TCGA: The Cancer Genome Atlas; GEO: Gene Expression Omnibus. *Chi-square test for the comparison of characteristics between TCGA database and the GSE27020 database for each clinical variable.

identified to predict survival in the univariate Cox regression analysis. To study their interactions, the STRING biological database was utilized to construct the PPI network, containing 11 nodes and 22 edges. Based on the degree of genes, *IL1A, CTLA4, CCR8, IL12RB2, TNFRSF4, CXCL13,* and *PLAU* appeared to be the core genes among these IRGs (Figure 3(a)). As for functional analysis in Figure 3(b), the 136 immune-related DEGs were mostly enriched in immune response/cytokine mediation (BP), immunoglobulin complex/external side of plasma membrane (CC), and cytokine activity/signaling receptor activator activity/receptor ligand activity (MF) by GO analysis. By KEGG pathway analysis, the genes were mostly enriched in cytokine-cytokine receptor interaction, viral protein interaction with cytokine and cytokine receptor, and chemokine signaling pathway.

3.2. Development and Verification of the IRG-Based Prognostic Signature. The detailed characteristics along with population demographics are given in Table 1. To develop a

TABLE 2: The detailed information of the immune-related gene signature for the survival of HNSCC patients.

Gene name	Coef	HR (95% CI)	P value
DKK1	0.006062	1.006 (0.998-1.014)	0.118
GAST	0.010886	1.011 (1.001-1.021)	0.024
IGHM	-0.000928	0.999 (0.998-1.000)	0.108
IL12RB2	-0.051088	0.950 (0.894-1.010)	0.099
SLURP1	-0.001863	0.998 (0.997-1.000)	0.012
STC2	0.025190	1.026 (1.006-1.046)	0.011
TNFRSF4	-0.089341	0.915 (0.831-1.007)	0.069

HNSCC: head and neck squamous cell carcinoma; Coef: regression coefficient value; HR: hazard ratio; CI: confidence interval.

predictive IRG-based signature, seven IRGs were chosen after univariate and multivariate Cox analyses (Table 2). Meanwhile, the expression levels of the seven IRGs were further investigated. Compared with normal tissues, only *SLURP1*

(a)

(b)

(c)

(d)

(e)

(f)

Figure 4: Continued.

(g)
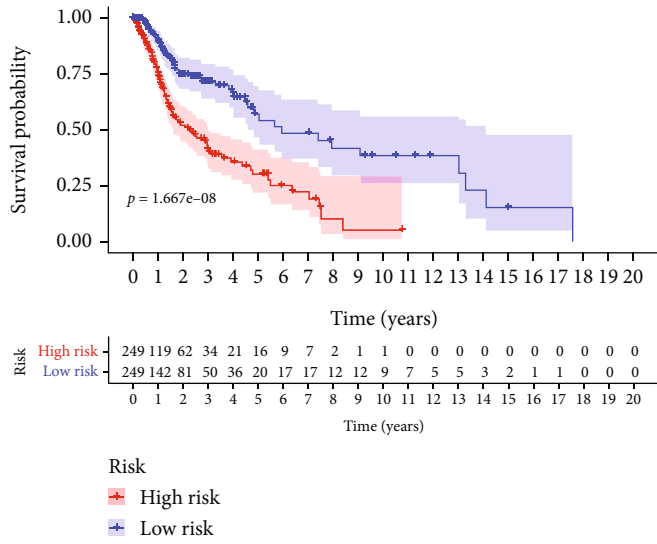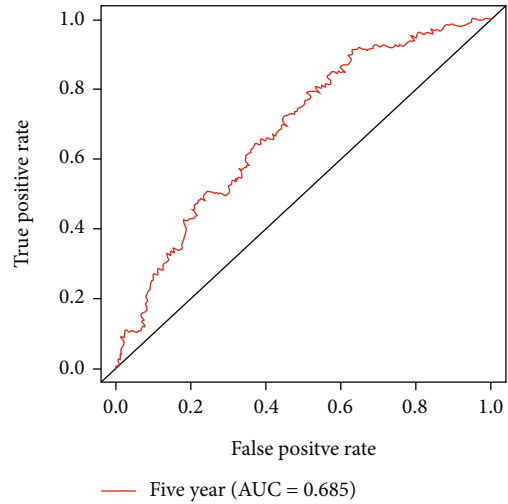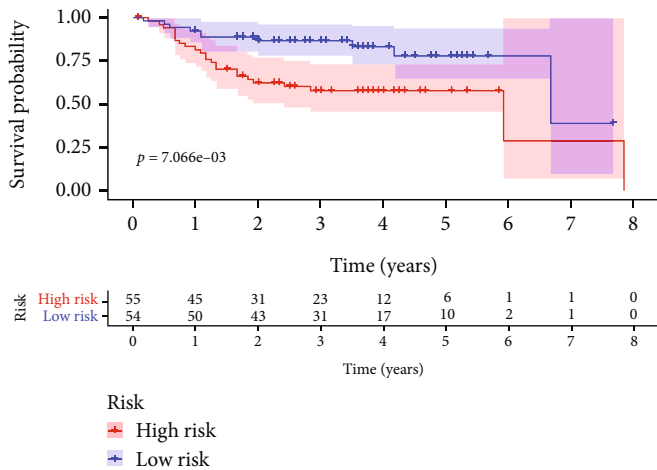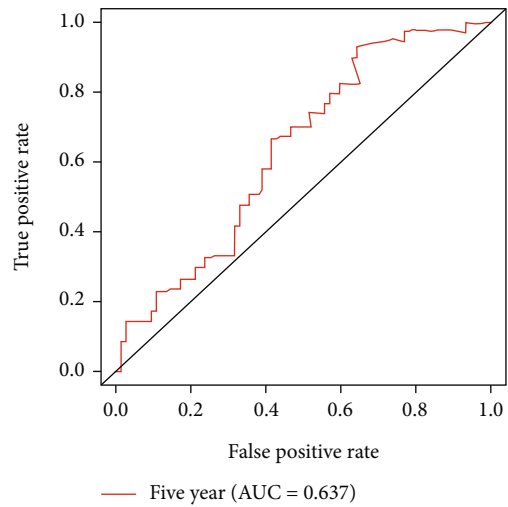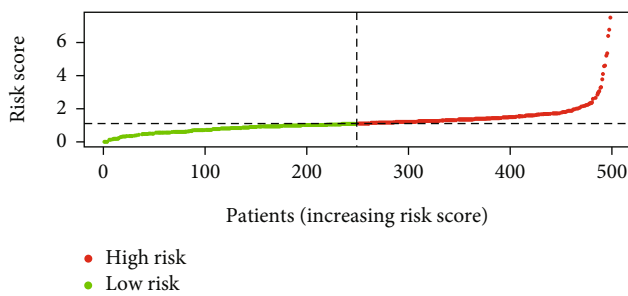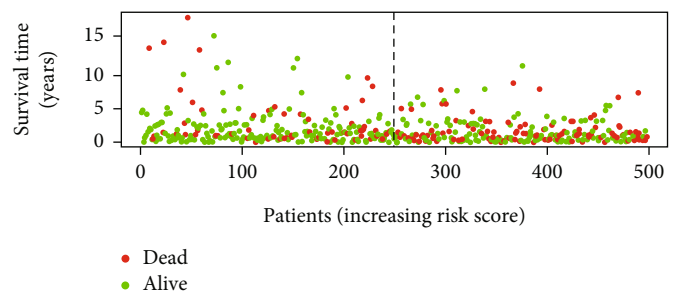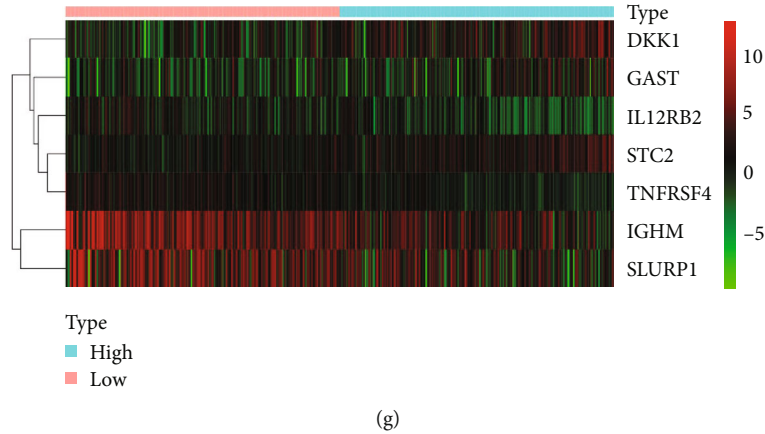
FIGURE 4: Development and validation of prognostic signature derived from immune-related genes. (a) K-M analysis of the effect of the prognostic signature on OS of HNSCC patients in TCGA database. (b) ROC curves of the prognostic signature in TCGA database. (c) K-M analysis of the effect of the prognostic signature on OS of HNSCC patients in the GEO database. (d) ROC curves of the prognostic signature in the GEO database. (e) The RS distribution in HNSCC patients. (f) The survival status of HNSCC patients. (g) Heatmap of the expression of nine immune-related genes in the low-risk and high-risk groups.

was downregulated in tumor tissues, while the expression levels of *DKK1*, *GAST*, *IGHM*, *IL12RB2*, *STC2*, and *TNFRSF4* were upregulated in tumor tissues (Figure 3(c)). Then, the calculation of the RS of this IRG-based signature was done as follows: RS = (0.006062^*DKK1) + (0.010886^*GAST) + (-0.000928^*IGHM) + $(-0.051088^*IL12RB2)$ + $(-0.001863^*SLURP1)$ + (0.025190^*STC2) + $(-0.089341^*TNFRSF4)$.

Moreover, individuals with HNSCC were categorized into the low-risk group ($n = 249$) and the high-risk group ($n = 249$) as per the median RS. HNSCC patients at high risk showed a worse survival in the K-M analysis, in comparison to the patients at low risk ($P < 0.001$) (Figure 4(a)), with the AUC of 0.685 for the 5-year ROC curve (Figure 4(b)), indicating a certain predictive value of the signature in predicting the survival of individuals with HNSCC. Meanwhile, this IRG-based signature was validated in the GEO database (GSE27020) of 109 HNSCC patients who were also grouped into the low-risk group ($n = 54$) and the high-risk group ($n = 55$). Consistent with TCGA database, the K-M analysis of the GEO data exhibited that high-risk HNSCC individuals presented a worse survival in comparison with the low-risk group ($P < 0.05$) (Figure 4(c)), with the AUC of 0.637 for 5-year ROC curve (Figure 4(d)).

Additionally, there were more deaths in HNSCC patients with the elevation in the value of RS (Figures 4(e) and 4(f)), and the seven genes showed differences in mRNA expression across the two groups in the heat map (Figure 4(g)).

3.3. Use of IRG-Based Signature as an Independent Prognostic Marker for HNSCC.
Univariate and multivariate Cox regression analyses were conducted for assessing the correlations between the IRG-based signature and clinical variables (age, gender, grade, tumor stage, and TNM stage). The findings indicated that OS of HNSCC patients was significantly associated with age (HR = 1.022, 95%CI = 1.008 – 1.037, $P = 0.003$), M stage (HR = 3.595, 95%CI = 1.137 – 11.370, $P = 0.029$), and the RS calculated from the IRG-

based signature (HR = 1.650, 95%CI = 1.452 – 1.876, $P < 0.001$) (Figure 5(a)) in univariate Cox regression analysis and also with age (HR = 1.020, 95%CI = 1.005 – 1.036, $P = 0.010$), M stage (HR = 4.643, 95%CI = 1.334 – 16.163, $P = 0.016$), and the RS (HR = 1.634, 95%CI = 1.432 – 1.864, $P < 0.001$) in multivariate Cox regression analysis (Figure 5(b)).

Furthermore, the associations between clinicopathological parameters and the RS and associations between the seven genes and clinical variables were also evaluated (Table 3, Figure 5(c)). The results revealed that the male gender, high tumor stage, and T stage were linked to a greater value of RS. In addition, mRNA expression levels of *IGHM* and *SLURP1* appeared to be elevated in females in comparison to males. The mRNA expression level of STC2 appeared to be elevated in males when compared with females, and a high pathological grade was correlated with lower mRNA expression of *GAST* and *SLURP1*. The results also suggested that higher mRNA expression of *IGHM* was remarkably linked to a high grade. Greater mRNA expression of *GAST* was significantly linked to a more advanced tumor stage. The elevated mRNA expression level of *DKK1* and *GAST* was correlated with the advanced T stage. Moreover, lower mRNA expression of *IGHM*, as well as higher mRNA expression of *SLURP1* and *STC2*, was correlated with the advanced M stage.

3.4. Construction of a Predictive Nomogram.
The clinical variables and RS were included in the nomogram. As indicated in the nomogram, the RS had the largest contribution to survival of patients with HNSCC both in TCGA and GSE27020 databases (Figures 6(a) and 6(b)).

3.5. Somatic Mutation Analysis.
We obtained somatic mutation profiles of 528 patients in TCGA database. Around 241 (97.57%) and 229 (93.47%) samples possessed somatic mutations in the high-risk and low-risk groups, respectively. The top 30 mutated genes for high-risk and low-risk groups
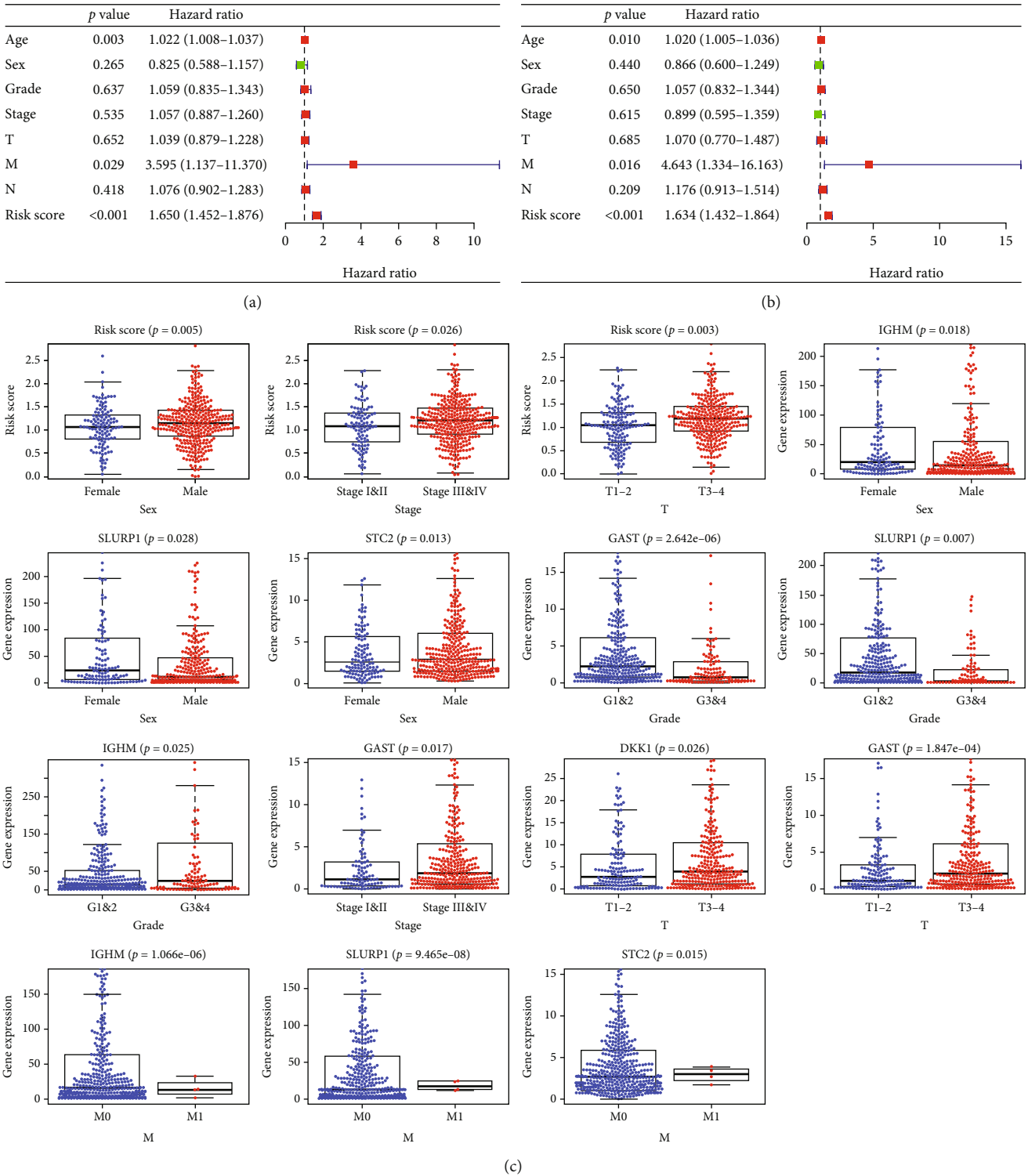
FIGURE 5: Correlations between the prognostic signature and clinical characteristics of HNSCC. (a) Forest plot of univariate Cox analysis. (b) Forest plot of multivariate Cox analysis. (c) Correlations between the risk score of expression of the seven genes and clinical characteristics.

are shown in Figures 7(a) and 7(b). The results indicated that the *TP53* mutated most frequently approximately accounting for 78% and 62% in the high-risk and low-risk groups, respectively.

3.6. *Immune Microenvironment Analysis.* The association between 23 immune cells infiltration differences and different risk groups was analyzed in TCGA and GSE27020 databases. Patients in the low-risk group showed higher

TABLE 3: Correlations between the seven immune-related genes and clinical characteristics.

Gene name	Age (P value)	Sex (P value)	Grade (P value)	Stage (P value)	T (P value)	M (P value)	N (P value)
DKK1	1.314 (0.190)	-0.346 (0.730)	-1.882 (0.062)	-1.725 (0.086)	-2.233 (0.026)	-0.502 (0.649)	-1.181 (0.238)
GAST	-1.550 (0.123)	-0.787 (0.432)	4.759 (<0.001)	-2.389 (0.017)	-3.773 (<0.001)	0.013 (0.990)	-0.107 (0.915)
IGHM	0.207 (0.836)	-2.370 (0.018)	-2.271 (0.025)	0.009 (0.993)	1.094 (0.275)	5.116 (<0.001)	-1.114 (0.266)
IL12RB2	-0.347 (0.729)	1.676 (0.095)	-0.499 (0.618)	1.820 (0.071)	1.411 (0.160)	0.459 (0.677)	1.261 (0.208)
SLURP1	0.071 (0.943)	2.221 (0.028)	2.717 (0.007)	1.622 (0.107)	0.632 (0.528)	5.777 (<0.001)	1.517 (0.130)
STC2	-1.203 (0.230)	-2.498 (0.013)	-1.658 (0.100)	-1.140 (0.256)	-0.647 (0.518)	3.320 (0.015)	0.085 (0.932)
TNFRSF4	1.154 (0.250)	-1.014 (0.311)	-1.484 (0.140)	-0.900 (0.368)	1.407 (0.161)	0.662 (0.535)	-1.381 (0.169)

(a)

(b)
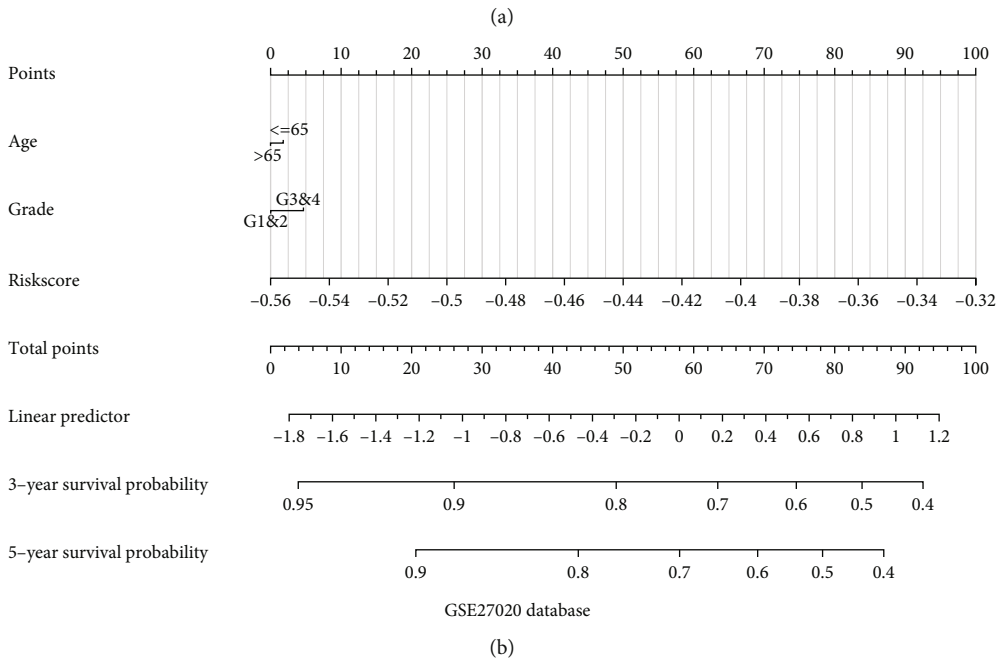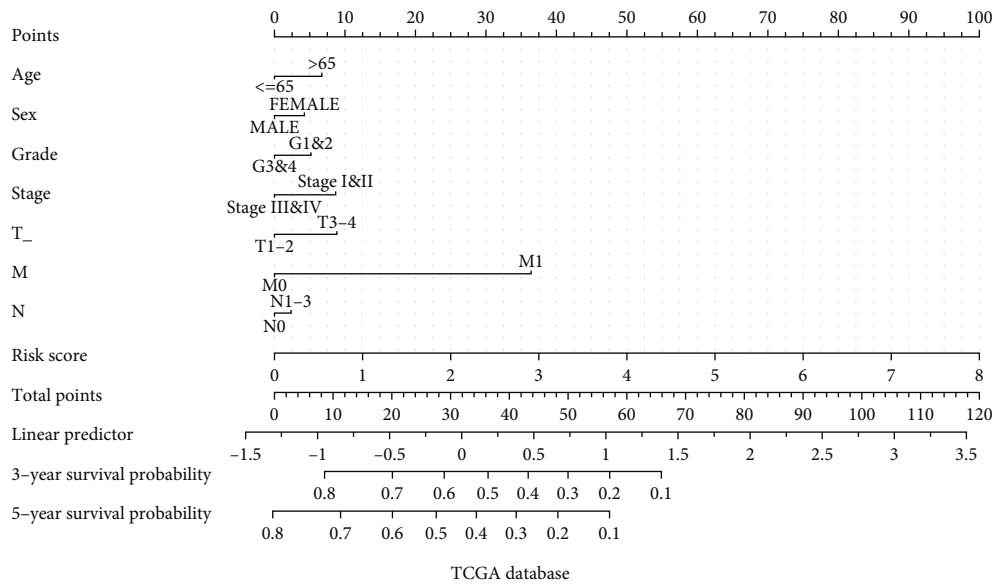
FIGURE 6: Nomogram for the prediction of survival for patients with HNSCC. (a) Nomogram for the prediction of survival at 3 and 5 years in TCGA database. (b) Nomogram for the prediction of survival at 3 and 5 years in the GSE27020 database.
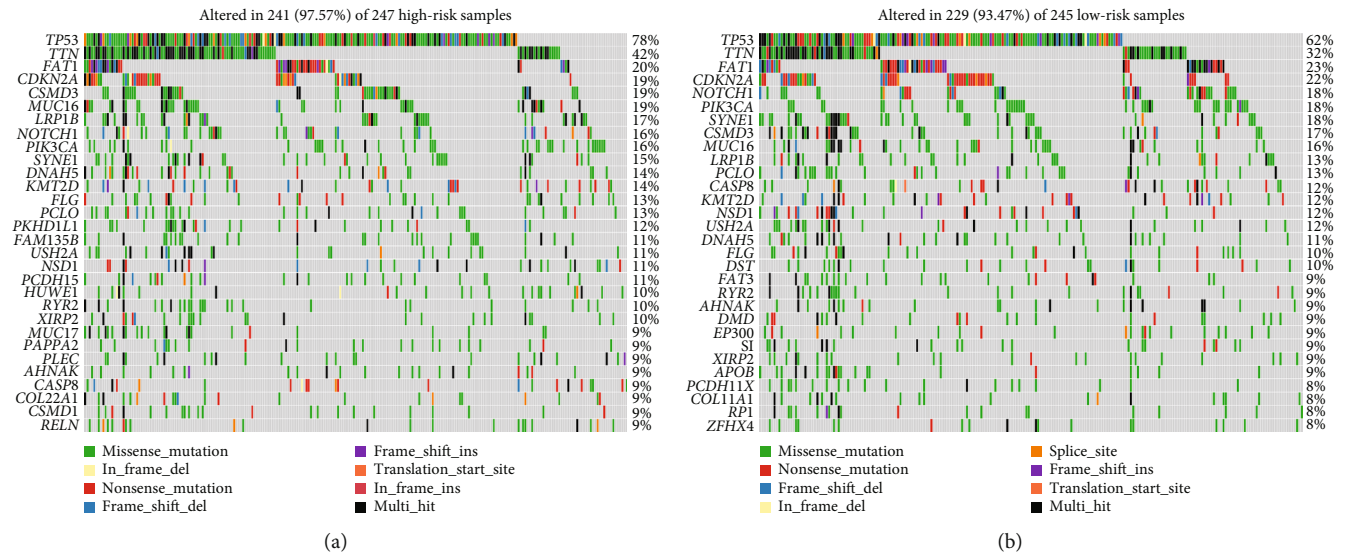
FIGURE 7: Evaluation of somatic mutation. (a) The mutation profile of the top 30 mutation genes in high-risk patients. (b) The mutation profile of the top 30 mutation genes in low-risk patients.

infiltration levels of these 23 immune cells in TCGA database (Figure 8(a)), and patients in the low-risk group were more correlated with the infiltration of activated CD8 T cell, activated dendritic cell, CD56dim natural killer cell, eosinophil, immature B cell, mast cell, MDSC, monocyte, natural killer cell, natural killer T cell, neutrophil, T follicular helper cell, type 1 T helper cell, and type 17 T helper cell in the GSE27020 database (Figure 8(b)).

In addition, the relationship between immune pathway scores and RS were analyzed in order to better explore the immune-related biological functions. Functions with a correlation greater than 0.2 and $P < 0.05$ are shown in Supplementary Figure 1. The results indicated that 14 immune-related pathways were correlated negatively with the RS in TCGA database (Supplementary Figure 1A). In the GSE27020 database, 8 immune-related pathways were correlated negatively with the RS, while 1 was correlated positively (Supplementary Figure 1B). These immune-related pathway scores vary with increasing levels of RS, implying that an imbalance in these pathways is closely related to tumor development.

3.7. Prediction of Clinical Application. The association of risk with the therapeutic efficacy of common chemotherapeutic agents in HNSCC was also studied. The findings exhibited that the low-risk HNSCC patients presented increased sensitivity to Elesclomol, GW843682X, Midostaurin, Pazopanib, QS11, and Salubrinal in TCGA database (Figure 9(a)), and the low-risk group was more likely with higher sensitivity of Bexarotene, BI.2536, MG.132, QS11, Salubrinal, and Thapsigargin in the GSE27020 database (Figure 9(b)). The results indicated that HNSCC patients with low risk represented higher sensitivity to chemotherapy.

3.8. Investigation of the Expression of the Seven IRGs. The expression of the seven IRGs in HNSCC was explored with the help of the GEPIA database. The expression levels of

the seven IRGs varied remarkably across cancerous and healthy tissues (Figure 10(a)). However, to validate these findings, more experimental analyses were required. Moreover, the HPA database was employed to investigate the expression of the seven IRGs at the translation level. Among the seven IRGs, expressions of *IGHM* and *SLURP1* were lower in the HNSCC tissues. Moreover, *STC2* showed higher expression in HNSCC by immunohistochemistry. No remarkable variations were observed in the expressions of *GAST*, *IL12RB2*, and *TNFRSF4* across normal and HNSCC tissues, while *DKK1* was not detected by immunohistochemistry in the HPA database (Figure 10(b)). However, to further validate the translational relevance of the seven IRGs on HNSCC, more clinical analyses on HNSCC samples are needed.

4. Discussion

During this research, an IRG-based signature was established, which was capable of anticipating the clinical landscapes of HNSCC patients and correlated with clinicopathological characteristics of affected individuals, the numbers of tumor-infiltrating immune cells, and the efficacy of common chemotherapeutics. These findings suggested that this signature may be valuable for predicting HNSCC-related prognosis and provide good clinical application in immunotherapy and chemotherapy.

The IRG-based signature consisted of seven genes (i.e., *DKK1*, *GAST*, *IGHM*, *IL12RB2*, *SLURP1*, *STC2*, and *TNFRSF4*). Among them, *DKK1* is a member of the DKK family and regulates cell proliferation, migration, and apoptosis in various tumor tissues through β-catenin-dependent and β-catenin-independent mechanisms [28]. Moreover, as a tumor suppressor gene, *DKK1* causes apoptosis and suppresses cell proliferation [29]. Gao et al. suggested that elevated *DKK1* expression levels can predict poor prognosis in HNSCC patients [30]. *STC2* regulates tumor cell

(a)

(b)
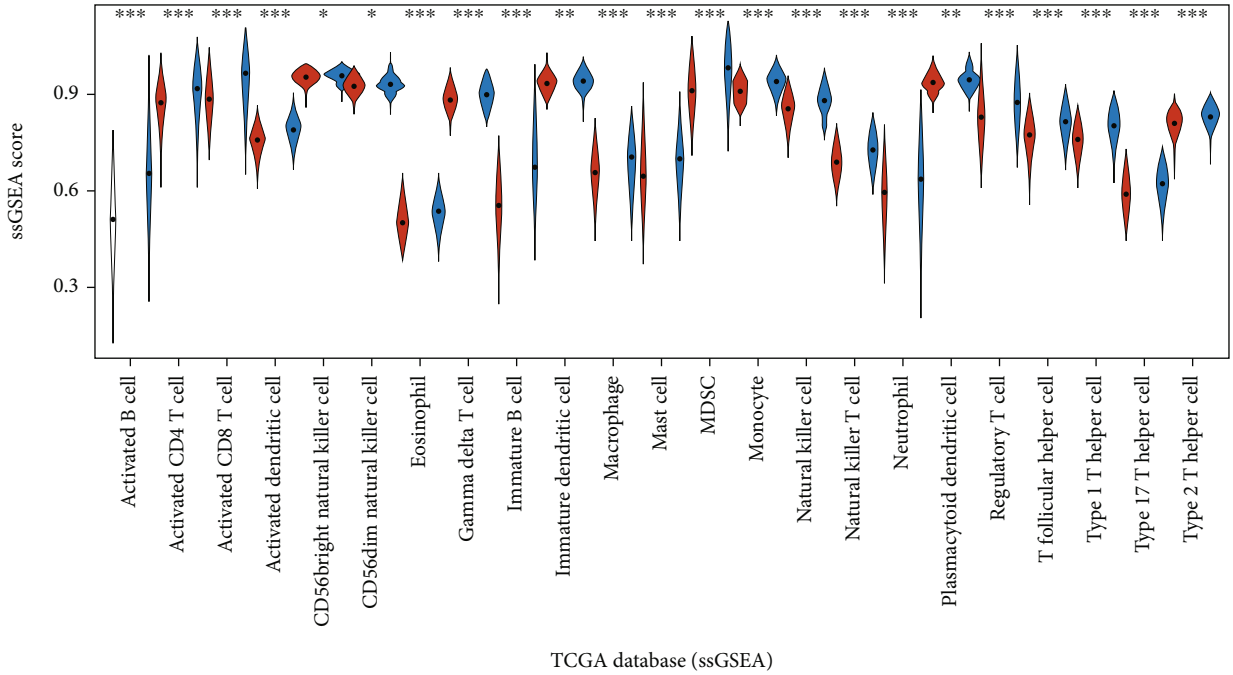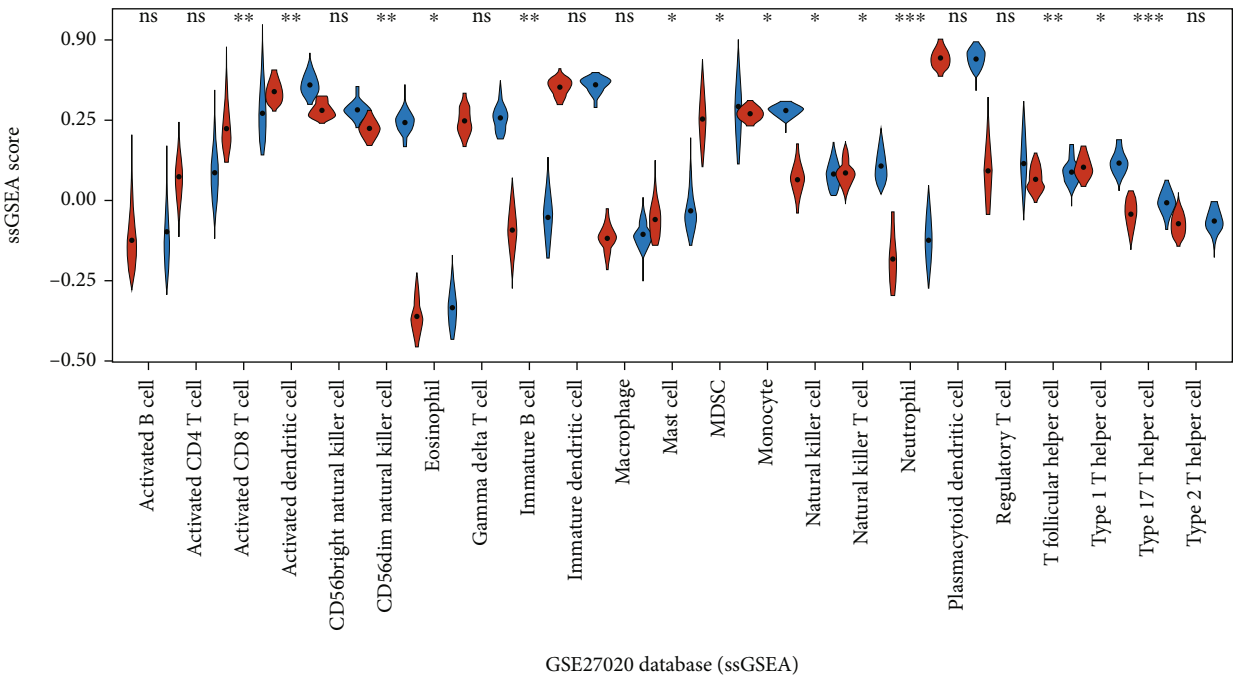
FIGURE 8: Evaluation of tumor immune microenvironment. Violin plots showed the detailed differences for 23 immune cells between high-risk and low-risk patients in TCGA database (a) and GSE27020 database (b). $^{*}P < 0.05$, $^{**}P < 0.01$, and $^{***}P < 0.001$.
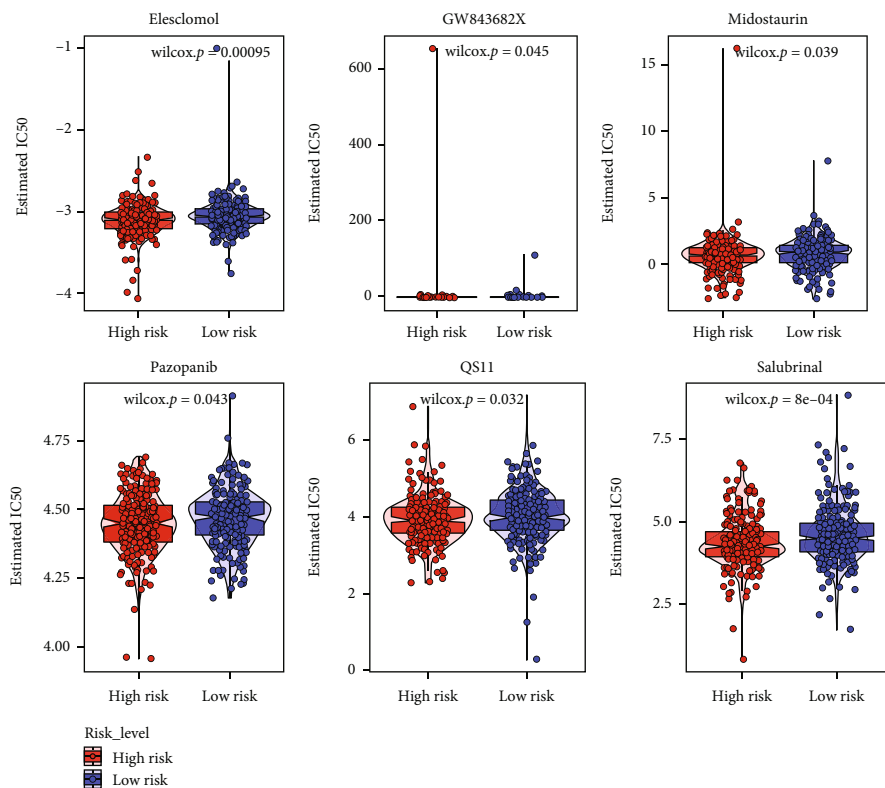
(a)
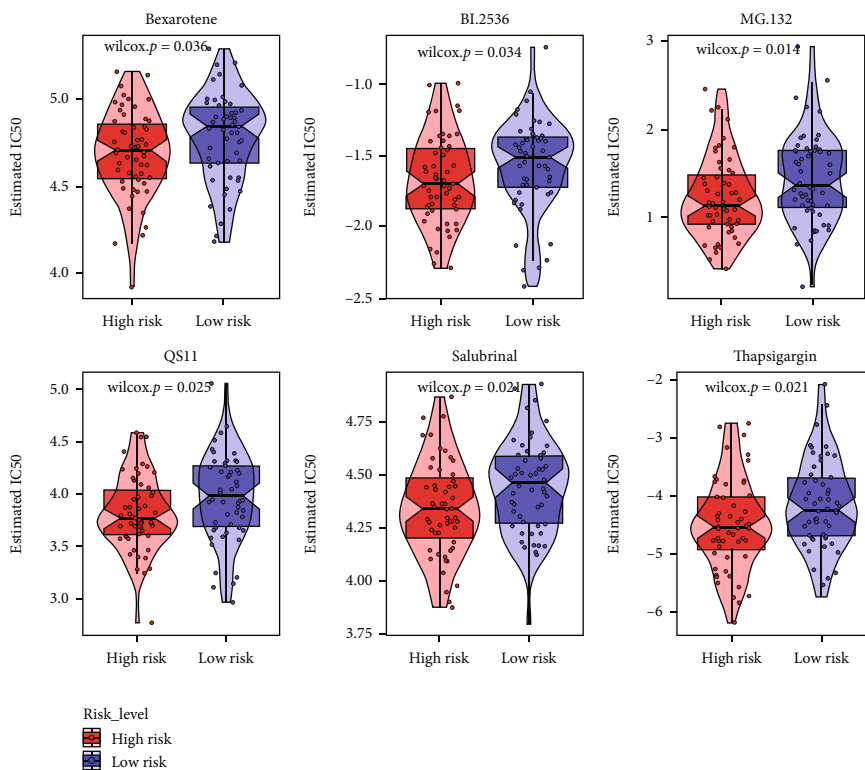
(b)

FIGURE 9: Prediction of clinical application. Correlations between the risk score of the prognostic signature and the efficacy of common chemotherapeutics in TCGA database (a) and GSE27020 database (b).

(a)

(b)
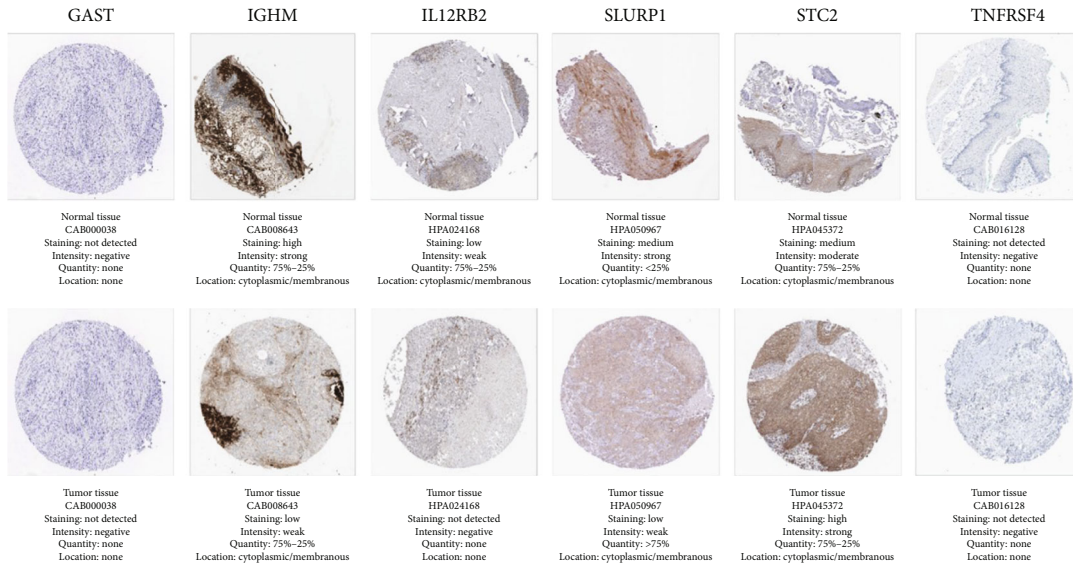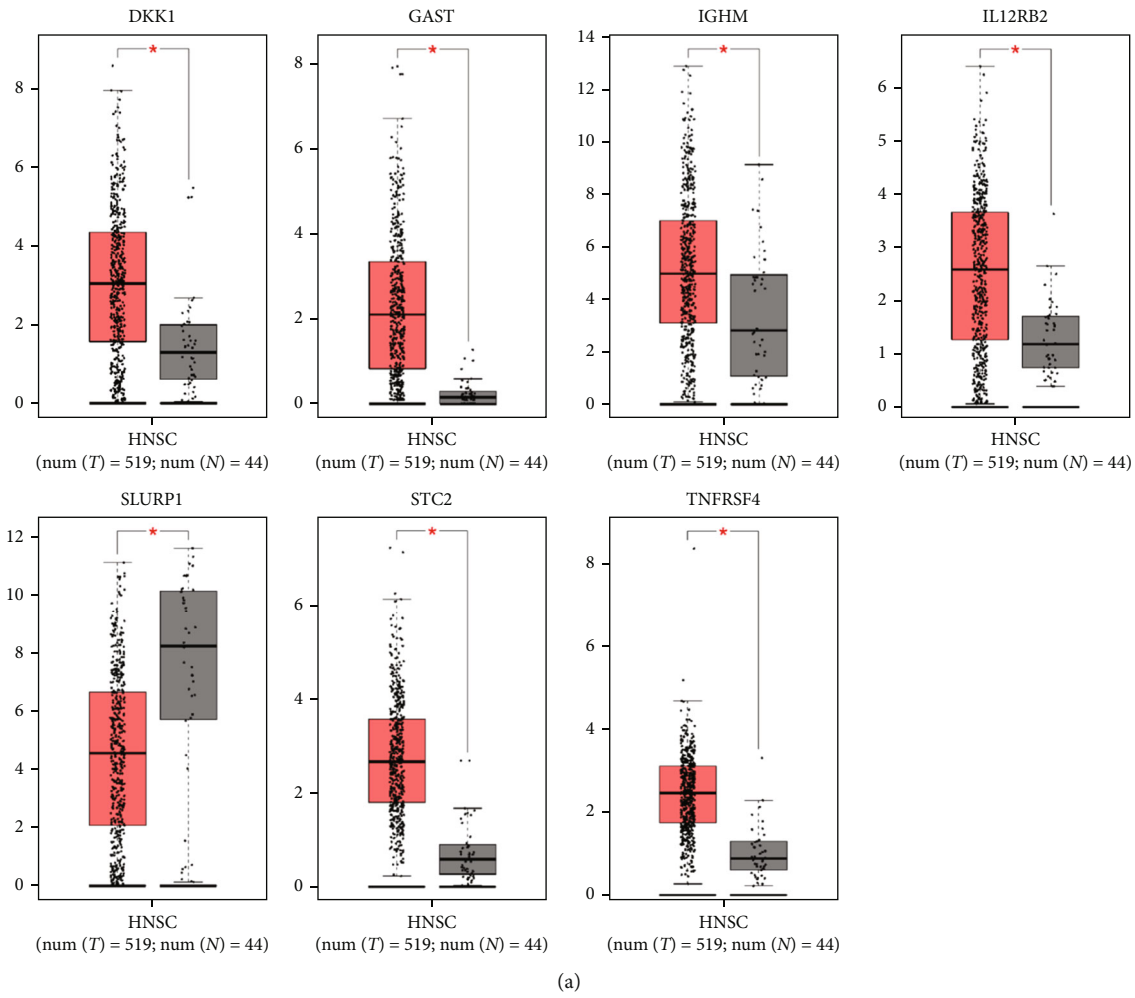
FIGURE 10: The expression of the seven IRGs. (a) The mRNA expressions of the hub genes from the GEPIA database. (b) Validation of the hub genes on a translational level using the HPA database.

proliferation, apoptosis, and angiogenesis and is also vital for the invasiveness and metastasis of HNSCC [31]. *IL12RB2* is a subunit of the IL-12 receptor, and an increased ratio of *IL12RB2*-positive tumor-infiltrating lymphocytes is indicative of a good prognosis in laryngeal cancer [32]. *SLURP1* belongs to the Ly6/uPAR family that lacks a GPI-anchoring signal sequence and is associated with a poor prognosis of HNSCC [33]. Furthermore, one of the tumor necrosis factor receptors, *TNFRSF4*, could be a useful target for immunotherapy of HNSCC [34]. Although there are no published reports on *GAST* and *IGHM* for HNSCC, these genes may be related to tumorigenesis and development [35, 36]. In general, these previous findings emphasize the importance of these seven genes in HNSCC prognosis prediction. Furthermore, the expression levels of *GAST*, *IL12RB2*, and *TNFRSF4* in HNSCC samples appeared to be elevated in healthy tissues from the GEPIA database, while no apparent variations were observed between cancerous and healthy tissues from the HPA data. Except for *SLURP1* and *STC2*, *IGHM* expression in HNSCC tissues was remarkably increased compared to that in healthy samples from the GEPIA database, which was inconsistent with the HPA database. This could be due to abnormal methylation. However, further experimentation is required to confirm this finding.

In the multivariate analysis for the associations between clinicopathological factors and the risk IRG-based signature, a high-immune RS was linked to a high tumor stage and T stage. Also, the signature predicted the possible clinical features of HNSCC subjects, likely by regulating the tumor immune microenvironment. The tumor-infiltrating immune cells are known to be correlated with the progression and OS of HNSCC subjects [37], and a high level of infiltrating immune cells is often a good predictor for the OS of patients [38, 39]. Therefore, the risk IRG-based signature is expected to correlate with infiltrating immune cells. As expected, low-risk HNSCC patients had increased infiltration rates of 23 immune cells, indicating the effectiveness of immunotherapy in the low-risk category compared with that in the high-risk category. Owing to the importance of chemotherapy in HNSCC, the IC_{50} values of various chemotherapeutic agents were compared in the two groups. A lower RS was linked to a higher IC_{50} of QS11 and Salubrinal in both TCGA and GSE27020 databases. The QS11 is an inhibitor of ADP-ribosylation factor GTPase-activating protein 1, which modulates Wnt/β-catenin signaling through an effect on protein trafficking [40]; and the Salubrinal is a selective cell complex inhibitor that inhibits endoplasmic reticulum stress-mediated apoptosis. Despite these two drugs are not commonly used as chemotherapy drugs for HNSCC, the findings of this study may be valuable for future research.

This study had some limitations. (i) Owing to limited HNSCC samples in TCGA and GSE27020 databases, an issue of the time period was evident in this study. (ii) The analyses were performed using publicly available data from retrospective studies, and the outcomes must be validated in further research with larger samples and functional experiments. (iii) There is a need for further exploration of other possible predictive factors linked to clinical outcomes in HNSCC. (iv) There is a need for further investigation of

the mechanisms underlying the functions of the IRG-based signature in HNSCC. Bioinformatics analysis with a specific reference value was used as a basis to conclude this study. Further corresponding molecular experiments are required to validate these findings.

To conclude, a risk signature based on seven IRGs (*DKK1*, *GAST*, *IGHM*, *IL12RB2*, *SLURP1*, *STC2*, and *TNFRSF4*) was developed. This signature serves as a potential biological marker and treatment target for immunotherapy and chemotherapy of HNSCC. These findings may facilitate future studies on the molecular mechanisms of HNSCC.

Data Availability

The datasets analyzed during the current study are available in TCGA database (https://portal.gdc.cancer.gov/), ImmPort database (https://immport.niaid.nih.gov/), GEO database (https://www.ncbi.nlm.nih.gov/gds/), TIMER (https://cistrome.shinyapps.io/timer/), STRING biological database (https://string-db.org/), GEPIA database (http://gepia.cancer-pku.cn/), and HPA database (https://www.proteinatlas.org/).

Conflicts of Interest

The authors declare that there is no conflict of interest regarding the publication of this article.

Acknowledgments

Supplementary Materials

Supplementary Figure 1: immune-related biological functions. (*Supplementary Materials*)

References

[1] H. Liu, G. Li, E. M. Sturgis et al., "Genetic variants in CYP2B6 and HSD17B12 associated with risk of squamous cell carcinoma of the head and neck," *International Journal of Cancer*, vol. 151, no. 4, pp. 553–564, 2022.

[2] R. L. Siegel, K. D. Miller, H. E. Fuchs, and A. Jemal, "Cancer statistics, 2022," *CA: a Cancer Journal for Clinicians*, vol. 72, no. 1, pp. 7–33, 2022.

[3] C. R. Leemans, P. J. F. Snijders, and R. H. Brakenhoff, "The molecular landscape of head and neck cancer," *Nature Reviews. Cancer*, vol. 18, no. 5, pp. 269–282, 2018.

[4] D. E. Johnson, B. Burtness, C. R. Leemans, V. W. Y. Lui, J. E. Bauman, and J. R. Grandis, "Head and neck squamous cell carcinoma," *Nature reviews Disease primers*, vol. 6, no. 1, p. 92, 2020.

[5] M. Badr, K. Jöhrens, M. Allgäuer et al., "Morphomolecular analysis of the immune tumor microenvironment in human head and neck cancer," *Cancer Immunology, Immunotherapy*, vol. 68, no. 9, pp. 1443–1454, 2019.

[6] S. M. Y. Chen, A. L. Krinsky, R. A. Woolaver, X. Wang, Z. Chen, and J. H. Wang, "Tumor immune microenvironment in head and neck cancers," *Molecular Carcinogenesis*, vol. 59, no. 7, pp. 766–774, 2020.

[7] C. Fu, H. Zhao, Y. Wang et al., "Tumor-associated antigens: Tn antigen, sTn antigen, and T antigen," *Hla*, vol. 88, no. 6, pp. 275–286, 2016.

[8] R. L. Ferris, J. L. Hunt, and S. Ferrone, "Human leukocyte antigen (HLA) class I defects in head and neck cancer: molecular mechanisms and clinical significance," *Immunologic Research*, vol. 33, no. 2, pp. 113–134, 2005.

[9] M. Canning, G. Guo, M. Yu et al., "Heterogeneity of the head and neck squamous cell carcinoma immune landscape and its impact on immunotherapy," *Frontiers in Cell and Development Biology*, vol. 7, p. 52, 2019.

[10] M. Fiedler, F. Weber, M. G. Hautmann, C. Bohr, T. E. Reichert, and T. Ettl, "Infiltrating immune cells are associated with radiosensitivity and favorable survival in head and neck cancer treated with definitive radiotherapy," *Oral Surgery, Oral Medicine, Oral Pathology, Oral Radiology*, vol. 129, no. 6, pp. 612–620, 2020.

[11] R. Duhen, C. Ballesteros-Merino, A. K. Frye et al., "Neoadjuvant anti-OX40 (MEDI6469) therapy in patients with head and neck squamous cell carcinoma activates and expands antigen-specific tumor- infiltrating T cells," *Nature Communications*, vol. 12, no. 1, p. 1047, 2021.

[12] Y. Peng, L. Xiao, H. Rong et al., "Single-cell profiling of tumor-infiltrating TCF1/TCF7$^+$ T cells reveals a T lymphocyte subset associated with tertiary lymphoid structures/organs and a superior prognosis in oral cancer," *Oral Oncology*, vol. 119, article 105348, 2021.

[13] O. Kaidar-Person, Z. Gil, and S. Billan, "Precision medicine in head and neck cancer," *Drug Resistance Updates*, vol. 40, pp. 13–16, 2018.

[14] J. D. Horton, H. M. Knochelmann, T. A. Day, C. M. Paulos, and D. M. Neskey, "Immune evasion by head and neck cancer: foundations for combination therapy," *Trends Cancer*, vol. 5, no. 4, pp. 208–232, 2019.

[15] E. E. W. Cohen, R. B. Bell, C. B. Bifulco et al., "The Society for Immunotherapy of Cancer consensus statement on immunotherapy for the treatment of squamous cell carcinoma of the head and neck (HNSCC)," *Journal for Immunotherapy of Cancer*, vol. 7, no. 1, p. 184, 2019.

[16] Y. Yao, Z. Yan, S. Lian et al., "Prognostic value of novel immune-related genomic biomarkers identified in head and neck squamous cell carcinoma," *Journal for Immunotherapy of Cancer*, vol. 8, no. 2, p. e000444, 2020.

[17] Y. Chen, Z. Y. Li, G. Q. Zhou, and Y. Sun, "An immune-related gene prognostic index for head and neck squamous cell carcinoma," *Clinical Cancer Research*, vol. 27, no. 1, pp. 330–341, 2021.

[18] Y. Zhang, P. Chen, Q. Zhou et al., "A novel immune-related prognostic signature in head and neck squamous cell carcinoma," *Frontiers in Genetics*, vol. 12, article 570336, 2021.

[19] T. Liu, H. Wu, J. Qi, C. Qin, and Q. Zhu, "Seven immune-related genes prognostic power and correlation with tumor-infiltrating immune cells in hepatocellular carcinoma," *Cancer Medicine*, vol. 9, no. 20, pp. 7440–7452, 2020.

[20] Z. Wang, Q. Song, Z. Yang, J. Chen, J. Shang, and W. Ju, "Construction of immune-related risk signature for renal papillary cell carcinoma," *Cancer Medicine*, vol. 8, no. 1, pp. 289–304, 2019.

[21] M. E. Ritchie, B. Phipson, D. Wu et al., "Limma powers differential expression analyses for RNA-sequencing and microarray studies," *Nucleic Acids Research*, vol. 43, no. 7, article e47, 2015.

[22] C. Y. Li, J.-H. Cai, J. J. P. Tsai, and C. C. N. Wang, "Identification of hub genes associated with development of head and neck squamous cell carcinoma by integrated bioinformatics analysis," *Frontiers in Oncology*, vol. 10, p. 681, 2020.

[23] J. Yang, K. Xie, and C. Li, "Immune-related genes have prognostic significance in head and neck squamous cell carcinoma," *Life Sciences*, vol. 256, article 117906, 2020.

[24] Z. Hu, J. Zhou, Y. Li et al., "Peripheral immune signature resembles tumor microenvironment and predicts clinical outcomes in head and neck squamous cell carcinoma," *Frontiers in Immunology*, vol. 13, article 915207, 2022.

[25] J. X. Liang, Q. Chen, W. Gao et al., "A novel glycosylation-related gene signature predicts survival in patients with lung adenocarcinoma," *BMC Bioinformatics*, vol. 23, no. 1, p. 562, 2022.

[26] N. T. Doncheva, J. H. Morris, J. Gorodkin, and L. J. Jensen, "Cytoscape StringApp: network analysis and visualization of proteomics data," *Journal of Proteome Research*, vol. 18, no. 2, pp. 623–632, 2019.

[27] G. Yu, L. G. Wang, Y. Han, and Q. Y. He, "clusterProfiler: an R package for comparing biological themes among gene clusters," *OMICS*, vol. 16, no. 5, pp. 284–287, 2012.

[28] G. Zhu, J. Song, W. Chen et al., "Expression and role of Dickkopf-1 (Dkk1) in tumors: from the cells to the patients," *Cancer Management and Research*, vol. Volume 13, pp. 659–675, 2021.

[29] J. Niu, X. M. Li, X. Wang et al., "DKK1 inhibits breast cancer cell migration and invasion through suppression of β-catenin/MMP7 signaling pathway," *Cancer Cell International*, vol. 19, no. 1, p. 168, 2019.

[30] H. Gao, L. Li, M. Xiao et al., "Elevated DKK1 expression is an independent unfavorable prognostic indicator of survival in head and neck squamous cell carcinoma," *Cancer Management and Research*, vol. Volume 10, pp. 5083–5089, 2018.

[31] H. F. Ma, G. X. Lv, and D. H. Zhang, "miR-381 mediates the development of head and neck squamous cell carcinoma via targeting STC2," *Oncotargets and Therapy*, vol. Volume 13, pp. 4485–4493, 2020.

[32] Y. Tao, N. Gross, Y. Liu et al., "A high ratio of IL-12Rβ2-positive tumor-infiltrating lymphocytes indicates favorable prognosis in laryngeal cancer," *Oral Oncology*, vol. 74, pp. 148–156, 2017.

[33] H. Zheng, H. Liu, Y. Lu, and H. Li, "Identification of a novel signature predicting overall survival in head and neck squamous cell carcinoma," *Frontiers in Surgery*, vol. 8, article 717084, 2021.

[34] S. M. Loick, A. Fröhlich, J. Gabrielpillai et al., "DNA methylation and mRNA expression of OX40 (TNFRSF4) and GITR (TNFRSF18, AITR) in head and neck squamous cell

carcinoma correlates with HPV status, mutational load, an interferon-γ signature, signatures of immune infiltrates, and survival," *Journal of Immunotherapy*, vol. 45, no. 4, pp. 194–206, 2022.

[35] E. Ness-Jensen, E. A. Bringeland, F. Mattsson et al., "Hypergastrinemia is associated with an increased risk of gastric adenocarcinoma with proximal location: a prospective population-based nested case-control study," *International Journal of Cancer*, vol. 148, no. 8, pp. 1879–1886, 2020.

[36] Z. Lu and Y. Gao, "Screening differentially expressed genes between endometriosis and ovarian cancer to find new biomarkers for endometriosis," *Annals of Medicine*, vol. 53, no. 1, pp. 1377–1389, 2021.

[37] A. Almangush, I. Leivo, and A. A. Mäkitie, "Overall assessment of tumor-infiltrating lymphocytes in head and neck squamous cell carcinoma: time to take notice," *Acta Oto-Laryngologica*, vol. 140, no. 3, pp. 246–248, 2020.

[38] M. E. Spector, E. Bellile, L. Amlani et al., "Prognostic value of tumor-infiltrating lymphocytes in head and neck squamous cell carcinoma," *JAMA Otolaryngology. Head & Neck Surgery*, vol. 145, no. 11, pp. 1012–1019, 2019.

[39] Q. Xu, C. Wang, X. Yuan, Z. Feng, and Z. Han, "Prognostic value of tumor-infiltrating lymphocytes for patients with head and neck squamous cell carcinoma," *Translational Oncology*, vol. 10, no. 1, pp. 10–16, 2017.

[40] M. K. Singh, H. Gao, W. Sun et al., "Structure-activity relationship studies of QS11, a small molecule Wnt synergistic agonist," *Bioorganic & Medicinal Chemistry Letters*, vol. 25, no. 21, pp. 4838–4842, 2015.

Research Article

GPR176 Is a Biomarker for Predicting Prognosis and Immune Infiltration in Stomach Adenocarcinoma

Lin Ni [1], **Shuming Chen** [1], **Jianyong Liu** [2], **He Li** [1], **Hu Zhao** [1], **Chunhua Zheng** [1], **Yawei Zhang** [1], **Hancong Huang** [1], **Junjie Huang** [1], **Bing Wang** [1], and **Chengzhi Lin** [1]

[1]Department of General Surgery, 900TH Hospital of Joint Logistics Support Force (Fuzong Clinical Medical College) (Former Fuzhou General Hospital), Fuzhou, Fujian, China
[2]Department of Hepatobiliary Surgery, 900TH Hospital of Joint Logistics Support Force (Fuzong Clinical Medical College) (Former Fuzhou General Hospital), Fuzhou, Fujian, China

Correspondence should be addressed to Bing Wang; wang213bing@163.com and Chengzhi Lin; 469872103@qq.com

Immunotherapy based on immune checkpoint inhibitors (ICIs) is considered to be a promising treatment for stomach adenocarcinoma (STAD), but only a minority of patients benefit from it. It is believed that the poor therapeutic efficacy is attributed to the complex tumor immune microenvironment (TIM) of STAD. Therefore, elucidating the specific regulatory mechanism of TIM in STAD is critical. Previous study suggests that GRP176 may be involved in regulating the pace of circadian behavior, and its role in tumors has not been reported. In this study, we first found that GPR176 was highly expressed in STAD and negatively correlated with patient prognosis. Next, we investigated the relationship between GPR176 and clinical characteristics, and the results showed that the stage is closely related to the level of GPR176. In addition, our further analysis found that GRP176 expression level was significantly correlated with chemotherapeutic drug sensitivity and ICI response. KEGG and GO analyses showed that GPR176 might be involved in stromal remodeling of STAD. Furthermore, we analyzed the association between GPR176 expression and immune implication, and the results revealed that GPR176 was negatively related to the infiltration of various immune cells. Interestingly, GPR176 induced the conversion of TIM while reducing the tumor immune burden (TMB). The expression of GRP176 is closely related to the level of various immunomodulators. Moreover, we performed univariate and multivariate regression analyses on the immunomodulators and finally obtained 4 genes (CRCR4, TNSF18, PDCD1, and TGFB1). Then, we constructed a GRP176-related immunomodulator prognostic model (GRIM) based on the above 4 genes, which was validated to have good predictive power. Finally, we developed a nomogram based on the risk score of GRIM and verified its accuracy. These results suggested that GPR176 is closely related to the prognosis and TIM of STAD. GPR176 may be a new potential target for immunotherapy in STAD.

1. Introduction

Stomach adenocarcinoma (STAD) is the most common pathological type of gastric cancer (GC), accounting for more than 95% of all GC [1]. Currently, STAD is the fifth most common malignancy and the third leading cause of cancer-related death globally [2]. To date, the classic treatment strategies for STAD are surgery, chemotherapy, anti-angiogenic therapy, and radiation therapy [3]. However,

these traditional treatments are increasingly difficult to improve the prognosis of STAD, especially for patients with advanced patients. Therefore, exploring new treatment options is extremely important and urgent to improve the prognosis of STAD.

Immunotherapy based on immune checkpoint inhibitors (ICIs) has steadily developed into a research hotspot for STAD treatment with the advent of a number of therapeutic alternatives [4]. Patients with STAD are now being treated

(a)

(b)

(c)

FIGURE 1: Continued.

(d)

(e)
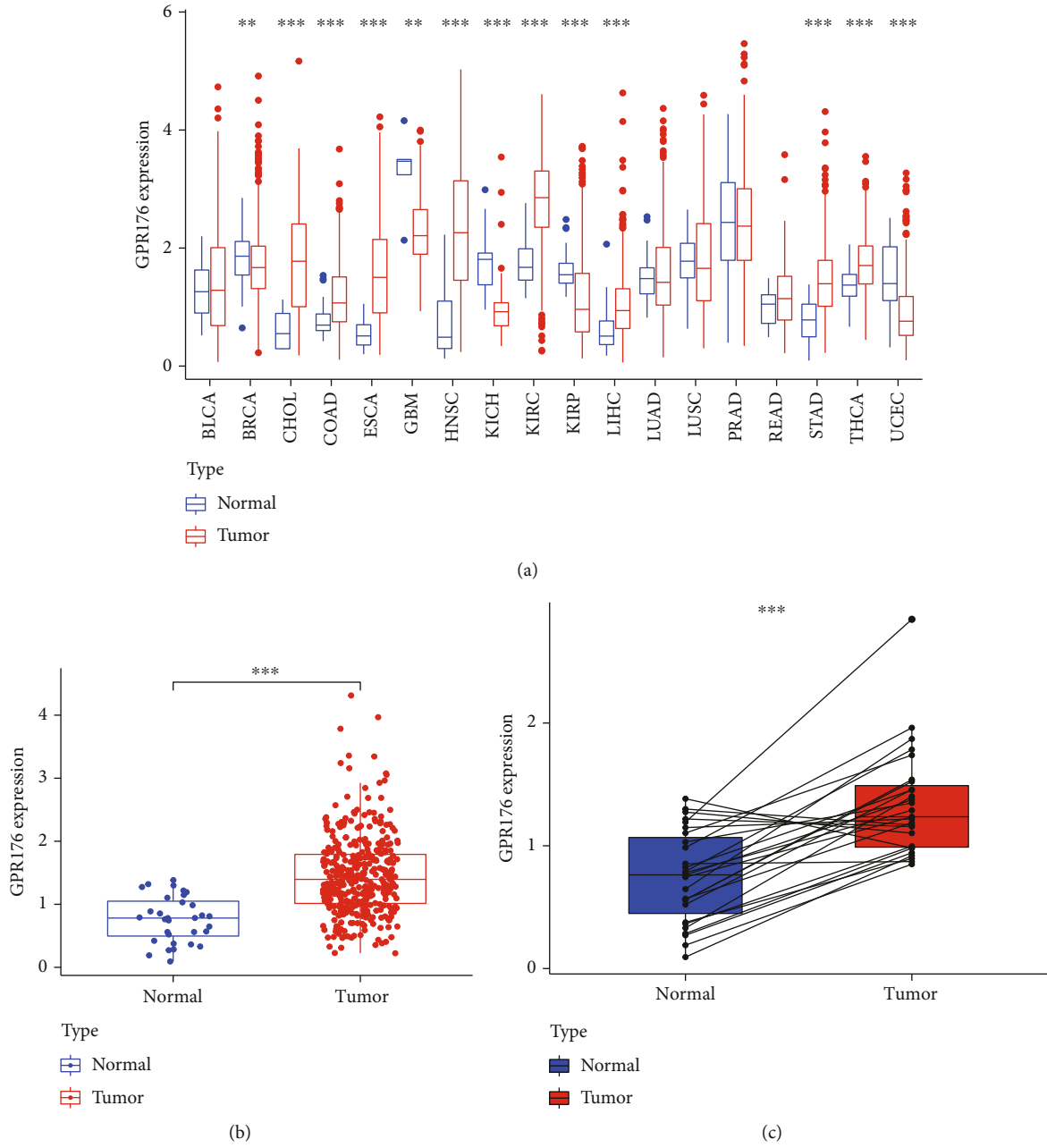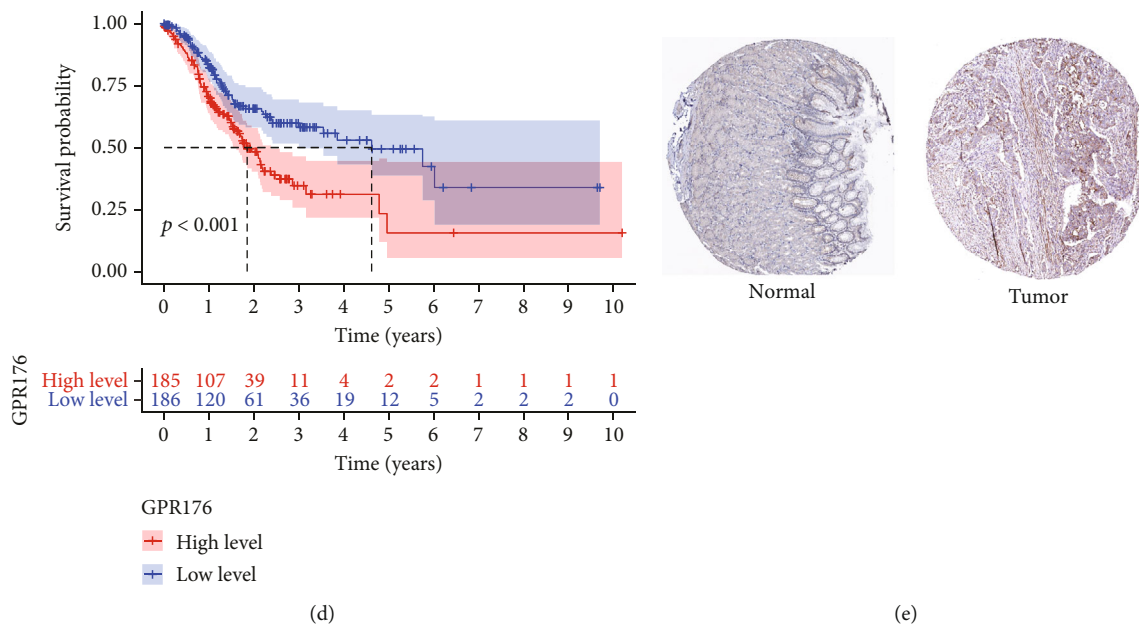
Figure 1: Expression level of GPR176 and its correlation with prognosis in STAD. (a) mRNA expression level of GPR176 in pancancer. (b) GRP176 mRNA expression levels in the STAD cohort. (c) Expression level of GRP176 mRNA in STAD and its paired normal tissues. (d) Comparison of overall survival in patients with high and low expressions of GRP176 in STAD. (e) Protein expression levels of GRP176 in STAD and normal gastric tissues.

with a range of ICIs, and considerable therapeutic results have been attained [5]. Unfortunately, due to heterogeneity of tumors, only a majority of advanced STAD patients benefit from ICIs [6]. Numerous studies have shown a strong correlation between the efficacy to immunotherapy and the percentage of immune cells in the TIM [7]. Therefore, it is particularly important to elucidate the specific mechanisms regulating TIM in STAD for guiding immunotherapy.

GPR176 is a member of the G protein-coupled receptor family, as a membrane receptor protein, widely involved in the response to hormones, growth factors, and neurotransmitters [8]. Previous study showed that GPR176 is involved in the pace of circadian behavior [8]. However, the function and role of GPR176 in malignant tumors are unknown, especially in TIM.

In this study, we first analyzed the expression of GRP176 in STAD and explored the correlation with patient prognosis and various clinical features. The underlying mechanism of GPR176 regulating STAD progression was preliminarily elucidated. We discovered the effectiveness of GPR176 to predict STAD on chemotherapy drugs and ICIs. We revealed the correlation between GPR176 and immune profile in STAD. Critically, we constructed a GPR176-based prognostic model and demonstrated its accuracy.

2. Materials and Methods

2.1. Acquisition of STAD Data from the Public Database.
TCGA database is an open platform for global users, which contains many types of malignant tumor data. The STAD transcription data was downloaded from TCGA database (https://portal.gdc.cancer.gov/). We applied the corresponding functions in the limma package of R software to process

the obtained data. In this study, a total of 371 STAD samples were obtained after excluding samples with incomplete clinical information.

2.2. Analysis of Immune Cell Infiltration in STAD.
We applied multiple databases to study the relationship between GPR176 and immune cell infiltration, including TIMER, TISIDB, and Cell-Type Identification by Estimating Relative Subsets of RNA Transcripts (CIBERSORT). TISIDB is a web server [9]. CIBERSORT is a novel calculation method that can use the characteristic genes in the transcription group data to mark the type of immune cells. CIBERSORT relied on a matrix file called LM22 to analyze the immune cells in the data to distinguish various immune cells [10].

2.3. Prediction of GPR176 Expression on the Effect of ICIs and Chemotherapy Drugs.
Immunophenoscore (IPS) is an indicator for predicting reactions to ICIs (anti-CTLA-4 or anti-PD-1) response [11]. This method is quantitatively immune-related genes, including MHC-related molecules, immune checking points, or effector cells and suppressor cells. Finally, the final score is obtained by the average weight. In this study, we analyze the expression level of GPR176 through algorithms and then predict the sensitivity of chemotherapy drugs. The principle of this algorithm is to analyze the different expression genes between the GPR176 high and low expressions. Then, the results were submitted to the CMap (Connectivity Map) database and then analyze the corresponding chemical drugs.

2.4. Statistics.
In this study, various function packages based on R software are used for calculation and statistical analysis. $p < 0.05$ were considered statistically significant.

(a)

(b)

(c)

(d)

(e)

(f)
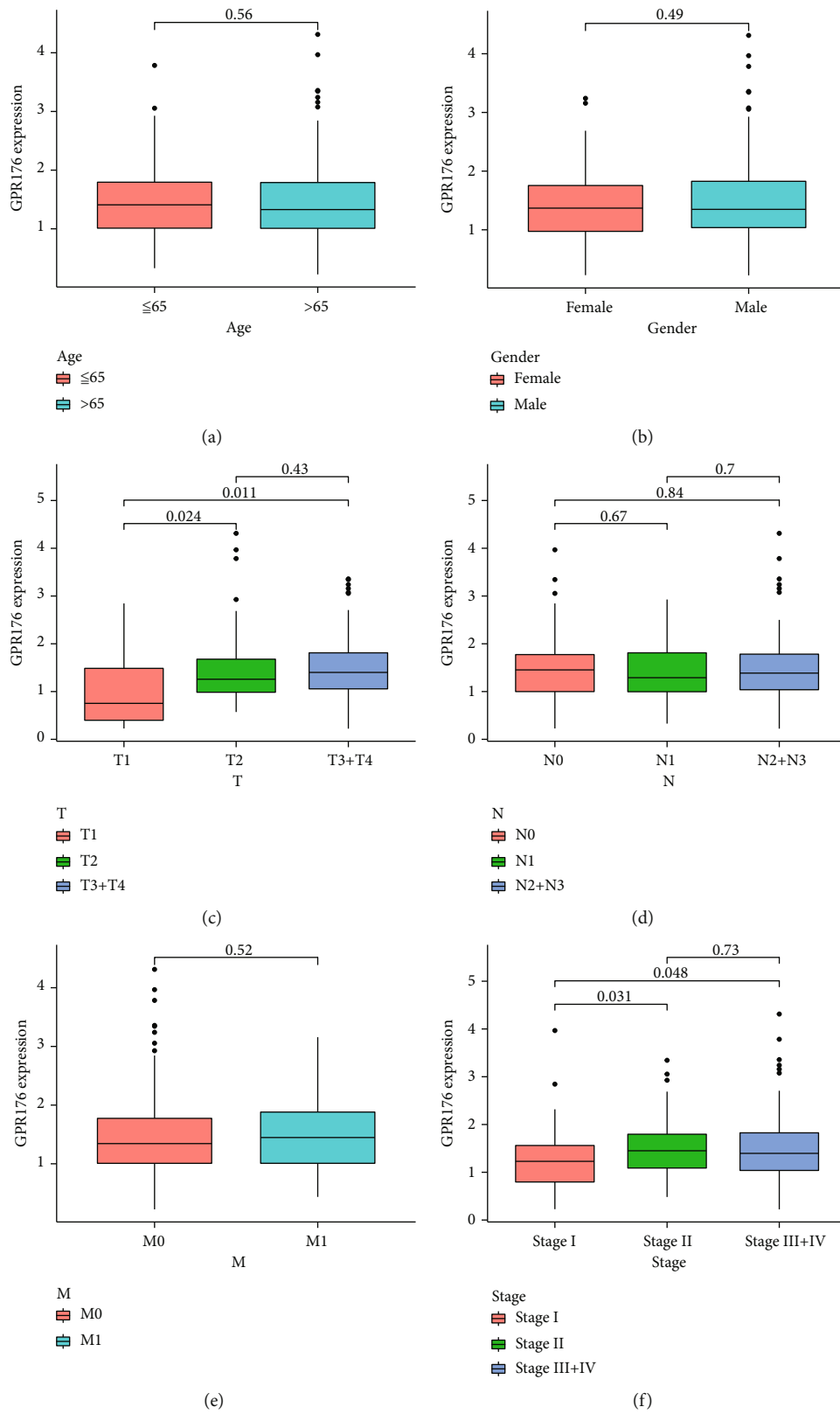
FIGURE 2: Correlation analysis between GRP176 and STAD clinical features. (a–f) Correlation of clinical features between high and low expressions of GRP176 in STAD.

(a)

(b)

(c)

(d)

(e)

(f)

Figure 3: Continued.

(g)

(h)

(i)

(j)

(k)

(l)
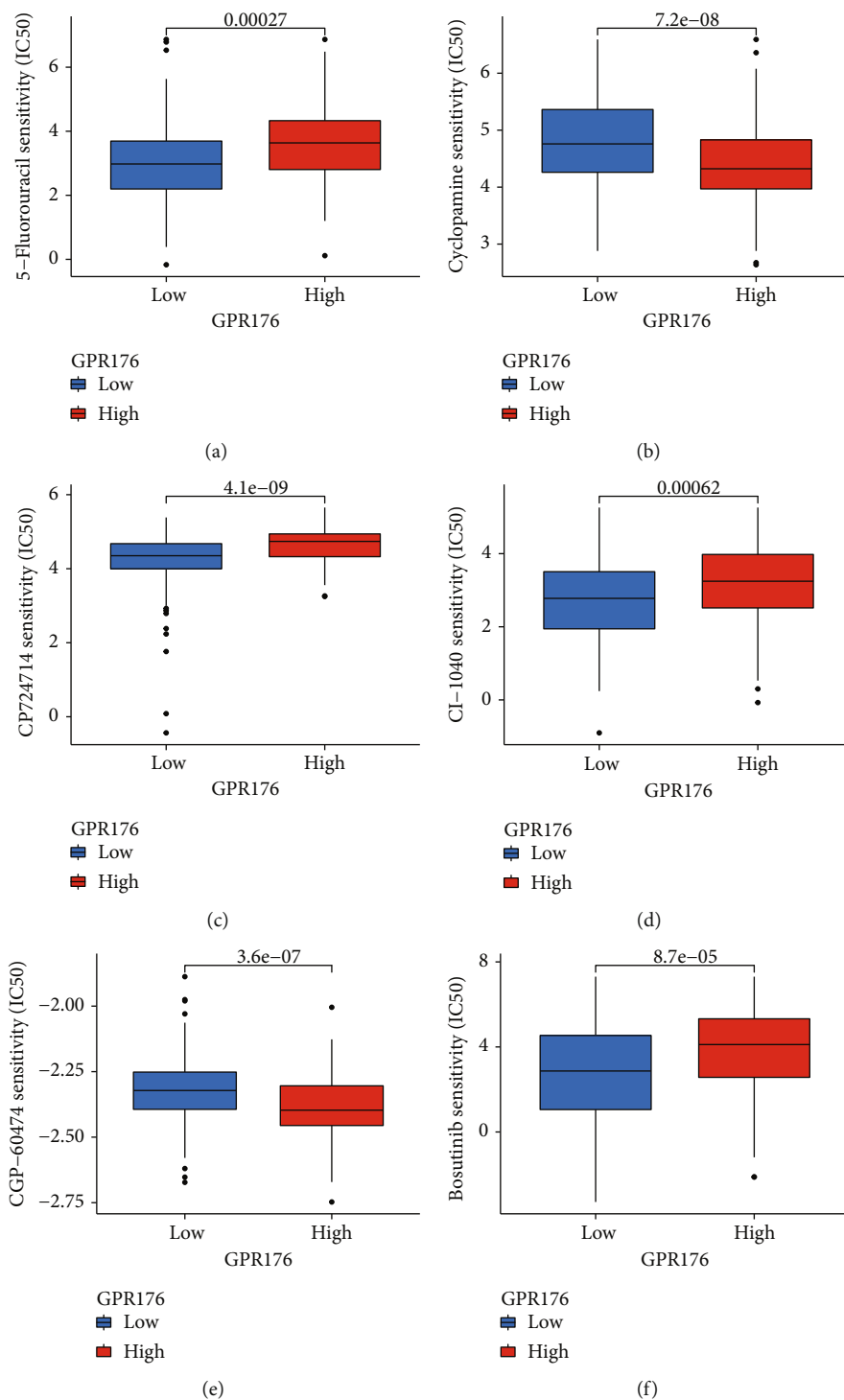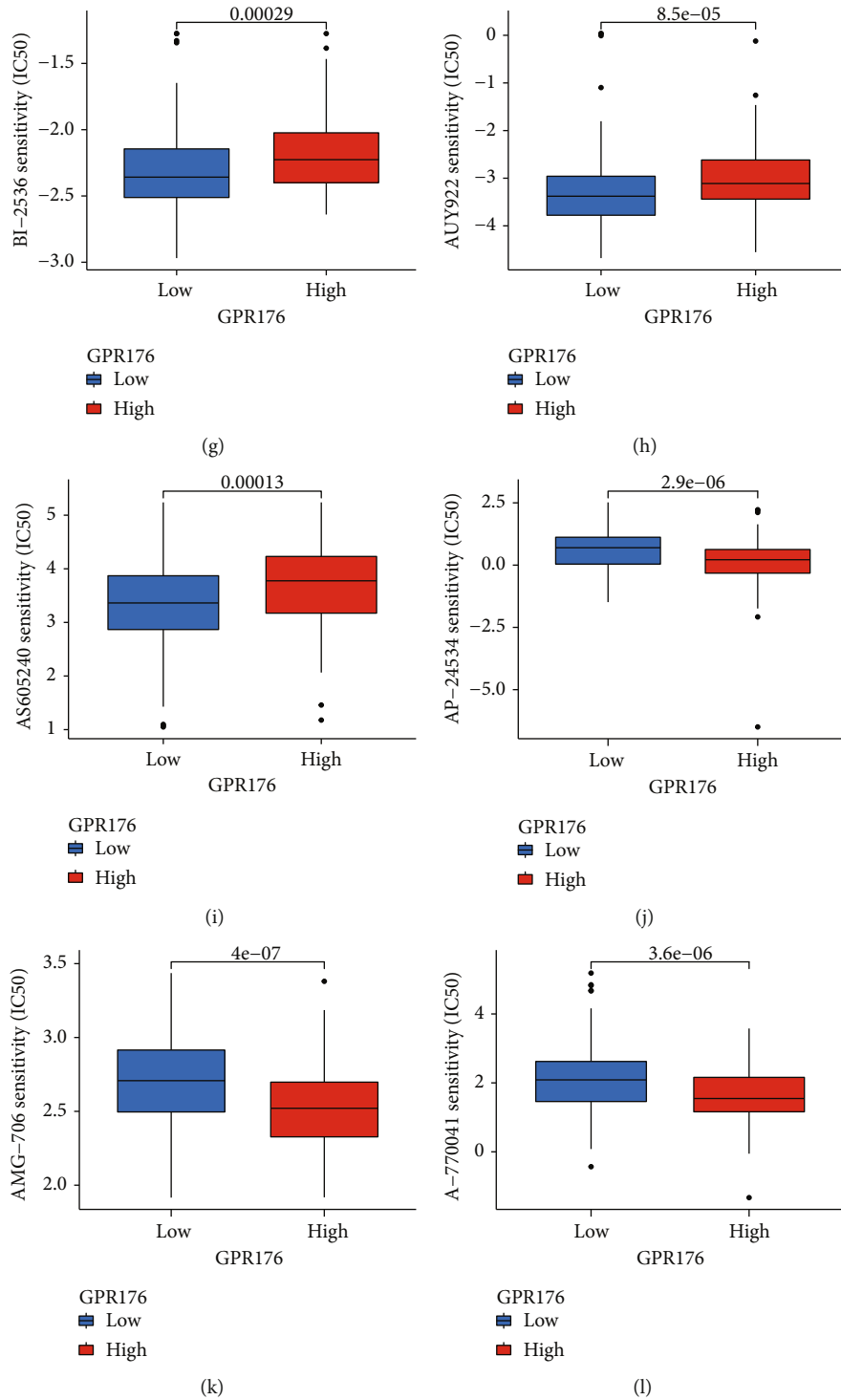
FIGURE 3: Analysis of GPR176 expression level and drug sensitivity in LIHC. (a–l) Sensitivity comparison of high and low expressions of GRP176 to various chemical drugs.

3. Results

3.1. GRP176 Is Highly Expressed and Associated with Poor Prognosis in STAD. Given that the role of GRP176 in tumors is unclear, we first evaluated the GPR176 expression levels in pan-cancer tissues. The result showed that the expression of GRP176 was significantly upregulated in most tumors,

including STAD (Figures 1(a) and 1(b)). Consistently, further analysis found that GPR176 was significantly higher in STAD than in paired normal gastric tissue (Figure 1(c)). In addition, we performed survival analysis on STAD patients with high and low expressions of GPR176, and the result demonstrated that patients with high expression of GPR176 had a worse prognosis (Figure 1(d)). Moreover,

(a)

(b)

(c)

(d)
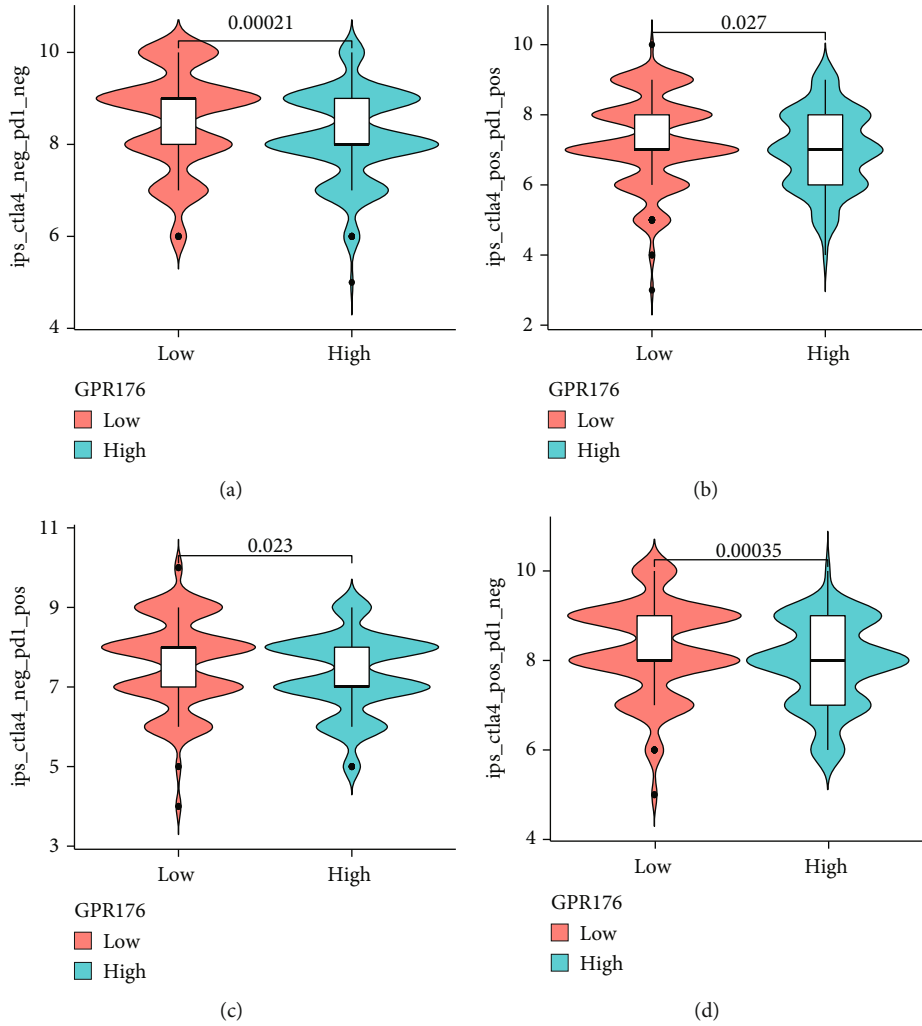
FIGURE 4: Expression levels of GPR176 and prediction of response to immunotherapy in LIHC. (a) In the case of both CTLA4 and PD-1 double negative, the low GPR176 cohort had higher IPS. (b) In the case of both CTLA4 and PD-1 double positive, the low GPR176 cohort had higher IPS. (c) In the case of CTLA4 negative but PD1 positive, the high GPR176 cohort had higher IPS. (d) In the case of CTLA4 positive but PD1 negative, the high GPR176 cohort had higher IPS.

we conducted public database (https://www.proteinatlas.org/) to investigate the protein level of GPR176 in STAD, and the results were consistent with the previous data (Figure 1(e)). The above results indicated that the upregulation of GPR176 in STAD is closely related to patient prognosis.

3.2. The Expression Level of GPR176 Is Related to the Clinical Characteristics in STAD. The previous results demonstrated the close association of GPR176 with poor prognosis of STAD. We intended to analyze the relationship between GPR176 and clinical characteristics. As shown in Figures 2(a) and 2(b), the distribution level of GPR176 does not have significant correlation with gender and age. The level of GPR176 in T2 patients was obviously higher than that in T1 patients, but no further upregulation was observed in T3+T4 (Figure 2(c)). Interestingly, GPR176 levels were not correlated with N and M in STAD patients (Figures 2(d) and 2(e)). In addition, the level of GPR176 in

stage II patients was higher than that in stage I patients, but no further upregulation was observed in III+IV (Figure 2(f)).

3.3. Prediction of Sensitivity to Immunotherapy and Chemotherapeutics by the Expression Level of GPR176 in STAD. Our previous analysis implied that upregulation of GPR176 is closely associated with the prognosis of STAD and its pathological features. We further explored whether GPR176 can instruct chemotherapy and immunotherapy in STAD. As shown in Figures 3(a)–3(l), the STAD cohort with high GPR176 expression had lower drug sensitivity to 5-fluoridine, CP724714, CL-1040, bosutinib, BL-2536, AUY922, and AS605240. Conversely, the STAD cohort with low GPR176 expression had lower drug sensitivity to cyclopamine, CGP-60474, AP-24534, and A-770041. In addition, when CTLA4 and PD-1 are negative, the cohort of low GPR176 had a stronger immune response to immunotherapy (Figure 4(a)). When CTLA4 and PD-1 are positive, the

(a)

Figure 5: Continued.

(b)

FIGURE 5: Continued.

(c)
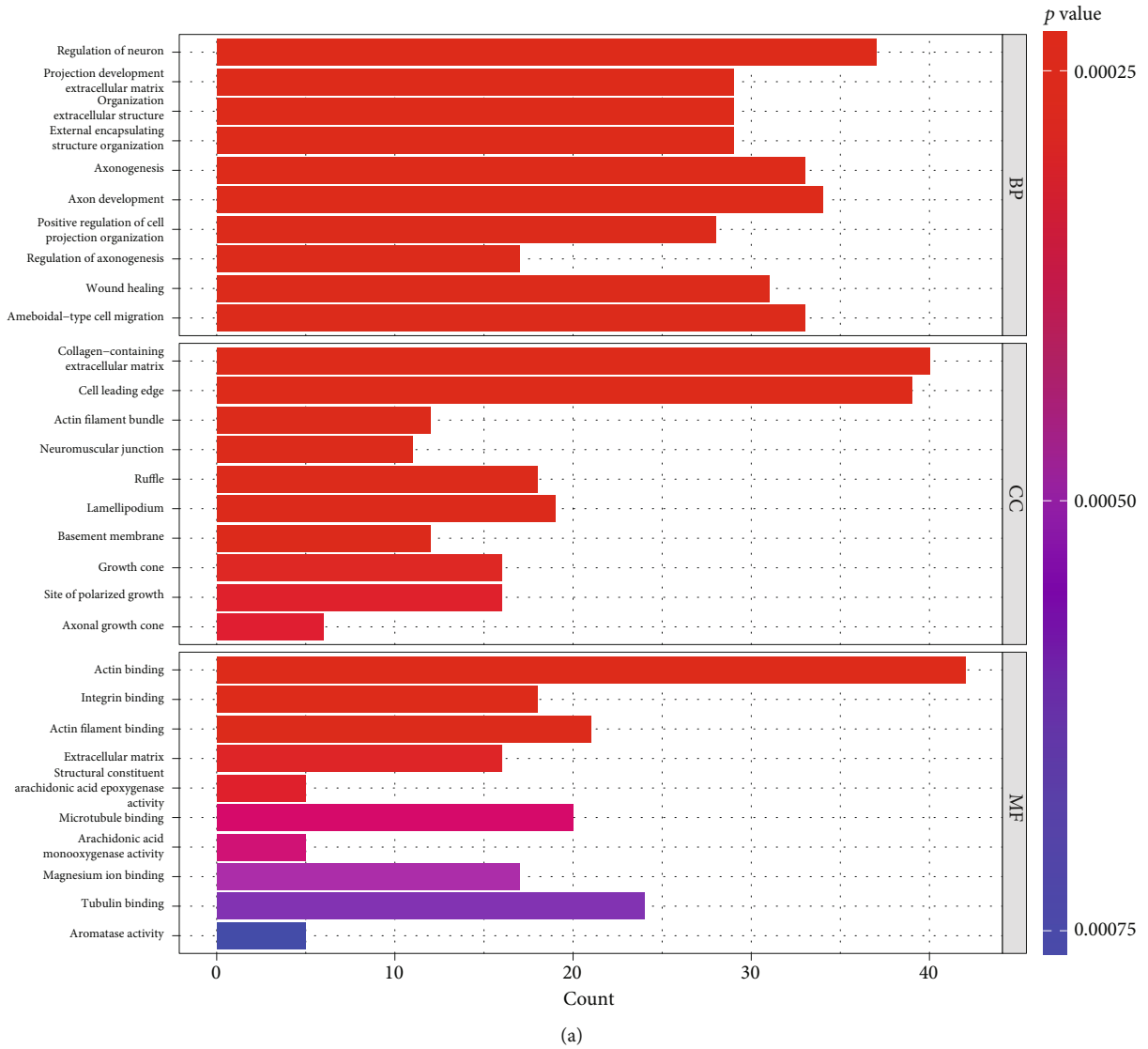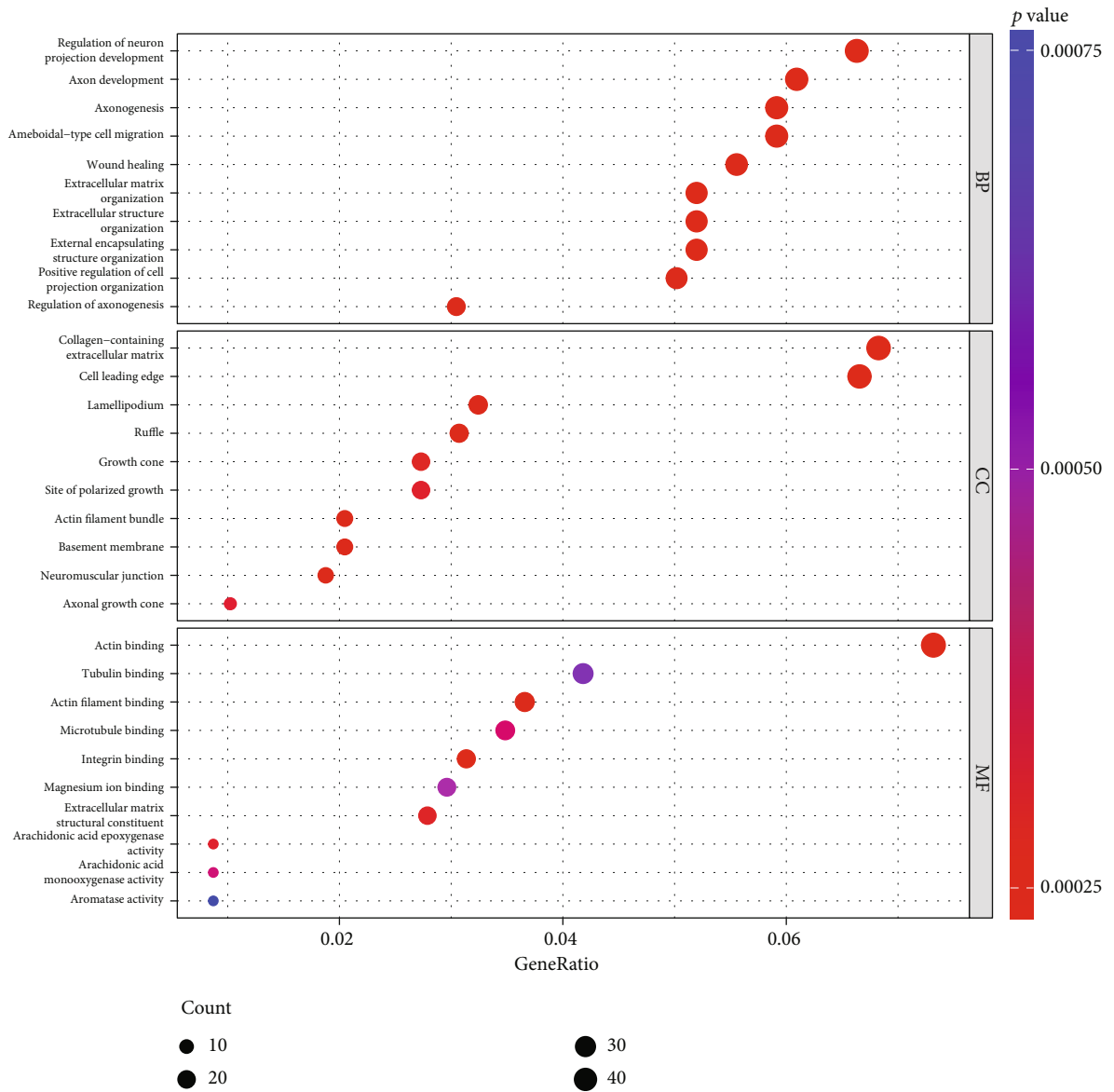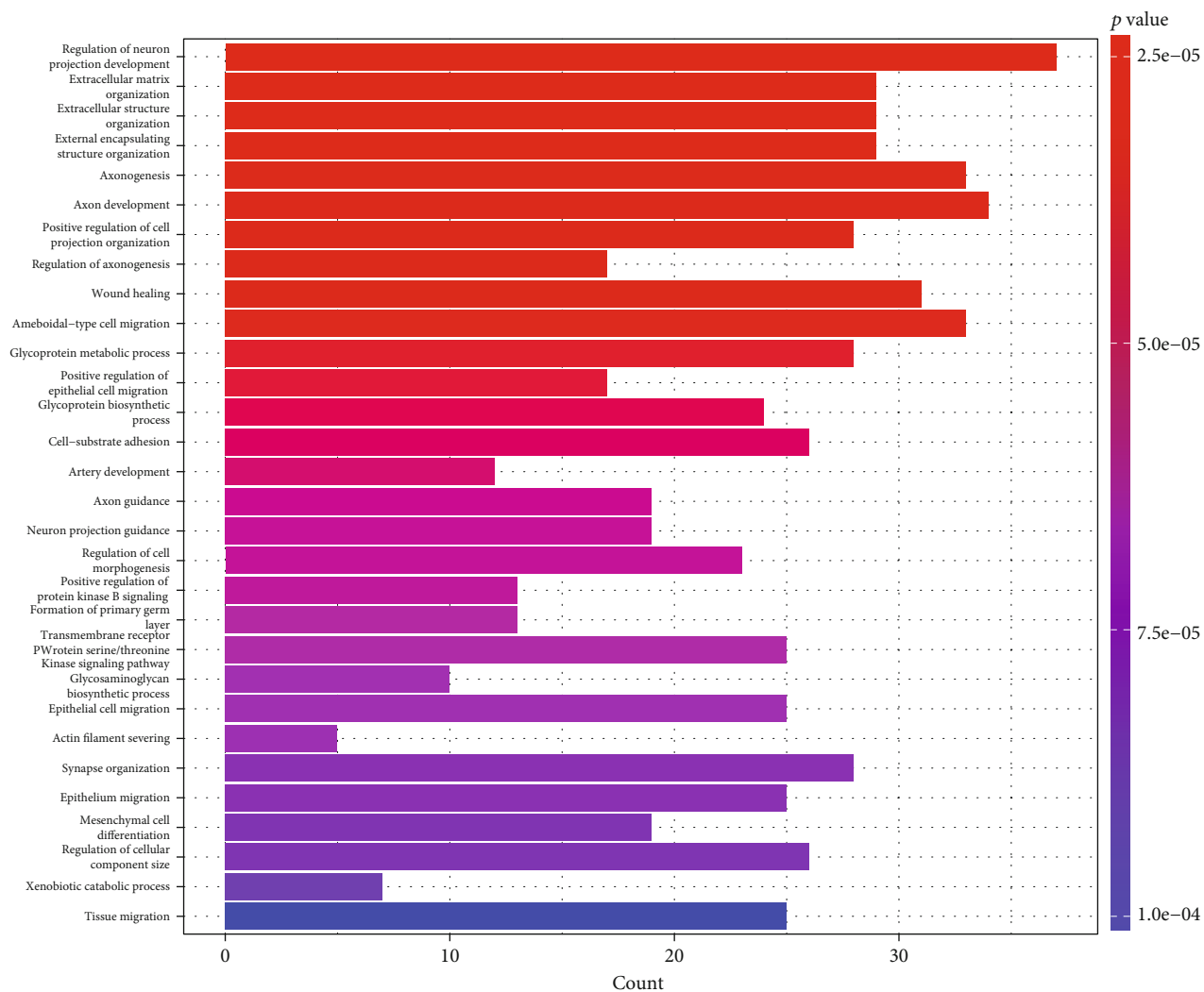
FIGURE 5: Continued.
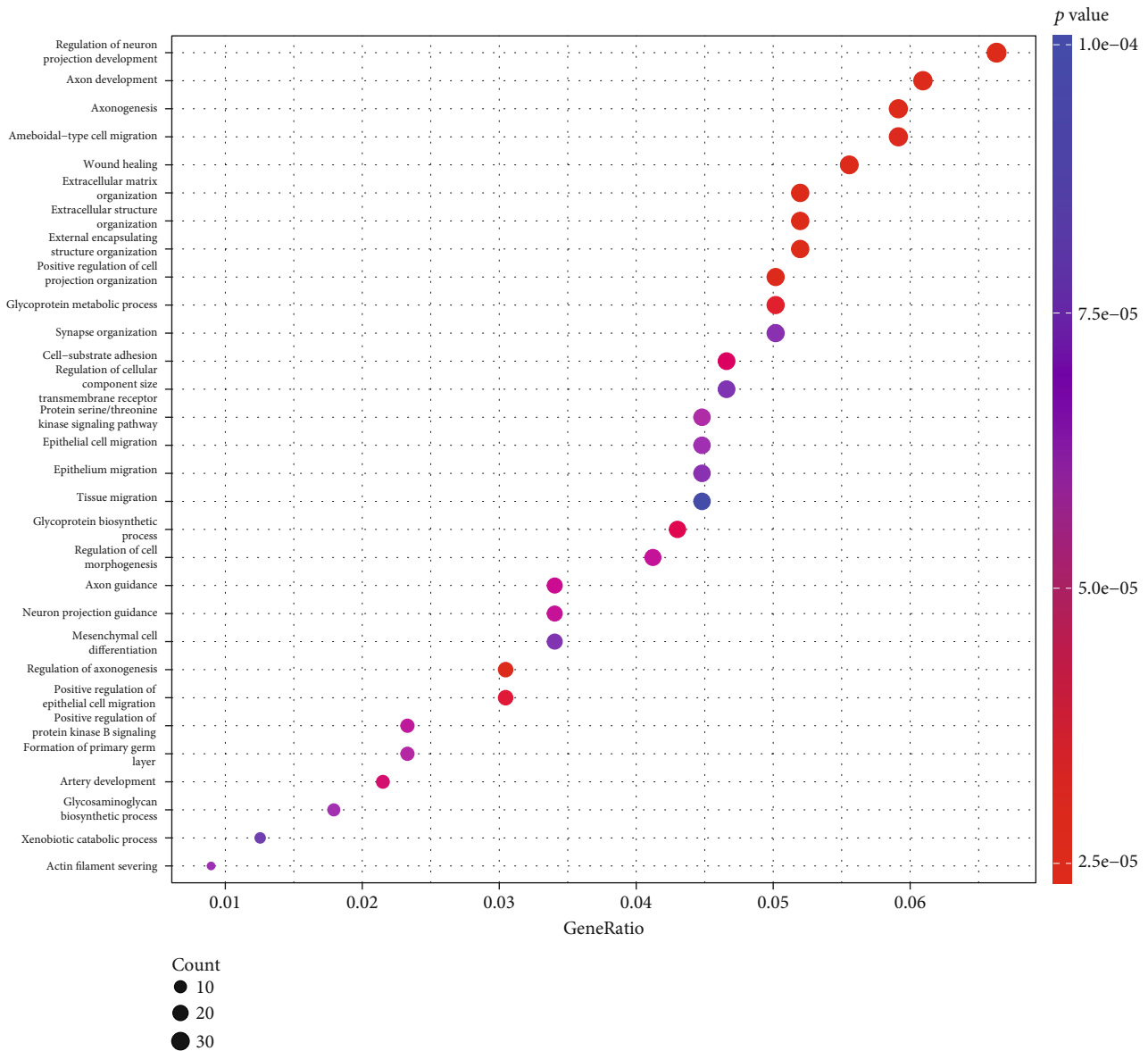
(d)

Figure 5: Enrichment analysis of GPR176 expression levels in STAD. (a and b) GO analysis of LIHC cohorts with high and low expressions ofGPR176. (c and d) KEGG analysis of LIHC cohorts with high and low expressions of GPR176.

cohort of low GPR176 showed a stronger immune response to immunotherapy (Figure 4(b)). In the case of CTLA4 negative but PD1 positive, the high GPR176 cohort showed a stronger immune response to immunotherapy (Figure 4(c)). In the case of CTLA4 positive but PD1 negative, the high GPR176 cohort demonstrated a stronger immune response to immunotherapy (Figure 4(d)).

3.4. Enrichment Analysis of GPR176 in STAD. To initially investigate the potential mechanism of GPR176, we performed KEGG and GO enrichment analyses by differentially expressed genes of GPR176 in STAD. The enrichment analysis of the GO function set showed that GPR176 may participate in cell migration, extracellular matrix ingredients, and

cell matrix reshaping (Figures 5(a) and 5(b)). The enrichment analysis of the KEGG function set shows that GPR176 may regulate cell migration, cell matrix, cell adhesion, and migration of epithelial cells (Figures 5(c) and 5(d)).

3.5. Correlation Analysis of GPR176 Expression Level and Immune Cell Infiltration. It is well-known that tumor immunological dysfunction plays a crucial role in tumorigenesis and progression [12]. We analyzed the relationship between GPR176 expression levels and immune profile in STAD. We implemented CIBERSORT to evaluate the relationship between GPR176 and various immune cells. The results indicated that GPR176 is negatively related to the infiltration

(a)

(b)

(c)

(d)

(e)

(f)
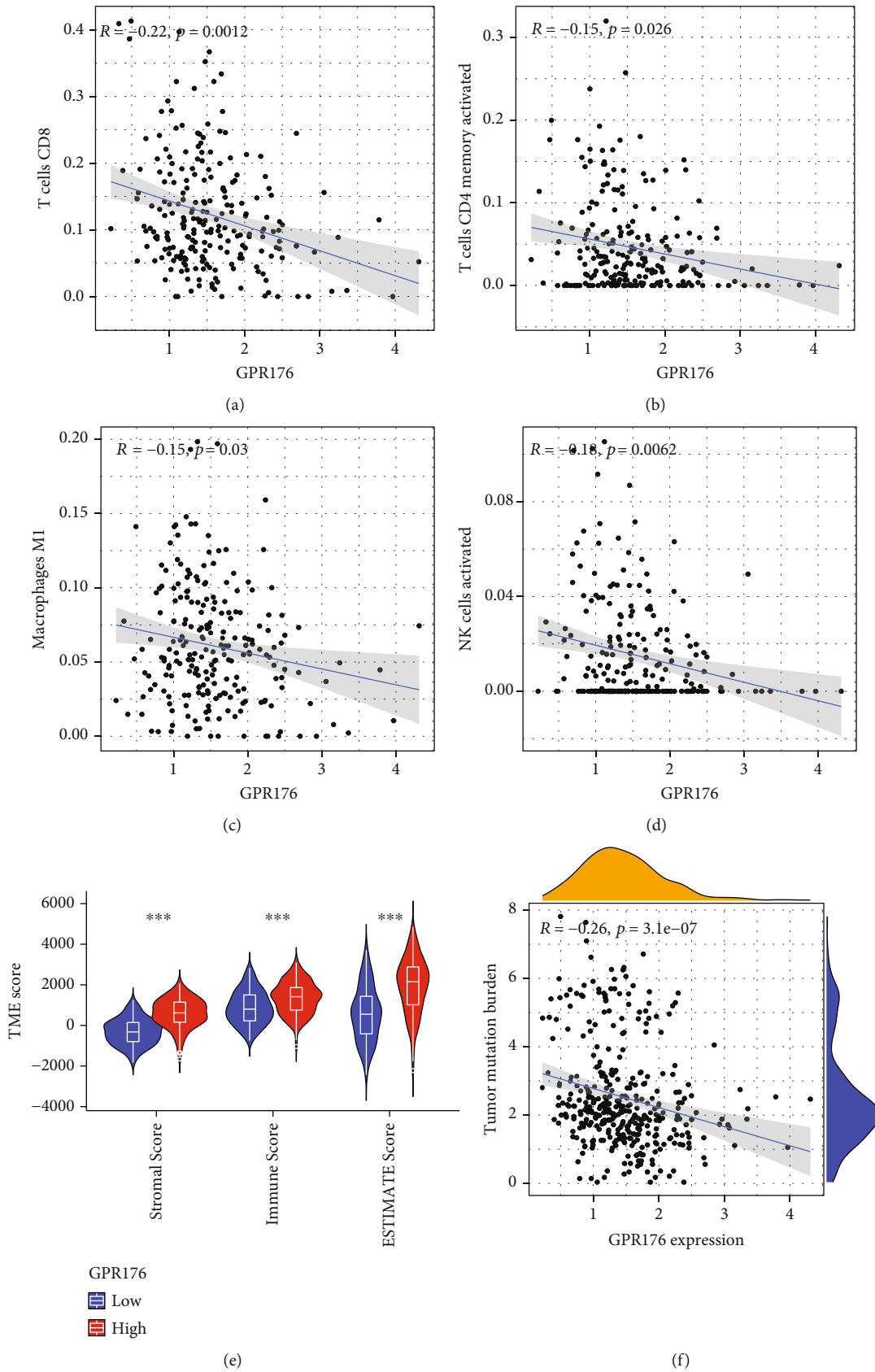
FIGURE 6: Correlation of GPR176 expression level with immune profile in STAD. (a–d) Correlation between GPR176 expression level and immune cell infiltration in STAD. (e) Correlation between GPR176 expression level and TME score in STAD. (f) Correlation between GPR176 expression level and TMB in STAD.

(a)

STAD (415 samples)

Spearman correlation test:
rho = 0.443, $p < 2.2e-16$

(b)

STAD (415 samples)

Spearman correlation test:
rho = 0.165, $p = 0.000754$

(c)
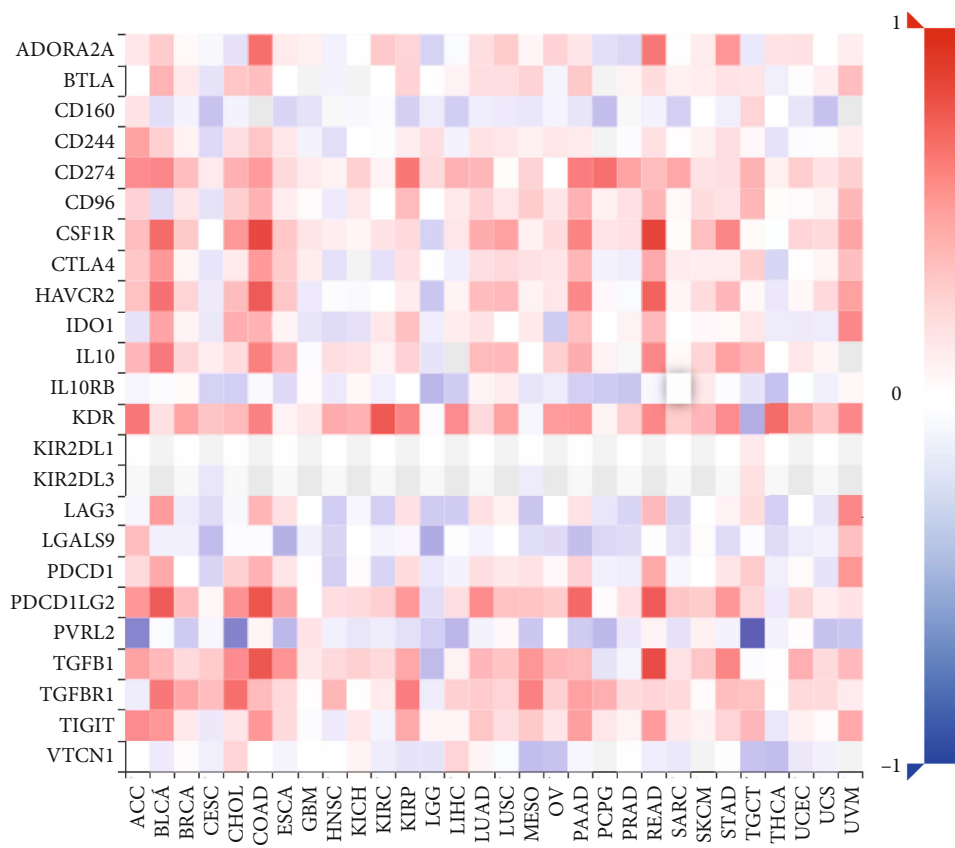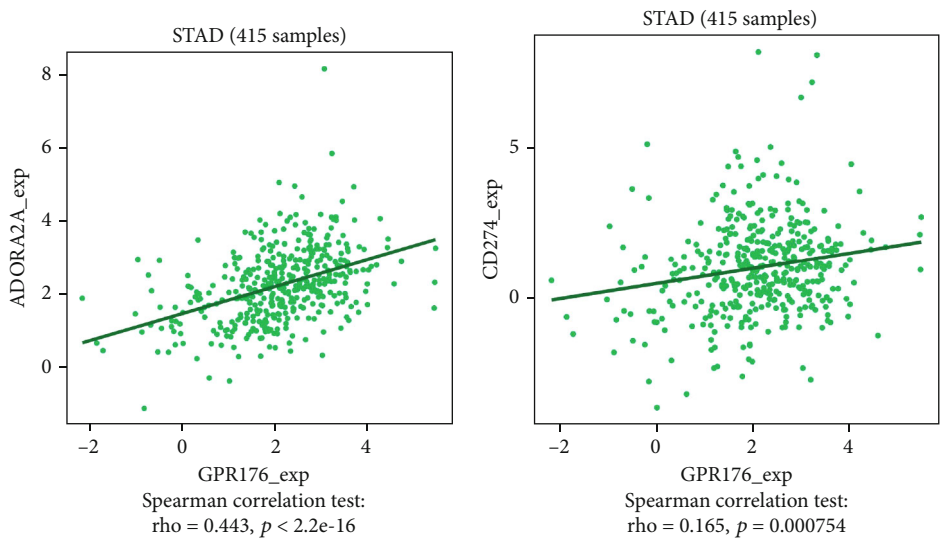
FIGURE 7: Continued.

(d)

(e)

Figure 7: Continued.

STAD (415 samples)

Spearman correlation test:
rho = −0.071, $p = 0.148$

(f)

STAD (415 samples)

Spearman correlation test:
rho = −0.208, $p = 2.01\text{e-}05$

(g)

STAD (415 samples)

Spearman correlation test:
rho = −0.096, $p = 0.0498$

(h)
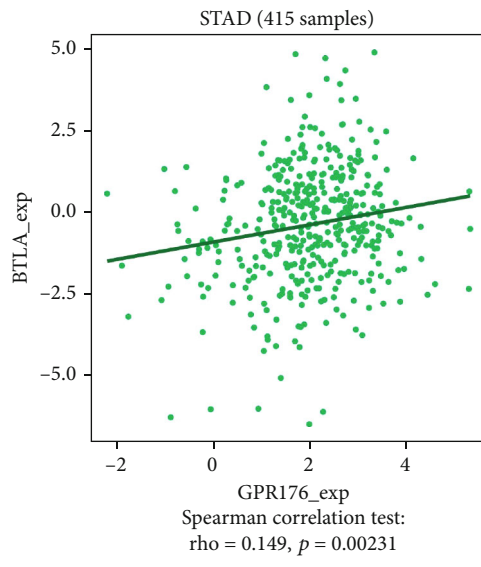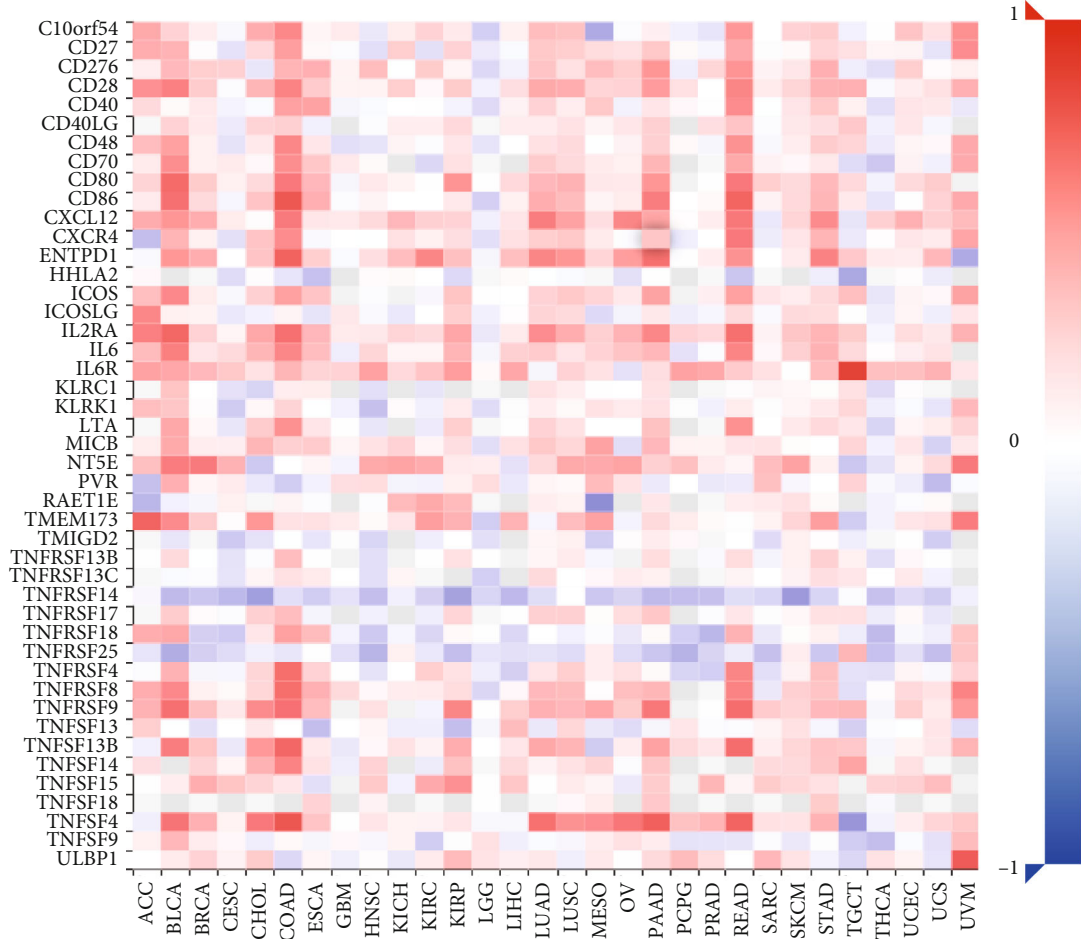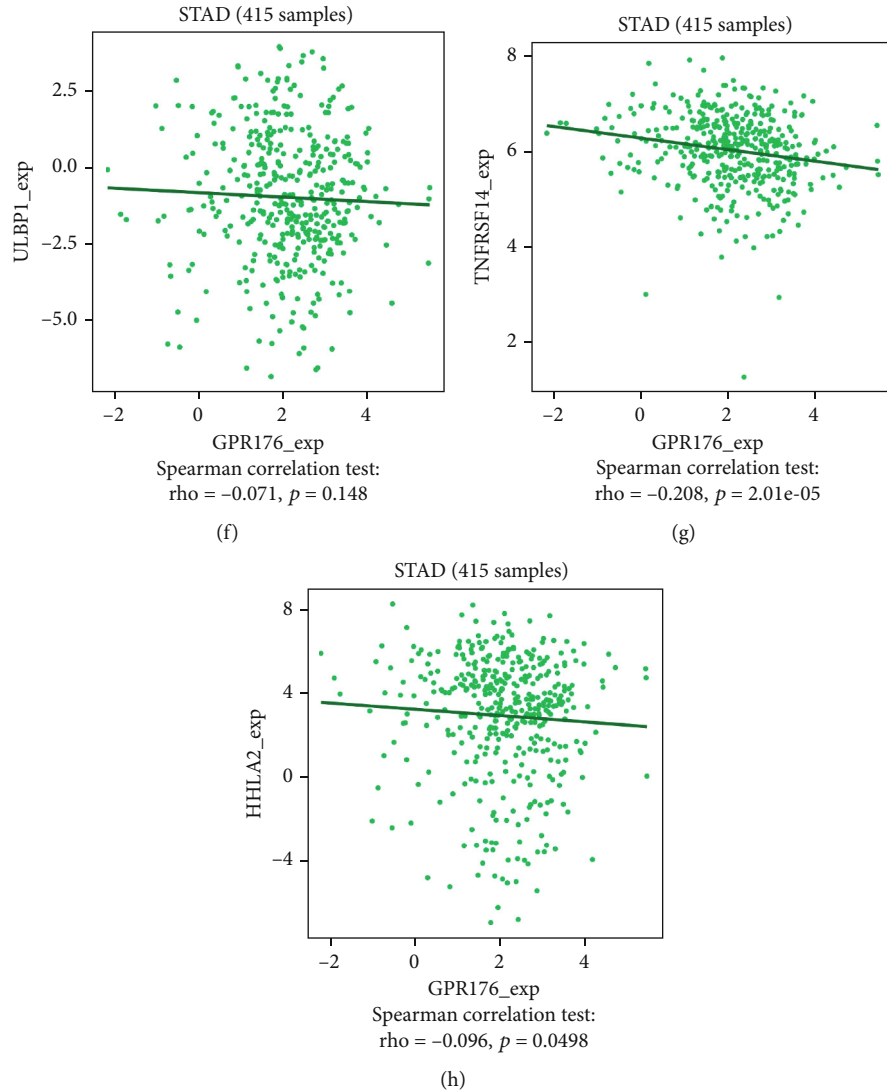
FIGURE 7: Correlation between GPR17 and immune checkpoints in STAD. (a) Heatmap of correlations between GPR17 expression levels and immunoinhibitor in STAD. (b–d) Correlation between GPR17 expression level and immunoinhibitor. (e) Heatmap of correlations between GPR17 expression levels and immunostimulator in STAD. (f–h) Correlation between GPR17 expression level and immunostimulator.

level of CD8$^+$ T cells, CD4 memory activation cells, M1 macrophages, and activated NK cells (Figures 6(a)–6(d)). In addition, we also found that patients with GPR176 have higher TME scores (Figure 6(e)). Interestingly, the expression level of GPR176 was negatively related to the TMB of STAD (Figure 6(f)). These data revealed that GPR176 plays a vital role in regulating the immun cells infiltration of STAD. Furthermore, we further explored whether the GPR176 level alters the expression of each immune checkpoint in STAD. As shown in Figure 7(a), GPR176 was positively related to the expression level of multiple immunoinhibitors, including ADORA2A, CD274, and BTLA (Figures 7(b)–7(d)). Meanwhile, GPR176 was negatively related to the expression level of multiple immunostimulator, including ULBP1, TNFRSF14, and HHLA2 (Figures 7(e)–7(h)). The above results strongly implied that GPR176 plays a vital role in regulating STAD immune profile.

3.6. Construction of Risk Score Model Based on GPR176-Related Immunomodulators. The previous results revealed that the GPR176 participate in regulating the immune function of STAD. We further intended to construct a prognostic model based on GPR176-related immunomodulators. We first conducted univariate and multivariate regression analyses to the obtained GPR176-related immunomodulators, and 4 GPR176-related genes were identified, including CXCR4, TNFSF18, PDCD1, and TGFB1 (Figures 8(a) and 8(b)). Furthermore, we constructed a prognosis model derived from the above 4 GPR176-related immunomodulators (GRIM). We further verified the prediction capabilities of the above model, and the results demonstrated that it has good prediction capabilities (Figures 8(c)–8(f)).

3.7. Construction of a Nomogram Based on GRIM. We intended to further explore the value of GRIM model in

(a)

(b)

Figure 8: Continued.

(c)

(d)

(e)

(f)
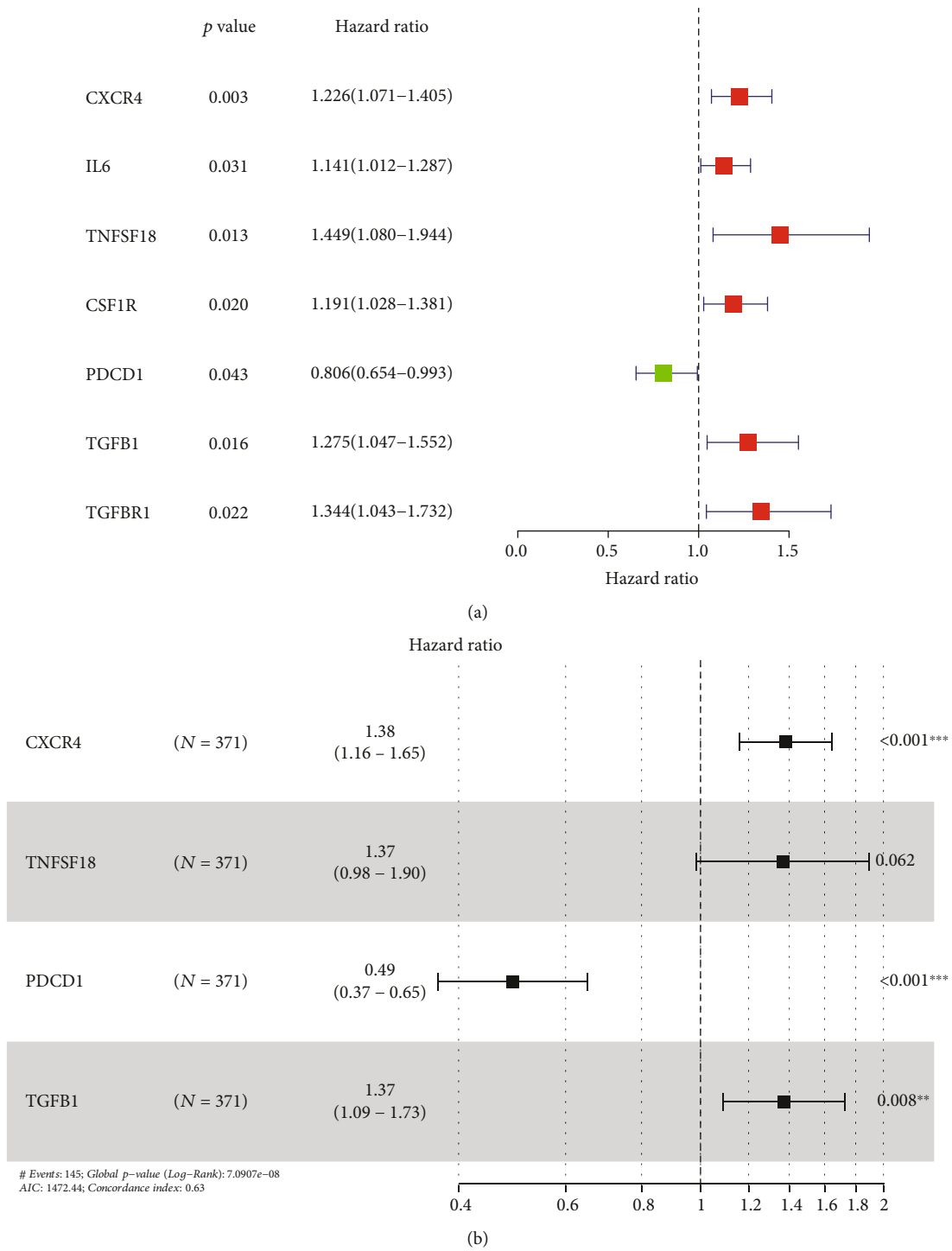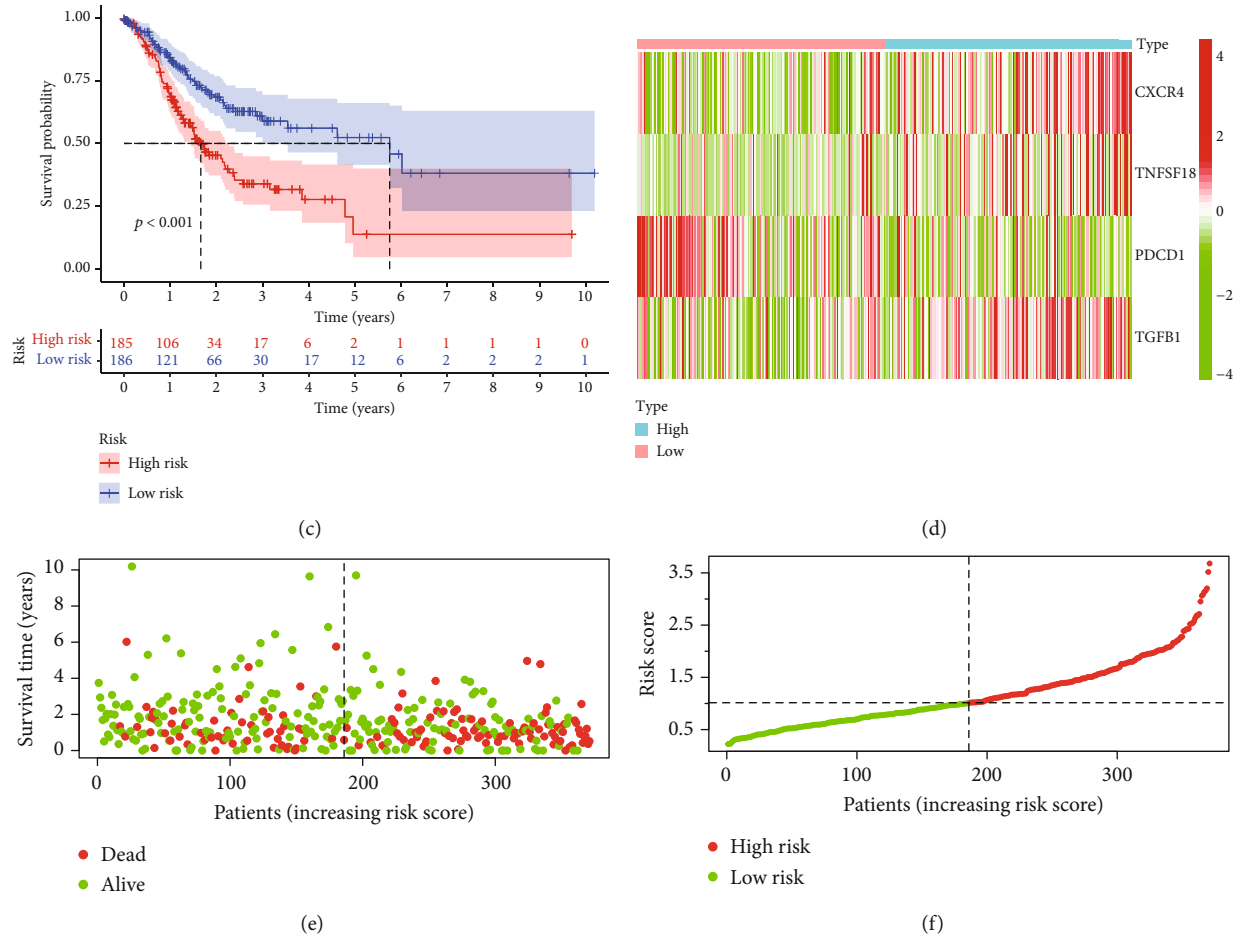
Figure 8: Construction of risk score model derived from GPR176-associated immunomodulators. (a) Univariate regression analysis of GPR176-related immunomodulators on STAD prognosis. (b) Multivariate regression analysis of GPR176-related immunomodulators on STAD prognosis. (c) OS comparison between high- and low-risk cohorts. (d) Distribution plot of immune checkpoints in high- and low-risk cohorts. (e) Distribution plot of survival status of patients according to risk score ranking. (f) Risk score ranking for high- and low-risk patients.

STAD. The risk score of GRIM model is identified as a prognostic risk factor for STAD by univariate and multivariate regression analyses (Figures 9(a) and 9(b)). As shown in Figure 9(c), the area under the ROC curve of the risk score reached 0.710. In addition, we developed a nomogram based on clinical features and risk score of GRIM model to predict the prognosis of STAD. The calibration curve indicated that the nomogram of GRIM model has excellent prognosis prediction capabilities for STAD patients in 1, 2, and 3 years (Figures 9(e)–9(g)).

4. Discussion

Immunotherapy brings new hopes for patients with advanced STAD. Therefore, it is particularly important to clarify the specific regulation mechanism of TIM. In this study, we first analyzed the expression of GRP176 in STAD and explored the correlation between its expression level and patient prognosis. We revealed that the level of GPR176 is significantly related to multiple clinical features. In addition, we found that GPR176 can be used to predict the efficacy of STAD on chemotherapy drugs and immunotherapy. KEGG and GO analyses were conducted to initially

explore the potential mechanisms by which GPR176 regulates STAD progression. Moreover, we further analyzed the correlation between GPR176 and immune profile of STAD. Finally, we constructed a prognostic model based on GPR176 and verified its accuracy and effectiveness through multiple methods. In the present study, we first revealed that GPR176 was closely related to the prognosis of STAD. GRP176 may participate in the regulation the TIM of patients with STAD.

At present, the TNM classification of malignant tumors is widely used in staging STAD, and its effectiveness and accuracy are confirmed [13]. In this study, we analyzed the correlation between GPR176 and TNM. It was found that the expression level of GPR176 at T2 was significantly upregulated compared to T1, and there was no further increase in T3 and T4. In N and M, there is no difference in expression of GPR176. Interestingly, the expression level of GPR176 at stage II was significantly upregulated compared to stage I. Given the above-mentioned abnormal results, this may be due to the fact that STAD is primarily involved in the regulation of STAD proliferative capacity, or to the insufficient number of samples adopted in this study.
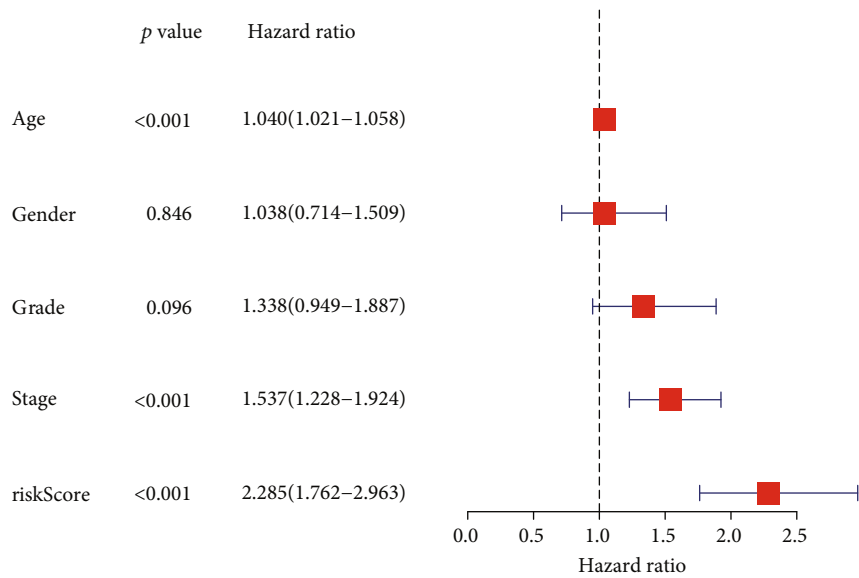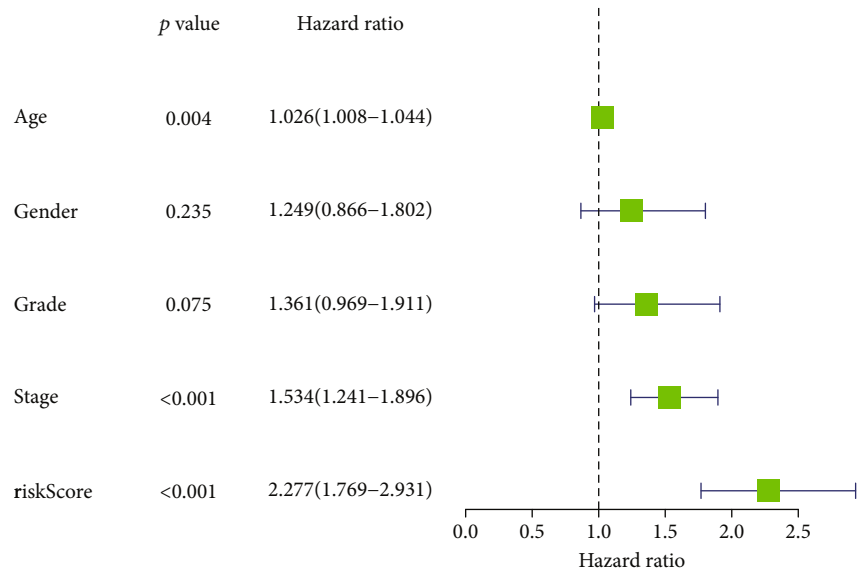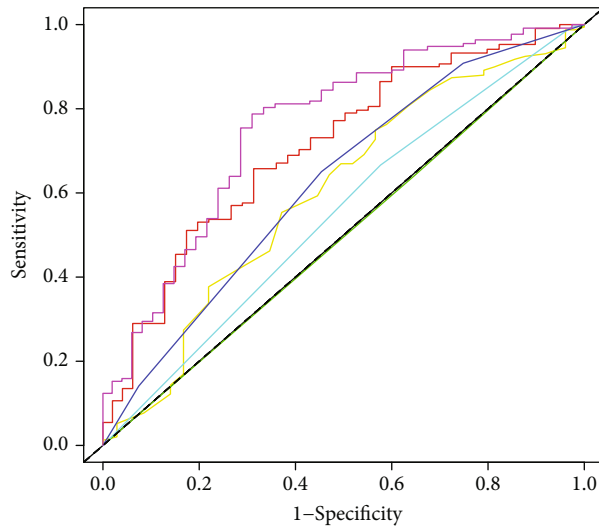
	p value	Hazard ratio	
Age	<0.001	1.040(1.021−1.058)	
Gender	0.846	1.038(0.714−1.509)	
Grade	0.096	1.338(0.949−1.887)	
Stage	<0.001	1.537(1.228−1.924)	
riskScore	<0.001	2.285(1.762−2.963)	

Hazard ratio

(a)

	p value	Hazard ratio	
Age	0.004	1.026(1.008−1.044)	
Gender	0.235	1.249(0.866−1.802)	
Grade	0.075	1.361(0.969−1.911)	
Stage	<0.001	1.534(1.241−1.896)	
riskScore	<0.001	2.277(1.769−2.931)	

Hazard ratio

(b)

Figure 9: Continued.

(c)
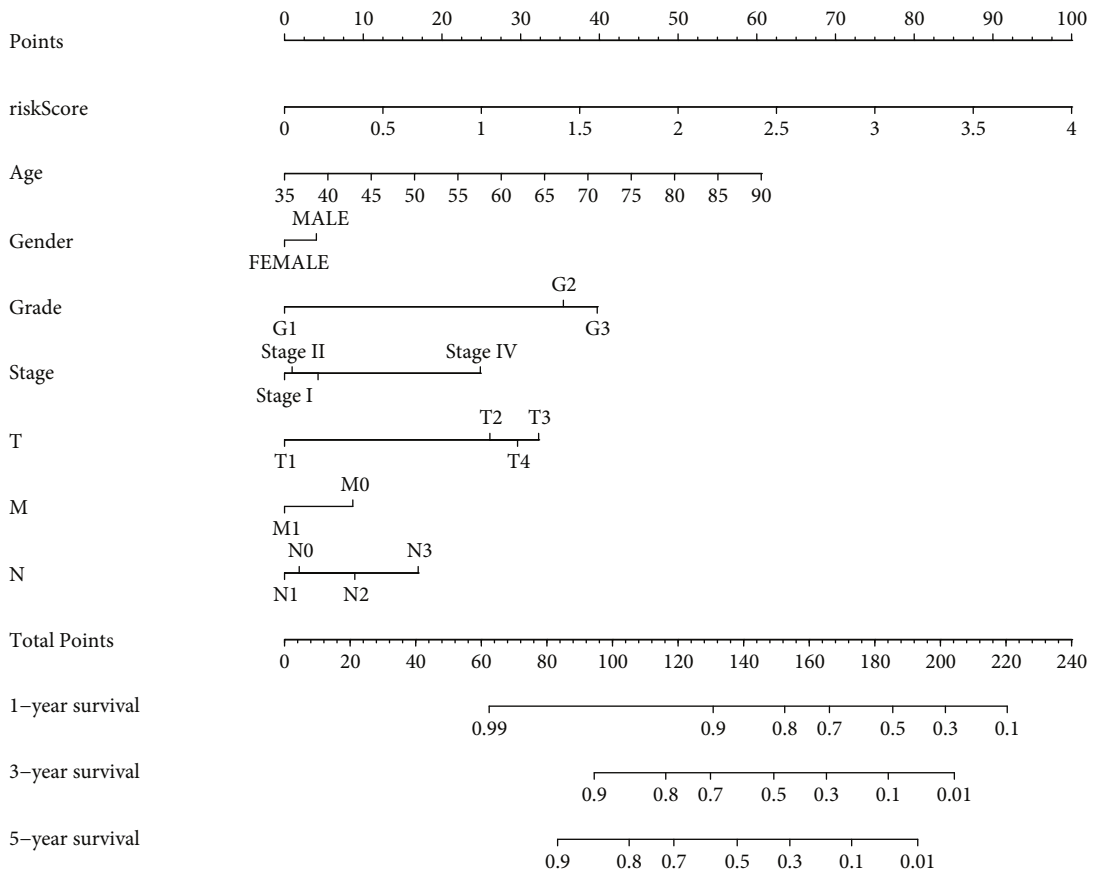
(d)

Figure 9: Continued.

(e)

(f)

(g)
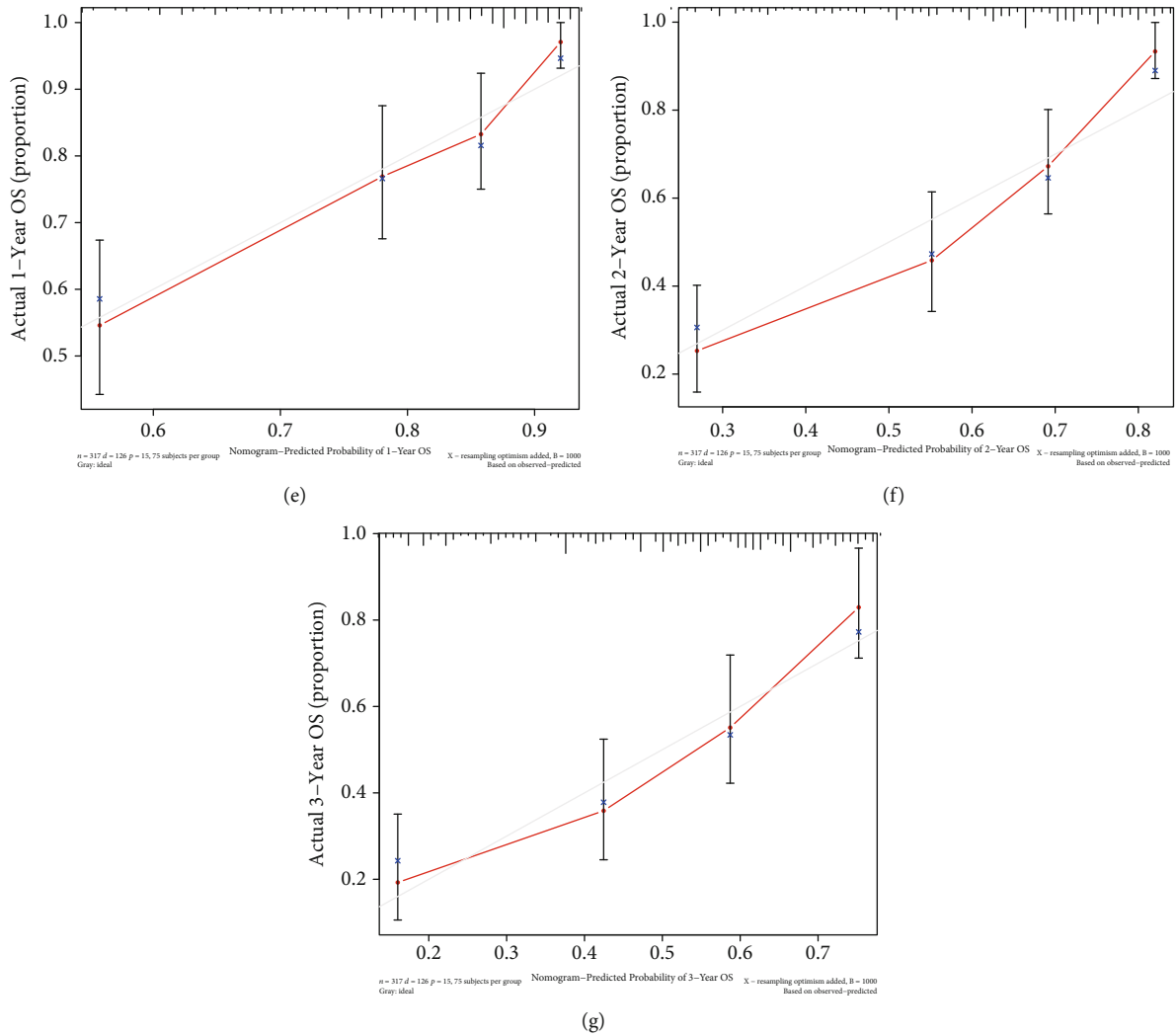
FIGURE 9: Construction of prognostic nomogram based on the risk scores of GRIM in STAD. (a) Univariate regression analysis of risk scores of GRIM and various clinical characteristics for STAD prognosis. (b) Multivariate regression analysis of risk scores of GRIM and various clinical characteristics for STAD prognosis. (c) ROC curves for risk score (GRIM) and clinical features. (d) Construction of GRIM nomogram and various clinical features in STAD. (e–g) Verification of the accuracy of the nomogram.

Malignant tumors have extremely complex gene networks, including a series of oncogenes and tumor suppressor genes, which regulate the occurrence and development of tumors [14]. In recent years, prognostic models based on various functional gene sets have emerged to evaluate the prognosis of tumors. In breast cancer, Hong et al. constructed a prognostic model based on the tumor microenvironment-related gene set, and the area under the ROC curve of the model risk score reached 0.67 [15]. Wang et al. analyzed the miRNA data of central lymph node metastasis in papillary thyroid carcinoma and then constructed a differential miRNA prognostic model with an area under the ROC curve of 0.7 [16]. In this study, the area under the ROC curve of the GRP176-based prognostic model we constructed was 0.71. The single-gene model based on GPR176 in this study also had excellent prognostic assessment compared with previous multigene prognostic models. This result indicated that the prognostic model derived from a single gene has a good application prospect.

The present study provided strong evidence to support the important role of GPR176 in STAD, but there are significant shortcomings. All the data in this study were obtained from public databases and lacked in vivo and in vitro validation, we will further confirm this in the follow-up study.

Collectively, our findings revealed a novel role of GRP176 in STAD, and GRP176 may be a promising potential target for STAD immunotherapy.

Data Availability

The data and result in this study are available from the corresponding authors upon reasonable request.

Ethical Approval

The study was conducted in accordance with the Declaration of Helsinki, and the protocol was approved by the Ethics

Committee of 900TH Hospital of Joint Logistics Support Force.

Conflicts of Interest

The authors declare no conflicts of interest.

Authors' Contributions

Lin Ni, Shuming Chen, and Jianyong Liu contributed equally to this work. All authors read and approved the final manuscript.

Acknowledgments

References

[1] J. A. Ajani, T. A. D'Amico, D. J. Bentrem et al., "Gastric cancer, version 2.2022, NCCN clinical practice guidelines in oncology," *Journal of the National Comprehensive Cancer Network*, vol. 20, pp. 167–192, 2022.

[2] Q. Liu, J. Jiang, X. Zhang, M. Zhang, and Y. Fu, "Comprehensive analysis of IGFBPs as biomarkers in gastric cancer," *Frontiers in Oncology*, vol. 11, article 723131, 2021.

[3] S. S. Joshi and B. D. Badgwell, "Current treatment and recent progress in gastric cancer," *CA: a Cancer Journal for Clinicians*, vol. 71, no. 3, pp. 264–279, 2021.

[4] A. Hogner and M. Moehler, "Immunotherapy in gastric cancer," *Current Oncology*, vol. 29, no. 3, pp. 1559–1574, 2022.

[5] Q. Zhao, L. Cao, L. Guan et al., "Immunotherapy for gastric cancer: dilemmas and prospect," *Brief Funct Genomics*, vol. 18, no. 2, pp. 107–112, 2019.

[6] J. Xie, L. Fu, and L. Jin, "Immunotherapy of gastric cancer: past, future perspective and challenges," *Pathology, Research and Practice*, vol. 218, article 153322, 2021.

[7] P. K. Darcy, P. Neeson, C. S. Yong, and M. H. Kershaw, "Manipulating immune cells for adoptive immunotherapy of cancer," *Current Opinion in Immunology*, vol. 27, pp. 46–52, 2014.

[8] K. Goto, M. Doi, T. Wang, S. Kunisue, I. Murai, and H. Okamura, "G-protein-coupled receptor signaling through Gpr176, Gz, and RGS16 tunes time in the center of the circadian clock [review]," *Endocrine Journal*, vol. 64, no. 6, pp. 571–579, 2017.

[9] T. Li, J. Fu, Z. Zeng et al., "TIMER2.0 for analysis of tumor-infiltrating immune cells," *Nucleic Acids Research*, vol. 48, no. W1, pp. W509–W514, 2020.

[10] B. Chen, M. S. Khodadoust, C. L. Liu, A. M. Newman, and A. A. Alizadeh, "Profiling tumor infiltrating immune cells with CIBERSORT," *Methods in Molecular Biology*, vol. 1711, pp. 243–259, 2018.

[11] Z. Zhao, B. He, Q. Cai et al., "Combination of tumor mutation burden and immune infiltrates for the prognosis of lung adenocarcinoma," *International Immunopharmacology*, vol. 98, article 107807, 2021.

[12] K. Nakamura, M. J. Smyth, and L. Martinet, "Cancer immunoediting and immune dysregulation in multiple myeloma," *Blood*, vol. 136, no. 24, pp. 2731–2740, 2020.

[13] T. Sano, D. G. Coit, H. H. Kim et al., "Proposal of a new stage grouping of gastric cancer for TNM classification: International Gastric Cancer Association staging project," *Gastric Cancer*, vol. 20, no. 2, pp. 217–225, 2017.

[14] A. J. Singh, S. A. Ramsey, T. M. Filtz, and C. Kioussi, "Differential gene regulatory networks in development and disease," *Cellular and Molecular Life Sciences*, vol. 75, no. 6, pp. 1013–1025, 2018.

[15] K. Hong, Y. Zhang, L. Yao, J. Zhang, X. Sheng, and Y. Guo, "Tumor microenvironment-related multigene prognostic prediction model for breast cancer," *Aging*, vol. 14, no. 2, pp. 845–868, 2022.

[16] M. Wang, R. Li, X. Zou et al., "A miRNA-clinicopathological nomogram for the prediction of central lymph node metastasis in papillary thyroid carcinoma-analysis from TCGA database," *Medicine*, vol. 99, no. 35, article e21996, 2020.

Research Article

A Prognostic Model Based on NSUN3 Was Established to Evaluate the Prognosis and Response to Immunotherapy in Liver Hepatocellular Carcinoma

Jianlin Zhu ⓘ,[1,2] **Junxi Kuang** ⓘ,[3,4] **Yi Yang** ⓘ,[1,2] **Lei Zhang** ⓘ,[1] **Bo Leng** ⓘ,[1] **Risheng She** ⓘ,[1,4] **and Ling Zou** ⓘ[1,2]

[1]*Dongguan Institute of Clinical Cancer Research, The Tenth Affiliated Hospital of Southern Medical University, China*
[2]*Dongguan Key Laboratory of Precision Diagnosis and Treatment for Tumors,*
 The Tenth Affiliated Hospital of Southern Medical University, China
[3]*Department of Cardiovascular Medicine, The Third Affiliated Hospital of Sun Yat-sen University, China*
[4]*Department of Emergency, The Tenth Affiliated Hospital of Southern Medical University, China*

Correspondence should be addressed to Risheng She; rishengshe2022@163.com and Ling Zou; zlbsetss@aliyun.com

It is difficult for traditional therapies to further improve the prognosis of hepatocellular carcinoma (LIHC), and immunotherapy is considered to be a promising approach to overcome this dilemma. However, only a minority of patients benefit from immunotherapy, which greatly limits its application. Therefore, it is particularly urgent to elucidate the specific regulatory mechanism of tumor immunity so as to provide a new direction for immunotherapy. NOP2/Sun RNA methyltransferase 3 (NSUN3) is a protein with RNA binding and methyltransferase activity, which has been shown to be involved in the occurrence and development of a variety of tumors. At present, the relationship between NSUN3 and immune implication in LIHC has not been reported. In this study, we first revealed that NSUN3 expression is upregulated in LIHC and that patients with high NSUN3 expression have a poor prognosis through multiple databases. Pathway enrichment analysis demonstrated that NSUN3 may be participated in cell adhesion and cell matrix remodeling. Next, we obtained a set of genes coexpressed with NSUN3 (NCGs). Further LASSO regression was performed based on NCGs, and a risk score model was constructed, which proved to have good predictive power. In addition, Cox regression analysis revealed that the risk score of NCGs model was an independent risk factor for LIHC patients. Moreover, we established a nomogram based on the NCGs-related model, which was verified to have a good predictive ability for the prognosis of LIHC. Furthermore, we investigated the relationship between NCGs-related model and immune implication. The results implied that our model was closely related to immune score, immune cell infiltration, immunotherapy response, and multiple immune checkpoints. Finally, the pathway enrichment analysis of NCGs-related model showed that the model may be involved in the regulation of various immune pathways. In conclusion, our study revealed a novel role of NSUN3 in LIHC. The NSUN3-based prognostic model may be a promising biomarker for inspecting the prognosis and immunotherapy response of LIHC.

1. Introduction

Liver hepatocellular carcinoma (LIHC) is a highly lethal malignancy originating from the digestive system and one of the leading causes of cancer-related deaths worldwide [1]. Global cancer epidemiological statistics in 2020 show that there are about one million new cases of liver cancer, most of which are LIHC [2]. Various risk factors are known to predispose to the development of liver cancer, including chronic hepatitis virus infection, aflatoxin B, and alcoholism [3, 4]. Currently, surgical resection is still the preferred treatment option for LIHC. Unfortunately, the overall recurrence rate of LIHC remains high, with a 5-year survival rate of less than 50% [5]. In addition to classic surgical resection, other

(a)

(b)

(c)

(d)

(e)

FIGURE 1: Continued.

(f)
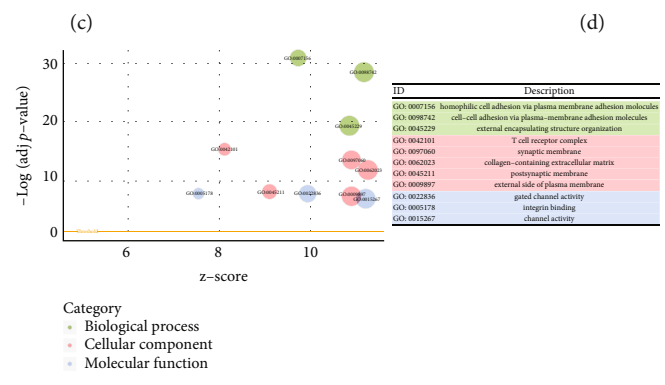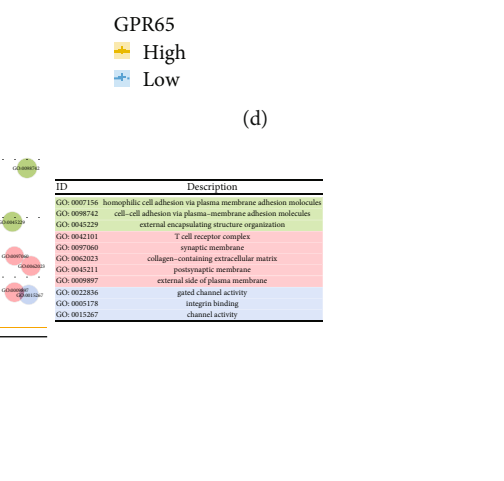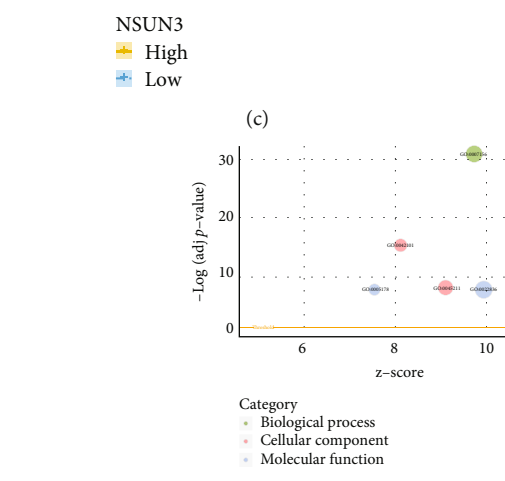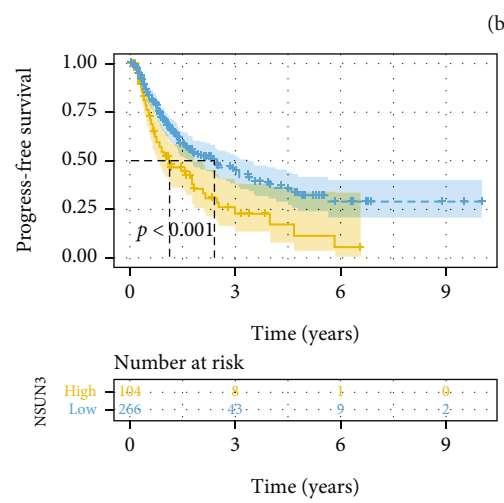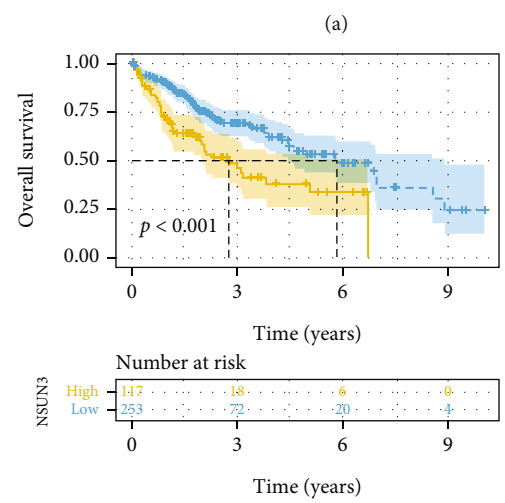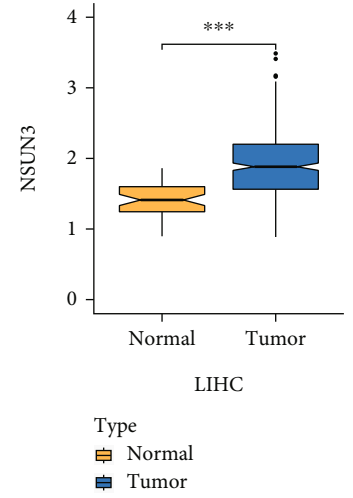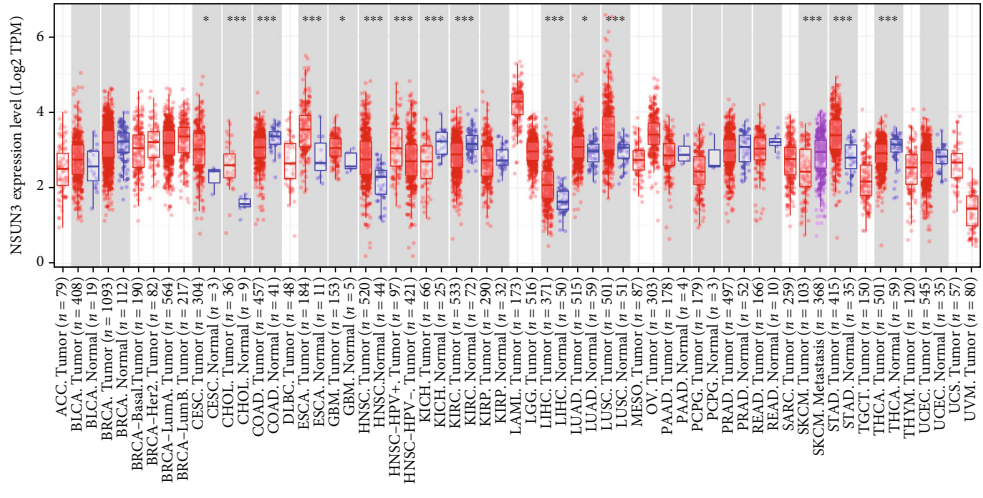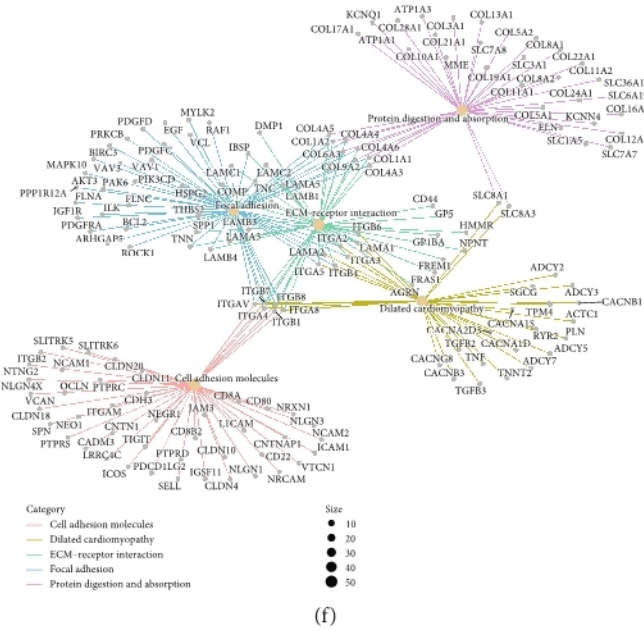
FIGURE 1: Analysis of NSUN3 expression and prognosis in LIHC and pathway enrichment analysis. (a) Expression level of NSUN3 in pancancer (TIMER database). (b) Differential expression of NSUN3 in LIHC and normal tissues. (c, d) Effects of NSUN3 expression level on overall survival (OS) and progression-free survival (PFS). (e) GO analysis based on NSUN3 expression level. (f) KEGG analysis based on NSUN3 expression level.

treatment options for LIHC including ablation, catheterization, and noncatheterization have been widely applied, but the 5-year survival is still less than 20% [6–8]. Traditional treatment strategies are extremely limited to further improve the prognosis of LIHC [9]. Therefore, elucidating the pathogenesis of LIHC is crucial for its treatment.

With the breakthrough of immunotherapy theory of tumor in recently years, immune checkpoint inhibitors (ICIs) based on various immune checkpoints have been developed, and they have brought new hope to LIHC patients [10]. At present, a variety of ICIs have been used in the treatment of LIHC, including PD1 antibody and CTLA-4 antibody [3]. However, in the practical application of ICIs, only a minority of patients benefit from ICIs treatment [11]. Several studies have shown that the level of leukocyte infiltration in the tumor immune microenvironment (TIM) is closely related to the efficacy of immunotherapy [12, 13]. Therefore, it is crucial to explore the specific situation and mechanism of TIM in LIHC for the guidance of LIHC immunotherapy.

NOP2/Sun RNA methyltransferase 3 (NSUN3) is a protein-coding gene with RNA binding and methyltransferase activities [14]. It has been reported that NSUN3-mediated m5C modification of mitochondrial tRNA enhances energy supply by promoting protein synthesis in the mitochondrial respiratory chain, thereby promoting cancer cell invasion and metastasis [14]. Currently, there is no report on the relationship between NSUN3 and immune function in LIHC.

In this study, we first found that NSUN3 was highly expressed in LIHC and correlated with poor patient progno-

sis. We constructed a prognostic model based on NSUN3 coexpressed genes (NCGs) and validated its applicability for evaluating the prognosis and immunotherapy response of LIHC. Our study revealed a novel role of NSUN3 in LIHC, which may be a potential therapeutic target.

2. Materials and Methods

2.1. Acquisition of LIHC Transcriptional Data. LIHC transcription data downloaded from The Cancer Genome Atlas (TCGA, https://portal.gdc.cancer.gov/) and GEO (https://www.ncbi.nlm.nih.gov/geo/) public databases. We merged the obtained survival information of LIHC samples with transcriptome data and finally got 342 LIHC samples with survival information (TCGA).

2.2. Construction of Risk Scoring Model. We performed LASSO regression analysis on the coexpressed genes of NSUN3. Risk score was assigned to each LIHC patient according to the following established formula: risk score = $(\beta i^* \text{Exp}i)$, where Exp$i$ refers to the expression level of the target gene and βi represents the coefficient of the target gene. The ROC curve was implemented to evaluate the predictive ability of the model.

2.3. Analysis of Immune Cell Infiltration in LIHC. In this study, we applied CIBERSORT to assess the immune cell infiltration ratio. CIBERSORT is a novel algorithm that relies on a gene expression matrix file called LM22, which

(a)

(b)

(c)

Figure 2: Continued.

(d)
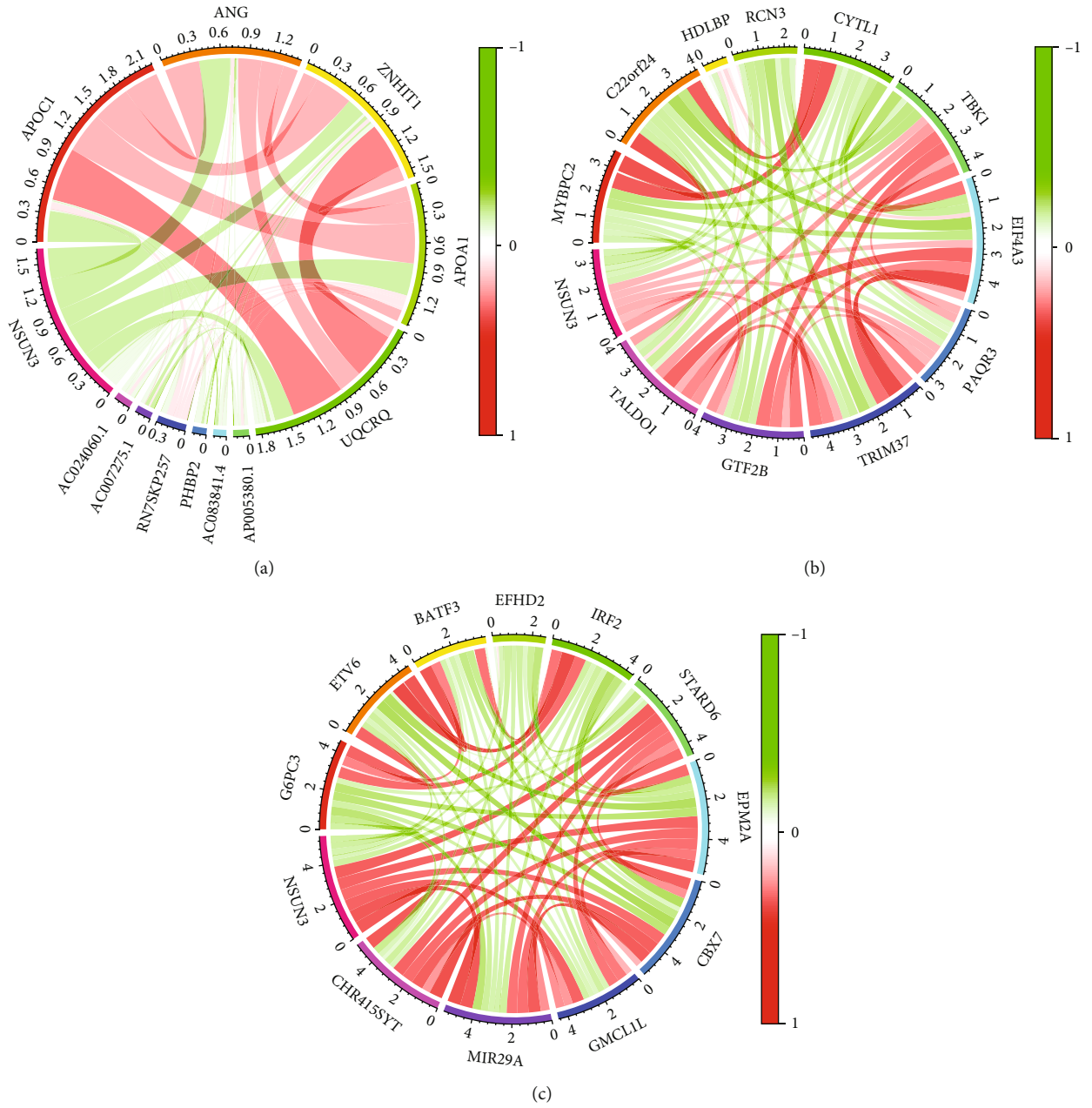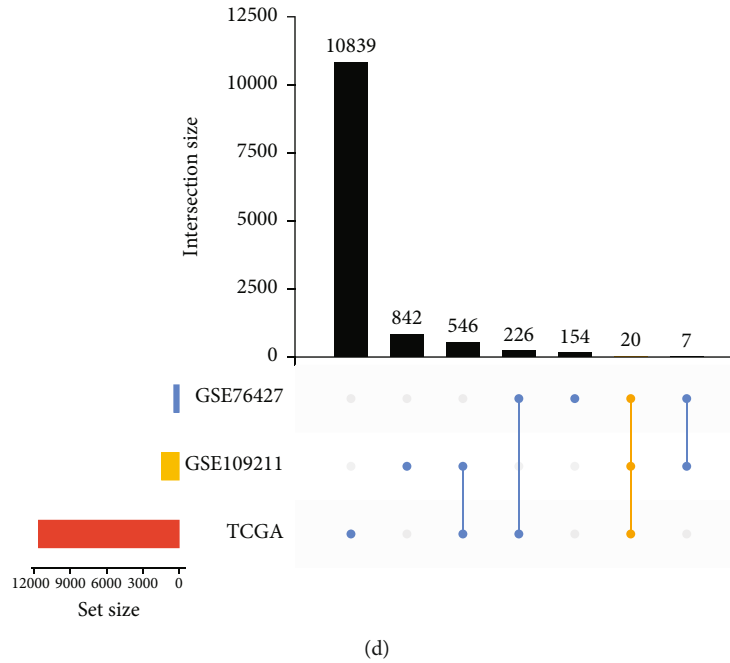
FIGURE 2: Analysis of NSUN3 coexpressed genes (NCGs). (a–c) Coexpressed genes of NSUN3 in different transcriptome datasets (GSE76427, GSE109211, and TCGA-LIHC cohorts). (d) Intersection of NSUN3 coexpressed genes obtained from different datasets.

can analyze immune cells by identifying and counting specific genes in them [15].

2.4. Evaluation of the Correlation between Risk Scores and Immune Profiles. In this study, we applied IPS, TIDE, and ESTIMATE to analyze the correlation of risk score and immune profile. The immunophenoscore (IPS) is a method for predicting response to immune checkpoints by quantifying tumor immunogenicity. The method incorporates multiple parameters, such as immunomodulators, effector cells, and suppressor cells, by weighted quantification of these components, resulting in a final IPS score [16]. ESTIMATE (Estimation of Stromal and Immune cells in Malignant Tumor Tissues using Expression Data) is a novel algorithm to infer tumor tissue components from unique characteristic genes in tumor tissue transcriptional data. In this study, we conducted the ESTIMATE algorithm to analyze the correlation of immune and stromal scores with risk scores [17]. Tumor immune dysfunction and rejection (TIDE) is a predictor of patient response to immune checkpoint inhibitors. Patients with low TIDE scores may be more responsive to immunotherapy, whereas patients with high TIDE scores may respond less to immunotherapy [18].

2.5. Statistics. In this study, R software (4.2.2) was applied for calculation and statistical analysis. $p < 0.05$ was considered statistically significant.

3. Results

3.1. NSUN3 Is Highly Expressed and Associated with Poor Prognosis in LIHC. We first analyzed the mRNA expression levels of NSUN3 in pan-cancer via the TIMER database, and

the result showed that NSUN3 was significantly upregulated in LIHC (Figure 1(a)). Next, we further explored the expression of NSUN3 in TCGA-LIHC and found that it was significantly elevated in tumor tissues (Figure 1(b)). In addition, we performed survival analysis based on NSUN3 expression, and the results demonstrated that NSUN3 was closely associated with poor prognosis (Figures 1(c) and 1(d)). Moreover, we applied GO and KEGG enrichment analyses to preliminarily explore the potential role and mechanism of NSUN3 in LIHC. GO analysis showed that the function of NSUN3 was mainly enriched in extracellular matrix remodeling (Figure 1(e)), and KEGG pathway analysis revealed that NSUN3 was enriched in cell adhesion, extracellular matrix remodeling, and focal adhesion junctions (Figure 1(f)). These pathways obtained above suggested that NSUN3 plays an important role in the regulation of LIHC immune function.

3.2. Coexpression Gene Analysis of NSUN3. The previous data strongly suggested a strong correlation between NSUN3 levels and prognosis, we intended to investigate the coexpressed genes of NSUN3 in LIHC. We analyzed the coexpressed gene network of NSUN3 by 3 LIHC datasets (GSE76427, GSE109211, and TCGA), and the correlation coefficient was set at 0.2 ($p < 0.05$). We presented the top 10 most correlated genes in these three datasets in Figures 2(a)–2(c). Next, the upset plot was applied to intersect the coexpressed genes of the three datasets, and 20 coexpressed genes were obtained finally (Figure 2(d)).

3.3. Construction of a Model Based on NSUN3 Expression Levels in LIHC. We previously obtained a gene set with 20 genes coexpressed with NSUN3. Next, we performed LASSO
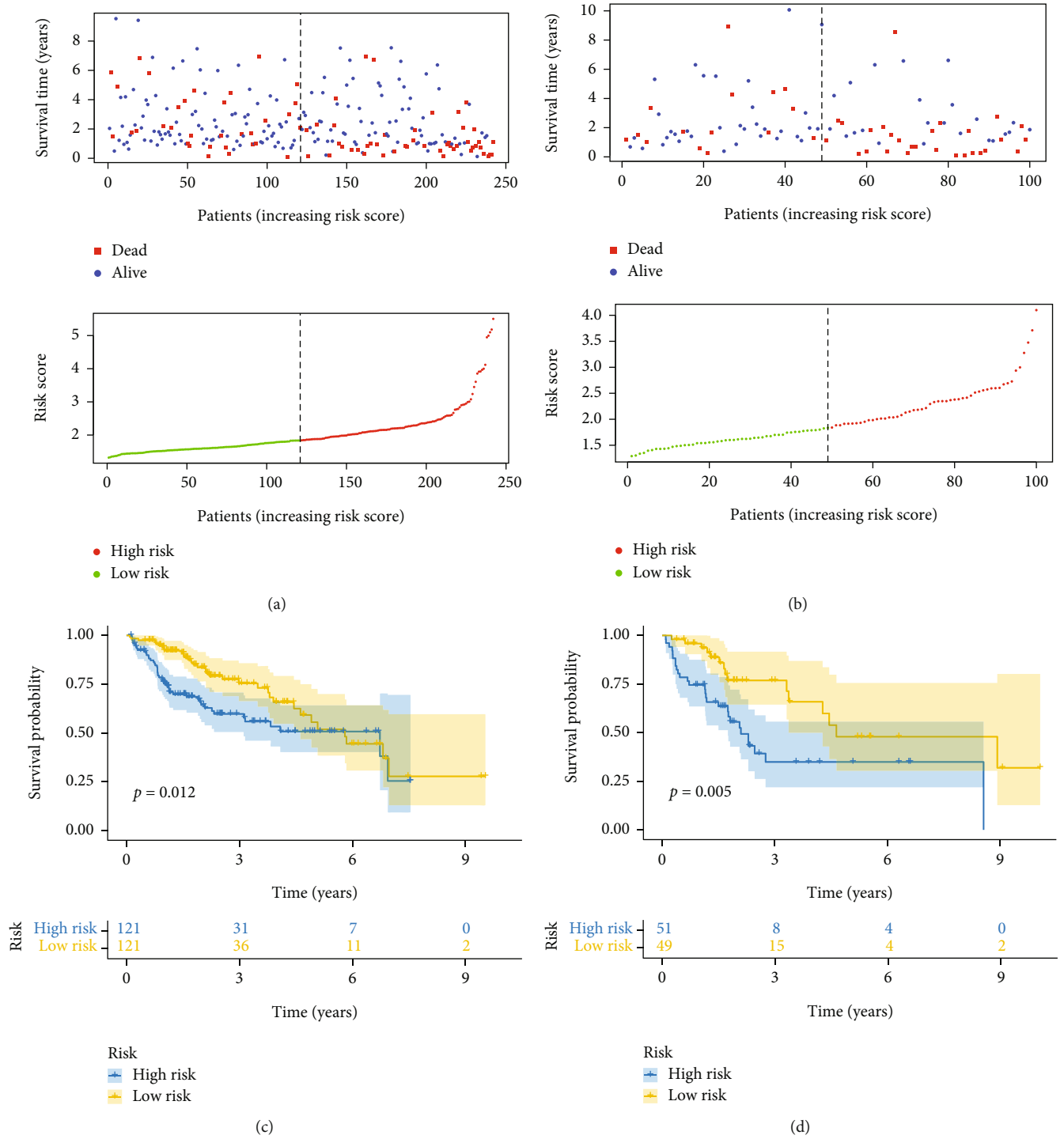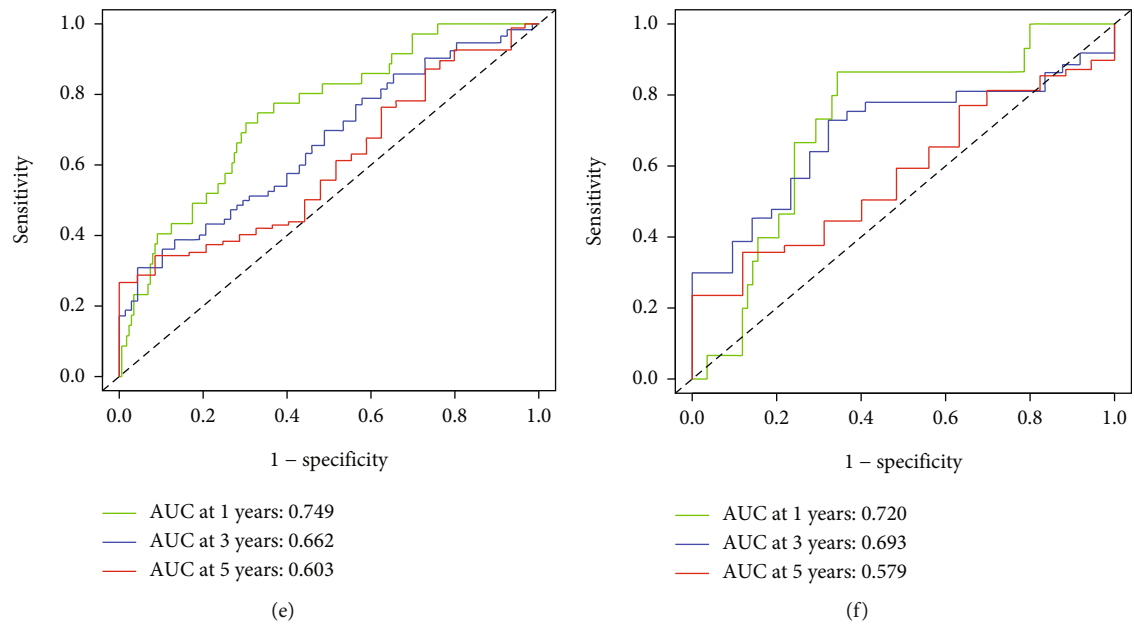
(a)

(b)

(c)

(d)

Figure 3: Continued.

regression analysis to screen this gene set and obtained 6 coexpression genes with associated NSUN3 (NCGs). Furthermore, based on the obtained 6 genes, we constructed a risk prognostic model based on NSUN3 coexpressed genes in LIHC and randomly divided the LIHC cohort in TCGA into two cohorts at a ratio of 7:3, namely, training cohort and validation cohort queues. As shown in Figures 3(a) and 3(b), we risk scored and ranked these patients and found consistent changes in mortality and risk scores among patients. In addition, we further verified that there were significant prognostic differences between high- and low-risk patients in this model (Figures 3(c) and 3(d)). Finally, we evaluated the predictive power of the training and validation cohorts by ROC curves. The AUC of the training cohort at years 1, 3, and 5 was 0.749, 0.662, and 0.603, respectively; the AUC of the validation cohort at years 1, 3, and 5 was 0.720, 0.693, and 0.579, respectively (Figures 3(e) and 3(f)). These data strongly indicated that the model has good predictive performance.

3.4. Construction and Verification of Nomogram Based on Predictive Model.

We first performed univariate and multivariate analyses on the risk model, and the results both showed that the HR values of the risk score of the model were 1.969 and 1.871, respectively (Figures 4(a) and 4(b)). Next, we constructed a nomogram integrating the prognostic model and its multiple clinical features, including gender, age, histological grade, and pathological stage (Figure 4(c)). Meanwhile, we verified the accuracy of the nomogram, and the results showed that the nomogram had accurate predictive capacity (Figure 4(d)). Interestingly, the accuracy of the risk model that we further evaluated by the C index also

demonstrated good performance in the assessment of LIHC prognosis (Figure 4(e)).

3.5. Correlation between NCG-Related Model Risk Scores and Immune Microenvironment in LIHC.

Immune cells in the tumor immune microenvironment (TIM) induce immune escape by interacting with tumor cells [13]. To clarify their complex relationship, we applied the ESTIMATE algorithm to analyze the TIM of LIHC and observed the differences in matrix score, immune score, and comprehensive score between the high-risk group and the low-risk group, respectively. The results demonstrated that the TME score of the low-risk group was significantly higher than in the high-risk cohort (Figure 5(a)). Next, we investigated the infiltration abundance of 21 immune cells in high- and low-risk patients by the CIBORESORT algorithm, and the results showed that the infiltration abundance of M0 macrophage cells in the low-risk group was higher than that in the high-risk group (Figure 5(b)). In addition, we further explored the correlation between 6 NCGs genes and 21 types of immune cells, the results revealed that AGPS was positively correlated with M0 macrophages but negatively correlated with gamma delta T cells and CD8 T cells; CCDC50 was negatively correlated with activated NK cells and $\gamma\delta$T cells; NSUN3 was negatively correlated with Treg cells and $\gamma\delta$T cells; SLC38A6 was negatively correlated with naive B cells and memory resident CD4$^+$ T cells; TFDP2 was negatively correlated with M1 macrophages; ZNF691 was negatively correlated with Treg cells (Figure 5(c)).

3.6. Risk Scores for NCGs-Related Models Predict Immunotherapy Response.

Immune checkpoints play a key role in the regulation of immune cell function and are

	p value	Hazard ratio
Age	0.406	1.175 (0.803–1.721)
Gender	0.156	0.754 (0.511–1.113)
Grade	0.400	1.118 (0.862–1.450)
Stage	< 0.001	1.806 (1.461–2.232)
riskScore	< 0.001	1.969 (1.560–2.486)

(a)

	p value	Hazard ratio
Age	0.706	1.079 (0.727–1.603)
Gender	0.774	0.941 (0.623–1.421)
Grade	0.722	1.053 (0.793–1.397)
Stage	< 0.001	1.741 (1.396–2.170)
riskScore	< 0.001	1.811 (1.404–2.336)

(b)

(c)

(d)

(e)
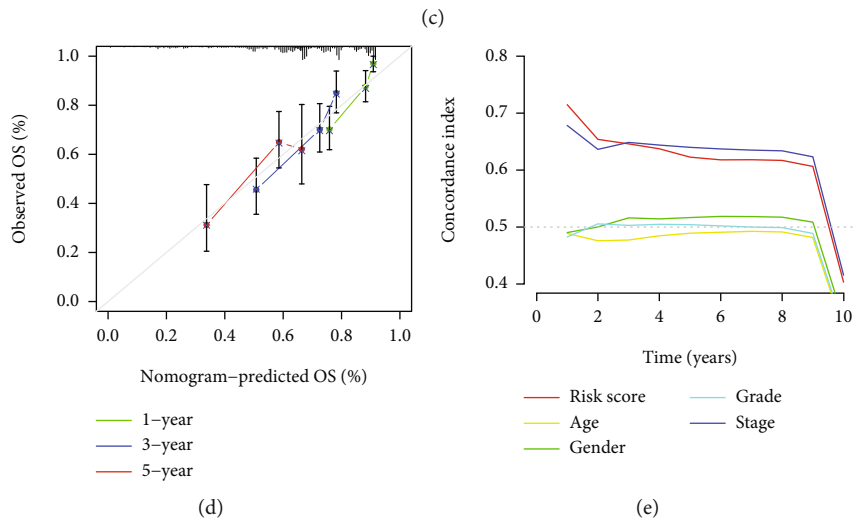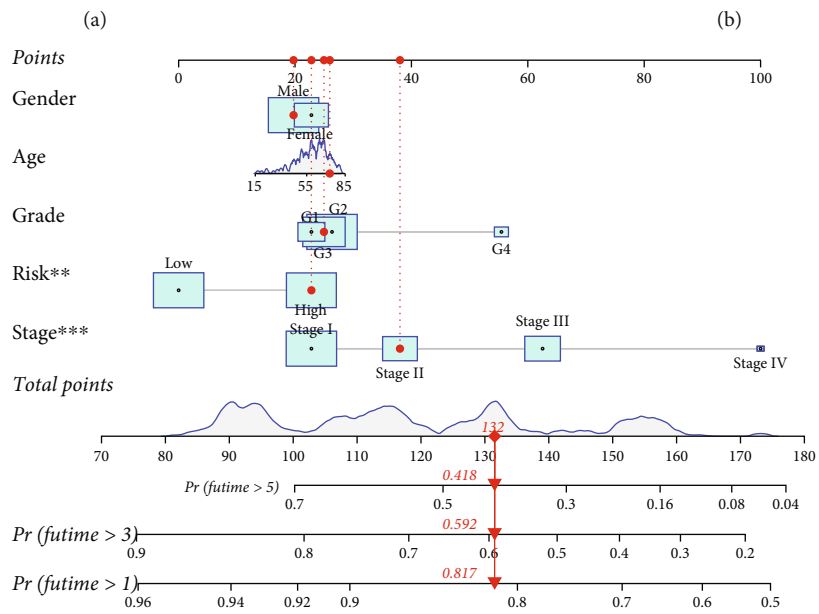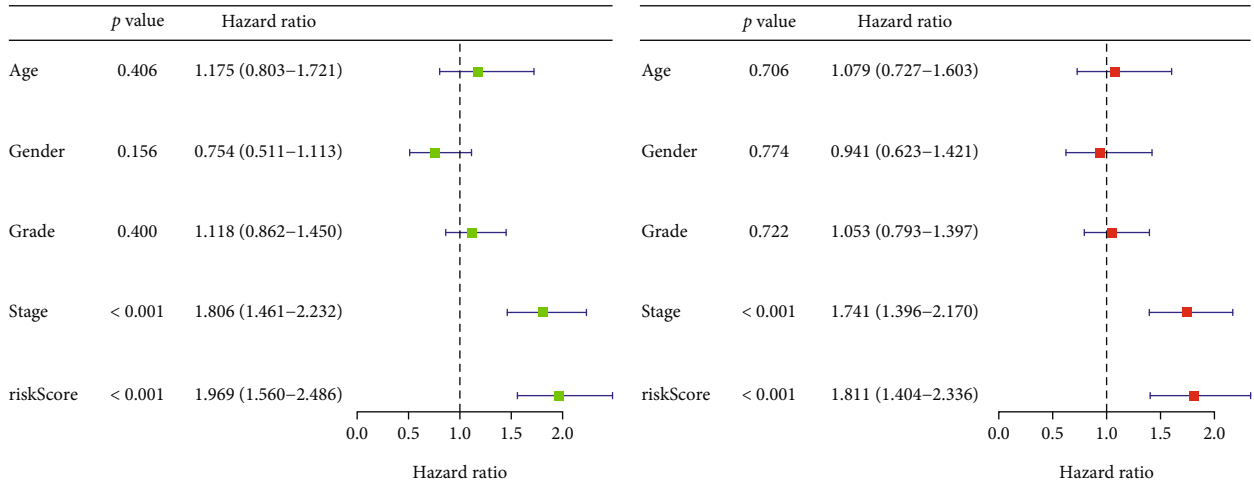
Figure 4: Construction and validation of nomogram based on NCGs-related model and clinical features. (a, b) Univariate and multivariate regression analyses of NCGs model risk score and clinical characteristics. (c) Construction of risk score and nomogram of various clinical characteristics based on NCGs-related model. (d) Validation of the predictive power of the nomogram at years 1, 3, and 5. (e) Analyze the predictive power of the model's risk score by the C-index.

(a)

(b)

(c)

*** $p < 0.001$
** $p < 0.01$
* $p < 0.05$
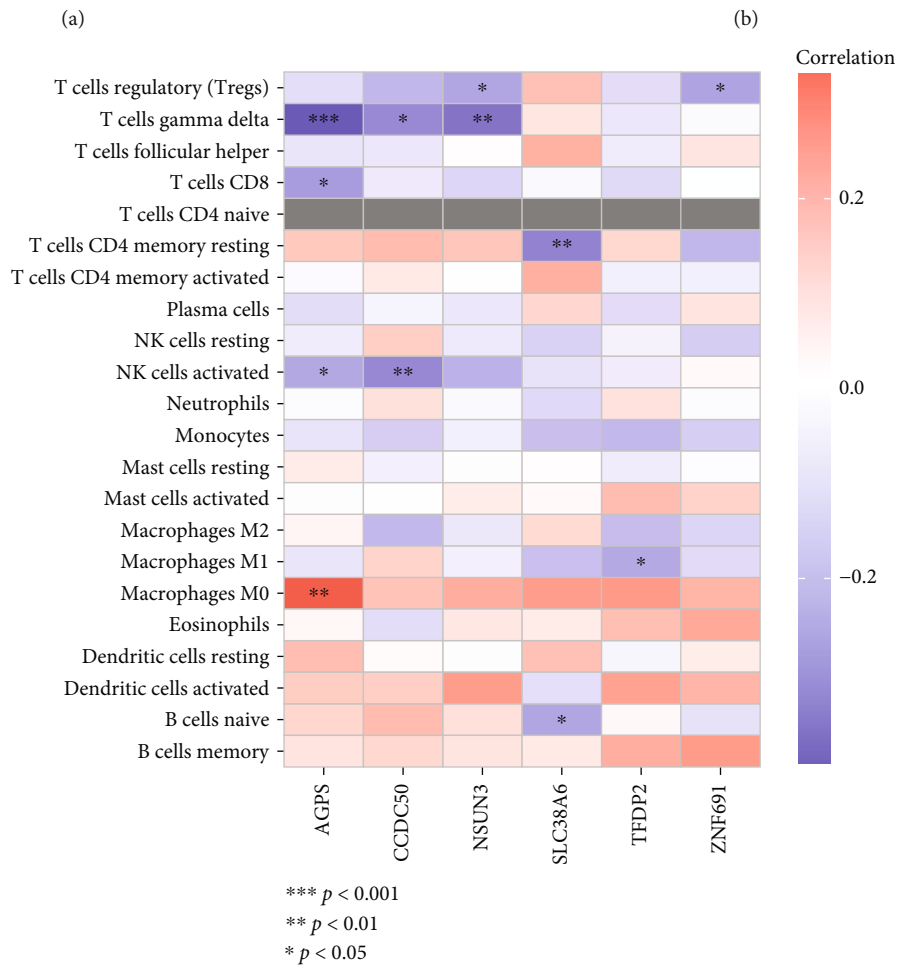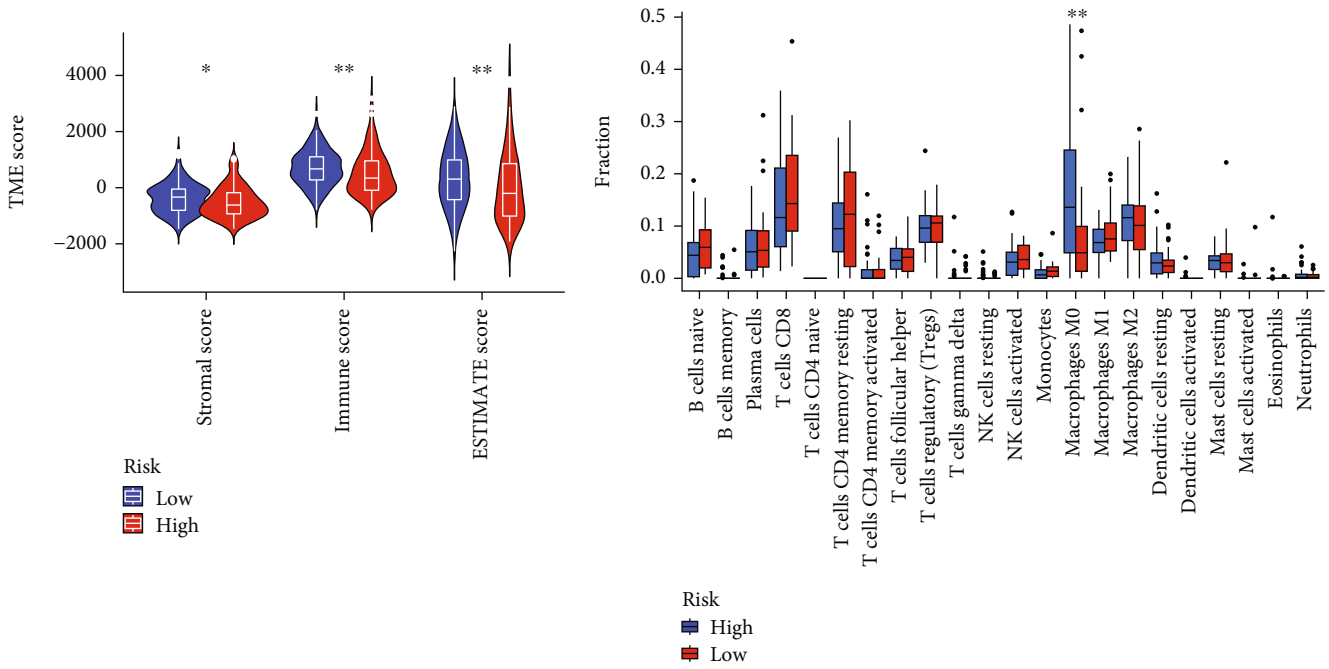
FIGURE 5: Analysis of the TIM of LIHC via risk scores of NCGs-related model. (a) Correlation between high and low NCGs risk score and TME score. (b) Correlation between high and low NCGs risk scores and 21 types of immune cell infiltration. (c) Correlation between NSUN3 coexpressed genes and immune cell infiltration.

(a)

(b)

Figure 6: Continued.

(c)

(d)

(e)

(f)

(g)

(h)
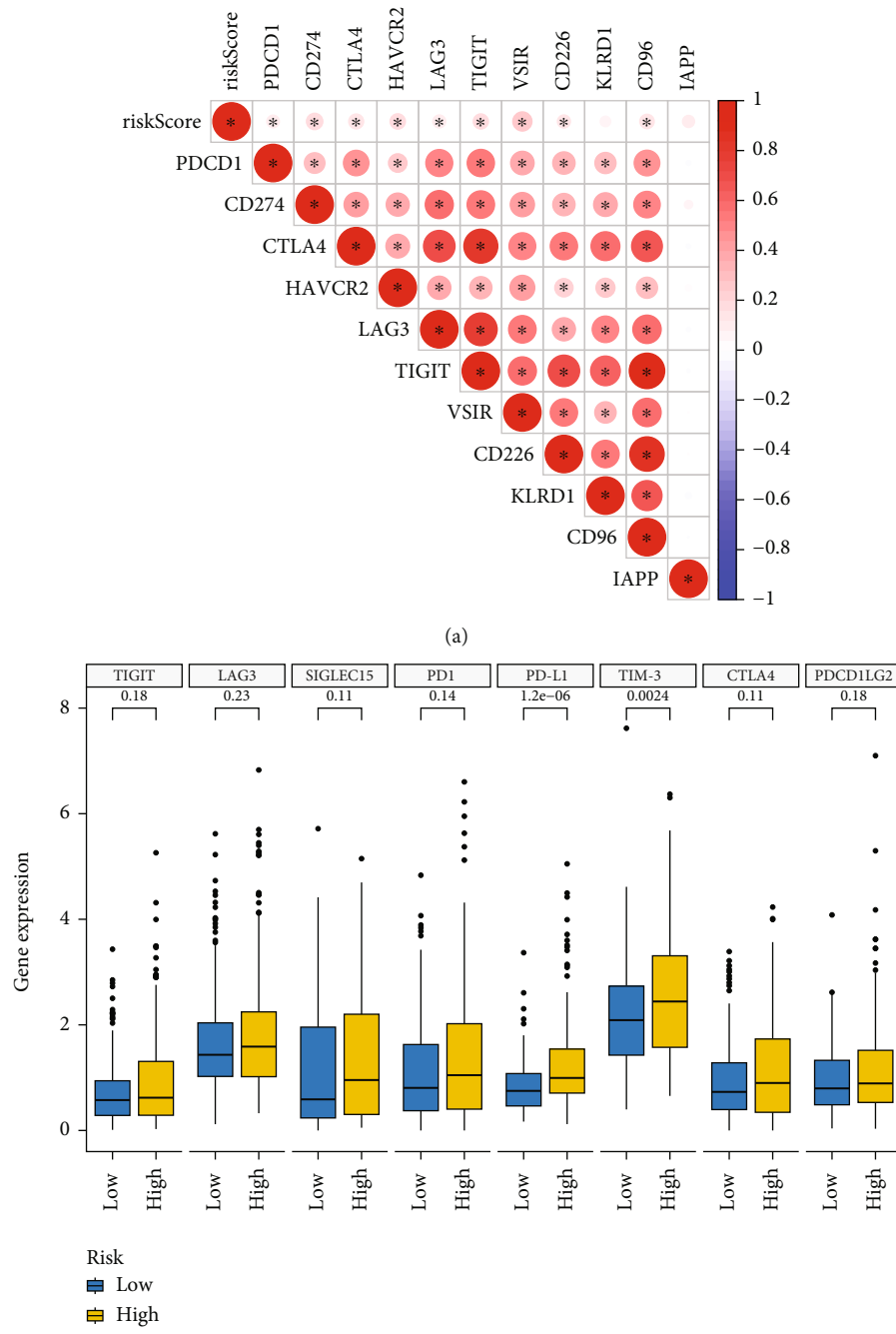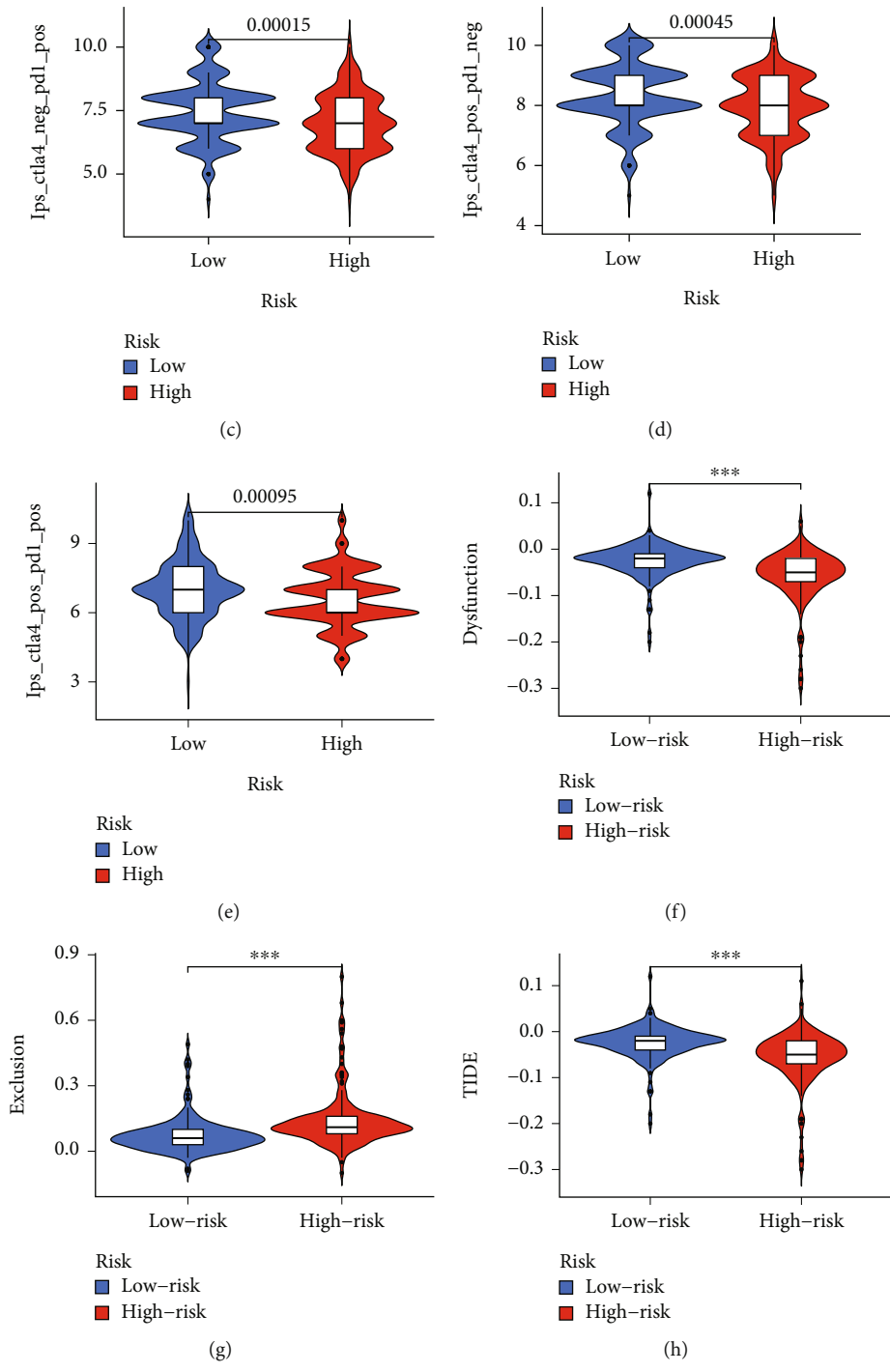
FIGURE 6: Risk scores from NCGs-related model predict LIHC response to immunotherapy. (a) Correlation of NCGs risk score with multiple immune checkpoints. (b) Differences in expression of multiple immune checkpoints in the high- and low-risk groups. (c) In the case of CTLA4 negative but PD1 positive, the high-risk group had lower IPS. (d) In the case of CTLA4 positive but PD1 negative, the high-risk group had lower IPS. (e) In the case of CTLA4 and PD1 negative, the high-risk group had lower IPS. (f) Low-risk patients have more pronounced immune dysfunction. (g) High-risk patients have a stronger tendency to immune exclusion. (h) Low-risk patients have lower TIDE scores.

important predictors for assessing immunotherapy response. Therefore, in the present study, we first analyzed the correlation between 11 immune checkpoints and risk scores of NCGs-related models, and the results showed that the risk scores of the NCGs-related models were strongly associated with most immune checkpoints (Figure 6(a)), except for KLRD1 and IAPP. As shown in Figure 6(b), we further explored the differences of 8 immune checkpoints in high- and low-risk cohorts, and the results revealed that PD-L1 and TIM-3 were significantly higher in high-risk

(a)

(b)

Figure 7: Continued.

*** $p < 0.001$
** $p < 0.01$
 * $p < 0.05$

(c)
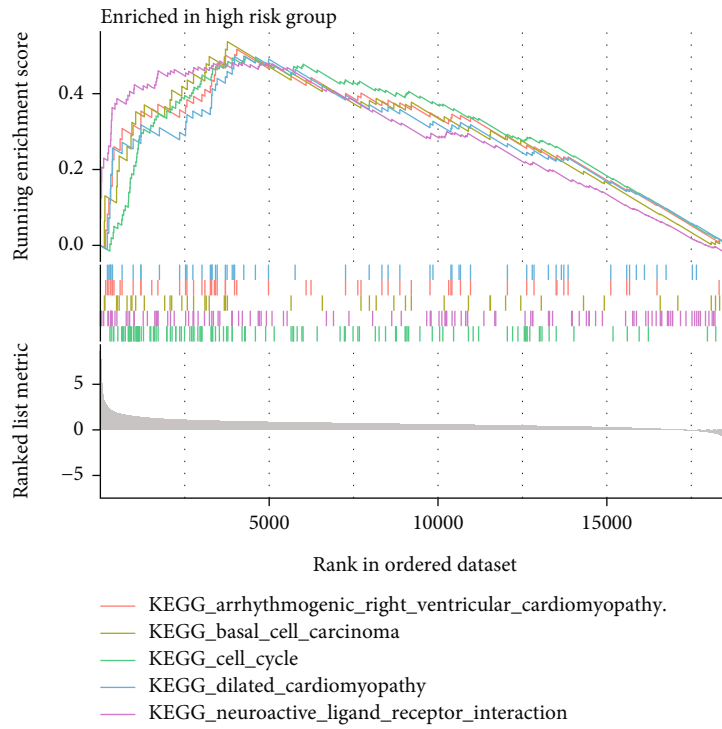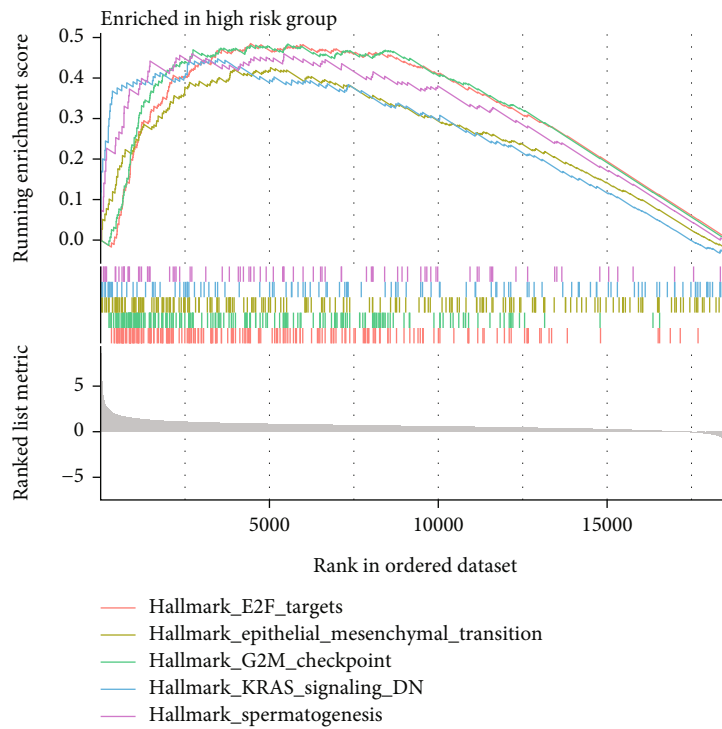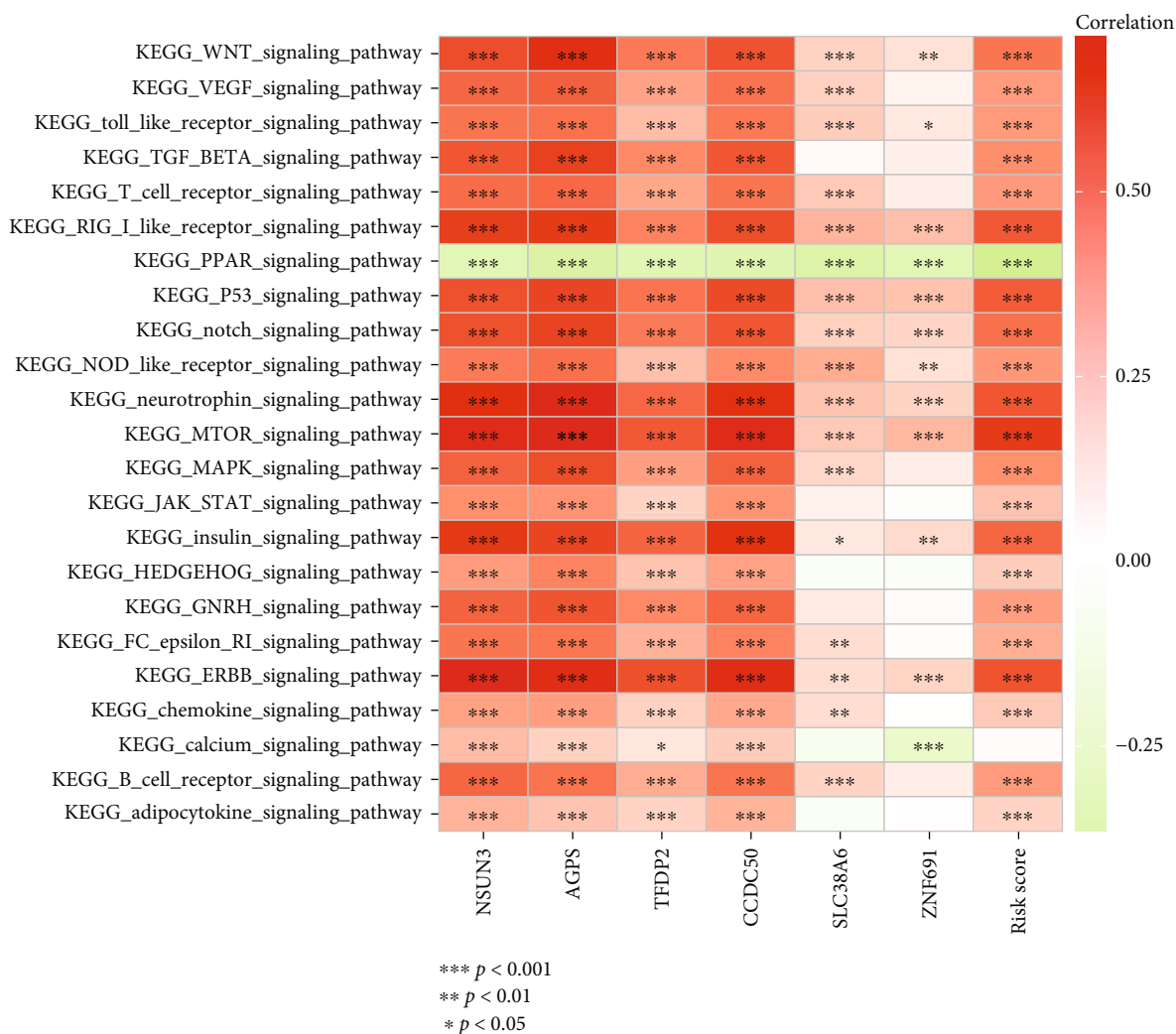
FIGURE 7: Continued.

(d)

Figure 7: Enrichment analysis of NCG-related model. (a) KEGG pathway enrichment analysis based on the risk score of NCG-related model. (b) HALLMARKER enrichment analysis based on the risk score of NCG-related model. (c) Correlation analysis between NCGs and KEGG enrichment pathway. (d) Correlation analysis between NCGs and Hallmark enrichment pathway.

cohorts than in low-risk cohorts. Furthermore, given the strong correlation between the risk score of the NCG-related model and immune checkpoints, we explored whether the risk score of this model could predict the response of LIHC patients to treatment with ICIs. In addition, IPS and TIDE have been widely used to assess tumor response to immunotherapy in recent years. The results of our analysis demonstrated that in the low-risk score group, PD1-positive and CTLA4-negative patients had significantly higher IPS; interestingly, high-risk patients had significantly lower IPS scores in CTLA-positive and PD1-negative patients (Figures 6(c)–6(e)). Finally, the results of the TIDE

algorithm implied that the low-risk group had higher immune dysfunction than the high-risk group, while the immune exclusion was lower than that of the high-risk group (Figures 6(f) and 6(g)).

3.7. Enrichment Analysis of NCGs-Related Model. Our previous studies revealed that risk stratification of NCGs-related models in LIHC is closely related to cell infiltration. To explore the underlying mechanism, we performed pathway enrichment analysis on high- and low-risk cohorts of the NCGs-related risk scoring model by the KEGG and HALL-MARK gene sets. The results of gene set enrichment analysis

showed that cell cycle-related pathways were significantly enriched NCGs-related models (Figures 7(a) and 7(b)). Next, we further analyzed the correlation of each NCGs with the enrichment pathway. The results revealed that in the KEGG gene set, multiple signaling pathways were positively correlated with NCGs, such as WNT, VEGF, TGF-β, and NOTCH signaling pathways. In the HALLMARK gene set, multiple signaling pathways were positively correlated with NCGs, such as unfolded protein pathway, KRAS, and angiogenesis (Figures 7(c) and 7(d)).

4. Discussion

The occurrence and development of tumors is a multistep process that is regulated by gene network [19]. Immune response is a special situation of inflammatory reactions [20]. The maintenance of normal immune function can effectively eliminate tumors. However, tumors in progress are often accompanied by immune evasion, which in turn induces the distant metastasis of the tumor [21]. Therefore, it is critical to clarify the specific mechanism of tumor immune function to the treatment of malignant tumors. In this study, we first discovered that NSUN3 upregulation was related to poor prognosis in LIHC. Then, by multiple database LIHC cohorts, we constructed a prognostic model based on NSUN3 coexpression genes and confirmed its accuracy and effectiveness. More importantly, we further explored the value of the model. We found that the risk score of NSUN3-related model is related to immune profile and can instruct the choice of immunotherapy.

The prognostic model based on various functional genes has become a hot spot in guiding the prognosis of tumor. Ruan et al. analyzed the expression of ZEB1-AS1 in colorectal cancer and found that its high expression was positively associated with poor prognosis. Furthermore, a prognostic model based on ZEB1-AS1 coexpression gene was constructed. The ROC curve areas of the model in the training cohort were 0.650, 0.706, and 0.706, respectively, and in the validation cohort were 0.705, 0.592, and 0.753, respectively [22]. Li et al. revealed that AHCYL1 acts as an oncogene in colorectal cancer. A prognostic model based on AhCYL1-related genes was constructed. To further explore the effectiveness of the model, the results showed that the areas of the ROC curves of the 1, 3, and 5 years in the training cohort were 0.665, 0.634, and 0.695, and the areas of the ROC curves of the 1, 3, and 5 years in the validation cohort were 0.691, 0.754, and 0.726, respectively [23]. In the present study, we constructed the prognostic model of NUSN3-related genes, and the areas under the ROC curve of 1, 3, and 5 years in the training cohort were 0.749, 0.662, and 0.603, while the areas under the ROC curve of 1, 3, and 5 years in the validation cohort were 0.720, 0.693, and 0.597. This result indicated that the predictive power of our constructed model is not weaker than that of other previous studies.

The prediction of immunotherapy therapy has always been difficult for immunotherapy [24]. The development of models that accurately predict the response to immunotherapy has been a goal we have pursued. In this study, we con-

structed a prognostic model based on NSUN3-related genes. The level of risk scores of this model shows different responses to immunotherapy. The results further revealed that NSUN3 participated in regulating LIHC immune profile. The data of this study mainly derived from the public database and lacked corresponding clinical evidence support, which requires us to be validated in our follow-up studies.

In conclusion, this study demonstrated a novel role for NSUN3 in regulating the immune implication of LIHC. The development of targeted NSUN3 drugs may be a promising research direction for the treatment of LIHC.

Data Availability

The data and results in this study are available from the corresponding authors upon reasonable request.

Ethical Approval

The study was conducted in accordance with the Declaration of Helsinki, and the protocol was approved by the Ethics Committee of Dongguan People's Hospital Affiliated to Southern Medical University.

Conflicts of Interest

The authors declare no conflicts of interest.

Authors' Contributions

Jianlin Zhu, Junxi Kuang, and Yi Yang contributed equally to this work. Jianlin Zhu, Ling Zou, and Junxi Kuang conceived and designed the experiments. Yi Yang and Lei Zhang performed the bioinformatic analyses. Bo Leng and Risheng She performed and guided the statistical analysis. Ling Zou and Risheng She wrote the manuscript. All the authors read and approved the final manuscript.

Acknowledgments

References

[1] S. Caruso, D. R. O'Brien, S. P. Cleary, L. R. Roberts, and J. Zucman-Rossi, "Genetics of hepatocellular carcinoma: approaches to explore molecular diversity," *Hepatology*, vol. 73, Suppl 1, pp. 14–26, 2021.

[2] A. Cucchetti, J. Zhong, S. Berhane et al., "The chances of hepatic resection curing hepatocellular carcinoma," *Journal of Hepatology*, vol. 72, no. 4, pp. 711–717, 2020.

[3] J. M. Llovet, F. Castet, M. Heikenwalder et al., "Immunotherapies for hepatocellular carcinoma," *Nature Reviews. Clinical Oncology*, vol. 19, no. 3, pp. 151–172, 2022.

[4] T. K. Lee, X. Y. Guan, and S. Ma, "Cancer stem cells in hepatocellular carcinoma – from origin to clinical implications," *Nature Reviews. Gastroenterology & Hepatology*, vol. 19, no. 1, pp. 26–44, 2022.

[5] P. A. Shah, R. Patil, and S. A. Harrison, "NAFLD-related hepatocellular carcinoma: the growing challenge," *Hepatology*, vol. 77, no. 1, pp. 323–338, 2023.

[6] Y. Sugawara and T. Hibi, "Surgical treatment of hepatocellular carcinoma," *Bioscience Trends*, vol. 15, no. 3, pp. 138–141, 2021.

[7] C. A. Arciero and E. R. Sigurdson, "Liver-directed therapies for hepatocellular carcinoma," *Journal of the National Comprehensive Cancer Network*, vol. 4, no. 8, pp. 768–774, 2006.

[8] F. Chino, S. J. Stephens, S. S. Choi et al., "The role of external beam radiotherapy in the treatment of hepatocellular cancer," *Cancer*, vol. 124, no. 17, pp. 3476–3489, 2018.

[9] C. Y. Liu, K. F. Chen, and P. J. Chen, "Treatment of liver cancer," *Cold Spring Harbor Perspectives in Medicine*, vol. 5, no. 9, article a021535, 2015.

[10] D. Anwanwan, S. K. Singh, S. Singh, V. Saikam, and R. Singh, "Challenges in liver cancer and possible treatment approaches," *Biochimica Et Biophysica Acta. Reviews on Cancer*, vol. 1873, no. 1, article 188314, 2020.

[11] B. Sangro, P. Sarobe, S. Hervás-Stubbs, and I. Melero, "Advances in immunotherapy for hepatocellular carcinoma," *Nature Reviews. Gastroenterology & Hepatology*, vol. 18, no. 8, pp. 525–543, 2021.

[12] K. Oura, A. Morishita, J. Tani, and T. Masaki, "Tumor immune microenvironment and immunosuppressive therapy in hepatocellular carcinoma: a review," *International Journal of Molecular Sciences*, vol. 22, no. 11, p. 5801, 2021.

[13] X. Lei, Y. Lei, J. K. Li et al., "Immune cells within the tumor microenvironment: biological functions and roles in cancer immunotherapy," *Cancer Letters*, vol. 470, pp. 126–133, 2020.

[14] L. Van Haute, C. A. Powell, and M. Minczuk, "Dealing with an unconventional genetic code in mitochondria: the biogenesis and pathogenic defects of the 5-formylcytosine modification in mitochondrial tRNA(Met)," *Biomolecules*, vol. 7, no. 1, p. 24, 2017.

[15] T. Shi and G. Gao, "Identify potential prognostic indicators and tumor-infiltrating immune cells in pancreatic adenocarcinoma," *Bioscience Reports*, vol. 42, no. 2, article BSR20212523, 2022.

[16] J. Mei, Y. Xing, J. Lv et al., "Construction of an immune-related gene signature for prediction of prognosis in patients with cervical cancer," *International Immunopharmacology*, vol. 88, article 106882, 2020.

[17] Q. Ma, Y. Chen, F. Xiao et al., "A signature of estimate-stromal-immune score-based genes associated with the prognosis of lung adenocarcinoma," *Translational Lung Cancer Research*, vol. 10, no. 3, pp. 1484–1500, 2021.

[18] Q. Wang, M. Li, M. Yang et al., "Analysis of immune-related signatures of lung adenocarcinoma identified two distinct subtypes: implications for immune checkpoint blockade therapy," *Aging (Albany NY)*, vol. 12, no. 4, pp. 3312–3339, 2020.

[19] K. Inamura, "Clinicopathological characteristics and mutations driving development of early lung adenocarcinoma: tumor initiation and progression," *International Journal of Molecular Sciences*, vol. 19, no. 4, p. 1259, 2018.

[20] P. Kubes and C. Jenne, "Immune responses in the liver," *Annual Review of Immunology*, vol. 36, no. 1, pp. 247–277, 2018.

[21] K. Eddy and S. Chen, "Overcoming immune evasion in melanoma," *International Journal of Molecular Sciences*, vol. 21, no. 23, p. 8984, 2020.

[22] L. Ruan, W. Chen, X. Zhao, N. Fang, and T. Li, "Predictive potentials of ZEB1-AS1 in colorectal cancer prognosis and their correlation with immunotherapy," *Journal of Oncology*, vol. 2022, Article ID 1084555, 13 pages, 2022.

[23] X. Li, M. Zhang, X. Yu et al., "AHCYL1 is a novel biomarker for predicting prognosis and immunotherapy response in colorectal cancer," *Journal of Oncology*, vol. 2022, Article ID 5054324, 13 pages, 2022.

[24] T. A. Chan, M. Yarchoan, E. Jaffee et al., "Development of tumor mutation burden as an immunotherapy biomarker: utility for the oncology clinic," *Annals of Oncology*, vol. 30, no. 1, pp. 44–56, 2019.

Research Article

Prognostic Biomarker SLCO4A1 Is Correlated with Tumor Immune Infiltration in Colon Adenocarcinoma

Xiaolong Chen, Gangfeng Yi, Yu Zhou, Weijun Hu, Lingyun Xi, Weilan Han, and Fei Wang [ID]

Department of General Surgery, Xi'an No. 1 Hospital, The First Affiliated Hospital of Northwestern University, Xi'an, Shaanxi Province, China

Correspondence should be addressed to Fei Wang; wfeipw@163.com

Background. Solute carrier organic anion transporter family member 4A1 (SLCO4A1), a member of solute carrier organic anion family, is a key gene regulating bile metabolism, organic anion transport, and ABC transport. However, the association of SLCO4A1 with prognosis and tumor immune infiltration in colon adenocarcinoma (COAD) remains indistinct. *Methods.* Firstly, we explored the expression level of SLCO4A1 in COAD via GEPIA, Oncomine, and UALCAN databases. Secondly, we used the Kaplan-Meier plotter and PrognoScan databases to investigate the effect of SLCO4A1 on prognosis in COAD patients. In addition, the correlation between SLCO4A1 and tumor immune infiltration was studied by using TIMER and TISIDB databases. *Results.* Our results showed that SLCO4A1 was overexpressed in COAD tissues. At the same time, our study showed that high expression of SLCO4A1 was associated with poor overall survival, disease-free survival, and disease-specific survival in COAD patients. The expression level of SLCO4A1 was negatively linked to the infiltrating levels of B cells, CD8+ T cells, and dendritic cells in COAD. Moreover, the expression of SLCO4A1 was significantly correlated with numerous immune markers in COAD. *Conclusions.* These results indicated that SLCO4A1 could be associated with the prognosis of COAD patients and the levels of tumor immune infiltration. Our study suggested that SLCO4A1 could be a valuable biomarker for evaluating prognosis and tumor immune infiltration in COAD patients.

1. Introduction

In recent decades, colorectal cancer (CRC) has become one of the most common malignancies in the world [1]. Morbidity and mortality of CRC are increasing every year, particularly in developing countries, where the morbidity and mortality of CRC increase by about 20 percent per year [2]. The disease has emerged as one of the major challenges facing global health. Although there are significant advances in cancer diagnosis and treatment, overall survival (OS) in CRC patients remains unsatisfactory. When many CRC patients are diagnosed, their tumors are already in the middle and advanced stage, and the patients often have regional lymph node metastasis or distant organ metastasis. Therefore, there is an urgent need to understand the pathogenesis

of CRC and to identify potential biomarkers to assess the prognosis and treatment effect of CRC patients.

Immunotherapy is the most promising treatment for colorectal cancer, especially for the microsatellite instability-high (MSI-H) phenotype [3–5]. MSI-H colorectal cancer has many mutations that produce many new antigens, stimulating tumor immune infiltration and improving immune checkpoint suppression [6, 7]. Programmed death ligand-1 (PD-L1) is an important target of tumor immunotherapy in clinical trials and has a significant therapeutic effect on liver hepatocellular carcinoma (LIHC) and non-small-cell lung cancer (NSCLC) [8, 9]. Numerous studies have confirmed that tumor-infiltrating immune cells (TIICs), especially cytotoxic T lymphocyte (CD8+ T) cells, significantly affect the prognosis of cancer patients and the

effect of immunotherapy and chemotherapy [10–12]. For example, CD8+ tumor-infiltrating lymphocyte was found to be positively associated with PD-L1 status in colorectal cancer patients [13]. However, clinical immunotherapy outcomes show that many monoclonal antibodies have poor clinical efficacy in advanced colorectal cancer, although anti-PD-1 and anti-PD-L1 monoclonal antibodies have obvious efficacy in the treatment of metastatic colorectal cancer [14–17]. There is an urgent need to explore new biomarkers to better assess the prognosis of CRC patients and to identify novel immune-based therapeutic targets.

Solute carrier organic anion transporter family member 4A1 (SLCO4A1), also known as organic anion-transporting polypeptide 4A1 (OATP4A1), is an important member of solute carrier organic anion transporter (SLCO) family, responsible for the Na^+-independent transmembrane transport of many substrates, such as many drugs, thyroid hormone, some toxins [18]. The changes in the uptake of these substrates may lead to variations in the concentration of anticancer drugs in cancer cells, thus playing an important role in the chemical sensitivity of cancer cells and influencing tumor progression [19]. For example, cisplatin activates SLCO4A1 and affects the progression and metastasis of lung cancer NCIH417 cells [20]. In addition, SLCO4A1 has been found to be overexpressed in pancreatic cancer and is expected to be an important biomarker for targeted therapy of pancreatic cancer [21]. At present, the biological role of SLCO4A1, its prognostic value, and the relationship of SLCO4A1 with tumor immune infiltration in COAD are still unclear.

In this study, the expression level and prognostic value of SLCO4A1 in patients with COAD were analyzed using multiple bioinformatic databases, such as Oncomine, UALCAN, PrognoScan, GEPIA, and Kaplan-Meier plotter. Using the interactive online websites STRING and OmicShare tools, the functional enrichment analysis was conducted to explore the potential molecular mechanism of SLCO4A1 in the progress of COAD. In addition, the relationship of SLCO4A1 with tumor immune infiltration in COAD was verified via TIMER and TISIDB databases. Our study examined whether SLCO4A1 could be used as an important biomarker to evaluate the prognosis and the efficacy of immunotherapy in COAD patients.

2. Materials and Methods

2.1. Bioinformatic Analysis of SLCO4A1 Expression. Oncomine (http://www.oncomine.org/) is currently the world's largest oncogene chip database and integrated data mining platform [22, 23]. We compared the mRNA expression of SLCO4A1 in COAD tissues and matched normal tissues using the Oncomine database. Firstly, we enter SLCO4A1 into the search box to get the expression profile of SLCO4A1 for various cancers. Secondly, tumor vs. normal analysis was used, and the tumor type was selected as COAD. Then, we set $P < 0.05$ and fold change > 1.5. Finally, the statistical values were obtained from the analysis results of related databases. UALCAN (http://ualcan.path.uab.edu/index .html/) is a powerful online database for analyzing cancer-

related data, and we assessed the expression of SLCO4A1 in COAD via the UALCAN database [24]. Moreover, we investigated the relationship of different clinical features with the expression level of SLCO4A1, such as race, sex, weight, age, lymph node metastasis, individual cancer stage, histological subtype, and TP53 mutation. In addition, we further explored the relationship between the mutation status of seven important clinically detected proteins (MLH1, PMS2, MSH2, MSH6, BRAF, KRAS, and NRAS) and the expression of SLCO4A1 by TIMER (http://timer.cistrome .org/) [25]. Immunohistochemical staining for the SLCO4A1 protein in COAD tissue was obtained from the Human Protein Atlas (https://www.proteinatlas.org/). The three-dimensional structural model of the SLCO4A1 protein was constructed by using the SWISS-MODEL (https:// swissmodel.expasy.org/) [26]. We followed the methods of Huang et al. [27].

2.2. Prognostic Survival Analysis. The prognostic value of SLCO4A1 in COAD patients was studied by using GEPIA, PrognoScan, and Kaplan-Meier plotter. GEPIA (http:// gepia.cancer-pku.cn/) is a concise, easy-to-use platform for analyzing the relationship between SLCO4A1 and survival in COAD patients [28, 29]. PrognoScan (http://www .prognoscan.org/) is a new online platform that can predict the association of different genes with cancer patients' prognosis [30]. The Kaplan-Meier plotter (https://kmplot.com/ analysis/) is an online database to assess the effect of targeted genes on the survival in 21 cancer types and is used to further validate our survival analysis [31]. COAD patients were divided into two groups based on their expression level of the SLCO4A1 gene. Survival analysis was evaluated using the hazard ratios (HRs) and P value, with $P = 0.05$ being the cut-off value for significance. We followed the methods of Huang et al. [27].

2.3. cBioPortal Database. Using the cBioPortal database (https://www.cbioportal.org/), the genetic alterations of the SLCO4A1 gene were explored [32]. Firstly, we selected three study datasets "DFCI, Cell Reports 2016," "TCGA, Firehose Legacy," and "TCGA PanCancer Atlas" and imported SLCO4A1 into "Gene Symbols" box. Secondly, the structural variation data, mutation data, and CNA data were analyzed separately in the "Tumor Types Summary" module. Thirdly, we also showed the SLCO4A1 gene mutation via a schematic diagram. In addition, we selected "comparison/survival" module to evaluate the effect of SLCO4A1 gene mutation on the survival in COAD patients. We followed the methods of Huang et al. [27].

2.4. SLCO4A1-Related Gene Enrichment Analysis. STRING (http://string-db.org/) was used for exploring SLCO4A1 protein-protein interactions [33]. The minimum interaction score required was 0.400, and the maximum number of these interactions was 50. The top 50 interacting proteins of SLCO4A1 were regarded as SLCO4A1-binding proteins. Furthermore, we clicked SLCO4A1 on the "Query Search" module to get the top 100 SLCO4A1-related genes via GEPIA. OmicShare tools (http://omicsshare.com/tools) was

an efficient online platform which was used for functional enrichment analysis of SLCO4A1-related genes [34].

2.5. Analysis of Tumor Immune Infiltration. TIMER (https://cistrome.shinyapps.io/timer/) is a comprehensive online platform for immune infiltration analysis in various tumors [35]. TIMER uses various deconvolutional statistical methods to predict the abundance of infiltrating immune cells in different tumors. In this study, we explored the relationship between the SLCO4A1 expression and tumor-infiltrating immune cell abundance in COAD patients using TIMER. Tumor-infiltrating immune cells (TIICs) are mainly composed of CD8+ T cells, CD4+ T cells, B cells, neutrophils, natural killer cells, dendritic cells, monocytes, macrophages, and T-helper cells. Molecular markers of these immune cells have been used in many previous studies [36–38]. The "Correlations" module may produce scatterplots of Spearman correlation for an interesting pair of genes in a specific cancer type. The expression level of specific genes was represented with $\log_2$ RSEM.

TISIDB (http://cis.hku.hk/TISIDB/index.php/), an open online platform to explore the interaction of tumors and immune system, was used for analyzing the relationship between SLCO4A1 expression levels and different immune components [39].

3. Results

3.1. Overexpression of SLCO4A1 in COAD. The expression level of SLCO4A1 in human tumors was analyzed via the GEPIA database. The results showed that SLCO4A1 was downregulated in BLCA, BRCA, CESC, SLCO4A1, CHOL, ESCA, GBM, HNSC, KIRC, LUAD, LUSC, PCPG, and SARC while SLCO4A1 was significantly upregulated in COAD, READ, PAAD, and STAD (Figure 1(a)). An interactive bodymap of SLCO4A1 is shown in Figure 1(b). In addition, the 3D structural model of the SLCO4A1 protein was constructed by using the SWISS-MODEL (Figure 1(c)). The abbreviation of each tumor is shown in Supplementary Table 1.

Moreover, we also used Oncomine and UALCAN databases to detect the mRNA expression level of SLCO4A1 in COAD. SLCO4A1 was highly expressed in colorectal cancer (including COAD and READ) compared with the corresponding normal tissues (Figures 2(a) and 2(b)). In addition, the expression level of the SLCO4A1 protein was elevated in COAD tumor tissues obtained from the Human Protein Atlas (Figure 2(c)).

3.2. The Relationship between the Expression Level of SLCO4A1 and Clinical Characteristics in COAD. In this study, the UALCAN database was used to explore the relationship between the expression level of SLCO4A1 and clinical characteristics in COAD. Different race, gender, weights, age, and nodal metastasis status were not linked to SLCO4A1 mRNA expression in patients with COAD. However, in terms of individual cancer stages, stage 1 group had a lower expression level than the stage 3 or 4 group. Mucinous adenocarcinoma presented with higher SLCO4A1

expression than adenocarcinoma in patients with COAD. Furthermore, SLCO4A1 had a higher expression level in those COAD tissues carrying a TP53 mutation. The relationships between the expression level of SLCO4A1 and clinical characteristics in COAD are shown in Table 1. In addition, the SLCO4A1 expression level was significantly related to the mutation status of MSH2 ($P = 0.01$) and BRAF ($P = 0.036$), but was not linked to the mutation status of MSH6 ($P = 0.098$), PMS2 ($P = 0.81$), MLH1 ($P = 0.9$), KRAS ($P = 0.39$), or NRAS ($P = 0.67$) (Supplementary Figure 1A–1G).

3.3. Correlation between the Expression of SLCO4A1 and Prognosis in COAD. The prognostic role of SLCO4A1 in COAD patients was explored via several databases. Overexpression of SLCO4A1 was associated with shorter OS ($P = 135$, HR = 2, $P = 0.0045$) using GEPIA (Figure 3(a)). Moreover, there were significant differences in DFS ($n = 135$, HR = 1.7, $P = 0.038$) (Figure 3(b)). Although SLCO4A1 was not associated with prolonged OS ($n = 165$, HR = 0.53, $P = 0.099$), it was significantly correlated with DFS ($n = 47$, HR = 10.55, $P = 0.008$) via the Kaplan-Meier plotter (Figures 3(c) and 3(d)).

The correlation between the expression of SLCO4A1 and prognosis in COAD patients was further explored using the PrognoScan database. The results showed that overexpression of SLCO4A1 was associated with shorter OS ($n = 177$, HR = 0.0, cox-$P = 0.019$) and DSS ($n = 177$, HR = 0.24, cox-$P = 0.0202$) in COAD patients (Figures 3(e)–3(g)) but no significant difference in DFS ($n = 145$, HR = 0.46, cox-$P = 0.3276$) (Figure 3(f)).

In short, based on these databases, this study explored the correlation between the expression of SLCO4A1 and prognosis in COAD patients and found that SLCO4A1 was a valuable biomarker for evaluating prognosis in patients with COAD.

3.4. Genetic Alterations of SLCO4A1 in COAD. Numerous studies have shown that genetic variation plays a pivotal role in the pathogenesis and development of various tumors. Our study investigated the genetic alterations of SLCO4A1 via the cBioPortal database. The results showed that somatic mutation of SLCO4A1 was present in about 7.6% of COAD samples (Figure 4(a)). In COAD, copy number variation (CNV) was the main mutation type of SLCO4A1 genetic alterations. The mutation types and the proportions of these mutations are shown in Figure 4(b). Information such as mutation site, mutation type, and number of cases was displayed on the mutation diagram and colored according to the corresponding mutation type (Figure 4(c)). In addition, we also explored the relationship between SLCO4A1 genetic alterations and COAD patients' survival. However, our study showed that SLCO4A1 gene alterations were not associated with OS ($P = 0.664$), PFS ($P = 0.528$), DFS ($P = 0.882$), or DSS ($P = 0.946$) in COAD patients (Supplementary Figure 2A–2D).

3.5. GO and KEGG Enrichment Analyses of SLCO4A1. In this study, the binding proteins of SLCO4A1 and the genes

(a)

Interactive Bodymap
The median expression of tumor and normal samples in bodymap

Log$_2$(TPM + 1) Scale

OFF

(b)

(c)
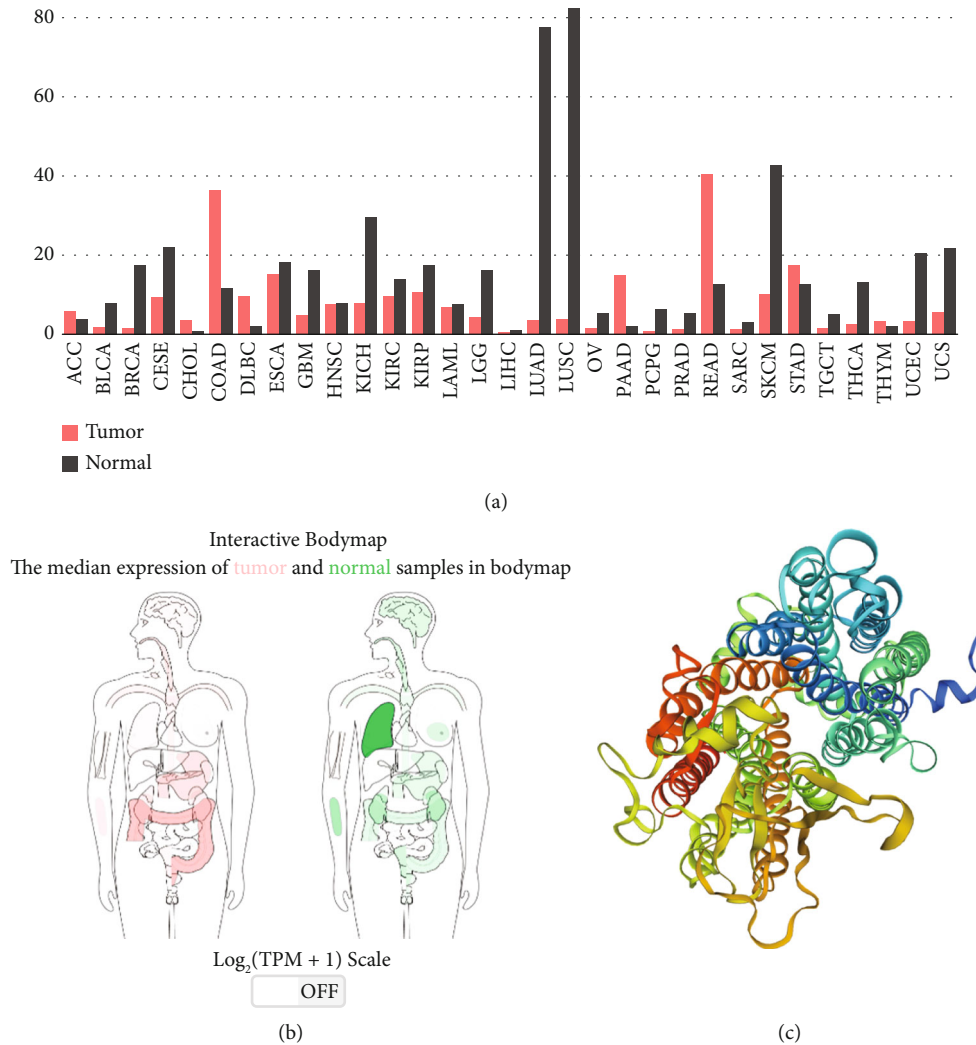
FIGURE 1: Expression levels of SLCO4A1 in a variety of cancers and its 3D protein model structure. (a) Expression levels of SLCO4A1 in different cancer samples were investigated via the GEPIA database. (b) The interactive bodymap of SLCO4A1 was shown using the GEPIA database. (c) The 3D structure of the SLCO4A1 protein was constructed via the SWISS-MODEL.

related to SLCO4A1 expression were identified using the STRING and GEPIA databases. The top 50 binding proteins of SLCO4A1 and the top 100 genes related to the expression of SLCO4A1 are summarized in Supplementary Table 2, and SLCO4A1-binding protein interacting network is shown in Figure 5(a). Furthermore, we also used the SLCO4A1-binding proteins to explore GO enrichment analysis and KEGG pathway analysis. GO enrichment analysis showed that these genes were obviously enriched in organic anion transmembrane transporter activity, anion transmembrane transporter activity, organic anion transport, anion transport, bile acid and bile salt transport, carboxylic acid transport, organic acid transport, active transmembrane transporter activity, carboxylic acid transmembrane transporter activity, organic acid transmembrane transporter activity, ion transport, transmembrane transport, monocarboxylic acid transport, transmembrane transporter activity, monocarboxylic acid transmembrane transport, transporter activity, plasma membrane region, bile acid transmembrane transporter activity, secondary

active transmembrane transporter activity, and ion transmembrane transporter activity (Figure 5(b)). In addition, KEGG pathway analysis found that SLCO4A1-interacting proteins were enriched in bile secretion, ABC transporters, antifolate resistance, thyroid hormone signaling pathway, primary bile acid biosynthesis, PPAR signaling pathway, glutamatergic synapse, cholesterol metabolism, hippo signaling pathway, and protein digestion and absorption (Figure 5(c)).

3.6. Correlation between SLCO4A1 and Tumor Immune Infiltration in COAD. The correlation of the expression level of SLCO4A1 with tumor immune infiltration in COAD was investigated using the TIMER database. Our study found that the expression level of SLCO4A1 gene was closely related to B lymphocytes (cor = −0.126, $P = 1.10e − 02$), CD8+ T lymphocytes (cor = −0.188, $P = 1.41e − 04$), and dendritic cells (cor = −0.101, $P = 4.29e − 2$) (Figure 6(a)). However, the expression of SLCO4A1 was not associated with tumor purity (cor = 0.097, $P = 5.06e − 2$), CD4+ T cells (cor = −0.006, $P =$

(a)

(b)

(c)
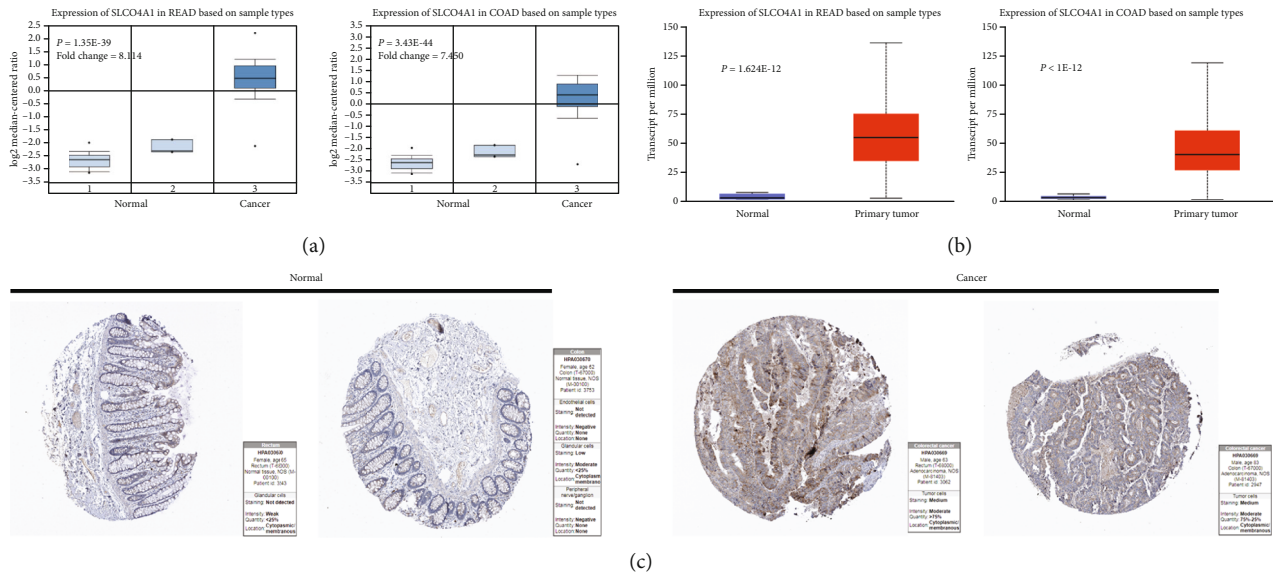
FIGURE 2: SLCO4A1 expression levels in CRC samples. (a) SLCO4A1 expression levels in COAD and READ samples were explored via the Oncomine database. (b) SLCO4A1 expression levels in COAD and READ were explored using the UALCAN database. (c) Immunohistochemical images of SLCO4A1 protein in COAD and READ tissues from the Human Protein Atlas.

TABLE 1: SLCO4A1 expression based on different clinical indicators.

Clinical indicators	Number of patients	Comparison	P value
Individual cancer stages	45/110/80/39 (stage 1/stage 2/stage 3/stage 4)	Stage 1 vs. stage 2	$2.921600E-01$
		Stage 1 vs. stage 3	$1.616230E-02$
		Stage 1 vs. stage 4	$2.207800E-02$
		Stage 2 vs. stage 3	$9.105500E-02$
		Stage 2 vs. stage 4	$1.213800E-01$
Patient's race	193/55/11 (Caucasian/African-American/Asian)	Caucasian vs. African-American	$7.265600E-01$
		Caucasian vs. Asian	$8.521000E-01$
		African-American vs. Asian	$9.166000E-01$
Patient's gender	156/127 (male/female)	Male vs. female	$7.154000E-01$
Patient's weight	70/74/56 (normal/extreme_weight/obese)	Normal_weight vs. extreme_weight	$8.504800E-01$
		Normal_weight vs. obese	$8.111000E-01$
		Extreme_weight vs. obese	$6.531800E-01$
Patient's age	12/90/149 (21-40 Yrs/41-60 Yrs/61-80 Yrs)	Age (21-40 Yrs) vs. age (41-60 Yrs)	$1.452190E-01$
		Age (21-40 Yrs) vs. age (61-80 Yrs)	$6.386100E-02$
Histological subtype	243/37 (adenocarcinoma/mucinous adenocarcinoma)	Adenocarcinoma vs. mucinous adenocarcinoma	$6.228500E-05$
Nodal metastasis status	166/70/47 (N0/N1/N2)	N0 vs. N1	$1.299810E-01$
		N0 vs. N2	$6.704200E-02$
		N1 vs. N2	$2.874600E-01$
TP53 mutation status	160/122 (mutant/nonmutant)	Mutant vs. nonmutant	$1.982530E-05$

$9.10e-1$), macrophages ($cor = -0.053$, $P = 2.92e-1$), and neutrophils ($cor = 0.038$, $P = 4.49e-1$) (Figure 6(a)). So we speculated that these three immune cells (B lymphocytes, CD8+ T lymphocytes, and dendritic cells) were more likely to

be responsible for the prognosis and survival difference between patients with different expression of SLCO4A1.

Using the TIMER database, we deeply explored the relationship between SLCO4A1 and immune specific markers.
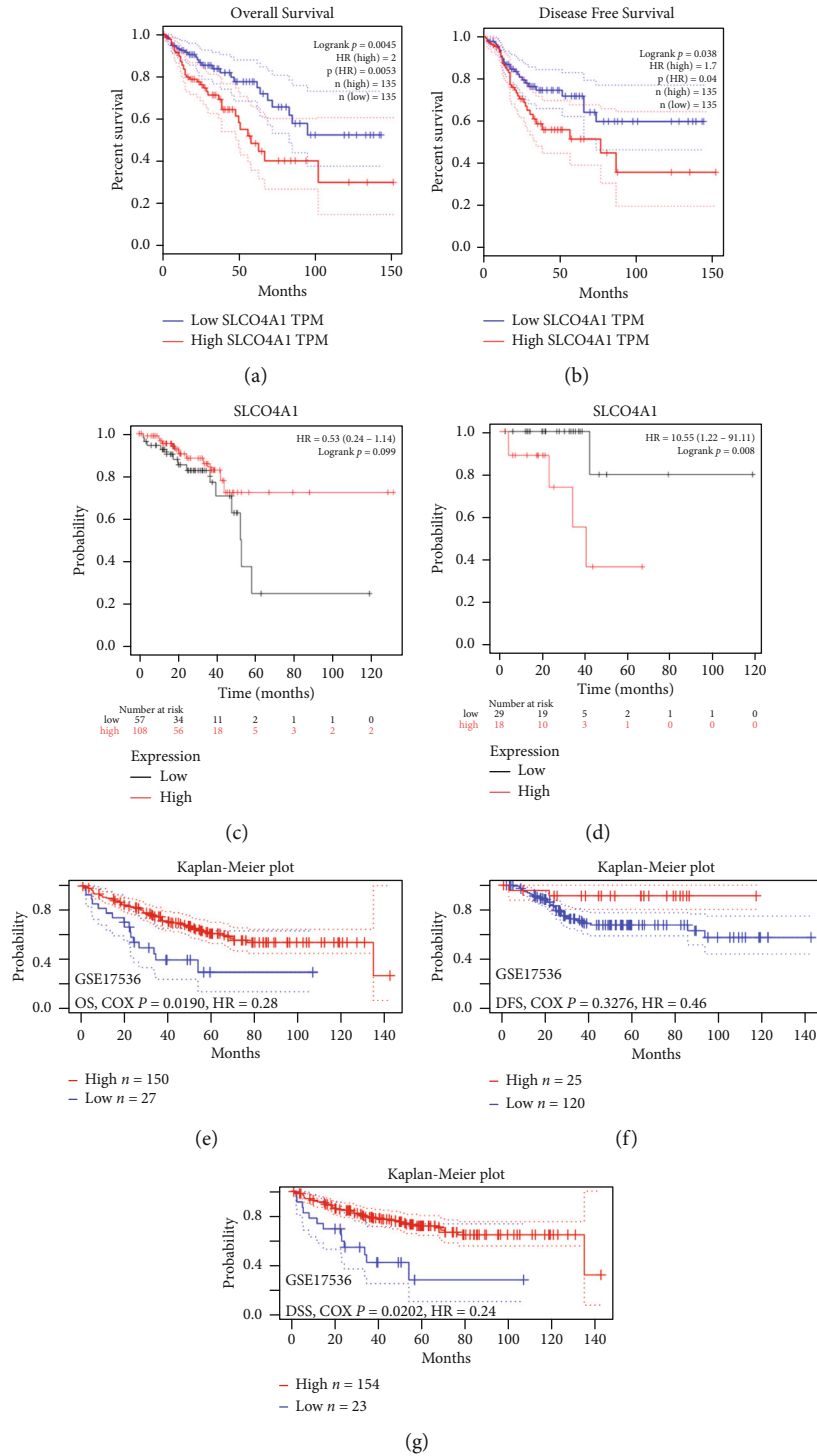
Figure 3: The relationship between SLCO4A1 expression levels and COAD patients' prognosis. (a) OS and (b) DFS of COAD patients based on SLCO4A1 expression levels via GEPIA. (c) OS and (d) DFS of COAD patients based on SLCO4A1 expression levels via the Kaplan-Meier plotter. (e) OS, (f) DFS, and (g) DDS of COAD patients based on SLCO4A1 expression levels via the PrognoScan database. OS: overall survival; DFS: disease-free survival; DSS: disease-specific survival.

Our study showed that SLCO4A1 was negatively correlated with a large number of immune specific markers, such as CD8A, CD8B, CD3D, CD3E, CD2, CD79A, CD86, KIR3DL2, CD1C, STAT4, and STAT6, and was positively correlated with CEACAM8 (Figure 6(b)). The more detailed results from the database are shown in Table 2. It was suggested that SLCO4A1 could play an important role in regulating immune cell infiltration in COAD. In addition, we further investigated the association of SLCO4A1 with other four important immune markers CD274 (also known as

(a)

(b)

(c)
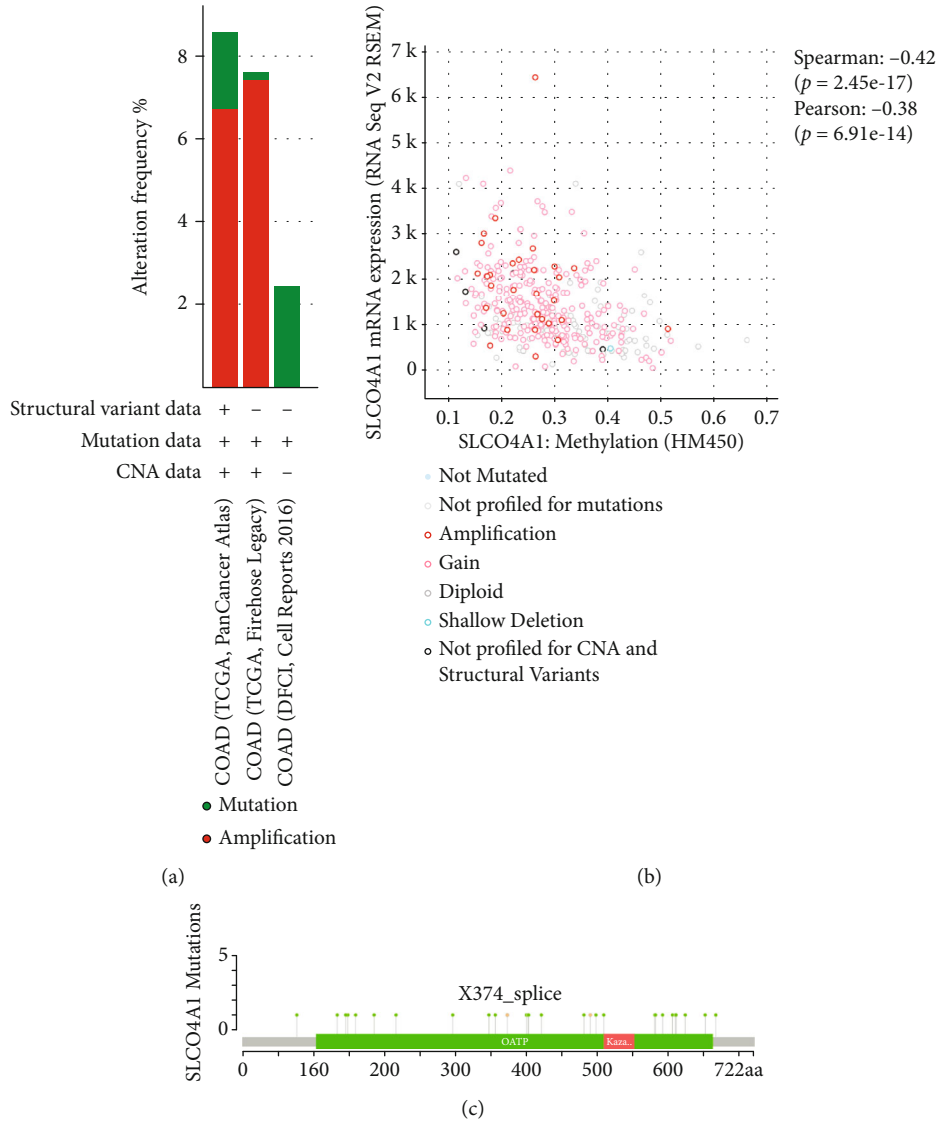
FIGURE 4: Genetic alterations of SLCO4A1 in COAD. (a) Alteration frequency of SLCO4A1 gene in three COAD studies. (b) Methylation levels of SLCO4A1 based on 372 samples with data in both axes. (c) Mutation diagram showing mutation sites, mutation types, and the number of cases; these results are colored according to the corresponding mutation type.

PD-L1), CTLA4, TIGIT, and HAVCR2. There was significant correlation between SLCO4A1 and two immune markers (TIGIT and HAVCR2) but no significant correlation between SLCO4A1 and two other immune markers (CD274 and CTLA4) in COAD (Figure 6(c)).

In this study, the TISIDB database was used to investigate the relationship between the expression of SLCO4A1 in COAD and three immune components (lymphocytes, immunomodulators, and chemokines). Firstly, the relationship between SLCO4A1 expression level and the abundance of tumor infiltrating lymphocytes was explored to identify which types of TIICs could be regulated by SLCO4A1 gene. The results showed that SLCO4A1 expression level was negatively correlated with Tem_CD8 cells (rho = −0.209, $P = 6.36e − 06$), Tfh cells (rho = −0.194, $P = 2.88e − 05$), Treg cells (rho = −0.164, $P = 0.00041$), Th1 cells (rho = −0.19, $P = 4.49e − 05$), Act_CD4 cells (rho = −0.217, $P = 2.99e − 06$

), and macrophages (rho = −0.266, $P = 7.72e − 09$) (Supplementary Figure 3A). Secondly, we identified the correlation between SLCO4A1 expression and immunomodulators (Supplementary Figure 3B–3D). Finally, we investigated the relationships of SLCO4A1 expression with chemokines and receptors. The correlation between SLCO4A1 and chemokines is shown in Supplementary Figure 3E, and the correlation between SLCO4A1 and receptors is shown in Supplementary Figure 3F. These results strongly suggested that SLCO4A1 could regulate a variety of immune components via multiple pathways and then influence tumor immune infiltration in COAD.

4. Discussion

COAD is a common and important pathological type in CRC. In the current clinical practice, radical surgery is the

(a)

(b)

(c)

FIGURE 5: The protein-protein interaction network of SLCO4A1 and functional enrichment analysis. (a) The protein-protein interaction network based on SLCO4A1-binding proteins using the STRING tool. (b) GO enrichment analysis (top 20 terms) by genes binding to SLCO4A1. (c) KEGG enrichment analysis (top 10 terms) by genes binding to SLCO4A1.

only possible cure treatment for most CRC patients. However, surgical operations are sometimes limited or even unable to carry out due to tumor location, depth of tumor invasion, or tumor metastasis. In recent years, new technologies, such as molecular targeted therapy and immunotherapy, have become one of the important means of treating cancer, and the therapeutic effect on some patients with advanced cancer has been significantly improved [40]. As an emerging treatment modality, immunotherapy has become a promising treatment method [41]. However, immunotherapy has only a good response to a small number of CRCs showing microsatellite instability (MSI), but most CRCs belong to the microsatellite stable type (MSS). Compared with MSS tumors, immunostimulatory factors, such as CD28, IL-15, CCL3, and CXCL16, have higher expression in MSI tumors [42]. Activated tumor-infiltrating immune cells could increase the expression level of HLA and checkpoint-related proteins in MSI tumors and then effectively inhibit the immune escape of tumor cells. Therefore,

in the future, how to activate immune cells in tumors is an urgent problem to be solved [43, 44].

In recent years, a large number of studies have focused on identifying key immune-related genes in many types of cancers, screening out high-risk populations, and testing the effectiveness of immune-targeted drugs [45–47]. In our study, we found that SLCO4A1 played an important role in the prognosis and tumor immune infiltration in COAD.

Firstly, we studied the expression level of SLCO4A1 in COAD and the relationship of SLCO4A1 abnormal expression with clinical characteristics in patients with COAD. SLCO4A1 was overexpressed in COAD and READ, compared with normal tissues (Figures 1 and 2). Moreover, the expression of SLCO4A1 was associated with individual cancer stages, histological subtype, and TP53 mutation status in patients with COAD (Table 1). In addition, SLCO4A1 overexpression was associated with a shorter OS or DFS (Figure 3). Interestingly, our results are similar to those of some studies, but the role of SLCO4A1 in the occurrence

(a)

(b)

(c)

Figure 6: Correlation of the SLCO4A1 expression level with immune infiltration in COAD via the TIMER database. (a) Correlation of the SLCO4A1 expression with different tumor-infiltrating immune cells. (b) Correlation between SLCO4A1 expression and immune cell-specific markers. (c) Correlation between SLCO4A1 expression and four important immune markers (CD274, CTLA4, TIGIT, and HAVCR2).

and development of COAD still needs to be further researched [48, 49].

The results of our study showed that the expression level of SLCO4A1 increased in COAD, which affected the prognosis of COAD patients, indicating that SLCO4A1 could play an important role in the pathogenesis of COAD. SLCO4A1 was a valuable research topic not only in genetic alterations (Figure 4) but also in the role of the occurrence and development of COAD. Previous studies have shown that abnormalities of the SLCO4A1 gene have multifaceted

TABLE 2: Correlation analysis between SLCO4A1 and related genes and markers of immune cells in TIMER.

Description	Gene markers	cor	P
CD8+ T cell	CD8A	-0.144	$1.97E-03$
	CD8B	-0.097	$3.72E-02$
T cell	CD3D	-0.197	$2.17E-05$
	CD3E	-0.150	$1.34E-03$
	CD2	-0.176	$1.62E-04$
B cell	CD19	-0.053	$2.58E-01$
	CD79A	-0.094	$4.49E-02$
Monocyte	CD86	-0.121	$9.76E-03$
	CSF1R	-0.072	$1.22E-01$
TAM	CCL2	-0.072	$1.26E-01$
	CD68	-0.028	$5.46E-01$
	IL10	-0.014	$1.44E-02$
M1 macrophage	INOS (NOS2)	-0.061	$1.93E-01$
	IRF5	0.115	$1.38E-02$
	COX2 (PTGS2)	-0.038	$4.15E-01$
M2 macrophage	CD163	-0.091	$5.26E-02$
	VSIG4	-0.089	$5.83E-02$
	MS4A4A	-0.133	$4.51E-03$
Neutrophils	CD66b (CEACAM8)	0.186	$6.08E-05$
	CD11b (ITGAM)	-0.032	$4.96E-01$
	CCR7	-0.076	$1.06E-01$
Natural killer cell	KIR2DL1	-0.046	$3.21E-01$
	KIR2DL3	0.000	$9.95E-01$
	KIR3DL1	-0.069	$1.39E-01$
	KIR3DL2	-0.106	$2.34E-02$
Dendritic cell	HLA-DPB1	-0.075	$1.11E-01$
	HLA-DRA	-0.130	$5.52E-03$
	BDCA-1 (CD1C)	-0.127	$6.31E-03$
Th1	STAT4	-0.161	$5.47E-04$
	STAT1	-0.040	$3.39E-01$
	TNF-α (TNF)	-0.015	$7.53E-01$
Th2	GATA3	-0.062	$1.85E-01$
	STAT6	0.126	$6.94E-03$
	IL13	-0.210	$6.62E-01$
Tfh	BCL6	0.087	$6.17E-02$
	IL21	-0.050	$2.87E-01$
Th17 cell	STAT3	-0.004	$9.36E-01$
	IL17A	0.098	$3.52E-02$
Treg cell	FOXP3	-0.100	$3.20E-02$

TABLE 2: Continued.

Description	Gene markers	cor	P
	CCR8	-0.145	$8.26E-04$

effects for many tumors. Overexpression of the SLCO4A1 gene in prostate cancer and thyroid cancer indicated a poor prognosis [48, 50]. Buxhofer-Ausch et al. have shown that SLCO4A1 may affect the accumulation of anticancer drugs in specific cancer cells [19].

Therefore, we hypothesized that SLCO4A1 could be an oncogene in COAD. Then, GO enrichment analysis showed that SLCO4A1-interacting genes were mainly enriched in organic anion transmembrane transporter activity, anion transmembrane transporter activity, bile acid and bile salt transport, carboxylic acid transport, active transmembrane transporter activity, ion transport, monocarboxylic acid transport, plasma membrane region, and secondary active transmembrane transporter activity (Figure 5(b)). The KEGG pathway analysis showed that SLCO4A1 and its coexpressed genes were mainly enriched in bile secretion, ABC transporters, antifolate resistance, thyroid hormone signaling pathway, primary bile acid biosynthesis, PPAR signaling pathway, glutamatergic synapse, cholesterol metabolism, hippo signaling pathway, and protein digestion and absorption (Figure 5(c)). The organic anion transmembrane transport mediates the uptake of many important drugs and hormones, thus affecting the drug distribution and intracellular drug concentration [51]. Because many anticancer drugs are the substrates of SLCOs, the abnormal expression of these transporters in cancer cells will affect the intracellular concentration of anticancer drugs and then affect the efficacy of these drugs. In addition, these influx transporters, which can act together with efflux transporters and drug metabolic enzymes, may play a key role in chemoresistance.

Another major result of our study was that the expression of SLCO4A1 was associated with multiple tumor-infiltrating immune cells and abundant immune molecules (Figure 6). These results strongly suggested that SLCO4A1 could be involved in tumor immune infiltration in COAD. An increased density of CD8+ T cell in tumor tissue has been found to be associated with a reduced risk of tumor recurrence [19]. Tumor-specific CD8+ T cells and CD4+ T cells are required for the effective clearance of tumor cells. We inferred that the suppression of CD8+ T cells could downregulate some important signals on immune cells and then reduce the aggregation of other immune cells, such as CD4+ T cells and dendritic cells, which could explain the simultaneous inhibition phenomenon of several tumor-infiltrating immune cells in our study. Furthermore, the correlation analysis obtained from the TISIDB database revealed the relationship between SLCO4A1 expression levels and lymphocyte, immunomodulators, and chemokines in COAD (Supplementary Figure 3). Our study clearly showed that SLCO4A1 was closely linked to tumor immune infiltration in COAD and might be a new molecular target, which was worth further exploration.

5. Conclusions

In conclusion, our study showed that SLCO4A1 was overexpressed in COAD tissues, and we have identified the relationship between SLCO4A1 overexpression and poor prognosis by using several authoritative databases. Moreover, our study also explored the correlation between the expression of SLCO4A1 and tumor immune infiltration in COAD. At the same time, we also studied the association of SLCO4A1 expression with specific markers of diverse immune cells. These results in our study showed that the expression level of SLCO4A1 was significantly related to the abundance of various lymphocytes, immunomodulators, and chemokines in COAD. Therefore, we can better predict the prognosis of COAD and evaluate the status of tumor immune infiltration by testing the expression level of SLCO4A1 in COAD.

There are still some shortcomings in the study. Although the study was based on multiple publicly authoritative databases, the same data in individual research aspects were still limited. In addition, we need to further explore the role of SLCO4A1 in regulating tumor immune infiltration in COAD. However, our current study strongly suggests that SLCO4A1 could be a novel prognostic biomarker and an important immune-related factor for evaluating the immunotherapy in COAD patients.

Data Availability

All data generated or analyzed during this study are included in this article (and its supplementary information files).

Ethical Approval

The study is a comprehensive and integrated bioinformatics analysis of available data which are all from public databases, and users can download relevant data for free for research. So there are no ethical issues and other conflicts of interest in the study.

Conflicts of Interest

The authors declare that there is no conflict of interest.

Authors' Contributions

Xiaolong Chen and Fei Wang contributed equally to this work.

Supplementary Materials

Supplementary 1. Table S1: the abbreviations for 31 cancers. Table S2: top 100 expression-correlated genes and 50 SLC04A1-binding proteins.

Supplementary 2. Supplementary Figure 1: relationship between SLCO4A1 expression and clinical molecular indicators in patients with COAD. Different SLCO4A1 expression levels in COAD based on (A) PMS2, (B) MSH2, (C) MSH6, (D) MLH1, (E) BRAF, (F) KRAS, and (G) NRAS, respectively. Supplementary Figure 2: analysis of SLCO4A1 genetic alterations via the cBioPortal database. Relationship of SLCO4A1 with genetic alterations (A) OS, (B) PFS, (C) DFS, and (D) DSS for patients with COAD. OATP: organic anion-transporting polypeptide; OS: overall survival; PFS: progression-free survival; DFS: disease-free survival; DSS: disease-specific survival. Supplementary Figure 3: relationship between SLCO4A1 expression and immune components in patients with COAD, including lymphocytes, immunomodulators, chemokines, and receptors. (A) Relationship between the SLCO4A1 expression level and lymphocytes. (B–D) Relationship between the SLCO4A1 expression level and immunomodulators. (E) Correlation between SLCO4A1 expression level and chemokines. (F) Correlation between SLCO4A1 expression level and receptors.

References

[1] H. Sung, J. Ferlay, R. L. Siegel et al., "Global cancer statistics 2020: GLOBOCAN estimates of incidence and mortality worldwide for 36 cancers in 185 countries," *CA: a cancer journal for clinicians*, vol. 71, no. 3, pp. 209–249, 2021.

[2] M. Arnold, M. S. Sierra, M. Laversanne, I. Soerjomataram, A. Jemal, and F. Bray, "Global patterns and trends in colorectal cancer incidence and mortality," *Gut*, vol. 66, no. 4, pp. 683–691, 2017.

[3] R. H. Vonderheide, S. M. Domchek, and A. S. Clark, "Immunotherapy for breast cancer: what are we missing?," *Clinical Cancer Research*, vol. 23, no. 11, pp. 2640–2646, 2017.

[4] L. Pusztai, T. Karn, A. Safonov, M. M. Abu-Khalaf, and G. Bianchini, "New strategies in breast cancer: immunotherapy," *Clinical Cancer Research*, vol. 22, no. 9, pp. 2105–2110, 2016.

[5] M. J. Overman, S. Lonardi, K. Y. M. Wong et al., "Durable clinical benefit with nivolumab plus ipilimumab in DNA mismatch repair-deficient/microsatellite instability–high metastatic colorectal cancer," *Journal of Clinical Oncology*, vol. 36, no. 8, pp. 773–779, 2018.

[6] D. T. Le, J. N. Uram, H. Wang et al., "PD-1 blockade in tumors with mismatch-repair deficiency," *The New England Journal of Medicine*, vol. 372, no. 26, pp. 2509–2520, 2015.

[7] L. B. Alexandrov, S. Nik-Zainal, D. C. Wedge et al., "Signatures of mutational processes in human cancer," *Nature*, vol. 500, no. 7463, pp. 415–421, 2013.

[8] M. Reck, D. Rodríguez-Abreu, A. G. Robinson et al., "Pembrolizumab versus chemotherapy for PD-L1-positive non-small-cell lung cancer," *The New England Journal of Medicine*, vol. 375, no. 19, pp. 1823–1833, 2016.

[9] L. Gandhi, D. Rodríguez-Abreu, S. Gadgeel et al., "Pembrolizumab plus chemotherapy in metastatic non–small-cell lung cancer," *The New England Journal of Medicine*, vol. 378, no. 22, pp. 2078–2092, 2018.

[10] S. Loi, N. Sirtaine, F. Piette et al., "Prognostic and predictive value of tumor-infiltrating lymphocytes in a phase III randomized adjuvant breast cancer trial in node-positive breast cancer comparing the addition of docetaxel to doxorubicin with doxorubicin-based chemotherapy: BIG 02-98," *Journal of Clinical Oncology*, vol. 31, no. 7, pp. 860–867, 2013.

[11] V. Deschoolmeester, M. Baay, E. van Marck et al., "Tumor infiltrating lymphocytes: an intriguing player in the survival of colorectal cancer patients," *BMC Immunology*, vol. 11, no. 1, p. 19, 2010.

[12] J. Eugène, N. Jouand, K. Ducoin et al., "The inhibitory receptor CD94/NKG2A on CD8+ tumor- infiltrating lymphocytes in colorectal cancer: a promising new druggable immune check-point in the context of HLAE/β2m overexpression," *Modern Pathology*, vol. 33, no. 3, pp. 468–482, 2020.

[13] M. W. Rosenbaum, J. R. Bledsoe, V. Morales-Oyarvide, T. G. Huynh, and M. Mino-Kenudson, "PD-L1 expression in colorectal cancer is associated with microsatellite instability, _BRAF_ mutation, medullary morphology and cytotoxic tumor- infiltrating lymphocytes," *Modern Pathology*, vol. 29, no. 9, pp. 1104–1112, 2016.

[14] C. Ralph, E. Elkord, D. J. Burt et al., "Modulation of lymphocyte regulation for cancer therapy: a phase II trial of tremelimumab in advanced gastric and esophageal adenocarcinoma," *Clinical Cancer Research*, vol. 16, no. 5, pp. 1662–1672, 2010.

[15] K. Y. Chung, I. Gore, L. Fong et al., "Phase II study of the anti-cytotoxic T-lymphocyte–associated antigen 4 monoclonal antibody, tremelimumab, in patients with refractory metastatic colorectal cancer," *Journal of Clinical Oncology*, vol. 28, no. 21, pp. 3485–3490, 2010.

[16] S. P. D'Angelo, J. Russell, C. Lebbé et al., "Efficacy and safety of first-line avelumab treatment in patients with stage IV metastatic Merkel cell carcinoma: a preplanned interim analysis of a clinical trial," *JAMA Oncology*, vol. 4, no. 9, article e180077, 2018.

[17] Y. K. Kang, N. Boku, T. Satoh et al., "Nivolumab in patients with advanced gastric or gastro-oesophageal junction cancer refractory to, or intolerant of, at least two previous chemotherapy regimens (ONO-4538-12, ATTRACTION-2): a randomised, double-blind, placebo- controlled, phase 3 trial," *Lancet*, vol. 390, no. 10111, pp. 2461–2471, 2017.

[18] B. Hagenbuch and P. J. Meier, "Organic anion transporting polypeptides of the OATP/ SLC21 family: phylogenetic classification as OATP/SLCO superfamily, new nomenclature and molecular/functional properties," *Pflügers Archiv*, vol. 447, no. 5, pp. 653–665, 2004.

[19] V. Buxhofer-Ausch, L. Secky, K. Wlcek et al., "Tumor-specific expression of organic anion-transporting polypeptides: transporters as novel targets for cancer therapy," *Journal of drug delivery*, vol. 2013, Article ID 863539, 12 pages, 2013.

[20] S. Brenner, L. Klameth, J. Riha et al., "Specific expression of OATPs in primary small cell lung cancer (SCLC) cells as novel biomarkers for diagnosis and therapy," *Cancer Letters*, vol. 356, no. 2, pp. 517–524, 2015.

[21] A. Hays, U. Apte, and B. Hagenbuch, "Organic anion transporting polypeptides expressed in pancreatic cancer may serve as potential diagnostic markers and therapeutic targets for early stage adenocarcinomas," *Pharmaceutical Research*, vol. 30, no. 9, pp. 2260–2269, 2013.

[22] D. R. Rhodes, S. Kalyana-Sundaram, V. Mahavisno et al., "Oncomine 3.0: genes, pathways, and networks in a collection of 18,000 cancer gene expression profiles," *Neoplasia*, vol. 9, no. 2, pp. 166–180, 2007.

[23] D. R. Rhodes, J. Yu, K. Shanker et al., "_ONCOMINE_ : a cancer microarray database and integrated data-mining platform," *Neoplasia*, vol. 6, no. 1, pp. 1–6, 2004.

[24] D. S. Chandrashekar, B. Bashel, S. A. H. Balasubramanya et al., "UALCAN: a portal for facilitating tumor subgroup gene expression and survival analyses," *Neoplasia*, vol. 19, no. 8, pp. 649–658, 2017.

[25] B. Li, E. Severson, J. C. Pignon et al., "Comprehensive analyses of tumor immunity: implications for cancer immunotherapy," *Genome Biology*, vol. 17, no. 1, p. 174, 2016.

[26] A. Waterhouse, M. Bertoni, S. Bienert et al., "SWISS-MODEL: homology modelling of protein structures and complexes," *Nucleic Acids Research*, vol. 46, no. W1, pp. W296–W303, 2018.

[27] Z. Huang, H. Lai, J. Liao et al., "Upregulation of ADAM12 is associated with a poor survival and immune cell infiltration in colon adenocarcinoma," *Frontiers in Oncology*, vol. 11, article 729230, 2021.

[28] Z. Tang, C. Li, B. Kang, G. Gao, C. Li, and Z. Zhang, "GEPIA: a web server for cancer and normal gene expression profiling and interactive analyses," *Nucleic Acids Research*, vol. 45, no. W1, pp. W98–W102, 2017.

[29] Z. Tang, B. Kang, C. Li, T. Chen, and Z. Zhang, "GEPIA2: an enhanced web server for large-scale expression profiling and interactive analysis," *Nucleic Acids Research*, vol. 47, no. W1, pp. W556–W560, 2019.

[30] H. Mizuno, K. Kitada, K. Nakai, and A. Sarai, "PrognoScan: a new database for meta-analysis of the prognostic value of genes," *BMC Medical Genomics*, vol. 2, no. 1, p. 18, 2009.

[31] Á. Nagy, G. Munkácsy, and B. Győrffy, "Pancancer survival analysis of cancer hallmark genes," *Scientific Reports*, vol. 11, no. 1, p. 6047, 2021.

[32] J. Gao, B. A. Aksoy, U. Dogrusoz et al., "Integrative analysis of complex cancer genomics and clinical profiles using the Cbioportal," *Science Signaling*, vol. 6, no. 269, p. pl1, 2013.

[33] D. Szklarczyk, A. Franceschini, S. Wyder et al., "STRING V10: protein-protein interaction networks, integrated over the tree of life," *Nucleic Acids Research*, vol. 43, no. D1, pp. D447–D452, 2015.

[34] L. Liang, J. H. Zhu, G. Chen, X. G. Qin, and J. Q. Chen, "Prognostic values for the mRNA expression of the ADAMTS family of genes in gastric cancer," *Journal of Oncology*, vol. 2020, Article ID 9431560, 24 pages, 2020.

[35] T. Li, J. Fan, B. Wang et al., "TIMER: a web server for comprehensive analysis of tumor-infiltrating immune cells," *Cancer Research*, vol. 77, no. 21, pp. e108–e110, 2017.

[36] N. O. Siemers, J. L. Holloway, H. Chang et al., "Genome-wide association analysis identifies genetic correlates of immune infiltrates in solid tumors," *PLoS One*, vol. 12, no. 7, article e0179726, 2017.

[37] P. Danaher, S. Warren, L. Dennis et al., "Gene expression markers of tumor infiltrating leukocytes," *Journal for Immunotherapy of Cancer*, vol. 5, no. 1, p. 18, 2017.

[38] S. Sousa and J. Maatta, "The role of tumour-associated macrophages in bone metastasis," *Journal of bone oncology*, vol. 5, no. 3, pp. 135–138, 2016.

[39] B. Ru, C. N. Wong, Y. Tong et al., "TISIDB: an integrated repository portal for tumor-immune system interactions," *Bioinformatics*, vol. 35, no. 20, pp. 4200–4202, 2019.

[40] E. Dekker, P. J. Tanis, J. L. A. Vleugels, P. M. Kasi, and M. B. Wallace, "Colorectal cancer," *Lancet*, vol. 394, no. 10207, pp. 1467–1480, 2019.

[41] K. Ganesh, Z. K. Stadler, A. Cercek et al., "Immunotherapy in colorectal cancer: rationale, challenges and potential," *Nature Reviews. Gastroenterology & Hepatology*, vol. 16, no. 6, pp. 361–375, 2019.

[42] B. Mlecnik, G. Bindea, H. K. Angell et al., "Integrative analyses of colorectal cancer show immunoscore is a stronger predictor of patient survival than microsatellite instability," *Immunity*, vol. 44, no. 3, pp. 698–711, 2016.

[43] M. J. Overman, M. S. Ernstoff, and M. A. Morse, "Where we stand with immunotherapy in colorectal cancer: deficient mismatch repair, proficient mismatch repair, and toxicity management," *American Society of Clinical Oncology Educational Book*, vol. 38, pp. 239–247, 2018.

[44] D. Y. Lizardo, C. Kuang, S. Hao, J. Yu, Y. Huang, and L. Zhang, "Immunotherapy efficacy on mismatch repair-deficient colorectal cancer: from bench to bedside," *Biochimica Et Biophysica Acta. Reviews on Cancer*, vol. 1874, no. 2, article 188447, 2020.

[45] J. H. Pan, H. Zhou, L. Cooper et al., "LAYN is a prognostic biomarker and correlated with immune infiltrates in gastric and colon cancers," *Frontiers in Immunology*, vol. 10, p. 6, 2019.

[46] I. Wasserman, L. H. Lee, S. Ogino et al., "SMAD4 loss in colorectal cancer patients correlates with recurrence, loss of immune infiltrate, and chemoresistance," *Clinical Cancer Research*, vol. 25, no. 6, pp. 1948–1956, 2019.

[47] X. Dong, S. Lv, X. Zhang, and R. Hao, "Upregulation of LAGE3 correlates with prognosis and immune infiltrates in colorectal cancer: a bioinformatic analysis," *International Immunopharmacology*, vol. 85, article 106599, 2020.

[48] X. S. Wang, S. L. Wu, Z. Peng, and H. H. Zhu, "SLCO4A1 is a prognosis-associated biomarker involved in neutrophil-mediated immunity in thyroid cancer," *International Journal of General Medicine*, vol. Volume 14, pp. 9615–9628, 2021.

[49] M. J. Ban, S. H. Ji, C. K. Lee et al., "Solute carrier organic anion transporter family member 4A1 (SLCO4A1) as a prognosis marker of colorectal cancer," *Journal of Cancer Research and Clinical Oncology*, vol. 143, no. 8, pp. 1437–1447, 2017.

[50] J. L. Wright, E. M. Kwon, E. A. Ostrander et al., "Expression of SLCO transport genes in castration-resistant prostate cancer and impact of genetic variation in SLCO1B3 and SLCO2B1 on prostate cancer outcomes," *Cancer Epidemiology, Biomarkers & Prevention*, vol. 20, no. 4, pp. 619–627, 2011.

[51] B. Stieger and B. Hagenbuch, "Organic anion-transporting polypeptides," *Current topics in membranes*, vol. 73, pp. 205–232, 2014.

Research Article

Benefits of Dynamic Nomogram Models for Elderly Diffuse Large B-Cell Lymphoma Patients' Early Death Prediction and Clinical Application

Lingke Zhang, Hongmei Jing ⬤, Shuhan Tang, Jing Wang, and Ping Yang

Department of Hematology, Peking University Third Hospital, Beijing 100191, China

Correspondence should be addressed to Hongmei Jing; j13263299069@stu.pku.edu.cn

Background. Diffuse large B-cell lymphoma (DLBCL) is an aggressive malignancy, and about 60% of the patients are diagnosed in their elderly age (≥65 years old). However, little is known about the early mortality and risk factors related to elderly patients with DLBCL. *Methodology.* From 2000 to 2019, elderly patients diagnosed with DLBCL in the Surveillance, Epidemiology, and End Result (SEER) database were involved in this research and served as test cohort. Moreover, elderly DLBCL patients from Peking University Third Hospital were used for external validation cohort. Risk factors were identified by univariate and multivariate logistic regression analyses. Nomogram models were constructed based on significance risk factors to predict the overall and cancer-specific early death. Besides that, the predictive value of the models was validated by receiver operating characteristic (ROC) analysis. Calibration plots were used to evaluate the calibrating ability. Clinical benefits of nomogram were evaluated by decision curve analysis (DCA). *Results.* 15242 elderly DLBCL patients obtained from the SEER database and 152 patients from Peking University Third Hospital were enrolled in this research. In the SEER database, 36.6% (5584/15242) of the patients had early death and 30.7% (4680/15242) of them were cancer-specific early death. Marital status, Ann Arbor stage, surgical treatment, radiotherapy, and chemotherapy were significant risk factors for overall and cancer-specific early death of elderly DLBCL patients. Nomograms were constructed according to these risk factors. Then, ROC analysis showed that the AUC of OS was 0.764 (0.756~0.772), and CSS was 0.742 (0.733~0.751). In the validation group, the AUC of OS was 0.767 (0.689~0.846) and CSS was 0.742 (0.743~0.83). *Conclusion.* The calibration plots and DCA analysis revealed that the nomograms were good at early death prediction and clinical application. Predictive dynamic nomogram models for elderly DLBCL patients were established and validated, which might play an essential role in helping physicians enact better treatment strategies.

1. Introduction

Diffuse large B-cell lymphoma (DLBCL) is one of the most common subtypes of non-Hodgkin lymphoma (NHL), which accounts for approximately 30% to 40% of patients with NHL [1, 2]. DLBCL is known as an aggressive carcinoma, with the features including rapidly growing cancers in the liver, bone marrow, lymph nodes, and other organs [3]. As the wide application of radiotherapy, chemotherapy, and immunotherapy combined with autologous stem cell transplantation, the survival of DLBCL patients improves

dramatically and DLBCL is found to be a curable carcinoma [4]. Such as it is, there are still about 30%~40% DLBCL patients failing to achieve remission or relapsing, which contributes to the morbidity and mortality of DLBCL patients [5, 6]. Moreover, about 60% of the DLBCL patients are diagnosed at the age of ≥65 years old [7], and it is found that the risk of death significantly increases with age [8, 9]. However, there is little research focused on the early death of elderly DLBCL patients.

DLBCL has a wide range of prognoses in the worldwide population. The identification of risk factors and prognosis

Table 1: Clinicopathological characteristics of patients in the SEER database and external cohort.

	Variable	SEER	External validation
n		15242	152
Sex (%)	Male	7485 (49.1)	77 (50.7)
	Female	7757 (50.9)	75 (49.3)
Race (%)	White	13122 (86.1)	NA
	Black	658 (4.3)	NA
	AI/AN	75 (0.5)	NA
	API	1387 (9.1)	NA
Marital status (%)	Married	8139 (53.4)	87 (57.2)
	Unmarried	7103 (46.6)	65 (42.8)
Median household income (%)	<$40,000	540 (3.5)	NA
	$40,000–$54,999	2892 (19.0)	NA
	$55,000–$69,999	5950 (39.0)	NA
	>$70,000	5860 (38.4)	NA
Tumor site (%)	Nodal	9784 (64.2)	96 (63.2)
	Extranodal	5458 (35.8)	56 (36.8)
Ann Arbor stage (%)	I	3829 (25.1)	33 (21.7)
	II	2710 (17.8)	26 (17.1)
	III	2572 (16.9)	28 (18.4)
	IV	5282 (34.7)	60 (39.5)
	Unknown	849 (5.6)	5 (3.3)
Surgery (%)	No	11027 (72.3)	111 (73.0)
	Yes	4215 (27.7)	41 (27.0)
Radiation (%)	No/unknown	12838 (84.2)	134 (88.2)
	Yes	2404 (15.8)	18 (11.8)
Chemotherapy (%)	No/unknown	5466 (35.9)	37 (24.3)
	Yes	9776 (64.1)	115 (75.7)

prediction is particularly vital for health care and making treatment decisions. Early death is defined as survival time less than 3 months, and the factors for early death of patients with DLBCL are still unknown. Nomogram is a type of prognostic model combined with risk factors to predict outcomes of patients, which has obtained a lot of attention in the oncology field [10–13]. Besides that, dynamic nomogram is useful for explaining the heterogeneity in the outcomes of elderly DLBCL patients with diverse clinical characteristics, providing individual prediction for the probability of outcome events. Therefore, the aim of this research was to identify risk factors, meanwhile constructing dynamic nomograms to predict the overall and cancer-specific early death of elderly DLBCL patients.

2. Methods

2.1. Patients. In this research, data of elderly (≥65 years old) patients with DLBCL from the dataset "incidence SEER research plus data 17 registries, Nov 2021 Sub (2000-2019)" was extracted from the Surveillance, Epidemiology,

and End Results (SEER) database, which is a public database that contains about 27.8% of the US cancer patients [14]. Histology codes from the third edition of the International Classification of Diseases for Oncology (ICD-O-3) including 9680/3, 9684/3, and 9688/3 were used to obtain the interesting cohort. All patients included in this research were confirmed as positive histology, who had one primary tumor only and completed clinical information. Therefore, a total of 15242 DLBCL patients from the SEER database were included in this research. Moreover, 152 elderly DLBCL patients from Peking University Third Hospital were utilized as external validation cohort. Early death was defined as survival time less than 3 months after diagnosis. This research was approved by the ethics committee of Peking University Third Hospital. The ethics committee approval number is M2021034.

2.2. Statistical Analysis. Categorized data was described by numbers and percentages (*N* and %). Univariate and multivariate logistic analyses were utilized to identify the risk factors associated with OS and CSS early death of elderly

Table 2: Rate of early death in older patients with DLBCL.

	Variable	Overall	No early death	Total early death	Cancer-specific early death
n		15242	9658	5584	4680
Sex (%)	Male	7485 (49.1)	4724 (48.9)	2761 (49.4)	2263 (48.4)
	Female	7757 (50.9)	4934 (51.1)	2823 (50.6)	2417 (51.6)
Race (%)	White	13122 (86.1)	8320 (86.1)	4802 (86.0)	4016 (85.8)
	Black	658 (4.3)	406 (4.2)	252 (4.5)	217 (4.6)
	AI/AN	75 (0.5)	54 (0.6)	21 (0.4)	19 (0.4)
	API	1387 (9.1)	878 (9.1)	509 (9.1)	428 (9.1)
Marital status (%)	Married	8139 (53.4)	5423 (56.2)	2716 (48.6)	2266 (48.4)
	Unmarried	7103 (46.6)	4235 (43.8)	2868 (51.4)	2414 (51.6)
Median household income (%)	<$40,000	540 (3.5)	329 (3.4)	211 (3.8)	174 (3.7)
	$40,000–$54,999	2892 (19.0)	1800 (18.6)	1092 (19.6)	906 (19.4)
	$55,000–$69,999	5950 (39.0)	3714 (38.5)	2236 (40.0)	1892 (40.4)
	>$70,000	5860 (38.4)	3815 (39.5)	2045 (36.6)	1708 (36.5)
Tumor site (%)	Nodal	9784 (64.2)	6224 (64.4)	3560 (63.8)	3018 (64.5)
	Extranodal	5458 (35.8)	3434 (35.6)	2024 (36.2)	1662 (35.5)
Ann Arbor stage (%)	I	3829 (25.1)	2663 (27.6)	1166 (20.9)	925 (19.8)
	II	2710 (17.8)	1824 (18.9)	886 (15.9)	739 (15.8)
	III	2572 (16.9)	1703 (17.6)	869 (15.6)	733 (15.7)
	IV	5282 (34.7)	2951 (30.6)	2331 (41.7)	2018 (43.1)
	Unknown	849 (5.6)	517 (5.4)	332 (5.9)	265 (5.7)
Surgery (%)	No	11027 (72.3)	6735 (69.7)	4292 (76.9)	3621 (77.4)
	Yes	4215 (27.7)	2923 (30.3)	1292 (23.1)	1059 (22.6)
Radiation (%)	No/unknown	12838 (84.2)	7677 (79.5)	5161 (92.4)	4314 (92.2)
	Yes	2404 (15.8)	1981 (20.5)	423 (7.6)	366 (7.8)
Chemotherapy (%)	No/unknown	5466 (35.9)	2013 (20.8)	3453 (61.8)	2868 (61.3)
	Yes	9776 (64.1)	7645 (79.2)	2131 (38.2)	1812 (38.7)

DLBCL patients. Discrimination was judged by the receiver operating characteristic (ROC) curve; the higher the area under the curve (AUC) was, the better the accuracy of the nomogram would be (13). Calibration plots were used to evaluate calibrating ability. Moreover, the clinical benefits of nomogram were evaluated by decision curve analysis (DCA). All analyses were performed by R software (4.1.3). P value < 0.05 (two-tail) was regarded as statistically significant.

3. Results

3.1. Demographic and Clinical Characteristics of Elderly Patients with DLBCL. The demographic and clinicopathological characteristics of elderly patients with DLBCL from the SEER database ($n = 15242$) and external validation cohort ($n = 152$) are shown in Table 1. From the SEER database, most of the patients were white (86.1%), while the black, AI/AN patients, and API patients accounted for 4.3%, 0.5%, and 9.1%, respectively. The gender distributions were

not different. The most common Ann Arbor stage was IV (34.7%), followed by stages I (25.1%), II (17.8%), and III (16.9%). About two-thirds of the patients was nodal (64.2%). Compared with chemotherapy (64.1%), few of the patients recepted surgical treatment (27.7%) or radiation (15.8%). There was no significant difference between the SEER cohort and the external validation cohort.

3.2. Mortality of Early Death of Elderly Patients with DLBCL. As shown in Table 2, 36.6% (5584/15242) of the patients suffered from early death and 30.7% (4680/15242) of them were cancer-specific early death. Unmarried patients had slightly higher early mortality than married patients. White patients had the highest early (86.0%) and cancer-specific (85.8%) mortality, followed by API, black, and AI/AN patients. Mortality rates increased with household income and peaked at the median household income of $55,000–$69,999. Tumor site at nodal caused a higher early mortality compared with extranodal. The highest early mortality was shown in Ann Arbor stage IV. Moreover, patients recepted surgical

Table 3: Univariate and multivariate logistic analyses of variables associated with risk of OS for older DLBCL patients.

Variable	Univariate analysis			Multivariate analysis		
	OR	95% CI	P	OR	95% CI	P
Sex						
Male						
Female	0.98	0.92-1.05	0.527			
Race						
White						
Black	1.08	0.92-1.26	0.377			
AI/AN	0.67	0.41-1.12	0.126			
API	1	0.9-1.13	0.94			
Marital status						
Married						
Unmarried	1.35	1.27-1.44	<0.001	1.1	1.02-1.18	0.017
Median household income						
< $40,000						
$40,000–$54,999	0.95	0.78-1.14	0.563			
$55,000–$69,999	0.94	0.78-1.12	0.493			
> $70,000	0.84	0.7-1	0.052			
Tumor site						
Nodal						
Extranodal	1.03	0.96-1.1	0.392			
Ann Arbor stage						
I						
II	1.11	1-1.23	0.054	1.26	1.12-1.42	<0.001
III	1.17	1.05-1.3	0.005	1.48	1.31-1.67	<0.001
IV	1.8	1.65-1.97	<0.001	2.17	1.96-2.4	<0.001
Unknown	1.47	1.26-1.71	<0.001	0.86	0.72-1.02	0.077
Surgery						
No						
Yes	0.69	0.64-0.75	<0.001	0.67	0.61-0.73	<0.001
Radiation						
No/unknown						
Yes	0.32	0.28-0.35	<0.001	0.33	0.29-0.37	<0.001
Chemotherapy						
No/unknown						
Yes	0.16	0.15-0.17	<0.001	0.14	0.13-0.15	<0.001

treatment, radiotherapy, or chemotherapy had lower early mortality compared with those not performed. There were no significant differences in the sex group.

3.3. Risk Factors Associated with Early Death of Elderly DLBCL Patients. Risk factors of early death of elderly DLBCL patients were identified by univariate and multivariate logistic regressions. As displayed in Tables 3 and 4, variables including marital status (OR: 1.1, 95% CI: 1.02-1.18), Ann Arbor stage, surgical treatment (OR: 0.67, 95% CI: 0.61-0.73), radiotherapy (OR: 0.33, 95% CI: 0.29-0.37), and chemotherapy (OR: 0.14, 95% CI: 0.13-0.15) were significantly associated with the probability of overall early death of elderly DLBCL patients. Moreover, multivariate logistic

regression analysis showed that unmarried status, advanced Ann Arbor stage, no surgical treatment, no radiotherapy, and no chemotherapy were significant risk factors for cancer-specific early death of elderly DLBCL patients, all of which were $P < 0.05$.

3.4. Dynamic Nomogram Construction. Risk prediction nomogram of the SEER cohort was constructed according to the multivariate logistic regression analysis results. The odds of early death among elderly DLBCL patients could be predicted by calculating the scores of each factor. As shown in Figure 1, Ann Arbor stage, surgical treatment, radiotherapy, and chemotherapy were great predictors for elderly DLBCL patients' overall and cancer-specific early

TABLE 4: Univariate and multivariate logistic analyses of variables associated with risk of CSS for older DLBCL patients.

Variable	Univariate analysis			Multivariate analysis		
	OR	95% CI	P	OR	95% CI	P
Sex						
Male						
Female	1.04	0.97-1.12	0.216			
Race						
White						
Black	1.12	0.94-1.32	0.198			
AI/AN	0.77	0.46-1.3	0.324			
API	1.01	0.9-1.14	0.846			
Marital status						
Married						
Unmarried	1.33	1.25-1.43	<0.001	1.11	1.03-1.19	0.009
Median household income						
< $40,000						
$40,000–$54,999	0.96	0.79-1.17	0.681			
$55,000–$69,999	0.98	0.81-1.18	0.84			
> $70,000	0.87	0.72-1.05	0.134			
Tumor size						
Nodal						
Extranodal	0.98	0.91-1.05	0.612			
Ann Arbor stage						
I						
II	1.18	1.05-1.32	0.004	1.32	1.16-1.49	<0.001
III	1.25	1.12-1.4	<0.001	1.54	1.36-1.75	<0.001
IV	1.94	1.77-2.13	<0.001	2.24	2.02-2.49	<0.001
Unknown	1.42	1.21-1.68	<0.001	0.89	0.75-1.07	0.216
Surgery						
No						
Yes	0.69	0.63-0.74	<0.001	0.69	0.63-0.75	<0.001
Radiation						
No/unknown						
Yes	0.35	0.32-0.4	<0.001	0.39	0.35-0.45	<0.001
Chemotherapy						
No/unknown						
Yes	0.21	0.19-0.22	<0.001	0.18	0.17-0.2	<0.001

death in the nomogram prediction models. To obtain the dynamic nomogram for OS, visit https://zhanglingbao .shinyapps.io/DynNomapp/, and dynamic nomogram for CSS, visit https://zhanglingbao.shinyapps.io/DynNomapp_ CSS/.

3.5. Nomogram Validation. The ROC, DCA analysis, and calibration plots were utilized to detect prediction efficiency on the probability of early death, and the results showed that nomograms had a good prediction efficiency. As shown in Figure 2, the area under the curve (AUC) of overall survival (OS) was 0.764 (0.756~0.772) and cancer-specific survival (CSS) was 0.742 (0.733~0.751). In the validation group, the AUC of OS was 0.767 (0.689~0.846) and CSS was 0.742

(0.656~0.83). The calibration plots (Figure 3) and DCA analysis (Figure 4) revealed that the nomograms were good at elderly DLBCL patients' early death prediction and clinical application.

4. Discussion

DLBCL is an aggressive carcinoma and mainly affects the older population. Age is a negative prognostic factor for patients with DLBCL, which has been involved in the International Prognostic Index (IPI) [15, 16]. The prognosis of elderly DLBCL patients is worse than that of young patients [17]. Research revealed that the 5-year survival rate of young patients with DLBCL (≤55 years old) was
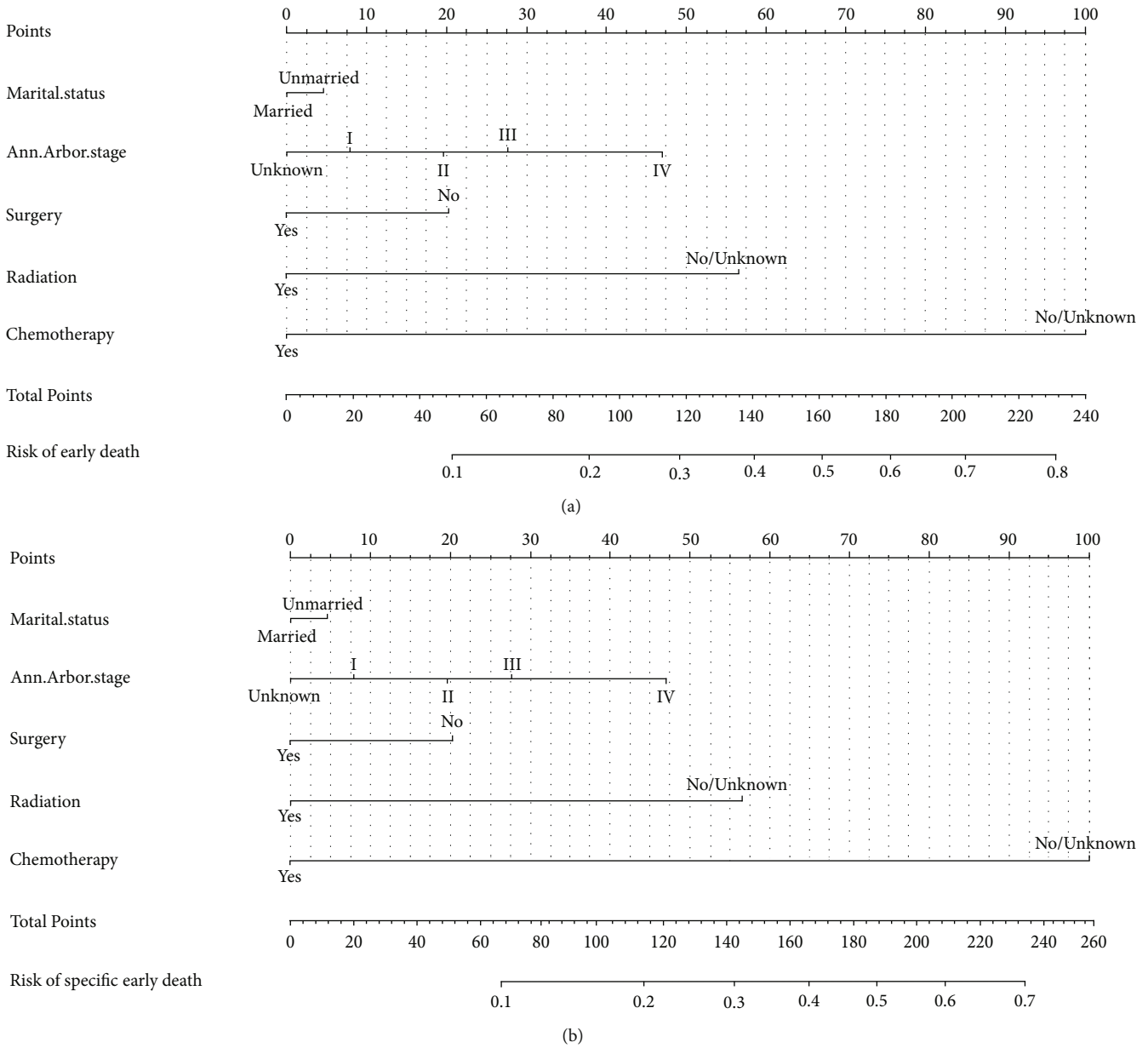
FIGURE 1: The predictive nomogram for the overall early death (a) and specific early death (b) for DLBCL patients.

78%, which was only 54% among patients over 65 years old [18], illustrating the importance of predicting prognosis in elderly DLBCL patients. IPI contains five variables, including age, Ann Arbor stage, the number of extranodal sites, lactate dehydrogenase (LDH), and the Eastern Cooperative Oncology Group performance status [15]. At present, IPI is used as a guide for patients' survival and prognosis. However, IPI fails to identify patients at extreme risk [19, 20].

In this population-based research, we found that the overall early mortality of elderly DLBCL patients was 36.6% and 30.7% of them were DLBCL-specific early death, indicating the poor prognosis of elderly DLBCL patients, which consisted with the previous studies [16, 21].

The prognosis of the elderly DLBCL patients has always been a concern, and most studies are mainly focused on its long-term survival. In recent years, early death of DLBCL patients has attracted much attention. Cho et al. found that the patients suffering DLBCL with a survival time of less than 120 days accounted for 25%; meanwhile, old age, bone marrow involvement, and high-risk IPI score were risk factors for early mortality caused by DLBCL [22]. In 2016, Olszewski et al. quantified the risk factors for death and hospitalization within the first 30 days of rituximab-based immunochemotherapy [7]. We fully included clinical characteristic variables in this research, finding that marital status, Ann Arbor stage, surgical treatment, radiotherapy, and chemotherapy were significantly associated with the

(a)

(b)

(c)

(d)
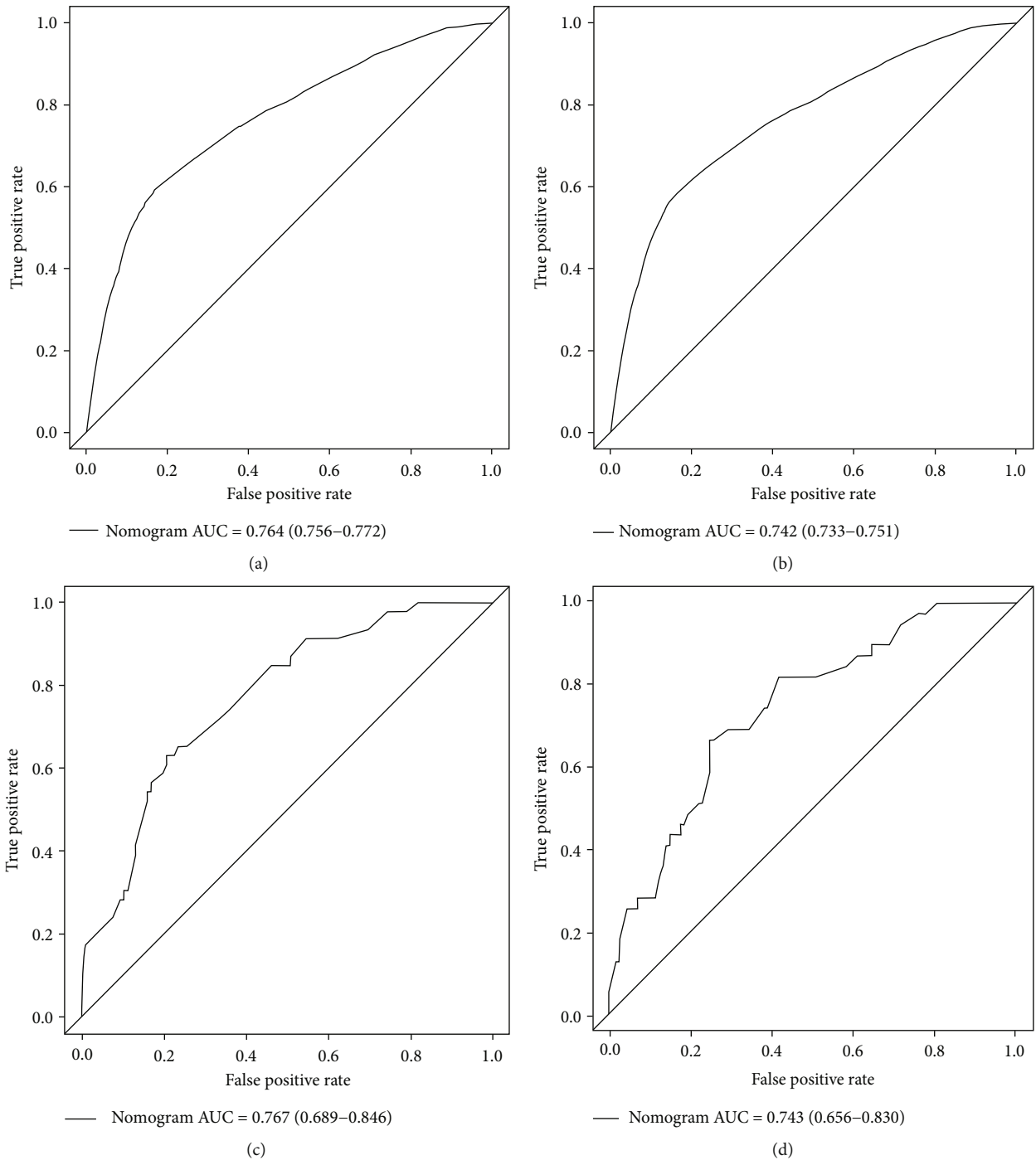
FIGURE 2: The ROC curves for the nomogram of overall early death (a) and specific early death (b) in the SEER database. The ROC curves for the nomogram of overall early death (c) and specific early death nomogram (d) in the validation cohort.

probability of early OS and CSS of elderly DLBCL patients. As a common clinical staging method for NHL, Ann Arbor staging is reasonably used as a predictor for elderly DLBCL patients.

The studies focused on early deaths have been applied to many types of carcinomas, which have shown an important clinical significance. Nomogram is a popular prognostic tool, which plays an important role in the identification of risk factors and personalized treatment [23, 24]. The research of IPI-DLBCL model is mainly focused on the medical indexes while ignoring the influence of families [25]. In this research, marital status, Ann Arbor stage, surgical treatment, radiotherapy, and chemotherapy were used to construct the predictive nomogram models. Therefore, this research may provide a new way to explore a better prognostic model. Moreover, as a dynamic model,

(a)

(b)

(c)

(d)
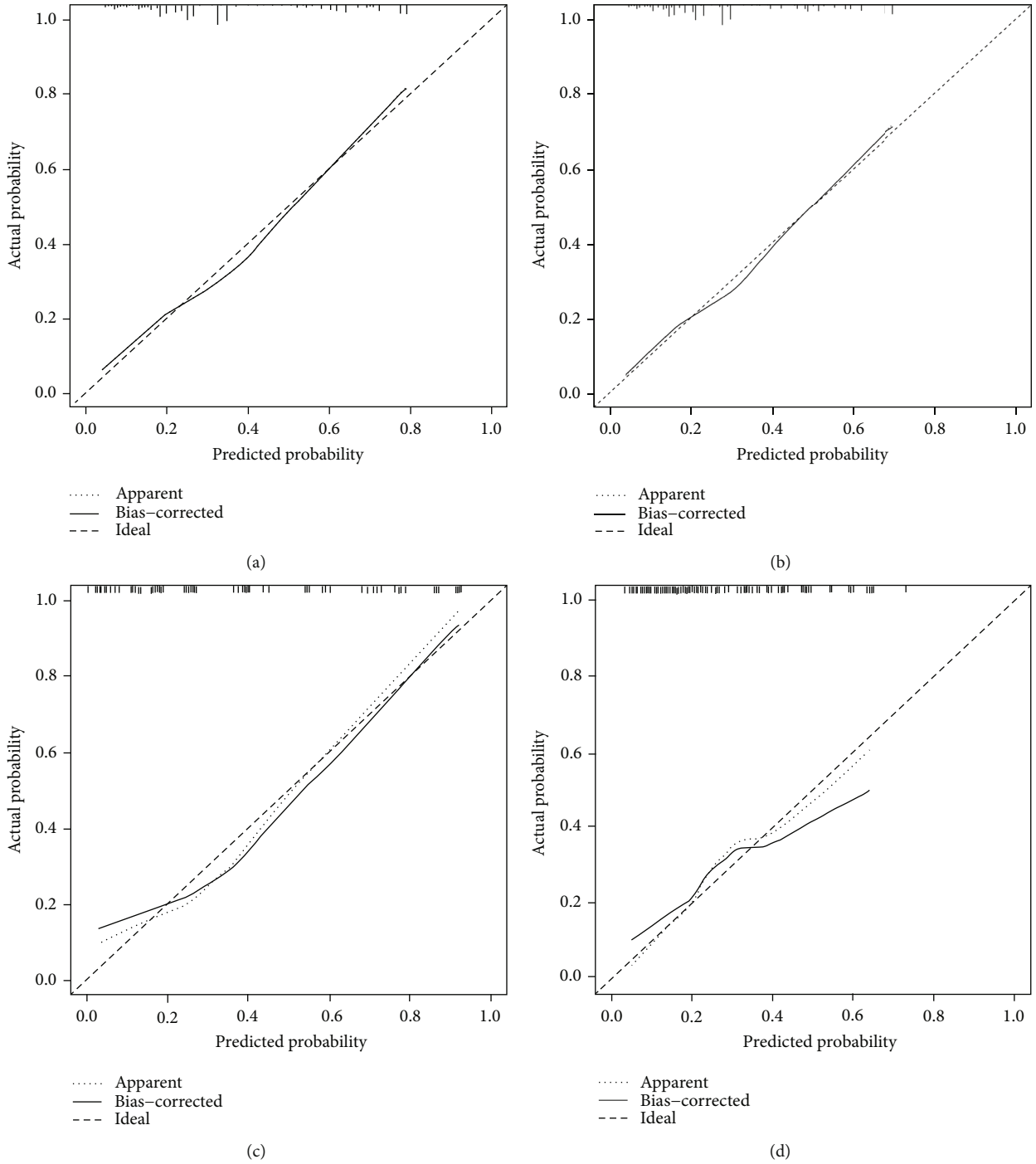
FIGURE 3: The calibration plots for the nomogram of overall early death (a) and specific early death (b) in the SEER database. The calibration plots for the nomogram of overall early death (c) and specific early death nomogram (d) in the validation cohort.

nomogram plays an important role in disease heterogeneity and individualized therapy. In validation, we found that there was a good agreement between predicted early deaths and actual deaths. Besides that, DCA analysis revealed that our nomogram models had a good clinical value and utility in predicting survival.

The research has several strengths. Firstly, SEER database contains information of DLBCL patients, which

involves about 27.8% of cancerous patients in the US; thus, the information is reliable. Secondly, external data is used for validation, which makes the predictive models more realistic and credible. However, our study also exists some limitations. For instance, SEER is a high-quality registry that collects clinically relevant features for risk prediction and does not collect the frailty characteristics and gene information of older individuals. Besides, the

(a)

(b)

(c)

(d)
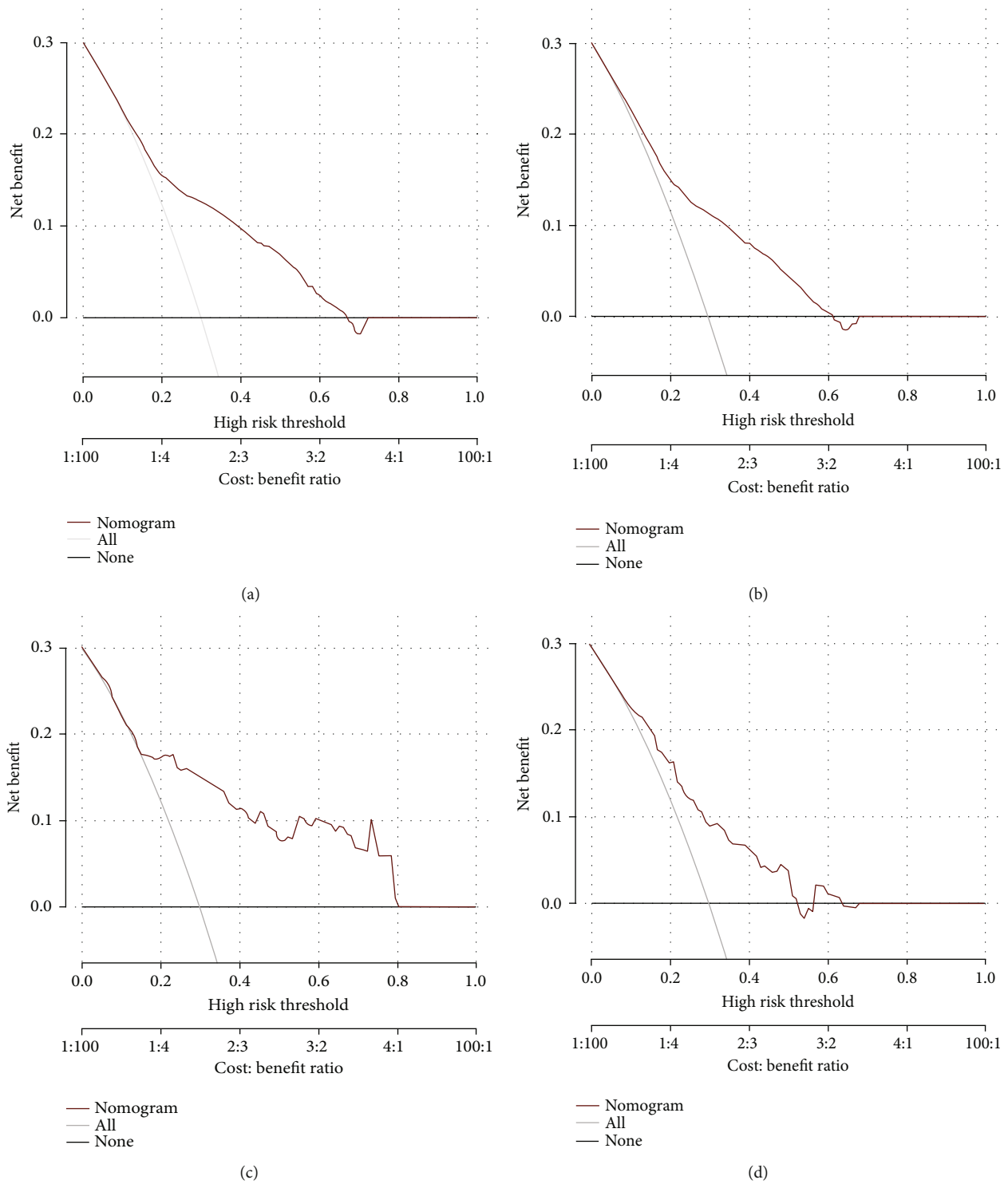
FIGURE 4: The decision curve analysis (DCA) for the nomogram of overall early death (a) and specific early death (b) in the SEER database. The decision curve analysis (DCA) for the nomogram of overall early death (c) and specific early death nomogram (d) in the validation cohort.

information of specific drugs of chemotherapy regimens is incomplete, and molecular pathological indicators are not involved in this research, which are also the limitation of our study.

5. Conclusion

In conclusion, marital status, Ann Arbor stage, surgical treatment, radiotherapy, and chemotherapy were risk factors

for elderly DLBCL patients. Dynamic nomogram models were constructed to predict the early OS and CSS of elderly DLBCL patients, which might be beneficial to elderly DLBCL patients' early death prediction and clinical application.

Data Availability

The datasets used and analyzed during the current study are available from the corresponding author on reasonable request.

Conflicts of Interest

The authors declare that they have no competing interests.

References

[1] N. Sukswai, K. Lyapichev, J. D. Khoury, and L. J. Medeiros, "Diffuse large B-cell lymphoma variants: an update," *Pathology*, vol. 52, no. 1, pp. 53–67, 2020.

[2] X. Gu, R. Zheng, C. Xia et al., "Interactions between life expectancy and the incidence and mortality rates of cancer in China: a population-based cluster analysis," *Cancer Communications*, vol. 38, no. 1, p. 44, 2018.

[3] J. Zhao, L. Su, and J. Zhong, "Risk factors for cancer-specific mortality and cardiovascular mortality in patients with diffuse large B-cell lymphoma," *Clinical Lymphoma Myeloma and Leukemia*, vol. 20, no. 11, pp. e858–e863, 2020.

[4] M. Pfreundschuh, L. Trümper, A. Osterborg et al., "CHOP-like chemotherapy plus rituximab versus CHOP-like chemotherapy alone in young patients with good-prognosis diffuse large-B-cell lymphoma: a randomised controlled trial by the MabThera International Trial (MInT) Group," *The Lancet Oncology*, vol. 7, no. 5, pp. 379–391, 2006.

[5] N. Howlader, L. M. Morton, E. J. Feuer, C. Besson, and E. A. Engels, "Contributions of subtypes of non-Hodgkin lymphoma to mortality trends," *Cancer Epidemiology, Biomarkers & Prevention*, vol. 25, no. 1, pp. 174–179, 2016.

[6] R. Camicia, H. C. Winkler, and P. O. Hassa, "Novel drug targets for personalized precision medicine in relapsed/refractory diffuse large B-cell lymphoma: a comprehensive review," *Molecular Cancer*, vol. 14, no. 1, p. 207, 2015.

[7] A. J. Olszewski, K. C. Mantripragada, and J. J. Castillo, "Risk factors for early death after rituximab-based immunochemotherapy in older patients with diffuse large B-cell lymphoma," *Journal of the National Comprehensive Cancer Network*, vol. 14, no. 9, pp. 1121–1129, 2016.

[8] P. A. Fields and D. C. Linch, "Treatment of the elderly patient with diffuse large B cell lymphoma," *British journal of haematology*, vol. 157, no. 2, pp. 159–170, 2012.

[9] K. Boslooper, R. Kibbelaar, H. Storm et al., "Treatment with rituximab, cyclophosphamide, doxorubicin, vincristine and prednisolone is beneficial but toxic in very elderly patients with diffuse large B-cell lymphoma: a population-based cohort study on treatment, toxicity and outcome," *Leukemia & Lymphoma*, vol. 55, no. 3, pp. 526–532, 2014.

[10] V. P. Balachandran, M. Gonen, J. J. Smith, and R. P. DeMatteo, "Nomograms in oncology: more than meets the eye," *The Lancet Oncology*, vol. 16, no. 4, pp. e173–e180, 2015.

[11] C. Jin, J. Cao, Y. Cai et al., "A nomogram for predicting the risk of invasive pulmonary adenocarcinoma for patients with soli-tary peripheral subsolid nodules," *The Journal of thoracic and cardiovascular surgery*, vol. 153, no. 2, pp. 462–469.e1, 2017.

[12] Q. Tao, Q. Zeng, W. Liu et al., "A novel prognostic nomogram for hepatocellular carcinoma after thermal ablation," *American Journal of Cancer Research*, vol. 11, no. 10, pp. 5126–5140, 2021.

[13] J. Wu, H. Zhang, L. Li et al., "A nomogram for predicting overall survival in patients with low-grade endometrial stromal sarcoma: a population-based analysis," *Cancer Communications*, vol. 40, no. 7, pp. 301–312, 2020.

[14] D. Chihara, Y. Oki, M. A. Fanale et al., "Stage I non-Hodgkin lymphoma: no plateau in disease-specific survival ?," *Annals of Hematology*, vol. 98, no. 5, pp. 1169–1176, 2019.

[15] International Non-Hodgkin's Lymphoma Prognostic Factors Project, "A predictive model for aggressive non-Hodgkin's lymphoma," *The New England Journal of Medicine*, vol. 329, no. 14, pp. 987–994, 1993.

[16] Z. Zhou, L. H. Sehn, A. W. Rademaker et al., "An enhanced International Prognostic Index (NCCN-IPI) for patients with diffuse large B-cell lymphoma treated in the rituximab era," *Blood*, vol. 123, no. 6, pp. 837–842, 2014.

[17] L. Oberic, F. Peyrade, M. Puyade et al., "Subcutaneous rituximab-MiniCHOP compared with subcutaneous rituximab-MiniCHOP plus lenalidomide in diffuse large B-cell lymphoma for patients age 80 years or older," *Journal of Clinical Oncology*, vol. 39, no. 11, pp. 1203–1213, 2021.

[18] M. Di, S. F. Huntington, and A. J. Olszewski, "Challenges and opportunities in the management of diffuse large B-cell lymphoma in older patients," *The Oncologist*, vol. 26, no. 2, pp. 120–132, 2021.

[19] K. T. Prochazka, T. Melchardt, F. Posch et al., "NCCN-IPI score-independent prognostic potential of pretreatment uric acid levels for clinical outcome of diffuse large B-cell lymphoma patients," *British Journal of Cancer*, vol. 115, no. 10, pp. 1264–1272, 2016.

[20] C. Montalbán, A. Díaz-López, I. Dlouhy et al., "Validation of the NCCN-IPI for diffuse large B-cell lymphoma (DLBCL): the addition of β2-microglobulin yields a more accurate GEL-TAMO-IPI," *British Journal of Haematology*, vol. 176, no. 6, pp. 918–928, 2017.

[21] M. Ziepert, D. Hasenclever, E. Kuhnt et al., "Standard international prognostic index remains a valid predictor of outcome for patients with aggressive CD20+ B-cell lymphoma in the rituximab era," *Journal of Clinical Oncology*, vol. 28, no. 14, pp. 2373–2380, 2010.

[22] S. F. Cho, Y. C. Liu, H. H. Hsiao et al., "Investigation on treatment strategy, prognostic factors, and risk factors for early death in elderly Taiwanese patients with diffuse large B-cell lymphoma," *Scientific reports*, vol. 7, no. 1, p. 44282, 2017.

[23] W. van Gijn, R. van Stiphout, C. van de Velde et al., "Nomograms to predict survival and the risk for developing local or distant recurrence in patients with rectal cancer treated with optional short-term radiotherapy," *Annals of Oncology*, vol. 26, no. 5, pp. 928–935, 2015.

[24] Z. Huang, C. Hu, K. Liu et al., "Risk factors, prognostic factors, and nomograms for bone metastasis in patients with newly diagnosed infiltrating duct carcinoma of the breast: a population-based study," *BMC Cancer*, vol. 20, no. 1, p. 1145, 2020.

[25] Y. Wang, J. Song, S. Wen, and X. Zhang, "A visual model for prognostic estimation in patients with primary diffuse large

B-cell lymphoma of small intestine and colon: analysis of 1,613 cases from the SEER database," *Translational Cancer Research*, vol. 10, no. 4, pp. 1842–1855, 2021.

Hindawi

Research Article

Prognosis and Novel Drug Targets for Key lncRNAs of Epigenetic Modification in Colorectal Cancer

Peng Zhang ⬤,[1] Tingting Zhang,[2] Denggang Chen,[1] Li Gong,[3] and Min Sun ⬤[1]

[1]*Department of General Surgery, Taihe Hospital, Hubei University of Medicine, Shiyan, China*
[2]*Department of Clinical Oncology, Taihe Hospital, Hubei University of Medicine, Shiyan, China*
[3]*Department of Endocrinology, Taihe Hospital, Hubei University of Medicine, Shiyan, China*

Correspondence should be addressed to Min Sun; sunmin-0715@163.com

Peng Zhang, Tingting Zhang, and Denggang Chen contributed equally to this work.

Background. Colorectal cancer (CRC) has been the 3rd most commonly malignant tumor of the gastrointestinal tract in the world. 5-Methylcytosine (m^5C) and long noncoding RNAs (lncRNAs) have an essential role in predicting the prognosis and immune response for CRC patients. Therefore, we built a m^5C-related lncRNA ($m^5CRlncRNA$) model to investigate the prognosis and treatment methods for CRC patients. *Methods.* Firstly, we secured the transcriptome and clinical data for CRC from The Cancer Genome Atlas (TCGA). Then, $m^5CRlncRNAs$ were recognized by coexpression analysis. Then, univariate Cox, least absolute shrinkage and selection operator (LASSO), and multivariate Cox regression analyses were utilized to build m^5C-related prognostic characteristics. Besides, Kaplan-Meier analysis, ROC, PCA, *C*-index, enrichment analysis, and nomogram were performed to investigate the model. Additionally, immunotherapy responses and antitumor medicines were explored for CRC patients. *Results.* A total of 8 m^5C-related lncRNAs (AC093157.1, LINC00513, AC025171.4, AC090948.2, ZEB1-AS1, AC109449.1, AC009041.3, and LINC02516) were adopted to construct a risk model to investigate survival and prognosis for CRC patients. CRC samples were separated into low- and high-risk groups, with the latter having a worse prognosis. The m^5C-related lncRNA model helps us to better distinguish immunotherapy responses and IC50 of antitumor medicines in different groups of CRC patients. *Conclusion.* The research may give new perspectives on tailored therapy approaches as well as novel theories for forecasting the prognosis of CRC patients.

1. Introduction

In terms of cancer-related deaths, colorectal cancer (CRC) is the third most frequent malignant tumor worldwide [1]. The recent epidemiological surveys showed that CRC contributes to 10% of all diagnosed cancers and 9.4% of cancer-related deaths [2]. The high incidence and low survival rate of CRC imposed a heavy economic burden and enormous public health pressure on the government. At present, the main clinical treatment strategies for CRC include surgery, chemotherapy, and radiotherapy, but with poor prognosis, easy recurrence, and significant side effects [3]. In order to better understand CRC, it is urgently needed to select key CRC-related genes, elucidate the potential path-

ogenesis of CRC, and develop novel diagnostic and therapeutic strategies for CRC.

Numerous studies have found that RNA modifications in epigenetic changes are intimately related to the progression of different types of tumors [4, 5]. At present, more than 150 RNA modifications have been recognized, such as N1-methyladenosine (m^1A), 5-methylcytosine (m^5C), N6-methyladenosine (m^6A), 7-methylguanosine (m^7G), microRNA, and long noncoding RNA (lncRNA) [6]. With the in-depth study of RNA modification, m^5C has received increasing attention from scholars around the world. As a widespread RNA modification of noncoding and coding RNAs, m^5C has a crucial function in the regulation of physiological and pathological processes in the organism [7]. A

study demonstrated that m^{5}C regulators were linked to the occurrence and progression of cancer [8]. In bladder cancer, the m^{5}C modification writer NSUN2 modulates HDGF expression in a m^{5}C-dependent manner in order to promote cancer development [9].

lncRNA is the nonprotein-coding RNA fraction of over 200 nucleotides in length that cannot be translated into protein [10]. It has been shown that RNA methylation of lncRNAs could impact cancer progression [11]. With the advancement of sequencing technology, m^{5}C was found to be extensively distributed in lncRNAs. However, the utility of m^{5}C in lncRNAs is still uncertain. Therefore, identifying m^{5}C-related lncRNAs (m^{5}CRlncRNAs) in CRC pathogenesis may help provide a rational basis for targeted therapy and prognosis.

In this study, bioinformatics analysis was used to examine the potential contribution of m^{5}CRlncRNAs to CRC. The Cancer Genome Atlas was used to obtain a database of m^{5}C genes and lncRNAs (TCGA). Then, using Pearson's correlation analysis, we were able to identify the m^{5}CRlncRNA. Additionally, a brand-new risk model for the m^{5}CRlncRNA was developed to forecast overall survival (OS) in CRC patients. We also created a nomogram incorporating clinical data to predict the overall survival of CRC patients. Finally, we looked for the connection between immunotherapy responses.

2. Materials and Methods

2.1. Data Acquisition. TCGA database was utilized to retrieve RNA transcriptome data, relevant clinical information, and mutation data from CRC samples. We used the R package to process the downloaded files. To reduce statistical bias, we excluded CRC patients with absent OS values and short OS values (<30 days).

2.2. Identification m^{5}C Genes and m^{5}CRlncRNAs. Based on previous publications [12, 13], we extracted 17 m^{5}C regulators from TCGA-CRC, including expression data on 11 writers, 2 readers, and 4 erasers (Supplementary Table 1). Then, we screened m^{5}CRlncRNA by Pearson correlation analysis, and we derived 2,028 m^{5}CRlncRNA. $|R| > 0.5$ and $p < 0.001$ were the threshold criteria.

2.3. Construction of a Risk Model. TCGA dataset was randomly distributed into a training set and a testing set (ratio: 0.7 : 0.3; sample: 355 : 148). We used the entire set to construct a m^{5}CRlncRNA risk model, and the training set and testing set were employed to verify the risk model. No significant differences were found in the clinical features of CRC patients between the two sets (Table 1). We utilized univariate Cox analysis of the filtered 14 m^{5}CRlncRNA in combination with CRC survival information ($p < 0.01$). Besides, we adopted the least absolute shrinkage and selection operator (LASSO) and Cox regression analyses to construct a risk assessment model that consisted of 8 m^{5}CRlncRNAs via the R package "glmnet" [14]. According to median risk scores, the CRC patients were assigned to low- and high-risk groups [15]. And the risk score was calculated as follows: $\sum_{i=1}^{k} \beta i S i$.

2.4. Validation of the Risk Signature. By using the "survminer" and "survive" packages in the R programming language, Kaplan-Meier survival analysis was employed to compare the clinical outcomes of the two groups. The time-dependent receiver-operating characteristic curves (ROC) and the area under the curve (AUC) were employed to confirm the accuracy of the model. We also grouped patients according to clinical characteristics to assess the ability of the model to predict prognosis across clinical characteristics. Principal component analysis (PCA) was employed for effective dimension reduction, model recognition, and exploratory visualization of high-dimensional data of the whole gene expression profiles, m^{5}C genes, m^{5}CRlncRNAs, and a risk model on the basis of the expression patterns of the m^{5}CRlncRNAs. A consistency index (*C*-index) was applied to determine the accuracy of the model compared to the traditional clinical features.

2.5. Construction of Predictive Nomogram. We developed a nomogram to predict the clinical features for the 1-, 3-, and 5-year OS of CRC patients via the R package of "rms.".

2.6. Evaluation of Enrichment Analysis. A clusterProfiler R package was used to perform GO enrichment analysis and KEGG pathway analysis to explore possible biological functions. $p < 0.05$ indicated that the functional pathways had significant enrichment.

2.7. Assessment of the Prognostic Features in the Tumor Immune Microenvironment. Studying how the model interacts with the tumor microenvironment, we measured the infiltration values for TCGA-CRC dataset samples on the basis of these algorithms: XCELL [16], TIMER [17], QUANTISEQ [18], MCPCOUNTER [19], EPIC [20], CIBERSORT-ABS [21], and CIBERSORT [22]. Additionally, we adopted single-sample GSEA (ssGSEA) for scoring CRC-infiltrating immune cells to quantify the tumor-infiltrating immune cells between different groups. Furthermore, we also evaluated the immune checkpoint activation among different groups.

2.8. Investigation of Immunotherapy Response. The mutation data was assessed and summarized by the "maftools" of R package. Based on tumor-specific mutated genes, we calculated the tumor mutational burden (TMB). In addition, the tumor immune dysfunction and exclusion (TIDE) algorithm was performed to estimate the probability of an immunotherapeutic response.

2.9. Exploration of Antitumor Agents. To predict therapeutic response, the "pRRophetic" R package was employed to determine the half-maximal inhibitory concentration (IC50) of commonly used antitumor drugs in different risk groups.

3. Results

3.1. Screen of m^{5}CRlncRNAs in CRC Patients. A total of 17 m^{5}C genes and 16,876 lncRNAs were selected from TCGA datasets. We found 2,028 lncRNAs that were strongly linked to one of the 17 m^{5}C genes ($|R| > 0.5$ and $p < 0.001$)

TABLE 1: The clinical characteristics of the different sets.

| Covariates	Type	Total set	Training set	Testing set	p value
Age	≤65	227 (45.13%)	161 (45.35%)	66 (44.59%)	0.9543
	>65	276 (54.87%)	194 (54.65%)	82 (55.41%)	
Gender	Female	225 (44.73%)	157 (44.23%)	68 (45.95%)	0.7985
	Male	278 (55.27%)	198 (55.77%)	80 (54.05%)	
Race	Asian	9 (1.79%)	6 (1.69%)	3 (2.03%)	0.9398
	Black or African American	246 (48.91%)	175 (49.3%)	71 (47.97%)	
	White	248 (49.3%)	174 (49.01%)	74 (50%)	
Radiation	No	466 (92.64%)	329 (92.68%)	137 (92.57%)	1
	Yes	37 (7.36%)	26 (7.32%)	11 (7.43%)	
Pharmaceutical therapy	No	301 (59.84%)	212 (59.72%)	89 (60.14%)	1
	Yes	202 (40.16%)	143 (40.28%)	59 (39.86%)	
Pathological stage	Stage I	91 (18.09%)	61 (17.18%)	30 (20.27%)	0.7053
	Stage II	180 (35.79%)	129 (36.34%)	51 (34.46%)	
	Stage III	155 (30.82%)	113 (31.83%)	42 (28.38%)	
	Stage IV	77 (15.31%)	52 (14.65%)	25 (16.89%)	
Stage T	T1	17 (3.38%)	12 (3.38%)	5 (3.38%)	0.0901
	T2	92 (18.29%)	60 (16.9%)	32 (21.62%)	
	T3	343 (68.19%)	253 (71.27%)	90 (60.81%)	
	T4	50 (9.94%)	30 (8.45%)	20 (13.51%)	
	Tis	1 (0.2%)	0 (0%)	1 (0.68%)	
Stage M	M0	377 (74.95%)	267 (75.21%)	110 (74.32%)	0.7588
	M1	77 (15.31%)	52 (14.65%)	25 (16.89%)	
	Mx	49 (9.74%)	36 (10.14%)	13 (8.78%)	
Stage N	N0	283 (56.26%)	200 (56.34%)	83 (56.08%)	0.7087
	N1	126 (25.05%)	86 (24.23%)	40 (27.03%)	
	N2	92 (18.29%)	67 (18.87%)	25 (16.89%)	
	Nx	2 (0.4%)	2 (0.56%)	0 (0%)	
Status	Alive	403 (80.12%)	284 (80%)	119 (80.41%)	1
	Dead	100 (19.88%)	71 (20%)	29 (19.59%)	

No: the patient have not receive the treatment; Tis: carcinoma in situ; Mx: unknown M stage; Nx: unknown N stage.

(Supplementary Table 2). As shown in Figure 1(a), the m^{5}C-lncRNA expression network was visualized via the Sankey diagram. Figure 1(b) depicts the relationship between m^{5}C genes and m^{5}CRlncRNAs in TCGA datasets.

3.2. Construction and Validation of a Risk Model. We adopted univariate Cox regression analysis to select 14 prognostic m^{5}CRlncRNAs (Supplementary Figure S1A). The LASSO-Cox regression algorithm was performed to construct the risk signature, including 8 m^{5}CRlncRNAs (AC093157.1, LINC00513, AC025171.4, AC090948.2, ZEB1-AS1, AC109449.1, AC009041.3, and LINC02516) in CRC (Figures 2(a)–2(c)). In addition, Kaplan-Meier analysis revealed a significant difference between distinct groups ($p < 0.05$, Figure 2(d)). In Figure 2(e), the 1-, 3-, and 5-year AUC values were 0.746, 0.717, and 0.792,

which demonstrated that CRC patients have a better prognosis. Furthermore, the AUC value of the signature was 0.792, which was notably higher than that of clinicopathological characteristics, including age (0.646), gender (0.481), and stage (0.737; Figure 2(f)). The Kaplan-Meier analyses and ROC curves of training set and testing set indicated that the prediction accuracy of the model is satisfactory (Supplementary Figure S1B-E).

Next, we studied the differences in clinical outcomes among distinct groups stratified by clinical characteristics. Kaplan-Meier survival analysis demonstrated that our model can be applied to a variety of clinical characteristics (Figure 3(a)). The PCA analysis showed that the distributions of the two groups were relatively dispersed, which indicated diverse groups had different distributions on the basis of the signature (Figure 3(b)). And the C-index of the model
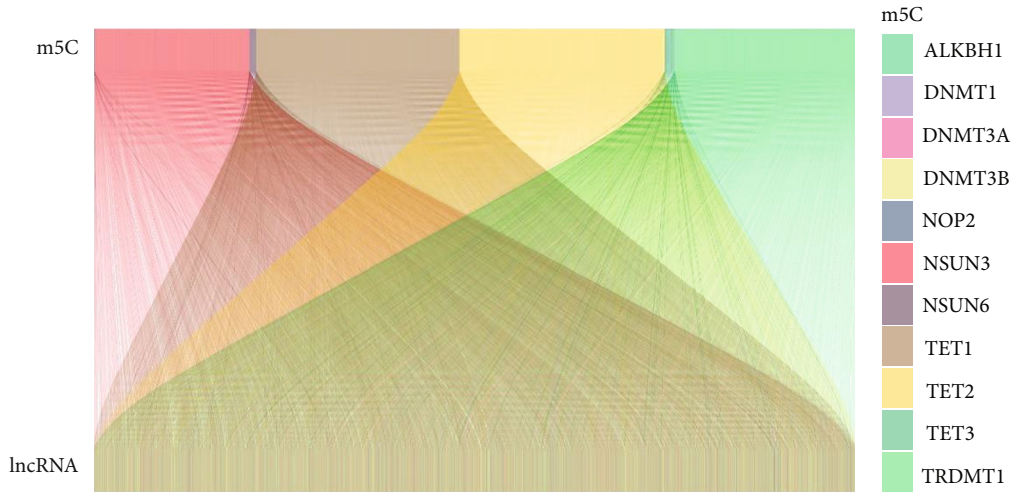
(a)
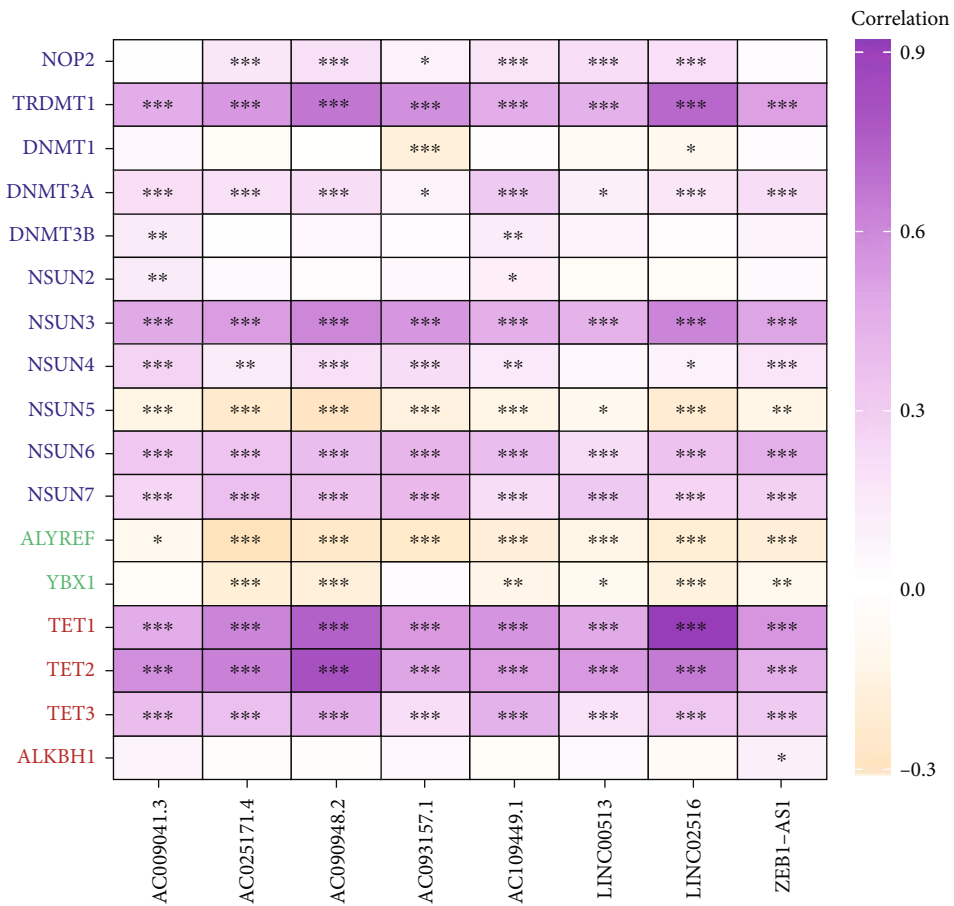
***$p < 0.001$
**$p < 0.01$
*$p < 0.05$

(b)

FIGURE 1: Identification of m⁵CRlncRNAs. (a) A Sankey plot for the network of m⁵C genes and associated m⁵CRlncRNAs. (b) Heatmap for correlation between 17 m⁵C genes and 8 m⁵CRlncRNAs.

was superior to the clinicopathological features, indicating that this model could better predict the prognosis of CRC patients (Figure 4(a)).

3.3. Construction of Nomogram and Calibration in CRC Patients. As shown in Figure 4(b), the calibration curves of a nomogram revealed good accordance between the predicted
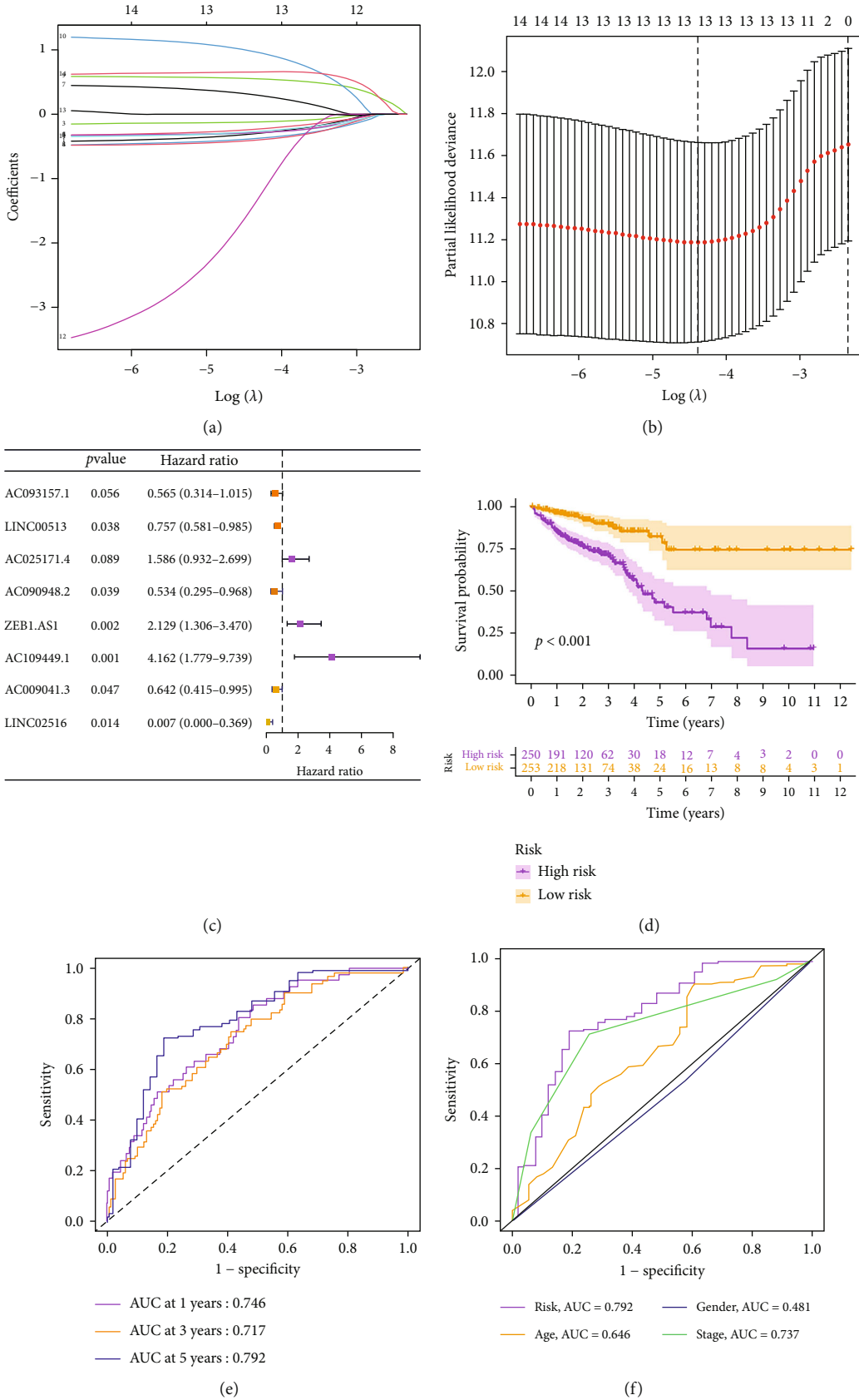
FIGURE 2: Construction of a risk signature for m⁵CRlncRNAs. (a, b) The LASSO regression algorithm to screen candidate m⁵CRlncRNAs. (c) Multivariate Cox regression analysis to develop a risk model. (d) Kaplan-Meier curves. (e) The 1-, 3-, and 5-year ROC curves of the entire set. (f) The 5-year ROC curves of the model and clinical characteristics.
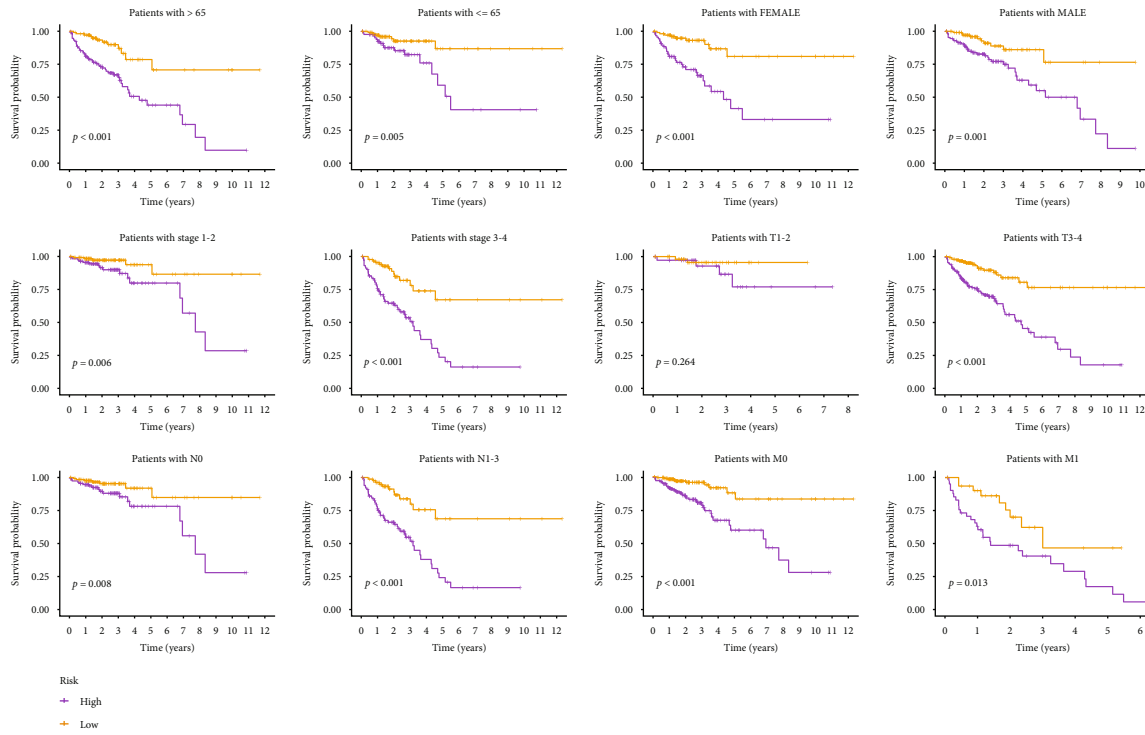
(a)
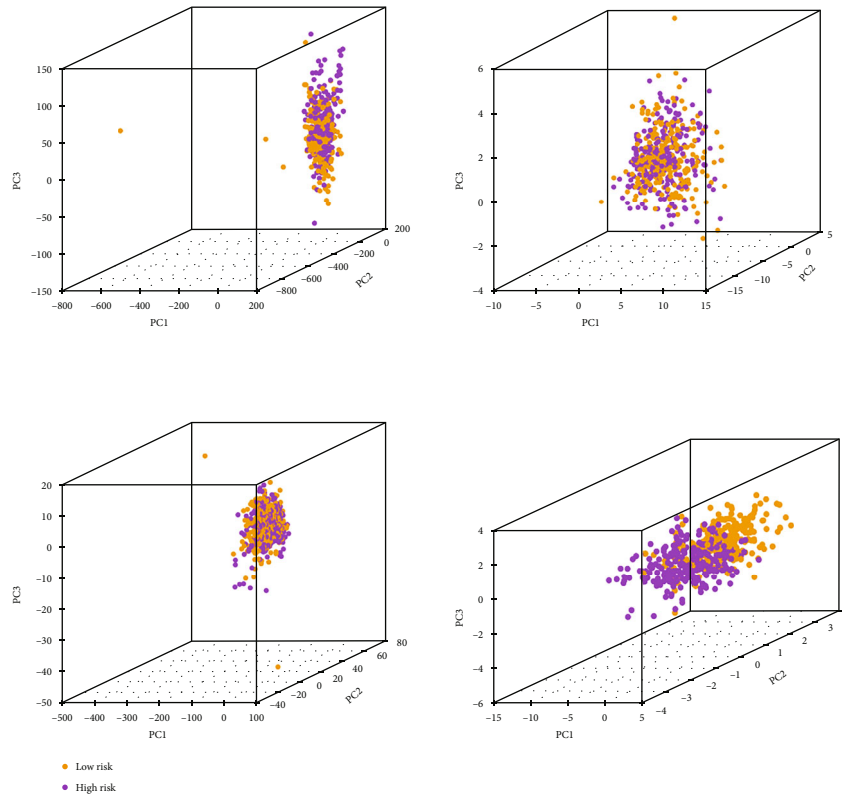
(b)

FIGURE 3: Validation of a risk signature. (a) Kaplan-Meier curves grouped by age, gender, clinical stage, T, N, or M. (b) PCA comparison on the basis of entire gene profiles, m^5C genes, lncRNAs, and m^5CRlncRNAs in TCGA entire set.

(a)

(b)

(c)
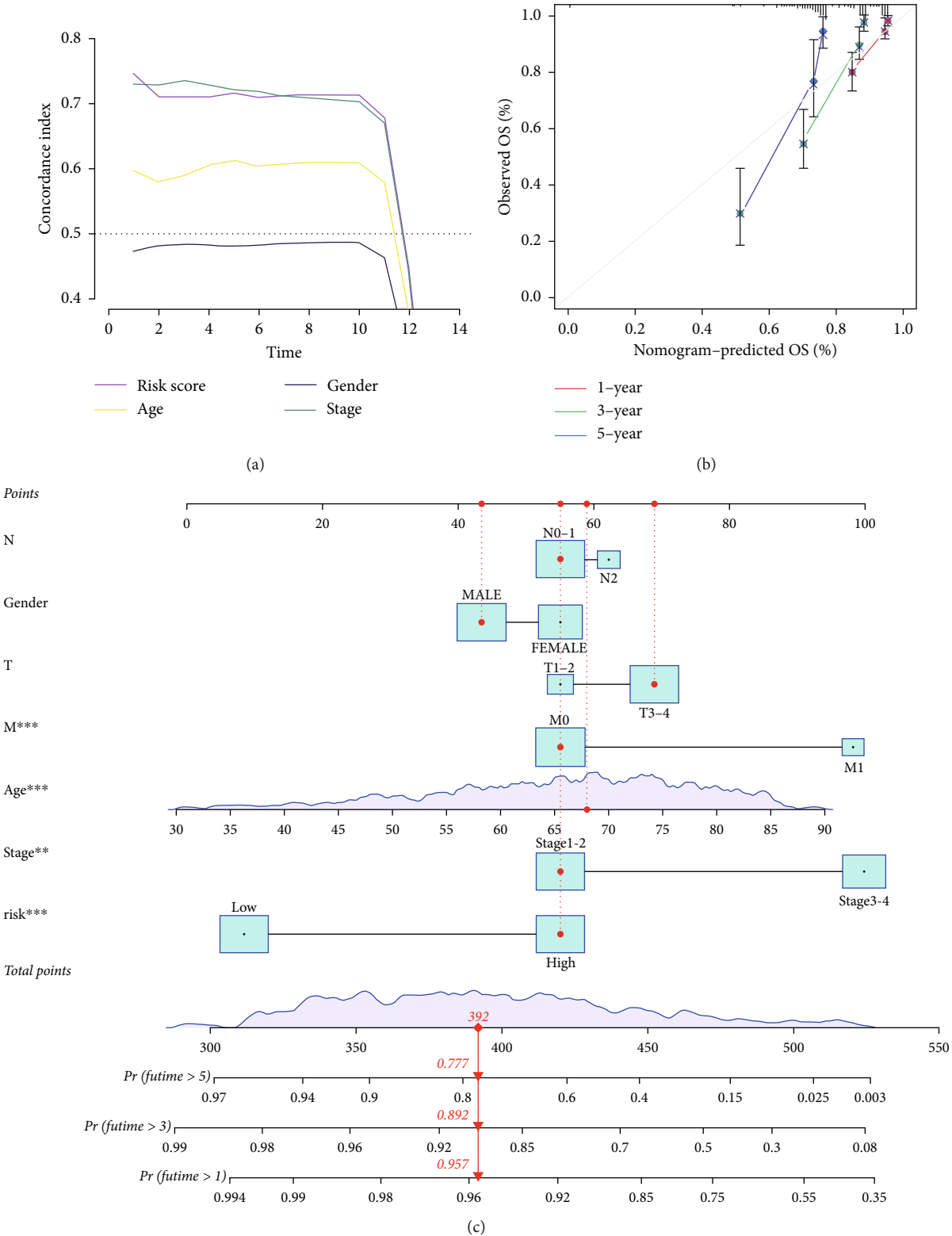
FIGURE 4: Evaluation of the m⁵CRlncRNAs model and development of a nomogram. (a) *C*-index of clinical characteristics and the model. (b) Calibration plot of a nomogram. (c) The nomogram predicts the ability of 1-, 3-, and 5-years OS rates of CRC patients.

1-, 3-, and 5-year OS rates and actual observations. And the nomogram was established to demonstrate the superior predictive power of m⁵C compared to clinical features (Figure 4(c)).

3.4. *Functional Enrichment Analysis.* The GO analysis (Figure 5(a)) showed that the terms were mainly enriched in the signaling receptor activator activity and receptor ligand activity of biological processes (BP), the apical part

(a)

(b)

FIGURE 5: The enrichment analyses. (a) The GO analyses results. (b) The KEGG analysis results.

of cell and presynapse of cellular component (CC), and the epidermis development and skin development of molecular function (MF) (Supplementary Table 3). The KEGG analysis showed that the terms were mainly enriched in hsa04978, hsa04972, hsa04020, hsa00040, hsa05226, and hsa04390 (Figure 5(b)) (Supplementary Table 4).

3.5. Evaluation of Tumor Immune Microenvironment. To further explore whether the m⁵CRlncRNA was related to the TIME, we assessed the relationship between the signature and tumor-infiltrating im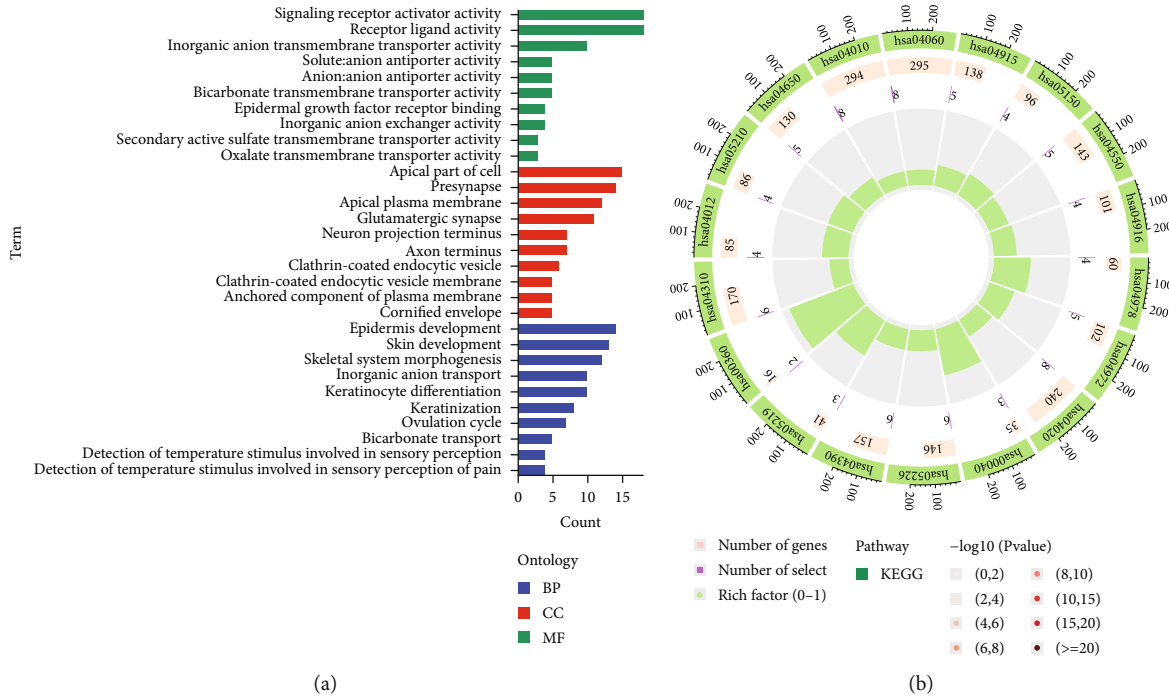mune cells. Significant correlations were noted between the abundance of these tumor-infiltrating immune cells and increased CRC risk (Figure 6(a)) (Supplementary Table 5). The ssGSEA results showed that HLA, type I IFN response, and type II IFN response of patients in the low-risk group were lower compared to high-risk group ($p < 0.05$, Figure 6(b)). We further investigated the immune checkpoints, and the results revealed significant differences in the distribution of immune checkpoint-related molecule expression among different groups. We examined the expression levels of 46 immune checkpoint genes, 14 of which differed in expression in the high- and low-risk groups. The immune checkpoints of TNFRSF15 and HHLA2 in the low-risk group were higher ($p < 0.05$) (Figure 6(c)). The above findings might imply that the low-risk group was more immunologically active and might be more sensitive to immunotherapy.

3.6. Evaluation of Immunotherapy. On the basis of the somatic mutational data from TCGA, we calculated the mutation frequency among different groups. And the mutation frequencies of the different groups were depicted by the

waterfall chart. It found that 223 of 232 (96.12%) CRC samples in the high-risk group and 219 of 234 (93.59%) CRC samples in the low-risk group displayed genetic mutations, and missense mutation was the most common variant classification. In addition, APC had high genetic alterations (72%), which was only lower than that of TP53 (60%) in the high-risk group (Figure 7(a)). APC had the highest genetic alterations (79%) (Figure 7(b)). Then, we evaluated the relationship between different groups and immunotherapy biomarkers. As exhibited in Figures 7(c) and 7(d), we observed that the high-risk group was more sensitive to immunotherapy, suggesting that the m⁵C-based classifier index may be a predictor of tumor mutation burden and TIDE. Finally, we used Kaplan-Meier curve analysis of patient OS based on TMB. As displayed in Figure 7(e), a significant difference was observed between patients in the high TMB and low TMB groups ($p < 0.05$). We further investigated whether the m⁵CRlncRNA model could predict OS outcomes greater than TMB alone. Compared with other groups, the low-risk group with high TMB had the best prognosis among those of the other three groups ($p < 0.001$) (Figure 7(f)). In summary, the signature of m⁵CRlncRNA has greater prognostic implications than that of TMB.

3.7. Selection Potential Antitumor Drugs by m⁵CRlncRNA Model. To identify for potential drugs targeting the m⁵CRlncRNA model for the treatment of CRC patients, the pRRophetic algorithm was implemented to assess therapeutic efficacy according to the IC50 of each data. In addition, we noticed that the sensitivity of the two groups differed significantly for 23 compounds by predicting the potential therapeutic agents. As shown in Figure 8, we

(a)

(b)

(c)
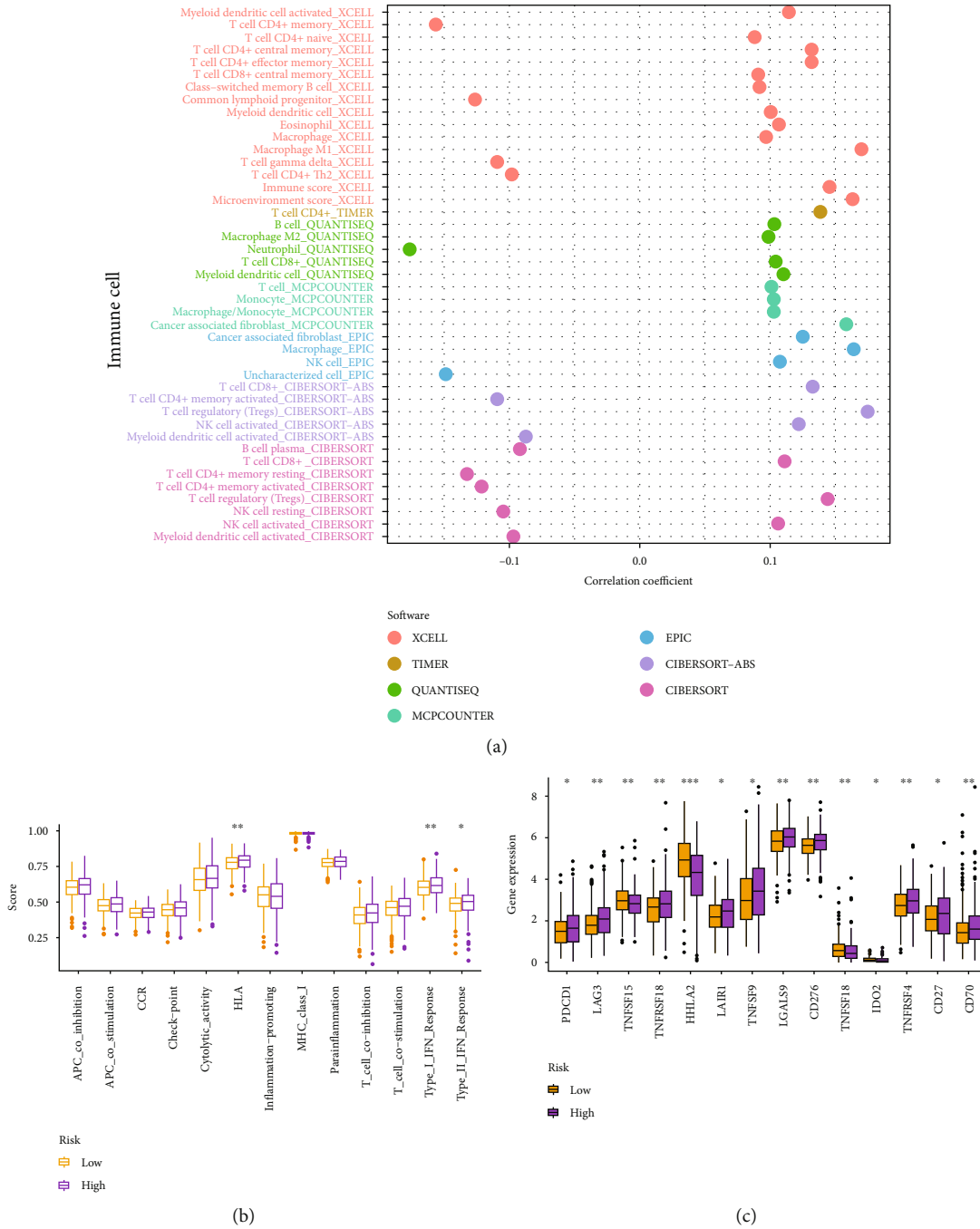
FIGURE 6: Immune analysis based on m⁵CRlncRNAs signature. (a) The immune cell bubble. (b) Immune functions scores between different groups. (c) Expression of immune checkpoint-related molecules.

detected that the low-risk group was closely connected with chemotherapeutic agents with higher IC50, suggesting that low-risk patients were more responsive to chemotherapeutic drugs.

4. Discussion

Many experts and scholars have concentrated on exploring the pathogenesis and treatment strategies of CRC in recent years [23]. Despite the fact that surgery, chemotherapy, radiotherapy, and targeted therapy were used for CRC patients, treatment outcomes were poor, and 5-year survival rates were low [24]. In recent years, research has demonstrated that cancer patients with different clinical characteristics and subgroups are likely to have a different prognosis and response to treatment [25, 26]. Thus, it is vital to investigate effective and personalized treatment options for the prognosis and management of CRC.

Firstly, we downloaded the lncRNA data of CRC patients from TCGA database. According to univariate Cox, LASSO,

(a)

(b)

(c)

(d)

(e)

(f)
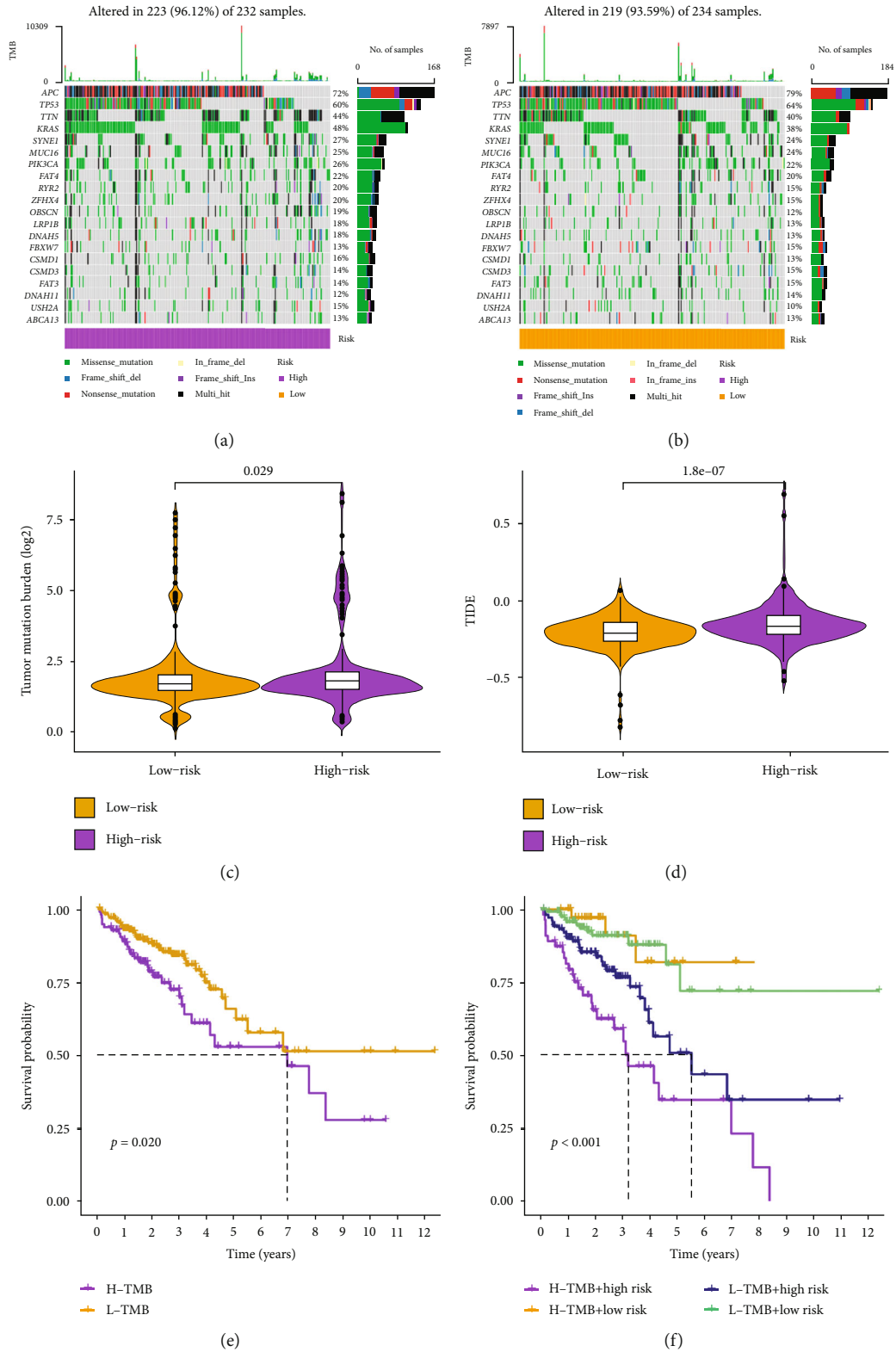
FIGURE 7: Assessment of immunotherapy response. (a, b) Waterfall plots revealed mutation information for genes with high mutation frequency. (c, d) TMB and TIDE of different groups. (e) Kaplan-Meier curve analysis different TMB groups. (f) Kaplan-Meier curve analysis of patient OS according to TMB and different risk groups.
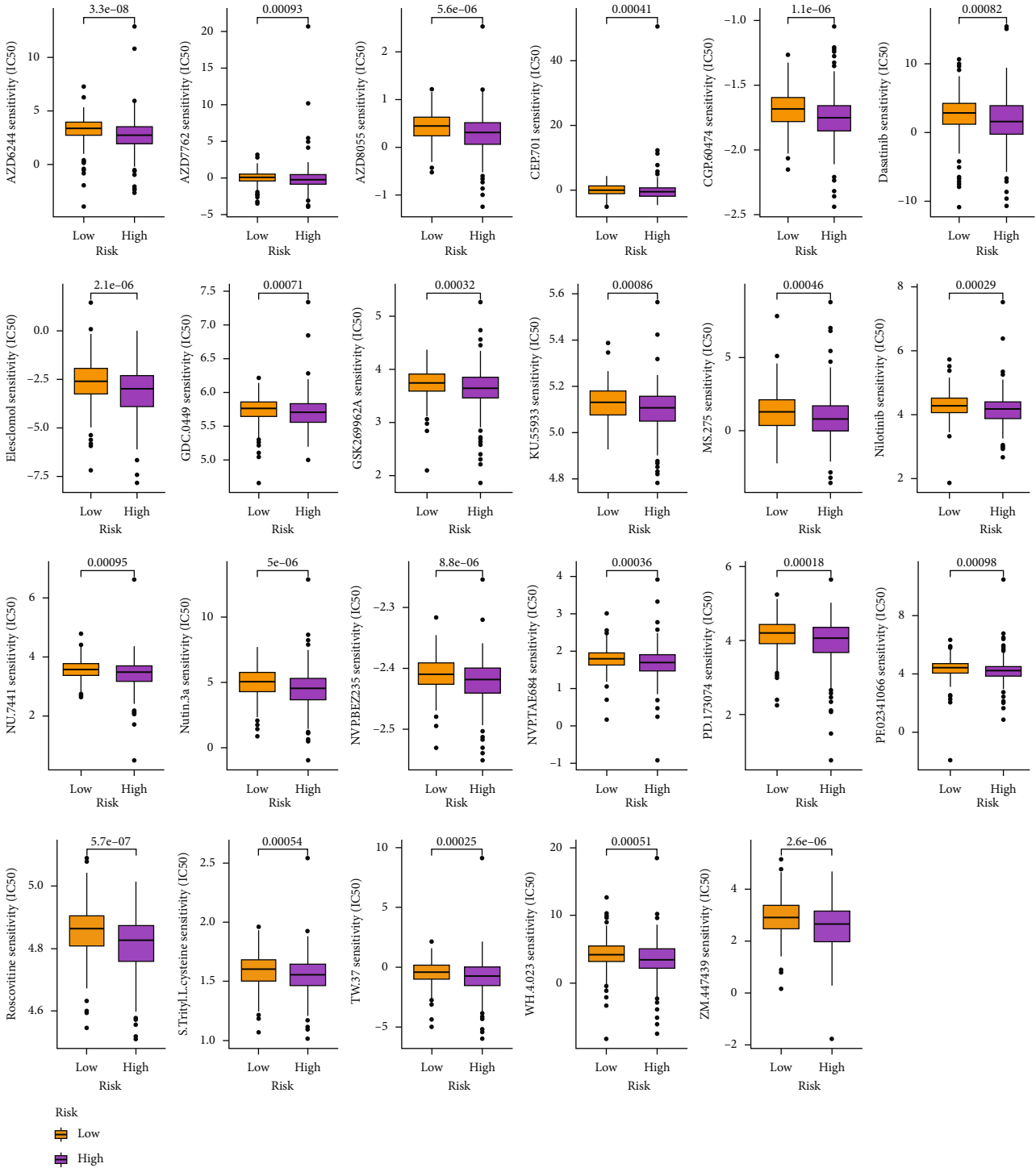
FIGURE 8: Selection of antitumor drugs.

and multivariate Cox regression analysis, 8 m5CRlncRNAs (AC093157.1, LINC00513, AC025171.4, AC090948.2, ZEB1-AS1, AC109449.1, AC009041.3, and LINC02516) were determined to be significant prognostic factors to explore the prognostic function in CRC. In recent years, lncRNAs have been linked to cancer survival and development in many studies [27, 28]. And ZEB1-AS1 was found to be a tumor-related lncRNA prognostic factor in CRC

[29]. In addition, a study revealed that regulation of LINC00513 lncRNA expression can affect disease susceptibility in systemic lupus erythematosus [30]. Besides, other lncRNAs were screened for the first time as prognostic markers for CRC. Based on 8 m5CRlncRNAs, we built a risk assessment model to further investigate the association between m5CRlncRNA and CRC. Next, CRC patients were divided into different risk groups based on median scores,

and the high-risk group had a lower clinical survival rate. There were similar results found in the analysis of subgroups categorized by gender, age, and tumor stage. Additionally, PCA analysis also supported the grouping ability of m^{5}C. As part of the present study, we developed a nomogram with clinical characteristics and m^{5}CRlncRNAs. These results suggest that OS was shorter in the high-risk group, with better concordance between 1-year, 3-year, and 5-year observation and predicted OS rates.

Furthermore, we investigated the associations between risk groups and TMB and TIME. The TMB is regarded as the total number of somatic cell-encoded mutations that lead to neoantigens being generated that trigger antitumor immunity [31]. A large number of studies have proven that TMB is a powerful biomarker for predicting the efficacy of checkpoint inhibitors in cancer [32, 33]. In the high-risk group, TMB appeared to be significantly higher. Additionally, TIDE is a computational framework for simulating tumor immune evasion and is usually applied to forecast the effects of immune checkpoint inhibition therapy [34]. Our results demonstrated that the low-risk group was predicted to have a superior response to immunotherapy. To probe the therapeutic potential of the identified m^{5}CRlncRNAs for CRC patients, we analyzed their sensitivity to different drugs. And we discovered that the low-risk group was significantly related to chemotherapeutic agents with higher IC50. Altogether, the above results help us to further predict the prognosis of CRC and elucidate the molecular biological mechanism between m^{5}CRlncRNAs and CRC.

However, there are several issues with the research. First off, we lack external datasets to validate the prediction accuracy of the risk model since there are not any lncRNA-related CRC datasets in the Gene Expression Omnibus (GEO) database. Second, because of the study's limited sample size, there could be some bias in the data analysis. Thirdly, there is no experimental validation of analytical findings in the research to demonstrate the use of the risk model in clinical treatment. Therefore, we will try to verify the validity of the signature utilizing animal and cellular tests.

Overall, our study did provide not only new insights into individualized treatment strategies for patients with CRC but also new ideas for predicting the prognosis of these patients. In addition, this study might contribute to further exploring the biological functions of m^{5}C-regulated lncRNAs.

Data Availability

The original contributions presented in the study are included in the article/Supplementary Material. Further inquiries can be directed to the corresponding author.

Conflicts of Interest

The authors declare that the research was conducted in the absence of any commercial or financial relationships that could be construed as a potential conflict of interest.

Authors' Contributions

MS and PZ designed the study. PZ, TTZ, DGC, and LG performed data analysis. PZ, TTZ, DGC, and LG drafted the manuscript. TTZ, LG, and MS revised the manuscript. All authors read and approved the final manuscript. Peng Zhang, Tingting Zhang, and Denggang Cheng contributed equally to this work.

Acknowledgments

Supplementary Materials

Supplementary 1. Supplementary Figure S1: (a) the prognostic m^{5}CRlncRNAs by univariate Cox regression analysis. (b–e) Kaplan-Meier curves and the 1-, 3-, and 5-year ROC curves of the training and testing sets.

Supplementary 2. Supplementary Table S1: the list of m^{5}C genes.

Supplementary 3. Supplementary Table S2: the details of m^{5}CRlncRNAs.

Supplementary 4. Supplementary Table S3: the details of GO enrichment analysis.

Supplementary 5. Supplementary Table S4: the details of KEGG enrichment analysis.

Supplementary 6. Supplementary Table S5: the abundance of these tumor-infiltrating immune cells and increased CRC risk.

References

[1] W. Zhang, C. Peng, X. Shen et al., "A bioactive compound from Sanguisorba officinalis L. inhibits cell proliferation and induces cell death in 5-fluorouracil-sensitive/resistant colorectal cancer cells," *Molecules*, vol. 26, no. 13, 2021.

[2] Y. Xi and P. Xu, "Global colorectal cancer burden in 2020 and projections to 2040," *Translational Oncology*, vol. 14, no. 10, article 101174, 2021.

[3] W. Zhang, S. Sang, C. Peng et al., "Network pharmacology and transcriptomic sequencing analyses reveal the molecular mechanism of Sanguisorba officinalis against colorectal cancer," *Frontiers in Oncology*, vol. 12, article 807718, 2022.

[4] M. Bai and C. Sun, "M5C-related lncRNA predicts lung adenocarcinoma and tumor microenvironment remodeling: computational biology and basic science," *Frontiers in Cell and Development Biology*, vol. 10, article 885568, 2022.

[5] D. Shao, Y. Li, J. Wu et al., "An m6A/m5C/m1A/m7G-related long non-coding RNA signature to predict prognosis and immune features of glioma," *Frontiers in Genetics*, vol. 13, article 903117, 2022.

[6] I. Barbieri and T. Kouzarides, "Role of RNA modifications in cancer," *Nature Reviews Cancer*, vol. 20, no. 6, pp. 303–322, 2020.

[7] M. Li, Z. Tao, Y. Zhao et al., "5-Methylcytosine RNA methyltransferases and their potential roles in cancer," *Journal of Translational Medicine*, vol. 20, no. 1, p. 214, 2022.

[8] X. Liu, D. Wang, S. Han et al., "Signature of m5C-related lncRNA for prognostic prediction and immune responses in pancreatic cancer," *Journal of Oncology*, vol. 2022, Article ID 7467797, 2022.

[9] X. Chen, A. Li, B. F. Sun et al., "5-Methylcytosine promotes pathogenesis of bladder cancer through stabilizing mRNAs," *Nature Cell Biology*, vol. 21, no. 8, pp. 978–990, 2019.

[10] L. Liu, X. Li, Y. Shi, and H. Chen, "Long noncoding RNA DLGAP1-AS1 promotes the progression of glioma by regulating the miR-1297/EZH2 axis," *Aging (Albany NY)*, vol. 13, no. 8, pp. 12129–12142, 2021.

[11] J. Pan, Z. Huang, and Y. Xu, "m5C-related lncRNAs predict overall survival of patients and regulate the tumor immune microenvironment in lung adenocarcinoma," *Frontiers in Cell and Development Biology*, vol. 9, article 671821, 2021.

[12] J. Zhang, N. Wang, J. Wu et al., "5-Methylcytosine related lncRNAs reveal immune characteristics, predict prognosis and oncology treatment outcome in lower-grade gliomas," *Frontiers in Immunology*, vol. 13, article 844778, 2022.

[13] H. Zhang, P. Xu, and Y. Song, "Machine-learning-based m5C score for the prognosis diagnosis of osteosarcoma," *Journal of Oncology*, vol. 2021, Article ID 1629318, 2021.

[14] H. Wang, J. Cui, J. Yu, J. Huang, and M. Li, "Identification of fatty acid metabolism-related lncRNAs as biomarkers for clinical prognosis and immunotherapy response in patients with lung adenocarcinoma," *Frontiers in Genetics*, vol. 13, article 855940, 2022.

[15] W. Hong, L. Liang, Y. Gu et al., "Immune-related lncRNA to construct novel signature and predict the immune landscape of human hepatocellular carcinoma," *Molecular Therapy-Nucleic Acids*, vol. 22, pp. 937–947, 2020.

[16] D. Aran, Z. Hu, and A. J. Butte, "xCell: digitally portraying the tissue cellular heterogeneity landscape," *Genome Biology*, vol. 18, no. 1, p. 220, 2017.

[17] T. Li, J. Fan, B. Wang et al., "TIMER: a web server for comprehensive analysis of tumor-infiltrating immune cells," *Cancer Research*, vol. 77, no. 21, pp. e108–e110, 2017.

[18] F. Finotello, C. Mayer, C. Plattner et al., "Molecular and pharmacological modulators of the tumor immune contexture revealed by deconvolution of RNA-seq data," *Genome Medicine*, vol. 11, no. 1, p. 34, 2019.

[19] R. Dienstmann, G. Villacampa, A. Sveen et al., "Relative contribution of clinicopathological variables, genomic markers, transcriptomic subtyping and microenvironment features for outcome prediction in stage II/III colorectal cancer," *Annals of Oncology: Official Journal of the European Society for Medical Oncology*, vol. 30, no. 10, pp. 1622–1629, 2019.

[20] J. Racle, K. de Jonge, P. Baumgaertner, D. E. Speiser, and D. Gfeller, "Simultaneous enumeration of cancer and immune cell types from bulk tumor gene expression data," *eLife*, vol. 6, 2017.

[21] M. Tamminga, T. J. N. Hiltermann, E. Schuuring, W. Timens, R. S. Fehrmann, and H. J. Groen, "Immune microenvironment composition in non-small cell lung cancer and its association with survival," *Clinical & Translational Immunology*, vol. 9, no. 6, article e1142, 2020.

[22] A. M. Newman, C. L. Liu, M. R. Green et al., "Robust enumeration of cell subsets from tissue expression profiles," *Nature Methods*, vol. 12, no. 5, pp. 453–457, 2015.

[23] W. Jia, L. Yuan, H. Ni, B. Xu, and P. Zhao, "Prognostic value of platelet-to-lymphocyte ratio, neutrophil-to-lymphocyte ratio, and lymphocyte-to-white blood cell ratio in colorectal cancer patients who received neoadjuvant chemotherapy," *Technology in Cancer Research & Treatment*, vol. 20, 2021.

[24] X. Wang and T. Li, "Development of a 15-gene signature for predicting prognosis in advanced colorectal cancer," *Bioengineered*, vol. 11, no. 1, pp. 165–174, 2020.

[25] A. Xu, Q. Wang, and T. Lin, "Low-frequency magnetic fields (LF-MFs) inhibit proliferation by triggering apoptosis and altering cell cycle distribution in breast cancer cells," *International Journal of Molecular Sciences*, vol. 21, no. 8, 2020.

[26] L. Ping, K. Zhang, X. Ou, X. Qiu, and X. Xiao, "A novel pyroptosis-associated long non-coding RNA signature predicts prognosis and tumor immune microenvironment of patients with breast cancer," *Frontiers in Cell and Development Biology*, vol. 9, article 727183, 2021.

[27] Z. Wang, J. Chen, F. Sun et al., "lncRNA CRLM1 inhibits apoptosis and promotes metastasis through transcriptional regulation cooperated with hnRNPK in colorectal cancer," *Cell & Bioscience*, vol. 12, no. 1, p. 120, 2022.

[28] P. Samadi, M. Soleimani, F. Nouri, F. Rahbarizadeh, R. Najafi, and A. Jalali, "An integrative transcriptome analysis reveals potential predictive, prognostic biomarkers and therapeutic targets in colorectal cancer," *BMC Cancer*, vol. 22, no. 1, p. 835, 2022.

[29] L. Ruan, W. Chen, X. Zhao, N. Fang, and T. Li, "Predictive potentials of ZEB1-AS1 in colorectal cancer prognosis and their correlation with immunotherapy," *Journal of Oncology*, vol. 2022, Article ID 1084555, 2022.

[30] Z. Xue, C. Cui, Z. Liao et al., "Identification of lncRNA Linc00513 containing lupus-associated genetic variants as a novel regulator of interferon signaling pathway," *Frontiers in Immunology*, vol. 9, p. 2967, 2018.

[31] Y. Bai, Y. Xu, X. Wang et al., "Whole exome sequencing of lung adenocarcinoma and lung squamous cell carcinoma in one individual: a case report," *Thoracic Cancer*, vol. 11, no. 8, pp. 2361–2364, 2020.

[32] H. Li, L. Liu, T. Huang et al., "Establishment of a novel ferroptosis-related lncRNA pair prognostic model in colon adenocarcinoma," *Aging (Albany NY)*, vol. 13, no. 19, pp. 23072–23095, 2021.

[33] Z. Jiang, W. Yin, H. Zhu et al., "METTL7B is a novel prognostic biomarker of lower-grade glioma based on pan-cancer analysis," *Cancer Cell International*, vol. 21, no. 1, p. 383, 2021.

[34] M. Y. Lv, W. Wang, M. E. Zhong et al., "DNA repair-related gene signature in predicting prognosis of colorectal cancer patients," *Frontiers in Genetics*, vol. 13, article 872238, 2022.

Research Article

CLDN4 as a Novel Diagnostic and Prognostic Biomarker and Its Association with Immune Infiltrates in Ovarian Cancer

Pan Hu,[1,2] **Li Lei,**[1,2] **Ying Wang,**[1,2] **Xue Tian,**[3] **Xia Wei,**[4] **Ni Jiang,**[1,2] **and Lubin Liu** [1,2]

[1]*Department of Obstetrics and Gynecology, Chongqing Health Center for Women and Children, Chongqing, China*
[2]*Department of Obstetrics and Gynecology, Women and Children's Hospital of Chongqing Medical University, Chongqing, China*
[3]*Department of Gynecology, Women and Children's Hospital of Xiushan County, Chongqing, China*
[4]*People's Hospital of Kunming, Xishan District, Kunming, Yunnan, China*

Correspondence should be addressed to Lubin Liu; liulubin1975@126.com

Ovarian cancer (OC) is the seventh most prevalent type of cancer in women and the second most common cause of cancer-related deaths in women worldwide. Because of the high rates of relapse, there is an immediate and pressing need for the discovery of innovative sensitive biomarkers for OC patients. Using TCGA and GSE26712 datasets, we were able to identify 17 survival-related DEGs in OC that had differential expression. CLDN4 was the gene that caught our attention the most out of the 17 important genes since its expression was much higher in OC samples than in nontumor samples. The findings of the ROC assays then confirmed the diagnostic utility of the test in screening OC specimens to differentiate them from nontumor specimens. Patients with high CLDN4 expression predicted a shorter overall survival (OS) and disease-specific survival (DSS) than those with low CLDN4 expression, according to clinical research. Patients with low CLDN4 expression predicted longer OS and DSS. Analysis using both univariate and multivariate techniques revealed that CLDN4 expression was an independent factor associated with a poor prognosis for OS and DSS. Based on multivariate analysis, the *C*-indexes and calibration plots of the nomogram suggested an effective predictive performance for OC patients. After that, we investigated whether or not there was a link between the infiltration of immune cells and the expression of the CLDN4 gene. We found that the expression of CLDN4 was positively associated with Th17 cells, NK CD56bright cells, while negatively associated with Th2 cells, pDC, and T helper cells. In the end, we carried out RT-PCR on our cohort and confirmed that the level of CLDN4 expression was noticeably elevated in OC specimens in comparison to nontumor tissues. The diagnostic usefulness of CLDN4 expression for OC was also validated by the findings of ROC tests. Thus, our findings revealed that CLDN4 may serve as a predictive biomarker in OC to assess both the clinical outcome of OC patients and the level of immune infiltration.

1. Introduction

Ovarian cancer (OC), which is one of the most prevalent but lethal forms of gynecological cancer, places a significant burden on the overall health of women all over the world [1]. Because of the lack of symptoms that are typically associated with OC until its more advanced phases, it has been given the nickname "the silent killer" [2, 3]. It is generally agreed that OC is a heterogeneous disease that includes at least five distinct subtypes, each of which possesses unique biological and molecular characteristics [4, 5]. Most people with OC

were diagnosed at more advanced stages, which have a lower five-year survival rate (44% worldwide) [6]. This is because there are no evident symptoms in the early stages of the disease, despite the fact that many modern therapeutic approaches, like as surgery, immunotherapy, and targeted therapies, have been successful [7, 8]. The overall prognosis of patients with OC is not encouraging, and the risk of recurrence following treatment is high. As a result, they are unable to take advantage of the most beneficial treatment chances and do not utilize treatment strategies that are efficient, which leads to an unfavorable prognosis. Thus, we

(a)

(b)

Figure 1: Continued.

Survival-related genes   Differentially expressed genes
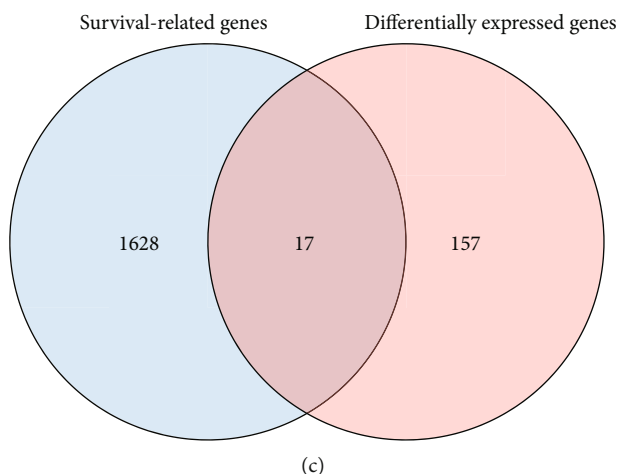

1628   17   157

(c)

Figure 1: Identification of the survival-related DEGs between OC specimens and nontumor specimens. DEGs between OC tissues and nontumor specimens based on GSE26712 datasets were depicted in heat map and volcano plots, respectively (a, b). (c) The genes that are shared by the DEG GSE26712 datasets and the genes that are connected to survival according to TCGA datasets.

need to find better prognostic markers to better stratify patients and develop personalized therapeutic treatment strategies.

As more research on cancer development and metastasis has been carried out, there has been a corresponding surge in interest in tumor junctions (TJs) [9]. Several studies have indicated that the TJ plays a significant role in the advancement of cancer. As a constituent of tight junctions (TJs), the transmembrane protein CLDN, which has a size of around 20–27 kDa, is responsible for promoting cell-cell adhesion [10]. The CLDN molecule traverses the cell membrane four times on its way to the cytoplasm, where both its N- and C-termini are found. Because of their function as regulators of intercellular adhesion, CLDNs play significant roles in the process of carcinogenesis and have the potential to influence both the aggressive development and motility of tumors [11, 12]. In point of fact, there is mounting data suggesting that CLDN dysregulation is a characteristic shared by a wide variety of cancers, including gastric, lung, breast, ovarian, and colorectal cancer. Claudin-4, also known as CLDN4, is a key structural protein that is found in epithelial tight junctions [13]. It has a role in epithelial development, the maintenance of polarity, and considerable transport. Multiple research over the past few years have pointed to an essential function for CLDN4 in the development of various distinct types of cancer. On the other hand, very little information regarding the expression and function of CLDN4 was found in OC.

Tumor microenvironment (TME) was an intricate and dynamic multicellular ecosystem that included a variety of cell types, including immune cells, stromal cells, cancer cells, and other constituents [14]. Immune cells in the TME have long been recognized as a critical and core field of oncology inquiry [15]. These cells play an important part in the prognosis of cancer patients, as well as in immune evasion and treatment resistance. In terms of the release of cytokines and the recruitment of immune cells, the immunological microenvironment has an influence on the survival, proliferation, and migration of tumor cells [16–18]. Within this

group, invading M2 macrophages plays a very significant role in the process. M2 macrophages develop from macrophages in the extraordinarily complex microenvironment of a tumor. These macrophages play a significant role in the regulation of tumor growth as well as invasion and metastasis. A deeper and more comprehensive understanding of endogenous antitumor immunity can be obtained through the examination of the density of immunocellular infiltration in tumor regions. In this study, our objective was to investigate the predictive usefulness of CLDN4 in OC as well as its connection with immune infiltration in OC.

2. Materials and Methods

2.1. Patients and Clinical Samples. All tissue samples, including those of the tumor as well as matched normal ovarian surface tissue, were taken from twenty ovarian cancer patients who had surgery at Chongqing Health Center for Women and Children between July 2020 and April 2022. None of the patients who were enrolled for this study had previously been treated with chemotherapy or radiation before their operations. Following the completion of the surgical excision, tumor specimens and the normal renal tissues that were close to the tumor were collected and frozen in liquid nitrogen until further use. The Research Ethics Committee of Chongqing Health Center for Women and Children gave their blessing to the current study before it was conducted. Consent to participate in the study was obtained from each individual patient.

2.2. RNA Extraction and Quantitative Real-Time PCR (qRT-PCR). Through the use of TRIzol reagent (Invitrogen, Carlsbad, CA, USA), total RNA was isolated from frozen OC tissues. Using a PrimeScript RT Master Mix and one microgram of total RNA, high-quality cDNA was produced by the process of reverse transcription (Vazyme Biotech, Nanjing, China). Quantitative real-time PCR with a SYBR Premix Ex TaqII Kit (TaKaRa, Japan) was used to analyze
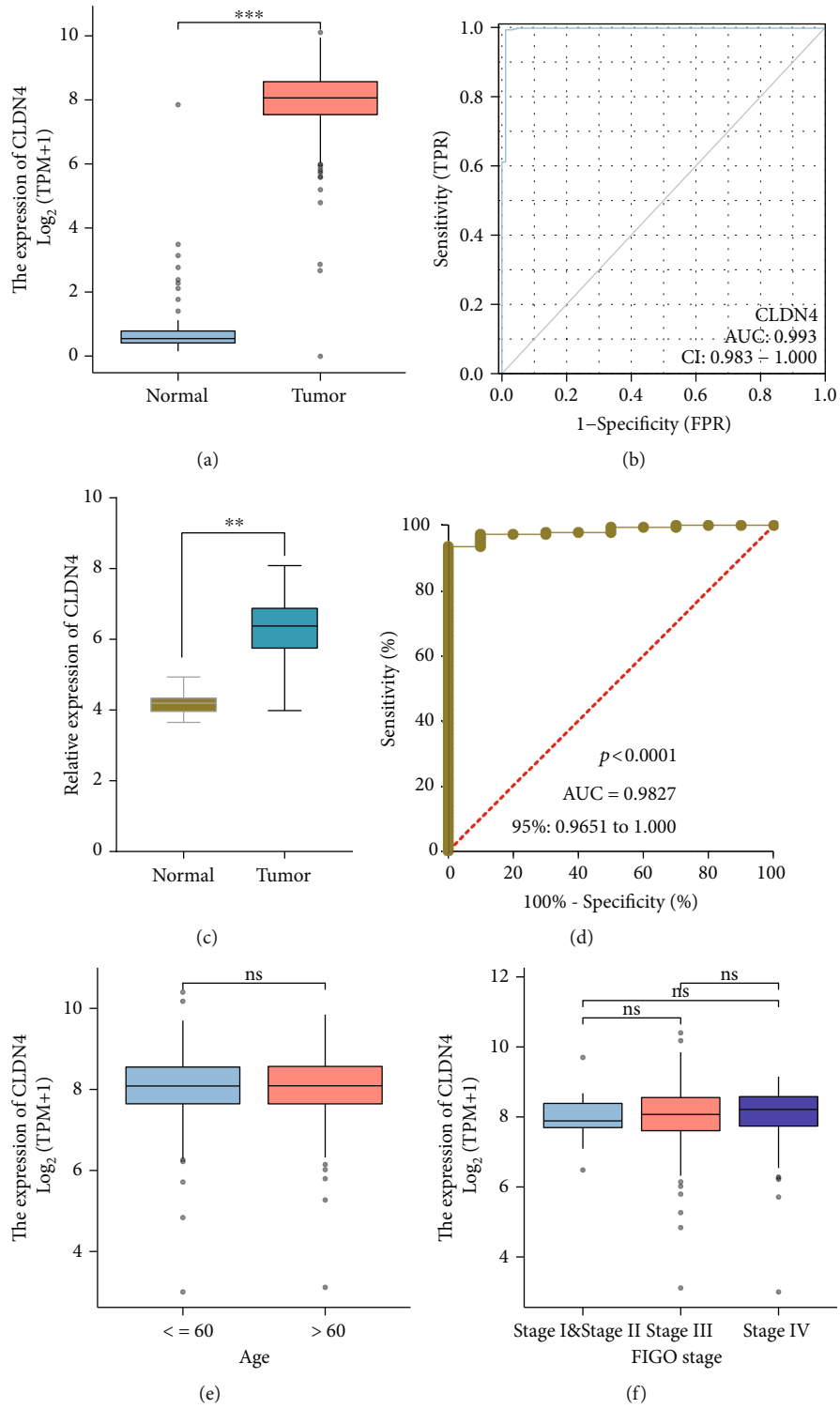
(a)

(b)

(c)

(d)
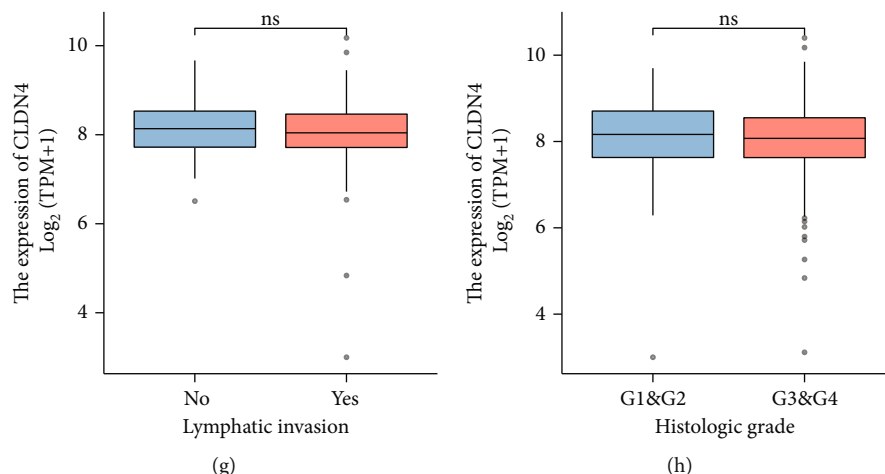

(e)

(f)

Figure 2: Continued.

(g)

(h)

FIGURE 2: The expression of CLDN4 in OC and the clinical importance of its presence has been investigated. (a) When compared with nontumor specimens, OC were found to have a significantly higher level of CLDN4 overexpression. (b) ROC assays were utilized in order to provide evidence that CLDN4 expression have diagnostic value. (c) The expression of CLDN4 in OC as determined by the GSE26712 datasets. (d) ROC assays based on the data found in GSE26712. (e–h) Association between CLDN4 expression and clinicopathological parameters, such as age, FIGO stage, lymphatic invasion, and histologic grade.

TABLE 1: Association of CLDN4 expression levels with clinical factors in ovarian cancer patients.

Characteristic	Low expression of CLDN4	High expression of CLDN4	P
n	189	190	
Age, n (%)			1.000
≤60	104 (27.4%)	104 (27.4%)	
>60	85 (22.4%)	86 (22.7%)	
FIGO stage, n (%)			0.203
Stage I	0 (0%)	1 (0.3%)	
Stage II	14 (3.7%)	9 (2.4%)	
Stage III	150 (39.9%)	145 (38.6%)	
Stage IV	23 (6.1%)	34 (9%)	
Histologic grade, n (%)			0.269
G1	1 (0.3%)	0 (0%)	
G2	19 (5.1%)	26 (7%)	
G3	165 (44.7%)	157 (42.5%)	
G4	0 (0%)	1 (0.3%)	
Lymphatic invasion, n (%)			0.817
No	23 (15.4%)	25 (16.8%)	
Yes	52 (34.9%)	49 (32.9%)	
Age, median (IQR)	59 (50, 69)	58.5 (52, 67)	0.786

the samples in triplicate to determine the amounts of mRNA. The primers used in this experiment were designed in-house (Tsingke, China). Internal quality check for the mRNA was performed with GAPDH. The $2'$Ct technique was utilized for the purpose of determining the levels of CLDN4 expression. The PCR primer sequences were as follows: CLDN4 sense, $5'$-TGGGGC TACAGGTAATGGG-$3'$ and reverse, $5'$-GGTCTGCGA GGTGACAATGTT-$3'$; GAPDH reverse, $5'$-ACAACTTTG GTATCGTGGAAGG-$3'$ and reverse, $5'$-GCCATCACG CCACAGTTTC-$3'$.

2.3. Data Collection. The RNA-seq data were evaluated, and this included 427 individuals who had ovarian cancer that were obtained from TCGA database, as well as 88 samples of nondi-seased ovarian tissue that were retrieved from the GTEx (Geno-type-Tissue Expression) database. In addition, the RNA-Seq data of 185 OC patients were retrieved from the Gene Expression Omnibus (GEO) database. These data were based on the GPL96 platform and were included in the GSE26712 dataset.

2.4. Identification of DEGs in GSE26712 Datasets. Back-ground errors were fixed, arrays were normalized, and differential expression analysis of 185 OC and 10 nontumor
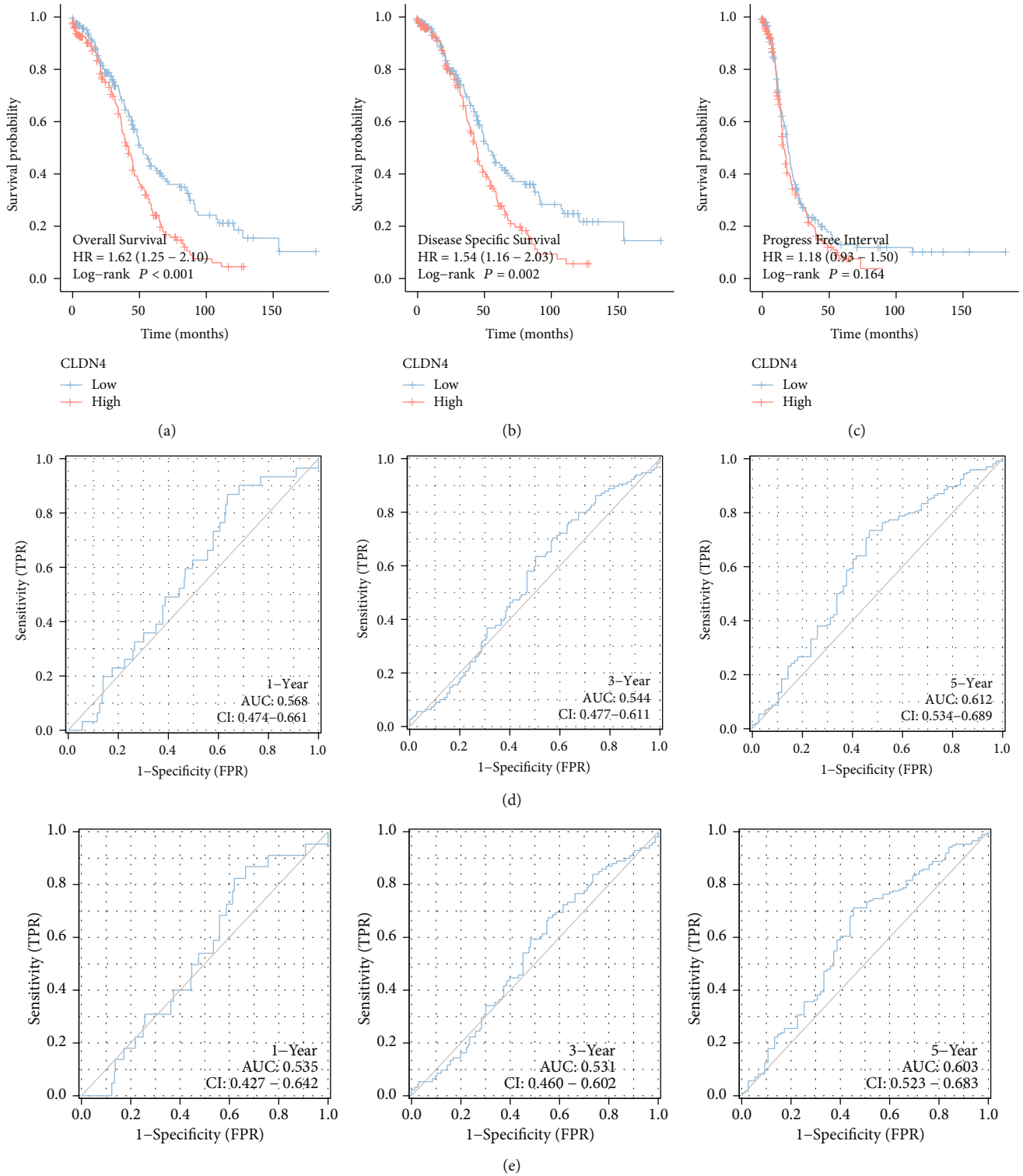
(a)

(b)

(c)
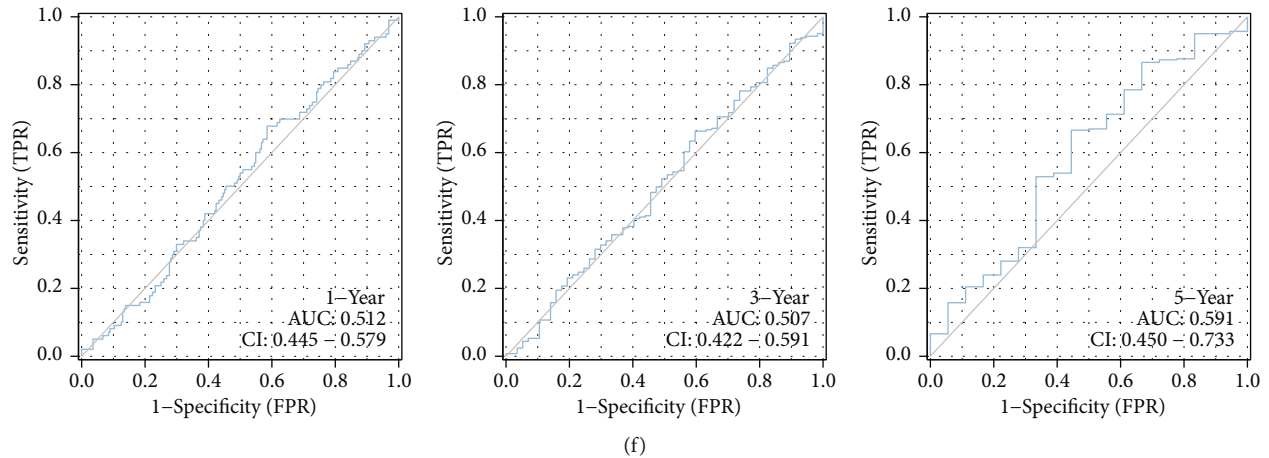

(d)

(e)

FIGURE 3: Continued.

(f)

FIGURE 3: The survival study of CLDN4 expression in individuals diagnosed with OC. (a–c) Survival curves of overall survival, disease-specific survival, and progression-free survival for patients with OC who had high or low levels of CLDN4. The ROC curve was used to confirm that the expression of CLDN4 for (d) OS, (e) DSS, and (f) PFI is effective as a prediction tool.

samples was performed with the help of the limma package of the R programming language. The threshold points for differentially expressed genes (DEGs) were determined to be samples that had an adjusted false discovery rate P that was less than 0.05 and a |log fold change (FC)| that was more than 2.

2.5. Survival Analysis. In order to study the relationship between gene expression and the overall survival (OS), disease-specific survival (DSS), and progress free interval (PFI) of OC patients, Kaplan-Meier plots were generated. A log-rank test was utilized in order to investigate the statistical significance of the correlation.

2.6. Identification of Independent Prognostic Parameters of OC. In order to validate the independent prognostic value of the gene signature and to identify independent prognostic parameters, univariate- and multivariate Cox regression analyses were performed in TCGA dataset on the prognostic gene signature and clinicopathological parameters. These analyses focused on validating the independent prognostic value of the gene signature. When P was less than 0.05, statistical significance was assumed. Only the parameters that had a P value that was less than 0.05 based on the univariate analysis were included in the subsequent multivariate Cox regression analysis.

2.7. Predictive Nomogram Construction and Validation. The independent prognostic indicators acquired from multivariate analysis were utilized to build nomograms, which individualized the expected survival probability for one, three, and five years. These nomograms were established on the basis of Cox regression models. It was decided to make use of the RMS software in order to generate nomograms that contained important clinical characteristics as well as calibration plots. The calibration curves were graphically evaluated by mapping the nomogram-predicted probability against the observed occurrences; the 45° line represented the best predictive values among all of the lines in the assessment. To evaluate the accu-

racy of the nomogram's discrimination, a concordance index, abbreviated as C-index, was utilized, and its value was determined using a bootstrap method with a total of 1,000 resamples. The C-index was utilized to make a comparison between the prediction accuracies of the nomogram and those of the individual prognostic parameters. In this particular research endeavor, all statistical tests were performed using two different sets of data, and the level of statistical significance was established at 0.05.

2.8. Function Enrichment Analysis of Differentially Expressed Genes between Groups with High CLDN4 Expression and Groups with CLDN4 Expression. In order to investigate the biological and molecular functions that CLDN4 played in OC, Gene Ontology (GO) and Kyoto Encyclopedia of Genes and Genomes (KEGG) were used. An investigation on the BP, CC, and MF that are related with CLDN4 was carried out using GO analysis. The Cluster Profiler program in R was used throughout each step of the three separate studies.

2.9. Infiltration of Immune Cells. The data from TCGA gene expression profile were used to quantify the infiltration of immune cells in tumor tissues using a method called ssGSEA (single-sample gene set enrichment analysis) [19]. The results of this study showed that there was an infiltration of 24 immune cells. SsGSEA calculates an enrichment score showing the degree to which genes in a certain gene set are coordinately up- or downregulated within a single sample. This score is based on the results of a collection of genes that have been studied. A gene's enrichment score is calculated by the ssGSEA by integrating the differences between the empirical cumulative distribution functions of its ranked genes. Genes are ranked according to the absolute expression they have in a given sample.

2.10. Statistical Analysis. All statistical analyses were performed in R (v3.6.2). The Wilcoxon signed-rank test was utilized for the analysis of paired samples, whilst the Wilcoxon rank-sum test was utilized for the analysis of unpaired
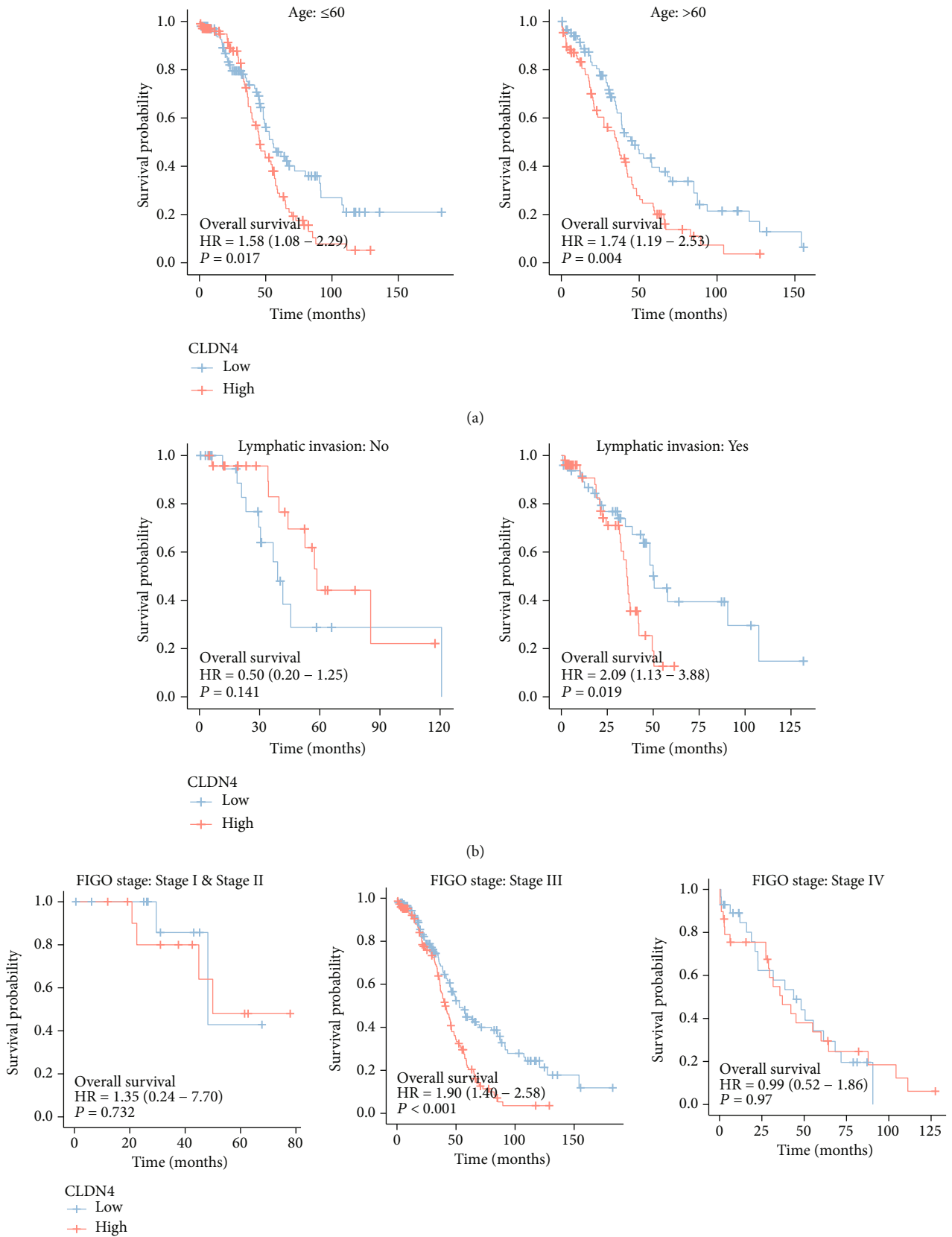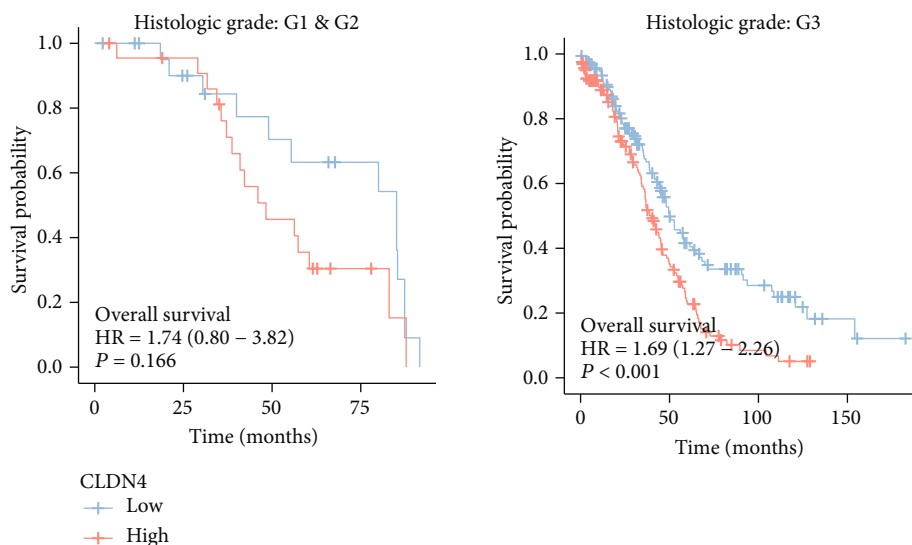
(a)

(b)

(c)

Figure 4: Continued.

(d)

FIGURE 4: The survival analysis of CLDN4 expression in different subgroup of OC patients. (a) Age, (b) lymphatic invasion, (c) FIGO stage, and (d) histologic grade.

TABLE 2: Univariate and multivariate analysis of overall survival in patients with ovarian cancer.

Characteristics	Total (N)	Univariate analysis		Multivariate analysis	
		Hazard ratio (95% CI)	P value	Hazard ratio (95% CI)	P value
Age	377				
≤60	206	Reference			
>60	171	1.355 (1.046-1.754)	**0.021**	1.410 (1.088-1.828)	**0.009**
FIGO stage	374				
Stage I and stage II	24	Reference			
Stage III and stage IV	350	2.115 (0.938-4.766)	0.071	2.122 (0.942-4.781)	0.070
Histologic grade	367				
G1 and G2	46	Reference			
G3 and G4	321	1.229 (0.830-1.818)	0.303		
Lymphatic invasion	148				
No	48	Reference			
Yes	100	1.413 (0.833-2.396)	0.200		
CLDN4	377				
Low	187	Reference			
High	190	1.647 (1.263-2.147)	**<0.001**	1.693 (1.297-2.209)	**<0.001**

samples. The receiver-operating characteristic (ROC) curve was used to analyze whether CLDN4 expression could be the diagnostic marker. In order to investigate the connection that exists between the expression of CLDN4 and the clinicopathological features, either the chi-square test or the Fisher exact test was carried out. A statistically significant P value was set at 0.05.

3. Results

3.1. Identification of Survival-Related DEGs in OC.
In this study, a retrospective analysis of the data was performed on a total of 175 OC samples and 10 nontumor samples taken from the GSE26712 datasets. A total of 174 differen-

tially expressed genes (DEGs) were found, with 49 genes showing significant upregulation and 125 genes showing significant downregulation (Figures 1(a) and 1(b)). After that, we carried out survival study by making use of TCGA datasets, and we discovered 1645 genes in OC patients that are associated to survival. Figure 1(c) illustrates the findings of a Venn diagram that confirmed 17 overlapping genes between 174 differentially expressed genes and 1645 genes related to survival (Figure 1(c)). CLDN4 was the primary focus of our research among the 17 genes that overlapped.

3.2. The Expression of CLDN4 in OC and Its Association with Clinical Factors.
First, we looked at the levels of CLDN4 expression in OC and found that it was significantly higher

TABLE 3: Univariate and multivariate analysis of disease-specific survival in patients with ovarian cancer.

Characteristics	Total (N)	Univariate analysis Hazard ratio (95% CI)	P value	Multivariate analysis Hazard ratio (95% CI)	P value
Age	352				
≤60	196	Reference			
>60	156	1.255 (0.950-1.658)	0.110		
FIGO stage	350				
Stage I and stage II	23	Reference			
Stage III and stage IV	327	2.276 (0.935-5.541)	0.070	2.283 (0.938-5.555)	0.069
Histologic grade	342				
G1 and G2	42	Reference			
G3 and G4	300	1.394 (0.893-2.178)	0.144		
Lymphatic invasion	144				
No	48	Reference			
Yes	96	1.397 (0.810-2.408)	0.229		
CLDN4	352				
Low	183	Reference			
High	169	1.554 (1.171-2.063)	**0.002**	1.553 (1.170-2.061)	**0.002**

TABLE 4: Univariate and multivariate analysis of progress-free interval in patients with ovarian cancer.

Characteristics	Total (N)	Univariate analysis Hazard ratio (95% CI)	P value	Multivariate analysis Hazard ratio (95% CI)	P value
Age	377				
≤60	206	Reference			
>60	171	1.076 (0.848-1.366)	0.547		
FIGO stage	374				
Stage I and stage II	24	Reference			
Stage III and stage IV	350	1.573 (0.918-2.694)	0.099	1.573 (0.918-2.694)	0.099
Histologic grade	367				
G1 and G2	46	Reference			
G3 and G4	321	1.188 (0.835-1.688)	0.338		
Lymphatic invasion	148				
No	48	Reference			
Yes	100	1.115 (0.729-1.704)	0.615		
CLDN4	377				
Low	187	Reference			
High	190	1.183 (0.933-1.500)	0.165		

in OC samples than in nontumor samples. This data led us to conclude that CLDN4 is strongly upregulated in OC (Figure 2(a)). As a result, we conducted more research on the diagnostic potential of CLDN4. The findings of ROC testing revealed that CLDN4 efficiently distinguished OC specimens from normal specimens with an area under the ROC curves (AUC) of 0.993 (95% confidence interval [CI]: 0.983 to 1.000). These results are displayed in Figure 2(b). In addition, based on the findings from the GSE26712 datasets, we discovered that CLDN4 was substantially expressed in OC samples (Figure 2(c)). In addition, ROC testing proved the diagnostic utility of this method (Figure 2(d)). Using a pancancer investigation, we discovered that multiple

different types of tumors had a dysregulated level of CLDN4, which suggests that this gene plays a significant role in the progression of cancers (Figure S1A and S1B). Following that, we investigated the potential relationships between CLDN4 expression and clinical factors. Despite this, we found that the expression of CLDN4 was not connected to a number of clinical variables, including age, FIGO stage, lymphatic invasion, and histologic grade (Figures 2(e)–2(h) and Table 1).

3.3. Survival Analysis of CLDN4 Expression in OC Patients. The next step consisted of conducting a survival study to investigate the predictive value of CLDN4 in OC patients.
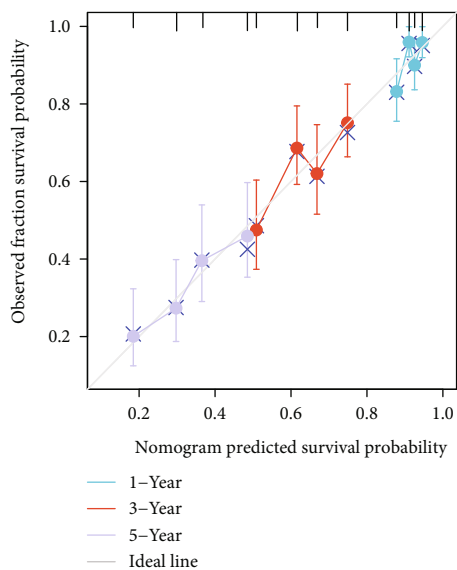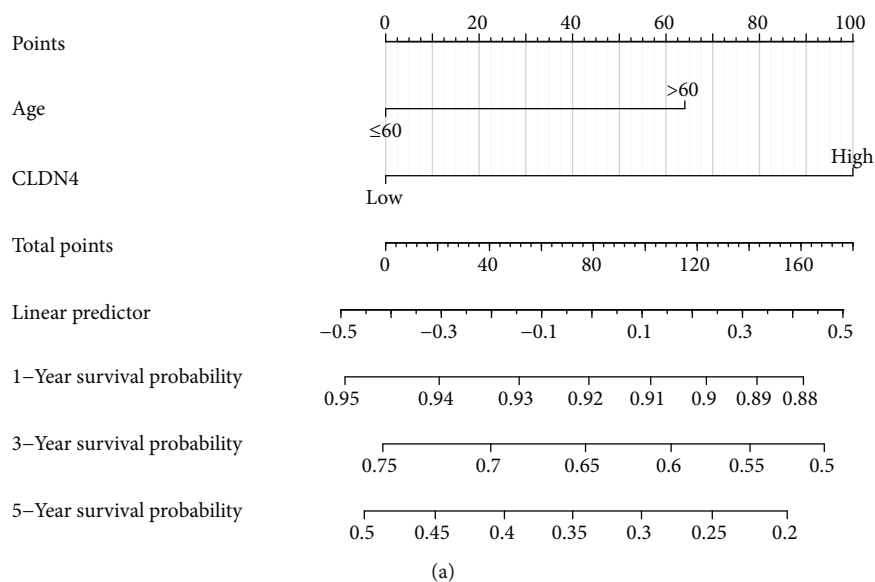
(a)

(b)

FIGURE 5: A quantitative method to forecast the probability of OC patients surviving one, three, or five years after their diagnosis. (a) A nomogram that estimates the likelihood that OC patients will be alive at 1, 3, and 5 years after diagnosis. (b) The calibration plots of the nomogram, which are used to forecast the likelihood of having OS at 1, 3, and 5 years.

Patients who had high levels of CLDN4 expression predicted a shorter overall survival time and disease-free survival time than patients who had low levels of CLDN4 expression, as can be seen in Figures 3(a) and 3(b). On the other hand, we found no correlation between the expression of CLDN4 and the PFI of OC patients (Figure 3(c)). ROC curves illustrated the degree to which CLDN4 expression in TCGA cohort was able to accurately predict outcomes (Figures 3(d)–3(f)). In addition, we carried out subgroup analysis, which revealed that elevated CLDN4 expression demonstrated a significant correlation in both younger and older ovarian cancer patients (Figure 4(a)). CLDN4 expression was not linked with OS in patients with ovarian cancer who had nonlymphatic

invasion (Figure 4(b)), early clinical stage (Figure 4(c)), and early histologic grade (Figure 4(d)). We performed univariate and multivariate analyses to demonstrate the predictive value of CLDN4 expression in OC patients. Importantly, both univariate and multivariate analyses showed that CLDN4 expression was an independent predictor associated with a poor prognosis for overall survival (Table 2) and disease-specific survival (Table 3). On the other hand, CLDN4 expression cannot be used to accurately forecast the PFI (Table 4).

3.4. Construction and Validation of a Nomogram Based on the CLDN4 Expression. In order to give a quantitative method for predicting the outcome of patients with OC, a nomogram
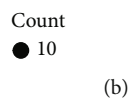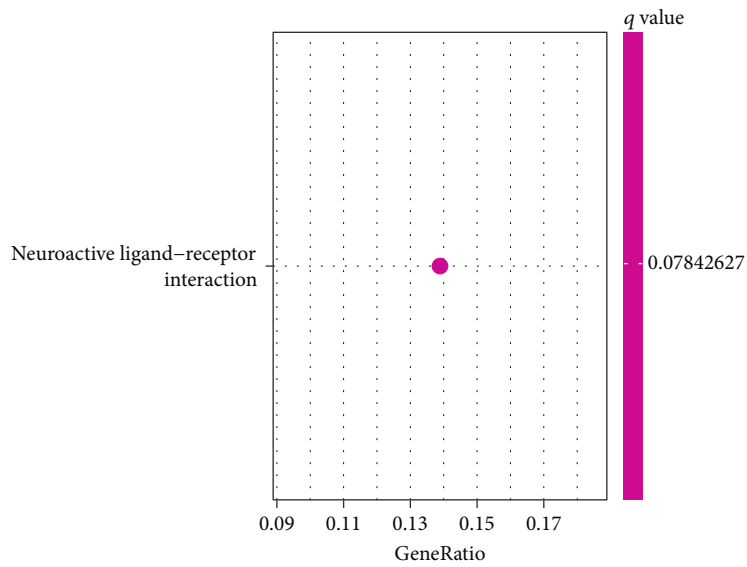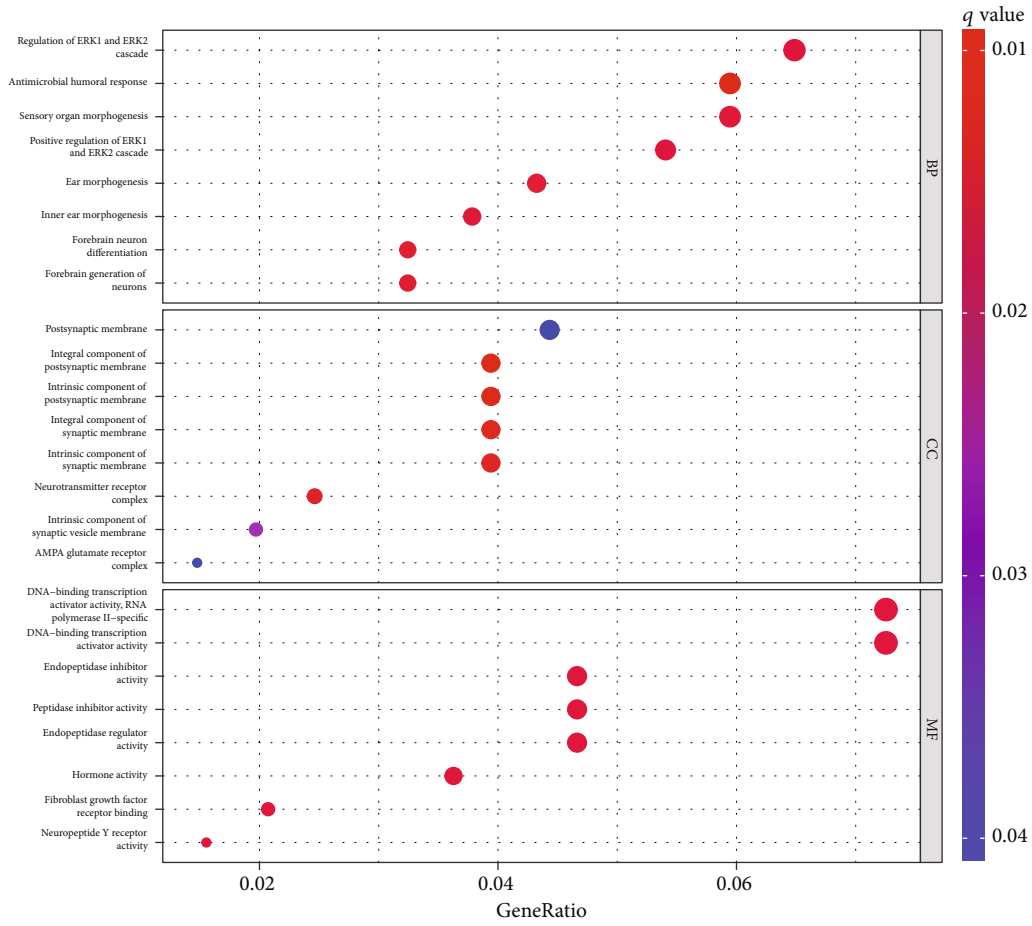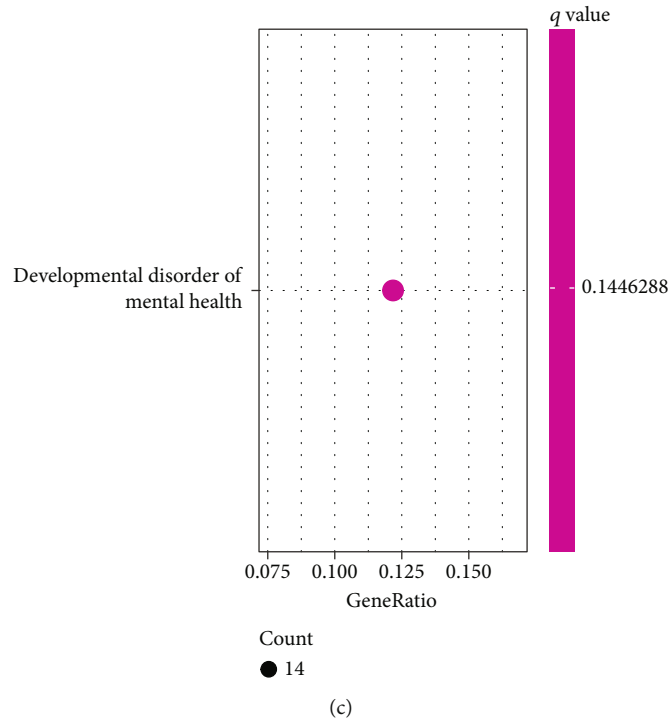
(a)

(b)

FIGURE 6: Continued.

(c)

Figure 6: Functional bioassay. (a) GO functional analysis. (b) KEGG functional analysis. (c) DO functional analysis.

was constructed using CLDN4 in conjunction with independent clinical risk indicators (Figure 5(a)). A point scale was utilized in the construction of the nomogram that was based on the multivariate Cox analysis. The variables were each given a certain number of points depending on the scale. The total number of points that were given to each variable was recalculated to fall within the range of one to one hundred. The sum of the points earned across all of the variables was then used as the basis for the final score. Drawing a vertical line immediately downward from the total point axis to the outcome axis allowed for the calculation of the chance of survival in OC patients at 1, 3, and 5 years. We also performed an analysis of the nomogram's ability to make correct predictions, and the findings showed that the C-index of the model was 0.584 (CI: 0.562-0.606), which indicated that the nomogram's ability to make accurate predictions is approximately accurate to a modest degree. The bias-corrected line in the calibration plot was employed to be close to the ideal curve, which was the line at 45 degrees, which showed that the forecast and the observation were in close agreement with one another (Figure 5(b)).

3.5. Functional Enrichment Analysis. A total of 224 DEGs were discovered. After that, we carried out GO analysis with the help of 224 DEGs. As shown in Figure 6(a), we found that 224 DEGs were mainly enriched in regulation of ERK1 and ERK2 cascade, antimicrobial humoral response, sensory organ morphogenesis, postsynaptic membrane, integral component of postsynaptic membrane, endopeptidase inhibitor activity, peptidase inhibitor activity, and endopeptidase regulator activity. In addition, the results of KEGG revealed that the 224 DEGs were associated with neuroactive

ligand-receptor interaction (Figure 6(b)). In order to learn more about the function of DEGs, enrichment analysis of DO pathways was carried out. According to the findings, the majority of the disorders that were enriched by DEGs were related to developmental disorder of mental health (Figure 6(c)). Our findings suggested that CLDN4 may be involved in the progression of several tumors.

3.6. The Association between CLDN4 Expression and Immune Cell Infiltration. Then, we explored the correlation between immune infiltration and CLDN4 expression. As shown in Figures 7(a) and 7(b), we found that the expression of CLDN4 was positively associated with Th17 cells and NK CD56bright cells, while negatively associated with Th2 cells, pDC, and T helper cells.

3.7. The Confirmation of CLDN4 Expression and Its Diagnostic in Our Cohort. We used RT-PCR to investigate the level of CLDN4 expression in our sample population so that we could validate our previous findings. As can be seen in Figure 8(a), we discovered that the level of CLDN4 expression was noticeably higher in OC specimens in comparison to nontumor tissues. Following that, an investigation into the diagnostic utility of CLDN4 for OC patients was carried out. The ROC assays revealed that increased CLDN4 expression had an AUC value of 0.735 for OC (Figure 8(b)).

4. Discussion

The mortality rate from ovarian cancer, which already has the second highest rate among gynecological malignances, is on the rise in China, but the prevalence of the disease is
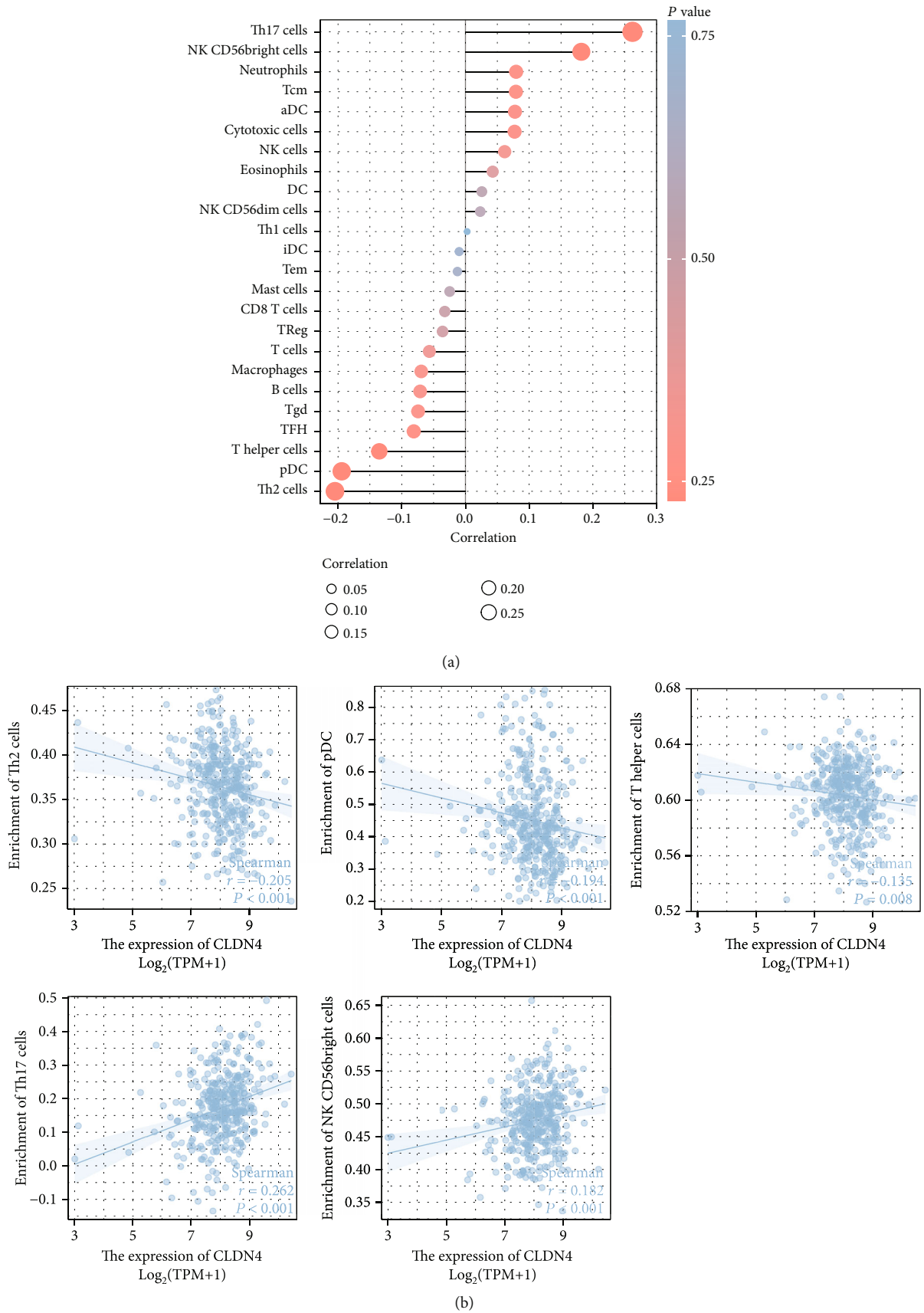
(a)

(b)

Figure 7: (a, b) Relationships between CLDN4 expression and infiltrating immune cells in OC.
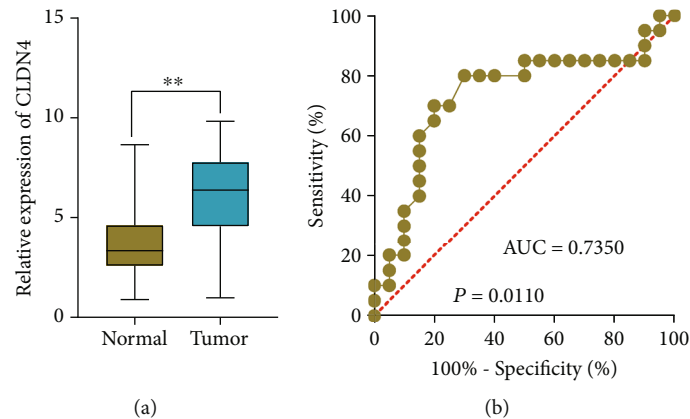
(a)

(b)

FIGURE 8: The level of expression of CLDN4 in OC in our cohort and the diagnostic value of this gene. (a) RT-PCR to analyze the expression of CLDN4 in OC and nontumor specimens. (b) The diagnostic usefulness of CLDN4 expression in screening OC specimens and differentiating them from nontumor specimens was validated by ROC analysis.

decreasing [20, 21]. It is difficult to detect in its early stages; thus, the majority of individuals are diagnosed when the disease has already progressed significantly [22, 23]. Even though there have been significant advancements in the treatment of OC, including chemotherapy, radiation, surgery, and targeted therapies, the 5-year overall survival rate for individuals with advanced OC is only about 30% [24, 25]. Thus, it is necessary to investigate the potential biomarkers related to the fundamental mechanisms of OC progression.

In recent years, a number of studies have indicated that an improper control of CLDN4 played a role in the evolution of a number of different cancers. For example, Hao and colleagues found that the expression of CLDN4 was abnormally increased in acute myeloid leukemia cells. In acute myeloid leukemia cells, inhibiting the expression of CLDN4 led to a significant reduction in cell proliferation as well as an increase in the rate of apoptosis. In addition, we discovered that inhibiting the expression of CLDN4 mRNA results in a suppression of the activation of AKT and ERK1/2. This suppression was achieved by knocking down CLDN4. Most notably, activating the AKT branch with SC79 partially counteracted the effects of CLDN4 knockdown on the suppression of cell survival. We also discovered that a higher expression of CLDN4 is associated with poorer survival and is an independent indication of shorter disease-free survival (DFS) in patients with acute myeloid leukemia [26]. According to the findings of Luo and colleagues, the expression of CLDN4 was much lower in gastric cancer tissues and cell lines when compared to nearby normal tissues or stomach epithelial cells. The silencing of CLDN4 led to a rise in the degree to which PI3K and Akt were phosphorylated, as well as in the proliferation, migration, invasion, and tumorigenesis of GC cells. Concurrently, apoptosis and the sensitivity of GC cells to chemotherapy were decreased. In conclusion, CLDN4 may play a critical role in improving the sensitivity of GC cells to chemotherapy and reducing the rate of GC cell proliferation by inactivating the PI3K/Akt signaling pathway. This may be achieved by inhibiting the activity of PI3K [27]. Jie et al.

demonstrated that ELFN1-AS1 speeds up cell proliferation, invasion, and migration in ovarian cancer by modulating the miR-497-3p/CLDN4 axis. This finding suggests that CLDN4 acts as a tumor promotor in ovarian cancer. On the other hand, very little is known about the clinical importance of CLDN4 in OC. In this particular investigation, we discovered that OC specimens exhibited a markedly elevated level of CLDN4 expression. It was determined through survival assays that a high level of CLDN4 expression was related with a bad prognosis. Importantly, the results of the multivariate analysis suggested that the expression of CLDN4 was an independent factor associated with a poor prognosis for OS and DSS. Based on our findings, CLDN4 may serve as an innovative diagnostic as well as prognostic biomarker for patients with OC. In addition, our findings suggested that CLDN4 was highly expressed and predicted a poor prognosis. Thus, targeting CLDN4 may improve the clinical prognosis of OC patients.

The interaction between the TME and cancer cells is quite intricate, and the TME has strong ties to tumor cell proliferation, apoptosis, and the spread of the cancer to other organs [28, 29]. It has been hypothesized that the immune cells that make up healthy tissue, neighboring tissue, and malignant tissue are structurally distinct from one another in basic ways. It has been proven that the intrinsic mechanisms that contribute to immunotherapy resistance include the expression of particular genes and pathways in tumor cells. These genes and pathways have the ability to block the invasion or activity of immune cells in the TME. TME has been found to have a dual function in both the development of tumors and their initial appearance, according to a significant number of studies. Alterations to the TME have the potential to not only encourage the normalization of tumor cells but also to encourage tumor growth, invasion, and metastasis. B cells have been shown in a variety of studies to perform an anticancer role, either by directly interacting with tumor cells or by supporting in the operation of other immune functions. Treg cells are generally responsible for suppressing antitumor immunity, whereas CD8+ T cells are the primary antitumor effector

cells [30]. During the course of this investigation, we came to the conclusion that the expression of CLDN4 was inversely linked with Th2 cells, pDC, and T helper cells, while it was positively associated with Th17 cells and NK CD56bright cells. Our findings suggested that CLDN4 was intimately connected to the invasion of immune cells and possesses significant potential as a therapeutic target in the treatment of cancer.

This study had certain shortcomings that need to be addressed. First, the predictive and prognostic usefulness of CLDN4 for the immune system needs to be verified in a larger number of OC patients who come from multiple real-world multicenters. Second, additional preclinical and clinical research is required to determine whether or not OC patients who have greater CLDN4 levels are more responsive to immune checkpoint inhibitors. Third, additional research, both experimental and clinical, is required to investigate potential techniques for enhancing immune function while minimizing the effects of an inhibitive milieu by focusing on CLDN4.

5. Conclusion

In the current investigation, we provide evidence that there was a connection between CLDN4 and OC. The results of this research showed that CLDN4 was an important gene in OC that has the potential to act as a predictive biomarker. Additionally, the researchers found that the expression of CLDN4 might be utilized to analyze immune infiltration in OC patients. To evaluate the accuracy of these predictors, however, additional research and experiments are required because the sample sizes were too small, and there was neither an internal nor an external validation of the data. In addition, more research is required to investigate the processes that underlie the pathogenic involvement of CLDN4 in OC.

Data Availability

The data used to support the findings of this study are available from the corresponding author upon request.

Conflicts of Interest

The authors declare that they have no competing interests.

Authors' Contributions

Pan Hu and Lubin Liu designed and supervised the study. Pan Hu and Li Lei performed most experiments and wrote the manuscript. Ni Jiang, Ying Wang, Xue Tian, and Xia Wei helped to perform parts of the experiments. Pan Hu and Li Lei analyzed the data and revised the article. All authors contributed to the article and approved the submitted version.

Acknowledgments

Supplementary Materials

Figure S1: pancancer analysis of CLDN4 based on (A) TCGA datasets or (B) TCGA and GTEx database. (*Supplementary Materials*)

References

[1] C. Stewart, C. Ralyea, and S. Lockwood, "Ovarian cancer: an integrated review," *Seminars in Oncology Nursing*, vol. 35, no. 2, pp. 151–156, 2019.

[2] M. A. Roett and P. Evans, "Ovarian cancer: an overview," *American Family Physician*, vol. 80, no. 6, pp. 609–616, 2009.

[3] E. A. Eisenhauer, "Real-world evidence in the treatment of ovarian cancer," *Annals of Oncology*, vol. 28, 2017.

[4] P. P. Santoiemma and D. J. Powell Jr., "Tumor infiltrating lymphocytes in ovarian cancer," *Cancer Biology & Therapy*, vol. 16, no. 6, pp. 807–820, 2015.

[5] A. Chandra, C. Pius, M. Nabeel et al., "Ovarian cancer: current status and strategies for improving therapeutic outcomes," *Cancer Medicine*, vol. 8, no. 16, pp. 7018–7031, 2019.

[6] M. Friedrich, D. Friedrich, C. Kraft, and C. Rogmans, "Multimodal treatment of primary advanced ovarian cancer," *Anticancer Research*, vol. 41, no. 7, pp. 3253–3260, 2021.

[7] E. Emmings, S. Mullany, Z. Chang, C. N. Landen Jr., S. Linder, and M. Bazzaro, "Targeting mitochondria for treatment of chemoresistant ovarian cancer," *International Journal of Molecular Sciences*, vol. 20, no. 1, p. 229, 2019.

[8] D. Trudel, D. P. Labbé, I. Bairati, V. Fradet, L. Bazinet, and B. Têtu, "Green tea for ovarian cancer prevention and treatment: a systematic review of the *in vitro*, *in vivo* and epidemiological studies," *Gynecologic Oncology*, vol. 126, no. 3, pp. 491–498, 2012.

[9] N. Defamie, A. Chepied, and M. Mesnil, "Connexins, gap junctions and tissue invasion," *FEBS Letters*, vol. 588, no. 8, pp. 1331–1338, 2014.

[10] A. A. Bhat, N. Syed, L. Therachiyil et al., "Claudin-1, a double-edged sword in cancer," *International Journal of Molecular Sciences*, vol. 21, no. 2, p. 569, 2020.

[11] H. Du, X. Yang, J. Fan, and X. Du, "Claudin 6: therapeutic prospects for tumours, and mechanisms of expression and regulation (review)," *Molecular Medicine Reports*, vol. 24, no. 3, 2021.

[12] Y. Hashimoto, Y. Okada, K. Shirakura et al., "Anti-claudin antibodies as a concept for development of claudin-directed drugs," *The Journal of Pharmacology and Experimental Therapeutics*, vol. 368, no. 2, pp. 179–186, 2019.

[13] Y. X. Song, J. X. Sun, J. H. Zhao et al., "Non-coding RNAs participate in the regulatory network of CLDN4 via ceRNA mediated miRNA evasion," *Nature Communications*, vol. 8, no. 1, p. 289, 2017.

[14] B. Arneth, "Tumor microenvironment," *Medicina*, vol. 56, no. 1, p. 15, 2019.

[15] M. Jarosz-Biej, R. Smolarczyk, T. Cichoń, and N. Kułach, "Tumor microenvironment as a "game changer" in cancer radiotherapy," *International Journal of Molecular Sciences*, vol. 20, no. 13, p. 3212, 2019.

[16] L. Hui and Y. Chen, "Tumor microenvironment: sanctuary of the devil," *Cancer Letters*, vol. 368, no. 1, pp. 7–13, 2015.

[17] T. Du, J. Gao, P. Li et al., "Pyroptosis, metabolism, and tumor immune microenvironment," *Clinical and Translational Medicine*, vol. 11, no. 8, article e492, 2021.

[18] Y. Li, L. Zhao, and X. F. Li, "Hypoxia and the tumor microenvironment," *Technology in Cancer Research & Treatment*, vol. 20, 2021.

[19] L. Liang, J. Yu, J. Li et al., "Integration of scRNA-Seq and bulk RNA-Seq to analyse the heterogeneity of ovarian cancer immune cells and establish a molecular risk model," *Frontiers in Oncology*, vol. 11, article 711020, 2021.

[20] C. Yang, B. R. Xia, Z. C. Zhang, Y. J. Zhang, G. Lou, and W. L. Jin, "Immunotherapy for ovarian cancer: adjuvant, combination, and neoadjuvant," *Frontiers in Immunology*, vol. 11, article 577869, 2020.

[21] K. M. Elias, J. Guo, and R. C. Bast Jr., "Early detection of ovarian cancer," *Hematology/Oncology Clinics of North America*, vol. 32, no. 6, pp. 903–914, 2018.

[22] M. Barani, M. Bilal, F. Sabir, A. Rahdar, and G. Z. Kyzas, "Nanotechnology in ovarian cancer: diagnosis and treatment," *Life Sciences*, vol. 266, article 118914, 2021.

[23] H. D. Liu, B. R. Xia, M. Z. Jin, and G. Lou, "Organoid of ovarian cancer: genomic analysis and drug screening," *Clinical & Translational Oncology*, vol. 22, no. 8, pp. 1240–1251, 2020.

[24] X. Dong, X. Men, W. Zhang, and P. Lei, "Advances in tumor markers of ovarian cancer for early diagnosis," *Indian Journal of Cancer*, vol. 51, Supplement 3, pp. e72–e76, 2014.

[25] W. Tian, N. Lei, J. Zhou et al., "Extracellular vesicles in ovarian cancer chemoresistance, metastasis, and immune evasion," *Cell Death & Disease*, vol. 13, no. 1, p. 64, 2022.

[26] S. Hao, C. Yang, P. Song et al., "CLDN4 promotes growth of acute myeloid leukemia cells via regulating AKT and ERK1/2 signaling," *Biochemical and Biophysical Research Communications*, vol. 619, pp. 137–143, 2022.

[27] J. Luo, H. Wang, H. Chen, G. Gan, and Y. Zheng, "CLDN4 silencing promotes proliferation and reduces chemotherapy sensitivity of gastric cancer cells through activation of the PI3K/Akt signalling pathway," *Experimental Physiology*, vol. 105, no. 6, pp. 979–988, 2020.

[28] Y. Pan, Y. Yu, X. Wang, and T. Zhang, "Tumor-associated macrophages in tumor immunity," *Frontiers in Immunology*, vol. 11, article 583084, 2020.

[29] J. Kim and J. S. Bae, "Tumor-associated macrophages and neutrophils in tumor microenvironment," *Mediators of Inflammation*, vol. 2016, Article ID 6058147, 11 pages, 2016.

[30] K. G. K. Deepak, R. Vempati, G. P. Nagaraju et al., "Tumor microenvironment: challenges and opportunities in targeting metastasis of triple negative breast cancer," *Pharmacological Research*, vol. 153, article 104683, 2020.

Research Article

Identification of GPD1L as a Potential Prognosis Biomarker and Associated with Immune Infiltrates in Lung Adenocarcinoma

Zhengyang Fan,[1] Song Wu,[1] Hongyang Sang,[1] Qianping Li,[1] Shaofei Cheng [iD],[1] and Hongling Zhu [iD][2]

[1]*Department of Cardiothoracic Surgery, Shanghai Sixth People's Hospital Affiliated to Shanghai Jiao Tong University School of Medicine, Shanghai, China*
[2]*Department of Oncology, Shanghai Sixth People's Hospital Affiliated to Shanghai Jiao Tong University School of Medicine, Shanghai, China*

Correspondence should be addressed to Shaofei Cheng; dr_chengshaofei@163.com
and Hongling Zhu; zhuhongling199101@163.com

Lung adenocarcinoma (LUAD) is one of the most prevalent pathological kinds of lung cancer, which is a common form of cancer that has a high death rate. Over the past several years, growing studies have indicated that GPD1L was involved in the advancement of a number of different cancers. However, its clinical significance in LUAD has not been investigated. In this study, following an examination of the TGCA datasets, we found that GPD1L displayed a dysregulated state in a wide variety of cancers; this led us to believe that GPD1L is an essential regulator in the progression of malignancies. In addition, we found that the expression of GPD1L was much lower in LUAD tissues when compared with nontumor specimens. According to the findings of ROC tests, GPD1L was able to effectively identify LUAD specimens from nontumor samples with an AUC value of 0.828 (95% confidence interval: 0.793 to 0.863). On the basis of the clinical study, a low expression of GPD1L was clearly related with both the N stage and the clinical stage. Moreover, based on the findings of a Kaplan-Meier survival study, elevated GPD1L expression was a strong indicator of considerably improved overall survival (OS) and disease-specific survival (DSS). GPD1L expression and clinical stages were found to be independent prognostic indicators for overall survival and disease-free survival in LUAD patients, according to multivariate analyses. Based on multivariate analysis, the C-indexes and calibration plots of the nomogram demonstrated an effective prediction performance for LUAD patients. Besides, the expression of GPD1L was positively related to mast cells, eosinophils, Tcm, TFH, iDC, DC, and macrophages, while negatively associated with Th2 cells, NK CD56dim cells, Tgd, Treg, and neutrophils. Finally, qRT-PCR was able to demonstrate that GPD1L had a significant amount of expression in LUAD. Additionally, according to the results of functional tests, overexpression of GPD1L had a significant inhibiting effect on the proliferation of LUAD cells. In general, the results of our study suggested that GPD1L had the potential to serve as a diagnostic and prognostic marker for LUAD.

1. Introduction

Over twenty-seven percent of all cancer-related deaths worldwide are attributable to lung cancer, with non-small cell lung cancer (NSCLC) being responsible for eighty percent of all lung cancer cases [1]. The histological subtype of non-small cell lung cancer that occurs most frequently is known as lung adenocarcinoma (LUAD) [2]. It has virtually reached the position of being the primary contributor to death among those living in urban regions of China [3]. Even with all of the advancements that have been made over the years in cancer diagnosis and treatment, the death rate of lung cancer is still rather high, which is particularly relevant to smokers [4, 5]. As a direct consequence of this, numerous patients who were diagnosed with early lung cancer did not receive adjuvant therapy following their surgeries [6, 7].
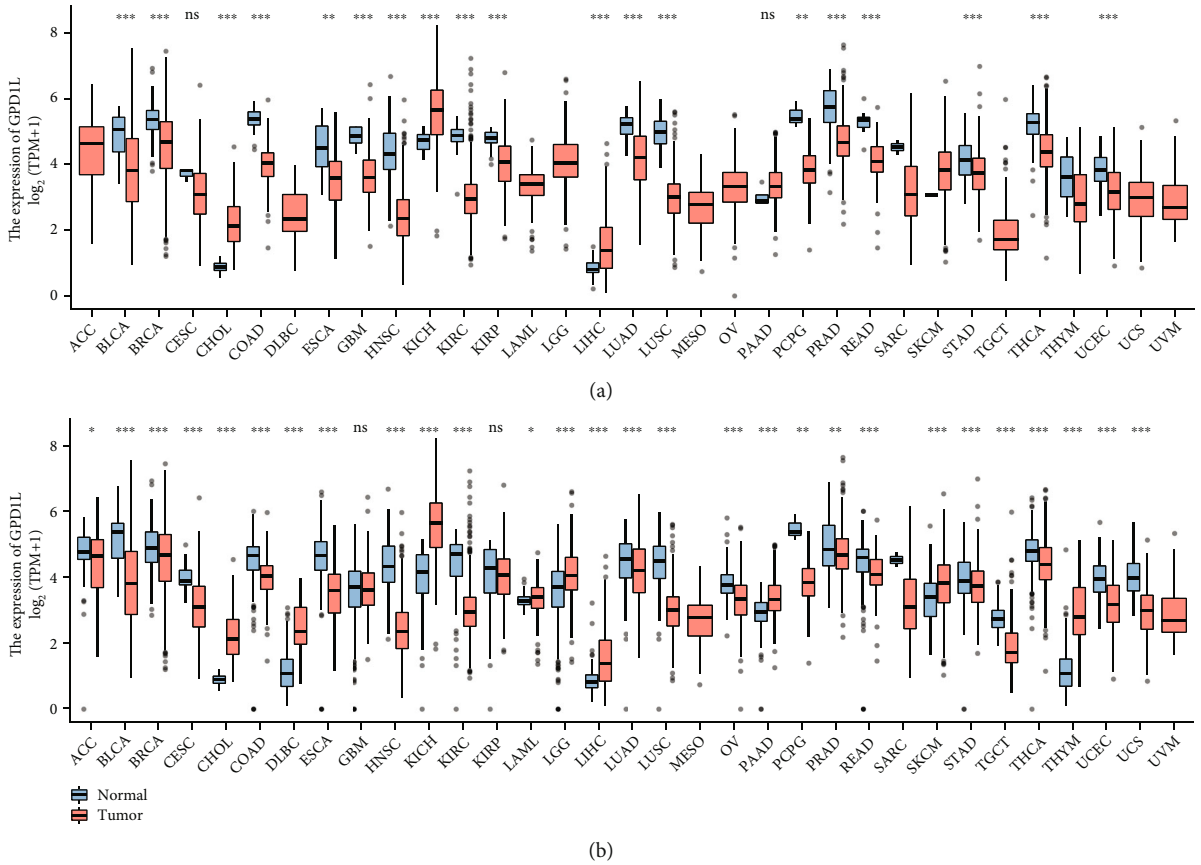
(a)

(b)

Figure 1: GPD1L levels that are either higher or lower in various malignancies when compared with normal tissues in (a) the TCGA datasets and (b) the TCGA and GTEx database. $^*p < 0.05$, $^{**}p < 0.01$, $^{***}p < 0.001$; ns: no significance.

Consequently, the disease returned or spread to other parts of the body in some of the patients due to a number of variables, including that some people are diagnosed at an advanced stage of lung cancer [8, 9]. That may be one of the many reasons why this is the case. Besides, lung cancer patients do not receive an accurate picture of their prognosis through the use of the guided staging technique that is currently in place, which is another possible explanation [10, 11]. At this time, the histopathologic diagnosis and the neoplasm staging system are the only things that can accurately predict a patient's prognosis [12]. However, conventional approaches do not provide a precise enough picture of a patient's outlook to be used. In order to further aid doctors to treat LUAD, therefore, a trustworthy and precise marker for prognosis prediction needs to be established.

The protein known as glycerol 3-phosphate dehydrogenase 1-like (GPD1L) is encoded by the gene GPD1L, which is located on chromosome 3p22.3 [13]. This protein is responsible for catalyzing the conversion of sn-glycerol 3-phosphate to glycerone phosphate [14]. The GPD1L protein was discovered in the cytoplasm, and it was connected to the plasma membrane [15]. It was found in 2002 when the Mammalian Gene Collection (MGC) program of the National Institutes of Health attempted to find and sequence a cDNA clone [16]. Studies done in the past have found evidences that GPD1L was involved in more than one type of tumor. For example, Liu et al. discovered that the mRNA

expression of GPD1L, which was found to be downregulated, and HIF1, which was found to be upregulated, exhibited a negative association ($r = -.496$, $p = .001$) in cT1-2 N0 head and neck squamous cell carcinoma (HNSCC) [17]. In addition to this, GPD1L has been shown to have a negative association with HIF1 expression and to be a factor that predicts lymph node metastases in cases of oral and HPV-related oropharyngeal cancer [18]. Zhao et al. showed that the expression level of GPD1L was low in colorectal cancer, and it had a strong correlation with the clinical stage, grade, and TNM stage of colorectal cancer [19]. In addition, GPD1L protein levels were also measured in HNSCC patients and found to be associated with a dismal prognosis for those patients with HNSCC [18]. However, on the other hand, very little is known about the function of GPD1L in LUAD.

Tumor microenvironment (TME) refers to the collection of cancer cells, immune cells, stromal cells, and extracellular matrix that together play a significant role in the progression of cancer [20]. Cancer cells are present in the TME, and these cells have the ability to infect neighboring tissues either directly or indirectly by traveling through blood and lymphatic channels [21]. These infiltrating cells have the capability of provoking an immune response through the release of cytokines and other substances that influence the growth of the tumor [22]. Growing researches have indicated that TME affected the procedures of tumor
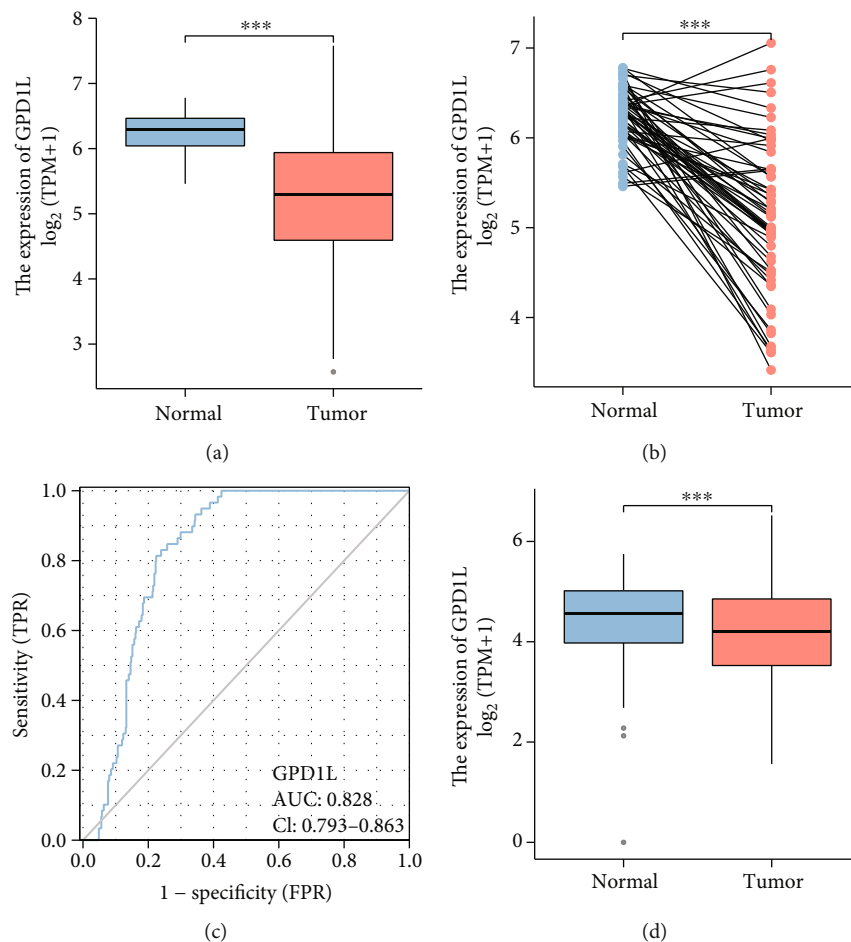
(a)

(b)

(c)

(d)

Figure 2: The levels of GPD1L expression in LUAD, as well as the diagnostic usefulness of this protein. (a, b) The levels of GPD1L expression found in LUAD specimens as compared to those found in nontumor tissues. (c) The ROC tests were utilized to evaluate the diagnostic potential of GPD1L. (d) The levels of GPD1L expression found in LUAD specimens compared to those found in non-tumor specimens, as determined by the TCGA or GTEx database. $^*p < 0.05$, $^{**}p < 0.01$, $^{***}p < 0.001$; ns: no significance.

progression and have shown a possible predictive value for the clinical outcome of patients, including LUAD [23, 24].

The rapid growth of precision medicine has led to an increase in the number of studies in which researchers use statistical algorithms to investigate new diagnostic and therapeutic targets. The Cancer Genome Atlas (TCGA) delivered genomic profiles as well as clinical data, which made it feasible to study the association between genomic features and clinical as well as prognostic aspects. The purpose of this research was to investigate the clinical relevance of GPD1L in LUAD patients and to determine whether or not it was associated with immune cell infiltration.

2. Materials and Methods

2.1. Cell Lines and Cell Transfection. LUAD cell lines, including A549, H1299, HCC827, H226, and H23 cells, as well as normal bronchial epithelial cells (BEAS-2B), were purchased from the American Type Culture Collection (ATCC, Manassas, VA, USA). Next, the LUAD cell lines were cultured in a 5% CO_2 incubator at 37°C in RPMI-1640 medium (Cat#11875119, Gibco, Shanghai, China) containing 10%

fetal bovine serum (FBS) (Cat#12664025, Gibco, Shanghai, China). After mixing for 20 minutes at room temperature, 2μl of the overexpress plasmids targeting GPD1L in 100μl of RMPI 1640 media were combined with μl of lipofectamine 3000 (Cat#L3000001, Invitrogen, Shanghai, China) that had been diluted in 100μl of RMPI 1640 media. Following a transfection time of 48 hours, the cells were harvested to carry out the following experiments.

2.2. Quantitative Real-Time PCR (qRT-PCR). Trizol reagents (Cat#15596026, Invitrogen, MA, USA) were employed to isolate the total RNAs from various tissues and cells, and the concentration of total RNAs was examined by Nano-Drop 2000 device (Cat#ND-2000-GL, Thermo, Waltham, MA, USA). Subsequently, 2μg of total RNAs was subjected to reverse reaction using EpiNext Hi-Fi cDNA Synthesis kit (AmyJet, Wuhan, Hubei, China) to obtain the cDNAs. Then, the qRT-PCR assays were carried out with the use of PrimeScriptTM RT Master Mix kits, which were purchased from Takara company (Dalian, Liaoning, China), and the Bio-Rad CFX96 PCR System (Bio-Rad, CA, USA). The relative expression levels were determined using the $2^{-\triangle\triangle Ct}$
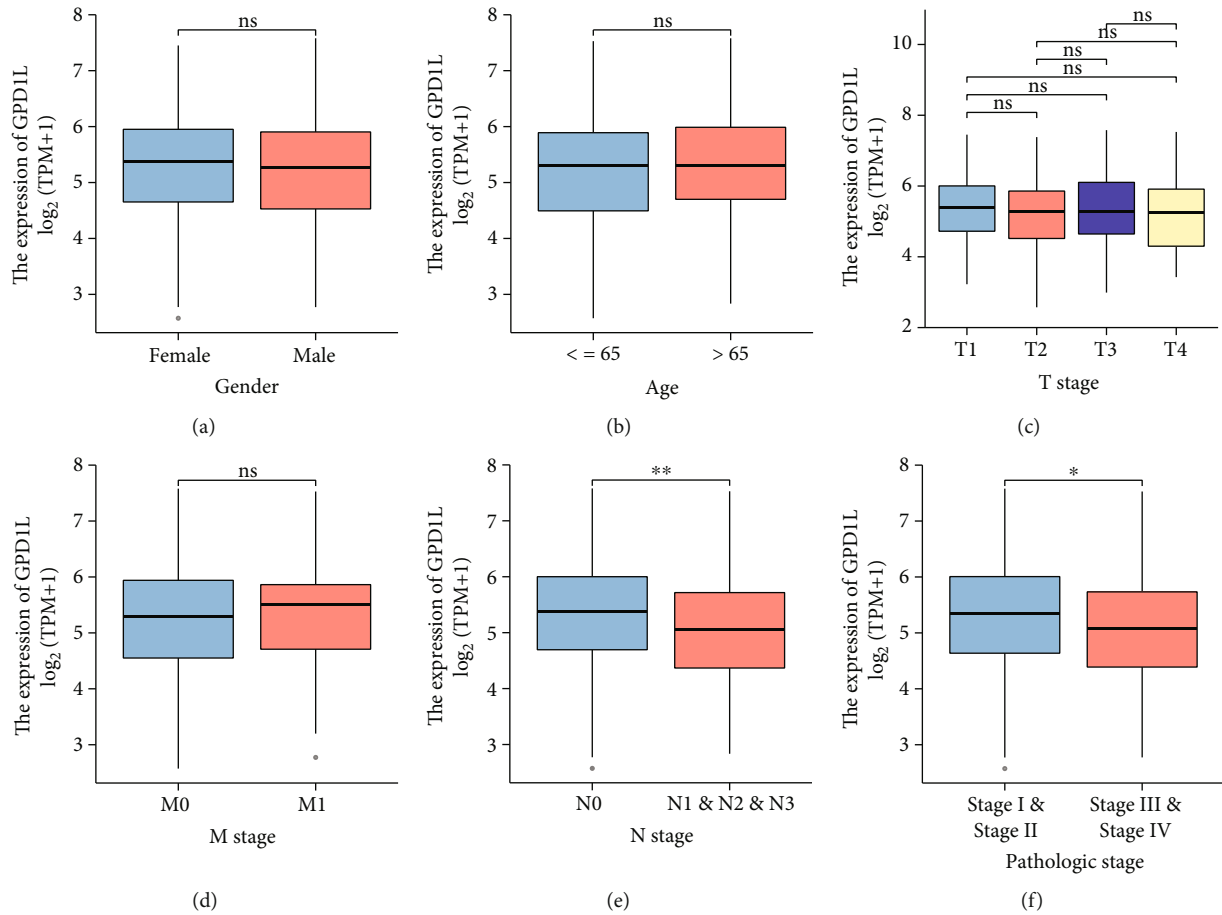
(a)

(b)

(c)

(d)

(e)

(f)

Figure 3: GPD1L expression and the clinical characteristics of LUAD patients have been found to have a correlation with one another. GPD1L expression was found to be associated with a number of clinicopathologic variables, such as (a) gender, (b) age, (c) T stage, (d) M stage, (e) N stage, and (f) pathologic stage. $^*p < 0.05$, $^{**}p < 0.01$, $^{***}p < 0.001$; ns: no significance.

method, with GAPDH serving as the control for the standardization process. The primer sequence for GPD1L was listed as follows: F-primer: 5'ATCAAGGGCATAGACGAGGG3'; R-primer: 5'TCTGCATCATCAACCACGGTA3'. The primer sequence for GAPDH was: F-primer: 5'TCAAGCTCATT TCCTGGTATGAC3'; R-primer: 5'CTTGCTCAGTGTCC TTGCTG3'.

2.3. Cell Viability Assay.
The Cell Counting Kit-8 (CCK-8) test kits (Cat#HY-K0301, MedChemExpress, Shanghai, China) was utilized in order to determine the cellular proliferation of H1299 and H226 cells with overexpressing GPD1L. The cells were firstly inserted onto 96-well plates (2500 cells per well, 100 μl) after GPD1L-overexpressing plasmids were transfected. Afterwards, the cells were applied for CCK-8 assays at 24, 48, 72, and 96 hours. After adding 10 μl of CCK-8 reagents from MedChemExpress company (Cat#HY-K0301, Shanghai, China) and allowing the mixture to incubate for one hour, the optical density was measured using a microplate reader from BioTek (BioTek, Winooski, VT, USA) at a wavelength of 450 nm.

2.4. Data Collection and Processing.
The TCGA Data Portal (http://www.tcgaportal.org/) was mined for the high-throughput gene expression data in order to collect it. This data was obtained not just from LUAD tissues but also from normal lung tissues in the TCGA Data Portal. Besides, these RNA-seq data (HTSeq-count) were obtained through the data portal of the Genomic Data Commons (GDC), which is open to the general public (https://gdc.cancer.gov/). The Illumina HiSeq RNA-seq platform was the source of these data, which included 535 LUAD samples in addition to 59 noncancerous samples.

2.5. Identification of the Aberrantly Expressed Genes in LUAD.
In order to determine which genes were differentially expressed, the expression patterns of LUAD tissues and normal tissues were compared using R software. The edgeR Bioconductor package was used to undertake an investigation on the differential expression of particular genes. For the purpose of differentially expressed genes (DEGs) identification, the threshold values were determined to be |log 2(fold change [FC])| greater than 2, p value less than 0.01, and false discovery rate (FDR) less than 0.01.

2.6. GPD1L Differential Expression in Pan-Cancer in the TCGA Database. In order to calculate the differential expression of GPD1L, boxplots and scatter plots were produced using the disease state as the variable. The illness condition was either tumor or normal. Receiver operating characteristic (ROC) curves were utilized to create an estimate of GPD1L's diagnostic performance. The statistical ranking for GPD1L expression that was designated as GPD1L high or GPD1L low, respectively, was determined by whether it was above or below the median value.

2.7. Prognostic Analysis. In order to determine the overall survival (OS) of patients who were part of the TCGA cohort, a Kaplan-Meier analysis was carried out. Univariate Cox regression analyses were carried out to determine the importance of GPD1L in evaluating overall survival (OS) and disease-specific survival (DSS) in patients with LUAD.

2.8. Analysis of DEGs between GPD1L High and Low Expression LUAD Groups. The unpaired Student *t*-test that is included in the DESeq2 (3.8) package was used to find differentially expressed genes (DEGs) comparing patients with high and low levels of GPD1L in the TCGA datasets.

2.9. Functional Enrichment Analysis. Disease Ontology (DO) enrichment analyses were carried out on DEGs with the help of the "clusterProfiler" and DOSE packages in the R programming language [25, 26]. The "clusterProfiler" R package was used to carry out the analyses based on DEGs that were conducted by GO and KEGG.

2.10. Nomogram Construction. Combining the findings of the genetic risk score model with clinical characteristics led to the development of a nomogram that was able to accurately forecast 3- and 5-year LUAD overall survival (OS). Calibration plots were used to evaluate the nomogram's ability to make accurate predictions. The area under the curve (AUC) was employed to analyze the time-dependent sensitivities and specificities of the nomogram for both the 3-year and 5-year OS ROC curves. R software was used as the statistical program for all of the studies that were done (version 3.4.1). The rms package of R software was used to construct the nomogram and calibration plots, and the time-ROC package was used to conduct the analysis of the time-dependent ROC curve. The Hmisc package of the R program was utilized in order to do comparisons of the C-index between the nomogram and the staging systems developed by the American Joint Committee on Cancer. If the *p* values were lower than 0.05, then the null hypothesis, which states that there was no difference, was rejected.

2.11. Statistical Analysis. R (version 3.6.3) was used to carry out all statistical assays. The statistical analyses were performed on one-way analysis of variance (ANOVA) or two-tailed Student's *t*-test, and the results with a *p* value of less than 0.05 were determined as statistically significant.

TABLE 1: The association between GPD1L expression and clinicopathological features.

Characteristic	Low expression of GPD1L	High expression of GPD1L	*p*
n	267	268	
Gender, *n* (%)			0.280
Female	136 (25.4%)	150 (28%)	
Male	131 (24.5%)	118 (22.1%)	
Age, *n* (%)			1.000
< =65	128 (24.8%)	127 (24.6%)	
>65	130 (25.2%)	131 (25.4%)	
Pathologic stage, *n* (%)			0.004
Stage I	128 (24.3%)	166 (31.5%)	
Stage II	72 (13.7%)	51 (9.7%)	
Stage III	52 (9.9%)	32 (6.1%)	
Stage IV	12 (2.3%)	14 (2.7%)	
T stage, *n* (%)			0.692
T1	81 (15.2%)	94 (17.7%)	
T2	150 (28.2%)	139 (26.1%)	
T3	25 (4.7%)	24 (4.5%)	
T4	10 (1.9%)	9 (1.7%)	
N stage, *n* (%)			0.002
N0	159 (30.6%)	189 (36.4%)	
N1	60 (11.6%)	35 (6.7%)	
N2	44 (8.5%)	30 (5.8%)	
N3	2 (0.4%)	0 (0%)	
M stage, *n* (%)			0.893
M0	186 (48.2%)	175 (45.3%)	
M1	12 (3.1%)	13 (3.4%)	
Age, median (IQR)	66 (58, 72)	66 (60, 73)	0.372

3. Results

3.1. Pan-Cancer Analysis of GPD1L. First, we carried out a pan-cancer study utilizing data from either TCGA or both TCGA and GTEx. Our research revealed that GPD1L demonstrated a dysregulated expression in a wide variety of malignancies, as illustrated in Figures 1(a) and 1(b). Furthermore, the expression pattern of GPD1L was shown to be variable in various types of cancers, which led researchers to hypothesize that GPD1L might act as tumor promoters or tumor suppressors.

3.2. The Expression of GPD1L in LUAD and Its Diagnostic Value. After that, we performed an analysis on the expression of GPD1L in LUAD and discovered that the expression of GPD1L was much lower in LUAD specimens when compared to specimens of nontumorous tissues (Figures 2(a) and 2(b)). Thereafter, the diagnostic utility of GPD1L was investigated further by us. The findings of ROC assays revealed that GPD1L was successful in differentiating LUAD specimens from normal specimens with an area under the ROC curves (AUC) of 0.828 (95% confidence interval: 0.793 to 0.863). These results are displayed in Figure 2(c).
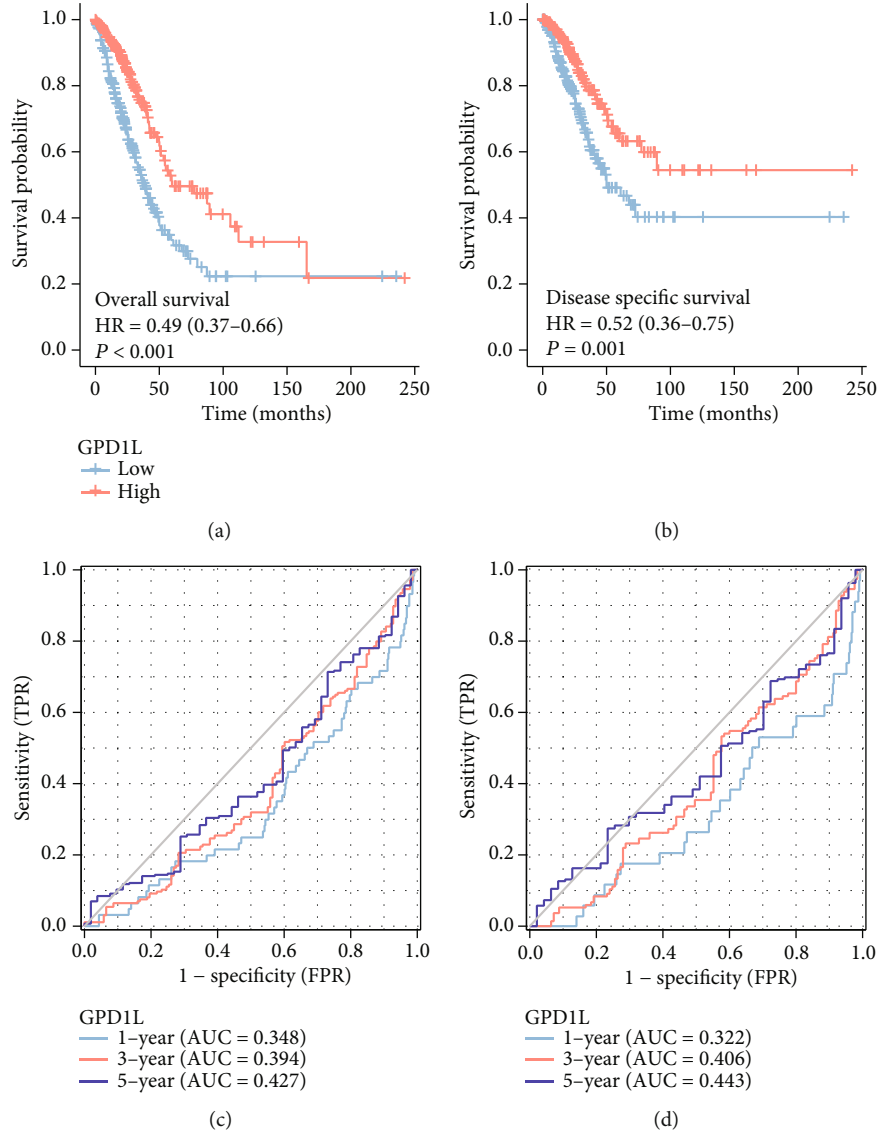
FIGURE 4: Analysis of the prognosis of GPD1L in patients with LUAD who were part of the TCGA cohort. Expression of GPD1L has been shown to have a correlation with both (a) overall survival and (b) survival specific to the disease. (c, d) The predictive performance of GPD1L expression in TCGA is evaluated using time-dependent receiver operating characteristic curves.

In addition, a discovery that is analogous to this one was discovered based on the TCGA and GTEx data (Figure 2(d)).

3.3. The Associations between GPD1L Expressions and Clinical Factors of LUAD Patients.
For the purpose of elucidating the function and importance of GPD1L expression, the TCGA data on all LUAD samples containing GPD1L expression data together with the characteristics of all patients were studied. As observed in Figures 3(a)–3(f) and Table 1, our investigation revealed that a low expression of GPD1L was inextricably linked to both the N stage and the clinical stage.

3.4. The Prognostic Values of GPD1L Expressions in LUAD.
Through the use of survival analysis, we were able to further investigate whether or not GPD1L levels were connected with LUAD prognosis. According to the results of a

Kaplan-Meier survival analysis, greater GPD1L expression predicted significantly improved OS ($p < 0.001$, Figure 4(a)) and DSS ($p = 0.001$, Figure 4(b)). GPD1L expression had a good predictive potential for the OS (AUC = 0.427, Figure 4(c)) and disease-specific survival (AUC = 0.443, Figure 4(d)) of LUAD patients, according to data from the TCGA. We performed univariate and multivariate analyses using Cox's proportional hazard model to further investigate the prognostic value of GPD1L expression in LUAD. Specifically, we demonstrated that the expression of GPD1L and the clinical stages were both independent prognostic indicators for overall survival (Table 2) and disease-specific survival (Table 3) in LUAD patients.

3.5. Construction and Validation of a Nomogram Based on the GPD1L Expression.
In order to give a quantitative method for predicting the prognosis of LUAD patients, a

Table 2: Univariate and multivariate analysis of overall survival in LUAD patients.

Characteristics	Total (n)	Univariate analysis Hazard ratio (95% CI)	p value	Multivariate analysis Hazard ratio (95% CI)	p value
Gender	526				
Female	280	Reference			
Male	246	1.070 (0.803-1.426)	0.642		
Age	516				
< =65	255	Reference			
>65	261	1.223 (0.916-1.635)	0.172		
Pathologic stage	518				
Stage I and stage II	411	Reference			
Stage III and stage IV	107	2.664 (1.960-3.621)	<0.001	2.490 (1.829-3.391)	<0.001
GPD1L	526				
Low	263	Reference			
High	263	0.492 (0.365-0.662)	<0.001	0.521 (0.386-0.705)	<0.001

Table 3: Univariate and multivariate analysis of disease-specific survival in LUAD patients.

Characteristics	Total (n)	Univariate analysis Hazard ratio (95% CI)	p value	Multivariate analysis Hazard ratio (95% CI)	p value
Gender	491				
Female	262	Reference			
Male	229	0.989 (0.687-1.424)	0.954		
Age	481				
< =65	243	Reference			
>65	238	1.013 (0.701-1.464)	0.944		
Pathologic stage	483				
Stage I and stage II	389	Reference			
Stage III and stage IV	94	2.436 (1.645-3.605)	<0.001	2.269 (1.530-3.367)	<0.001
GPD1L	491				
Low	241	Reference			
High	250	0.517 (0.355-0.752)	<0.001	0.545 (0.373-0.798)	0.002

nomogram was constructed using GPD1L and clinical stage as its two primary variables (Figure 5(a)). A point scale was utilized in the construction of the nomogram that was based on the multivariate Cox analysis. The variables were each given a certain number of points depending on the scale. When calculating the likelihood of surviving for LUAD patients at 1, 3, and 5 years, we drew a vertical line immediately downward from the total point axis to the outcome axis. Next, we also performed an analysis on the nomogram's ability to make accurate predictions, and the findings showed that the C-index of the model was 0.671 (CI: 0.650-0.691), which indicated that the nomogram's ability to make accurate predictions is only to a moderate degree (Figure 5(b)). In addition, we discovered a result that was comparable based on the DSS model (Figures 6(a) and 6(b)).

3.6. Functional Enrichment Analysis. We first discovered a total of 454 DEGs. After that, we carried out a GO analysis with the 454 DEGs. As shown in Figure 7(a), we found that the 454 DEGs were mainly enriched in humoral immune response, defense response to the bacterium, antimicrobial humoral response, presynapse, neuronal cell body, dense core granule, receptor ligand activity, signaling receptor activator activity, and hormone activity. The results of KEGG revealed that the 454 DEGs were associated with neuroactive ligand-receptor interaction, complement and coagulation cascades, and Staphylococcus aureus infection (Figure 7(b)). In order to reveal more about the function of DEGs, an enrichment analysis of DO pathways was carried out. According to the findings, the majority of the disorders that were enriched by DEGs were related to nutrition disease, coronary artery disease, a developmental disorder of mental health, myocardial infarction, and overnutrition (Figure 7(c)).

3.7. The Expressions of GPD1L Were Associated with Immune Cell Infiltration. In order to evaluate the extent of immune cell infiltration that was present, the TCGA LUAD cohort's transcriptomes were analyzed using the ssGSEA methodology. This was done so that the researchers could determine the level of immune cell presence. In order to estimate the amount of immune cells that are present in the microenvironment of a tumor, the study included a total of
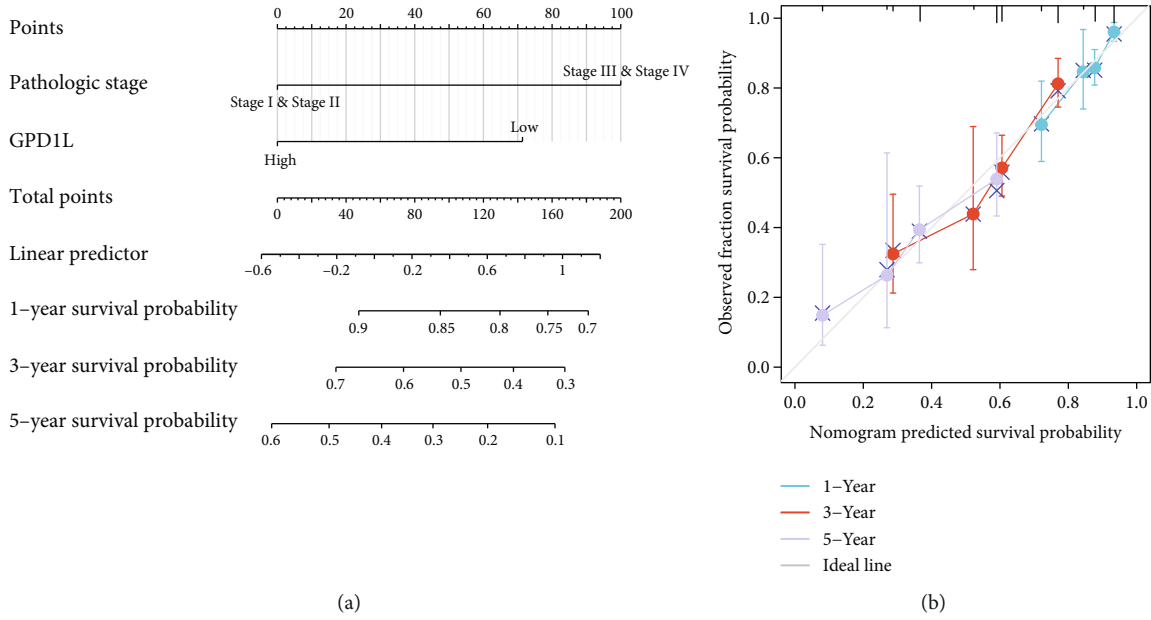
(a)

(b)

FIGURE 5: A quantitative method to predict the chance of 1-, 3-, and 5-year overall survival for patients diagnosed with LUAD. (a) A nomogram that estimates the likelihood of 1-, 3-, and 5-year overall survival for patients diagnosed with LUAD. (b) Calibration plots of the nomogram used to assess the overall likelihood of survival at 1, 3, and 5 years.
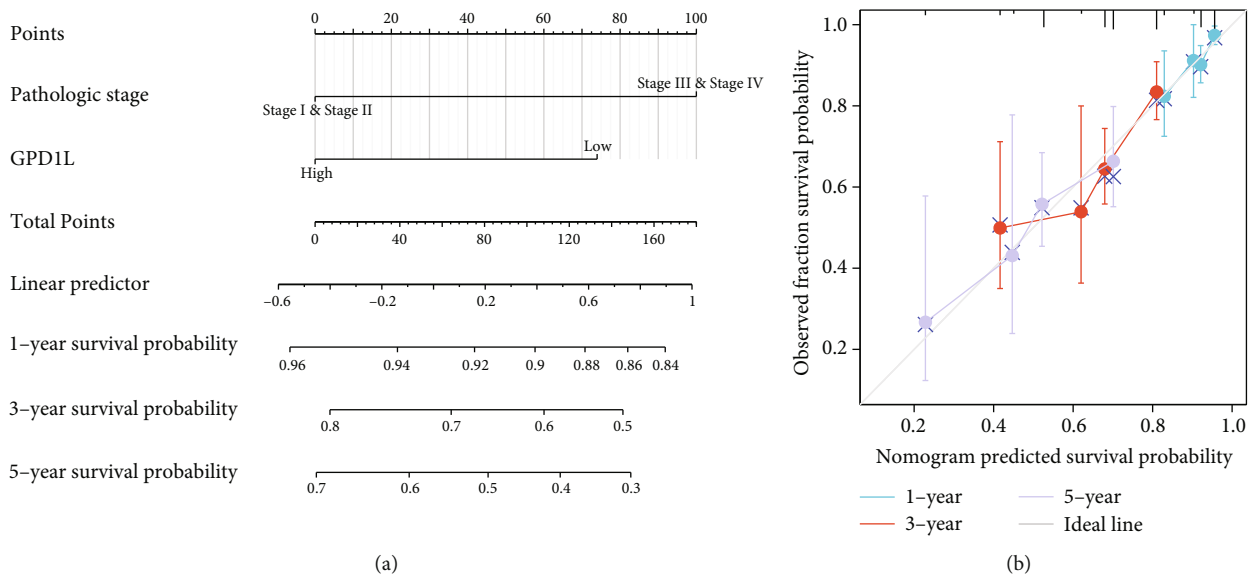

(a)

(b)

FIGURE 6: A quantitative method for estimating the likelihood that LUAD patients would develop the illness at 1, 3, and 5 years. (a) A nomogram that estimates the chance of disease-specific survival for LUAD patients at 1, 3, and 5 years. (b) Calibration plots of the nomogram used to assess the overall likelihood of survival at 1, 3, and 5 years.

twenty-four different words that were connected to the immune system. Our group observed that the expression of GPD1L was positively related to mast cells, eosinophils, Tcm, TFH, iDC, DC, and macrophages, while negatively associated with Th2 cells, NK CD56dim cells, Tgd, Treg, and neutrophils (Figures 8(a) and 8(b)).

3.8. Overexpression of GPD1L Suppressed the Proliferation of LUAD Cells. In order to provide more evidences for the presence of GPD1L in LUAD, we next carried out qRT-PCR

examination and discovered that the expression of GPD1L was much lower in A549, H1299, HCC827, H226, and H23 cells when compared with BEAS-2B cells. This difference was rather noticeable (Figure 9(a)). In addition to this, it was demonstrated that treatment with GPD1L overexpressing plasmids (ov-GPD1L) resulted in a clear elevating expression of GPD1L (Figure 9(b)). Furthermore, we conducted CCK-8 tests, which enabled us to establish that the overexpression of GPD1L markedly inhibited the proliferation of H1299 and H226 cells (Figures 9(c) and 9(d)).
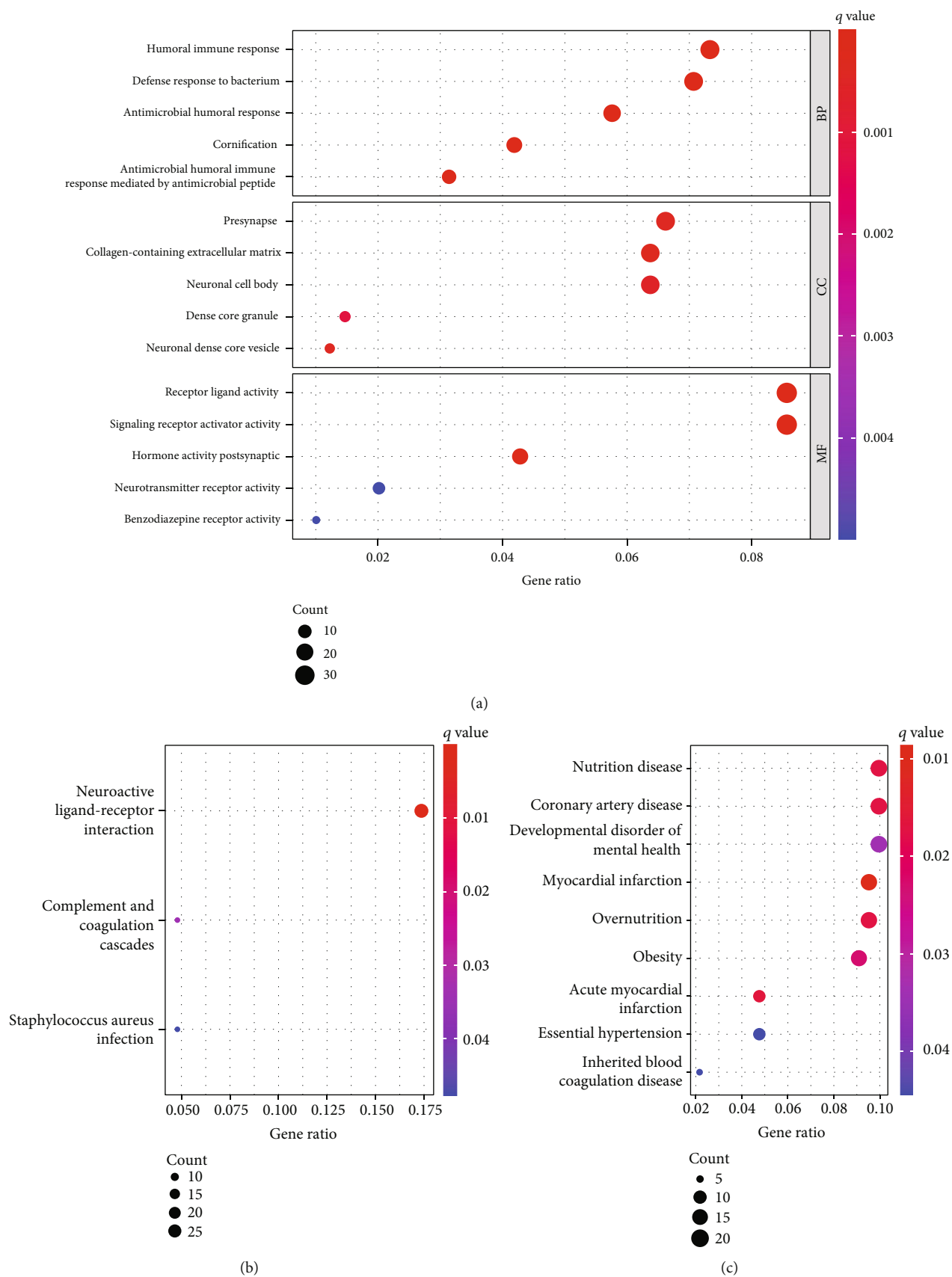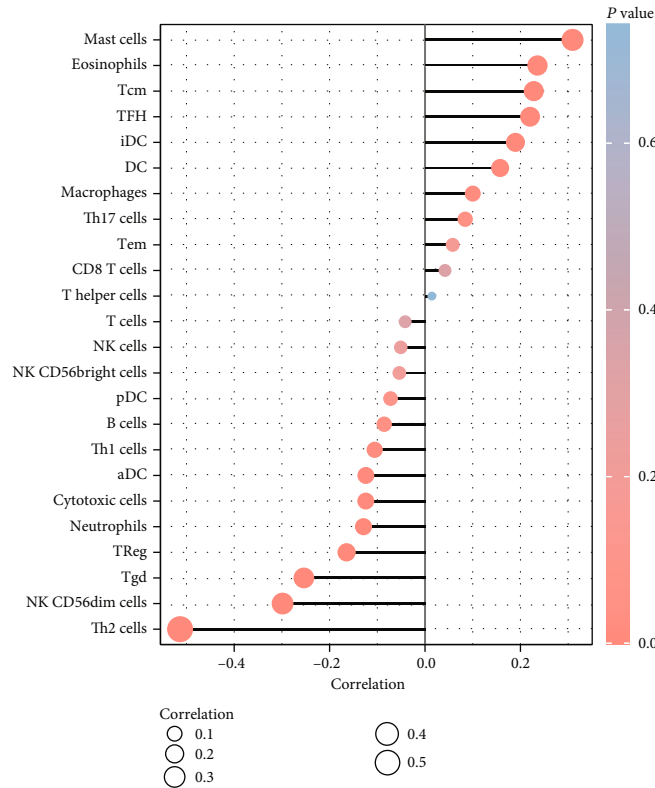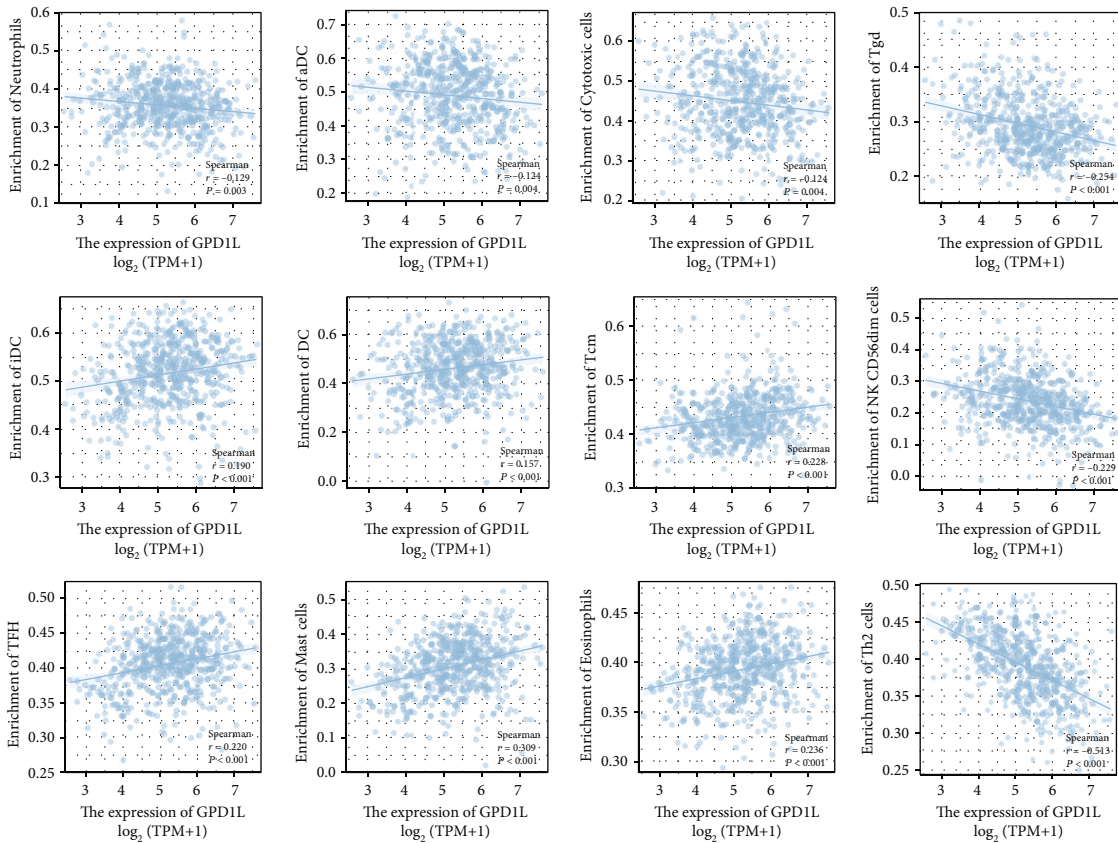
FIGURE 7: Functional enrichment analyses to identify potential biological processes. (a) The top 10 enriched BP, CC, and MF terms. (b) KEGG pathways. (c) Disease ontology enrichment analysis.

(a)

(b)

Figure 8: (a, b) Relationships between GPD1L and infiltrating immune cells in LUAD.
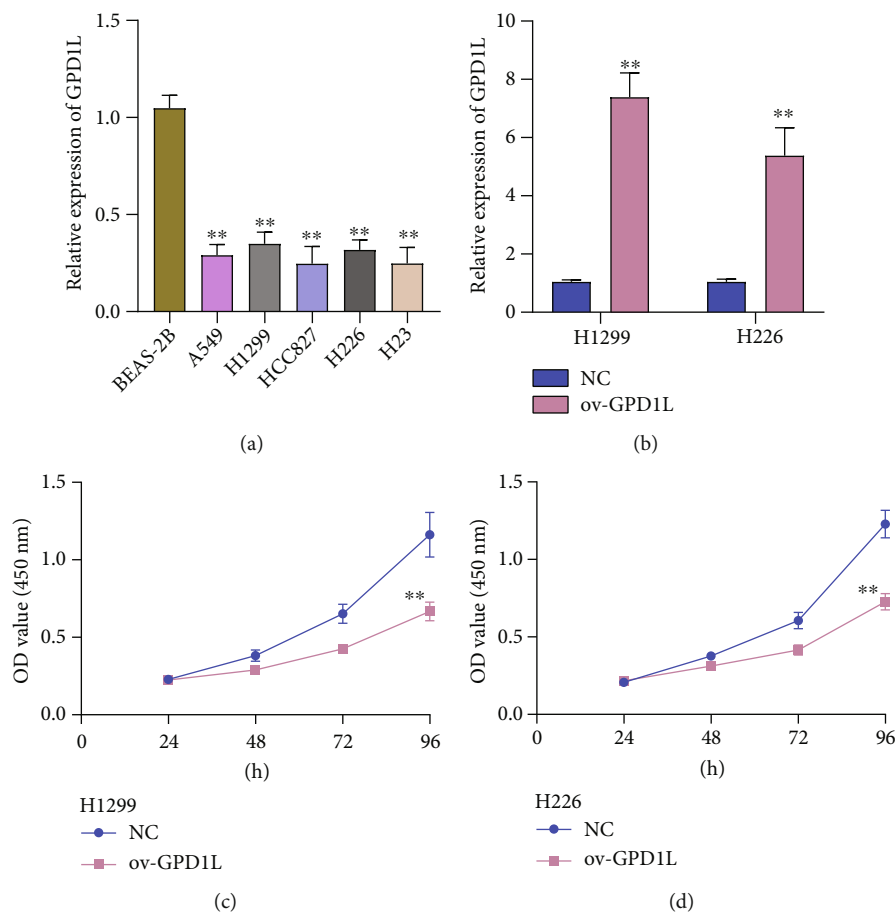
FIGURE 9: The overexpression of GPD1L in LUAD cells has been shown to limit cell growth. (a) The amount of GPD1L mRNA that is expressed relatively in LUAD cells (A549, H1299, HCC827, H226, and H23 cells) compared to BEAS-2B cells. (b) After treatment, there was an increase in the amount of GPD1L that was expressed in H1299 and H226. (c, d) The CCK-8 assay was utilized to determine whether or not the cells were viable. $^*p < 0.05$, $^{**}p < 0.01$, $^{***}p < 0.001$; ns: no significance.

4. Discussion

In spite of the significant progress that has been made over the course of the past several years, LUAD continues to be regarded as a malignant tumor that has a dismal outlook when it is discovered at an advanced clinical stage [27, 28]. As a result, the investigation of the etiological factors and molecular mechanisms underlying LUAD is of the utmost significance for both treatment and prevention [29]. The quantity of data pertaining to genes has significantly expanded as a result of the ongoing development of gene chip and sequencing technology of the second generation [30, 31]. Therefore, one of the most pressing challenges facing researchers today is figuring out how to put these data to use to assist humans in better understanding the connection between genes and cancer.

The current study used data from the TCGA dataset to gather gene expression information. We discovered a new gene called GPD1L that was associated with cancer and found that its expression was aberrant in a wide variety of cancers. Previous researches had uncovered the roles that GPD1L played in a number of different cancers. For example, Tu et al. found that low levels of GPD1L expression in hepatocellular carcinoma were predictive of shorter overall survival times for patients with hepatocellular carcinoma [32]. Importantly, we discovered that the level of GPD1L expression was significantly lower in LUAD specimens compared to nontumor specimens, which suggested that it might play a role as a tumor suppressor gene in the evolution of LUAD. In addition, ROC assays demonstrated their diagnostic utility in screening LUAD specimens to differentiate them from nontumor specimens. The expression of GPD1L was shown to be an independent predictive factor for both overall survival and disease-free survival in the LUAD patients who were studied. Based on our findings, GPD1L may serve as a potential diagnostic and prognostic biomarker for patients suffering from LUAD.

After that, a total of 454 DEGs were discovered. Then, we carried out GO and KEGG assays and found that the 454 DEGs were primarily enriched in the following categories: antimicrobial humoral response; humoral immune response; defense response to bacterium; presynapse; neuronal cell body; dense core granule; receptor ligand activity; signaling receptor activator activity; hormone activity; and

defense response to the bacterium. Based on our findings, GPD1L may be engaged in a number of different pathways that are associated with tumors.

TME can influence the development and progression of a tumor. In addition, it is made up of both cells that are part of the tumor and cells that are not part of the tumor, such as fibroblasts and immune cells [33, 34]. Immune cells that infiltrate tumors are strongly linked to angiogenesis and oncogenesis, as well as to the spread and proliferation of tumor cells [35, 36]. This connection may modulate the number of immune cells and how they differentiate. Recent researches had shed light on how inconsistencies between the advancement of a tumor and the immunological response of its host could contribute to the growth of the tumor [37]. TME was an essential component in both the beginning and the development of the tumorigenic process. Exploring the possible therapeutic targets that contribute to the remodeling of TME and supporting the transition of the TME from being tumor-friendly to being tumor-suppressed is of tremendous benefit [38, 39]. The significance of the immune microenvironment in the development of tumors was demonstrated by a significant number of research. Our findings from the study of the transcriptome based on the LUAD data in the TCGA database suggested that the immunological components present in the TME contributed to the prognosis of patients. Here, our group found that the expressions of GPD1L were positively associated with mast cells, eosinophils, Tcm, TFH, iDC, DC, and macrophages, while negatively associated with Th2 cells, NK CD56dim cells, Tgd, Treg, and neutrophils. Due to the fact that there was a correlation between the amounts of eosinophils, Th2 cells, and GPD1L expression in LUAD patients, it was shown that GPD1L might be responsible for the maintenance of an immune-active status in the TME.

Nevertheless, our investigation had a few drawbacks. First, we only used the data from the TCGA database for internal validation; in order to evaluate the applicability of the predictive signature, we require data from additional databases for external validation. Besides, experiments need to be conducted further in order to deeply uncover the mechanism of GPD1L in LUAD.

5. Conclusion

According to the results of our research, GPD1L expression is lower in patients with LUAD. Furthermore, the level of GPD1L expression is connected to the clinical case characteristics and prognosis of LUAD patients. The extent of immune cell infiltration, which may increase the antitumor impact, is directly tied to the level of expression of GPD1L. GPD1L is a biomarker that can be utilized in the diagnosis, treatment, and evaluation of the prognosis of LUAD.

Data Availability

All data are available from the corresponding authors under reasonable conditions.

Conflicts of Interest

The authors declare that they have no conflicts of interest.

References

[1] R. L. Siegel, K. D. Miller, and A. Jemal, "Cancer statistics, 2019," *CA: a Cancer Journal for Clinicians*, vol. 69, no. 1, pp. 7–34, 2019.

[2] A. M. Romaszko and A. Doboszyńska, "Multiple primary lung cancer: a literature review," *Advances in Clinical and Experimental Medicine*, vol. 27, no. 5, pp. 725–730, 2018.

[3] F. Wu, L. Wang, and C. Zhou, "Lung cancer in China: current and prospect," *Current Opinion in Oncology*, vol. 33, no. 1, pp. 40–46, 2021.

[4] F. R. Hirsch, G. V. Scagliotti, J. L. Mulshine et al., "Lung cancer: current therapies and new targeted treatments," *The Lancet*, vol. 389, no. 10066, pp. 299–311, 2017.

[5] Y. Zhang, F. Fu, and H. Chen, "Management of ground-glass opacities in the lung cancer spectrum," *The Annals of Thoracic Surgery*, vol. 110, no. 6, pp. 1796–1804, 2020.

[6] H. J. Park, S. H. Lee, and Y. S. Chang, "Recent advances in diagnostic technologies in lung cancer," *The Korean Journal of Internal Medicine*, vol. 35, no. 2, pp. 257–268, 2020.

[7] N. Hasan, R. Kumar, and M. S. Kavuru, "Lung cancer screening beyond low-dose computed tomography: the role of novel biomarkers," *Lung*, vol. 192, no. 5, pp. 639–648, 2014.

[8] X. Wu, H. Chen, and X. Wang, "Can lung cancer stem cells be targeted for therapies?," *Cancer Treatment Reviews*, vol. 38, no. 6, pp. 580–588, 2012.

[9] G. Veronesi, "Lung cancer screening: the European perspective," *Thoracic Surgery Clinics*, vol. 25, no. 2, pp. 161–174, 2015.

[10] D. R. Aberle and K. Brown, "Lung cancer screening with CT," *Clinics in Chest Medicine*, vol. 29, no. 1, pp. 1–14, 2008, v.

[11] M. Okada, N. Tsubota, M. Yoshimura, Y. Miyamoto, and R. Nakai, "Evaluation of TMN classification for lung carcinoma with ipsilateral intrapulmonary metastasis," *The Annals of Thoracic Surgery*, vol. 68, no. 2, pp. 326–330, 1999.

[12] R. Rami-Porta and P. Goldstraw, "Strength and weakness of the new TNM classification for lung cancer," *The European Respiratory Journal*, vol. 36, no. 2, pp. 237–239, 2010.

[13] K. Shrestha, A. E. Onasanya, I. Eisenberg et al., "miR-210 and GPD1L regulate EDN2 in primary and immortalized human granulosa-lutein cells," *Reproduction*, vol. 155, no. 2, pp. 197–205, 2018.

[14] M. Yuan, Y. Guo, H. Xia, H. Xu, H. Deng, and L. Yuan, "Novel SCN5A and GPD1L variants identified in two unrelated Han-Chinese patients with clinically suspected Brugada syndrome," *Frontiers in Cardiovascular Medicine*, vol. 8, article 758903, 2021.

[15] C. R. Valdivia, K. Ueda, M. J. Ackerman, and J. C. Makielski, "GPD1L links redox state to cardiac excitability by PKC-dependent phosphorylation of the sodium channel SCN5A," *American Journal of Physiology Heart and Circulatory Physiology*, vol. 297, no. 4, pp. H1446–H1452, 2009.

[16] R. L. Strausberg, E. A. Feingold, L. H. Grouse et al., "Generation and initial analysis of more than 15,000 full-length human and mouse cDNA sequences," *Proceedings of the National Academy of Sciences of the United States of America*, vol. 99, no. 26, pp. 16899–16903, 2002.

[17] H. Liu, S. Wang, A. Cheng, Z. Han, Z. Feng, and C. Guo, "GPD1L is negatively associated with HIF1α expression and predicts lymph node metastasis in oral and HPV- Oropharyngeal cancer," *Oral Diseases*, vol. 27, no. 7, pp. 1654–1666, 2021.

[18] Z. Feng, J. N. Li, L. Wang, Y. F. Pu, Y. Wang, and C. B. Guo, "The prognostic value of glycerol-3-phosphate dehydrogenase 1-like expression in head and neck squamous cell carcinoma," *Histopathology*, vol. 64, no. 3, pp. 348–355, 2014.

[19] Z. Zhao, X. Cui, G. Guan et al., "Bioinformatics analysis reveals the clinical significance of GIPC2/GPD1L for colorectal cancer using TCGA database," *Translational Cancer Research*, vol. 11, no. 4, pp. 761–771, 2022.

[20] B. Arneth, "Tumor Microenvironment," *Medicina*, vol. 56, no. 1, 2020.

[21] I. Vitale, G. Manic, L. M. Coussens, G. Kroemer, and L. Galluzzi, "Macrophages and metabolism in the tumor microenvironment," *Cell Metabolism*, vol. 30, no. 1, pp. 36–50, 2019.

[22] M. Jarosz-Biej, R. Smolarczyk, T. Cichoń, and N. Kułach, "Tumor microenvironment as a "game changer" in cancer radiotherapy," *International Journal of Molecular Sciences*, vol. 20, no. 13, p. 3212, 2019.

[23] J. Wu, L. Li, H. Zhang et al., "A risk model developed based on tumor microenvironment predicts overall survival and associates with tumor immunity of patients with lung adenocarcinoma," *Oncogene*, vol. 40, no. 26, pp. 4413–4424, 2021.

[24] H. Zhang, Y. B. Luo, W. Wu et al., "The molecular feature of macrophages in tumor immune microenvironment of glioma patients," *Computational and Structural Biotechnology Journal*, vol. 19, pp. 4603–4618, 2021.

[25] G. Yu, L. G. Wang, Y. Han, and Q. Y. He, "clusterProfiler: an R package for comparing biological themes among gene clusters," *Omics: a Journal of Integrative Biology*, vol. 16, no. 5, pp. 284–287, 2012.

[26] G. Yu, L. G. Wang, G. R. Yan, and Q. Y. He, "DOSE: an R/Bioconductor package for disease ontology semantic and enrichment analysis," *Bioinformatics*, vol. 31, no. 4, pp. 608-609, 2015.

[27] M. M. Jacobsen, S. C. Silverstein, M. Quinn et al., "Timeliness of access to lung cancer diagnosis and treatment: a scoping literature review," *Lung Cancer*, vol. 112, pp. 156–164, 2017.

[28] L. Succony, D. M. Rassl, A. P. Barker, F. M. McCaughan, and R. C. Rintoul, "Adenocarcinoma spectrum lesions of the lung: detection, pathology and treatment strategies," *Cancer Treatment Reviews*, vol. 99, article 102237, 2021.

[29] H. A. Hamann, E. S. Ver Hoeve, L. Carter-Harris, J. L. Studts, and J. S. Ostroff, "Multilevel opportunities to address lung cancer stigma across the cancer control continuum," *Journal of Thoracic Oncology*, vol. 13, no. 8, pp. 1062–1075, 2018.

[30] E. O'Dowd, J. Mackenzie, and H. Balata, "Lung cancer for the non-respiratory physician," *Clinical Medicine*, vol. 21, no. 6, pp. e578–e583, 2021.

[31] S. B. Goldberg, J. N. Contessa, S. B. Omay, and V. Chiang, "Lung cancer brain metastases," *Cancer Journal*, vol. 21, no. 5, pp. 398–403, 2015.

[32] K. Tu, J. Li, H. Mo, Y. Xian, Q. Xu, and X. Xiao, "Identification and validation of redox-immune based prognostic signature for hepatocellular carcinoma," *International Journal of Medical Sciences*, vol. 18, no. 9, pp. 2030–2041, 2021.

[33] K. Liu, A. Huang, J. Nie et al., "IL-35 regulates the function of immune cells in tumor microenvironment," *Frontiers in Immunology*, vol. 12, article 683332, 2021.

[34] R. R. Malla, G. Shailender, and M. A. Kamal, "Exosomes: critical mediators of tumour microenvironment reprogramming," *Current Medicinal Chemistry*, vol. 28, no. 39, pp. 8182–8202, 2021.

[35] J. Zheng and P. Gao, "Toward normalization of the tumor microenvironment for cancer therapy," *Integrative Cancer Therapies*, vol. 18, p. 153473541986235, 2019.

[36] P. Wu, W. Gao, M. Su et al., "Adaptive mechanisms of tumor therapy resistance driven by tumor microenvironment," *Frontiers in Cell and Developmental Biology*, vol. 9, article 641469, 2021.

[37] R. Zhang, Q. Liu, T. Li, Q. Liao, and Y. Zhao, "Role of the complement system in the tumor microenvironment," *Cancer Cell International*, vol. 19, no. 1, p. 300, 2019.

[38] A. Puthenveetil and S. Dubey, "Metabolic reprograming of tumor-associated macrophages," *Annals of Translational Medicine*, vol. 8, no. 16, p. 1030, 2020.

[39] M. W. Zhang, K. Fujiwara, X. Che, S. Zheng, and L. Zheng, "DNA methylation in the tumor microenvironment," *Journal of Zhejiang University Science B*, vol. 18, no. 5, pp. 365–372, 2017.

Research Article

COX7B Is a New Prognostic Biomarker and Correlates with Tumor Immunity in Esophageal Carcinoma

Yinsen Song,[1] **Na Gao,**[2] **Zhenzhen Yang,**[2] **Sisen Zhang,**[2] **Tanli Fan** ⓘ**,**[3] **and Baojun Zhang** ⓘ[4]

[1]*School of Basic Medical Sciences, Xi'an Jiaotong University, Translational Medicine Research Center, Zhengzhou People's Hospital, Zhengzhou, China*
[2]*Translational Medicine Research Center, Zhengzhou People's Hospital, Zhengzhou, China*
[3]*School of Basic Medical Sciences, Zhengzhou University, Zhengzhou, China*
[4]*Department of Pathogenic Microbiology and Immunology, School of Basic Medical Sciences, Xi'an Jiaotong University, Xi'an, China*

Correspondence should be addressed to Baojun Zhang; bj.zhang@mail.xjtu.edu.cn

Esophageal carcinoma (ESCA) refers to the most common type of malignant tumor, which reveals that it occurs often all over the world. ESCA is also correlated with an advanced stage and low survival rates. Thus, the development of new prognostic biomarkers is an absolute necessity. In this study, the aim was to investigate the potential of COX7B as a brand-new predictive biomarker for ESCA patients. COX7B expression in pancancer was examined using TIMER2. The statistical significance of the predictive value of COX7B expression was explored. The relationship between COX7B expression and tumor-infiltrating immune cells in ESCA was analyzed by using ssGSEA. In this study, the result indicated that several types of cancers had an abnormally high amount of COX7B. COX7B expression in samples from patients with ESCA was considerably higher than in nontumor tissues. A more advanced clinical stage may be anticipated from higher COX7B expression. According to the findings of Kaplan-Meier survival curves, patients with low COX7B levels had a more favorable prognosis than those with high COX7B levels. The result of multivariate analysis suggested that COX7B expression was a standalone prognostic factor for the overall survival of ESCA patients. A prognostic nomogram including gender, clinical stage, and COX7B expression was constructed, and TCGA-based calibration plots indicated its excellent predictive performance. An analysis of immune infiltration revealed that COX7B expression has a negative correlation with TFH, Tcm, NK cells, and mast cells. COX7B may serve as an immunotherapy target and as a biomarker for ESCA diagnosis and prognosis.

1. Introduction

Esophageal carcinoma (ESCA) is one of the most frequent malignancies in the world and is the cause of a significant number of deaths annually [1]. Men had a significantly greater incidence of the condition than women did. It is also one of the prevalent malignant tumors of the digestive system in China, with squamous carcinoma and adenocarcinoma being the primary histological forms [2, 3]. Consumption of tobacco and alcohol is the primary environmental risk factor correlated with ESCA. Although there has been significant progress in recent years in the development of early diagnostic and treatment techniques for ESCA, the five-year survival rate of just 15-20% is unacceptable [4–6]. For patients diagnosed with ESCA, the development of a reliable prognostic predictor takes on a critical significance in providing exact customized therapy [7, 8]. The existing indication is the node, tumor, and metastasis (TNM) staging system that is employed for ESCA staging and prognostic prediction with the greatest frequency [9]. Besides the
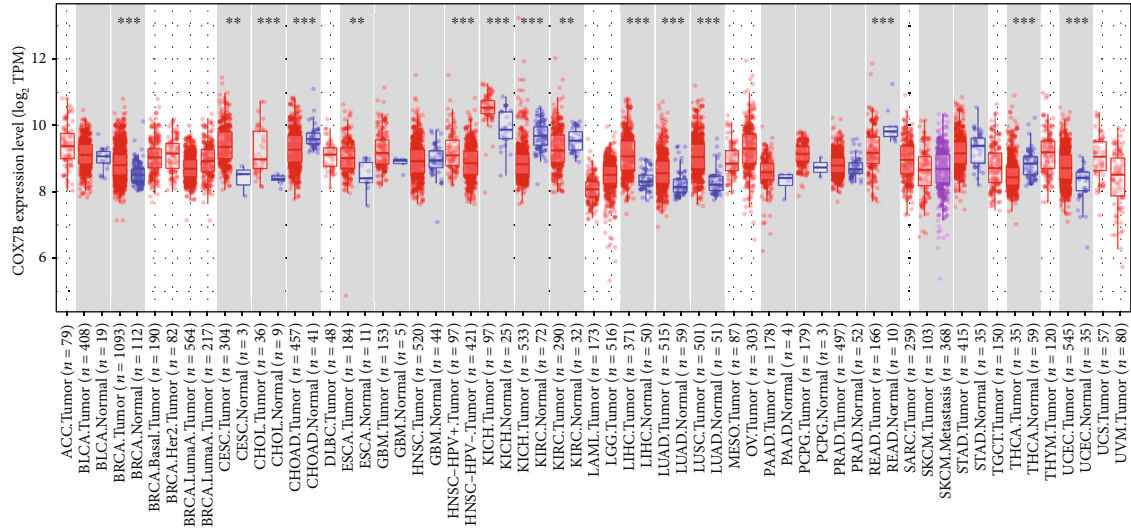
Figure 1: Pancancer analysis of COX7B expression.

TNM staging system, unique and accurate prognostic indicators should be identified to create effective treatment options for ESCA.

Mammalian Cox, often termed complex IV, refers to a multiheteromeric enzyme with 13 subunits that catalyzes the reduction of molecular oxygen to water and the oxidation of cytochrome c at the final step of OXPHOS in the mitochondrial electron transport chain [10, 11]. This occurs at the end of the oxidative phosphorylation step of the electron transport chain (ETC). Within the complex, COX7B refers to a small transmembrane protein of 80 amino acids, and it is encoded by the nucleus [12]. It is linked to the four catalytic redox centers of the enzyme that were found in the mitochondrial subunits (Cox1, Cox2, and Cox3), which were encoded by the above genes. The result indicated that the structural protein cyclooxygenase 7b (COX7B), a part of complex IV of the mitochondrial electron transport chain, was a member of a protein family that may be bigger than the one that was previously believed to account for the brain tropism in mice caused by breast cancer [13, 14]. With the help of this proof-of-concept research, it is now possible to look for metabolic sensors that are responsible for cancer organotropism and could be therapeutically addressed. This is important for therapies that prevent metastasis. Currently, there has been rare information about the role of COX7B in malignancies.

There is mounting evidence to suggest that the process of tumorigenesis is intimately connected to immunological surveillance and defense mechanisms that are activated throughout the progression of the disease [15, 16]. The above functions play an important part in determining how well a patient will respond to treatment. Immunotherapy, embodied by immune checkpoint inhibitors (ICIs), has evolved into the norm of treatment for several malignancies; yet, immunotherapy is only beneficial for a limited number of patients [17, 18]. Thus, it is essential

for the treatment of cancer to conduct research into the discovery of new biomarkers that may accurately predict a patient's response to immunotherapy and to create novel therapeutic approaches that combine immunotherapy with other forms of treatment. The tumor microenvironment (TME) significantly affects the prognosis of the tumor, the likelihood of survival, and the response to treatment [19, 20]. Accordingly, acquiring a better knowledge of the pathogenic impact and dynamics of various ESCA immune cells is of great significance to the development of an effective TIME-related prognostic biomarker.

Throughout the course of this study, TCGA database was adopted to investigate the expression, prognosis, and immune infiltration of COX7B in ESCA.

2. Materials and Methods

2.1. Data Collection. The Cancer Genome Atlas (TCGA), a database for cancer genomics, can be accessed at https://cancergenome.nih.gov/. This database contains genetic data on matched normal samples and more than 2,000 primary tumors. TCGA database was used to retrieve case data for our study, including mRNA expression profiles and clinical features. This database originated from the UCSC Xena platform (https://xena.ucsc.edu/). The data from matched samples from 163 ESCA and 11 normal samples were collected for additional analysis.

2.2. Gene Expression Analysis of COX7B in Cancers. "COX7B" was used as the variable of interest in an investigation of the "Gene DE" component of the Tumor Immune Estimation Resource 2.0 (TIMER2) (http://timer.cistrome.org) web server's tumor immune estimation resource. In TCGA datasets, the researchers explored the ways in which the COX7B gene's expression varies between malignancies and healthy tissues.
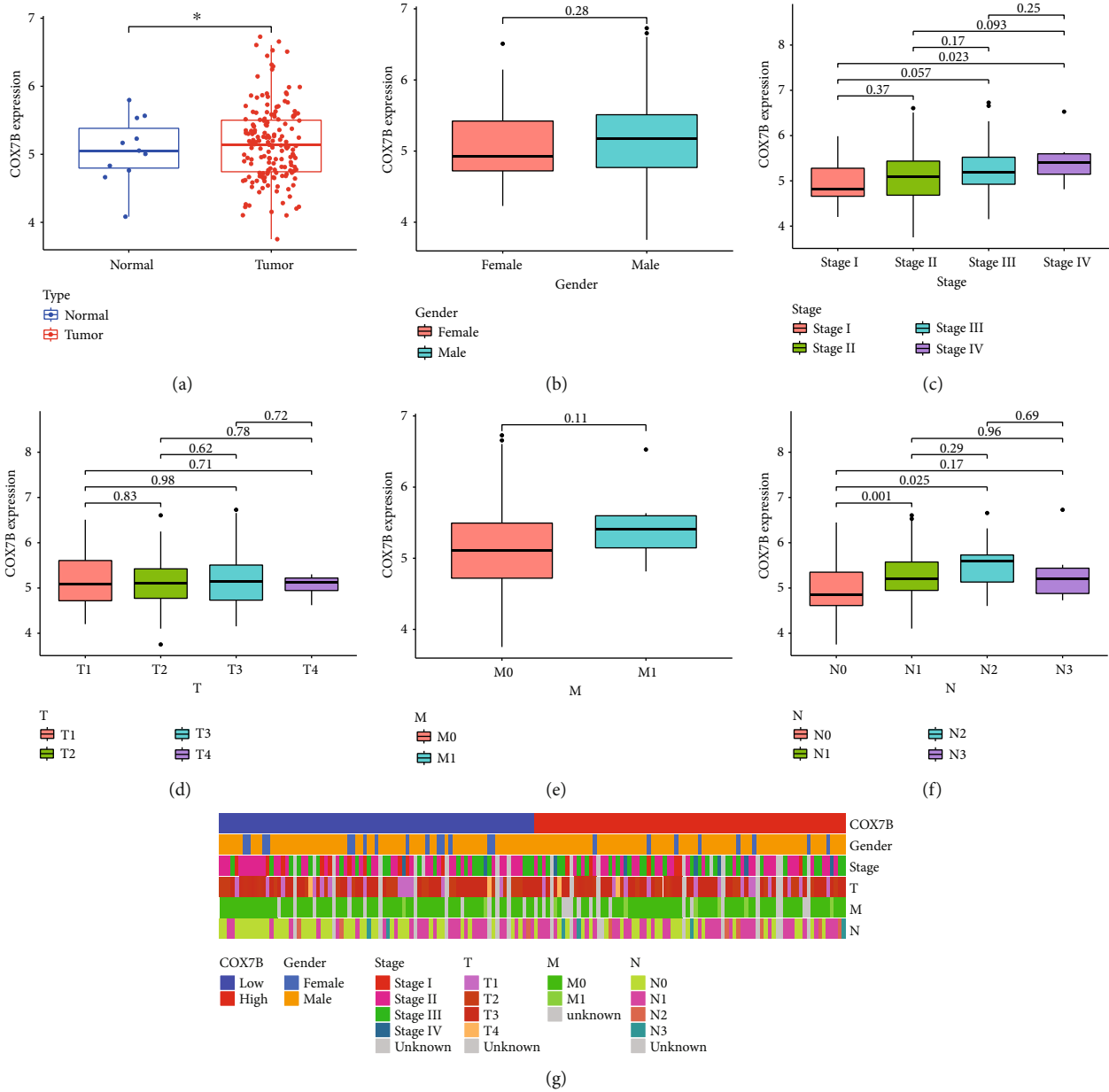
(a)

(b)

(c)

(d)

(e)

(f)

(g)

FIGURE 2: Correlations between COX7B expression in ESCA and clinical variables. (a) The distinct upregulation of COX7B was observed in ESCA specimens compared with nontumor specimens based on TCGA datasets. (b–g) Clinical features of ESCA and COX7B mRNA expression.

2.3. Survival Evaluation.
The Youden index [(sensitivity + specificity) 1] was adopted to determine the ideal COX7B cut-off value. The ESCA samples were assigned to two groups in accordance with COX7B expression levels (high and low). The survival rates of the two groups were compared using the log-rank test, and the differences in survival rates were examined using the Kaplan-Meier (K-M) method. $p < 0.05$ indicated a difference with statistical significance.

2.4. Analysis Using GO, KEGG, GSEA, and GSVA.
KEGG pathway analysis and Gene Ontology enrichment analysis were conducted for all the differentially expressed genes

(DEGs) for biological processes (BP), cellular components (CC), and molecular functions (MF). We could look at the cellular and molecular functions that COX7B performs in ESCA tissues using GO analysis. GSEA and GSVA were also used to assess the potential molecular pathways of COX7B in the same tissues. The same organs underwent the above examinations. All the analyses made use of the ClusterProfiler R tool [21].

2.5. Immune Infiltration Analysis.
We examined the infiltration of 24 immune cell types (ICTs) in tumor tissues using the ssGSEA method, a component of the Gene Set Variation Analysis (GSVA) package of the R software. According to

(a)

(b)

(c)
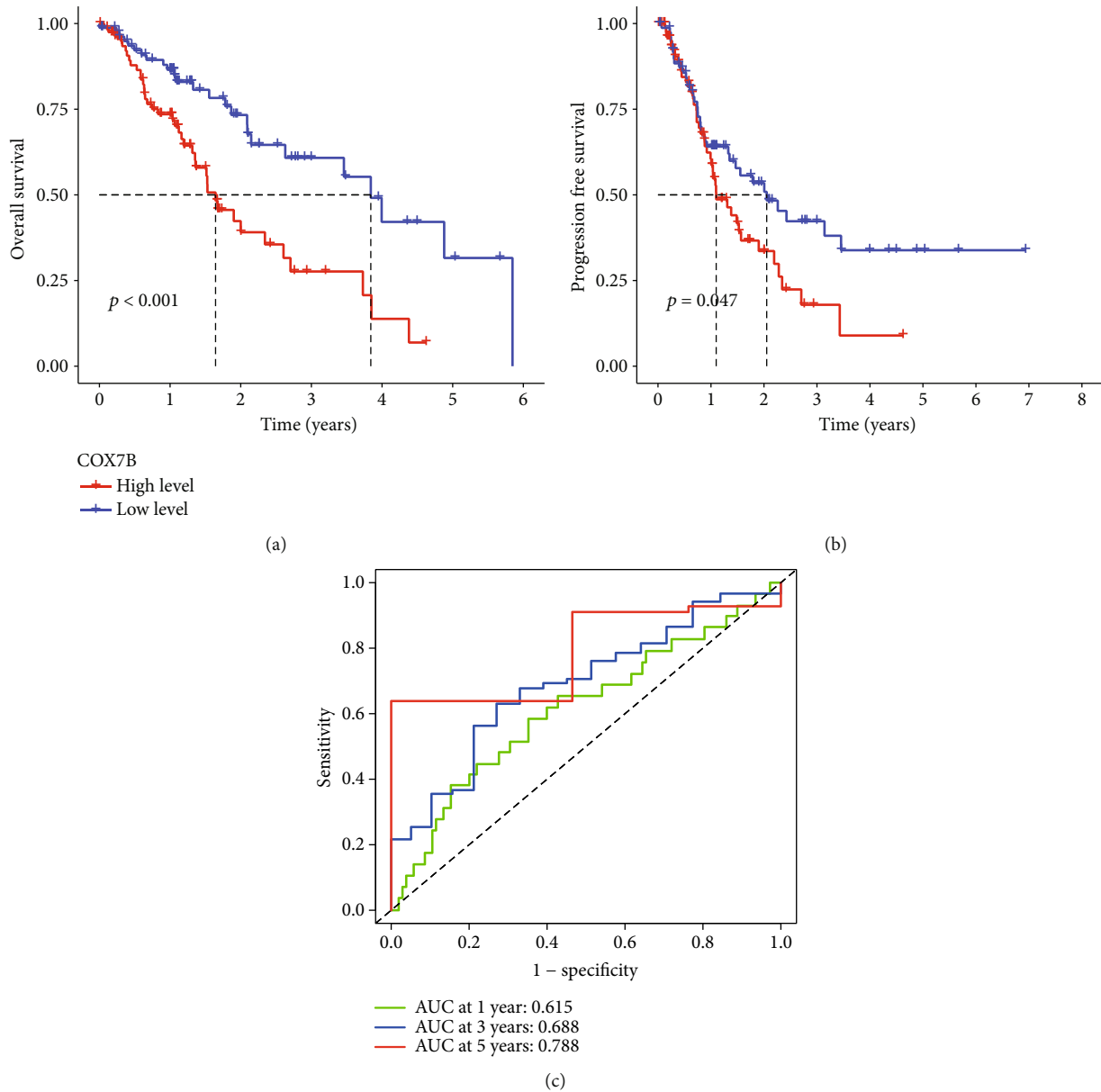
FIGURE 3: The survival analysis of COX7B in ESCA patients. (a) The OS and (b) survival distributions for PFS were plotted for patients with high and low COX7B expression in ESCA. (c) Estimating the likelihood of survival at 1, 3, and 5 years in ESCA patients using a ROC curve that changes over time.

this study, tumor growth was substantially suppressed by ICTs. The GSA assessed the absolute expression of genes in each tumor sample, which was used to calculate an enrichment score based on the marker genes of the 24 ICTs revealed in the study. The Wilcoxon rank-sum and Spearman correlation tests were used to examine the relationship between immune cells and COX7B.

3. Statistical Analysis

All statistical analyses were performed using R. To determine the nature of the connection that exists between clinicopathologic features and COX7B expression, a logistic regression analysis was conducted. Using the Kaplan-Meier method and the Cox regression analysis, researchers explored the relationship between clinicopathologic features and overall survival in ESCA patients. To carry out both univariate and multivariable studies of survival, the Cox regression model was utilized. A multivariate Cox analysis was used to compare the impact of COX7B expression on survival to the impact of the other variables. A value of $p < 0.05$ was regarded as significantly different.

4. Results

4.1. Pancancer Analysis of COX7B and Its Association with Clinical Factors in ESCA. To begin, we analyzed the COX7B expression profiles in several cancer types using data from
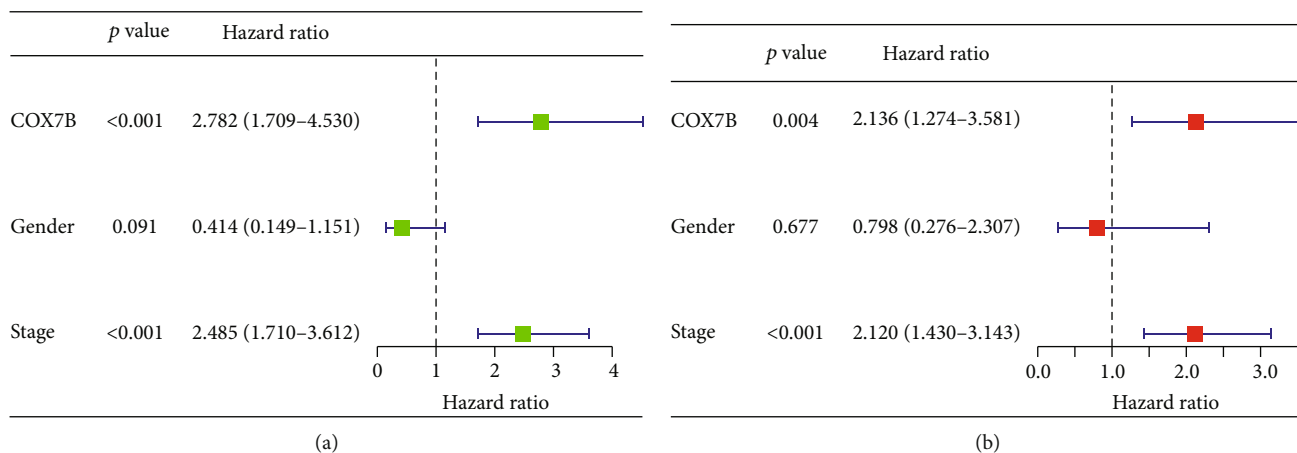
FIGURE 4: Univariate (a) and multivariate (b) analyses of prognostic factors in ESCA patients.

TCGA's RNA sequencing project (including those cancers without normal tissues for comparison). According to the prediction of TIMER data, we observed that COX7B expression was higher in BRCA, CESC, CHOL, ESCA, HNSC, KICH, LIHC, LUAD, LUSC, and UCEC. Conversely, COX7B was expressed low in KIRC, KIRP, READ, and THCA (Figure 1). The full names of all tumor types are shown in Table S1.

The histogram revealed COX7B as an overexpressed gene in ESCA samples against control samples (Figure 2(a)). Then, we analyzed its association with clinical factors in ESCA. Expression of COX7B was not correlated with either sex, as we found (Figure 2(b)). Importantly, we observed that COX7B expressed markedly higher at stage IV than stage I in ESCA (Figure 2(c)). Furthermore, there was no correlation between the T stage and M stage and COX7B expression (Figures 2(d) and 2(e)). Importantly, higher levels of COX7B were observed in the N1-N2 stage than the N0 stage (Figure 2(f)). The heatmap showed the distribution of ESCA patients with different clinical factors in the group with low or high COX7B expression (Figure 2(g)).

4.2. Relationship between COX7B Expression and the Clinical Outcome of ESC Patients. We analyzed the associations between COX7B mRNA levels and OS and PFS in patients with ESCA to investigate the potential prognostic significance of COX7B in ESCA. Patients with high COX7B mRNA expression had significantly poorer OS ($p < 0.001$, Figure 3(a)) and PFS ($p = 0.047$, Figure 3(b)) compared with the low expression group, as shown by Kaplan-Meier analysis. Based on TCGA data, COX7B expression has a high predictive capacity for the survival of ESCA patients, as indicated by an area under the ROC curve (AUC) of 0.788 (Figure 3(c)). Univariate and multivariate analyses were conducted to verify whether COX7B was an independent prognostic factor for ESCA. Clinical stage and COX7B expression were separate prognostic variables for ESCA patients (Figures 4(a) and 4(b)). A nomogram

was developed using COX7B and clinical risk indicators to provide a quantitative way to predict the prognosis of ESCA patients. Clinicians now have a quantifiable tool in COX7B expression level to forecast their patients' odds of surviving 1, 3, and 5 years after initial diagnosis with ESCA (Figures 5(a) and 5(b)).

4.3. Enrichment Analysis. To explore the potential function of COX7B in ESCA progression, we screened the differentially expressed genes (DEGs) among ESCA samples ranging from high to low COX7B expression. Finally, we screened 463 DEGs (Table S2 and Figure 6). The results of GO analysis revealed that the 463 DEGs were mainly correlated with extracellular structure organization, extracellular matrix organization, axonogenesis, external encapsulating structure organization, collagen-containing extracellular matrix, neuron projection extension, glutamatergic synapse, endoplasmic reticulum lumen, microfibril, and metalloendopeptidase activity, extracellular matrix structural constituent, and integrin binding (Figures 7(a) and 7(b)). Moreover, we performed KEGG analysis and found that the 463 DEGs were mainly enriched in focal adhesion and ECM-receptor interaction (Figure 7(c)). In addition, based on the results of the Gene Set Enrichment Analysis (GSEA), GPX1 was found to have a role in the following processes: cytokine-receptor interaction, extracellular matrix receptor interaction, focal adhesion, JAK/STAT signaling pathway, and neuroactive ligand-receptor interaction (Figure 8).

4.4. COX7B Expression in ESCA and the Presence of Immune Cell Infiltration. We performed the Spearman correlation analysis to find a link between COX7B expression and immune cell infiltration in the ESCA microenvironment. It was revealed that COX7B expression was inversely related to TFH, Tcm, NK cells, and mast cells (Figure 9). The above results suggested that COX7B may be critical in controlling immune cell infiltration in the tumor microenvironment.
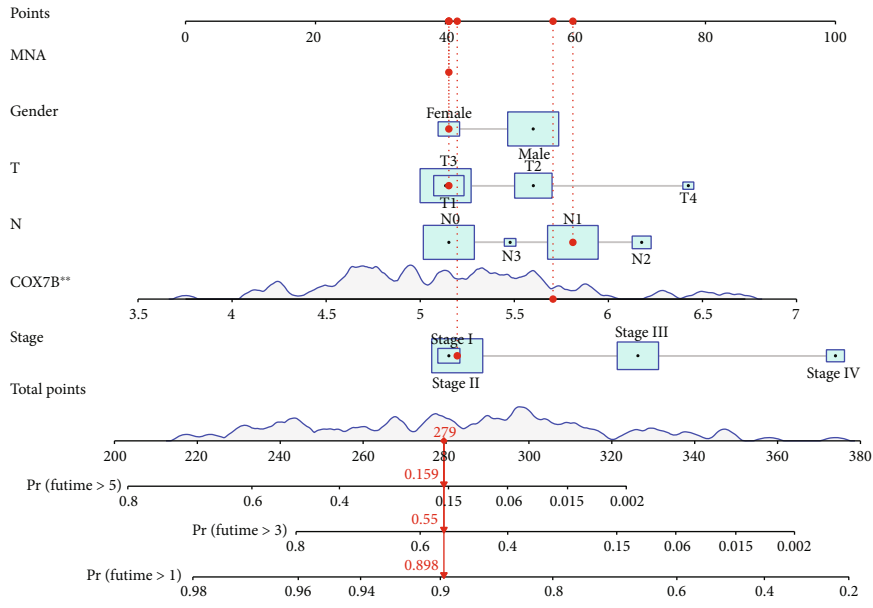
(a)
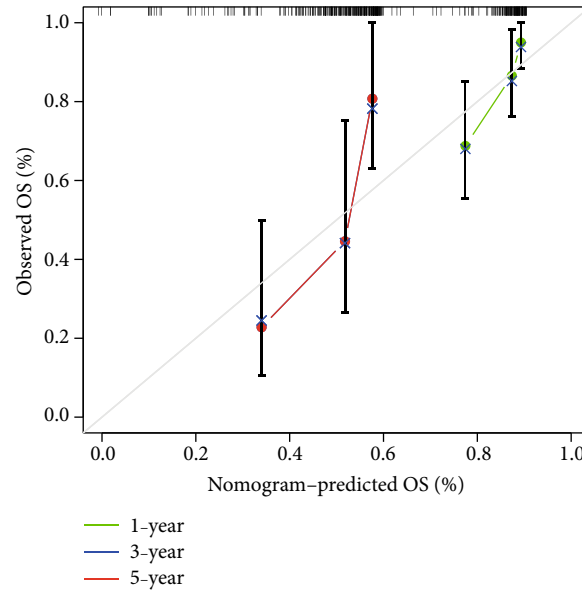
(b)

FIGURE 5: (a) Survival nomogram for estimating the likelihood of survival for ESCA patients over the course of 1, 3, and 5 years. (b) An ideal nomogram is represented by the diagonal dashed line in the calibration curve for the overall survival nomogram.

5. Discussion

In 2018, there were around 572,000 patients who were given a diagnosis of ESCA for the first time [22]. The recurrence of ESCA and the poor prognosis correlated with it continue to make it difficult to treat the condition [23, 24]. Due to the advanced stage of the disease when it is diagnosed (usually stage III or stage IV), the overall 5-year survival rate of ESCA can be as low as 20% due to the disease's high invasiveness [25, 26]. Over the course of the last couple of decades, genetic and epigenomic variables that contribute to the

development of precancerous squamous lesions in the esophagus into ESCA have been the subject of an extensive amount of research and investigation [27, 28]. It has been revealed that besides cancer genetics, aberrant epigenetic regulation, which can include aberrant DNA methylation, aberrant histone modifications, and alterations of numerous noncoding RNAs, plays a crucial role in what causes and what keeps ESCA going.

Researchers have recently suggested that mutations in the COX7B gene are linked to the development of malignancies. Cox7b is a structural subunit of the mitochondrial
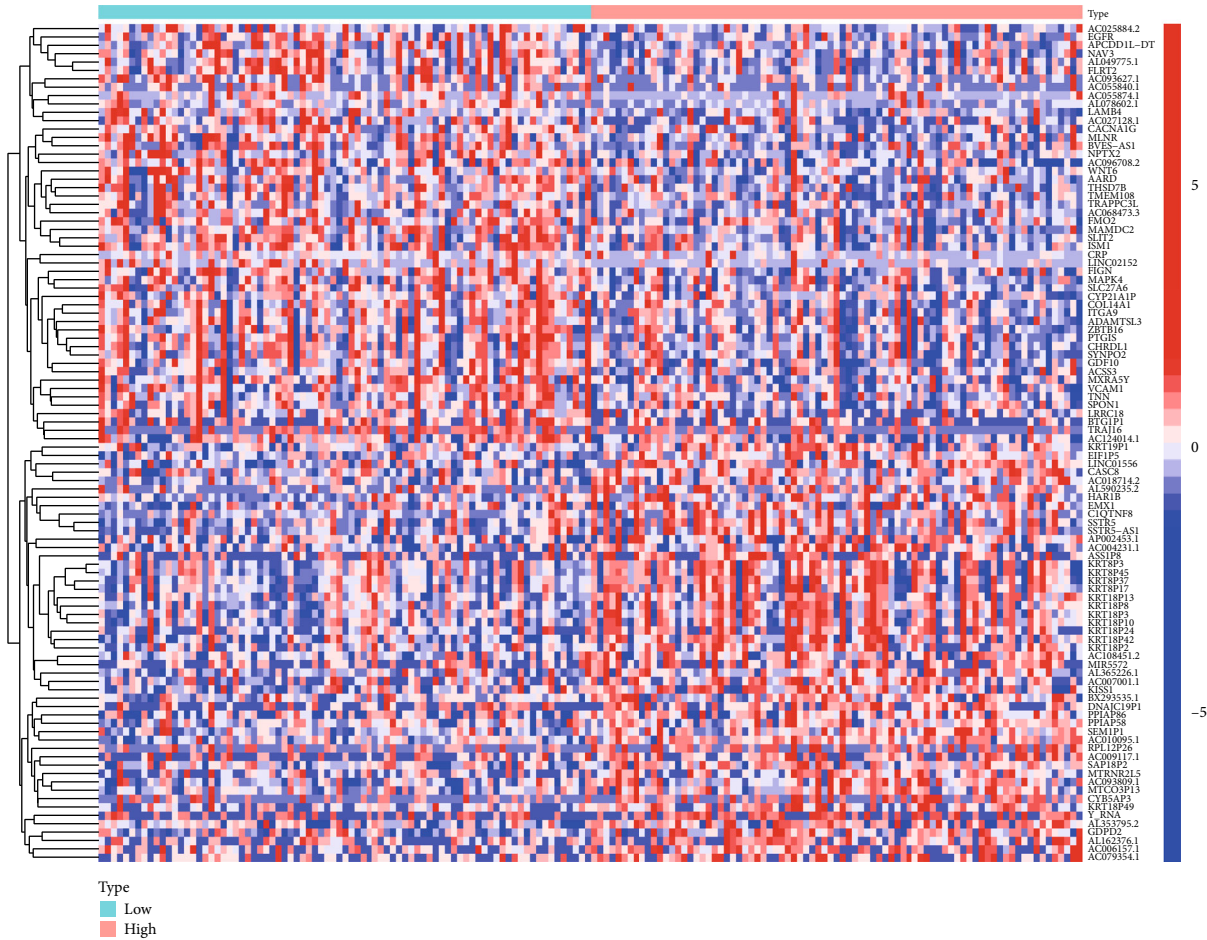
FIGURE 6: Heatmap of the DEGs between ESCA specimens with high COX7B expression and ESCA specimens with low COX7B expression.

electron transport chain (complex IV). Cox7b refers to the part of a likely wider family of proteins important for breast cancer brain tropism in mice [29]. They employed human triple-negative MDA-MB-231 breast cancer cells and two separate brain-seeking variants as models. Mice were employed in this study. This preliminary research confirmed the feasibility of a search for metabolic sensors that drive cancer organotropism and could be targeted therapeutically, which takes on a critical significance to therapies aiming at preventing metastasis. Expression of it and reports of its function were extremely infrequent in other tumor types. In this study, we performed an investigation of pancancer and revealed that COX7B displayed a dysregulated level in various types of tumors. This finding suggests that COX7B may play a role in the progression of malignancies. Because the level of COX7B expression varied in accordance with the variety of cancers, we speculated that it may act either as a tumor promotor or a tumor suppressor. We confirmed that COX7B expression is significantly greater in ESCA samples than in control samples. Patients with high COX7B expression were correlated with lower overall survival and progression-free survival compared to those with low COX7B expression,

according to the results of the survival research. It is important to note that multivariate analysis indicated that COX7B expression served as an independent prognostic factor for ESCA patients. Based on our findings, COX7B may serve as an innovative predictive biomarker for patients with ESCA.

Immunotherapy with immune checkpoint inhibitors has achieved promising results in treating various cancers [30]. Significant advancements have also been made in treating advanced ESCA thanks to the use of monoclonal antibodies targeting PD-1 or PD-L1 in combination with angiogenesis inhibitors or TKIs [31]. On the other hand, there are just a few patients that have a satisfactory response to treatment. Accordingly, clarifying the immunological heterogeneity of ESCA will help doctors determine which patients are most likely to benefit from immunotherapy, and it will make it easier to screen synergistic therapeutic targets, thus increasing the efficacy of treatment. The result indicated an inverse relationship between COX7B expression and TFH, Tcm, NK cells, and mast cells. Previous research indicated that immune-inhibited cell types (e.g., reduced CD8+ T cells and M2 macrophages) were present in high numbers in ESCA [32, 33]. Undifferentiated M0 macrophages may
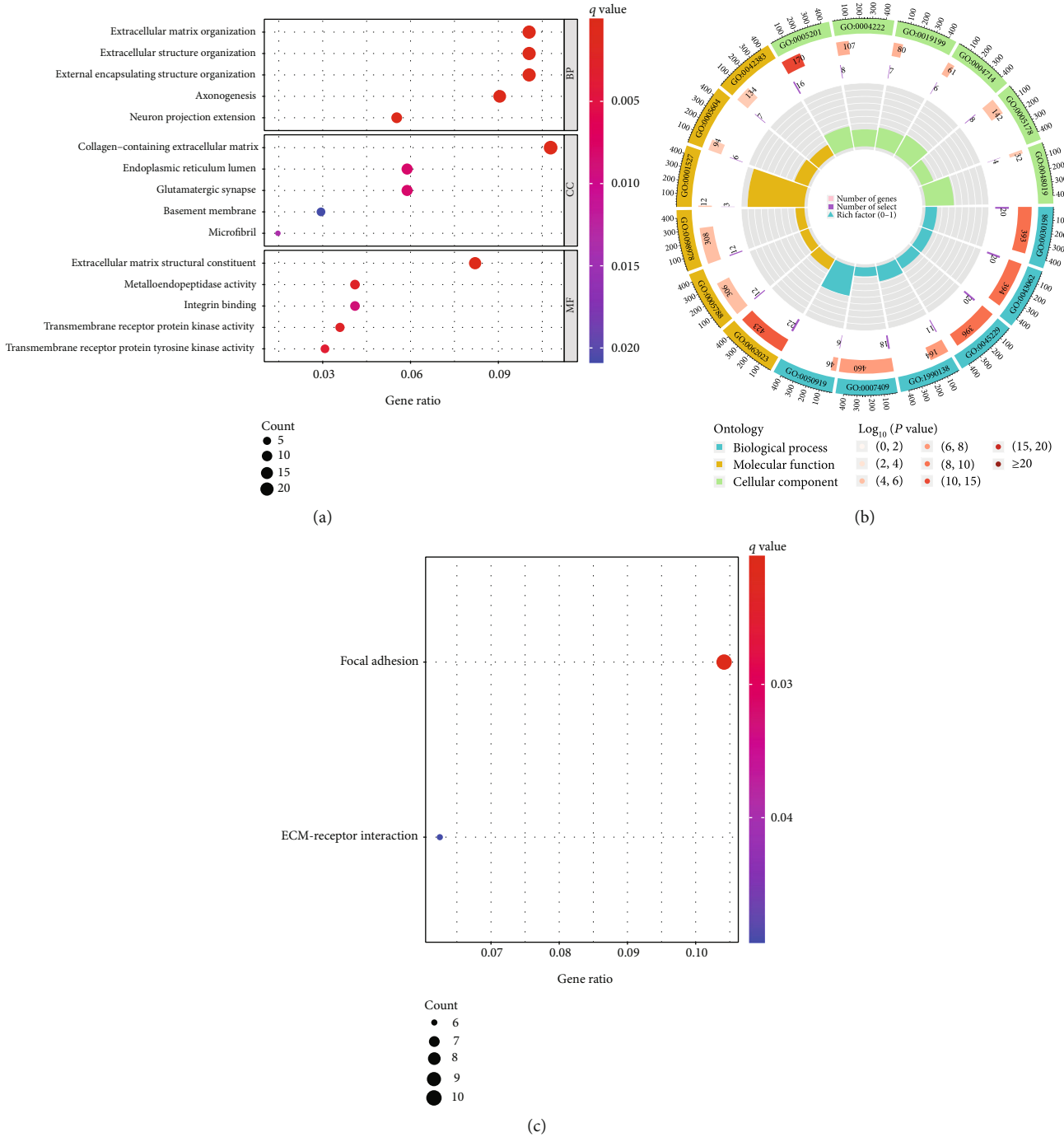
(a)

(b)

(c)

Figure 7: Functional enrichment analysis of DEGs in ESCA. (a, b) The GO analysis-identified biological processes with an abundance of DEGs. (c) KEGG analysis reveals enhanced pathways for DEGs.

develop into usually activated M1 macrophages, which have a phenotype that is proinflammatory and antitumorous, as revealed by the findings of a previous study [34, 35]. Besides, it has the potential to differentiate into alternatively activated macrophages (M2) that have an immune-inhibited and protumoral character. According to the results of this study, a possible prognostic indicator for ESCA is COX7B involved in immune cell infiltration. Individuals who have

a low expression of COX7B and are undergoing tumor immunotherapy for ESCA may benefit more from this medication than other patients.

This study has some important caveats and restrictions. First, TCGA cohorts were mined for data used to build the diagnostic and prognostic models; however, not all the clinical parameter information may have been captured. The above cohorts were adopted to collect the data that was
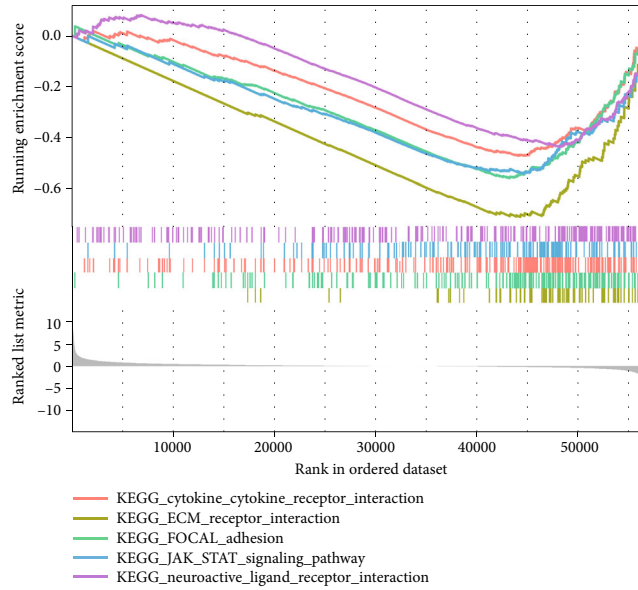
FIGURE 8: GSEA enrichment analysis of COX7B expression in ESCA patients from TCGA datasets.
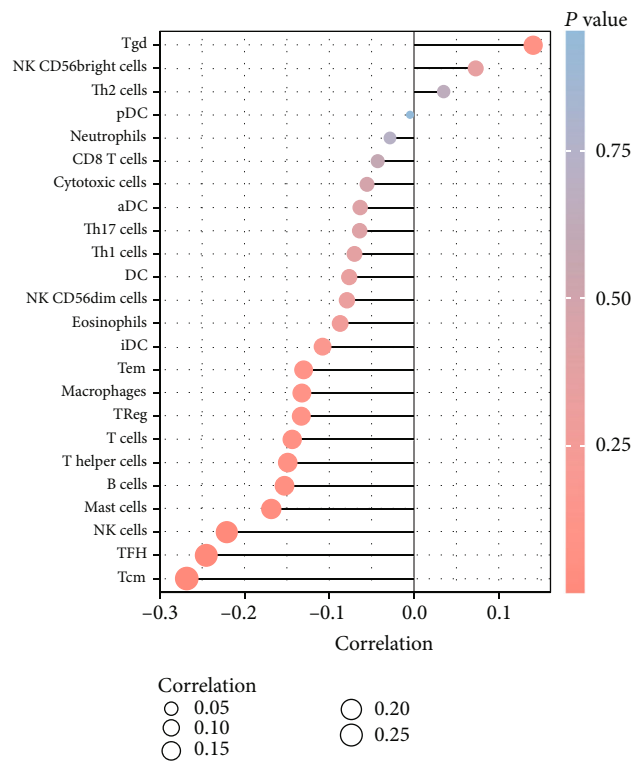
FIGURE 9: Associations of the COX7B expression level with tumor immune infiltration in ESCA. COX7B expression was inversely related to TFH, Tcm, NK cells, and mast cells.

employed. Because of this, the outcomes may have varied from what was expected. Second, we did not give any direct in vivo proof that the COX7B upregulation had any consequences that promoted the development of cancer. As a result, an additional study should be conducted using more advanced in vivo models (e.g., a knockout mouse).

6. Conclusion

COX7B may be a unique prognostic biomarker and a possible therapeutic target for ESCA patients. This study underlined the clinical value of COX7B in ESCA and analyzed the effect of COX7B on immune infiltration in the tumor microenvironment.

Data Availability

The data used to support the findings of this study are included in the article.

Conflicts of Interest

The authors state no conflict of interest.

Acknowledgments

Supplementary Materials

Supplementary 1. Table S1: the full names of all tumor types.

Supplementary 2. Table S2: the differentially expressed genes between ESCA specimens with high COX7B expression and ESCA specimens with low COX7B expression.

References

[1] R. L. Siegel, K. D. Miller, and A. Jemal, "Cancer statistics, 2019," *CA: a Cancer Journal for Clinicians*, vol. 69, no. 1, pp. 7–34, 2019.

[2] Y. Lin, Y. Totsuka, Y. He et al., "Epidemiology of esophageal cancer in Japan and China," *Journal of Epidemiology*, vol. 23, no. 4, pp. 233–242, 2013.

[3] C. Niu, Y. Liu, J. Wang et al., "Risk factors for esophageal squamous cell carcinoma and its histological precursor lesions in China: a multicenter cross-sectional study," *BMC Cancer*, vol. 21, no. 1, article 1034, 2021.

[4] M. J. Domper Arnal, Á. Ferrández Arenas, and Á. Lanas Arbeloa, "Esophageal cancer: risk factors, screening and endoscopic treatment in Western and Eastern countries," *World Journal of Gastroenterology*, vol. 21, no. 26, pp. 7933–7943, 2015.

[5] T. E. Lerut, P. de Leyn, W. Coosemans, D. Van Raemdonck, P. Cuypers, and B. Van Cleynenbreughel, "Advanced esophageal carcinoma," *World Journal of Surgery*, vol. 18, no. 3, pp. 379–387, 1994.

[6] M. C. S. Wong, Y. Deng, J. Huang et al., "Performance of screening tests for esophageal squamous cell carcinoma: a systematic review and meta-analysis," *Gastrointestinal Endoscopy*, vol. 96, no. 2, pp. 197–207.e34, 2022.

[7] J. E. Rogers, M. Sewastjanow-Silva, R. E. Waters, and J. A. Ajani, "Esophageal cancer: emerging therapeutics," *Expert Opinion on Therapeutic Targets*, vol. 26, no. 2, pp. 107–117, 2022.

[8] E. Morgan, I. Soerjomataram, H. Rumgay et al., "The global landscape of esophageal squamous cell carcinoma and esophageal adenocarcinoma incidence and mortality in 2020 and projections to 2040: new estimates from GLOBOCAN 2020," *Gastroenterology*, vol. 163, no. 3, pp. 649–658.e2, 2022.

[9] N. Sudo, H. Ichikawa, Y. Muneoka et al., "Clinical utility of ypTNM stage grouping in the 8th edition of the American joint committee on cancer TNM staging system for esophageal squamous cell carcinoma," *Annals of Surgical Oncology*, vol. 28, no. 2, pp. 650–660, 2021.

[10] S. M. I. Mahboubi Rabbani and A. Zarghi, "Selective COX-2 inhibitors as anticancer agents: a patent review (2014-2018)," *Expert Opinion on Therapeutic Patents*, vol. 29, no. 6, pp. 407–427, 2019.

[11] P. Rao and E. E. Knaus, "Evolution of nonsteroidal anti-inflammatory drugs (NSAIDs): cyclooxygenase (COX) inhibition and beyond," *Journal of Pharmacy & Pharmaceutical Sciences*, vol. 11, no. 2, pp. 81s–110s, 2008.

[12] N. Tanaka, S. Katayama, A. Reddy et al., "Single-cell RNA-seq analysis reveals the platinum resistance gene COX7B and the surrogate marker CD63," *Cancer Medicine*, vol. 7, no. 12, pp. 6193–6204, 2018.

[13] Y. P. Zhang, X. Wang, L. G. Jie et al., "Osteoarticular involvement-associated biomarkers and pathways in psoriasis: the shared pathway with ankylosing spondylitis," *Frontiers in Immunology*, vol. 13, article 836533, 2022.

[14] M. Brischigliaro, A. Cabrera-Orefice, M. Sturlese et al., "CG7630 is the Drosophila melanogaster homolog of the cytochrome c oxidase subunit COX7B," *EMBO Reports*, vol. 23, no. 8, article e54825, 2022.

[15] A. Maia and S. Wiemann, "Cancer-associated fibroblasts: implications for cancer therapy," *Cancers*, vol. 13, no. 14, p. 3526, 2021.

[16] X. Wang, L. Zhong, and Y. Zhao, "Oncolytic adenovirus: a tool for reversing the tumor microenvironment and promoting cancer treatment (review)," *Oncology Reports*, vol. 45, no. 4, 2021.

[17] T. Eggert and T. F. Greten, "Tumor regulation of the tissue environment in the liver," *Pharmacology & Therapeutics*, vol. 173, pp. 47–57, 2017.

[18] A. Puthenveetil and S. Dubey, "Metabolic reprograming of tumor-associated macrophages," *Annals of translational medicine*, vol. 8, no. 16, p. 1030, 2020.

[19] M. W. Zhang, K. Fujiwara, X. Che, S. Zheng, and L. Zheng, "DNA methylation in the tumor microenvironment," *Journal of Zhejiang University-SCIENCE B*, vol. 18, no. 5, pp. 365–372, 2017.

[20] B. Arneth, "Tumor Microenvironment," *Medicina*, vol. 56, no. 1, p. 15, 2020.

[21] G. Yu, L. G. Wang, Y. Han, and Q. Y. He, "clusterProfiler: an R package for comparing biological themes among gene clusters," *Omics: a journal of integrative biology*, vol. 16, no. 5, pp. 284–287, 2012.

[22] M. A. Blum, T. Taketa, K. Sudo, R. Wadhwa, H. D. Skinner, and J. A. Ajani, "Chemoradiation for esophageal cancer," *Thoracic Surgery Clinics*, vol. 23, no. 4, pp. 551–558, 2013.

[23] G. Businello, C. A. D. Pozzo, M. Sbaraglia et al., "Histopathological landscape of rare oesophageal neoplasms," *World Journal of Gastroenterology*, vol. 26, no. 27, pp. 3865–3888, 2020.

[24] S. Killcoyne and R. C. Fitzgerald, "Evolution and progression of Barrett's oesophagus to oesophageal cancer," *Nature Reviews Cancer*, vol. 21, no. 11, pp. 731–741, 2021.

[25] H. Kuwano, M. Nagamatsu, S. Ohno, H. Matsuda, M. Mori, and K. Sugimachi, "Coexistence of intraepithelial carcinoma and glandular differentiation in esophageal squamous cell carcinoma," *Cancer*, vol. 62, no. 8, pp. 1568–1572, 1988.

[26] E. G. Yegin and D. G. Duman, "Staging of esophageal and gastric cancer in 2014," *Minerva Medica*, vol. 105, no. 5, pp. 391–411, 2014.

[27] K. B. Berg and D. F. Schaeffer, "Tumor budding as a standardized parameter in gastrointestinal carcinomas: more than just the colon," *Modern Pathology*, vol. 31, no. 6, pp. 862–872, 2018.

[28] A. L. Racette and R. T. Miller, "Esophageal carcinoma: matching patients with treatment methods," *Journal of the American Academy of Physician Assistants*, vol. 24, no. 1, p. 28, 2011.

[29] M. C. N. M. Blackman, T. Capeloa, J. D. Rondeau et al., "Mitochondrial protein Cox7b is a metabolic sensor driving brain-specific metastasis of human breast cancer cells," *Cancers*, vol. 14, no. 18, p. 4371, 2022.

[30] L. B. Kennedy and A. K. S. Salama, "A review of cancer immunotherapy toxicity," *CA: a Cancer Journal for Clinicians*, vol. 70, no. 2, pp. 86–104, 2020.

[31] R. S. Riley, C. H. June, R. Langer, and M. J. Mitchell, "Delivery technologies for cancer immunotherapy," *Nature Reviews Drug Discovery*, vol. 18, no. 3, pp. 175–196, 2019.

[32] M. Abbott and Y. Ustoyev, "Cancer and the immune system: the history and background of immunotherapy," *Seminars in Oncology Nursing*, vol. 35, no. 5, article 150923, 2019.

[33] H. Zhao, Y. Xu, Y. Xie et al., "m6A regulators is differently expressed and correlated with immune response of esophageal cancer," *Frontiers in cell and developmental biology*, vol. 9, article 650023, 2021.

[34] Y. Baba, D. Nomoto, K. Okadome et al., "Tumor immune microenvironment and immune checkpoint inhibitors in esophageal squamous cell carcinoma," *Cancer Science*, vol. 111, no. 9, pp. 3132–3141, 2020.

[35] S. He, J. Xu, X. Liu, and Y. Zhen, "Advances and challenges in the treatment of esophageal cancer," *Acta Pharmaceutica Sinica B*, vol. 11, no. 11, pp. 3379–3392, 2021.

Hindawi

Research Article

The Prognostic Model Established by the Differential Expression Genes Based on CD8+ T Cells to Evaluate the Prognosis and the Response to Immunotherapy in Osteosarcoma

Yu Chen [1], **Wei Yan** [2], **Hongqing Wang** [3], **Zhiliang Ou** [1], **Huihong Chen** [1], **Zhenhua Huang** [4], **Jinlian Yang** [5], **Biqiong Liu** [6], **Fanjie Ou** [6], and **Huang Zhang** [1]

[1]*The Third Department of Surgery, Xianyou County General Hospital, Putian, Fujian, China*
[2]*Xianyou County General Hospital, Putian, Fujian, China*
[3]*The Second Orthopedic Rehabilitation Center, Beijing Rehabilitation Hospital, Capital Medical University, Beijing, China*
[4]*The Department of Neurosurgery, Xianyou County General Hospital, Putian, Fujian, China*
[5]*Pulmonary and Critical Care Medicine, Xianyou County General Hospital, Putian, Fujian, China*
[6]*Department of Nephrology, Xianyou County General Hospital, Putian, Fujian, China*

Correspondence should be addressed to Fanjie Ou; ojie56@163.com and Huang Zhang; 18344980996@163.com

Osteosarcoma (OS) is a malignant tumor with an extremely poor prognosis, especially in progressive patients. Immunotherapy based on immune checkpoint inhibitors (ICIs) is considered to be a promising treatment option for OS. Due to tumor heterogeneity, only a minority of patients benefit from immunotherapy. Therefore, it is urgent to explore a model that can accurately assess the response of OS to immunotherapy. In this study, we obtained the single-cell RNA sequencing datasets of OS patients from public databases and defined 34 cell clusters by dimensional reduction and clustering analysis. PTPRC was applied to identify immune cell clusters and nonimmune cell clusters. Next, we performed clustering analysis on the immune cell clusters and obtained 25 immune cell subclusters. Immune cells were labeled with CD8A and CD8B to obtain CD8+ T cell clusters. Meanwhile, we extracted the differentially expressed genes (DEGs) of CD8+ T cell clusters and other immune cell clusters. Furthermore, we constructed a prognostic model (CD8-DEG model) based on the obtained DEGs of CD8+ T cells, and verified the excellent predictive ability of this model for the prognosis of OS. Moreover, we further investigated the value of the CD8-DEG model. The results indicated that the risk score of the CD8-DEG model was an independent risk factor for OS patients. Finally, we revealed that the risk score of the CD8-DEG model correlates with the immune profile of OS and can be used to evaluate the response of OS to immunotherapy. In conclusion, our study revealed the critical role of CD8 cells in OS. The risk score model based on CD8-DEGs can provide guidance for prognosis and immunotherapy of OS.

1. Introduction

Osteosarcoma (OS) is a rare and highly lethal malignancy, accounting for more than 50% of malignant primary bone tumors [1]. OS originates from primitive mesenchymal cells and occurs mostly in the metaphysis of long bones, including the distal femur and proximal tibia [2]. OS is also the second leading cause of tumor-related deaths in children and adolescents after lymphoma and brain tumors [3]. It is widely recognized that environmental factors and genetic mutations are high-risk factors for OS [4]. Given that tumors are regulated by complex gene networks, the pathogenesis of OS has not been fully elucidated. Surgery, chemotherapy, and radiotherapy are still the classic treatment options for OS currently [5]. For patients with local OS, traditional treatment regimens can achieve a 5-year survival rate of more than 70% [6]. However, for OS patients with recurrence and metastasis, the 5-year survival rate does not

exceed 20% [7]. Therefore, it is extremely urgent to explore a new treatment method that can fundamentally improve the prognosis of OS.

An increasing number of studies have shown that the tumor immune microenvironment (TIM) play a vital role in the occurrence and development of tumors, including OS [8]. Under normal conditions, the immune function is in a state of dynamic equilibrium, and immune suppression and immune activation restrict each other [9]. However, the TIM of tumor tends to be immunosuppressive, thereby prompting tumor cells to evade immune surveillance [10]. How to relieve the immunosuppressive state of tumors is the focus and difficulty of tumor immunotherapy. The immune process of tumors is regulated by a variety of immune cells, and the killing of tumors by $CD8^+$ T cells is the core of the whole process [11]. Therefore, elucidating the functional mechanism of CD8+ T cells is the key to the success of immunotherapy.

In recent years, a variety of immunotherapy drugs, such as PD-L1/PD-1 monoclonal antibody and CTLA4 monoclonal antibody, have been used in the treatment of malignant tumors and achieved satisfactory therapeutic effects, including OS [12]. However, in the application of immunotherapy, only a minority of patients benefit from immunotherapy [13]. It is currently believed that the cause of this dilemma is due to the abnormal immune microenvironment and immune cell function [14]. Therefore, developing a model that can accurately predict the efficacy of immunotherapy is crucial for patients of OS.

In this study, we obtained $CD8^+$ T cell clusters and differentially expressed genes (DEGs). Next, we constructed a prognostic model based on the DEGs of $CD8^+$, which was proved to have excellent predictive performance for the prognosis of OS patients. Moreover, we further revealed that the risk score of this model is closely related to the immune microenvironment of OS and multiple immune checkpoints, which can be used to predict immunotherapy response.

2. Materials and Methods

2.1. Acquisition of OS Single-Cell Sequencing Data and Transcriptome Data.
Single-cell osteosarcoma data, including 11 OS patients, were obtained from the GEO dataset (https://www.ncbi.nlm.nih.gov/geo/, GSE152048). The OS transcriptome data TARGET-OS was downloaded from XENA (http://xenabrowser.net), including 88 OS samples.

2.2. Single-Cell RNA-Seq Data Quality Control and Data Processing.
Single-cell samples of OS were processed by the R package Seurat package. Three-dimensional controls were applied to the original matrix of each cell: $nFeature\_RNA > 200$ and $percent.mt < 10$ and $nCount\_RNA > 3$. 3000 highly variable genes were identified using the FindVariableFeatures function, and principal component analysis- (PCA-) based dimensionality reduction was performed using RunPCA. Batch effects were removed on a sample-by-sample basis by the Harmony package. The distribution of cell components is mapped with R package "UMAP" with resolution = 0.5. Immune cells are distinguished from non-

immune cells based on the expression level of PRPDC (CD45). The resolution of cluster analysis of immune cells was 0.9. Findmarkers were used to screen signature genes, log 2FC > 1 and $p < 0.05$.

2.3. Construction of Random Forest Prognostic Model.
The characteristic genes we screened were firstly subjected to univariate prognostic analysis in TARGET-OS, and 6 genes were screened for inclusion in the prognostic model. Next, in this study, we randomly defined 70% of the TARGET-OS cohort as the training cohort and 30% as the validation cohort. The random forest prognostic model generates 1000 binary survival trees by default. When the number of survival trees increases to a certain number, the error rate curve tends to be stable.

2.4. Evaluation of the Predictive Power of the Model.
We conducted the timeROC package to draw ROC curves to evaluate the predictive ability of the model. Next, patients were divided into high- and low-risk cohorts according to the model score best cutoff value, and the KM survival curve was used to compare the prognostic differences between the high-risk group and the low-risk group. Finally, univariate prognostic analysis was performed with model scores and clinical characteristics, and ROC curves were drawn.

2.5. GO and KEGG Enrichment Analysis.
In this study, we carried out the GO analysis and KEGG to explore the value of our model risk score. The Database for Annotation, Visualization, and Integrated Discovery was used to integrate functional genomic annotations.

2.6. Evaluation to Immunotherapy Reactions.
The ClusterProfiler package was used to perform GO and KEGG enrichment analysis of high- and low-risk patients [15]. OS immune cell infiltration analysis was performed by the ESTIMATE and XCELL algorithms [16]. The TIDE algorithm was used to evaluate the immune evasion ability of OS patients and predict the sensitivity to immunotherapy [17].

2.7. Statistics.
In this study, R software (4.2.2) was used for calculation and statistical analysis of all data. We applied univariate and multivariate Cox regression analyses to assess the association of each factor with overall survival. The Student's t-test was conducted to compare the mean of different dataset. $p < 0.05$ were considered statistically significant.

3. Results

3.1. Identification of Immune Cells in OS Tissue.
To reveal the cellular heterogeneity of OS tissue, we collected single-cell RNA-sequencing (RNA-seq) datasets from 11 OS patients from the GEO database. We eliminated low-quality cells and identified 34 cell clusters from OS tissue by the dimensional reduction and clustering analysis (Figure 1(a)). PRPDC (CD45) is widely used as a characteristic marker of immune cells [18]. To clearly identify immune cells and nonimmune cells in OS tissue, we applied PRPDC to label immune cell clusters, and the results are
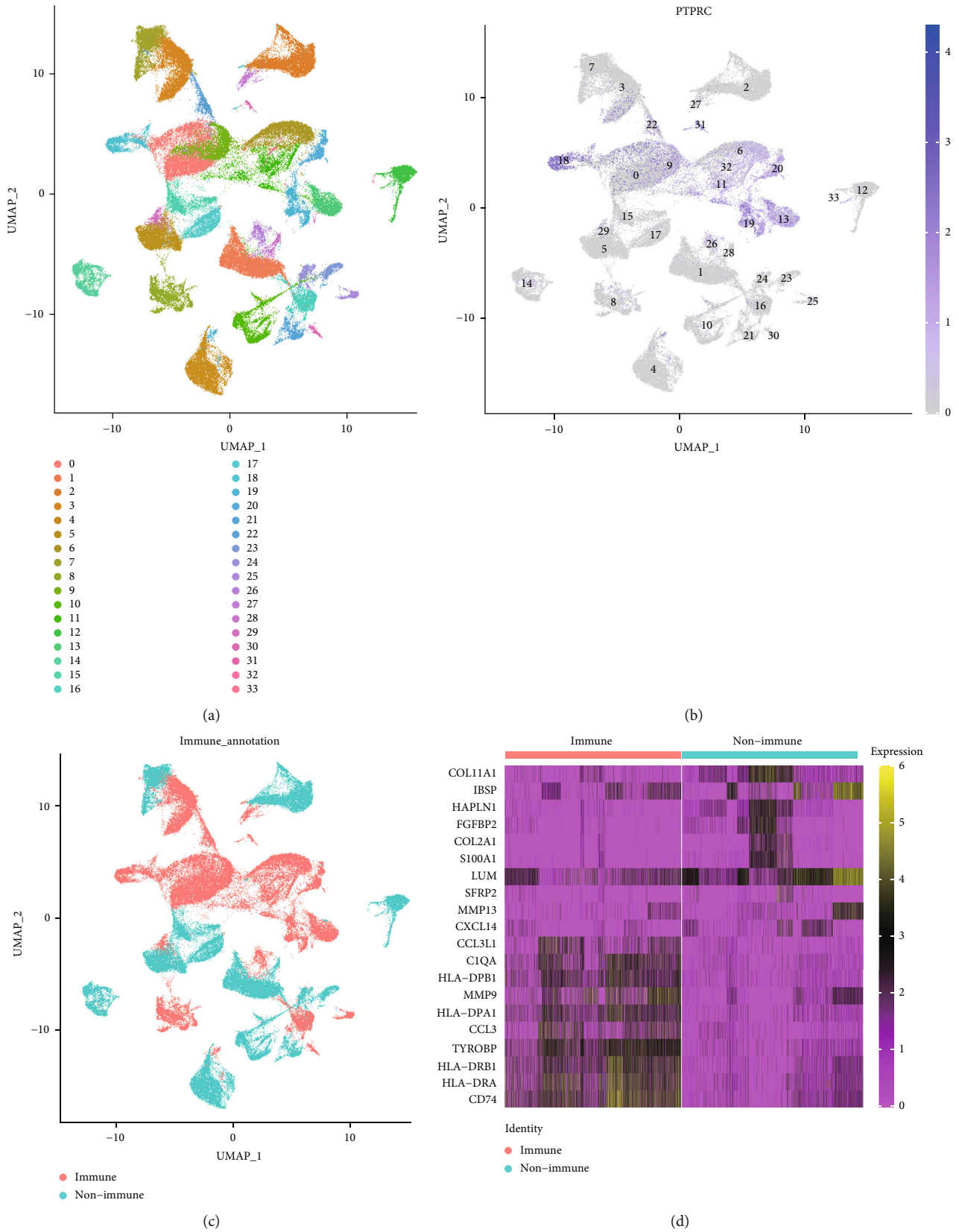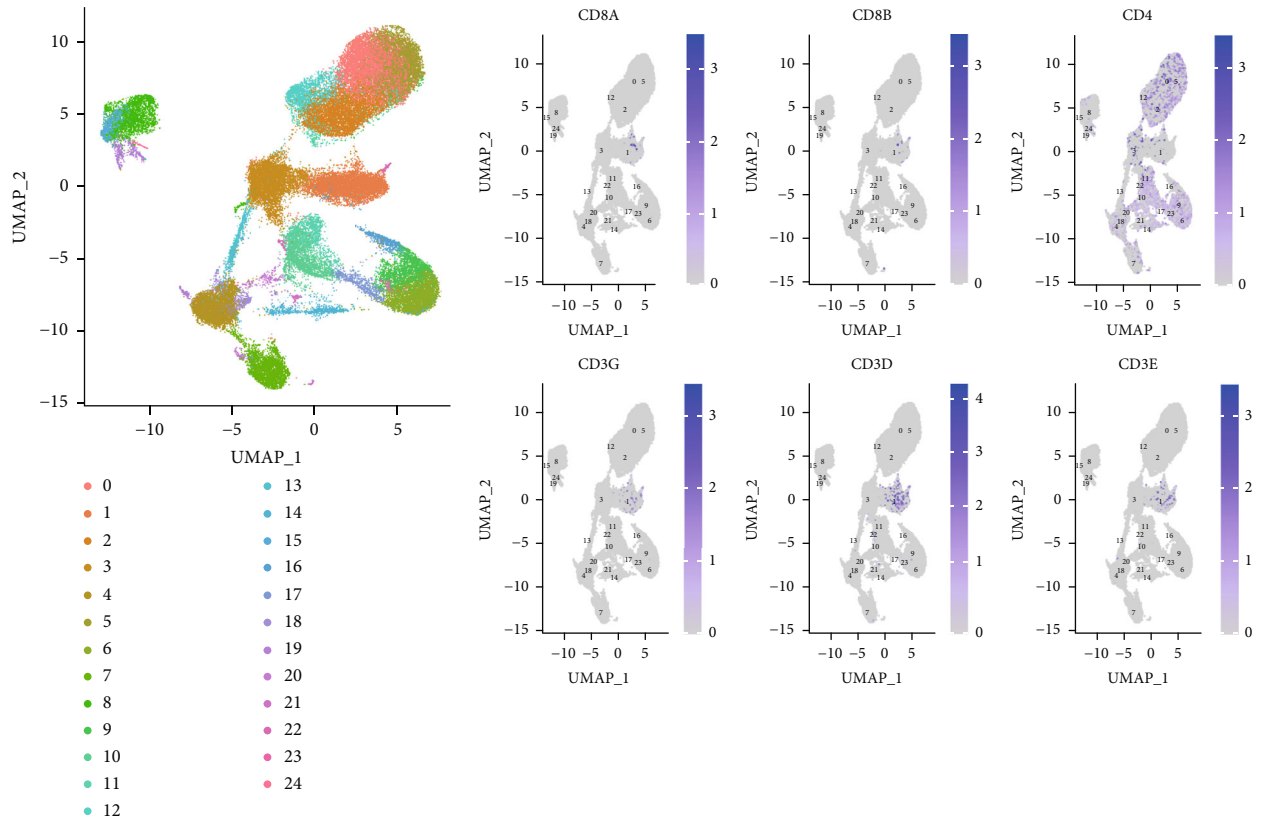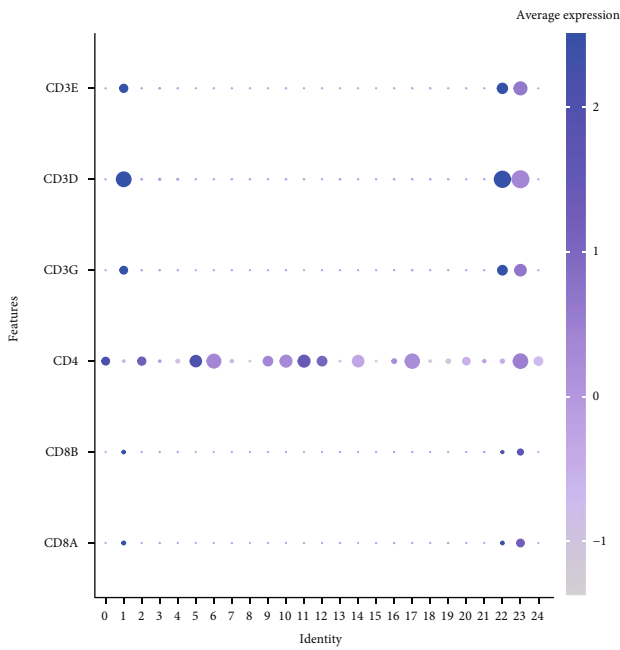
(a)

(b)

(c)

(d)

Figure 1: Identification of cell types in OS scRNA-seq sample. (a) UMAP plot of OS scRNA-seq data with 34 clusters (resolution = 0.5). (b) Expression of immune marker PTPRC (CD45) across all clusters, shown by UMAP plot. (c) Clustering of OS tissue via immune markers to obtain immune and nonimmune cells. (d) Heatmap of marker gene expression levels in different clusters.
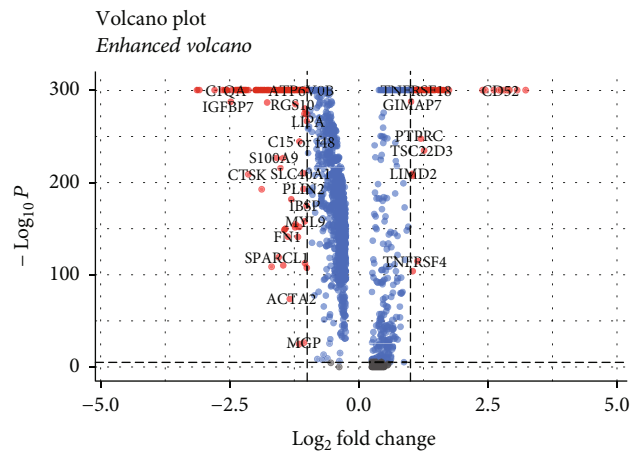
(a)

(b)

(c)

(d)

FIGURE 2: Identification of CD8+ T cell clusters and extraction of differentially expressed genes (DEGs). (a) UMAP plot of leukocyte scRNA-seq data with 25 clusters. (b) UMAP plots of single-cell expression levels of different marker genes. (c) Expression of different marker genes in immune cell subsets. (d) Analysis of DEGs between the 1st subset of immune cells and other cells.

(a)

(b)

(c)

(d)
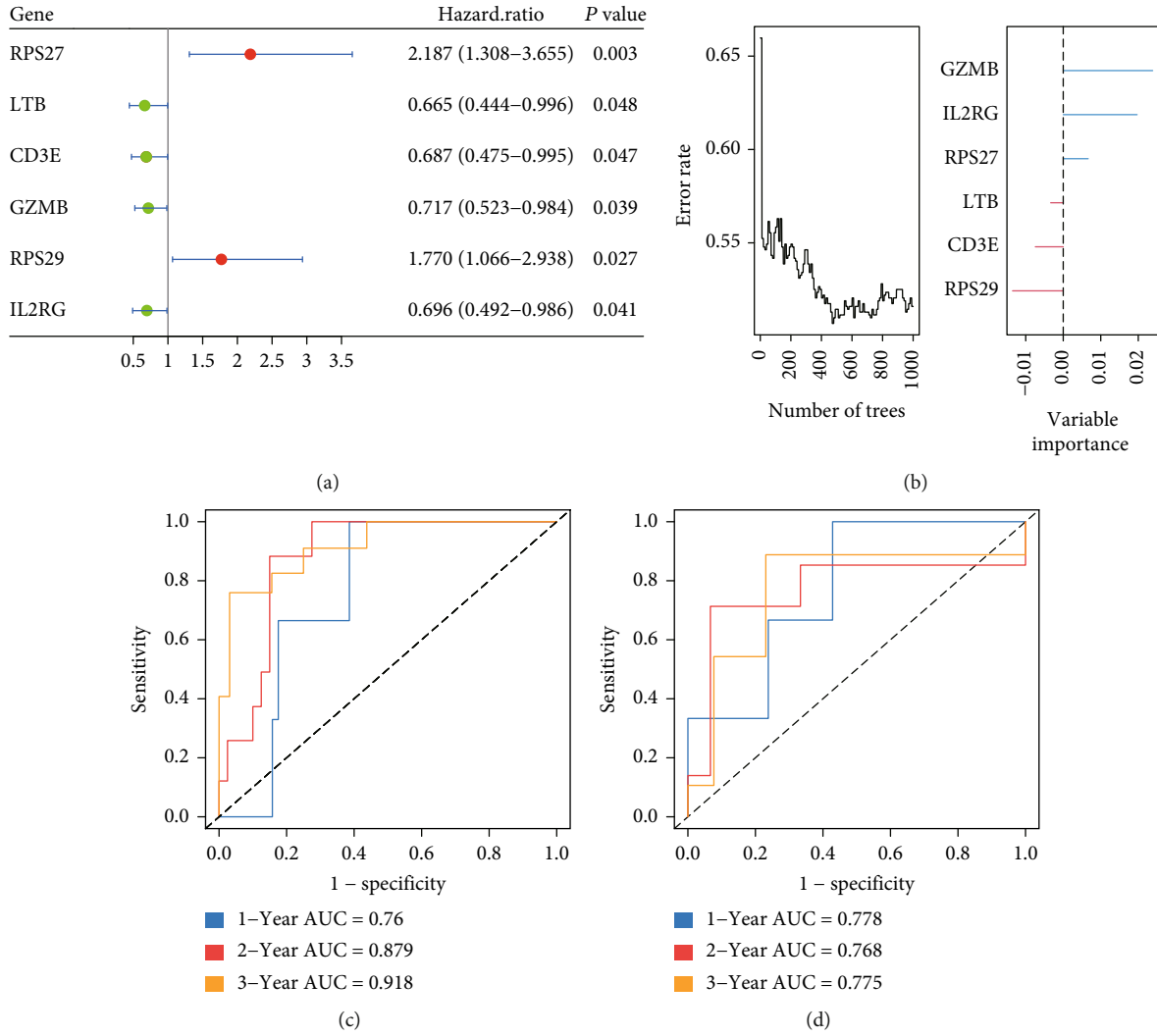
FIGURE 3: Construction of risk models. (a) Univariate regression analysis of CD8-DEGs. (b) Plot of the out of bag (OOB) prediction error rate for each tree constructed in the CD8-DEG model (left panel). Plot of variable importance in the CD8-DEG model (right panel). (c, d) ROC curves showed the predictive efficiency of the CD8-DEG risk score for 1-, 3-, and 5-year survival in the training and validation cohorts.

shown in Figures 1(b) and 1(c). Finally, we further analyzed the signature genes of immune cell clusters and nonimmune cell clusters and found that immune cells highly expressed immune signature genes, which suggested that immune cells are well characterized by PTPRC (Figure 1(d)).

3.2. Definition of CD8⁺ T Cell Clusters and Extraction of Differentially Expressed Genes (DEGs). We previously labeled OS tissues with corresponding marker genes and obtained immune cell clusters. We performed cluster analysis on the previous immune cell clusters and finally obtained 25 cell clusters (Figure 2(a)). Next, we applied CD8A and CD8B to label CD8⁺ T cell clusters, CD4 to label CD4⁺ T cell clusters, and CD3G, CD3D, and CD3E to label T cell clusters, respectively. The results indicated that the cluster analysis had good clustering performance (Figure 2(b)). In addition, to further isolate CD8⁺ T cells, we analyzed the expression levels of marker genes in different immune cell clusters. The results suggested that cluster1 could represent the optimal choice for CD8⁺ T cell clusters (Figure 2(c)). We per-

formed differentially expressed gene (DEG) analysis on the obtained CD8⁺ cell clusters and the remaining cells ($Log_2FC > 1$, $p < 0.05$) and finally obtained 59 genes with statistical significance (Figure 2(d) and Supplementary Table 1).

3.3. Construction of Risk Score Model Based on DEGs in CD8⁺ T Cells (CD8-DEGs). Given the DEG analysis by CD8⁺ T cells, we finally obtained 59 genes. We performed univariate analysis in the TARGET-OS dataset and finally obtained 6 genes (RPS27, LTB, CD3E, GZMB, RPS29, and IL2RG). The results showed that RPS27 and RPS29 were high-risk factors, while LTB, CD3E, GZMB, and IL2RG were low-risk factors in OS (Figure 3(a)). In addition, we divided the TARGET-OS patients into training cohort and validation cohort by 70% and 30%. We adopted these 6 genes and constructed a random survival forest model (CD8-DEGs model) based on the DEGs of CD8⁺ T cells. As shown in Figure 3(b), our model exhibited high accuracy, and GZMB and IL2RG play a major role in this model. We
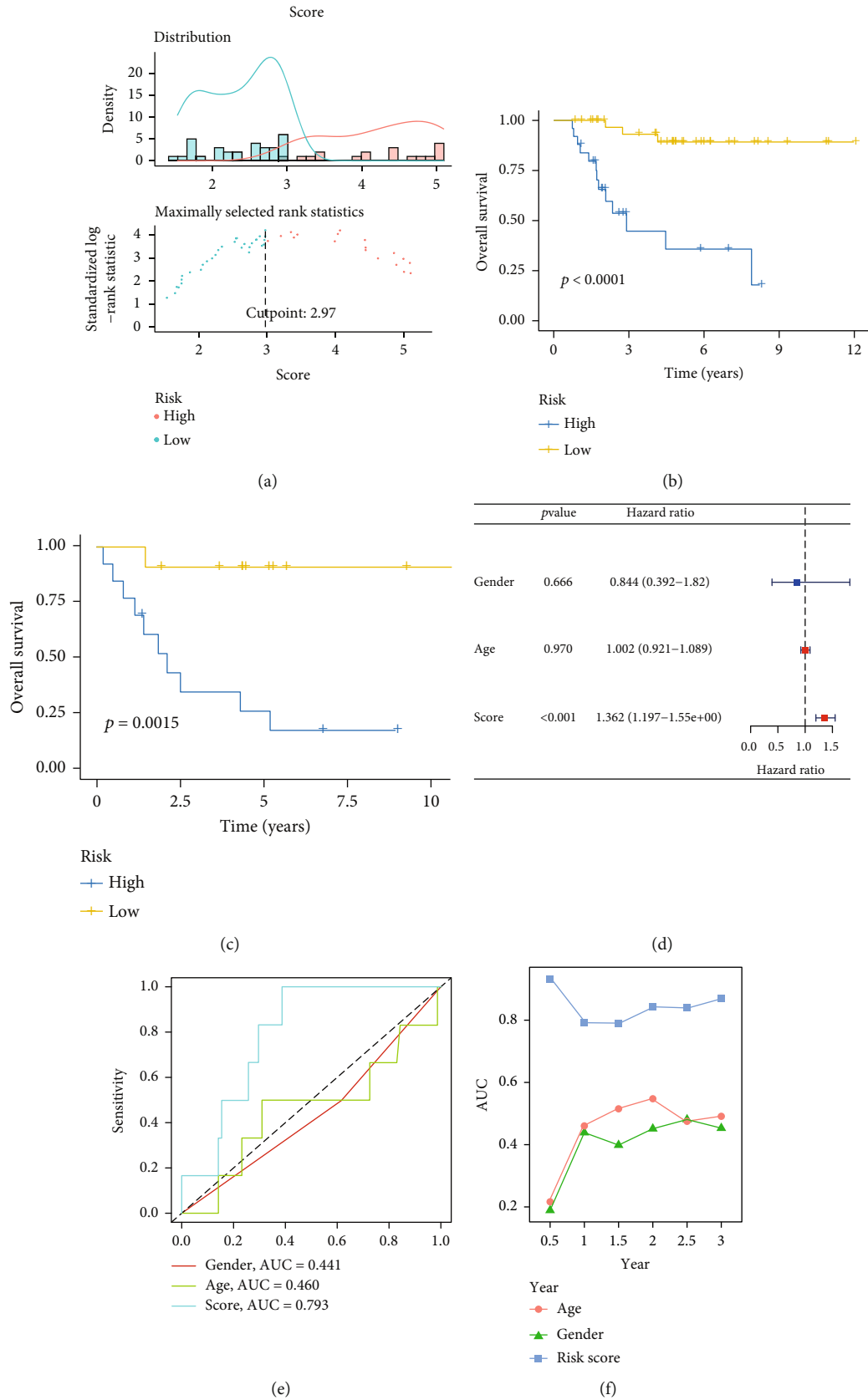
(a)

(b)

(c)

(d)

(e)

(f)

FIGURE 4: Evaluation of risk models for CD8-DEGs. (a) OS patients were divided into high- and low-risk groups according to the optimal cutoff (2.97) value. (b, c) Comparison of OS between high- and low-risk scores in the training and validation cohorts. (d) Univariate analysis of CD8-DEG risk scores and clinical characteristics. (e, f) Comparison of the predictive power of CD8-DEG risk models and their clinical Inharacteristics.
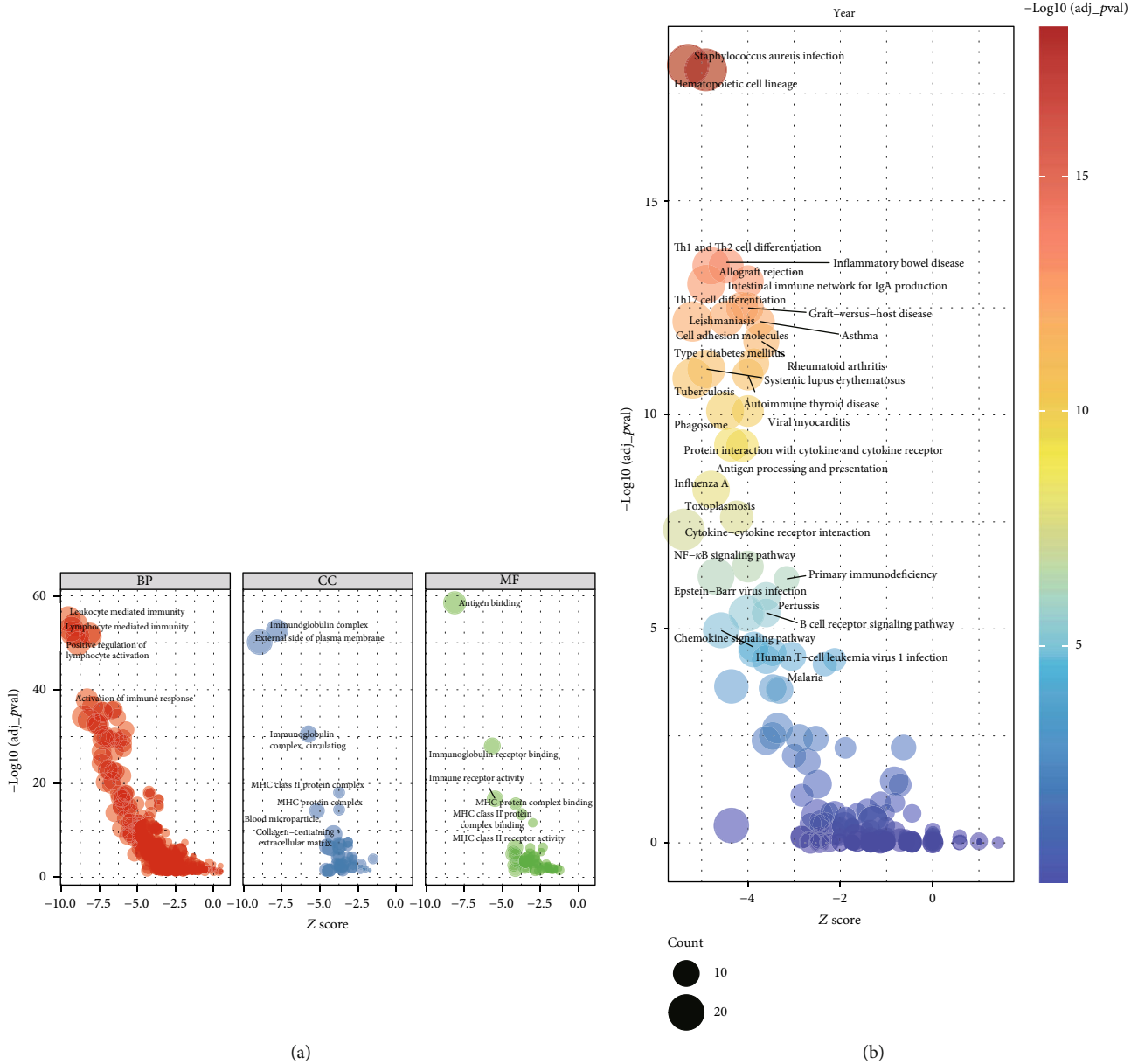
(a)

(b)

FIGURE 5: Pathway enrichment analysis of high- and low-risk scores in CD8-DEG model. (a) GO analysis of CD8-DEGs model. (b) KEGG analysis of CD8-DEG model.

further evaluated the accuracy of our model by ROC curve, and the results demonstrated that in the training cohort, the ROC curve area reached 0.75, 0.879, and 0.918 at 1, 3, and 5 years (Figure 3(c)). Likewise, in the validation cohort, the ROC curve areas reached 0.778, 0.768, and 0.775 at 1, 3, and 5 years (Figure 3(d)).

3.4. Evaluating the Performance of the CD8-DEG Model. To further investigate the value of CD8-DEGs model, we assessed the predictive power of this model by various measures. As shown in Figure 4(a), we took 2.97 as the cutoff value to classify the TARGET-OS cohort patients into high- and low-risk cohorts. The results demonstrated that high-risk patients had worse prognosis in both the training and validation cohorts (Figures 4(b) and 4(c)). In addition, we

further adopted the corresponding clinical characteristics (gender and age) and their risk scores for univariate analysis. We found that risk score was a high-risk factor for OS patient prognosis (=1.362) (Figure 4(d)). Meanwhile, the area under the ROC curve of the risk score reached 0.793 (Figure 4(e)). Finally, *C*-index analysis showed that risk scores had higher AUC curve values compared to gender and age (Figure 4(f)). These data strongly indicated that the CD8-DEG model has good performance in predicting the prognosis of OS patients.

3.5. Pathway Enrichment Analysis of Risk Scores for the CD8-DEG Model. The CD8-DEG model showed excellent ability in predicting the prognosis of OS patients. To initially revealed the mechanism, we performed GO and KEGG
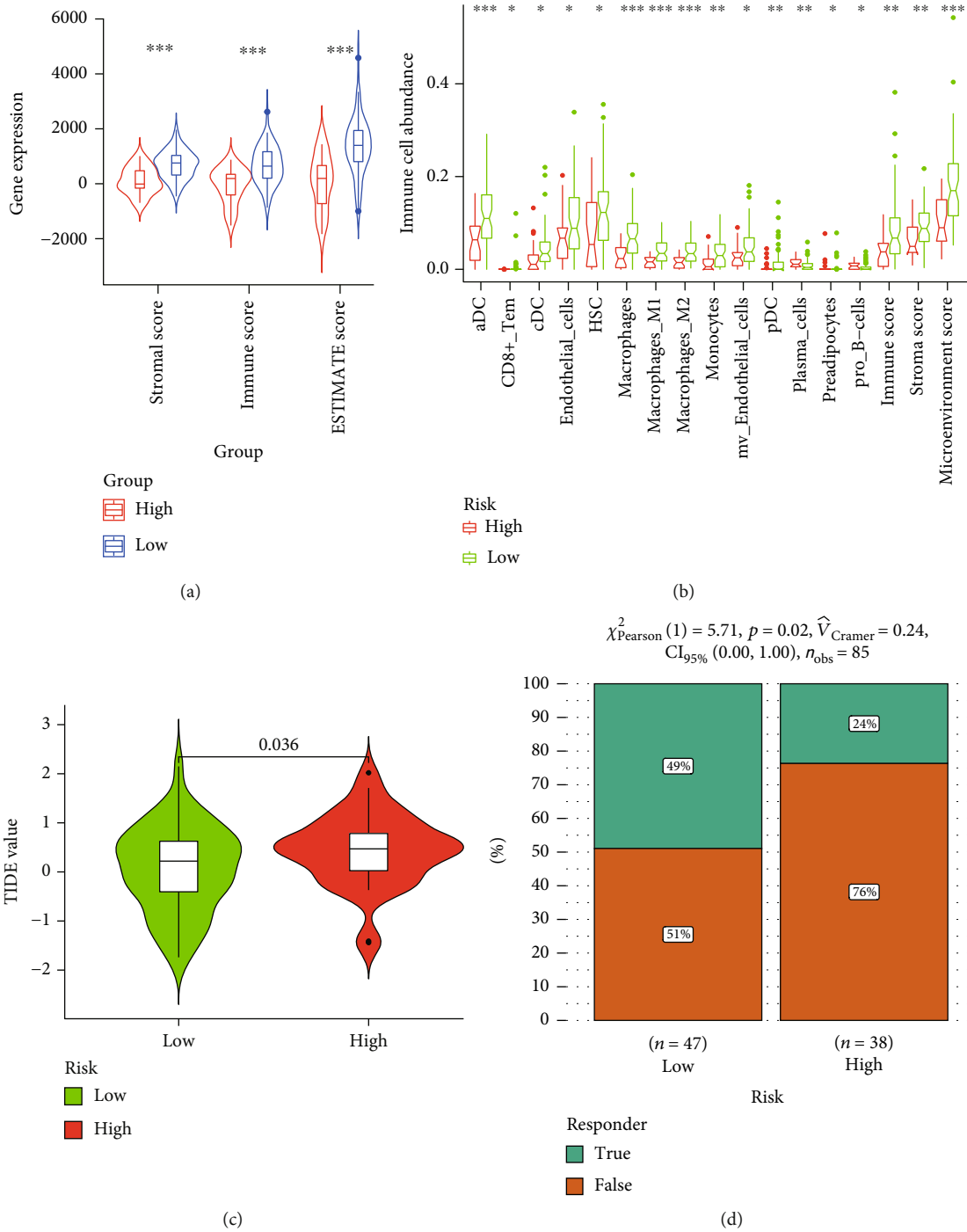
(a)

(b)

(c)

(d)

Figure 6: Correlation of risk scores with immune profiles of OS. (a) Comparison of the stromal score, immune score, and ESTIMATE score between high-risk and low-risk groups. (b) Comparison of immune cell infiltration between high-risk and low-risk groups. (c) Comparison of TIDE value between high-risk and low-risk groups. (d) Comparison of the response to immunotherapy in patients with OS in high-risk and low-risk groups.

enrichment analysis. The results of GO analysis showed that the risk score of the CD8-DEGs model was closely related to multiple immune functions, such as leukocyte-mediated immunity, activation of immune response, MHC complexes, and antigen binding (Figure 5(a)). KEGG analysis revealed that the risk score of the CD8-DEG model was associated with multiple immune-related pathways, such as Th1 and Th2 cell

differentiation, intestinal immune network for IgA production, cell adhesion molecules, cytokine-cytokine receptor interactions and NF-kappa B pathway (Figure 5(b)).

3.6. Correlations between Risk Scores and OS Immune Profiles. The previous results indicated that the risk score of CD8-DEG model is closely related to multiple immune

(a)

(b)

(c)
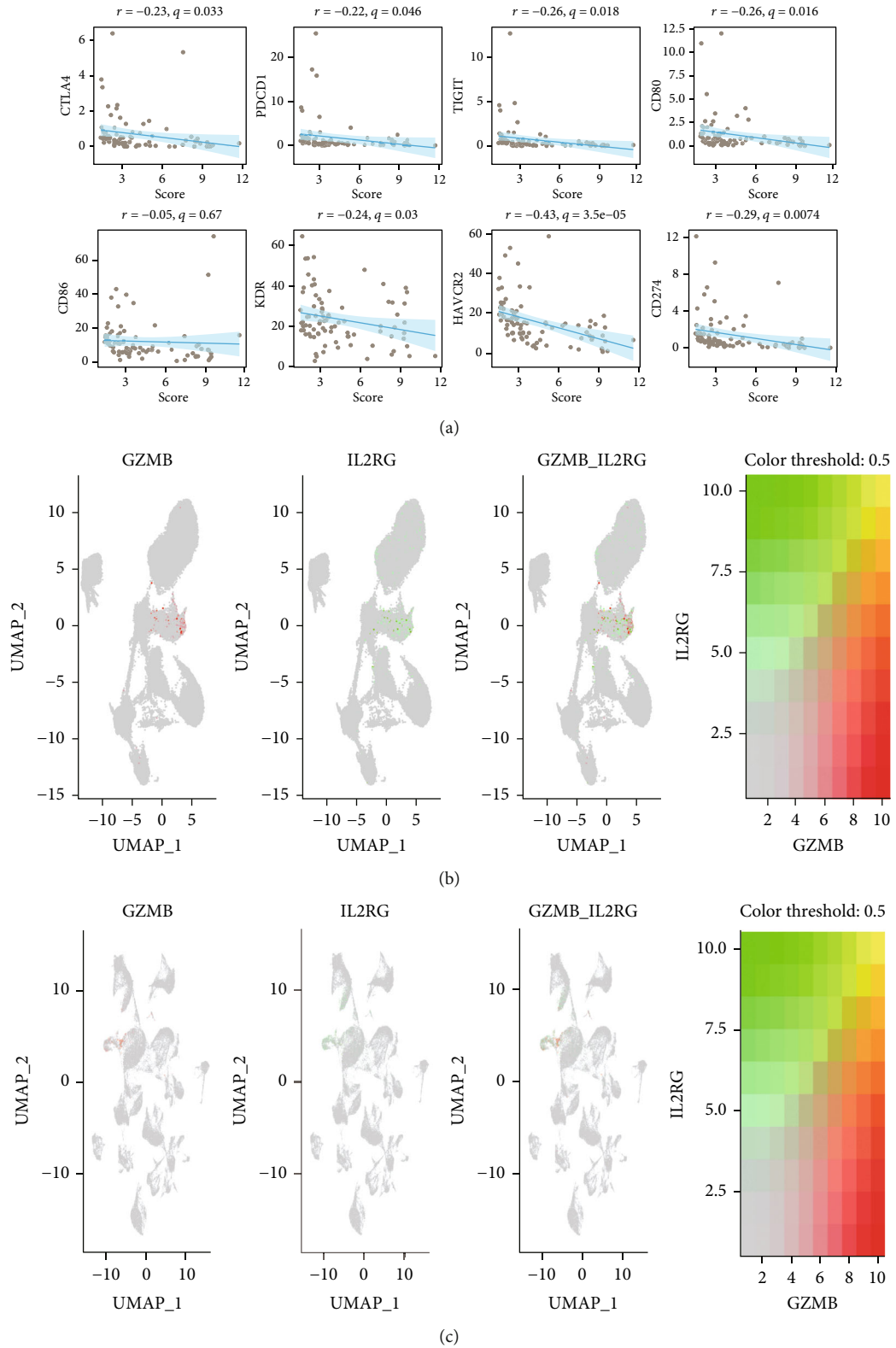
FIGURE 7: Correlation of risk scores with immune checkpoints and validation of risk genes. (a) Correlation analysis of immune checkpoints and risk scores. (b) Expression of GZMB and IL2RG in UMAP plots of OS scRNA-seq data. (c) Expression of GZMB and IL2RG in UMAP plots of leukocyte scRNA-seq data.

pathways. We analyzed the association of risk scores and OS immune profile. As shown in Figure 6(a), low-risk patients had higher scores in stromal score, immune score, and ESTI-MATE score. We applied CIBERSORT to assess the effect of risk score on immune cell infiltration. It was found that high-risk patients negatively regulate the infiltration of various immune cells, such as CD8^{+} T cells, macrophages, and M1-like macrophages (Figure 6(b)). In recent years, TIDE has been widely used as an indicator for tumor immune evasion ability. As presented in Figure 6(c), high-risk patients had lower TIDE scores. Finally, we further assessed whether risk scores could be used as a predictor of response to immunotherapy in OS. The results showed that OS patients with high-risk scores tended to be insensitive to immunotherapy (Figure 6(d)).

3.7. Correlation of Risk Scores with Immune Checkpoints and Validation of Risk Genes. Due to the immune checkpoints play an important role in regulating immune cell function, we further analyzed the relationship between risk scores and immune checkpoints. As shown in Figure 7(a), the risk score was negatively correlated with the expression of multiple immune checkpoints, including CTLA4, PDCD1, TIGIT, CD80, CD86, KDR, HAVCR2, and CD274. Finally, we further verified the expression of GZMB and IL2RG in OS scRNA-seq and leukocyte scRNA-seq data. The results revealed that GZMB and IL2RG similarly clustered in the UMAP plot of OS scRNA-seq data (Figure 7(b)). Similarly, GZMB and IL2RG were clustered in UMAP plots of leukocyte scRNA-seq data (Figure 7(c)).

4. Discussion

The poor prognosis of OS has plagued and threatens the physical and mental health of human beings. Immunotherapy is considered a promising treatment for improving OS prognosis [19]. Given the current dilemma of immunotherapy for OS, it is urgent to develop an effective method to predict the response to immunotherapy. In this study, we first downloaded and processed the single-cell sequencing data of OS from the GEO database. Next, we clustered the above data and further marked it by specific markers to obtain immune cell clusters and nonimmune cells. In addition, we performed cluster analysis on the obtained immune cell clusters, while applying specific markers to extract CD8^{+} T cell clusters, and obtained DEGs of CD8^{+} T cells by gene differential analysis. Furthermore, we combined TCGA-OS cohort data to perform univariate regression analysis on DEGs to obtain prognostic-related genes. A random forest model (CD8-DEG model) was constructed for the above-mentioned prognosis-related genes, and further verification found that it has good predictive performance. Moreover, we revealed that the risk score of CD8-DEG model was significantly associated with the immune profile and could also be used as a predictor of OS immunotherapy response. Finally, we demonstrated the correlation between risk score and the expression of multiple immune checkpoints.

Prognostic models based on various functional gene sets of tumors, such as ferroptosis, pyroptosis, and autophagy,

have gradually become a research hotspot in recent years. Tang et al. constructed a ferroptosis-related lncRNA prognostic model in head and neck squamous cell carcinoma, and the area under the ROC curve of the model risk score reached 0.782 [20]. Zhang et al. analyzed the expression levels of pyroptosis-related genes in human endometrial cancer and constructed a prognostic model based on pyroptosis-related genes. The ROC value of the model was 0.613 [21]. Duan et al. analyzed the expression levels of autophagy-related gene lncRNAs in colorectal cancer, obtained 11 lncRNAs related to autophagy, and further constructed a prognostic model. The ROC area of this model reached 0.808 [22]. In this study, constructed a prognostic model based on the differentially expressed genes of CD8^{+} cells, the area under the ROC curve was 0.793. The prognostic model of DEGs based on CD8^{+} T cells we established has a predictive ability that is not inferior to other previous prognostic models of functional gene sets, which provided a valuable reference for evaluating the prognosis of OS.

Single-cell transcriptome sequencing is performed by analyzing the mRNA expression level of each cell in a sample. In this study, we performed two cluster analyses. We first performed cluster analysis on the single-cell data of OS, resulting in 34 cell clusters. Then, we defined immune cell clusters by PTPRC. Next, we again performed cluster analysis on the immune cell clusters. In this study, we applied two clustering analyses to more precisely define CD8^{+}T cells. This is more reliable than previous analysis of BULK sequencing data.

The model we established has a high application prospect, but there are also some obvious shortcomings. First, all data are derived from public data and lack in vivo and in vitro validation. Second, the specific mechanisms by which the model predicts immune signatures and immunotherapy have not been further explored. These are worthy of further clarification in our follow-up research.

In conclusion, the CD8-DEG model can not only be used to analyze the immune profile of OS but also can be used as a marker to evaluate the efficacy of OS on immunotherapy.

Data Availability

All data generated or analyzed in this study are available from the corresponding author for reasonable request.

Ethical Approval

The study was conducted in accordance with the Declaration of Helsinki, and the protocol was approved by the Ethics Committee of Xianyou County General Hospital.

Conflicts of Interest

All authors in this study declare no conflict of interest.

Authors' Contributions

Yu Chen, Wei Yan, and Hongqing Wang contributed equally to this work. All authors read and approved the final manuscript.

Acknowledgments

Supplementary Materials

Supplementary Table: differentially expressed genes between CD8$^+$ cell clusters and remaining cells. *(Supplementary Materials)*

References

[1] R. L. Siegel, K. D. Miller, and A. Jemal, "Cancer statistics, 2018," *CA: a Cancer Journal for Clinicians*, vol. 68, no. 1, pp. 7–30, 2018.

[2] S. Prater and B. McKeon, *Osteosarcoma*, StatPearls, Treasure Island (FL), 2022.

[3] G. N. Yan, X. F. Tang, X. C. Zhang et al., "TSSC3 represses self-renewal of osteosarcoma stem cells and Nanog expression by inhibiting the Src/Akt pathway," *Oncotarget*, vol. 8, no. 49, pp. 85628–85641, 2017.

[4] G. Ottaviani and N. Jaffe, "The etiology of osteosarcoma," *Cancer Treatment and Research*, vol. 152, pp. 15–32, 2009.

[5] F. Jafari, S. Javdansirat, S. Sanaie et al., "Osteosarcoma: a comprehensive review of management and treatment strategies," *Annals of Diagnostic Pathology*, vol. 49, article 151654, 2020.

[6] D. J. Harrison, D. S. Geller, J. D. Gill, V. O. Lewis, and R. Gorlick, "Current and future therapeutic approaches for osteosarcoma," *Expert Review of Anticancer Therapy*, vol. 18, no. 1, pp. 39–50, 2018.

[7] X. Zhang and Z. Guan, "PET/CT in the diagnosis and prognosis of osteosarcoma," *Front Biosci (Landmark Ed)*, vol. 23, no. 11, pp. 2157–2165, 2018.

[8] I. Corre, F. Verrecchia, V. Crenn, F. Redini, and V. Trichet, "The osteosarcoma microenvironment: a complex but targetable ecosystem," *Cell*, vol. 9, 2020.

[9] T. F. Gajewski, Y. Meng, and H. Harlin, "Immune suppression in the tumor microenvironment," *Journal of Immunotherapy*, vol. 29, no. 3, pp. 233–240, 2006.

[10] K. Shimizu, T. Iyoda, M. Okada, S. Yamasaki, and S. I. Fujii, "Immune suppression and reversal of the suppressive tumor microenvironment," *International Immunology*, vol. 30, no. 10, pp. 445–455, 2018.

[11] J. S. Dolina, N. Van Braeckel-Budimir, G. D. Thomas, and S. Salek-Ardakani, "CD8(+) T cell exhaustion in cancer," *Frontiers in Immunology*, vol. 12, article 715234, 2021.

[12] M. Abbott and Y. Ustoyev, "Cancer and the immune system: the history and background of immunotherapy," *Seminars in Oncology Nursing*, vol. 35, no. 5, article 150923, 2019.

[13] B. Li, H. L. Chan, and P. Chen, "Immune checkpoint inhibitors: basics and challenges," *Current Medicinal Chemistry*, vol. 26, no. 17, pp. 3009–3025, 2019.

[14] J. Cable, B. Greenbaum, D. Pe'er et al., "Frontiers in cancer immunotherapy—a symposium report," *Annals of the New York Academy of Sciences*, vol. 1489, no. 1, pp. 30–47, 2021.

[15] J. Ding and Y. Zhang, "Analysis of key GO terms and KEGG pathways associated with carcinogenic chemicals," *Combinatorial Chemistry & High Throughput Screening*, vol. 20, 2017.

[16] Z. Wang, H. Wu, Y. Chen, H. Chen, W. Yuan, and X. Wang, "The heterogeneity of infiltrating macrophages in metastatic osteosarcoma and its correlation with immunotherapy," *Journal of Oncology*, vol. 2021, Article ID 4836292, 13 pages, 2021.

[17] Q. Wang, M. Li, M. Yang et al., "Analysis of immune-related signatures of lung adenocarcinoma identified two distinct subtypes: implications for immune checkpoint blockade therapy," *Aging (Albany NY)*, vol. 12, no. 4, pp. 3312–3339, 2020.

[18] N. Hilger, J. Glaser, C. Muller et al., "Attenuation of graft-versus-host-disease in NOD scid IL-2Rγ−/− (NSG) mice by ex vivo modulation of human CD4+ T cells," *Cytometry. Part A*, vol. 89, no. 9, pp. 803–815, 2016.

[19] K. Yahiro and Y. Matsumoto, "Immunotherapy for osteosarcoma," *Human Vaccines & Immunotherapeutics*, vol. 17, no. 5, pp. 1294-1295, 2021.

[20] Y. Tang, C. Li, Y. J. Zhang, and Z. H. Wu, "Ferroptosis-related long non-coding RNA signature predicts the prognosis of head and neck squamous cell carcinoma," *International Journal of Biological Sciences*, vol. 17, no. 3, pp. 702–711, 2021.

[21] X. Zhang and Q. Yang, "A pyroptosis-related gene panel in prognosis prediction and immune microenvironment of human endometrial cancer," *Frontiers in Cell and Development Biology*, vol. 9, article 705828, 2021.

[22] L. Duan, Y. Xia, C. Li, N. Lan, and X. Hou, "Identification of autophagy-related lncRNA to predict the prognosis of colorectal cancer," *Frontiers in Genetics*, vol. 13, article 906900, 2022.

Research Article

Comprehensively Analyze the Prognosis Significance and Immune Implication of PTPRO in Lung Adenocarcinoma

Zhimin Lin [ID],[1,2] **Jinjun Zhang** [ID],[3] **Biqiong Liu** [ID],[4] **Zhiqian Hong** [ID],[5] **Zengguang Chen** [ID],[6] **and Xiaoyan Huang** [ID][7]

[1]*Department of General Surgery, 900 Hospital of Joint Logistics Support Force, Fujian, Fuzhou, China*
[2]*Fuzhou General Clinical Medical College of Fujian Medical University, Fujian, Fuzhou, China*
[3]*The First Department of Surgery, Xianyou County General Hospital, Putian, Fujian, China*
[4]*Department of Nephrology, Xianyou County General Hospital, Putian, Fujian, China*
[5]*Longgang District Maternity & Child Healthcare Hospital of Shenzhen City, Shenzhen, Guangdong, China*
[6]*Department of Orthopedics, Xiuyu District Hospital, Fujian, Putian, China*
[7]*Department of Oncology, 900 Hospital of Joint Logistics Support Force, Fujian, Fuzhou, China*

Correspondence should be addressed to Zengguang Chen; 50018068@qq.com
and Xiaoyan Huang; huangxiaoyan202208@163.com

Immunotherapy for lung adenocarcinoma (LUAD) is considered to be a promising treatment option, but only a minority of patients benefit from it. Therefore, it is essential to clarify the regulation mechanism of the tumor immune microenvironment (TIM) of the LUAD. Receptor-type protein tyrosine phosphatase (PTPRO) has been shown to be a tumor suppressor in a variety of tumor; however, its role in LUAD has never been reported. In this study, we first found that PTPRO was lowly expressed in LUAD and positively correlated with patient prognosis. Next, we investigated the relationship between PTPRO and clinical characteristics, and the results showed that gender, age, T, and stage were closely related to the expression level of PTPRO. Moreover, we performed univariate and multivariate analyses, and the results revealed that PTPRO was a protective factor for LUAD. By constructing a nomogram based on the expression level of PTPRO and various clinical characteristics, it was proved that the nomogram has a good predictive capacity. Furthermore, we analyzed the coexpression network of PTPRO through multiple databases and performed GO and KEGG enrichment analyses. The results demonstrated that PTPRO was involved in the regulation of multiple immune pathways. In addition, we analyzed whether PTPRO expression of LUAD regulate immune cell infiltration and the results demonstrated that PTPRO was closely related to the infiltration of various immune cells. Finally, we predicted LUAD sensitivity to chemotherapeutics and response to immunotherapy by PTPRO expression levels. The results showed that PTPRO expression level affect the sensitivity of various chemotherapeutic drugs and may be involved in the efficacy of immunotherapy. These results we obtained suggested that PTPRO is closely related to the prognosis and TIM of LUAD, which may be a potential immunotherapeutic target for LUAD.

1. Introduction

Lung cancer (LC) is the second most common malignancy worldwide and one of the leading causes of cancer-related death currently [1]. LC is a heterogeneous malignancy, which is roughly divided into non-small-cell lung cancer (NSCLC) and small-cell lung cancer, and lung adenocarci-

noma (LUAD) is the main pathological type of LC [2]. Currently, the traditional treatment options for LUAD mainly include surgery, chemotherapy, and radiation therapy [3]. However, the prognosis of LUAD is unsatisfactory, especially for advanced patients [4]. In the past two decades, with the further exploration of the mechanism of occurrence and development of LUAD, more treatment methods have been

applied, such as targeted drugs and immunotherapy, which have significantly improved the prognosis of LUAD [5].

At present, a variety of immunotherapy methods have been developed, including vaccine therapy, chimeric antigen receptor (CAR) T cells, and immune checkpoint inhibitors (ICIs), including against cytotoxic T-lymphocyte-related antigen 4 (CTLA-4) antibodies, programming cell death 1 (PD-1), and programmatic cell death ligand 1 (PD-L1) [6]. The unique treatment effect of ICIs has gradually become a research hotspot in tumor treatment. Unfortunately, only a small percentage of patients benefit from immunotherapy [6]. Several studies have shown that the proportion of leukocytes infiltrating the tumor immune microenvironment (TIM) is closely related to the response to immunotherapy [7–10]. Therefore, elucidating the TIM regulation mechanism of LUAD is crucial for developing therapeutic strategies for LUAD.

Receptor-type protein tyrosine phosphatase (PTPRO) is a member of the PTP family and plays an important role in regulating human physiological and pathological processes [11, 12]. Based on previous studies, PTPRO has been shown to act as a tumor suppressor in the development of various tumors. The initial study found that overexpression of PTPRO inhibited the progression of lung cancer [13]. Another study revealed that PTPRO suppress tumor cell proliferation and promotes apoptosis by dephosphorylating signal transducer and activator of transcription 3 (STAT3) in liver cancer [14]. Not only that, PTPRO has also been found to be involved in regulating the TIM of various tumors in recent years. Gan and Zhang found that the expression level of PTPRO in human clear cell renal cell carcinoma is closely related to patient prognosis and immune infiltration [15]. Paradoxically, the expression level of PTPRO in pancreatic cancer is negatively correlated with patient prognosis and has the function of worsening the TIM [16]. However, there is no study of the relationship between PTPRO and immune function in LUAD.

In this study, we first analyzed the relationship between the PTPRO expression and prognosis in LUAD and further explored the correlation between PTPRO and clinical characteristics. Furthermore, the potential mechanism of PTPRO regulation of LUAD progression was explored by KEGG and GO analyses. In addition, we analyzed the correlation between PTPRO and immune cell infiltration status by multiple public databases. Finally, we further predicted the level of PTPRO and the sensitivity of LUAD to multiple chemotherapeutic agents and immunotherapy.

2. Methods and Materials

2.1. TIMER2.0. Tumor Immune Estimation Resource 2.0 (TIMER2.0) is a public database that can be used to analyze immune cell infiltration in variety of cancers. The database has a variety of analysis modules, such as gene, survival, and copy number variation, to analyze tumor immune function [17].

2.2. Acquisition of LUAD Transcription Data from the TCGA Database. The LUAD transcription data was obtained from the TCGA database. The LUAD cohort contains LUAD and normal tissues, and all LUAD tissues contain relevant clinical information. We use corresponding functions in the limma package of the R software to further process these obtained data.

2.3. Analysis of Immune Cell Infiltration in LUAD. To investigate the relationship between PTPRO and cellular immune infiltration using multiple databases, including TIMER2.0, TISIDB, and cell type identification by estimating relative subsets of RNA transcripts (CIBERSORT). TIMER and TISIDB are web databases [17, 18]. CIBERSORT identifies immune cell types based on the expression profiles of characteristic genes in RNA-sequencing data. CIBERSORT relies on a gene expression matrix file (named LM22) to parse immune cells in tissues to distinguish human hematopoietic cell phenotypes [19].

2.4. Prediction of PTPRO Expression on the Effect of Immunotherapy. The immunophenotype score (IPS) is a predictor of response to anti-CTLA-4 and anti-PD-1 therapy that quantifies determinants of tumor immunogenicity [20]. The principle for this protocol is based on immune-related genes including MHC-associated molecules, checkpoints or immunomodulators, effector cells, and suppressor cells. This method obtains the final IPS by quantifying the abovementioned genes and then weighting them equally.

2.5. Prediction of PTPRO Expression on the Efficacy of Chemotherapy Drugs. The principle of this algorithm is based on differentially expressed genes (DEGs) between samples with high and low expressions of the target gene. Then, the top 1000 DEGs will be submitted to the CMap database to match the corresponding potential chemical drugs.

2.6. KEGG and GO Enrichment Analyses. GO (http://geneontology.org) and KEGG (https://www.genome.jp/kegg) analyses were frequently used in functional enrichment study and investigated the biological pathways that involve differentially expressed mRNAs. ClusterProfiler (v3.12.0) and Database for Annotation, Visualization and Integrated Discovery tools were conducted to analyze the functional enrichment conditions for dysregulated mRNAs. The false discovery rate (FDR) was calculated to correct the p value.

2.7. Statistics. In this study, R software was used for calculation and statistical analysis. Their responses to immunotherapy were compared using the Wilcoxon rank-sum test. Differences between high and low target gene classes were determined using Kaplan-Meier curves and log-rank tests. $p < 0.05$ were considered statistically significant.

3. Results

3.1. PTPRO Is Lowly Expressed in LUAD and Associated with Prognosis. We first analyzed the expression levels of PTPRO in pan-cancer tissues via the TIMER database. As shown in Figure 1(a), the expression level of PTPRO in LUAD was
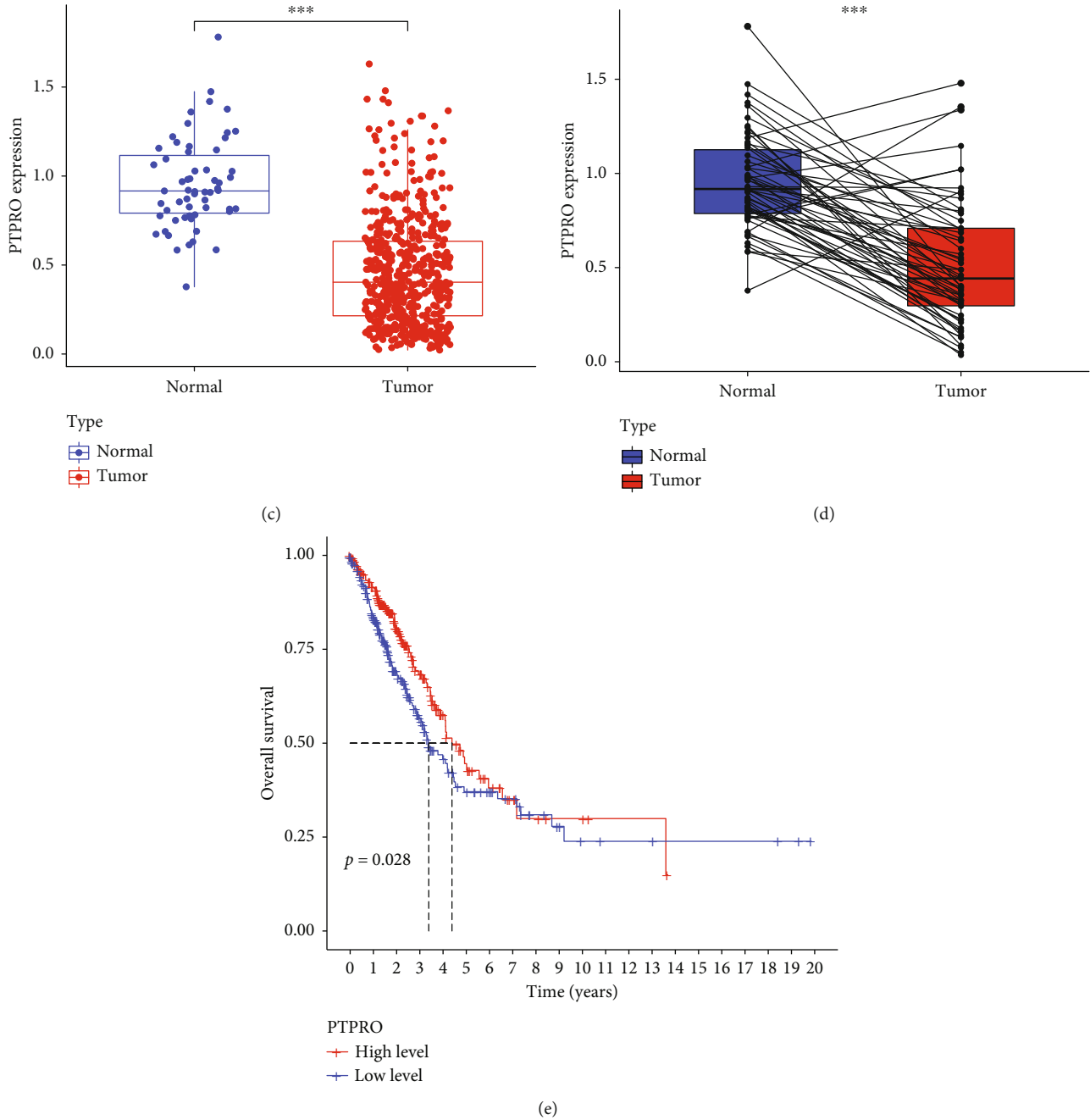
(a)

(b)

Figure 1: Continued.

(c)

(d)

(e)
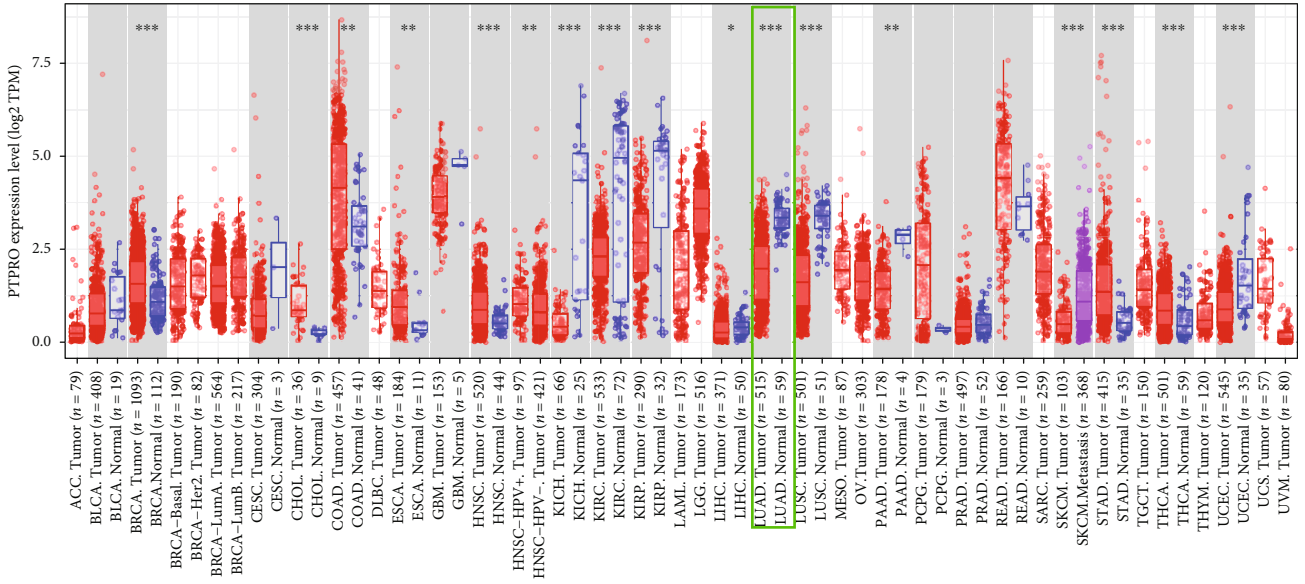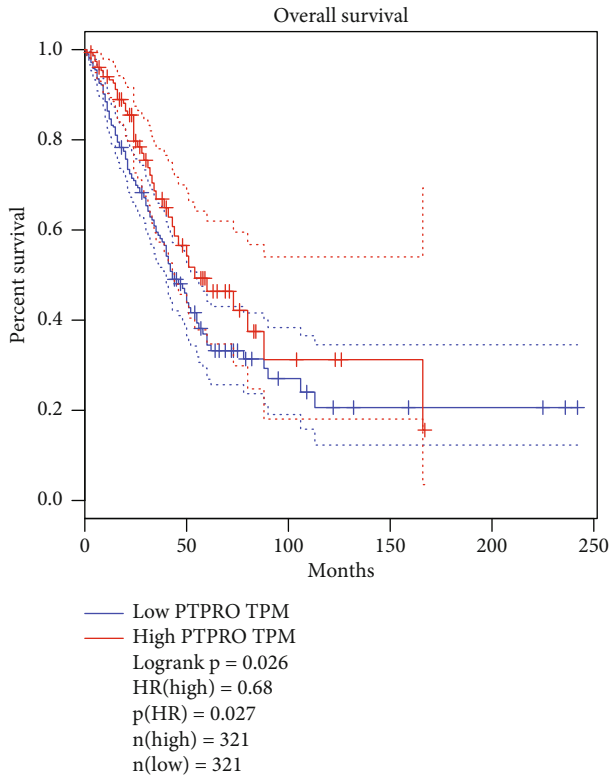
FIGURE 1: Expression level of PTPRO in LUAD and its correlation with prognosis. (a) Analysis of the expression level of PTPRO in pancancer by GEPIA database. (b) Kaplan-Meier survival analysis for high vs. low expression level of PTPRO in LUAD (GEPIA database). (c) Differences in mRNA expression levels of PTPRO in LUAD and normal tissues (TCGA database). (d) Differences in mRNA expression levels of PTPRO in LUAD and paired normal tissues (TCGA database). (e) Kaplan-Meier survival analysis for high vs. low expression level of PTPRO in LUAD (TCGA database).

significantly lower than that in normal tissues. Further survival prognostic analysis showed that LUAD with high PTPRO expression had better prognosis (Figure 1(b)). Furthermore, we analyzed the expression of PTPRO in LUAD by the TCGA database. The results indicated that the expression of PTPRO was significantly higher in LUAD than in normal tissues (Figure 1(c)). The expression levels of PTPRO in LUAD and its paired normal tissues also showed the same results as above (Figure 1(d)). Interestingly, the

further analysis revealed that the TCGA-LUAD cohort with a high expression of PTPRO had a better prognosis (Figure 1(e)). These above results indicated that the expression of PTPRO was significantly downregulated and correlated with the prognosis of patients in LUAD.

3.2. The Correlation Analysis between the Clinical Features and PTPRO Expression Level for LUAD Patients. The TNM system is widely used in evaluating the classification of
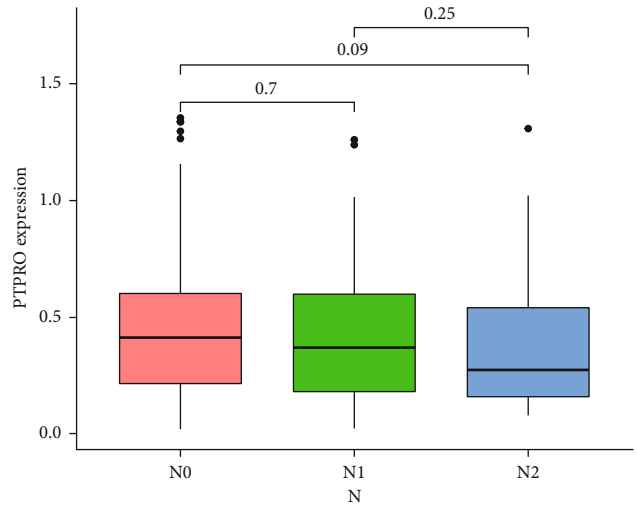
(a)

(b)

(c)
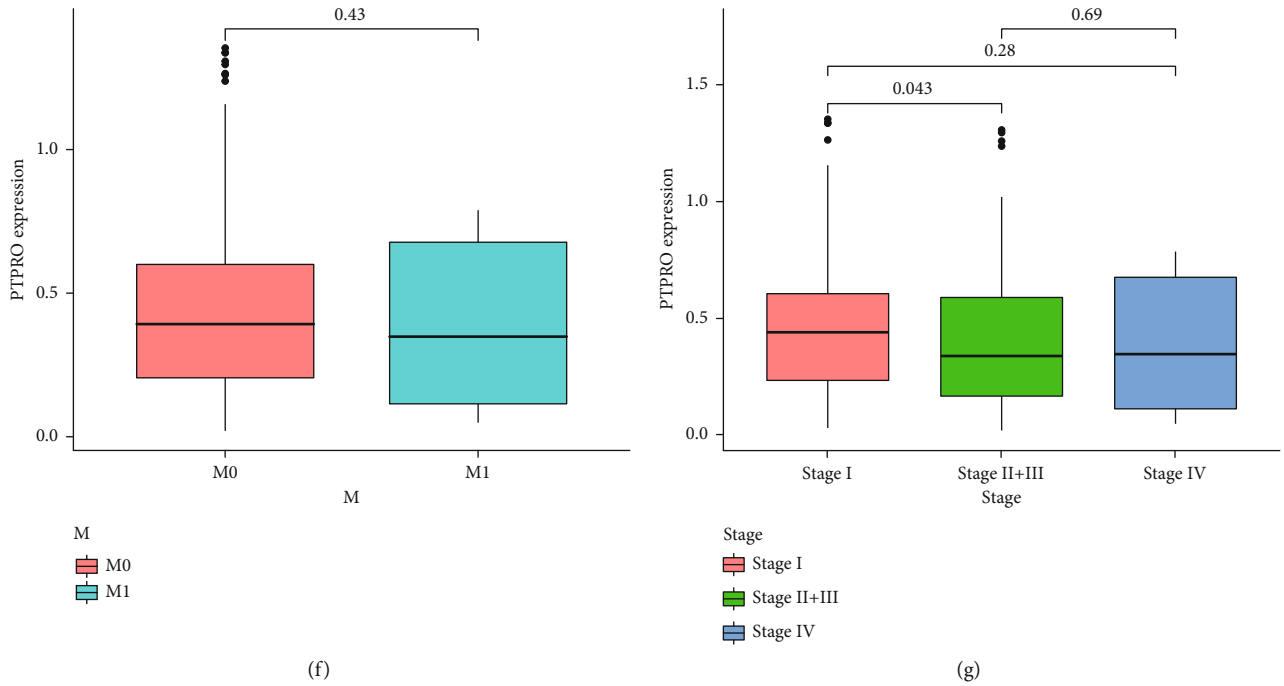

(d)

(e)

FIGURE 2: Continued.

(f)

(g)
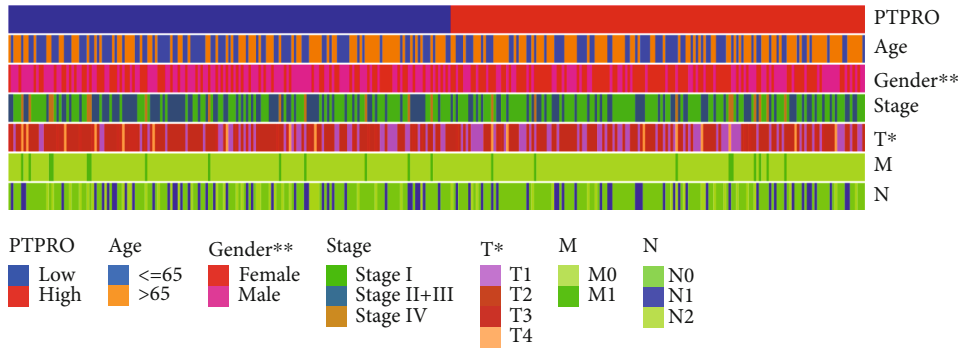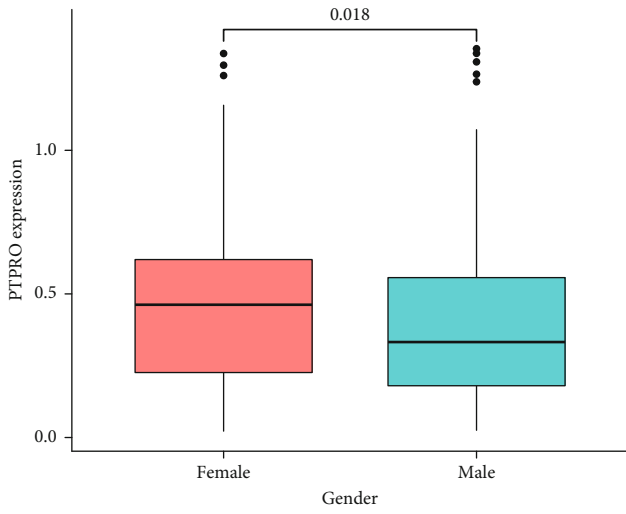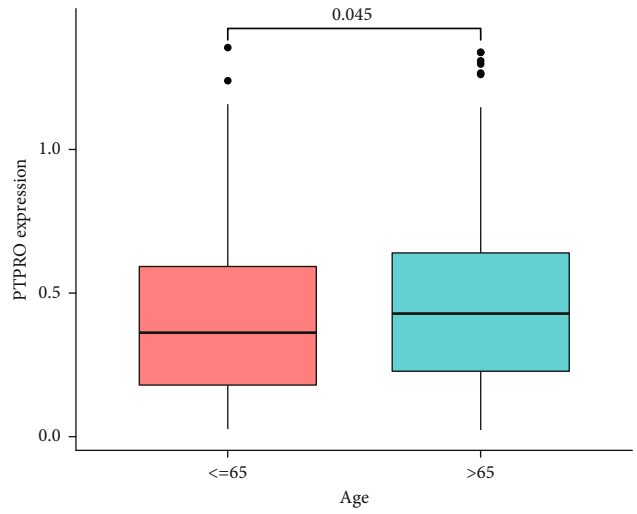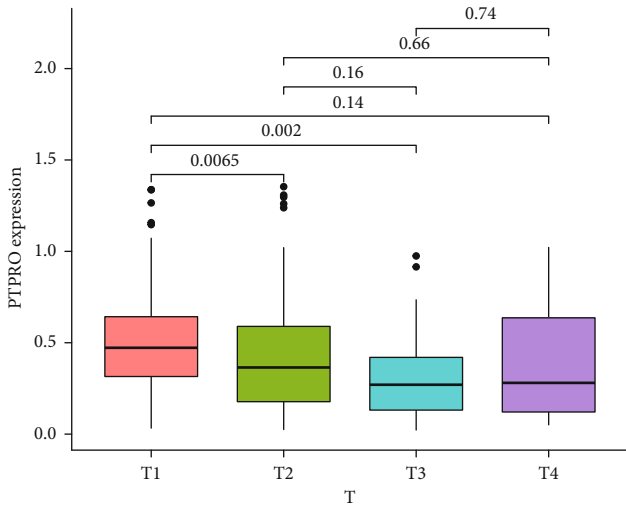
Figure 2: Correlation between the expression level of PTPRO and clinical features in LUAD. (a) Heatmap of the clinical relevance of PTPRO expression level. (b–g) Differences in PTPRO expression level between different clinical subgroups (gender, age, TNM and stage).

LUAD. [21]. Our previous findings suggested that the expression level of PTPRO was closely related to the prognosis of LUAD patients. To further explore the role of PTPRO in LUAD, we analyzed the relationship between PTPRO and clinical characteristics. First, we created a heatmap to show the distribution of clinicopathological feature subtypes in patients with high and low PTPRO expressions (Figure 2(a)). Moreover, we found that PTPRO was expressed at higher levels in female patients, while patients younger than 65 years old had lower levels of PTPRO expression (Figures 2(b) and 2(c)). More interestingly, we found that PTPRO levels were significantly lower in T2 and T3 patients compared to T1 patients (Figure 2(d)). The expression levels of PTPRO in patients were not significantly different in N and M stages (Figures 2(e) and 2(f)). Finally, the correlation between pathological stage and PTPRO level showed that stage II+III patients had lower PTPRO levels than stage I patients (Figure 2(g)).
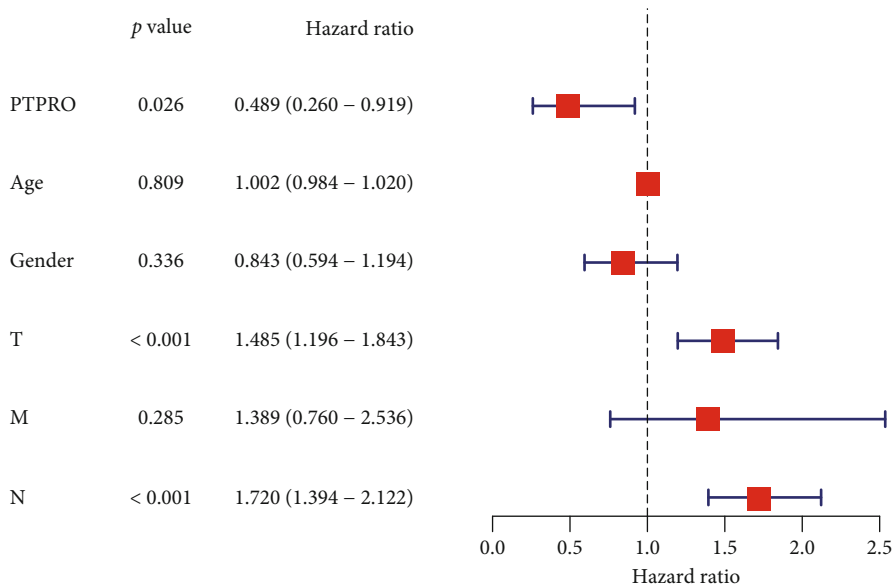
3.3. Construction of a Nomogram Based on PTPRO Expression Levels. The previous results of this study showed that the expression level of PTPRO was positively correlated with the prognosis of various solid tumor and was also closely related to the clinical characteristics [12, 22]. Therefore, we further explored whether PTPRO could be used to assess the prognosis of LUAD. Univariate and multivariate regression analyses indicated that PTPRO was a protective factor for the prognosis of LUAD (Figures 3(a) and 3(b)). Next, we established a nomogram based on PTPRO expression levels and clinicopathological features to predict the prognosis of LUAD (Figure 3(c)). The calibration curve implied that the nomogram has good predictive capacity (Supplementary Figure 1).

3.4. Construction of PTPRO-Related Gene Network and Enrichment Analysis of GO and KEGG. Based on the above results, we constructed PTPRO-related gene networks by multiple databases (TCGA, STRING, and GeneMANIA) to investigate the potential role of PTPRO in LUAD (Figures 4(a)–4(c)). Next, we extracted different expression genes (DEGs) from patients with high and low PTPRO expressions (Figure 5(a)). Furthermore, we performed GO enrichment analysis to clarify the biological processes, cellular components, and molecular function of PTPRO based on the above DEGs. As shown in Figures 5(b) and 5(c), the results showed that the foremost biological processes were leukocyte cell-cell adhesion, T cell activation, and regulation of leukocyte cell-cell adhesion; the top three cellular components were T cell receptor complex, plasma membrane signaling receptor complex, and external side of plasma membrane; the top three molecular functions were immune receptor activity, signaling receptor activator activity, and receptor ligand activity. KEGG enrichment analysis showed that PTPRO was involved in multiple immune-related pathways, including cytokine-cytokine receptor interaction, cell adhesion molecules, chemokine signaling pathway, Th1 and Th2 cell differentiation, and Th17 cell differentiation. These results strongly suggested that PTPRO may be involved in regulating the TIM of LUAD (Figures 5(d) and 5(e)).

3.5. Correlation Analysis of PTPRO Expression Level and Immune Cell Infiltration. It is well known that tumor immune dysfunction is a critical step in tumorigenesis and progression [23]. We further analyzed the correlation between PTPRO expression levels and immune cell infiltration via multiple databases. We first analyzed the
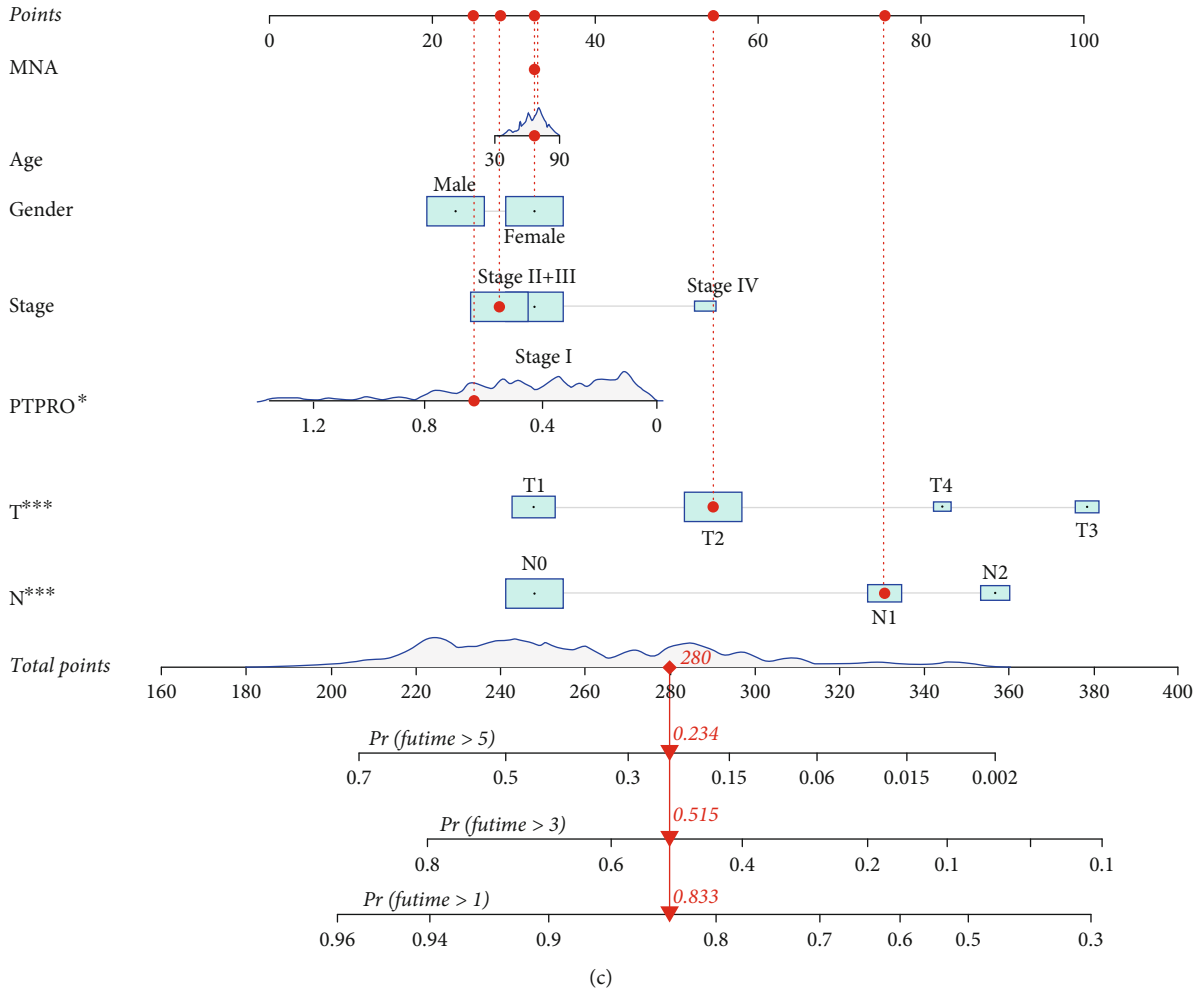
(a)

(b)
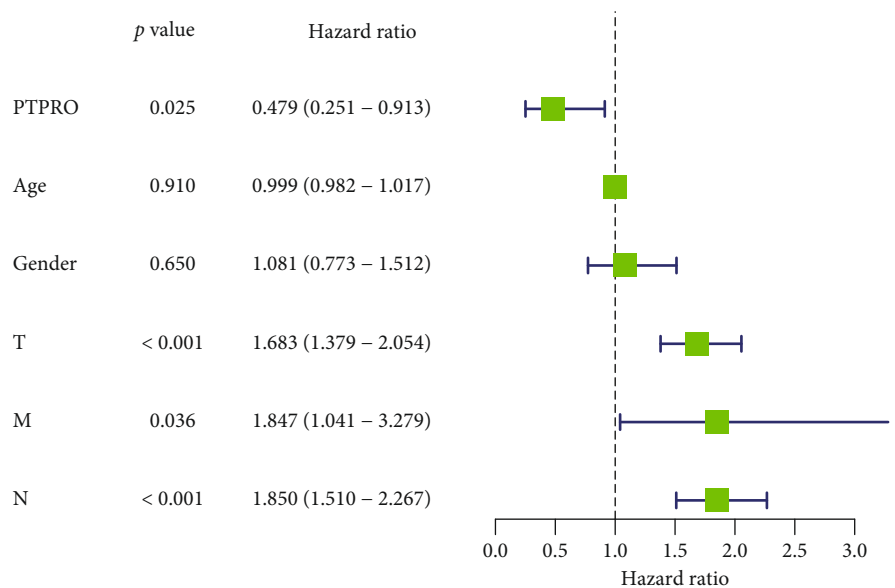
Figure 3: Continued.

FIGURE 3: The value of PTPRO expression level in evaluating the prognosis of LUAD. (a, b) Univariate and multivariate regression analyses of PTPRO expression levels and clinical parameters. (c) Construction of nomogram by the PTPRO expression level and clinical characteristics for predicting the probability of 1-, 3-, and 5-year OS of LUAD patients.

TCGA-LUAD cohort by the CIBERSORT algorithm, and the results showed that PTPRO was positively associated with a variety of immune cells, including CD8, M2 macrophages, and follicular helper T cells (Figure 6(a)). In addition, the results obtained from the TIMER and TISIDB databases demonstrated that the PTPRO was positively correlated with CD8, CD4 and macrophages (Figures 6(b) and 6(c)). These results indicated that PTPRO may be involved in regulating the infiltration of various immune cells in LUAD.

3.6. Prediction of PTPRO Expression Levels within LUAD for Sensitivity to Chemotherapy and Immunotherapy. We analyzed the association between the PTPRO expression level and the chemosensitivity in the treatment of LUAD. As shown in Figure 7, we found that patients with high PTPRO expression showed higher sensitivity to various chemotherapy drugs, such as BLX02189, BHG712, BEZ235, AC220, sunitinib, ruxolitinib, rapamycin, phenformin, masitinib, CH5424802, CGP-06474, and BX912. Given that the function of immune cells is regulated by a variety

of immune checkpoints [24]. Therefore, we further analyzed the relationship between PTPRO and various immune checkpoints, and the results demonstrated that the expression level of PTPRO was closely related to various immune checkpoints (Figure 8(a)). Moreover, we evaluated the TIM of LUAD by the ESTIMATE algorithm and observed that LUAD patients with high PTPRO expression had higher TIM scores (Figure 8(b)). Currently, the immunophenoscore (IPS) is a widely used algorithm to predict the immune response [25]. We divided all patients into 4 groups according to the expression of PD1 and CTLA4, namely, PD1_negative_CTLA4_negative, PD1_positive_ CTLA4_positive, PD1_negative_CTLA4_positive, and PD1_positive_CTLA4_negative. The results showed that in the PD1_positive_CTLA4_positive and PD1_positive_ CTLA4_negative groups, patients with high PTPRO expression had higher IPS scores. In the PD1_negative_CTLA4_ negative group, patients with low expression of PTPRO had higher IPS scores, while in the PD1_negative_ CTLA4_positive group, the expression level of PTPRO had no effect on the IPS score (Figures 8(c)–8(f)).
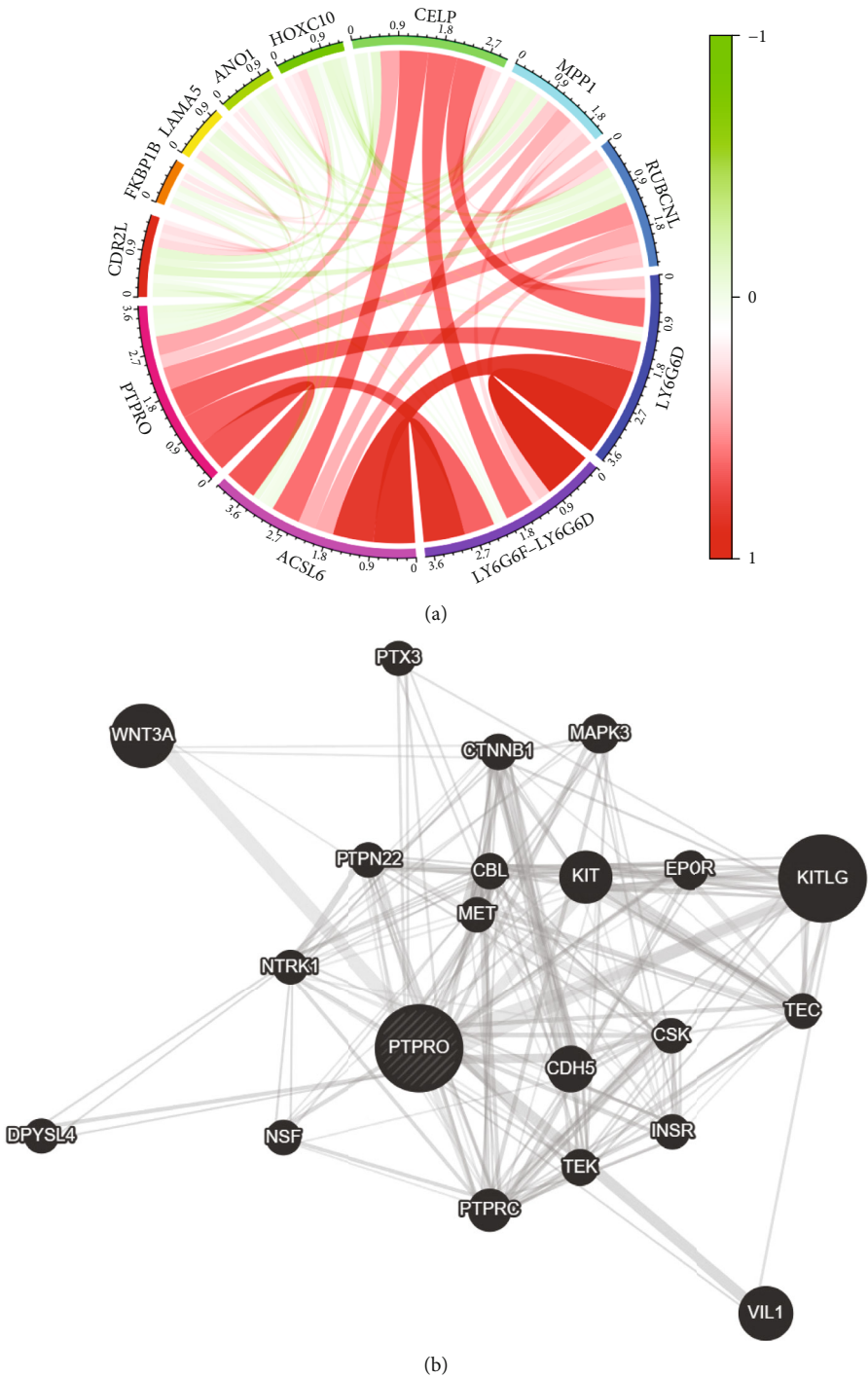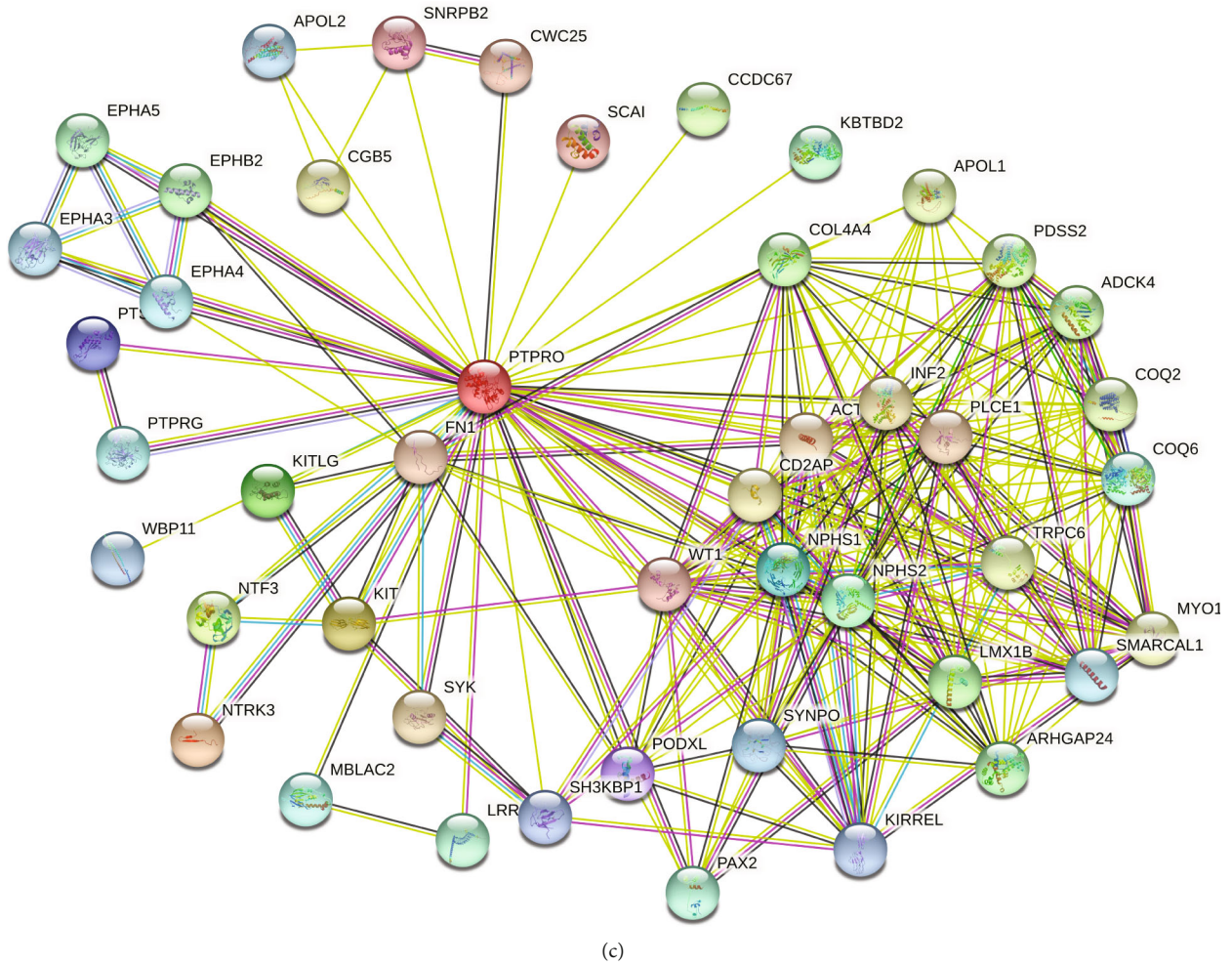
(a)

(b)

Figure 4: Continued.

(c)

FIGURE 4: Coexpression network analysis of PTPRO-related genes. (a) Coexpressed genes of PTPRO were analyzed by TCGA-LUAD cohorts. (b) Coexpressed genes of PTPRO were analyzed by GeneMANIA database. (c) Coexpressed genes of PTPRO were analyzed by STRING database.

4. Discussions

LUAD is a highly lethal malignant tumor that seriously threatens the health of human [26]. Conventional treatments, such as surgery, chemotherapy, and radiotherapy, have significantly improved patient outcomes, but further improvements are more difficult [27]. In recent years, immunotherapy for LUAD based on immune checkpoint inhibitors has gradually attracted people's attention [28]. However, only a minority of patients benefit from it, which greatly limits the application of ICIs [5]. In the present study, we found that PTPRO was significantly downregulated in LUAD and positively correlated with patient prognosis. Next, we found that age, gender, T, and stage of patients affected PTPRO expression levels. In addition, we further analyzed the results and showed that PTPRO was a protective factor for LUAD; we further established a nomogram based on PTPRO expression, which was shown to have good predictive capacity for patient prognosis. Furthermore, we preliminarily explored the mechanism of PTPRO in LUAD by GO and KEGG analyses. Moreover, we also found

that the expression level of PTPRO was closely related to the infiltration of various immune cells. Finally, we applied an algorithm to predict the sensitivity of PTPRO to chemotherapeutic drugs and immunotherapy response.

Tumor immunotherapy is an extremely complex process, and the execution of leukocyte function is the key to the whole step. The entire tumor immune process mainly includes the following steps: recognition of tumor antigens, presentation of tumor antigens, activation of T cell function, overcoming immune suppression, and killing tumor cells [29–31]. The above steps are not independent but intersect each other. In this study, we confirmed the relationship between PTPRO and the tumor immune microenvironment for the first time, which provided more theoretical support for guiding the immunotherapy of LUAD.

In recent years, a large number of studies have attempted to establish prognostic models based on various gene expressions, in order to provide help for the prognosis of malignant tumors. Guo et al. constructed a prognostic model by analyzing the expression levels of ferroptosis-related lncRNAs from head and neck squamous carcinoma in
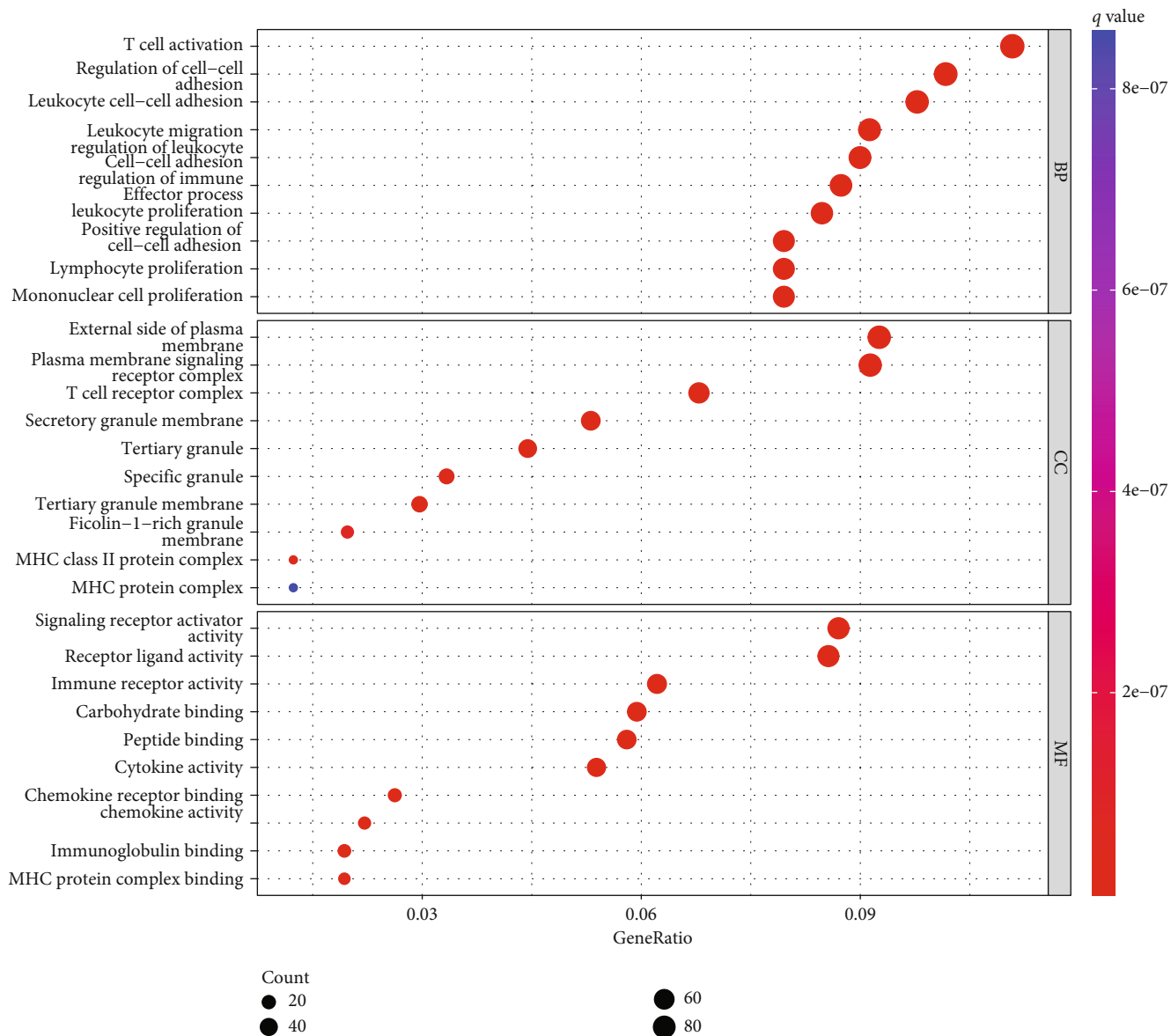
(a)

Figure 5: Continued.

(b)

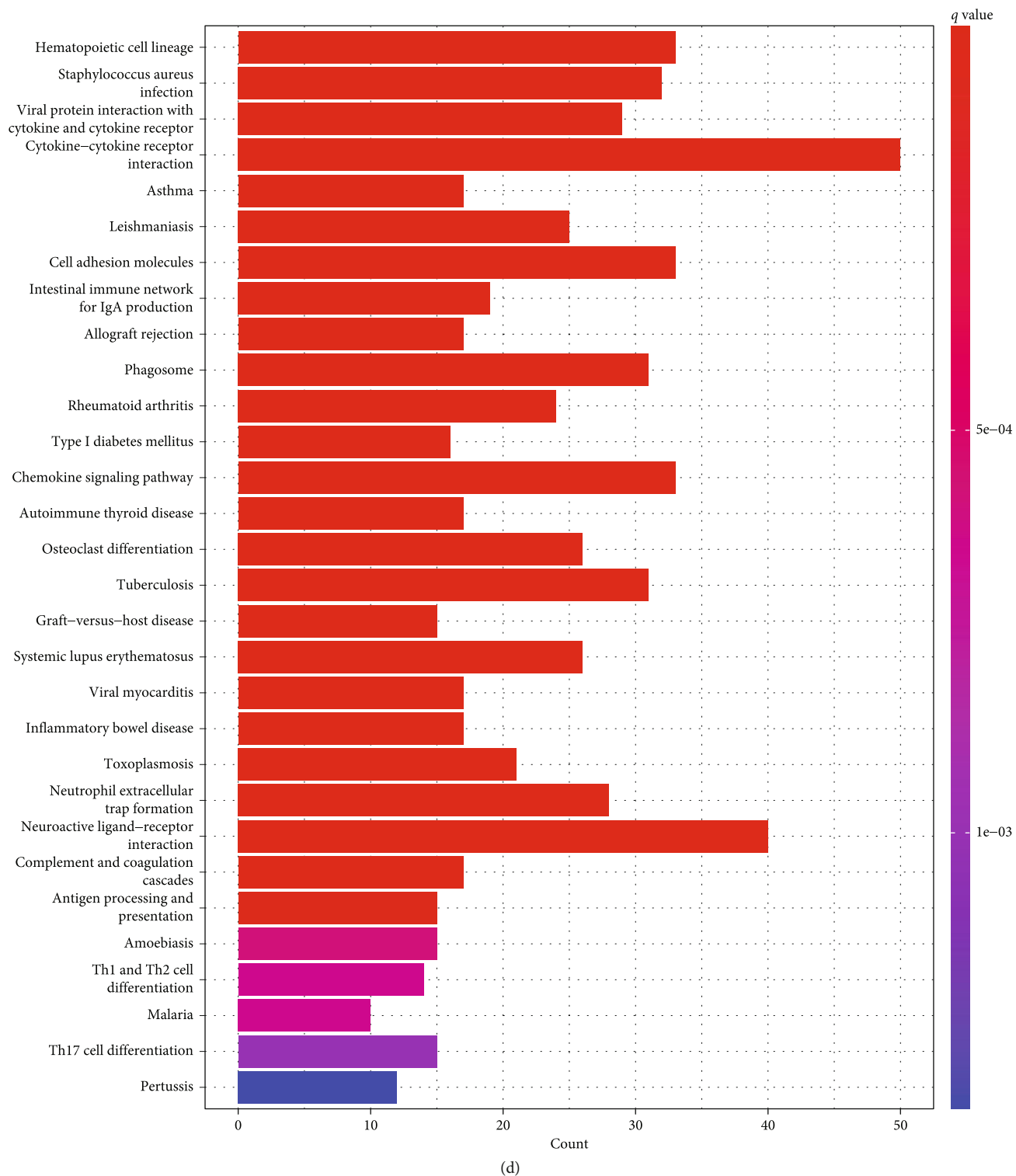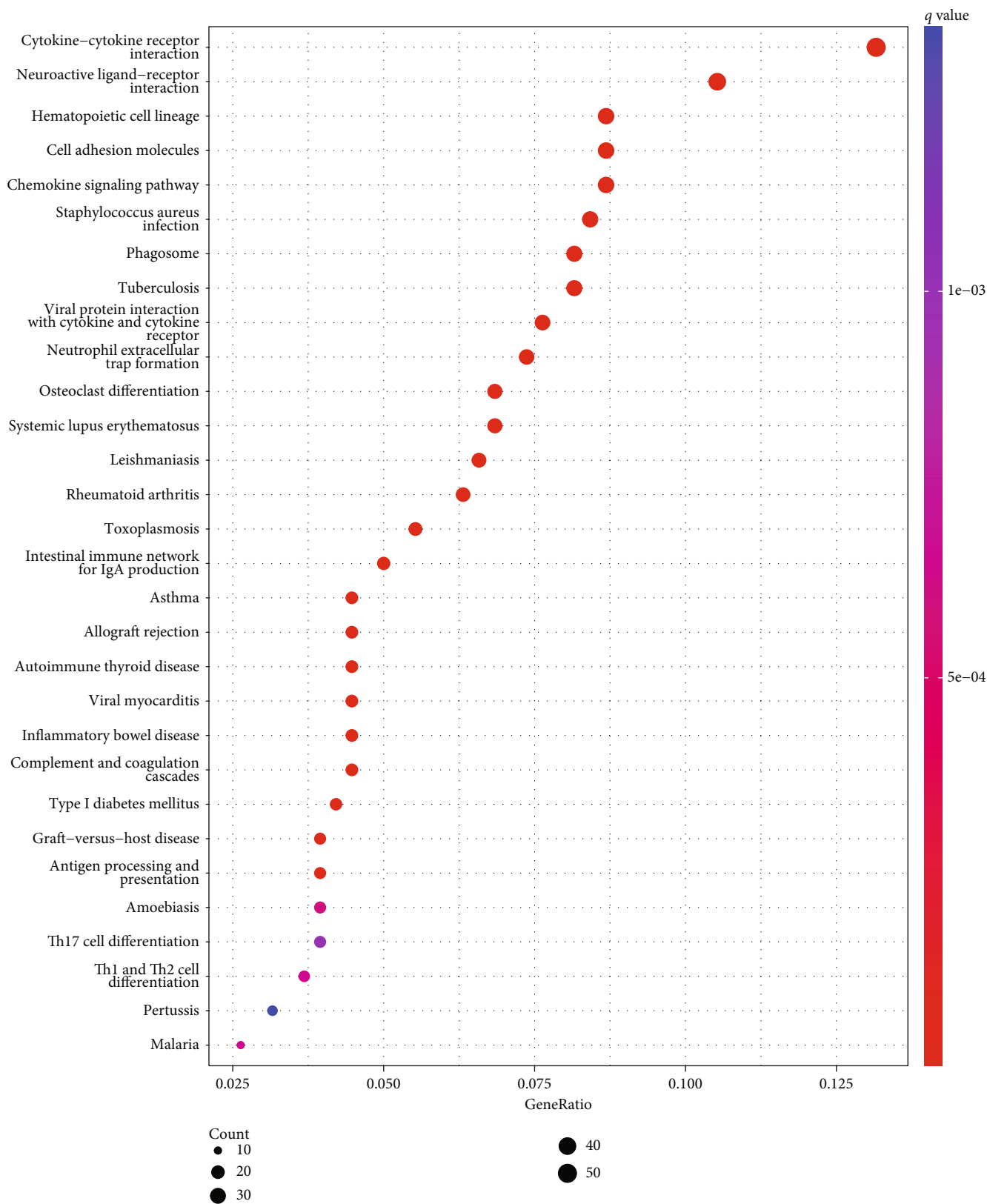Figure 5: Continued.

(c)
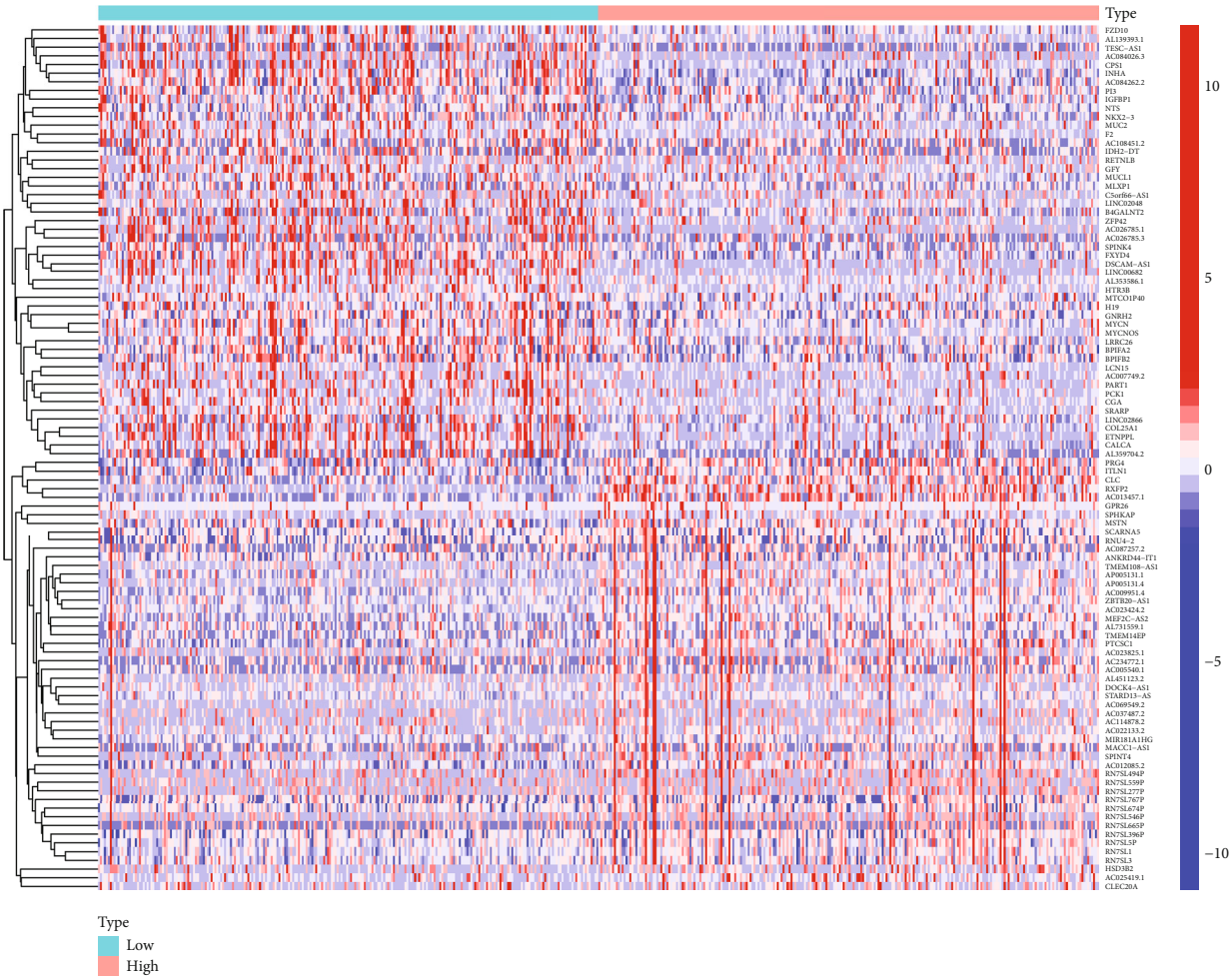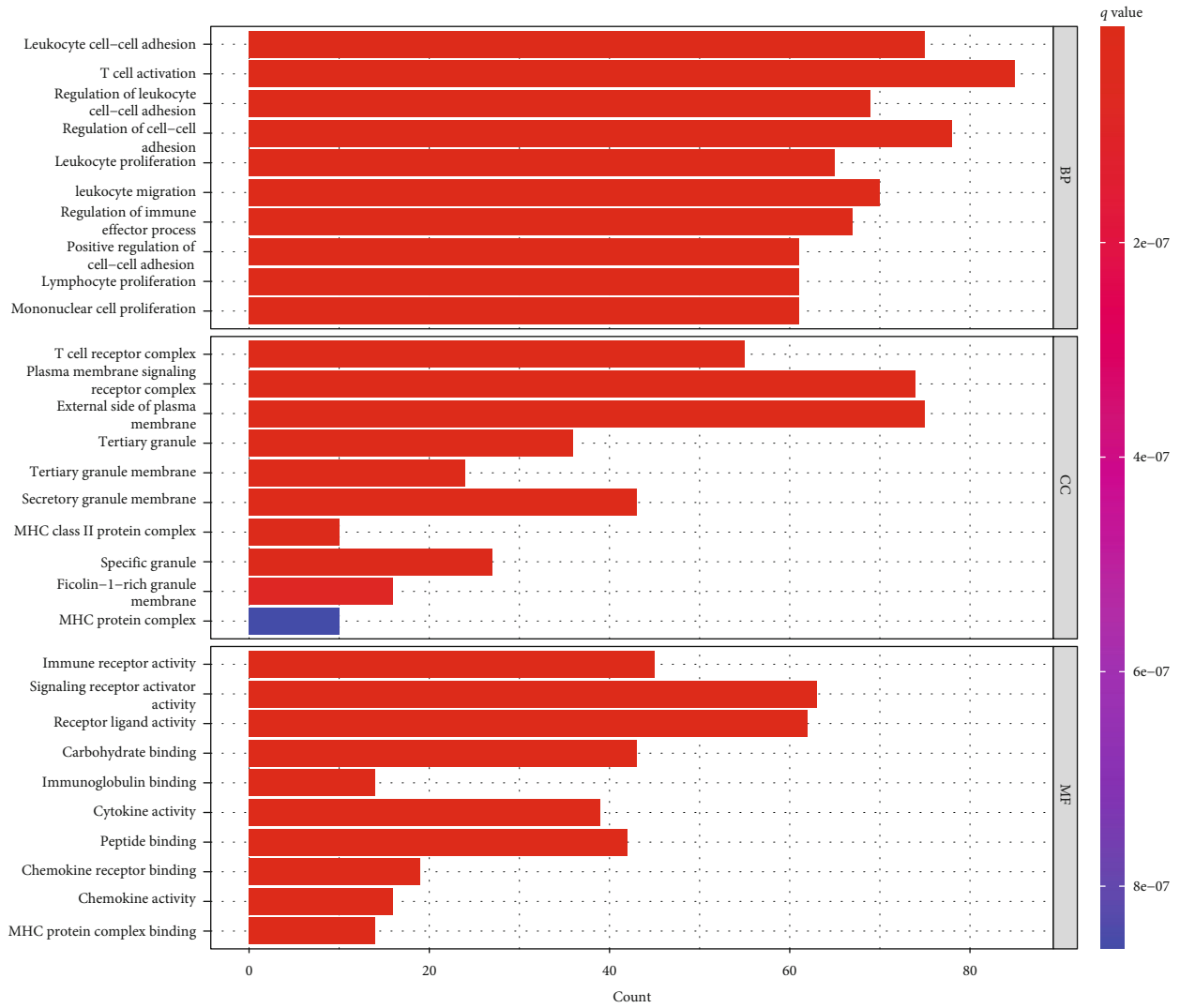
Figure 5: Continued.

(d)

FIGURE 5: Continued.

(e)

FIGURE 5: GO and KEGG pathway enrichment analyses for PTPRO-related genes. (a) Heatmap of differential genes (DEGs) with high and low PTPRO expression level in LUAD patients. (b, c) Top 10 results of the GO enrichment analysis based on PTPRO-related DEGs. (d, e) The plots of the KEGG pathway enrichment analysis for PTPRO-related DEGs.
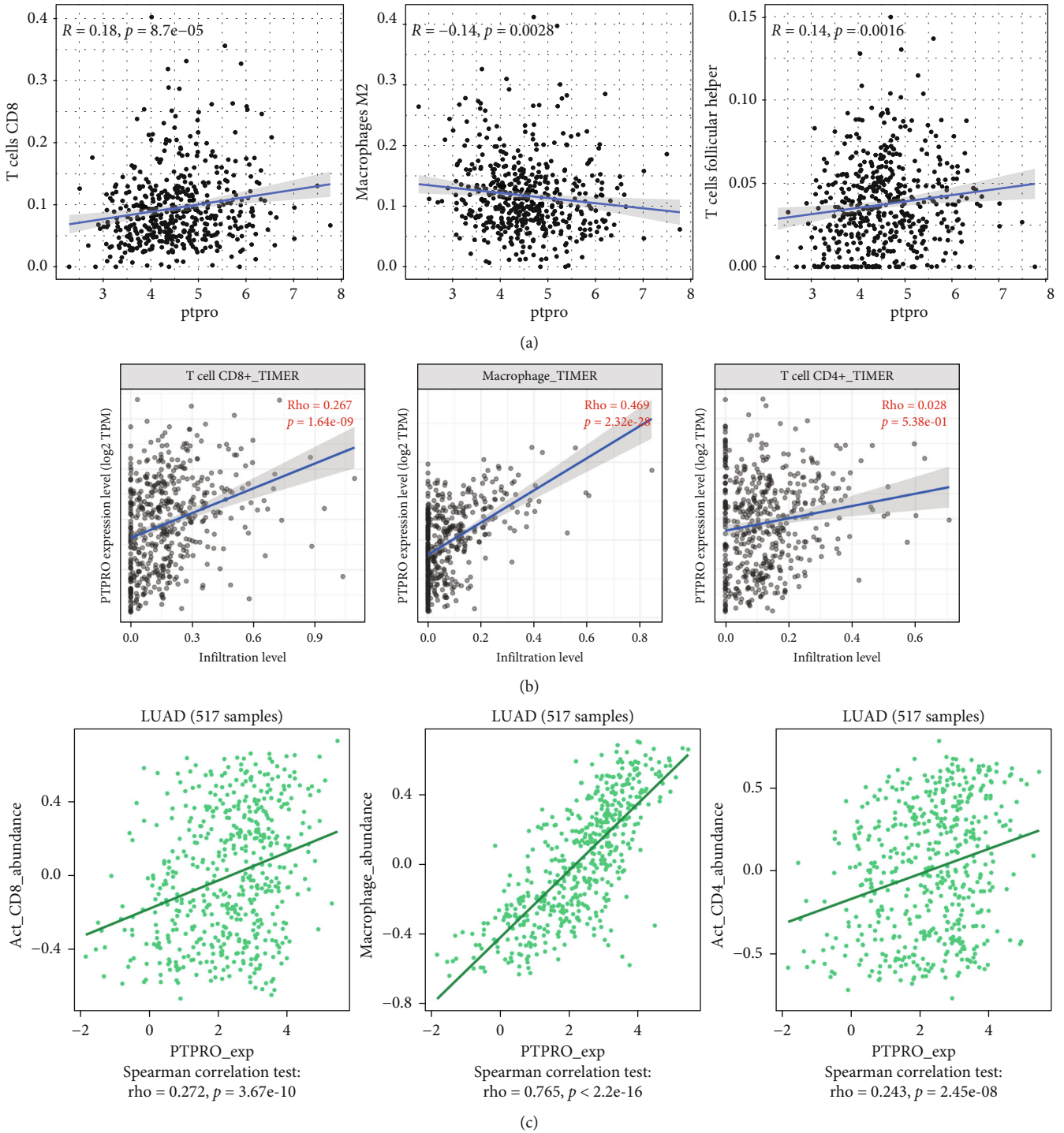
(a)

(b)

(c)

Figure 6: Correlation analysis of PTPRO expression level and immune cell infiltration. (a–c) TIMER, TISIDB, and CIBERSORT tools were used to analyze the correlation between the expression level of PTPRO and the infiltration of LUAD immune cells, respectively.

public databases and confirmed that the model has a good predictive ability for patient prognosis [32]. In the present study, we found that PTPRO was a protective factor for LUAD by univariate and multivariate analyses. Next, we constructed a nomogram based on PTPRO expression levels and multiple clinical characteristics, and the associated calibration curve showed that the nomogram had a good pre-

dictive ability for 1-, 3-, and 5-year survival, which indirectly confirmed PTPRO plays a vital role in LUAD.

In this study, we evaluated the relationship between the expression level of PTPRO in LUAD and immune cell subsets in the tumor through multiple databases, and the results showed that the expression level of PTPRO significantly affected the infiltration of various immune cells. It is well
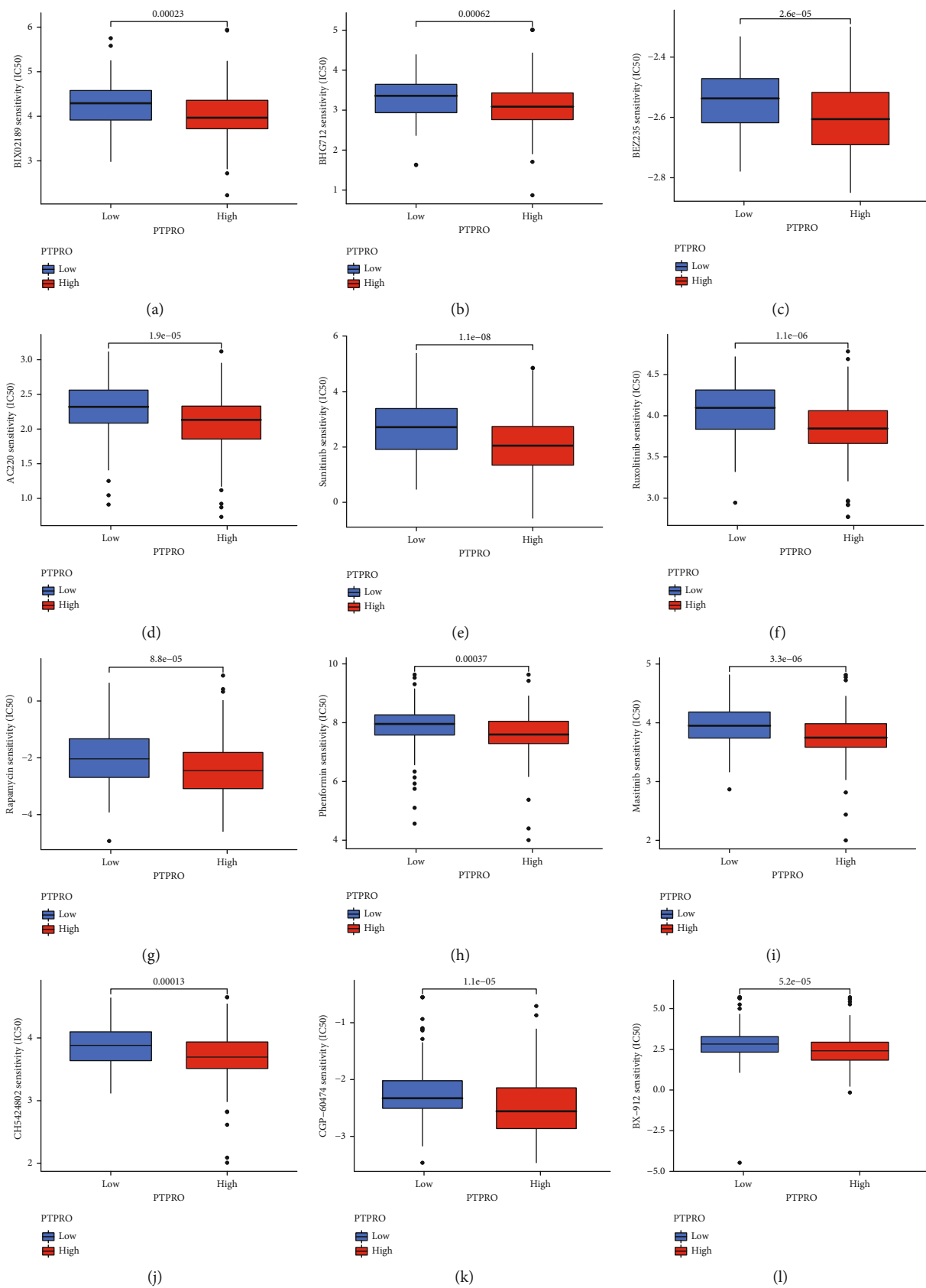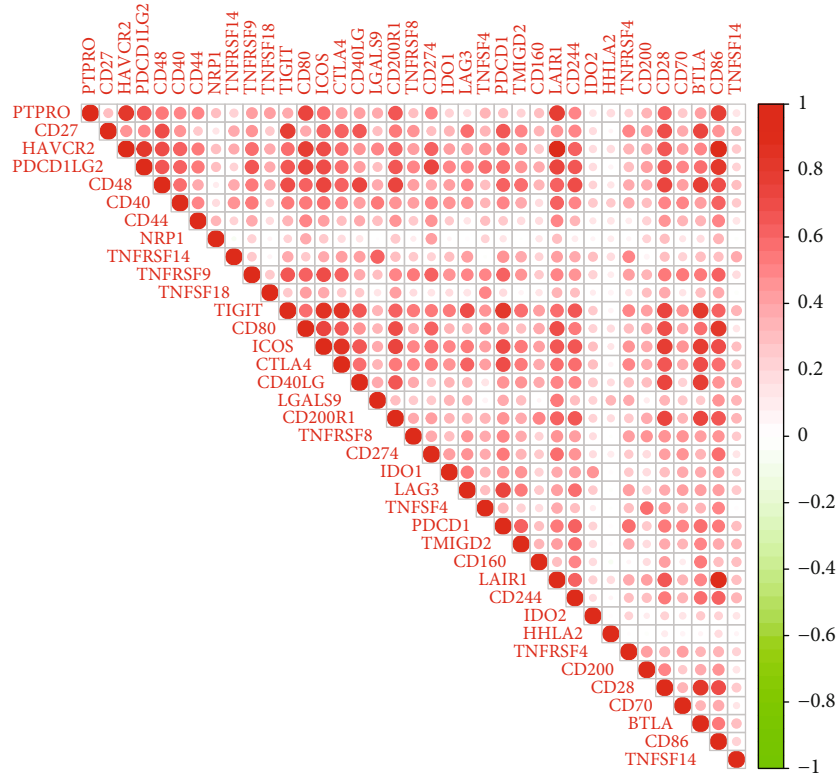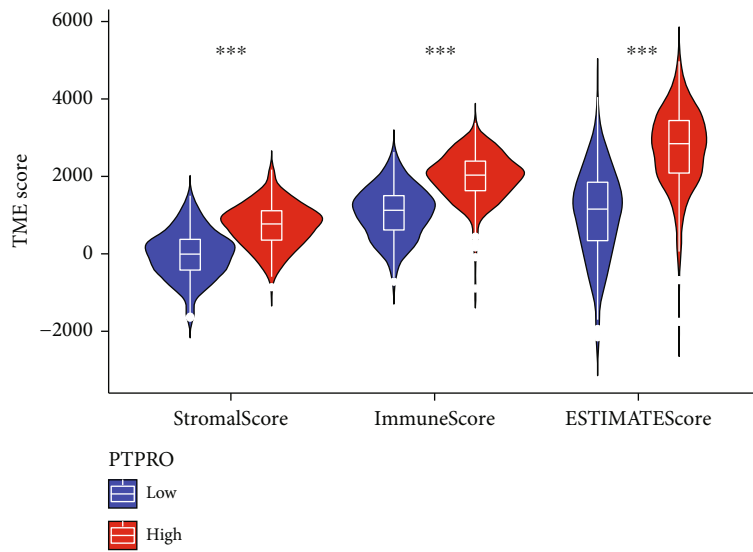
FIGURE 7: Prediction of sensitivity to chemotherapeutic drugs based on PTPRO expression levels. (a–l) Prediction of PTPRO expression levels in LUAD for sensitivity to multiple chemotherapeutics.

(a)

(b)

FIGURE 8: Continued.
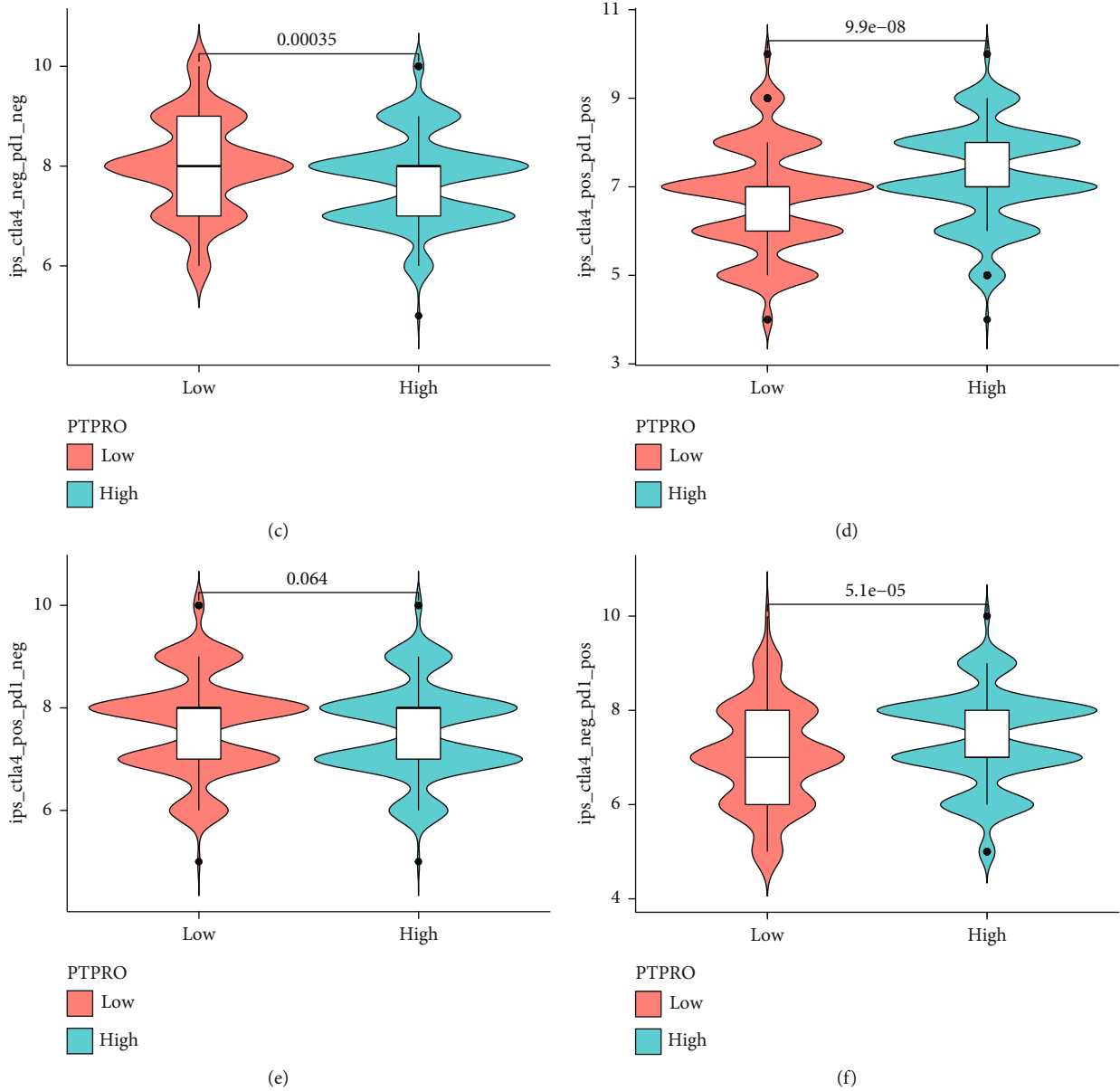
(c)

(d)

(e)

(f)

FIGURE 8: Prediction of sensitivity to immunotherapy based on PTPRO expression levels. (a) Correlation analysis of immune checkpoints and PTPRO expression level. (b) Immune, stromal, and ESTIMATE scores for high and low PTPRO expressions in LUAD. (c–f) The IPS scores between high and low expressions of the PTPRO groups when CTLA-4 or/and PD1 positive.

known that CD8^{+} cells and macrophages are key cell subsets that perform leukocyte immune function against tumors [31, 33]. A previous study demonstrated that PTPRO can improve TIM in renal cancer, and given the findings we obtained, PTPRO has a similar effect in LUAD [15]. It is worth noting that the results obtained in this study are derived from multiple databases and have high reliability.

Our study demonstrates the important role of PTPRO in LUAD; however, there are still many shortcomings. First, all data in this study were derived from public databases and have not been verified by relevant experiments. In addition, the specific mechanism by which PTPRO regulates the TIM of LUAD has not been fully elucidated in this study.

In conclusion, our results suggested PTPRO expression level is closely related to the prognosis and TIM of LUAD.

In LUAD, PTPRO is not only an independent prognostic predictor but also a potential immunotherapy target.

Data Availability

All data generated in this study are available from the corresponding author.

Ethical Approval

The study was conducted in accordance with the Declaration of Helsinki, and the protocol was approved by the Ethics Committee of 900 Hospital of Joint Logistics Support Force.

Conflicts of Interest

The authors declare that they have no conflicts of interest.

Authors' Contributions

Zhimin Lin, Jinjun Zhang, and Biqiong Liu contributed equally to this work.

Acknowledgments

Supplementary Materials

Supplementary Figure 1: calibration curves of Norman plots constructed based on PTPRO and clinical feature information. *(Supplementary Materials)*

References

[1] T. Houston, "Screening for lung cancer," *The Medical Clinics of North America*, vol. 104, no. 6, pp. 1037–1050, 2020.

[2] A. A. Thai, B. J. Solomon, L. V. Sequist, J. F. Gainor, and R. S. Heist, "Lung cancer," *The Lancet*, vol. 398, no. 10299, pp. 535–554, 2021.

[3] Q. Xu, Q. Cha, H. Qin, B. Liu, X. Wu, and J. Shi, "Identification of master regulators driving disease progression, relapse, and drug resistance in lung adenocarcinoma," *Frontiers in Bioinformatics*, vol. 2, p. 813960, 2022.

[4] C. Y. Jin, L. Du, A. H. Nuerlan, X. L. Wang, Y. W. Yang, and R. Guo, "High expression of RRM2 as an independent predictive factor of poor prognosis in patients with lung adenocarcinoma," *Aging*, vol. 13, no. 3, pp. 3518–3535, 2020.

[5] M. Santarpia, A. Aguilar, I. Chaib et al., "Non-small-cell lung cancer signaling pathways, metabolism, and PD-1/PD-L1 antibodies," *Cancers*, vol. 12, no. 6, p. 1475, 2020.

[6] M. Spella and G. T. Stathopoulos, "Immune resistance in lung adenocarcinoma," *Cancers*, vol. 13, no. 3, p. 384, 2021.

[7] V. Kurbatov, A. Balayev, A. Saffarzadeh et al., "Digital inference of immune microenvironment reveals low-risk subtype of early lung adenocarcinoma," *The Annals of Thoracic Surgery*, vol. 109, no. 2, pp. 343–349, 2020.

[8] X. Yang, Y. Shi, M. Li et al., "Identification and validation of an immune cell infiltrating score predicting survival in patients with lung adenocarcinoma," *Journal of Translational Medicine*, vol. 17, no. 1, p. 217, 2019.

[9] A. J. Gentles, A. M. Newman, C. L. Liu et al., "The prognostic landscape of genes and infiltrating immune cells across human cancers," *Nature Medicine*, vol. 21, no. 8, pp. 938–945, 2015.

[10] X. Liu, S. Wu, Y. Yang, M. Zhao, G. Zhu, and Z. Hou, "The prognostic landscape of tumor-infiltrating immune cell and immunomodulators in lung cancer," *Biomedicine & Pharmacotherapy*, vol. 95, pp. 55–61, 2017.

[11] Y. Li, A. Jia, H. Yang et al., "Protein tyrosine phosphatase PTPRO signaling couples metabolic states to control the development of granulocyte progenitor cells," *Journal of Immunology*, vol. 208, no. 6, pp. 1434–1444, 2022.

[12] W. Dai, W. Xiang, L. Han et al., "PTPRO represses colorectal cancer tumorigenesis and progression by reprogramming fatty acid metabolism," *Cancer Communications*, vol. 42, no. 9, pp. 848–867, 2022.

[13] Y. Chen and B. Sun, "PTPRO activates TLR4/NF-κB signaling to intensify lipopolysaccharide-induced pneumonia cell injury," *Allergologia et Immunopathologia*, vol. 50, no. 3, pp. 119–124, 2022.

[14] J. Hou, J. Xu, R. Jiang et al., "Estrogen-sensitive PTPRO expression represses hepatocellular carcinoma progression by control of STAT3," *Hepatology*, vol. 57, no. 2, pp. 678–688, 2013.

[15] J. Gan and H. Zhang, "PTPRO predicts patient prognosis and correlates with immune infiltrates in human clear cell renal cell carcinoma," *Translational Cancer Research*, vol. 9, pp. 4800–4810, 2020.

[16] X. Hou, J. Du, and H. Fang, "PTPRO is a therapeutic target and correlated with immune infiltrates in pancreatic cancer," *Cancer*, vol. 12, no. 24, pp. 7445–7453, 2021.

[17] T. Li, J. Fu, Z. Zeng et al., "TIMER2.0 for analysis of tumor-infiltrating immune cells," *Nucleic Acids Research*, vol. 48, no. W1, pp. W509–W514, 2020.

[18] B. Ru, C. N. Wong, Y. Tong et al., "TISIDB: an integrated repository portal for tumor-immune system interactions," *Bioinformatics*, vol. 35, no. 20, pp. 4200–4202, 2019.

[19] B. Chen, M. S. Khodadoust, C. L. Liu, A. M. Newman, and A. A. Alizadeh, "Profiling tumor infiltrating immune cells with CIBERSORT," *Methods in Molecular Biology*, vol. 1711, pp. 243–259, 2018.

[20] Z. Zhao, B. He, Q. Cai et al., "Combination of tumor mutation burden and immune infiltrates for the prognosis of lung adenocarcinoma," *International Immunopharmacology*, vol. 98, article 107807, 2021.

[21] G. D. Jones, W. S. Brandt, R. Shen et al., "A genomic-pathologic annotated risk model to predict recurrence in early-stage lung adenocarcinoma," *JAMA Surgery*, vol. 156, no. 2, article e205601, 2021.

[22] M. M. Kang, S. L. Shan, X. Y. Wen, H. S. Shan, and Z. J. Wang, "Tumor-suppression mechanisms of protein tyrosine phosphatase O and clinical applications," *Asian Pacific Journal of Cancer Prevention*, vol. 16, no. 15, pp. 6215–6223, 2015.

[23] A. Sica and V. Bronte, "Altered macrophage differentiation and immune dysfunction in tumor development," *The Journal of Clinical Investigation*, vol. 117, no. 5, pp. 1155–1166, 2007.

[24] B. Li, H. L. Chan, and P. Chen, "Immune checkpoint inhibitors: basics and challenges," *Current Medicinal Chemistry*, vol. 26, no. 17, pp. 3009–3025, 2019.

[25] J. Mei, Y. Xing, J. Lv et al., "Construction of an immune-related gene signature for prediction of prognosis in patients with cervical cancer," *International Immunopharmacology*, vol. 88, article 106882, 2020.

[26] R. L. Siegel, K. D. Miller, H. E. Fuchs, and A. Jemal, "Cancer statistics, 2022," *CA: a Cancer Journal for Clinicians*, vol. 72, no. 1, pp. 7–33, 2022.

[27] F. Wei, Y. Ge, W. Li, X. Wang, and B. Chen, "Role of endothelin receptor type B (EDNRB) in lung adenocarcinoma," *Thorac Cancer*, vol. 11, pp. 1885–1890, 2020.

[28] R. Ruiz-Cordero and W. P. Devine, "Targeted therapy and checkpoint immunotherapy in lung cancer," *Surgical Pathology Clinics*, vol. 13, no. 1, pp. 17–33, 2020.

[29] T. J. Tan, J. J. Chan, S. Kamis, and R. A. Dent, "What is the role of immunotherapy in breast cancer?," *Chinese Clinical Oncology*, vol. 7, no. 2, p. 13, 2018.

[30] K. Pilipow, A. Darwich, and A. Losurdo, "T-cell-based breast cancer immunotherapy," *Seminars in Cancer Biology*, vol. 72, pp. 90–101, 2021.

[31] S. L. Goff and D. N. Danforth, "The role of immune cells in breast tissue and immunotherapy for the treatment of breast cancer," *Clinical Breast Cancer*, vol. 21, no. 1, pp. e63–e73, 2021.

[32] Q. Guo, X. Zhang, T. Shen, and X. Wang, "Identification of autophagy- and ferroptosis-related lncRNAs functioned through immune-related pathways in head and neck squamous carcinoma," *Life*, vol. 11, no. 8, p. 835, 2021.

[33] B. Farhood, M. Najafi, and K. Mortezaee, "CD8$^+$ cytotoxic T lymphocytes in cancer immunotherapy: a review," *Journal of Cellular Physiology*, vol. 234, no. 6, pp. 8509–8521, 2019.